Victor E. Saouma
M. Amin Hariri-Ardebili

Aging, Shaking and Cracking of Infrastructures

Concrete Dams and Nuclear Structures

March 9, 2020

Springer Nature

To all those whose safety depends on the independent and rigorous application of sound science by regulatory agencies

Foreword

About 1.5 pages

Place, month year *First name Surname*

Preface

A major challenge confronting Structural Engineers in the 21st century is how to exploit modern computational techniques to assess the true safety of the infrastructure against the inevitable ravages of the second law of thermodynamics and the forces of nature: aging, shaking and cracking.

The need for advanced analysis is widely recognized in codes, guidelines, and bulletins. Yet, none of them is explicit enough on how to conduct such an advanced analysis, which would be nonlinear finite element for all practical purposes. This vagueness, coupled with the potential complexity of such an analysis and the lack of authoritative references, has discouraged the profession from embracing it.

As if complexity of nonlinear analyses was not enough, there has been much interest in probabilistic based safety prognosis of structures. Conveniently, this performance-driven assessment will ineluctably necessitate a nonlinear analysis framework.

While this self-contained book will ultimately focus its applications on two major types of structures, dams and nuclear reactors, the first four parts would also be of interest in the analysis of other structures.

The geometry of the structures addressed in this book appear to be quite simple: a trapezoidal or arch retaining water on one hand, or a cylinder capped by a dome on the other. But, in both cases, not only is the devil in the details, but any form of failure could be hugely consequential.

True seismic nonlinear analysis of dams or containment enclosure buildings (CEB) are already challenging enough. However, when their complexity is compounded by a relatively recently discovered aging mechanism (alkali silica reaction or ASR), and again when framed in a probabilistic context, this may become quite challenging.

Hence, this book is a first attempt to provide clear guidance on how to perform a comprehensive nonlinear analysis of concrete dams and CEB subjected to aging, shaking and cracking. It will first cast the mathematical formalism and engineering rigor with which such advanced analysis is to be conducted and much of this coverage is based on the authors' teaching, research and experience.

What this book is not about, it is not about the design of new structures, for those are code-driven processes driven by (simple) linear elastic analyses and not particularly

challenging. Instead, it is about how to perform a risk assessment of a dam or CEB subjected to extraordinary loads using advanced methods.

In carrying out this task, there lie two major dangers. First, there is a glaring absence of codes for the assessment of existing structures. This is particularly troublesome in light of the fact that the aging of our infrastructure is widely recognized. The second is the danger of entrusting engineers, reared in the design of new structures, with the safety assessment of existing ones. Those two tasks require two very different skill sets. Simply put the design of a new structure may be accomplished by a good Professional Engineer (PE). However the safety assessment, at a minimum, would necessitate engineers (not necessarily a PE) with graduate studies (and possibly some with a Ph.D. in some circumstances).

This dichotomy was glaring when the first author recently evaluated the technical basis for a license amendment request for the life extension of a major nuclear reactor suffering from ASR. The regulating agency evaluation was shockingly simplistic and ill informed, and yet the license for continued operation for an additional 30 years was approved. Indeed, what happened is that the safety assessment was entrusted to code-based engineers who may have failed to grasp the full complexity of a safety assessment.

Hence, this book is essentially a self-contained one and is organized in seven parts, starting from basic mechanics, and then gradually leading to a complex case study.

The first part, *Fundamentals*, provide the reader, lacking exposure to some of the graduate courses needed to fully understand the subsequent coverage, with the theoretical underpinning needed. Coverage is detailed, possibly too theoretical at times, but certainly comprehensive.

The second part, *Damage*, addresses the types of damages that can affect concrete structures, such as fracture, ASR, and chloride ingress.

The third part is an introduction to *Finite Elements*. It covers not only the formulation of the method, but also nonlinear finite element techniques, and how the method can be used to model fracture.

Hence, it is not until the fourth part that *Engineering Models* are covered. This is the last intermediary stage before applications can be presented.

Parts five and six cover *Applications; Dams* and *Applications; Nuclear* with numerous examples based on models previously presented.

Finally, the last part covers the impact of ASR on *Massive Reinforced Concrete Structures*, and a detailed *Case study of Seabrook* station, the first nuclear power plant in the US reported to have ASR, relying on extensive public documents.

The book greatly borrows from lecture notes (especially the first parts), and from journal papers (especially the last part). Its structure is very hierarchical (task greatly facilitated by LaTeX), and the reader should find it easy to either "zoom in" or "zoom out" from a particular topic.

It is hoped that this exhaustive coverage will inspire young researchers and encourage regulators not to be afraid of embracing modern tools to fully and convincingly ensure infrastructure safety. The authors also hope that the case study provided in Chapter 35 will stimulate government regulators to consider how advanced scientific methods can be applied to current industrial problems to ensure the safety and serviceability

of ASR-affected facilities for which they have ultimate responsibility. **Victor E. Saouma** **M. Amin Hariri-Ardebili**
Boulder, CO 2020

Acknowledgments

The first author would like to acknowledge his major research sponsors over the years, in particular, the Electric Power Research Institute (EPRI), the Tokyo Electric Power Company (TEPCO), the US Nuclear Regulatory Commission (NRC), the US Bureau of Reclamation (BOR) and the Oak Ridge National Laboratory (ORNL) that made this book possible.

Such work would not have been possible without the help of a few highly talented and dedicated students: Jan Cervenka, Eric Hansen, Gary Haussmann, Chandra Kishen, Wiwat Puatsananon, and Ron Reich; as well as the support of Daniel Rypl for the countless complex finite element meshes used in this book.

Finally, the first author would like to acknowledge the support of the College of Engineering at the University of Colorado for having provided him a one semester fellowship to complete this manuscript.

Contents

I Fundamentals

1 Review of Solid Mechanics; Vector Fields 3
1.1 Introduction 3
1.1.1 Indicial Notation 3
1.1.1.1 Notation 5
1.1.2 Tensors 5
1.1.2.1 Operations 6
1.1.2.2 Rotation of Axes 7
1.1.2.3 Tensor Transformation 8
1.1.2.4 Principal Values of Symmetric Second Order Tensors 9
1.1.3 Physical interpretation of Stress Invariants 10
1.1.4 Review Integral Equations 11
1.2 Vector Fields; Solid Mechanics 13
1.2.1 Forces 13
1.2.2 Cauchy's Stress Tensor 14
1.2.3 Hydrostatic and Deviatoric Stress Tensors 15
1.2.4 Geometric Representation of Stress States 16
1.3 Kinematics 16
1.3.1 Position and Displacement 16
1.3.2 Strains 18
1.4 Fundamental Laws of Continuum Mechanics 19
1.4.1 Conservation of Mass; Continuity Equation 21
1.4.2 Conservation of Momentum; Equation of Motion 21
1.4.3 Conservation of Energy; First Principle of Thermodynamics 22
1.4.4 Constitutive Equations 25
1.4.4.1 General 3D 25
1.4.4.2 Transversly Isotropic Case 27
1.4.4.3 Special 2D Cases 27
1.4.4.4 Pore Pressures 28

1.5 Boundary Conditions 28

2 Review of Scalar Field Diffusion Problems 31
2.1 Introduction 31
2.2 Derivation of the Diffusion Problem 32
2.2.1 Simplified; 2D 32
2.2.2 Generalized Derivation; 3D 35
2.3 Boundary Conditions for Exposed Concrete 37
2.3.1 Essential; Temperature 38
2.3.1.1 Special Considerations for Dams 38
2.3.1.1.1 Air Temperature 38
2.3.1.1.2 Reservoir Temperature 39
2.3.2 Natural; Convection 40
2.3.2.1 Special Considerations for Exposed Concrete Surfaces 40
2.3.3 Radiation 41
2.3.3.1 Irradiation; Stefan-Boltzman 41
2.3.3.2 Solar Radiation; Approximation 41
2.4 Summary 44
2.5 Summary and Tonti Diagrams 44

3 Plasticity 49
3.1 Introduction 49
3.2 Plastic Yield Conditions 49
3.2.1 Hydrostatic Pressure Independent Models 50
3.2.2 Hydrostatic Pressure Dependent Models 51
3.3 Laboratory Observations 53
3.3.1 Metals 53
3.3.2 Concrete 54
3.4 Microscopic Failures 55
3.4.1 Chemical Bonds 55
3.4.2 Ductile and Brittle Failures 55
3.4.3 Dislocation 56
3.5 Fundamentals of Plasticity 57
3.5.1 Introduction 57
3.5.2 Tangent Elastic Modulus 58
3.5.2.1 Generalized Derivation 58
3.5.2.1.1 Yield Function; Isotropic Hardening Model 58
3.5.2.1.2 Flow Rule 59
3.5.2.1.2.1 Kuhn-Tucker Conditions . 60
3.5.2.1.3 Consistency Condition 60
3.5.2.1.4 Tangent Modulus 60
3.5.2.2 Tangent Modulus; Engineering 61

4 Fracture Mechanics 63
4.1 Introduction 63
4.2 Stress Concentrations in Hollowed Plates under Uniform Traction . . 63
4.3 Linear Elastic Fracture Mechanics 66
4.3.1 Order of Stress Singularity 66
4.3.2 Stress Intensity Factors 66
4.3.3 Design Philosophy Based on Linear Elastic Fracture Mechanics 68
4.3.4 Stress Intensity Factors 69
4.3.5 Fracture Properties of Materials 71
4.3.6 Mixed Mode Crack Propagation 72
4.3.7 Some Practical Considerations 74
4.3.7.1 Leak Before Break (LBB) Paradigm 74
4.3.7.2 Damage Tolerance Assessment 75
4.3.7.2.1 Inspection 75
4.3.7.2.2 Fracture Control Plan 77
4.4 Thermodynamics Approach 78
4.5 Elasto-Plastic Fracture: Metals 79
4.5.1 Plastic Zone Size 79
4.5.2 J Integral 81
4.5.2.1 Proof of Path Independence 81
4.5.2.2 Nonlinear Elastic Energy Release Rate 83
4.5.3 Nonlinear Energy Release Rate 85
4.5.4 J_1 and J_2 Generalization. 86
4.6 Fatigue Crack Propagation 88
4.6.1 Variable Amplitude Loading with Load Interaction 88

5 Creep 91
5.1 Time-dependent Inelastic Strains 91
5.2 Origin of Inelastic Behavior 92
5.3 Classification of Inelastic Strains 92
5.3.1 Hygrothermal Strain 93
5.3.2 Mechanical Strain 94
5.4 Basic Expressions for Inelastic Strains 94
5.4.1 Empirical Expressions 94
5.4.2 Theoretically-based Rheological Expressions 95
5.4.3 Creep Coefficient 96
5.5 Creep and Shrinkage Prediction Models 96
5.5.1 fib Model Code 2010 97
5.5.2 B3 Model 99
5.5.3 Age-Adjusted Effective Modulus 101
5.6 Effects of Creep on Structures 102
5.6.1 Harmful Effects of Creep 102
5.6.2 Effects of Prestressed Structures 102
5.6.3 Mass Structures 102

6 Seismology and Seismicity 103
6.1 Causes and Consequences of Earthquake 103
6.1.1 Earth's Layers 103
6.1.2 Natural Earthquakes 103
6.1.3 Induced Earthquakes 104
6.1.4 Earthquake Damage 105
6.2 Theory of Plate Tectonics 105
6.3 Reid's Elastic Rebound Theory 106
6.4 Fault Mechanisms 107
6.5 Seismic Waves 108
6.5.1 Terminology 108
6.5.2 Equation of Motion 109
6.5.3 Location of Earthquake 111
6.6 Shaking Intensity 111
6.7 Earthquake Magnitude 113
6.7.1 Classification 113
6.7.2 Energy Released 115
6.8 Source-to-Site Effects 116
6.8.1 Directional Effects 116
6.8.2 Site Effects 117
6.8.3 Dispersion and Incoherence Effects 117

7 Transient Dynamic Analysis 119
7.1 Introduction 119
7.2 Variational Formulation 119
7.2.1 Explicit Time Integration; Central Difference 121
7.2.2 Implicit Time Integration 122
7.2.2.1 Linear Case 122
7.2.2.2 Nonlinear Case 123
7.3 Time Discretization 123
7.3.1 Explicit Time Integration 124
7.3.1.1 Linear Systems 124
7.3.1.2 Nonlinear Systems 128
7.3.2 Implicit Case 128
7.3.2.1 Newmark Method; Forward Difference 128
7.3.2.2 Hughes α Method 130
7.4 Free Vibration 132

8 Probability and Statistics 135
8.1 Introduction to Probability 135
8.1.1 Deterministic *vs.* Probabilistic 135
8.1.2 Fundamentals 135
8.1.3 Conditional Probability 137
8.1.4 Discrete Random Variables 137
8.1.5 Continuous Random Variables 138

8.1.6 Cumulative Distribution Function . . . 139
8.1.7 Expectations . . . 140
8.1.8 Statistics of Discrete Variables . . . 141
8.2 Univariate Distributions . . . 143
8.2.1 Uniform distribution . . . 143
8.2.2 Normal distribution . . . 143
8.2.3 Lognormal distribution . . . 144
8.2.4 Weibull distribution . . . 145
8.2.5 Gumbel distribution . . . 146
8.3 Multivariate Distributions . . . 146
8.3.1 Bivariate distribution . . . 147
8.3.2 Multivariate normal distribution . . . 148
8.3.3 Bivariate normal distribution . . . 148

II Damage

9 Fracture Mechanics of Concrete . . . 153
9.1 Macro Cracks . . . 153
9.1.1 Experimental Observations . . . 153
9.1.2 σ-COD Diagram, Hillerborg's Model . . . 154
9.1.3 Fracture Energies . . . 156
9.1.3.1 G_F . . . 156
9.1.3.2 G_f . . . 156
9.1.4 Impact of Hillerborg's Model on Strength . . . 157
9.1.5 Localization . . . 160
9.1.6 Size Effect . . . 160
9.1.6.1 Bažant's Original Derivation . . . 160
9.1.6.2 Saouma's Derivation . . . 163
9.2 Micro Cracks . . . 171
9.2.1 Theoretical Considerations . . . 171
9.2.1.1 Strength . . . 171
9.2.1.2 Compliance . . . 171
9.2.1.2.1 Experimental Evidence . . . 171
9.2.1.2.2 Analytical Considerations . . . 172
9.2.2 Micro Cracks in Concrete . . . 174
9.2.2.1 Conjectures . . . 174
9.2.2.2 Physical Evidences . . . 174
9.2.3 Creep Fracture . . . 177
9.2.3.1 Load Carrying Capacity . . . 177
9.2.3.2 Fracture Energy . . . 178
9.2.4 Coalescence of Micro-Cracks . . . 180

10 Chloride, Carbonation and Corrosion . . . 183
10.1 Introduction . . . 183
10.2 Chloride Diffusion Analysis in Concrete . . . 185
10.2.1 Fick's Laws . . . 186
10.2.2 Chloride Diffusion in Concrete . . . 187
10.2.2.1 Binding Capacity of Concrete . . . 188
10.2.2.2 Chloride Diffusivity of Concrete . . . 190
10.2.2.2.1 f_1, Effect of Aggregates . . . 190
10.2.2.2.2 f_2, Effect of w/c and curing time . . . 191
10.2.2.2.3 f_3, Effect of Temperature . . . 191
10.2.2.2.4 f_4, Effect of Pore Relative Humidity . . . 191
10.2.2.2.5 f_5, Effect of Chloride Concentration . . . 192
10.2.3 Final Algorithm for Chloride Diffusion . . . 192
10.3 Carbonation . . . 192
10.3.1 Physical Description . . . 192
10.3.1.1 Effects of carbonation on concrete durability . . . 194
10.3.1.2 Factors affecting the carbonation rate . . . 194
10.3.1.2.1 Environmental conditions . . . 194
10.3.1.2.2 Compositions of concrete . . . 195
10.3.2 Governing Differential Equation . . . 196
10.3.2.1 Carbonation Process . . . 196
10.3.2.2 Carbon dioxide diffusion . . . 197
10.4 Corrosion . . . 198
10.4.1 Passivity . . . 199
10.4.1.1 Reinforcement . . . 199
10.4.1.2 Passivity and pH . . . 199
10.4.2 Corrosion Process . . . 199
10.4.2.1 Anodes and Cathodes . . . 200
10.4.2.2 Corrosion product . . . 201
10.5 Coupling . . . 202

11 Alkali Aggregate Reaction; Theory . . . 205
11.1 Introduction . . . 205
11.2 Model . . . 205
11.2.1 Premises . . . 205
11.3 Kinetics . . . 206
11.3.1 Volumetric Expansion . . . 208
11.3.2 AAR Strain Redistribution . . . 210
11.3.3 Degradation . . . 214
11.4 Bureau of Reclamation Study . . . 215
11.4.0.1 Effect of Confinement . . . 216
11.4.1 Compressive Strength . . . 216
11.4.2 Tensile Strength . . . 216
11.4.3 Case Studies . . . 217
11.5 AAR Properties through System Identification . . . 219

11.5.1 Algorithm . . . 221
11.6 Prediction of Past & Future Expansion . . . 222

III Finite Element

12 Science and Art of Finite Element Modeling . . . 227
12.1 Tasks . . . 228
12.1.1 Problem Definition . . . 228
12.1.2 Mathematical Model . . . 229
12.1.3 Finite Element Analyses . . . 229
12.1.4 Final Evaluation . . . 230
12.2 Key Considerations . . . 230
12.2.1 Modeling . . . 230
12.2.2 Loads and Boundary Conditions . . . 231
12.2.3 Material Properties . . . 232
12.2.4 Software Selection . . . 233
12.2.5 Concepts of Model Verification and Validation . . . 234
12.2.6 Expert Selection . . . 235
12.2.7 Finite Element Mesh/Analysis Verification . . . 235
12.2.8 Singularities . . . 236

13 Finite Elements . . . 237
13.1 Principle of Virtual Work (Displacement) . . . 237
13.2 Element Stiffness Matrix Formulation . . . 240
13.3 Isoparametric Elements . . . 242
13.3.1 Element Formulation . . . 244
13.3.1.1 Bar Element . . . 244
13.3.1.2 Linear Quadrilateral (Q4) . . . 247
13.3.1.3 Quadratic Quadrilateral (Q8) . . . 252
13.3.1.4 Lagrangian Quadrilateral (Q9) . . . 253
13.3.2 Numerical Integration . . . 255
13.3.2.1 Gauss-Legendre Quadrature for $n = 2$ . . . 256
13.3.3 Stress Recovery; Nodal Stresses . . . 257
13.3.4 Nodal Equivalent Loads . . . 259
13.3.4.1 Gravity Load . . . 259
13.3.4.2 Traction Load . . . 260
13.3.4.3 Initial Strains/Stresses; Thermal Load . . . 262
13.4 Finite Element Formulation of the Heat Equation . . . 262
13.4.1 Derivation of the Weak Form . . . 262
13.4.2 Finite Element Discretization . . . 264
13.4.2.1 No Convection . . . 264
13.4.2.2 Convection . . . 265
13.5 Equilibrium and Compatibility in the Solution . . . 266
13.6 Convergence . . . 266

14 Nonlinear Finite Element Analysis . . . 269
14.1 Introduction . . . 269
14.2 Types of Non-Linearities . . . 270
14.3 Incremental Load/Displacement . . . 271
14.4 Numerical Integration . . . 272
14.4.1 Explicit . . . 272
14.4.2 Implicit . . . 274
14.4.2.1 Linearization . . . 274
14.4.2.2 Solution Strategies . . . 275
14.4.2.3 Quasi-Newton Numerical Solution . . . 276
14.4.2.3.1 Multi-dimensional . . . 277
14.4.2.3.2 Convergence and Error Estimate . . . 279
14.4.2.3.3 Final Remarks . . . 280
14.4.2.3.4 Variations . . . 280
14.5 Relationship to Structural Mechanics; Implicit . . . 280
14.6 Integration Methods . . . 281
14.6.1 Newton-Raphson . . . 283
14.6.1.1 Newton-Raphson/Tangent Stiffness Method . . . 284
14.6.1.2 Modified Newton-Raphson . . . 285
14.6.1.3 Secant Newton . . . 286
14.6.2 Convergence Criteria . . . 287
14.7 Modeling Reinforcement . . . 288
14.7.1 Smeared Reinforcement . . . 288
14.7.2 Embedded Reinforcement . . . 289
14.7.3 Discrete Reinforcement . . . 291
14.8 Modeling ASR . . . 291

15 Fracture Mechanics Analysis with Finite Elements . . . 293
15.1 Linear Elastic Fracture Mechanics . . . 293
15.1.1 Quarter Point Singular Elements . . . 293
15.1.2 Review of Isoparametric Finite Elements . . . 294
15.1.3 How to Distort the Element to Model the Singularity . . . 295
15.1.4 Order of Singularity . . . 297
15.1.5 Stress Intensity Factors Extraction . . . 298
15.2 J Integral . . . 299
15.2.1 Equivalent Domain Integral (EDI) Method . . . 303
15.2.2 Energy Release Rate J . . . 304
15.2.2.1 2D case . . . 304
15.2.2.2 3D Generalization . . . 307
15.2.3 Extraction of SIF . . . 309
15.2.3.1 J Components . . . 309
15.2.3.2 σ and u Decomposition . . . 309
15.3 Fictitious Crack Model for concrete . . . 310
15.3.1 Premises . . . 310
15.3.2 Failure Function . . . 311

15.3.3 Evolution of the Failure Function . . . 312
15.3.4 Stiffness Degradation . . . 314

IV Engineering Models

16 Soil Structure Interaction . . . 319
16.1 Rocking . . . 319
16.1.1 Rock Free-Field . . . 320
16.1.2 Concrete-Rock . . . 321
16.2 Deconvolution . . . 321
16.2.1 Preliminary Considerations . . . 322
16.2.2 Procedure . . . 324
16.2.2.1 One-Dimensional . . . 324
16.2.2.2 Three-Dimensional . . . 325
16.2.2.3 Simplification . . . 325
16.3 Soil Structure Interaction . . . 326
16.3.1 Wave Equation . . . 326
16.3.2 Lysmer Model . . . 328
16.3.3 Miura-Saouma Model . . . 329
16.3.3.1 Theory . . . 330
16.3.3.2 Finite Element Implementation . . . 335
16.3.3.3 Finite Element Implementation . . . 338
16.3.4 Validation Problems . . . 340
16.4 Modeling Aspects . . . 341
16.4.1 Inhibition of Lateral Rigid Body Motion . . . 342
16.4.2 Alternative Boundary Conditions for Dynamic Analysis . . . 342

17 Fluid Structure Interactions . . . 345
17.1 Uplift . . . 345
17.1.1 Models for Rigid Body Equilibrium Analysis . . . 346
17.1.2 Finite Element Modeling of Uplift . . . 347
17.1.3 Steady State Seepage Analysis . . . 349
17.1.4 Dynamic Uplift . . . 351
17.2 Hydro-Dynamic Pressures . . . 351
17.2.1 Lumped Mass Models . . . 352
17.2.1.1 Westergaard . . . 352
17.2.1.2 Zangar . . . 354
17.2.2 Continuum Model I: Displacement Based Formulation . . . 355
17.2.3 Continuum Model II: Pressure Based Formulation . . . 357
17.2.3.1 Governing Equations . . . 357
17.2.3.1.1 Boundary Condition at Fluid-Solid Interface . . . 357
17.2.3.1.2 Boundary Condition at Free Surface . . . 358
17.2.3.1.3 Discretized Equation of Fluid Domain . 358
17.2.3.1.4 Coupling Matrix . . . 358

17.2.3.1.5 Damping within the Fluid Domain 359
17.2.3.2 Coupled Equations of the Solid and Fluid 359
17.2.3.2.1 Time-Stepping Scheme of the Coupled Equations 359
17.2.3.3 Dam-Reservoir Interaction Boundary Conditions .. 361
17.2.3.4 Simplified Crack-Pressure Interaction 362

18 Uncertainty Quantification 365
18.1 Uncertainty Quantification 365
18.1.1 Classification of Random Variables 365
18.1.2 Sensitivity Analysis 366
18.1.3 Uncertainty Analysis 367
18.1.4 Sampling Techniques 367
18.1.4.1 Limited Number of Simulations 368
18.1.4.1.1 Taylor's Series-Finite Difference Estimation 368
18.1.4.1.2 Point Estimate Method 369
18.1.4.2 Variable Number of Simulations 369
18.1.5 Correlation of Random Variables 369
18.2 Terminology of Risk-Based Assessment 371
18.2.1 Reliability 371
18.2.1.1 Time-invariant Case 373
18.2.1.2 Time-variant Case 375
18.2.2 Hazard 376
18.2.3 Risk 379
18.2.4 Fragility 381
18.2.5 Vulnerability 383
18.2.6 Resilience 384
18.2.7 Sustainability 387
18.3 Estimation of Failure Probability 389
18.3.1 Direct Integration 389
18.3.2 First order Reliability Method (FORM) 389
18.3.3 Second order Reliability Method (SORM) 390
18.3.4 Crude Monte Carlo Simulation 391
18.3.5 Latin Hypercube Sampling 391
18.3.6 Importance Sampling 392

19 Probabilistic and Random FEM 393
19.1 Uncertainty Propagation 393
19.1.1 Fundamentals 393
19.1.2 Crude Monte Carlo Simulation 394
19.1.3 Latin Hypercube Sampling (LHS) 395
19.1.4 Halton Sequence 395
19.1.5 Sobol Sequence 396
19.1.6 Comparison of Sampling Techniques 397

19.2 Random Response Spectrum Method (RRSM) 398
19.3 Random Fields 409
19.3.1 Random Fields Classifications 409
19.3.2 Random Fields Generators 410
19.3.3 Efficient Random Field Generator 411
19.3.4 FE Implementation of RF 414

20 Metamodeling and Machine Learning 417
20.1 Introduction 417
20.2 Concept of Metamodeling 418
20.3 Design of Experiment 419
20.3.1 Randomized Complete Block Design (RCBD) 420
20.3.2 Latin Square Experimental Design (LSED) 421
20.3.3 Higher Order LSED 421
20.3.4 Full Factorial Design (FFD) 421
20.3.5 Fractional Factorial Design (FrFD) 422
20.3.6 Star Experimental Design (SED) 422
20.3.7 Central Composite Design (CCD) 422
20.3.8 Box-Behnken Experimental Design (BBED) 423
20.3.9 Plackett-Burman Experimental Design (PBED) 423
20.3.10 Taguchi Experimental Design (TED) 424
20.3.11 Comparison of DOE Techniques 424
20.4 Response Surface Method 425
20.4.1 Polynomial Metamodel 425
20.4.2 Goodness-of-fit 426
20.5 Polynomial Chaos Expansions 426
20.5.1 Constructing the Polynomial Basis 426
20.5.2 Computing the Expansion Coefficients 428
20.6 Concept of Machine Learning 430
20.6.1 Hints on Machine Learning Modeling 430
20.7 Classification Techniques 434
20.7.1 K-Nearest Neighbor 435
20.7.2 Support Vector Machine 436
20.7.3 Naive Bayes Classifier 438
20.8 Regression Techniques 439
20.8.1 Support Vector Regression 439
20.8.2 Decision Tree Regression 440
20.8.3 Random Forest 441
20.8.4 Tree Bagging 441
20.8.5 Extreme Gradient Boosting 442
20.8.6 Artificial Neural Networks 442
20.8.7 Extreme Learning Machine 443
20.8.8 Gaussian Process Regression 444
20.8.9 Multi Adaptive Regression Splines 444

21 Performance Based Earthquake Engineering 445
21.1 Basic Definitions 445
21.1.1 Performance Based Engineering (PBE) 445
21.1.2 Performance Based Earthquake Engineering (PBEE) 446
21.1.3 Performance Based Seismic Design (PBSD) 446
21.1.4 Performance Based Assessment (PBA) 446
21.2 PBEE Predecessors 446
21.2.1 ATC-13 (1985) and ATC-14 (1987) 447
21.2.2 SEAOC Vision 2000 (1995) 447
21.2.3 ATC-40 (1996) 447
21.2.4 FEMA 273 (1997) and FEMA 274 (1997) 447
21.2.5 FEMA 356 (2000) 448
21.2.6 Global Framework for PBEE 448
21.3 First Generation of PBEE 449
21.4 Second Generation of PBEE 451
21.4.1 Intensity-Based Performance Assessments (IBPA) 453
21.4.2 Scenario-Based Performance Assessments (SBPA) 454
21.4.3 Time Based Performance Assessments (TBPA) 454

22 Ground Motion Intensity Measures 455
22.1 Ground Motion Records 455
22.1.1 Sources 455
22.1.2 Time Histories 455
22.2 Frequency Content Parameters 456
22.2.1 Fourier Spectra 456
22.2.2 Power Spectral Density Function 458
22.3 Response Spectrum 458
22.3.1 Elastic Response Spectra 458
22.3.2 Pseudo Response Spectra 459
22.3.3 Damping Effects 460
22.4 Ground Motion Duration 460
22.4.1 Fundamentals 460
22.4.2 Classification 461
22.5 Time-Dependent IM Functions 462
22.6 Ground Motion IMs 463
22.6.1 Category I: Unscalable IMs 463
22.6.2 Category II: Ground Motion Dependent Scalar IMs 463
22.6.3 Category III: Ground Motion Dependent Compound IMs . . . 465
22.6.4 Category IV: Structure-Independent Spectral IMs 467
22.6.5 Category V: Structure-Dependent Spectral IMs 468
22.6.6 Category VI: Vector-Based IMs 469
22.6.7 Category VII: IM for Multiple-Component Ground Motions 470
22.7 Optimal IM Selection 470

23 Seismic Hazard Analysis 473
23.1 Recurrence Relationship 473
23.2 Attenuation Model 476
23.2.1 Fundamentals 476
23.2.2 Boore, Joyner, and Fumel (1997) 476
23.2.3 Parametric Evaluation 478
23.3 Deterministic Seismic Hazard Analysis 479
23.4 Probabilistic Seismic Hazard Analysis 479
23.5 Occurrence Time 482
23.6 Seismic Hazard Curves 483
23.7 Seismic Hazard Maps 484
23.8 Seismic Hazard Deaggregation 485
23.9 Target Response Spectra 486
23.10 Stochastic Ground Motion Simulation 488
23.10.1 Rezaeian and Der Kiureghian (R-D) Modal 489
23.10.2 Yamamoto and Baker (Y-B) Model 490
23.11 Endurance Time Excitation Functions 492
23.11.1 First Generation of ETEFs 493
23.11.2 Second Generation of ETEFs 494
23.11.3 Third Generation of ETEFs 495
23.11.4 Fourth Generation of ETEFs 495
23.11.5 Fifth Generation of ETEFs 496

24 Capacity Functions 499
24.1 Fundamentals 499
24.2 Generalized Capacity Functions 501
24.2.1 Basic Definitions 501
24.2.2 Mathematical model 501
24.3 Single-Hazard Capacity Functions 504
24.3.1 Strength Reserve Factor (SRF) 504
24.3.2 Time-dependent Strength Degradation (TSD) 504
24.3.3 Hydro-pressure Overload Factor (HPOF) 506
24.3.4 Flood Overload Factor (FOF) 506
24.3.5 Pushover-based Analysis (POA) 507
24.3.5.1 Invariant single-load vectors 508
24.3.5.2 Invariant multi-mode vectors 509
24.3.5.3 Hybrid load vector 510
24.3.6 Cyclic Pushover Procedure (CPP) 512
24.3.7 Equivalent Static Lateral Force (ESLF) 515
24.3.8 Incremental Dynamic Analysis (IDA) 517
24.3.8.1 Single-Record IDA (SR-IDA) 517
24.3.8.2 Multi-Record IDA (MR-IDA) 520
24.3.9 Cloud Analysis (CLA) 522
24.3.10 Endurance Time Analysis (ETA) 523
24.4 Multi-Hazard Capacity Functions 525

24.4.1 Extended Capacity Function . . . 525
24.4.2 Combined Capacity Function . . . 526

25 Fragility Functions . . . 529
25.1 Fundamentals . . . 529
25.1.1 Fragility Curve *vs.* Surface . . . 529
25.1.2 Fragility *vs.* Vulnerability *vs.* Hazard . . . 530
25.1.3 Continuous Function *vs.* Discrete Matrix . . . 532
25.1.4 Classification Based on Data Type . . . 533
25.1.5 Fragility in the Context of PBEE . . . 534
25.1.6 Treatment of Collapse (Large Data Point) . . . 534
25.2 Analytical Models Based on Generalized Linear Models . . . 535
25.3 Analytical Models Based on Lognormality Assumption . . . 537
25.3.1 IM-based Rule . . . 537
25.3.2 EDP-based Rule . . . 538
25.4 Analysis Techniques and Data Fitting . . . 538
25.4.1 Incremental Dynamic Analysis (IDA) . . . 538
25.4.2 Multiple Stripe Analysis (MSA) . . . 541
25.4.3 Cloud Analysis (CLA) . . . 544

26 Damage Index . . . 547
26.1 Damage Index for RC Structures . . . 547
26.1.1 Damage Index vs. Damage Variable . . . 547
26.1.2 Classification of Damage Index . . . 548
26.2 Damage Index for Gravity Dams . . . 550
26.3 Damage Index for Arch Dams . . . 555
26.3.1 Displacement-dependent DIs . . . 556
26.3.2 Crack-dependent DIs . . . 559
26.3.3 Energy-dependent DIs . . . 560

V Applications; Dams

27 Potential Failure Mode Analysis . . . 565
27.1 Historical Seismic Damage in Concrete Dams . . . 565
27.2 Potential Failure Mode Analysis . . . 567
27.3 Initiators . . . 568
27.4 Determination of PFMs . . . 569
27.4.1 Gravity Dams . . . 569
27.4.2 Arch Dams . . . 569
27.4.3 Buttress Dams . . . 571
27.4.4 Foundation-related PFMs . . . 571
27.5 Classification of PFMs . . . 571
27.6 Event Tree and Fault Tree . . . 573
27.7 Quantitative Assessment of PFMs . . . 577
27.7.1 Linear System . . . 578
27.7.1.1 Indices . . . 578

27.7.1.1.1 Demand capacity ratio (DCR): 578
27.7.1.1.2 Cumulative inelastic duration (CID): . . 578
27.7.1.1.3 Cumulative inelastic area (CIA): 578
27.7.1.1.4 Damage spatial distribution ratio (DSDR): 579
27.7.1.2 Criteria 579
27.7.2 Nonlinear System 580

28 Risk-Informed Decision Making 583
28.1 Basic Terminology 583
28.2 Risk Analysis 585
28.2.1 Risk Types 585
28.2.2 Risk Measures 586
28.2.2.1 Life Safety Risk 586
28.2.2.2 Annual Probability of Failure 586
28.2.2.3 Economic Considerations 587
28.2.2.4 Environment Consequences 587
28.2.3 Levels of Risk Analysis 588
28.2.3.1 Screening Level Risk Analyses 588
28.2.3.2 Periodic Risk Analyses 590
28.2.3.3 Semi-Quantitative Risk Analyses 590
28.2.3.3.1 Failure Likelihood Categories 591
28.2.3.3.2 Consequences Categories 591
28.2.3.3.3 Confidence Level 591
28.2.3.3.4 Risk Matrix 592
28.2.3.3.5 SQRA Procedure 592
28.2.3.4 Quantitative Risk Analyses 593
28.3 Risk Assessment 595
28.3.1 Tolerable Risk 595
28.3.2 Risk Guidelines 596
28.3.2.1 Life Safety 596
28.3.2.2 Annual Probability of Failure 597
28.3.3 Comparison of Different Guidelines 597

29 Deterministic Analyses of Concrete Dams: Examples 599
29.1 Potential Failure Mode Analysis 599
29.1.1 Model 600
29.1.2 Finite Element Analysis 601
29.1.3 Safety Factors against Sliding 604
29.1.4 Summary 605
29.2 AAR in an Arch Gravity Dam; Isola 605
29.2.1 Data Preparation 606
29.2.2 Stress Analysis 610
29.2.3 Results 610
29.3 AAR in a Hollow Buttress Dam; Poglia 613

29.3.1 Transient Thermal Analysis . . . 615
29.3.2 Stress Analysis . . . 616
29.3.3 Analysis and Results . . . 617
29.4 Seismic Analysis of High Arch Dam: Dez . . . 621
29.4.1 Dam Description . . . 621
29.4.2 Finite Element Model . . . 622
29.4.3 Thermal Analysis . . . 623
29.4.3.1 Applied Initial Temperature . . . 623
29.4.3.2 Determination of Meteorological Parameters . . . 624
29.4.3.2.1 Air Temperature . . . 624
29.4.3.2.2 Reservoir Water Temperature . . . 624
29.4.3.2.3 Effect of Solar Radiation . . . 625
29.4.3.2.4 Reservoir Water Level Changes . . . 626
29.4.3.3 Thermal Calibration of Model . . . 627
29.4.3.4 Thermal Analysis Considering Solar Radiation Effects . . . 628
29.4.3.5 Thermal Analysis Neglecting Solar Radiation Effects . . . 629
29.4.4 Structural Calibration . . . 629
29.4.5 Modal Analysis . . . 631
29.4.6 Seismic Safety Evaluation . . . 634
29.4.7 Post-Earthquake Safety Evaluation . . . 638
29.4.8 Impact of Water Level Variation . . . 642
29.4.8.1 Detailed Single Ground Motion . . . 642
29.4.8.2 Generalized Findings . . . 643
29.4.9 Endurance Time Analysis Method . . . 646
29.4.9.1 ETAFs and Equivalent Target Time . . . 646
29.4.9.2 Response Prediction . . . 647
29.5 Dam Foundation Interaction: Karaj . . . 649
29.5.1 Modeling the Dam-Foundation Interaction . . . 649
29.5.2 Numerical Model of the Coupled System . . . 652
29.5.3 Loading of the Coupled System . . . 653
29.5.4 Near- vs. Far-Field Responses . . . 656
29.6 Soil Structure Interaction: Folsom Dam . . . 658
29.6.1 Dam Description . . . 659
29.6.2 Analyses . . . 660
29.6.2.1 No Absorbing Boundary Conditions . . . 661
29.6.2.2 Lysmer Boundary Condition . . . 662
29.6.2.3 Miura Model . . . 665
29.6.3 Observations . . . 667

30 Probabilistic Analysis of Dams; Examples . . . 671
30.1 Probabilistic Seismic Demand Model Analysis of a Gravity Dam . . . 671
30.1.1 Case Study Dam . . . 672
30.1.2 Ground motion Characteristics . . . 673

30.1.3 IM Distribution Models for Selected GMs 673
30.1.4 Cloud Analysis 674
30.1.5 Optimal IM, (EDP = Displacement) 674
30.1.6 Fragility Curves 675
30.2 Incremental Dynamic Analysis of a Gravity Dam 676
30.2.1 Case Study Dam 676
30.2.2 Ground motion Characteristics 676
30.2.3 Capacity Curves 677
30.2.3.1 Single Record IDA 677
30.2.3.2 Resurrection Phenomenon 678
30.2.3.3 Multiple Record IDA 678
30.2.4 Collapse Fragility Curves 678
30.3 Epistemic Uncertainty Quantification in a Gravity Dam 680
30.3.1 Case Study Dam 680
30.3.2 Material Properties 680
30.3.3 Uncertainty of Mode I and II Fracture Mechanics 681
30.3.4 Sensitivity Analysis of Dam (Mixed-Mode Fracture) 682
30.3.5 Quantification of Uncertainties in Dam 682
30.4 Comprehensive Fragility Analysis of Concrete Dams 684
30.4.1 Contextual Framework 684
30.4.2 Review of Current Applications 687
30.5 Response Surface Meta-Model for a Linear Gravity Dam 687
30.5.1 Case Study Dam 688
30.5.2 Material Uncertainty Quantification 689
30.5.3 Meta-Model for Material Uncertainty 690
30.5.4 Meta-Model for Ground motion Uncertainty 691
30.6 Response Surface Meta-Model for a Nonlinear Arch Dam 693
30.6.1 Case Study Dam 693
30.6.2 Selection of DOE Model 693
30.6.3 Nonlinear Transient Analyses 694
30.6.4 Develop a Meta-Model 696
30.7 Meta-Model based Reliability Analysis of a Gravity Dam 696
30.7.1 Case Study Dam 697
30.7.2 Dynamic Sensitivity 697
30.7.3 Reliability Assessment 697
30.8 Fracture Mechanics based Reliability Analysis of a Gravity Dam . . . 700
30.8.1 Dam Description 700
30.8.2 Analysis 701
30.8.2.1 Point Estimate Method 701
30.8.2.2 Taylor's Series-Finite Difference Estimation 702
30.9 Classical Reliability Analysis of a Gravity Dam with LEM 703
30.9.1 Case Study Dam 703
30.9.2 Classical Reliability Methods 703
30.9.3 Reduced Model Reliability 705
30.10Failure Probability of Gravity Dam Classes 705

30.10.1Case Study Dam 706
30.10.2Step by Step Procedure 706
30.10.3Dam Class Failure Probability 707
30.11Random Field Vibration Anatomy of Arch Dams 708
30.11.1Case Study Dams 709
30.11.2Vibration Response for Homogeneous Pilot Dam 710
30.11.3Vibration Response of Heterogeneous Pilot Dam 710
30.11.4Generalized Model 711
30.11.5DOE-Based Analytical Model 712
30.12Random Field Linear Seismic Analysis of a Gravity Dam 712
30.12.1Case Study Dams 713
30.12.2Anatomy of Random Field Responses 714
30.12.3Impact of Spatial Correlation Length 715
30.12.4Impact of the Double Random Field Distribution 716
30.13Random Field Damage Assessment of a Gravity Dam 717
30.13.1Case Study Dams 717
30.13.2Anatomy of Pilot Model 718
30.13.3Crack Pattern 720
30.14SVM for Nonlinear Seismic Analysis of a Gravity Dam 720
30.14.1Case Study Dam 721
30.14.2Hybrid FEM-SVM 721
30.14.3Detecting Failure from Non-Failure 723
30.14.4Regression of Non-Failure Results 724
30.15Ground motions Meta-Features for Dam Response Prediction 724
30.15.1Case Study Dam 725
30.15.2Employing All the Features 725
30.15.3Employing the Selective Features 728
30.16Machine Learning based Multi Hazard Reliability of Gravity Dams . 729
30.16.1Case Study Dam 729
30.16.2Methodology of Machine Learning 730
30.16.3Hydrological Hazard 730
30.16.4Aging Hazard 732
30.16.5Seismic Hazard 733
30.17Soft Computing based Material and Modeling Uncertainty Quantification in Gravity Dams 733
30.17.1Case Study Dam 734
30.17.2Prediction Tasks 734
30.17.3PT-1: Pilot Model 735
30.17.4PT-4: Material and Modeling Effect 737
30.18Polynomial Chaos Expansion for Uncertainty Quantification in Dam Engineering 739
30.18.1Case Study Dam 740
30.18.2Analytical Gravity Dam Model 741
30.18.3Simplified Gravity Dam Finite Element Model 743
30.18.4Coupled Arch Dam-Reservoir-Foundation Model 744

30.18.5 Layered Arch Dams Vibration Characteristics 746

VI Applications; Nuclear Structures

31 Analysis of Nuclear Containment Structures; I Introduction 751
31.1 Introduction 751
31.1.1 Guidelines 752
31.1.2 Challenges 752
31.2 Contextual Framework 754
31.2.1 Historical Development 754
31.2.2 Literature Survey 756
31.2.2.1 Seismic Hazard Analysis 756
31.2.2.2 Numerical Simulations 757
31.2.2.3 Probabilistic Risk Evaluation 758
31.2.3 Anatomy of a Probabilistic Seismic Analysis 759
31.3 Revisit of Sandia's Report 759
31.3.1 Background 760
31.3.1.1 Historical Context 760
31.3.1.2 Containment Design 762
31.3.1.3 Toward Containment Testing at Sandia 762
31.3.2 Preliminary Considerations 763
31.3.2.1 Failure 763
31.3.3 Tests 763
31.3.4 Containment Capacity Analysis Guidelines 765
31.3.4.1 Introduction 765
31.3.4.2 Analysis Goals and Planning 766
31.3.4.3 Simulation Code Selection 768
31.3.4.4 Model Development 768
31.3.4.4.1 Geometric Considerations 768
31.3.4.4.1.1 Element Types for Concrete Containments . . 770
31.3.4.4.2 Constitutive Modeling of Concrete Containment 771
31.3.4.5 Interpretation and Evaluation of Results 772
31.3.4.5.1 Basic Model Checks 772
31.3.4.5.2 Failure Criteria and Interpreting Analytic Solution 773

32 Analysis of Nuclear Containment Structures; II Reported Analyses . . 775
32.1 AAR: Gentilly 775
32.1.1 Reported Analyses/Investigation 775
32.1.1.1 Material Aspects and Laboratory Testing 777
32.1.1.2 Material Modeling 778
32.1.1.3 Structural Modeling 778

32.1.1.4 Non-Destructive Testing and *in-situ* Condition Assessment . . . 780
32.1.1.5 Conclusions . . . 784
32.1.2 Critical Review . . . 785
32.2 AAR: Ikata . . . 786
32.2.1 Reported Analyses/Investigation . . . 786
32.2.2 Critical Review . . . 788
32.3 Crystal River Delamination . . . 788
32.3.1 Introduction . . . 788
32.3.2 Reported Analyses/Investigation . . . 789
32.3.2.1 Finite Element Models . . . 794
32.3.2.2 Failure Modes in Group 1: Containment Design . . . 798
32.3.2.3 Failure Modes in Group 7: SGR Activities . . . 800
32.3.2.3.1 Discussions . . . 800
32.3.2.3.2 Global Radial Response . . . 801
32.3.2.3.3 Delamination Explained . . . 801
32.3.3 Critical Review . . . 802
32.3.3.1 Analysts/Analysis . . . 803
32.3.3.2 Validation . . . 804
32.3.3.3 Elastic Modulus and Visco-Elasticity . . . 805
32.3.3.4 Tensile Strength . . . 806
32.3.3.5 Modeling . . . 807
32.4 Saint Laurent . . . 809
32.5 Tihange 2 . . . 809

33 Analysis of Nuclear Containment Structures; III Analyses by the Authors . . . 813
33.1 Crystal River Delamination . . . 813
33.1.1 Assumption and Model . . . 813
33.1.2 Results . . . 815
33.1.3 Conclusion . . . 815
33.2 CEB Subjected to ASR and Seismic Loads . . . 816
33.2.1 Finite Element Mesh . . . 817
33.2.2 Stochastic Seismic Excitation . . . 820
33.2.3 Results . . . 822
33.2.3.1 Static + ASR Analyses . . . 822
33.2.3.2 Impact of ASR on Capacity Curves: ETA Method . 822
33.2.3.3 Impact of ASR on Fragility Curves: Stochastic Analysis . . . 825

VII Applications; Others & Case Study

34 Massive Reinforced Concrete Structures 831
34.1 Introduction 831
34.2 Massive Reinforced Concrete Structure 831
34.2.1 Description 831
34.2.2 Model 832
34.2.3 Results 833
34.2.3.1 Seismic Analysis Following AAR Expansion 835
34.3 Segmental Bridge 837
34.3.1 Description of the Viaduct 837
34.3.2 Concrete Conditions 837
34.3.3 Finite Element Model 838
34.3.4 Preliminary Deterministic Analysis 840
34.3.5 Uncertainty Quantification Framework 841
34.3.6 Analyses Results 843
34.3.6.1 Effect of Kinetics (classification) 844
34.3.6.2 Probabilistic Based Assessment 846
34.3.7 Risk Informed Conditional Assessment 847

35 Case Study: Seabrook Station Unit 1 ASR Problem 851
35.1 Reported Analyses/Investigation 853
35.1.1 Background 853
35.1.2 The Process 854
35.1.3 License Amendment Request 855
35.1.3.1 Ferguson Structural Engineering Laboratory 856
35.1.3.1.1 In/out-of-plane Shear Transfer 856
35.1.3.1.2 Concrete Mix 856
35.1.3.1.3 Beam Tests 857
35.1.3.1.3.1 Dimensions and Loading . 857
35.1.3.1.3.2 Structural Crack 857
35.1.3.1.3.3 Shear Failure 858
35.1.3.2 Building Deformation Aging Management 860
35.1.3.2.1 Crack Index 860
35.1.3.2.2 out-of-plane Expansion 860
35.1.3.2.3 Recorded Expansion 862
35.1.3.3 Building Deformation Assessment 863
35.1.3.3.1 Screening Evaluations 863
35.1.3.3.2 Factored Self-Straining Loads 864
35.1.3.3.3 Finite Element Analysis 865
35.2 Critical Review 867
35.2.1 The Process and Concepts for Development and Review of LAR 868
35.2.1.1 Role of NRC 869
35.2.1.2 Competence and Independence of LAR Preparation and Reviewers 870
35.2.1.3 Code approach 871

35.2.1.4 Tests Based on Tunnel not CEB 871
35.2.1.5 Scaling and Boundary Conditions 872
35.2.1.6 Box Limits not Applicable for Applications to Seabrook Site 873
35.2.2 License Amendment Request 874
35.2.2.1 Ferguson Structural Engineering Laboratory 874
35.2.2.1.1 In/out-of-plane Shear Transfer Mechanisms 874
35.2.2.1.2 Concrete representativeness 875
35.2.2.1.3 Beam Tests 876
35.2.2.1.3.1 Splitting crack 876
35.2.2.1.3.2 Chemical Prestressing Side Effects 878
35.2.2.1.3.3 Fracturing of stirrups 878
35.2.2.1.3.4 Size Effect 879
35.2.2.1.3.5 Creep 880
35.2.2.2 Building Deformation Aging Management 880
35.2.2.2.1 Crack Index 880
35.2.2.2.2 out-of-plane Expansion 883
35.2.2.2.3 Unaddressed Concerns 884
35.2.2.2.3.1 Internal Cracks 884
35.2.2.2.3.2 Potential Delamination . . . 886
35.2.2.2.3.3 Uncertainty in Future Expansion; Threshold Factors 887
35.2.2.2.3.4 “Elastic” Margin for Future Expansion 888
35.2.2.3 Building Deformation Assessment 888
35.2.2.3.1 Screening Evaluation 888
35.2.2.3.2 Factored Self-Straining Loads 889
35.2.2.3.3 Finite Element modeling 890
35.2.2.3.3.1 Lack of Verification and Validation 890
35.2.2.3.3.2 Shell Elements 891
35.2.2.3.3.3 Nonlinear Analysis 891
35.2.2.3.3.4 Demand and Capacity . . . 892
35.2.2.3.3.5 ASR Model 893
35.2.2.3.3.6 ASR Demand 893
35.2.2.3.3.7 Modeling chemical prestressing 894
35.2.2.3.3.8 Static Soil Structure Interaction 895
35.2.2.3.3.9 Dynamic Analysis Model . 895
35.2.2.3.3.10 Dynamic Analysis Time Integration 896

35.2.2.3.3.11 Nonlinear Analysis 896
35.2.2.3.3.12 Dynamic Uplift/Rocking . 897
35.3 Conclusion 897

Bibliography 901

Index Subject 958

Index Names 970

A Testing Method for Concrete Fracture Properties 987
A.1 Apparatus 989
A.2 Test Specimens 989
A.3 Procedure 991
A.4 Calculation 992
A.4.1 Fracture Energy G_F 992
A.4.2 Tensile Softening Diagram 993
A.4.3 Fracture Energy G_f 993
A.4.4 Fracture Toughness 994
A.5 Report 995
A.6 Additional Illustrations 996

B Computational Tools for Probabilistic Analyses 999
B.1 Motivation 999
B.2 Probabilistic Performance Assessment of Structures 1000
B.3 Detailed Steps 1002
B.3.1 `P0.m` 1002
B.3.2 `P1.m` 1002
B.3.3 `P2.m` 1006
B.3.4 `P3.m` 1006
B.3.5 `P4.m` 1008
B.3.6 `P5.m` 1008

List of Figures

1.1 Vector transformation 8
1.2 Principal directions of tensor of order two 10
1.3 Octahedral plane 11
1.4 Surface forces 13
1.5 Cauchy: Tetrahedron to stress 14
1.6 Geometric representation of stress 17
1.7 Position and displacement vectors 17
1.8 Flux Through Area dS 20
1.9 Equilibrium of stresses, Cartesian coordinates 23
1.10 Plate from Hooke's lecture on springs 25

2.1 Flux vector 31
2.2 Flux Through Sides of Differential Element 32
2.3 Heat transfer mechanism for a concrete dam in 3D space; adopted from [596] 38
2.4 Air and reservoir temperatures 39
2.5 Azimuth angle of the sun 42
2.6 Zenith angle θ_p, azimuth angle of a vertical plane ϕ_p, and angle of incidence of sun on the vertical plane θ_i [510] 44
2.7 Heat Transfer Analysis in Concrete 45
2.8 Components of Tonti's Diagram, [293] 46
2.9 Fundamental Equations of Solid Mechanics and Heat Flow 47

3.1 Yield surface; Definition 50
3.2 Hydrostatic pressure independent models 50
3.3 Pressure Dependent Yield Surfaces 52
3.4 Hydrostatic pressure dependent models 53
3.5 Representative stress-strain of metals 54
3.6 Bauschinger Effect 54
3.7 Concrete micro-cracks 55
3.8 Chemical bonds 55

3.9 Ductile and brittle bonds . . . 56
3.10 Slip planes . . . 56
3.11 Dislocation . . . 57
3.12 Elasto-Plastic stress strain response . . . 58
3.13 Isotropic Hardening and Kinematic Hardening . . . 59

4.1 Infinite plates with holes and uniform traction . . . 64
4.2 Infinite plate with elliptical hole (curvilinear coordinate system) . . . 64
4.3 Hollowed plates with circular and elliptical holes . . . 65
4.4 Comparison of different singularity strengths . . . 66
4.5 Crack tip stresses, and independent crack displacements . . . 67
4.6 SIF geometries . . . 70
4.7 Mixed Mode Crack Propagation and Biaxial Failure Modes . . . 73
4.8 Mixed mode crack propagation crack tip stresses . . . 73
4.9 Concept of break through in fracture mechanics . . . 74
4.10 Concept of leak before failure in fracture mechanics (Courtesy Dr. Brian Rose) . . . 75
4.11 Residual strength diagrams . . . 76
4.12 Some NDE/NDT Techniques, [624] . . . 76
4.13 Fracture control plan and cost . . . 78
4.14 Determination of Plastic Zone Sizes . . . 80
4.15 J Integral definition around a Crack . . . 82
4.16 Closed contour for proof of J path independence . . . 83
4.17 Virtual crack extension definition of J . . . 84
4.18 Elastic-Plastic versus nonlinear elastic materials . . . 85
4.19 Nonlinear energy release rate, [30] . . . 86
4.20 Fatigue crack growth . . . 89
4.21 Retardation in fatigue crack growth . . . 89

5.1 Typical behavior of concrete shrinkage [480] . . . 93
5.2 Creep strain evolution at various stress levels and shrinkage strain evolution of various sized samples . . . 95

6.1 Schematic of earth's layers . . . 104
6.2 Seismic belts of the world; adopted from Wikipedia . . . 104
6.3 Different types of plate boundaries; image courtesy of the USGS . . . 106
6.4 Reid's Elastic Rebound Theory . . . 107
6.5 Classification of fault mechanisms . . . 108
6.6 Classification of seismic waves; [147] . . . 109
6.7 Different fault-to-site distance terminologies . . . 109
6.8 Approximate location of earthquake . . . 112
6.9 Shaking intensity definitions . . . 112
6.10 Comparison of epicentral and hypocentral based Richter standard event . . . 114
6.11 Definition of parameters in body wave correction factor . . . 114

6.12 Earthquake directional effects 116
6.13 Earthquake dispersion and incoherence effects 117

7.1 Secant and Tangent Stiffnesses for α Method 131

8.1 Inter-connection of concepts incorporated in probabilistic analysis . . . 136
8.2 The concept of sample space and mutually disjoint events 137
8.3 Comparison of histograms due to 100 samples for three times 138
8.4 Comparison of histograms due to 1,000 to 100,000 samples 138
8.5 Examples of three continuous distributional functions 139
8.6 Relation between PDF and CDF 139
8.7 Relation between bounded PDF and CDF 140
8.8 The concept of percentile within a continuous distribution 141
8.9 Uniform distribution 144
8.10 Normal distribution 144
8.11 Lognormal distribution 145
8.12 Bivariate normal distribution 149
8.13 Impact of correlation on the bivariate normal distribution 149

9.1 Post-peak response of a concrete specimen under uniaxial tension in terms of gauge locations 154
9.2 Hillerborg's model 155
9.3 Impact of Hillerborg's model on structural response 158
9.4 Localization of cracks in concrete structures 161
9.5 Size effect derivation in cohesive materials 162
9.6 Implications of the size effect law 162
9.7 Example of size effect in shear for reinforced concrete members without stirrups [117] 163
9.8 Central Crack With Constant Cohesive Stresses 164
9.9 Nominal strength in terms of size for a center crack plate with constant cohesive stresses 165
9.10 Dugdale's Model 166
9.11 Size Effect Law for an Edge Crack with Constant Cohesive Stresses . 167
9.12 Linear Cohesive Stress Model 167
9.13 Energy Transfer During Infinitesimal Crack Extension 168
9.14 Size Effect Law for an Edge Crack with Linear Softening and Various Orders of Approximation 169
9.15 Three Point Bend Specimen with Linear Cohesive Stresses 170
9.16 Experimental evidence of the role of micro-cracks Nemat-Nasser and Hori [625] 172
9.17 Analytical model of micro-cracks Nemat-Nasser and Hori [625] 173
9.18 Development of cracking due to ASR 175
9.19 Measure of volumetric crack density $N_v < a^3 >$ versus compressive strain for cement paste, w/c = 0.7, 0.5-, 0.3, and mortar, w/c= 0.5 [71] 176

9.20 Micro-cracks in solids [521] 176
9.21 Creep fracture of concrete 177
9.22 Concrete creep study of Bažant, Ž. and Gettu, R. [104] 179
9.23 Crack coalescence 181
9.24 Crack coalescence 181

10.1 Reinforced Concrete Deterioration Modes (excluding AAR) 184
10.2 Outline of mechanical damage in reinforced concrete initiated by chloride diffusion 185
10.3 Normalized solution of Fick's second law of diffusion 187
10.4 Algorithm for chloride diffusion analysis 193
10.5 Flowchart of Carbon Dioxide Diffusion and Carbonation Process 198
10.6 Schematic of the corrosion process 200
10.7 Coupled thermal, diffusion, corrosion and stress analyses 203

11.1 Definition of the expansion curve 206
11.2 Stress Induced Cracks with Potential Gel Absorption, [779] 209
11.3 Graphical Representation of Γ_c and Γ_t 209
11.4 Effect of confinement on AAR strain redistribution 210
11.5 Weight of Volumetric AAR Redistribution in Selected Cases 211
11.6 Weight Regions 212
11.7 Relative Weights 214
11.8 Degradation of E and f'_t 215
11.9 Impact of ASR on ASR on compressive and tensile strengths in concrete dams [250] 217
11.10 Impact of ASR on field measured elastic properties of Parker and Seminoe dams [250] 218
11.11 Principle of the system identification approach 219
11.12 System identification for ASR properties 222
11.13 Estimate of past and future ASR expansions 223

12.1 Finite Element Process (inspired by Bathe [89]) 227
12.2 Unstructured *vs.* structured *vs.* shell meshes 229
12.3 Uniformly distributed model complexity 231
12.4 Meshing in the presence of stress singularity in a re-entry corner [431] 236

13.1 Two-Dimensional Mapping of Some Elements 243
13.2 Iso, Super, and Sub Parametric Elements 244
13.3 Pascal Triangles for Quadrilateral Elements 245
13.4 Three-noded quadratic bar element 245
13.5 Four noded Isoparametric element 247
13.6 Differential Element in Curvilinear Coordinate System 250
13.7 Cross Product of Two Vectors 251
13.8 Elements with Possible Singular Jacobians [89] 252
13.9 Serendipity and Lagrangian Quadratic Quadrilaterals 252

13.10 Serendipity Isoparametric Quadratic Finite Element: Global and Parent Element . . . 253
13.11 Shape functions for various isoparametric elements . . . 254
13.12 Extrapolation from 4-Node Quad Gauss Points [292] . . . 258
13.13 Gravity Loading . . . 259
13.14 Traction Load in Isoparametric Elements . . . 260
13.15 Traction Load in Contiguous Isoparametric Elements . . . 261
13.16 h, p and r Convergence . . . 267

14.1 Linear *vs* non-linear analyses . . . 269
14.2 Level of Analysis . . . 270
14.3 Explicit integration scheme . . . 273
14.4 Test Controls . . . 275
14.5 Newton's method for the solution of a non-linear equation . . . 277
14.6 Newton's method in structural engineering . . . 282
14.7 Newton-Raphson Method . . . 284
14.8 Modified Newton-Raphson Method, Initial Tangent in Increment . . . 285
14.9 Modified Newton-Raphson Method, Initial Problem Tangent . . . 286
14.10 Incremental Secant, Quasi-Newton Method . . . 287
14.11 Effective Young's modulus of reinforced concrete) . . . 289
14.12 Embedded Reinforcement Across a Crack/Joint . . . 290

15.1 Isoparametric quadratic finite element: global and parent element . . . 294
15.2 Singular element (quarter-point quadratic isoparametric element) . . . 296
15.3 Finite element discretization of the crack tip using singular elements . 298
15.4 Displacement correlation method to extract sif from quarter point singular elements . . . 298
15.5 Singular quarter point isoparametric elements in 3D . . . 300
15.6 Numerical extraction of the J integral [672] . . . 301
15.7 Simply connected region A^* enclosed by contours Γ_1, Γ_0, Γ_+, and Γ_-, [30] . . . 305
15.8 Surface enclosing a tube along a three dimensional crack front, [30] . 307
15.9 Interpretation of q in terms of a Virtual Crack Advance along ΔL, [30] . . . 308
15.10 Inner and outer surfaces enclosing a tube along a three dimensional crack front . . . 308
15.11 Interface idealization and notations. . . . 311
15.12 Interface fracture . . . 312
15.13 Failure function . . . 313
15.14 Bi-linear softening laws . . . 314
15.15 Stiffness degradation in the equivalent uniaxial case . . . 315

16.1 Rocking due to finite size foundation support . . . 320
16.2 Rocking due to concrete-rock interface . . . 321
16.3 Deconvolution . . . 322

16.4 Comparison of Butterworth filters . . . 323
16.5 Transfer function . . . 323
16.6 Deconvolution applied in finite element analysis . . . 324
16.7 Infinitesimal element subjected to elastic wave . . . 326
16.8 Elastic waves in an infinite medium . . . 328
16.9 Lysmer Modeling for Lateral Excitation . . . 329
16.10 Conceptual model . . . 330
16.11 2D Idealization and Γ_i planes . . . 333
16.12 Foundation boundary conditions for radiating flexible foundation . . . 336
16.13 Finite element discretization of the free field . . . 337
16.14 Discretization of 2D dam foundation with free field velocities . . . 338
16.15 2D Finite Element Modeling . . . 339
16.16 3D extension; procedure outline . . . 339
16.17 Selected results for 2D analyses; Crest accelerations, deformed shapes with contour lines of V_X and V_Y . . . 340
16.18 Selected results for 3D analyses; Crest accelerations, accelerations at h = 0, h/8, h/4, 3h/8, h/2, 5h/8, 3h/4, 7h/8 and h; deformed shapes with contour lines of V_X . . . 341
16.19 Soil structure interaction models . . . 343

17.1 Uplift pressures in a dam . . . 345
17.2 Uplift models from three US agencies [262] . . . 346
17.3 Details of the FERC uplift model [309] . . . 347
17.4 FERC finite element model for uplift [309, Fig. 11] . . . 348
17.5 Finite element models to model uplift; a) Dam; b) Assumed uplift loading; c) Finite element discretization; d) Loading on finite element model . . . 348
17.6 Three-dimensional uplift model in Saouma, Červenka, and Reich [767] . . . 349
17.7 Boundary Conditions for Seepage Analysis . . . 350
17.8 Dynamic uplift . . . 351
17.9 Hydrodynamic water pressure and force . . . 352
17.10 Comparison of the approximate and exact solutions for a hypothetical dam . . . 354
17.11 Electric Analog Tray Model used by [904] . . . 355
17.12 Zangar [904] model . . . 355
17.13 Dam-reservoir-massed foundation coupled system and boundary conditions . . . 361
17.14 Implementation of the water pressure inside the opened contraction joints, (a) calculation of hydrostatic and hydrodynamic pressure at considered level, (b) Joint opening direction on plane view of the dam body at considered level, (c) Calculation of effective area and force for each node . . . 363

18.1 Aleatory vs. epistemic uncertainty . . . 366

18.2 Sensitivity analysis using Tornado diagram . . . 367
18.3 Crude vs. quasi Monte Carlo methods . . . 370
18.4 Sampling of a system with two RVs . . . 370
18.5 A multivariate partial correlation matrix with 10,000 samples . . . 371
18.6 Three samples of spatial correlation of fracture energy . . . 371
18.7 Temporal correlation in concrete elastic modulus of an AAR-affected structure . . . 371
18.8 Capacity and demand reliability index . . . 372
18.9 Probability of failure in terms of reliability index β . . . 374
18.10 Concept of the reliability analysis with basic random variables . . . 375
18.11 Probabilistic Seismic Hazard . . . 379
18.12 2% probability of exceedance in 50 years map of PGA [846] . . . 379
18.13 Structural safety risk management . . . 380
18.14 HSE tolerability of risk framework; adopted from HSE [432] . . . 381
18.15 Typical risk assessment process for a dam; adopted from ANCOLD [29] . . . 382
18.16 Fragility function . . . 383
18.17 Vulnerability function . . . 384
18.18 Resilience curve . . . 386
18.19 Framework for resilience-based collaboration in dam/levee safety; adopted from National Research Council [622] . . . 387
18.20 Hierarchy levels in sustainability; adopted from Bocchini et al. [132] 388
18.21 FORM; Isoparametric transform from physical to standard normal space . . . 389
18.22 FORM vs. SORM . . . 390
18.23 Crude MCS vs. IS . . . 392

19.1 Comparison of sampling techniques and impact of sample size . . . 397
19.2 Detailed random ESLF calculations for the gravity dams . . . 400
19.3 Graphical representation of Chopra's 4D standard values for the ESLF method . . . 401
19.4 Standard values for the period lengthening ratio due to hydrodynamic effects, R_r . . . 402
19.5 Standard values for the period lengthening ratio due to hydrodynamic effects, ζ_r . . . 404
19.6 Standard values for the normalized hydrodynamic pressure function with a full reservoir, $gp(\hat{y})/wH_w$ . . . 406
19.7 Standard values for the hydrodynamic force coefficient, A_p . . . 407
19.8 Classification of random field based on location of observation; adopted from [854] . . . 410
19.9 Classification of random field based on generators; adopted from [853] . . . 411
19.10 Comparison of auto-correlation functions with different length . . . 412
19.11 Sample application of random field on a square with unit length and 25 nodes in each direction . . . 413

19.12 Four realizations of the generated two-dimensional random field with different correlation length . . . 415
19.13 Step-by-step RF generation by covariance matrix decomposition and midpoint discretization method; from left to right: 1) continuum RF with l_{corr}=0.2 m; 2) a uniform grid of 50×150 (green) points for RF, element (red) midpoint of irregular FE mesh, and closest matching (black) point from grid to mesh; 3) irregular FE mesh; 4) transfered continuum RF to discrete form; 5) discrete RF in the FE program; and 6) sample damage response of the model subjected to an arbitrary loading . . . 416

20.1 The general uncertainty quantification framework; adapted from [570] 418
20.2 Composition of commonly used metamodeling techniques, adapted from [792] and [865] . . . 419
20.3 Three-factor DOE techniques with two, three and five levels . . . 420
20.4 Relationship between number of simulations, technique type, number of factors and levels . . . 424
20.5 Illustration of the hyperbolic truncation set with varying p (3 to 5) and q (0.5 to 1.0) . . . 428
20.6 Different learning styles in machine learning algorithms . . . 430
20.7 Some of the important Machine Learning algorithms by Jason Brownlee . . . 431
20.8 Selection of right machine learning model . . . 432
20.9 Generalizability of machine learning models . . . 432
20.10 Developing an optimized machine learning model . . . 433
20.11 Imbalance data set . . . 434
20.12 Three classification techniques in machine learning. From left to right: K-Nearest Neighbor (KNN), Support Vector Machine (SVM), and Naive Bayes Classifier (NBC). In KNN, a new observation is classified based on the labels of K nearest neighbors. SVM solves an optimization problem to find a separating hyperplane with maximum margin and a new observation is classified based on its position. NBC is a probabilistic approach to find the most likely class for a new observation using Bayes theorem. . . . 435

21.1 Comparison of general methodologies in PFMA and PBEE . . . 445
21.2 Recommended minimum seismic performance design objectives for buildings . . . 448
21.3 Global framework for performance based earthquake engineering . . . 449
21.4 The disciplines contribute in global framework of performance based earthquake engineering . . . 450
21.5 Conceptual description of first generation of PBEE . . . 450
21.6 General framework of PEER PBEE methodology [700] . . . 452
21.7 Comparison of ground motion selection and scaling for IBPA, SBPA and TBPA . . . 453

22.1 Time history of acceleration, velocity, and displacement for a sample ground motion record . . . 456
22.2 Frequency dependent parameters of a sample ground motion record . 457
22.3 Response spectra for a sample ground motion record . . . 459
22.4 Comparison of response spectra and pseudo response spectra for a sample ground motion record . . . 460
22.5 Damping effects on response spectra . . . 461
22.6 Determination of different ground motion durations . . . 462
22.7 Characterization of a time-dependent function $f(t)$ . . . 463
22.8 PSDM and criteria for optimal IM selection . . . 471

23.1 The (bounded) Gutenberg-Richter recurrence law . . . 474
23.2 Classification of seismic sources . . . 475
23.3 Classification of site-to-source distances . . . 478
23.4 Parametric investigation on GMPEs . . . 479
23.5 Deterministic Seismic Hazard Analysis . . . 480
23.6 Probabilistic Seismic Hazard Analysis . . . 481
23.7 Poisson's probability model . . . 482
23.8 Sample of mean and fractile seismic hazard curves . . . 483
23.9 Samples of US hazard maps . . . 485
23.10 Samples of seismic deaggregation plots for the University of Colorado Boulder . . . 486
23.11 Comparison of different response spectra . . . 487
23.12 Sample ETEF . . . 494
23.13 CAV of ETA40lc01 versus target . . . 496
23.14 Hysteretic energy of ETA20kd01 versus target . . . 497

24.1 Global framework for PBE and the role of capacity function . . . 500
24.2 A sample idealized capacity function (normalized form) . . . 502
24.3 Fitting an analytical capacity function . . . 503
24.4 Various forms of the nonlinear function f_N based on Eq. 24.4 . . . 504
24.5 Capacity estimation using mechanics-based methods . . . 505
24.6 AAR and creep interaction [772] . . . 505
24.7 Capacity estimation by hydraulic-based methods . . . 507
24.8 Classification of the pushover-based capacity functions . . . 509
24.9 Modal analysis of concrete gravity dams . . . 511
24.10 Algorithm to find the derivation of a capacity function using the hybrid load vector . . . 513
24.11 Cyclic pushover procedure for the New Zealand protocol . . . 514
24.12 Standard contribution factors for the dam-reservoir interaction [546] . 516
24.13 Standard contribution factors for the dam-foundation interaction [546] 517
24.14 Standard values of the hydrodynamic pressure for a full reservoir [546] . . . 517
24.15 Single-Record IDA capacity functions . . . 520

24.16 Multi-Record IDA capacity functions using different interpolation techniques . . . 520
24.17 Comparison of various 3D MR-IDA capacity functions . . . 522
24.18 Cloud-based data power-form capacity function . . . 523
24.19 ETA-based capacity function generation . . . 525
24.20 IDA-based extended capacity function generation . . . 526
24.21 Time-dependent strength degradation with material uncertainty . . . 527
24.22 Combination of time-dependent and seismic capacity functions . . . 527

25.1 Comparison of seismic fragility, vulnerability and hazard curves . . . 531
25.2 Different aspects of seismic fragility surfaces . . . 531
25.3 Relationship between fragility curve and damage probability matrix . 533
25.4 Link functions for binomial data and their relationship . . . 536
25.5 Conceptual collapse fragility curves based on IDA method . . . 542
25.6 Conceptual collapse fragility curves based on MSA method . . . 545

26.1 Relationship between damage variable and damage index . . . 548
26.2 Potential failure mechanism of a typical gravity dam, critical locations and crack paths . . . 551
26.3 Different cracking scenarios for gravity dams under earthquake excitation . . . 554
26.4 FSS-based DS matrix [35] . . . 556
26.5 ETA-based capacity functions for a generic arch dam (no scale) . . . 557
26.6 Direct relation between DI and $\Omega(\Delta)$ . . . 559
26.7 Evolution of energy terms under the ETA method . . . 561

27.1 Steps towards PFMA of concrete dams based on qualitative approach; adapted from FERC [308] and USBR-manual [845] . . . 566
27.2 Initiators in concrete dams . . . 568
27.3 Damage response of gravity dam under earthquake ground motion . . 569
27.4 Damage response of arch dam under earthquake ground motion . . . 570
27.5 Damage response of buttress dam under earthquake ground motion . . 571
27.6 Event tree for an independent three-component system indicating accident sequences; $P(X_A|I) = P(X_A)$, $P(X_B|X_A, I) = P(X_B)$, and $P(X_{Ci}|X_B, X_A, I) = P(X_{Ci})$ . . . 574
27.7 Failure modes of a gravity dam using fault tree approach . . . 575
27.8 Transformation of event tree to fault tree and vice versa . . . 576
27.9 Slenderness of concrete arch dams and susceptibility to damage . . . 577
27.10 Calculation of the CID and CIA for two DCRs using stress (or strain) time histories . . . 579
27.11 Failure surface for concrete dams under linear analysis (no scale); t_{tot} is total ground motion duration . . . 580

28.1 General framework of risk-based dam safety; [310] . . . 584
28.2 The Four Inundation Scenarios; [843] . . . 585
28.3 Level of Risk Framework; [310] . . . 588

28.4 SLPRA risk index scoring matrix; [310] . . . 589
28.5 USACE-USBR incremental risk matrix; [844] . . . 592
28.6 SIR (F-N chart) and AALL (f-$\bar{N}$ chart); [310] . . . 597
28.7 F-N or f-N charts by different agencies/organizations . . . 598

29.1 Gilboa dam, [922] . . . 600
29.2 Modeling considerations . . . 602
29.3 Selected results . . . 603
29.4 Joint 36 (between Block 5 and 6) . . . 603
29.5 Arch gravity dam geometry . . . 605
29.6 Preliminary load data to be collected for the AAR analysis of a dam . 606
29.7 Data preparation for thermal analysis of a dam subjected to AAR . . . 607
29.8 3D Finite element mesh for the stress analysis . . . 608
29.9 Computed internal temperature distribution variation . . . 609
29.10 Data preparation, cyclic load . . . 610
29.11 System identification process for the AAR analysis of an arch gravity dam . . . 611
29.12 Crest displacement comparison . . . 612
29.13 Internal AAR and stresses . . . 612
29.14 "Lift-off" of central portion of dam due to AAR . . . 613
29.15 Observed internal crack . . . 613
29.16 Section (central element) and layout of Poglia Dam . . . 614
29.17 Measured crest vertical displacement . . . 614
29.18 Adiabatic boundary conditions for the thermal analysis . . . 615
29.19 Internal temperature of Poglia Dam . . . 616
29.20 Analysis results for the Poglia Dam . . . 617
29.21 Deformed shape of the Poglia Dam . . . 618
29.22 Contour plots of the main rock/concrete joint, joint opening displacements (m), normal stresses (MPa), uplift pressures (MPa), joint sliding displacements (m) and joint shear stresses (MPa) . . . 619
29.23 Effects of lateral constraints on AAR expansion . . . 619
29.24 Deformed mesh and AAR strains in the lateral directions for both free and fixed boundary conditions . . . 620
29.25 Possible failure mechanism at a joint connecting two parts of the dam 621
29.26 Finite element model of dam, reservoir, foundation and used elements 623
29.27 Proposed algorithm for calculation of the real initial temperature distribution . . . 624
29.28 Comparison of the results obtained from thermal analysis and thermometers . . . 625
29.29 Variation of the air temperature recorded in Dez Dam site . . . 625
29.30 Comparison of the results obtained from thermal analysis and thermometers at upstream face of block number 9 . . . 626
29.31 Solar radiation at Dez Dam site . . . 626
29.32 Variation of the reservoir level in Dez Dam site . . . 627
29.33 Variation of the reservoir level in Dez Dam site . . . 627

29.34 Comparison of the results from thermal calibration analysis with thermometers data 629
29.35 Temperature distribution on the upstream and downstream surfaces of the dam for the year 1973 considering solar radiation effects (°C) . 630
29.36 Temperature distribution on the upstream and downstream surfaces of the dam for the year 1973 neglecting solar radiation effects (°C) . . 631
29.37 Comparison of the calculated results and the geodetic measurement for the reference block 632
29.38 Modal analysis of dam and calculation of Rayleigh damping coefficients 633
29.39 Dynamic inputs at MCL: (left) acceleration response spectra and, (right) acceleration time histories of the scaled main shock, Manjil ground motion 634
29.40 Water pressure (left) hydrostatic pressure distribution (MPa) and (right) time history of the pressure at the index point 635
29.41 Comparison of the displacement time histories (first 20s) under the main shock 636
29.42 Comparison of the non-concurrent maximum first principal stresses (MPa) 637
29.43 Response of the central block (left) maximum displacement and (right) maximum joint opening and sliding 638
29.44 Cracked elements in the full nonlinear model, DYN4, under the main shock 639
29.45 A comprehensive methodology for seismic safety evaluation of the existing concrete dams 640
29.46 Displacement time histories under the main shock and after shock events 641
29.47 Time history of the crest displacement in stream direction for Tabas ground motion 643
29.48 Non-concurrent envelope of the maximum and minimum principal stresses on US and DS faces (Pa) for Tabas ground motion 644
29.49 Extension of the overstressed areas on upstream and downstream faces for Tabas ground motion 644
29.50 Comparison of the non-concurrent displacement envelope of the central cantilever in stream direction for the three scaled ground motions 645
29.51 Non-concurrent envelope of the maximum first principal stress and minimum third principal stress along the height of the central cantilever 645
29.52 Non-concurrent envelope of the maximum first principal stress and minimum third principal stress along the height of the central cantilever 646
29.53 Displacement time history at crest point in stream direction 648
29.54 ETA curves for the crest displacement, left: linear, right: nonlinear . . 648
29.55 Crack profiles from real ground motions and ETAFs 650

29.56Summary of cracked elements from real ground motions and ETAFs 651
29.57Different foundation models 652
29.58Karaj Dam 653
29.59Mode shapes 654
29.60Scaled acceleration and velocity time-histories for near-fault and far-field ground motions 654
29.61Scaled acceleration response spectra of selected records based on the target spectrum 655
29.62Rotational effect 655
29.63The effects of considering permutations of all three earthquake components 656
29.64Non-concurrent envelope of displacement in the stream direction at the central cantilever for the 657
29.65Percentage of overstressed area on the dam face at various DCR values 658
29.66Folsom Dam Geometry and Corresponding Finite Element Mesh . . . 659
29.67Folsom Dam Eigenvalues 659
29.68San Fernando Earthquake 660
29.69Analyses Performed 661
29.70Size effect on foundation analysis (no dam), 5hz 662
29.71Size effect on foundation analysis (no dam), San Fernando 662
29.72Effect of E on crest acceleration, model C, foundation only 662
29.73Effect of mass modeling on foundation and dam using foundation model C, San Fernando; Dam base accelerations 663
29.74Effect of finite element mesh size, Dam Foundation only, San Fernando 663
29.75Effect of Lysmer boundary conditions, dam crest accelerations, foundation model C, San Fernando 664
29.76Effect of mass modeling in Lysmer with foundation model C, foundation and dam, San Fernando 664
29.77Effect of foundation size, Model C, foundation and dam, San Fernando 664
29.78Effect of frequency 665
29.79Effect of frequency, foundation (model C) and dam, optimized height 665
29.80Comparaison Miura/Lysmer San Fernando 666
29.81Effect of frequency, Optimized Height 666
29.82Effect of Rock-Concrete Interface on Acceleration 666
29.83Effect of Rock-Concrete Interface on Stresses 667
29.84Acceleration Comparison of a refined model (no damping) and a Simplified model (massless foundation) at 10% Damping 667
29.85Stress Comparison of a refined model (no damping) and a Simplified model (massless foundation) at 10% Damping 667

30.1 Big picture and the elements of the next-generation dam safety framework 672
30.2 Tallest non-overflow monolith of Pine Flat dam 673

30.3 General characteristics of the selected ground motions; mean = green solid line, median = red solid line, 95% confidence interval = blue dashed lines 674
30.4 Histograms and distributional models for some IMs 674
30.5 Different versions of cloud-based fragility functions for a gravity dam 676
30.6 Response spectra for 21 un-scaled ground motions (Gray: individual ground motions, red: arithmetic mean, blue: geometric mean) 677
30.7 SR-IDA curves for gravity dams 677
30.8 Progressive failure with single record IDA; * means failure; number refers to intensity level 678
30.9 Impact of IM on the MR-IDA curves and their summary 679
30.10 Comparison of different methods for collapse fragility curves fitting . 679
30.11 Sampling of the RVs for mode I and II fracture mechanics (no scale) . 681
30.12 Comparison of fragility curves for mode I and II fracture 682
30.13 Tornado diagram for the mixed-mode fracture 683
30.14 Comparison of all RVs for four LSs under mixed-mode fracture condition 683
30.15 Impact of RV correlation on the uncertainty quantification of the mixed-mode fracture 684
30.16 Outline of the concrete dams fragility analysis 685
30.17 Outline of the concrete dams fragility analysis 687
30.18 Samples of seismic fragility curves and surfaces for concrete dams . . 689
30.19 Comparison of convergence rate and statistics of four UQ techniques 690
30.19 Comparing CMCS-based seismic analyses results computed from FEM and estimated from DOE 692
30.20 Estimation of 55 polynomial coefficients to develop a meta-model for seismic uncertainty 693
30.21 Distribution of first crack on upstream face; top left: Sim-1; first row: 1 to 6; bottom right: Sim-24 695
30.22 Validation of the predicted response surface using LHS method 696
30.23 Dynamic sensitivity of material RVs 698
30.24 Proposed Taguchi based meta-modeling for seismic reliability analysis 698
30.25 Seismic reliability assessment of the cases study example including material uncertainties 700
30.26 Case study dam for reliability analysis and rehabilitation 701
30.27 LEM based model description (loads and geometry) 704
30.28 Estimated failure probability and the confidence intervals for three simulation-based methods; full analytical model 705
30.29 Impact of correlation on the reliability index in reduced model 706
30.30 Box-plots showing dependency of failure probability on dam class and varying parameters (Left to right: crack length, water height, coherency, friction angle, and drain efficiency) 708
30.31 Parametric computed failure probabilities for different dam classes based on finite element simulations; in each plot, the provided range is the bottom-to-top order of the surfaces 709

30.32 Geometry and finite element mesh of the studied arch dams; no scale; with one sample random fields of E_c 710
30.33 Detailed vibration anatomy of the homogeneous pilot dam 710
30.34 Detailed vibration anatomy of the heterogeneous pilot dam 711
30.35 Summary of frequency variation for all six dams 712
30.36 Finite element model of the coupled dam-reservoir-foundation system, including three realizations of a heterogeneous dam with different correlation lengths 713
30.37 Anatomy of outputs from the random field simulation of a gravity dam 715
30.38 Impact of spatial correlation length on the variability of results 716
30.39 Impact of a single- or double-random field assumption 716
30.40 Preparing the numerical models with concrete heterogeneity and different correlation length 718
30.41 Response summary of the pilot dam model; E_c as random field with correlation length ratio of 0.04 719
30.42 DV^1 (crack 1) profile of all 24 E_c RF models with normalized correlation length of 0.04; all the plots are at t=15 s 720
30.43 FEM based model description (loads and boundary conditions) 721
30.44 Proposed hybrid FEM-SVM methodology for seismic analysis of concrete dams 722
30.45 Binary classification of seismic responses with two RVs 724
30.46 SVM regression for non-failure crest displacement [mm] 724
30.47 Correlation map between input IM parameters 726
30.48 Quality of prediction based on different forecasting techniques and QoIs. 727
30.49 Feature selection using different subsets for two response quantities. . 728
30.50 Failure probability estimation error using various machine learning techniques for the pilot hydrological hazard model 731
30.51 Estimated failure probability under aging risk 732
30.52 Estimated failure probability for different dam classes, correlation and water level subjected to seismic hazard 733
30.53 Description of case study, Koyna Dam, including the dam body, foundation, and reservoir 734
30.54 Schematic presentation of different prediction tasks 736
30.55 Prediction accuracy of the algorithms in PT-1 considered for the validation set (8,000 cases) and 100 iterations 737
30.56 The first 60 random gravity dam shapes generated based on a Matlab code; the box size is 150 $\times$ 225 m in all cases 738
30.57 Prediction accuracy for the algorithms in PT-4 (only based on MAPE) 738
30.58 Relative influence of the predictors for 100 training repetitions; and partial dependence on WL and shape 739
30.59 Partial dependence plots for 14 RVs in PT-4 740

30.60Model description of four case studies in this paper including geometry, loads, and sample QoIs; (a) analytical gravity dam; (b) 2D simplified finite element gravity dam model for seismic analysis; (c) 3D reservoir-foundation-arch-dam for both seismic analysis and free vibration 741
30.61Example 1; PCE meta-model; LAR technique; Reference model $N_{LHS} = 1000$; N_{DOE} is variable; meta-modeling is based on Z 742
30.62Example 1; Uncertainty quantification of PCE meta-model based on 100 replications of the analyses; N_{DOE} is variable; meta-modeling is based on Z 743
30.63Example 2; Uncertainty quantification of PCE meta-model; N_{DOE} is variable; black line: crest displacement in [mm]; red line: heel vertical stress in [MPa]; Note: the red curves are shifted a bit right to avoid overlapping with black ones 744
30.64Example 3; Coupled arch dam; PCE meta-model; LHS-based $N_{DOE} = 50$; elemental principal stresses over dam body; Unit = [Pa] 745
30.65Example 4; Layered arch dam; $N_{LHS} = 1000$; $N_{DOE} = 200$; two QoIs 746

31.1 Concerns with nonlinear analysis 754
31.2 Anatomy of a Seismic Probability Risk Assessment in Nuclear structures 760
31.3 1:6 scale model reinforced containment vessels 764
31.4 PCCV Model 765

32.1 Containment structure (reactor building envelope), vertical and horizontal sections [344] 776
32.2 Distribution of coefficient of deterioration β due to own weight, post-tensioning and after 25 years of combined ASR and creep effects (a) before an earthquake and (b) after an earthquake (Analysis of structural state in 2010; Interior view) [344] 784
32.3 Ikata Turbine generator foundation [816] 787
32.4 Crystal River Unit 3 characteristics [712] 790
32.5 Post-tensioning cables [712] 790
32.6 Six anchoring buttresses [712] 791
32.7 Five inch tendon conduits [712] 791
32.8 Concrete and liner removal sequence [712] 792
32.9 Tendon pattern [712] 792
32.10Delamination of Crystal River [712] 793
32.11Group 7 Finite element analyses; global sub-model [649] 797
32.12Detailed model [649] 798
32.13Group 1 Finite Element Analyses [649] 799
32.14CR-3 Containment radial displacements [649] 802
32.15CR-3 bay 34, cracking and crack opening displacement [649] 803

32.16Plot of delamination damage in Bay 34. Shown are the measurements of the delamination gap both by impulse response test and by core bores [649] . . . 803
32.17Maximum principal stresses (psi) [649] . . . 804
32.18Bay 34 wall segment delamination . . . 804
32.19Plot of maximum principal stresses in delamination. f'_t =360 psi. [649] . . . 804
32.20Models . . . 807
32.21Impact of AAR on the Saint-Laurent nuclear power station . . . 809
32.22Reported impact of ASR on Tihange nuclear power plant [821] . . . 810

33.1 CR Idealization . . . 814
33.2 Finite element mesh . . . 814
33.3 Delamination of CR captured by a fracture mechanics based approach 816
33.4 Three scenarios of investigation: A: No ASR; B: ASR with 40% damage; and C: ASR without Damage. . . . 817
33.5 Geometry, material groups, role of joint elements, and finite element mesh . . . 818
33.6 Reinforcement details . . . 818
33.7 Seismic hazard characterization around the nuclear site . . . 821
33.8 Six adopted ETF . . . 821
33.9 Acceleration and displacement time history of 25 random signals for each scenario . . . 822
33.10Response of CEB under static + ASR analysis after 40 years . . . 823
33.11ETA-based displacements and the mean differences . . . 824
33.12Principal stresses capacity curves . . . 824
33.13Crack profile from a sample ETA simulation at identical time steps . . 825
33.14Displacement-based fragility curves . . . 826
33.15Displacement-based fragility surfaces . . . 827

34.1 Heavily reinforced transmission tower foundation partially affected by AAR . . . 832
34.2 Geometry of the massive reinforced concrete structure . . . 833
34.3 Field strain measurements . . . 834
34.4 Reinforcement . . . 834
34.5 Finite element mesh . . . 835
34.6 Finite element analysis of various cases . . . 835
34.7 Finite Element Analysis summary; COD . . . 836
34.8 Close-up of analysis 4: Strains . . . 836
34.9 Kinetics of analysis 4 . . . 836
34.10General view of the viaduct [511] . . . 837
34.11Finite element mesh . . . 839
34.12Comparison of the uniform, partial and fully non-uniform models . . . 841
34.13Domain of investigation for AAR expansion (1970-2015: dry and 2016-2070: wet condition) . . . 842

34.14Latin Hypercube based sampling method 843
34.15Predicting degradation of E and f_t based on optimization of experimental tests 844
34.16Identification of two distinct structural responses attributed to delayed AAR expansion 845
34.17Rebar spatial and temporal stress distributions and cracking for two identified structural responses 846
34.18Individual probabilistic-based simulations and the 16, 50 and 84% fractiles 847
34.19Fragility curves 848
34.20Engineering interpretation of results 848

35.1 Cracking at Seabrook 854
35.2 Integration of the three major components of the LAR, adapted from [794] 855
35.3 Concrete and specimens 856
35.4 Shear beam tests 858
35.5 Splitting structural crack 859
35.6 Shear test results 859
35.7 Crack index measurements 860
35.8 Determination of volumetric ASR expansion 862
35.9 Directional expansion measurements [859] 863
35.10Representative plots of the finite element analyses 867
35.11in-plane and out-of-plane shear in a CEB 875
35.12Finite element simulation of specimen splitting 877
35.13Issues about shear tests 879
35.14Impacts of temperature, relative humidity, and reinforcement on limited surface CI measurements 881
35.15Early age compressive strength increase in concrete [228] 883
35.16Concerns about out-of-plane expansion measurements 884
35.17Crack patterns caused by reactive sand and aggregates 885
35.18Causes and examples of delamination in walls without out-of-plane reinforcement 887
35.19Example of overlayed four noded shell element 892
35.20Stress induced anisotropy during volumetric ASR expansion 893
35.21Problems arising from fitting $y = f(x)$ through interpolation 894

A.1 Test set-up and acting forces, for a prismatic specimen 988
A.2 Principle of the Wedge Splitting Test Set-up 988
A.3 Dimensions of the specimens for the wedge splitting test (all dimensions in mm) 990
A.4 Specimen preparation 990
A.5 Representative Experimental Load-COD Curve 991
A.6 Definition of the work of fracture and specific fracture energy 992
A.7 Bilinear softening diagram 993

A.8 G_F *vs* G_f 994
A.9 Compliance and stress intensity factors in terms of crack length a . . . 995
A.10 Measuring specimen dimensions 996
A.11 Wedge Splitting Test Parts dimensions 997
A.12 From cores to small prismatic specimens 997
A.13 Details of the specimens 998

B.1 Interaction among KumoNoSu, Merlin and Spider 1000
B.2 Interaction among different programs in Matlab-based code 1001
B.3 General algorithm in `P0.m` 1003
B.4 Different types of uncertainties in PPACS 1004
B.5 General algorithm in `P1Sta.m` 1005
B.6 User defined Excel file with distribution models, mean, standard deviation and L/U bounds. 1005
B.7 User defined Excel file with possible correlation coefficients. 1006
B.8 Sampling the material properties based on algorithm in figure B.5 . . . 1006
B.9 General algorithm in `P1Dyn.m` 1007
B.10 Different types of dynamic analysis methodologies in PPACS 1007
B.11 Treatment of IMs in `P4.m` 1008

List of Tables

1.1 Examples of boundary conditions in structural analysis 29

2.1 Selected Examples of Diffusion Problems 35
2.2 Reflectivity of the selected surfaces [510] 44
2.3 Comparison of Scalar and Vector Field Problems 45

4.1 Fracture toughness of selected materials 72

5.1 Empirically fitted parameters for the B3 model 101

6.1 Amplitude of standard event as a function of epicenter 113

9.1 Similarities between column equation and size effect laws 164
9.2 Experimentally Determined Values of Bf_t', [92] 171

10.1 Activation energies for various cement pastes 192
10.2 Typical rate of penetration of carbonation 195
10.3 The influence of curing time on carbonation rate in $mm/w^{0.5}$ (Adapted from [421]) 196

11.1 Variation of $\epsilon(\infty)$, τ_c and τ_l for 4 specimens, [523] 208
11.2 Triaxial Weights 213
11.3 Average compressive strength and elastic properties of concrete dams subject to aging [250] 216

12.1 Sample of Excel file storing load information 232
12.2 Example of Data Repository 233
12.3 Example of Correlation Between Random variables 233

13.1 Shape Functions and Natural Derivatives for Q8 Element 253
13.2 Integration Points and Weights for Gauss-Quadrature Formulaes Over the Interval $[-1, 1]$ 256

13.3 Natural Coordinates of Bilinear Quadrilateral Nodes 258

14.1 Non-linear analyses types 272
14.2 Benchmark problems for ASR code “validation” 292

16.1 Evaluation of Various Boundary Conditions 342

17.1 Required Material Properties for Seepage Analysis 349

18.1 Reliability of steel and concrete structures 374
18.2 Sample maturity matrix for assessing community engagement; adopted from National Research Council [622] 388

19.1 Parameters considered in the pilot example 401

20.1 Relationship between m and k in polynomial form 425

21.1 The range of damage of structural and non-structural components for various target building performance levels (Table C1-2) [296] . . . 449

23.1 Period-dependent coefficients of Boore, Joyner, and Fumal [139] model 477
23.2 Estimated V_S based on site class 478

26.1 Definition of the proposed damage states for gravity dams 555

27.1 Common foundation-related PFMs for concrete dams 572
27.2 Categories used to rank identified PFMs 573
27.3 Proposed index criteria for linear analysis 579

29.1 FSS Calculation for the upper crack of block 6 604
29.2 Thermal properties found in an arch gravity dam 607
29.3 Initial and final parameter values in system identification study; Reference temperature 60°C 611
29.4 Temperatures used for the Poglia Dam analysis 615
29.5 Main characteristics of Dez Dam 621
29.6 Recommended values of n for different months (average day of the month) [596] 626
29.7 Thermal properties of dam-environmental system 628
29.8 Mechanical properties of materials based on calibration 632
29.9 Mechanical and strength properties of concrete in static and dynamic conditions 635
29.10 Foundation Sizes and Properties 659
29.11 Evaluation of Various Boundary Conditions 660

30.1 Safety assessment examples and cross-referencing to corresponding theory 671

30.2 Demand models and IM comparisons for displacement response 675
30.3 Parameters defining the zero thickness joint element 681
30.4 Characteristics of concrete and rock 682
30.5 Summary of the fragility analysis of concrete dams, adopted from [391] 688
30.6 Material properties and modeling parameters 690
30.7 Material properties for the finite element model 694
30.8 Tabulated simulations in a BBED with $k = 4$ 694
30.9 Summary of the BBED simulations 695
30.10 Tabulation of Point Estimate Method; Nonlinear Analysis; Retrofitted Dam. 702
30.11 Tabulation of Taylor's Series Finite Difference Estimate Method; Nonlinear Analysis; Retrofitted Dam. 702
30.12 Parameters considered for the LEM analytical limit state function ... 704
30.13 Comparison of classical reliability methods 705
30.14 Model and material parameters for probabilistic finite element simulations (Note: for the lognormal distribution in the form of $LogN(\mu, \sigma)$, the mean and standard deviations are: $e^{\mu+\sigma^2/2}$ and $\sqrt{(e^{\sigma^2-1})e^{2\mu+\sigma^2}}$, respectively.) 707
30.15 Basic characteristics and material properties of concrete arch dams .. 709
30.16 Coefficients of the analytical model for a shape-dependent frequency analysis 713
30.17 Summary of the ground motion IMs for gravity dam 722
30.18 GOF for the displacement with all the features 726
30.19 GOF for the stress with all the features 726
30.20 Model parameters for analytical limit state function 729
30.21 Material properties for the concrete and foundation 735

31.1 Analogy between nuclear and building safety guidelines 756

32.1 Input values adjusted for matching 795
32.2 Material properties for Group 1 Analyses 799
32.3 Material properties used in the detensioning simulations 801

33.1 Load increment in CR analysis by authors 815
33.2 Concrete mechanical properties 819
33.3 Characteristics of the ASR model 820
33.4 Rebar mechanical properties 820

34.1 Mean and minimum values of concrete properties [511] 838
34.2 Central fractiles for the two conditional assessments of Class I case; number inside the parentheses represents absolute date 849

35.1 Severity zones [794] 861
35.2 Acceptance criteria for CI measurements [635] 861

35.3 Recommendations for confirming expansion behavior at Seabrook Station is similar to test programs [635] 863
35.4 ASR Expansion Limits For Structural Limit States 865
35.5 Load combinations [794] 866
35.6 Some commonly used scale factors [778]. 872
35.7 Comparison between FSEL test conditions and Seabrook Station 882

Part I
Fundamentals

Chapter 1
Review of Solid Mechanics; Vector Fields

Abstract
Mechanics is where it all starts. Rooted in mathematics, it provides a solid underpinning for subsequent engineering solutions. Rather than providing a classical introductory "Mechanics of Materials" approach, we have opted for the more concise and powerful continuum mechanics based one. Far from exhaustive, this chapter limits itself to the fundamental concepts.
As the title indicates, we focus on solid mechanics characterized by vectorial fields. A subsequent chapter will address scalar field problems in mechanics (such as the heat equation).

1.1 Introduction

Coverage of the advanced structural analysis of infrastructure requires a solid grounding in the fundamentals of mechanics and finite element. The objective of this chapter is indeed to provide a succinct review. The approach taken is to proceed from a rigorous *continuum mechanics* paradigm using tensorial notation first, and then expand in the more traditionally used Cartesian coordinate system.

1.1.1 Indicial Notation

Different sets of notations are commonly used in engineering:

Matrix: Finite Element, $[A]$, $[\sigma]$, $\{F\}$
Indicial: Mechanics cartesian, F_x, σ_{ij}, C_{ijkl}
Tensorial: Mechanics cartesian/curvilinear, $\mathbf{F}$, $\boldsymbol{\sigma}$, $\mathbf{C}$
Engineering: (Timoshenko/Voigt) Elasticity, σ_x, γ_{xy}

$$\underbrace{\mathbf{x}.\mathbf{A}.\mathbf{x}}_{\text{tensor}} = \underbrace{\lfloor \mathbf{x} \rfloor \, [\mathbf{A}] \, \{\mathbf{x}\}}_{\text{matrix}} = \underbrace{x_i A_{ij} x_j}_{\text{indicial}} \tag{1.1}$$

In the following sections, we shall briefly explain the last two.
Whereas the Engineering notation may be the simplest and most intuitive one, it often leads to long and repetitive equations. Alternatively, the tensor will lead to shorter and more compact forms.

While working on general relativity, Einstein got tired of writing the summation symbol with its range of summation below and above (such as $\sum_{i=1}^{n=3} a_{ij}b_i$) and noted that most of the time the upper range (n) was equal to the dimension of space (3 for us, 4 for him), and that when the summation involved a product of two terms, the summation was over a repeated index (i in our example). Hence, he decided that there is no need to include the summation sign $\sum$ if there were repeated indices (i), and thus any repeated index is a dummy index and is summed over the range 1 to 3. An index that is not repeated is called a free index and assumed to take a value from 1 to 3. Hence, this so called indicial notation is also referred to Einstein's notation. The following rules define indicial notation:

1. If there is one letter index, that index goes from i to n (range of the tensor). For instance:
$$a_i = a^i = \lfloor\, a_1 \; a_2 \; a_3 \,\rfloor = \left\{ \begin{array}{c} a_1 \\ a_2 \\ a_3 \end{array} \right\} \qquad i = 1, 3 \tag{1.2}$$
assuming that $n = 3$.
2. A repeated index will take on all the values of its range, and the resulting tensors summed. For instance:
$$a_{1i}x_i = a_{11}x_1 + a_{12}x_2 + a_{13}x_3 \tag{1.3}$$
3. Tensor's order:
   - First order tensor (such as force) has only one free index:
   $$a_i = a^i = \lfloor\, a_1 \; a_2 \; a_3 \,\rfloor \tag{1.4}$$
   other first order tensors are $a_{ij}b_j$, F_{ikk}, $\varepsilon_{ijk}u_jv_k$.
   - Second order tensor (such as stress or strain) will have two free indices.
   $$D_{ij} = \begin{bmatrix} D_{11} & D_{12} & D_{13} \\ D_{21} & D_{22} & D_{23} \\ D_{31} & D_{32} & D_{33} \end{bmatrix} \tag{1.5}$$
   other examples are A_{ijip}, $\delta_{ij}u_kv_k$.
   - A fourth order tensor (such as Elastic constants) will have four free indices.
4. Derivatives of tensor with respect to x_i is written as $,i$. For example:
$$\frac{\partial \Phi}{\partial x_i} = \Phi_{,i}; \; \frac{\partial v_i}{\partial x_i} = v_{i,i}; \; \frac{\partial v_i}{\partial x_j} = v_{i,j}; \; \frac{\partial T_{i,j}}{\partial x_k} = T_{i,j,k}; \tag{1.6}$$

Usefulness of the indicial notation is in presenting systems of equations in compact form. For instance:

$$x_i = c_{ij}z_j \equiv \left\{ \begin{array}{l} x_1 = c_{11}z_1 + c_{12}z_2 + c_{13}z_3 \\ x_2 = c_{21}z_1 + c_{22}z_2 + c_{23}z_3 \\ x_3 = c_{31}z_1 + c_{32}z_2 + c_{33}z_3 \end{array} \right. \tag{1.7}$$

1.1.1.1 Notation

Tensor Notation In tensor notation the indices are not shown. While cartesian indicial equations apply only to Cartesian coordinates, expressions in tensor notation are independent of the coordinate system and apply to other coordinate systems such as cylindrical, curvilinear, etc.

In tensor notation, we indicate tensors of order one or greater in boldface letters. It is usually recommended to use lower case letters for tensors of order one and upper case letters for tensors of order 2 and above. We distinguish between tensor notation and matrix notation by using dots and colons between terms, as in $\mathbf{a}.\mathbf{b} \equiv a_i b_i$ (the '.' indicates a contraction of a pair of repeated indices which appear in the same order), and $\mathbf{A} : \mathbf{B} \equiv A_{ij} B_{ij}$. or $\sigma_{ij} = C_{ijkl}\varepsilon_{kl}$ is equivalent to $\boldsymbol{\sigma} = \mathbf{C} : \boldsymbol{\varepsilon}$.

Voigt Notation In finite element, symmetric second-order tensors are often written as column matrices. This conversion, and the one of other higher-order tensors into column matrices, is called Voigt notation. The Voigt rule depends on whether the tensor is a kinetic quantity (such as stress) or a kinematic one (such as strain).

$$\boldsymbol{\sigma} \equiv \begin{bmatrix} \sigma_{11} & \sigma_{12} \\ \sigma_{21} & \sigma_{22} \end{bmatrix} \rightarrow \begin{Bmatrix} \sigma_{11} \\ \sigma_{22} \\ \sigma_{12} \end{Bmatrix} = \begin{Bmatrix} \sigma_1 \\ \sigma_2 \\ \sigma_3 \end{Bmatrix} = \{\boldsymbol{\sigma}\} \tag{1.8}$$

$$\boldsymbol{\varepsilon} \equiv \begin{bmatrix} \varepsilon_{11} & \varepsilon_{12} \\ \varepsilon_{21} & \varepsilon_{22} \end{bmatrix} \rightarrow \begin{Bmatrix} \varepsilon_{11} \\ \varepsilon_{22} \\ 2\varepsilon_{12} \end{Bmatrix} = \begin{Bmatrix} \varepsilon_1 \\ \varepsilon_2 \\ \varepsilon_3 \end{Bmatrix} = \{\boldsymbol{\varepsilon}\} \tag{1.9}$$

1.1.2 Tensors

We generalize the concept of a vector by introducing the tensor ($\mathbf{T}$), which essentially *exists to operate on vectors* $\mathbf{v}$ *to produce other vectors* (or on tensors to produce other tensors!). We designate this operation by $\mathbf{T}\cdot\mathbf{v}$ or simply $\mathbf{T}\mathbf{v}$. We hereby adopt the tensor (or dyadic notation) for tensors as linear vector operators

$$\mathbf{u} = \mathbf{T}\cdot\mathbf{v} \text{ or } u_i = T_{ij} v_j \tag{1.10}$$

$$\mathbf{u} = \mathbf{v}\cdot\mathbf{S} \text{ where } \mathbf{S} = \mathbf{T}^T \tag{1.11}$$

Whereas a tensor is essentially an operator on vectors (or other tensors), it is also a physical quantity independent of any particular coordinate system yet specified most conveniently by referring to an appropriate system of coordinates.

Tensors frequently arise as physical entities whose components are the coefficients of a linear relationship between vectors. A tensor is classified by the rank or order. A Tensor of order zero is specified in any coordinate system by one coordinate and is a scalar. A tensor of order one has three coordinate components in space, hence it is a vector. In general 3-D, space the number of components of a tensor is 3^n where n is the order of the tensor. Force and stress are tensors of order 1 and 2 respectively.

1.1.2.1 Operations

The sum of two tensors (must be of the same order) is simply defined as:

$$\mathbf{S}_{ij} = \mathbf{T}_{ij} + \mathbf{U}_{ij} \tag{1.12}$$

The scalar multiplication of a (second order) tensor is defined by:

$$\mathbf{S}_{ij} = \lambda \mathbf{T}_{ij} \tag{1.13}$$

The outer product of two tensors is the tensor whose components are formed by multiplying each component of one of the tensors by every component of the other. This produces a tensor with an order equal to the sum of the orders of the factor tensors.

$$\begin{aligned} a_i b_j &= T_{ij} \quad \text{or} \left\{ \quad \right\}_{nx1} \lfloor \quad \rfloor_{1xm} = \left[\quad \right]_{nxm} \\ v_i F_{jk} &= b_{ijk} \\ D_{ij} T_{km} &= \phi_{ijkm} \end{aligned} \tag{1.14}$$

The inner product of two tensors: contraction of one index from each tensor

$$\begin{aligned} & a_i b_i \\ a_i E_{ik} &= f_k \quad \text{or} \lfloor \quad \rfloor_{1xm} \left[\quad \right]_{mxn} = \lfloor \quad \rfloor_{1xn} \\ E_{ij} F_{jm} &= G_{im} \text{ or } \left[\quad \right]_{nxp} \left[\quad \right]_{pxm} = \left[\quad \right]_{nxm} \end{aligned} \tag{1.15}$$

The cross product can be defined

$$\mathbf{a} \times \mathbf{b} = \varepsilon_{pqr} a_q b_r \mathbf{e}_p = (a_y b_z - a_z b_y)\mathbf{i} + (a_z b_x - a_x b_z)\mathbf{j} + (a_x b_y - a_y b_x)\mathbf{k} \tag{1.16}$$

In the second equation, there is one free index p thus there are three equations, there are two repeated (dummy) indices q and r, thus each equation has nine terms. ε_{pqr} is called the permutation symbol and is defined as

$$\varepsilon_{pqr} = \begin{cases} 1 & \text{If the value of } i,j,k \text{ are an even permutation of 1,2,3} \\ & \text{(i.e. if they appear as 1 2 3 1 2)} \\ -1 & \text{If the value of } i,j,k \text{ are an odd permutation of 1,2,3} \\ & \text{(i.e. if they appear as 3 2 1 3 2)} \\ 0 & \text{If the value of } i,j,k \text{ are not a permutation of 1,2,3} \\ & \text{(i.e. if two or more indices have the same value)} \end{cases} \tag{1.17}$$

The scalar product of two tensors is defined as

$$\mathbf{T} : \mathbf{U} = T_{ij} U_{ij} \tag{1.18}$$

in any rectangular system. The following inner product axioms are satisfied:

$$\begin{aligned}\mathbf{T}:\mathbf{U} &= \mathbf{U}:\mathbf{T}\\ \mathbf{T}:(\mathbf{U}+\mathbf{V}) &= \mathbf{T}:\mathbf{U}+\mathbf{T}:\mathbf{V}\\ \alpha(\mathbf{T}:\mathbf{U}) &= (\alpha\mathbf{T}):\mathbf{U}=\mathbf{T}:(\alpha\mathbf{U})\\ \mathbf{T}:\mathbf{T} &> 0 \text{ unless } \mathbf{T}=\mathbf{0}\end{aligned}$$

1.1.2.2 Rotation of Axes

Consider two different sets of Cartesian orthogonal coordinate systems $\{\mathbf{e}_1,\mathbf{e}_2,\mathbf{e}_3\}$ and $\{\overline{\mathbf{e}}_1,\overline{\mathbf{e}}_2,\overline{\mathbf{e}}_3\}$, any vector $\mathbf{v}$ can be expressed in one system or the other

$$\mathbf{v} = v_j\mathbf{e}_j = \overline{v}_j\overline{\mathbf{e}}_j \tag{1.19}$$

To determine the relationship between the two sets of components, we consider the dot product of $\mathbf{v}$ with one (any) of the base vectors

$$\overline{\mathbf{e}}_i\cdot\mathbf{v} = \overline{v}_i = v_j(\overline{\mathbf{e}}_i\cdot\mathbf{e}_j) \tag{1.20}$$

We can thus define the nine scalar values

$$a_i^j \equiv \overline{\mathbf{e}}_i\cdot\mathbf{e}_j = \cos(\overline{x}_i, x_j) \tag{1.21}$$

which are the direction cosines between the nine pairs of base vectors. A covariant transformation will transform a tensor from one basis to another:

$$\overline{v}_j = a_j^p v_p \tag{1.22}$$

note that the free index in the first and second equations appear on the upper and lower index respectively.
Consider the transformation of a vector $\mathbf{V}$ from $(\mathbf{X},\mathbf{Y},\mathbf{Z})$ coordinate system to $(\mathbf{x},\mathbf{y},\mathbf{z})$. From Eq. 1.22

$$V_j = a_j^p\overline{V}_p \text{ or } \begin{cases} V_1 = a_1^1\overline{V}_1 + a_1^2\overline{V}_2 + a_1^3\overline{V}_3\\ V_2 = a_2^1\overline{V}_2 + a_1^2\overline{V}_2 + a_2^3\overline{V}_3\\ V_3 = a_3^1\overline{V}_3 + a_1^2\overline{V}_2 + a_3^3\overline{V}_3\end{cases} \tag{1.23}$$

or,

$$\begin{Bmatrix} V_x\\ V_y\\ V_z\end{Bmatrix} = \underbrace{\begin{bmatrix} a_x^X & a_x^Y & a_x^Z\\ a_y^X & a_y^Y & a_y^Z\\ a_z^X & a_z^Y & a_z^Z\end{bmatrix}}_{a_j^k} \begin{Bmatrix} V_X\\ V_Y\\ V_Z\end{Bmatrix} \tag{1.24}$$

where a_i^j is the direction cosine of axis i with respect to axis j

- $a_x^j = (a_x^X, a_x^Y, a_x^Z)$ direction cosines of $\mathbf{x}$ with respect to $\mathbf{X},\mathbf{Y}$ and $\mathbf{Z}$
- $a_y^j = (a_y^X, a_y^Y, a_y^Z)$ direction cosines of $\mathbf{y}$ with respect to $\mathbf{X},\mathbf{Y}$ and $\mathbf{Z}$
- $a_z^j = (a_z^X, a_z^Y, a_z^Z)$ direction cosines of $\mathbf{z}$ with respect to $\mathbf{X},\mathbf{Y}$ and $\mathbf{Z}$

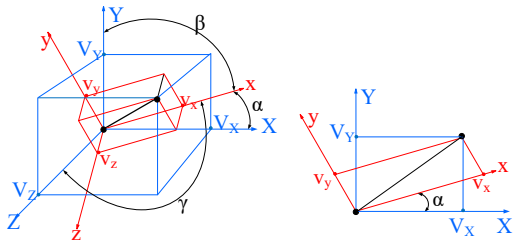

(a) 3D (b) 2D

Fig. 1.1: Vector transformation

For the 2D case, the transformation matrix is written as

$$T = \begin{bmatrix} a_1^1 & a_1^2 \\ a_2^1 & a_2^2 \end{bmatrix} = \begin{bmatrix} \cos\alpha & \cos\beta \\ \cos\gamma & \cos\alpha \end{bmatrix} \tag{1.25}$$

but since $\gamma = \frac{\pi}{2} + \alpha$ and $\beta = \frac{\pi}{2} - \alpha$, then $\cos\gamma = -\sin\alpha$ and $\cos\beta = \sin\alpha$, thus the transformation matrix becomes

$$T = \begin{bmatrix} \cos\alpha & \sin\alpha \\ -\sin\alpha & \cos\alpha \end{bmatrix} \tag{1.26}$$

1.1.2.3 Tensor Transformation

Rotation of a second order tensor T_{jq}:

$$\begin{aligned} \overline{u}_j &= T_{jq}\overline{v}_q \\ \overline{u}_i &= a_i^j u_j \\ &= a_i^j T_{jq} v_q \\ &= a_i^j T_{jq} a_p^q \overline{v}_p \end{aligned}$$

But we also have $\overline{u}_i = \overline{T}_{ip}\overline{v}_p$ in the barred system, equating these two expressions we obtain

$$\overline{T}_{ip} = a_i^j a_p^q T_{jq} \tag{1.27}$$

hence,

$$\overline{T}_{ip} = a_i^j a_p^q T_{jq} \text{ in Matrix Form } [\overline{T}] = [A]^T[T][A] \tag{1.28}$$

$$T_{jq} = a_i^j a_p^q \overline{T}_{ip} \text{ in Matrix Form } [T] = [A][\overline{T}][A]^T \tag{1.29}$$

If we consider the 2D case, from Eq. 1.26

$$A = \begin{bmatrix} \cos\alpha & \sin\alpha & 0 \\ -\sin\alpha & \cos\alpha & 0 \\ 0 & 0 & 1 \end{bmatrix}$$

$$T = \begin{bmatrix} T_{xx} & T_{xy} & 0 \\ T_{xy} & T_{yy} & 0 \\ 0 & 0 & 0 \end{bmatrix}$$

$$\overline{T} = \begin{bmatrix} \overline{T}_{xx} & \overline{T}_{xy} & 0 \\ \overline{T}_{xy} & \overline{T}_{yy} & 0 \\ 0 & 0 & 0 \end{bmatrix} = A^T T A$$

Substituting and simplifying ($\sin 2\alpha = 2\sin\alpha\cos\alpha$ and $\cos 2\alpha = \cos^2\alpha - \sin^2\alpha$)

$$\begin{Bmatrix} \overline{T}_{xx} \\ \overline{T}_{yy} \\ \overline{T}_{xy} \end{Bmatrix} = \begin{bmatrix} \cos^2\theta & \sin^2\theta & 2\sin\theta\cos\theta \\ \sin^2\theta & \cos^2\theta & -2\sin\theta\cos\theta \\ -\sin\theta\cos\theta & \cos\theta\sin\theta & \cos^2\theta - \sin^2\theta \end{bmatrix} \begin{Bmatrix} T_{xx} \\ T_{yy} \\ T_{xy} \end{Bmatrix} \tag{1.30}$$

1.1.2.4 Principal Values of Symmetric Second Order Tensors

Two fundamental tensors in continuum mechanics are second order and symmetric (stress and strain); we examine some important properties of these tensors. For every symmetric tensor T_{ij} defined at some point in space, there is associated with each direction (specified by unit normal n_j) at that point a vector given by the inner product

$$v_i = T_{ij} n_j \tag{1.31}$$

If the direction is one for which v_i is parallel to n_i, the inner product is

$$T_{ij} n_j = \lambda n_i \tag{1.32}$$

and the direction n_i is called a principal direction of T_{ij}. Since $n_i = \delta_{ij} n_j$, this can be rewritten as

$$(T_{ij} - \lambda\delta_{ij}) n_j = 0 \tag{1.33}$$

which represents a system of three equations for the four unknowns n_i and λ.

$$\begin{aligned} (T_{11} - \lambda) n_1 + T_{12} n_2 + T_{13} n_3 &= 0 \\ T_{21} n_1 + (T_{22} - \lambda) n_2 + T_{23} n_3 &= 0 \\ T_{31} n_1 + T_{32} n_2 + (T_{33} - \lambda) n_3 &= 0 \end{aligned}$$

To have a non-trivial solution ($n_i \neq 0$), the determinant of the coefficients must be zero:

$$|T_{ij} - \lambda\delta_{ij}| = 0 \tag{1.34}$$

Expansion of this determinant leads to the following characteristic equation

$$\lambda^3 - I_T\lambda^2 + II_T\lambda - III_T = 0 \tag{1.35}$$

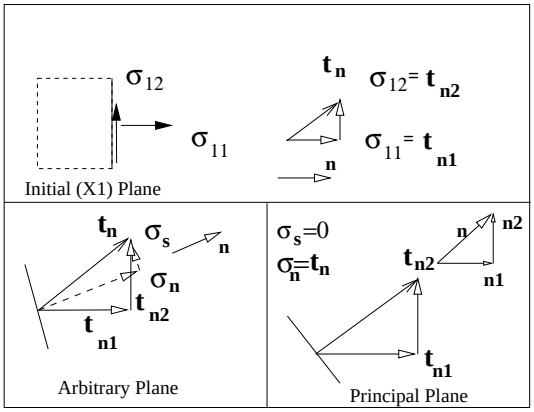

Fig. 1.2: Principal directions of tensor of order two

where the roots are called the principal values of T_{ij} and

$$\begin{aligned} I_T &= T_{ii} = \text{tr}\, T_{ij} \\ II_T &= \frac{1}{2}(T_{ii}T_{jj} - T_{ij}T_{ij}) \\ III_T &= |T_{ij}| = \det T_{ij} \end{aligned}$$

are called the first, second, and third invariants respectively of T_{ij}. It is customary to order those roots as $\lambda_{(1)} > \lambda_{(2)} > \lambda_{(3)}$. In terms of the principal stresses, those invariants can be simplified into

$$I_T = T_{(1)} + T_{(2)} + T_{(3)} \tag{1.36}$$

$$II_T = -(T_{(1)}T_{(2)} + T_{(2)}T_{(3)} + T_{(3)}T_{(1)}) \tag{1.37}$$

$$III_T = T_{(1)}T_{(2)}T_{(3)} \tag{1.38}$$

For a symmetric tensor with real components, the principal values are also real. If those values are distinct, the three principal directions are mutually orthogonal.

1.1.3 Physical interpretation of Stress Invariants

An octahedral plane is one which makes equal angles with respect to each of the principal-stress directions; the normal to this plane is given by

$$\mathbf{n} = \frac{1}{\sqrt{3}} \begin{Bmatrix} 1 \\ 1 \\ 1 \end{Bmatrix} \tag{1.39}$$

The vector of traction on this plane is

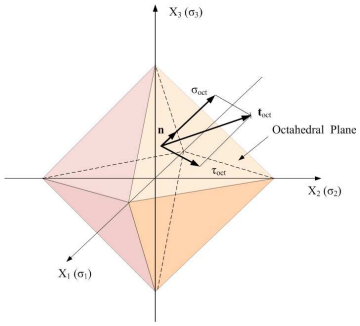

Fig. 1.3: Octahedral plane

$$\mathbf{t}_{oct} = \frac{1}{\sqrt{3}} \begin{Bmatrix} \sigma_1 \\ \sigma_2 \\ \sigma_3 \end{Bmatrix} \tag{1.40}$$

and the normal component of the stress on the octahedral plane is given by

$$\sigma_{oct} = \mathbf{t}_{oct} \cdot \mathbf{n} = \frac{\sigma_1 + \sigma_2 + \sigma_3}{3} = \frac{1}{3}\mathbf{I}_1 = \sigma_{hyd} \tag{1.41}$$

The octahedral shear stress is obtained from

$$\tau_{oct}^2 = |\mathbf{t}_{oct}|^2 - \sigma_{oct}^2 = \frac{\sigma_1^2}{3} + \frac{\sigma_2^2}{3} + \frac{\sigma_3^2}{3} - \frac{(\sigma_1 + \sigma_2 + \sigma_3)^2}{9} \tag{1.42}$$

Upon algebraic manipulation, it can be shown that

$$\tau_{oct} = \sqrt{\frac{2}{3} J_2} \tag{1.43}$$

and finally, the direction of the octahedral shear stress is given by

$$\cos 3\theta = \sqrt{2} \frac{J_3}{\tau_{oct}^3} \tag{1.44}$$

The elastic strain energy (total) per unit volume can be decomposed into two parts: $U = U_1 + U_2$, where

$$\begin{array}{ll} U_1 = \frac{1-2\nu}{E} I_1^2 & \text{Dilational energy} \\ U_2 = \frac{1+\nu}{E} J_2 & \text{Distortional energy} \end{array} \tag{1.45}$$

1.1.4 Review Integral Equations

Basic Operations

$$\mathbf{A}+\mathbf{B}=\mathbf{B}+\mathbf{A} \tag{1.46}$$

$$\mathbf{A}\times\mathbf{B}=-\mathbf{B}\times\mathbf{A} \tag{1.47}$$

$$\mathbf{A}=A_x\mathbf{i}+A_y\mathbf{j}+A_z\mathbf{k} \tag{1.48}$$

$$\mathbf{A}\cdot\mathbf{B}=|\mathbf{A}||\mathbf{B}|\cos(\mathbf{A},\mathbf{B}) \tag{1.49}$$

$$=A_xB_x+A_yB_y+A_zB_z \tag{1.50}$$

$$\mathbf{A}\otimes\mathbf{B}=\begin{vmatrix}\mathbf{i} & \mathbf{j} & \mathbf{k}\\ A_x & A_y & A_z\\ B_x & B_y & B_z\end{vmatrix} \tag{1.51}$$

Gradient

$$\text{grad } A=\boldsymbol{\nabla}A=\mathbf{i}\frac{\partial A}{\partial x}+\mathbf{j}\frac{\partial A}{\partial y}+\mathbf{k}\frac{\partial A}{\partial z} \tag{1.52}$$

Divergence

$$\text{div } \mathbf{A}=\boldsymbol{\nabla}\cdot\mathbf{A}=\left(\mathbf{i}\frac{\partial}{\partial x}+\mathbf{j}\frac{\partial}{\partial y}+\mathbf{k}\frac{\partial}{\partial z}\right) \tag{1.53}$$

$$\cdot(\mathbf{i}A_x+\mathbf{j}A_y+\mathbf{k}A_z)$$

$$=\frac{\partial A_x}{\partial x}+\frac{\partial A_y}{\partial y}+\frac{\partial A_z}{\partial z} \tag{1.54}$$

Lapalacian

$$\boldsymbol{\nabla}^2=\boldsymbol{\nabla}\cdot\boldsymbol{\nabla}=\frac{\partial^2 A}{\partial x^2}+\frac{\partial^2 A}{\partial y^2}+\frac{\partial^2 A}{\partial z^2} \tag{1.55}$$

Integration by parts

$$\int_a^b u(x)v'(x)\mathrm{d}x=u(x)v(x)|_a^b-\int_a^b v(x)u'(x)\mathrm{d}x \tag{1.56}$$

$$\int_a^b udv=uv|_a^b-\int_a^b vdu \tag{1.57}$$

Green-Gradient Theorem

$$\oint(R\mathrm{d}x+S\mathrm{d}y)=\int_\Gamma\left(\frac{\partial S}{\partial x}-\frac{\partial R}{\partial y}\right)\mathrm{d}x\mathrm{d}y \tag{1.58}$$

Gauss-Divergence Theorem

$$\int_{\Gamma} \mathbf{v}.\mathbf{n}\mathrm{d}\Gamma = \int_{\Omega} \mathrm{div}\mathbf{v}\mathrm{d}\Omega \tag{1.59}$$

$$\int_{\Gamma} v_i n_i \mathrm{d}\Gamma = \int_{\Omega} v_{i,i}\mathrm{d}\Omega \tag{1.60}$$

$$\int_{\Omega} \mathrm{div}\ \mathbf{q}\mathrm{d}\Omega = \int_{\Gamma} \mathbf{q}^T.\mathbf{n}\mathrm{d}\Gamma \tag{1.61}$$

$$\int_{\Omega} v_{i,i}\mathrm{d}\Omega = \int_{\Gamma} v_i n_i \mathrm{d}\Gamma \tag{1.62}$$

1.2 Vector Fields; Solid Mechanics

1.2.1 Forces

There are two kinds of forces in continuum mechanics

Body forces: act on the elements of volume or mass inside the body, e.g. gravity, electromagnetic fields. $\mathrm{d}\mathbf{F} = \rho \mathbf{b}\mathrm{d}Vol.$

Surface forces: (or traction) are contact forces acting on the free body at its bounding surface. Those will be defined in terms of force per unit area, Figure 1.4, Eq. 1.63.

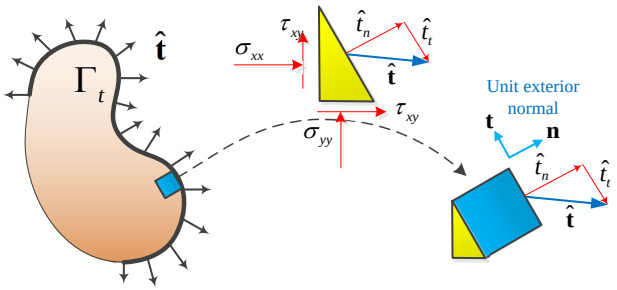

Fig. 1.4: Surface forces

$$\int_{\Gamma} \mathbf{t}\mathrm{d}\Gamma = \mathbf{i}\int_{\Gamma} t_x \mathrm{d}\Gamma + \mathbf{j}\int_{\Gamma} t_y \mathrm{d}\Gamma + \mathbf{k}\int_{\Gamma} t_z \mathrm{d}\Gamma \tag{1.63}$$

We usually limit the term traction to an actual bounding surface of a body and use the term stress vector for an imaginary interior surface. The traction vectors on planes perpendicular to the coordinate axes are particularly useful. When the vectors acting at a point on three such mutually perpendicular planes is given, the stress vector at

that point on any other arbitrarily inclined plane can be expressed in terms of the first set of tractions.

1.2.2 Cauchy's Stress Tensor

The concept of force was at first abstract, Aristotelian physics referred to impetus. Galileo and Newton (1687) formalized it. As to the concept of stress it was not firmly understood until 1822 when Cauchy presented the idea of traction vector that contains both the normal and tangential components $\mathbf{t} = t_n \mathbf{e}_n + t_t \mathbf{e}_t$. His "genius" was to consider what became known as the Cauchy tetrahedron, Figure 1.5(a), and applied Newton's second law (or more precisely its extension to particles by Euler: Euler's first law of motion) Equilibrium of the Cauchy tetrahedron yields

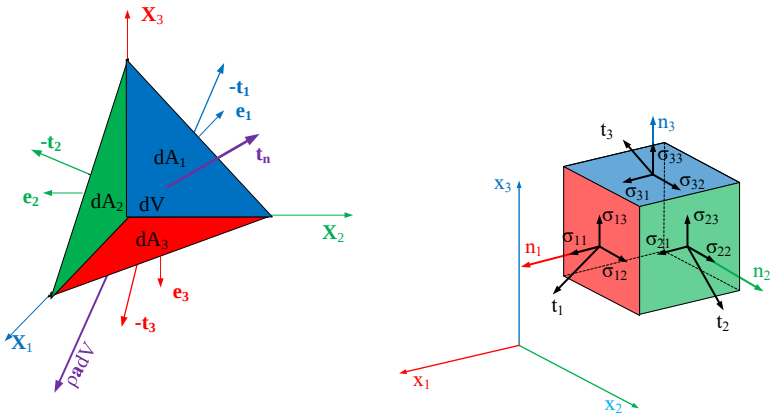

(a) Tetrahedron (b) Stresses

Fig. 1.5: Cauchy: Tetrahedron to stress

$$\mathbf{t}dA - \mathbf{t}_1 dA_1 - \mathbf{t}_2 dA_2 - \mathbf{t}_3 dA_3 = \rho dV \mathbf{a} \tag{1.64}$$

where $\mathbf{a}$ is the acceleration and ρ the mass density. The areas of the faces are given by

$$\begin{aligned} dA_1 &= \mathbf{n}.\mathbf{e}_1 dA = n_1 dA \\ dA_2 &= \mathbf{n}.\mathbf{e}_1 dA = n_2 dA \\ dA_3 &= \mathbf{n}.\mathbf{e}_1 dA = n_3 dA \end{aligned} \tag{1.65}$$

Substituting in the equilibrium equation, and considering the limiting case where $dV \to 0$

$$\mathbf{t} = \mathbf{t}_1 n_1 + \mathbf{t}_2 n_2 + \mathbf{t}_3 n_3 \tag{1.66}$$

The traction vectors must have components

$$\begin{aligned}\mathbf{t}_1 &= \sigma_{11}\mathbf{e}_1 + \sigma_{12}\mathbf{e}_2 + \sigma_{13}\mathbf{e}_3\\ \mathbf{t}_2 &= \sigma_{21}\mathbf{e}_1 + \sigma_{22}\mathbf{e}_2 + \sigma_{23}\mathbf{e}_3\\ \mathbf{t}_3 &= \sigma_{31}\mathbf{e}_1 + \sigma_{32}\mathbf{e}_2 + \sigma_{33}\mathbf{e}_3\end{aligned} \tag{1.67}$$

It should be noted that historically and traditionally in continuum mechanics the stress is denoted by $\mathbf{T}$. This was replaced by σ. Substituting into Eq. 1.66

$$\begin{aligned}\mathbf{t} &= n_1(\sigma_{11}\mathbf{e}_1 + \sigma_{12}\mathbf{e}_2 + \sigma_{13}\mathbf{e}_3) + n_2(\sigma_{21}\mathbf{e}_1 + \sigma_{22}\mathbf{e}_2 + \sigma_{23}\mathbf{e}_3)\\ &\quad + n_3(\sigma_{31}\mathbf{e}_1 + \sigma_{32}\mathbf{e}_2 + \sigma_{33}\mathbf{e}_3)\\ &= (n_1\sigma_{11} + n_2\sigma_{21} + n_3\sigma_{31})\mathbf{e}_1 + (n_1\sigma_{12} + n_2\sigma_{22} + n_3\sigma_{32})\mathbf{e}_2\\ &\quad + (n_1\sigma_{13} + n_2\sigma_{23} + n_3\sigma_{33})\mathbf{e}_3\end{aligned} \tag{1.68}$$

or simply

$$\mathbf{t}_n = \mathbf{n}\cdot\boldsymbol{\sigma} \tag{1.69}$$

Hence, there is a second order tensor called Cauchy stress tensor where the 1st subscript (i) refers to the direction of outward facing normal, and the second one (j) to the direction of component force.

$$\begin{Bmatrix}\mathbf{t}_1\\ \mathbf{t}_2\\ \mathbf{t}_3\end{Bmatrix} = \underbrace{\begin{bmatrix}\sigma_{11} & \sigma_{12} & \sigma_{13}\\ \sigma_{21} & \sigma_{22} & \sigma_{23}\\ \sigma_{31} & \sigma_{32} & \sigma_{33}\end{bmatrix}}_{\boldsymbol{\sigma}} \tag{1.70}$$

The preceding equations played a major role in the foundation of Continuum mechanics.
Finally, Voigt Notation (commonly used in engineering) is a way to represent the symmetric tensor by reducing its order.

$$\boldsymbol{\sigma} = \begin{bmatrix}\sigma_{xx} & \sigma_{xy} & \sigma_{xz}\\ \sigma_{yx} & \sigma_{yy} & \sigma_{yz}\\ \sigma_{zx} & \sigma_{zy} & \sigma_{zz}\end{bmatrix} \rightarrow \lfloor\, \sigma_{xx} \;\sigma_{yy} \;\sigma_{zz} \;\sigma_{xy} \;\sigma_{xz} \;\sigma_{yz} \,\rfloor \tag{1.71}$$

Note: we have not yet introduced the equation of equilibrium (momentum equation).

1.2.3 Hydrostatic and Deviatoric Stress Tensors

Let σ denote the mean normal stress p:

$$\sigma = -p = \frac{1}{3}(\sigma_{11} + \sigma_{22} + \sigma_{33}) = \frac{1}{3}\sigma_{ii} = \frac{1}{3}\text{tr}\,\boldsymbol{\sigma} \tag{1.72}$$

Then the stress tensor can be written as the sum of two tensors:

Hydrostatic stress in which each normal stress is equal to $-p$ and the shear stresses are zero. The hydrostatic stress produces volume change without change in shape in an isotropic medium.

$$\sigma_{hyd} = -p\mathbf{I} = \begin{bmatrix} -p & 0 & 0 \\ 0 & -p & 0 \\ 0 & 0 & -p \end{bmatrix} \tag{1.73}$$

Deviatoric Stress: which causes the change in shape.

$$\sigma_{dev} = \begin{bmatrix} \sigma_{11} - p & \sigma_{12} & \sigma_{13} \\ \sigma_{21} & \sigma_{22} - p & \sigma_{23} \\ \sigma_{31} & \sigma_{32} & \sigma_{33} - p \end{bmatrix} \tag{1.74}$$

1.2.4 Geometric Representation of Stress States

Using the three principal stresses σ_1, σ_2, and σ_3, as the coordinates, a three-dimensional stress space can be constructed, Figure 1.6. This stress representation is known as the Haigh-Westergaard stress space.
$\mathbf{OP} = \mathbf{ON}+\mathbf{NP}$. The former is along the direction of the unit vector $(1\sqrt{3}, 1/\sqrt{3}, 1/\sqrt{3})$ and $\mathbf{NP}\perp\mathbf{ON}$.
$\mathbf{ON}$ is the hydrostatic component of the stress state, axis $O\xi$ is called the hydrostatic axis ξ, and every point on this axis has $\sigma_{(1)} = \sigma_{(2)} = \sigma_{(3)} = p$, or $\xi = \sqrt{3}p$. $\mathbf{NP}$ represents the deviatoric component of the stress state (s_1, s_2, s_3) and is perpendicular to the ξ axis. Any plane perpendicular to the hydrostatic axis is called the deviatoric plane and is expressed as $\frac{1}{\sqrt{3}}(\sigma_{(1)} + \sigma_{(2)} + \sigma_{(3)}) = \xi$. A plane which passes through the origin is called the π plane and is represented by $\xi = 0$. Any plane containing the hydrostatic axis is called a meridian plane. The vector $\mathbf{NP}$ lies in a meridian plane and has $\rho = \sqrt{s_1^2 + s_2^2 + s_3^2} = \sqrt{2J_2}$.

1.3 Kinematics

1.3.1 Position and Displacement

Figure 1.7 shows the un-deformed configuration of a material continuum at time $t = 0$ together with the deformed configuration at $t = t$.
In the initial configuration, P_0 has the position vector

$$\mathbf{X} = X_1\mathbf{I}_1 + X_2\mathbf{I}_2 + X_3\mathbf{I}_3 \tag{1.75}$$

which is here expressed in terms of the material coordinates (X_1, X_2, X_3). In the deformed configuration, the particle P_0 has now moved to the new position P and has the following position vector

$$\mathbf{x} = x_1\mathbf{i}_1 + x_2\mathbf{i}_2 + x_3\mathbf{i}_3 \tag{1.76}$$

which is expressed in terms of the spatial coordinates. The displacement vector $\mathbf{u}$ connecting P_0 and P is the displacement vector which can be expressed in both the material or spatial coordinates

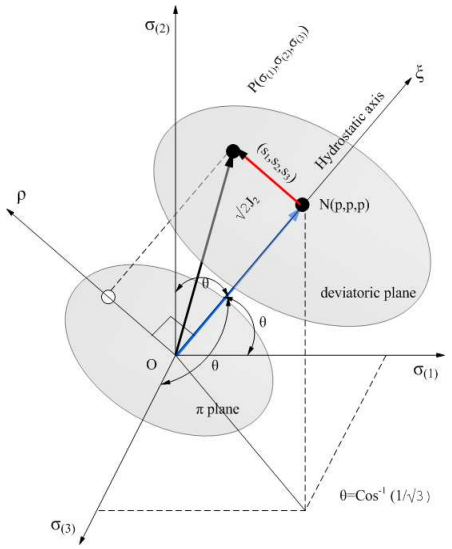

Fig. 1.6: Geometric representation of stress

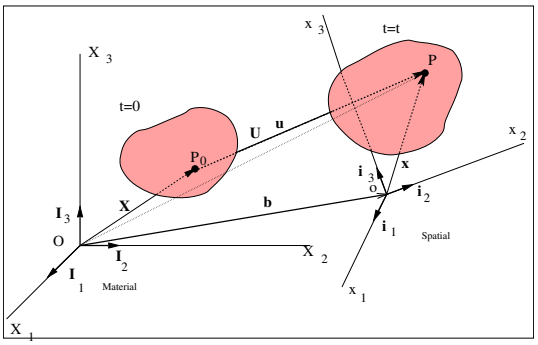

Fig. 1.7: Position and displacement vectors

$$\mathbf{U} = U_K \mathbf{I}_K \tag{1.77}$$

$$\mathbf{u} = u_k \mathbf{i}_k \tag{1.78}$$

From the preceding figure we can express motion as

$$\begin{array}{l} x_i = x_i(X_1, X_2, X_3, t) \text{ Lagrangian formulation} \\ X_i \ = X_i(x_1, x_2, x_3, t) \text{ Eulerian formulation} \end{array} \tag{1.79}$$

1.3.2 Strains

In continuum mechanics, we differentiate between

Material coordinates (X_1, X_2, X_3) defined in the undeformed original coordinate system which gives rise to the Lagrangian coordinate system.

Spatial Coordinates (x_1, x_2, x_3) defined in the deformed coordinate system. This gives rise to the Eulerian coordinate system.

If both the displacement gradients and the displacements themselves are small, then $\frac{\partial u_i}{\partial X_j} \approx \frac{\partial u_i}{\partial x_j}$, and thus the Eulerian and the Lagrangian infinitesimal strain tensors may be taken as equal, $E_{ij} = E^*_{ij}$.

If the displacement gradients are small but the displacements are large, we should use the Eulerian infinitesimal representation.

If the displacement gradients are large but the displacements are small, use the Lagrangian finite strain representation.

If both the displacement gradients and the displacements are large, use the Eulerian finite strain representation.

If large deformation is accounted for (such as in buckling), the Eulerian finite strains are:

$$\varepsilon_{xx} = \frac{\partial u}{\partial x} + \frac{1}{2}\left[\left(\frac{\partial u}{\partial x}\right)^2 + \left(\frac{\partial v}{\partial x}\right)^2 + \left(\frac{\partial w}{\partial x}\right)^2\right] \tag{1.80}$$

$$\varepsilon_{yy} = \frac{\partial v}{\partial y} + \frac{1}{2}\left[\left(\frac{\partial u}{\partial y}\right)^2 + \left(\frac{\partial v}{\partial y}\right)^2 + \left(\frac{\partial w}{\partial y}\right)^2\right] \tag{1.81}$$

$$\varepsilon_{zz} = \frac{\partial w}{\partial z} + \frac{1}{2}\left[\left(\frac{\partial u}{\partial z}\right)^2 + \left(\frac{\partial v}{\partial z}\right)^2 + \left(\frac{\partial w}{\partial z}\right)^2\right] \tag{1.82}$$

$$\varepsilon_{xy} = \frac{1}{2}\left(\frac{\partial v}{\partial x} + \frac{\partial u}{\partial y} + \frac{\partial u}{\partial x}\frac{\partial u}{\partial y} + \frac{\partial v}{\partial x}\frac{\partial v}{\partial y} + \frac{\partial w}{\partial x}\frac{\partial w}{\partial y}\right) \tag{1.83}$$

$$\varepsilon_{xz} = \frac{1}{2}\left(\frac{\partial w}{\partial x} + \frac{\partial u}{\partial z} + \frac{\partial u}{\partial x}\frac{\partial u}{\partial z} + \frac{\partial v}{\partial x}\frac{\partial v}{\partial z} + \frac{\partial w}{\partial x}\frac{\partial w}{\partial z}\right) \tag{1.84}$$

$$\varepsilon_{yz} = \frac{1}{2}\left(\frac{\partial w}{\partial y} + \frac{\partial v}{\partial z} + \frac{\partial u}{\partial y}\frac{\partial u}{\partial z} + \frac{\partial v}{\partial y}\frac{\partial v}{\partial z} + \frac{\partial w}{\partial y}\frac{\partial w}{\partial z}\right) \tag{1.85}$$

or

$$\varepsilon_{ij} = \frac{1}{2}\left(u_{i,j} + u_{j,i} + u_{k,i}u_{k,j}\right) \tag{1.86}$$

Note that the (commonly used) engineering shear strain is defined as

$$\gamma_{ij} = 2\varepsilon_{ij} \qquad (i \neq j) \tag{1.87}$$

In most cases the deformations are small enough for the quadratic terms to be dropped, the resulting equations reduce to

$$\begin{array}{lll} \varepsilon_{xx} = \frac{\partial u}{\partial x}; & \varepsilon_{yy} = \frac{\partial v}{\partial y}; & \varepsilon_{zz} = \frac{\partial w}{\partial z}; \\ \gamma_{xy} = \frac{\partial v}{\partial x} + \frac{\partial u}{\partial y}; & \gamma_{xz} = \frac{\partial w}{\partial x} + \frac{\partial u}{\partial z}; & \gamma_{yz} = \frac{\partial w}{\partial y} + \frac{\partial v}{\partial z}; \end{array} \tag{1.88}$$

or

$$\varepsilon_{ij} = \frac{1}{2}\left(u_{i,k} + u_{k,i}\right) \tag{1.89}$$

which is called the Cauchy strain. In finite element, the strain is often expressed through the linear operator $\mathbf{L}$:

$$\boldsymbol{\varepsilon} = \mathbf{L}\mathbf{u} \tag{1.90}$$

or

$$\underbrace{\begin{Bmatrix} \varepsilon_{xx} \\ \varepsilon_{yy} \\ \varepsilon_{zz} \\ \varepsilon_{xy} \\ \varepsilon_{xz} \\ \varepsilon_{yz} \end{Bmatrix}}_{\boldsymbol{\varepsilon}} = \underbrace{\begin{bmatrix} \frac{\partial}{\partial x} & 0 & 0 \\ 0 & \frac{\partial}{\partial y} & 0 \\ 0 & 0 & \frac{\partial}{\partial z} \\ \frac{\partial}{\partial y} & \frac{\partial}{\partial x} & 0 \\ \frac{\partial}{\partial z} & 0 & \frac{\partial}{\partial x} \\ 0 & \frac{\partial}{\partial z} & \frac{\partial}{\partial y} \end{bmatrix}}_{\mathbf{L}} \underbrace{\begin{Bmatrix} u_x \\ u_y \\ u_z \end{Bmatrix}}_{\mathbf{u}} \tag{1.91}$$

1.4 Fundamental Laws of Continuum Mechanics

In this section, we will derive differential equations governing the way stress and deformation vary at a point and with time. They will apply to any continuous medium, yet we will not have enough equations to determine unknown tensor field. For that we need to wait for the next section where constitututive laws relating stress and strain will be introduced. Only with constitutive equations and boundary and initial conditions will we be able to obtain a well defined mathematical problem to solve for the stress and deformation distribution or the displacement or velocity fields. In this section, we shall summarize the differential equations which express locally the conservation of mass, momentum, and energy. These differential equations of balance will be derived from integral forms of the equation of balance expressing the fundamental postulates of continuum mechanics.

Conservation laws constitute a fundamental component of classical physics. A conservation law establishes a balance of a scalar or tensorial quantity in voulme V bounded by a surface S. In its most general form, such a law may be expressed as

$$\underbrace{\frac{\mathrm{d}}{\mathrm{d}t}\int_V \mathcal{A}\mathrm{d}V}_{\text{Rate of variation}} + \underbrace{\int_S \boldsymbol{\alpha}\mathrm{d}S}_{\text{Exchange by Diffusion}} = \underbrace{\int_V \mathbf{A}\mathrm{d}V}_{\text{Source}} \tag{1.92}$$

where $\mathcal{A}$ is the volumetric density of the quantity of interest $\mathbf{a}$ (mass, linear momentum, energy, ...), $\mathbf{A}$ is the rate of volumetric density of what is provided from the outside, and $\boldsymbol{\alpha}$ is the rate of surface density of what is lost through the surface S of V and will be a function of the normal to the surface $\mathbf{n}$.

Hence, we read the previous equation as: The input quantity (provided by the right hand side) is equal to what is lost across the boundary and to modify $\mathcal{A}$ which is the

quantity of interest. The dimensions of various quantities are given by

$$\dim(\mathbf{a}) = \dim(\mathcal{A}L^{-3}) \tag{1.93}$$
$$\dim(\boldsymbol{\alpha}) = \dim(\mathcal{A}L^{-2}t^{-1}) \tag{1.94}$$
$$\dim(\mathbf{A}) = \dim(\mathcal{A}L^{-3}t^{-1}) \tag{1.95}$$

Hence this section will apply the previous conservation law to mass, momentum, and energy. The resulting differential equations will provide additional interesting relations with regard to the incompressibility of solids (important in classical hydrodynamics and plasticity theories), equilibrium and symmetry of the stress tensor, and the first law of thermodynamics. The enunciation of the preceding three conservation laws plus the second law of thermodynamics constitute what is commonly known as the fundamental laws of continuum mechanics.

Prior to the enunciation of the first conservation law, we need to define the concept of flux across a bounding surface. The flux across a surface can be graphically defined through the consideration of an imaginary surface fixed in space with continuous "medium" flowing through it. If we assign a positive side to the surface, and take $\mathbf{n}$ in the positive sense, then the volume of "material" flowing through the infinitesimal surface area $\mathrm{d}S$ in time dt is equal to the volume of the cylinder with base $\mathrm{d}S$ and slant height vdt parallel to the velocity vector $\mathbf{v}$, Figure 1.8.

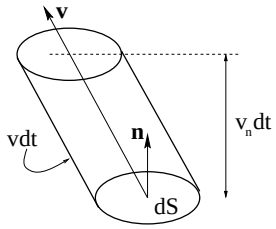

Fig. 1.8: Flux Through Area dS

(If $\mathbf{v}\cdot\mathbf{n}$ is negative, then the flow is in the negative direction). Hence, we define the volume flux as

$$\text{Volume Flux } = \int_S \mathbf{v}\cdot\mathbf{n}\mathrm{d}S = \int_S v_j n_j \mathrm{d}S \tag{1.96}$$

where the last form is for rectangular Cartesian components. We can generalize this definition and define the following fluxes per unit area through $\mathrm{d}S$:

$$\text{Mass Flux} = \int_S \rho \mathbf{v}\cdot\mathbf{n}\mathrm{d}S = \int_S \rho v_j n_j \mathrm{d}S \tag{1.97}$$

$$\text{Momentum Flux} = \int_S \rho \mathbf{v}(\mathbf{v}\cdot\mathbf{n})\mathrm{d}S = \int_S \rho v_k v_j n_j \mathrm{d}S \tag{1.98}$$

$$\text{Heat flux} = \int_S \mathbf{q}\cdot\mathbf{n}\mathrm{d}S = \int_S q_j n_j \mathrm{d}S \tag{1.99}$$

1.4.1 Conservation of Mass; Continuity Equation

$$\frac{\mathrm{d}\rho}{\mathrm{d}t} + \rho\frac{\partial v_i}{\partial x_i} = 0 \text{ or } \frac{\mathrm{d}\rho}{\mathrm{d}t} + \rho\boldsymbol{\nabla}\cdot\mathbf{v} = 0 \tag{1.100}$$

The vector form is independent of any choice of coordinates. This equation shows that the divergence of the velocity vector field equals $(-1/\rho)(d\rho/dt)$ and measures the rate of flow of material away from the particle and is equal to the unit rate of decrease of density ρ in the neighborhood of the particle.
If the material is incompressible so that the density in the neighborhood of each material particle remains constant as it moves, then the continuity equation takes the simpler form

$$\frac{\partial v_i}{\partial x_i} = 0 \text{ or } \boldsymbol{\nabla}\cdot\mathbf{v} = 0 \tag{1.101}$$

This is the condition of incompressibility.

1.4.2 Conservation of Momentum; Equation of Motion

The time rate of change of the total momentum of a given set of particles equals the vector sum of all external forces acting on the particles of the set, provided Newton's Third Law applies. The continuum form of this principle is a basic postulate[1] of continuum mechanics. Starting with

$$\frac{\mathrm{d}}{\mathrm{d}t}\int_V \underbrace{\rho\mathbf{v}}_{\mathcal{A}}\,\mathrm{d}V - \int_S \underbrace{\mathbf{t}}_{\alpha}\,\mathrm{d}S = \int_V \underbrace{\rho\mathbf{b}}_{\mathbf{A}}\,\mathrm{d}V \tag{1.102}$$

and noting that

$$\begin{aligned} \dim(\mathcal{A}) &= \rho\mathbf{v} = \tfrac{m}{L^2 t} \\ \dim(\alpha) &= \mathbf{t} = \tfrac{ma}{L^2} = \tfrac{m}{Lt^2} \\ \dim(\mathbf{A}) &= = \rho\mathbf{b} = \tfrac{m}{L^3}\tfrac{L}{t^2} = \tfrac{m}{L^2 t^2} \end{aligned} \tag{1.103}$$

recall Divergence Theorem

$$\int_V v_{i,i} dV = \int_S \underbrace{v_i n_i}_{\text{flux}} dS \tag{1.104}$$

[1] postulate: a statement, also known as an axiom, which is taken to be true without proof.

The flux of a vector function through some closed surface equals the integral of the divergence of that function over the volume enclosed by the surface. We substitute $t_i = T_{ij} n_j$ and apply the divergence theorem to obtain

$$\int_V \left(\frac{\partial T_{ij}}{\partial x_j} + \rho b_i \right) \mathrm{d}V = \int_V \rho \frac{\mathrm{d}v_i}{\mathrm{d}t} \mathrm{d}V \tag{1.105}$$

$$\int_V \left[\frac{\partial T_{ij}}{\partial x_j} + \rho b_i - \rho \frac{\mathrm{d}v_i}{\mathrm{d}t} \right] \mathrm{d}V = 0 \tag{1.106}$$

or for an arbitrary volume

$$\frac{\partial T_{ij}}{\partial x_j} + \rho b_i = \rho \frac{\mathrm{d}v_i}{\mathrm{d}t} \tag{1.107}$$

which is Cauchy's (first) equation of motion, or the linear momentum principle, or more simply the equilibrium equation. When expanded in 3D and for static problems, this equation yields:

$$\begin{array}{l} \frac{\partial T_{11}}{\partial x_1} + \frac{\partial T_{12}}{\partial x_2} + \frac{\partial T_{13}}{\partial x_3} + \rho b_1 = 0 \\ \frac{\partial T_{21}}{\partial x_1} + \frac{\partial T_{22}}{\partial x_2} + \frac{\partial T_{23}}{\partial x_3} + \rho b_2 = 0 \\ \frac{\partial T_{31}}{\partial x_1} + \frac{\partial T_{32}}{\partial x_2} + \frac{\partial T_{33}}{\partial x_3} + \rho b_3 = 0 \end{array} \tag{1.108}$$

or

$$\underbrace{\begin{bmatrix} \frac{\partial}{\partial x_1} & 0 & 0 & \frac{\partial}{\partial x_2} & \frac{\partial}{\partial x_x} & 0 \\ 0 & \frac{\partial}{\partial x_2} & 0 & \frac{\partial}{\partial x_1} 0 & \frac{\partial}{\partial x_3} & \\ 0 & 0 & \frac{\partial}{\partial x_3} & 0 & \frac{\partial}{\partial x_1} & \frac{\partial}{\partial x_2} \end{bmatrix}}_{\mathbf{L}} \underbrace{\begin{Bmatrix} T_{11} \\ T_{22} \\ T_{33} \\ T_{12} \\ T_{13} \\ T_{23} \end{Bmatrix}}_{\mathbf{T}} + \rho \underbrace{\begin{Bmatrix} b_1 \\ b_2 \\ b_3 \end{Bmatrix}}_{\mathbf{T}} = \begin{Bmatrix} 0 \\ 0 \\ 0 \end{Bmatrix} \tag{1.109}$$

We note that these equations could also have been derived from the free body diagram with the assumption of equilibrium (via Newton's second law) considering an infinitesimal element of dimensions $\mathrm{d}x_1 \times \mathrm{d}x_2 \times \mathrm{d}x_3$, Figure 1.9.

1.4.3 Conservation of Energy; First Principle of Thermodynamics

The first principle of thermodynamics relates the work done on a (closed) system and the heat transfer into the system to the change in energy of the system. We shall assume that the only energy transfers to the system are by mechanical work done on the system by surface traction and body forces and by heat transfer through the boundary.

If mechanical quantities only are considered, the principle of conservation of energy for the continuum may be derived directly from the equation of motion given by Eq. 1.108. This is accomplished by taking the integral over the volume V of the scalar

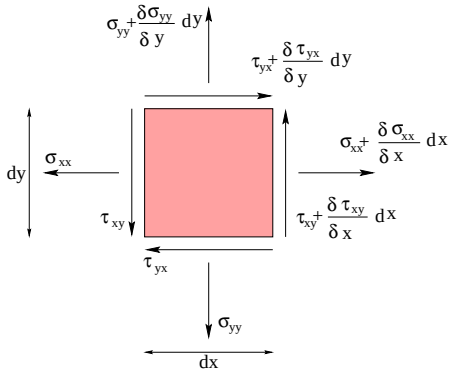

Fig. 1.9: Equilibrium of stresses, Cartesian coordinates

product between Eq. 1.108 and the velocity v_i.

$$\int_V \rho v_i \frac{\mathrm{d}v_i}{\mathrm{d}t}\mathrm{d}V = \int_V v_i T_{ji,j}\mathrm{d}V + \int_V \rho b_i v_i \mathrm{d}V \tag{1.110}$$

Consider the left hand side

$$\int_V \rho v_i \frac{\mathrm{d}v_i}{\mathrm{d}t}\mathrm{d}V = \frac{d}{\mathrm{d}t}\int_V \frac{1}{2}\rho v_i v_i \mathrm{d}V = \frac{d}{\mathrm{d}t}\int_V \frac{1}{2}\rho v^2 \mathrm{d}V = \frac{\mathrm{d}K}{\mathrm{d}t} \tag{1.111}$$

which represents the time rate of change of the kinetic energy K in the continuum. If we consider thermal processes, the rate of increase of total heat into the continuum is given by

$$Q = -\int_S q_i n_i \mathrm{d}S + \int_V \rho r \mathrm{d}V \tag{1.112}$$

Q has the dimension[2] of power, that is ML^2T^{-3}, and the SI unit is the Watt (W). $\mathbf{q}$ is the heat flux per unit area by conduction, its dimension is MT^{-3} and the corresponding SI unit is Wm^{-2}. Finally, r is the radiant heat constant per unit mass, its dimension is $MT^{-3}L^{-4}$ and the corresponding SI unit is Wm^{-6}. We thus have

$$\frac{\mathrm{d}K}{\mathrm{d}t} + \int_V D_{ij}T_{ij}\mathrm{d}V = \int_V (v_i T_{ji})_{,j}\mathrm{d}V + \int_V \rho v_i b_i \mathrm{d}V + Q \tag{1.113}$$

We next convert the first integral on the right hand side to a surface integral by the divergence theorem ($\int_V \boldsymbol{\nabla}\cdot\mathbf{T}dV = \int_S \mathbf{T}.\mathbf{n}\mathrm{d}S$) and since $t_i = T_{ij}n_j$ we obtain

[2] Work=$FL = ML^2T^{-2}$; Power=Work/time

$$\frac{\mathrm{d}K}{\mathrm{d}t} + \int_V D_{ij} T_{ij} \mathrm{d}V = \int_S v_i t_i \mathrm{d}S + \int_V \rho v_i b_i \mathrm{d}V + Q \tag{1.114}$$

$$\frac{\mathrm{d}K}{\mathrm{d}t} + \frac{\mathrm{d}U}{\mathrm{d}t} = \frac{\mathrm{d}W}{\mathrm{d}t} + Q \tag{1.115}$$

This equation relates the time rate of change of total mechanical energy of the continuum on the left side to the rate of work done by the surface and body forces on the right hand side.

If both mechanical and non mechanical energies are to be considered, the first principle states that *the time rate of change of the kinetic plus the internal energy is equal to the sum of the rate of work plus all other energies supplied to, or removed from, the continuum per unit time (heat, chemical, electromagnetic, etc.).* For a thermomechanical continuum, it is customary to express the time rate of change of internal energy by the integral expression

$$\frac{\mathrm{d}U}{\mathrm{d}t} = \frac{d}{\mathrm{d}t} \int_V \rho u \mathrm{d}V \tag{1.116}$$

where u is the internal energy per unit mass or specific internal energy. We note that U appears only as a differential in the first principle, hence if we really need to evaluate this quantity, we need to have a reference value for which U will be null.

The dimension of U is one of energy: dim $U = ML^2T^{-2}$, and the SI unit is the Joule. Similarly dim $u = L^2T^{-2}$ with the SI unit of Joule/Kg.

In terms of energy integrals, the first principle can be rewritten as

$$\overbrace{\underbrace{\frac{d}{\mathrm{d}t}\int_V \frac{1}{2}\rho v_i v_i \mathrm{d}V}_{\frac{dK}{dt}=\dot{K}} + \underbrace{\frac{d}{\mathrm{d}t}\int_V \rho u \mathrm{d}V}_{\frac{dU}{dt}=\dot{U}}}^{\text{Rate of increase}} = \underbrace{\overbrace{\int_S t_i v_i \mathrm{d}S}^{\text{Exchange}} + \overbrace{\int_V \rho v_i b_i \mathrm{d}V}^{\text{Source}}}_{\frac{dW}{dt}(\mathcal{P}_{ext})}$$

$$+ \underbrace{\overbrace{\int_V \rho r \mathrm{d}V}^{\text{Source}} - \overbrace{\int_S q_i n_i \mathrm{d}S}^{\text{Exchange}}}_{Q(\mathcal{P}_{cal})} \tag{1.117}$$

or

$$\frac{\mathrm{d}K}{\mathrm{d}t} + \frac{\mathrm{d}U}{\mathrm{d}t} = \frac{\mathrm{d}W}{\mathrm{d}t} + Q \tag{1.118}$$

In ideal elasticity, heat transfer is considered insignificant, and all of the input work is assumed converted into internal energy in the form of recoverable stored elastic strain energy which can be recovered as work when the body is unloaded.

In general, however, the major part of the input work into a deforming material is not recoverably stored but dissipated by the deformation process causing an increase in the body's temperature and eventually being conducted away as heat.

1.4.4 Constitutive Equations

Hooke[3] published in 1676 an anagram *c.e.i.i.n.o.s.s.t.t.u.u.* Only in 1678 did he publish the key (in Latin) *ut tension, sic vis*, meaning "as the extension, so the force." In this own words: *The Power of any Spring is in the same proportion with the Tension thereof: That is, if one power stretch or bend is one space, two will bend it two, and three will bend it three, and so forward*. Indeed, it was said that Hooke was "too little and too lately known."

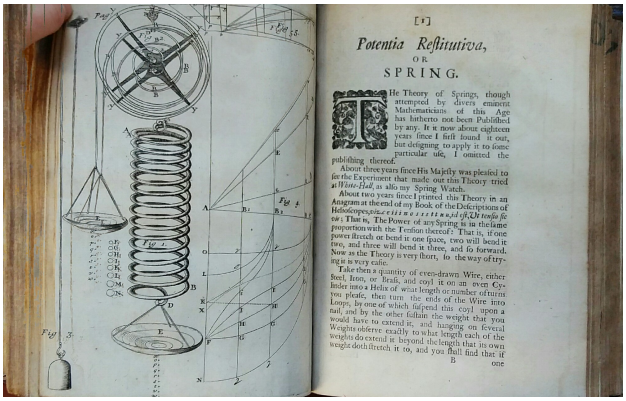
[1]

Potentia Restitutiva,

OR

SPRING.

THe Theory of Springs, though attempted by divers eminent Mathematicians of this Age has hitherto not been Published by any. It is now about eighteen years since I first found it out, but designing to apply it to some particular use, I omitted the publishing thereof.

About three years since His Majesty was pleased to see the Experiment that made out this Theory tried at *White-Hall*, as also my Spring Watch.

About two years since I printed this Theory in an Anagram at the end of my Book of the Descriptions of Helioscopes, *viz. c e i i n o s s t t u u*, *id est*, *Ut tensio sic vis*: That is, The Power of any Spring is in the same proportion with the Tension thereof: That is, if one power stretch or bend it one space, two will bend it two, and three will bend it three, and so forward. Now as the Theory is very short, so the way of trying it is very easie.

Take then a quantity of even-drawn Wire, either Steel, Iron, or Brass, and coyl it on an even Cylinder into a Helix of what length or number of turns you please, then turn the ends of the Wire into Loops, by one of which suspend this coyl upon a nail, and by the other sustain the weight that you would have to extend it, and hanging on several Weights observe exactly to what length each of the weights do extend it beyond the length that its own weight doth stretch it to, and you shall find that if

B one

Fig. 1.10: Plate from Hooke's lecture on springs

From there on, Hooke became the undisputed father of elasticity.

1.4.4.1 General 3D

The Generalized Hooke's Law can be written as:

$$\sigma_{ij} = D_{ijkl}\varepsilon_{kl} \qquad i,j,k,l = 1,2,3 \tag{1.119}$$

The (fourth order) tensor of elastic constants D_{ijkl} has 81 (3^4) components; however, due to the symmetry of both $\boldsymbol{\sigma}$ and $\boldsymbol{\varepsilon}$, there are at most 36 $\left(\frac{9(9-1)}{2}\right)$ distinct elastic terms.

For the purpose of writing Hooke's Law, the double indexed system is often replaced by a simple indexed system with a range of six:

$$\sigma_k = \overbrace{D_{km}}^{6^2=36}\,\varepsilon_m \qquad k,m = 1,2,3,4,5,6 \tag{1.120}$$

[3] Hooke, a contemporary of Newton, was very secretive, bitter and jealous (not unlike Salieri and Mozart) as he felt that he had been denied credit for many discoveries.

In terms of Lame's constants, Hooke's Law for an isotropic body is written as

$$T_{ij} = \lambda\delta_{ij}E_{kk} + 2\mu E_{ij} \quad \text{or} \quad \mathbf{T} = \lambda\mathbf{I}_E + 2\mu\mathbf{E} \tag{1.121}$$

$$E_{ij} = \frac{1}{2\mu}\left(T_{ij} - \frac{\lambda}{3\lambda+2\mu}\delta_{ij}T_{kk}\right) \quad \text{or} \quad \mathbf{E} = \frac{-\lambda}{2\mu(3\lambda+2\mu)}\mathbf{I}_T + \frac{1}{2\mu}\mathbf{T} \tag{1.122}$$

In terms of engineering constants:

$$\frac{1}{E} = \frac{\lambda+\mu}{\mu(3\lambda+2\mu)}; \nu = \frac{\lambda}{2(\lambda+\mu)} \tag{1.123}$$

$$\lambda = \frac{\nu E}{(1+\nu)(1-2\nu)}; \mu = G = \frac{E}{2(1+\nu)} \tag{1.124}$$

Similarly in the case of pure shear in the x_1x_3 and x_2x_3 planes, we have

$$\sigma_{21} = \sigma_{12} = \tau \quad \text{all other } \sigma_{ij} = 0 \tag{1.125}$$

$$2\varepsilon_{12} = \frac{\tau}{G} \tag{1.126}$$

and μ is equal to the shear modulus G. Hooke's law for isotropic material in terms of engineering constants becomes

$$\sigma_{ij} = \frac{E}{1+\nu}\left(\varepsilon_{ij} + \frac{\nu}{1-2\nu}\delta_{ij}\varepsilon_{kk}\right) \quad \text{or} \quad \boldsymbol{\sigma} = \frac{E}{1+\nu}\left(\boldsymbol{\varepsilon} + \frac{\nu}{1-2\nu}\mathbf{I}_\varepsilon\right) \tag{1.127}$$

$$\varepsilon_{ij} = \frac{1+\nu}{E}\sigma_{ij} - \frac{\nu}{E}\delta_{ij}\sigma_{kk} \quad \text{or} \quad \boldsymbol{\varepsilon} = \frac{1+\nu}{E}\boldsymbol{\sigma} - \frac{\nu}{E}\mathbf{I}_\sigma \tag{1.128}$$

When the strain equation is expanded in 3D Cartesian coordinates, it yields:

$$\begin{Bmatrix} \varepsilon_{xx} \\ \varepsilon_{yy} \\ \varepsilon_{zz} \\ \gamma_{xy}(2\varepsilon_{xy}) \\ \gamma_{yz}(2\varepsilon_{yz}) \\ \gamma_{zx}(2\varepsilon_{zx}) \end{Bmatrix} = \frac{1}{E}\begin{bmatrix} 1 & -\nu & -\nu & 0 & 0 & 0 \\ -\nu & 1 & -\nu & 0 & 0 & 0 \\ -\nu & -\nu & 1 & 0 & 0 & 0 \\ 0 & 0 & 0 & 1+\nu & 0 & 0 \\ 0 & 0 & 0 & 0 & 1+\nu & 0 \\ 0 & 0 & 0 & 0 & 0 & 1+\nu \end{bmatrix}\begin{Bmatrix} \sigma_{xx} \\ \sigma_{yy} \\ \sigma_{zz} \\ \tau_{xy} \\ \tau_{yz} \\ \tau_{zx} \end{Bmatrix} \tag{1.129}$$

If we invert this equation, we obtain

$$\begin{Bmatrix} \sigma_{xx} \\ \sigma_{yy} \\ \sigma_{zz} \\ \tau_{xy} \\ \tau_{yz} \\ \tau_{zx} \end{Bmatrix} = \begin{bmatrix} \frac{E}{(1+\nu)(1-2\nu)}\begin{bmatrix} 1-\nu & \nu & \nu \\ \nu & 1-\nu & \nu \\ \nu & \nu & 1-\nu \end{bmatrix} & 0 \\ 0 & G\begin{bmatrix} 1 & 0 & 0 \\ 0 & 1 & 0 \\ 0 & 0 & 1 \end{bmatrix} \end{bmatrix}\begin{Bmatrix} \varepsilon_{xx} \\ \varepsilon_{yy} \\ \varepsilon_{zz} \\ \gamma_{xy}(2\varepsilon_{xy}) \\ \gamma_{yz}(2\varepsilon_{yz}) \\ \gamma_{zx}(2\varepsilon_{zx}) \end{Bmatrix} \tag{1.130}$$

1.4.4.2 Transversly Isotropic Case

For transversely isotropic, we can express the stress-strain relation in terms of

$$\begin{aligned}
\varepsilon_{xx} &= a_{11}\sigma_{xx} + a_{12}\sigma_{yy} + a_{13}\sigma_{zz} \\
\varepsilon_{yy} &= a_{12}\sigma_{xx} + a_{11}\sigma_{yy} + a_{13}\sigma_{zz} \\
\varepsilon_{zz} &= a_{13}(\sigma_{xx} + \sigma_{yy}) + a_{33}\sigma_{zz} \\
\gamma_{xy} &= 2(a_{11} - a_{12})\tau_{xy} \\
\gamma_{yz} &= a_{44}\tau_{xy} \\
\gamma_{xz} &= a_{44}\tau_{xz}
\end{aligned} \tag{1.131}$$

and

$$a_{11} = \frac{1}{E}; \quad a_{12} = -\frac{\nu}{E}; \quad a_{13} = -\frac{\nu'}{E'}; \quad a_{33} = -\frac{1}{E'}; \quad a_{44} = -\frac{1}{\mu'} \tag{1.132}$$

where E is the Young's modulus in the plane of isotropy and E' the one in the plane normal to it. ν corresponds to the transverse contraction in the plane of isotropy when tension is applied in the plane; ν' corresponds to the transverse contraction in the plane of isotropy when tension is applied normal to the plane; μ' corresponds to the shear moduli for the plane of isotropy and any plane normal to it, and μ is shear moduli for the plane of isotropy.

1.4.4.3 Special 2D Cases

Often times one can make simplifying assumptions to reduce a 3D problem into a 2D one.

Plane Strain For problems involving a long body in the z direction with no variation in load or geometry, then $\varepsilon_{zz} = \gamma_{yz} = \gamma_{xz} = \tau_{xz} = \tau_{yz} = 0$. Thus, replacing into Eq. 1.130 we obtain

$$\begin{Bmatrix} \sigma_{xx} \\ \sigma_{yy} \\ \sigma_{zz} \\ \tau_{xy} \end{Bmatrix} = \frac{E}{(1+\nu)(1-2\nu)} \begin{bmatrix} (1-\nu) & \nu & 0 \\ \nu & (1-\nu) & 0 \\ \nu & \nu & 0 \\ 0 & 0 & \frac{1-2\nu}{2} \end{bmatrix} \begin{Bmatrix} \varepsilon_{xx} \\ \varepsilon_{yy} \\ \gamma_{xy} \end{Bmatrix} \tag{1.133}$$

Axisymmetry In solids of revolution, we can use a polar coordinate system and

$$\varepsilon_{rr} = \frac{\partial u}{\partial r} \tag{1.134}$$

$$\varepsilon_{\theta\theta} = \frac{u}{r} \tag{1.135}$$

$$\varepsilon_{zz} = \frac{\partial w}{\partial z} \tag{1.136}$$

$$\varepsilon_{rz} = \frac{\partial u}{\partial z} + \frac{\partial w}{\partial r} \tag{1.137}$$

The constitutive relation is again analogous to 3D/plane strain

$$\begin{Bmatrix} \sigma_{rr} \\ \sigma_{zz} \\ \sigma_{\theta\theta} \\ \tau_{rz} \end{Bmatrix} = \frac{E}{(1+\nu)(1-2\nu)} \begin{bmatrix} 1-\nu & \nu & \nu & 0 \\ \nu & 1-\nu & \nu & 0 \\ \nu & \nu & 1-\nu & 0 \\ 0 & 0 & 0 & \frac{1-2\nu}{2} \end{bmatrix} \begin{Bmatrix} \varepsilon_{rr} \\ \varepsilon_{zz} \\ \varepsilon_{\theta\theta} \\ \gamma_{rz} \end{Bmatrix} \tag{1.138}$$

Plane Stress If the longitudinal dimension in z direction is much smaller than in the x and y directions, then $\tau_{yz} = \tau_{xz} = \sigma_{zz} = \gamma_{xz} = \gamma_{yz} = 0$ throughout the thickness. Again, substituting into Eq. 1.130 we obtain:

$$\begin{Bmatrix} \sigma_{xx} \\ \sigma_{yy} \\ \tau_{xy} \end{Bmatrix} = \frac{1}{1-\nu^2} \begin{bmatrix} 1 & \nu & 0 \\ \nu & 1 & 0 \\ 0 & 0 & \frac{1-\nu}{2} \end{bmatrix} \begin{Bmatrix} \varepsilon_{xx} \\ \varepsilon_{yy} \\ \gamma_{xy} \end{Bmatrix} \tag{1.139}$$

$$\varepsilon_{zz} = -\frac{1}{1-\nu}\nu(\varepsilon_{xx} + \varepsilon_{yy}) \tag{1.140}$$

1.4.4.4 Pore Pressures

In porous material, the water pressure is transmitted to the structure as a body force of magnitude

$$b_x = -\frac{\partial p}{\partial x} \qquad b_y = -\frac{\partial p}{\partial y} \tag{1.141}$$

where p is the pore pressure.
The effective stresses are the forces transmitted between the solid particles and are defined in terms of the total stresses $\boldsymbol{\sigma}$ and pore pressure p:

$$\sigma'_{ij} = \sigma_{ij} + m_{ij}p \qquad \mathbf{m}^T = [-1, -1, 0] \tag{1.142}$$

i.e simply removing the hydrostatic pressure component from the total stress.

1.5 Boundary Conditions

In general, boundary conditions can be obtained from the Euler-Lagrange equations corresponding to the governing differential equation (conservation of momentum or equilibrium in solid mechanics).

For field variables in which the highest derivative in the governing differential equation is of order $2m$, then we have

Essential (or forced, or geometric) boundary conditions (because it was essential for the derivation of the Euler equation) if $\eta(a)$ or $\eta(b)$ =0. Essential boundary conditions involve derivatives of order zero (the field variable itself) through m-1. Mathematically, this corresponds to Dirichlet boundary-value problems.

Natural (or static) if we left η to be arbitrary, then it would be necessary to use $\frac{\partial F}{\partial u'} = 0$ at $x = a$ or b. Natural boundary conditions involve derivatives of order m and higher. Mathematically, this corresponds to Neuman boundary-value problems.

Mixed Boundary-Value problems in which both essential and natural boundary conditions are specified on complementary portions of the boundary (such as Γ_u and Γ_t).

Table 1.1 provides examples in structural analysis.

Table 1.1: Examples of boundary conditions in structural analysis

Problem	Axial Member Distributed load	Flexural Member Distributed load
Differential Equation	$AE\frac{d^2u}{dx^2} - q = 0$	$EI\frac{d^4w}{dx^4} - q = 0$
m	1	2
Essential B.C. $[0, m-1]$	u	w, $\frac{dw}{dx}$
Natural B.C. $[m, 2m-1]$	$\frac{du}{dx}$ or $\sigma_{xx} = Eu_{,x}$	$\frac{d^2w}{dx^2}$ and $\frac{d^3w}{dx^3}$ or $M = EIw_{,xx}$ and $V = EIw_{,xxx}$

Chapter 2
Review of Scalar Field Diffusion Problems

Abstract
Following the previous chapter that addressed solid mechanics problems, this one will focus on the most common scalar field diffusion problem (heat). Moisture diffusion will not be covered, and chloride diffusion will be separately covered.

2.1 Introduction

A good understanding of the mechanics of heat transfer in concrete is essential in multiple applications covered in this book. In concrete deterioration, the process of chloride diffusion hinges on the moisture diffusivity which is temperature dependent. Alkali aggregate reaction is a thermodynamic one, hence through Arhenius law, the kinetics of the reaction is temperature dependent. Finally, temperature can substantially impact the response of concrete dams (especially the thin arch dams) which must consider it as a load. Hence, this chapter will begin by examining the fundamentals of heat transfer in solids. For radiation (there the problem is highly nonlinear) some simplification will be presented along with the geographical role in this mode of heat exchange.
There are three fundamental modes of heat transfer:

Conduction: takes place when a temperature gradient exists within a material and is governed by Fourier's Law, Figure 2.1 on Γ_q:

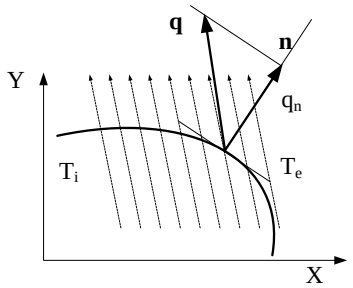

Fig. 2.1: Flux vector

$$q_x = -k_x \frac{\partial T}{\partial x}; \qquad q_y = -k_y \frac{\partial T}{\partial y}; \tag{2.1}$$

where $T = T(x, y)$ is the temperature field in the medium, q_x and q_y are the components of the heat flux (W/m^2 or Btu/h-ft^2), k is the thermal conductivity (W/m.^{o}C or Btu/h-ft-^{o}F), and $\frac{\partial T}{\partial x}$, $\frac{\partial T}{\partial y}$ are the temperature gradients along the x and y, respectively. Note that heat flows from "hot" to "cool" zones, hence the negative sign.

Convection: heat transfer takes place when a material is exposed to a moving fluid which is at different temperature. It is governed by Newton's Law of Cooling

$$q = h(T - T_\infty) \text{ on } \Gamma_c \tag{2.2}$$

where q is the convective heat flux and h is the convection heat transfer coefficient or film coefficient (W/m^2.^{o}C or Btu/h-ft^2.^{o}F). It depends on various factors, such as whether convection is natural or forced, laminar or turbulent flow, type of fluid, and geometry of the body. T and T_∞ are the surface and fluid temperature, respectively. This mode is considered as part of the boundary condition.

Radiation: is the energy transferred between two separated bodies at different temperatures by means of electromagnetic waves. The fundamental law is the Stefan-Boltzman Law of Thermal Radiation for black bodies in which the flux is proportional to the fourth power of the absolute temperature, which causes the problem to be non-linear. This mode is not addressed.

2.2 Derivation of the Diffusion Problem

2.2.1 Simplified; 2D

If we examine a solid (for simplification, a 2D differential body of dimensions dx by dy with unit thickness) as in Figure 2.2 (note similarity with Figure 1.9) and consider that there is flow $\mathbf{q}$ of some quantity (mass, heat, chemical) through it. Then, the

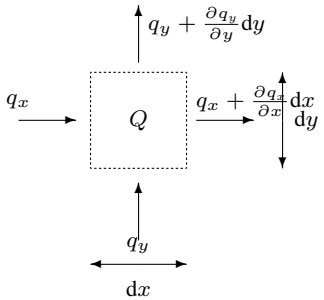

Fig. 2.2: Flux Through Sides of Differential Element

rate of transfer per unit area, $\mathbf{q}$, is called the flux. The direction of flow will be in the direction of maximum "potential" (such as temperature, piezometric head, or ion concentration) decrease (as governed by Fourrier, Darcy, or Fick laws respectively). Hence the flux is equal to the gradient of the scalar quantity.

$$\mathbf{q} = \left\{ \begin{array}{c} q_x \\ q_y \\ q_z \end{array} \right\} = -\mathbf{D} \left\{ \begin{array}{c} \frac{\partial \phi}{\partial x} \\ \frac{\partial T}{\partial y} \\ \frac{\partial T}{\partial z} \end{array} \right\} = -\mathbf{D} \boldsymbol{\nabla} T \tag{2.3}$$

$\mathbf{D}$ is a three by three (symmetric) constitutive/conductivity matrix.
The conductivity can be either

Isotropic

$$\mathbf{D} = k \begin{bmatrix} 1 & 0 & 0 \\ 0 & 1 & 0 \\ 0 & 0 & 1 \end{bmatrix} \tag{2.4}$$

Anisotropic

$$\mathbf{D} = \begin{bmatrix} k_{xx} & k_{xy} & k_{xz} \\ k_{yx} & k_{yy} & k_{yz} \\ k_{zx} & k_{zy} & k_{zz} \end{bmatrix} \tag{2.5}$$

Orthotropic

$$\mathbf{D} = \begin{bmatrix} k_{xx} & 0 & 0 \\ 0 & k_{yy} & 0 \\ 0 & 0 & k_{zz} \end{bmatrix} \tag{2.6}$$

Note that for flow through porous media, Darcy's equation is only valid for laminar flow. For the two dimensional (unit thickness) solid, the heat balance will be composed of three terms:

1. Rate of heat generation/sink:

$$I_2 = Q \mathrm{d}x \mathrm{d}y \tag{2.7}$$

2. Heat flux across the boundary of the element:

$$\begin{aligned} I_1 &= \left[\left(q_x + \frac{\partial q_x}{\partial x} \mathrm{d}x \right) - q_x \right] \mathrm{d}y + \left[\left(q_y + \frac{\partial q_y}{\partial y} \mathrm{d}y \right) - q_y \right] \mathrm{d}x \\ &= \frac{\partial q_x}{\partial x} \mathrm{d}x \mathrm{d}y + \frac{\partial q_y}{\partial y} \mathrm{d}y \mathrm{d}x \end{aligned} \tag{2.8}$$

3. Change in stored energy:

$$I_3 = c\rho \frac{\mathrm{d}T}{\mathrm{d}t} . \mathrm{d}x \mathrm{d}y \tag{2.9}$$

where we define the specific heat, c, as the amount of heat required to raise a unit mass by one degree.

From the first law of thermodynamics, energy produced, I_2, plus the net energy across the boundary, I_1, must be equal to the energy absorbed, I_3, thus

$$I_1 + I_2 - I_3 = 0 \tag{2.10}$$

$$\underbrace{\frac{\partial q_x}{\partial x}\mathrm{d}x\mathrm{d}y + \frac{\partial q_y}{\partial y}\mathrm{d}y\mathrm{d}x}_{I_1} + \underbrace{Q\mathrm{d}x\mathrm{d}y}_{I_2} - \underbrace{c\rho\frac{\mathrm{d}T}{\mathrm{d}t}\mathrm{d}x\mathrm{d}y}_{I_3} = 0 \tag{2.11}$$

Replacing the flux by its expression in Eq. 2.3, we obtain

$$\frac{\partial}{\partial x}\left(k(x,y)\frac{\partial T}{\partial x}\right) + \frac{\partial}{\partial y}\left(k(x,y)\frac{\partial T}{\partial y}\right) + Q = \rho(x,y)C(x,y)\frac{\partial T}{\partial t} \tag{2.12}$$

where

- k = thermal conductivity of concrete in W/m^oC
- T = temperature in ^oC
- t = time in sec
- Q = rate of heat per unit volume generated within the body W/m^3
- ρ = density in kg/m^3
- C = specific heat of concrete in J/kg^oC

Finally, it should be noted that scalar field problems (of which the heat equation is a special case) are encountered in almost all branches of engineering and physics. Most of them can be viewed as special forms of the general Helmholtz equation given by

$$\frac{\partial}{\partial x}\left(k_x\frac{\partial \phi}{\partial x}\right) + \frac{\partial}{\partial y}\left(k_y\frac{\partial \phi}{\partial y}\right) + \frac{\partial}{\partial z}\left(k_z\frac{\partial \phi}{\partial z}\right) + Q = c\rho\frac{\partial \phi}{\partial t} \tag{2.13}$$

where $\phi(x,y,z)$ is the field variable to be solved.
Note the similarity between Eq. 2.12 (scalar variable) and the equation of equilibrium (conservation of momentum in terms of a vectorial variable, Eq. 1.109).

$$\frac{\partial \sigma_{xx}}{\partial x} + \frac{\partial \sigma_{xy}}{\partial y} + \rho b_x = \rho m\frac{\partial^2 u_x}{\partial t^2} \tag{2.14}$$

$$\frac{\partial \sigma_{yy}}{\partial y} + \frac{\partial \sigma_{xy}}{\partial x} + \rho b_y = \rho m\frac{\partial^2 u_y}{\partial t^2} \tag{2.15}$$

1. For steady state problems, the previous equation does not depend on t, and for 2D problems, it reduces to

$$\left[\frac{\partial}{\partial x}\left(k_x\frac{\partial T}{\partial x}\right) + \frac{\partial}{\partial y}\left(k_y\frac{\partial T}{\partial y}\right)\right] + Q = 0 \tag{2.16}$$

2. For steady state isotropic problems,

$$\frac{\partial^2 T}{\partial x^2} + \frac{\partial^2 T}{\partial y^2} + \frac{\partial^2 T}{\partial z^2} = -\frac{Q}{k} \tag{2.17}$$

which is Poisson's equation in 3D.

3. If the heat input $Q = 0$, then the previous equation reduces to

$$\frac{\partial^2 T}{\partial x^2} + \frac{\partial^2 T}{\partial y^2} + \frac{\partial^2 T}{\partial z^2} = 0 \tag{2.18}$$

which is an Elliptic equation (or Laplace equation). Solutions of Laplace equations are termed harmonic functions (right hand side is zero) which is why Eq. 2.16 is referred to as the quasi-harmonic equation.

4. If the function depends only on x and t, then we obtain

$$\rho c \frac{\partial T}{\partial t} = \frac{\partial}{\partial x}\left(k_x \frac{\partial T}{\partial x}\right) + Q \tag{2.19}$$

which is a parabolic (or Heat) equation. Note that this equation will be revisited in Section 10.2.1 under Fick's Law.

2.2.2 Generalized Derivation; 3D

We rederive the previous equations through a more rigorous approach, and for the sake of generalization, replace T by ϕ as the diffusion equation governs a number of different physical phenomena, Table 2.1. The amount of flow per unit time into an

$\text{div}(\mathbf{D}\boldsymbol{\nabla}\phi) + Q = 0$					
Equation	ϕ	$\mathbf{D}$	Q	$\mathbf{q}$	Constitutive law
Heat Flow	Temperature T	Thermal conductivity	Heat supply/sink	Heat flux	Fourrier $\mathbf{q} = -\mathbf{D}\boldsymbol{\nabla}T$
Fluid flow through porous media	Piezometric head h	Permeability Coefficients	Fluid supply	Volume flux	Darcy $\mathbf{q} = -\mathbf{D}\boldsymbol{\nabla}\phi$
Diffusion	ion concentration	Permeability coefficients	Ion supply	Ion flux	Fick $\mathbf{q} = -\mathbf{D}\boldsymbol{\nabla}\phi$
Saint-Venant Torsion	Prandtl's stress function	$\frac{1}{\mu}$	Rate of twist $\frac{\theta}{2}$		Hooke

Table 2.1: Selected Examples of Diffusion Problems

element of volume Ω and surface Γ is

$$I_1 = \int_\Gamma \mathbf{q}(-\mathbf{n})\mathrm{d}\Gamma = \int_\Gamma \mathbf{D}\boldsymbol{\nabla}\phi.\mathbf{n}\mathrm{d}\Gamma \tag{2.20}$$

where $\mathbf{n}$ is the unit exterior normal to Γ. Using the divergence theorem

$$\int_{\Gamma} \mathbf{v}\cdot\mathbf{n}\mathrm{d}\Gamma = \int_{\Omega} \mathrm{div}\ \mathbf{v}\mathrm{d}\Omega \tag{2.21}$$

Eq. 2.20 transforms into

$$I_1 = \int_{\Omega} \mathrm{div}\ (\mathbf{D}\boldsymbol{\nabla}\phi)\mathrm{d}\Omega \tag{2.22}$$

Furthermore, if the instantaneous volumetric rate of "heat" generation or removal at a point x, y, z inside Ω is $Q(x, y, z, t)$, then the total amount of heat/flow produced per unit time is

$$I_2 = \int_{\Omega} Q(x, y, z, t)\mathrm{d}\Omega \tag{2.23}$$

Finally, we define the *specific heat* of a solid, c, as the amount of heat required to raise a unit mass by one degree. Thus if $\Delta\phi$ is a temperature change which occurs in a mass m over a time Δt, then the corresponding amount of heat that was added must have been $cm\Delta\phi$, or

$$I_3 = \int_{\Omega} \rho c\Delta\phi\mathrm{d}\Omega \tag{2.24}$$

where ρ is the density. Note that another expression of I_3 is $\Delta t(I_1 + I_2)$. The balance equation, or conservation law, states that the energy produced, I_2, plus the net energy across the boundary, I_1, must be equal to the energy absorbed, I_3, (note similarity with Eq. 1.102 and 2.11), thus

$$I_1 + I_2 - I_3 = 0 \tag{2.25}$$

$$\int_{\Omega} \left(\mathrm{div}\ (\mathbf{D}\boldsymbol{\nabla}\phi) + Q - \rho c\frac{\Delta\phi}{\Delta t}\right) d\Omega = 0 \tag{2.26}$$

Since t and Ω are both arbitrary, then

$$\mathrm{div}\ (\mathbf{D}\boldsymbol{\nabla}\phi) + Q - \rho c\frac{\partial\phi}{\partial t} = 0 \tag{2.27}$$

or

$$\mathrm{div}\ (\mathbf{D}\boldsymbol{\nabla}\phi) + Q = \rho c\frac{\partial\phi}{\partial t} \tag{2.28}$$

This equation can be rewritten as

$$\frac{\partial q_x}{\partial x} + \frac{\partial q_y}{\partial y} + Q = \rho c\frac{\partial\phi}{\partial t} \tag{2.29}$$

1. Note the similarity between this last equation, and the equation of equilibrium (Eq. 1.108)

$$\frac{\partial \sigma_{xx}}{\partial x} + \frac{\partial \sigma_{xy}}{\partial y} + \rho b_x = \rho m \frac{\partial^2 u_x}{\partial t^2} \tag{2.30}$$

$$\frac{\partial \sigma_{yy}}{\partial y} + \frac{\partial \sigma_{xy}}{\partial x} + \rho b_y = \rho m \frac{\partial^2 u_y}{\partial t^2} \tag{2.31}$$

In this case, we are dealing with a scalar quantity (ϕ) whereas in mechanics it was a vectorial quantity $\mathbf{u}$.

2. For steady state problems, the previous equation does not depend on t, and for 2D problems, it reduces to

$$\left[\frac{\partial}{\partial x}\left(k_x \frac{\partial \phi}{\partial x}\right) + \frac{\partial}{\partial y}\left(k_y \frac{\partial \phi}{\partial y}\right)\right] + Q = 0 \tag{2.32}$$

3. For steady state isotropic problems,

$$\frac{\partial^2 \phi}{\partial x^2} + \frac{\partial^2 \phi}{\partial y^2} + \frac{\partial^2 \phi}{\partial z^2} = -\frac{Q}{k} \tag{2.33}$$

which is *Poisson's equation* in 3D.

4. If the heat input $Q = 0$, then the previous equation reduces to

$$\frac{\partial^2 \phi}{\partial x^2} + \frac{\partial^2 \phi}{\partial y^2} + \frac{\partial^2 \phi}{\partial z^2} = 0 \tag{2.34}$$

which is an Elliptic (or *Laplace*) equation. Solutions of Laplace equations are termed *harmonic functions* (right hand side is zero) which is why Eq. 2.32 is refered to as the *quasi-harmonic* equation.

5. If the function depends only on x and t, then we obtain

$$\rho c \frac{\partial \phi}{\partial t} = \frac{\partial}{\partial x}\left(k_x \frac{\partial \phi}{\partial x}\right) + Q \tag{2.35}$$

which is a parabolic (or Heat) equation.

2.3 Boundary Conditions for Exposed Concrete

As in solid mechanics (Section 1.5), boundary conditions must be defined and are of two types:

Essential: Temperatures prescribed over Γ_T.
Natural: Flux prescribed over Γ_q, which in turn can be broken into

Specified Flux or q =cst over Γ_q.
Convection or Radiation $q = f(T)$ over Γ_q.

2.3.1 Essential; Temperature

At the boundary or the surface of the concrete, there is energy transferred between the surface of the concrete and the surrounding air. The rate of energy transferred by the surrounding air to or from the concrete surface (q_a) must be equal to the rate of energy transferred through the concrete (q_c) by conduction or

$$q_c = q_a \qquad \text{at the boundary,} \tag{2.36}$$

where q_c is the rate of heat transfer by conduction which is defined by

$$q_c = -k\left(\frac{\partial T}{\partial x}n_x + \frac{\partial T}{\partial y}n_y\right) \tag{2.37}$$

where n_x and n_y are the direction cosines of the unit outward normal to the boundary surface.

2.3.1.1 Special Considerations for Dams

As stated earlier, thermal analysis of dams is particularly important and subjected to different mechanisms of heat transfer, Figure 2.3.

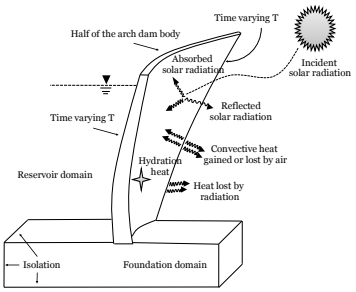

Fig. 2.3: Heat transfer mechanism for a concrete dam in 3D space; adopted from [596]

2.3.1.1.1 Air Temperature Estimation of the dam site's air temperature usually depends on the data obtained from the nearest weather station. In the current study, the following data were collected from weather stations:

- Daily mean temperature, T_i
- Daily maximum, $(T_{max})_i$, and daily minimum temperatures, $(T_{min})_i$
- The maximum monthly mean temperature, T_{max}
- The minimum monthly mean temperature, T_{min}
- Annual mean temperature, T_{mean}
- The highest and lowest recorded temperature at the site

If there is no information about the air temperature at the dam site, it is possible to use the sinusoidal function with the acceptable accuracy as:

$$T_a(t) = \bar{A} \sin\left(\frac{2\pi(t-\xi)}{P}\right) + \bar{B} \tag{2.38}$$

where $\bar{A}$ is the amplitude, $\bar{B}$ is the annual mean temperature, t is time in day, ξ is time in day at which $T_a(\xi) = \bar{B}$, and P is period of the sine function, here it is 365 days. In this function, $\bar{A}$ can be obtained as:

$$\bar{A} = \frac{1}{2}\left(|T_{max} - T_{mean}| + |T_{min} - T_{mean}|\right) \tag{2.39}$$

in which

$$\begin{cases} T_{max} = \frac{\sum_{i=1}^{n}(T_{max})_i}{n} \\ T_{min} = \frac{\sum_{i=1}^{n}(T_{min})_i}{n} \\ T_{mean} = \frac{\sum_{i=1}^{P} T_i}{P} \end{cases} \tag{2.40}$$

where n is the number of days per month. Figure 2.4(a) compares a sample recorded air temperature and the estimated one for a hypothetical station.

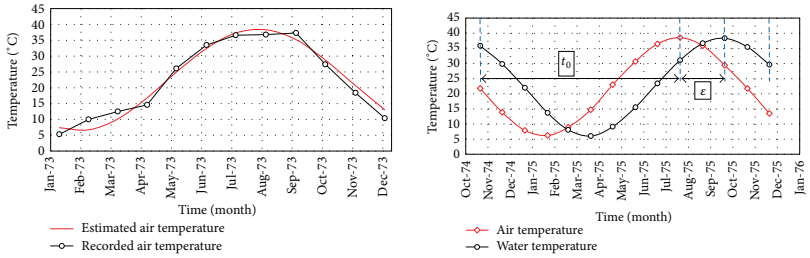

(a) Estimated vs. recorded air temperature

(b) Physical concept of ε and t_0

Fig. 2.4: Air and reservoir temperatures

2.3.1.1.2 Reservoir Temperature Distribution of the temperature within the dam body is strongly affected by the reservoir water temperature. The best source for this information is the collected statistical data from similar reservoirs. This type of information is collected by USBR and reported in engineering supplement No.34 [834]. The proposed method by Zhu [920] is another way for estimation of the reservoir temperature which is used in the present study (see the following equation). He showed that the proposed method is in good agreement with the recitation values from China reservoirs and can be used for other reservoirs with small changes in the parameters:

$$T(y,t) = T_m(y) + A(y)\cos\omega(t - t_0 - \varepsilon) \tag{2.41}$$

where y is reservoir depth, t is time in day, $T(y,t)$ is the reservoir temperature at time t and depth y, $T_m(y)$ is the mean annual temperature of the reservoir, $A(y)$ is the amplitude of the annual variations in the reservoir temperature, ω is the frequency of temperature variations, and the parameters ε and t_0 are illustrated in Figure 2.4(b). The mean annual temperature of the reservoir, $T_m(y)$, can be obtained as follows [920]:

$$\begin{cases} T_m(y) = c + (T_s - c).\exp(-\alpha y) \\ c = \frac{T_b - gT_s}{1-\exp(-0.04H)} \end{cases} \tag{2.42}$$

where T_s is the mean annual temperature of the reservoir at the surface, T_b is the mean annual temperature of the reservoir at the bottom, H is the reservoir depth, and the parameter α is 0.04. The detailed formulations on how T_s and T_b are calculated can be found in Zhu [920]. Moreover, the amplitude of the annual variations in the reservoir temperature, $A(y)$, is:

$$A(y) = \left(\frac{T_{max} - T_{min}}{2}\right)\exp(-\beta_0 y) \tag{2.43}$$

The parameter β_0 is a function of reservoir height and is calculated as:

$$\beta_0 = -0.058545 + 7.2727 \times 10^{-4} H \tag{2.44}$$

The minimum allowed value for β_0 is 0.018. Finally the parameter ε may be calculated by the following equation:

$$\varepsilon = d - f.\exp(-\gamma y) \tag{2.45}$$

where the parameters γ, d, and f are 0.085, 2.15, and 1.30, respectively.

2.3.2 Natural; Convection

Convection is the heat transfer due to the moving air contacts at the concrete surface at different temperatures. It is expressed by Newton's law of cooling as

$$q_{conv} = h_c(T_s - T_a) \tag{2.46}$$

where

- h_c = convection coefficient $W/m^{2o}C$
- T_s = temperature of the concrete surface ^oC
- T_a = temperature of the surrounding air ^oC

2.3.2.1 Special Considerations for Exposed Concrete Surfaces

For the convection over the planes, the convection coefficient is a function of the length of the surface in the direction of the flow, L, and the wind speed, v. It is given by [510]

1. if $vL < 15\ ft^2/s$ or $1.4\ m^2/s$

$$h_c = 0.35\left(\frac{v}{L}\right)^{1/2} \quad \text{[US unit]} \tag{2.47}$$

$$h_c = 2.0\left(\frac{v}{L}\right)^{1/2} \quad \text{[SI unit]} \tag{2.48}$$

2. if $vL > 15\ ft^2/s$ or $1.4\ m^2/s$

$$h_c = 0.54\left(\frac{v^4}{L}\right)^{1/5} \quad \text{[US unit]} \tag{2.49}$$

$$h_c = 6.2\left(\frac{v^4}{L}\right)^{1/5} \quad \text{[SI unit]} \tag{2.50}$$

2.3.3 Radiation

2.3.3.1 Irradiation; Stefan-Boltzman

Irradiation refers to the heat transfer from the surface to the surrounding air and is governed by the Stefan-Boltzman law as

$$q_{ir} = C_s \epsilon (T_s^4 - T_a^4) \tag{2.51}$$

where

- C_s = Stefan-Boltzman constant = $5.677 \times 10^{-8} W/m^2K^4$
- ϵ = emissivity coefficient of concrete
- T_s = concrete surface temperature in $Kelvin$
- T_a = surrounding air temperature in $Kelvin$

2.3.3.2 Solar Radiation; Approximation

Solar Radiation refers to the power (J/m^2) received by the sun in the form of electromagnetic radiation. It is a function of the orientation of the surface with respect to the sun. An exact mathematical model for solar radiation is quite complex, and an approximation by Kreider and Rabl [510] offered the following linear simplification

$$q_s = \alpha\, I(s,t) \tag{2.52}$$

where I is total solar radiation or global radiation on a surface s at time t and α is the absorptivity of the surface which is defined by the fraction of I absorbed by the surface structure. For concrete, α = 0.94.
The global radiation ,I_{glo}, is sum of the diffuse radiation, I_{diff} (i.e. solar radiation scattered by aerosols, dust and by the Rayleigh mechanism), and direct radiation, I_{dir} (solar radiation intercepted by a surface with negligible direction change and scattering in the atmosphere).

1. Solar radiation on the horizontal surface
   The total radiation on the horizontal surface or, in other words, global horizontal radiation is given by

$$I_{glo,hor} = I_{dir} \cos\theta_s + I_{diff} \tag{2.53}$$

   where θ_s is zenith angle of the sun or the angle between the normal of the surface at point P and the line from point P to the sun as shown in Figure 2.5

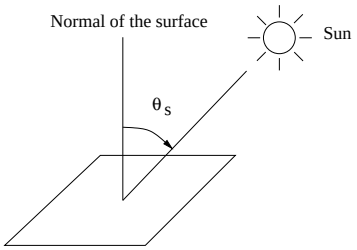

Fig. 2.5: Azimuth angle of the sun

2. Zenith angle of the sun, θ_s
   The zenith angle of the sun is given by

$$\cos\theta_s = \cos\lambda\cos\delta\cos\omega + \sin\lambda\sin\delta \tag{2.54}$$

   where

   - λ = latitude of the the location (north is positive)
   - δ = solar declination
   - ω = solar hour angle which can be expressed by

$$\omega = \frac{t_{sol} - 12}{24} \times 360^o \tag{2.55}$$

     where t_{sol} is the solar time in $hours$.

3. Solar Time, t_{sol}
   The solar time is given by

$$t_{sol} = t_{std} + \frac{L_{std} - L_{loc}}{15} + \frac{ET}{60} \tag{2.56}$$

   where

- L_{std} = longitude of the standard time zone ($degrees$). For example, in the United States, the longitudes of the standard time zones are 75^oW for Eastern, 90^oW for Central, 105^oW for Mountain, and 120^oW for Pacific.
- L_{loc} = site longitude ($degrees$)
- ET = equation of time which is defined by the following:

$$ET = 9.87 \sin 2\left(360^o \times \frac{n-81}{364}\right) - 7.53 \cos\left(360^o \times \frac{n-81}{364}\right) - 1.5 \sin\left(360^o \times \frac{n-81}{364}\right) \tag{2.57}$$

where n is day of the year (i.e. $n = 1$ for Jan 1).

4. Solar Declination, δ
The solar declination can be expressed by

$$\sin \delta = -\sin 23.45^o \cos \frac{360^o \times (n+10)}{365.25} \tag{2.58}$$

where n is defined as mentioned before.

The heat flux, q_s, can only be applied during the hours between sunrise and sunset. The sunrise (t_{sr}) and sunset times (t_{ss}) can be determined from the following:

$$\begin{aligned} t_{sr} &= 12 + \frac{1}{15} \cos^{-1}(-\tan\lambda \tan\delta) \\ t_{ss} &= 12 - \frac{1}{15} \cos^{-1}(-\tan\lambda \tan\delta) \end{aligned} \tag{2.59}$$

in which λ is latitude of the location and δ is solar declination.
The total radiation on the vertical surface or global vertical radiation is given by

$$I_{glo,ver} = I_{dir} \cos\theta_i + \frac{I_{diff}}{2} + \frac{I_{glo,hor}\,\rho_g}{2} \tag{2.60}$$

where θ_i is angle between the normal of the plane and the line of the sun. It is given by

$$\cos\theta_i = \sin\theta_s \cos(\phi_s - \phi_p) \tag{2.61}$$

in which

- ϕ_p = azimuth angle of the surface in $degrees$ (positive for the the orientations west of south); it can be shown in Figure 2.6
- ϕ_s = azimuth angle of the sun which is defined by

$$\sin\phi_s = \frac{\cos\delta \sin\omega}{\sin\theta_s} \tag{2.62}$$

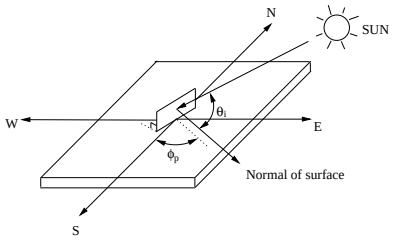

Fig. 2.6: Zenith angle θ_p, azimuth angle of a vertical plane ϕ_p, and angle of incidence of sun on the vertical plane θ_i [510]

- ρ_g = Reflectivity of the ground. The values of the reflectivity of some selected surfaces can be tabulated in Table 2.2

Table 2.2: Reflectivity of the selected surfaces [510]

Surface	Reflectivity ρ_g
Soils	0.75
Water	0.07
Concrete, new	0.35
Concrete, old	0.25
Earth roads	0.04
Grass, dry	0.20
Grass, green	0.26

2.4 Summary

The complexity introduced by the empirical relationships to approximate radiation heat transfer is non-negligible. Hence, the inter connectivity of the various equations previously presented in shown in Figure 2.7.

2.5 Summary and Tonti Diagrams

There are many similarities between the scalar field problem addressed in this chapter and the vectorial one addressed in Chapter 1; those are compared in Table 2.3.
A Tonti diagram represents governing equations as arrows linking boxes containing kinematic and static quantities, Figure 2.8.

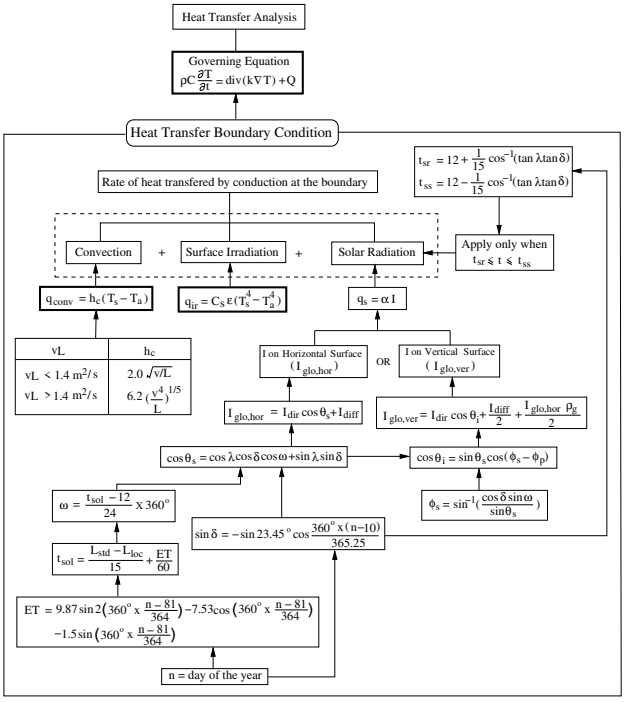

Fig. 2.7: Heat Transfer Analysis in Concrete

Table 2.3: Comparison of Scalar and Vector Field Problems

Scalar	Vector	
Conduction	Solid Mechanics	
Variables		
T	$\mathbf{u}$	State
g	$\boldsymbol{\varepsilon}$	Intermediate
$\mathbf{q}$	$\boldsymbol{\sigma}$	Flux
Field Equations		
$\mathrm{div}\,\mathbf{q} + Q = 0$	$\mathbf{L}^T\boldsymbol{\sigma} + \mathbf{b} = 0$	Balance
$g = \boldsymbol{\nabla} T$	$\boldsymbol{\varepsilon} = \mathbf{L}\mathbf{u}$	kinematic
$\underbrace{\mathbf{q} = -\mathbf{D}g}_{\text{Fourrier}}$	$\underbrace{\boldsymbol{\sigma} = \mathbf{D}\boldsymbol{\varepsilon}}_{\text{Hooke}}$	Constitutive
Boundary Conditions		
T on Γ_T	$\mathbf{u}$ on Γ_u	Essential BC
$q_n = \mathbf{q}^T\mathbf{n}$ on $\Gamma_q \cup \Gamma_c$	$\mathbf{t} = \boldsymbol{\sigma}\mathbf{n}$ on Γ_t	Natural BC (Flux)

For the scalar and vectorial field problems studied, the corresponding Tonti diagrams are shown in Figure 2.9.

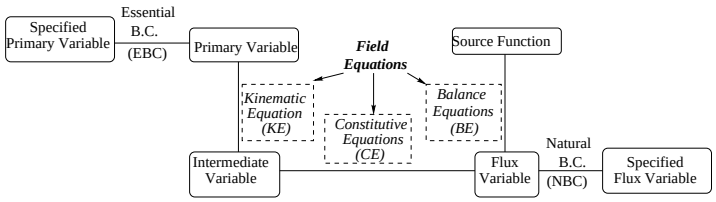

Fig. 2.8: Components of Tonti's Diagram, [293]

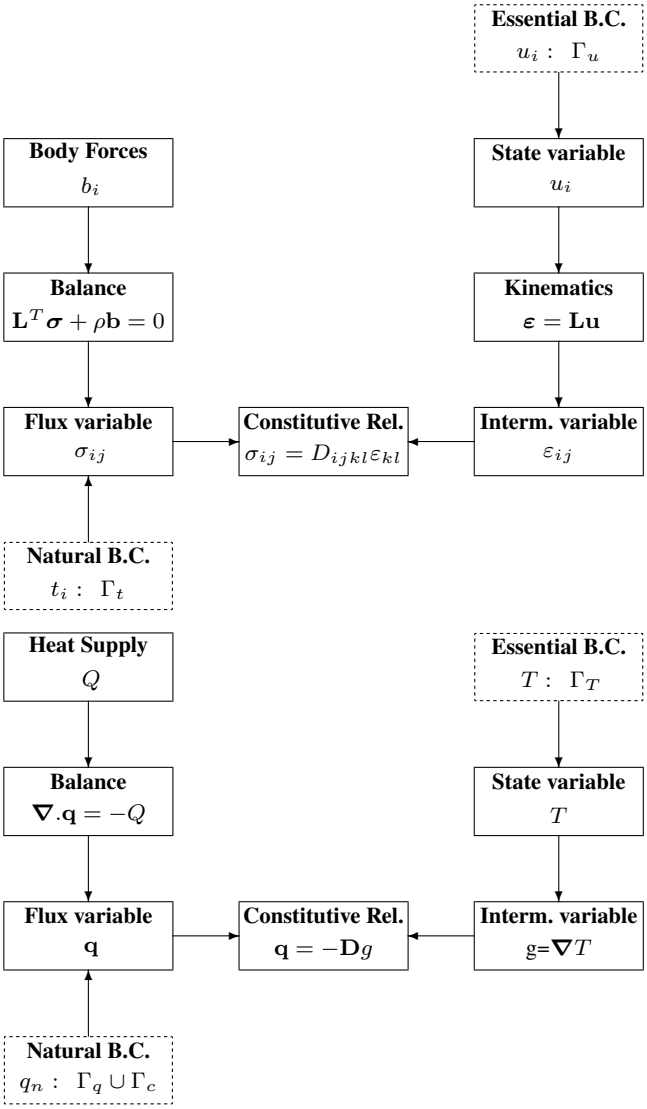

Fig. 2.9: Fundamental Equations of Solid Mechanics and Heat Flow

Chapter 3
Plasticity

Abstract
Plasticity is probably the most commonly studied failure mechanism. Its usage in metals is wide-spread; however, it has its limitations in capturing concrete failure (especially in tension). Failure modes, causes of plastic failures, and implications on computational plasticity will be addressed.

3.1 Introduction

There are three major types of failure: cracking/fracture, buckling/instability, and yielding/plasticity. The first was addressed in Chapter 4, and plasticity will be briefly addressed in this one. It can be argued that although most structure failures are caused by (one way or another) fracture, far fewer are caused by yielding or excessive plastic deformation.
For concrete, plastic failure tends to be associated with "crushing" of concrete (see Section 3.2.1), or yielding of the reinforcement (Section 3.2.2).
This chapter will provide a brief introduction to plasticity based failure criteria which are nearly universally used in non-linear finite element analyses.

3.2 Plastic Yield Conditions

Yielding in a uniaxially loaded structural element can be easily determined from $|\frac{\sigma}{\sigma_{yld}}| \overset{?}{\geq} 1$. But what about a general three dimensional stress state?
This is accomplished by introducing a yield function F as a function of the principal stresses and the uniaxial yield stress

$$F(\sigma_{(1)}, \sigma_{(2)}, \sigma_{(3)}; \sigma_y) \begin{cases} < 0 & \text{Elastic} \\ = 0 & \text{Plastic} \\ > 0 & \text{Impossible} \end{cases} \quad \begin{vmatrix} \frac{\mathrm{d}\varepsilon^P}{\mathrm{d}t} \end{vmatrix} = 0 \\ \begin{vmatrix} \frac{\mathrm{d}\varepsilon^P}{\mathrm{d}t} \end{vmatrix} \geq 0 \tag{3.1}$$

Note that F can not be greater than zero, for the same reason that a uniaxial stress can not exceed the yield stress. In terms of the two principal stresses $\sigma_{(1)} - \sigma_{(2)}$, F is shown in Figure 3.1. The area defined by F constitutes the yield surface.

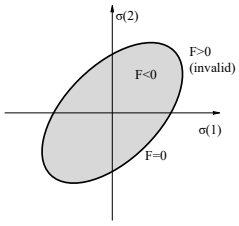

Fig. 3.1: Yield surface; Definition

There are two classes of yield surfaces: those which are independent of the hydrostatic stress (Eq. 1.72) and those which are dependent [187].

3.2.1 Hydrostatic Pressure Independent Models

For hydrostatic pressure independent yield surfaces (such as for steel), their meridians are straight lines parallel to the hydrostatic axis. Hence, shearing stress must be the major cause of yielding for this type of material. Since it is the magnitude of the shear stress that is important, and not its direction, it follows that the elastic-plastic behavior in tension and in compression should be equivalent for hydrostatic pressure independent materials (such as steel).

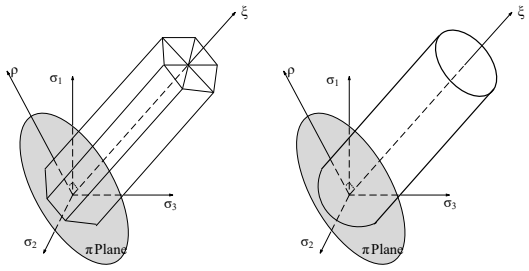

(a) Tresca (b) von Mises

Fig. 3.2: Hydrostatic pressure independent models

Tresca: criterion postulates that yielding occurs when the maximum shear stress reaches a limiting value k, Figure 3.2(a).

$$F\left(\max\left(\frac{1}{2}|\sigma_1-\sigma_2|,\frac{1}{2}|\sigma_2-\sigma_3|,\frac{1}{2}|\sigma_3-\sigma_1|\right)-k\right)=0 \qquad (3.2)$$

From a uniaxial tension test, we determine that $k = \sigma_y/2$, and from a pure shear test, $k = \tau_y$. Hence in Tresca, tensile strength and shear strength are related by

$$\sigma_y = 2\tau_y \tag{3.3}$$

Tresca's criterion can also be represented as

$$2\sqrt{J_2}\sin\left(\theta + \frac{\pi}{3}\right) - \sigma_y = 0 \;\text{ for }\; 0 \le \theta \le \frac{\pi}{3} \tag{3.4}$$

The Tresca criterion is the first one proposed, used mostly for elastic-plastic problems. However, because of the singular corners, it causes numerous problems in numerical analysis.

Von Mises: There are multiple physical interpretations for the von Mises criteria postulate (all equivalent), Figure 3.2(b):

1. Material will yield when the second deviatoric stress invariant reaches a critical value

$$F(J_2) = J_2 - k^2 = 0 \tag{3.5}$$

$$= \frac{(\sigma_1 - \sigma_2)^2 + (\sigma_2 - \sigma_3)^2 + (\sigma_1 - \sigma_3)^2}{2} - \sigma_y^2 = 0 \tag{3.6}$$

2. Material will yield when the maximum distorsional (shear) energy reaches the same critical value as for yield as in uniaxial tension.
3. When the distance (ρ) between the stress point P and the hydrostatic axis ξ is equal to

$$\rho_0 = \tau_y\sqrt{2} \tag{3.7}$$

Using Eq. 3.6 and from the uniaxial test, k is equal to $k = \sigma_y/\sqrt{3}$, and from the pure shear test, $k = \tau_y$. Hence in von Mises, tensile strength and shear strength are related by

$$\sigma_y = \sqrt{3}\tau_y \tag{3.8}$$

Hence, we can rewrite Eq. 3.5 as

$$f(J_2) = J_2 - \frac{\sigma_y^2}{3} = 0 \tag{3.9}$$

3.2.2 Hydrostatic Pressure Dependent Models

Pressure sensitive frictional materials (such as soil, rock, concrete) need to consider the effects of both the first and second stress invariants, better explained in terms of the yield surface.

The cross-sections of a yield surface are the intersection curves between the yield surface and the deviatoric plane (ρ, θ) which is perpendicular to the hydrostatic axis, ξ, and with ξ = constant. The cross-sectional shapes of this yield surface will have threefold symmetry.

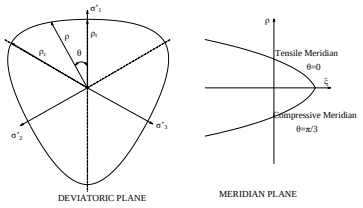

Fig. 3.3: Pressure Dependent Yield Surfaces

The meridians of a yield surface are the intersection curves between the surface and a meridian plane (ξ, ρ) which contains the hydrostatic axis. The meridian plane with $\theta = 0$ is the tensile meridian and passes through the uniaxial tensile yield point. The meridian plane with $\theta = \pi/3$ is the compressive meridian and passes through the uniaxial compression yield point, Figure 3.3. The radius of a yield surface on the tensile meridian is ρ_t and on the compressive meridian is ρ_c.

Rankine: criterion postulates that yielding occurs when the maximum principal stress reaches the tensile strength, Figure 3.4(a).

$$\sigma_1 = \sigma_y; \qquad \sigma_2 = \sigma_y; \qquad \sigma_3 = \sigma_y; \tag{3.10}$$

Mohr-Coulomb: criteria can be considered as an extension of the Tresca criterion. The maximum shear stress is a constant plus a function of the normal stress acting on the same plane, Figure 3.4(b).

$$|\tau| = c - \sigma \tan\phi \tag{3.11}$$

where c is the cohesion and ϕ the angle of internal friction. Both c and ϕ are material properties which can be calibrated from uniaxial tensile and uniaxial compressive tests.

$$\begin{cases} \sigma_t = \frac{2c\cos\phi}{1+\sin\phi} \\ \sigma_c = \frac{2c\cos\phi}{1-\sin\phi} \end{cases} \tag{3.12}$$

In terms of invariants, the Mohr-Coulomb criteria can be expressed as:

$$\frac{1}{3} I_1 \sin\phi + \sqrt{J_2}\sin\left(\theta + \frac{\pi}{3}\right) + \sqrt{\frac{J_2}{3}}\cos\left(\theta + \frac{\pi}{3}\right)\sin\phi - c\cos\phi = 0 \quad \text{for } 0 \le \theta \le \frac{\pi}{3} \tag{3.13}$$

Drucker-Prager: postulate is a simple extension of the von Mises criterion to include the effect of hydrostatic pressure on the yielding of the materials through I_1, Figure 3.4(c):

$$F(I_1, J_2) = \alpha I_1 + J_2 - k \tag{3.14}$$

The strength parameters α and k can be determined from the uniaxial tension and compression tests:

$$\begin{cases} \sigma_t = \frac{\sqrt{3}k}{1+\sqrt{3}\alpha} \\ \sigma_c = \frac{\sqrt{3}k}{1-\sqrt{3}\alpha} \end{cases} \tag{3.15}$$

or

$$\begin{cases} \alpha = \frac{m-1}{\sqrt{3}(m+1)} \\ k = \frac{2\sigma_c}{\sqrt{3}(m+1)} \end{cases} \tag{3.16}$$

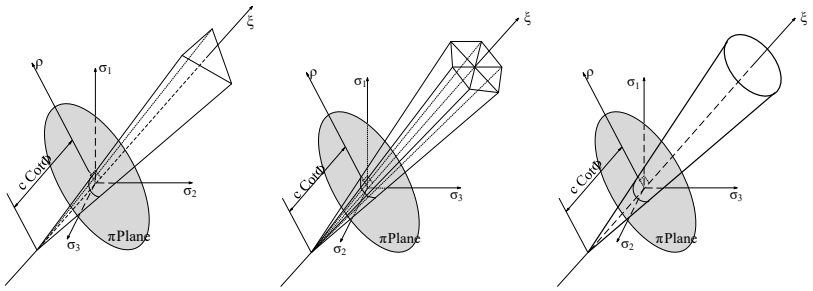

(a) Rankine (b) Mohr-Coulomb (c) Drucker-Prager

Fig. 3.4: Hydrostatic pressure dependent models

3.3 Laboratory Observations

3.3.1 Metals

Loading and unloading a steel coupon at various stages, Figure 3.5, we observe that up to A, there would be a linearly elastic unloading following the initial loading path. O-A behavior is load path independent. At A, we reach the elastic limit. Then, the material becomes plastic and behaves irreversibly: First yielding occurs (A-D) and then hardening. Upon unloading, the material experiences permanent strain or plastic strain ε^p. Thus, only part of the total strain ε_B at B is recovered upon unloading, i.e., the elastic strain ε^e_A.

Strain hardening in one direction followed by reversed loading in the other leads to a different stress-strain curve than the one obtained from pure tension or compression. The new yield point in compression at B corresponds to a stress σ_y^B smaller than σ_y^0, and much smaller than the previous yield stress at A. This phenomenon is called the Bauschinger effect, or kinematic hardening (as opposed to isotropic hardening).

Finally, the stress-strain behavior in the plastic range is path dependent, i.e. strain will not depend on the the current stress state. It also depends on the entire loading history, i.e. stress history and deformation history.

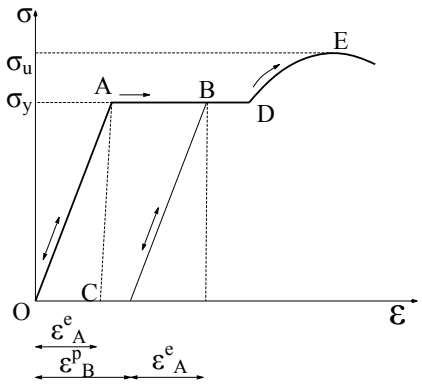

Fig. 3.5: Representative stress-strain of metals

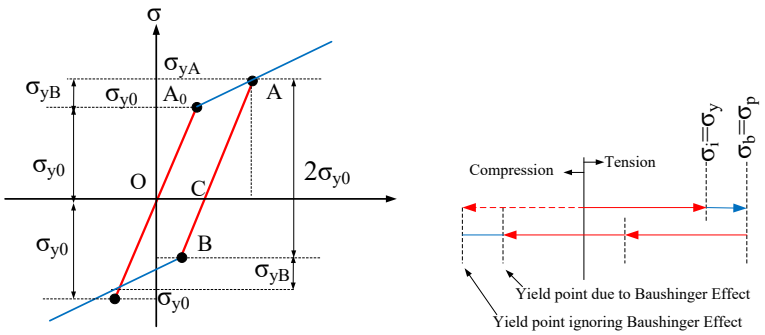

Fig. 3.6: Bauschinger Effect

3.3.2 Concrete

Concrete contains microcracks due to shrinkage and is originally isotropic. Under compression as the stress reaches $\simeq 0.5 f_c'$, interface cracks around the aggregates propagate and tend to align themselves with the compressive stress. At peak stress, a mechanism is formed (coalescence of the micro-cracks) [433] [795].
If a load is applied, sudden failure at the peak occurs, and if displacement is imposed, post-peak softening occurs.

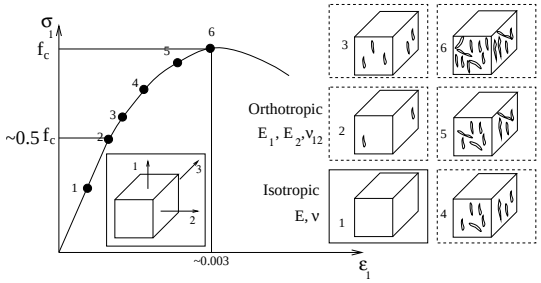

Fig. 3.7: Concrete micro-cracks

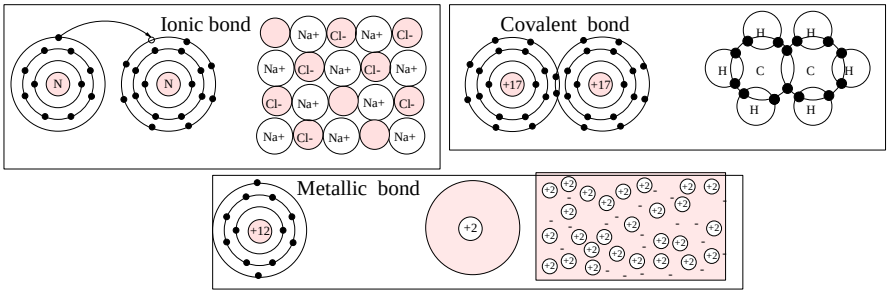

Fig. 3.8: Chemical bonds

3.4 Microscopic Failures

3.4.1 Chemical Bonds

Understanding chemical bonds is important to explaining both ductile failure and dislocation. Ionic bond atoms are held together by electrostatic attraction as electrons are transferred from one atom to a neighboring one. The atom giving up the electron becomes positively charged, and the atom receiving it becomes negatively charged. A covalent bond occurs when electrons are shared more or less equally between neighboring atoms. Although the electrostatic force of attraction between adjacent atoms is less than it is in ionic bonds, covalent bonds tend to be highly directional, meaning that they resist motion of atoms past one another. Diamond has covalent bonds. In a metallic bond, electrons are delocalized or distributed equally through a metallic crystal, and the bond is not localized between two atoms. These are best described as positive ions in a sea of electrons.

3.4.2 Ductile and Brittle Failures

In an ionic solid, each ion is surrounded by oppositely charged ions, thus slipping is much more difficult to achieve, and the material responds by breaking in a brittle behavior.

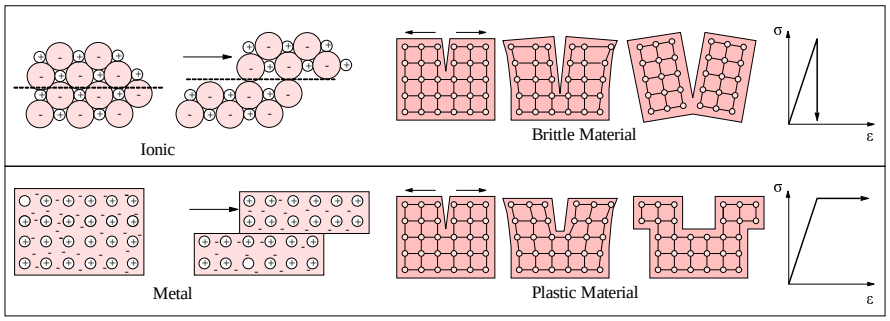

Fig. 3.9: Ductile and brittle bonds

When a force of sufficient magnitude displaces atoms from one equilibrium position to another, we have a plastic deformation along the slip plane.
When a shear stress is applied on a metal bond, atoms can slip and slide past one another without regard to electrical charge constraint, and thus it gives rise to a ductile response.

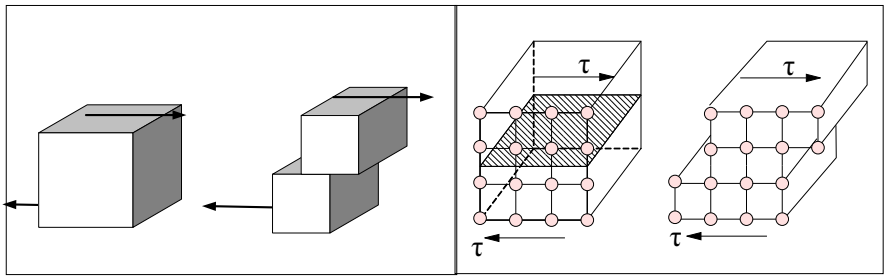

Fig. 3.10: Slip planes

3.4.3 Dislocation

The theoretical strength of perfect crystals (stress it takes to separate two adjacent atoms) is about $E/10$, but it is never achieved due to the presence of random imperfections.
Edge dislocation is caused by internal flaws in the atomic plane. Due to τ, there is a driving force for breaking atomic bonds between atoms A and C until the dislocation passes entirely out of the crystal. This is called dislocation glide, Figure 3.11.
When the dislocation leaves the crystal, there will be a permanent offset.

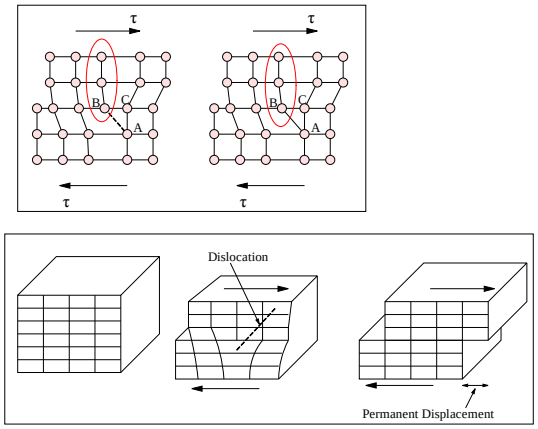

Fig. 3.11: Dislocation

The yield stress is reached once the applied shear stress equals the shear stress necessary to provide the dislocations with enough energy to overcome short range forces exerted by the obstacles.
Work-Hardening in turn can be explained when plastic deformation dislocations multiply, and greater stresses are needed to overcome this resistance and strain hardening occurs.
Finally, the Bauschinger Effect occurs when deformations or dislocations accumulate causing dislocation pile-ups. Since strain hardening is related to increased dislocation density, reducing the number of dislocations (through stress reversal) reduces strength.

3.5 Fundamentals of Plasticity

3.5.1 Introduction

There are two major theories for elastoplasticity:

Deformation Theory (or Total) of Hencky and Nadai, where the total strain, ε_{ij}, is a function of the current stress. $\varepsilon = \varepsilon_e + \varepsilon_p$ leads to a secant-type formulation of plasticity that is based on the additive decomposition of total strain into elastic and plastic components (Hencky).

Rate Theory (or incremental) of Prandtl-Reuss, defined by

$$\dot{\varepsilon} = \dot{\varepsilon}_e + \dot{\varepsilon}_p \tag{3.17}$$

Rate theory is the most widely used one.
With reference to Figure 3.12, the total strain increment can be decomposed into an elastic and a plastic one:

$$\dot{\varepsilon} = \dot{\varepsilon}^e + \dot{\varepsilon}^p \tag{3.18}$$

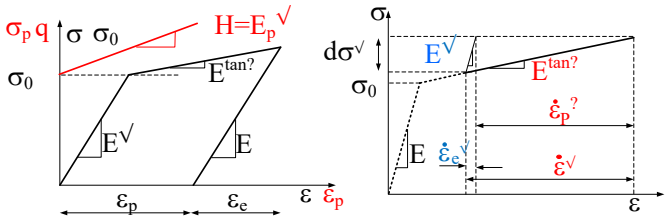

Fig. 3.12: Elasto-Plastic stress strain response

However, we only know the elastic part from the constitutive law:

$$\dot{\sigma} = E(\dot{\varepsilon} - \dot{\varepsilon}^p) \tag{3.19}$$

The plastic strain and corresponding plastic stress increment are:

$$\dot{\sigma_p} = \dot{q} = H\dot{\varepsilon_p} \tag{3.20}$$

3.5.2 Tangent Elastic Modulus

With reference to Figure 3.12, the total incremental strain is $\dot{\varepsilon}$, and we seek to determine the corresponding incremental plastic stress, $\dot{\sigma}$, such that

$$\dot{\sigma} = E^{tan}\dot{\varepsilon} \tag{3.21}$$

This would necessitate the so-called tangent elastic modulus E^{tan} (not to be confused with H).
Two approaches are possible:

1. Generalized 3D Mechanics; this will require
   a. Yield function
   b. Flow rule
   c. Consistency condition
2. Engineering 1D

Each will be separately addressed.

3.5.2.1 Generalized Derivation

3.5.2.1.1 Yield Function; Isotropic Hardening Model The yield function denotes the current level of stress minus the initial yield stress to which one may add a

function of α which describes the type of hardening. In 1D, it can be defined as

$$h(\sigma, q) = |\sigma| - q \leq 0 \tag{3.22}$$

$\mathbf{q}$ determines the motion and deformation of the yield surface (Hardening or Softening). If $h < 0$, then the stress is within the elastic domain, and if $h = 0$, the stress has reached its plastic limit.
First the strain reaches yielding ($\sigma_0 = \sigma_y$). At that point, further increase in strain results in an expansion of q which will in turn expand the elastic domain.

3.5.2.1.2 Flow Rule When the stress is inside the yield surface, it is elastic, Hooke's law is applicable, strains are recoverable, and there is no dissipation of energy . Hence, when the load on the structure pushes the stress tensor to be beyond the yield surface, the stress tensor locks up on the yield surface, and the structure deforms plastically. If the material exhibits hardening as opposed to elastic-perfectly plastic response, then the yield surface expands or moves with the stress point still on the yield surface. The crucial question is what will be the direction of the plastic flow (that is the relative magnitude of the components of $\boldsymbol{\varepsilon}^P$). This question is addressed by the flow rule, or normality rule.

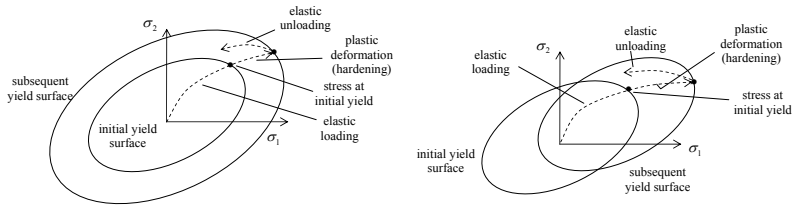

Fig. 3.13: Isotropic Hardening and Kinematic Hardening

Flow rule assumes that the plastic strain increment and deviatoric stress tensor have the same principal directions, and it defines the evolution of plastic strain as:

$$\dot{\varepsilon}^p := \lambda \cdot \frac{\partial g(\sigma, \varepsilon^p, q)}{\partial \sigma} = \lambda \cdot h(\sigma,\ q) \tag{3.23}$$

where $g(\sigma, \varepsilon^p, q)$ is the plastic potential and λ is a plastic multiplier that measures the magnitude of the plastic deformation (as we shall see later, this term will drop and lead to E^{tan} which is what we are ultimately seeking). If $g \equiv h$, we have an associated flow rule (usually in metals). If $g \neq h$ we have a non associated flow rule (concrete and geomaterials exhibiting dilatancy).
For isotropic hardening models and an associated flow rule,

$$g(\sigma, \varepsilon^p, q) = h(\sigma, q) = |\sigma| - q \Rightarrow \frac{\partial g}{\partial \sigma} = \text{sign}(\sigma) \tag{3.24}$$

where sign(σ) is 1 if $\sigma \geq 0$ or -1 if $\sigma < 0$. Then from Eq. 3.23,

$$\dot{\varepsilon}^p = \lambda \cdot \text{sign}(\sigma) \tag{3.25}$$

or

$$\lambda = |\dot{\varepsilon}^p| \geq 0 \tag{3.26}$$

For simplicity and under the assumption of an elasto-plastic hardening material with a bilinear curve,

$$h(\sigma,\ q) = -\frac{\partial g}{\partial q} = 1 \tag{3.27}$$

Therefore, we can express the stress (Eq. 3.19) as

$$\dot{\sigma} = E(\dot{\varepsilon} - \dot{\varepsilon}^p) \Rightarrow \dot{\sigma} = E \cdot (\dot{\varepsilon} - \lambda \cdot \frac{\partial g}{\partial \sigma}) = E \cdot (\varepsilon - \lambda \cdot \dot{\text{sign}}(\sigma)) \tag{3.28}$$

and from Eq. 3.20

$$\dot{q} = H\dot{\varepsilon_p} \Rightarrow \dot{q} = H \cdot \lambda \cdot h(\sigma,\ q) = H \cdot \lambda \tag{3.29}$$

3.5.2.1.2.1 Kuhn-Tucker Conditions In the elastic regime, the yield function f must remain negative, and the plastic multiplier is zero. During plastic flow, the yield function f must be zero while plastic multiplier is positive. These constraints can be succinctly expressed by the so-called Kuhn-Tucker condition,

$$\begin{aligned} \text{Elastic loading and unloading} &: f < 0,\ \dot{\gamma} = 0 \\ \text{Plastic loading} &: f = 0,\ \dot{\gamma} > 0 \end{aligned}$$

Or combined for the general case of $f \leq 0$ and $\dot{\gamma} \geq 0$

$$f \cdot \dot{\gamma} = 0 \tag{3.30}$$

3.5.2.1.3 Consistency Condition During plastic loading, the stress path is constrained to move along the yield surface, thus this consistency condition precludes us from going beyond the yield surface and is mathematically expressed as $\dot{f}(\sigma, q) = 0$, or

$$\begin{aligned} \dot{f}(\sigma,\ q) &= \frac{\partial f}{\partial \sigma} \cdot \frac{\partial \sigma}{\partial t} + \frac{\partial f}{\partial q} \cdot \frac{\partial q}{\partial t} \\ &= \frac{\partial f}{\partial \sigma} \cdot \dot{\sigma} + \frac{\partial f}{\partial q} \cdot \dot{q} = 0 \end{aligned} \tag{3.31}$$

3.5.2.1.4 Tangent Modulus Now, we can finally solve Eq. 3.21

$$\dot{\sigma} = E^{tan}\dot{\varepsilon} \tag{3.32}$$

where the tangent modulus is the slope of the stress-strain curve at any specified stress or strain. Below the proportional limit, the tangent modulus is equivalent to Young's modulus, not to be confused with $\dot{\sigma_p} = \dot{q} = H\dot{\varepsilon_p}$. Substituting

$$\begin{array}{ll} \text{Flow Rule Eq. 3.28} & \dot{\sigma} = E \cdot (\dot{\varepsilon} - \lambda \cdot \frac{\partial g}{\partial \sigma}) \\ \text{Eq. 3.29} & \dot{q} = H \cdot \lambda \cdot h(\sigma,\ q) \\ \text{Consistency Eq. 3.31} & \dot{f}(\sigma,\ q) = \frac{\partial f}{\partial \sigma} \cdot \dot{\sigma} + \frac{\partial f}{\partial q} \cdot \dot{q} = 0 \end{array} \tag{3.33}$$

we obtain

$$\frac{\partial f}{\partial \sigma} \cdot E \cdot \left(\dot{\varepsilon} - \lambda \cdot \frac{\partial g}{\partial \sigma} \right) + \frac{\partial f}{\partial q} \cdot H \cdot \lambda \cdot h(\sigma,\ q) = 0 \tag{3.34}$$

Therefore,

$$\lambda = \frac{\frac{\partial f}{\partial \sigma} \cdot E \cdot \dot{\varepsilon}}{\frac{\partial f}{\partial \sigma} \cdot E \cdot \frac{\partial g}{\partial \sigma} - \frac{\partial f}{\partial q} \cdot H \cdot h(\sigma,\ q)} \tag{3.35}$$

Substituting back into

$$\dot{\sigma} = E \cdot (\dot{\varepsilon} - \dot{\gamma} \cdot \text{sign}(\sigma)) \tag{3.36}$$

we obtain an explicit expression for the incremental stress,

$$\begin{aligned} \dot{\sigma} &= E \cdot \left(\dot{\varepsilon} - \lambda \cdot \frac{\partial g}{\partial \sigma} \right) \\ &= \underbrace{\left(E - \frac{\frac{\partial f}{\partial \sigma} \cdot E^2 \cdot \frac{\partial g}{\partial \sigma}}{\frac{\partial f}{\partial \sigma} \cdot E \cdot \frac{\partial g}{\partial \sigma} - \frac{\partial f}{\partial q} \cdot H \cdot h(\sigma,\ q)} \right)}_{(\textit{by definition})\ E^{tan}} \cdot \dot{\varepsilon} \end{aligned} \tag{3.37}$$

For an elasto-plastic hardening material with a bilinear curve in one dimension,

$$\lambda = \frac{\text{sign}(\sigma) \cdot E \cdot \dot{\varepsilon}}{E + H} \tag{3.38}$$

and the tangent modulus reduces to

$$E^{tan} = E - \frac{\text{sign}(\sigma) \cdot E^2 \cdot \text{sign}(\sigma)}{\text{sign}(\sigma) \cdot E \cdot \text{sign}(\sigma) - (-1) \cdot H \cdot (1)} \tag{3.39}$$

$$= E - \frac{E^2}{E + H} = \frac{E \cdot H}{E + H} \tag{3.40}$$

Note that if $H = E/9$, then $E^{tan} = E/10$.

3.5.2.2 Tangent Modulus; Engineering

A simpler (and more intuitive) derivation of the tangent modulus is derived next. Rate theory is defined by

$$\dot{\varepsilon} = \dot{\varepsilon}_e + \dot{\varepsilon}_p \tag{3.41}$$

If $\sigma \leq \sigma_y$ (elasticity), then

$$\dot{\varepsilon} = \dot{\varepsilon}_e = \frac{\dot{\sigma}}{E} \tag{3.42}$$

and if $\sigma > \sigma_y$ (plasticity), then

$$\dot{\varepsilon} = \dot{\varepsilon_e} + \dot{\varepsilon}_p$$
$$\dot{\varepsilon} = \frac{\dot{\sigma}}{E} + \frac{\dot{\sigma}}{H} = \frac{\dot{\sigma}}{E^{tan}}$$

where

$$E^{tan} = \frac{E.H}{E+H} \tag{3.43}$$

We note that

$$E^{tan} = \begin{cases} > 0, \, Hardening \\ = 0, \, Perfectly \, Plastic \\ < 0, \, Softening \end{cases} \tag{3.44}$$

E_t is independent of the type of hardening (isotropic or kinematic). Note: There is a counterpart in nonlinear structural analysis where we seek to determine the tangent stiffness matrix of an element at a given time step. The procedure is conceptually identical to what was done analytically in the first part.
Note the analogy with an equivalent resistor when multiple ones are in parallel.

Chapter 4
Fracture Mechanics

Abstract
Ultimately and at different scales, fracture is the leading cause of material failures. As continuum mechanics by its very essence can not capture fracture, a different branch of mechanics addresses this complex failure mode.
Hence, this chapter will be devoted to the fundamentals of theoretical fracture mechanics. Coverage will be substantially more expansive than the previous chapter on plasticity as it is, to some extent, more complex to tackle fracture of both brittle and quasi-brittle (such as concrete) materials. Both linear and nonlinear fracture mechanics will be addressed.

4.1 Introduction

The most common modes of failure are cracking and yielding. The first is addressed through fracture mechanics, and the other through the theory of plasticity.
Fracture mechanics is a (relatively) complex branch of applied mechanics (akin of fluid mechanics) that has attracted the attention of mathematicians (given the complexity of closed-formed solutions), physicists (relating fracture to debonding of atoms and the notion of surface energy), metallurgists (who study the nucleation of cracks), and civil-mechanical-aerospace engineers who apply it to better understand the mechanism of fracture whether for anticipating and preventing cracks or in forensic studies.
It should be noted that though this book focuses on concrete structures, this chapter covers basic concepts, and their applications are mostly geared to metallic structural elements.

4.2 Stress Concentrations in Hollowed Plates under Uniform Traction

Before stress singularities (present in a crack) are addressed within the context of linear elastic fracture mechanics, it may be helpful to remind ourselves that stress concentration factors are present around openings in plates subjected to uniform traction, Figure 4.1. By way of introduction, let us consider the simple classical

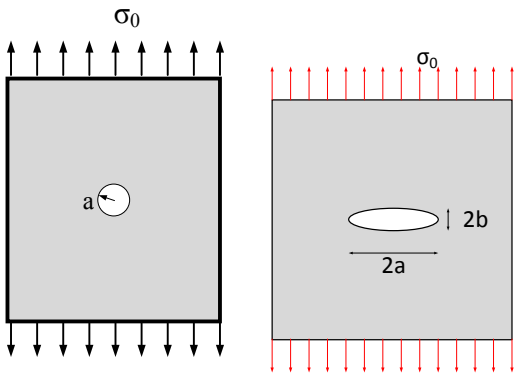

(a) Circular hole (b) Circular hole

Fig. 4.1: Infinite plates with holes and uniform traction

problem of a plate with a circular hole subjected to a uniform far field traction [504] It can be shown that around the edges of the hole, the stresses are given by

$$\sigma_{rr} = 0 \tag{4.1}$$

$$\sigma_{r\theta} = 0 \tag{4.2}$$

$$\sigma_{\theta\theta}|_{r=a} = \sigma_0(1 - 2\cos 2\theta) \tag{4.3}$$

which for $\theta = \frac{\pi}{2}$ and $\frac{3\pi}{2}$ gives a stress concentration factor (SCF) of 3. For $\theta = 0$ and $\theta = \pi$, $\sigma_{\theta\theta} = -\sigma_0$. For an elliptical hole in an infinite plate under uniform stress, Figure 4.1(b), Inglis [460] who was investigating failure around elliptical openings in British ships, solved this complex problem using curvilinear coordinate systems (α and β correspond to ellipses and orthogonal hyperbolae respectively), Figure 4.2.

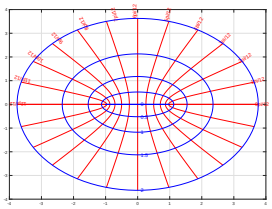

Fig. 4.2: Infinite plate with elliptical hole (curvilinear coordinate system)

$$(\sigma_{\beta\beta})_{\alpha=\alpha_0}^{\beta=0,\pi} = \sigma_0\left(1 + 2\frac{a}{b}\right) \tag{4.4}$$

where a and b are the major and minor elliptical dimensions, respectively.
We observe that for $a = b$, we recover the stress concentration factor of 3 of a circular hole, and that for a degenerated ellipse (i.e a crack), there is an infinite (theoretical) stress.
Alternatively, let ρ be the radius of curvature of a parametric curve. Then at the tip of the ellipse $x_2 = 0$ and $x_1 = \pm a$, and another form of the equation would be:

$$(\sigma_{\beta\beta})_{\alpha=\alpha_0}^{\beta=0,\pi} = \sigma_0 \left(1 + 2\sqrt{\frac{a}{\rho}}\right) \tag{4.5}$$

From this equation, we note that the stress concentration factor is inversely proportional to the radius of curvature of an opening. Examining the circumferential stresses around the hole (and considering a plate where the radius of the hole is small compared to the radius of the disk), the stress concentration factor is apparent for the circular hole, and it rapidly increases as the elliptical hole is flattened. In Figure 4.3, the left figure shows the contour line of the circumferential stresses, and the one on the right shows the magnitude of the stresses in the third (z) dimension. When

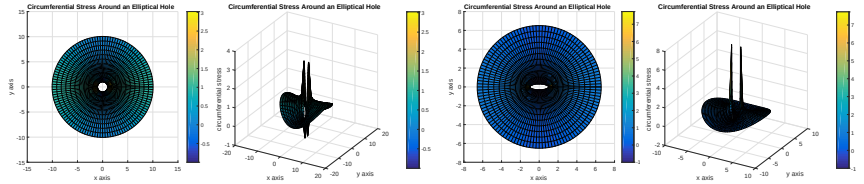

(a) Circular hole: $a_x = a_y = 1$

(b) Elliptical hole; $a_x = 0.3$, $a_y = 1$

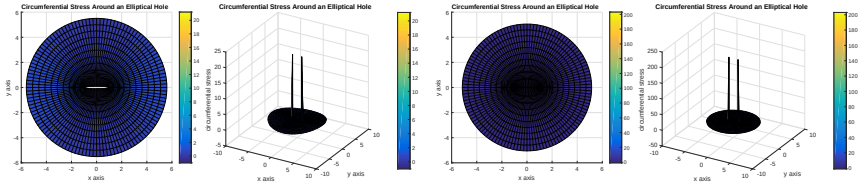

(c) Elliptical hole;$a_x = 0.1$, $a_y = 1$

(d) Elliptical hole; $a_x = 0.01$, $a_y = 1$

Fig. 4.3: Hollowed plates with circular and elliptical holes

the ellipse is completely flattened, i.e. as a approaches zero, the stress concentration factor approaches infinity. Given that the stress goes to infinity at the tip of the crack, it is by now evident that plasticity based failure criteria are no longer applicable (as the yield stress will be reached for even an infinitesimal load unlikely to propagate the crack), and a new paradigm must be used. This is where fracture mechanics comes in with tools to answer three fundamental questions:

1. What material parameter(s) should be used to characterize the material resistance to crack propagation?

2. Under which load combination/magnitude will the crack propagate?
3. If the crack were to propagate, along which direction would it propagate?

Having established that plasticity can not provide an objective failure criteria, a different one is needed.

4.3 Linear Elastic Fracture Mechanics

4.3.1 Order of Stress Singularity

Though it was shown that a collapsed ellipse yields a stress singularity, the order of the singularity is unknown. It could be any of the following

$$\begin{aligned} \sigma &= \tfrac{1}{r^{0.5}} && \text{Figure 4.4(a)} \\ \sigma &= \tfrac{1}{r} && \text{Figure 4.4(b)} \\ \sigma &= \tfrac{1}{r^2} && \text{Figure 4.4(c)} \end{aligned} \tag{4.6}$$

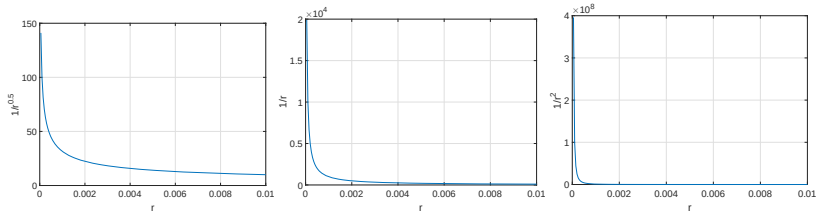

(a) $\sigma = \frac{1}{r^{0.5}}$ (b) $\sigma = \frac{1}{r}$ (c) $\sigma = \frac{1}{r}$

Fig. 4.4: Comparison of different singularity strengths

Westergaard [880] showed that the order of the stress singularity is $1/\sqrt{r}$.

4.3.2 Stress Intensity Factors

Irwin [466] subsequently identified three independent modes of crack displacements defined as:

$$\begin{Bmatrix} K_{\mathrm{I}} \\ K_{\mathrm{II}} \\ K_{\mathrm{III}} \end{Bmatrix} = \lim_{r \to 0, \theta = 0} \sqrt{2\pi r} \begin{Bmatrix} \sigma_{yy} \\ \sigma_{xy} \\ \sigma_{xz} \end{Bmatrix} \tag{4.7}$$

where the stresses are the near crack tip stresses ($r \ll a$) and K_i are associated with three independent kinematic movements of the upper and lower crack surfaces with respect to each other.

Opening Mode, I: The two crack surfaces are pulled apart in the y direction, but the deformations are symmetric about the $x - z$ and $x - y$ planes.

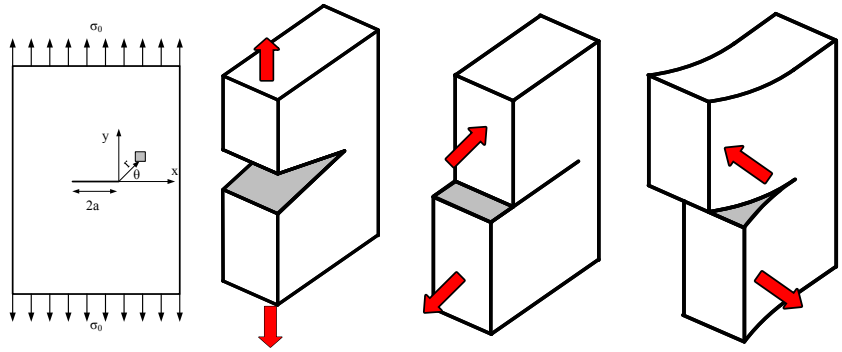

(a) Westerglaad's plate (not to scale) (b) Mode I: Crack Opening Displacement (COD) (c) Mode II: Crack Sliding Displacement (CSD) (d) Mode III: Crack Tearing Displacement (CTD)

Fig. 4.5: Crack tip stresses, and independent crack displacements

Shearing Mode, II: The two crack surfaces slide over each other in the x-direction, but the deformations are symmetric about the $x-y$ plane and skew symmetric about the $x-z$ plane.

Tearing Mode, III: The crack surfaces slide over each other in the z-direction, but the deformations are skew symmetric about the $x-y$ and $x-z$ planes.

For an infinite plate with a central crack of length $2a$ subjected to a uniform traction σ_0, the stress intensity factor is simply

$$K_I = \sigma_0 \sqrt{\pi a} \tag{4.8}$$

The stress intensity factor (SIF) is an indicator of the strength singularity (by analogy the stress concentration factor in plates with holes). It can be expressed as

$$K = \beta \sigma \sqrt{\pi a} \tag{4.9}$$

where β is a parameter that depends on the specimen, crack geometry, and loading. In the previous case $\beta = 1$.

The stress field in the very close vicinity of the crack tip ($r \ll a$) is always expressed as:

Pure mode I loading:

$$\sigma_{xx} = \frac{K_{\mathrm{I}}}{\sqrt{2\pi r}} \cos\frac{\theta}{2}\left[1 - \sin\frac{\theta}{2}\sin\frac{3\theta}{2}\right] + \cdots \tag{4.10}$$

$$\sigma_{yy} = \frac{K_{\mathrm{I}}}{\sqrt{2\pi r}} \cos\frac{\theta}{2}\left[1 + \sin\frac{\theta}{2}\sin\frac{3\theta}{2}\right] + \cdots \tag{4.11}$$

$$\tau_{xy} = \frac{K_{\mathrm{I}}}{\sqrt{2\pi r}} \sin\frac{\theta}{2}\cos\frac{\theta}{2}\cos\frac{3\theta}{2} + \cdots \tag{4.12}$$

$$\sigma_{zz} = \nu(\sigma_x + \sigma_y) + \cdots \tag{4.13}$$

$$\tau_{xz} = \tau_{yz} = 0 \tag{4.14}$$

$$v = \frac{K_{\mathrm{I}}}{2\mu}\left[\frac{r}{2\pi}\right]^{\frac{1}{2}} \sin\frac{\theta}{2}\left[\kappa + 1 - 2\cos^2\frac{\theta}{2}\right] + \cdots \tag{4.15}$$

Pure mode II loading:

$$\sigma_{xx} = -\frac{K_{\mathrm{II}}}{\sqrt{2\pi r}} \sin\frac{\theta}{2}\left[2 + \cos\frac{\theta}{2}\cos\frac{3\theta}{2}\right] + \cdots \tag{4.16}$$

$$\sigma_{yy} = \frac{K_{\mathrm{II}}}{\sqrt{2\pi r}} \sin\frac{\theta}{2}\cos\frac{\theta}{2}\cos\frac{3\theta}{2} + \cdots \tag{4.17}$$

$$\tau_{xy} = \frac{K_{\mathrm{II}}}{\sqrt{2\pi r}} \cos\frac{\theta}{2}\left[1 - \sin\frac{\theta}{2}\sin\frac{3\theta}{2}\right] + \cdots \tag{4.18}$$

Pure mode III loading:

$$\tau_{xz} = -\frac{K_{\mathrm{III}}}{\sqrt{2\pi r}} \sin\frac{\theta}{2} + \cdots \tag{4.19}$$

$$\tau_{yz} = \frac{K_{\mathrm{III}}}{\sqrt{2\pi r}} \cos\frac{\theta}{2} + \cdots \tag{4.20}$$

$$\sigma_{xx} = \sigma_y = \sigma_z = \tau_{xy} = 0 \tag{4.21}$$

where $\kappa = 3 - 4\nu$ for plane strain and $\kappa = \frac{3-\nu}{1+\nu}$ for plane stress.
Hence, the elastic stress field distribution close to the crack can be fully described by K_I, K_{II}, and K_{III}. Since these solutions are based on a linear elastic approach, the SIFs are additive.

4.3.3 Design Philosophy Based on Linear Elastic Fracture Mechanics

One of the underlying principles of (linear elastic) fracture mechanics is that unstable fracture occurs when the SIF reaches a critical value, K_{Ic}. K_{Ic} or fracture toughness represents the inherent ability of a material to withstand a given stress field intensity at the tip of a crack and to resist progressive tensile crack extensions. K_{Ic} represents the inherent ability of a material to withstand a given stress field intensity at the tip of a crack and to resist progressive tensile crack extension.
Hence, a crack will propagate (under pure mode I), whenever the stress intensity factor, K_I (which characterizes the strength of the singularity for a given problem),

reaches a material constant K_{Ic}. Hence, under the assumptions of linear elastic fracture mechanics (LEFM), at the point of incipient crack growth:

$$K_{Ic} = \beta\sigma\sqrt{\pi a} \tag{4.22}$$

Thus for the design of a cracked or potentially cracked structure, the engineer would have to decide what design variables can be selected, as only two of these variables can be fixed, and the third must be determined. The design variables are:

Material properties: (such as special steel to resist corrosive liquid) $\Rightarrow$ K_c is fixed.
Design stress level: (which may be governed by weight considerations) $\Rightarrow$ σ is fixed.
Flaw size a: In assessing the safety of a cracked body, it is essential that the crack length a[1] be properly known. In most cases it is not. Thus assumptions must be made for its value, and those assumptions are dependent upon the crack detection methodology adopted. The presence of a crack, equal to the smallest one that can be detected, must be assumed. Thus, a simpler inspection procedure would result in a larger minimum crack size than one detected by expensive nondestructive techniques. In return, simplified inspection would result in larger crack size assumptions.

Once two parameters are specified, the third one is fixed. Finally, it should be mentioned that whereas in most cases the geometry is fixed (hence β), occasionally there is the possibility to alter it in such a way to reduce (or maximize) β.

4.3.4 Stress Intensity Factors

Analytical expressions of stress intensity factors are notoriously complex to derive. Hence, one has to rely either on numerical methods (finite element) or consult stress intensity factor handbooks: [813], [739], [613].
An example of such an expression is listed below:

Middle Tension Panel (MT), Figure 4.6(a)

$$K_I = \underbrace{\sqrt{\sec\frac{\pi a}{W}}}_{\beta}\sigma\sqrt{\pi a} \tag{4.23}$$

$$= \underbrace{\left[1 + 0.256\left(\frac{a}{W}\right) - 1.152\left(\frac{a}{W}\right)^2 + 12.2\left(\frac{a}{W}\right)^3\right]}_{\beta}\sigma\sqrt{\pi a} \tag{4.24}$$

We note that for W very large with respect to a, $\sqrt{\pi \sec\frac{\pi a}{W}} = 1$ as anticipated.
Single Edge Notch Tension Panel (SENT) for $\frac{L}{W} = 2$, Figure 4.6(b)

[1] In most cases, a refers to half the total crack length.

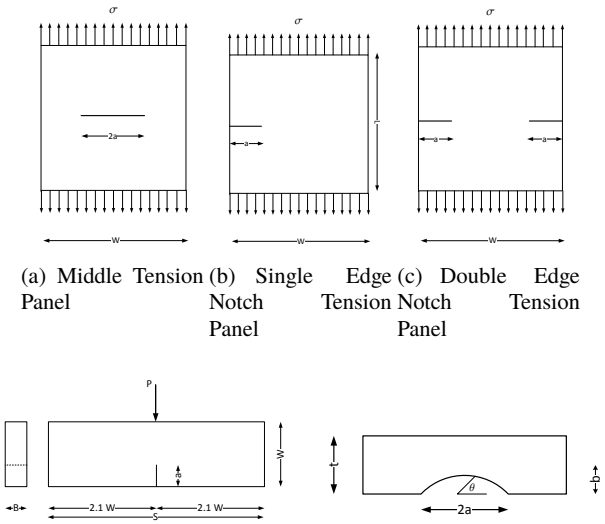

(a) Middle Tension Panel (b) Single Edge Notch Tension Panel (c) Double Edge Notch Tension Panel

(d) Three Point Bend Beam (e) Thumbnail crack

Fig. 4.6: SIF geometries

$$K_I = \underbrace{\left[1.12 - 0.23\left(\frac{a}{W}\right) + 10.56\left(\frac{a}{W}\right)^2 - 21.74\left(\frac{a}{W}\right)^3 + 30.42\left(\frac{a}{W}\right)^4\right]}_{\beta} \sigma\sqrt{\pi a} \tag{4.25}$$

We observe that here the β factor for small crack ($\frac{a}{W} \ll 1$) is greater than one and is approximately 1.12.

Double Edge Notch Tension Panel (DENT), Figure 4.6(c)

$$K_I = \underbrace{\left[1.12 + 0.43\left(\frac{a}{W}\right) - 4.79\left(\frac{a}{W}\right)^2 + 15.46\left(\frac{a}{W}\right)^3\right]}_{\beta} \sigma\sqrt{\pi a} \tag{4.26}$$

Three Point Bend (TPB), Figure 4.6(d)

$$K_I = \frac{3\sqrt{\frac{a}{W}}\left[1.99 - \left(\frac{a}{W}\right)\left(1 - \frac{a}{W}\right)\left(2.15 - 3.93\frac{a}{W} + 2.7\left(\frac{a}{W}\right)^2\right)\right]}{2\left(1 + 2\frac{a}{W}\right)\left(1 - \frac{a}{W}\right)^{\frac{3}{2}}} \frac{PS}{BW^{\frac{3}{2}}} \tag{4.27}$$

Thumbnail crack or surface cracks. Using the results of three dimensional finite element analysis, Newman and Raju [627] developed an empirical SIF equation for semi-elliptical surface cracks, Figure 4.6(e). This is perhaps the most accurate

solution and is almost universally used:

$$K = \sigma\sqrt{\pi b}\left[M_1 + M_2\left(\frac{b}{t}\right)^2 + M_3\left(\frac{b}{t}\right)^4\right]\left[1 + 1.464\left(\frac{b}{a}\right)^{1.65}\right]^{-\frac{1}{2}} \left[\left(\frac{b}{a}\right)^2\cos^2\theta + \sin^2\theta\right]^{\frac{1}{4}}\left\{1 + \left[0.1 + 0.35\left(\frac{b}{t}\right)^2\right](1 - \sin\theta)^2\right\} \quad (4.28)$$

$$M_1 = 1.13 - 0.09\left(\frac{b}{a}\right)$$
$$M_2 = 0.89\left[0.2 + \left(\frac{b}{a}\right)\right]^{-1} - 0.54$$
$$M_3 = 0.5 - \left[0.65 + \left(\frac{b}{a}\right)\right]^{-1} + 14\left[1. - \left(\frac{b}{a}\right)\right]^{24}$$

This equation is accurate within ± 5 percent, provided $0 < \frac{b}{a} \leq 1.0$ and $\frac{b}{t} \leq 0.8$.
For $\frac{b}{a}$ approximately equal to 0.25, K is roughly independent of θ.
For shallow cracks $\frac{b}{t} \ll 1$, Equation 4.28 reduces to

$$K = 1.13\sigma\sqrt{\pi b}\left[1 - .08\left(\frac{b}{a}\right)\right]\left[1 + 1.464\left(\frac{b}{a}\right)^{1.65}\right]^{-\frac{1}{2}} \quad (4.29)$$

For very long cracks $\frac{b}{a} \ll 1$, Equation 4.28 reduces to

$$K = 1.13\sigma\sqrt{\pi b}\left[1 + 3.46\left(\frac{b}{t}\right)^2 + 11.5\left(\frac{b}{t}\right)^4\right] \quad (4.30)$$

4.3.5 Fracture Properties of Materials

There are countless references for the fracture toughness of metallic alloys [445] [446]. However, as shall be seen in Chapter 9, the concept of linear elastic fracture mechanics is seldom applicable to concrete structures, and thus there is little interest in determining the fracture toughness of concrete.
For rocks, fracture toughness values have been compiled by Ouchterlony [670].
Finally, Table 4.1 provides an indication of the fracture toughness of selected materials.
Note that stress intensity factors in metric units are commonly expressed in $\text{Mpa}\sqrt{\text{m}}$, and that

$$1\text{ksi}\sqrt{\text{in}} = 1.099\text{Mpa}\sqrt{\text{m}} \quad (4.31)$$

Table 4.1: Fracture toughness of selected materials

Material Type	K_{Ic} ksi$\sqrt{\text{in}}$
Steel, Medium Carbon	49
Steel, Pressure Vessel	190
Hardened Steel	20
Aluminum	20-30
Titanium	70
Copper	100
Lead	18
Glass	0.7
Westerly Granite	16
Cement Paste	0.5
Concrete	1
Nylon	3

4.3.6 Mixed Mode Crack Propagation

Practical engineering cracked structures are subjected to mixed mode loading. In general, K_I and K_{II} are both nonzero, yet we usually measure only mode I fracture toughness, K_{Ic} (K_{IIc} concept is seldom used). So far the only fracture propagation criterion we have is for mode I only (K_I vs K_{Ic} and G_I vs R). Whereas under pure mode I in a homogeneous isotropic material, crack propagation is collinear, in all other cases the propagation will be curvilinear and at an angle θ_0 with respect to the crack axis. Thus for the general mixed mode case, we seek to formulate a criterion that will determine:

1. The angle of incipient propagation, θ_0, with respect to the crack axis.
2. If the stress intensity factors are in such a critical combination as to render the crack locally unstable and force it to propagate.

Once again, for pure mode I problems, fracture initiation occurs if:

$$K_{\mathrm{I}} \geq K_{\mathrm{Ic}} \tag{4.32}$$

The determination of a fracture initiation criterion for an existing crack in mode I and II would require a relationship between K_{I}, K_{II}, and K_{Ic} of the form

$$F\left(K_{\mathrm{I}}, K_{\mathrm{II}}, K_{\mathrm{Ic}}\right) = 0 \tag{4.33}$$

and would be analogous to the one between the two principal stresses and a yield stress, Figure 4.7.

$$F_{yld}(\sigma_1, \sigma_2, \sigma_y) = 0 \tag{4.34}$$

Such an equation may be the familiar von Mises criterion.
Erdogan, F. and Sih, G.C. [279] presented the first mixed-mode fracture initiation theory: the maximum circumferential tensile stress theory. It is based on the knowledge of the stress state near the tip of a crack written in polar coordinates. The

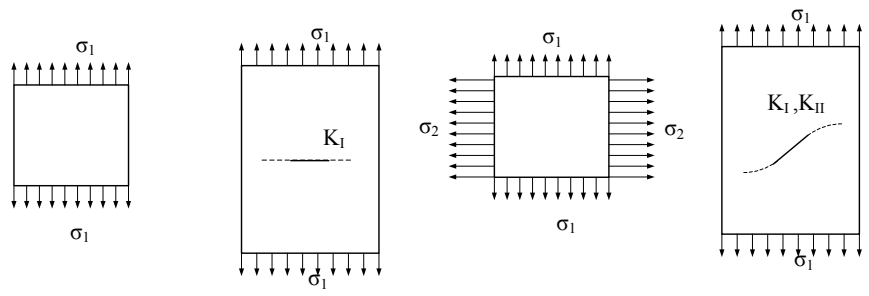

Fig. 4.7: Mixed Mode Crack Propagation and Biaxial Failure Modes

maximum circumferential stress theory states that the crack extension starts, Figure 4.8:

1. At its tip in a radial direction
2. In the plane perpendicular to the direction of greatest tension, i.e at an angle θ_0 such that $\tau_{r\theta} = 0$
3. When $\sigma_{\theta max}$ reaches a critical material constant

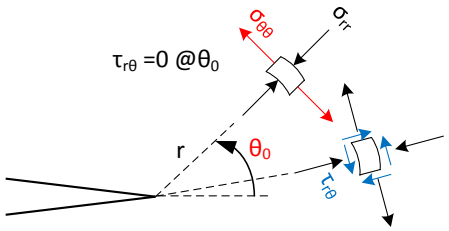

Fig. 4.8: Mixed mode crack propagation crack tip stresses

It can be easily shown that σ_θ reaches its maximum value when $\tau_{r\theta} = 0$. Replacing $\tau_{r\theta}$ for mode I and II by their expressions:

$$\tau_{r\theta} = \frac{K_{\mathrm{I}}}{\sqrt{2\pi r}} \sin\frac{\theta}{2}\cos^2\frac{\theta}{2} + \frac{K_{\mathrm{II}}}{\sqrt{2\pi r}}\left(\frac{1}{4}\cos\frac{\theta}{2} + \frac{3}{4}\cos\frac{3\theta}{2}\right) \tag{4.35}$$

$$\Rightarrow \cos\frac{\theta_0}{2}\left[K_{\mathrm{I}}\sin\theta_0 + K_{\mathrm{II}}\left(3\cos\theta_0 - 1\right)\right] = 0 \tag{4.36}$$

This equation has two solutions:

$$\theta_0 = \pm\pi \quad \text{trivial} \tag{4.37}$$

$$K_{\mathrm{I}} \sin\theta_0 + K_{\mathrm{II}} \left(3\cos\theta_0 - 1\right) = 0 \tag{4.38}$$

Solution of the second equation yields the angle of crack extension θ_0

$$\tan\frac{\theta_0}{2} = \frac{1}{4}\frac{K_{\mathrm{I}}}{K_{\mathrm{II}}} \pm \frac{1}{4}\sqrt{\left(\frac{K_{\mathrm{I}}}{K_{\mathrm{II}}}\right)^2 + 8} \tag{4.39}$$

For the crack to extend, the maximum circumferential tensile stress, σ_θ,

$$\sigma_\theta = \frac{K_{\mathrm{I}}}{\sqrt{2\pi r}} \cos\frac{\theta_0}{2}\left(1 - \sin^2\frac{\theta_0}{2}\right) + \frac{K_{\mathrm{II}}}{\sqrt{2\pi r}}\left(-\frac{3}{4}\sin\frac{\theta_0}{2} - \frac{3}{4}\sin\frac{3\theta_0}{2}\right) \tag{4.40}$$

must reach a critical value which is obtained by rearranging the previous equation

$$\sigma_{\theta max}\sqrt{2\pi r} = K_{\mathrm{Ic}} = \cos\frac{\theta_0}{2}\left[K_{\mathrm{I}}\cos^2\frac{\theta_0}{2} - \frac{3}{2}K_{\mathrm{II}}\sin\theta_0\right] \tag{4.41}$$

which can be normalized as

$$\frac{K_{\mathrm{I}}}{K_{\mathrm{Ic}}}\cos^3\frac{\theta_0}{2} - \frac{3}{2}\frac{K_{\mathrm{II}}}{K_{\mathrm{Ic}}}\cos\frac{\theta_0}{2}\sin\theta_0 = 1 \tag{4.42}$$

This equation can be used to define an equivalent stress intensity factor, K_{eq}, for mixed mode problems:

$$K_{eq} = K_{\mathrm{I}}\cos^3\frac{\theta_0}{2} - \frac{3}{2}K_{\mathrm{II}}\cos\frac{\theta_0}{2}\sin\theta_0 \tag{4.43}$$

4.3.7 Some Practical Considerations

4.3.7.1 Leak Before Break (LBB) Paradigm

As observed from the preceding example, many pressurized vessels are subject to crack growth if internal flaws are present. Two scenarios may happen:

Break-through: In this case critical crack configuration is reached before the crack has "daylighted," and there is a sudden and unstable crack growth, Figure 4.9.

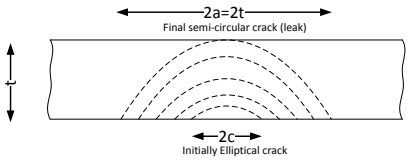

Fig. 4.9: Concept of break through in fracture mechanics

Leak Before Fail: In this case, crack growth occurs, and the crack "pierces" through the thickness of the vessel before unstable crack growth occurs. This in turn will result in a sudden depressurization, and this will stop any further crack growth, Figure 4.10.

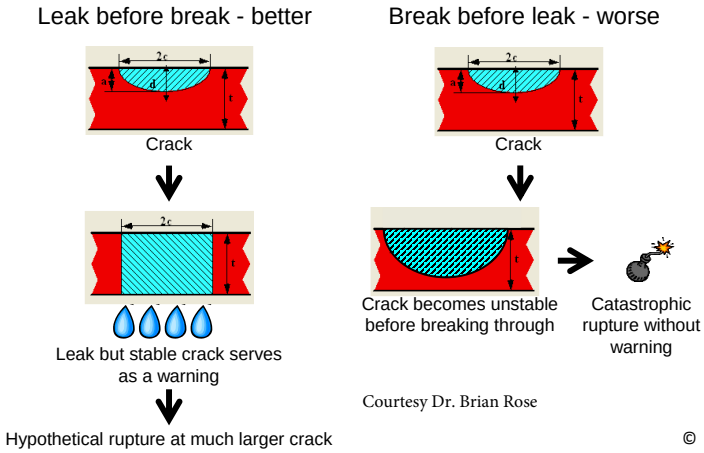

Fig. 4.10: Concept of leak before failure in fracture mechanics (Courtesy Dr. Brian Rose)

Pressurized vessels should be designed to ensure a leak before fail scenario, as this would usually be immediately noticed and corrected (assuming that there is no leak of flammable gas!).
Leak before break assessment should be made on the basis of a complete residual strength diagram for both the part and the through crack. Various ratios should be considered.

4.3.7.2 Damage Tolerance Assessment

Fracture mechanics is not limited to determining the critical crack size, load, or stress combination. It can also be applied to establish a fracture control plan or damage tolerance analysis with the following objectives:

1. Determine the effect of cracks on strength. This will result in a plot of crack size versus residual strength, or a Residual Strength Diagram, Figure 4.11(a).
2. Note analogy with column curve where one can have either plastic failure or (in)elastic buckling in terms of the slenderness ratio kL/r Figure 4.11(b).
3. Determine crack growth with time, resulting in a Crack Growth Curve.

4.3.7.2.1 Inspection `Adapted from [624]`

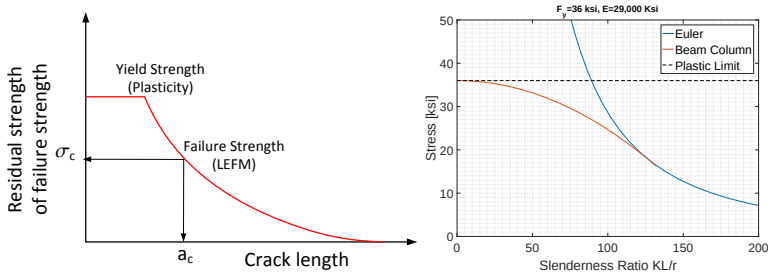

(a) Fracture (b) Euler buckling

Fig. 4.11: Residual strength diagrams

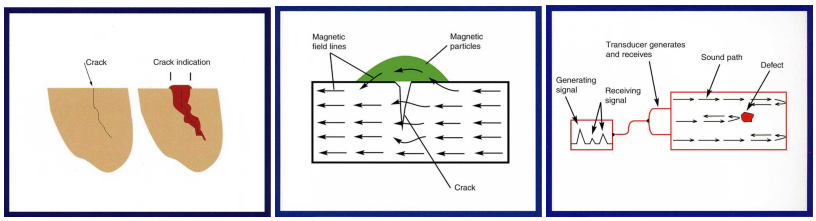

(a) Penetran testing (b) Magnetic particle testing (c) Ultrasoninc testing

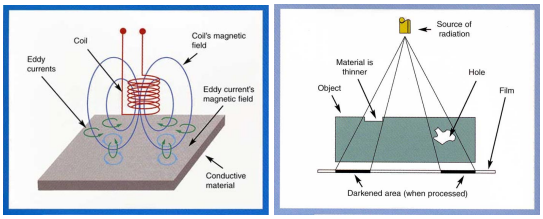

(d) Eddy current testing (e) Radiographic testing

Fig. 4.12: Some NDE/NDT Techniques, [624]

Penetrant Testing: Figure 4.12(a), Penetrant solution is applied to the surface of a precleaned component. The liquid is pulled into surface-breaking defects by capillary action. Excess penetrant material is carefully cleaned from the surface. A developer is applied to pull the trapped penetrant back to the surface where it is spread out and forms an indication. The indication is much easier to see than the actual defect.

Magnetic Particle Testing: Figure 4.12(b), A magnetic field is established in a component made from ferromagnetic material. The magnetic lines of force travel through the material and exit and reenter the material at the poles. Defects such as crack or voids cannot support as much flux and force some of the flux outside

of the part. Magnetic particles distributed over the component will be attracted to areas of flux leakage and produce a visible indication.

Ultrasonic Testing: Figure 4.12(c), High frequency sound waves are sent into a material by use of a transducer. The sound waves travel through the material and are received by the same transducer or a second transducer. The amount of energy transmitted or received and the time the energy is received is analyzed to determine the presence of flaws. Changes in material thickness and changes in material properties can also be measured.

Eddy Current Testing: Figure 4.12(d), Alternating electrical current is passed through a coil producing a magnetic field. When the coil is placed near a conductive material, the changing magnetic field induces current flow in the material. These currents travel in closed loops and are called eddy currents. Eddy currents produce their own magnetic field that can be measured and used to find flaws and characterize conductivity, permeability, and dimensional features.

Radiographic Testing: Figure 4.12(e), X-rays are used to produce images of objects using a film or other detector that is sensitive to radiation. The test object is placed between the radiation source and detector. The thickness and the density of the material that X-rays must penetrate affects the amount of radiation reaching the detector. This variation in radiation produces an image on the detector that often shows internal features of the test object.

It is most important to always assume the existence of a crack equal to the smallest detectable one.

4.3.7.2.2 Fracture Control Plan Fracture mechanics is not limited to determining the critical crack size, load, or stress combination. It can also be applied to establish a fracture control plan. Knowing the critical crack length, a_{cr}, that may result in failure, a safety factor is first established and the maximum allowable crack length, a_{al}, determined. Then, the minimum detectable crack length, a_{det}, is determined on the basis of inspection methodology (naked eye, ultra-sonic equipment, or other).
If an inspection found no crack, then the minimum detectable crack is assumed to be present, and an estimate time interval Δt needed for a_{det} to reach a_{al} is computed. This will determine the next date of inspection. Now if a crack is detected, then the inspection interval will naturally be reduced to $\alpha\Delta t$ ($\alpha < 1$). Finally, if a crack equal to the maximum allowable one is detected, then the structure must be retired, Figure 4.13(a).
It should be apparent that the cost associated with crack detection: a) is inversely proportional to the size of the detectable crack size and b) has associated with it a probability distribution factor, Figure 4.13(b). Hence, increasing cost of detection equipment reduces the frequency of inspection.

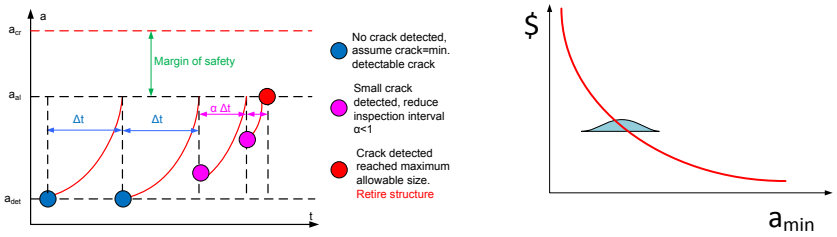

(a) Inspection interval (b) Cost of crack detection

Fig. 4.13: Fracture control plan and cost

4.4 Thermodynamics Approach

So far a so-called "Newtonian" approach was followed, i.e. one in terms of vectorial quantities (e.g. stresses at the crack tip). An alternative "Lagrangian" approach can be used to provide an alternative framework (especially for crack propagation criteria). The first Law of Thermodynamics (Eq. 1.118) can be expressed as

$$\dot{W} = \dot{U} + \dot{K} + \dot{\Gamma} \tag{4.44}$$

where W is work, K kinetic energy, U internal energy (elastic and plastic), and Γ surface energy (energy needed to increase the crack area). Derivative is with respect to time. Since all changes with respect to time are caused by changes in crack size, we can write

$$\frac{\partial}{\partial t} = \frac{\partial A}{\partial t}\frac{\partial}{\partial A} \tag{4.45}$$

In a adiabatic system (no heat exchange) and if loads are applied in a quasi static manner (no kinetic energy), then Q and K are zero.
For unit thickness, replace A by a:

$$\underbrace{\frac{\partial W}{\partial a}}_{\text{External}} = \underbrace{\left(\frac{\partial U^e}{\partial a} + \frac{\partial U^p}{\partial a}\right) + \frac{\partial \Gamma}{\partial a}}_{\text{Internal}} \tag{4.46}$$

We can rewrite it as

$$\underbrace{\frac{\partial W}{\partial a} - \frac{\partial U^e}{\partial a}}_{G} = \underbrace{\frac{\partial U^p}{\partial a} + \frac{\partial \Gamma}{\partial a}}_{R} \tag{4.47}$$

where R is the rate of energy dissipation during stable crack growth which equals plastic deformation plus energy consumed during crack propagation.
In terms of Potential Energy, Π:

$$\Pi \equiv U^e - W \tag{4.48}$$
$$-\frac{\partial \Pi}{\partial a} = -\frac{\partial U^e}{\partial a} + \frac{\partial W}{\partial a} = \frac{\partial U^p}{\partial a} + \frac{\partial \Gamma}{\partial a}$$

Crack stability can be assessed from

$$-\frac{\partial \Pi}{\partial a} \begin{cases} < \frac{\partial U^p}{\partial a} + \frac{\partial \Gamma}{\partial a} & \text{No crack growth} \\ = \frac{\partial U^p}{\partial a} + \frac{\partial \Gamma}{\partial a} & \text{Quasi static crack growth} \\ > \frac{\partial U^p}{\partial a} + \frac{\partial \Gamma}{\partial a} & \text{Dynamic crack growth} \end{cases} \tag{4.49}$$

For quasi-static crack growth, the rate of potential energy decrease during crack growth is equal to the rate of energy dissipated in plastic deformation and crack growth.
For brittle materials ($U^p = 0$), potential energy is released from a volume ($\propto L^3$) whereas surface energy is consumed over a surface ($\propto L^2$), thus we have a size discrepancy or a size effect (which will be studied later).
It can be shown that the energy release rate, G, is related to the stress intensity factor, K_I, through

$$G = \frac{K_{\mathrm{I}}^2}{E'} \tag{4.50}$$

4.5 Elasto-Plastic Fracture: Metals

A stress singularity implies an infinite stress at the crack tip. Clearly at some distance r_p away from the crack tip, the stress will reach the yield stress σ_{yld}. The zone inbetween the crack tip and the end of this zone is labeled as:

Plastic Zone for metals. Three of the most widely used models to determine this zone will be discussed below.

Fracture Process Zone for cementitious materials and ceramics. This zone was first postulated by Hillerborg, Modéer, and Petersson [419].

If this zone is small compared to the crack size, then our linear elastic assumptions are correct; if not, LEFM is not applicable (thus it would be incorrect to use a K) and a non-linear model must be used. Thus there are two important issues associated with non-linear fracture:

1. What is the size of the plastic or process zone?
2. What are the criteria for crack growth?

4.5.1 Plastic Zone Size

There are three major approaches to determine the size of the plastic zone r_p, Figure 4.14(a). Once determined, we can consider an effective crack length of $a + r_p^*$ which would result in:

$$K_{eff} = f(g)\sigma\sqrt{\pi(a + r_p)} \tag{4.51}$$

and for linear elastic fracture mechanics to remain applicable, we must have:

$$\text{LEFM} \Leftrightarrow K \approx K_{eff} \tag{4.52}$$

Three of the most commonly used models for determination of the plastic zone:

Irwin postulated that as a result of the finite stress at the tip of the crack, a stress redistribution is to take place. Since equilibrium of vertical forces must be maintained then areas A and B must be equal [467].

$$r_p = \frac{1}{\pi}\frac{K_I^2}{\sigma_{\text{yld}}^2} = \left(\frac{\sigma}{\sigma_{\text{yld}}}\right)^2 a \tag{4.53}$$

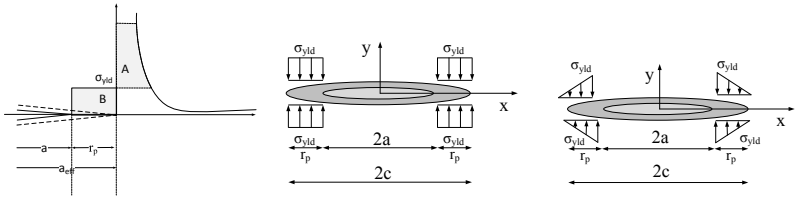

(a) Irwin (b) Dugdale (c) Barenblatt

Fig. 4.14: Determination of Plastic Zone Sizes

Dugdale postulated that the actual physical crack of length $2a$ is to be replaced by a total effective crack of length $2c$, where $c = a + \rho$ such that [260] a constant stress σ_{yld} is applied over ρ where $a < x < c$ causing (a negative) K_ρ, and c is selected in such a manner that $\sum K = 0$ or $K_{remote} = -K_\rho$. This results in

$$r_p = \frac{\pi^2}{8}\left(\frac{\sigma}{\sigma_{\text{yld}}}\right)^2 a = \frac{\pi}{8}\frac{K_I^2}{\sigma_{yld}^2} \tag{4.54}$$

Barenblatt model is a variation of the one of Dugdale, however rather than having a constant stress distribution ahead of the crack tip, it is assumed to be linear [85].

As an example, consider an infinite plate with central crack of size $2a = 16$ mm, a far field applied stress $\sigma_{app} = 350$ MPa, and the plate has a yield stress $\sigma_{\text{yld}} = 1,400$ MPa.

1. Using Irwin's approximation:

$$r_p = \frac{\sigma^2 a}{\sigma_{\text{yld}}^2} = \frac{(350)^2(.008)}{1,400^2} \approx .00050 \text{ m} = .5 \text{ mm}$$

Since $\frac{r_p}{a}$ is very small, $K_{\text{eff}} \approx K_{\text{applied}}$

2. The effective SIF are then given by

$$K_{\text{eff}} = \sigma\sqrt{\pi(a+r_p)} = 350\sqrt{\pi(.008+.00050')} = 57.18MPa\sqrt{m}$$
$$K_{\text{app}} = \sigma\sqrt{\pi a} = 350\sqrt{\pi(.008)} = 55.5MPa\sqrt{m}$$

3. We note that there is only a 2 percent difference between those two solutions, hence LEFM is applicable.
4. If yield stress was decreased by heat treatment to 385 MPa, then

$$r_p = \frac{(350)^2(.008)}{385^2} = 6.6\text{mm} \tag{4.55}$$
$$K_{eff} = 350\sqrt{\pi(.008+.0066)} = 74.9\text{MPa}\sqrt{\text{m}} \tag{4.56}$$

and in this case LEFM may no longer be applicable.

4.5.2 J Integral

There are two criteria for crack propagation in elasto-plastic fracture. The first (akin to the stress intensity factor) is based on the crack tip opening displacement (CTOD) [875] seldom used in the U.S., and the J integral (akin to the energy release rate G). Eshelby [280] has defined a number of contour integrals that are path independent by virtue of the theorem of energy conservation. The two-dimensional form of one of these integrals can be written as:

$$J = \oint_\Gamma \left(w\mathrm{d}y - \mathbf{t}\frac{\partial \mathbf{u}}{\partial x}\mathrm{d}\Gamma \right) = 0 \tag{4.57}$$

with

$$w = \int_0^\varepsilon \sigma_{ij}\mathrm{d}\varepsilon_{ij} \tag{4.58}$$

where w is the strain energy density; Γ is a closed contour followed counter-clockwise, as shown in Figure 4.15; $\mathbf{t}$ is the traction vector on a plane defined by the outward drawn normal $\mathbf{n}$ and $\mathbf{t} = \boldsymbol{\sigma}\mathbf{n}$; $\mathbf{u}$ the displacement vector, and $\mathrm{d}\Gamma$ is the element of the arc along the path Γ. Whereas Eshelby has defined a number of similar path independent contour integrals, he had not assigned them with a particular physical meaning.

4.5.2.1 Proof of Path Independence

Before we establish the connection between Eshelby's expression for J and the energy release rate J, we need to show that the former is indeed equal to zero for a closed path.

$$J = \oint_\Gamma \left(w\mathrm{d}y - t_i\frac{\partial u_i}{\partial x}\mathrm{d}\Gamma \right) \tag{4.59}$$

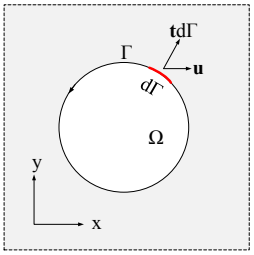

Fig. 4.15: J Integral definition around a Crack

and assuming Γ to be defined counterclockwise, then $\mathrm{d}x = -n_y \mathrm{d}\Gamma$, $\mathrm{d}y = n_x \mathrm{d}\Gamma$, and $t_i = n_j \sigma_{ij}$ where n_x, n_y and n_j are direction cosines. Substituting

$$J = \oint_\Gamma \left(w n_x - n_j \sigma_{ij} \frac{\partial u_i}{\partial x} \right) \mathrm{d}\Gamma \tag{4.60}$$

Invoking Green's theorem (Eq. 1.58)

$$\oint_\Gamma v_i n_i \mathrm{d}\Gamma = \int_\Omega v_{i,i} \mathrm{d}\Omega \tag{4.61}$$

we obtain

$$J = \int_\Omega \left[\frac{\partial w}{\partial x} - \frac{\partial}{\partial x_j} \left(\sigma_{ij} \frac{\partial u_i}{\partial x} \right) \right] \mathrm{d}x \mathrm{d}y \tag{4.62}$$

Applying the chain rule, the first term in the square bracket becomes

$$\frac{\partial w}{\partial x} = \frac{\partial w}{\partial \varepsilon_{ij}} \frac{\partial \varepsilon_{ij}}{\partial x} = \sigma_{ij} \frac{\partial \varepsilon_{ij}}{\partial x} \tag{4.63}$$

where the strain is given by

$$\varepsilon_{ij} = \frac{1}{2} \left(u_{i,j} + u_{j,i} \right) \tag{4.64}$$

Substituting for the first term

$$\frac{\partial w}{\partial x} = \frac{1}{2} \sigma_{ij} \left[\frac{\partial}{\partial x} \left(\frac{\partial u_i}{\partial x_j} \right) + \frac{\partial}{\partial x} \left(\frac{\partial u_j}{\partial x_i} \right) \right] \tag{4.65}$$

$$= \sigma_{ij} \frac{\partial}{\partial x_j} \left(\frac{\partial u_i}{\partial x} \right) \tag{4.66}$$

On the other hand, we have for the second term

$$\frac{\partial}{\partial x_j}\left(\sigma_{ij}\frac{\partial u_i}{\partial x}\right) = \sigma_{ij}\frac{\partial}{\partial x_j}\left(\frac{\partial u_i}{\partial x}\right) + \underbrace{\frac{\partial \sigma_{ij}}{\partial x_j}}_{0}\frac{\partial u_i}{\partial x} \tag{4.67}$$

Hence,

$$\frac{\partial w}{\partial x} = \sigma_{ij}\frac{\partial}{\partial x_j}\left(\frac{\partial u_i}{\partial x}\right) \tag{4.68}$$

which is identical to the second term of Eq. 4.62. Thus the integrand of Eq. 4.59 vanishes and $J = 0$ for any closed contour.
Having shown that indeed $J = 0$, we will now exploit this to proove that around a crack, J is non-zero and is independent of the path.
With reference to Figure 4.16, we consider the closed path $\Gamma = \Gamma_1 + \Gamma_2 + \Gamma_3 + \Gamma_4$ in which Γ_1 and Γ_3 are arbitrarily chosen contours. Obviously $J = 0$ over Γ in order to satisfy compatibility conditions, provided that the stresses and displacement gradients are continuous. Along paths Γ_2 and Γ_4, the traction vector $t_i = 0$ and also $\mathrm{d}y = 0$. Consequently, the contributions to J from Γ_2 and Γ_4 vanish. Taking into account the different sense of integration along paths Γ_1 and Γ_3, we arrive at the conclusion that the values of J integrated over paths Γ_1 and Γ_3 are identical. Because these two paths were arbitrarily chosen, the path independence of J is assured.

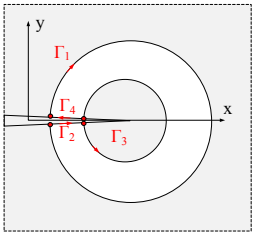

Fig. 4.16: Closed contour for proof of J path independence

4.5.2.2 Nonlinear Elastic Energy Release Rate

Let us now establish the connection between the two previous interpretations of J: the one mathematically defined by Eshelby and the one associated with the energy release rate (yet to be proven). We shall prove that when J is applied along a contour around a crack tip, it represents the change in potential energy for a virtual crack extension $\mathrm{d}a$.
Consider a two-dimensional crack surrounded by a line Γ which encompasses an area Ω. Under quasi-static conditions and in the absence of body forces, the potential energy is given by

$$\Pi = \underbrace{\int_\Omega w \mathrm{d}\Omega}_{U} - \underbrace{\oint_\Gamma t_i u_i \mathrm{d}\Gamma}_{W} \tag{4.69}$$

For a virtual crack extension, the change in potential energy is

$$\frac{\mathrm{d}\Pi}{\mathrm{d}a} = \int_\Omega \frac{\mathrm{d}w}{\mathrm{d}a}\mathrm{d}\Omega - \oint_\Gamma \left[t_i \frac{\mathrm{d}u_i}{\mathrm{d}a} + u_i \frac{\mathrm{d}t_i}{\mathrm{d}a} \right] \mathrm{d}\Gamma \tag{4.70}$$

$$= \int_\Omega \frac{\mathrm{d}w}{\mathrm{d}a}\mathrm{d}\Omega - \underbrace{\oint_{\Gamma_u}}_{0} \left[t_i \frac{\mathrm{d}u_i}{\mathrm{d}a} + u_i \frac{\mathrm{d}t_i}{\mathrm{d}a} \right] \mathrm{d}\Gamma - \oint_{\Gamma_t} \left[t_i \frac{\mathrm{d}u_i}{\mathrm{d}a} + \underbrace{u_i \frac{\mathrm{d}t_i}{\mathrm{d}a}}_{0} \right] \mathrm{d}\Gamma \tag{4.71}$$

We have decomposed the contour path into two parts, the first one with prescribed displacement (Γ_u) and a second one with prescribed traction (Γ_t). Since Γ_u is zero along the path, we maintain a closed contour integral along Γ_t.
Furthermore, the second term inside the square bracket will be zero along Γ_t because the traction is constant during crack growth.
For a crack extension, the coordinate axis also moves, Figure 4.17. Thus we can

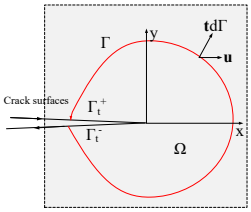

Fig. 4.17: Virtual crack extension definition of J

write

$$\frac{\mathrm{d}}{\mathrm{d}a} = \frac{\partial}{\partial a} + \frac{\partial}{\partial x}\frac{\partial x}{\partial a} = \frac{\partial}{\partial a} - \frac{\partial}{\partial x} \tag{4.72}$$

for a crack extension along a ($\frac{\partial x}{\partial a} = -1$) with respect to the new coordinate system. Substituting into Eq. 4.71

$$\frac{\mathrm{d}\Pi}{\mathrm{d}a} = \int_\Omega \left[\frac{\partial w}{\partial a} - \frac{\partial w}{\partial x} \right] \mathrm{d}\Omega - \oint_{\Gamma_t} t_i \left(\frac{\partial u_i}{\partial a} - \frac{\partial u_i}{\partial x} \right) \mathrm{d}\Gamma \tag{4.73}$$

We can also rewrite:

$$\underbrace{\frac{\partial w}{\partial a} = \frac{\partial w}{\partial \varepsilon_{ij}}\frac{\partial \varepsilon_{ij}}{\partial a}}_{\text{Eq. 4.63}} = \underbrace{\sigma_{ij}\frac{\partial}{\partial x_j}\left(\frac{\partial u_i}{\partial a}\right)}_{\text{Eq. 4.66}} \tag{4.74}$$

But from the divergence theorem,

$$\oint_{\Gamma_t} t_i \frac{\partial u_i}{\partial a} \mathrm{d}\Gamma = \int_{\Omega} \sigma_{ij} \frac{\partial}{\partial x_j} \left(\frac{\partial u_i}{\partial a} \right) \mathrm{d}\Omega \tag{4.75}$$

$$= \int_{\Omega} \frac{\partial w}{\partial a} \tag{4.76}$$

Hence from this Equation and Eq. 4.74, the first terms in each of the two integrals in Eq. 4.73 cancel out, and we are left with

$$\frac{\mathrm{d}\Pi}{\mathrm{d}a} = \oint_{\Gamma_t} t_i \frac{\partial u_i}{\partial x} \mathrm{d}\Gamma - \int_{\Omega} \frac{\partial w}{\partial x} \mathrm{d}\Omega \tag{4.77}$$

We now apply the divergence theorem (Eq. 1.59), multiply both sides by -1, and recall that $n_x \mathrm{d}\Gamma = \mathrm{d}y$

$$-\frac{\mathrm{d}\Pi}{\mathrm{d}a} = \oint_{\Gamma_t} \left(w n_x - t_i \frac{\partial u_i}{\partial x} \right) \mathrm{d}\Gamma \tag{4.78}$$

$$= \oint_{\Gamma_t} \left(w \mathrm{d}y - t_i \frac{\partial u_i}{\partial x} \mathrm{d}\Gamma \right) \tag{4.79}$$

which is the same as Eq. 4.57. Henceforth, the J integral is equal to the energy release rate for linear and nonlinear elastic material under quasi-static conditions.

4.5.3 Nonlinear Energy Release Rate

Whereas LEFM is restricted to linear elastic materials, most metals have a nonlinear stress-strain curve. Figure 4.18 illustrates the uniaxial stress-strain behavior of elastic-plastic and nonlinear elastic materials. Though the loading behavior of both materials

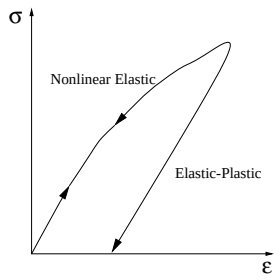

Fig. 4.18: Elastic-Plastic versus nonlinear elastic materials

is identical, they differ when they are unloaded. Thus, as long as there is no unloading, we can assume a nonlinear elastic behavior, and the deformation theory of plasticity which relates the total strains to stresses is applicable.

For nonlinear elastic solids, we have already shown that J is the energy release rate in nonlinear elastic materials:

$$J = -\frac{\mathrm{d}\Pi}{\mathrm{d}a} \tag{4.80}$$

for a unit thickness crack extension.
Next, we consider the load displacement curve of a notched specimen made of nonlinear elastic material for two different conditions, Figure 4.19, during crack extension from a to $a + \mathrm{d}a$:

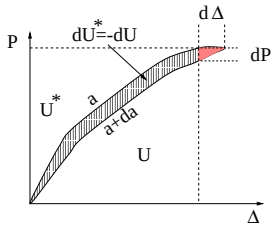

Fig. 4.19: Nonlinear energy release rate, [30]

Load control we have $\mathrm{d}\Delta = 0$ and

$$\Pi = U - W = U - P\Delta = -U^* \tag{4.81}$$

where

$$U^* \stackrel{\text{def}}{=} \int_0^P \Delta \mathrm{d}P \tag{4.82}$$

is the complimentary strain energy. Thus for constant load

$$J_P = \left(\frac{\mathrm{d}U^*}{\mathrm{d}a}\right)_P \tag{4.83}$$

Constant displacement $\mathrm{d}P = 0$, and

$$J_\Delta = -\left(\frac{\mathrm{d}U}{\mathrm{d}a}\right)_\Delta \tag{4.84}$$

From Figure 4.19, the difference between J_P and J_Δ is $\frac{1}{2}\mathrm{d}P d\Delta$ which is vanishingly small compared to $\mathrm{d}U$. Therefore J for load control is equal to J for displacement control and for linear elastic materials $J = G = \frac{K^2}{E'}$.

4.5.4 J_1 and J_2 Generalization.

Rice has shown that in linear elastic fracture, and in terms of the stress intensity factors, J can be written as:

$$(1-\nu^2)(K_I^2+K_{II}^2)+(1+\nu)K_{III}^2=EJ_1 \tag{4.85}$$

where J_1 is expressed in indicial notation by:

$$J_1=\int_\Gamma\left(w\mathrm{d}y-\mathbf{t}\frac{\partial\mathbf{u}}{\partial x}\mathrm{d}\Gamma\right) \tag{4.86}$$

$$=\int_\Gamma\left(wn_1-t_i\frac{\partial u_i}{\partial x_1}\mathrm{d}\Gamma\right) \tag{4.87}$$

where w is the strain energy density, n_i are the direction cosines of the normal to the contour, T_i are the components of traction, and the contour of integration is around the tip.
Knowles and Stenberg [506] noted that this can be considered as the first component of a vector

$$J_k=\int\{wn_k-t_i\frac{\partial u_i}{\partial x_k}\}\mathrm{d}\Gamma \tag{4.88}$$

which is also path independent. When written in vector form, this gives

$$J_1=\int_\Gamma\left(w\mathrm{d}y-\mathbf{t}\frac{\partial\mathbf{u}}{\partial x}\mathrm{d}\Gamma\right) \tag{4.89}$$

$$J_2=\int_\Gamma\left(w\mathrm{d}x-\mathbf{t}\frac{\partial\mathbf{u}}{\partial y}\mathrm{d}\Gamma\right) \tag{4.90}$$

Hellen and Blackburn [411] showed that

$$J=J_1-iJ_2 \tag{4.91}$$

$$=\frac{(1+\nu)(1+\kappa)}{4E}(K_I^2+K_{II}^2+2iK_IK_{II}) \tag{4.92}$$

Thus the values of energy release rates (J_1 and J_2) for crack extensions parallel and perpendicular to the crack, respectively, will be given by:

$$J_1=\frac{K_I^2+K_{II}^2}{H} \tag{4.93}$$

$$J_2=\frac{-2K_IK_{II}}{H} \tag{4.94}$$

where

$$H=\begin{cases}E & \text{plane strain}\\ \frac{E}{1-\nu^2} & \text{plane stress}\end{cases} \tag{4.95}$$

Note that solution of Eq. 4.93 and 4.94 is the intersection of a circle and a hyperbola. Hence, there exists more than one pair of stress intensity factors (or none).

4.6 Fatigue Crack Propagation

Subcritical crack propagation (when $a < a_{cr}$) can occur under fatigue loading (low amplitude cyclic load), Figure 4.20(a), or be driven by corrosion (crack propagating with time while in a corrosive environment). The most widely used fatigue crack growth is Paris (empirical) Law [681]

$$\frac{\mathrm{d}a}{\mathrm{d}N} = C\,(\Delta K)^n \tag{4.96}$$

which is a straight line on a log-log plot of $\frac{\mathrm{d}a}{\mathrm{d}N}$ vs ΔK, and

$$\Delta K = K_{max} - K_{min} = (\sigma_{max} - \sigma_{min}) f(g) \sqrt{\pi a} \tag{4.97}$$

where a is the crack length; N is the number of load cycles; C is the intercept of the line along $\frac{\mathrm{d}a}{\mathrm{d}N}$ (of the order of 10^{-6}) units of m/cycle/(MPa$\sqrt{m}$)^n; n is the slope of the line and ranges from 2 to 10 (for metals). C and n are experimentally determined (an expensive test).
Paris law can be rewritten as :

$$\Delta N = \frac{\Delta a}{C\,[\Delta K(a)]^n} \tag{4.98}$$

or

$$N = \int \mathrm{d}N = \int_{a_i}^{a_f} \frac{\mathrm{d}a}{C\,[\Delta K(a)]^n} \tag{4.99}$$

It is thus evident that a small error in the SIF calculations would be magnified greatly given the values of n. Whereas there have been many extensions of Paris law, two of the most commonly used are the ones of Foreman and Walker.
A simple extension of Paris law was proposed by Walker [862]. It accounts for the stress ratio only

$$\frac{\mathrm{d}a}{\mathrm{d}N} = C \left[\frac{\Delta K}{(1-R)^{(1-m)}} \right]^n \tag{4.100}$$

with $R = \frac{K_{min}}{K_{max}} = \frac{\sigma_{min}}{\sigma_{max}}$. Foreman, Kearney, and Engle [316] extended Paris law to account for: a) increase in crack growth rate as K_{max} approaches K_{Ic} and b) slow increase in crack growth at $K_{min} \approx K_{th}$, Figure 4.20(b).

$$\frac{\mathrm{d}a}{\mathrm{d}N} = \frac{C(\Delta K)^n}{(1-R)K_c - \Delta K} \tag{4.101}$$

4.6.1 Variable Amplitude Loading with Load Interaction

If the cyclic load contains a spike, this may significantly reduce the rate of crack growth during the subsequent cycles. This phenomena is called Retardation. This can be explained by the presence of a plastically deformed zone ahead of the crack tip. When the spike is unloaded, the surrounding material is elastically unloaded

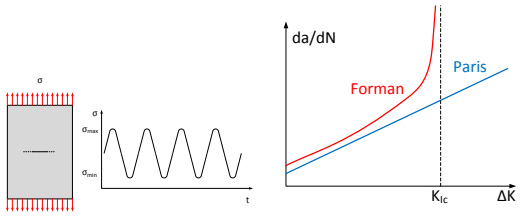

(a) Cyclic load (b) Forman law for fatigue crack growth

Fig. 4.20: Fatigue crack growth

and a part of the plastic zone experiences compressive stresses that will slow crack growth. Once the crack tip emerges from the previously formed large plastic zone, then the crack growth rate returns to its typical steady-state level, [881] [884].

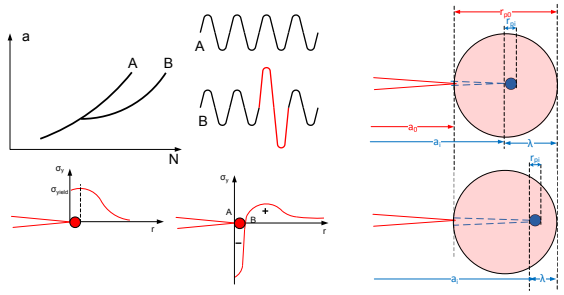

(a) Plastic zone retarding crack growth (b) Willerborg model

Fig. 4.21: Retardation in fatigue crack growth

Chapter 5
Creep

Written by Mija Hubler

Abstract
Creep is a quintessential form of concrete aging. It has been the subject of countless studies, and indeed in many cases it is a phenomenon that must be properly accounted for. Though it should never be discounted, its importance may be minimized by other aging mechanisms (such as ASR).
This chapter, will provide a basic coverage that should assist engineers in their investigation.

5.1 Time-dependent Inelastic Strains

The deformation of concrete increases with time under a constant applied stress. This behavior is referred to as the creep of concrete. While the creep of concrete is a time-dependent strain, it is unlike the flow of other materials, which are described by a strain rate, e.g. Newton's law for viscosity. In concrete, the stress-strain relation itself is a function of time [626]. The observed strain is a function of the duration of applied stress. Complexities in describing creep of concrete structures arise from the heterogeneous nature of the microstructure from which the phenomenon originates and the anisotropy introduced with reinforcement during design.
Another source of inelastic behavior in concrete is drying shrinkage driven by the loss of water to the environment. Volumetric changes due to shrinkage can act with or against creep strains. Since the stress-strain behavior of the cement paste depends on its hydration state, which drying directly impacts, the mechanisms driving creep and shrinkage are inherently coupled. As a result, these two behaviors must be considered jointly when describing time-dependent inelastic strains of any concrete member. Early studies by McMillan [584] captured both of these behaviors and concluded that concrete shows a time-dependent stress-strain behavior both in the loaded (creep & shrinkage) and unloaded (shrinkage only) states. The combined time-dependent strains pose a significant challenge in structural design since they can accumulate to up to three times in magnitude of the initial elastic response within one year of loading.
Recent research on the topic of time-dependent inelastic strains in concrete has focused on describing the mechanisms driving creep and shrinkage behaviors [6]. Since the cement paste contributes the dominant deformations while aggregate acts to restrain the behavior, the heterogeneous bonded composite microstructure of

concrete plays a role. The rheological properties of the cement paste must theoretically arise from processes occurring at the molecular and atomic level. However, these are difficult to confirm experimentally and cannot capture the impact of the heterogeneous microstructure at larger scales. Thus, phenomenological approaches which express the behavior of creep and shrinkage in terms of physical models have been developed. Empirical calibration of rheological models provides a means of prediction of creep and shrinkage of concrete for design purposes.

5.2 Origin of Inelastic Behavior

A complete understanding of concrete creep requires empirical knowledge of concrete behavior as well as theoretical understanding of the molecule scale behavior of cement paste. Creep and shrinkage strains originate from the deformation of the hydrating cement paste. The hydrating cement paste consists of a matrix of cement hydration products with interspersed grains of un-hydrated cement. The hydration products form a gel with a discontinuous, partially saturated pore network. The initial hydration reaction rapidly progresses upon contact with water under non-equilibrium conditions and forms an amorphous gel structure. When this gel structure is placed under loading, it has the potential to reform bonds mechanically and restructure chemically through dissolution at any point with a high local stress concentration [534]. The long-term ongoing chemical hydration processes are driven by thermodynamics [464], so restructuring may continue indefinitely. Additionally, movement of water out of the sample causes the rise in capillary tension on water trapped in the cement pores, which contracts the cement gel, reducing its volume and shrinking the pore network. The ongoing chemical reactions within the cement can consume water and similarity induce shrinkage or create bubbles which forms voids and alternatively increase the volume of the cement.
While typical aggregate does not show significant strains, it impacts the response in other ways [423, 47]. During early hydration, the aggregate provides the internal surface area on which the cement hydrate precipitates. The topology of this surface area affects the rate of reaction of the cement and ultimately can change the tendency of the cement paste to exhibit creep and shrinkage behavior. After hydration is complete, the aggregate responds to the local cement strains by acting as a restraint and distributing the stresses that are generated. The resulting bulk deformation is what is measured in creep and shrinkage tests of concrete. The measurement of bulk deformation of the concrete composite captures the inelastic deformations of the cement, but may also capture any cracking or microcracking induced by shrinkage stress gradients [109, Ch. 12].

5.3 Classification of Inelastic Strains

The classification terminology of the time dependent strain in concrete was developed based on the various controlled environmental and loading conditions in which it was observed. When unloaded, any deformation is described by hygrothermal strain,

and when loaded, the additional deformations in the loading direction are described as mechanical strain of the material.

5.3.1 Hygrothermal Strain

The term shrinkage, denoted as $\varepsilon_{sh}(t)$, describes the bulk deformation of a concrete observed in a dry environment. It typically has the form of an increasing function with time, t, which approaches a bound at a decreasing rate as illustrated in Figure 5.1. In a wet environment, a positive valued ε_{sh} is used to describe bulk swelling or expansion behavior. When plotted, shrinkage is typically illustrated as the positive strain since it is the dominant effect whereas swelling is shown in the negative axis direction.

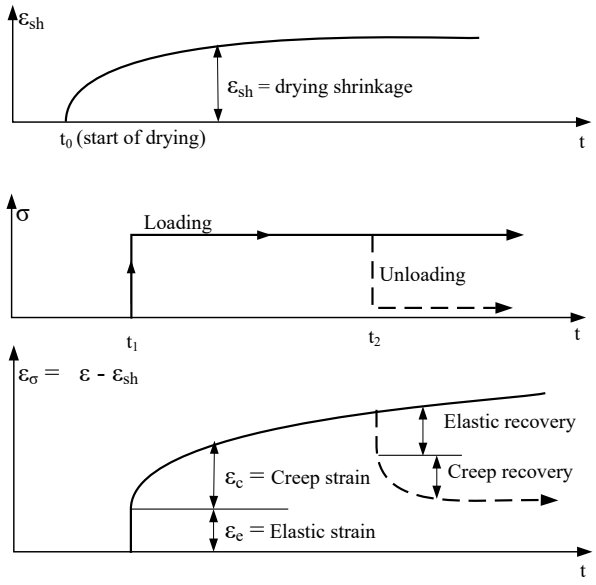

Fig. 5.1: Typical behavior of concrete shrinkage [480]

Unique experimental conditions have identified mechanism-specific components of shrinkage. The dominant contribution is drying shrinkage, which is caused by stresses induced in the cement matrix as diffusion changes the surface interactions of water in the pore network [368]. Another contribution is autogenous shrinkage, which is caused by stresses induced in the cement matrix by the ongoing hydration reaction. Autogenous shrinkage can be observed as a bulk measure of volumetric change under sealed conditions [823, 551]. The term chemical shrinkage has been introduced since the hydration reaction also may generate voids which create a bulk

expansion. Chemical shrinkage describes the internal volume change of the cement without the addition to any void volume that is generated in the process[824, 524].

5.3.2 Mechanical Strain

The instantaneous response of concrete to loading with a uniaxial stress, σ, is an elastic strain, denoted as ε_e. With time, an additional creep strain, denoted as ε_c, is observed, acting to increase the deformation in the loaded direction. It typically has the form of an increasing function with time, t, which approaches a bound at a decreasing rate as illustrated in Figure 5.1. Upon unloading, the elastic strain is instantaneously recovered while the creep strain is partially recovered at a decreasing rate over time. The ongoing hydration reaction of the cement changes its mechanical properties with time so that it will respond differently by the time it is unloaded. This phenomenon is termed aging and is observed as the gradual increase of strength and elastic modulus of concrete.
To describe the interaction between environmental conditions and creep strain, additional types of creep have been defined based on the environmental conditions under which they are measured. Basic creep is measured at constant moisture, while drying creep is measured simultaneous drying conditions [693].

5.4 Basic Expressions for Inelastic Strains

5.4.1 Empirical Expressions

Experimentally observed trends in creep and shrinkage strains are seen in Figure 5.2. The shape of the creep curve changes systematically based on relevant parameters and is initially steep, approaching what seems to be a finite value in a linear time scale. However, it has been observed that structures continue to measurably creep over 30 years [835]. Since some of the associated mechanisms are driven by thermodynamic processes, it is reasonable to expect that while creep measurements seem to approach a finite value, they may indefinitely increase at a very slow rate. Generally a semi-logarithmic plot and testing sequence best captures the rapid changes in the creep and shrinkage curves during early ages, followed by decades of gradual changes in strain. Based on these observations, two types of empirical expressions for creep prediction may be found in literature: those approaching a limit based on observations, and those that increase indefinitely based on observations and theory. Note that empirical and semi-empirical models that are only based on the early-age functional form and do not match the long-term continued strain evolution will not be able to correctly predict long-term strains. In fact, they may significantly under-predict the long-term strains in a structure, even after matching the short-term behavior [110]. Empirical expressions which have been proposed in literature include: power expressions [807, 782], exponential expressions [831, 582], hyperbolic expressions [740, 547], and logarithmic expressions [840].

Fig. 5.2: Creep strain evolution at various stress levels and shrinkage strain evolution of various sized samples

5.4.2 Theoretically-based Rheological Expressions

When concrete is loaded within service stress levels (up to 40% of the compressive strength), the creep exhibits a linear relationship to the applied stress, σ. The two dashed curves in Figure 5.2 are within this load limit and illustrate a linear scaling with load. Creep strains under service stress levels can thus be described with viscoelastic expressions.
An expression which qualitatively captures the rheological properties of concrete should capture the following characteristics [848]:

1. instantaneous elastic deformations,
2. delayed-elastic deformations,
3. a creep behavior dependent on stress and time,
4. instantaneous elastic recovery,
5. delayed elastic recovery,
6. permanent residual deformation.

Many such models have been developed with varying degrees of success in capturing the observed behavior of concrete.
Generally, the loading history of a standard creep test in which a sample is subjected to a uniaxial stress of magnitude $\bar{\sigma}$ at time t' may be mathematically described as

$$\sigma(t) = \bar{\sigma} H(t - t') \tag{5.1}$$

where H is the heaviside step function. The resulting strain response is $\varepsilon(t)$. By the principle of superposition, the compliance function of the material, J, may be obtained by dividing the strain response by the applied stress.

$$\varepsilon(t) = \bar{\sigma} J(t, t') \tag{5.2}$$

J provides the strain at time t due to a stress acting from t' to t. It is the mathematical kernel mapping the stress rate to the strain. Thus, if the compliance of a given concrete is known, it is possible to integrate any general stress history to obtain the strain evolution.

$$\varepsilon(t) = \int_0^t J(t, t') d\sigma(t') \tag{5.3}$$

Typical loading histories for concrete begin at some loading age $t_1 > 0$ at which point the stress jumps from zero. The strain equation thus takes the form:

$$\varepsilon(t) = J(t, t_1)\sigma_1 + \int_{t_1}^t J(t, t')\dot{\sigma}(t')dt' \tag{5.4}$$

where the dot represents the partial derivative with respect to t. Differentiating, the strain rate becomes

$$\dot{\varepsilon}(t) = \frac{\dot{\sigma}(t)}{E(t)} + \int_0^t \dot{J}(t,t')d\sigma(t') \tag{5.5}$$

where $E(t)$ is the instantaneous elastic modulus at age t which equals $1/J(t,t')$.
The stress-strain history can be described in integral form by introducing the relaxation function, $R(t,t_1)$, which is the stress history caused by a constant strain induced at age t'.

$$\sigma(t) = R(t,t_1)\varepsilon_1 + \int_{t_1^+}^t R(t,t')\dot{\varepsilon}(t')dt' \tag{5.6}$$

The compliance of concrete is often reported over time and used for empirical fitting of creep and shrinkage prediction equations. Plotted in a semi-logarithmic time scale in terms of the concrete age $t-t'$, the long-term creep curves take the form of parallel lines.
Note that concrete is at times placed in conditions above service stress levels – caused by extreme moisture gradients in dry environments or by high stresses. Under these conditions, the creep exhibits a nonlinear relationship to the applied stress. The natural extension of the viscoelastic description above would be to capture such nonlinear behavior using a viscoelastic formulation. However, since the origin of the nonlinearity is from irreversible microcracking and cracking of the material, there is no true plastic behavior.

5.4.3 Creep Coefficient

For analysis of creep in structural components in practice, a dimensionless creep coefficient, i.e. ϕ, is often defined [211]. This is a convenient dimensionless quantity that captures the long-term deformations due to loading, *i.e.* creep strains which are most significant for design.

$$\begin{aligned}\phi(t,t') &= \frac{\text{creep strain at time } t}{\text{elastic strain at time of loading } t'} \\ &= \frac{\bar{\sigma}J(t,t') - \bar{\sigma}/E(t')}{\bar{\sigma}/E(t')} = E(t')J(t,t') - 1\end{aligned} \tag{5.7}$$

Since the creep coefficient does not explicitly specify the initial elastic strain, it is an insufficient measure to describe the full strain response of concrete, but it may be used judiciously.

5.5 Creep and Shrinkage Prediction Models

A number of international recommendations by design code institutes and academics provide comprehensive compliance functions for predicting creep and shrinkage strains of concrete. Here the B3 and fib models are summarized. Further models

have been published by the American Concrete Institute (ACI) [1], the Japan Society of Civil Engineers (JSCE) [206], the Comité Euro-International du Béton (CEB) [191], and Eurocode committee [113].

5.5.1 fib Model Code 2010

The *fib* model [123] provides a creep and shrinkage compliance function in terms a concrete characteristic compressive strength, f_c. This is defined as a bounding value from strength measurements below which only 5% of all tests fall. The mean compressive strength is estimated as $\bar{f}_c = f_c + 8\text{MPa}$.
First, the modulus of elasticity is estimated from the compressive strength at 28 days. Here the modulus is assumed to be obtained from a static unloading after loading the concrete sample to 40% of the compressive strength.

$$E_{28} = 21.5\text{GPa} \times \alpha_E \times \left(\frac{\bar{f}_c}{10\text{MPa}}\right)^{1/3} \tag{5.8}$$

where α_E captures the effect of different aggregate and is 1.0 for quartzite, 1.2 for basalt and dense limestone, 0.9 for typical limestone, and 0.7 for sandstone aggregate. The evolution of the elastic modulus due to aging is estimated next.

$$E(t) = E_{28}\sqrt{\exp\left(s\left[1 - \sqrt{28/t}\right]\right)} \tag{5.9}$$

where s captures the effect of different cement types and is 0.25 for normal hardening cement of strength class 42.5.
The compliance equation is given in terms of two creep curves: basic creep (φ_{bc}) and drying creep (φ_{dc}).

$$J(t,t') = \frac{1}{E(t')} + \frac{\varphi_{28}(t,t')}{E_{28}} \tag{5.10}$$

$$\varphi_{28}(t,t') = \varphi_{bc}(t,t') + \varphi_{dc}(t,t') \tag{5.11}$$

Here the basic creep is given as a logarithmic function without limit:

$$\varphi_{bc}(t,t') = \frac{1.8}{\bar{f}_c^{0.7}} \ln\left[1 + \left(0.035 + \frac{30}{t'_{adj}}\right)^2 (t - t')\right] \tag{5.12}$$

The drying creep approaches a bound:

$$\varphi_{dc}(t,t') = \frac{412}{\bar{f}_c^{1.4}} \frac{\phi_{RH}}{0.1 + (t'_{adj})^{0.2}} \left(\frac{t - t'}{\beta_H + t - t'} \right)^{\gamma(t'_{adj})} \quad \text{where} \quad \gamma(t'_{adj}) = \frac{1}{2.3 + 3.5/\sqrt{t'_{adj}}} \tag{5.13}$$

where t'_{adj} is the adjusted age at loading which takes into account effects of elevated and reduced temperatures and cement type on the shape of the creep curves. For normal strength concrete, the adjusted age defaults to the temperature-adjusted age t'_T which uses an Arrhenius rate equation to approximate temperature effects on aging:

$$\frac{dt'_T}{dt} = \exp\left(\frac{Q_T}{RT_0} - \frac{Q_T}{RT} \right) \tag{5.14}$$

Reference values for adjustment are $Q_T/R = 4000$K, $T_0 = 293$K. T is the mean temperature of the concrete section in Kelvin. For other types of concrete, the temperature-adjusted age is further modified by

$$t'_{adj} = t'_T \left(1 + \frac{9}{2 + (t'_T)^{1.2}} \right)^{\alpha}, t'_{adj} \geq 0.5\text{days} \tag{5.15}$$

where α is selected as -1 for 32.5 N concrete strength, 0 for 32.5 R and 42.5 N concrete, and 1 for 42.5 R, 52.5 N, and 52.5 R concrete.
In the drying creep equation, the effect of member size is captured in β_H in terms of cross-sectional area, A_c, and the perimeter of the surface in contact with the atmosphere, u (in mm).

$$\beta_H = 1.5 \frac{2A_c}{u} + 250 \sqrt{\frac{35}{\bar{f}_c}} \tag{5.16}$$

Similarly, the effect of the environmental humidity is captured in ϕ_{RH} in terms of the relative environmental humidity, h_{env}.

$$\phi_{RH} = 10 \frac{1 - h_{env}}{\sqrt[3]{2A_c/u}} \tag{5.17}$$

β_H should be multiplied by another factor, β_T, to take into account the effect of temperature on the creep. Additionally, the creep coefficients should be multiplied by factors in terms of ϕ_T to capture this effect. The corrections look at follows:

$$\beta_T = exp\left(\frac{1500}{T} - 5.12 \right) \tag{5.18}$$

$$\phi_T = exp\left[0.015(T - T_0) \right] \tag{5.19}$$

$$\varphi_{28}\left(t,t'\right)=\varphi_{bc}\left(t,t'\right)\phi_T+\varphi_{dc}\left(t,t'\right)\phi_T^{1.2} \tag{5.20}$$

5.5.2 B3 Model

The B3 model [109] provides a creep and shrinkage compliance function in terms of the standard mean 28-day compression strength $\bar{f}_c$. This is 30% higher than the the reduced strength, f'_c, used for the design of concrete components.
The compliance equation is given in terms of three parts:

$$J(t,t')=\frac{1}{E_0}+J_b(t,t')+J_d(t,t') \tag{5.21}$$

where E_0 is the asymptotic modulus, J_b is the basic creep compliance, and J_d is the drying creep compliance.
The asymptotic modulus, E_0, captures the very early creep value by extrapolating the creep curve to very short loading durations. This value is empirically assumed to be age-independent. A practical estimate of the asymptotic modulus may simply be taken as $E_0 = E_{28}/0.6$. If only the compressive strength, $\bar{f}_c$, is available, the empirical relation provided by the ACI (1999) recommendation [1] may be applied to estimate E_{28}:

$$E_{28}=57\text{ksi}\sqrt{\frac{\bar{f}_c}{1\text{psi}}} \tag{5.22}$$

Generally the short-term modulus of elasticity and its aging is defined as

$$E(t')=\frac{1}{J(t'+\Delta t_s,t')} \tag{5.23}$$

where Δt_s is a chosen loading duration. Selecting $\Delta t_s \approx 0.01\text{day} \approx 15\text{min}$ gives the 28-day elastic modulus defined in the ACI Building Code 318-05 [211]. When relying on empirically fitted parameters, the term $\frac{1}{E_0}$ is typically referred to as q_1.
The simplest basic creep compliance is given as a double-power law:

$$J_b(t,t')=\frac{\phi_1}{E_0}\left((t')^{-m}+\alpha\right)(t-t')^n \tag{5.24}$$

which gives approximate concrete behavior for ages less than one year and load times $t' = 14 - 365$ days when $n = 0.1$, $m = 1/3$, $\alpha = 0.05$, and $\phi_1 = 2 - 6$, depending on the type of concrete. With these default values, the asymptotic modulus $E_0 = (1 + 0.239\phi_1)E_{28}$. A log-double-power law form of this expression is also available [100] and provides better predictions. The full theoretically-based formulation provides the best predictions [96].

$$J_b(t,t')=q_2Q(t,t')q_3\ln\left[1+(t-t')\right]+q_4\ln\left(\frac{t}{t'}\right) \tag{5.25}$$

$$\text{where}\quad Q(t,t')=\int_{t'}^{t}\frac{ns^{-m}}{(s-t')+(s-t')^{1-n}}ds$$

The equation for Q can be numerically integrated, interpolated from a table in [108] [97] or estimated from an approximate explicit formula as:

$$Q(t,t') = Q_f(t')\left[1 + \left(\frac{Q_f(t')}{}\right)^{r(t')}\right]^{-1/r\left(t'\right)} \tag{5.26}$$

in which,

$$r(t') = 1.7(t')^{0.12} + 8 \tag{5.27}$$

$$Z(t,t') = (t')^{-m}\ln\left[1 + (t-t')^{n}\right] \tag{5.28}$$

$$Q_f(t') = \left[0.086(t')^{\frac{2}{9}} + 1.21(t')^{\frac{4}{9}}\right]^{-1} \tag{5.29}$$

The drying creep on a concrete section is estimated with a bounded formulation in terms of the time of exposure to the environment, t_0.

$$J_d(t,t') = q_5\sqrt{\langle e^{-g(t-t_0)} - e^{-g(\langle t'-t_0\rangle)}\rangle} \tag{5.30}$$

where $\langle x\rangle \equiv \max(x,0)$ are Macauley brackets. When using the simple basic creep compliance, the best experimental agreement is found with function g selected as:

$$g(t-t_0) = 3\left[1 - (t - h_{env})S(t-t_0)\right], \text{where } \; q_5 = 0.0006/\bar{f}_c \tag{5.31}$$

For the full model B3 function, g should instead be:

$$g(t-t_0) = 8\left[1 - (1 - h_{env}S(t-t_0)\right], \text{where } \; q_5 = \frac{7.57\times 10^5}{\bar{f}_c(\varepsilon_{sh}^{\infty})^{0.6}} \tag{5.32}$$

$\varepsilon_{sh}^{\infty}$ represents the final shrinkage strain corresponding to a perfectly dry environment ($h_{env} = 0$).
The function $S(t-t_0)$ is given by:

$$S(t-t_0) = \tanh\sqrt{\frac{t-t_0}{\tau_{sh}}}, \text{where } \; \tau_{sh} = k_t(k_s D)^2 \tag{5.33}$$

where k_s captures the effect of member shape and should be selected as 1.00 for an infinite slab, 1.15 for an infinite cylinder, 1.25 for an infinite square prism, 1.30 for a sphere, and 1.55 for a cube. This function is used to capture the shape of the drying curve for the drying creep as well as the shrinkage strain on the cross section. The average shrinkage strain is given by

$$\varepsilon_{sh}(t) = -\varepsilon_{sh}^{\infty}k_h S(t-t_0), \text{where } \; k_h = 1 - h_{env}^3 \tag{5.34}$$

To conduct a complete prediction of the compliance functions and shrinkage using this model, the parameters $q_1 - q_5$, $\varepsilon_{sh}^{\infty}$, and k_t must be obtained by optimization to

experimental data or from functions fitted to large data sets of experiments, Table 5.1.

Table 5.1: Empirically fitted parameters for the B3 model

Line	Phenomenon	Parameter	Inch-pound formula	Units	SI formula	Units
1		q_1	$10.526\overline{f}_c^{-0.5}$	10^{-6}/psi	$126.77\overline{f}_c^{-0.5}$	10^{-6}/Mpa
2	Basic creep	q_2	$451.1\, c^{0.5}\overline{f}_c^{-0.9}$	10^{-6}/psi	$185.4\, c^{0.5}\overline{f}_c^{-0.9}$	10^{-6}/Mpa
3		q_3	$0.29(\text{w/c})^4 q_2$	10^{-6}/psi	$0.29(\text{w/c})^4 q_2$	10^{-6}/Mpa
4		q_4	$0.14\,(\text{a/c})^{-0.7}$	10^{-6}/psi	$20.3\,(\text{a/c})^{-0.7}$	10^{-6}/Mpa
5		k_t	$190.8t_0^{-0.08}\overline{f}_c^{-1/4}$	days/in^2	$0.085t_0^{-0.08}\overline{f}_c^{-1/4}$	days/mm^2
6	Shrinkage	ε_s^∞	$\alpha_1\alpha_2(26w^{2.1}\overline{f}_c^{-0.28}+270)$	10^{-6}	$\alpha_1\alpha_2(0.019w^{2.1}\overline{f}_c^{-0.28}+270)$	10^{-6}
7		ε_{sh}^∞	$\varepsilon_s^\infty \times 0.57514\sqrt{3+14/(t_0+\tau_{sh}}$	10^{-6}	$\varepsilon_s^\infty \times 0.57514\sqrt{3+14/(t_0+\tau_{sh}}$	10^{-6}
8	Drying creep	q_5	$7.57\times10^5\overline{f}_c^{-1}(\varepsilon_{sh}^\infty)^{-0.6}$	10^{-6}/psi	$7.57\times10^5\overline{f}_c^{-1}(\varepsilon_{sh}^t nfty)^{-0.6}$	10^{-6}/MPa

5.5.3 Age-Adjusted Effective Modulus

Creep compliance functions inherently result in functional forms which require tedious step-wise numerical implementation. This is not well suited for preliminary design of structures or simple structures for which time-dependent deformations do not dominate strains. The age-adjusted effective modulus is used as an approximate solution method for design calculations. The AAEM method assumes that the stress and strain histories between the initial and current state can be approximated as a linear combination of creep (at constant stress) and relaxation (at constant strain). Using this assumption, the stress-strain history equation may be approximated as

$$\sigma(t) = R(t,t_1)\varepsilon_1 + E'_{eff}(t,t_1)\Delta\varepsilon(t) \tag{5.35}$$

for simpler implementation. Here E'_{eff} is the age-adjusted effective modulus:

$$E'_{eff}(t,t_1) = \frac{E(t_1) - R(t,t_1)}{\varphi(t,t_1)} = \frac{E(t_1) - R(t,t_1)}{E(t_1)J(t,t_1) - 1}, t > t_1 \tag{5.36}$$

For a single-step loading history, the effective modulus can be written in terms of the creep coefficient.

$$E_{eff} = \frac{1}{J(t,t_1)} = \frac{E(t_1)}{1+\phi(t,t_1)} \tag{5.37}$$

which is also enshrined in Eq. 3.1 of ACI-209 [8]
Hence in a two step finite element analysis, one can apply the initial load with the original E, and then in the next increment transition from an incremental formulation to a secant one and replace E by E_{eff}.

5.6 Effects of Creep on Structures

The ability of concrete to creep is directly related to the observed ductile failure of reinforced concrete members. Developing large strains before failure causes stress redistribution in structures and the preferential ductile failure we see in concrete structures. To make use of these beneficial effects of creep during design, careful consideration and prediction of time dependent strains and environmental effects are critical. Recent research in the field of concrete creep aims to engineer these behaviors to control crack development by redistributing stresses locally within the concrete microstructure.

5.6.1 Harmful Effects of Creep

Creep can cause loss of prestress in pre-stressed structures, initiate cracking in mass structures due to thermal cycles, encourage column buckling, and complicate stress analysis in arches and indeterminate structures. Indeterminate structures are more likely to exhibit creep since they may be subjected to loading stresses as well as stresses developed due to deformation restraints.

5.6.2 Effects of Prestressed Structures

Compressive stresses are induced with prestressing steel tendons in the tension zone of concrete structures. The time-dependent strains in concrete act to reduce this compressive stress. With inadequate compression, the concrete in the tension zone forms cracks. This gradual redistribution of stress is complicated by the fact that the steel tendons exhibit viscoplastic relaxation which is sensitive to temperature changes. Standard texts on the topic of design of prestressed concrete structures detail approximate design calculations which take into account the effects of the time-dependent strains in the concrete and steel. However, classical bending theory is insufficient if the resulting deflections of a bridge are to be predicted. Finite element models of the construction process with considerations for environmental fluctuations are necessary to fully capture the interplay of the time-dependent stress redistribution between the concrete and steel and any cracking.

5.6.3 Mass Structures

Mass structures experience thermal cycles during hydration. The initial stresses caused by thermal expansion strains are relieved by creep. However, since the creep of concrete gradually diminishes with age, subsequent cooling produces stresses that are no longer relieved by creep and the material suffers cracking. This detrimental phenomenon is more accurately a consequence of insufficient relaxation behavior of the concrete. Relaxation governs the concrete's ability to resist cracking due to shrinkage and the redistribution of stress in hydrostatic structures.

Chapter 6
Seismology and Seismicity

Abstract
Seismology is the scientific study of earthquakes and the propagation of elastic waves through the earth. A seismologist is a scientist who does research in seismology. A field that uses geology to infer information regarding past earthquakes is paleoseismology. On the other hand, the seismicity refers to the geographic and historical distribution of earthquakes.
Earthquake design of a structure always depends on degree of regional seismic activity. Many seismological factors directly influence the work of a structural engineer such as: 1) distribution of earthquake sources affecting the construction site, 2) fault mechanisms of various sources, 3) seismic activity of various sources in terms of recurrence of magnitudes, 4) ground motion intensity level, and 5) attenuation of the ground motion signal with distance. This chapter is an introduction to the fundamental characteristics of the engineering seismology.

6.1 Causes and Consequences of Earthquake

6.1.1 Earth's Layers

The Earth is layered with the core at its center, then the mantle, and the crust on the outside, Figure 6.1. The crust and uppermost part of the mantle is the layer between the crust and the outer core. Together the crust and the upper mantle make up the solid layer called the lithosphere. The lithosphere is made up of large moving and broken pieces of rock called tectonic plates. Most of the natural earthquakes occur in the earth's crust.

6.1.2 Natural Earthquakes

Deformations occur in the rock, which cause a build up of elastic energy. Rupture or slip along a fault line causes a sudden release of energy into a seismic shock (an earthquake) which, in turn, causes propagation of seismic waves and ground shaking. Most earthquakes occur in two specific zones on the planet, Figure 6.2:

- Circum Pacific Belt (ring of fire): South America, the California coast, Alaska, Japan, Formosa, Philippines, New Zealand. About 90% of the world's earthquakes and 81% of the world's largest earthquakes occur along the ring of fire.

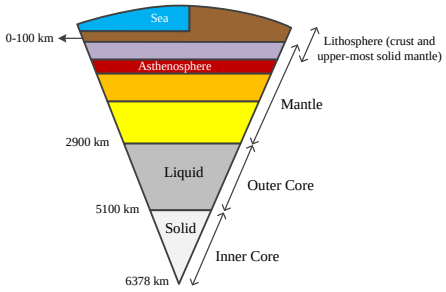

Fig. 6.1: Schematic of earth's layers

- Alpine Belt: the Mediterranean, North India, Indonesia. About 5-6% of earthquakes and 17% of the world's largest earthquakes occur along the Alpine Belt.

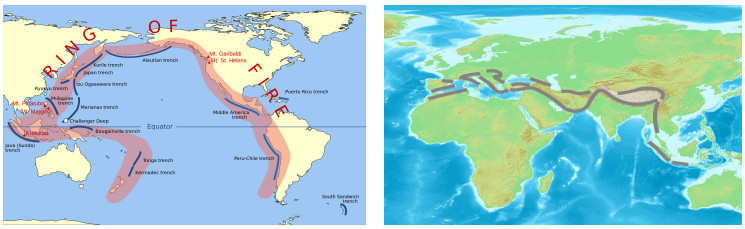

(a) Circum Pacific Belt (b) Alpine Belt

Fig. 6.2: Seismic belts of the world; adopted from Wikipedia

6.1.3 Induced Earthquakes

Not all earthquakes are natural. Some human activities influence amplitude and distribution of strains in the earth's crust such as:

- Filling of a reservoir (artificial lake)
  - Usually causes most severe induced earthquakes
  - May reach magnitude 6.0 on the Richter scale
  - More than 70 earthquakes of this type have been recorded world wide
- Mining
- Excavation of huge quarries
- High pressure injection of fluids to generate geothermic energy
- Groundwater extraction
- Oil wells
- Underground nuclear explosions

6.1.4 Earthquake Damage

Earthquakes may damage structures and the environment in different ways:

- **Ground shaking** is the most familiar effect of earthquakes. It is a result of the passage of seismic waves through the ground. Buildings and infra-structures can be damaged or destroyed, people and animals have trouble standing up or moving around, and objects can be tossed around due to strong ground shaking in earthquakes.
- **Fault (ground) rupture** is an important effect of earthquakes which occurs when the earthquake movement along a fault actually breaks the Earth's surface. Rupture causes problems for humans by rupturing things; pipelines, tunnels, aqueducts, railway lines, roads, and airport runways which cross an area of active rupture can easily be destroyed or severely damaged.
- **Soil liquefaction** describes a phenomenon whereby a saturated or partially saturated soil substantially loses strength and stiffness in response to an applied stress (earthquake shaking in our case) or other sudden change in stress condition, causing it to behave like a liquid. It is most often observed in saturated, loose, sandy soils.
- **Fires**, often associated with broken electrical and gas lines, are one of the common side effects of earthquakes. Gas is set free as gas lines are broken and a spark will start bringing "inferno". To complicate things, water lines are broken so there is no water to extinguish the fire.
- **Tsunamis** are a series of water waves caused when the sea floor moves vertically in an earthquake and which can travel vast distances in a short period of time. Tsunami speeds in the deep ocean have been measured at more than 700 km/hr, and when tsunamis reach shallow water near the coast, they can reach heights of more than 100 ft.
- **Seismic seiches** are standing waves set up on rivers, reservoirs, ponds, and lakes when seismic waves from an earthquake pass through the area. They are in direct contrast to tsunamis which are giant sea waves created by the sudden uplift of the sea floor.
- **Flood**: an earthquake can rupture (break) dams or levees along a river. The water from the river or the reservoir would then flood the area, damaging buildings and maybe sweeping away or drowning people.

6.2 Theory of Plate Tectonics

The earth is characterized by a small number of lithospheric plates that float on a viscous under-layer called the asthenosphere. Geological evidence shows that plates undergo constant, gradual change. Magma is continually upwelling at the mid-oceanic ridges and rises as the sea floor spreads apart. In some areas, large sections of plates are forced to move beneath other plates (surface layers of rocks are absorbed into the earth's interior). These areas are called subduction zones.
Theory of plate tectonics, proposed in the early 1960's, is an accepted explanation for the occurrence of most earthquakes. Earth's crust is composed of several large

plates that float on a viscous medium. Continents and oceans are supported by those plates. Continents were originally all linked together but started drifting apart 200 million years ago. Plates move 1 to 15 cm every year.
Generally, three types of plate boundaries exist, with a fourth, mixed type, Figure 6.3:

- Transform boundaries (Conservative) occur where two lithospheric plates slide (grind) past each other. Plates are neither created nor destroyed. Strong earthquakes can occur along a fault, e.g the San Andreas Fault in California.

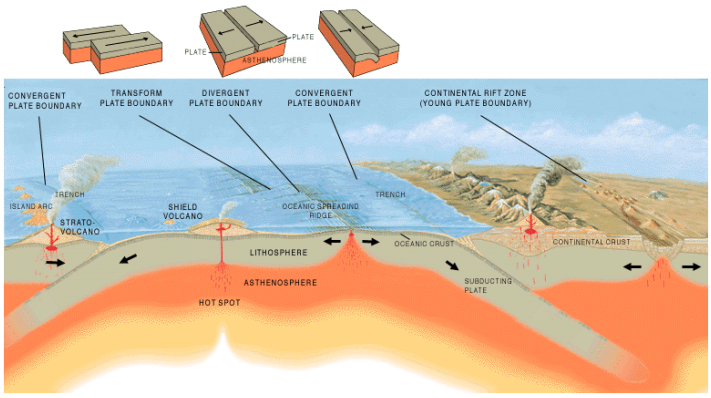

Fig. 6.3: Different types of plate boundaries; image courtesy of the USGS

- Divergent boundaries (Constructive) occur where two plates slide apart from each other. At zones of ocean-to-ocean rifting, divergent boundaries form by seafloor spreading, allowing for the formation of new ocean basin. As the continent splits, the plate area increases causing many small volcanoes and/or shallow earthquakes.

- Convergent boundaries (Destructive) occur where two plates slide toward each other to form either a subduction zone (one plate moving underneath the other) or a continental collision. At zones of ocean-to-continent subduction, the dense oceanic lithosphere plunges beneath the less dense continent. Earthquakes then trace the path of the downward-moving plate as it descends into asthenosphere. A trench forms, and as the subducted plate partially melts, magma rises to form continental volcanoes.

6.3 Reid's Elastic Rebound Theory

Following a 1906 San Francisco earthquake, Prof. H.F. Reid (Johns Hopkins University) proposed an explanation for the immediate cause of an earthquake know as "Reid's elastic rebound theory." Tectonic stress is an important variable in the cre-

ation of an earthquake. The elastic rebound theory involves following steps, Figure 6.4:

- (a) the rock on the fault line begins in its original position,
- (b) there is a buildup of strain that deforms the rock,
- (c) the strain becomes too much for the rock to handle and there is a rupture of the rock that releases the stored-up energy out as seismic waves,
- (d) the rock springs back to its original undeformed position.

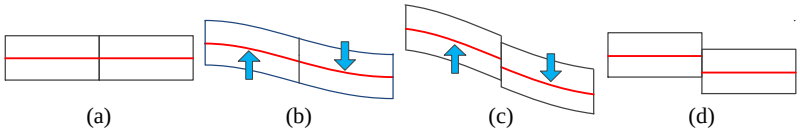

Fig. 6.4: Reid's Elastic Rebound Theory

6.4 Fault Mechanisms

A fault is a fracture or zone of fractures between two blocks of rock. Fault movement may occur rapidly in the form of an earthquake, or may occur slowly in the form of creep. Faults may range in length from a few millimeters to thousands of kilometers. The fault surface (know as the "dip") can be horizontal or vertical or some arbitrary angle in between. There are three fault mechanisms, Figure 6.5:

- Dip-slip faults are inclined fractures where the blocks have mostly shifted vertically
  - Normal faults are caused by divergent boundaries (tension). The hanging wall slides downward.
  - Reverse (thrust) faults are caused by convergent boundaries (compression). The hanging wall is pushed upward.
- Strike-slip faults are nearly vertical fractures where the blocks have mostly moved horizontally.
  - Right-lateral fault: if the block opposite an observer looking across the fault moves to the right.
  - Left-lateral fault: if the block moves to the left.
- Oblique-slip faults show both dip-slip and strike-slip motion.

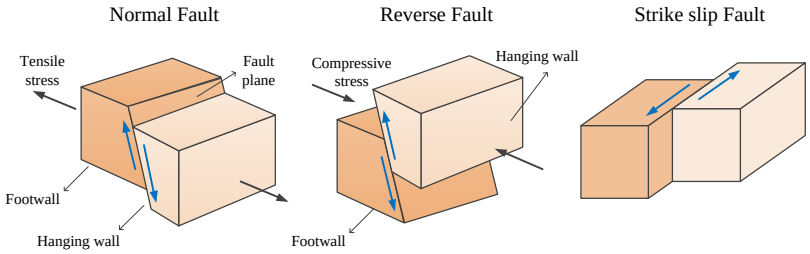

Fig. 6.5: Classification of fault mechanisms

6.5 Seismic Waves

6.5.1 Terminology

Seismic waves are waves of energy that travel through the earth's layers as a result of an earthquake. The wave velocity depends on density and elasticity of the medium. The velocity tends to increase with depth. It ranges from approximately 2 to 8 km/s in the earth's crust, and up to 13 km/s in the deep mantle. Seismic waves can be classified as, Figure 6.6:

- Body waves: which are traveling within solid earth
  - Primary waves (P-waves): Horizontal tension and compression waves, which travel in the direction of the wave front. They are high frequency and the first waves to reach a structure, Figure 6.6(a).
  - Secondary waves (S-waves); Horizontal (SH-waves) and Vertical (SV-waves): Shear waves which travel perpendicularly to the wave front. They are lower frequency, larger amplitude, and cause the most destructive vibrations, Figure 6.6(b).
- Surface waves: which are traveling near the ground surface. They travel more slowly than body waves.
  - Rayleigh waves: Vertical waves traveling on the ground surface. They are slower than body waves, roughly 90% of the velocity of S-waves for typical homogeneous elastic media, Figure 6.6(c).
  - Love waves: Horizontal waves traveling on the ground. They usually travel slightly faster than Rayleigh waves, Figure 6.6(d).

Moreover, depending on the location of the earthquake source to the desired site, the following terminology is used, Figure 6.7:

- Hypocentre: Focal point or focus where the earthquake occurs.
- Epicentre: Vertical projection of focal point on ground surface.
- Focal depth: Vertical distance between focal point and epicenter.
- Hypocentral distance: The distance from the site to the hypocenter.

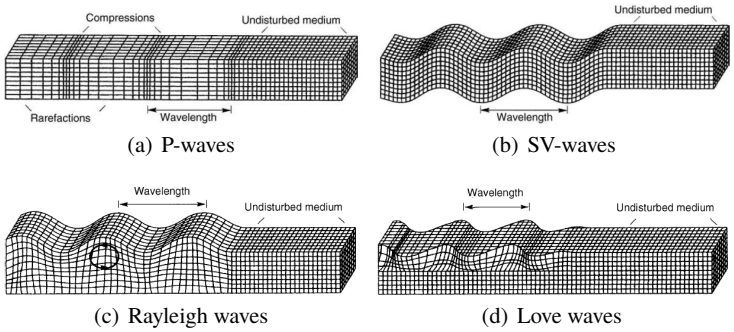

(a) P-waves (b) SV-waves

(c) Rayleigh waves (d) Love waves

Fig. 6.6: Classification of seismic waves; [147]

- Epicentral distance: The distance from the site to the epicenter.
- Rupture distance: The distance from the site to the closest point on the fault plane.

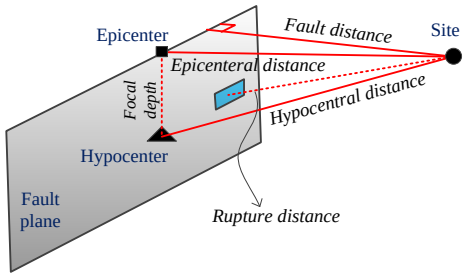

Fig. 6.7: Different fault-to-site distance terminologies

6.5.2 Equation of Motion

The equation of motion (also called Navier's equation) for seismic waves in the general format can be written as [314]:

$$(\Gamma + G)\,\nabla D + G\nabla^2 \mathbf{u} = \rho \frac{\partial^2 \mathbf{u}}{\partial t^2} \tag{6.1}$$

where Γ is Lame's constant:

$$\Gamma = \frac{\upsilon E}{(1+\upsilon)(1-2\upsilon)} \tag{6.2}$$

where υ and E are Poisson's ratio and Young's modulus, respectively; G is the shear modulus; and D is dilatation (negative compression). Dilatation is a scalar value that shows the increase in volume of a unit cube of the earth

$$D = \varepsilon_{ii} = \varepsilon_{11} + \varepsilon_{22} + \varepsilon_{33} \tag{6.3}$$

where ε_{ii} are three principal strains in principal directions.
ρ is rock density at the earth's crest; t is time; $\mathbf{u}$ is the displacement vector; ∇ is the gradient (grad) of a function, f ($\nabla f = \frac{\partial f}{\partial x}\mathbf{i} + \frac{\partial f}{\partial y}\mathbf{j} + \frac{\partial f}{\partial z}\mathbf{k}$, where $\mathbf{i}$, $\mathbf{j}$, $\mathbf{k}$ are the standard unit vectors); ∇^2 is the Laplacian of any tensor field $\mathbf{T}$ ($\nabla^2\mathbf{T} = \nabla\cdot(\nabla\mathbf{T})$). There are several major assumptions in this formulation:

- The earth's crust is assumed to be a perfectly elastic medium in which the theory of elasticity applies.
- Large strains near the earthquake source are neglected.
- Geological anisotropy is not considered.
- Discontinuities near the source due to fractures and faults in the earth's crust are omitted.

The standard wave equation governing the propagation of dilatational waves (P-waves) can be obtained using the divergent on both sides of Eq. 6.1:

$$\left(\frac{\Gamma + 2G}{\rho}\right)\nabla^2 D = \frac{\partial^2 D}{\partial t^2} \tag{6.4}$$

Comparing to the classical acoustic wave equation:

$$c^2\nabla^2 u = \frac{\partial^2 u}{\partial t^2} \tag{6.5}$$

The P-wave velocity (which has no rotation) is given by:

$$V_P = \sqrt{\frac{\Gamma + 2G}{\rho}} \tag{6.6}$$

On the other hand, waves which involve a distortion of the earth's crust may be expected to produce a relative rotation of neighboring particles causing shear stresses. The standard wave equation governing the pure rotational disturbance (S-waves) can be obtained using the curl ($\nabla\times$) on both sides of Eq. 6.1:

$$(\Gamma + G)(\nabla\times\nabla D) + G\nabla^2(\nabla\times\mathbf{u}) = \rho\frac{\partial^2(\nabla\times\mathbf{u})}{\partial t^2} \tag{6.7}$$

where the curl of a gradient is equal to zero $(\nabla\times\nabla D) = 0$.
Thus, the simplified equation of motion for S-waves is:

$$\frac{G}{\rho}\nabla^2(\nabla\times\mathbf{u}) = \frac{\partial^2(\nabla\times\mathbf{u})}{\partial t^2} \tag{6.8}$$

The S-wave velocity (which has no volume change) is given by:

$$V_S = \sqrt{\frac{G}{\rho}} \tag{6.9}$$

Finally, the one-dimensional solution for the wave equation can be obtained by assuming a region without sources:

$$c^2 \nabla^2 \eta = \frac{\partial^2 \eta}{\partial t^2} \tag{6.10}$$

where η is the wave-function and could be either dilatation or the vector potential, and c is either P- or S-wave velocity. The 1D solution to this equation is:

$$\eta\left(x,t\right) = A_0 \ \cos\left[k\left(x - ct\right) - \phi\right] \tag{6.11}$$

where A_0 is wave amplitude, k is wave-number, and ϕ is phase angle.
Alternatively, it can be written as:

$$\eta\left(x,t\right) = A_0 \cos\left[\frac{2\pi}{\lambda}x - \frac{2\pi}{T}t - \phi\right] \tag{6.12}$$

where λ is wave-length, T is period, $\omega = \frac{2\pi}{T}$ is angular frequency.

6.5.3 Location of Earthquake

Location of the epicenter can be estimated by at least three geological stations. The arrival times for the P- and S-waves are computed as: $t_P = \frac{d}{V_P}$ and $t_S = \frac{d}{V_S}$, respectively. Since P-waves arrive earlier than S-waves, the distance between site and earthquake epicenter, d, is:

$$t_S - t_P = \frac{d}{V_S} - \frac{d}{V_P} \Rightarrow d = \frac{t_S - t_P}{\frac{1}{V_S} - \frac{1}{V_P}} \tag{6.13}$$

Next, by plotting three circles, Figure 6.8, and finding the "approximate" intersection point, one can estimate the location of earthquake.

6.6 Shaking Intensity

In 1902, G. Mercalli (Italian seismologist) introduced an intensity scale when there were no recording instruments. Later, this intensity scale was adapted and modified by two Californian seismologists and was known as the "Modified Mercalli Intensity" (MMI) scale. The MMI is based on subjective human feelings and observations of local damage and varies from I (1) to XII (12), Figure 6.9(a). Data required to determine MMI of an earthquake is obtained by interviews and surveys. The results of MMI scale is usually expressed in terms of contours of intensities called "isoseismal

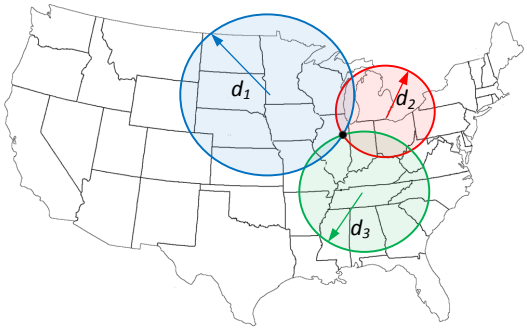

Fig. 6.8: Approximate location of earthquake

lines". The so-called "Instrumental intensity" is USGS's term for equivalent MMI values as measured by instruments, Figure 6.9(b).

I. Not felt	Not felt except by a very few under especially favorable conditions.
II. Weak	Felt only by a few persons at rest, especially on upper floors of buildings.
III. Weak	Felt quite noticeably by persons indoors, especially on upper floors of buildings. Many people do not recognize it as an earthquake. Standing motor cars may rock slightly. Vibrations similar to the passing of a truck. Duration estimated.
IV. Light	Felt indoors by many, outdoors by few during the day. At night, some awakened. Dishes, windows, doors disturbed; walls make cracking sound. Sensation like heavy truck striking building. Standing motor cars rocked noticeably.
V. Moderate	Felt by nearly everyone; many awakened. Some dishes, windows broken. Unstable objects overturned. Pendulum clocks may stop.
VI. Strong	Felt by all, many frightened. Some heavy furniture moved; a few instances of fallen plaster. Damage slight.
VII. Very Strong	Damage negligible in buildings of good design and construction; slight to moderate in well-built ordinary structures; considerable damage in poorly built or badly designed structures; some chimneys broken.
VIII. Severe	Damage slight in specially designed structures; considerable damage in ordinary substantial buildings with partial collapse. Damage great in poorly built structures. Fall of chimneys, factory stacks, columns, monuments, walls. Heavy furniture overturned.
IX. Violent	Damage considerable in specially designed structures; well-designed frame structures thrown out of plumb. Damage great in substantial buildings, with partial collapse. Buildings shifted off foundations.
X. Extreme	Some well-built wooden structures destroyed; most masonry and frame structures destroyed with foundations. Rails bent.
XI. Extreme	Few, if any, (masonry) structures remain standing. Bridges destroyed. Broad fissures in ground. Underground pipe lines completely out of service. Earth slumps and land slips in soft ground. Rails bent greatly.
XII. Extreme	Damage total. Waves seen on ground surfaces. Lines of sight and level distorted. Objects thrown upward into the air.

(a) MMI scale; adopted from www.tes.com

Perceived Shaking	Not Felt	Weak	Light	Moderate	Strong	Very Strong	Severe	Violent	Extreme
Potential Damage	None	None	None	Very Light	Light	Moderate	Moderate / Heavy	Heavy	Very Heavy
Instrumental Intensity	I	II-III	IV	V	VI	VII	VIII	IX	X+

(b) Instrumental intensity; adopted from www.reddit.com

Fig. 6.9: Shaking intensity definitions

On the other hand, the Richter scale was developed in the 1930s by Charles Francis Richter (seismologist at CalTech). This scale (also called "local" magnitude) assigns a magnitude number to quantify the energy released by an earthquake. It is a base-10 logarithmic scale, which defines magnitude as the logarithm of the ratio of the amplitude, A, of the seismic waves to an arbitrary, minor amplitude, A_0.

$$M_L = \log_{10}\left(\frac{A}{A_0(d)}\right) = \log_{10}A - \log_{10}A_0(d) \tag{6.14}$$

where A is the Wood-Anderson seismograph amplitude of the event in [mm], $A_0(d)$ is the amplitude of a standard event for the same epicentral distance, d, Table 6.1. For d = 100 km, amplitude on the seismograph of the standard event is equal to $A_0(100)$ = 0.001 mm ($-\log_{10}A_0(100)$ = 3).

Table 6.1: Amplitude of standard event as a function of epicenter

d	$-log_{10}A_0$	d	$-log_{10}A_0$	d	$-log_{10}A_0$	d	$-log_{10}A_0$	d	$-log_{10}A_0$
0	1.4	80	2.9	160	3.3	280	3.9	440	4.6
10	1.5	90	3	170	3.4	300	4	460	4.6
20	1.7	100	3	180	3.4	320	4.1	480	4.7
30	2.1	110	3.1	190	3.5	340	4.2	500	4.7
40	2.4	120	3.1	200	3.5	360	4.3	520	4.8
50	2.6	130	3.2	220	3.65	380	4.4	540	4.8
60	2.8	140	3.2	240	3.7	400	4.5	560	4.9
70	2.8	150	3.3	260	3.8	420	4.5	580	4.9

Because the fundamental period of the Wood-Anderson seismograph is about 0.8 s, it amplifies those seismic waves with periods ranging $[0.5, 1.5]$ s. In Richter's logarithmic scale, $M_L = 7$ means that the earthquake produces waves 10 times the amplitude of an earthquake with $M_L = 6$ and 100 times the amplitude of $M_L = 5$. Hutton and Boore [453] analyzed about 10,000 records from 972 earthquakes recorded in Southern California and proposed a new expression for the Richter scale's standard event as:

$$-\log_{10}A_0(d') = 1.110\,\log_{10}\left(\frac{d'}{100}\right) + 0.00189\,(d' - 100) + 3.0 \tag{6.15}$$

where d' is hypocentral distance in [km] and is valid up to $\sim$ 700 km. This equation is pretty close to the Richter model, Figure 6.10.

6.7 Earthquake Magnitude

6.7.1 Classification

There are other definitions (rather than local magnitude, M_L) for the earthquake magnitude.

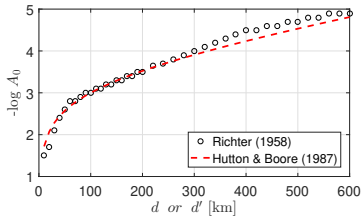

Fig. 6.10: Comparison of epicentral and hypocentral based Richter standard event

Body wave magnitude, m_b, measures the amplitude of P-waves with a period of about 1.0 s. It is suitable for deep earthquakes that have few surface waves. Body wave magnitude can be estimated as:

$$m_b = \log\left(\frac{A}{T}\right) + Q(d,h) \tag{6.16}$$

where $Q(d,h)$ is a correction factor that is a function of epicentral distance, d [degrees], and focal depth, h [km], of the earthquake, Figure 6.11.

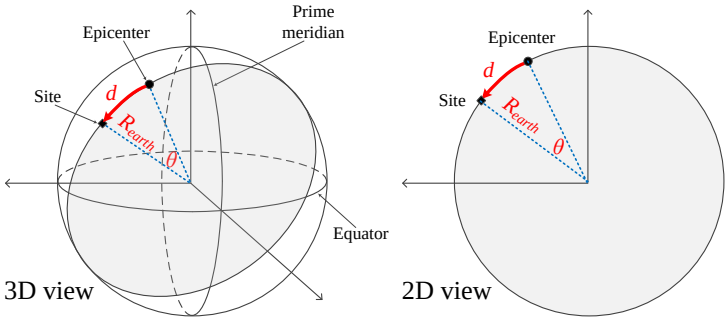

Fig. 6.11: Definition of parameters in body wave correction factor

Surface wave magnitude, M_S, is a measure of the amplitudes of Rayleigh waves with a period of 20 s. It is common for very distant earthquakes (epicentral distance more than 2,000 km). M_S is used for large earthquakes, but it cannot be used for deep ones as well. Surface wave magnitude can be estimated as:

$$M_S = \log\left(\frac{A}{T}\right) + 1.66\,\log(d) + 3.30 \tag{6.17}$$

where A is the maximum amplitude in microns, T is the corresponding period [s], d is the epicentral distance [degrees].

- This equation is applicable for $d > 15^o$.
- Note that the average radius of the earth is 6,370 km and the circumference is about 40,000 km.

Seismic moment, M_0, is related to fundamental parameters of the faulting process and is defined as:

$$M_0 = G\ A\ \Delta u \tag{6.18}$$

where G is the shear modulus of the material surrounding the fault, A is the fault rupture area and Δu is the average slip between opposite sides of the fault.

- M_0 has units of work or energy and is usually reported in [dyn.cm] (10^{-7} [N.m]).
- Note that 1 [dyn] = 1 [g-cm/s^2].
- The modulus G can be assumed to be 32,000 and 75,000 MPa in the crest and mantle, respectively.

Moment magnitude, M_w, accounts for the mechanisms of shear that take place at earthquake sources. It is not related to any specific period. Therefore, M_w can be used to measure the whole spectrum of ground motions. M_w is defined as a function of the seismic moment, M_0:

$$M_w = \frac{2}{3}\ \log M_0 - 10.7 \tag{6.19}$$

where M_0 is in [dyn.cm]. The M_0 of 2.5 $\times 10^{30}$, 7.5 $\times 10^{29}$, 10^{12} and 10^5 has been reported for Chile 1960, Alaska 1964, Micro earthquakes, and Micro fracture (lab), respectively.

6.7.2 Energy Released

The amount of energy radiated by an earthquake is a measure of the potential for damage to structures and infra-structures. Because of instrumental limitations, most estimates of energy have historically relied on the empirical relationship developed by Gutenberg and Richter [355]:

$$\log E = 11.8 + 1.5\ M_S \tag{6.20}$$

where E is in [ergs].

- 1 [erg] = 99.9 $\times\ 10^{-9}$ [N-m] = 73.7 x $^{-9}$ [ft-pound].
- As the magnitude increases by one unit, the energy increases by a factor of ~ 32 and the difference between two units of magnitude is a factor of 1,000 on energy release.

Moreover, there is a relation between body wave magnitude and the seismic energy as:

$$\log E = -1.3 + 2.4\, m_b \tag{6.21}$$

where E is expressed in [joules] (1 [joules] = 10^7 [ergs]).

6.8 Source-to-Site Effects

The characteristics of seismic waves are altered as they travel from the source to the site due to wave dispersion at geological interfaces, damping, and change in the wavefront shape. The latter are referred to as "distance and travel path effects." On the other hand, the site effect refers to the potential changes in the amplitude of earthquake ground motion due to the local site condition. Structural responses are also highly affected by: 1) directional effect, 2) site amplification (site effect), and 3) dispersion and incoherence.

6.8.1 Directional Effects

The assumption of "point source" is only acceptable for for small magnitude earthquakes. For large earthquakes, fault rupture traces may be a few hundred kilometers and thus, affect the wave radiation. Directivity means seismic waves propagate away from the fault rupture with different intensity along different directions.
Based on the rupture mechanism and slip direction relative to the site, ground motions in the near-fault zone can exhibit the dynamic consequences of forward-directivity (FD), neutral-directivity (ND), or backward-directivity (BD), Figure 6.12. The FD motions typically present the most severe loading of structures. The FD motions are usually shorter in duration than BD motions, but are more intense.

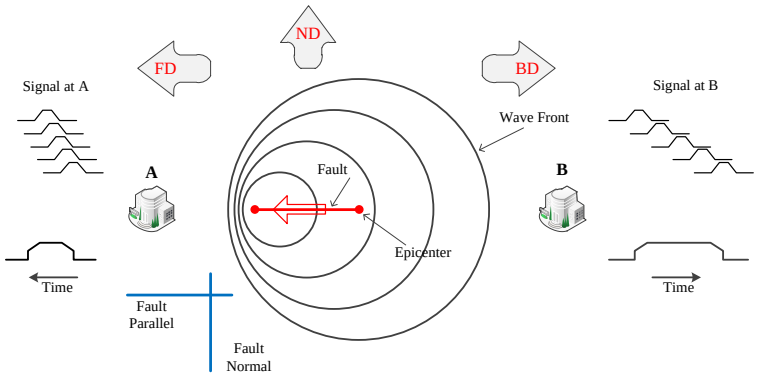

Fig. 6.12: Earthquake directional effects

6.8.2 Site Effects

Site characteristics affect the frequency and duration of earthquake ground motions. The structures founded on rock are, in general, subjected to short-period motion, whereas soft sites result in longer period excitation. The ratio between the period of the site and that of the structure is important in estimating the amplification effects, known as "site resonance effect." The resonance is a frequency-dependent phenomenon. The site period, T_S, for uniform single soil layer on bedrock can be estimated as:

$$T_{S,n} = \frac{1}{2n-1}\frac{4H}{V_S} \tag{6.22}$$

where T is in [sec], H is soil depth in [m], V_S is soil shear wave velocity in [m/s], and n represents the number of vibrational modes.

6.8.3 Dispersion and Incoherence Effects

Dispersion and incoherence may be caused by several factors, among them, Figure 6.13:

- Wave passage effect: represents the time delay in the arrival of seismic waves on the ground surface at different stations. This is due to the finite traveling velocity of seismic waves.
- Extended source effect: number and size of earthquake sources affecting the seismicity at a site may cause delays in the arrival time of waves.
- Ray path effect (scattering effect): caused by reflection and refraction of waves through the soil during their propagation, inhomogeneities of soil layers and other differences in local soil.

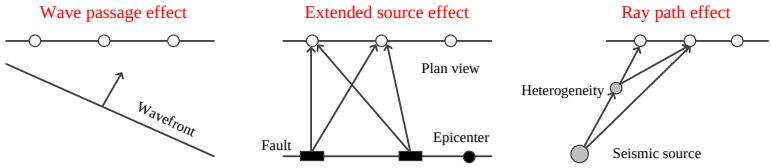

Fig. 6.13: Earthquake dispersion and incoherence effects

Note that this phenomenon does not generally affect short-span structures (buildings), but they may significantly influence the dynamic response of large infra-structures (e.g. bridges, pipelines, dams).

Chapter 7
Transient Dynamic Analysis

Abstract
Dynamics is a sine qua non *for seismic investigation of structures. Rather than reviewing its fundamentals, this chapter will focus on the computational aspects as implemented in finite element analysis codes.*

7.1 Introduction

When the frequency of excitation of a structure is less than about a third of its lowest natural frequency of vibration, we can neglect inertia effects and treat the problem as a quasi-static one.
If the structure is subjected to an impact load, then one must be primarily concerned with (stress) wave propagation. In such a problem, we often have high frequencies, and the duration of the dynamic analysis is about the time it takes for the wave to travel across the structure.
If inertia forces are present, then we are confronted with a dynamic problem and can analyze it through any one of the following solution procedures:

1. Natural frequencies and mode shapes (only linear elastic systems)
2. Time history analysis through modal analysis (again linear elastic) or direct integration.

Methods of structural dynamics are essentially independent of finite element analysis, as these methods presume that we already have the stiffness, mass, and damping matrices. Those matrices may be obtained from a single degree of freedom system, from an idealization/simplification of a frame structure, or from a very complex finite element mesh. The time history analysis procedure remains the same.

7.2 Variational Formulation

In a general three-dimensional continuum, the equation of motion of an elementary volume Ω without damping is

$$\mathbf{L}^T\boldsymbol{\sigma} + \mathbf{b} = \mathbf{m}\ddot{\mathbf{u}} \tag{7.1}$$

where $\mathbf{m}$ is the mass density matrix equal to $\rho\mathbf{I}$, and $\mathbf{b}$ is the vector of body forces. The Differential operator $\mathbf{L}$ is

$$\mathbf{L} = \begin{bmatrix} \frac{\partial}{\partial x} & 0 & 0 \\ 0 & \frac{\partial}{\partial y} & 0 \\ 0 & 0 & \frac{\partial}{\partial z} \\ \frac{\partial}{\partial y} & \frac{\partial}{\partial x} & 0 \\ \frac{\partial}{\partial z} & 0 & \frac{\partial}{\partial x} \\ 0 & \frac{\partial}{\partial z} & \frac{\partial}{\partial y} \end{bmatrix} \tag{7.2}$$

For linear elastic material

$$\boldsymbol{\sigma} = \mathbf{D}_e\boldsymbol{\varepsilon} \tag{7.3}$$

and for non-linear material, the constitutive equations can be written as

$$\dot{\boldsymbol{\sigma}} = \mathbf{D}_i\dot{\boldsymbol{\varepsilon}} \tag{7.4}$$

where $\mathbf{D}_i$ is the tangent stiffness matrix.
Whereas Eq. 7.1 describes the body motion in a strong sense, a weak formulation is obtained by the principle of minimum complementary virtual work (or Weighted Residual/Galerkin)

$$\int_\Omega \delta\mathbf{u}^T[\mathbf{L}^T\boldsymbol{\sigma} + \mathbf{b} - \mathbf{m}\ddot{\mathbf{u}}]\mathrm{d}\Omega = 0 \tag{7.5}$$

Applying Gauss divergence theorem, Eq. 1.59:

$$\int\int_A \phi\,\mathrm{div}\ \mathbf{q}\mathrm{d}A = \oint_s \phi\mathbf{q}^T\mathbf{n}\mathrm{d}s - \int\int_A (\boldsymbol{\nabla}\phi)^T\mathbf{q}\mathrm{d}A \tag{7.6}$$

and recalling that $\mathbf{Lu} = \boldsymbol{\varepsilon}$,

$$\int_\Omega \delta\mathbf{u}^T\mathbf{L}^T\boldsymbol{\sigma}\mathrm{d}\Omega = -\int_\Omega \delta\boldsymbol{\varepsilon}^T\boldsymbol{\sigma}\mathrm{d}\Omega + \int_\Gamma \delta\mathbf{u}^T\boldsymbol{\sigma}\mathbf{n}\mathrm{d}\Gamma \tag{7.7}$$

Thus, Eq. 7.5 transforms into

$$\int_\Omega [\delta\mathbf{u}^T(\mathbf{m}\ddot{\mathbf{u}} - \mathbf{b}) + \delta\boldsymbol{\varepsilon}^T\boldsymbol{\sigma}]\mathrm{d}\Omega - \int_\Gamma \delta\mathbf{u}^T\mathbf{t}\mathrm{d}\Gamma = 0 \tag{7.8}$$

So far no assumption has been made with regard to material behavior.
Next we will seek the spatial discretization of the virtual work equation (Eq. 7.8). From fundamentals of finite elements, we have the following relations:

$$\begin{aligned}
\mathbf{u} &= \mathbf{N}\overline{\mathbf{u}} \\
\delta\mathbf{u}^T &= \delta\overline{\mathbf{u}}^T\mathbf{N}^T \\
\ddot{\mathbf{u}} &= \mathbf{N}\ddot{\overline{\mathbf{u}}} \\
\mathbf{B} &= \mathbf{L}\mathbf{N} \\
\boldsymbol{\varepsilon} &= \mathbf{B}\overline{\mathbf{u}} \\
\delta\boldsymbol{\varepsilon}^T &= \delta\overline{\mathbf{u}}^T\mathbf{B}^T \\
\dot{\boldsymbol{\varepsilon}} &= \mathbf{B}\dot{\overline{\mathbf{u}}}
\end{aligned} \tag{7.9}$$

7.2.1 Explicit Time Integration; Central Difference

For explicit integration, we consider the virtual work (Eq. 7.8) at time t

$$\int_\Omega \delta\mathbf{u}^T\mathbf{m}\mathrm{d}\Omega\ddot{\mathbf{u}}^t = \int_\Omega \delta\mathbf{u}^T\mathbf{b}^t\mathrm{d}\Omega + \int_\Gamma \delta\mathbf{u}^T\mathbf{t}^t\mathrm{d}\Gamma - \int_\Omega \delta\boldsymbol{\varepsilon}^T\boldsymbol{\sigma}^t\mathrm{d}\Omega \tag{7.10}$$

Substituting

$$\delta\overline{\mathbf{u}}^T\left[\underbrace{\int_\Omega \mathbf{N}^T\mathbf{m}\mathbf{N}\mathrm{d}\Omega}_{\mathbf{M}}\ddot{\overline{\mathbf{u}}}^t - \underbrace{\left[\int_\Omega \mathbf{N}^T\mathbf{b}^t\mathrm{d}\Omega + \int_\Gamma \mathbf{N}^T\mathbf{t}^t\mathrm{d}\Gamma\right]}_{\mathbf{f}_e^t} + \underbrace{\int_\Omega \mathbf{B}^T\boldsymbol{\sigma}^t\mathrm{d}\Omega}_{\mathbf{f}_i^t}\right] = 0 \tag{7.11}$$

Since this identity must hold for any admissible $\delta\overline{\mathbf{u}}$, we conclude that

$$\mathbf{M}\ddot{\overline{\mathbf{u}}}^t = \mathbf{f}_e^t - \mathbf{f}_i^t \tag{7.12}$$

which represents the semi-discrete linear equation of motion in the explicit time integration in terms of the mass matrix,

$$\mathbf{M} = \int_\Omega \mathbf{N}^T\mathbf{m}\mathbf{N}\mathrm{d}\Omega \tag{7.13}$$

the vector of external forces,

$$\mathbf{f}_e^t = \int_\Omega \mathbf{N}^T\mathbf{b}^t\mathrm{d}\Omega + \int_\Gamma \mathbf{N}^T\mathbf{t}^t\mathrm{d}\Gamma \tag{7.14}$$

and the vector of internal forces,

$$\mathbf{f}_i^t = \int_\Omega \mathbf{B}^T\boldsymbol{\sigma}^t\mathrm{d}\Omega \tag{7.15}$$

But since $\boldsymbol{\sigma} = \mathbf{D}\boldsymbol{\varepsilon} = \mathbf{D}\mathbf{B}$, then

$$\mathbf{f}_i^t = \int_\Omega \mathbf{B}^T \mathbf{D}\mathbf{B} \mathrm{d}\Omega \mathbf{u} \tag{7.16}$$

It should be noted that Eq. 7.13 defines the consistent mass matrix which is a fully populated matrix. Alternatively, a *lumped mass matrix* can be defined, resulting only in a diagonal matrix. For an axial element, the lumped mass matrix is obtained by placing half of the total element mass as a particle at each node.
For linear elastic systems and if damping was considered,

$$\mathbf{M}\ddot{\overline{\mathbf{u}}}^t + \mathbf{C}\dot{\overline{\mathbf{u}}}^t + \mathbf{K}\overline{\mathbf{u}} = \mathbf{f}_e^t \tag{7.17}$$

The damping matrix is often expressed in terms of the mass and stiffness matrices, called Rayleigh damping, as

$$\mathbf{C} = \alpha\mathbf{M} + \beta\mathbf{K} \tag{7.18}$$

7.2.2 Implicit Time Integration

7.2.2.1 Linear Case

For implicit time integration we consider the virtual work equation at time $t + \Delta t$ (instead of t in the explicit method), thus Eq. 7.8 transforms into

$$\int_\Omega \delta\mathbf{u}^T \mathbf{m} \mathrm{d}\Omega \ddot{\mathbf{u}}^{t+\Delta t} + \int_\Omega \delta\boldsymbol{\varepsilon}^T \boldsymbol{\sigma}^{t+\Delta t} \mathrm{d}\Omega = \int_\Gamma \delta\mathbf{u}^T \mathbf{t}^{t+\Delta t} \mathrm{d}\Gamma + \int_\Omega \delta\mathbf{u}^T \mathbf{b}^{t+\Delta t} \mathrm{d}\Omega \tag{7.19}$$

For linear problems

$$\boldsymbol{\sigma}^{t+\Delta t} = \mathbf{D}_e \mathbf{B} \overline{\mathbf{u}}^{t+\Delta t} \tag{7.20}$$

Again, upon proper substitution, this would yield

$$\delta\overline{\mathbf{u}}^T \left[\underbrace{\int_\Omega \mathbf{N}^T \mathbf{m} \mathbf{N} \mathrm{d}\Omega}_{\mathbf{M}} \ddot{\overline{\mathbf{u}}}^{t+\Delta t} + \underbrace{\int_\Omega \mathbf{B}^T \mathbf{D}_e \mathbf{B} \mathrm{d}\Omega}_{\mathbf{K}} \overline{\mathbf{u}}^{t+\Delta t} - \underbrace{\left(\int_\Omega \mathbf{N}^T \mathbf{b}^{t+\Delta t} \mathrm{d}\Omega + \int_\Gamma \mathbf{N}^T \mathbf{t}^{t+\Delta t} \mathrm{d}\Gamma \right)}_{\mathbf{f}_e^{t+\Delta t}} \right] = 0 \tag{7.21}$$

or

$$\mathbf{M}\ddot{\overline{\mathbf{u}}}^{t+\Delta t} + \mathbf{K}\overline{\mathbf{u}}^{t+\Delta t} = \mathbf{f}_e^{t+\Delta t} \tag{7.22}$$

Which represents the semi-discrete linear equation of motion in the implicit time integration.

7.2.2.2 Nonlinear Case

In non-linear problems, the constitutive matrix $\mathbf{D}$ is no longer constant, and we must use the tangential relation which is linearized as

$$\boldsymbol{\Delta\sigma} = \mathbf{D}_i \boldsymbol{\Delta\varepsilon} \tag{7.23}$$

with the stress at time $t + \Delta t$:

$$\boldsymbol{\sigma}^{t+\Delta t} = \boldsymbol{\sigma}^t + \boldsymbol{\Delta\sigma} \tag{7.24}$$

Substituting into the virtual work equation (Eq. 7.19)

$$\begin{aligned} &\int_\Omega \delta\mathbf{u}^T \mathbf{m} \mathrm{d}\Omega \ddot{\mathbf{u}}^{t+\Delta t} + \int_\Omega \delta\boldsymbol{\varepsilon}^T \Delta\boldsymbol{\sigma} \mathrm{d}\Omega \\ &= \int_\Gamma \delta\mathbf{u}^T \mathbf{t}^{t+\Delta t} \mathrm{d}\Gamma + \int_\Omega \delta\mathbf{u}^T \mathbf{b}^{t+\Delta t} \mathrm{d}\Omega - \underbrace{\int_\Omega \delta\boldsymbol{\varepsilon}^T \boldsymbol{\sigma}^t \mathrm{d}\Omega}_{\text{new term}} \end{aligned} \tag{7.25}$$

Again, combining with

$$\boldsymbol{\Delta\sigma} = \mathbf{D}_i \mathbf{B} \boldsymbol{\Delta}\overline{\mathbf{u}} \tag{7.26}$$

and substituting:

$$\begin{aligned} \delta\overline{\mathbf{u}}^T [&\underbrace{\int_\Omega \mathbf{N}^T \mathbf{m} \mathbf{N} \mathrm{d}\Omega}_{\mathbf{M}} \ddot{\overline{\mathbf{u}}}^{t+\Delta t} + \underbrace{\int_\Omega \mathbf{B}^T \mathbf{D}_i \mathbf{B} \mathrm{d}\Omega}_{\mathbf{K}^t} \boldsymbol{\Delta}\overline{\mathbf{u}} \\ &- \underbrace{(\int_\Omega \mathbf{N}^T \mathbf{b}^{t+\Delta t} \mathrm{d}\Omega + \int_\Gamma \mathbf{N}^T \mathbf{t}^{t+\Delta t} \mathrm{d}\Gamma)}_{\mathbf{f}_e^{t+\Delta t}} - \underbrace{\int_\Omega \mathbf{B}^T \boldsymbol{\sigma}^t \mathrm{d}\Omega}_{\mathbf{f}_i^t}] = 0 \end{aligned} \tag{7.27}$$

or

$$\mathbf{M} \ddot{\overline{\mathbf{u}}}^{t+\Delta t} + \mathbf{K}^t \boldsymbol{\Delta}\overline{\mathbf{u}} = \mathbf{f}_e^{t+\Delta t} - \mathbf{f}_i^t \tag{7.28}$$

Which represents the semi-discrete non-linear equation of motion in the implicit time integration.

7.3 Time Discretization

Mathematically, Equation 7.28 represents a system of linear differential equations of second order, and in principle, the solution of the equations can be obtained by standard procedures for the solution of differential equations with constant coefficients. However, the procedures proposed for the solution of general systems of differential equations can become very expensive if the order of the matrices is large - unless specific advantage is taken of the special characteristics of the coefficient matrices $\mathbf{M}$, $\mathbf{C}$, and $\mathbf{K}$.

In practical finite element analysis, we are therefore mainly interested in a few effective methods, namely direct integration and mode superposition. These two techniques are closely related, and the choice for one method or the other is determined only by their numerical effectiveness. In the present implementation, the direct integration method is employed.
In the direct integration method, Eq. 7.28 is integrated using a numerical step by step procedure; the term "direct" meaning that prior to the numerical integration, no transformation of the equations into a different form is carried out.

7.3.1 Explicit Time Integration

For the explicit time integration, we adopt at starting point a slight variation of the differential equation previously derived, one which includes the effects of damping.

$$\underbrace{\mathbf{M}\ddot{\overline{\mathbf{u}}}}_{\mathbf{F}_I(t)} + \underbrace{\mathbf{C}\dot{\overline{\mathbf{u}}}}_{\mathbf{F}_D(t)} + \underbrace{\mathbf{K}\overline{\mathbf{u}}}_{\mathbf{F}_i(t)} = \underbrace{\mathbf{f}_e}_{\mathbf{f}_e(t)} \tag{7.29}$$

where $\mathbf{M}$, $\mathbf{C}$, and $\mathbf{K}$ are the mass, damping, and stiffness matrices; $\mathbf{f}_e$ is the external load vector; and $\ddot{\mathbf{u}}$, $\dot{\mathbf{u}}$, and $\mathbf{u}$ are the acceleration, velocity, and displacement vectors of the finite element assemblage.
An alternative way to consider this equation is to examine the equation of statics at time t, where $\mathbf{F}_I(t), \mathbf{F}_D(t), \mathbf{F}_i(t), \mathbf{F}_e(t)$ are the inertia, damping, internal and external elastic forces, respectively.

7.3.1.1 Linear Systems

For the semi-discretized equation of motion, we adopt the *central difference method*. This method is based on a finite difference approximation of the time derivatives of displacement (velocity and acceleration). Assuming a linear change in displacement over each time step, the velocity and the acceleration at time t are:

$$\dot{\overline{\mathbf{u}}}^t = \frac{\overline{\mathbf{u}}^{t+\Delta t} - \overline{\mathbf{u}}^{t-\Delta t}}{2\Delta t} \tag{7.30}$$

$$\ddot{\overline{\mathbf{u}}}^t = \frac{\overline{\mathbf{u}}^{t-\Delta t} - 2\overline{\mathbf{u}}^t + \overline{\mathbf{u}}^{t+\Delta t}}{\Delta t^2} \tag{7.31}$$

where Δt is the time step.

Substituting into Eq. 7.17 ($\mathbf{M}\ddot{\overline{\mathbf{u}}}^t + \mathbf{C}\dot{\overline{\mathbf{u}}}^t + \mathbf{K}_e\overline{\mathbf{u}} = \mathbf{f}_e^t$), we obtain

$$\underbrace{\left(\underbrace{\frac{1}{\Delta t^2}}_{a_0}\mathbf{M} + \underbrace{\frac{1}{2\Delta t}}_{a_1}\mathbf{C}\right)}_{\mathbf{M}\widehat{\mathbf{M}}}\overline{\mathbf{u}}^{t+\Delta t} = \underbrace{\mathbf{f}_e^t - \left(\mathbf{K} - \underbrace{\frac{2}{\Delta t^2}}_{a_2}\mathbf{M}\right)\overline{\mathbf{u}}^t - \left(\underbrace{\frac{1}{\Delta t^2}}_{a_0}\mathbf{M} - \underbrace{\frac{1}{2\Delta t}}_{a_1}\mathbf{C}\right)\overline{\mathbf{u}}^{t-\Delta t}}_{\mathbf{f}\hat{\mathbf{f}}_e^t} \tag{7.32}$$

from which we can solve for $\overline{\mathbf{u}}^{t+\Delta t}$.
It should be noted that:

- The solution is based on the equilibrium condition at time, t.
- No factorization of the stiffness matrix, $\mathbf{K}$, is necessary (i.e. no $\mathbf{K}^{-1}$ term appears in the equation).
- To initiate the method, we should determine the displacement, velocity, and acceleration at time $-\Delta t$.

Algorithm:

1. Form the stiffness matrix $\mathbf{K}$, mass matrix $\mathbf{M}$, and damping matrix $\mathbf{C}$.
2. Initialize $\overline{\mathbf{u}}^0, \dot{\overline{\mathbf{u}}}^0, \ddot{\overline{\mathbf{u}}}^0$ at time $t = 0$.
3. Select the time step $\Delta t \leq \Delta t_{cr}$.
4. Determine the constants $a_0 = \frac{1}{\Delta t^2}$, $a_1 = \frac{1}{2\Delta t}$, $a_2 = 2a_0$, $a_3 = \frac{1}{a_2}$.
5. Compute
$$\overline{\mathbf{u}}^{-\Delta t} = \overline{\mathbf{u}}^0 - \Delta t\dot{\overline{\mathbf{u}}}^0 + a_3\ddot{\overline{\mathbf{u}}}^0 \tag{7.33}$$
6. Compute the effective mass matrix, $\hat{\mathbf{M}} = a_0\mathbf{M} + a_1\mathbf{C}$.
7. Triangularize $\hat{\mathbf{M}}$ (not necessary if lumped mass matrix is used):
$$\hat{\mathbf{M}} = \mathbf{L}\mathbf{D}\mathbf{L}^T \tag{7.34}$$
8. For each time step:
   a. Determine the effective loads at time t:
   $$\hat{\mathbf{f}}_e^t = \mathbf{f}_e^t - (\mathbf{K} - a_2\mathbf{M})\overline{\mathbf{u}}^t - (a_0\mathbf{M} - a_1\mathbf{C})\overline{\mathbf{u}}^{t-\Delta t} \tag{7.35}$$
   b. Solve for the displacements at time $t + \Delta t$
   $$\mathbf{L}\mathbf{D}\mathbf{L}^T\overline{\mathbf{u}}^{t+\Delta t} = \hat{\mathbf{f}}_e^t \tag{7.36}$$
   c. If required, solve for velocities and accelerations, strains and stresses at time t

$$\ddot{\overline{\mathbf{u}}}^t = a_0(\overline{\mathbf{u}}^{t-\Delta t} - 2\overline{\mathbf{u}}^t + \overline{\mathbf{u}}^{t+\Delta t}) \tag{7.37}$$

$$\dot{\overline{\mathbf{u}}}^t = a_1(-\overline{\mathbf{u}}^{t-\Delta t} + \overline{\mathbf{u}}^{t+\Delta t}) \tag{7.38}$$

$$\boldsymbol{\varepsilon}^{t+\Delta t} = \mathbf{B}\overline{\mathbf{u}}^{t+\Delta t} \tag{7.39}$$

$$\boldsymbol{\sigma}^{t+\Delta t} = \mathbf{D}_e\boldsymbol{\varepsilon}^{t+\Delta t} \tag{7.40}$$

d. Update next time $t = t + \Delta t$ and go back to (a).

An explicit time integration has many advantages; the major one is that it does not require factorization of the stiffness matrix.
If we adopt a lumped (instead of consistent) mass matrix, and there is no damping, then no factorization is necessary, and Eq. 7.32 reduces to:

$$\left(\frac{1}{\Delta t^2}\mathbf{M}\right)\overline{\mathbf{u}}^{t+\Delta t} = \hat{\mathbf{f}}_e^t \tag{7.41}$$

where

$$\hat{\mathbf{f}}_e^t = \mathbf{f}_e^t - \left(\mathbf{K} - \frac{2}{\Delta t^2}\mathbf{M}\right)\overline{\mathbf{u}}^t - \left(\frac{1}{\Delta t^2}\mathbf{M}\right)\overline{\mathbf{u}}^{t-\Delta t} \tag{7.42}$$

Hence if the mass is diagonal, there is no need to factorize. Furthermore, if the structure stiffness matrix need not be triangularized, then it is not necessary to assemble the global stiffness matrix. It can be shown that

$$\mathbf{K}\overline{\mathbf{u}}^t = \sum_i^n \mathbf{K}_{(e)}\overline{\mathbf{u}}^t = \sum \mathbf{F}_{(e)}^t \tag{7.43}$$

which means that $\mathbf{K}_{(i)}\overline{\mathbf{u}}^t$ needed in Eq. 7.42 can be evaluated on the element level by summing the contributions from each element to the effective load vector. Thus

$$\hat{\mathbf{f}}_e^t = \mathbf{f}_e^t - \sum_i \mathbf{F}_{(i)}^t - \frac{1}{\Delta t^2}\mathbf{M}(\overline{\mathbf{u}}^{t-\Delta t} - 2\overline{\mathbf{u}}^t) \tag{7.44}$$

Since no structural stiffness matrix needs to be assembled, very large problems can be effectively solved. This includes quasi-static problems (linear and non-linear) where the load is applied incrementally in time.
A major disadvantage of the explicit method is that it converges only if

$$\Delta t < \Delta t_{cr} = \frac{2}{\omega_{max}} \tag{7.45}$$

where ω_{max} is the highest natural frequency (or smallest wave length) of the structure [222]. Recall that $\omega = \frac{2\pi}{T}$. If this condition is violated, numerical instability occurs. Hence, an eigenvalue analysis of the complete system must first be undertaken. But since the global structural stiffness matrix is not necessarily assembled, an upper bound estimate of ω_{max} is obtained from

$$\omega_{max} < \omega_{max}^{(e)} \tag{7.46}$$

where $\omega_{max}^{(e)}$ is the maximum frequency of a single finite element (usually the smallest one). It can in turn be determined from

$$\det(\mathbf{K}^{(e)} - (\omega_{max}^{e})^2\mathbf{M}^{e}) = 0 \tag{7.47}$$

In non-linear problems, $\mathbf{K}$ is the tangent stiffness. Note that the determination of the eigenvalues (which correspond to ω^2) of the simple problem without damping $(\mathbf{K} - \omega^2\mathbf{M})$ can be solved by either expanding the determinant of the resulting matrix, or simply determining the eigenvalues of $\mathbf{M}^{-1}\mathbf{K}$.
Alternatively,

$$\omega_{max}^{e} = \frac{2c}{L} \tag{7.48}$$

where c is the acoustic wave speed, $c = \sqrt{E/\rho}$, and L is a representative length of element (e).
Essentially, this means that Δt must be small enough so that information does not propagate across more than one element per time step.

```
%================================================================
%I N I T I A L I Z A T I O N
%================================================================
% Initialize the matrices
M=[2 0;0 1]; K=[6 2; 2 4];C=[0 0;0 0];P=[0 ; 10];
% determine the eigenvalues, minimum frequency, and delta t critical
omega2=eig(inv(M)*K);
Tcrit=min(2*pi./sqrt(omega2));
Delta_t=Tcrit/10;
% Initialize the displacement and velocity vectors at time = 0;
u_t(1:2,:)=0;
du_t(1:2,:)=0;
Phat_t(1:2,:)=0;
% solve for the initial acceleration at time 0
ddu_t(1:2,:)=inv(M)*(P K*u_t);
% Initialize the constants
a_0=1/(Delta_t^2);a_1=1/(2*Delta_t);a_2=2*a_0;a_3=1/a_2;
% Determine displacement at t Delta_t;
u_tmdt=u_t Delta_t*du_t+a_3*ddu_t;
% Determine the effective mass matrix
Mhat=a_0*M+a_1*C;
MhatInv=inv(Mhat);
u(1:2,1:13)=0;
d(1:2,1)=u_t;
%================================================================
% I T E R A T I O N S
%================================================================
for i=2:13
% Effective Load
Phat=P (K a_2*M)*u_t (a_0*M a_1*C)*u_tmdt;
% Solve for the displacement
u_tpdt=MhatInv*Phat;
u_tmdt=u_t;
u_t=u_tpdt;
d(1:2,i)=u_tpdt;
end
```

7.3.1.2 Nonlinear Systems

In the non-linear systems the incremental displacements $\Delta\overline{\mathbf{u}}$, the incremental strains and stresses, and the stiffness matrix are updated according to

$$\Delta\overline{\mathbf{u}} = \overline{\mathbf{u}}^{t+\Delta t} - \overline{\mathbf{u}}^{t} \tag{7.49}$$

$$\Delta\boldsymbol{\varepsilon} = \mathbf{B}\Delta\overline{\mathbf{u}} \tag{7.50}$$

$$\Delta\boldsymbol{\sigma} = \mathbf{D}_i^{t+\Delta t}\Delta\boldsymbol{\varepsilon} \tag{7.51}$$

$$\boldsymbol{\sigma}^{t+\Delta t} = \boldsymbol{\sigma}^{t} + \Delta\boldsymbol{\sigma} \tag{7.52}$$

$$\mathbf{K}_i^{t+\Delta t} = \int_{\Omega} \mathbf{B}^T D_i^{t+\Delta t}\mathbf{B}\mathrm{d}\Omega \tag{7.53}$$

In the algorithm shown above, we must evaluate $\mathbf{K}_i$ at each time step.

7.3.2 Implicit Case

7.3.2.1 Newmark Method; Forward Difference

Consider the Taylor series expansions of the displacement and velocity terms about the values at t

$$\overline{\mathbf{u}}^{t+\Delta t} = \overline{\mathbf{u}}^{t} + \frac{\partial\overline{\mathbf{u}}^{t}}{\partial t}\Delta t + \frac{\partial^2\overline{\mathbf{u}}^{t}}{\partial t^2}\frac{\Delta t^2}{2!} + \frac{\partial^3\overline{\mathbf{u}}^{t+\Delta t}}{\partial t^3}\frac{\Delta t^3}{3!} \tag{7.54}$$

$$\dot{\overline{\mathbf{u}}}^{t+\Delta t} = \dot{\overline{\mathbf{u}}}^{t} + \frac{\partial^2\overline{\mathbf{u}}^{t}}{\partial t^2}\Delta t + \frac{\partial^3\overline{\mathbf{u}}^{t+\Delta t}}{\partial t^3}\frac{\Delta t^2}{2!} \tag{7.55}$$

The above two equations represent the approximate displacement and velocity ($\overline{\mathbf{u}}^{t+\Delta t}$ and $\dot{\overline{\mathbf{u}}}^{t+\Delta t}$) by a truncated Taylor series. Looking at the remainder term (last term above),

$$\begin{aligned}\mathbf{R}_1 = \frac{\partial^3\overline{\mathbf{u}}^{t+\Delta t}}{\partial t^3}\frac{\Delta t^3}{3!} &\simeq \frac{\frac{\partial^2\overline{\mathbf{u}}^{t+\Delta t}}{\partial t^2} - \frac{\partial^2\overline{\mathbf{u}}^{t}}{\partial t^2}}{\Delta t}\frac{\Delta t^3}{3!} \\ &\simeq (\ddot{\overline{\mathbf{u}}}^{t+\Delta t} - \ddot{\overline{\mathbf{u}}}^{t})\frac{\Delta t^2}{3!} \\ &\simeq \beta(\ddot{\overline{\mathbf{u}}}^{t+\Delta t} - \ddot{\overline{\mathbf{u}}}^{t})\Delta t^2\end{aligned} \tag{7.56}$$

Note the presence of $t+\Delta t$ because of the forward difference nature of the algorithm. Similarly,

$$\begin{aligned}\mathbf{R}_2 = \frac{\partial^3\overline{\mathbf{u}}^{t+\Delta t}}{\partial t^3}\frac{\Delta t^2}{2!} &\simeq \frac{\frac{\partial^2\overline{\mathbf{u}}^{t+\Delta t}}{\partial t^2} - \frac{\partial^2\overline{\mathbf{u}}^{t}}{\partial t^2}}{\Delta t}\frac{\Delta t^2}{2!} \\ &\simeq \gamma(\ddot{\overline{\mathbf{u}}}^{t+\Delta t} - \ddot{\overline{\mathbf{u}}}^{t})\Delta t\end{aligned} \tag{7.57}$$

β and γ are parameters representing numerical approximations.

Those parameters will account for $\mathbf{R}_1$ and $\mathbf{R}_2$ plus additional terms which were dropped from our Taylor series approximation. Substituting Equations 7.56 and 7.57 into Equations 7.54 and 7.55 respectively, we obtain:

$$\overline{\mathbf{u}}^{t+\Delta t} = \overline{\mathbf{u}}^{t} + \dot{\overline{\mathbf{u}}}^{t}\Delta t + \ddot{\overline{\mathbf{u}}}^{t}\frac{\Delta t^2}{2} + \beta(\ddot{\overline{\mathbf{u}}}^{t+\Delta t} - \ddot{\overline{\mathbf{u}}}^{t})\Delta t^2 \tag{7.58}$$

$$\dot{\overline{\mathbf{u}}}^{t+\Delta t} = \dot{\overline{\mathbf{u}}}^{t} + \ddot{\overline{\mathbf{u}}}^{t}\Delta t + \gamma(\ddot{\overline{\mathbf{u}}}^{t+\Delta t} - \ddot{\overline{\mathbf{u}}}^{t})\Delta t \tag{7.59}$$

By rearrangement, we obtain:

$$\dot{\overline{\mathbf{u}}}^{t+\Delta t} = \dot{\overline{\mathbf{u}}}^{t} + [(1-\gamma)\ddot{\overline{\mathbf{u}}}^{t} + \gamma\ddot{\overline{\mathbf{u}}}^{t+\Delta t}]\Delta t \tag{7.60}$$

$$\overline{\mathbf{u}}^{t+\Delta t} = \overline{\mathbf{u}}^{t} + \dot{\overline{\mathbf{u}}}^{t}\Delta t + [(1/2-\beta)\ddot{\overline{\mathbf{u}}}^{t} + \beta\ddot{\overline{\mathbf{u}}}^{t+\Delta t}]\Delta t^2 \tag{7.61}$$

$$\mathbf{f}_e^{t+\Delta t} = \mathbf{M}\ddot{\overline{\mathbf{u}}}^{t+\Delta t} + \mathbf{C}\dot{\overline{\mathbf{u}}}^{t+\Delta t} + \mathbf{K}\overline{\mathbf{u}}^{t+\Delta t} \tag{7.62}$$

where the last equation is the equation of equilibrium, Eq. 7.22, expressed at time $t + \Delta t$.

It can be shown that Newmark's forward difference assumes constant average acceleration over the time step.

Both β and γ are parameters that can be determined to obtain integration accuracy and stability. If $\gamma = 1/2$ and $\beta = 1/6$, then we recover the linear acceleration method. The scheme is explicit when β is 0. When γ is 1/2, this explicit form has the same numerical properties as the central difference method.

It can be shown that the Newmark method is

1. Unconditionally stable if

$$\gamma \geq \frac{1}{2} \tag{7.63}$$

$$\beta \geq \frac{\gamma}{2} \tag{7.64}$$

2. Conditionally stable if

$$\gamma \geq \frac{1}{2} \tag{7.65}$$

$$\beta < \frac{\gamma}{2} \tag{7.66}$$

with the following stability limit:

$$\omega\Delta t_{crit} = \frac{\xi(\gamma - 1/2) + [\gamma/2 - \beta + \xi^2(\gamma - 1/2)^2]^{1/2}}{(\gamma/2 - \beta)} \tag{7.67}$$

where ξ is the damping parameter.

7.3.2.2 Hughes α Method

A major drawback of the Newmark β method is the tendency for high frequency noise to persist in the solution. On the other hand, when linear damping or artificial viscosity is added via the parameter γ, the accuracy is markedly degraded. The α method [416] improves numerical dissipation for high frequency without degrading the accuracy as much [114].
Hughes α method [416] is an implicit method in which the equation of motion (ignoring damping for now) is written at time $t + \Delta t$ (forward difference):

$$\mathbf{M}\ddot{\mathbf{u}}^{t+\Delta t} + \mathbf{K}\mathbf{u}^{t+\Delta t} = \mathbf{f}_e^{t+\Delta t} \tag{7.68}$$

Seeking an approximate solution of this equation by one-step difference, we write

$$\mathbf{M}\ddot{\mathbf{u}}^{t+\Delta t} + (1+\alpha)\mathbf{K}\mathbf{u}^{t+\Delta t} - \alpha\mathbf{K}\mathbf{u}^{t} = \mathbf{f}_e^{t+\Delta t} \tag{7.69}$$

with

$$\mathbf{u}^{t+\Delta t} = \mathbf{u}^t + \Delta t\dot{\mathbf{u}}^t + \Delta t^2\left[\left(\frac{1}{2}-\beta\right)\ddot{\mathbf{u}}^t + \beta\ddot{\mathbf{u}}^{t+\Delta t}\right] \tag{7.70}$$

$$\dot{\mathbf{u}}^{t+\Delta t} = \dot{\mathbf{u}}^t + \Delta t\left[(1-\gamma)\ddot{\mathbf{u}}^t + \gamma\ddot{\mathbf{u}}^{t+\Delta t}\right] \tag{7.71}$$

We note that the α method introduces $\alpha\mathbf{K}(\mathbf{u}^{t+\Delta t} - \mathbf{u}^t)$ which is akin to stiffness proportional damping.
If the above equation is expanded [450], the effect of damping introduced, and possible material non-linearity introduced, we obtain:

$$\mathbf{M}\ddot{\mathbf{u}}^{t+\Delta t} + (1+\alpha)\mathbf{C}\dot{\mathbf{u}}^{t+\Delta t} - \alpha\mathbf{C}\dot{\mathbf{u}}^{t} + (1+\alpha)\mathbf{f}_i^{t+\Delta t} - \alpha\mathbf{f}_i^t = (1+\alpha)\mathbf{f}_e^{t+\Delta t} - \alpha\mathbf{f}_e^t \tag{7.72}$$

$$\mathbf{u}^{t+\Delta t} = \tilde{\mathbf{u}}^{t+\Delta t} + \beta\Delta t^2\ddot{\mathbf{u}}^{t+\Delta t} \tag{7.73}$$

$$\dot{\mathbf{u}}^{t+\Delta t} = \tilde{\dot{\mathbf{u}}}^{t+\Delta t} + \gamma\Delta t\ddot{\mathbf{u}}^{t+\Delta t} \tag{7.74}$$

where

$$\tilde{\mathbf{u}}^{t+\Delta t} = \mathbf{u}^t + \Delta t\dot{\mathbf{u}}^t + \Delta t^2\left(\frac{1}{2}-\beta\right)\ddot{\mathbf{u}}^t \tag{7.75}$$

$$\tilde{\dot{\mathbf{u}}}^{t+\Delta t} = \dot{\mathbf{u}}^t + \Delta t(1-\gamma)\ddot{\mathbf{u}}^t \tag{7.76}$$

and $\mathbf{f}_i$ is the internal restoring force and $\mathbf{f}_e$ the external driving force.
Hence, the 3 equations and the (possibly non-linear) constitutive equation must all be simultaneously satisfied through an iterative method.
Assuming that we have obtained the response at time t (i.e. $\mathbf{u}^t$, $\dot{\mathbf{u}}^t$, and $\ddot{\mathbf{u}}^t$) which satisfy the equation of motion, we now seek to determine the solution at time $t+\Delta t$ by iteration (since $\mathbf{f}_i^{t+\Delta t} = \mathbf{K}(\mathbf{u}^{t+\Delta t})\mathbf{u}^{t+\Delta t}$). Given iteration step k, the trial solution is $\mathbf{u}_k^{t+\Delta t}$, $\dot{\mathbf{u}}_k^{t+\Delta t}$, and $\ddot{\mathbf{u}}_k^{t+\Delta t}$; it does not yet satisfy the equation of motion, Eq. 7.72. Hence, for this particular step we can write:

$$\mathbf{M}\ddot{\mathbf{u}}_k^{t+\Delta t} + (1+\alpha)\mathbf{C}\dot{\mathbf{u}}_k^{t+\Delta t} - \alpha\mathbf{C}\dot{\mathbf{u}}^{t} + (1+\alpha)\mathbf{f}_{i,k}^{t+\Delta t} - \alpha\mathbf{f}_i^t = (1+\alpha)\mathbf{f}_e^{t+\Delta t} - \alpha\mathbf{f}_e^t - \mathbf{R}_k^{t+\Delta t} \tag{7.77}$$

where $\mathbf{f}_{i,k}^{t+\Delta t}$ is evaluated from the trial displacement, $\mathbf{u}_k^{t+\Delta t}$, and $\mathbf{R}_k^{t+\Delta t}$ is the residual force error. If we subtract this equation from the exact equilibrium equation (Eq. 7.72), we have:

$$\mathbf{R}_k^{t+\Delta t} = \mathbf{M}\Delta\ddot{\mathbf{u}}_k^{t+\Delta t} + (1+\alpha)\mathbf{C}\Delta\dot{\mathbf{u}}^{t+\Delta t} + (1+\alpha)\Delta\mathbf{f}_{i,k}^{t+\Delta t} \tag{7.78}$$

where

$$\Delta\ddot{\mathbf{u}}_k^{t+\Delta t} = \ddot{\mathbf{u}}^{t+\Delta t} - \ddot{\mathbf{u}}_k^{t+\Delta t} \tag{7.79}$$
$$\Delta\dot{\mathbf{u}}_k^{t+\Delta t} = \dot{\mathbf{u}}^{t+\Delta t} - \dot{\mathbf{u}}_k^{t+\Delta t} \tag{7.80}$$
$$\Delta\mathbf{u}_k^{t+\Delta t} = \mathbf{u}^{t+\Delta t} - \mathbf{u}_k^{t+\Delta t} \tag{7.81}$$
$$\Delta\mathbf{f}_{i,k}^{t+\Delta t} = \mathbf{f}_i^{t+\Delta t} - \mathbf{f}_{i,k}^{t+\Delta t} \tag{7.82}$$

Hence if we know the exact secant stiffness $\mathbf{K}_{k,sec}^{t+\Delta t}$, we can solve for $\mathbf{u}^{t+\Delta t}$, $\dot{\mathbf{u}}^{t+\Delta t}$, and $\ddot{\mathbf{u}}^{t+\Delta t}$ directly. However in the context of a nonlinear model, the secant stiffness will have to be determined at each time step, Figure 7.1.

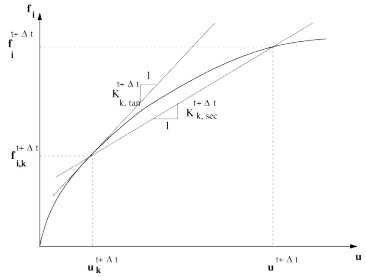

Fig. 7.1: Secant and Tangent Stiffnesses for α Method

The solution process can now proceed as follows: from Figure 7.1 we have

$$\Delta\mathbf{f}_{i,k}^{t+\Delta t} = \mathbf{K}_{k,sec}^{t+\Delta t}\Delta\mathbf{u}_k^{t+\Delta t} \tag{7.83}$$

However from Eq. 7.73 and 7.74

$$\mathbf{u}_k^{t+\Delta t} = \tilde{\mathbf{u}}^{t+\Delta t} + \beta\Delta t^2\ddot{\mathbf{u}}_k^{t+\Delta t} \tag{7.84}$$
$$\dot{\mathbf{u}}_k^{t+\Delta t} = \tilde{\dot{\mathbf{u}}}^{t+\Delta t} + \gamma\Delta t\ddot{\mathbf{u}}_k^{t+\Delta t} \tag{7.85}$$

Subtracting the above equations from the corresponding exact ones

$$\Delta\ddot{\mathbf{u}}_k^{t+\Delta t} = \frac{\Delta\mathbf{u}_k^{t+\Delta t}}{\beta\Delta t^2} \tag{7.86}$$
$$\Delta\dot{\mathbf{u}}_k^{t+\Delta t} = \gamma\Delta t\Delta\ddot{\mathbf{u}}_k^{t+\Delta t} = \frac{\gamma}{\beta\Delta t}\Delta\mathbf{u}_k^{t+\Delta t} \tag{7.87}$$

Substituting the above equation into the residual equation (Eq. 7.78), we obtain

$$\mathbf{R}_k^{t+\Delta t} = \frac{\Delta \mathbf{u}_k^{t+\Delta t}}{\beta \Delta t^2}\mathbf{M} + (1+\alpha)\frac{\gamma}{\beta \Delta t}\Delta \mathbf{u}_k^{t+\Delta t}\mathbf{C} + (1+\alpha)\mathbf{K}_{k,sec}^{t+\Delta t}\Delta \mathbf{u}_k^{t+\Delta t} \quad (7.88)$$

which can be rearranged as

$$\tilde{\mathbf{K}}_k^{t+\Delta t}\Delta \mathbf{u}_k^{t+\Delta t} = \mathbf{R}_k^{t+\Delta t} \quad (7.89)$$

where the effective stiffness matrix is given by

$$\tilde{\mathbf{K}}_k^{t+\Delta t} = \frac{1}{\beta \Delta t^2}\mathbf{M} + \frac{\gamma(1+\alpha)}{\beta \Delta t}\mathbf{C} + (1+\alpha)\mathbf{K}_{k,sec}^{t+\Delta t} \quad (7.90)$$

It should be noted that Eq. 7.89 is analogous to the simple static equilibrium equation, and we can directly evaluate $\Delta \mathbf{u}_k^{t+\Delta t}$ and obtain the exact solution. However, since we do not know $\mathbf{u}^{t+\Delta t}$ *a priori*, we can not evaluate the secant stiffness matrix $\mathbf{K}_{k,sec}^{t+\Delta t}$. This can be numerically estimated from Figure 7.1 by the tangent stiffness matrix if need be. In this later case, we will need to iterate to converge to the exact solution.
Finally, we note that:

1. Alpha introduces a damping that grows with the ratio of time increment to the period of vibration of a node.
2. Negative values of α provide damping.
3. If $\alpha = 0$, we have no artificial damping (energy preserving) and is exactly the trapezoidal rule (Newmark's method if $\beta = 1/4$ and $\gamma = 1/2$).
4. Maximum value is $\alpha = -1/3$ which provides the maximum artificial damping. This results in a damping ratio of about 6% when the time increment is 40% of the period of oscillation of the mode being studied and smaller if the oscillation period increases.
5. This artificial damping is not very substantial for realistic time increments and low frequencies but is non-negligible for high frequencies.
6. A default value of -0.05 is recommended.

7.4 Free Vibration

The governing equation for the free (undamped) vibration of a structure is

$$\mathbf{M}\ddot{\mathbf{u}} + \mathbf{K}\mathbf{u} = 0 \quad (7.91)$$

where the motion is referred to being free since there are no applied loads. By assuming a harmonic motion

$$\mathbf{u} = \boldsymbol{\phi} \sin \omega t \quad (7.92)$$

the natural frequencies, ω, and the corresponding mode shapes, $\boldsymbol{\phi}$, can be determined from the generalized eigenvalue problem

$$\omega^2 \mathbf{M}\boldsymbol{\phi} = \mathbf{K}\boldsymbol{\phi} \tag{7.93}$$

or

$$(\mathbf{K} - \omega^2 \mathbf{M})\boldsymbol{\phi} = 0 \tag{7.94}$$

Since $\boldsymbol{\phi}$ is nontrivial,

$$|\mathbf{K} - \omega^2 \mathbf{M}| = 0 \tag{7.95}$$

or with $\omega^2 = \lambda$

$$|\mathbf{K} - \lambda \mathbf{M}| = 0 \tag{7.96}$$

which is the characteristic equation; λ is called the eigenvalue of the equation, and the structure is said to respond in the mode corresponding to a particular frequency. For computational purposes, if we premultiply each side of the preceding equation by $\mathbf{M}^{-1}$, then

$$(\mathbf{M}^{-1}\mathbf{K} - \lambda \mathbf{I})\boldsymbol{\phi} = 0 \tag{7.97}$$

It should be noted that a zero eigenvalue is obtained for each possible rigid body motion of a structure that is not completely supported. Depending on which mass matrix is adopted, slightly different results are obtained. In general, lumped mass matrices approach the exact value (consistent mass matrix) from below.

The mode shapes, $\boldsymbol{\phi}$, are "shapes", and give a relative magnitude of the DOF, not the absolute values (since they are the solution to a set of homogeneous equations). Both, the natural frequencies and mode shapes provide a fundamental description of the vibrating structure.

Chapter 8
Probability and Statistics

Abstract
This chapter aims to provide the fundamentals of probability and statistics. This is an essential topic, and most of the advanced topics and majority of the applied examples are rooted in probabilistic-based simulations. First the differences between discrete and continuous random variables are explained. Next, the properties of several widely-used distributional models are discussed. Finally, the concept of multivariate distributions and joint probability functions is presented.

8.1 Introduction to Probability

8.1.1 Deterministic *vs*. Probabilistic

Traditionally, evaluations of structural adequacy have been expressed by safety factors $SF = \frac{C}{D}$, where C is the capacity (i.e., strength) and D is the demand (i.e., load). Although this evaluation is quite simple to understand, it suffers from many limitations: it 1) treats all loads equally; 2) does not differentiate between capacity and demand's respective uncertainties; 3) is restricted to service loads; and last but not least 4) does not allow comparison of relative reliability among different structures for different performance modes. Another major deficiency is that all parameters are assigned a single value in an analysis which is then deterministic.
On the other hand, the so-called probabilistic approach is, in fact, an extension of the deterministic one which accounts for the uncertainties. They include but are not limited to uncertainties in demand, capacity, analysis type, interpretation of results, etc. Different concepts play role in a probabilistic analysis depending on the goal of the project and expected results. These parameters which are schematically shown in Figure 8.1 will be explained later.

8.1.2 Fundamentals

The probability of an event, A, is a fraction between 0 and 1.

$$0 \leq P\{A\} \leq 1 \tag{8.1}$$

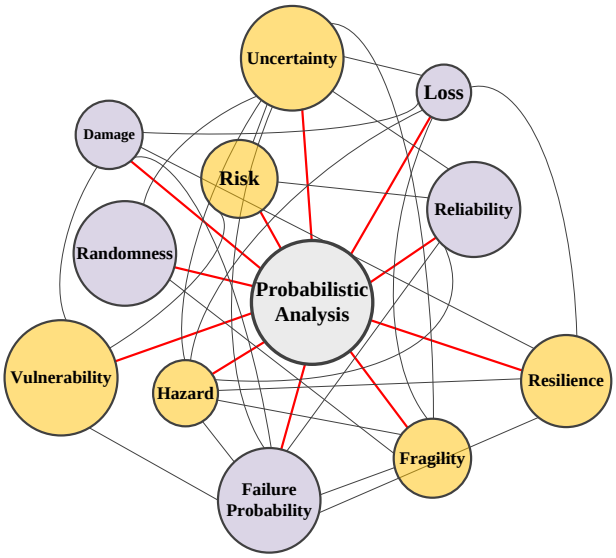

Fig. 8.1: Inter-connection of concepts incorporated in probabilistic analysis

One is the probability of an event that is sure to happen. Zero is the probability of an event that cannot happen.
A random variable (RV) is the outcome of a natural process that can not be predicted with certainty. The set of all possible outcomes for a RV is called the "sample space," Ω.

$$P\{\Omega\} = 1 \tag{8.2}$$

A random variable is either "qualitative" or "quantitative" depending on the type of value in the sample space. Quantitative RVs express values like mass, tensile strength, and modulus of elasticity. Qualitative RVs express values like gender and race.
The more times a trial is repeated, the more likely it is that the relative frequency of any particular event will be close to the probability of that event. This is called "Law of Large Numbers." For example, if we flip a coin many times, the more times we flip it, the more likely it is that the number of "heads" divided by the total number of tosses will be close to 1/2.
For each sequence A_1, A_2, ... of mutually disjoint events, Figure 8.2:

$$P\left\{\bigcup_{i=1}^{\infty} A_i\right\} = \sum_{i=1}^{\infty} P\{A_i\} \tag{8.3}$$

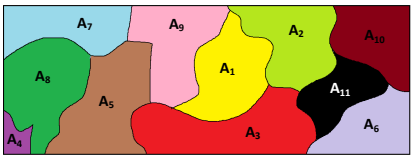

Fig. 8.2: The concept of sample space and mutually disjoint events

8.1.3 Conditional Probability

The conditional probability of A, given B, written as $P\{A|B\}$, is defined to be

$$P\{A|B\} = \frac{P\{A \cap B\}}{P\{B\}} \tag{8.4}$$

$P\{A \cap B\}$ is interpreted as the likelihood/probability that A occurs given knowledge that B has occurred.
Two events A and B are "independent" of one another if

$$P\{A|B\} = P\{A\} \tag{8.5}$$

or,

$$P\{A \cap B\} = P\{A\}.P\{B\} \tag{8.6}$$

It means knowledge of B's occurrence has no effect on the likelihood that A will occur.

8.1.4 Discrete Random Variables

If X is a RV (i.e. a function defined over the elements of a sample space) with a finite number of possible values $x_i \in R_X$ with i = 1,2,..., where R_X is the range of values of the RV, then it is a "discrete random variable."
The probability of X having a specific value x_i, $p(x_i) = P(X = x_i)$ is a number such that

$$p(x_i) \geq 0 \tag{8.7}$$

for every i = 1,2,..., and

$$\sum_{i=1}^{\infty} p(x_i) = 1 \tag{8.8}$$

The collection of pairs $(x_i; p(x_i))$, i = 1,2,... is called the "probability distribution" of X, in which $p(x_i)$ is the "probability mass function" of X.

For small number of samples, the results may not reflect exactly the true distributional model. For example all of the plots in Figure 8.3 are generated with only 100 random samples. One can see the clear differences among them.

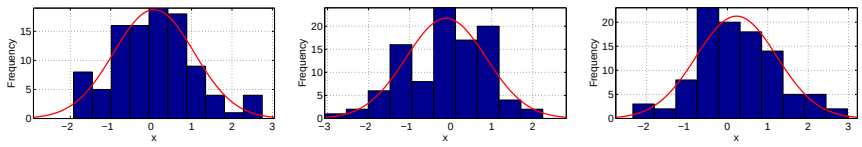

(a) 100 samples, first try (b) 100 samples, second try (c) 100 samples, third try

Fig. 8.3: Comparison of histograms due to 100 samples for three times

Increasing the number of samples will help. The plots in Figure 8.4 are based on 1,000, 10,000 and 100,000 samples, respectively.

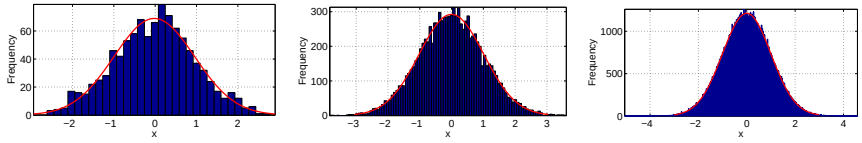

(a) 1,000 samples (b) 10,000 samples (c) 100,000 samples

Fig. 8.4: Comparison of histograms due to 1,000 to 100,000 samples

8.1.5 Continuous Random Variables

If R_X is an interval rather than a discrete set then X is a "continuous random variable." The probability that $X \in [a, b]$ is

$$P\left(a \leq X \leq b\right) = \int_a^b f(x)dx \tag{8.9}$$

where $f(x)$ is the "probability density function" (PDF) of X satisfying equation 8.9 (for all $x \in R_X$). Always,

$$f(x) \geq 0 \tag{8.10}$$

and,

$$\int_{R_X} f(x)dx = 1 \tag{8.11}$$

and, if $x \notin R_X$, then $f(x) = 0$.
Figure 8.5 shows three samples of PDFs for three different types of continuous functions. These functions will be explained later in detail.

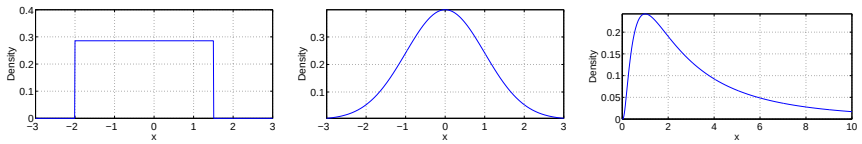

(a) Uniform distribution (b) Normal distribution (c) Lognormal distribution

Fig. 8.5: Examples of three continuous distributional functions

8.1.6 Cumulative Distribution Function

The probability that $X \leq x$, $P(X \leq x) = F(x)$ is the "cumulative distribution function" (CDF) and is defied as follows:

- For discrete $X \leq x_n$:

$$F(x) = \sum_{i=1}^{n} p(x_i) \tag{8.12}$$

- For continuous $X \leq x$:

$$F(x) = \int_{-\infty}^{x} f(\tau) d\tau \tag{8.13}$$

Figure 8.6 shows the relation between the PDF and CDF for a normal distribution.

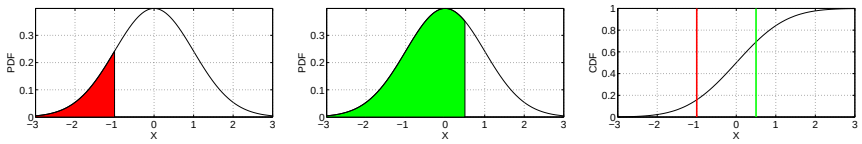

(a) PDF; low probability (b) PDF; high probability (c) Corresponding CDF

Fig. 8.6: Relation between PDF and CDF

Some key feature of the CDF can be summarized as follows:

- If $a < b$, then $F(a) < F(b)$
- $\lim_{x \to \infty} F(x) = 1$

- $\lim_{x \to -\infty} F(x) = 0$
- $P\left(a \leq X \leq b\right) = F(b) - F(a)$

Figure 8.7 shows the relationship between a bounded PDF and its corresponding CDF.

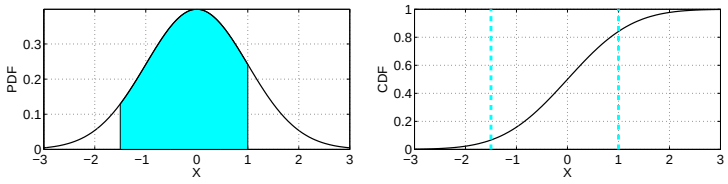

(a) Uniform distribution (b) Normal distribution

Fig. 8.7: Relation between bounded PDF and CDF

8.1.7 Expectations

In probability theory, the expected value of a random variable is intuitively the long-run average value of repetitions of the experiment it represents. The expected value is also known as the "expectation," EV, mean, or "first moment." The expected value of a dice roll is 3.5 because, the average of an extremely large number of dice rolls is practically always nearly equal to 3.5.
Expectation is coupled with the "law of large numbers." It is defined as follows:

- For discrete RV:

$$E\left[X\right] = \sum_{i=1}^{n} x_i p(x_i) \tag{8.14}$$

- For continuous RV:

$$E\left[X\right] = \int_{-\infty}^{\infty} x f(x) dx \tag{8.15}$$

Consequently, the following terms can be defined:

- The "mean" of a random variable X is just its expectation $E[X]$.
- The "variance" of X is

$$Var\left[X\right] = \sigma^2 = E\left[\left(X - E\left[X\right]\right)^2\right] = E\left[X^2\right] - \left(E\left[X\right]\right)^2 \tag{8.16}$$

- The "standard deviation" of X is

$$\sigma = \sqrt{Var\left[X\right]} \tag{8.17}$$

This is a measure of variability that scales appropriately under a change in the units used to measure X.

- "Median" of X is the value m having the property that

$$P\{X \leq m\} = P\{X \geq m\} = \frac{1}{2} \tag{8.18}$$

It is a measure of the "central tendency" of X that complements the mean. Its advantage, relative to the mean, is that it is "less sensitive" to "outliers" (i.e. observations that are in the "tails" of X that have a big influence on the mean but very little influence on the median).

- If X is a continuous random variable, then the $(100p)^{th}$ percentile is a number π_p such that the area under $f(x)$ and to the left of π_p is p.

$$p = \int_{-\infty}^{\pi_p} f(x)dx \tag{8.19}$$

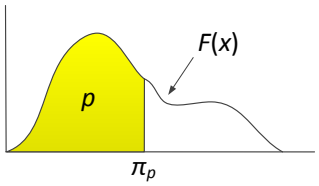

Fig. 8.8: The concept of percentile within a continuous distribution

- Covariance of two random variables X and Y is

$$Cov(X,Y) = E[XY] - E[X]E[Y] \tag{8.20}$$

If $Cov(X,Y) = 0$ the variables are said to be uncorrelated, and if $Cov(X,Y) = 1$ they are fully correlated.

8.1.8 Statistics of Discrete Variables

For a set of N quantities x_i the following central values can be defined:

Mean: estimates the value around which the data clusters.

$$\mu = \frac{1}{N}\sum_{i=1}^{N} x_i \tag{8.21}$$

It is, in fact, the arithmetic average of all the data points.

Median: of a sorted series ($x_{i-1} < x_i < x_{i+1}$) is defined as:

$$x_{med} = \begin{cases} x_{\frac{N+1}{2}} & N \text{ odd} \\ \frac{1}{2}(x_{\frac{N}{2}} + x_{\frac{N}{2}+1}) & N \text{ even} \end{cases} \tag{8.22}$$

Variance: is an indication of the "width" of the cluster:

$$\sigma^2 = \frac{1}{N-1}\Sigma_{i=1}^{N}(x_i - \mu)^2 \tag{8.23}$$

or

$$\sigma^2 = \frac{1}{N}\Sigma_{i=1}^{N}(x_i - \mu)^2 \tag{8.24}$$

Note that if N is less than 10, it is more appropriate to use the second equation, otherwise use the first one.

Standard deviation: is defined as the square root of the variance:

$$\sigma = \sqrt{\sigma^2} \tag{8.25}$$

Coefficient of variation: is the standard deviation normalized with respect to the mean

$$\text{COV} = \frac{\sigma}{\mu} \tag{8.26}$$

Covariance: measures the combined effect of how two variables vary together.

$$\sigma_{xy} = \frac{1}{N}\sum_{i=1}^{N}(x_i - \mu_x)(y_i - \mu_y) \tag{8.27}$$

Correlation coefficient: ρ_{xy} is a non-dimensional measure of the degree of correlation

$$\rho_{xy} = \frac{\sigma_{xy}}{\sigma_x \sigma_y} \tag{8.28}$$

A correlation coefficient of 1.0 or -1.0 indicates a perfect linear correlation. A positive value indicates that the variables either increase or decrease together, a negative one indicates that one value increases while the other decreases. A zero value indicates that there is no linear correlation between the variables.

Skewness: characterizes the degree of asymmetry of a distribution around its mean. It is defined in a non-dimensional value. A positive one signifies a distribution with an asymmetric tail extending out toward more positive x

$$\text{Skew} = \frac{1}{N}\Sigma_{i=1}^{N}\left[\frac{x_i - \mu}{\sigma}\right]^3 \tag{8.29}$$

Kurtosis: is a non-dimensional quantity which measures the "flatness" or "peakedness" of a distribution. It is normalized with respect to the curvature of a normal distribution. Hence a negative value would result from a distribution resembling a loaf of bread, while a positive one would be induced by a sharp peak:

$$\text{Kurt} = \frac{1}{N}\Sigma_{i=1}^{N}\left[\frac{x_i - \mu}{\sigma}\right]^4 - 3 \tag{8.30}$$

the -3 term makes the value zero for a normal distribution.

8.2 Univariate Distributions

In a probabilistic analysis, each of the uncertain parameters can be represented by a random variable and its associated PDF in the form of $X \sim f_X(x)$. This section shows some of the commonly used univariate distributional models in civil engineering and their main characteristics. The most important ones are:

- Uniform distribution
- Gaussian/Normal distribution
- Lognormal distribution
- Weibull distribution
- Extreme Value (Gumbel) distribution

8.2.1 Uniform distribution

Uniform distributions are usually used to represent random variables with unknown moments and known support.

- Notation: $X \sim \mathcal{U}(a, b)$
- PDF:

$$f(x) = \begin{cases} \frac{1}{b-a} & a \leq x \leq b \\ 0 & \text{otherwise} \end{cases} \tag{8.31}$$

- CDF:

$$F(x) = \begin{cases} 0 & x < a \\ \frac{x-a}{b-a} & a \leq x < b \\ 1 & x \geq b \end{cases} \tag{8.32}$$

- Statistics:

$$\begin{cases} \mu_X = \frac{a+b}{2} \\ \sigma_X = \frac{b-a}{\sqrt{12}} \end{cases} \tag{8.33}$$

Figure 8.9 shows a sample PDF and the corresponding CDF of a uniform distribution.

8.2.2 Normal distribution

Normal distributions are widely used in many applied science and engineering fields to represent measurement error, noise term, etc.

- Notation: $X \sim \mathcal{N}(\mu, \sigma)$

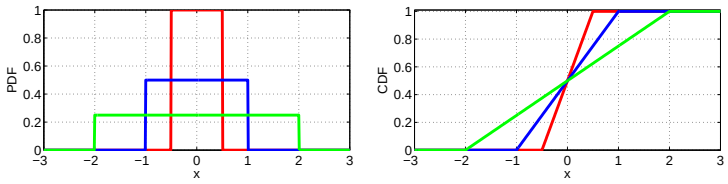

(a) PDF (b) CDF

Fig. 8.9: Uniform distribution

- PDF:

$$f(x) = \frac{1}{\sqrt{2\pi\sigma^2}} e^{-\frac{(x-\mu)^2}{2\sigma^2}} \tag{8.34}$$

- CDF:

$$F(x) = \int_{-\infty}^{x} \frac{1}{\sqrt{2\pi\sigma^2}} e^{-\frac{(\tau-\mu)^2}{2\sigma^2}} d\tau \tag{8.35}$$

- Statistics:

$$\begin{cases} \mu_X = \mu \\ \sigma_X = \sigma \end{cases} \tag{8.36}$$

Figure 8.10 shows a sample PDF and the corresponding CDF of a uniform distribution.

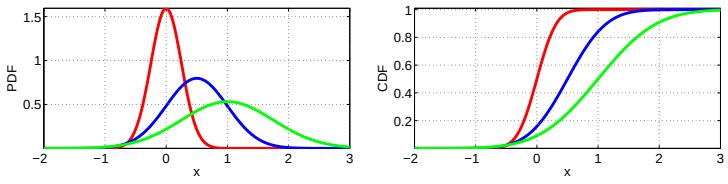

(a) PDF (b) CDF

Fig. 8.10: Normal distribution

8.2.3 Lognormal distribution

Lognormal distributions are widely used in many applied science and engineering fields to represent measurement error, noise term, etc.

- Notation: $X \sim \mathcal{LN}(\lambda, \zeta)$

- PDF:

$$f(x) = \frac{1}{x\sqrt{2\pi\zeta^2}} \exp(-\frac{(\ln x - \lambda)^2}{2\zeta^2}) \tag{8.37}$$

- CDF:

$$F(x) = \frac{1}{2} + \frac{1}{2}\text{erf}\left(\frac{\ln x - \lambda}{\sqrt{2}\zeta}\right) = \Phi\left(\frac{\ln x - \lambda}{\zeta}\right) \tag{8.38}$$

where erf is called error function and and Φ is the cumulative distribution function of the standard normal distribution.

- Statistics:

$$\begin{cases} \mu_X = e^{\lambda+\zeta^2/2} \\ \sigma_X = e^{\lambda+\zeta^2/2}\sqrt{e^{\zeta^2}-1} \end{cases} \tag{8.39}$$

where λ and ζ are the mean and standard deviation of the natural logarithm of the variable.
Figure 8.11 shows a sample PDF and the corresponding CDF of a lognormal distribution.

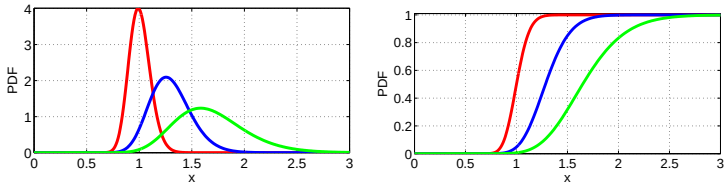

(a) PDF (b) CDF

Fig. 8.11: Lognormal distribution

8.2.4 Weibull distribution

This model is usually used to characterize time-to-failure type variables. It is can be used for material strength and lifetime parameters for brittle materials,

- Notation: $X \sim \mathcal{W}(\alpha, \beta)$
- PDF:

$$f(x) = \begin{cases} \frac{\beta}{\alpha}\left(\frac{x}{\alpha}\right)^{\beta-1} \exp -\left(\frac{x}{\alpha}\right)^{\beta} & \text{if } x \geq 0 \\ 0 & \text{if } x < 0 \end{cases} \tag{8.40}$$

- CDF:

$$F(x) = \begin{cases} 1 - \exp - \left(\frac{x}{\alpha}\right)^{\beta} & \text{if } x \geq 0 \\ 0 & \text{if } x < 0 \end{cases} \tag{8.41}$$

- Statistics:

$$\begin{cases} \mu_X = \alpha\Gamma\left(1 + \frac{1}{\beta}\right) \\ \sigma_X = \alpha\sqrt{\Gamma\left(1 + \frac{2}{\beta}\right) - \Gamma\left(1 + \frac{1}{\beta}\right)^2} \end{cases} \tag{8.42}$$

8.2.5 Gumbel distribution

The Gumbel distribution (or Generalized Extreme Value distribution Type-I) is used to model the distribution of the maximum (or the minimum) of a number of samples of various distributions.

- Notation: $X \sim \mathcal{G}(\mu, \beta)$
- PDF:

$$f(x) = \frac{1}{\beta} e^{-\frac{x-\mu}{\beta} - e^{-\frac{x-\mu}{\beta}}} \tag{8.43}$$

- CDF:

$$F(x) = e^{-e^{-\frac{x-\mu}{\beta}}} \tag{8.44}$$

- Statistics:

$$\begin{cases} \mu_X = \mu + \beta\gamma_e \\ \sigma_X = \frac{\pi\beta}{\sqrt{6}} \end{cases} \tag{8.45}$$

  where $\gamma_e = 0.577216...$ is the Euler constant.

8.3 Multivariate Distributions

A natural extension of univariate distributions are multivariate ones. Given the random variables X, Y, Z, ..., the joint probability distribution for X, Y, Z, ... is a probability distribution that gives the probability that each of X, Y, Z, ... falls in any particular range of values specified for that variable.
The joint probability distribution can be expressed:

- Joint probability density function (for the continuous variables), and joint probability mass function (for the discrete variables)
- Joint cumulative distribution function

Two major concepts are usually studied when dealing with multivariate distributions:

- Marginal distribution: gives the probabilities for each of the random variables with no reference to any specific ranges of the other variables.

- Conditional probability distribution: gives the probabilities for any subset of the random variables conditional on specific values of the other variables.

The following sections explains the simplified models for the bivariate and normal distribution case.

8.3.1 Bivariate distribution

Given two continuous random variables, X and Y, the joint cumulative bivariate distribution function is:

$$F_{X,Y}(x,y) = \mathbb{P}\left(X \leq x, Y \leq y\right) \tag{8.46}$$

The joint density is defined as

$$f(x,y) = \frac{\partial^2 F(x,y)}{\partial x \partial y} \tag{8.47}$$

or,

$$F(x,y) = \int_{-\infty}^{x}\int_{-\infty}^{y} f(x,y)\mathrm{d}x\mathrm{d}y \tag{8.48}$$

Consequently, the probability that $(X,Y) \in A$ is:

$$\mathbb{P}(A) = \int_A f(x,y)\mathrm{d}x\mathrm{d}y \tag{8.49}$$

Some of the main features of bivariate distributions are:

- $F\left(-\infty,-\infty\right) = 0$
- $F\left(\infty,\infty\right) = 1$
- If $x_1 \leq x_2$ and $y_1 \leq y_2$ then $F(x_1,y_1) \leq F(x_2,y_2)$.
- $\int_{-\infty}^{+\infty}\int_{-\infty}^{+\infty} f(x,y)\mathrm{d}x\mathrm{d}y = 1$

Main concepts in relationship of bivariate distributions:

- Marginal distribution function of X is defined as

$$\begin{aligned} F_X(x) &= F\left(X \leq x, -\infty < Y < +\infty\right) \\ &= F\left(x,\infty\right) = \mathbb{P}\left(X \leq x\right) = \lim_{y\to\infty} F(x,y) \end{aligned} \tag{8.50}$$

  According to above, y is integrated out:

$$f_X(x) = \int_{-\infty}^{+\infty} f(x,y)\mathrm{d}y \tag{8.51}$$

- Independency of two random variables can be examined as:

$$F_{X,Y}(x,y) = \mathbb{P}(X \leq x, Y \leq y) \\ = \mathbb{P}(X \leq x) \times \mathbb{P}(Y \leq y) = F_X(x) \times F_Y(y) \tag{8.52}$$

- Conditional density of Y given $X = x$ (i.e., what is the conditional distribution of Y when X is fixed at the value $X = x$?)

$$f_{Y|X}(y) = \frac{f(x,y)}{f_X(x)} \tag{8.53}$$

Note that if X and Y are independent then "conditional" is equal to "marginal."

8.3.2 Multivariate normal distribution

The multivariate normal (Gaussian) distribution is a generalization of the univariate normal distribution to higher dimensions. A random vector is said to be k-variate normally distributed if every linear combination of its k components has a univariate normal distribution.
The multivariate normal distribution of a k-dimensional random vector $\mathbf{x} = [X_1, X_2, ..., X_k]$ can be written in the following notation

$$\mathbf{x} \sim \mathcal{N}_k(\boldsymbol{\mu}, \boldsymbol{\Sigma}) \tag{8.54}$$

with k-dimensional mean vector and $k \times k$ covariance matrix:

$$\begin{cases} \boldsymbol{\mu} = & [\mathrm{E}[X_1], \mathrm{E}[X_2], \ldots, \mathrm{E}[X_k]] \\ \boldsymbol{\Sigma} = & [\mathrm{Cov}[X_i, X_j]], i = 1, 2, \ldots, k; j = 1, 2, \ldots, k \end{cases} \tag{8.55}$$

The multivariate normal distribution is said to be "non-degenerate" when the symmetric covariance matrix $\boldsymbol{\Sigma}$ is positive definite. In this case the distribution has density as:

$$f_{\mathbf{x}}(x_1, \ldots, x_k) = \frac{1}{\sqrt{(2\pi)^k |\boldsymbol{\Sigma}|}} \exp\left(-\frac{1}{2}(\mathbf{x} - \boldsymbol{\mu})^{\mathrm{T}} \boldsymbol{\Sigma}^{-1} (\mathbf{x} - \boldsymbol{\mu})\right) \tag{8.56}$$

where $\mathbf{x}$ is a real k-dimensional column vector and $|\boldsymbol{\Sigma}|$ is the determinant of $\boldsymbol{\Sigma}$.

8.3.3 Bivariate normal distribution

In the two-dimensional case ($k = 2$), the probability density function is defined as:

$$f(x,y) = \frac{1}{2\pi\sigma_X\sigma_Y\sqrt{1-\rho^2}} \exp \\ \left(-\frac{1}{2(1-\rho^2)}\left[\frac{(x-\mu_X)^2}{\sigma_X^2} + \frac{(y-\mu_Y)^2}{\sigma_Y^2} - \frac{2\rho(x-\mu_X)(y-\mu_Y)}{\sigma_X\sigma_Y}\right]\right) \tag{8.57}$$

where ρ is the correlation between X and Y and $\sigma_X > 0$ and $\sigma_Y > 0$. In this case,

Figure 8.12 shows a sample PDF and CDF of bivariate normal distribution in which $\mu_X = \mu_Y = 0.0$, $\sigma_X = 0.707$ and $\sigma_Y = 1.000$.

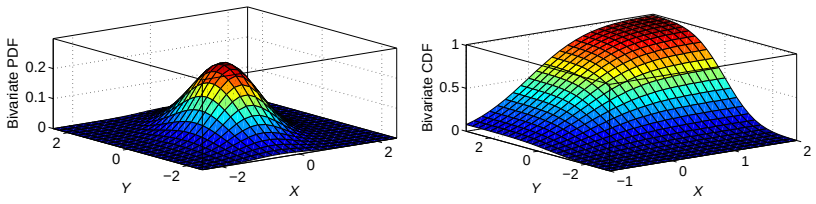

(a) Bivariate PDF (b) Bivariate CDF

Fig. 8.12: Bivariate normal distribution

Figure 8.13 shows impact of correlation on the bivariate normal distribution.

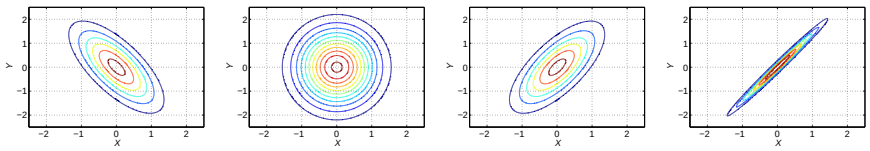

(a) $\rho = -0.5$ (b) $\rho = 0.0$ (c) $\rho = +0.5$ (d) $\rho = +0.7$

Fig. 8.13: Impact of correlation on the bivariate normal distribution

Part II
Damage

Chapter 9
Fracture Mechanics of Concrete

Abstract
In many respects, concrete is a far more complex material to model in the inelastic range than steel. Only relatively recently has the research community embraced fracture mechanics as a model to capture its cracking. Given the importance of the topic, a separate chapter is hence devoted to this form of fracture. It is composed of two parts: macro and micro cracks.
In the former, emphasiz will be on Hillerborg's model that is by now universally accepted for the fracture of cementitious material. Then the important phenomenon of strain localization and accompanying size effect laws will be addressed.
In the second part of the chapter, the impact of micro-cracks in concrete will be addressed.

Concrete being inherently brittle, it was at first thought that one could directly apply the concepts of linear elastic fracture mechanics (developed for metals). Kaplan [488], Walsh [864] and Walsh [863] early on found out that the measured fracture toughness was highly dependent on the specimen size. This was further confirmed by Kesler, Naus, and Lott [501].
This chapter will explain why linear elastic fracture mechanics is not applicable to concrete, and why a cohesive crack model is a more appropriate model.

9.1 Macro Cracks

9.1.1 Experimental Observations

Considering a concrete cylinder subjected to uniaxial tensile displacement (not load), possibly slightly notched in the center to trigger cracking, then the load displacement response will greatly vary, Figure 9.1. It should be noted that in this case, there is no crack propagation from the notch, but rather a gradual formation of a crack in between the notches and a gradual opening of the crack.
There are three possibilities:

Elastic unloading: if the gage does not cover the crack. In this case, the concrete is first elastically stressed, and when the peak load is reached (thus causing crack formation along the notch), the concrete will elastically unload.

Strain softening: for a gage tightly covering the crack. In this case, once the peak load is reached, there is a decrease of the load carrying capacity accompanying the increased displacement. The recorded core displacement corresponds to the crack opening displacement.

Snap-back: occurs when the gage records both the crack opening (localized softening) and the elastic unloading.

For case 2, and if we were to homogenize by taking $\sigma = F/A$, and $\varepsilon = u/L$, it is clear that we can not provide a unique definition of the strain across the crack. At this location, the strain can no longer be defined, and instead we should characterize the crack by its crack opening displacement COD which will then be plotted along with the stress (σ-COD). Capability of transmitting stresses across a crack under controlled displacement is a characteristic of *softening materials* such as concrete, rock, ceramics, and even solid rocket propellants [766].

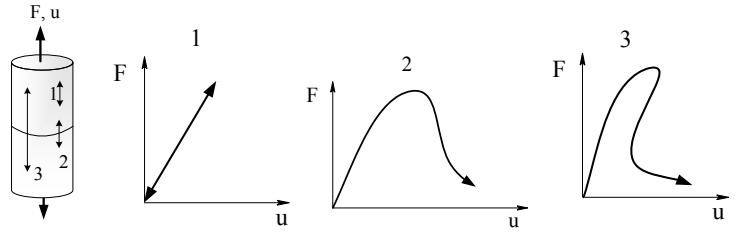

(a) Gauge locations (b) Elastic unloading (c) Elastic softening (d) Snap-Back

Fig. 9.1: Post-peak response of a concrete specimen under uniaxial tension in terms of gauge locations

9.1.2 σ-COD Diagram, Hillerborg's Model

Cementitious material softening is characterized by a stress-crack opening width curve (and not stress-strain). The exact characterization of the softening response should ideally be obtained from a uniaxial test of an uncracked specimen. This is extremely difficult, so the softening curve is often indirectly determined by testing notched specimens.

Hillerborg, Modéer, and Petersson [419] presented a very simple and elegant model. In this cohesive crack model, the crack is composed of two parts, Figure 9.2:

True or physical crack across which no stresses can be transmitted. Along this zone we have both displacement and stress discontinuities.

Fictitious crack or Fracture Process Zone (FPZ) ahead of the previous one, characterized by:

- Peak stress at its tip equal to the tensile strength of cementitious material

- Decreasing stress distribution from f_t' at the tip of the fictitious crack to zero at the tip of the physical crack

Along FPZ, we have displacement discontinuity and stress continuity.

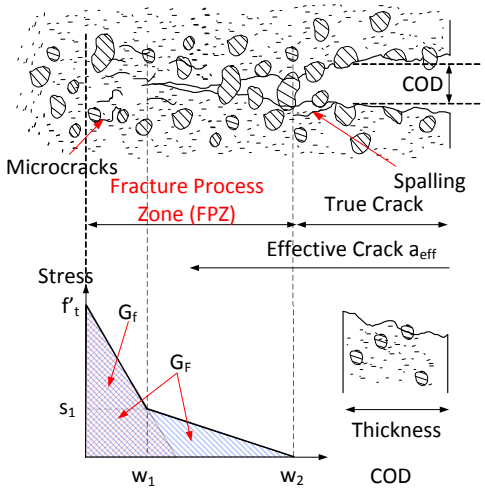

Fig. 9.2: Hillerborg's model

This model is a natural extension of the ones of Dugdale [260] (Figure 9.10) and Barenblatt [85] (Figure 4.14(c)). There is an inflection point in the descending branch; the first part has been associated with (unconnected) microcracking ahead of the stress-free crack. The second part with bridging of the crack by aggregates.
The area under the curve is the *fracture energy,* G_F, (not to be confused with G_c or critical energy release rate) and is a measure of the energy that needs to be spent to generate a unit surface of crack.
The characteristic length in concrete is given by

$$l_{ch} = \frac{EG_F}{f_t'^2} \tag{9.1}$$

(and is to be compared to the plastic zone size of Irwin, Eq. 4.53). For the shape of the softening diagram ($\sigma - COD$), in general a bilinear model for the strain softening should be used.

9.1.3 Fracture Energies

9.1.3.1 G_F

The determination of the fracture energy G_F has been investigated by [172, 691, 887, 477, 346, 259, 343]. There are many models for concrete softening, and the two most commonly used ones are the one based on an exponential decay [214] or bilinear [887], Figure 9.2. This last model can be uniquely defined in terms of the tensile strength, f'_t, and the fracture energy, G_F. It was found that the optimal points for concrete with 1" maximum size aggregate are [155]:

$$s_1 = 0.4 f'_t \tag{9.2}$$

$$w_1 = 0.8 \frac{G_F}{f'_t} \tag{9.3}$$

$$w_2 = 3 \frac{G_F}{f'_t} \tag{9.4}$$

whereas for structural concrete the corresponding values are [887]:

$$s_1 = \frac{f'_t}{4} \tag{9.5}$$

$$w_1 = 0.75 \frac{G_F}{f'_t} \tag{9.6}$$

$$w_2 = 5 \frac{G_F}{f'_t} \tag{9.7}$$

where f'_t is the uniaxial tensile strength.
As f'_t is seldom determined experimentally, it is assumed to be 9% of f'_c [594]. In lieu of a direct tension test, a flexural test can be performed under strain control, and the fracture energy, G_F, could still be determined from the area under the load and corresponding displacement curve. For dynamic analysis, the fracture properties of dam concrete depend on both rate of loading and preloadings. Test results [155] show that the fracture properties generally increase with increasing loading rate. However, dynamic compressive preloading leads to a reduction of the fracture properties at both quasi-static and high loading rates.

9.1.3.2 G_f

The maximum loads of structures depend mainly on the initial tangent of the softening stress-separation curve, which is fully characterized by G_f. They are almost independent of the tail of this curve, which depends mainly of G_F, Figure 9.2.
The prediction of the entire post-peak softening load-deflection curve of a structure, which is often of secondary interest for design, depends mainly on the tail of the stress-separation curve of the cohesive crack model, and thus on G_F.
G_f and G_F are two different material characteristics which are only partially correlated. G_F can be estimated from G_f and vice versa, but not accurately. Ideally, both

G_f and G_F should be measured and used for calibrating the initial slope and the tail of the softening curve of the cohesive crack model (or crack band model), which are both needed for fracture analysis of structures. A rough approximation

$$G_F \approx 2.5 G_f \tag{9.8}$$

is reported by Planas and Elices [698] and further verified by Bažant and Becq-Giraudon [98].

Bažant and Becq-Giraudon [98] analyzed 238 tests reported in the literature, conducted extensive nonlinear optimization studies based on the Levenberg-Marquardt algorithm, and obtained two simple approximate formulae for the means of G_f and G_F as functions of the compressive strength f'_c, maximum aggregate size d_a, water-cement ratio w/c, and shape of aggregate (crushed or river):

$$\begin{aligned} G_f &= \alpha_0 \left(\tfrac{f'_c}{0.051}\right)^{0.46} \left(1+\tfrac{d_a}{11.27}\right)^{0.22} \left(\tfrac{w}{c}\right)^{-0.30} && \omega_{G_f} = 17.8\% \\ G_F &= 2.5\alpha_0 \left(\tfrac{f'_c}{0.051}\right)^{0.46} \left(1+\tfrac{d_a}{11.27}\right)^{0.22} \left(\tfrac{w}{c}\right)^{-0.30} && \omega_{G_F} = 29.9\% \\ c_f &= \exp\left[\gamma_0 \left(\tfrac{f'_c}{0.022}\right)^{-0.019} \left(1+\tfrac{d_a}{15.05}\right)^{0.72} \left(\tfrac{w}{c}\right)^{0.2}\right] && \omega_{c_f} = 47.6\% \end{aligned} \tag{9.9}$$

where $\alpha_0 = \gamma_0 = 1$ for rounded aggregates, while $\alpha_0 = 1.44$ and $\gamma_0 = 1.12$ for crushed or angular aggregates; ω_{G_f} and ω_{G_F} are the coefficients of variation of the ratios G_f^{test}/G_f and G_F^{test}/G_F for which a normal distribution may be assumed. ω_{c_f} is the coefficient of variation of c_f^{test}/c_f for which a lognormal distribution should be assumed (ω_{c_f} is approximately equal to the standard deviation of $\ln c_f$). Because there is not yet a standardized test to determine the fracture energies of concrete, one is proposed by the authors in Appendix A.

9.1.4 Impact of Hillerborg's Model on Strength

Accepting Hillerborg's model, we seek to assess its impact on the response of an idealized structure: a bar subjected to uniaxial imposed displacement.

First, we consider a representative volume element (RVE) small enough that abstraction can be made of the localized crack and can be characterized by a stress strain curve, Figure 9.3(a).

Prior to reaching the peak stress f_t, we have a linear stress strain relationship $\sigma = E\varepsilon$. Once peak load is reached, the concrete softens, and the peak strain is ε_u. At that point, the load carrying capacity of the bar is exhausted. The post-peak stress is given by $\sigma = f_t + h(\varepsilon - \varepsilon_0)$ for degrading (softening) material, where h is the (negative) softening modulus, and for linear softening

$$h = -\frac{f_t}{\varepsilon_u - \varepsilon_0}, \quad \varepsilon_0 = f_t/E \tag{9.10}$$

Next, we consider an assemblage of m "elements" assembled in series, Figure 9.3(b) and assume that one of the elements is weaker than the other $m-1$ ones. Thus when

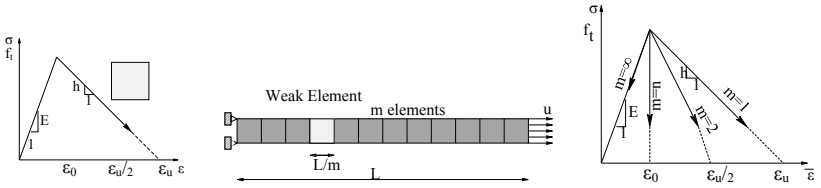

(a) Idealized RVE (b) Concrete elements assembled in series

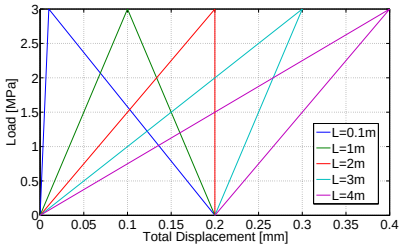

(c) Numerical example

Fig. 9.3: Impact of Hillerborg's model on structural response

this element reaches its own tensile strength (lower than f_t), it fails. Upon failure of this element, the other ones will have to unload elastically. In the post-peak zone, the displacement will be

$$\begin{aligned} u &= \frac{L}{m}\varepsilon_f + (m-1)\frac{L}{m}\varepsilon_e \\ \varepsilon_f &= \frac{f_t}{E} + \frac{\sigma - f_t}{h} \\ \varepsilon_e &= \frac{\sigma}{E} \\ \overline{\varepsilon} &= \frac{u}{L} \\ \Rightarrow \overline{\varepsilon} &= \frac{\sigma}{E} + \frac{E-h}{Eh}\frac{\sigma - f_t}{m} \end{aligned} \tag{9.11}$$

Defining $n = \frac{\varepsilon_u}{\varepsilon_0}$, then $h = -E/(n-1)$ and the last equation reduces to

$$\overline{\varepsilon} = \frac{\sigma}{E} + \frac{n(f_t - \sigma)}{mE}$$

Note "similarity" with the tangent modulus in plasticity. From the figure, we note that depending on the number of elements used (m), there is a wide range of possible responses.

- For $m = 1$, softening curve reproduced.

- For $m = n$, brittle failure.
- For $m = 2$, half the bar localizes.
- For $m > n$, strain decrease, i.e. snap-back behavior, impossible to achieve experimentally. Physically, that implies that the localization zone can not absorb the elastic energy released by the elastic part of the bar.

If $m \to \infty$, elastic unloading. Physically, this is impossible as it would imply failure occurred without dissipation of energy. As a result we would have: a) Loss of local material stability, b) Loss of structural stability, c) Loss of ellipticity, d) Mesh dependence. This can be illustrated with a simple numerical example where a softening material member is subjected to uniaxial displacement with the following properties: $f_t' = 3$MPa, $E = 30$ GPa, w_{max}=.02 cm, and the fracture energy can be easily determined: $G_F = \frac{1}{2}(3 \times 10^6)(2 \times 10^{-4}) = 300$N/m. From these properties, the peak elastic strain is $\varepsilon_0 = \frac{3 \times 10^6}{3 \times 10^{10}} = 10^{-4}$, and the maximum elastic displacement is $10^{-4}L$. Plotting the load displacement curve ($P - u$) of this member for various lengths, L:

- In all cases the peak load will be $P_{max} = 3A$ where A is the cross sectional area (since results are independent of A we shall assume A=1).
- The corresponding displacement will be given by $u = \varepsilon_0 \times L$.
- Similarly, in all cases the maximum displacement will be $u_{max} = w_{max} = 0.02$ cm and the corresponding load will obviously be equal to zero.
- The displacement corresponding to peak load will be equal to w_{max} if: $L = \frac{w_{max}}{\epsilon_0} = \frac{2 \times 10^4}{10^{-4}} = 2$m, and results shown in Figure 9.3(c).

This figure calls for the following observations:

1. Specimens less than 2 m long do exhibit a softening branch which can be experimentally obtained only through displacement controlled tests.
2. For a 2 m specimen, we do have a perfectly brittle response.
3. For specimens larger than 2 m, there is a snap-back which can only be hypothesized but not experimentally obtained.
4. Large specimens could still be tested, however rather than using the entire specimen length as "gage length" (or displacement/stroke control test), we would have to use a smaller gage length (through strain control tests) across a potential crack. Thus a notched specimen should be used.

In summary, the load displacement curve of this simple test is clearly size dependent. The larger the specimen, the larger the stored strain energy which would be released to form surface energy.
An energetic interpretation of this figure would lead us to compare the elastic energy, $U = \frac{1}{2} f_t' \epsilon_u AL = \frac{1}{2}(3 \times 10^6)(10^{-4})AL = 150AL$, at peak load with the fracture energy $G_F = 300$ N/m, thus $300A = 150AL$ and $L = 2$ m.
As long as the strain energy is smaller than the fracture energy, then we do have structural softening. If the two energies are equal, then we would have a perfectly brittle response. If the elastic energy exceeds the fracture energy, then we would have a sudden failure with snap-back.

L (m)	0.1	1.	2.	3.	4.
$\frac{U}{A}$	15.	150.	**300.**	450.	600.

We observe that $\frac{U}{A} = G_F$ for $L = 2$ m. Thus as long as the energy released can be transformed into fracture energy, we have a stable configuration. However if the accumulated strain energy being released (including not only the one stored in the specimen but also in the experimental set-up) is greater than the one which can be absorbed to create new surface energy (cracks), then we have instability.
For experimentalists, the implication is that for a successful post-peak experiment, the total strain energy (of the specimen and of the testing frame) should be less than the fracture energy. Hence to avoid snap-backs, the testing frame should be as stiff as possible.

9.1.5 Localization

The concept of crack localization in concrete is illustrated next. Considering a plate subjected to uniform imposed displacement, Figure 9.4(a), we seek to map the strain history (which is to some extent counterintuitive but essential to understand concrete cracking). The plate is initially crack free, but it is assumed that there is a minute imperfection in the middle that will trigger failure (cracking) at this location. Units are irrelevant here, and all values are normalized.
Up to an imposed displacement just under 0.7, the strain is uniformly distributed and increases linearly with load up to a maximum of 1,000, Figure 9.4(c). From that point onward, the strain localizes in the middle (assumed to contain the weakest point), with a corresponding increase in strain. Adjacent to that location, the strain bounces back elastically and gradually decreases to zero. This is also shown schematically in Figure 9.4(b).

9.1.6 Size Effect

The Size Effect law stems from the fact that potential energy stored in $\mathbb{R}^3$ is released to create a surface energy (crack) in $\mathbb{R}^2$; hence it has profound influence in assessing the strength of "large" structures.

9.1.6.1 Bažant's Original Derivation

The law was originally derived by Bažant [94] who considered a notched plate subjected to uniaxial force, Figure 9.5, and examined the energy exchanged during infinitesimal crack extension. The energy released can be approximated by $b2k(a_0 + c_f)\Delta a\sigma_n^2/2E$, which must be equal to the energy consumed during crack growth: $bG_F\Delta a$. Hence

$$b2k(a_0 + c_f)\Delta a\sigma_n^2/2E = bG_F\Delta a \tag{9.12}$$

yielding

$$\sigma_n = \frac{Bf_t'}{\sqrt{1 + \frac{D}{D_0}}}$$

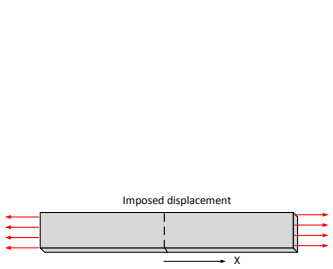

(a) Concrete plate under imposed displacement

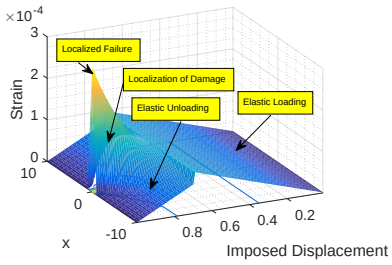

(b) Plate response

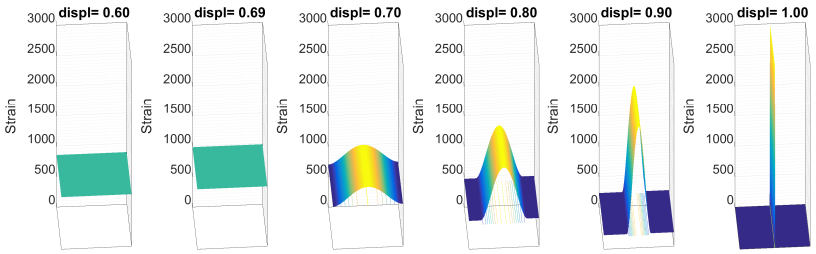

(c) Strains in terms of imposed displacement

Fig. 9.4: Localization of cracks in concrete structures

where

$$Bf_t' = \sqrt{\frac{G_F E}{kc_f}} \quad \text{and} \quad \frac{D}{D_0} = \frac{a_0}{c_f} = \beta$$

In his original paper, Bažant noted that analytical or numerical derivation of B and β is too difficult, and they are best obtained through statistical regression analysis of test data.

A subsequent derivation, in the spirit of Dugdale and Barenblatt, was derived by Saouma, Natekar, and Hansen [760] who derived explicit expressions for β for various geometries. A further extension accounted for the fractal nature of concrete fracture surfaces [758].

One can rewrite Eq. 9.12 as

$$f_t^* = \frac{f_t'}{\sqrt{1+\beta}} = \frac{\sigma_N}{B}, \tag{9.13}$$

where f_t^* is termed the size-reduced-strength and is a characteristic of the entire structure and not only of the material.

Bažant has defined $\beta = \frac{\lambda}{\lambda_0} = \frac{D}{D_0}$ where D is a representative dimension of the structure and D_0 the average aggregate size.

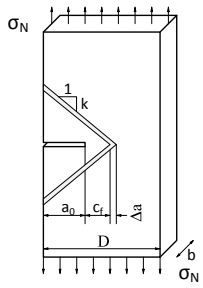

Fig. 9.5: Size effect derivation in cohesive materials

Undoubtedly the size effect law is a very elegant generalized model for concrete fracture. It attempts to provide a unified mathematical model for concrete cracking by merging two different approaches. Furthermore, it has been experimentally validated with numerous tests, many of which involved uncracked (initial) structures.

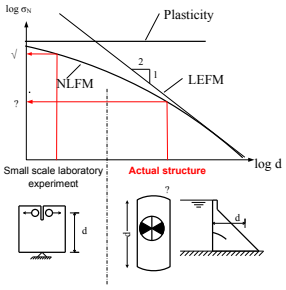

(a) Size effect law

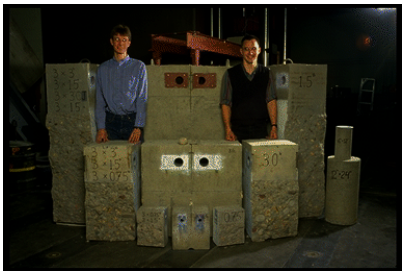

(b) Tests by Saouma et al. [768] $1' < h < 5', 3/4" < d_a < 3"$

Fig. 9.6: Implications of the size effect law

For structures:

Small Structures: i.e. small size relative to the size of aggregate or small λ. Then $\frac{\lambda}{\lambda_0}$ in Eq. 9.13 may be neglected in comparison to 1 yielding $f_t^* \simeq f_t'$, and the classical strength criterion governs. Furthermore, $B = \frac{\sigma_N}{f_t'}$ and can be determined from plastic limit analysis.

Large Structures: i.e. very large size compared to aggregate size, $\frac{\lambda}{\lambda_0} \gg 1$. Thus Eq. 9.13 reduces to $f_t^* \simeq f_t' \sqrt{\frac{\lambda_0}{\lambda}}$, and we see that "for very large concrete structures, such as dams (or large rock masses), Eq. 9.13 asymptotically approaches the size effect of linear elastic fracture mechanics."

In general, Eq. 9.13 represents a gradual transition from the strength criterion for small structures to linear elastic fracture mechanics for large structures. To assess the size effect law, geometrically identical specimens with different sizes must be tested, Figure 9.6(b). Then Eq. 9.13 can be cast in the form:

$$Y = a + b\lambda = \frac{1}{\sigma_N^2} \tag{9.14}$$

where $a = \frac{1}{B^2}$ and $b = \frac{1}{B^2 \lambda_0}$ and plotted on a log-log plot. From statistical regression analysis, the intercept a and the slope b can be determined, and then $B = \frac{1}{\sqrt{a}}$ and $\lambda_0 = \frac{a}{b}$. If $\frac{\lambda}{\lambda_0} = \beta$ is less than 0.1, then a strength criterion must be used, and if β is greater than 10, then an LEFM criterion is to be used. Note that those are arbitrary guidelines. The point of intersection of the two asymptotes corresponds to $\beta = 1$.
An example of experimentally observed size effect is the shear strength of reinforced concrete without stirrups, shown in Figure 9.7 [117].

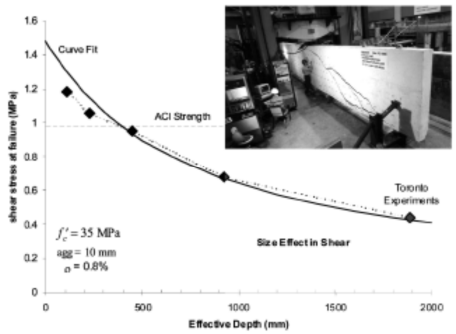

Fig. 9.7: Example of size effect in shear for reinforced concrete members without stirrups [117]

Finally, the strong analogy between the size effect and column buckling should be mentioned, Table9.1.

9.1.6.2 Saouma's Derivation

In this section, based on Saouma, Natekar, and Hansen [760], an alternate derivation of the size effect law is presented. Though it hinges (for simplifying reasons) on Dugdale's or Barenblatt's model for the cohesive stresses (in lieu of Hillerborg's fracture energy), it will be shown that a purely analytical expression could be derived; hence problem specific numerical values of B can be obtained.

Table 9.1: Similarities between column equation and size effect laws

Column Buckling	Size Effect
Euler Equation	LEFM
Slenderness ratio	Size
Plastic failure	Plastic failure
Inelastic stresses	Cohesive stresses
Inelastic Buckling	NLFM
Column Equation (SSRC)	Size Effect law (Bažant)
$\sigma_{cr} = \sigma_y \left[1 - \frac{\sigma_y}{4\pi^2 E}\left(\frac{KL}{r_{min}}\right)^2\right]$	$\sigma_n = \frac{B f_t'}{\sqrt{1+\beta}}$

This approach is based on classical elasto-plastic fracture mechanics [154] where in its simplest form the stress intensity factors caused by the cohesive stresses (in a plastic zone or process zone) are assumed to cancel the ones caused by the far field load. Hence contrary to the original derivation by Bažant, the size effect law will be shown to have explicit roots in plasticity and linear elastic fracture mechanics theories. As a result, it will be shown that not only quasi-brittle materials exhibit a size effect, but elasto-plasticones as well.
The model was subsequently extended to fractal cracks [758].

Constant Cohesive Stresses

Central Crack Starting with a general case, we consider an infinite plate subjected to a far field uniform tensile stress, σ, and a crack of length $2a$ at the tip of which we have a uniform cohesive compressive stress (Dugdale type) equal to the tensile strength, f_t', Figure 9.8.

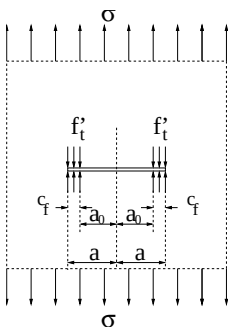

Fig. 9.8: Central Crack With Constant Cohesive Stresses

The stress intensity factors due to the far field and cohesive stresses are:

$$K_a = \sigma\sqrt{\pi a} \tag{9.15}$$

$$K_b = f'_t\sqrt{\pi a}\left(1 - \frac{2}{\pi}\arcsin\frac{a - c_f}{a}\right) \tag{9.16}$$

respectively, [189].
Equating those two stress intensity factors, we obtain the nominal strength:

$$\sigma_n = f'_t\left[1 - \frac{2}{\pi}\arcsin\left(1 - \frac{c_f}{a}\right)\right] \tag{9.17}$$

For small sizes when $a \simeq c_f$, σ_n asymptotically approaches f'_t. On the other hand, for large sizes when $c_f \simeq 0$, σ_n will asymptotically approach zero.
Whereas the expression of σ_n appears to have the same limits as the Size Effect Law, it is not mathematically similar to it. This will only become apparent if one takes a series expansion of the ArcSin function and substituting c_f/a by s:

$$\sigma_n = \sigma_n = f'_t\left[1 - \frac{2}{\pi}\arcsin(1 - s)\right] \tag{9.18}$$

$$\simeq \frac{2\sqrt{2}f'_t}{\pi}s^{1/2} + \frac{f'_t}{3\sqrt{2}\pi}s^{3/2} + \frac{3f'_t}{40\sqrt{2}\pi}s^{5/2} + O[s]^{7/2} \tag{9.19}$$

Neglecting the terms of power greater than 1 (since s is at most equal to 1) and substituting $s = 1/(1 + r)$ where $r = a_0/c_f$, we obtain

$$\sigma_n = \underbrace{\frac{2\sqrt{2}}{\pi}}_{B} f'_t\sqrt{\frac{1}{1 + \underbrace{r}_{\beta}}} \tag{9.20}$$

We have thus recovered the size effect law as originally derived by Bažant as expressed by Eq. 9.1.6.1, with the additional benefit that B is quantified for this combination of geometry and cohesive stresses, Figure 9.9.

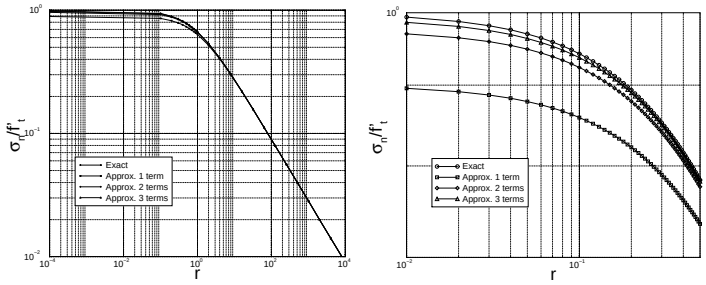

Fig. 9.9: Nominal strength in terms of size for a center crack plate with constant cohesive stresses

Edge Crack We next consider an arbitrary geometry of a cracked structure whose stress intensity factor due to the far field stress can be expressed as

$$K_a = \alpha\sigma\sqrt{\pi a} \tag{9.21}$$

where α is a coefficient which accounts for geometry, boundary conditions, and load. On the other hand, the stress intensity factor corresponding to a constant stress, Figure 9.10, is given by [805] as

$$K_b = -f_t'\sqrt{\pi a} f_b \tag{9.22}$$

where

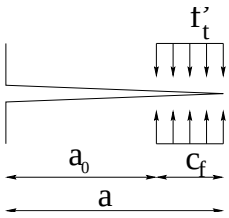

Fig. 9.10: Dugdale's Model

$$f_b = 0.903s^{1/2} + \frac{1}{3}0.4406s^{3/2} + \frac{1}{5}0.4997s^{5/2} - \frac{1}{7}0.1438s^{7/2} - \frac{1}{9}0.04578s^{9/2} \tag{9.23}$$

and $s = c_f/a$. Since at most $s = 1$, we keep only the first term which has an exponent lower than one.
Equating K_a to K_b, we solve for the far field nominal stress, σ_n, which would result in a zero net stress intensity factor at the tip of the crack. For this problem, we obtain

$$\sigma_n = \frac{0.903}{\alpha} f_t'\sqrt{s} \tag{9.24}$$

Expressed in terms of $r = a_0/c_f$ and $s = 1/(1+r)$, the far field nominal stress will be

$$\sigma_n = \underbrace{\frac{0.903}{\alpha}}_{B} f_t' \sqrt{\frac{1}{1+\underbrace{r}_{\beta}}} \tag{9.25}$$

For an infinite plate with an edge crack, $\alpha = 1.1215$ [813], and the resulting nominal stress will be

$$\sigma_n = \underbrace{0.805}_{B} f_t' \sqrt{\frac{1}{1+\underbrace{r}_{\beta}}} \tag{9.26}$$

This equation is shown in Figure 9.11.

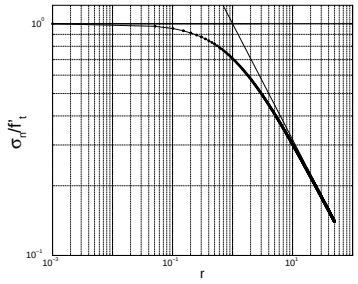

Fig. 9.11: Size Effect Law for an Edge Crack with Constant Cohesive Stresses

Linear Cohesive Stresses

Edge Crack The stress intensity factor for an edge crack subjected to a pair of point forces on opposite faces at a distance x from the crack mouth, Figure 9.12, is given by [327] as

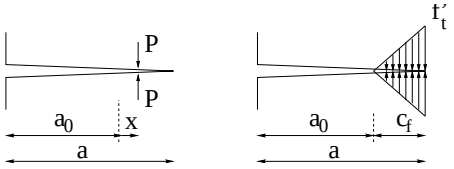

Fig. 9.12: Linear Cohesive Stress Model

$$K_b^P = \frac{2}{\sqrt{\pi}} \frac{1+F(x/a)}{\sqrt{a^2-x^2}} P\sqrt{a} \text{ or } \mathrm{d}K_b^P = \frac{2}{\sqrt{\pi}} \frac{1+F(x/a)}{\sqrt{a^2-x^2}} \mathrm{d}P\sqrt{a} \tag{9.27}$$

where

$$\begin{aligned} F(x/a) = [1-(x/a)^2][0.2945 - 0.3912(x/a)^2 + 0.7685(x/a)^4 \\ -0.9942(x/a)^6 + 0.5094(x/a)^8] \end{aligned} \tag{9.28}$$

The stress intensity factor for a linearly varying stress distribution (analogous to, but not exactly, Barenblatt's model) is simply obtained by replacing $\mathrm{d}P$ by $\frac{\mathrm{d}x}{c_f} f_t'$ in Eq. 9.27 and integrating

$$K_b = \int_{a_0}^{a} K_b^P \mathrm{d}x = \frac{2}{\sqrt{\pi}} \int_{a_0}^{a} \frac{1 + F(x/a)}{\sqrt{a^2 - x^2}} \frac{x}{c_f} f_t' \sqrt{a} \mathrm{d}x \tag{9.29}$$

Equating this stress intensity factor, caused by local plastification, to the far field stress intensity factor given by Eq. 9.21 (with $\alpha = 1.1215$) we solve for the nominal stress σ_n which would cause the net stress intensity factor to be equal to zero. Using $s = (a - a_0)/a$ and expanding in terms of s about $s = 0$, we obtain

$$\begin{aligned} \frac{\sigma_n}{f_t'} = {} & \frac{0.000124102}{s} - \frac{0.0000668046}{\sqrt{s}} - 0.000124102 + 0.535096\sqrt{s} \\ & + 0.0675175 s^{3/2} - 0.388195 s^{5/2} + 0.19108 s^{7/2} - 0.411846 s^{9/2} \\ & + O[s]^5 \end{aligned} \tag{9.30}$$

Even though s is very small, we can drop the first three terms which are negligibly small compared to the others. This is first confirmed by replacing s with $1/(1 + r)$ and plotting Eq. 9.30 with all the terms up to $s^{3/2}$ and the very same equation with the first three terms omitted, Figure 9.13. We observe that those two graphs (plotted on a linear scale to enhance the potential discrepancies) are practically identical with a small deviation in the high range of r.

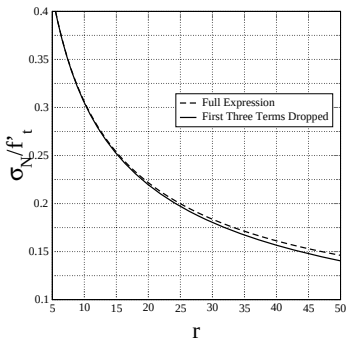

Fig. 9.13: Energy Transfer During Infinitesimal Crack Extension

Hence, we may now justifiably drop the first three terms in Eq. 9.30 and rewrite this equation as:

$$\sigma_n = \frac{0.5351 f_t'}{\sqrt{1+r}} \left(1 + \frac{0.126182}{1+r}\right) + O[s]^2 \tag{9.31}$$

$$= \frac{0.5351 f_t'}{\sqrt{1+r}} \left[-0.0728836 \left(-4.66957 + \frac{1}{1+r}\right) \left(2.93828 + \frac{1}{1+r}\right)\right] + O[s]^3 \tag{9.32}$$

$$= \frac{0.5351 f_t'}{\sqrt{1+r}} \left[0.357092 \left(2.21298 + \frac{1}{(1+r)^2} - \frac{1.46954}{1+r}\right) \left(1.26544 + \frac{1}{1+r}\right)\right] + O[s]^4 \tag{9.33}$$

$$= \frac{0.5351 f_t'}{\sqrt{1+r}} \left[-0.769662 \left(1.16279 + \frac{1}{(1+r)^2 - \frac{0.164699}{1+r}}\right) \left(-1.21723 + \frac{1}{1+r}\right) \left(0.917969 + \frac{1}{1+r}\right)\right] + O[s]^5 \tag{9.34}$$

We note that the derived size effect law contains higher order terms than those originally derived by Bažant through Eq. 9.1.6.1.
Bažant size effect law is recovered through Eq. 9.31 by dropping the second term in the parenthesis. As for Eq. 9.32-9.34, they definitely contain even higher order terms, Figure 9.14.

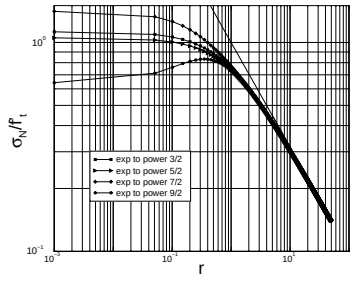

Fig. 9.14: Size Effect Law for an Edge Crack with Linear Softening and Various Orders of Approximation

Three-Point Bend Specimen We then turn our attention to a slightly more complex geometry: a three point bend specimen, Figure 9.15, for which the stress intensity factor is now given by [327] as:

$$K_a = \frac{PS}{BW^{3/2}} \left[2.9(a/W)^{1/2} - 4.6(a/W)^{3/2} + 21.8(a/W)^{5/2} - 37.6(a/W)^{7/2} + 38.7(a/W)^{9/2}\right] \tag{9.35}$$

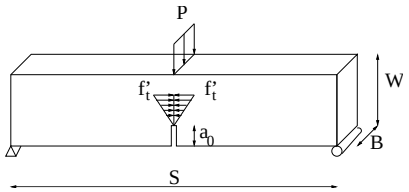

Fig. 9.15: Three Point Bend Specimen with Linear Cohesive Stresses

The stress intensity factor for an edge crack subjected to a linearly varying cohesive stress (Barenblatt's type) K_b, Figure 9.12, was given by Equation 9.29.
As before, equating the two stress intensity factors, solving for σ, substituting $s = (a - a_0)/a$, and expanding in terms of s about $s = 0$, we obtain

$$\frac{\sigma}{f'_t} = -\frac{0.000067298}{s} + \frac{0.0000597828}{\sqrt{s}} + 0.000067298 + 1.06378\sqrt{s} \\ +8.32667 \times 10^{-17}s + 0.132783s^{3/2} + O[s]^2 \tag{9.36}$$

As for Eq. 9.30, it can be shown that we can retain the terms in $s^{1/2}$ and $s^{3/2}$ without loss of accuracy and thus obtain

$$\sigma_n = \frac{1.06738 f'_t}{\sqrt{1+r}} \left(1 + \frac{0.124401}{1+r}\right) + O[s]^2 \tag{9.37}$$

Again, this newly derived size effect law for a three point bend beam with a linearly varying cohesive stress along the fracture process zone is to be contrasted with Eq. 9.1.6.1. Should we drop the second term within the parenthesis, then and only then we will recover an equation analogous to Eq. 9.1.6.1.

Comparison with Experimental Data

In order to assess the results, we closely examine experimental size effects tests on three point bending concrete specimens as reported in Table 1.5.2 of [92].
Table 9.2 gives the compressive strength and $B f'_t$. For the sake of simplification, we assume $f'_t = 0.1 f'_c$ and thus determine the experimental value of the B coefficient. The average experimentally determined value is 1.39 (with a standard deviation of 0.61) and compares relatively well (given the assumption of a Barenblatt cohesive stress model) with the analytically derived value of 1.07 in Eq. 9.37. Interestingly enough, we note that the experimentally determined B value is clearly inversely proportional to the nominal specimen size D_0.

Table 9.2: Experimentally Determined Values of Bf_t', [92]

Series	f_c' MPa	Bf_t' MPa	B	D_0 mm	Reference
A5	46.8	2.9	0.62	212.	[864]
A2	35.4	2.8	0.79	157.	[864]
A4	15.6	1.7	1.09	126.	[864]
B1	34.1	6.0	1.76	60.	[102]
A6	32.7	4.1	1.25	55.	[864]
A1	23.1	4.5	1.95	36.	[864]
A3	14.3	3.2	2.24	34.	[864]

9.2 Micro Cracks

9.2.1 Theoretical Considerations

9.2.1.1 Strength

Griffith [349] addressed the impact of imperfections to the strength of (perfect crystalline) solids by revisiting the work of Inglis [460], and more specifically Equation 4.5. Simply put the nominal strength of a solids with imperfections would be given by

$$\sigma_{nominal} = \sigma_{the}\left(1 + 2\sqrt{\frac{a}{\rho}}\right) \tag{9.38}$$

where σ_{th} is the theoretical strength of solids estimated to be [495]

$$\sigma_{th} \approx \frac{E}{10} \tag{9.39}$$

Which explains why smaller solids, in defiance to the theory of plasticity, have higher strength.

9.2.1.2 Compliance

The impact of imperfections, Figure 9.16(a) on the formation, propagation and compliance in brittle material was experimentally and analytically investigated by the seminal book of Nemat-Nasser and Hori [625].

9.2.1.2.1 Experimental Evidence Figure 9.16(b) is indeed an illustration of the response of flawed (inherently caused by "manufacturing") solids to increasing compressive load. First crack will nucleate (Figure 9.16(c), then they coalesce ((Figure 9.16(d)) and finally failure occurs and is driven by a predominantly coalesced crack ((Figure 9.16(e)).

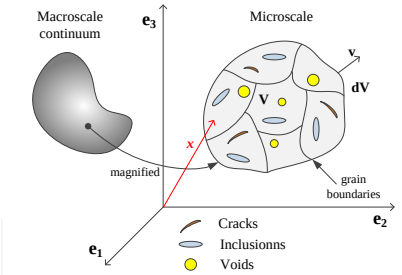

(a) Macro (a) and micro (b) structures of a representative volume in the neighborhood of P [625]



(b) Specimen containing a large number of flaws



(c) Under axial compression without confinement, cracks nucleate first at larger flaws



(d) Axial splitting by the growth and coalescence of cracks



(e) Shattering of a part of the specimen while many flaws in the remaining part are inactive

Fig. 9.16: Experimental evidence of the role of micro-cracks Nemat-Nasser and Hori [625]

9.2.1.2.2 Analytical Considerations In a comprehensive and detailed study, Nemat-Nasser and Hori [625] derived analytical expressions for the impact of microcracks on the compliance (E) of a brittle solid by c Considering penny-shaped microcracks defined by their radius a_α and orientation given by the unit normal $\mathbf{n}_\alpha = \mathbf{n}$, Figure 9.17(a)

$$n_1 = \sin\Psi\cos\theta; \qquad n_2 = \sin\Psi\sin\theta; \qquad n_3 = \cos\Psi \tag{9.40}$$

When there are a very large number of microcracks with radii ranging from a_m to a_M, and with unit normals ranging over all orientations, a density function, $w = w(a,\theta,\Psi)$, may be introduced such that the number of cracks per unit volume with radii in the range of a to $a + da$, and orientations in the range of (θ,Ψ) to $(\theta + d\theta, \Psi + d\Psi)$ is given by $w(a,\theta,\Psi)\sin\Psi da d\theta d\Psi$, then the total number of cracks per unit volume, N, is

$$N = \frac{1}{4\pi}\int_{a_m}^{a_M}\int_0^{2\pi}\int_0^{\pi} w(a,\theta,\Psi)\sin\Psi da d\theta d\Psi \tag{9.41}$$

$\sin\Psi d\theta d\Psi$ defines the elementary solid angle with orientation (θ, Ψ). With θ ranging from 0 to 2π and Ψ ranging from 0 to π, the corresponding unit vector traces a unit sphere. When the crack size distribution is independent of the crack orientation, the density function may be expressed as

$$w(a, \theta, \Psi) = w_r(a) w_0(\theta, \Psi) \tag{9.42}$$

and

$$N = \int_{a_m}^{a_M} w_r(a) da \tag{9.43}$$

$$1 = \frac{1}{4\pi} \int_0^{2\pi} \int_0^{\pi} w_0(\theta, \Psi) \sin\Psi d\theta d\Psi \tag{9.44}$$

Now, if we consider a simple case where: (1) the distribution of microcracks is

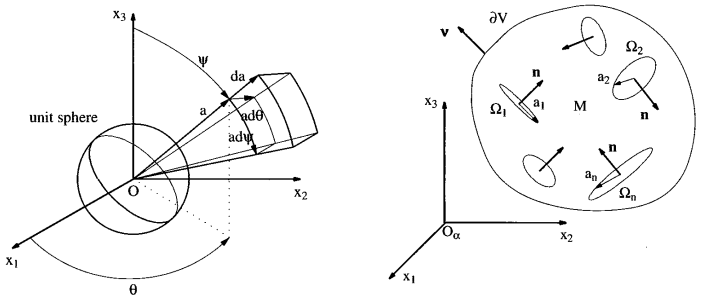

(a) Distribution of radii and unit normals of penny-shaped cracks

(b) A random dilute distribution of microcracks

Fig. 9.17: Analytical model of micro-cracks Nemat-Nasser and Hori [625]

dilute (which assumes that the inhomogeneities are small and far apart, so that their interaction may be neglected) and (2) the crack orientation distribution is random; and (3) the crack size distribution is independent of the crack orientation, Figure 9.17(b). Then, the crack orientation distribution function, $w_0(\theta, \Psi)$ given by Eq. 9.42 becomes

$$w_0(\theta, \Psi) = \text{constant} = 1 \tag{9.45}$$

Then Nemat-Nasser and Hori [625] have shown that

$$\frac{\bar{E}}{E} = 1 - f \frac{16(1-\nu^2)(10-3\nu)}{45(2-\nu)} + O(f^2) \tag{9.46}$$

where
f is the crack density parameter

$$f \equiv \int_{a_n}^{a_M} a^3 w_r(a) da \tag{9.47}$$

and since the microcracks distribution is dilute $f << 1$, for a uniform crack size distribution

$$w_r(a) = \frac{N}{a_M - a_m} \tag{9.48}$$

and the crack density parameter f becomes

$$f = \frac{N}{a_n - a_M} \int_{a_n}^{a_M} a^3 da = \frac{N}{4}(a_M^3 + a_M^2 a_m + a_M a_m^2 + a_m^3) \tag{9.49}$$

if all the microcracks in the RVE have the same radius a then

$$f = N a^3 \tag{9.50}$$

9.2.2 Micro Cracks in Concrete

9.2.2.1 Conjectures

Micro-cracks are omnipresent in concrete. Under tension, we have a macro-crack, and in this context, the model of Hillerborg, Modéer, and Petersson [419] (Figure 9.2) is by now universally accepted, and is characterized by a so-called fracture process zone composed of multiple micro-cracks.
Under compression, micro cracks are most likely to initiate at Interface Transition Zones (ITZ) around (non-shrinking) aggregate, then we do have micro-cracks due to poor vibration.
Micro-cracks will form and extend due to external strain or internal swelling. Hsu et al. [433] were the first to connect the formation (and propagation) of micro-cracks to the nonlinear (compressive) stress strain curve of concrete, Figure 9.18(a). ASR, by virtue of the (often constrained) expansion will induce the formation of micro cracks that will propagate as a result of additional swelling, Figure 9.18(b) and 9.18(c). Indeed, for ASR, the reduced elastic modulus due to ASR (§11.3.3) could conceivably be interpreted through the prisms of Nemat-Nasser and Hori [625]'s model.

9.2.2.2 Physical Evidences

Experimental quantification of the impact of micro-crack on the macro response of concrete is notoriously difficult to achieve.
In a seminal paper, Attiogbe and Darwin [71] measured the submicroscopic cracking of cement paste and mortar under uniaxial compression and compared them to applied strain. They showed that

1. Crack density in cement paste and mortar increases with increasing uniaxial compressive strain, starting at strains as low as 0.0005.

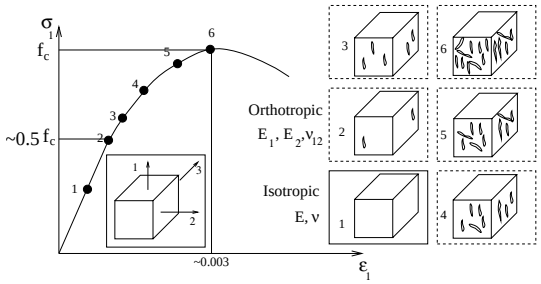

(a) Concrete Stress-Strain Curve Relation to Microcracking

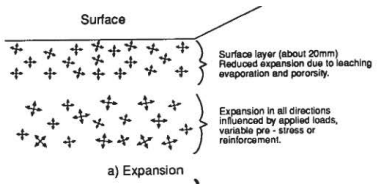

(b) Expansion due to ASR [463]

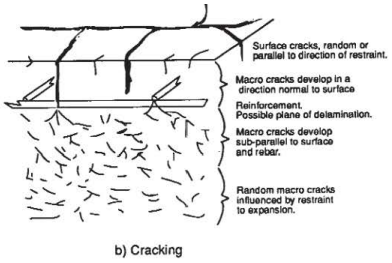

(c) Cracking due to ASR [463]

Fig. 9.18: Development of cracking due to ASR

2. The density of surface cracks in cement paste and mortar is an order of magnitude greater than the density of bond and mortar microcracks in concrete at the same values of compressive strain.
3. Under uniaxial compressive loading, the mean size of submicroscopic cracks increases with increasing strain, Figure 9.19, while the number of cracks per unit volume decreases. This suggests that as compressive strain increases, small cracks *coalesce* to form larger cracks.
4. Under increasing uniaxial compression, three-dimensional distributions of submicroscopic cracks become skewed towards the direction of applied stress.
5. On the average, three-dimensional crack distributions in cement paste show only small variations with water to cement (w/c) ratio. However, at high strains volumetric crack density increases more rapidly the lower the w/c.
6. Crack density is lower initially but increases more rapidly in mortar than in cement paste. Thus, sand particles appear to act as stress raisers that result in a greater degree of softening and a lower strain capacity for mortar than for cement paste.

Landis [521] used three-dimensional measurements of internal cracking and simple relationships were made between the quantity of cracking and a corresponding scalar damage variable. A scalar damage variable was determined from the changes in stiffness measured in successive loading cycles. Results showed a nearly linear relationship between the damage variable and the fractal dimension of the internal

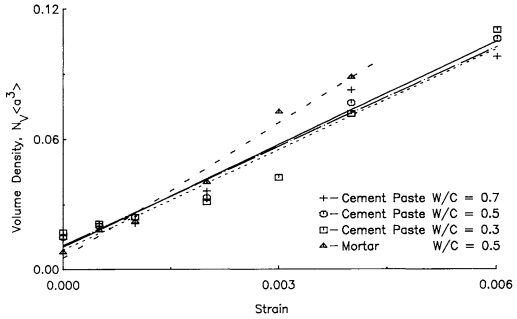

Fig. 9.19: Measure of volumetric crack density $N_v < a^3 >$ versus compressive strain for cement paste, w/c = 0.7, 0.5-, 0.3, and mortar, w/c= 0.5 [71]

crack system. In contrast, results showed a nonlinear relationship between the damage variable and the crack surface area.

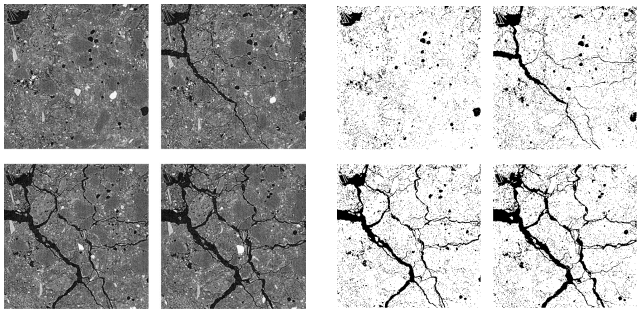

(a) Images of specimen section at different levels of damage

(b) Binary images highlighting crack and void space in the same sections as

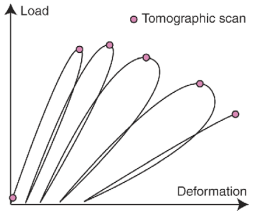

(c) Load-unload cycles and tomographic scans

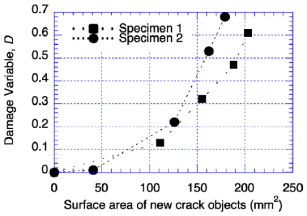

(d) Damage variable plotted against the cumulative increase in crack object surface area

Fig. 9.20: Micro-cracks in solids [521]

Finally, those micro-crack may propagate as a result of creep, and may coalesce leading to failure (of a concrete cylinder or worst a delamination in the absence of reinforcement). This will be addressed next.

9.2.3 Creep Fracture

The structures considered in this book are likely to sustain large, sustained compressive stresses i the presence of internal damage (micro-cracks) possibly caused by ASR. Accordingly their long term response must be ascertained and possibly accounted for in some critical cases.
The time dependence of fracture has two sources: 1) the viscoelasticity of material behavior in the bulk of the structure and 2) the rate process of the breakage of bonds in the fracture process zone which causes the softening law for the crack opening to be rate-dependent [91]. The former is covered in Chapter 5, the later in this section.

9.2.3.1 Load Carrying Capacity

Zhou [917] was the first to experimentally investigate creep fracture in his doctoral research Time-Dependent Crack Growth and Fracture of Concrete). His experimental work has been extensively referenced thereafter, and to the best of the authors knowledge, they have never since been replicated. The premises of the investigation is the observation that if we increase the rate of loading, there is an increase in "strength" [564], would there be a corollary, that is for very slow loading (such as effect of time, or simply creep), there would be a decrease in "strength"? Hence, fracture tests under sustained loading were performed, and an empirical relationship for the rate effect on the fracture energy was determined. It was found that if the stress is close to the tensile strength, then under sustained static loading, we may have a rupture point, Fig. 9.21(a).

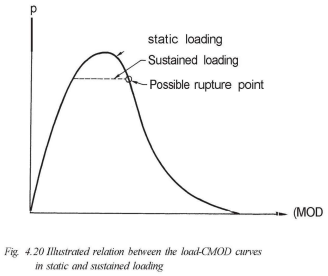

Fig. 4.20 Illustrated relation between the load-CMOD curves in static and sustained loading

(a) Possible Failure Under Sustained Load [917]

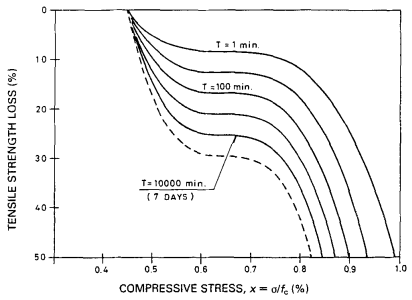

(b) Tensile strength loss *vs* time and sustained compressive stress,[543]

Fig. 9.21: Creep fracture of concrete

Analogous results were obtained by Bažant, Ž. and Gettu, R. [104] who followed a fracture mechanics interpretation, and showed that under sustained loading, behavior shifts from quasi-brittle material to brittle material, Figure 9.22(a). In other words whereas under normal load energy is smeared along the fracture process zone, under sustained load, the fracture process zone tends to shrink to almost zero, and we are now closer to the linear elastic fracture mechanics condition (with singularity at the tip). Likewise, it was found that the load

The work of Zhou [917] (with A. Hillerborg) has been widely referenced by modelers and seldom replicated by experimentalists. It provides ample experimental evidence that creep fracture is a phenomenon to be reckoned with. Carpinteri et al. [167] did carry out additional tests (with Zhou), and those results have been primarily used by the "Italian" school of fracture. They have shown that a slow rate of loading will reduce the peak load, Figure 9.22(b), and more importantly that the mode of failure is altered from one of a quasi-brittle to brittle (i.e approaching linear elastic fracture mechanics), Figure 9.22(a). Likewise, it was found that the load rate will have an influence on the peak load carrying capacity of concrete, Figure 9.22(b).

A theoretical framework for creep fracture was set by Bažant, Ž and Xiang, Y. [105] and Bažant and Li [91].

Application to nuclear container was (indirectly) addressed by Masuero and Creus [578], and most recently by Zijl, Rots, and deBorst [927] who analyzed the test results of Zhou [917] through the models of Bažant and Li [91].

Mihashi and Wittman [591] presented a power low for the tensile strength of concrete in terms of the load rate, which is actually analogous to the one of Zhou [917].

To the best of the authors knowledge, the only experimental work reporting on the decrease of tensile strength due to compression induced "damage" is the one of Liners [543] who first applied compressive loads on concrete specimens, and then determined the splitting tensile strength using a "Brazilian Tests". it was determined that for compressive stresses over 40% of compressive strength there is a substantial (up to 50%) decrease in tensile strength reduction. This tensile strength reduction is further exacerbated by time as shown in Fig. 9.21(b). On a related issue, the role of pre-damage (micro-cracks) in tension of the compressive strength of concrete has also been studied [493].

9.2.3.2 Fracture Energy

In the preceding section, we reported on the impact of creep on load carrying capacity (compression or tension). However, for applications relevant to this book, one seeks to quantify the decrease in G_F and f_t following creep fracture.

Specifically, based on his tests, Zhou [917] has shown that the fracture energy decreases as loading rate decreases. For the tested beams, the fracture energy was found to be related to deflection rate in a poser law

$$\frac{G_F}{G_{F0}} = \left(\frac{\dot{u}}{\dot{u}_0}\right)^{0.04} \tag{9.51}$$

where $\dot{u}$ is the displacement rate, and $\dot{u}_0$=2μm/s.

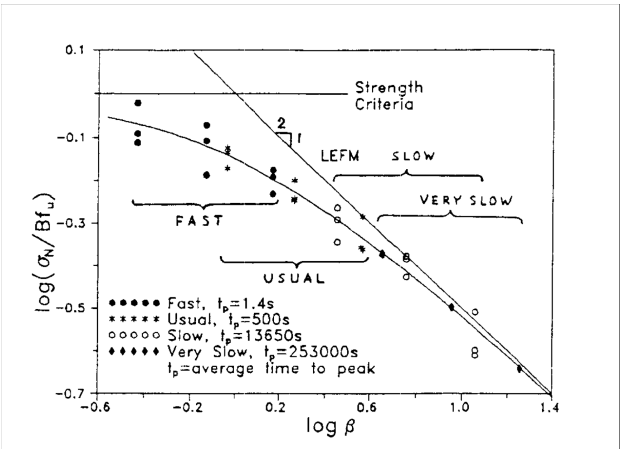

(a) Change in Mode of Failure with Loading Rate

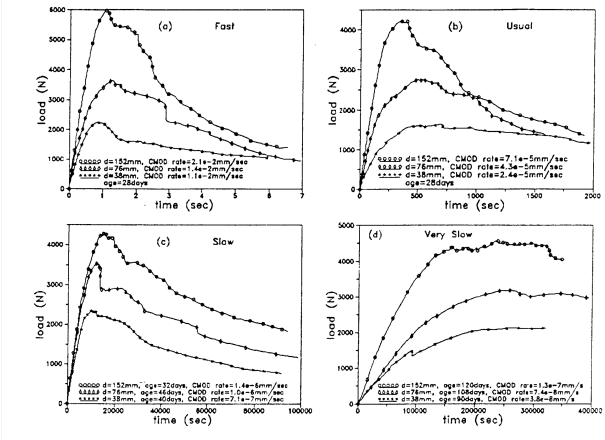

(b) Effect of Loading Rate on Peak Load

Fig. 9.22: Concrete creep study of Bažant, Ž. and Gettu, R. [104]

Alternatively, one can attempt to infer the decrease in G_F from the one of the elastic modulus E. Recalling that the characteristic length is given by (Eq. 9.1)

$$l_{ch} = \frac{EG_F}{f_t^2} \tag{9.52}$$

Bažant [95] estimates that it should drop about 10 times, the long term tensile strength being about 80% of the static one. If we use Equation 5.37 $E_{eff} = E/(1+\Phi)$, then

$$\frac{G_F^{\infty}}{G_F^0} = \frac{\frac{(0.1)l_0(0.8)^2 f_t^2}{\frac{E}{(1+\Phi)}}}{\frac{l_0 f_t^2}{E}}, \; or \quad G_F^{\infty} = 0.192 G_F^0 \tag{9.53}$$

Thus, we could have a decrease of about 80% in G_F as a result of creep fracture.

9.2.4 Coalescence of Micro-Cracks

Using a highly analytical approach, the interaction of adjacent cracks, (such as those in a fracture process zone, or possibly caused by ASR), were first investigated by Hori and Nemat-Nasser [424] and explicit asymptotic expressions are obtained for the stress intensity factors of the macro-crack, as well as those of the micro-cracks. The mechanism of fracture coalescence in hard, porous material has been investigated experimentally and through numerical simulation [784].

It was found that fracture coalescence can be generated by mode I failure, mode II failure, or mixed mode I and II failure, Figure 9.23(a) and 9.23(b). The mode II failure plays an important role in the coalescence between two non-overlapping cracks. The mechanism of coalescence observed in gypsum does not agree with previous experimental results where glass and polymer have been used. For those materials coalescence only occurs between overlapping cracks and is caused by mode I failure. The possible reason why mode II failure can occur in gypsum and other earth materials such as rock and concrete is the existence of voids and pores in these materials. Porous material can absorb the shear dilation in the fracture process zone and prevent the development of resistant stress due to shear dilation. The mode II fracture toughness of material with high porosity is known to be low (in concrete G_F^{II} is about 10 times smaller than G_F^I.

A (mixed mode) crack propagation model was developed for the failures in compression. It is an extension of the classical maximum energy release rate G [452]. However, the authors found that when applied to crack propagation under compressive load, the original G criterion can lead to wrong results, especially for the direction of wing crack initiation and it does not consider difference between mode I surface energy (G_{Icr}) and mode II surface energy (G_{IIcr}). Therefore, a modified G criterion, (called the F criterion, was proposed

$$F = \frac{G_I}{G_{Icr}} + \frac{G_{II}}{G_{IIcr}} \geq 1.0 \tag{9.54}$$

where G_I and G_{II} are the mode I and II energy release rates during crack growth. Extension occurs in the direction θ which maximizes F. Whereas the previous model was experimentally driven(or heuristic in nature), a mechanics based one was followed by Ortiz [669] (albeit for mode I crack propagation only). In this model the author studied the analytical estimation of the effect of microcracking on crack growth initiation in brittle solids, Figure 9.24(a). Particular attention was given to the counteracting effects of toughness degradation and shielding (reduction of the stress intensity factors) by macrocracking, with a view to determining the range of dominance of each mechanism. Crack growth initiation by coalescence

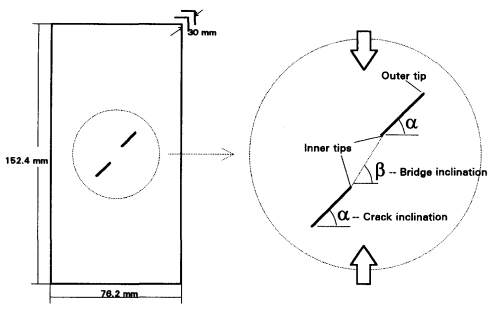

(a) Geometry of gypsum samples and pre-existing cracks [784]

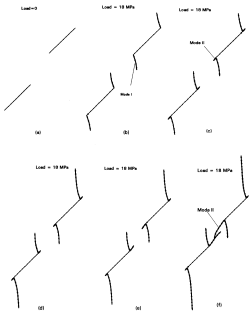

(b) Simulated coalescence of two 45 /105 closed cracks. [784]

Fig. 9.23: Crack coalescence

with microcracks was studied with the aid of a cohesive zone model (analogous to Figure 9.2). The extent of shielding of the crack tip by the intervening microcracks is estimated under isotropic damage conditions. A comparison of hese effects reveals that, were the crack capable of growing within its plane, the toughness enhancement derived from shielding would be almost exactly counterbalanced by the reduction of toughness in the microcracked material.

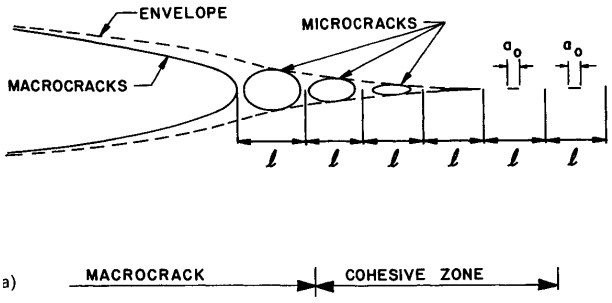

(a) Semi-infinite crack weakened by an array of microcracks [669]

Fig. 9.24: Crack coalescence

Chapter 10
Chloride, Carbonation and Corrosion

Abstract
There are two major forms of environmentally induced concrete deterioration: the first is caused by the ingress of chloride (in marine environments or whenever salt based de-icing is used) and the other by carbonation from the atmosphere. Although per se these ingress will not deteriorate the concrete, they will eventually cause internal rebar corrosion. Given sufficient time, the corrosion will lead to cracking, splitting of the concrete, exposure of the rebars, and formation of what is commonly referred as "pot-holes."
Each of the above-mentioned phenomena will be separately covered in this chapter.

10.1 Introduction

There are four major mechanisms for concrete aging (and thus deterioration): creep (Chapter 5, alkali aggregate reaction (Chapter 11), freeze and thaw (not covered) and chemical induced steel corrosion (this chapter). The three major causes of corrosion are, Figure 10.1:

Chloride Ions: Chlorides ions, present whenever de-icing salts are used or in marine/corrosive environments, will diffuse into the concrete. Concrete has an initial pH around 12-13 and thus protects the reinforcement from corrosion. Whereas chloride ingress will not weaken the concrete, it will lower its PH, and this in turn will depassivate[1] the reinforcing steel leading to the initiation of a half-cell, i.e. corrosion. An important result of corrosion is the volumetric increase around the anode which in turn will lead to cracking/spalling of the surrounding concrete.

Carbonation: Carbonation occurs as a result of the penetration of carbon dioxide from the atmosphere into the concrete. Carbon dioxide will in turn react with calcium hydroxide to form calcium carbonates, thereby reducing the concrete's alkalinity and lowering its pH value. From that point, just as with chloride, a corrosion and cracking process is initiated.

Atmospheric Pollution: Sulfur dioxide in the air (or through acid rain) collects with rain water to form sulfurous acid. This reacts with lime compounds in the

[1] Passivity is the loss of electrochemical reactivity, thereby decreasing the corrosion rate of the metal.

concrete, forming calcium sulfate. Calcium sulfate is only slightly soluble in water and is deposited on or near the surface, forming a skin. The calcium sulfate then crystallizes behind this skin, and differential movements between it and the concrete underneath loosen the concrete and cause disintegration. Polluted air causes erosion, and an originally smooth surface can be weathered away leaving coarse exposed aggregate highly susceptible to deterioration.

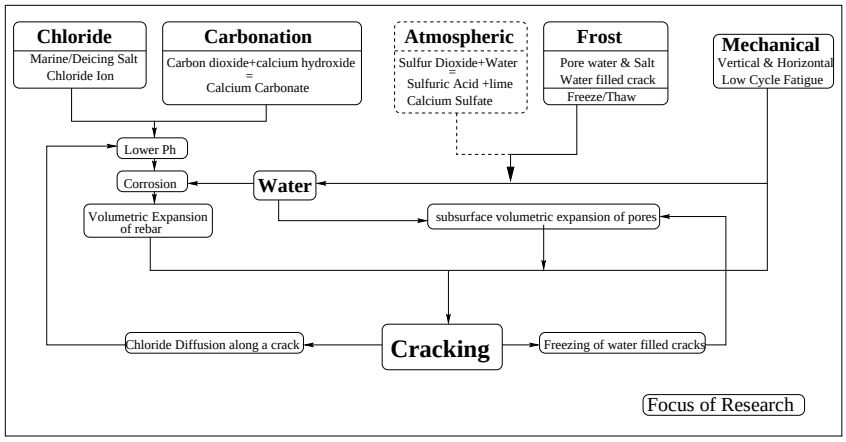

Fig. 10.1: Reinforced Concrete Deterioration Modes (excluding AAR)

Damage caused by chloride ingress into concrete being by far the most consequential one of the three root causes of corrosion, it will be be addressed first. Deterioration is composed of three consecutive phases, Figure 10.2.

1. Phase 1: diffusion of chloride through the concrete beginning at time $t = 0$ with a concrete surface free of chlorides. As time increases, the chloride concentration at the surface initially increases until it reaches its constant value, and the chlorides diffuse through the concrete toward the rebar. At some critical value of chloride and concentrations at the rebar, the pH of the pore solution is reduced enough for major corrosion to begin. Initially, the high pH of the pore solution protects the steel by maintaining its passivity. As the pH of the pore solution is reduced, the passivity of the steel is also reduced, and at a sufficiently low pH, corrosion initiates. The result of this first phase is the determination of chloride concentration at the rebar as a function of time. This in turn will be used to determine the formation of the anode and cathode.
2. Phase 2: corrosion of the rebar. Electric current will pass between anode and cathode. Knowing the value of the current will enable the determination of the corrosion rate. Once the corrosion rate is determined, the amount of rust produced over time can be computed and applied to the stress analysis of the concrete.
3. Phase 3: cracking of the concrete.

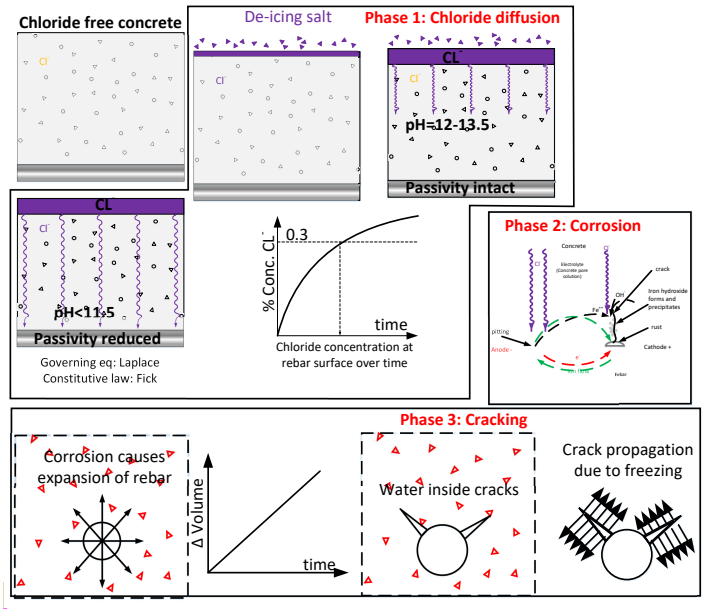

Fig. 10.2: Outline of mechanical damage in reinforced concrete initiated by chloride diffusion

Each one of those phases will be addressed separately.

10.2 Chloride Diffusion Analysis in Concrete

Again, concrete protects steel from corrosion; however when chloride concentration reaches a critical level (and its PH reaches $\sim$ 11.5), its protective environment is destroyed, and the corrosion of the reinforcing steel bars embedded in concrete starts. An important consideration is that when chloride ions penetrate into concrete, some of them will be bound to the internal surface of cement paste and aggregate. They are called bound chloride. The others, called free chloride, will diffuse freely throughout the concrete.
There are two approaches to simulate chloride penetration:

Fick's Law is the conventional diffusion theory based on mass conservation. The problem with this approach is that the differential equation parameters are all effective parameters at large scale, that is they are averaged over a representative volume. To account for chemical and physical mechanisms which occur on small scale, many simplified formulas are assumed resulting in as many empirical formulas.

Nernst-Plank Equation is a conservation of mass equation used to describe the motion of a charged chemical species in a fluid medium. It extends Fick's law of

diffusion for the case where the diffusing particles are also moved with respect to the fluid by electrostatic forces.

10.2.1 Fick's Laws

Fick's law describes the diffusion that occurs when solutions of different concentrations come into contact, with molecules moving from regions of higher concentration to regions of lower concentration. In the context of chloride diffusion, it governs the diffusion of the free chloride into the concrete. There are two variants to the law: the first and the second.
Fick's first law relates the diffusive flux to the concentration under the assumption of steady state. It postulates that the flux goes from regions of high concentration to regions of low concentration with a magnitude that is proportional to the concentration gradient (spatial derivative), or in simplistic terms, the concept that a solute will move from a region of high concentration to a region of low concentration across a concentration gradient. It is the counterpart of Fourier's law in the heat equation (Eq. 2.1).
In one (spatial) dimension, the law is:

$$q = -D\frac{d\phi}{dx} \tag{10.1}$$

where

- q is the "diffusion" of which the dimension is amount of substance per unit area per unit time, so it is expressed in such units as mol L^{-2} s^{-1}. It measures the amount of substance that will flow through a unit area during a unit time interval.
- D is the diffusion coefficient or diffusivity. Its dimension is area per unit time, so typical units for expressing it would be L^2/s.
- ϕ (for ideal mixtures) is the concentration, of which the dimension is amount of substance per unit volume. It might be expressed in units of mol/L^3.
- x is position, the dimension of which is length. It might thus be expressed in the unit m.
- D is proportional to the squared velocity of the diffusing particles, which depends on the temperature, viscosity of the fluid, and the size of the particles according to the Stokes-Einstein relation.

Fick's second law predicts how diffusion causes the concentration to change with time. From Eq. 2.35:

$$\rho c\frac{\partial\phi}{\partial t} = \frac{\partial}{\partial x}\left(k_x\frac{\partial\phi}{\partial x}\right) + Q \tag{10.2}$$

For k_x = constant and $Q = 0$ then we obtain Fick's second law:

$$\frac{\partial\phi}{\partial t} = \underbrace{\frac{k_x}{\rho c}}_{D}\frac{\partial^2\phi}{\partial^2 x} \tag{10.3}$$

The closed-form solution of Fick's law is given by

$$\phi(x,t) = \phi_o \left(1 - erf\left[\frac{x}{2\sqrt{Dt}}\right]\right) \tag{10.4}$$

where (and is shown in Figure 10.3)

- ϕ_o is the constant surface concentration, lbs/yd^3 (kg/m^3)
- erf = error function
- t = time of exposure to ϕ_o.
- D = diffusion constant, L^2/t.

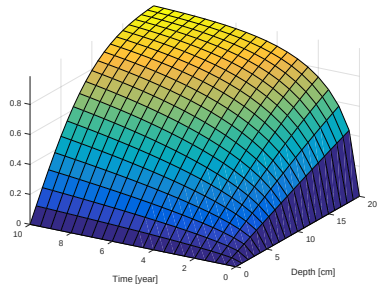

Fig. 10.3: Normalized solution of Fick's second law of diffusion

10.2.2 Chloride Diffusion in Concrete

This subsection is largely based on the work of Xi and Bažant [892] and Ababneh, Benboudjema, and Xi [2] for the theory and Puatatsananon and Saouma [714] and Hansen and Saouma [365] for the numerical implementation.
Dealing with chloride concentration, we now replace the general variable ϕ by C. For unsaturated concrete, the chloride diffusion is given by

$$\frac{\partial C_f}{\partial t} = \frac{\partial C_f}{\partial C_t}\left(\nabla.[D_{Cl}\nabla(C_f)] + \mu\frac{\partial W}{\partial t}C_f\right) \tag{10.5}$$

$$\frac{\partial C_f}{\partial t} = \frac{\partial C_f}{\partial C_t}\left(\nabla.[D_{Cl}\nabla(C_f)] + \mu\frac{\partial W}{\partial H}\frac{\partial H}{\partial t}C_f\right) \tag{10.6}$$

where

C_t = Total chloride concentration in grams of total chloride per gram of concrete (g/g)
C_f = Free chloride concentration in grams of free chloride per gram of concrete (g/g)
t = time in days
D_{Cl} = Chloride diffusivity of concrete (cm^2/day)
$\partial C_f/\partial C_t$ = Binding capacity of concrete
μ = $\frac{1}{\rho_{sol}\beta_{sol}}$ (unit converter to gram of chloride per gram of concrete)
β_{sol} = Ratio of the volume of pore solution to the weight of concrete
ρ_{sol} = Density of pore solution in grams of pore solution per liter
$\frac{\partial W}{\partial H}$ = Moisture capacity of concrete
$\frac{\partial H}{\partial t}$ = Rate of change of pore relative humidity

For saturated concrete the term $\frac{\partial H}{\partial t}$ vanishes, and the governing differential equation for chloride diffusion reduces to

$$\frac{\partial C_f}{\partial t} = \frac{\partial C_f}{\partial C_t}\nabla.[D_{Cl}\nabla(C_f)] \tag{10.7}$$

To solve Eq.10.7 and Eq.10.6, the two material parameters which are binding capacity (dC_f/dC_t) and chloride diffusivity (D_{Cl}) must be first determined.

10.2.2.1 Binding Capacity of Concrete

The total chloride concentration is defined as

$$C_t = C_f + C_b \tag{10.8}$$

where C_b is bound chloride concentration in grams of bound chloride per gram of concrete, and the binding capacity is defined as

$$\frac{dC_f}{dC_t} = \frac{1}{\frac{dC_t}{dC_f}} = \frac{1}{\frac{d(C_f+C_b)}{dC_f}}\frac{1}{1+\frac{dC_b}{dCf}} \tag{10.9}$$

The chloride isotherm, dC_b/dC_f, can be measured experimentally. The binding capacity of concrete can be evaluated by two different chloride isotherm models, namely Freundlich isotherm and Langmuir isotherm.
The relationship between free and bound chloride which was established on the basis of Freundlich isotherms [820] is given by

$$\log(C_b') = A\log(C_f') + B \text{ or } C_b' = (C_f')^A 10^B \tag{10.10}$$

where A and B are two material constants related to chloride adsorption, C_b' is the bound chloride expressed in milligrams of bound chloride per gram of calcium silicate hydrate (C-S-H) gel, and C_f' is the free chloride expressed in free chloride per liter of pore solution (mol/L).
It was shown in [820] that A = 0.3788 and B = 1.14; hence binding isotherm is nonlinear. The advantage of this unit system is that the Freundlich isotherms are now

independent of w/c and concrete aggregates. However in practice, it is necessary to use the unit system of C_b and C_f. Therefore, the conversion of the two unit systems is needed. It can be shown as follows:

$$C_f = 35.45\beta_{sol}C'_f \tag{10.11}$$

$$C_b = \frac{\beta_{\text{C-S-H}}C'_b}{1,000} \tag{10.12}$$

where β_{sol} is the ratio of volume of pore solution to weight of concrete (L/g); β_{C-S-H} is the ratio of weight of C-S-H gel to weight of concrete (g/g).
By substituting the values of C_b and C_f in Eq.10.12 into Eq. 10.10, we obtain

$$C_b = \frac{\beta_{\text{C-S-H}}}{1,000}\left(\frac{C_f}{35.45\beta_{sol}}\right)^A 10^B \tag{10.13}$$

The chloride isotherm can be determined by taking the derivative of C_b from Eq. 10.13 with respect to Cf. Then by substituting the chloride isotherm into Eq. 10.9, we obtain the binding capacity as follows[892]:

$$\frac{\partial C_f}{\partial C_t} = \frac{1}{1 + \frac{A10^B\beta_{\text{C-S-H}}}{35,450\beta_{sol}}\left(\frac{C_f}{35.45\beta_{sol}}\right)^{A-1}} \tag{10.14}$$

From this equation, the binding capacity is the function of the two parameters which are β_{sol} and $\beta_{\text{C-S-H}}$. β_{sol} in turn is given by

$$\beta_{sol} = \frac{V_{sol}}{W_{conc}} = \frac{W_{sol}}{\rho_{sol}W_{conc}} = \frac{n(H,T)}{\rho_{sol}} \tag{10.15}$$

where

ρ_{sol} = Density of the solution (g/L). Since it varies little, it is assumed to be equal to density of pore water
V_{sol} = Volume of pore solution
W_{sol} = Weight of pore solution
W_{conc} = Weight of concrete
$n(H,T)$ = Adsorption isotherm of concrete
H = Humidity, for saturated concrete $H = 1.0$

For the parameter $f_{\text{C-S-H}}$,

$$f_{\text{C-S-H}} = \frac{V_{\text{C-S-H}}}{V_{tot}} = \frac{V_{tot} - V1 - V_{cp}}{V_{tot}} = 1 - f_1 - f_{cp} \tag{10.16}$$

where V_{cp} is the volume of the capillary pores, V_1 and f_1 are the volume and the volume fraction of the anhydrous cores of cement grains and of all the crystalline phases, such as CH.
Since the specific gravities of concrete and C-S-H are very close, then $\beta_{\text{C-S-H}} \simeq f_{\text{C-S-H}}$.

10.2.2.2 Chloride Diffusivity of Concrete

The chloride diffusivity of concrete can be affected by several parameters, and it can be evaluated based on multi-factor method by Ababneh, Benboudjema, and Xi [2] as follows:

$$D_{cl} = f_1(g_i) f_2(w/c, t_0) f_3(T) f_4(H) f_5(C_f) \tag{10.17}$$

where
$f_1(g_i)$ = Effect of aggregate factor
$f_2(w/c, t_0)$ = Effect of water to cement ratio and curing time factors
$f_3(T)$ = Effect of temperature factor
$f_4(H)$ = Effect of pore relative humidity factor
$f_5(C_f)$ = Effect of chloride concentration factor

10.2.2.2.1 f_1, Effect of Aggregates

The effective diffusivity of the concrete, which accounts for the presence of aggregates, can be determined by means of the composite material theory. It is given by

$$f_1(g_i) = D_m \left[1 + \frac{g_i}{\frac{1-g_i}{3} + \frac{D_m}{D_i - D_m}} \right] \tag{10.18}$$

where
D_i = Diffusivity of inclusions (aggregates)
D_m = Diffusivity of the matrix (cement paste)
g_i = Volume fraction of the inclusions
D_{eff} = Effective diffusivity
The interface transition zone (ITZ) between aggregates and cement paste can also play an important role. It has a higher porosity (thus diffusivity) than the cement paste. This should be accounted for if there is a low aggregate contents(less than 50%). For higher values (as in this study) most of the cement paste is constituted of ITZ, and thus the cement property is considered to be constant.
The diffusivity of porous materials can be determined by the Kozeny-Carman equation (used in fluid mechanics to calculate the pressure drop of a fluid flowing through a packed bed of solids):

$$D = \frac{V_p^3}{S^2 K_k} \tag{10.19}$$

where D is the diffusivity, V_p is the porosity, S is the specific area, and K_k is the a factor which accounts for the tortuosity. However, this equation is not often applied since 1) not all the porosity is available for transport of moisture, chloride or other chemicals, and 2) the specific surface area almost always overestimates the length scale for fluid flow.
One modification of this equation is

$$D = \frac{2[1 - (V_p - V_p^c)]}{S^2} (V_p - V_p^c)^f \tag{10.20}$$

where $f = 4.2$ and V_p^c is the critical porosity which is 3%.
D_i can be evaluated from Eq. 10.20 (if S, V_p and V_p^c for the aggregates are known) or may be taken as a constant equal to 1×10^{-12} cm/s. D_m can be evaluated also from Eq. 10.20 if S can be estimated through V_m. Porosity V_p for the cement paste can be estimated by using the adsorption isotherm at saturation ($H = 1$), and note that $n(H, T)$ is defined as a weight ratio and must be converted to a volume fraction by multiplying by bulk specific gravity of cement paste which has an estimated value about 2.5.

10.2.2.2.2 f_2, Effect of w/c and curing time

To account for the effect of water to cement ratio and the curing time, the factor is evaluated as follows:

$$f_2(w/c, t_0) = \left[\frac{1}{4} + \frac{(28 - t_0)}{300}\right]\left(\frac{w}{c}\right)^{6.55} + \frac{28 - t_0}{62,500} \tag{10.21}$$

which is valid for concrete with t_0 less than 28 days; for concrete older than 28 days, f_{Cl} takes the 28 day values.

10.2.2.2.3 f_3, Effect of Temperature

The temperature has an important effect on the diffusivity. It changes the the adsorption heat, and its effect has already been included in the BET adsorption model. It also increases the frequency of thermal vibrations of the diffusant, which can be accounted for by the Arthenius's law:

$$f_3(T) = \exp\left[\frac{U}{R}\left(\frac{1}{T_0} - \frac{1}{T}\right)\right] \tag{10.22}$$

where
T_0 = Reference temperature (K)
T = Current temperature (K)
D_T = Diffusivity at temperature T
D_0 = Reference diffusivity
R = Gas constant
U = The activation energy of the diffusion process.
It depends on w/c which can be shown in Table 10.1.

10.2.2.2.4 f_4, Effect of Pore Relative Humidity

The effect of pore relative humidity on chloride diffusivity can be taken into account using the model proposed by Bažant and Najjar [101] as follows:

Table 10.1: Activation energies for various cement pastes

	U (KI/mol)	
w/c	Ordinary Portland cement	Cement with Pozzolans
0.4	41.8±4.0	-
0.5	44.6±4.3	4.18
0.6	32.0±2.4	-

$$f_4(H) = \frac{1}{1 + \left(\frac{1-H}{1-H_c}\right)^4} \tag{10.23}$$

where H_c = 0.75 is critical pore relative humidity.

10.2.2.2.5 f_5, Effect of Chloride Concentration

The chloride diffusivity is concentration dependent, which makes Eq. 10.7 nonlinear. The major resistance to the diffusion process is due to wall effect, i.e. interaction of the diffusant with the pore wall.
However for ions, the movement is restricted by the electrostatic field introduced by the other ions present in the solution. The effect of free chloride concentration on the chloride diffusivity can be expressed by

$$f_5(C_f) = 1 - k_{ion}(C_f)^m \tag{10.24}$$

where $m = 0.5$ and $k_{ion} = \sqrt{70}$[892].

10.2.3 Final Algorithm for Chloride Diffusion

Finally, the algorithm to determine chloride diffusion can be schematically represented by Figure 10.4 and can relatively easily be implemented in a Matlab based finite difference code [714].

10.3 Carbonation

10.3.1 Physical Description

The carbonation of concrete is a chemical reaction in the presence of water between the hydration product of hardened cement and carbon dioxide which diffuses from the surrounding environment into the concrete leading to the formation of calcium carbonates.
The chemical reaction between CO_2 with each hydration product and the final products of each reaction can be shown as follows:

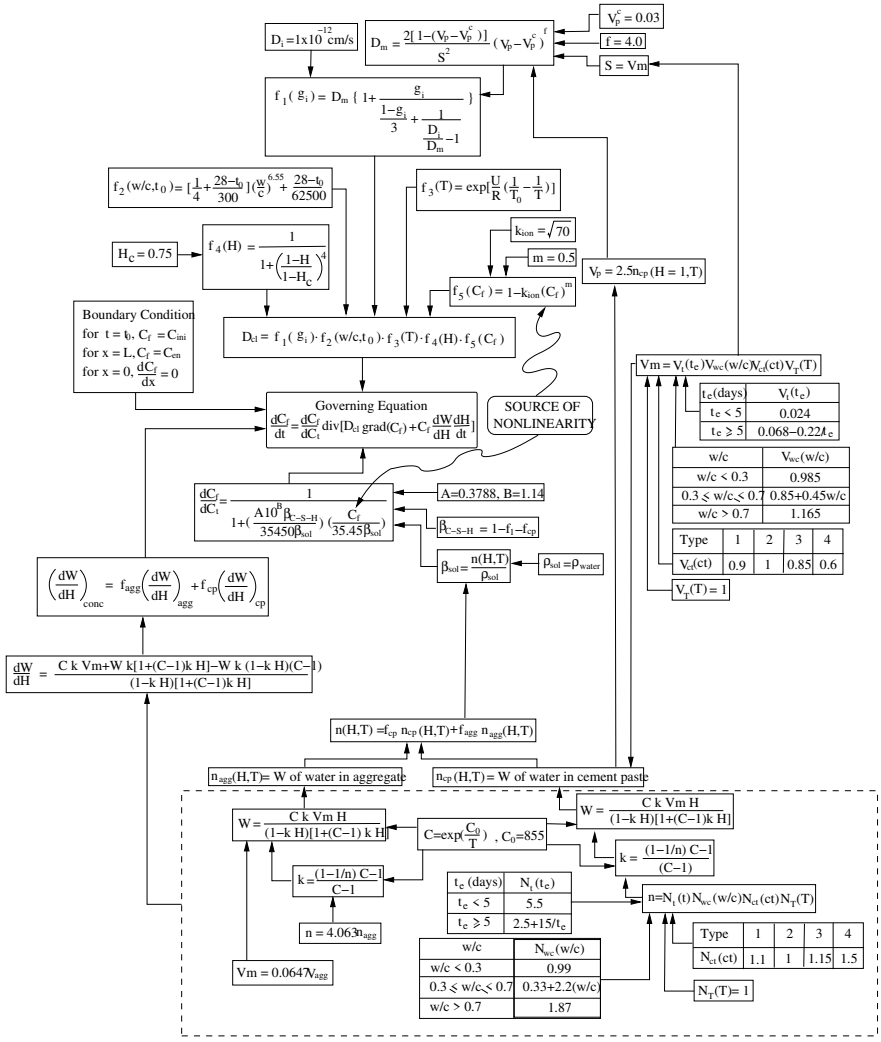

Fig. 10.4: Algorithm for chloride diffusion analysis

1. Calcium hydroxide $Ca(OH)_2$ [679]

$$CO_2 + Ca(OH)_2 \xrightarrow{H_2O} Ca(CO)_3 + H_2O \tag{10.25}$$

2. CaO in calcium silicate hydrate(CSH) [679]

$$(3\text{CaO.2SIO}_2\text{.3H}_2\text{O}) + 3CO_2 \xrightarrow{H_2O} (3\text{CaCO}_3\text{.2SIO}_2\text{.3H}_2\text{O}) \tag{10.26}$$

3. Alumina-containing hydrate phases ($CAF, CAFH$ and $CASH$) [18] also react with carbon dioxide. The final products of this reaction are calcium aluminum hydroxide and chemically bound water.

Since the concentration of calcium hydroxide in the normal concrete is higher than the concentration of the other hydration products, the reaction between $Ca(OH)_2$ and CO_2 predominates[745].
The reaction, illustrated by Eq. 10.25, actually occurs in two steps:

$$H_2O + CO_2 \longrightarrow \mathrm{HCO_3^-} + \mathrm{H^+} \tag{10.27}$$

$$\mathrm{HCO_3^-} \longrightarrow \mathrm{CO_3^{2-}} + \mathrm{H^+} \tag{10.28}$$

$$Ca(OH)_2 + 2\mathrm{H^+} + \mathrm{CO_3^{2-}} \longrightarrow Ca(CO)_3 + 2H_2O \tag{10.29}$$

First, carbon dioxide in the surrounding environment (where its concentration is approximately 350 ppm or 0.03-0.04% by volume; higher values are present in urban areas) penetrates into the capillary pores of concrete and combines with pore water to form carbonic acid. The carbonic acid then reacts with the solid calcium hydroxide dissolved in the pores of concrete to form calcium carbonates according to Eq. 10.29.

10.3.1.1 Effects of carbonation on concrete durability

The main effect of carbonation is the drop of pH of the pore solution of concrete from 12.5-13.5 to ∼8.3. This in turn will result in the depassivation of the steel which may undergo an electrochemical or galvanic corrosion. Carbonation will also reduce the following properties of concrete:

1. Total porosity [429, 637]; it is shown in De Ceukelaire and Van Nieuwenburg [232] that in the conversion of $Ca(OH)_2$ to $CaCO_3$ there is a solid volume increase around 11%; hence a reduction of porosity.
2. Water adsorption isotherm [429, 131]
3. BET specific area [429]
4. Humidity diffusivity of concrete [430]
5. Hydraulic conductivity [773]
6. Chloride binding capacity [422]
7. Chloride diffusion [458]

10.3.1.2 Factors affecting the carbonation rate

The rate of the carbonation process is controlled physically by the carbon dioxide diffusion into concrete and chemically by the amount of calcium hydroxide in concrete [745]. The factors which affect the rate of carbonation can be divided into two groups which are environmental conditions and compositions of concrete.

10.3.1.2.1 Environmental conditions which will affect the rate of carbonation are relative humidity, temperature, the exposed condition of concrete, and the CO_2 concentration in the air.

Relative Humidity: From Eq. 10.25, the carbonation reaction can take place when there are water and carbon dioxide in the pores of concrete. That means the carbonation cannot occur when the concrete is completely dry. Also in the fully saturated concrete, carbonation hardly occurs because the water blocks the pores and reduces the diffusion of CO_2 (the rate of CO_2 diffusion in the water is 10^{-4} times slower than in the air [18]). It is generally accepted that the maximum rate of carbonation occurs when the concrete is exposed to the environmental relative humidity of 50-60% [799].

Temperature: Carbonation is a chemical reaction process. Therefore, the rate of it depends on temperature. The rate of carbonation will increase as the temperature increases [18].

Environmental CO_2 concentration: The rate of carbonation depends on the concentration of CO_2 (Eq.10.25). Therefore, under poor conditions where the concrete is exposed to a much higher CO_2 content from the average value 0.03% by volume, for example the environment of industrial or a large town, carbonation proceeds correspondingly faster[18].

Exposure: Soroka [799] has shown that the carbonation rate of the concrete stored under constant lab conditions is slower than the one of the same concrete exposed outdoors. Also, less carbonation occurs in concrete which is exposed outdoors unprotected from rain than in the same concrete which is protected from rain.

10.3.1.2.2 Compositions of concrete also plays an important role in causing carbonation. This includes:

Water to cement ratio: It was determined that high w/c ratios will lead to greater depth of penetration, Table 10.2; we note the importance of providing adequate cover to limit carbonation.

Table 10.2: Typical rate of penetration of carbonation

Depth of Carbonation (mm)	Age (years)	
	20 MPa Concrete	40 MPa Concrete
5	0.5	4
10	2	16
15	4	36
20	7	64

Curing time: Ho and Lewis [421] have shown that "the carbonation rate decreased as the curing duration was increased from one to seven days but remained practically unaffected when the curing was extended beyond seven days," Table 10.3.

Cement: Type and cement content [685] also affect carbonation rate.

Table 10.3: The influence of curing time on carbonation rate in $mm/w^{0.5}$ (Adapted from [421])

curing time	28 day strength (MPa)			
(days)	47	38	29	23
1	5.7	7.1	8.8	9.4
7	1.6	4.0	5.5	7.6
28	1.1	3.8	5.5	7.3
91	1.2	3.9	5.3	7.6
365	1.0	3.9	5.4	6.9

10.3.2 Governing Differential Equation

This section is based on the work of Saetta, Schrefler, and Vitaliani [745] and Saetta, Schrefler, and Vitaliani [746]. Since the diffusion of carbon dioxide depends on the moisture content of the pores, the temperature, and carbon dioxide atmospheric concentration, the equation for CO_2 diffusion is coupled with the differential equation governing heat and mass flow (expressed in terms of pore humidity) in concrete.

10.3.2.1 Carbonation Process

The amount of $Ca(CO)_3$ that forms in a unit of time depends on the degree of carbonation (i.e. availability of $Ca(OH)_2$), temperature T, CO_2 concentration, and the relative humidity H in the concrete pores. Thus, we can write

$$v = \frac{\partial Ca(CO)_3}{\partial t} = f(H,T) \times [Ca(OH)_2] \times [CO_2] = \frac{\partial c}{\partial t} \tag{10.30}$$

where we can express $f(H,T)$ as follows:

$$f(H,T) = f_1(H) \times \alpha_1 \times k \tag{10.31}$$

where $k = Ae^{-E_0/RT}$ represents the Arrhenius equation for thermally activated processes, α_1 is a material parameter, and $f_1(H)$ accounts for the influence of moisture on carbonation.
Hence, as suggested by Wittmann and Brieger [886], the rate of chemical reaction per unit time can be rewritten as

$$v = \frac{\partial c}{\partial t} = \frac{\partial Ca(CO)_3}{\partial t} = \alpha_1 . f_1(H) . f_2(g) . f_3(c) . f_4(T) \tag{10.32}$$

where $f_1(H)$ is introduced to reflect the fact that the reaction (Eq. 10.25) can only occur in the presence of water.

$$f_1(H) = \begin{cases} 0 & o \leq H \leq 0.5 \\ \frac{5}{2}(H - 0.5) & 0.5 \leq H \leq 0.9 \\ 1 & 0.9 \leq H \leq 1 \end{cases} \tag{10.33}$$

$f_2(g)$ ranges between 0 (where carbon dioxide has not yet penetrated) and 1 (where carbon dioxide concentration is equal to its maximum, g_{max}).

$$f_2(g) = \frac{g}{g_{max}} \tag{10.34}$$

$f_3(c)$ reflects the influence of degree of carbonation, $\mathcal{R}$, and will thus vary between 0 and 1.

$$f_3(c) = 1 - \mathcal{R}^m \tag{10.35}$$

where

$$\mathcal{R} = \frac{Ca(CO)_3}{Ca(CO)_{3\,max}} \tag{10.36}$$

$Ca(CO)_{3\,max}$ is the concentration for which the chemical degradation process reaches its maximum effect and m is usually taken as 1.

$$f_4(T) = Ae^{-E_0/RT} \tag{10.37}$$

Above is the Arrhenius equation where E_0 is the activation energy of the carbonation process, R the gas constant, and T is the absolute temperature. Finally, α_1 is a factor which reflects the concrete characteristics.

10.3.2.2 Carbon dioxide diffusion

The differential equation describing the carbon dioxide diffusion process into porous materials, such as concrete, can also be described by the usual diffusion equation:

$$\frac{\partial g}{\partial t} = \nabla.(D_g.\nabla g) - \frac{\partial g_c}{\partial t} \tag{10.38}$$

where D_g is the diffusivity of carbon dioxide which depends on temperature, relative humidity content of the concrete, curing time, and amount of carbonation which reduces the porosity of the concrete. It is given by

$$D_g(H, T, t_e, c) = D_{g28}.F_1^*(H).F_2(T).F_3(t_e).F_4(c) \tag{10.39}$$

$$F_1^*(H) = (1 - H)^{2.5} \tag{10.40}$$

$$F_2(T) = \exp\left(\frac{Q}{RT_0} - \frac{Q}{RT}\right) \tag{10.41}$$

$$F_3(t_e) = \chi + (1 - \chi)\sqrt{\frac{28}{t_e}} \tag{10.42}$$

$$F_4(c) = 1 - \zeta\mathcal{R} \tag{10.43}$$

where D_{g28} is the diffusivity of carbon dioxide in the standard condition (28 days curing, temperature = 25 ^{o} C); $F_1^*(H)$, $F_2(T)$, $F_3(t_e)$, and $F_4(c)$ take the effect of humidity, temperature, curing time, and the reduction of the diffusivity due to precipitation of carbonation, respectively, into account.
The second term in Eq. 10.38 accounts for the loss of carbon dioxide and

$$\frac{\partial g_c}{\partial t} = \alpha_4 \frac{\partial c}{\partial t} \tag{10.44}$$

where $\partial c/\partial t$ is given by Eq. 10.32. α_4 is a non dimensional parameter varying between 0 and 1 according to the concrete characteristics.
The equations of carbon dioxide diffusion and carbonation process are summarized in Figure 10.5.

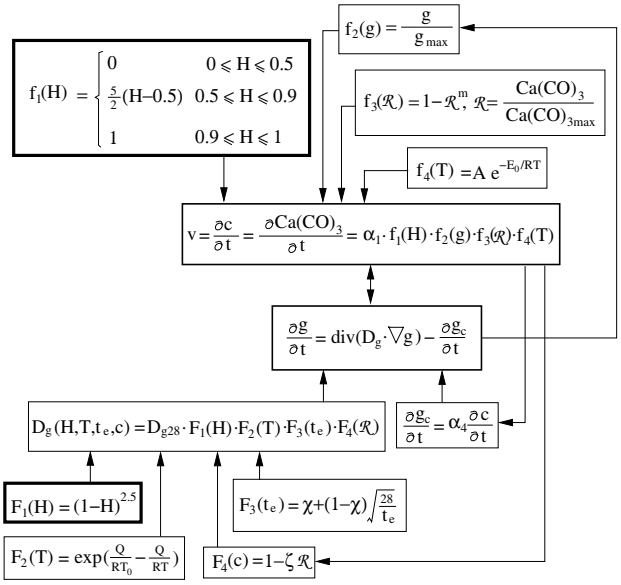

Fig. 10.5: Flowchart of Carbon Dioxide Diffusion and Carbonation Process

10.4 Corrosion

This section on corrosion is taken from Hansen [367] and Hansen and Saouma [366].

10.4.1 Passivity

10.4.1.1 Reinforcement

Reinforcing steel in concrete is initially protected from corrosion by passivity. Jones [483] defines passivity as "a condition of corrosion resistance due to formation of thin surface films under oxidizing conditions with high anodic polarization." The thin surface films are protective surfaces, shielding the metal from the corrosive solutions. A passive film forms for iron by a direct electrochemical reaction, Eq.10.45.

$$\mathrm{Fe} + 2H_2O \rightarrow \quad \mathrm{Fe(OH)_2} + \quad 2\mathrm{H^+} + \quad 2\mathrm{e^-} \tag{10.45}$$

The actual structure of the surface film has not been defined because it is very thin and fragile. Optical measurements have found the film to be 1 to 10 nm in thickness. The accepted structure of passive films on iron is an inner layer of Fe_3O_4 under an outer layer of Fe_2O_3. The overall anodic reaction for iron passivity is given by Eq. 10.45.
While the exact chemistry of passivity is complex and still not completely well understood, it is an important factor in corrosion of reinforcing steel in concrete. It will be shown in the next section that passivity is dependent on the pH of the concrete pore solution, which in turn is affected by chloride ions.

10.4.1.2 Passivity and pH

As discussed previously, the presence of OH^- ions in concrete create an alkaline environment, which has been shown to preserve steel passivity. Introducing Cl^- ions into the environment lowers the pH of the concrete enough to cause depassivation of the steel. The relation between pH and passivity is discussed in this section.
Gouda [347] studied the relation between pH and passivity while conducting experiments with steel bars submerged in alkaline solutions. He determined that in pure alkaline solutions, the critical pH above which passivity is preserved is 11.5. This critical pH value increases when the solution is contaminated with aggressive ions such as Cl^- . Gouda found that a linear relationship exists between the pH of the alkaline solution and the highest concentration of sodium chloride that can be tolerated (Cl^- /OH^-). This relation is expressed as

$$pH = n \log C_{Cl^-} + K \tag{10.46}$$

where n and K are constants.

10.4.2 Corrosion Process

With the protective passivity of reinforcing steel broken by chlorides, corrosion of the steel may begin.
Hertlein [414] summarizes the corrosion process as follows, Figure 10.6. In corrosion, small electrical currents flow between areas of different voltage potential on the reinforcing steel. The currents flow between the areas through an "electrolyte." In

concrete the electrolyte is the pore solution. The current transports electrons freed in the anodic reaction to the cathode, which uses the electrons in its chemical reaction to free OH^- ions, which are then transported back to the anode and combine with free Fe^{++} ions to form rust.

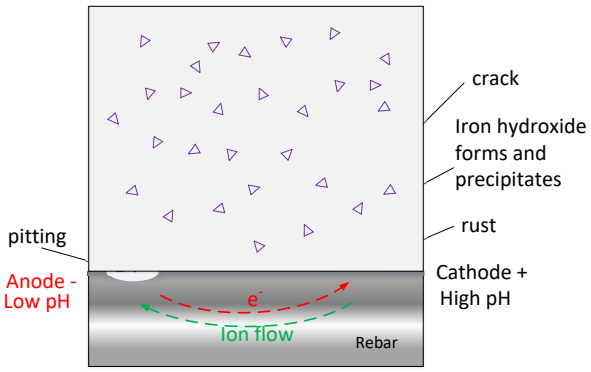

Fig. 10.6: Schematic of the corrosion process

Henceforth, there are three essential conditions for corrosion to occur:

1. There must be a difference in voltage potential between points on the steel surface or the surrounding material.
2. The concrete must be conductive to form the electrolyte (i.e. “close the circuit”).
3. The concrete must have electrical contact with the steel.

If these conditions are met, then corrosion can take place.
The first step in the corrosion process is the formation of an anode and cathode. The anode and cathode are locations of differing electric potentials on the reinforcing steel. This difference in potential between anode and cathode leads to the second step, the formation of an electric current. The current flows between the anode and cathode, transporting ions between the two areas. Finally, this ion transport leads to the third step, rust production. Ions from the cathode react with other ions at the anode to form rust, which is a product of the corrosion process.

10.4.2.1 Anodes and Cathodes

Corrosion is a process of oxidation and reduction. Oxidation frees electrons, while reduction consumes electrons. An example of each is

$$Zn \rightarrow Zn^{2+} + 2e^- \quad \text{Oxidation/Anode} \tag{10.47}$$

$$2H^+ + 2e^- \rightarrow H_2 \quad \text{Reduction/Cathode} \tag{10.48}$$

In the anodic reaction (oxidation), electrons are freed from the zinc. In the cathodic reaction (reduction), electrons are consumed by the hydrogen ion [483].
So what determines where anodes and cathodes form? In general, anodes form where the steel reinforcing is active, while cathodes occupy the passive areas of steel [351]. Being active means the steel has been depassivated and can readily corrode. Because steel passivation is affected by pH, anodes form where the pH of the pore solution is lower. They may also form at residual stress locations or on certain phases of steel microstructure, such as Fe_3C. Since the cathodic reaction requires O_2 , cathodes also form in areas where O_2 is higher [571]. The initial anodic reaction takes place at tiny areas on the steel and leads to the formation of narrow pits in the surface of the steel. Soon the small anodic areas become densely and uniformly distributed, forming a large anodic area [107].
The total reaction in the corrosion process is

$$2Fe^{++} + 2H_2O + O_2 \rightarrow 2Fe(OH)_2 \tag{10.49}$$

which may be broken into two partial or half-cell electrochemical reactions, each corresponding to the anodic or cathodic reaction [107]. The respective anodic and cathodic reactions for iron corrosion are

$$\text{anodic reaction: } 2Fe \rightarrow 2Fe^{++} + 4e^- \tag{10.50}$$

$$\text{cathodic reaction: } O_2 + 2H_2O + 4e^- \rightarrow 4OH^- \tag{10.51}$$

In any chemical reaction there is a change of free energy, denoted as ΔG. This holds for Eq. 10.49. The free-energy change may be associated with an electrochemical potential, E (volts), at equilibrium by the relationship

$$\Delta G = -nFE \tag{10.52}$$

where n is the number of electrons (or equivalents) exchanged in the reaction and F is Faraday's constant (96,500 coulombs per equivalent). The negative sign in Eq. 10.52 is included to conform to the convention that a positive potential results in a negative free-energy change for a spontaneous reaction.

10.4.2.2 Corrosion product

Reactive products from the anodic and cathodic reactions join together at the anode to form the corrosion product, commonly known as rust. The reaction at the anode may take many forms, one of which is

$$Fe^{++} + 2H_2O + O_2 \rightarrow 2Fe(OH)_2 \tag{10.53}$$

Since this reaction contains the anodic and cathodic reactions, it can be simplified by removing the cathodic reaction and replacing it with its product, $4OH^-$, to give

$$2Fe^{++} + 4OH^- \rightarrow 2Fe(OH)_2 \tag{10.54}$$

The product of this reaction, $2Fe(OH)_2$, is one form of rust. Other forms of rust are FeO, Fe_3O_4, Fe_2O_3, $Fe(OH)_2$, and $Fe(OH)_3$, depending upon the reactions.
Predicting the rate of formation of the corrosion product is important in determining the time to concrete damage. The proportionality between current, I, and mass reacted, m, is given by Faraday's Law:

$$m = \frac{Ita}{nF} \tag{10.55}$$

where F is Faraday's constant, n is the number of equivalents exchanged, a is the atomic weight, and t is the time. Dividing through by time t gives the corrosion rate in mass produced per unit time:

$$r = \frac{ia}{nF} \tag{10.56}$$

where r is the corrosion rate (mass/time), and i is the current density or current per area (I/A) [483]. It should be noted that current density, i, is only meaningful for uniform corrosion. With the current density determined from numerical or experimental methods, Eq. 10.56 can be used to find the mass of rust produced over time. This mass may be converted to volume of corrosion product, which can be applied as a boundary condition in a fracture analysis of the concrete [483].
The corrosion process can be summarized as follows:

Step 1 Formation of anodes and cathodes. The electrochemical potentials (voltage) at the anode and cathode are boundary conditions for an ion diffusion process.
Step 2 Ion diffusion process. The difference in potential between anode and cathode creates a potential distribution between them. e^- ions move from anode to cathode, and OH^- ions move from cathode to anode. This ion movement creates a current flow between anode and cathode.
Step 3 Rust production. OH^- ions at the anode react with Fe^{++} ions from the anodic reaction to form rust. The current determined in the previous step is used in Faraday's Law, Eq. 10.56, to determine the rust production rate.

10.5 Coupling

All processes addressed in this chapter are coupled among themselves and with the heat presented in Chapter 2. Of particular importance is the coupling between carbonation and chloride diffusion.
From Eq.10.25, the products of the carbonation process are water and calcium carbonate. As mentioned early on, carbonation causes the reduction of porosity; thus the humidity diffusivity of concrete is reduced. By using the same reduction factor of the diffusivity and the rate of the liberated water due to the effect of carbonation as introduced by Saetta, Schrefler, and Vitaliani [746], the moisture diffusion equation can then be given by

$$\frac{\partial H}{\partial t} = \frac{\partial H}{\partial W} \nabla.(D_H^* \nabla H) + \frac{\partial H_c}{\partial t} \tag{10.57}$$

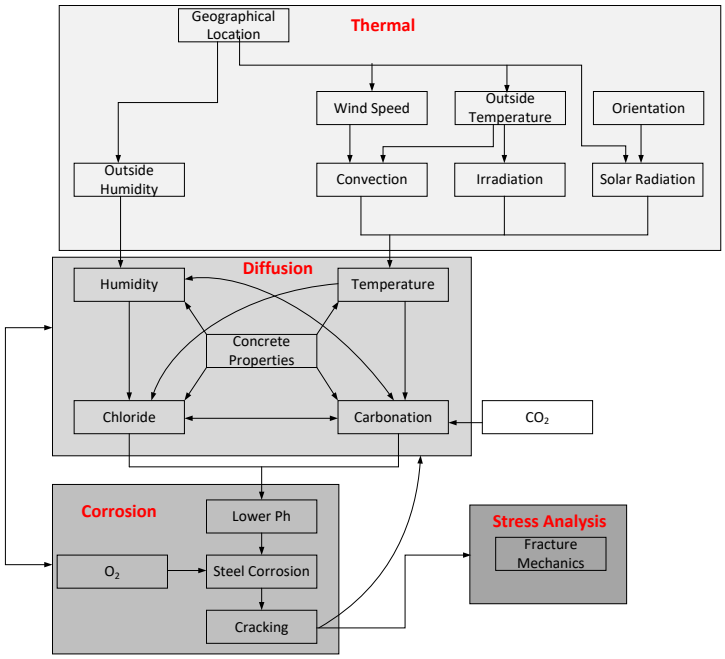

Fig. 10.7: Coupled thermal, diffusion, corrosion and stress analyses

where $\frac{\partial H_c}{\partial t} = \alpha_2 \frac{\partial c}{\partial t}$ is the term which accounts for the liberated water during the chemical reaction in the carbonation process D_H^* is the humidity diffusivity in the carbonated concrete which is given by

$$D_H^* = F_4(c) \cdot D_h \tag{10.58}$$

where $F_4(c)$, which is the same factor as the one in Eq. 10.43, is the reduction factor due to the reduction of porosity caused by carbonation.

Chapter 11
Alkali Aggregate Reaction; Theory

Abstract
Alkali aggregate reaction (AAR), also known as alkali silica reaction (ASR), is a major form of concrete deterioration for older structures. AAR will eventually weaken the concrete, induce cracking, and can jeopardize the integrity of dams and nuclear structures to the point of having them decommissioned.
This chapter will solely address a theoretical model for AAR developed by the first author and one that proved to be popular enough to have been implemented in numerous finite element codes.

11.1 Introduction

This chapter details an AAR model developed by the author [761], and its "validation" is reported in Saouma [749].
The model is complete, thorough, uncoupled from the concrete constitutive model, and yet easy to understand. As such, it has also been implemented in numerous other codes [736] [265] [595] [676] [437] [439] [115].

11.2 Model

11.2.1 Premises

Two different aspects of mathematical modeling of AAR in concrete may be distinguished: 1) the kinetics of the chemical reactions and diffusion processes involved and 2) the mechanics of fracture that affects volume expansion and causes loss of strength, with possible disintegration of the material [103]. The proposed model [761] [754] is driven by the following considerations:

1. AAR is a volumetric expansion, and as such can not be addressed individually along a principal direction without due regard to what may occur along the other two orthogonal ones.
2. The kinetics component is taken from the work of [523] and [839].
3. AAR is sufficiently influenced by temperature to account for its temporal variation in an analysis.

4. AAR expansion is constrained by compression and is redirected in other less constrained principal directions. This will be accomplished by assigning "weights" to each of the three principal directions.
5. Relatively high compressive or tensile stresses inhibit AAR expansion due to the formation of micro or macro cracks which absorb the expanding gel.
6. High compressive hydrostatic stresses slow down the reaction.
7. Triaxial compressive state of stress reduces but does not eliminate expansion.
8. Accompanying AAR expansion is a reduction in tensile strength and elastic modulus.

11.3 Kinetics

One of the most extensive and rigorous AAR investigations has been conducted by Larive [523], who tested more than 600 specimens with various mixes, ambient and mechanical conditions, and proposed a numerical model that governs concrete expansion. This thermodynamically-based, semi-analytical model was then calibrated using laboratory results in order to determine two key parameters: the latency time and characteristic times shown in Figure 11.1(a) for the normalized expansion.

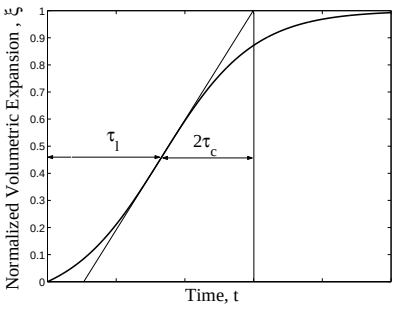

(a) Normalized Expansion Curve ($\xi(t) = \epsilon^{AAR}_{F,Vol}(t)/\epsilon(\infty)$)

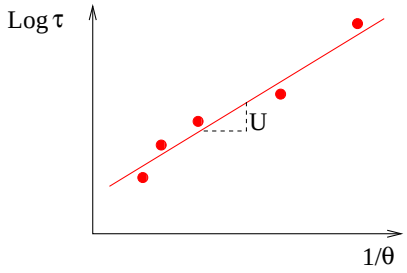

(b) Determination of Activation Energies

Fig. 11.1: Definition of the expansion curve

$$\xi(t,T) = \frac{1 - e^{-\frac{t}{\tau_c(T)}}}{1 + e^{-\frac{(t-\tau_l(T))}{\tau_c(T)}}} \tag{11.1}$$

or in rate form

$$\dot{\xi}(t,T) = \frac{e^{t/\tau_c}\left(e^{\frac{\tau_l}{\tau_c}} + 1\right)}{\tau_c\left(e^{t/\tau_c} + e^{\frac{\tau_l}{\tau_c}}\right)^2} \tag{11.2}$$

where τ_l and τ_c are the latency and characteristic times, respectively. The first corresponds to the inflection point while the second is defined relative to the intersection of the tangent at τ_L with the asymptotic unit value of ξ. Like all chemical reactions, AAR is subject to Arrhenius Law [48], which relates the dependence of the rate constant, k, of a chemical reaction on absolute temperature (T expressed in Kelvin, $TK = 273 + T^oC$) and activation energy, E_a.

$$k = Ae^{-\frac{E_a}{RT}} \tag{11.3}$$

Substituting k with τ_L and τ_C, Ulm et al. [839] has shown that these values at temperature T can be expressed in terms of the corresponding values at temperature T_0 through:

$$\begin{aligned} \tau_l(T) &= \tau_l(T_0) \exp\left[U_l\left(\tfrac{1}{T} - \tfrac{1}{T_0}\right)\right] \\ \tau_c(T) &= \tau_c(T_0) \exp\left[U_c\left(\tfrac{1}{T} - \tfrac{1}{T_0}\right)\right] \end{aligned} \tag{11.4}$$

where U_l and U_c are the activation energies required to trigger the reaction for latency and characteristic times, respectively. Activation energies can be easily determined by rewriting Eq. 11.4 in its non-exponential form:

$$\ln k = \ln\left(Ae^{-\frac{E_a}{RT}}\right) = \ln A - \frac{E_a}{RT} \tag{11.5}$$

which is the equation of a straight line with slope $-E_a/RT$ (Figure 11.1(b)). We can thus determine the activation energy from values of k observed at different temperatures by simply plotting k as a function of $1/T$, Figure 11.1(b). Activation energies for Eq. 11.4 were determined to be:

$$\begin{aligned} U_l &= 9,400 \pm 500K \\ U_c &= 5,400 \pm 500K \end{aligned} \tag{11.6}$$

To the best of the authors' knowledge, the only other tests for these values were performed by Haha [357], who obtained values within 20% of Larive's, while dependency on the types of aggregates and alkali content of the cement has not been investigated. In the absence of other tests, these values can thus be reasonably considered as representative.

It should be emphasized that not only are the latency and characteristic times temperature-dependent, but considerable variability can also be present for the same concrete specimen chosen from among others. This point is illustrated in Table 11.1 for four specimens (ϕ13H24 kept at 38^oC) tested by Larive [523].

Parameters affecting the kinetics of the ASR can be obtained by accelerated expansion tests. Saouma [749] has a compilation of numerous such tests, along with other investigative tools for a thorough diagnosis o ASR.

Table 11.1: Variation of $\epsilon(\infty)$, τ_c and τ_l for 4 specimens, [523]

specimen		501	475	287	19	Mean	NSD (%)
$\epsilon(\infty)$	%	0.198	0.195	0.168	0.230	0.198	12.8
τ_c	days	19.9	35.3	25.8	22.0	25.7	26.5
τ_l	days	102.1	83.9	94.8	64.8	86.4	18.8
τ_l/τ_c	-	5.1	2.4	3.7	2.9	3.4	0.7

11.3.1 Volumetric Expansion

The general (uncoupled) equation for the incremental free volumetric AAR strain is given by

$$\dot{\boldsymbol{\varepsilon}}_V^{AAR}(t) = \Gamma_t(f_t'|w_c, \sigma_I|COD_{max})\Gamma_c(\overline{\sigma}, f_c')g(h)\dot{\xi}(t,\theta)\ \varepsilon^{\infty}|_{\theta=\theta_0} \tag{11.7}$$

where COD is the crack opening displacement, $\xi(t,\theta)$ is a sigmoid curve expressing the volumetric expansion in time as a function of temperature and is given by Eq. 11.1, and ε^{∞} is the laboratory determined (or predicted) maximum free volumetric expansion at the reference temperature θ_0, Figure 11.1(a).
The retardation effect of the hydrostatic compressive stress manifests itself through τ_l. Hence, Eq. 11.4 is expanded as follows

$$\tau_l(\theta, \theta_0, I_\sigma, f_c') = f(I_\sigma, f_c')\tau_l(\theta_0)\exp\left[U_l\left(\frac{1}{\theta} - \frac{1}{\theta_0}\right)\right] \tag{11.8}$$

where

$$f(I_\sigma, f_c') = \begin{cases} 1 & \text{if } I_\sigma \geq 0 \\ 1 + \alpha\frac{I_\sigma}{3f_c'} & \text{if } I_\sigma < 0 \end{cases} \tag{11.9}$$

I_σ is the first invariant of the stress tensor and f_c' the compressive strength. Based on a careful analysis of [609], it was determined that $\alpha = 4/3$.
The stress dependency (through I_σ) of the kinetic parameter τ_l makes the model a truly coupled one between the chemical and mechanical phases.
Coupling with the thermal component is a loose one (hence a thermal analysis can be separately run); $0 < g(h) \leq 1$ is a reduction function to account for humidity given by

$$g(h) = h^m \tag{11.10}$$

where h is the relative humidity [165]. However, one can reasonably assume that (contrary to bridges) inside a dam, $g(h) = 1$ for all temperatures.
$\Gamma_t(f_t'|w_c, \sigma_I|COD_{max})$ accounts for AAR reduction due to tensile cracking (in which case gel is absorbed by macro-cracks), Figure 11.2.
A hyperbolic decay with a non-zero residual value is adopted, Figure 11.3:

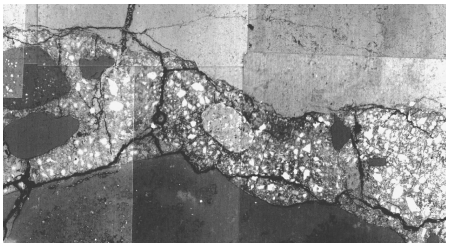

Fig. 11.2: Stress Induced Cracks with Potential Gel Absorption, [779]

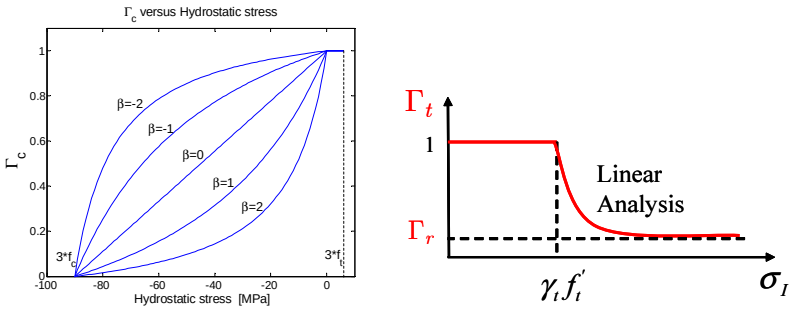

Fig. 11.3: Graphical Representation of Γ_c and Γ_t

$$\text{Smeared Crack} \begin{cases} \text{No } \Gamma_t = \begin{cases} 1 & \text{if } \sigma_I \leq \gamma_t f_t' \\ \Gamma_r + (1-\Gamma_r)\gamma_t \frac{f_t'}{\sigma_I} & \text{if } \gamma_t f_t' < \sigma_I \end{cases} \\ \text{Yes } \Gamma_t = \begin{cases} 1 & \text{if } \text{COD}_{max} \leq \gamma_t w_c \\ \Gamma_r + (1-\Gamma_r)\gamma_t \frac{w_c}{\text{COD}_{max}} & \text{if } \gamma_t w_c < \text{COD}_{max} \end{cases} \end{cases} \tag{11.11}$$

γ_t is the fraction of the tensile strength beyond which gel is absorbed by the crack; Γ_r is a residual AAR retention factor for AAR under tension. If an elastic model is used, then f_t' is the the tensile strength and σ_I the maximum principal tensile stress. If a smeared crack model is adopted, then COD_{max} is the maximum crack opening displacement at the current Gauss point, and w_c the maximum crack opening displacement in the tensile softening curve [887].

Concrete pores being seldom interconnected and the gel viscosity relatively high, gel absorption by the pores is not explicitly accounted for. Furthermore, gel absorption by the pores is accounted for by the kinetic equation through the latency time which depends on concrete porosity. The higher the porosity, the larger the latency time.

Γ_c in turn accounts for the reduction in AAR volumetric expansion under compressive stresses (in which case gel is absorbed by diffused micro-cracks) [609]:

$$\Gamma_c = \begin{cases} 1 & \text{if } \overline{\sigma} \leq 0. \text{ Tension} \\ 1 - \frac{e^{\beta}\overline{\sigma}}{1+(e^{\beta}-1.)\overline{\sigma}} & \text{if } \overline{\sigma} > 0. \text{ Compression} \end{cases} \tag{11.12}$$

$$\overline{\sigma} = \frac{\sigma_I + \sigma_{II} + \sigma_{III}}{3f'_c} \tag{11.13}$$

This expression will also reduce expansion under uniaxial or biaxial confinement, Figure 11.3; these conditions are more directly accounted for below through the assignment of weights.

11.3.2 AAR Strain Redistribution

The third major premise of the model is that the volumetric AAR strain must be redistributed to the three principal directions according to their relative propensity for expansion on the basis of a weight which is a function of the respective stresses.

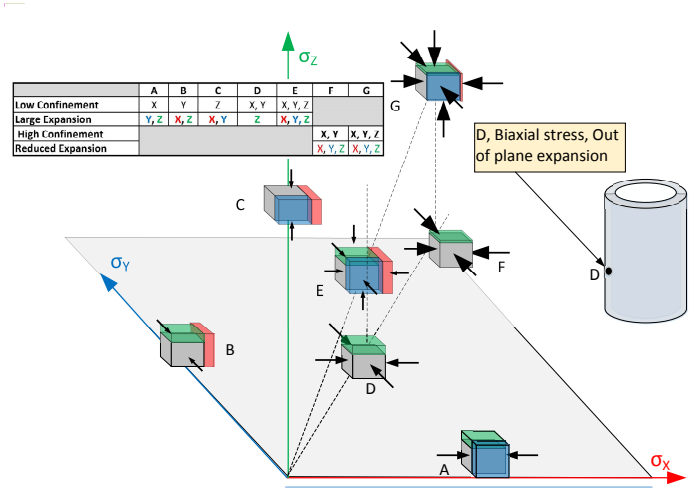

Fig. 11.4: Effect of confinement on AAR strain redistribution

The determination of the weight is relatively straightforward for triaxial AAR expansion under uniaxial confinement (for which some experimental data is available), but it is more problematic for biaxially or triaxially confined concrete. Given a principal stress vector defined by $\sigma_k, \sigma_l, \sigma_m$, we need to assign a weight to each of those three principal directions. These weights will control the AAR volumetric expansion distribution. For instance, with reference to Figure 11.5, we consider three scenarios.

Uniaxial state of stress, where we distinguish the following three cases:

1. In the first case, we have uniaxial tension, and hence, the volumetric AAR strain is equally redistributed in all three directions.

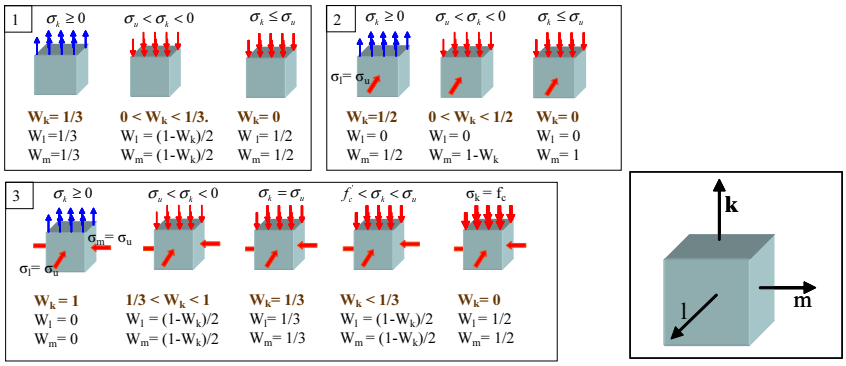

Fig. 11.5: Weight of Volumetric AAR Redistribution in Selected Cases

2. Under a compressive stress greater than the limiting one (σ_u), the weight in the corresponding (k) direction should be less than one third. The remaining AAR has to be equally redistributed in the other two directions.
3. If the compressive stress is lower than σ_u, than AAR expansion in the corresponding direction is prevented (weight equal zero), and thus the other two weights must be equal to one half.

Biaxial state of stress in which we have a compressive stress equal to σ_u in one of the three principal directions. In this case, the corresponding weight will always be equal to zero. As to the possible three combinations:

1. Tension in one direction, equal weights of one half.
2. Compression greater than σ_u in one direction, then the corresponding weight must be less than one half, and the remaining weight is assigned to the third direction.
3. Compression less than σ_u, then the corresponding weight is again zero, and a unit weight is assigned to the third direction.

Triaxial state of stress in which we have σ_u acting on two of the three principle directions. We identify the following five cases:

1. Tension along direction k, then all the expansion is along k.
2. Compressive stress greater than σ_u, then we have a triaxial state of compressive stress, and the corresponding weight will be between one and one third. The remaining complement of the weight is equally distributed in the other two directions.
3. Compression equal to σ_u, hence we have a perfect triaxial state of compressive stress. In this case we have equal weights of one third. It should be noted that the overall expansion is reduced through Γ_c.

4. Compression less than σ_u but greater than the compressive strength. In this case, the weight along k should be less than one third, and the remaining equally distributed along the other two directions.
5. Compression equal to the compressive strength. In this case, the corresponding weight is reduced to zero, and the other two weights are equal to one half each.

Based on the preceding discussion, we generalize this weight allocation scheme along direction k as follows

1. Given σ_k, identify the quadrant encompassing σ_l and σ_m, Figure 11.6[1]. Weight will be determined through a bilinear interpolation for those four neighboring nodes.

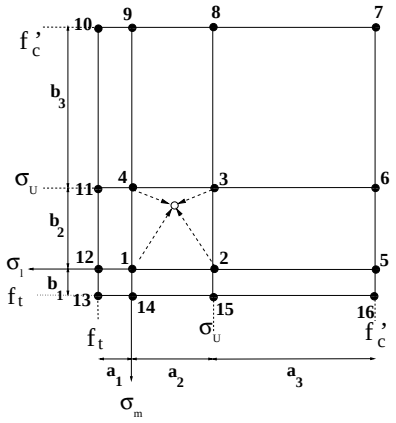

Fig. 11.6: Weight Regions

2. Determine the weights of the neighboring nodes from Table 11.2 through proper linear interpolation of σ_k.
3. Compute the weight from:

$$W_k(\sigma_k, \sigma_l, \sigma_m) = \sum_{i=1}^{4} N_i(\sigma_l, \sigma_m) W_i(\sigma_k) \tag{11.14}$$

where N_i is the usual two bilinear shape function used in finite element and is given by

[1] Since compressive stresses are quite low compared to the compressive strength, we ignore the strength gained through the biaxiality or triaxiality of the stress tensor [518]. Furthermore, the strength gain is only about 14% for equibiaxial compressive stresses [171].

Table 11.2: Triaxial Weights

Node			Weights		
No.	σ_l	σ_m	$\sigma_k \geq 0$	$\sigma_k = \sigma_u$	$\sigma_k = f'_c$
1	0.	0.	1/3	0.	0.
2	σ_u	0.	1/2	0.	0.
3	σ_u	σ_u	1.	1/3	0.
4	0.	σ_u	1/2	0.	0.
5	f'_c	0.	1/2	0.	0.
6	f'_c	σ_u	1.	1/2	0.
7	f'_c	f'_c	1.	1.	1/3
8	σ_u	f'_c	1.	1/2	0.
9	0.	f'_c	1/2	0.	0.
10	f'_t	f'_c	1/2	0.	0.
11	f'_t	σ_u	1/2	0.	0.
12	f'_t	0.	1/3	0.	0.
13	f'_t	f'_t	1/3	0.	0.
14	0.	f'_t	1/3	0.	0.
15	σ_u	f'_t	1/2	0.	0.
16	f'_c	f'_t	1/2	0.	0.

$$\mathbf{N}(\sigma_l, \sigma_m) = \frac{1}{ab} \lfloor\, (a-\sigma_l)(b-\sigma_m)\ \sigma_l(b-\sigma_m)\ \sigma_l\sigma_m\ (a-\sigma_l)\sigma_m \,\rfloor \tag{11.15}$$

$$\mathbf{W}(k) = \lfloor\, W_1(\sigma_k)\ W_2(\sigma_k)\ W_3(\sigma_k)\ W_4(\sigma_k) \,\rfloor^t \tag{11.16}$$

$$a = (a_1|a_2|a_3) \qquad b = (b_1|b_2|b_3) \tag{11.17}$$

$$\sigma_l = (\sigma_l|f'_c - \sigma_l) \qquad \sigma_m = (\sigma_m|f'_c - \sigma_m) \tag{11.18}$$

The $i-j$ stress space is decomposed into nine distinct regions, Figure 11.6, where σ_u is the upper (signed) compressive stress below which no AAR expansion can occur along the corresponding direction (except in triaxially loaded cases). Hence, a and b are the dimensions of the quadrant inside which σ_i and σ_j reside.

Weights of the individual nodes are in turn interpolated according to the principal stress component in the third direction σ_k, Table 11.2. Those weights are for the most part based on the work of [523] and [609], but in some cases due to lack of sufficient experimental data, based on simple "engineering common sense."

A simple example for weight determination is shown here. Assuming that the principal stresses are given by $\lfloor\, \sigma_l\ \sigma_m\ \sigma_k \,\rfloor = \lfloor\, -5.0\ -8.0\ -5.0 \,\rfloor$ MPa, and that f_c, f'_t, and σ_u are equal to -30.0, 2.0, and -10.0 MPa respectively, we seek to determine W_k. The stress tensor places us inside the quadrant defined by nodes 1-2-3-4 whose respective weights are equal to: $W_1 = \frac{1}{2}\left(\frac{1}{3}\right) = \frac{1}{6}$, $W_2 = \frac{1}{2}\left(\frac{1}{2}\right) = \frac{1}{4}$, $W_3 = \frac{1}{3} + \frac{1}{2}\left(1.0 - \frac{1}{3}\right) = \frac{2}{3}$, and $W_4 = \frac{1}{2}\left(\frac{1}{2}\right) = \frac{1}{4}$. Also, a and b are both equal to -10 MPa, and the "shape factors" will be $N_1 = \frac{1}{100}\left[(-10+5)(-10+8)\right] = \frac{1}{10}$, $N_2 = \frac{1}{100}\left[-5(-10+8)\right] = \frac{1}{10}$, $N_3 = \frac{1}{100}\left[(-5)(-8)\right] = \frac{4}{10}$, $N_4 = \frac{1}{100}\left[-8(-10+5)\right] = \frac{4}{10}$, and finally $W_k = \frac{1}{10} \times \frac{1}{6} + \frac{1}{10} \times \frac{1}{4} + \frac{4}{10} \times \frac{2}{3} + \frac{4}{10} \times \frac{1}{4} = 0.40833$.

Based on the earlier work of [808] in which it was reported that no gel expansion can occur at pressures above 11 MPa, σ_u is taken as -10 MPa. This value was also confirmed by [523]. f'_t and f'_c are the concrete tensile and compressive strengths respectively.
Individual strain is given by

$$\dot{\varepsilon}_i^{AAR} = W_i \dot{\varepsilon}_V^{AAR} \tag{11.19}$$

and the resulting relative weights are shown in Figure 11.7.

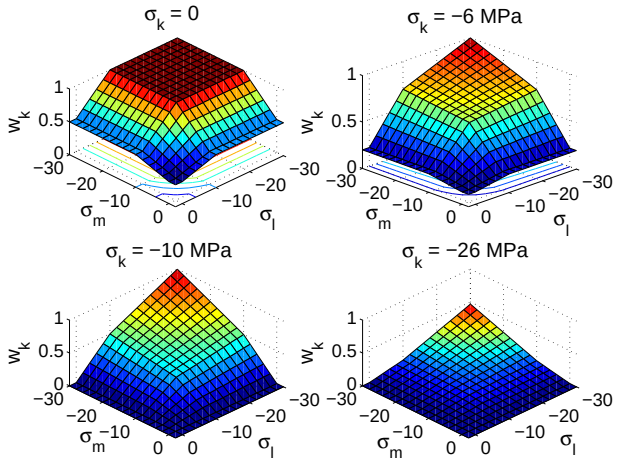

Fig. 11.7: Relative Weights

The proposed model will indeed result in an anisotropic AAR expansion. While not explicitly expressed in tensorial form, the anisotropy stems from the different weights assigned to each of the three principal directions.

11.3.3 Degradation

Deterioration being time dependent, the following time dependent non-linear model is considered, Figure 11.8.

$$E(t,\theta) = E_0 \left[1 - (1 - \beta_E)\, \xi(t,\theta)\right] \tag{11.20}$$

$$f'_t(t,\theta) = f'_{t,0} \left[1 - (1 - \beta_f)\, \xi(t,\theta)\right] \tag{11.21}$$

where E_0 and $f'_{t,0}$ are the original elastic modulus and tensile strength; β_E and β_f are the corresponding residual fractional values when ε_{AAR} tends to $\varepsilon^{\infty}_{AAR}$.

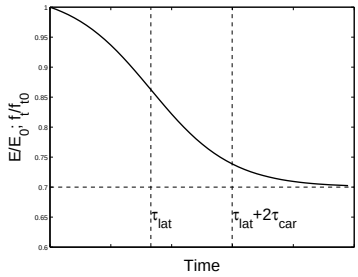

Fig. 11.8: Degradation of E and f'_t

11.4 Bureau of Reclamation Study

A very comprehensive investigation of the impact of AAR on the elastic properties of dam concrete was conducted by the Bureau of Reclamation over many years. This source could serve as an excellent starting point for preliminary analysis, and this section will provide an adaption of Dolen [250, 251] and the text/figures displayed herein have been reproduced with the permission of the Bureau of Reclamation.

A database model of aging concrete was developed to identify the changes in material properties over time. Data were input into the *Aging Concrete Information System* (ACIS) where they were analyzed for trends in the deterioration of concretes subject to aging, including the alkali aggregate reaction (AAR) and general aging of early 20th-century concrete with high water-to-cement ratios.

These aging concrete samples were then compared to dams from a similar period, yet without any adverse effects from aging processes. The aging concretes were also compared to known high quality concretes mixed after circa 1948 specifically to resist deterioration from AAR, freezing and thawing (FT), and sulfate attack. Trends were established so as to compare the compressive strength, splitting and direct tensile strength, and elastic properties of both aging and non-aging dams.

The strength and elastic properties of aging mass concrete differed significantly from those of comparable non-aging specimens. Both the spatial variations within a structure and long-term changes in strength and elastic properties could be identified.

Three Bureau of Reclamation concrete dams have sustained significant deterioration attributable to AAR and, in particular, ASR. Parker Dam, built in 1937-38, was the first Reclamation dam to be identified with ASR. American Falls Dam, which dates back to 1927, was actually the first Reclamation facility to experience deterioration caused by ASR and was ultimately replaced in 1977. Seminoe Dam was constructed in 1938 and has gradually deteriorated over time. Both Parker and Seminoe Dams feature comparable “reference” dams, i.e. dams built using similar materials and mixtures at about the same time with little deterioration.

11.4.0.1 Effect of Confinement

Confinement plays an important role in reducing the elastic properties of concrete. Samples taken above 20 feet differ markedly from those extracted below the 20-foot level due to the (beneficial) effect of confinement. Table 11.3 clearly illustrates this effect. These data are to be compared with the non-ASR-affected concrete modulus

Table 11.3: Average compressive strength and elastic properties of concrete dams subject to aging [250]

	Test Age years	Compressive strength lb/in^2	Modulus of Elasticity 10^6 lb/in^2	Poisson's ratio
AAR-affected dams*	53.1	3,695	2.28	0.20
AAR cores from above 20 ft	48.0	3,180	2.09	0.20
AAR cores from below 20 ft	49.0	4,090	2.35	0.10
ACIS aging dams (1902 to 1920)*	79.7	2,490	2.59	0.23

*The average is weighted by the number of tests for a given sample set.

value of approximately 5.410 ^{6} lb/in^2.

11.4.1 Compressive Strength

Figure 11.9(a) shows the relationship between compressive strength and modulus of elasticity for all concrete cores both with and without ASR. Although the correlation coefficient for these equations is poor, the trend lines have been added to indicate the demarcation between the two classes of concrete. Individual correlations between compressive strength and modulus of elasticity are typically much better for individual dams using the same types of aggregate. These trends reveal that the strength-to-modulus of elasticity relationship provides a good indicator of ASR and may be used to develop failure criteria for predictive models.

11.4.2 Tensile Strength

Tensile strength is becoming more critical in the structural analysis of concrete dams, particularly in the case of dynamic analyses involving earthquakes. Tensile strength tests were not normally performed until the 1970's, and tensile strength development in dams built before this era is unknown. The results of direct and splitting tensile strength tests on high quality concrete and aging/ASR-affected concrete specimens are shown in Figure 11.9(b).

Tensile strength data have typically been entered into the database as average values from just a few tests for each mixture. The aging data also include some tests on old dams not subject to ASR. It is clear however that the tensile strength of aging/ASR-affected dams is averaged at about 50 percent of the direct tensile strength and 30 percent less in splitting tensile strength when compared to dams without ASR degradation or aging. Also, aging concrete data are often based solely on "testable"

concrete and do not represent the condition of the deteriorated concrete that could not be tested.

11.4.3 Case Studies

The evolution in strength at both Parker and Seminoe Dams has been extensively studied for ASR effects. Cracking at Parker Dam was identified as ASR after examinations confirmed the process first identified by Stanton [803]. Widespread concrete coring and testing have been performed since 1940, and the resulting strength trends are well documented. Seminoe Dam was subjected to early freezing and thawing near the dam crest, but ASR was not identified as a significant contributing factor to degradation until more than 60 years after construction. The deterioration at Seminoe Dam seems more alarming because the mass concrete appears to have nearly reached its projected ultimate strength potential before the onset of ASR. The slow reaction rate may be due to both the nature of the aggregates and the cold temperatures at the site. Another dam built in a northern climate with the potential for similar behavior is Owyhee Dam in Idaho. Tests conducted near the crest of Owyhee Dam reveal a behavior close to that found at Seminoe Dam, and potentially reactive aggregates are indeed prevalent in the vicinity of Owyhee Dam.
The compressive strength trend lines in Figure 11.10(a) from the two ASR-affected dams show a relatively constant state for Parker Dam and a decreasing strength at Seminoe Dam. Some of the data scatter is caused by the fact that overall sampling has not been sorted by elevation and moreover includes test results on concrete not significantly affected by ASR due either to the cement alkali content of individual block placements or to location in the dam. When sorted by elevation, the rate of change can also be observed for both dams, as depicted in Figures 11.10(b).
These compressive strength trends do not indicate an overall change with time for Parker Dam, even though some spatial trends may be present. For Seminoe Dam, it is readily apparent that the overall compressive strength is decreasing with time, and

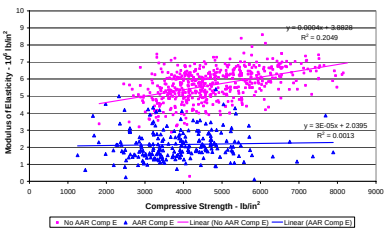

(a) Comparison of strength with modulus of elasticity in compression for mass concrete dams both with and without ASR

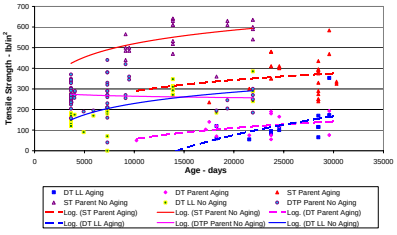

(b) Comparison of the effects of aging and ASR on the tensile strength of mass concrete dams

Fig. 11.9: Impact of ASR on ASR on compressive and tensile strengths in concrete dams [250]

the compressive strength exhibits significant spatial deterioration near the top of the dam, as shown in Figure 11.10(d).
This deterioration extends more deeply into the dam over time. The modulus of elasticity also displays the same trends (Figure 11.10(e)).

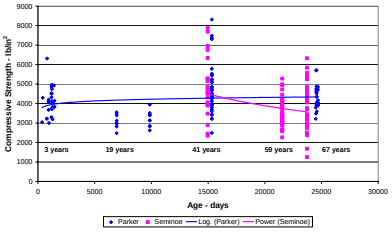

(a) Compressive strength development in ASR-affected concrete cores for Parker and Seminoe Dams

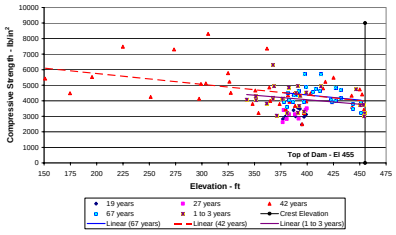

(b) Parker Dam concrete cores; Core compressive strength vs. dam elevation

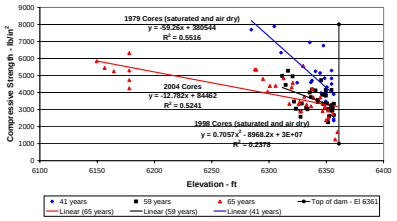

(c) Effect of both ASR reaction and freezing & thawing; Seminoe Dam; Compressive strength vs. elevation

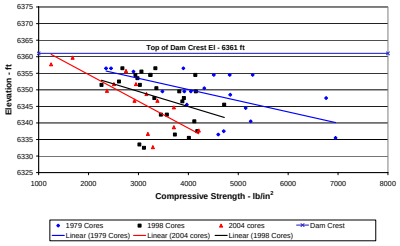

(d) Effect of ASR reaction and freezing & thawing; Top 30 feet of Seminoe Dam; Compressive strength vs. elevation

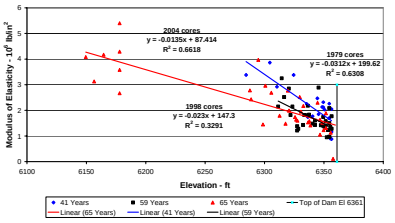

(e) Effect of ASR reaction and freezing & thawing; Seminoe Dam; Modulus of elasticity vs. elevation

Fig. 11.10: Impact of ASR on field measured elastic properties of Parker and Seminoe dams [250]

11.5 AAR Properties through System Identification

As previously noted, only the selected zones of a structure are most often affected by AAR; it is also possible for multiple pockets of AAR to differ in intensity. Great care should therefore be taken when assessing the spatial distribution of AAR properties. It is seldom feasible or realistic, however, to either identify these zones or characterize them, in which case an equivalent set of parameters must be assumed.
The three critical AAR parameters (τ_l, τ_c and $\varepsilon(\infty)$) cannot be derived from expansion tests performed on cores since these cores have already expanded by an unknown amount once they have been retrieved. Hence, the only effective procedure to derive AAR parameters for a time-history analysis would be through a system identification that compares measured quantities (typically displacements) with quantities obtained numerically. In case of discrepancy, the model parameters are to be adjusted until the error lies within an acceptable range. It is obvious that such a method can only be applied provided the availability of historical field data.
Mathematically speaking, the problem can be simply formulated as follows. The field-recorded displacements (e.g. crest displacement on a dam) are denoted by $\mathbf{u}(t)$, the target parameters by $\mathbf{x}$ (in our case $x(1) = \tau_c$, $x(2) = \tau_l$ and $(x(3) = \varepsilon(\infty))$, the finite element "operator" by $f(.)$, and computed results by $\mathbf{u}'(t)$. We thus have:

$$f(\mathbf{x}) = \mathbf{u}'(t) \neq \mathbf{u}(t) \tag{11.22}$$

and are seeking to minimize $(\mathbf{u}(t) - \mathbf{u}'(t))^2$, see Figure 11.11.

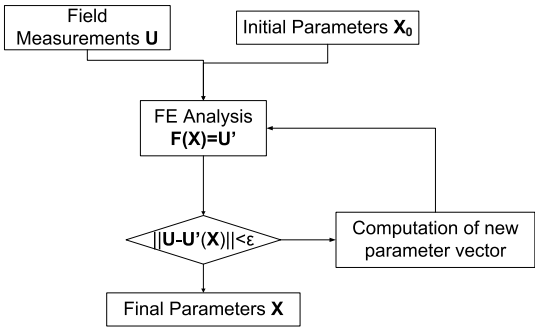

Fig. 11.11: Principle of the system identification approach

The corresponding objective function, Jacobian, gradient, and Hessian matrices [237] are then given by:

$$\omega(\mathbf{x}) = (\mathbf{u} - \mathbf{u}')^T(\mathbf{u} - \mathbf{u}') = \mathbf{r}^T \cdot \mathbf{r} = \sum_{i=1}^{m} (u_i - u_i')^2 \tag{11.23}$$

$$\mathbf{J}(\mathbf{x}) = \frac{\partial \mathbf{r}(\mathbf{x})}{\partial \mathbf{x}^T} = \frac{\partial}{\partial \mathbf{x}^T}\left[(\mathbf{u} - \mathbf{u}')\right] = \frac{\partial \mathbf{u}}{\partial \mathbf{x}^T} - \frac{\partial \mathbf{u}'}{\partial \mathbf{x}^T} = -\frac{\partial \mathbf{u}'}{\partial \mathbf{x}^T} = -\mathbf{L} \tag{11.24}$$

$$\nabla\omega(\mathbf{x}) = \frac{\partial \omega(\mathbf{x})}{\partial \mathbf{x}^T} = \frac{\partial}{\partial \mathbf{x}^T}\left[(\mathbf{u} - \mathbf{u}')^T(\mathbf{u} - \mathbf{u}')\right] = 2\mathbf{J}^T\mathbf{r} \tag{11.25}$$

$$\mathbf{H}(\mathbf{x}) = \frac{\partial^2 \omega}{\partial \mathbf{x}^T \partial \mathbf{x}} = \frac{\partial}{\partial \mathbf{x}}\left(\nabla\omega\left(\mathbf{x}\right)\right) = \frac{\partial}{\partial \mathbf{x}}\left[2\mathbf{J}^T\mathbf{r}\right] = 2\mathbf{J}^T\mathbf{J} + 2\frac{\partial^2 \mathbf{r}}{\partial \mathbf{x}^T \partial \mathbf{x}} \tag{11.26}$$

In nearing the minimum, $\frac{\partial^2 \mathbf{r}}{\partial \mathbf{x}^T \partial \mathbf{x}}\mathbf{r} \rightarrow 0$, we have $\mathbf{H}(\mathbf{x}) = 2\mathbf{J}^T\mathbf{J}$. Use of the Levenberg-Marquardt method [237] allows solving for $\mathbf{x}_{k+1}$ from:

$$\mathbf{x}_{k+1} = \mathbf{x}_k - \left[\varepsilon_k \mathbf{I} + \mathbf{H}\left(\mathbf{x}_k\right)\right]^{-1} \nabla\omega\left(\mathbf{x}_k\right) \tag{11.27}$$

where ε_k is such that all eigenvalues of $\left[\varepsilon_k \mathbf{I} + \mathbf{H}\left(\mathbf{x}_k\right)\right]$ are positive and greater than $\delta > 0$. A development of the Levenberg-Marquardt method, known as the trust region method, can ultimately be introduced. We have indeed sought to minimize the objective function, $\omega(\mathbf{x})$, inside a trust region where the quadratic approximation (as obtained by a Taylor series) is considered reliable:

$$\omega_{II}\left(\mathbf{x}, \mathbf{x}_k\right) = \omega\left(\mathbf{x}_k\right) + \nabla\omega\left(\mathbf{x}_k\right)^T\left(\mathbf{x} - \mathbf{x}_k\right) + \frac{1}{2}\left(\mathbf{x} - \mathbf{x}_k\right)^T \mathbf{H}\left(\mathbf{x}_k\right)\left(\mathbf{x} - \mathbf{x}_k\right) \tag{11.28}$$

The trust region is defined as follows:

$$\mathbf{\Omega}_k = \left\{\mathbf{x} : \|\mathbf{x} - \mathbf{x}_k\| \leq \Delta_k\right\}; \Delta_k > 0 \tag{11.29}$$

The optimization problem becomes:

$$\min_{\mathbf{x}} \left\{\omega_{II}\left(\mathbf{x}, \mathbf{x}_k\right) : \mathbf{x}_k \in \Omega_k\right\} \tag{11.30}$$

The condition needed to update the region is given by:

$$R_k = \frac{\omega\left(\mathbf{x}_k\right) - \omega\left(\mathbf{x}_{k+1}\right)}{\omega\left(\mathbf{x}_k\right) - \omega_{II}\left(\mathbf{x}_{k+1}\right)} \simeq 1 \tag{11.31}$$

The update of the starting point is the same as that illustrated for the Levenberg-Marquardt method. With this method, we are also able to define the upper and lower bounds for these parameters as:

$$\min_{\mathbf{x}} \left\{\omega_{II}\left(\mathbf{x}, \mathbf{x}_k\right) : \mathbf{x}_k \in \Omega_k\right\}; \mathbf{lb} \leq \mathbf{x} \leq \mathbf{ub} \tag{11.32}$$

From a practical standpoint, the three following considerations must be taken into account during the optimization process:
The starting point of the parameter identification process may be determined from laboratory tests (yielding an initial estimate of $\varepsilon^{\infty}|_{T=T_0}$, $\tau_L(T_0)$ and $\tau_C(T_0)$).

Alternatively, curve fitting of the dam crest displacement:

$$u_{irr}^{AAR}(t,\theta) = \frac{1 - e^{-\frac{t}{\tau_c(\theta)}}}{1 + e^{-\frac{(t-\tau_l(\theta))}{\tau_c(\theta)}}} u_{irr}^{AAR,\infty} \tag{11.33}$$

(where u_{irr}^{AAR} and $u_{irr}^{AAR,\infty}$ are the irreversible, time and temperature-dependent displacement and the final displacement due to AAR respectively) provides a conservative estimate for the times but not for $\varepsilon^{\infty}|_{T=T_0}$. The target parameters must be normalized such that all initial values have the same order of magnitude, i.e.: a) the initial variation must be large enough to produce a variation in the computed results (large normalized values can lead to an immediate stop of the identification process); and b) the final variation of parameters must be small enough to allow for a small final adjustment of the identified parameters without large oscillations around the final solution (an overly small normalized parameter may result in a large final oscillation).
A weight function can be introduced to assign importance to the last data field, which typically contains a major absolute value and is thus more representative of the irreversible effect of AAR expansion with respect to the effect of normal loads. Let's note that this system identification does not require a thermal analysis and, from a practical standpoint, entails a simple modification of three variables included in the stress analysis input file.

11.5.1 Algorithm

Of paramount importance to the long-term reliable prediction of dam response is the ability of the model to simulate past responses. A dam always contains a record of the irreversible crest displacement over time; this curve is precisely what a model should be able to replicate as closely as possible. In using the approach previously described, a MATLAB "driver" program has thus been written to identify the three key parameters, $\tau_l(\theta)$, $\tau_c(\theta)$ and $\varepsilon_{\theta}^{\infty}$, by means of continuously comparing the histogram of the computed crest displacement with the histogram of recordings. The driver will:

1. Launch an initial finite element analysis.
2. Open the output file and extract the crest displacement histogram.
3. Compare the numerical histogram with field recordings. If the results are nearly similar, stop execution.
4. Appropriately modify the input key parameters and launch the finite element analysis.

This procedure is best illustrated by Figure 11.12(a) where: Left: Matlab code; upper right: finite element analysis program execution; lower right: comparison of computed and recorded crest displacements (upper left) and variation of τ_l, τ_c and ε^{∞} vs. number of iterations.
Figure 11.12(b) shows that the computed crest displacement lies well within the seasonal variations of the final numerical predictions.

11.6 Prediction of Past & Future Expansion

As well established, ASR expansion will follow a sigmoid curve. But what if a structure built many years ago (at time t_0), and (as is always the case) ASR was uncovered many years later (at time t_1), we will then be confronted with a set of three questions, Figure 11.13.

1. What has been the past expansion, ε_1?
2. At what time t_2 will the reaction stop?
3. What would be the corresponding final expansion, ε_2?

Answer to the first question can be addressed through detailed petrographic studies as reported in [749, Appendix B], and answers to the last two can be addressed through accelerated expansion tests as again amply reported in [749]. Of course, one would have to associate a margin of errors to such predictions.

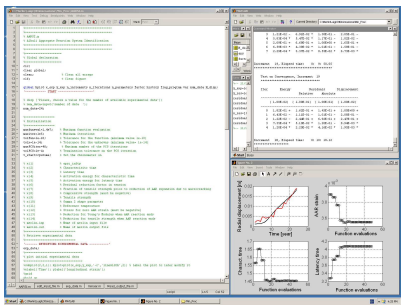

(a) Graphical user interface for AAR parameter identification

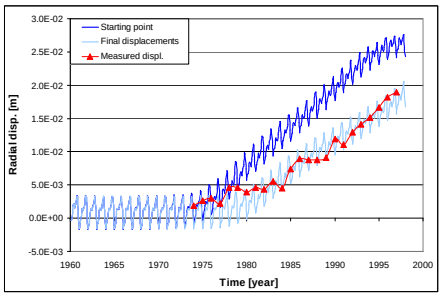

(b) Comparison between the first analysis estimate and the final analysis using optimized parameters

Fig. 11.12: System identification for ASR properties

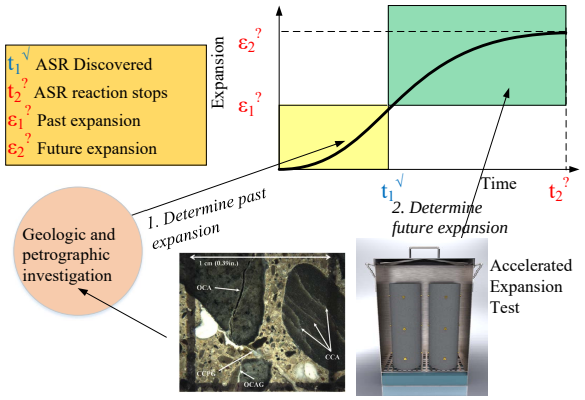

Fig. 11.13: Estimate of past and future ASR expansions

Part III
Finite Element

Chapter 12
Science and Art of Finite Element Modeling

Abstract
A key factor in finite element analysis is often neglected: modeling. As this chapter implies, this is both an art and a science whose exercise can impact results.
It will first cast the analysis within the general framework of an investigation and identify the associated tasks. More details are addressed subsequently in terms of key considerations to be accounted for.

This chapter provides the reader with basic recommendations prior to *any* finite element study. More specifically, how to understand and articulate and then mathematically define the problem, how to gather the required data from multiple sources and synthetize them, how to define the mathematical (finite element) model, how to identify the computer codes and assess the quality of the results, and finally how to prepare a report. In particular, it will address modeling which (in this context) is the science and art of addressing all of the above.

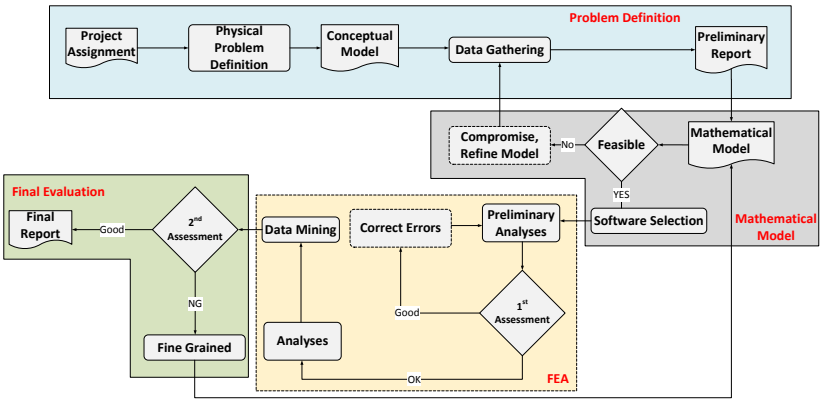

Fig. 12.1: Finite Element Process (inspired by Bathe [89])

Coverage (albeit condensed) of the finite element method is left to any of the multiple references on the method [925, 924, 449, 114]. Broadly speaking, the finite element

analysis of a major structure can be summarized by Figure 12.1. Each of the major blocks will be separately addressed below.

12.1 Tasks

12.1.1 Problem Definition

The first step consists in simply defining the problem in terms of the following:

Project Assignment is typically a document written with input from regulators, site and safety engineers, and others interested in assessing the structural safety of the structure. It is typically driven by safety and regulatory requirements and should not be unduly influenced by potential task complexity, lack of data, expertise or resources. In other words it is a "wish list."

Physical Problem Definition is a translation of the previous document to specific requirements of the analyses to be undertaken. It should include the specifically desired numerical results in a manner easily understood by the finite element analyst.

Conceptual Model this report will summarize all assumptions, algorithms, relationships, and data that describe the reality of interest from which the mathematical model and validation experiment can be constructed. It will also spell out the expectation, break down the project in clearly identifiable tasks, and translate what may be a partially legalistic document into an engineering one (see Section 12.2.5). This document should never be modified. If possible, prior to any analysis, it should include anticipated orders of magnitudes of the desired response bracketed between *minima* and *maxima* and anticipated failure modes. This will be important for subsequent "reality/sanity checks" in the first assessment.

Data Gathering is the first attempt by the analysis to translate the previous assignment into specific tasks such as:

- Are all necessary material properties available? Where could one get them (archives, site engineer, literature, others), and how reliable are they?
- Is there a need to perform laboratory tests; are the financial resources available; can one easily obtain regulatory authorization to extract cores?
- Software requirements should be spelled out before identifying the one to be used. It may very well be that the "commonly used one" does not have the required features. Eventual discrepancies should be duly noted.
- Is there in-house the expertise to
  1. Perform the numerical simulation.
  2. Supervise/review the simulation performed by others.
- Identify third party independent reviewers for the project.

Preliminary Report Report on data gatherings, and repeat the anticipated results (failure modes, order of magnitudes of results).

12.1.2 Mathematical Model

A mathematical model is the link between the problem statement and the actual finite element simulation. It consists of the following:

Mathematical Model This task involves selecting the material properties (Section 12.2.3), loads and boundary conditions (Section 12.2.2 below), and type of analysis (linear, non-linear, implicit, explicit).

Assess Feasibility This is a "reality check" on whether the *desiderata* can indeed be fulfilled realistically.

Compromise If the model can not fully respond to the needs articulated in the second report, then compromises must be made, recorded, and the process of data gathering is repeated.

Software Selection This is a critical step separately addressed in Section 12.2.4.

Whereas much could be written about mesh preparation, suffice it to say that as a rule, it is far better to use a structured mesh, Figure 12.2(b) rather than unstructured ones, Figure 12.2(a), as the former yield better convergence.

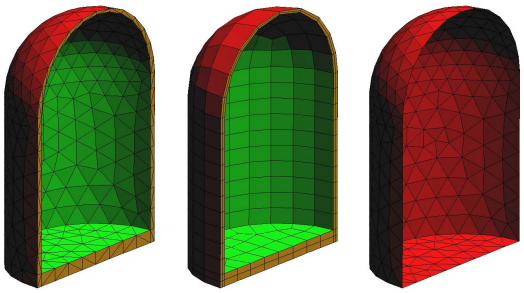

(a) Unstructured (b) Sructured (c) Shell

Fig. 12.2: Unstructured *vs.* **structured** *vs.* **shell meshes**

12.1.3 Finite Element Analyses

The finite element study *per-se* consists of the following parts:

Preliminary Analysis usually linear elastic to test definition of material properties, boundary conditions, and loads.

Preliminary Assessment Perform a "reality check" on the results. Are they out of bound (different orders of magnitude) of those anticipated in the preliminary report? Are there blatant erroneous data entries or mixed units? Are the displacements consistent with loads or boundary conditions? Is the load path realistic? Are there zones of the mesh which should be refined? Should one use a different number of increments or integration scheme? Are the convergence criteria too tight?

Correct Errors that may have resulted in unacceptable preliminary results.

Analyses of the structure going incrementally from the simplest to the most complex.

Data Mining Is the process of extracting all relevant results from piles of output. Some software allow specific data to be dumped on disk files, others not. Data may have to be extracted, either from the graphical post-processor or from the ascii-output, and stored. It is best to store all retrieved data in an Excel sheet, and then use programs such as Matlab or Python to read the data and plot them as is best suited for the demand.

12.1.4 Final Evaluation

A final evaluation of the series of analyses must be performed. This includes a 2nd assessment or a "fine grained" assessment of results to determine if they are truly meaningful and reflect a solution to the problem. If not, then the mathematical model itself must be revisited. In the end, the final report should have a short executive summary, the body of the report, and typically many appendices with plots and graphs.

12.2 Key Considerations

12.2.1 Modeling

Before we start, we should address some key questions:

- 2D or 3D? Plane stress, plane strain, or axisymmetric?
- Limit state? (only failure load is of interest, and not the displacements).
- Pushover or transient analysis?
- Damping: Rayleigh and/or hysteretic?
- How much non-linearity to expect? Up to peak? Post-peak?
- Rigorous single deterministic analysis, approximate multiple analyses, or detailed probabilistic assessment (Monte Carlo family)?

Ultimately, the selected finite element analysis is often a compromise between: a) needs and time constraint, b) our understanding of the problem and of nonlinear analysis, c) tools available, and d) quality of results expected. Likewise, if we are interested in a localized part of the structure, shall we model the entire structure with reasonable details to capture the local effect but may jeopardize a probabilistic analysis, or should one use a coarse global mesh, and then a fine grained mesh to capture detailed response?

Attention to details must be uniformly distributed over the entire process, Figure 12.3. On the one hand, one may inadvertently underestimate the importance of a particular modeling aspect, and this weakest link may then trigger failure. For instance bond failure may be overlooked, yet for seismic loads it is critical at the base of a CEB.

Similarly, disproportionate effort may be spent in modeling an aspect of the structure which is unlikely to play a critical role. For instance, modeling the stiffness of the

liner or of the sleeves inside which the post-tensioning cables are housed may require much effort, increase the complexity of the model, and is ultimately unnecessary.

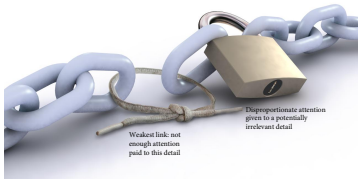

Fig. 12.3: Uniformly distributed model complexity

Contrary to linear elastic solutions, there are a multitude of acceptable non-linear solutions. Different software, models, and analysts will get different results, and this does not imply that they are all "wrong" (but some may be). It should be kept in mind that, often, large scale failure is driven by small overlooked details, which in retrospect could and should have been considered in the model while major effort may have been spent on modeling irrelevant other details. Hence, great care should be exercised in identifying what must be modeled, what is relevant, and what is not. In the end, the finite element analysis is just a tool to confirm or quantify a response anticipated through proper solid engineering judgment.

12.2.2 Loads and Boundary Conditions

Loads should receive special attention especially in the context of a nonlinear (incremental) analysis. Point loads should be completely discarded as they will induce a localized stress concentration which may slow down the analysis. Instead, distributed traction over a narrow strip should be used. Initial loads should be carefully applied initially through one or more increments even though they are unlikely to induce any non-linearity. This is mostly for the gravity loads and initial displacements.
In nonlinear analyses, load is applied incrementally. Too large of an increment will result in a slow convergence; too small will result in increased computational time. In a dynamic analysis, time steps should be a function of the type of analysis. In an implicit one (where equilibrium is nearly enforced through iterations within an increment), the "usual" time step is 0.02 sec. Whereas in an explicit analysis, the time step should be much smaller to make ensure that a stress wave does not cross an entire element during a time step (thus computation time is in this case conditioned on the smallest element size in the mesh) [222]. Depending on the computer program, some loads may be incremental and others not.
Whereas *a priori* boundary conditions may not be perceived as loads, they are. Indeed a non zero fixed support will induce loads. Careful to not drastically change the boundary conditions on an analysis without the "buffer" of a few increments to allow equilibrium to be properly recovered.

In an incremental nonlinear analysis, loading of each increment should be referenced, Table 12.1.

Table 12.1: Sample of Excel file storing load information

Increments			
From	**To**	**Description**	**Comments**
1	end	B.C.: Lateral support	*on patch 231*
1	3	Initial gravity load	*this is a total and not an increment load*
4	8	Initial thermal load	
9	50	Incremental load	
51	52	Detension cable 21	
53	300	Incremental AAR load	*Careful about the time increment here*
Save and restart with removed BC			
301	20,000	Seismic excitation	*uniform ground excitation hor. and ver.*

12.2.3 Material Properties

Material properties for a non-linear analysis go well beyond the traditional compressive strength, f'_c. Though each structure may be governed by different codes of construction (not to be confused with codes for safety assessment), in order of importance, the following data should be gathered for multiple site locations and prevalent standards recommended:

Compressive strength per ACI 349 [11] or ASTM, C39 [59].
Elastic Modulus per ACI 349 [11] or ASTM C469 [61]. Ideally, the full stress-strain curve should be measured and reported. If possible, tests should be conducted under strain control.
Tensile strength per ACI 349 [11] or ASTM C496 [62].
Fracture Energy is a most important parameter for modern non-linear analysis.
Creep Coefficients per ASTM C512 [63].

In a nonlinear analysis, some material properties are either unknown or widely guesstimated. As such, probabilistic analyses may be warranted. This entails selection of the distribution (normal and log-normal are the most common), the corresponding mean and standard deviation. Since the normal distribution goes from minus to plus infinity, it is advisable to use a truncated distribution at plus or minus two standard deviations. In the context of a probabilistic analysis, the probability distribution function should also be identified along with the normalized standard deviation and the truncated values (minimum and maximum).
A major tenet in the scientific and engineering community is that a paper or report should contain sufficient detail (data, figures, and others) and references to permit others to replicate the work. Hence, all input data should be clearly identified: value, symbol, and reference.
Data will be most efficiently stored in a multi-sheet excel file, Table 12.2 for the variables and Table 12.3 for the correlations.

Table 12.2: Example of Data Repository

Characteristics	Symbol	Unit	Distributional model	Mean/COV	[min, max]
Max. volumetric strain	$\varepsilon^{\infty}_{AAR}$	-	Trapezoidal	-	[0.004 0.020]
Characteristic time	τ_c	ATU	Trapezoidal	-	[40 75]
Latency time	τ_l	ATU	Trapezoidal	-	[480 610]
Activation energy for τ_c	U_C	^{o}K	Uniform Dist.	5,400	[4,900 5,900]
Activation energy for τ_l	U_L	^{o}K	Uniform Dist.	9,400	[8,900 9,900]
Residual reduction factor	Γ_r	-	Normal Dist.	0.15/0.2	[0.1 0.2]
Fraction of ε_t	γ_t	-	Normal Dist.	0.5/0.2	[0.3 0.7]
Compressive strength	f_c	MPa	Uniform Dist.	-67.0	[-77.0 -57.0]
Tensile strength	f_t	MPa	Uniform Dist.	4.5	[4.0 5.0]
Shape factor	a	-	Deterministic	-2	-
Reference temperature	T_0	^{o}C	-	10.1/0.3	[2 19]
Upper compressive stress lim.	σ_U	MPa	Deterministic	-8	
Reduction fraction for E	β_E	-	Uniform Dist.	-	[0.68 0.78]
Reduction faction for f'_t	β_{f_t}	-	Uniform Dist.	-	[0.10 0.41]

Table 12.3: Example of Correlation Between Random variables

Property	**RV**	**1**	**2**	**3**	**4**	**5**	**6**	**7**	**8**	**9**	**10**	**11**	**12**
Mass density	1	1											
Coefficient of thermal expansion	2	0	1										
Elastic/Young's modulus	3	0	0	1									
Poisson's ratio	4	0	0	0	1								
Tensile strength	5	0	0	0	0	1							
G_F - Exponential softening	6	0	0	0	0	0.5	1						
Compressive strength (must be negative)	7	0	0	0.5	0	0	0	1					
Compressive critical displacement	8	0	0	0	0	0.7	0	0	1				
Factor beta for return direction	9	0	0	0	0	0	0	0	0	1			
Factor e for roundness of failure surface	10	0	0	0	0	0	0	0	0	0	1		
Onset of non-linearity in compression	11	0	0	0	0	0	0	0	0	0	0	1	
Plastic strain at compressive stresngth	12	0	0	0	0	0	0	0	0	0	0	0	1

12.2.4 Software Selection

The first reaction is to assume that the readily available (in-house or with the consultant) software is adequate. This is not always correct. By the time a non-linear analysis must be performed, a serious and potentially grave problem exists, and the best tool should be selected. Software fall into four major categories:

Major Commercial ABAQUS, ADINA, ANSYS: none of them targets the civil engineering discipline (but rather aerospace, mechanical, and nuclear respectively). Code Aster is worth mentioning as it was developed by the French national utility company *EdF* and must be used by all analysts. The code is practically not used outside of France.

National Laboratories LS-Dyna (originally developed at Lawrence Livermore Laboratory) has been widely publicized [361]. It uses an explicit algorithm; thus results will always be obtained, but there is no assurance that equilibrium

(and thus nearly correct) results are obtained, Section 14.4.1. Another "up and coming" software is Grizzly (developed by the Idaho National Laboratory for modeling degradation of nuclear power plant systems, structures, and components) [438, 801] for concrete structures. However at this stage, it still lacks some essential features for the non-linear analysis of reinforced concrete.

Medium Size Specialized software for concrete such as DIANA [245] and ATENA [180]. The former grew from the TNO research laboratory at Delft university, and the second has been developed by Cervenka. Both of them have many concrete models, and to the best of the author's knowledge, only ATENA has been used for the simulation of an acNCS.

University Codes such as MERLIN [767], developed by the authors through funding from the Electric Power Research Institute, and then from the Tokyo Electric Power Company (TEPCO). This is not a commercial software as it does not contain safeguard for possible misuse by an unqualified analyst.

12.2.5 Concepts of Model Verification and Validation

Too often nonlinear finite element codes are presumed as "validated" by merely capturing the experimentally observed data (displacements typically). Often times, this is accompanied with very colorful figures and juxtapositions. It should be kept in mind that nonlinear models have sufficient variables to "tune" many of them and then obtain what is perceived as an acceptable model. Such a model should be scrutinized to make sure that all assumptions are sound and reasonable and that material properties adopted are realistic. In other words a mere superficial pictorial comparison is not sufficient.

It is commonly said that a finite element code must be validated or verified. A few definitions are in order [828] [806].

Verification Process of determining that a model implementation accurately represents the developer's conceptual description of the model and the solution to the model. It is concerned with identifying and removing errors in the model by comparing numerical solutions to analytical or highly accurate benchmark solutions. In short, verification deals with the mathematics associated with the model.

Validation Process of determining the degree to which a model is an accurate representation of the real world from the perspective of the intended uses of the model. It is concerned with quantifying the accuracy of the model by comparing numerical solutions to experimental data. In short, validation deals with the physics associated with the model.

Calibration Process of adjusting numerical or physical modeling parameters in the computational model for the purpose of improving agreement with experimental data.

Code Verification Process of determining that the computer code is correct and functioning as intended.

Computer Model Numerical implementation of the mathematical model, usually in the form of numerical discretization, solution algorithms, and convergence criteria.

Conceptual Model Collection of assumptions, algorithms, relationships, and data that describe the reality of interest from which the mathematical model and validation experiment can be constructed.

Confidence Probability that a numerical estimate will lie within a specified range.

Error is a recognizable deficiency in any phase or activity of modeling and simulation that is not due to lack of knowledge.

Fidelity The difference between simulation and experimental outcomes.

Irreducible Uncertainty Inherent variation associated with the physical system being modeled.

Mathematical Model The mathematical equations, boundary values, initial conditions, and modeling data needed to describe the conceptual model.

Model Conceptual/mathematical/numerical description of a specific physical scenario, including geometrical, material, initial, and boundary data.

Model Revision The process of changing the basic assumptions, structure, parameter estimates, boundary values, or initial conditions of a model to improve agreement with experimental outcomes.

Prediction Use of a model to foretell the state of a physical system under conditions for which the model has not been validated.

Reducible Uncertainty Potential deficiency that is due to lack of knowledge, e.g. incomplete information, poor understanding of physical process, imprecisely defined or nonspecific description of failure modes, etc.

12.2.6 Expert Selection

If a non-linear analysis is to be performed, great care should be exercised in selecting "experts" who could perform such an analysis. Most engineers in consulting firms are accustomed to performing linear elastic analyses and code regulated design. On the other hand, there are a handful of researchers in academia who are well versed in the conduct of non-linear analysis of a complex structure; however they often tend to simplify peripheral aspects of the model and focus on a narrow aspect.
It should be kept in mind that extraordinary problems will require extraordinary techniques to investigate by very well qualified analysts.

12.2.7 Finite Element Mesh/Analysis Verification

Once a finite element mesh has been put together, it is desirable to verify its representativity. This can be assessed by comparing the finite element and experimental modal models. The former is determined from a modal analysis and the determination of the first natural frequency of the finite element model. The latter can be obtained through a forced vibration of the structure by a shaker with an eccentrically placed mass.

For containment enclosure buildings (CEB), at the very least, the linear elastic response of the model should reasonably well match the results obtained from the structural integrity test (SIT), which involves pressurizing the container and recording displacements at various locations. Likewise for dams, the analysis should be able to predict the changes due to either seasonal temperature changes or the changes in pool elevation (not the absolute values but the variation). Finally, "validation" on the basis of linear elastic analysis does not imply validation of the non-linear model. Mesh for a nonlinear analysis could be verified by a "pushover" analysis to identify if it is capable of replicating an anticipated failure mode (for instance, are the joint elements properly defined to allow anticipated failure?) as in Figure 29.2(d). Finally, the non-linear model should be validated independently based on a representative structural component with a known experimental response.

12.2.8 Singularities

Singularities (theoretically infinite stress) appear in many finite element models whenever there are point/line loads, sharp corners, discontinuities in boundary conditions or loads. For instance under a point load, the stress is $\propto 1/R^2$ [140]. To circumvent their presence would be to unduly refine the mesh which may be very time consuming and not necessary. Hence in the presence of singularity, one should not try to excessively refine the mesh as the mesh will never be fine enough. In other words, the smaller the element size, the larger the stress (i.e. "tell me what stress you want, I can get it by merely playing with the element size"), Figure 12.4.

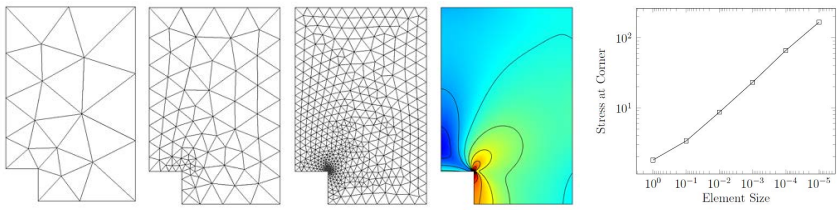

(a) Refined meshes (b) Stress *vs.* element size

Fig. 12.4: Meshing in the presence of stress singularity in a re-entry corner [431]

In the context of linear elastic analysis, this should not be a problem, however for non-linear analyses, singularities will have a very detrimental effect as they will slow the solution, and their impact will mask the stress distribution in the rest of the mesh (unless contour lines of stresses are plotted on the basis of a logarithmic scale).

Chapter 13
Finite Elements

Abstract
Two important aspects of the finite element method are summarized in this chapter. Starting with the derivation of the principle of virtual work (displacement), a general expression for the element stiffness matrix is derived. In the second part, details of the formulation of the most commonly used element (isoparametric) are presented. Though understanding of this chapter is not critical for the practitioner, it does nevertheless hint to practical issues that they may be confronted with (such as element distortion, nodal equivalent loads, stress recovery, or convergence) as the practicing engineer.

13.1 Principle of Virtual Work (Displacement)

It all starts with the principle of virtual work. Through the Euler's equation (calculus of variation), it can be derived from the equation of equilibrium (expressed in differential form) and vice versa. Its derivation starts with the assumption that forces are in equilibrium (§1.4.2) and satisfaction of the natural (traction) boundary conditions (Section1.5).
The equation of equilibrium (Eq. 1.108) is rewritten as

$$\frac{\partial \sigma_{xx}}{\partial x} + \frac{\partial \tau_{xy}}{\partial y} + b_x = 0 \tag{13.1}$$

$$\frac{\partial \sigma_{yy}}{\partial y} + \frac{\partial \tau_{xy}}{\partial x} + b_y = 0 \tag{13.2}$$

where $\mathbf{b}$ represents the body force. In matrix form, this can be rewritten as

$$\begin{bmatrix} \frac{\partial}{\partial x} & 0 & \frac{\partial}{\partial y} \\ 0 & \frac{\partial}{\partial y} & \frac{\partial}{\partial x} \end{bmatrix} \begin{Bmatrix} \sigma_{xx} \\ \sigma_{yy} \\ \tau_{xy} \end{Bmatrix} + \begin{Bmatrix} b_x \\ b_y \end{Bmatrix} = 0 \tag{13.3}$$

or

$$\underbrace{\mathbf{L}^T \boldsymbol{\sigma}}_{\nabla . \boldsymbol{\sigma}} + \mathbf{b} = 0 \tag{13.4}$$

Note that this equation can be generalized to 3D.

The surface Γ of the solid can be decomposed into two parts, Γ_t and Γ_u,

$$\Gamma = \Gamma_t \cup \Gamma_u \tag{13.5}$$

where tractions and displacements are respectively specified.

$$\mathbf{t} - \hat{\mathbf{t}} = 0 \quad \text{on } \Gamma_t \ \text{ Natural B.C.} \tag{13.6}$$

where the hat corresponds to known values.
Equations 13.4 and 13.6 constitute a statically admissible stress field.
We now express the local condition of equilibrium, Eq. 13.4, and the static boundary condition, Eq. 13.6, in global (or integral) form. This is accomplished (Galerkin's Method) by multiplying both equations by a virtual displacement $\delta\mathbf{u}$ and integrating the first equation over Ω and the second one over Γ_t. We then take the sum of these two integrals (each of which must be equal to zero):

$$-\int_\Omega \delta\mathbf{u}^T \underbrace{\left(\mathbf{L}^T\boldsymbol{\sigma} + \mathbf{b}\right)}_{\text{Equil.}} \mathrm{d}\Omega + \int_{\Gamma_t} \delta\mathbf{u}^T \underbrace{\left(\mathbf{t} - \hat{\mathbf{t}}\right)}_{\text{B.C.}} \mathrm{d}\Gamma = 0 \tag{13.7}$$

Note that since each term is equal to zero, the negative sign is introduced to maintain later on consistency with previous results. Furthermore, according to the fundamental lemma of the calculus of variation, this equation is still equivalent to Eq. 13.4. Next, we will focus our attention on $\int_{\Gamma_t} \delta\mathbf{u}^T\mathbf{t}\mathrm{d}\Gamma$ which will be replaced (from Eq. 13.5) by

$$\int_{\Gamma_t} \delta\mathbf{u}^T\mathbf{t}\mathrm{d}\Gamma = \int_{\Gamma} \delta\mathbf{u}^T\mathbf{t}\mathrm{d}\Gamma - \int_{\Gamma_u} \delta\mathbf{u}^T\mathbf{t}\mathrm{d}\Gamma \tag{13.8}$$

and which we seek to convert into a volume integral through Gauss Theorem, Eq. 1.59. But first let us recall the definition of the traction vector:

$$\mathbf{t} = \boldsymbol{\sigma}.\mathbf{n} \quad \text{or} \ \ t_i = \sigma_{ij} n_j \tag{13.9}$$

Applying Gauss theorem we obtain

$$\int_\Gamma \delta\mathbf{u}^T\mathbf{t}\mathrm{d}\Gamma = \int_\Gamma (\delta\mathbf{u}^T\boldsymbol{\sigma})\mathbf{n}\mathrm{d}\Gamma = \int_\Omega \mathrm{div}(\delta\mathbf{u}^T\boldsymbol{\sigma})\mathrm{d}\Omega \tag{13.10}$$

$$= \int_\Omega \mathrm{div}\delta\mathbf{u}^T\boldsymbol{\sigma}\mathrm{d}\Omega + \int_\Omega \delta\mathbf{u}^T\mathrm{div}\boldsymbol{\sigma}\mathrm{d}\Omega \tag{13.11}$$

However, from Eq. 13.4 we have $\mathrm{div}\boldsymbol{\sigma} = \mathbf{L}^T\boldsymbol{\sigma}$ thus,

$$\int_\Gamma \delta\mathbf{u}^T\mathbf{t}\mathrm{d}\Gamma = \int_\Omega \mathrm{div}\delta\mathbf{u}^T\boldsymbol{\sigma}\mathrm{d}\Omega + \int_\Omega \delta\mathbf{u}^T\mathbf{L}^T\boldsymbol{\sigma}\mathrm{d}\Omega \tag{13.12}$$

Combining Eq. 13.8 with the previous equation leads to

$$\int_{\Gamma_t} \delta\mathbf{u}^T \mathbf{t} \mathrm{d}\Gamma = \int_{\Omega} \mathrm{div}\delta\mathbf{u}^T \boldsymbol{\sigma} \mathrm{d}\Omega + \int_{\Omega} \delta\mathbf{u}^T \mathbf{L}^T \boldsymbol{\sigma} \mathrm{d}\Omega - \int_{\Gamma_u} \delta\mathbf{u}^T \mathbf{t} \mathrm{d}\Gamma \tag{13.13}$$

We next substitute this last equation into Eq. 13.7 and reduce

$$\begin{aligned} &- \int_{\Omega} \delta\mathbf{u}^T \mathbf{L}^T \boldsymbol{\sigma} \mathrm{d}\Omega - \int_{\Omega} \delta\mathbf{u}^T \mathbf{b} \mathrm{d}\Omega + \int_{\Omega} \mathrm{div}\delta\mathbf{u}^T \boldsymbol{\sigma} \mathrm{d}\Omega \\ &+ \int_{\Omega} \delta\mathbf{u}^T \mathbf{L}^T \boldsymbol{\sigma} \mathrm{d}\Omega - \int_{\Gamma_u} \delta\mathbf{u}^T \mathbf{t} \mathrm{d}\Gamma - \int_{\Gamma_t} \delta\mathbf{u}^T \hat{\mathbf{t}} \mathrm{d}\Gamma = 0 \end{aligned} \tag{13.14}$$

$$\Rightarrow - \int_{\Omega} \delta\mathbf{u}^T \mathbf{b} \mathrm{d}\Omega + \int_{\Omega} \mathrm{div}\delta\mathbf{u}^T \boldsymbol{\sigma} \mathrm{d}\Omega - \int_{\Gamma_u} \delta\mathbf{u}^T \mathbf{t} \mathrm{d}\Gamma - \int_{\Gamma_t} \delta\mathbf{u}^T \hat{\mathbf{t}} \mathrm{d}\Gamma = 0 \tag{13.15}$$

Since we must have a kinematically admissible virtual displacement, i.e. virtual displacements satisfy the essential boundary conditions, then

$$\mathbf{L}\delta\mathbf{u} = \mathrm{div}\delta\mathbf{u} = \delta\boldsymbol{\varepsilon} \tag{13.16}$$

Substituting in the previous equation, we get

$$- \int_{\Omega} \delta\mathbf{u}^T \mathbf{b} \mathrm{d}\Omega + \int_{\Omega} \delta\boldsymbol{\varepsilon}^T \boldsymbol{\sigma} \mathrm{d}\Omega - \int_{\Gamma_u} \delta\mathbf{u}^T \mathbf{t} \mathrm{d}\Gamma - \int_{\Gamma_t} \delta\mathbf{u}^T \hat{\mathbf{t}} \mathrm{d}\Gamma = 0 \tag{13.17}$$

Virtual displacement must be kinematically admissible, i.e. $\delta\mathbf{u}$ must satisfy the essential boundary conditions $\mathbf{u} = 0$ on Γ_u (note that the exact solution had to satisfy the natural/traction B.C. instead); hence the previous equation reduces to

$$\underbrace{\int_{\Omega} \delta\boldsymbol{\varepsilon}^T \boldsymbol{\sigma} \mathrm{d}\Omega}_{-\delta W_i = \delta U_i} \underbrace{- \int_{\Omega} \delta\mathbf{u}^T \mathbf{b} \mathrm{d}\Omega - \int_{\Gamma_t} \delta\mathbf{u}^T \hat{\mathbf{t}} \mathrm{d}\Gamma}_{-\delta W_e} = 0 \tag{13.18}$$

Each of the preceding equations is a work expression. The first one corresponds to the internal virtual work, and the last two are expressions of the work done by the body forces and the surface tractions through the corresponding virtual displacement, $\delta\mathbf{u}$; hence

$$-\delta W_i = \delta W_e \tag{13.19}$$

or

$$\delta U_i = \delta W_e \tag{13.20}$$

which is the expression of the *principle of virtual work* (or more specifically of virtual displacement) which can be stated as:

> A deformable system is in equilibrium (Eq. 13.4) if the sum of the external virtual work and the internal virtual work is zero for virtual displacements $\delta\mathbf{u}$ which are kinematically admissible (Eq. 13.16).

The major governing equations are summarized as follows:

$$\underbrace{\int_\Omega \delta\boldsymbol{\varepsilon}^T\boldsymbol{\sigma}\mathrm{d}\Omega}_{-\delta W_i} \underbrace{- \int_\Omega \delta\mathbf{u}^T\mathbf{b}\mathrm{d}\Omega - \int_{\Gamma_t} \delta\mathbf{u}^T\hat{\mathbf{t}}\mathrm{d}\Gamma}_{-\delta W_e} = 0 \tag{13.21}$$

$$\delta\boldsymbol{\varepsilon} = \mathbf{L}\delta\mathbf{u} \quad \text{in} \quad \Omega \tag{13.22}$$

$$\delta\mathbf{u} = 0 \quad \text{on} \quad \Gamma_u \tag{13.23}$$

Note that the principle is independent of material properties and that *both the real and virtual quantities must be expressed in terms of displacements*.
For one dimensional elements with no initial strains ($U = -W_i$),

$$\underbrace{\int \sigma\delta\varepsilon\mathrm{d}\Omega}_{\delta U} = \underbrace{P\delta v}_{\delta W} \tag{13.24}$$

13.2 Element Stiffness Matrix Formulation

The displacement, Δ, at any point inside an element can be written in terms of the shape functions $\lfloor\mathbf{N}\rfloor$ and the nodal displacements $\{\overline{\boldsymbol{\Delta}}\}$:

$$\Delta(x) \overset{\text{def}}{=} \lfloor\mathbf{N}(x)\rfloor\{\overline{\boldsymbol{\Delta}}\} \tag{13.25}$$

The strain is then defined as:

$$\varepsilon(x) \overset{\text{def}}{=} [\mathbf{B}(x)]\{\overline{\boldsymbol{\Delta}}\} \tag{13.26}$$

where $[\mathbf{B}]$ is the matrix which relates nodal displacements to strain field and is clearly expressed in terms of derivatives of $\mathbf{N}$.
In one dimensional elements with initial strain (temperature effect, support settlement, or other),

$$\varepsilon_{xx} = \underbrace{\frac{\sigma_{xx}}{E}}_{\text{due to load}} + \underbrace{\varepsilon^0_{xx}}_{\text{initial strain}} \tag{13.27}$$

Thus

$$\sigma_{xx} = E\varepsilon_{xx} - E\varepsilon^0_{xx} \tag{13.28}$$

Generalizing and in matrix form:

$$\{\boldsymbol{\sigma}\} = [\mathbf{D}]\{\boldsymbol{\varepsilon}\} - [\mathbf{D}]\{\boldsymbol{\varepsilon}^0\} \tag{13.29}$$

where $[\mathbf{D}]$ is the constitutive matrix which relates stress and strain vectors.
The element will be subjected to a load, $q(x)$, acting on its surface. Let us now apply the principle of virtual displacement and restate some known relations:

$$\delta U = \delta W \tag{13.30}$$

$$\delta U = \int_{\Omega} \lfloor \delta\varepsilon \rfloor \{\boldsymbol{\sigma}\} \mathrm{d}\Omega \tag{13.31}$$

$$\{\boldsymbol{\sigma}\} = [\mathbf{D}]\{\varepsilon\} - [\mathbf{D}]\{\varepsilon^0\} \tag{13.32}$$

$$\{\boldsymbol{\varepsilon}\} = [\mathbf{B}]\{\overline{\boldsymbol{\Delta}}\} \tag{13.33}$$

$$\{\delta\boldsymbol{\varepsilon}\} = [\mathbf{B}]\{\delta\overline{\boldsymbol{\Delta}}\} \tag{13.34}$$

$$\lfloor \delta\boldsymbol{\varepsilon} \rfloor = \lfloor \delta\overline{\boldsymbol{\Delta}} \rfloor [\mathbf{B}]^T \tag{13.35}$$

Combining Eqns. 13.30, 13.31, 13.32, 13.35, and 13.33, the internal virtual strain energy is given by

$$\begin{aligned} \delta U &= \int_{\Omega} \underbrace{\lfloor \delta\overline{\boldsymbol{\Delta}} \rfloor [\mathbf{B}]^T}_{\lfloor \delta\boldsymbol{\varepsilon} \rfloor} \underbrace{[\mathbf{D}][\mathbf{B}]\{\overline{\boldsymbol{\Delta}}\}}_{\{\boldsymbol{\sigma}\}} \mathrm{d}\Omega - \int_{\Omega} \underbrace{\lfloor \delta\overline{\boldsymbol{\Delta}} \rfloor [\mathbf{B}]^T}_{\lfloor \delta\boldsymbol{\varepsilon} \rfloor} \underbrace{[\mathbf{D}]\{\varepsilon^0\}}_{\{\boldsymbol{\sigma}^0\}} \mathrm{d}\Omega \\ &= \lfloor \delta\overline{\boldsymbol{\Delta}} \rfloor \int_{\Omega} [\mathbf{B}]^T [\mathbf{D}][\mathbf{B}] \, \mathrm{d}\Omega \{\overline{\boldsymbol{\Delta}}\} - \lfloor \delta\overline{\boldsymbol{\Delta}} \rfloor \int_{\Omega} [\mathbf{B}]^T [\mathbf{D}]\{\varepsilon^0\} \mathrm{d}\Omega \end{aligned} \tag{13.36}$$

The virtual external work in turn is given by

$$\delta W = \underbrace{\lfloor \delta\overline{\boldsymbol{\Delta}} \rfloor}_{\text{Virt. Nodal Displ.}} \underbrace{\{\overline{\mathbf{F}}\}}_{\text{Nodal Force}} + \int_{l} \lfloor \delta\Delta \rfloor q(x) \mathrm{d}x \tag{13.37}$$

Combining this equation with

$$\{\delta\Delta\} = [\mathbf{N}]\{\delta\overline{\boldsymbol{\Delta}}\} \tag{13.38}$$

yields:

$$\delta W = \lfloor \delta\overline{\boldsymbol{\Delta}} \rfloor \{\overline{\mathbf{F}}\} + \lfloor \delta\overline{\boldsymbol{\Delta}} \rfloor \int_0^l [\mathbf{N}]^T \, q(x) \, \mathrm{d}x \tag{13.39}$$

Equating the internal strain energy, Eqn. 13.36, with the external work, Eqn. 13.39, we obtain:

$$\begin{aligned} &\underbrace{\lfloor \delta\overline{\boldsymbol{\Delta}} \rfloor \underbrace{\int_{\Omega} [\mathbf{B}]^T [\mathbf{D}][\mathbf{B}] \, \mathrm{d}\Omega}_{[\mathbf{k}]} \{\overline{\boldsymbol{\Delta}}\} - \lfloor \delta\overline{\boldsymbol{\Delta}} \rfloor \underbrace{\int_{\Omega} [\mathbf{B}]^T [\mathbf{D}]\{\varepsilon^0\} \mathrm{d}\Omega}_{\{\overline{\mathbf{F}}^0\}}}_{\delta U} = \\ &\underbrace{\lfloor \delta\overline{\boldsymbol{\Delta}} \rfloor \{\overline{\mathbf{F}}\} + \lfloor \delta\overline{\boldsymbol{\Delta}} \rfloor \underbrace{\int_0^l [\mathbf{N}]^T \, q(x) \, \mathrm{d}x}_{\{\overline{\mathbf{F}}^e\}}}_{\delta W} \end{aligned} \tag{13.40}$$

or

$$[\mathbf{k}]\{\overline{\boldsymbol{\Delta}}\} - \{\overline{\mathbf{F}}^o\} = \{\overline{\mathbf{F}}\} + \{\overline{\mathbf{F}}^e\} \tag{13.41}$$

which is the counterpart of Eq. 13.29.
Canceling out the $\lfloor \delta\overline{\mathbf{\Delta}} \rfloor$ term, this is the same equation of equilibrium as the one written earlier. It relates the (unknown) nodal displacement $\left\{\overline{\mathbf{\Delta}}\right\}$, the structure stiffness matrix $[\mathbf{k}]$, the external nodal force vector $\left\{\overline{\mathbf{F}}\right\}$, the distributed element force $\left\{\overline{\mathbf{F}}^e\right\}$, and the vector of initial displacement.
From this relation we define:

The element stiffness matrix:

$$[\mathbf{k}] = \int_{\Omega} [\mathbf{B}]^T [\mathbf{D}][\mathbf{B}] \mathrm{d}\Omega \tag{13.42}$$

Element initial force vector:

$$\{\overline{\mathbf{F}}^0\} = \int_{\Omega} [\mathbf{B}]^T [\mathbf{D}]\{\varepsilon^0\} \mathrm{d}\Omega \tag{13.43}$$

Element equivalent load vector:

$$\{\overline{\mathbf{F}}^e\} = \int_0^L [\mathbf{N}]\, q(x)\, \mathrm{d}x \tag{13.44}$$

and the general equation of equilibrium can be written as:

$$[\mathbf{k}]\{\overline{\mathbf{\Delta}}\} - \{\overline{\mathbf{F}}^0\} = \{\overline{\mathbf{F}}\} + \{\overline{\mathbf{F}}^e\} \tag{13.45}$$

Next we seek to determine the internal (generalized) stresses which are more important than displacements in the context of design or safety assessment.
Recall that we have:

$$\{\boldsymbol{\sigma}\} = [\mathbf{D}]\{\varepsilon\} \tag{13.46}$$
$$\{\varepsilon\} = [\mathbf{B}]\{\overline{\mathbf{\Delta}}\} \tag{13.47}$$

With the vector of nodal displacement $\{\mathbf{\Delta}\}$ known, those two equations would yield:

$$\{\boldsymbol{\sigma}\} = [\mathbf{D}] \cdot [\mathbf{B}]\{\overline{\mathbf{\Delta}}\} \tag{13.48}$$

We note that the secondary variables (strain and stresses) are derivatives of the primary variables (displacement), and as such may not always be determined with the same accuracy.

13.3 Isoparametric Elements

In modern finite element codes, nearly all elements are so-called isoparameteric (that is, the displacement field and the deformed shape of the element are of the same order). In this formulation, the natural coordinates will be distorted into new curvilinear sets when plotted in a Cartesian x, y, z space, Figure 13.1.

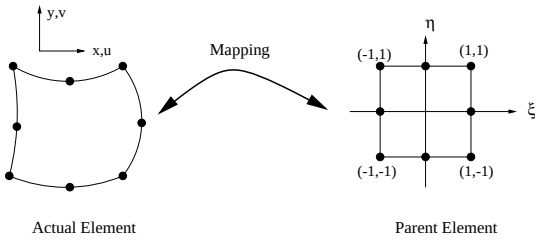

Fig. 13.1: Two-Dimensional Mapping of Some Elements

Displacements will be expressed in terms of natural coordinates; however they must be differentiated with respect to Cartesian coordinates x, y, z. This is accomplished through a transformation matrix $\mathbf{J}$, and integration can no longer be performed analytically but must be done numerically within the range of the natural coordinates range from -1 to +1.
Finally, nodal displacements at any point inside the element can be written in terms of the nodal known displacements and the shape functions

$$\begin{aligned} u &= N_1\overline{u}_1 + N_2\overline{u}_2 + \cdots = \mathbf{N}\left\{\begin{array}{c}\overline{u}_1\\ \overline{u}_2\\ \vdots\end{array}\right\} = \mathbf{N}\overline{\mathbf{u}}_e \\ v &= N_1\overline{v}_1 + N_2\overline{v}_2 + \cdots = \mathbf{N}\left\{\begin{array}{c}\overline{v}_1\\ \overline{v}_2\\ \vdots\end{array}\right\} = \mathbf{N}\overline{\mathbf{v}}_e \end{aligned} \tag{13.49}$$

or

$$\mathbf{u} = \lfloor\, u\ v\ w\,\rfloor^T = [\mathbf{N}]\overline{\mathbf{u}}_e \tag{13.50}$$

It should be noted that when elements are also distorted, the coordinates of any point can also be expressed in terms of nodal coordinates

$$\begin{aligned} x &= \tilde{N}_1\overline{x}_1 + \tilde{N}_2\overline{x}_2 + \cdots = \tilde{\mathbf{N}}\left\{\begin{array}{c}\overline{x}_1\\ \overline{x}_2\\ \vdots\end{array}\right\} = \tilde{\mathbf{N}}\overline{\mathbf{x}} \\ y &= \tilde{N}_1\overline{y}_1 + \tilde{N}_2\overline{y}_2 + \cdots = \tilde{\mathbf{N}}\left\{\begin{array}{c}\overline{y}_1\\ \overline{y}_2\\ \vdots\end{array}\right\} = \tilde{\mathbf{N}}\overline{\mathbf{y}} \end{aligned} \tag{13.51}$$

or

$$c = \lfloor\, x\ y\ z\,\rfloor^T = [\tilde{\mathbf{N}}]\overline{\mathbf{c}} \tag{13.52}$$

Shape function matrices, $[\mathbf{N}]$ and $[\tilde{\mathbf{N}}]$, are functions of ξ, η, and ζ. Hence, three possible cases arise, Figure 13.2.

Isoparamteric: $[\mathbf{N}]$ and $[\tilde{\mathbf{N}}]$ are identical
Subparamteric: $[\mathbf{N}]$ is of higher degree than $[\tilde{\mathbf{N}}]$
Superparamteric: $[\mathbf{N}]$ is of lower degree than $[\tilde{\mathbf{N}}]$

Note that sub and super parametric elements are very seldom used.

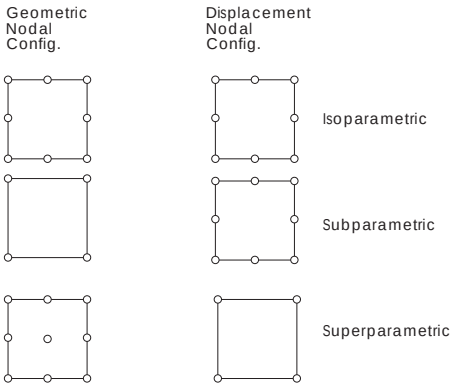

Fig. 13.2: Iso, Super, and Sub Parametric Elements

13.3.1 Element Formulation

The actual formulation of a finite element is rooted in an extension of the principle of virtual displacement: the so-called Rayleigh-Ritz method where one assumes a polynomial expansion of the displacement field, and the number of terms would have to be equal to the number of nodes. This is best illustrated through Pascal's triangle in Figure 13.3.
In the so-called serendipity elements, all relevant terms are present for the linear element but not for the quadratic one (eight noded). On the other hand, all terms are present in the so-called Lagrangian element (nine noded).
In the following, the element formulation of the bar and quadrilateral elements will be detailed.

13.3.1.1 Bar Element

The simplest introduction to isoparametric elements is through a straight, three noded quadratic element, Figure 13.4.
The shape functions for the element can be obtained from the Lagrangian interpolation function. The kth term in a polynomial of order $n-1$ would be

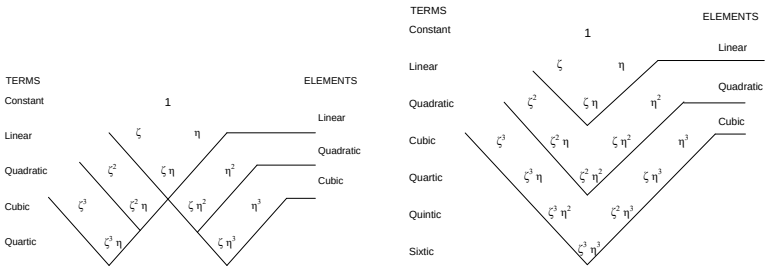

(a) Serendipity element (b) Lagrange element

Fig. 13.3: Pascal Triangles for Quadrilateral Elements

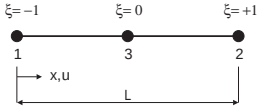

Fig. 13.4: Three-noded quadratic bar element

$$N_k^n = \frac{\prod_{i=1, i\neq k}^{n}(\xi - \xi_i)}{\prod_{i=1, i\neq k}^{n}(\xi_k - \xi_i)} \tag{13.53}$$

$$= \frac{(\xi-\xi_1)(\xi-\xi_2)\cdots(\xi-\xi_{k-1})(\xi-\xi_{k+1})\cdots(\xi-\xi_n)}{(\xi_k-\xi_1)(\xi_k-\xi_2)\cdots(\xi_k-\xi_{k-1})(\xi_k-\xi_{k+1})\cdots(\xi_k-\xi_n)} \tag{13.54}$$

For a three noded quadratic element, $\xi_1 = -1$, $\xi_2 = +1$, and $\xi_3 = 0$. Substituting, we obtain the three shape functions:

$$\begin{aligned} N_1(\xi) &= \tfrac{(\xi-\xi_2)(\xi-\xi_3)}{(\xi_1-\xi_2)(\xi_1-\xi_3)} = \tfrac{(\xi-1)(\xi-0)}{(-1-1)(-1-0)} &&= \tfrac{1}{2}(\xi^2-\xi) \\ N_2(\xi) &= \tfrac{(\xi-\xi_1)(\xi-\xi_3)}{(\xi_2-\xi_1)(\xi_2-\xi_3)} = \tfrac{(\xi+1)(\xi-0)}{(1+1)(1-0)} &&= \tfrac{1}{2}(\xi^2+\xi) \\ N_3(\xi) &= \tfrac{(\xi-\xi_1)(\xi-\xi_2)}{(\xi_3-\xi_1)(\xi_3-\xi_2)} = \tfrac{(\xi+1)(\xi-1)}{(0+1)(0-1)} &&= 1-\xi^2 \end{aligned} \tag{13.55}$$

Hence,

$$x(\xi) = \lfloor \mathbf{N} \rfloor \lfloor\, \overline{x}_1 \; \overline{x}_2 \; \overline{x}_3 \,\rfloor^T \quad \text{and} \quad u(\xi) = \lfloor \mathbf{N} \rfloor \lfloor\, \overline{u}_1 \; \overline{u}_2 \; \overline{u}_3 \,\rfloor^T \tag{13.56}$$

where

$$\lfloor \mathbf{N} \rfloor = \lfloor\, \tfrac{1}{2}(\xi^2-\xi) \;\; \tfrac{1}{2}(\xi^2+\xi) \;\; 1-\xi^2 \,\rfloor \tag{13.57}$$

The strain displacement relation is given by Eq. 1.91 $\boldsymbol{\varepsilon} = \mathbf{L}\mathbf{u} = \mathbf{L}\mathbf{N}\overline{\mathbf{u}}_e = \mathbf{B}\overline{\mathbf{u}}_e$, and the differential operator $\mathbf{L}$ is equal to $\frac{\mathrm{d}}{\mathrm{d}x}$. For this one dimensional case, this reduces to

$$\varepsilon_x = \frac{du}{\mathrm{d}x} = \underbrace{\underbrace{\frac{\mathrm{d}}{\mathrm{d}x}}_{L} \lfloor \mathbf{N} \rfloor}_{\mathbf{B}} \begin{Bmatrix} \overline{u}_1 \\ \overline{u}_2 \\ \overline{u}_3 \end{Bmatrix} \tag{13.58}$$

We next invoke the chain rule since the shape functions are expressed in terms of natural coordinates:

$$\mathbf{B} = \frac{\mathrm{d}\mathbf{N}}{\mathrm{d}x} = \frac{\mathrm{d}\mathbf{N}}{\mathrm{d}\xi}\frac{\mathrm{d}\xi}{\mathrm{d}x} \tag{13.59}$$

The first term may be readily available from the shape functions, Eq. 13.57, but the second one is not. Whereas, $\frac{\mathrm{d}\xi}{\mathrm{d}x}$ is not available, we may determine its inverse $\frac{\mathrm{d}x}{\mathrm{d}\xi}$ from Eq. 13.56, which we shall denote by J or **Jacobian**. The Jacobian operator J is a scale factor which relates Cartesian to natural coordinates, $\mathrm{d}x = J\mathrm{d}\xi$.

$$J(\xi) = \frac{\mathrm{d}x}{\mathrm{d}\xi} = \frac{\mathrm{d}}{\mathrm{d}\xi}\lfloor \mathbf{N} \rfloor \begin{Bmatrix} \overline{x}_1 \\ \overline{x}_2 \\ \overline{x}_3 \end{Bmatrix} = \underbrace{\underbrace{\lfloor \tfrac{1}{2}(2\xi - 1) \;\; \tfrac{1}{2}(2\xi + 1) \;\; -2\xi \rfloor}_{\frac{\mathrm{d}_\mathbf{N}}{\mathrm{d}_\xi}} \begin{Bmatrix} \overline{x}_1 \\ \overline{x}_2 \\ \overline{x}_3 \end{Bmatrix}}_{\frac{\mathrm{d}_x}{\mathrm{d}_\xi}} \tag{13.60}$$

We can rewrite Eq. 13.59 as

$$\mathbf{B} = \frac{\mathrm{d}\mathbf{N}}{\mathrm{d}x} = \underbrace{\frac{\mathrm{d}\xi}{\mathrm{d}x}}_{J^{-1}} \frac{\mathrm{d}\mathbf{N}}{\mathrm{d}\xi} \tag{13.61}$$

and the $\mathbf{B}$ matrix is thus obtained by substituting into Eq. 13.58:

$$\lfloor \mathbf{B}(\xi) \rfloor = \frac{1}{J}\frac{\mathrm{d}}{\mathrm{d}\xi}\lfloor \mathbf{N} \rfloor = \frac{1}{J}\lfloor \tfrac{1}{2}(2\xi - 1) \;\; \tfrac{1}{2}(2\xi + 1) \;\; -2\xi \rfloor \tag{13.62}$$

The differential area is

$$d\Omega = A\mathrm{d}x = AJd\xi \tag{13.63}$$

Substituting, the element stiffness matrix is finally obtained from Eq. 13.42

$$\mathbf{K}_e(\xi) = \int_0^L \mathbf{B}^T(\xi)AE\mathbf{B}(\xi)\mathrm{d}x = \int_{-1}^{+1} \mathbf{B}^T(\xi)AE\mathbf{B}(\xi)J(\xi)d\xi \tag{13.64}$$

We observe that $\mathbf{B}$, in general, contains ξ terms in both the numerator and denominator, and hence the expression can not be analytically integrated. Furthermore,

the limits of integration are now from -1 to +1, and we shall see later on how to numerically integrate it.

13.3.1.2 Linear Quadrilateral (Q4)

The previous derivation is now extended to a rectangular four noded element, Figure 13.5.

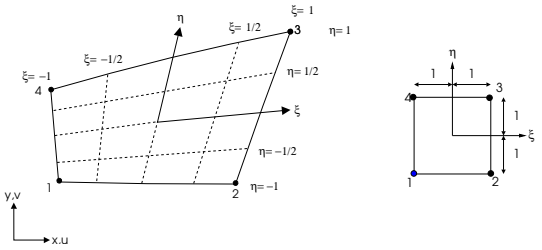

Fig. 13.5: Four noded Isoparametric element

For the two-dimensional case,

$$u(\xi,\eta) = \sum N_{ij}\overline{u}_k = \sum_{i=1}^{n}\sum_{j=1}^{m} N_j(\xi)N_i(\eta)\overline{u}_k \tag{13.65}$$

where $k = (i-1)m + j$.
For a bilinear element, $n = m = 2$, this can be rewritten as

$$\begin{aligned} u(\xi,\eta) &= \lfloor\, N_1(\xi)\ N_2(\xi)\,\rfloor \begin{bmatrix} \overline{u}_1 & \overline{u}_3 \\ \overline{u}_2 & \overline{u}_4 \end{bmatrix} \begin{Bmatrix} N_1(\eta) \\ N_2(\eta) \end{Bmatrix} = \mathbf{N}_\xi^T \overline{\mathbf{u}} \mathbf{N}_\eta \\ &= N_1(\xi)N_1(\eta)\overline{u}_1 + N_2(\xi)N_1(\eta)\overline{u}_2 + N_1(\xi)N_2(\eta)\overline{u}_4 + N_2(\xi)N_2(\eta)\overline{u}_3 \\ &= N_1(\xi,\eta)\overline{u}_1 + N_2(\xi,\eta)\overline{u}_2 + N_3(\xi,\eta)\overline{u}_3 + N_4(\xi,\eta)\overline{u}_4 \qquad (13.66) \\ &= \sum_{i=1}^{4} N_i\overline{u}_i \qquad (13.67) \end{aligned}$$

Applying the Lagrangian interpolation equation, Eq. 13.53, we obtain the shape functions illustrated in Figure 13.11(a).

$$N_1(\xi) = \frac{(\xi - \xi_2)}{(\xi_1 - \xi_2)} = \frac{(\xi - 1)}{(-1 - 1)} = \frac{1}{2}(1 - \xi) \tag{13.68}$$

$$N_2(\xi) = \frac{(\xi - \xi_1)}{(\xi_2 - \xi_1)} = \frac{(\xi + 1)}{(1 + 1)} = \frac{1}{2}(1 + \xi) \tag{13.69}$$

$$N_1(\eta) = \frac{(\eta - \eta_2)}{(\eta_1 - \eta_2)} = \frac{(\eta - 1)}{(-1 - 1)} = \frac{1}{2}(1 - \eta) \tag{13.70}$$

$$N_2(\eta) = \frac{(\eta - \eta_1)}{(\eta_2 - \eta_1)} = \frac{(\eta + 1)}{(1 + 1)} = \frac{1}{2}(1 + \eta) \tag{13.71}$$

Substituting into Eq. 13.66:

$$\begin{array}{l} N_1(\xi,\eta) = \frac{1}{4}(1-\xi)(1-\eta);\ N_2(\xi,\eta) = \frac{1}{4}(1+\xi)(1-\eta) \\ N_3(\xi,\eta) = \frac{1}{4}(1+\xi)(1+\eta);\ N_4(\xi,\eta) = \frac{1}{4}(1-\xi)(1+\eta) \end{array} \tag{13.72}$$

It should be noted that for this simple case, the shape functions could have been determined by mere inspection.
Coordinates and displacements are given by

$$\begin{array}{l} x = \sum N_i(\xi,\eta)\overline{x}_i;\ y = \sum N_i(\xi,\eta)\overline{y}_i \\ u = \sum N_i(\xi,\eta)\overline{u}_i;\ v = \sum N_i(\xi,\eta)\overline{v}_i \end{array} \tag{13.73}$$

The strain displacement relation is given by Eq. 1.91:

$$\{\varepsilon\} = \begin{Bmatrix} \varepsilon_{xx} \\ \varepsilon_{yy} \\ \gamma_{xy} \end{Bmatrix} = \underbrace{\begin{bmatrix} \frac{\partial}{\partial x} & 0 \\ 0 & \frac{\partial}{\partial y} \\ \frac{\partial}{\partial y} & \frac{\partial}{\partial x} \end{bmatrix}}_{\mathbf{L}} \underbrace{\begin{Bmatrix} u \\ v \end{Bmatrix}}_{\mathbf{u}} \tag{13.74}$$

However the displacements can be obtained from Eq. 13.73:

$$\underbrace{\begin{Bmatrix} u \\ v \end{Bmatrix}}_{\mathbf{u}} = \underbrace{\left[\begin{array}{cc|cc|cc|cc} N_1(\xi,\eta) & 0 & N_2(\xi,\eta) & 0 & N_3(\xi,\eta) & 0 & N_4(\xi,\eta) & 0 \\ 0 & N_1(\xi,\eta) & 0 & N_2(\xi,\eta) & 0 & N_3(\xi,\eta) & 0 & N_4(\xi,\eta) \end{array}\right]}_{\mathbf{N}} \underbrace{\begin{Bmatrix} \overline{u}_1 \\ \overline{v}_1 \\ \overline{u}_2 \\ \overline{v}_2 \\ \overline{u}_3 \\ \overline{v}_3 \\ \overline{u}_4 \\ \overline{v}_4 \end{Bmatrix}}_{\overline{\mathbf{u}}} \tag{13.75}$$

Combining Eq. 13.74 and 13.75 yields

$$\boldsymbol{\varepsilon} = \mathbf{LN}\overline{\mathbf{u}} = \mathbf{B}\overline{\mathbf{u}}$$

$$\begin{Bmatrix} \varepsilon_{xx}(\xi,\eta) \\ \varepsilon_{yy}(\xi,\eta) \\ \gamma_{xy}(\xi,\eta) \end{Bmatrix} = \underbrace{\sum_{i=1}^{4} \begin{bmatrix} \frac{\partial N_i(\xi,\eta)}{\partial x} & 0 \\ 0 & \frac{\partial N_i(\xi,\eta)}{\partial y} \\ \frac{\partial N_i(\xi,\eta)}{\partial y} & \frac{\partial N_i(\xi,\eta)}{\partial x} \end{bmatrix}}_{\mathbf{B}=\mathbf{LN}} \underbrace{\begin{Bmatrix} \overline{u}_i \\ \overline{v}_i \end{Bmatrix}}_{\overline{\mathbf{u}}} \tag{13.76}$$

$$= \underbrace{\left[\begin{array}{cc|cc|cc|cc} N_{1,x} & 0 & N_{2,x} & 0 & N_{3,x} & 0 & N_{4,x} & 0 \\ 0 & N_{1,y} & 0 & N_{2,y} & 0 & N_{3,y} & 0 & N_{4,y} \\ N_{1,y} & N_{1,x} & N_{2,y} & N_{2,x} & N_{3,y} & N_{3,x} & N_{4,y} & N_{4,x} \end{array}\right]}_{\mathbf{B}} \left\{\begin{array}{c} \overline{u}_1 \\ \overline{v}_1 \\ \hline \overline{u}_2 \\ \overline{v}_2 \\ \hline \overline{u}_3 \\ \overline{v}_3 \\ \hline \overline{u}_4 \\ \overline{v}_4 \end{array}\right\}$$

$$= \sum_{i=1}^{4} \begin{bmatrix} \frac{\partial N_i(\xi,\eta)}{\partial \xi} & 0 \\ 0 & \frac{\partial N_i(\xi,\eta)}{\partial \eta} \\ \frac{\partial N_i(\xi,\eta)}{\partial \eta} & \frac{\partial N_i(\xi,\eta)}{\partial \xi} \end{bmatrix} \underbrace{\begin{bmatrix} \frac{\partial \xi}{\partial x} & \frac{\partial \eta}{\partial x} \\ \frac{\partial \xi}{\partial x} & \frac{\partial \eta}{\partial y} \end{bmatrix}}_{[\mathbf{J}]^{-1}} \tag{13.77}$$

Considering the local set of coordinates (ξ, η) and the corresponding global one (x, y), the chain rules would give

$$\begin{Bmatrix} \frac{\partial N_i}{\partial \xi} \\ \frac{\partial N_i}{\partial \eta} \end{Bmatrix} = \underbrace{\begin{bmatrix} \frac{\partial x}{\partial \xi} & \frac{\partial y}{\partial \xi} \\ \frac{\partial x}{\partial \eta} & \frac{\partial y}{\partial \eta} \end{bmatrix}}_{\mathbf{J}} \begin{Bmatrix} \frac{\partial N_i}{\partial x} \\ \frac{\partial N_i}{\partial y} \end{Bmatrix} \tag{13.78}$$

$$\begin{Bmatrix} \frac{\partial N_i}{\partial x} \\ \frac{\partial N_i}{\partial y} \end{Bmatrix} = [\mathbf{J}]^{-1} \begin{Bmatrix} \frac{\partial N_i}{\partial \xi} \\ \frac{\partial N_i}{\partial \eta} \end{Bmatrix} \tag{13.79}$$

This last equation is the key to get all the components which will go inside the $\mathbf{B}$ matrix.
Next, expanding the definition of the Jacobian

$$\left\{ \begin{array}{c} \frac{\partial N_i(\xi,\eta)}{\partial \xi} \\ \frac{\partial N_i(\xi,\eta)}{\partial \eta} \end{array} \right\} = \underbrace{\left[\begin{array}{cc} \frac{\partial x}{\partial \xi} & \frac{\partial y}{\partial \xi} \\ \frac{\partial x}{\partial \eta} & \frac{\partial y}{\partial \eta} \end{array} \right]}_{\mathbf{J}} \left\{ \begin{array}{c} \frac{\partial N_i}{\partial x} \\ \frac{\partial N_i}{\partial y} \end{array} \right\} = \sum_{i=1}^{4} \left[\begin{array}{cc} \frac{\partial N_i}{\partial \xi}\overline{x}_i & \frac{\partial N_i}{\partial \xi}\overline{y}_i \\ \frac{\partial N_i}{\partial \eta}\overline{x}_i & \frac{\partial N_i}{\partial \eta}\overline{y}_i \end{array} \right] \left\{ \begin{array}{c} \frac{\partial N_i}{\partial x} \\ \frac{\partial N_i}{\partial y} \end{array} \right\} \tag{13.80}$$

$$= \left[\begin{array}{cccc} \frac{\partial N_1}{\partial \xi} & \frac{\partial N_2}{\partial \xi} & \frac{\partial N_3}{\partial \xi} & \frac{\partial N_4}{\partial \xi} \\ \frac{\partial N_1}{\partial \eta} & \frac{\partial N_2}{\partial \eta} & \frac{\partial N_3}{\partial \eta} & \frac{\partial N_4}{\partial \eta} \end{array} \right] \left[\begin{array}{c|c} \overline{x}_1 & \overline{y}_1 \\ \overline{x}_2 & \overline{y}_2 \\ \overline{x}_3 & \overline{y}_3 \\ \overline{x}_4 & \overline{y}_4 \end{array} \right] \left\{ \begin{array}{c} \frac{\partial N_i}{\partial x} \\ \frac{\partial N_i}{\partial y} \end{array} \right\} \tag{13.81}$$

$$= \underbrace{\frac{1}{4} \left[\begin{array}{cccc} -(1-\eta) & (1-\eta) & (1+\eta) & -(1+\eta) \\ -(1-\xi) & -(1+\xi) & (1+\xi) & (1-\xi) \end{array} \right] \left[\begin{array}{c|c} \overline{x}_1 & \overline{y}_1 \\ \overline{x}_2 & \overline{y}_2 \\ \overline{x}_3 & \overline{y}_3 \\ \overline{x}_4 & \overline{y}_4 \end{array} \right]}_{\mathbf{J}} \left\{ \begin{array}{c} \frac{\partial N_i}{\partial x} \\ \frac{\partial N_i}{\partial y} \end{array} \right\} \tag{13.82}$$

Back to the Jacobian

$$[\mathbf{J}]^{-1} \stackrel{\text{def}}{=} \left[\begin{array}{cc} \frac{\partial \xi}{\partial x} & \frac{\partial \eta}{\partial x} \\ \frac{\partial \xi}{\partial y} & \frac{\partial \eta}{\partial y} \end{array} \right] = \frac{1}{\det \mathbf{J}} \left[\begin{array}{cc} \frac{\partial y}{\partial \eta} & -\frac{\partial y}{\partial \xi} \\ -\frac{\partial x}{\partial \eta} & \frac{\partial x}{\partial \xi} \end{array} \right] = \frac{1}{\det \mathbf{J}} \sum_{i=1}^{4} \left[\begin{array}{cc} \frac{\partial N_i}{\partial \xi}\overline{y}_i & -\frac{\partial N_i}{\partial \eta}\overline{y}_i \\ -\frac{\partial N_i}{\partial \eta}\overline{x}_i & \frac{\partial N_i}{\partial \xi}\overline{x}_i \end{array} \right] \tag{13.83}$$

From calculus, if ξ and η are some arbitrary curvilinear coordinates, Figure 13.6,

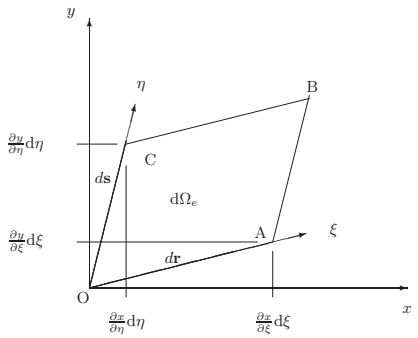

Fig. 13.6: Differential Element in Curvilinear Coordinate System

then

$$d\mathbf{r} = \left\{ \begin{array}{c} \frac{\partial x}{\partial \xi} \\ \frac{\partial y}{\partial \xi} \end{array} \right\} d\xi \quad \text{and} \quad d\mathbf{s} = \left\{ \begin{array}{c} \frac{\partial x}{\partial \eta} \\ \frac{\partial y}{\partial \eta} \end{array} \right\} \mathrm{d}\eta \tag{13.84}$$

are vectors directed tangentially to $\xi =$ constant and $\eta =$ constant, respectively. From vector algebra, the cross product of two vectors lying in the x-y plane, Figure 13.7, is

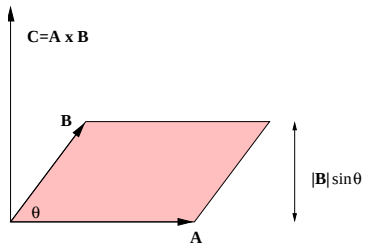

Fig. 13.7: Cross Product of Two Vectors

$$\mathbf{C} = \mathbf{A} \times \mathbf{B} \tag{13.85}$$

$$= |\mathbf{A}||\mathbf{B}| \sin\theta \mathbf{k} \tag{13.86}$$

$$= \begin{vmatrix} \mathbf{i} & \mathbf{j} & \mathbf{k} \\ A_x & A_y & 0 \\ B_x & B_y & 0 \end{vmatrix} = \underbrace{(A_x B_y - B_x A_y)}_{\text{Area}} \mathbf{k} \tag{13.87}$$

$$|\mathbf{C}| = |\mathbf{A}||\mathbf{B}| \sin\theta \tag{13.88}$$

Hence, the differential area $\mathrm{d}x\mathrm{d}y$ is equal to the length of the vector resulting from the cross product of $d\mathbf{r}d\mathbf{s}$ and is equal to

$$\mathrm{d}(area) = \mathrm{d}x\mathrm{d}y = \det \underbrace{\begin{bmatrix} \frac{\partial x}{\partial \xi} & \frac{\partial x}{\partial \eta} \\ \frac{\partial y}{\partial \xi} & \frac{\partial y}{\partial \eta} \end{bmatrix}}_{\mathbf{J}} \mathrm{d}\xi\mathrm{d}\eta \tag{13.89}$$

Finally, we can determine the element stiffness matrix from

$$[\mathbf{k}]_{8\times 8} = \int\int [\mathbf{B}]^T_{8\times 3} [\mathbf{D}]_{3x3} [\mathbf{B}]_{3\times 8} t \mathrm{d}x\mathrm{d}y \tag{13.90}$$

$$= \int_{-1}^{1}\int_{-1}^{1} [\mathbf{B}]^T [\mathbf{D}][\mathbf{B}] t |\mathbf{J}| \mathrm{d}\xi\mathrm{d}\eta \tag{13.91}$$

The evaluation of the element stiffness matrix involves dA. If we consider an infinitesimal element of length dr and ds at the vertex of an element, it has the boundaries of the element as its sides. Then, from Eq. 13.88,

$$dA = \mathrm{d}x.\mathrm{d}y.\sin\theta \tag{13.92}$$

However from Eq. 13.89, we have $dA = \det\mathbf{J}\mathrm{d}\xi.\mathrm{d}\eta$, thus

$$\det\mathbf{J} = \frac{\mathrm{d}x.\mathrm{d}y}{\mathrm{d}\xi.\mathrm{d}\eta} \sin\theta \tag{13.93}$$

Thus we observe that if θ is small or close to 180°, then det$\mathbf{J}$ will be very small; if the angle is greater than 180 ^{o}, the determinant is negative (implying a negative stiffness which will usually trigger an error/stop in an FE analysis).
In general it is recommended that $30^\circ < \theta < 150^o$. The inverse of the Jacobian exists as long as the element is not very distorted and does not fold back upon itself, Figure 13.8.

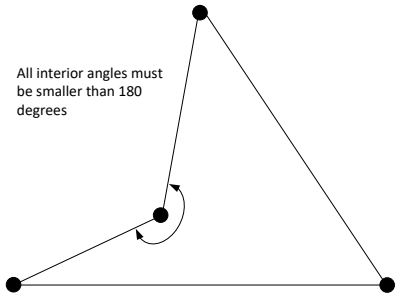

Fig. 13.8: Elements with Possible Singular Jacobians [89]

In those cases there is no unique relation between the coordinates. It can be easily shown that for parallelograms, the Jacobian is constant whereas for non-parallelograms it is not. In general, $\mathbf{J}$ is an indicator of the amount of element distortion with respect to a 2×2 square one. Some times it is constant; others it varies within the element.

13.3.1.3 Quadratic Quadrilateral (Q8)

For a quadratic quadrilateral element, there are two possibilities, Figure 13.9.

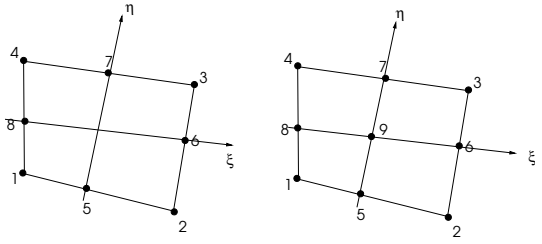

Fig. 13.9: Serendipity and Lagrangian Quadratic Quadrilaterals

Based on Pascal's triangle (Figure 13.3), the displacement field should be given by

$$u = \underbrace{a_1}_{\boxed{0}} + \underbrace{a_2 x + a_3 y}_{\boxed{1}} + \underbrace{a_4 x^2 + a_5 xy + a_6 y^2}_{\boxed{2}} + \underbrace{a_8 x^2 y + a_9 xy^2}_{\boxed{3}} \tag{13.94}$$

In this formulation, the x^2y^2 term is missing and the 8 terms in the assumed polynomial expansion correspond the 8 nodes (4 corner and 4 midside).

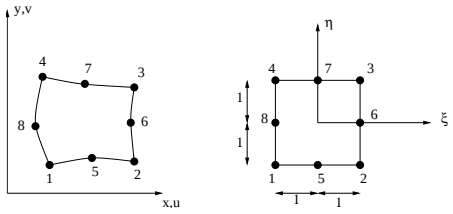

Fig. 13.10: Serendipity Isoparametric Quadratic Finite Element: Global and Parent Element

The shape functions may be obtained by mere inspection (i.e. **serendipitously**).

$$\begin{array}{ll} N_i = \frac{1}{4}\left(1+\xi\xi_i\right)\left(1+\eta\eta_i\right)\left(\xi\xi_i+\eta\eta_i-1\right) & i=1,2,3,4 \\ N_i = \frac{1}{2}\left(1-\xi^2\right)\left(1+\eta\eta_i\right) & i=5,7 \\ N_i = \frac{1}{2}\left(1+\xi\xi_i\right)\left(1-\eta^2\right) & i=6,8 \end{array} \tag{13.95}$$

They are tabulated in Table 13.1 and shown in Figure 13.11(b).

Table 13.1: Shape Functions and Natural Derivatives for Q8 Element

i	N_i	$N_{i,\xi}$	$N_{i,\eta}$
1	$\frac{1}{4}(1-\xi)(1-\eta)(-\xi-\eta-1)$	$\frac{1}{4}(2\xi+\eta)(1-\eta)$	$\frac{1}{4}(1-\xi)(2\eta+\xi)$
2	$\frac{1}{4}(1+\xi)(1-\eta)(\xi-\eta-1)$	$\frac{1}{4}(2\xi-\eta)(1-\eta)$	$\frac{1}{4}(1+\xi)(2\eta-\xi)$
3	$\frac{1}{4}(1+\xi)(1+\eta)(\xi+\eta-1)$	$\frac{1}{4}(2\xi+\eta)(1+\eta)$	$\frac{1}{4}(1+\xi)(2\eta+\xi)$
4	$\frac{1}{4}(1-\xi)(1+\eta)(-\xi-\eta-1)$	$\frac{1}{4}(2\xi-\eta)(1+\eta)$	$\frac{1}{4}(1-\xi)(2\eta-\xi)$
5	$\frac{1}{2}(1-\xi^2)(1-\eta)$	$-\xi(1-\eta)$	$-\frac{1}{2}(1-\xi^2)$
6	$\frac{1}{2}(1+\xi)(1-\eta^2)$	$\frac{1}{2}(1-\eta^2)$	$-(1+\xi)\eta$
7	$\frac{1}{2}(1-\xi^2)(1+\eta)$	$-\xi(1+\eta)$	$\frac{1}{2}(1-\xi^2)$
8	$\frac{1}{2}(1-\xi)(1-\eta^2)$	$-\frac{1}{2}(1-\eta^2)$	$-(1-\xi)\eta$

13.3.1.4 Lagrangian Quadrilateral (Q9)

If we were to follow a similar procedure to the one adopted to extract the bilinear shape functions, we would obtain 9 shape functions, which must in turn correspond to 9 (rather than 8) nodes.

In this element, the displacement field is given by

$$u = \underbrace{\underbrace{a_1}_{\boxed{0}} + \underbrace{a_2 x + a_3 y}_{\boxed{1}} + \underbrace{a_4 x^2 + a_5 xy + a_6 y^2}_{\boxed{2}} + \underbrace{a_8 x^2 y + a_9 x y^2}_{\boxed{3}}}_{\text{Serendipity}} + \underbrace{a_{12} x^2 y^2}_{\boxed{4}} \tag{13.96}$$

All the quadratic terms are present; hence there are 9 terms in the polynomial expansion, and the 9th node will correspond to an internal node. The shape functions in this case can be directly obtained from the Lagrangian interpolation functions, yielding

$$\begin{array}{ll} N_i = \frac{1}{4}\left(1+\xi\xi_i\right)\left(1+\eta\eta_i\right)\left(\xi\xi_i+\eta\eta_i-1\right) & i=1,2,3,4 \\ N_i = \frac{1}{2}\left(1-\xi^2\right)\left(1+\eta\eta_i\right) & i=5,7 \\ N_i = \frac{1}{2}\left(1+\xi\xi_i\right)\left(1-\eta^2\right) & i=6,8 \\ N_9 = \left(1-\xi^2\right)\left(1-\eta^2\right) & i=9 \end{array} \tag{13.97}$$

Note that the last shape function is often called the bubble function. Those shape functions differ slightly from those of the serendipity element, and the Q9 elements perform much better than the Q8 if edges are not parallel or slightly curved. Shape functions (Eq. 13.25) are shown in Figure 13.11(c).

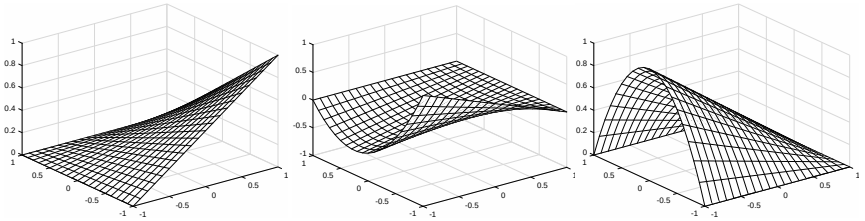

(a) Four noded, linear (b) Eight noded, quadratic

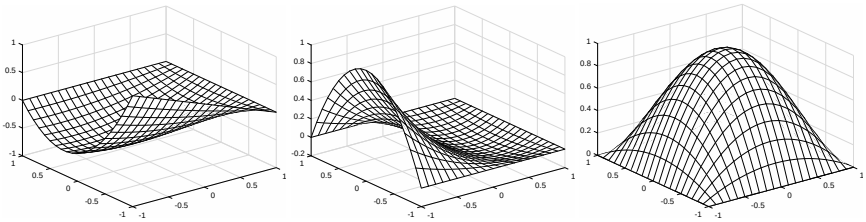

(c) Nine noded, quadratic

Fig. 13.11: Shape functions for various isoparametric elements

13.3.2 Numerical Integration

A crucial aspect of isoparametric element formulation is the numerical integration. The traditional Newton-Cotes method (with equally spaced sampling points) is replaced by the Gauss-Legendre quadrature where the points are not fixed and equally spaced, but are selected to achieve best accuracy.
Again we start with

$$\int_{-1}^{1} F(\xi)\mathrm{d}\xi \approx \int_{-1}^{1} P(\xi)\mathrm{d}\xi = \sum_{i=1}^{n} W_i^{(n)} F(\xi_i) \tag{13.98}$$

However in this formulation, **both** $W_i^{(n)}$ and ξ_i are unknowns to be yet determined. Thus, we have a total of $2n$ unknowns. At the integration points $P(\xi_i) = F(\xi_i)$, however, at intermediary points the difference can be expressed as

$$F(\xi) = P(\xi) + \underbrace{\chi(\xi)(\beta_0 + \beta_1\xi + \beta_2\xi^2 + \cdots)}_{0 \text{ at } \xi=\xi_i; i=1,2,\cdots,n} \tag{13.99}$$

Since we want the left side to be exactly equal to $P(\xi)$ at the integration points, we define

$$\chi(\xi) = (\xi - \xi_1)(\xi - \xi_2)...(\xi - \xi_n) \tag{13.100}$$

as a polynomial of order n, to be equal to zero at the integration points ξ_i. β_i should be appropriately selected in order to eliminate the gap between $F(\xi)$ and $P(\xi)$ at intermediary points. Integrating

$$\int_{-1}^{1} F(\xi)\mathrm{d}\xi = \int_{-1}^{1} P(\xi) + \sum_{j=0}^{\infty} \beta_j \int_{-1}^{1} \chi(\xi)\xi^j \mathrm{d}\xi \tag{13.101}$$

We split the last term

$$\sum_{j=0}^{\infty} \beta_j \int_{-1}^{1} \chi(\xi)\xi^j \mathrm{d}\xi = \sum_{j=0}^{n-1} \beta_j \int_{-1}^{1} \chi(\xi)\xi^j \mathrm{d}\xi + \sum_{j=n}^{\infty} \beta_j \int_{-1}^{1} \chi(\xi)\xi^j \mathrm{d}\xi \tag{13.102}$$

Truncating the last terms of the expansion,

$$\int_{-1}^{1} F(\xi)\mathrm{d}\xi \approx \int_{-1}^{1} P(\xi) + \sum_{j=0}^{n-1} \beta_j \int_{-1}^{1} \chi(\xi)\xi^j \mathrm{d}\xi \tag{13.103}$$

we observe that the first integral on the right-hand side involves a polynomial of order $n-1$, and the second integral a polynomial of order $2n-1$. Thus we set

$$\int_{-1}^{1} \chi(\xi)\xi^j \mathrm{d}\xi = 0 \qquad j = 0, 1, \cdots, n-1 \tag{13.104}$$

which would result in a set of n simultaneous equations of order n in terms of the unknowns (ξ_i, $i = 0, 1, \cdots, n-1$).
Back to Eq. 13.103:

$$\int_{-1}^{1} F(\xi)\mathrm{d}\xi \approx \int_{-1}^{1} P(\xi) = \sum_{i=1}^{n} F(\xi_i) \int_{-1}^{1} l_i(\xi)\mathrm{d}\xi = \sum_{i=1}^{n} W_i^{(n)} F(\xi_i) \tag{13.105}$$

or

$$\begin{array}{r|c} \text{Approximation} & \int_{-1}^{1} F(\xi)\mathrm{d}\xi \approx \sum_{i=1}^{n} W_i^{(n)} F(\xi_i) \\ \text{Weights} & W_i^{(n)} = \int_{-1}^{1} l_i(\xi)\mathrm{d}\xi \\ \text{Gauss Points} & \int_{-1}^{1} \chi(\xi)\xi^j \mathrm{d}\xi = 0 \qquad j = 0, 1, \cdots, n-1 \end{array} \tag{13.106}$$

Integration points ξ_i and weight coefficients $W_i^{(n)}$ are given in Table 13.2 [89].

Table 13.2: Integration Points and Weights for Gauss-Quadrature Formulaes Over the Interval $[-1, 1]$

n	ξ_i	$W_i^{(n)}$	Error
1	0	2	$\frac{1}{3}F^{(2)}(\xi)$
2	$-1/\sqrt{3}$ $1/\sqrt{3}$	1 1	$\frac{1}{135}F^{(4)}(\xi)$
3	$-\sqrt{3/5}$ 0 $\sqrt{3/5}$	5/9 8/9 5/9	$\frac{1}{15,750}F^{(6)}(\xi)$

The solutions (Gauss integration points) are equal to the roots of a Legendre polynomial defined by

$$\begin{array}{l} L_0(\xi) = 1 \\ L_1(\xi) = \xi \\ L_k(\xi) = \frac{2k-1}{k}\xi L_{k-1}(\xi) - \frac{k-1}{k}\xi L_{k-2}(\xi) \qquad 2 \leq k \leq n \end{array} \tag{13.107}$$

and the n Gauss integration points are determined by solving $L_n(\xi) = 0$ for its roots, ξ_i, $i = 0, 1, \cdots, n-1$. The weighting functions are then given by

$$W_i^{(n)} = \frac{2(1-\xi_i^2)}{[nL_{n-1}(\xi_i)]^2} \tag{13.108}$$

13.3.2.1 Gauss-Legendre Quadrature for $n = 2$

First we seek the integration points for $n = 2$, $\chi(\xi) = (\xi - \xi_1)(\xi - \xi_2)$, and the resulting equations are

$$\int_{-1}^{1}(\xi-\xi_1)(\xi-\xi_2)\xi^0 \mathrm{d}\xi = 0 \tag{13.109}$$

$$\int_{-1}^{1}(\xi-\xi_1)(\xi-\xi_2)\xi^1 \mathrm{d}\xi = 0 \tag{13.110}$$

(13.111)

Upon integration, we obtain

$$\xi_1\xi_2 = -\frac{1}{3} \quad \text{and} \quad \xi_1+\xi_2 = 0 \tag{13.112}$$

Hence

$$\xi_1 = -\frac{1}{\sqrt{3}} \quad \text{and} \quad \xi_2 = \frac{1}{\sqrt{3}} \tag{13.113}$$

The weight coefficients are

$$W_i^{(n)} = \int_{-1}^{1} l_i(\xi)\mathrm{d}\xi \tag{13.114}$$

$$W_1^{(2)} = \int_{-1}^{1}\frac{\xi-\xi_2}{\xi_1-\xi_2}\mathrm{d}\xi = \frac{-2\xi_2}{\xi_1-\xi_2} = 1.0 \tag{13.115}$$

$$W_2^{(2)} = \int_{-1}^{1}\frac{\xi-\xi_1}{\xi_2-\xi_1}\mathrm{d}\xi = \frac{-2\xi_1}{\xi_1-\xi_2} = 1.0 \tag{13.116}$$

13.3.3 Stress Recovery; Nodal Stresses

Stresses are evaluated from

$$\boldsymbol{\sigma} = \mathbf{DB}\bar{\mathbf{u}} \tag{13.117}$$

In general, it is desirable to have them evaluated at the element's nodal points. However, it should be kept in mind that stresses computed at a given node from different elements need not be the same (since stresses are not required to be continuous in displacement based finite element formulations).
Hence some sort of stress averaging at nodal points may be desirable. In the isoparametric formulation, nodal stresses are very poor, and best results are obtained at the Gauss points.
There are two approaches to evaluate nodal stresses:

1. Evaluate $\boldsymbol{\sigma}$ directly at the nodes ($\xi = \eta = \pm 1$)
2. Evaluate the stresses at the Gauss points and then extrapolate.

The second approach yields far better results.
Extrapolation from Gauss points will be illustrated through Figure 13.12 for the 4 noded isoparametric quadrilateral.
We specify an "internal" element with its own nodes and natural coordinates ξ' and η' which are related to ξ and η through Table 13.3.
or

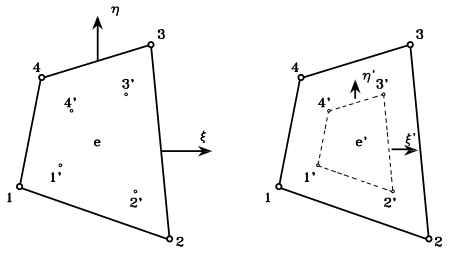

Fig. 13.12: Extrapolation from 4-Node Quad Gauss Points [292]

Table 13.3: Natural Coordinates of Bilinear Quadrilateral Nodes

Corner Node	ξ	η	ξ'	η'	Gauss Node	ξ	η	ξ'	η'
1	-1	-1	$-\sqrt{3}$	$-\sqrt{3}$	1'	$-1/\sqrt{3}$	$-1/\sqrt{3}$	-1	-1
2	$+1$	-1	$+\sqrt{3}$	$-\sqrt{3}$	2'	$+1/\sqrt{3}$	$-1/\sqrt{3}$	$+1$	-1
3	$+1$	$+1$	$+\sqrt{3}$	$+\sqrt{3}$	3'	$+1/\sqrt{3}$	$+1/\sqrt{3}$	$+1$	$+1$
4	-1	$+1$	$-\sqrt{3}$	$+\sqrt{3}$	4'	$-1/\sqrt{3}$	$+1/\sqrt{3}$	-1	$+1$

$$\xi' = \sqrt{3}\xi \qquad \eta' = \sqrt{3}\eta \tag{13.118}$$

Hence any scalar quantity σ (such as σ_{xx}) whose value σ'_i is known at the Gauss element corners can be interpolated through the usual bilinear shape functions now expressed in terms of ξ' and η':

$$\sigma(\xi', \eta') = \lfloor N_1^{e'} \; N_2^{e'} \; N_3^{e'} \; N_4^{e'} \rfloor \begin{Bmatrix} \sigma'_1 \\ \sigma'_2 \\ \sigma'_3 \\ \sigma'_4 \end{Bmatrix} \tag{13.119}$$

where

$$N_1^{e'} = \frac{1}{4}(1-\xi')(1-\eta') \tag{13.120}$$

$$N_2^{e'} = \frac{1}{4}(1+\xi')(1-\eta') \tag{13.121}$$

$$N_3^{e'} = \frac{1}{4}(1+\xi')(1+\eta') \tag{13.122}$$

$$N_4^{e'} = \frac{1}{4}(1-\xi')(1+\eta') \tag{13.123}$$

Similarly, we can **extrapolate** σ to the corners of the element. For corner 1, for instance, we replace ξ' and η' in the preceding equations by $-\sqrt{3}$. Doing that for the four corners, we obtain

$$\begin{Bmatrix} \sigma_1 \\ \sigma_2 \\ \sigma_3 \\ \sigma_4 \end{Bmatrix} = \begin{bmatrix} 1+\frac{1}{2}\sqrt{3} & -\frac{1}{2} & 1-\frac{1}{2}\sqrt{3} & -\frac{1}{2} \\ -\frac{1}{2} & 1+\frac{1}{2}\sqrt{3} & -\frac{1}{2} & 1-\frac{1}{2}\sqrt{3} \\ 1-\frac{1}{2}\sqrt{3} & -\frac{1}{2} & 1+\frac{1}{2}\sqrt{3} & -\frac{1}{2} \\ -\frac{1}{2} & 1-\frac{1}{2}\sqrt{3} & -\frac{1}{2} & 1+\frac{1}{2}\sqrt{3} \end{bmatrix} \begin{Bmatrix} \sigma'_1 \\ \sigma'_2 \\ \sigma'_3 \\ \sigma'_4 \end{Bmatrix} \tag{13.124}$$

As expected, the sum of each row is equal to one, and for stresses, we replace σ by σ_{xx}, σ_{yy}, and τ_{xy}.
As we know, different nodal stresses will be obtained from adjacent elements. To obtain a single value we can either take

- Unweighted average of all the nodal stresses.
- Weighted average of nodal stresses based on the relative sizes of the elements as determined from their area through det(J).

13.3.4 Nodal Equivalent Loads

In the finite element formulation, all loads must be replaced by an "energy equivalent" nodal load. We shall consider the following cases: nodal load, gravity, tractions, and thermal.

13.3.4.1 Gravity Load

Gravity forces are equivalent to a body force/unit volume acting within the solid in the direction of the gravity axis, Figure 13.13 (which need not be coincident with either of the coordinate axes).

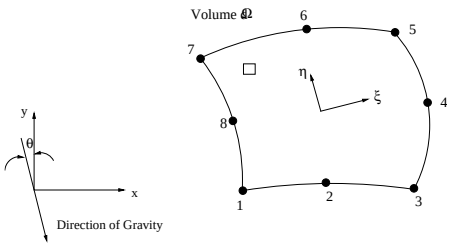

Fig. 13.13: Gravity Loading

$$dG_x = \rho g d\Omega \sin\theta \tag{13.125}$$
$$dG_y = -\rho g d\Omega \cos\theta \tag{13.126}$$

where g is the gravitational acceleration and ρ is the mass density.
The applied load can be readily defined from

$$\mathbf{P}_e = \int_{\Omega_e} \mathbf{N}^T \mathbf{b} \mathrm{d}\Omega + \int_{\Gamma_t} \mathbf{N}^T \hat{\mathbf{t}} \mathrm{d}\Gamma \tag{13.127}$$

hence,

$$\left\{ \begin{array}{c} P_{xi} \\ P_{yi} \end{array} \right\} = \int_{\Omega_e} N_i \rho g \left\{ \begin{array}{c} \sin\theta \\ -\cos\theta \end{array} \right\} d\Omega \tag{13.128}$$

or the energy equivalent nodal forces for node i are

$$\left\{ \begin{array}{c} P_{xi} \\ P_{yi} \end{array} \right\} = \sum_{j=1}^{ngaus} \sum_{k=1}^{ngaus} \rho g t \left\{ \begin{array}{c} \sin\theta \\ -\cos\theta \end{array} \right\} N_i(\xi_j \eta_k) W_j W_k \mathrm{det}\mathbf{J}(\xi_j, \eta_k) \tag{13.129}$$

The angle θ is to be measured counterclockwise from the positive y axis.

13.3.4.2 Traction Load

Any element edge can have a distributed load per unit length in a normal and tangential direction prescribed. The variation of the distributed load is polynomial, and its order can not exceed the order of the element. For the sake of consistency, loaded nodes are listed also counterclockwise.
First, we determine the components of the distributed loads in the x and y directions by considering the forces acting on an incremental length dS of the loaded edge, Figure 13.14:

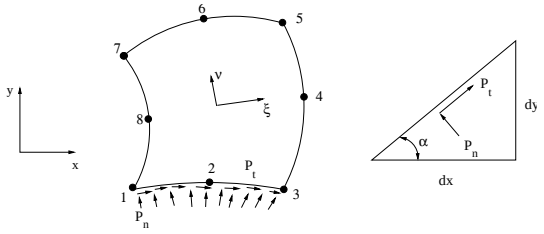

Fig. 13.14: Traction Load in Isoparametric Elements

$$\begin{array}{l} dP_x = (p_t dS \cos\theta - p_n dS \sin\theta) = (p_t \mathrm{d}x - p_n \mathrm{d}y) \\ dP_y = (p_n dS \cos\theta - p_t dS \sin\theta) = (p_n \mathrm{d}x - p_t \mathrm{d}y) \end{array} \tag{13.130}$$

But since integration is to be carried on in terms of natural coordinates:

$$\mathrm{d}x = \frac{\partial x}{\partial \xi} \mathrm{d}\xi \qquad \mathrm{d}y = \frac{\partial y}{\partial \xi} \mathrm{d}\xi \tag{13.131}$$

Substituting

$$dP_x = \left(p_t \frac{\partial x}{\partial \xi} - p_n \frac{\partial y}{\partial \xi} \right) \mathrm{d}\xi \tag{13.132}$$

$$dP_y = \left(p_n \frac{\partial x}{\partial \xi} + p_t \frac{\partial y}{\partial \xi} \right) \mathrm{d}\xi \tag{13.133}$$

$$\tag{13.134}$$

The initial force vector $\mathbf{f}_e$ can be defined as

$$\mathbf{f}_{0_e} = \int_{\Omega_e} \mathbf{B}^T \mathbf{D} \boldsymbol{\epsilon}_0 \mathrm{d}\Omega - \int_{\Omega_t} \mathbf{B}^T \boldsymbol{\sigma}_0 \mathrm{d}\Omega \tag{13.135}$$

or

$$P_{xi} = \int_{\Gamma_t} N_i \left(p_t \frac{\partial x}{\partial \xi} - p_n \frac{\partial y}{\partial \xi} \right) \mathrm{d}\xi \tag{13.136}$$

$$P_{yi} = \int_{\Gamma_t} N_i \left(p_n \frac{\partial x}{\partial \xi} + p_t \frac{\partial y}{\partial \xi} \right) \mathrm{d}\xi \tag{13.137}$$

The integration is again carried out numerically (along the edge), and the energy equivalent nodal forces for node i are

$$P_{xi} = \sum_{j=1}^{ngaus} N_i \left(p_t \frac{\partial x}{\partial \xi} - p_n \frac{\partial y}{\partial \xi} \right) W_j \tag{13.138}$$

$$P_{yi} = \sum_{j=1}^{ngaus} N_i \left(p_n \frac{\partial x}{\partial \xi} + p_t \frac{\partial y}{\partial \xi} \right) W_j \tag{13.139}$$

Note that $\frac{\partial x}{\partial \xi}$ and $\frac{\partial y}{\partial \xi}$ are taken straight out of the Jacobian matrix and that since integration is to be carried along the edge, we have used ξ. For adjacent elements, see Figure 13.15.

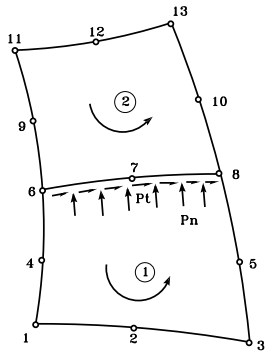

Fig. 13.15: Traction Load in Contiguous Isoparametric Elements

13.3.4.3 Initial Strains/Stresses; Thermal Load

We distinguish between two cases:

Plane Stress which is the simplest

$$\varepsilon^0_{xx} = \alpha\Delta T \tag{13.140}$$
$$\varepsilon^0_{yy} = \alpha\Delta T \tag{13.141}$$
$$\gamma^0_{xy} = 0 \tag{13.142}$$

Plane Strain we have

$$\varepsilon^0_{xx} = -\frac{\nu\sigma^0_{zz}}{E} + \alpha\Delta T \tag{13.143}$$
$$\varepsilon^0_{yy} = -\frac{\nu\sigma^0_{zz}}{E} + \alpha\Delta T \tag{13.144}$$
$$\gamma^0_{xy} = 0 \tag{13.145}$$
$$\varepsilon^0_{zz} = \frac{\sigma^0_{zz}}{E} + \alpha\Delta T = 0 \tag{13.146}$$

Using the last expression to eliminate σ^0_{zz}, we obtain

$$\varepsilon^0_{xx} = (1+\nu)\alpha\Delta T \tag{13.147}$$
$$\varepsilon^0_{yy} = (1+\nu)\alpha\Delta T \tag{13.148}$$
$$\gamma^0_{xy} = 0 \tag{13.149}$$
$$\sigma^0_{zz} = -E\alpha\Delta T \tag{13.150}$$

Those expressions are then substituted into Eq. 13.135

$$\mathbf{f}_{0_e} = \int_{\Omega_e} \mathbf{B}^T\mathbf{D}\boldsymbol{\epsilon}_0 \mathrm{d}\Omega - \int_{\Omega_t} \mathbf{B}^T\boldsymbol{\sigma}_0 \mathrm{d}\Omega \tag{13.151}$$

and integrated numerically.

13.4 Finite Element Formulation of the Heat Equation

Having "proven" the validity of the Galerkin method by its ability to recover the variational based formulation, we now turn our attention to a problem which (strictly speaking) could only be handled by such an approach. As a vehicle for such an application, we will consider the field equation.

13.4.1 Derivation of the Weak Form

Our starting point will be the field equation, Eq. 2.28

$$-\text{div}\,(\mathbf{D}\boldsymbol{\nabla}\phi) - Q = \rho c\frac{\partial\phi}{\partial t} \tag{13.152}$$

Recalling (Eq. 2.3) that $\mathbf{q} = -\mathbf{D}\boldsymbol{\nabla}\phi$, and that for steady state problems the right hand side reduces to zero, and finally (for the mere sake of clarity) substituting ϕ by T, this equation reduces to

$$\underbrace{\text{div}\,\mathbf{q} - Q}_{L\phi+g} = 0 \tag{13.153}$$

The boundary conditions are given by

$$\begin{array}{lll} \text{Essential, Temperature} & \Gamma_T & T = g \\ \text{Natural, Flux} & \Gamma_q & q_n = \mathbf{q}^t\mathbf{n} = q_f \\ \text{Natural, Convection Flux} & \Gamma_c & q_c = h(T - T_\infty) \end{array} \tag{13.154}$$

Note that in a fin, the convection heat loss can be considered as a negative heat source. Applying the Galerkin's residual method:

$$\int_\Omega w(\text{div}\,\mathbf{q} - Q)\text{d}\Omega = 0 \tag{13.155}$$

for 2D problems, we replace $\text{d}\Omega$ by $t\text{d}A$

$$\int_A w\text{div}\,\mathbf{q}t\text{d}A - \int_A wQt\text{d}A = 0 \tag{13.156}$$

Applying Green-Gauss Theorem[1], the first term becomes

$$\int_A w\text{div}\,\mathbf{q}t\text{d}A = \oint_\Gamma wt\mathbf{q}^T\mathbf{n}\text{d}\Gamma - \int_A(\boldsymbol{\nabla}w)^T\mathbf{q}t\text{d}A \tag{13.157}$$

Thus Eq. 13.156 becomes

$$\int_A(\boldsymbol{\nabla}w)^T\mathbf{q}t\text{d}A = \oint_\Gamma wt\mathbf{q}^T\mathbf{n}\text{d}\Gamma - \int_A wQt\text{d}A \tag{13.158}$$

which is the weak form. Applying the boundary conditions, $\Gamma = \Gamma_T + \Gamma_q$

$$\int_A(\boldsymbol{\nabla}w)^T\mathbf{q}t\text{d}A = \int_{\Gamma_q} wq_ft\text{d}\Gamma + \int_{\Gamma_T} wq_nt\text{d}\Gamma - \int_A wQt\text{d}A \tag{13.159}$$

where along Γ_q the flux (which may include convection) is known but the temperature is not, and along Γ_T, the temperature is known but flux is not. This equation is valid for any constitutive relation. Applying Fourrier Law, we obtain

$$\int_A(\boldsymbol{\nabla}w)^T\mathbf{D}\boldsymbol{\nabla}Tt\text{d}A = -\int_{\Gamma_q} wq_ft\text{d}\Gamma - \int_{\Gamma_T} wq_nt\text{d}\Gamma + \int_A wQt\text{d}A \tag{13.160}$$

[1] $\int\int_A \phi\text{div}\,\mathbf{q}dA = \oint_\Gamma \phi\mathbf{q}^T\mathbf{n}\text{d}\Gamma - \int\int_A(\boldsymbol{\nabla}\phi)^T\mathbf{q}dA$

This is the weak form of our problem. By extension, the weak form in 3D would be

$$\int_V (\boldsymbol{\nabla} w)^T \mathbf{D} \boldsymbol{\nabla} T \mathrm{d}V = \oint_{S_q} w q_f dS - \oint_{S_T} w q_n dS + \int_V w Q \mathrm{d}V \tag{13.161}$$

13.4.2 Finite Element Discretization

The temperature field is expressed in terms of the nodal ones

$$T = \mathbf{N}\overline{T} \tag{13.162}$$

where $\mathbf{N}$ are the shape functions, and $\overline{T}$ are the nodal known temperatures. The flux is given by $\mathbf{q} = -\mathbf{D}\nabla T$ where

$$\nabla T = \lfloor \frac{\partial T}{\partial x} \ \frac{\partial T}{\partial y} \rfloor^T \tag{13.163}$$

furthermore, the flux q_n at the boundary is given by $q_n = \mathbf{q}^T \mathbf{n}$. Substituting

$$\nabla T = \nabla \mathbf{N} \overline{T} = \mathbf{B} \overline{T} \tag{13.164}$$

where

$$\mathbf{B} = \begin{bmatrix} \frac{\partial N_i}{\partial x} \\ \frac{\partial N_i}{\partial y} \end{bmatrix} \tag{13.165}$$

Note, this definition of the $\mathbf{B}$ matrix for scalar field problems, should not be confused with the one for vector problems, Eq. 13.59

$$\mathbf{B} = \begin{bmatrix} \frac{\partial N_i}{\partial x} & 0 \\ 0 & \frac{\partial N_i}{\partial y} \\ \frac{\partial N_i}{\partial y} & \frac{\partial N_i}{\partial x} \end{bmatrix} = \mathbf{J}^{-1} \begin{bmatrix} \frac{\partial N_i}{\partial \xi} & 0 \\ 0 & \frac{\partial N_i}{\partial \eta} \\ \frac{\partial N_i}{\partial \eta} & \frac{\partial N_i}{\partial \xi} \end{bmatrix} \tag{13.166}$$

13.4.2.1 No Convection

Substituting the previous set of equations, Eq. 13.160 reduces to

$$\left(\int_A (\boldsymbol{\nabla} w)^T \mathbf{D} \mathbf{B} t \mathrm{d}A \right) \overline{T} = -\int_{\Gamma_q} w q_f t \mathrm{d}\Gamma - \int_{\Gamma_T} w q_n t \mathrm{d}\Gamma + \int_A w Q t \mathrm{d}A \tag{13.167}$$

In accordance with the Galerkin method, the weight function w is

$$w = \mathbf{N}\mathbf{c} \tag{13.168}$$

Since w is arbitrary, the matrix $\mathbf{c}$ is also arbitrary, thus

$$\boldsymbol{\nabla} w = \boldsymbol{\nabla} \mathbf{N} \mathbf{c} = \mathbf{B}\mathbf{c} \tag{13.169}$$

and since w is a scalar

$$w = \mathbf{c}^T \mathbf{N}^T \tag{13.170}$$

Inserting those equations into Eq. 13.167

$$\mathbf{c}^T \left[\left(\int_A \mathbf{B}^T \mathbf{D} \mathbf{B} t \mathrm{d}A \right) \overline{T} + \int_{\Gamma_q} \mathbf{N}^T q_f t \mathrm{d}\Gamma + \int_{\Gamma_T} \mathbf{N}^T q_n t \mathrm{d}\Gamma - \int_A \mathbf{N}^T Q t \mathrm{d}A \right] = 0 \tag{13.171}$$

But since this expression should hold for any arbitrary $\mathbf{c}^T$ matrix, we conclude that

$$\mathbf{K}^e \overline{T} = \mathbf{f}_b^e + \mathbf{f}_Q^e \tag{13.172}$$

$$\mathbf{K}^e = \int_A \mathbf{B}^T \mathbf{D} \mathbf{B} t \mathrm{d}A \tag{13.173}$$

$$\mathbf{f}_b^e = -\int_{\Gamma_q} \mathbf{N}^T q_f t \mathrm{d}\Gamma - \int_{\Gamma_T} \mathbf{N}^T q_n t \mathrm{d}\Gamma \tag{13.174}$$

$$\mathbf{f}_Q^e = -\int_A \mathbf{N}^T Q t \mathrm{d}A \tag{13.175}$$

13.4.2.2 Convection

Next we consider the effet of the convection term, and thus

$$\Gamma = \Gamma_q + \Gamma_T + \Gamma_c \tag{13.176}$$

The presence of the convection term affects only $\mathbf{f}_b$ in Eq. 13.174 which now becomes

$$\mathbf{f}_b = -\int_{\Gamma_q} \mathbf{N}^T q_f t \mathrm{d}\Gamma - \int_{\Gamma_T} \mathbf{N}^T q_n t \mathrm{d}\Gamma - \int_{\Gamma_c} \mathbf{N}^T q_c \mathrm{d}\Gamma \tag{13.177}$$

and based on Newton's convection boundary condition (Eq. 2.2)

$$q_c = h(T - T_\infty) \tag{13.178}$$

or

$$q_c = h\mathbf{N}\overline{T} - hT_\infty \tag{13.179}$$

Substituting into Eq. 13.177 yields

$$\mathbf{f}_b = -\int_{\Gamma_q} \mathbf{N}^T q_f t \mathrm{d}\Gamma - \int_{\Gamma_T} \mathbf{N}^T q_n t \mathrm{d}\Gamma - \left(\int_{\Gamma_c} h \mathbf{N}^T \mathbf{N} \mathrm{d}\Gamma \right) \overline{T} + T_\infty \int_{\Gamma_c} \mathbf{N}^T h \mathrm{d}\Gamma \tag{13.180}$$

Using this relation, Eq. 13.174 becomes

$$(\mathbf{K}^e + \mathbf{K}_c^e)\overline{T} = \mathbf{f}_b^e + \mathbf{f}_Q^e \tag{13.181}$$

$$\mathbf{K}^e = \int_A \mathbf{B}^T \mathbf{D}\mathbf{B} t \mathrm{d}A \tag{13.182}$$

$$\mathbf{K}_c^e = \int_{\Gamma_c} h \mathbf{N}^T \mathbf{N} \mathrm{d}\Gamma \tag{13.183}$$

$$\mathbf{f}_b^e = -\int_{\Gamma_q} \mathbf{N}^T q_f \mathrm{d}\Gamma - \int_{\Gamma_T} \mathbf{N}^T q_n \mathrm{d}\Gamma + T_\infty \int_{\Gamma_c} \mathbf{N}^T h \mathrm{d}\Gamma \tag{13.184}$$

$$\mathbf{f}_Q^e = -\int_A \mathbf{N}^T Q t \mathrm{d}A \tag{13.185}$$

It should be noted that convection occurs around the perimeter of an element, and conduction occurs inside its volume.

13.5 Equilibrium and Compatibility in the Solution

In an exact solution over each differential element, equilibrium and compatibility prevails; however in a finite element discretization, this is not necessarily the case:

Equilibrium of Nodal Forces: Those are automatically satisfied by definition ($\mathbf{k}^e\overline{\mathbf{u}} - \overline{\mathbf{f}} = 0$) at the nodes.

Compatibility at Nodes: Elements connected to one another have the same displacements (along corresponding dof) at the connecting node.

Interelement Continuity of Stress: This is usually not satisfied; that is equilibrium across the elements does not necessarily prevail.

Interelement Compatibility of Displacements: Most elements have this requirement satisfied.

Equilibrium Inside Elements: This is not always satisfied. In general, satisfaction of equilibrium at every point demands relations between dof which do not necessarily result from $\mathbf{k}^e\overline{\mathbf{u}} - \overline{\mathbf{f}} = 0$.

Displacement Compatibility Inside an Element: This is satisfied as we only require that the element displacement be continuous and single-valued.

It should be kept in mind that a numerical solution that is derived from the principle of virtual work (or minimum total potential energy) is a lower bound solution because the strain energy is smaller than the exact one (i.e. obtained from an infinite number of elements):

$$u_i^{approx} < u_i^{exact} \tag{13.186}$$

Hence, the solution is too stiff. This is circumvented by using reduced numerical integration (i.e. 2×2 when a 3×3 integration is needed).

13.6 Convergence

Convergence of a finite element analysis can be achieved by decreasing the element size or by increasing the interpolation order of an element (i.e the displacement field

inside an element can be linear or quadratic; very seldom are higher order used). Those are referred to as h or p convergence respectively. Hence, convergence to the exact solution can be accelerated by Figure 13.16.

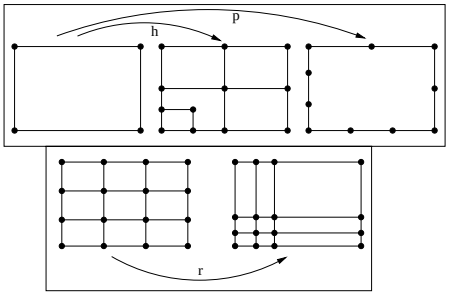

Fig. 13.16: h, p and r Convergence

h: Reducing the size of the elements (or mesh refinement).
p: Increasing the order of the polynomial (same number of elements but higher number of nodes/dof).

Approximation will yield an exact solution in the limit as the size h of elements approach zero. A third form of acceleration is the so-called *r* refinement in which the same number of nodes/elements is retained but the mesh is shifted around to increase its density in zones of high stress gradient.
The above convergence procedures can be accelerated within the context of a program which can accommodate adaptive remeshing techniques. Finally, additional errors may come from round-off within the computer. Typically, one would have to perform at least two analyses with two different element sizes (h) to make sure that mesh refinement is sufficient.

Chapter 14
Nonlinear Finite Element Analysis

Abstract
Safety assessment of structures can not be purely code based and certainly not based on linear elastic analyses. Hence, this chapter will cover key aspects of non-linear finite element analysis.

14.1 Introduction

Whereas linear elastic analyses are warranted for design or preliminary safety assessment, non-linear ones must be performed when the complete structural response is desired, the failure load is to be determined as accurately as possible, or the "true" factor of safety must be found.
In such cases, a simplistic linear elastic analysis will either overestimate the peak load, or underestimate the displacements. In the first case, the solution may lead to unnecessary retrofit; in the second to potentially dangerous situations arising from unanticipated large displacements, Figure 14.1. In both cases, stress redistribution is not captured, and it will be impossible to distinguish localized from global failure.

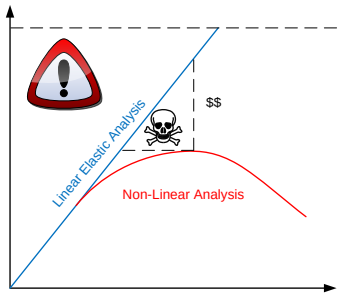

Fig. 14.1: Linear *vs* non-linear analyses

It should always be kept in mind that non-linear analysis is not a substitute to good engineering common sense; it should only be the last resort after common

sense, linear analysis, and simplified methods were exhausted. Ideally, it should be performed to validate/quantify a solid assumption.

14.2 Types of Non-Linearities

There are two sources of non-linearities:

Material when the non-linearity of the stress-strain curve (or of the constitutive model, C) is accounted for (e.g. concrete's response becomes non-linear at approximately $0.45f'_c$, and steel yields at f_y).

Geometric when the higher order terms of the strain displacements are accounted for (refer to Equation 1.80).

In civil engineering, one is mostly concerned about material non-linearity; geometric non-linearity is seldom an issue except for buckling, cable structures, and $P-\Delta$ effects in high rise buildings. With reference to Figure 14.2 and Table 14.1, we distinguish different levels (where C and K stand for constitutive and kinematic models, L and NL for linear and non-linear) of analyses:

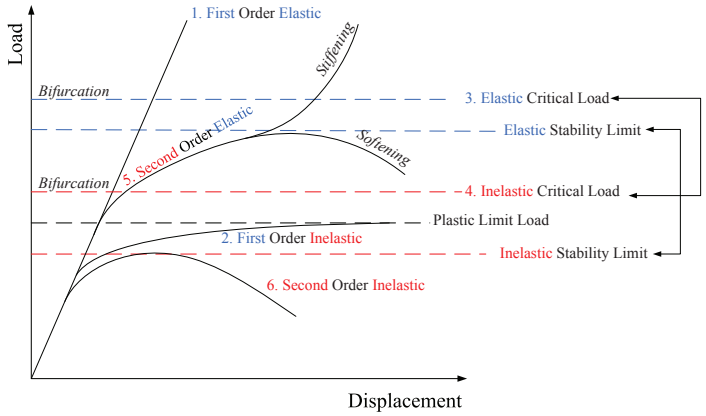

Fig. 14.2: Level of Analysis

First Order Elastic excludes any non-linearities. If the equilibrium equation is written in terms of

1) Undeformed Shape (C:L-K:L) This is the most common case, i.e. linear elastic. It is usually acceptable for service loads. For time dependent cases, we must consider visco-elastic models.
3) Bifurcation; Deformed shape (or "zero order") an eigenvalue analysis which would lead to the Elastic Critical Load. Note that we do not have a corresponding load-displacement curve but rather "buckling modes."

First Order Inelastic Accounts for material non-linearity. In such an analysis, the inelastic region (plastic zone) develops gradually, and it will provide a good estimate of the elasto-plastic response (note that instability is not addressed). We consider

- Non-linear Elasticity: reversible non-linear stress-strain (upon unloading, the strain goes back to zero).
- Plasticity: non reversible non-linear stress-strain.
- Damage.

If the equilibrium equation is written in terms of

2) Undeformed Shape (C:NL-K:L) Second most common form of analysis, typically conducted for ultimate/unusual loads.
4) Bifurcation; Deformed shape an eigenvalue analysis which would lead to the Inelastic Critical Load. Note that we do not have a corresponding load-displacement curve, but rather "buckling modes." This inelastic critical load will be smaller than the elastic one.

For time dependent cases, we consider visco-plasticity, fatigue, or continuous damage models.

Second-order elastic; 5 (C:L-K:NL) accounts for the effects of finite deformation and displacements; equilibrium equations are written in terms of the geometry of the deformed shape (Eulerian), does not account for material non-linearities, may be able to detect bifurcation and/or increased stiffness (when a member is subjected to a tensile axial load). Best for the analysis of cables, nets, catenary structures.

Second-order inelastic; 6 (C:NL-K:NL) equations of equilibrium written in terms of the geometry of the deformed shape, can account for both geometric and material non-linearities. Most suitable to determine failure or ultimate loads. By far the most complex form of analysis, used in Metal Forming simulation and fragmentation of structures (missile impact).

This is further summarized in Table 14.1, where kinematic equation refers to the strain-displacement relationship, and the equilibrium equation is written based on the deformed or undeformed shape.
This chapter will focus on case 2 (non-linear stress strain relationship, and linear strain displacements).

14.3 Incremental Load/Displacement

In the non-linear analysis of structures, the load is applied incrementally, and a solution is sought at the end of each increment:

1. "Break down" the external load into n increments (they need not be equal; as we approach the peak anticipated load, it is advisable to reduce the incremental one).
2. At each step, apply the incremental load vector, $\Delta \mathbf{P}_i$.

Table 14.1: Non-linear analyses types

		Constitutive Equations			
		Undeformed Shape		Deformed Shape	
		Elastic (Linear)	Inelastic (Non Linear)	Elastic (Linear)	Inelastic (Non Linear)
Kinematic Eq.	1st Order (Linear)	1 (C:L-K:L)	2 (C:NL-K:L)	Critical Load	
				3 Elastic	4 Inelastic
	2nd Order (Non Linear)	5 (C:L-K:NL)	6 (C:NL-K:NL)	-	-

3. Solve for the corresponding displacement, $\mathbf{u}_i$, that nearly satisfies equilibrium (in the implicit class of analysis, but not the explicit one).
4. Update the load and displacement vectors

$$\mathbf{P}_i = \mathbf{P}_{i-1} + \Delta\mathbf{P}_i \tag{14.1}$$

$$\mathbf{u}_i = \mathbf{u}_{i-1} + \Delta\mathbf{u}_i \tag{14.2}$$

An additional iterative loop is necessary in the implicit solution to ensure that equilibrium is (nearly) satisfied. Finally, it should be noted that whereas in most analyses the load is incrementally applied, such a solution strategy may fail to predict the post-peak-response. If this is desired, then the displacement vector (instead of the load vector) should be incrementally applied.

14.4 Numerical Integration

Good comprehension of the numerical algorithms used in the non-linear analysis of structures has to start with something quite simple: the solution of one or a set of non-linear equations [237]. Before one proceeds, it is important to make two important remarks:

1. Contrary to linear problems, one can not ensure the existence of a solution nor the uniqueness of one.
2. At best one can say that an approximate numerical solution of the problem can be found, or that an approximation does not exist (typically this implies local or global failure).

There are two classes of solutions: explicit and implicit. Each one will be reviewed separately.

14.4.1 Explicit

In an explicit integration scheme (also known as “step by step”), the load is applied incrementally and at the end of each increment: a) compute the tangent stiffness on the basis of the current displacements (this is the slope of the load displacement

curve); b) invert the stiffness matrix and multiply it by the incremental load to get the corresponding incremental displacement; c) add the incremental displacement to the sum of the previous ones to obtain the actual displacement corresponding to the actual load (sum of all previous incremental loads), Figure 14.3.
The major advantage of this technique is that a solution will always be found. The major disadvantage is that at the end of each increment we don't verify that equilibrium between internal and external forces is satisfied. This may result in a diverging solution as the load increases. A partial palliative to this problem is the adoption of very small load increments to minimize errors.
This method should be used extremely carefully, as a solution will always be obtained no matter how good or bad the model and its parameters are. Unfortunately, there are some constitutive models which are very fragile when run within an implicit integration scheme, and as a result they are used (or misused) in an explicit one. In

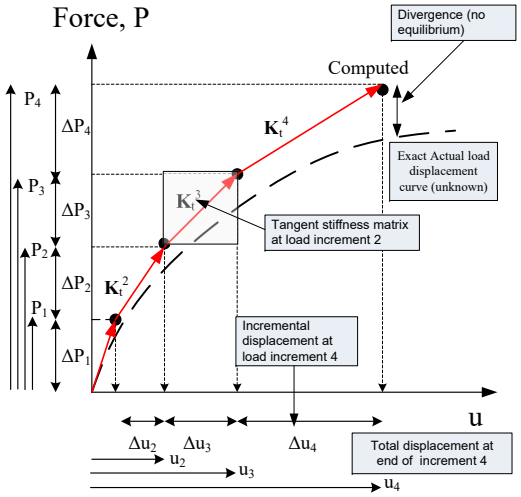

Fig. 14.3: Explicit integration scheme

an explicit integration scheme, no iterations are performed, and very small increments must be taken so as not to diverge from the solution.

$$\{\Delta\overline{\mathbf{u}}\}_i = \mathbf{K}_i^{-1} \{\Delta\overline{\mathbf{P}}\}_i \tag{14.3}$$

$$u_i = u_{i-1} + \Delta u_i \tag{14.4}$$

It should be evident that, contrary to the implicit techniques, a solution will always be obtained, and there is no indication as to whether equilibrium was (nearly) reached, and of course, there is no convergence criteria to satisfy.

14.4.2 Implicit

14.4.2.1 Linearization

We define a constitutive operator as

$$\boldsymbol{\sigma} = \tilde{\boldsymbol{\sigma}}(\varepsilon) \tag{14.5}$$

where $\tilde{\boldsymbol{\sigma}}$ denotes the constitutive operator (analogous to $\mathbf{L}$).
Given a strain stat0,e $\bar{\varepsilon}$, the corresponding stress will be $\bar{\boldsymbol{\sigma}} = \tilde{\boldsymbol{\sigma}}(\tilde{\varepsilon})$. Furthermore, the constitutive operator $\tilde{\boldsymbol{\sigma}}$ can be expanded into a Taylor series with respect to $\bar{\varepsilon}$

$$\tilde{\boldsymbol{\sigma}}(\overline{\varepsilon} + \delta\varepsilon) = \tilde{\boldsymbol{\sigma}}(\overline{\varepsilon}) + \left.\frac{\partial\tilde{\boldsymbol{\sigma}}}{\partial\boldsymbol{\varepsilon}}\right|_{\boldsymbol{\varepsilon}=\overline{\boldsymbol{\varepsilon}}} \delta\varepsilon + \cdots \tag{14.6}$$

Neglecting quadratic and higher order terms leads to a linearized constitutive law

$$\boldsymbol{\sigma} \approx \tilde{\boldsymbol{\sigma}}(\overline{\varepsilon}) + \mathbf{D}(\overline{\varepsilon})\delta\varepsilon \tag{14.7}$$

which approximates Eq. 14.5 for strains in the neighborhood of $\overline{\varepsilon}$, and

$$\mathbf{D} \equiv \frac{\partial\tilde{\boldsymbol{\sigma}}}{\partial\boldsymbol{\varepsilon}} \tag{14.8}$$

is the tangent stiffness matrix which is a function of the current strain.
We rewrite Eq. 13.42, 13.135 and 13.127 in terms of the newly defined constitutive operator

$$\underbrace{\int_{\Omega_e} \mathbf{B}^T\tilde{\boldsymbol{\sigma}}(\mathbf{B}\overline{\mathbf{u}})\mathrm{d}\Omega}_{\overline{\mathbf{f}}^{int}} = \underbrace{\underbrace{\int_{\Omega_e} \mathbf{B}^T\mathbf{D}\boldsymbol{\epsilon}_0\mathrm{d}\Omega - \int_{\Omega_t} \mathbf{B}^T\boldsymbol{\sigma}_0\mathrm{d}\Omega}_{\overline{\mathbf{f}}_{0_e}} + \underbrace{\int_{\Omega_e} \mathbf{N}^T\mathbf{b}\mathrm{d}\Omega + \int_{\Gamma_t} \mathbf{N}^T\hat{\mathbf{t}}\mathrm{d}\Gamma}_{\overline{\mathbf{f}}_e}}_{\overline{\mathbf{f}}^{ext}} \tag{14.9}$$

or

$$\overline{\mathbf{f}}^{int}(\overline{\mathbf{u}}) = \overline{\mathbf{f}}^{ext} \tag{14.10}$$

We now develop a linearized expression for the internal forces. Given $\overline{\mathbf{u}}$ as nodal displacements, the strain field $\overline{\boldsymbol{\varepsilon}} = \mathbf{B}\overline{\mathbf{u}}$, and the stress field $\overline{\boldsymbol{\sigma}} = \tilde{\boldsymbol{\sigma}}(\overline{\varepsilon}) = \tilde{\boldsymbol{\sigma}}(\mathbf{B}\overline{\mathbf{u}})$. Then, the Taylor expansion of the internal forces around $\overline{\mathbf{u}}$ yields

$$\overline{\mathbf{f}}^{int}(\overline{\mathbf{u}} + \Delta\overline{\mathbf{u}}) = \overline{\mathbf{f}}^{int}(\overline{\mathbf{u}}) + \left.\frac{\partial\overline{\mathbf{f}}^{int}}{\partial\overline{\mathbf{u}}}\right|_{\overline{\mathbf{u}}=\overline{\mathbf{u}}} \Delta\overline{\mathbf{u}} + \cdots \tag{14.11}$$

We again neglect the quadratic and higher order terms, leading to

$$\overline{\mathbf{f}}^{int}(\overline{\mathbf{u}} + \Delta\overline{\mathbf{u}}) \approx \overline{\mathbf{f}}^{int}(\overline{\mathbf{u}}) + \mathbf{K}_T(\overline{\mathbf{u}})\Delta\overline{\mathbf{u}} \tag{14.12}$$

where

$$\mathbf{K}_T \equiv \frac{\partial \bar{\mathbf{f}}^{int}}{\partial \bar{\mathbf{u}}} \tag{14.13}$$

is the tangent stiffness matrix of the structure. Differentiating Eq. 14.9:

$$\begin{aligned} \mathbf{K}_T = \frac{\partial \bar{\mathbf{f}}^{int}}{\partial \bar{\mathbf{u}}} = \frac{\partial}{\partial \bar{\mathbf{u}}} \int_\Omega \mathbf{B}^T \tilde{\boldsymbol{\sigma}} \mathrm{d}\Omega = \int_\Omega \mathbf{B}^T \frac{\partial \tilde{\boldsymbol{\sigma}}}{\partial \bar{\mathbf{u}}} \mathrm{d}\Omega \\ = \int_\Omega \mathbf{B}^T \frac{\partial \tilde{\boldsymbol{\sigma}}}{\partial \boldsymbol{\varepsilon}} \frac{\partial \boldsymbol{\varepsilon}}{\partial \bar{\mathbf{u}}} \mathrm{d}\Omega = \int_\Omega \mathbf{B}^T \mathbf{D} \mathbf{B} \mathrm{d}\Omega \end{aligned} \tag{14.14}$$

which is the well known formula for the stiffness matrix; however $\mathbf{D}_{el}$ is now replaced by the tangent moduli $\mathbf{D}$.

14.4.2.2 Solution Strategies

Before we discuss solution strategies, it may be helpful to point out the parallelism which exists between (numerical) solution strategies and (experimental) testing methods. Modern testing equipment can be programmed to apply a pre-determined rate of load (as measured by a load cell), displacement (as measured by an internal displacement transducer), or strain (or relative displacement such as crack mouth opening displacement) measured by a strain/clip gage or other instruments, Figure 14.4.

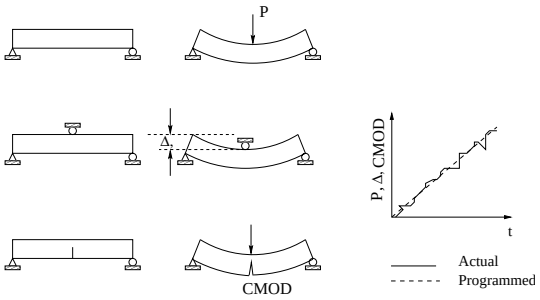

Fig. 14.4: Test Controls

Load Control: the cross-head applies an increasing load irrespective of the specimen deformation or response. For all materials, when the tensile strength is reached, there is a sudden and abrupt brittle failure. The strain energy accumulated in the specimen is suddenly released once the ultimate load of the specimen is reached; thus the sudden failure can be explosive.

Displacement/Stroke Control: the cross-head applies an increasing displacement to the specimen. For softening materials, there will be a post-peak response with a gradual decrease in stress accompanying an increase in displacement. In this

case, there is a gradual release of strain energy which is then transferred to surface energy during crack formation.

Strain Control: is analogous to displacement control except that the feedback is provided by a ("strategically positioned") strain gage, clip gage, or an arbitrary specimen deformation (not necessarily corresponding to the loading direction) such as a crack opening displacement (COD). To accomplish this test, a clip gage or a strain gage has to provide the feedback signal to the testing equipment in order to accordingly adjust the stroke.

Similarly, the objective of a non-linear finite element analysis is to trace the (non-linear) response of a structure subjected to a given load history. This is best done in an incremental-iterative procedure where the load (or the displacement) is applied through several increments, and within each increment we seek to satisfy equilibrium through an iterative procedure (caused by the non-linearity of the problem).The incremental analysis can be performed under:

1. Load control: Load is incrementally applied on the structure.
2. Direct displacement control: An imposed displacement is applied.
3. Indirect displacement control (such as relative displacements between two degrees of freedom)
4. Arc-Length control

Alternatively, iterative techniques include:

1. Newton-Raphson
2. Modified Newton-Raphson
3. Initial Stiffness
4. Secant Newton

Finally, essential ingredients of an incremental-iterative solution strategy are

1. Convergence Criteria
2. Convergence Accelerators (such as line-search or step-size adjustments)

14.4.2.3 Quasi-Newton Numerical Solution

The most widely used implicit class of numerical solution is attributed to Newton, [628] and is called "Newton Methods" or "Quasi Newton". Other methods may include the bisection method (only linearly convergent). The essence of the method, which seeks to solve $f(x) = 0$, is to linearize the equation about the current approximation, x_n, and solve for the resulting linear equation for the next approximation, x_{n+1}.

Traditionally, Newton's method starts with Taylor's series where we express a function as an infinite series with respect to point $\overline{x}$:

$$\begin{aligned} f(x) &= f(\overline{x}) + (x-\overline{x})f'(\overline{x}) + \frac{(x-\overline{x})^2}{2!}f''(\overline{x}) + ... \\ &= f(\overline{x}) + (x-\overline{x})f'(\overline{x}) + \mathcal{O}(\underbrace{|x-\overline{x}|^2|}_{\xi^2}) \end{aligned} \tag{14.15}$$

Ignoring the higher order terms gives a linear function:

$$L(x) = f(\overline{x}) + (x - \overline{x})f'(\overline{x}) \tag{14.16}$$

If we set $f(x) = 0 \Rightarrow x \simeq \overline{x} - \frac{f(\overline{x})}{f'(\overline{x})}$, this is an approximate solution at $\overline{x}$ which presumes that we also have $f'(x)$. In an iterative procedure, this equation can be rewritten as (Figure 14.5):

$$\frac{\mathrm{d}y}{\mathrm{d}x} = f'(x_n) \tag{14.17}$$

$$\Rightarrow \mathrm{d}x = \frac{\mathrm{d}y}{f'(x_n)} = \frac{\overbrace{f(x_{n+1})}^{0} - f(x_n)}{f'(x_n)} \tag{14.18}$$

$$x_{n+1} \simeq x_n \underbrace{- \frac{f(x_n)}{f'(x_n)}}_{\delta x_n} \tag{14.19}$$

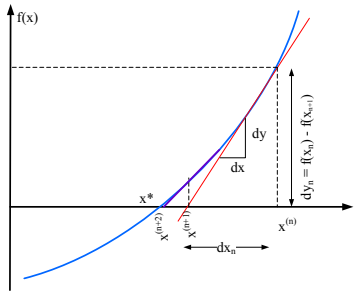

Fig. 14.5: Newton's method for the solution of a non-linear equation

Convergence will be ensured when

$$|\delta x_n| \leq \varepsilon_\delta \quad \text{or} \quad |f(x_{n+1})| \leq \varepsilon_f \tag{14.20}$$

14.4.2.3.1 Multi-dimensional

If we want to solve two equations with two unknowns, then we should linearize $f_1(\mathbf{x})$ and $f_2(\mathbf{x})$ and

$$L(\mathbf{x}) = \begin{bmatrix} f_1(\overline{\mathbf{x}}) + \frac{\partial f_1(\mathbf{x})}{\partial x_1}(x_1 - \overline{x}_1) + \frac{\partial f_1(\mathbf{x})}{\partial x_2}(x_2 - \overline{x}_2) \\ f_2(\overline{\mathbf{x}}) + \frac{\partial f_2(\mathbf{x})}{\partial x_1}(x_1 - \overline{x}_1) + \frac{\partial f_2(\mathbf{x})}{\partial x_2}(x_2 - \overline{x}_2) \end{bmatrix} \tag{14.21}$$

which can be rewritten as

$$L(\mathbf{x}) = \mathbf{f}(\overline{\mathbf{x}}) + J(\overline{\mathbf{x}})(\mathbf{x} - \overline{\mathbf{x}}) \tag{14.22}$$

where $J(\overline{\mathbf{x}})$ is the Jacobian matrix,

$$J(\overline{\mathbf{x}}) = \begin{bmatrix} \frac{\partial f_1(\mathbf{x})}{\partial x_1} & \frac{\partial f_1(\mathbf{x})}{\partial x_2} \\ \frac{\partial f_2(\mathbf{x})}{\partial x_1} & \frac{\partial f_2(\mathbf{x})}{\partial x_2} \end{bmatrix} \tag{14.23}$$

and $J(\overline{\mathbf{x}})(\mathbf{x} - \overline{\mathbf{x}})$ is a matrix vector product[1]. This is similar to Eq. 14.17 except that the scalar derivative has been replaced by the 2x2 Jacobian matrix of partial derivatives. We can further generalize the problem to one of m non-linear equations with m unknowns:

$$\mathbf{x} = \begin{Bmatrix} x_1 \\ x_2 \\ \vdots \\ x_m \end{Bmatrix} \text{ and } \mathbf{f}(\mathbf{x}) = \begin{Bmatrix} f_1(\mathbf{x}) \\ f_2(\mathbf{x}) \\ \vdots \\ f_m(\mathbf{x}) \end{Bmatrix} \tag{14.24}$$

The Jacobian matrix $J(\mathbf{x})$ for this matrix will be an $m \times m$ matrix with (i, j) entries corresponding to the partial derivative of the function i with respect to the variable j or $\frac{\partial f_i(\mathbf{x})}{\partial x_j}$, and the linearization of the function $f(\mathbf{x})$ about $\overline{\mathbf{x}} \in (R)^m$ is

$$L(\mathbf{x}) = f(\overline{\mathbf{x}}) + \frac{\partial f(\overline{\mathbf{x}})}{\partial x_1}(x_1 - \overline{x}_1) + \cdots \frac{\partial f(\overline{\mathbf{x}})}{\partial x_m}(x_m - \overline{x}_m) \tag{14.25}$$

$$= f(\overline{\mathbf{x}}) + J(\overline{\mathbf{x}})(\mathbf{x} - \overline{\mathbf{x}}) \tag{14.26}$$

At each step of the Newton method, we have an approximate value of $\mathbf{x}_n$ to the exact solution, $\mathbf{x}^*$, of the non-linear equations $\mathbf{f}(\mathbf{x}) = \mathbf{0}$. We thus determine $\mathbf{x}_{n+1}$ by solving the linearized system of equations, $L^{(n)}(\mathbf{x}_{n+1}) = \mathbf{0}$:

$$\mathbf{f}(\mathbf{x}_n) + J(\mathbf{x}_n)(\mathbf{x}_{n+1} - \mathbf{x}_n) = \mathbf{0} \tag{14.27}$$

or

$$\mathbf{x}_{n+1} = \mathbf{x}_n - J(\mathbf{x}_n)^{-1}\mathbf{f}(\mathbf{x}_n) \tag{14.28}$$

and note the similarity with Eq. 14.19 where $J(\mathbf{x}) = f'(x)$ for $m = 1$. Finally, we should note that at each step we should evaluate the Jacobian matrix at a new point, and then solve a linear system of equations using this new updated matrix.
Again convergence will be ensured when

$$\| \delta x_n \| \leq \varepsilon_\delta \quad \text{or} \quad \| f(x_{n+1}) \| \leq \varepsilon_f \tag{14.29}$$

where $\| \mathbf{v} \|$ is the Euclidian norm of $\mathbf{v}$ (strictly speaking, it should be written as $\| \mathbf{v} \|_2$) computed as the square root of the sum of the vector components squared:

[1] Note that the ith row corresponds to the gradient of the ith component function f_i ($\boldsymbol{\nabla} f_i$).

$$\| \mathbf{v} \| = \sqrt{\sum_{i=1}^{N} v_i^2} \tag{14.30}$$

in an N dimensional space. Finally, the solution algorithm is given by:

- Given an initial $\mathbf{x}$ and a required tolerance $\varepsilon > 0$,
  Repeat
  1. Evaluate $g = f(\mathbf{x})$ and $H = J(\mathbf{x})$
  2. If $\| g \| \leq \varepsilon$, **return** $\mathbf{x}$
  3. $\mathbf{v} = \mathbf{x}_n - \mathbf{x}_{n-1} = \frac{f(\mathbf{x})}{J(\mathbf{x})}$
  4. Solve $H\mathbf{v} = -g$
  5. $\mathbf{x} := \mathbf{x} + \mathbf{v}$

  until the maximum number of iterations is exceeded.
- Each iteration requires the evaluation of $(\mathbf{x})$ (n scalar functions evaluated in terms of $\mathbf{x}$) and $J(\mathbf{x})$ (n^2 derivatives).

14.4.2.3.2 Convergence and Error Estimate

Convergence must be ensured and the order of the error determined. Given $g(x) = x - \frac{f(x)}{f'(x)}$, define a convergence factor $\rho^{(n)}$ as the ratio of the error in x_{n+1} to the error in x_n. Near the exact solution x^* (where $g(x^*) = x^*$), $\rho^{(n)} \simeq g'(x^*)$ and is called the asymptotic convergence factor.
Determine $g'(x)$:

$$g'(x) = \frac{f(x)f''(x)}{f'(x)^2} \tag{14.31}$$

If $f'(x^*) \neq 0$ and $f''(x^*)$ is finite, then $g'(x^*)$=0, and we conclude that the convergence factor tends to zero when and if $x_n \to x^*$. To determine the error $x^* - x_n$,

$$\begin{aligned} x^* - x_{n+1} &= x^* - x_n - \frac{f(x^*) - f(x_n)}{f'(x_n)} \\ \Rightarrow x^* - x_{n+1} &= -\frac{1}{2}(x^* - x_n)^2 \frac{f''(\xi_n)}{f'(x_n)} \end{aligned} \tag{14.32}$$

Thus if the iteration converges to x^*, there follows

$$\underbrace{x^* - x_{n+1}}_{\text{error at } n+1} \simeq -\frac{f''(x^*)}{2f'(x^*)} \underbrace{(x^* - x_n)^2}_{\text{error at } n} \text{ as } n \to \infty \tag{14.33}$$

as long as $f'(x^*)$ and $f''(x^*)$ are both finite and nonzero. Hence we note that the error tends to be proportional to the square of the error in x_n as n tends to infinity. Other methods (such as bisection) have a linear convergence.

14.4.2.3.3 Final Remarks

Finally, the Newton method

1. Requires an analytical expression of the derivative.
2. If the initial value is too far from the correct value, convergence may not be ensured (which is why one must place an upper limit on the number of iterations).
3. Fails if the slope is close to zero (such as around the peak load).
4. Works best with curves with low curvatures.
5. Convergence is often quadratic:

$$\| x_{n+1} - x^* \| \leq c \| x_n - x^* \|^2 \tag{14.34}$$

However, in practice we do not know what c is.

14.4.2.3.4 Variations

Some variations to the classical Newton's method include:

Secant Method In many instances, it is nearly impossible to compute $J(\mathbf{x})$, as $\mathbf{f}(\mathbf{x})$ may not be analytically defined. In such cases, we will numerically determine the Jacobian based on the simple approximation

$$\mathbf{f}'(\mathbf{x}_{n+1}) \simeq \frac{\mathbf{f}(\mathbf{x}_n) - \mathbf{f}(\mathbf{x}_{n-1})}{\mathbf{x}_n - \mathbf{x}_{n-1}} \tag{14.35}$$

Substituting for $J(\mathbf{x}_n)^{-1}$ in Eq. 14.28

$$\mathbf{x}_{n+1} = \mathbf{x}_n - \underbrace{\frac{\mathbf{x}_n - \mathbf{x}_{n-1}}{\mathbf{f}(\mathbf{x}_n) - \mathbf{f}(\mathbf{x}_{n-1})}}_{\simeq J^{-1}(\mathbf{x}_n)} \mathbf{f}(\mathbf{x}_n) \tag{14.36}$$

Modified-Newton In some applications, the evaluation of the Jacobian is computationally expensive, and in such cases, J^{-1} is kept constant throughout the analysis (this will be referred to as the initial stiffness method) or the load increment (modified Newton).

14.5 Relationship to Structural Mechanics; Implicit

In structural analysis we seek to solve Eq. 13.41 as

$$\underbrace{\mathbf{k}\overline{\mathbf{\Delta}} - \overline{\mathbf{F}}^o}_{\mathbf{P}^{int}} - \underbrace{\overline{\mathbf{F}} + \overline{\mathbf{F}}^e}_{\mathbf{P}^{ext}} = 0 \tag{14.37}$$

Since the non-linear analysis is indeed an approximate method, one in which the imposed load is incrementally applied, after near equilibrium has been confirmed at the end of increment n, we can define

$$\mathbf{R} = \mathbf{P}_n^{ext} - \mathbf{P}_n^{int} = 0 \tag{14.38}$$

which is the residual force (should be approaching zero with increasing number of iterations, n). We precisely seek to solve

$$\mathbf{R}(\mathbf{u}) = 0 \tag{14.39}$$

In this context, Newton's method hinges on our ability to linearize (through a truncated Taylor series) the problem within load increment n as follows:

$$\mathbf{R}_n^k = \mathbf{P}_n^{ext} - \mathbf{P}_n^{int,k} \tag{14.40}$$
$$\delta\mathbf{u}_n^k = [\mathbf{K}_n^{k-1}]^{-1} \cdot \mathbf{R}_n^k \tag{14.41}$$
$$\mathbf{u}_n^k = \mathbf{u}_n^{k-1} + \delta\mathbf{u}_n^k \tag{14.42}$$

where

$$\mathbf{u}_n^{k=0} = \mathbf{u}_{n-1} \tag{14.43}$$
$$\mathbf{P}_n^{int,k=0} = \mathbf{P}_{n-1}^{int} \tag{14.44}$$

and subscript n refers to the load increment, and superscript k to the iteration number within a load. At each iteration, we determine the residual, $\mathbf{R}_i^{(n+1)}$, which corresponds to $\mathbf{P}_{ext} - \mathbf{P}_{int}$ and seek to minimize this residual. We also update (in the Newton method) the tangent stiffness matrix which corresponds to the Jacobian. The algorithm is illustrated in Figure 14.6. It is essentially the same as the explicit one; however it is broken into two steps:

Predictor (associated with an increment of load) to determine the incremental displacement as in the explicit method.
Corrector phase where we check for equilibrium iteratively.

1. Based on the predicted displacements, compute the corresponding internal forces (not evaluated in the explicit method).
2. Compute the residual force which is the difference between the external and internal forces (should be zero if equilibrium is reached).
3. If the residual is larger than a user specified convergence criteria, then update the displacement by multiplying the inverse of the tangent stiffness matrix (more about this later) by the residual force.
4. Update the total displacement vector. Hence for each load increment, we would have multiple iterations until equilibrium is satisfied within a numerical tolerance.

14.6 Integration Methods

`Adapted from [727]`
The fundamental equation to be solved in the non-linear analysis of structures

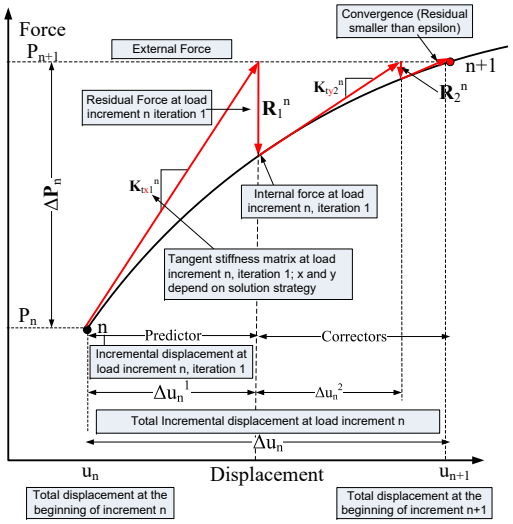

Fig. 14.6: Newton's method in structural engineering

$$\mathbf{P}^{ext} - \mathbf{P}^{int} = 0 \tag{14.45}$$

can be rewritten in incremental form at step n [89] as:

$$\mathbf{R}_n = \mathbf{P}_{t,n}^{ext} - \mathbf{P}_{t,n}^{int} = 0 \tag{14.46}$$

where R refers to the residual, and both $\mathbf{P}_{t,n}^{ext}$ and $\mathbf{P}_{t,n}^{int}$ are determined from the principle of virtual displacement. Since the internal nodal force vector $\mathbf{P}_{t,n}^{int}$ is a function of nodal displacements $\mathbf{u}_{t,n}$, the problem is non-linear, and a non-linear solver must be used to solve Eq. 14.46.

Assuming that forces are independent of the displacements (conservative system and ignoring $P-\Delta$ effects), it is customary to solve Eq. 14.46 by the Newton-Raphson method which will be described in more detail later.

Newton's methods hinge on our ability to linearize (through a truncated Taylor series) the problem as follows:

$$\mathbf{R}_n^k = \mathbf{P}_{t,n}^{ext} - \mathbf{P}_{t,n}^{int,k} \tag{14.47}$$

$$\delta\mathbf{u}_{t,n}^k = [\mathbf{K}_{tt,n}^{k-1}]^{-1} \cdot \mathbf{R}_n^k \tag{14.48}$$

$$\mathbf{u}_{t,n}^k = \mathbf{u}_{t,n}^{k-1} + \delta\mathbf{u}_{t,n}^k \tag{14.49}$$

where

$$\mathbf{u}_{t,n}^{k=0} = \mathbf{u}_{t,n-1}$$
$$\mathbf{P}_{t,n}^{int,k=0} = \mathbf{P}_{t,n-1}^{int}$$

and subscript n refers to the load increment, and superscript k to the iteration number within a load increment.
Within each iteration we determine the residual nodal force vector from Eq. 14.47, and this would yield an incremental nodal displacement vector given by Eq. 14.48. The iterations continue until the residual nodal force vector or the incremental nodal displacement vector is sufficiently small.
In the subsequent sections, different iterative methods will be explained in more detail. At the heart of all of them is the determination of the internal nodal force vector, $\mathbf{P}_{t,n}^{int,k}$, and the tangent stiffness matrix, $\mathbf{K}_{tt,n}^{k-1}$. Hence, we will focus only on the iterative methods to solve Equations 14.47-14.49.

14.6.1 Newton-Raphson

For the sake of discussion, we will assume in the following sections that the incremental analysis is under load control with increments of loads $\Delta\overline{\mathbf{f}}^{ext}$. At the end of each load increment, internal forces must be in equilibrium with the external ones. Hence, we define the vector of residual forces $\mathbf{R}_n^k$ as

$$\mathbf{R}_{n+1}^k \equiv \mathbf{R}_n^k(\overline{\mathbf{u}}_{n+1}) = \overline{\mathbf{f}}^{int}(\overline{\mathbf{u}}_{n+1}) - \overline{\mathbf{f}}^{ext} = 0 \tag{14.50}$$

where $\overline{\mathbf{f}}^{int}$ is the vector of internal forces, also commonly known as the reaction vector.
For equilibrium to be satisfied, the vector of internal forces, $\overline{\mathbf{f}}^{int}$, must be equal to the vector of external forces, $\overline{\mathbf{f}}^{ext}$. This is automatically satisfied in linear elastic analyses, but not necessarily in non-linear analyses. We start the analysis from an equilibrium configuration at the end of increment n such that

$$\overline{\mathbf{u}} = \overline{\mathbf{u}}_n, \quad \mathbf{R}_n^k = 0 \tag{14.51}$$

and apply an increment of load $\Delta\overline{\mathbf{f}}_n^{ext}$ such that

$$\overline{\mathbf{f}}_{n+1}^{ext} = \overline{\mathbf{f}}_n^{ext} + \Delta\overline{\mathbf{f}}_n^{ext} \tag{14.52}$$

and we seek to determine the corresponding change in displacement:

$$\overline{\mathbf{u}}_{n+1} = \overline{\mathbf{u}}_n + \Delta\overline{\mathbf{u}}_n \tag{14.53}$$

We will keep $\Delta\overline{\mathbf{f}}_n^{ext}$ reasonably small to capture the full non-linear response.

14.6.1.1 Newton-Raphson/Tangent Stiffness Method

This is the most rapidly convergent process (albeit computationally expensive) of non-linear problems. At the beginning of each step $n+1$, we start from the displacements $\overline{\mathbf{u}}_n$ that were computed in the previous step through equilibrium, $\mathbf{R}_n^k \approx 0$ or $\overline{\mathbf{f}}_n^{int} \approx \overline{\mathbf{f}}_n^{ext}$. The external forces are now increased from $\overline{\mathbf{f}}_n^{ext}$ to $\overline{\mathbf{f}}_{n+1}^{ext} = \overline{\mathbf{f}}_{n+1}^{ext} + \Delta\overline{\mathbf{f}}^{ext}$, and we seek to determine the corresponding displacements $\overline{\mathbf{u}}_{n+1}$ through equilibrium, $\mathbf{R}_{n+1}^k \approx 0$ or $\overline{\mathbf{f}}_{n+1}^{int} \approx \overline{\mathbf{f}}_{n+1}^{ext}$. Within the current step (identified through the subscript n), we will be iterating (through superscript k) in order to achieve equilibrium.
As an initial guess for $\overline{\mathbf{u}}_{n+1}^0$ we take it to be $\overline{\mathbf{u}}_n$, and based on the linearization around this initial state, we have

$$\overline{\mathbf{f}}_{int}(\overline{\mathbf{u}}_{n+1}^0) + \mathbf{K}_T(\overline{\mathbf{u}}_{n+1}^0)\Delta\overline{\mathbf{u}}_{n+1}^1 = \overline{\mathbf{f}}_{n+1}^{ext} \tag{14.54}$$

where $\Delta\overline{\mathbf{u}}_{n+1}^1$ is the first approximation for the unknown displacement increment, $\Delta\overline{\mathbf{u}}_{n+1} = \overline{\mathbf{u}}_{n+1} - \overline{\mathbf{u}}_n$.
Alternatively, we begin from a linearization of Eq. 14.50, Figure 14.7,

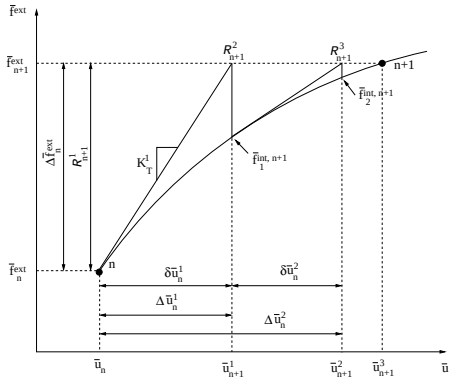

Fig. 14.7: Newton-Raphson Method

$$\mathbf{R}_n^k(\overline{\mathbf{u}}_{n+1}^{i+1}) \approx \mathbf{R}_n^k(\overline{\mathbf{u}}_{n+1}^i) + \left(\frac{\partial \mathbf{R}_n^k}{\partial \overline{\mathbf{u}}}\right)_{n+1}^i \delta\overline{\mathbf{u}}_n^i = 0 \tag{14.55}$$

where i is a counter starting from $\overline{\mathbf{u}}_{n+1}^1 = \overline{\mathbf{u}}_n$. We observe that

$$\frac{\partial \mathbf{R}_n^k}{\partial \overline{\mathbf{u}}} = \frac{\partial \overline{\mathbf{f}}^{int}}{\partial \overline{\mathbf{u}}} = \mathbf{K}_T \tag{14.56}$$

Assuming that $\overline{\mathbf{f}}^{ext}$ is constant and $\mathbf{K}_T$ is the tangent stiffness matrix, Eq. 14.55 yields

$$\mathbf{K}_T^i \delta \overline{\mathbf{u}}_n^i = -\mathbf{R}_{n+1}^i \tag{14.57}$$

or

$$\delta \overline{\mathbf{u}}_n^i = -(\mathbf{K}_T^i)^{-1} \mathbf{R}_{n+1}^i \tag{14.58}$$

Thus, a series of successive approximations yields

$$\overline{\mathbf{u}}_{n+1}^{i+1} = \overline{\mathbf{u}}_n + \Delta \overline{\mathbf{u}}_n^i = \overline{\mathbf{u}}_{n+1}^i + \delta \overline{\mathbf{u}}_n^i \tag{14.59}$$

with

$$\Delta \overline{\mathbf{u}}_n^i = \sum_{k \le i} \delta \overline{\mathbf{u}}_n^k \tag{14.60}$$

very rapidly. It should be noted that each iteration involves three computationally expensive steps:

1. Evaluation of internal forces (or reactions), $\overline{\mathbf{f}}^{int}$
2. Evaluation of the global tangent stiffness matrix, $\mathbf{K}_T$
3. Solution of a system of linear equations

14.6.1.2 Modified Newton-Raphson

This method is essentially the same as the Newton-Raphson; however in Eq. 14.58, $(\mathbf{K}_T^i)$ is replaced by $\overline{\mathbf{K}}_T$ which is the tangent stiffness matrix of the first iteration of either: 1) the first increment $\overline{\mathbf{K}}_T = \mathbf{K}_{T,0}^1$, Figure 14.9, or 2) the current increment $\overline{\mathbf{K}}_T = \mathbf{K}_{T,n}^1$, Figure 14.8.

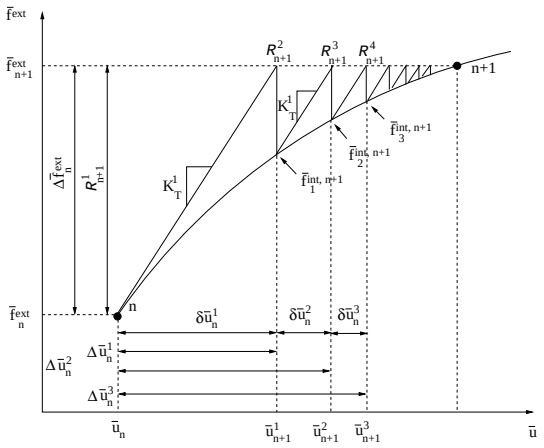

Fig. 14.8: Modified Newton-Raphson Method, Initial Tangent in Increment

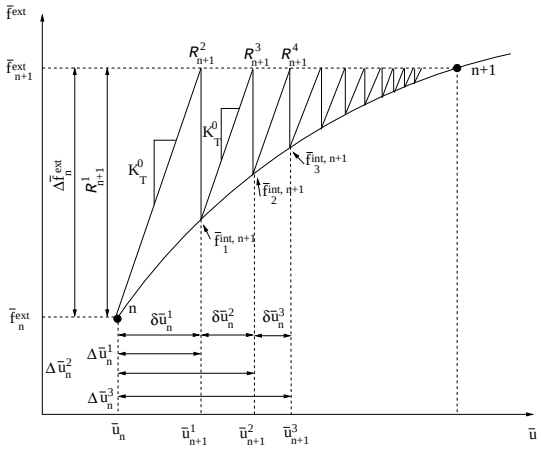

Fig. 14.9: Modified Newton-Raphson Method, Initial Problem Tangent

$$\delta\overline{\mathbf{u}}^i_n = -(\overline{\mathbf{K}}_T)^{-1}\mathbf{R}^i_{n+1} \tag{14.61}$$

In general, the CPU time required for the extra iterations required by this method is less than the time saved by the assembly and decomposition of the stiffness matrix for each iteration. It should be mentioned that the tangent stiffness matrix does not necessarily have to be the true tangent stiffness matrix; an approximation of the true tangent stiffness matrix or even the initial stiffness matrix will generally produce satisfactory results, albeit at the cost of additional iterations.

14.6.1.3 Secant Newton

This method is a compromise between the first two. First we seek two displacements by two cycles of modified Newton-Raphson; then a secant to the curve is established between those two points, and a step is taken along it, Figure 14.10.

$$\delta\overline{\mathbf{u}}^i_n = -(\overline{\mathbf{K}}_T)^{-1}\mathbf{R}^i_{n+1} \tag{14.62}$$

Subsequently, each step will be taken along a secant connecting the previous two points.
Starting with

$$\delta\overline{\mathbf{u}}^1_n = -\mathbf{K}_T^{-1}\mathbf{R}^1_{n+1} \tag{14.63}$$

the secant slope can be determined

$$(\mathbf{K}^2_S)^{-1} = -\frac{\delta\overline{\mathbf{u}}^1_n}{(\mathbf{R}^1_{n+1} - \mathbf{R}^2_{n+1})} \tag{14.64}$$

and then

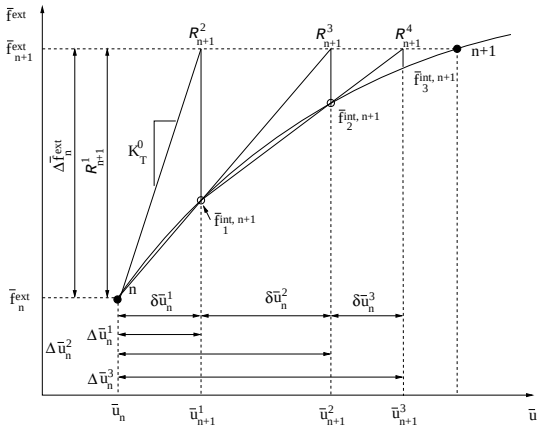

Fig. 14.10: Incremental Secant, Quasi-Newton Method

$$\delta\overline{\mathbf{u}}^2_n = -(\mathbf{K}^2_S)^{-1}\mathbf{R}^2_{n+1} \tag{14.65}$$

This process can be generalized to

$$\delta\overline{\mathbf{u}}^i_n = -(\mathbf{K}^i_S)^{-1}\mathbf{R}^i_{n+1} \tag{14.66}$$

$$(\mathbf{K}^i_S)^{-1} = -\frac{\delta\overline{\mathbf{u}}^i_n}{(\mathbf{R}^{i-1}_{n+1} - \mathbf{R}^i_{n+1})} \tag{14.67}$$

14.6.2 Convergence Criteria

In all preceding methods, iterations are performed until one or all of a variety of convergence criteria are satisfied. Relative convergence criteria are optionally enforced on the displacements, loads, and/or incremental energy to define the termination conditions. The relative displacement criteria is defined in terms of the displacement corrections, $\delta\overline{\mathbf{u}}^j$, and the updated incremental displacements, $\delta\overline{\mathbf{u}}^{j+1}$, as

$$\epsilon_u = \frac{\parallel \delta\overline{\mathbf{u}}^j \parallel_2}{\parallel \Delta\overline{\mathbf{u}}^{j+1} \parallel_2} \tag{14.68}$$

where $\parallel \ldots \parallel_2$ is the Euclidean norm.
The Euclidean norm, which is also known as the L_2 norm, of a vector $\mathbf{v}$ is defined as

$$\parallel \mathbf{v} \parallel_2 = \left[\sum_{i=1}^{N} v_i^2\right]^{1/2} \tag{14.69}$$

where N is the size of $\mathbf{v}$. The relative load criteria is defined in terms of the updated residual loads, $\mathbf{R}^{j+1}$, and the reactions, $\overline{\mathbf{f}}^{int}_{j+1}$, as either

$$\epsilon_r = \frac{\| \mathbf{R}^{j+1} \|_2}{\| \overline{\mathbf{f}}^{int}_{j+1} \|_2} \tag{14.70}$$

or

$$\epsilon_r = \frac{\| \mathbf{R}^{j+1} \|_\infty}{\| \overline{\mathbf{f}}^{int}_{j+1} \|_\infty} \tag{14.71}$$

where $\| \ldots \|_\infty$ is the infinity norm of $\mathbf{v}$ defined as

$$\| \mathbf{v} \|_\infty = \max \left(\sum_{i=1}^{N} |v_i| \right) \tag{14.72}$$

where N is the size of $\mathbf{v}$. The relative incremental energy criteria is defined in terms of displacement corrections $\delta\overline{\mathbf{u}}^j$, the updated residual loads $\mathbf{R}^{j+1}$, the updated incremental displacements $\Delta\overline{\mathbf{u}}^{j+1}$, and the updated reactions $\overline{\mathbf{f}}^{int}_{j+1}$ as

$$\epsilon_W = \frac{\delta\overline{\mathbf{u}}^j \cdot \mathbf{R}^{j+1}}{\Delta\overline{\mathbf{u}}^{j+1} \cdot \overline{\mathbf{f}}^{int}_{j+1}} \tag{14.73}$$

where the numerator is the change in the incremental energy for iteration j, and the denominator is the incremental energy.

14.7 Modeling Reinforcement

Modeling reinforcement in reinforced concrete structures can be challenging. Some key considerations include: a) are the reinforcement strains/stresses individually needed; b) can the pre-processor "line-up" element edges along the reinforcement so as not to penalize the mesh quality; and c) is bond slip important to capture? These concerns can be addressed by one of two techniques to model the reinforcement.

14.7.1 Smeared Reinforcement

In smeared reinforcement, the steel is not explicitly modeled; however the concrete directional stiffness is altered to reflect the presence of rebars [176]. With reference to Figure14.11, the concrete and steel stiffness act as parallel springs. Hence, the equivalent spring stiffness is simply obtained from

$$\left.\begin{array}{l} K_{eff} = K_c + K_s \\ K_c = \frac{Ebh}{t} \\ K_s = \frac{E_s A_s}{t} \\ K_{eq} = \frac{E_{eq} bh}{t} \end{array}\right\} E_{eq} = E_c + \frac{E_s A_s}{bt} = E_c + \rho E_s \tag{14.74}$$

where ρ is the reinforcement ratio (A_s/bh). This method does not allow the extraction of individual reinforcement strains or stresses from the completed analysis.

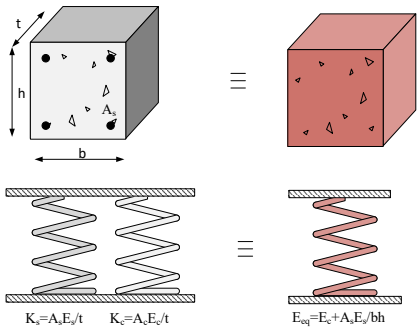

Fig. 14.11: Effective Young's modulus of reinforced concrete)

14.7.2 Embedded Reinforcement

The embedded reinforcement method will model each reinforcement bar individually by altering the stiffness matrices of individual finite elements crossed by the rebars. Start with the stiffness matrix of a rod element (Eq. 13.42),

$$\mathbf{K} = \int_{\Omega} \mathbf{B}^T \mathbf{D} \mathbf{B} \mathrm{d}\Omega \tag{14.75}$$

where $\mathbf{B}$ (Eq. 13.26) is really composed of two parts,

$$\underbrace{\mathbf{B}}_{1\times 4} = \underbrace{\mathbf{B}_1}_{1\times 2}\underbrace{\mathbf{B}_2}_{2\times 4} \tag{14.76}$$

where $\mathbf{B}_2$ transforms the displacements from global to local coordinates and $\mathbf{B}_1$ determines the derivative for the strain.
The stiffness matrix is a 4×4 matrix in 2D, and 6×6 in 3D, for an arbitrarily oriented element in space. The embedded reinforcement is going to intersect edges of continuum solid elements. At each one of those points, we can relate the bar displacements to those of the element through the shape functions. Consider a 3 noded triangle,

$$\left\{ \begin{array}{c} \mathbf{u}_1 \\ \mathbf{u}_2 \end{array} \right\} = \left[\begin{array}{c} \mathbf{N}(\boldsymbol{\xi}_1) \\ \mathbf{N}(\boldsymbol{\xi}_2) \end{array} \right] \mathbf{u}_s = \underbrace{\mathbf{B}^*}_{4\times 6} \mathbf{u}_s \tag{14.77}$$

where $\mathbf{u}_s$ is the nodal displacement vector of the solid element, $\mathbf{u}_i$ are the nodal displacements of the bar node i, and $N(\boldsymbol{\xi}_i)$ are shape function values of the solid element that are evaluated at bar node i with natural coordinates $\boldsymbol{\xi}_i$.
The stiffness matrix of the embedded element is thus added to the one of the solid element

$$\mathbf{K}^{total} = \mathbf{K}^{solid} + \mathbf{K}^{bar} \tag{14.78}$$

where

$$\underbrace{\mathbf{K}^{bar}}_{6\times6} = \int_{\Omega} \mathbf{B}'^{T}\mathbf{D}\mathbf{B}'\mathrm{d}\Omega \tag{14.79}$$

where

$$\underbrace{\mathbf{B}'}_{1\times6} = \underbrace{\mathbf{B}}_{1\times4}\underbrace{\mathbf{B}^{*}}_{4\times6} \tag{14.80}$$

$$\mathbf{D} = \frac{AE}{L} \tag{14.81}$$

When an embedded reinforcement crosses a crack, Figure 14.12, then

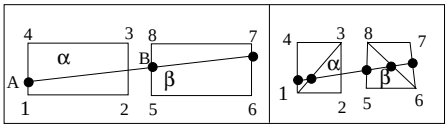

Fig. 14.12: Embedded Reinforcement Across a Crack/Joint

1. The element stiffness matrices of the two adjacent elements are computed and added to the global stiffness matrix.
2. A virtual super element, obtained by adding the connectivity vectors of the two elements α and β (1-2-3 and 5-6-8 or 1-2-3-4 and 5-6-7-8), is created. The $\mathbf{B}^{*}$ matrix is now given by

$$\begin{Bmatrix}\mathbf{u}_1\\ \mathbf{u}_2\end{Bmatrix} = \underbrace{\begin{bmatrix}\mathbf{N}(\boldsymbol{\xi}_\alpha) & 0\\ 0 & \mathbf{N}(\boldsymbol{\xi}_\beta)\end{bmatrix}}_{\underbrace{\mathbf{B}^{*}}_{4\times12}} \begin{Bmatrix}\mathbf{u}_\alpha\\ \mathbf{u}_\beta\end{Bmatrix} \tag{14.82}$$

   where $\boldsymbol{\xi}_\alpha$ are the natural coordinates of the first bar node in the first element and $\boldsymbol{\xi}_\beta$ the natural coordinates of the second bar node in the second element (the first bar node (1) contributes to the stiffness of element α, and the second node (2) contributes to the adjacent element β); $\mathbf{u}_\alpha$ and $\mathbf{u}_\beta$ are the nodal displacements of the two virtual elements.
3. Hence, the size of $\mathbf{B}'$ is

$$\underbrace{\mathbf{B}'}_{1\times12} = \underbrace{\mathbf{B}}_{1\times4}\underbrace{\mathbf{B}^{*}}_{4\times12} \tag{14.83}$$

   and

$$\underbrace{\mathbf{K}^{bar}}_{12\times12} = \int_{\Omega} \mathbf{B}'^{T}\mathbf{D}\mathbf{B}'\mathrm{d}\Omega \tag{14.84}$$

4. If the two elements have identical nodes (i.e. are not intersected by a crack), then we essentially recover Eq. 14.77 since the stiffness terms of the second bar node

will contribute to the same stiffness term in the global stiffness matrix (and the second bar node does not contribute to the stiffness terms corresponding to node 6).

This method allows for strain recovery of each segment of the rod.

14.7.3 Discrete Reinforcement

In this last method, internal elements adjacent to the reinforcement must have their edges aligned with it. In most cases, this will be difficult to achieve. Such an effort may be warranted only if the bond-slip is to be modeled by wrapping a "bond" element around the reinforcement. Such a bond-slip element can very well be a variation of the interface element separately discussed in Section 15.3.

14.8 Modeling ASR

By virtue of its time dependent volumetric expansion, the formation of internal micro-cracks, the degradation of the elastic modulus and tensile strength, ASR finite element modeling has to be nonlinear [772].
For a finite element code to capture the ASR response, it has to account for the following essential features [749]:

1. Environmental Conditions of the concrete
   a. Temperature
   b. Humidity
2. Constitutive models
   a. Solid concrete (tension, compression, creep, shrinkage)
   b. Cracks/joints/interfaces.
3. Load history
4. Mechanical Boundary Conditions
   a. Structural Arrangement
   b. Reinforcement
   c. Anchorage

This is followed by a battery of eleven problems that could be analyzed to "validate" (or as a minimum to lend some credibility to a code claiming to perform an ASR analysis), Table 14.2. There were five published submittals, including one by the authors [759].

Table 14.2: Benchmark problems for ASR code "validation"

No.	Description
P0	Textual description of finite element code/models
	Material Response
P1	Constitutive model
P2	Capturing drying and shrinkage
P3	Capturing creep
P4	Effect of Temperature
P5	Effect of RH
P6	Effect of confinement
	Structural Response
P7	Internal reinforcement
P8	Reinforced concrete beam
P9	Dam (simplified)
P10	Reinforced concrete panel expansion
P11	Nuclear containment vessel (Simplified)

Chapter 15
Fracture Mechanics Analysis with Finite Elements

Abstract
Whereas Chapters 4 and 9 addressed the theoretical underpinning of classical (linear and nonlinear) fracture mechanics and concrete fracture mechanics, this chapter will cover their implementation within the finite element method. It is broken into three parts: a) linear elastic fracture mechanics (use of singular elements to determine the stress intensity factors); 2) nonlinear fracture mechanics (J integral); and c) cohesive crack model for concrete.

15.1 Linear Elastic Fracture Mechanics

15.1.1 Quarter Point Singular Elements

`Based on [763]`
This section discusses the easiest and most powerful technique used in finite elements to model a stress singularity. Barsoum [86] and Henshell and Shaw [412] independently demonstrated that the inverse square root singularity characteristic of linear elastic fracture mechanics can be obtained in the 2D 8-noded isoparametric element (Q8) when the mid-side nodes near the crack tip are placed at the quarter point.
Thus, in order to model a stress singularity without altering the finite element code, the mid-side nodes adjacent to the crack tip must be shifted to their quarter-point positions. Since then, this element became known as the quarter-point element.
In light of the simplicity and accuracy achieved by this element, this section will:

1. Cover a brief review of the isoparametric element formulation
2. Show how the element can be distorted in order to achieve a stress singularity
3. Determine the order of the stress singularity
4. Provide a brief review of all the historical developments surrounding this element
5. Discuss the effect on numerical accuracy of element size, order of integration, and local meshing around the crack tip
6. Briefly mention references to other singular elements

15.1.2 Review of Isoparametric Finite Elements

In the isoparametric finite element representation, both the internal displacement and coordinates are related to their nodal values through the shape functions:

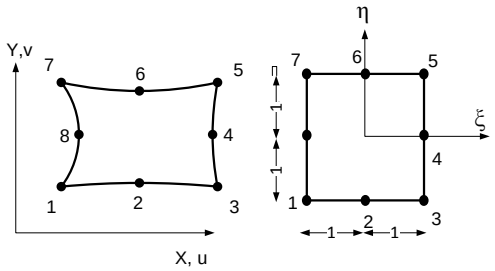

Fig. 15.1: Isoparametric quadratic finite element: global and parent element

$$\left\{ \begin{array}{c} x \\ y \end{array} \right\} = \sum_{i=1}^{8} \left[\begin{array}{cc} N_i & 0 \\ 0 & N_i \end{array} \right] \left\{ \begin{array}{c} \overline{x}_i \\ \overline{y}_i \end{array} \right\} \tag{15.1}$$

$$\{d\} = \left\{ \begin{array}{c} u \\ v \end{array} \right\} = \sum_{i=1}^{8} \left[\begin{array}{cc} N_i & 0 \\ 0 & N_i \end{array} \right] \left\{ \begin{array}{c} \overline{u}_i \\ \overline{v}_i \end{array} \right\} \tag{15.2}$$

where the N_i are the assumed shape functions.
The shape functions are obtained by mere inspection (i.e. **serendipitously**),

$$\begin{array}{ll} N_i = \frac{1}{4}\left(1+\xi\xi_i\right)\left(1+\eta\eta_i\right)\left(\xi\xi_i+\eta\eta_i-1\right) & i=1,2,3,4 \\ N_i = \frac{1}{2}\left(1-\xi^2\right)\left(1+\eta\eta_i\right) & i=5,7 \\ N_i = \frac{1}{2}\left(1+\xi\xi_i\right)\left(1+\eta^2\right) & i=6,8 \end{array} \tag{15.3}$$

and are tabulated in Table 13.1.
As the strain is the derivative of the displacement, we will later need to define $\frac{\partial N}{\partial x}$ and $\frac{\partial N}{\partial y}$. N has been defined in Eq. 15.3 in terms of the natural coordinates ξ and η. Thus the chain rule will have to be invoked, and the inverse of the Jacobian will be needed. In this case, the Jacobian matrix is:

$$[J] = \left[\begin{array}{cc} \frac{\partial x}{\partial \xi} & \frac{\partial y}{\partial \xi} \\ \frac{\partial x}{\partial \eta} & \frac{\partial y}{\partial \eta} \end{array} \right] = \left[\begin{array}{cc} \sum_{i=1}^{8} \frac{\partial N_i}{\partial \xi} x_i & \sum_{i=1}^{8} \frac{\partial N_i}{\partial \xi} y_i \\ \sum_{i=1}^{8} \frac{\partial N_i}{\partial \eta} x_i & \sum_{i=1}^{8} \frac{\partial N_i}{\partial \eta} y_i \end{array} \right] \tag{15.4}$$

The inverse Jacobian is then evaluated from:

$$[J]^{-1} = \begin{bmatrix} \frac{\partial \xi}{\partial x} & \frac{\partial \eta}{\partial x} \\ \frac{\partial \xi}{\partial y} & \frac{\partial \eta}{\partial y} \end{bmatrix} = \frac{1}{DetJ} \begin{bmatrix} \frac{\partial y}{\partial \eta} & -\frac{\partial y}{\partial \xi} \\ -\frac{\partial x}{\partial \eta} & \frac{\partial x}{\partial \xi} \end{bmatrix} \tag{15.5}$$

The strain displacement relationship is:

$$\{\epsilon\} = \sum_{i=1}^{8} [B_i] \left[\overline{d}_i\right] \tag{15.6}$$

where $[B_i]$ is the strain matrix given by:

$$[B_i] = \begin{bmatrix} \frac{\partial N_i}{\partial x} & 0 \\ 0 & \frac{\partial N_i}{\partial y} \\ \frac{\partial N_i}{\partial y} & \frac{\partial N_i}{\partial x} \end{bmatrix} \tag{15.7}$$

where the following chain rule is invoked to determine the coefficients of $[B]$:

$$\begin{Bmatrix} \frac{\partial N}{\partial x} \\ \\ \frac{\partial N}{\partial y} \end{Bmatrix} = [J]^{-1} \begin{Bmatrix} \frac{\partial N}{\partial \xi} \\ \\ \frac{\partial N}{\partial \eta} \end{Bmatrix} \tag{15.8}$$

Finally, it can be shown that the stiffness matrix of an element is given by [325, 926]:

$$[K] = \int_{-1}^{1} \int_{-1}^{1} [B(\xi, \eta)] [D] [B(\xi, \eta)] \, detJ d\xi d\eta \tag{15.9}$$

where the natural coordinates ξ and η are shown in Figure 15.1 and $[D]$ is the stress-strain or constitutive matrix.
The stress is given by:

$$\{\sigma\} = [D] [B] \begin{Bmatrix} \overline{u}_i \\ \overline{v}_i \end{Bmatrix} \tag{15.10}$$

15.1.3 How to Distort the Element to Model the Singularity

In Eq. 15.10, if the stresses are to be singular, then $[B]$ has to be singular as the two other components are constants. Consequently, if $[B]$ is to be singular, then the determinant of J must vanish to zero (Eq. 15.4) at the crack tip.
Now considering a rectangular element of length L along its first side (1-5-2, in Figure 15.1), we can readily see that both off-diagonal terms ($\frac{\partial y}{\partial \xi}$ and $\frac{\partial x}{\partial \eta}$) in J (Eq. 15.4) are zero. Thus, for the determinant of the Jacobian to be zero we must have either one of the diagonal terms equal to zero. It will suffice to force $\frac{\partial x}{\partial \xi}$ to be zero. Making the proper substitution for $\frac{\partial x}{\partial \xi}$ at $\eta = -1$ we have:

$$\begin{aligned}\left.\frac{\partial x}{\partial \xi}\right|_{\eta=-1} &= \sum_{i=1}^{8} \frac{\partial N_i}{\partial \xi} \overline{x}_i \\ &= \frac{1}{4}\left[-1+2\xi+2\xi-1\right](0) + \frac{1}{4}\left[1+2\xi+2\xi+1\right](L) \\ &\quad + \frac{1}{4}\left[-1+2\xi-2\xi+1\right](L) + \frac{1}{4}\left[1-2\xi+2\xi-1\right](0) \\ &\quad -2\xi\,(x_5) + \frac{1}{2}(1-1)L + \frac{1}{2}(1-1)(L) + \frac{1}{2}(1-1)\left(\frac{L}{2}\right) \\ &= \frac{1}{4}(2+4\xi)\,L - 2\xi x_5 \end{aligned} \tag{15.11}$$

After simplification, and considering the first corner node (where $\eta = \xi = -1$), we would have:

$$\left.\frac{\partial x}{\partial \xi}\right|_{\substack{\xi=-1\\ \eta=-1}} = 0 \Leftrightarrow (1-2)\frac{L}{2} + 2x_5 = 0 \Rightarrow x_5 = \frac{L}{4} \tag{15.12}$$

Thus all the terms in the Jacobian vanish if and only if the second node is located at $\frac{L}{4}$ instead of $\frac{L}{2}$, and subsequently both the stresses and strains at the first node will become singular.
Thus singularity at the crack tip is achieved by shifting the mid-side node to its quarter-point position, see Figure 15.2.
We should observe that instead of enforcing $\frac{\partial x}{\partial \xi}$ along edge 1-2 to vanish at the crack tip, we could have enforced $\frac{\partial y}{\partial \eta}$ along edge 1-7 to be zero at the crack tip.
A similar approach will show that if node 8 is shifted to its quarter-point position, the same radial strain variation would be obtained along sides 1-4. However, along rays within the element emanating from node 1, the strain variation is not singular. The next section will discuss this issue and other variations of this distorted element in more detail.

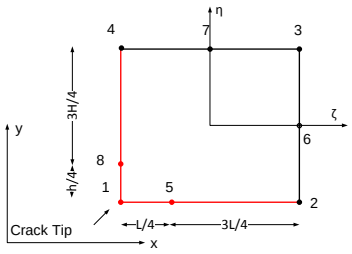

Fig. 15.2: Singular element (quarter-point quadratic isoparametric element)

15.1.4 Order of Singularity

Having shown that the stresses at the first node are singular, the obvious question is what is the degree of singularity.
First let us solve for ξ in terms of x and L at $\eta = -1$ (that is, along side 1-5-2):

$$\begin{aligned} x &= \sum_{i=1}^{8} N_i \overline{x}_i \\ &= \frac{1}{2}\left(1-\xi^2\right)(1+1)\frac{L}{4} + \frac{1}{4}(1+\xi)(1+1)(\xi)L \\ &= \frac{1}{2}\xi(1+\xi)L + \left(1-\xi^2\right)\frac{L}{4} \\ \Rightarrow \xi &= -1+2\sqrt{\frac{x}{L}} \end{aligned} \tag{15.13}$$

Recalling that in isoparametric elements the displacement field along $\eta = -1$ is given by:

$$u = -\frac{1}{2}\xi(1-\xi)\overline{u}_1 + \frac{1}{2}\xi(1+\xi)\overline{u}_5 + \left(1-\xi^2\right)\overline{u}_2 \tag{15.14}$$

we can rewrite Eq. 15.14 by replacing ξ with the previously derived expression (Eq. 15.14):

$$\begin{aligned} u = &-\frac{1}{2}\left(-1+2\sqrt{\frac{x}{L}}\right)\left(2-2\sqrt{\frac{x}{L}}\right)\overline{u}_1 \\ &+ \frac{1}{2}\left(-1+2\sqrt{\frac{x}{L}}\right)\left(2\sqrt{\frac{x}{L}}\right)\overline{u}_5 \\ &+ \left(4\sqrt{\frac{x}{L}} - 4\frac{x}{L}\right)\overline{u}_2 \end{aligned} \tag{15.15}$$

This complex equation can be rewritten in the form:

$$u = A + Bx + C\sqrt{\frac{x}{L}} \tag{15.16}$$

We thus note that the displacement field has had its quadratic term replaced by $x^{\frac{1}{2}}$, which means that when the derivative of the displacement is taken, the strain (and stresses) are of the form:

$$\epsilon_x = -\frac{1}{2}\left(\frac{3}{\sqrt{xL}} - \frac{4}{L}\right)\overline{u}_1 + \frac{1}{2}\left(\frac{-1}{\sqrt{xL}} + \frac{4}{L}\right)\overline{u}_5 + \left(\frac{2}{\sqrt{xL}} - \frac{4}{L}\right)\overline{u}_2 \tag{15.17}$$

Thus the strength of the singularity is of order $\frac{1}{2}$, just as we wanted it to be for linear elastic fracture mechanics!

15.1.5 Stress Intensity Factors Extraction

A number of techniques (including the ones discussed in the subsequent section) can be used to determine the SIF when quarter-point elements are used, Figure 15.3, but by far the simplest one to use and implement is the one based on the nodal

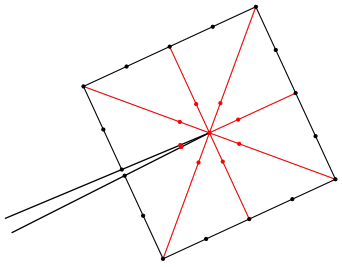

Fig. 15.3: Finite element discretization of the crack tip using singular elements

displacement correlation technique.
This technique, first introduced by Shih, Lorenzi, and German [786], equates the displacement field in the quarter-point singular element with the theoretical one. This method was subsequently refined by Lynn and Ingraffea [552], who introduced the transition elements, and extended by Ingraffea and Manu [461] to three-dimensional isotropic problems. This method was finally extended to full three-dimensional anisotropic cases by Saouma and Sikiotis [764].
For the quarter-point singular element, in two dimensions and with reference to Figure 15.4, the displacement field is given by Eq. 15.17:

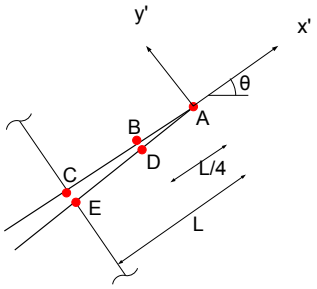

Fig. 15.4: Displacement correlation method to extract sif from quarter point singular elements

$$u' = \overline{u}'_A + \left(-3\overline{u}'_A + 4\overline{u}'_B - \overline{u}'_C\right)\sqrt{\tfrac{r}{L}} + \left(2\overline{u}'_A + 2\overline{u}'_C - 4\overline{u}'_B\right)\tfrac{r}{L} \quad (15.18)$$

$$v' = \overline{v}'_A + \left(-3\overline{v}'_A + 4\overline{v}'_B - \overline{v}'_C\right)\sqrt{\tfrac{r}{L}} + \left(2\overline{v}'_A + 2\overline{v}'_C - 4\overline{v}'_B\right)\tfrac{r}{L} \quad (15.19)$$

where $\overline{u}'$ and $\overline{v}'$ are the local displacements (with x' aligned with the crack axis) of the nodes along the crack in the singular elements.
On the other hand, the analytical expression for v is given by Eq. 4.15 with $\theta = 180$, yielding:

$$v = K_{\mathrm{I}}\frac{\kappa+1}{2G}\sqrt{\frac{r}{2\pi}} \quad (15.20)$$

Equating the terms of equal power ($\frac{1}{2}$) in the preceding two equations, the $\sqrt{r}$ term vanishes and we obtain:

$$K_{\mathrm{I}} = \frac{2G}{\kappa+1}\sqrt{\frac{2\pi}{L}}\left(-3\overline{v}'_A + 4\overline{v}'_B - \overline{v}'_C\right) \quad (15.21)$$

If this approach is generalized to mixed mode problems, then the two stress intensity factors are given by:

$$\left\{\begin{array}{c} K_{\mathrm{I}} \\ K_{\mathrm{II}} \end{array}\right\} = \frac{1}{2}\frac{2G}{\kappa+1}\sqrt{\frac{2\pi}{L}}\begin{bmatrix} 0 & 1 \\ 1 & 0 \end{bmatrix}\begin{bmatrix} -3\overline{u}'_A + 4\left(\overline{u}'_B - \overline{u}'_D\right) - \left(\overline{u}'_C - \overline{u}'_E\right) \\ -3\overline{v}'_A + 4\left(\overline{v}'_B - \overline{v}'_D\right) - \left(\overline{v}'_C - \overline{v}'_E\right) \end{bmatrix} \quad (15.22)$$

Thus it can be readily seen that the extraction of the SIF can be accomplished through a "post-processing" routine following a conventional finite element analysis in which the quarter-point elements have been used. The method can easily be extended to 3D; however meshing can be problematic.

15.2 J Integral

Within linear elastic fracture mechanics, the J integral is equivalent to G and we have:

$$G = J = -\frac{\partial \Pi}{\partial a} = \int_r (w\mathrm{d}y - \mathbf{t}\cdot\frac{\partial \mathbf{d}}{\partial x}\mathrm{d}s) \quad (15.23)$$

Thus it is evident that we do have two methods of evaluating J: the first one stems from its equivalence to the energy release rate, and the second one from its definition as an integral along a closed contour. Evaluation of J according to the first approach is identical to the one of G and has been previously presented.
In this section, we shall present the algorithm to evaluate J on the basis of its contour line integral definition. Whereas derivation will be for the J integral only, its extension to J_i is quite straightforward.
If the stresses are to be determined at the nodes, then the numerical evaluation of J will be relatively simple. However, most standard finite element codes only provide Gauss point stresses, and hence care must be exercised in properly determining the J integral along a path passing through them.

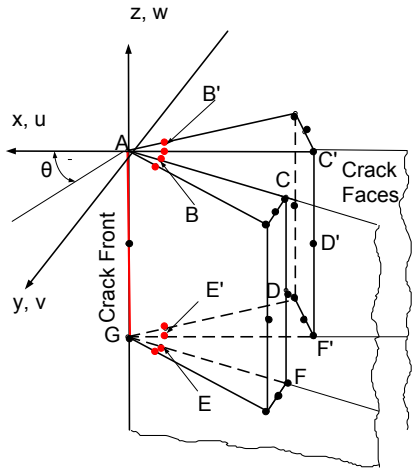

Fig. 15.5: Singular quarter point isoparametric elements in 3D

The algorithm for the J calculation closely follows the method presented in [672], and is as follows:

1. First let us restrict ourselves to the more general case in which isoparametric elements are used. Because the stresses are most accurately evaluated at the Gauss points, the path can be conveniently chosen to coincide with $\xi = \xi_{cst}$ and/or $\eta = \eta_{cst}$. For the sake of discussion, let us assume that the element connectivity is such that the path is along $\xi = \xi_{cst}$, as in Figure 15.6. We note that for corner elements, the integration will have to be performed twice along the two directions.
2. Now let us start from the basic definition of J:

$$J = \int_{\Gamma} w \mathrm{d}y - \mathbf{t} \cdot \frac{\partial \mathbf{d}}{\partial x} \mathrm{d}s \tag{15.24}$$

   where $\mathbf{t}$ is the traction vector along $\mathbf{n}$, which is normal to the path; $\mathbf{d}$ is the displacement vector; $\mathrm{d}s$ is the element of arc along path Γ; and w is the strain energy density. We note that the crack is assumed to be along the x axis. If it is not, stresses and displacements would first have to be rotated. Let us now determine each term of Eq. 15.24.
3. The traction vector is given by:

$$t_i = \sigma_{ij} n_j \Rightarrow \mathbf{t} = \left\{ \begin{array}{l} \sigma_{xx} n_1 + \tau_{xy} n_2 \\ \tau_{xy} n_1 + \sigma_{yy} n_2 \end{array} \right\} \tag{15.25}$$

4. The displacement vector is:

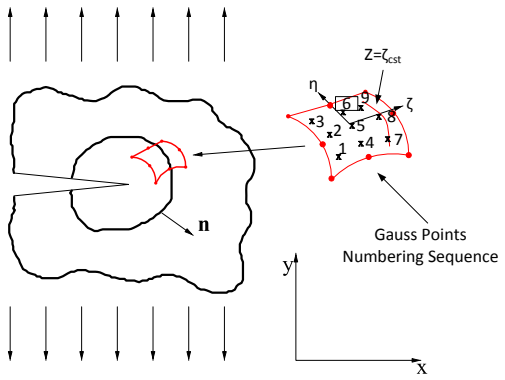

Fig. 15.6: Numerical extraction of the J integral [672]

$$\mathbf{d} = \begin{Bmatrix} u \\ v \end{Bmatrix} \tag{15.26}$$

5. The strain energy density w is:

$$\begin{aligned} w &= \frac{1}{2}(\sigma_{xx}\varepsilon_{xx} + 2\tau_{xy}\gamma_{xy} + \sigma_{yy}\varepsilon_{yy}) \\ &= \frac{1}{2}[\sigma_{xx}\frac{\partial u}{\partial x} + \tau_{xy}(\frac{\partial u}{\partial y} + \frac{\partial v}{\partial x}) + \sigma_{yy}\frac{\partial v}{\partial y}] \end{aligned} \tag{15.27}$$

6. The arc length $\mathrm{d}s$ and $\mathrm{d}y$ are given by:

$$\mathrm{d}s = \sqrt{\mathrm{d}x^2 + \mathrm{d}y^2} = \sqrt{\left(\frac{\partial x}{\partial \eta}\right)^2 + \left(\frac{\partial y}{\partial \eta}\right)^2}\,\mathrm{d}\eta \tag{15.28}$$

$$\mathrm{d}y = \frac{\partial y}{\partial \eta}\mathrm{d}\eta \tag{15.29}$$

7. Next we can evaluate part of the second term of J:

$$\mathbf{t} \cdot \frac{\partial \mathbf{d}}{\partial x} = (\sigma_x n_1 + \tau_{xy} n_2)\frac{\partial u}{\partial x} + (\tau_{xy} n_1 + \sigma_y n_2)\frac{\partial v}{\partial x} \tag{15.30}$$

   where n_1 and n_2 are the components of **n**, which is a unit vector normal to the contour line at the Gauss point under consideration.
8. Having defined all the terms of J, we substitute in Eq. 15.24 to obtain the contribution to J from a particular Gauss point within an element.

$$J^e = \int_{-1}^{1} \left\{ \underbrace{\frac{1}{2}\left[\sigma_x \frac{\partial u}{\partial x} + \tau_{xy}\left(\frac{\partial u}{\partial y} + \frac{\partial v}{\partial x}\right) + \sigma_y \frac{\partial v}{\partial y}\right]}_{w} \underbrace{\frac{\partial y}{\partial \eta}}_{\mathrm{d}y} \right.$$
$$\underbrace{- \left[(\sigma_x n_1 + \tau_{xy} n_2)\frac{\partial u}{\partial x} + (\tau_{xy} n_1 + \sigma_y n_2)\frac{\partial v}{\partial x}\right]}_{\mathbf{t}\cdot\frac{\partial \mathbf{d}}{\partial x}}$$
$$\left. \underbrace{\sqrt{\left(\frac{\partial x}{\partial \eta}\right)^2 + \left(\frac{\partial y}{\partial \eta}\right)^2}}_{\mathrm{d}s} \right\} \mathrm{d}\eta = \int_{-1}^{1} I \mathrm{d}\eta \tag{15.31}$$

9. Since the integration is to be carried out numerically along the path (using the same integration points used for the element stiffness matrix), we have:

$$J^e = \sum_{q=1}^{NGAUS} I(\xi_p, \eta_q) W_q \tag{15.32}$$

where W_q is the weighting factor corresponding to η_q and $NGAUS$ is the order of integration (2 or 3).

10. Stresses $\sigma_x,\ \sigma_y,\ \tau_{xy}$ are readily available at the Gauss points.
11. $\frac{\partial u}{\partial x}$, $\frac{\partial u}{\partial y}$, $\frac{\partial v}{\partial x}$, and $\frac{\partial v}{\partial y}$ are obtained through the shape function. For instance $\frac{\partial u}{\partial x} = \lfloor \frac{\partial N_i}{\partial x} \rfloor \{u_i\}$ where the u_i are the nodal displacements and $\frac{\partial N_i}{\partial x}$ is the Cartesian derivative of the shape function stored in the $[B]$ matrix:

$$[\mathbf{B}] = \begin{bmatrix} \frac{\partial N_i}{\partial x} & 0 \\ 0 & \frac{\partial N_i}{\partial y} \\ \frac{\partial N_i}{\partial y} & \frac{\partial N_i}{\partial x} \end{bmatrix} \tag{15.33}$$

where i ranges from 1 to 8 for quadrilateral elements.

12. Another term not yet defined in Eq. 15.31 is $\frac{\partial y}{\partial \eta}$. This term is actually stored already in the Gauss point Jacobian matrix:

$$[J] = \begin{bmatrix} \frac{\partial x}{\partial \xi} & \frac{\partial y}{\partial \xi} \\ \frac{\partial x}{\partial \eta} & \frac{\partial y}{\partial \eta} \end{bmatrix} \tag{15.34}$$

13. Finally we are left to determine n_1 and n_2 (components of **n**). Since there are an infinite number of vectors normal to ξ, we want the one which is in the $\xi - \eta$ plane. It should be noted that if we had a rectangular element, then η is orthogonal to ξ in the physical space, but in general we have a distorted element, and thus η and ξ are not necessarily orthogonal to each others in the physical space. Hence, we determine the normal is determined as follows:

a. Define two arbitrary vectors: $\mathbf{A}$ along $\xi = \xi_{cst}$ and $\mathbf{B}$ along $\eta = \eta_{cst}$ such that:

$$\mathbf{A}^t = \lfloor \frac{\partial x}{\partial \eta}, \frac{\partial y}{\partial \eta}, 0 \rfloor \tag{15.35}$$

$$\mathbf{B}^t = \lfloor \frac{\partial x}{\partial \xi}, \frac{\partial y}{\partial \xi}, 0 \rfloor \tag{15.36}$$

Note that we have defined the three-dimensional components of those two vectors.

b. Now we define a third vector, which is normal to the plane defined by the preceding two: $\mathbf{C} = \mathbf{A} \times \mathbf{B}$, or:

$$\begin{bmatrix} \mathbf{i} & \mathbf{j} & \mathbf{k} \\ \frac{\partial x}{\partial \eta} & \frac{\partial y}{\partial \eta} & 0 \\ \frac{\partial x}{\partial \xi} & \frac{\partial y}{\partial \xi} & 0 \end{bmatrix} \tag{15.37}$$

This leads to:

$$\mathbf{C} = \lfloor 0, 0, \frac{\partial x}{\partial \eta}\frac{\partial y}{\partial \xi} - \frac{\partial y}{\partial \eta}\frac{\partial x}{\partial \xi} \rfloor \tag{15.38}$$

c. With $\mathbf{C}$ defined, we can now return to the original plane and define

$$\mathbf{D} = \mathbf{C} \times \mathbf{A} \Rightarrow \mathbf{D} = \lfloor \underbrace{\frac{\partial y}{\partial \eta}\left(\frac{\partial y}{\partial \eta}\frac{\partial x}{\partial \xi} - \frac{\partial x}{\partial \eta}\frac{\partial y}{\partial \xi}\right)}_{D_1}, \underbrace{\frac{\partial x}{\partial \eta}\left(\frac{\partial x}{\partial \eta}\frac{\partial y}{\partial \xi} - \frac{\partial y}{\partial \eta}\frac{\partial x}{\partial \xi}\right)}_{D_2}, 0 \rfloor \tag{15.39}$$

d. The unit normal vector is now given by:

$$\mathbf{n} = \begin{Bmatrix} n_1 \\ n_2 \\ 0 \end{Bmatrix} = \begin{Bmatrix} \frac{D_1}{N} \\ \frac{D_2}{N} \\ 0 \end{Bmatrix} \tag{15.40}$$

where $N = \sqrt{D_1^2 + D_2^2}$ and all terms are taken from the Jacobian matrix.

K_I and K_{II} can be readily determine from Eq. 4.88 (Section 15.2) by redefining:

$$\mathrm{d}x = -n_2 \mathrm{d}s \tag{15.41}$$

$$\mathrm{d}x = -\frac{\partial x}{\partial \eta}\mathrm{d}\eta \tag{15.42}$$

15.2.1 Equivalent Domain Integral (EDI) Method

In this section, we shall derive an alternative expression for the energy release rate. Contrary to the virtual crack extension method where two analyses (or a stiffness derivative) had to be evaluated, in this method we have to perform only one analysis. The method is really based on Rice's J integral. However, it is recognized that the evaluation of J in 2D involves a line integral only or a line integral plus a volume

(area in 2D) integral if body forces are present [235]. For 3D problems, the line integral is replaced by a surface integral (and a volume integral for body forces).
Recognizing that surface integrals may not be easily evaluated in 3D, Green's theorem is invoked, and J will be evaluated through a volume integral in 3D and a surface integral in 2D. Thus computationally, this method is quite attractive.
Again as for the previous case, we will start by evaluating the energy release rate, and only subsequently we shall derive expressions for the SIF.
The essence of the method consists in replacing the contour integral by a closed integral (outer and inner) while multiplying the expression of J by a function q equal to zero on the outer surface and unity on the inner one. We adopt the expression of J derived for a propagating crack (determined around a path close to the crack tip). Having defined a closed path, we then apply Green's theorem and replace a contour integral by a surface integral.

15.2.2 Energy Release Rate J

15.2.2.1 2D case

The energy release rate of a propagating crack is given by

$$J = \lim_{\Gamma_0 \to 0} \int_{\Gamma_0} \left[(w + T)\, \delta_{1i} - \sigma_{ij} \frac{\partial u_j}{\partial x_1} \right] n_i \mathrm{d}\Gamma \tag{15.43}$$

where w is the strain energy density, T is the kinetic energy:

$$T = \frac{1}{2} \rho \frac{\partial u_i}{\partial t} \frac{\partial u_i}{\partial t} \tag{15.44}$$

and δ the Kronecker delta.
An alternative form of this equation [30] is

$$J = \lim_{\Gamma_0 \to 0} \int_{\Gamma_0} \left[(w + T)\, \mathrm{d}y - \sigma_{ij} n_i \frac{\partial u_j}{\partial x} \mathrm{d}\Gamma \right] \tag{15.45}$$

Unlike the conventional J integral, the contour path for this equation can not be arbitrarily selected.
This equation is derived from an energy balance approach and is thus applicable to all types of material models. However, this J integral is path independent only if Γ is within an elastic zone; if it is taken within the plastic zone, then it will be path dependent.
This equation is not well suited for numerical evaluation as the path would have to be a vanishingly small one where the stresses and strains could not be determined. As such, [536], we will be rewriting an alternative form of this equation by considering the contour shown in Figure 15.7 where Γ_1 is the outer finite contour, Γ_0 is the inner vanishingly small contour, and Γ_+ and Γ_- are respectively the upper and lower crack surfaces along the contour.

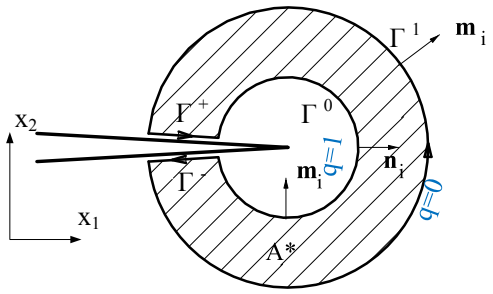

Fig. 15.7: Simply connected region A^* enclosed by contours $\Gamma_1, \Gamma_0, \Gamma_+$, and Γ_-, [30]

For quasi-static cases ($T = 0$), let us construct a closed contour by connecting inner and outer contours. The outer one, Γ_1, is finite while the inner one, Γ_0, is vanishingly small. For linear (or nonlinear) elastic materials, J can be evaluated along either one of those two contours, but only the inner one gives the exact solution in the general case. Thus, we can rewrite Eq. 15.43 around the following closed contour:

$$\Gamma^* = \Gamma_1 + \Gamma_+ + \Gamma_- - \Gamma_0 \tag{15.46}$$

yielding (and assuming that the crack faces are traction free)

$$J = \int_{\Gamma^*} \left[\sigma_{ij} \frac{\partial u_j}{\partial x_1} - w\delta_{1i} \right] q m_i \mathrm{d}\Gamma - \int_{\Gamma_+ \cup \Gamma_-} \sigma_{2j} \frac{\partial u_j}{\partial x_1} q \mathrm{d}\Gamma \tag{15.47}$$

where m_i is the outward normal to Γ^* (thus $m_i = n_i$ on Γ_1, $m_i = -n_i$ on Γ_0, $m_1 = 0$ and $m_2 = \pm 1$ on Γ_+ and Γ_-), and q is an arbitrary but smooth function which is equal to unity on Γ_0 and zero on Γ_1. Note that since the integral is taken along the contours, by explicitly specifying $q = 0$ on the outer one and $q = 1$ on the inner one, Eqs. 15.43 and 15.47 are identical. Furthermore, in the absence of crack surface tractions, the second term is equal to zero.
Applying the divergence theorem (Eq. 1.59) to Eq. 15.47

$$\oint_\Gamma \mathbf{v}.\mathbf{n} = \int_A \left(\frac{\partial v_x}{\partial x} + \frac{\partial v_y}{\partial y} \right) \mathrm{d}x\mathrm{d}y \tag{15.48}$$

we obtain

$$J = \int_{A^*} \frac{\partial}{\partial x_i} \left\{ \left[\sigma_{ij} \frac{\partial u_j}{\partial x_1} - w\delta_{1i} \right] q \right\} \mathrm{d}A \tag{15.49}$$

$$= \int_{A^*} \left[\left(\sigma_{ij} \frac{\partial u_j}{\partial x_1} - w\delta_{1i} \right) \frac{\partial q}{\partial x_i} + \left(\frac{\partial}{\partial x_i} \left(\sigma_{ij} \frac{\partial u_j}{\partial x_1} \right) - \frac{\partial w}{\partial x_1} \right) q \right] \mathrm{d}A \tag{15.50}$$

where A^* is the area enclosed by Γ^*.
Let us show that the second term is equal to zero:

$$\frac{\partial}{\partial x_i}\left(\sigma_{ij}\frac{\partial u_j}{\partial x_1}\right) = \underbrace{\sigma_{ij}\frac{\partial}{\partial x_i}\left(\frac{\partial u_j}{\partial x_1}\right)}_{\frac{\partial w}{\partial x}} + \underbrace{\frac{\partial \sigma_{ij}}{\partial x_i}}_{0}\frac{\partial u_i}{\partial x_1} \tag{15.51}$$

however from equilibrium we have

$$\frac{\partial \sigma_{ij}}{\partial x_i} = 0 \tag{15.52}$$

Furthermore, the derivative of the strain energy density is

$$\frac{\partial w}{\partial x} = \frac{\partial w}{\partial \varepsilon_{ij}}\frac{\partial \varepsilon_{ij}}{\partial x} = \sigma_{ij}\frac{\partial \varepsilon_{ij}}{\partial x} \tag{15.53}$$

substituting

$$\varepsilon_{ij} = \frac{1}{2}\left(\frac{\partial u_i}{\partial x_j} + \frac{\partial u_j}{\partial x_i}\right) \tag{15.54}$$

we obtain

$$\frac{\partial w}{\partial x} = \frac{1}{2}\sigma_{ij}\left[\frac{\partial}{\partial x}\left(\frac{\partial u_i}{\partial x_j}\right) + \frac{\partial}{\partial x}\left(\frac{\partial u_j}{\partial x_i}\right)\right] = \sigma_{ij}\frac{\partial}{\partial x_j}\left(\frac{\partial u_i}{\partial x}\right) \tag{15.55}$$

Hence, it is evident that the second term of Eq. 15.50 vanishes and that we are left with

$$J = \int_{A^*}\left[\sigma_{ij}\frac{\partial u_i}{\partial x_1} - w\delta_{1i}\right]\frac{\partial q}{\partial x_i}\mathrm{d}A \tag{15.56}$$

This expression is analogous to the one proposed by Babuska for a surface integral based method to evaluate stress intensity factors [76].
We note that deLorenzi, H.G. [235] has shown that the energy release rate is given by

$$G = \frac{1}{\Delta A}\int\left(\sigma_{ij}\frac{\partial u_j}{\partial x_1} - w\delta_{i1}\right)\frac{\partial \Delta x_1}{\partial x_i}\mathrm{d}A \tag{15.57}$$

for a unit crack growth extension along x_1. Thus comparing Eq. 15.56 with Eq. 15.57, we observe that the two expressions are identical for $q = \frac{\Delta x_1}{\Delta a}$, and thus q can be interpreted as a normalized virtual displacement. In this context it was merely a mathematical device.
In summary, we have replaced a contour integral by an equivalent area integral to determine J.

15.2.2.2 3D Generalization

In this section, we shall generalize to 3D our previous derivation [30]. From Figure 15.8 we define a local coordinate system such that x_1 is normal to the crack front, x_2 normal to the crack plane, and x_3 tangent to the crack front.

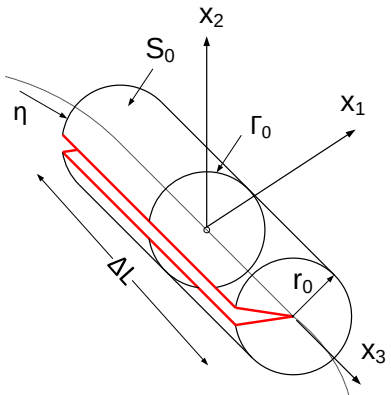

Fig. 15.8: Surface enclosing a tube along a three dimensional crack front, [30]

For an arbitrary point, the J integral is given by Eq. 15.43. We now consider a tube of length ΔL and radius r_0 that surrounds the segment of the crack front under consideration. We now define a weighted average J over the crack front segment of length ΔL as

$$\bar{J}\Delta L = \int_{\Delta L} J(\eta) q \mathrm{d}\eta \tag{15.58}$$

$$= \lim_{r_0 \to 0} \int_{S_0} \left[w\delta_{1i} - \sigma_{ij} \frac{\partial u_j}{\partial x_1} \right] q n_i \mathrm{d}s \tag{15.59}$$

where $J(\eta)$ is the point-wise value of J, S_0 is the vanishingly small surface area of the tube, and q is the weight function previously introduced. q can be again interpreted as a virtual crack advance, and Figure 15.9 illustrates an incremental crack advance over ΔL where q is defined as

$$\Delta a(\eta) = q(\eta) \Delta a_{max} \tag{15.60}$$

and the corresponding incremental area of the virtual crack is

$$\Delta A_c = \Delta a_{max} \int_{\Delta L} q(\eta) \mathrm{d}\eta \tag{15.61}$$

As in the previous case, this expression of J can not be numerically determined for a vanishingly small radius r_0. As such and as in the previous 2D case, we define a

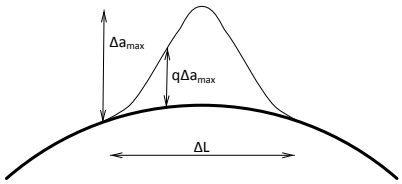

Fig. 15.9: Interpretation of q in terms of a Virtual Crack Advance along ΔL, [30]

second tube of radius r_1 around the crack front, Figure 15.10.

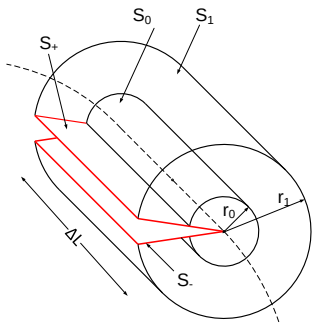

Fig. 15.10: Inner and outer surfaces enclosing a tube along a three dimensional crack front

$$\bar{J}\Delta L = \oint_{S^*} \left[\sigma_{ij}\frac{\partial u_i}{\partial x_1} - w\delta_{1i}\right] q m_i \mathrm{d}S - \oint_{S_-\cup S_+} \sigma_{2j}\frac{\partial u_j}{\partial x_1} q \mathrm{d}s \tag{15.62}$$

where

$$S^* = S_1 + S_+ + S_- - S_0 \tag{15.63}$$

and S_+ and S_- are the upper and lower crack surfaces respectively, S_0 and S_1 the inner and outer tube surfaces. Note that this equation is the 3D counterpart of Eq. 15.47 which was written in 2D.
Applying the divergence theorem (Eq. 1.59), this equation reduces to a volume integral

$$\bar{J}\Delta L = \int_{V^*} \left\{ \left[\sigma_{ij} \frac{\partial u_j}{\partial x_1} - w\delta_{1i} \right] \frac{\partial q}{\partial x_i} + \left[-\frac{\partial w}{\partial x_1} + \frac{\partial}{\partial x_j} \left(\sigma_{ij} \frac{\partial u_i}{\partial x_1} \right) \right] q \right\} dV + \int_{A_1 \cup A_2} \left(w\delta_{1i} - \sigma_{ij} \frac{\partial u_i}{\partial x_1} \delta_{1i} \right) q \mathrm{d}A \tag{15.64}$$

and q must be equal to zero at either end of ΔL, that is on A_1 and A_2. In [639] it is shown that in the absence of non-elastic (thermal and plastic) deformations, the second term would be equal to zero. The third term will also be equal to zero because q is arbitrarily selected to be zero at each end.

15.2.3 Extraction of SIF

From Eq. 15.64 it is impossible to extract the 3 distinct stress intensity factors. Hence we shall generalize this equation and write it as [639] (ignoring the second and third terms):

$$\bar{J}_k \Delta L = \int_{V^*} \left(\sigma_{ij} \frac{\partial u_i}{\partial x_k} \frac{\partial q}{\partial x_j} - w \frac{\partial q}{\partial x_k} \right) dV \tag{15.65}$$

Note that $k = 1, 2$ only thus defining $G_1 = J_1$ and $G_2 = J_2$. However, [639] have shown that G_3 has a similar form and is equal to

$$G_{III} = \int_{V^*} \left(\sigma_{3j} \frac{\partial u_3}{\partial x_1} \frac{\partial q}{\partial x_j} - w^{III} \frac{\partial q}{\partial x_1} \right) dV \tag{15.66}$$

With G_1, G_2 and G_3 known, we need to extract the three stress intensity factors K_I, K_{II} and K_{III}. Again there are two approaches.

15.2.3.1 J Components

Based on the solution by Nikishkov, [638]

$$\begin{aligned} K_I &= \tfrac{1}{2}\sqrt{E^*} \left(\sqrt{(J_1 - J_2 - G_3)} + \sqrt{(J_1 + J_2 - G_3)} \right) \\ K_{II} &= \tfrac{1}{2}\sqrt{E^*} \left(\sqrt{(J_1 - J_2 - G_3)} - \sqrt{(J_1 + J_2 - G_3)} \right) \\ K_{III} &= \sqrt{2\mu G_3} \end{aligned} \tag{15.67}$$

where [639]

$$E^* = E \left[\frac{1}{1-\nu^2} + \left(\frac{\nu}{1+\nu} \right) \frac{\varepsilon_{33}}{\varepsilon_{11} + \varepsilon_{22}} \right] \tag{15.68}$$

which is a weighted value of E such that we retrieve $E^* = \frac{E}{1-\nu^2}$ for plane strain and $E^* = E$ for plane stress.

15.2.3.2 σ and u Decomposition

As for the solution by Shah, we can decompose the displacement field as

$$\{u\} = \{u^I\} + \{u^{II}\} + \{u^{III}\}$$
$$= \frac{1}{2}\begin{Bmatrix} u_1 + u_1' \\ u_2 - u_2' \\ u_3 + u_3' \end{Bmatrix} + \frac{1}{2}\begin{Bmatrix} u_1 - u_1' \\ u_2 + u_2' \\ 0 \end{Bmatrix} + \frac{1}{2}\begin{Bmatrix} 0 \\ 0 \\ u_3 - u_3' \end{Bmatrix} \quad (15.69)$$

Similarly the stresses are decomposed as

$$\{\sigma\} = \{\sigma^I\} + \{\sigma^{II}\} + \{\sigma^{III}\}$$
$$= \frac{1}{2}\begin{Bmatrix} \sigma_{11} + \sigma_{11}' \\ \sigma_{22} + \sigma_{22}' \\ \sigma_{33} + \sigma_{33}' \\ \sigma_{12} - \sigma_{12}' \\ \sigma_{23} - \sigma_{23}' \\ \sigma_{31} - \sigma_{31}' \end{Bmatrix} + \frac{1}{2}\begin{Bmatrix} \sigma_{11} - \sigma_{11}' \\ \sigma_{22} - \sigma_{22}' \\ 0 \\ \sigma_{12} + \sigma_{12}' \\ 0 \\ 0 \end{Bmatrix} + \frac{1}{2}\begin{Bmatrix} 0 \\ 0 \\ \sigma_{33} - \sigma_{33}' \\ 0 \\ \sigma_{23} + \sigma_{23}' \\ \sigma_{31} + \sigma_{31}' \end{Bmatrix} \quad (15.70)$$

where

$$u_i'(x_1, x_2, x_3) = u_i(x_1, -x_2, x_3) \quad (15.71)$$
$$\sigma_{ij}'(x_1, x_2, x_3) = \sigma_{ij}(x_1, -x_2, x_3) \quad (15.72)$$

and the stress intensity factors are then determined from

$$K_I = \sqrt{E'G_I}\ K_{II} = \sqrt{E'G_{II}}\ K_{III} = \sqrt{2\mu G_{III}} \quad (15.73)$$

where

$$G_k = \int_{V^*} \left(\sigma_{kj} \frac{\partial u_k}{\partial x_1} \frac{\partial q}{\partial x_j} - w^k \frac{\partial q}{\partial x_1} \right) dV \quad (15.74)$$

Whereas this method may be difficult to use in conjunction with a 3D finite element mesh generated by triangularization (due to the lack of symmetry around the crack front), it has been successfully used by Cervenka (1994) in conjunction with a unit volume integration in the FE code MERLIN [767].

15.3 Fictitious Crack Model for concrete

15.3.1 Premises

As shown in Chapter 9, neither linear nor elasto-plastic fracture mechanics are applicable to concrete. Instead, the cohesive crack model of Hillerborg, Modéer, and Petersson [419] should be adopted (Section 9.1.2). This section, based on Červenka, J. [855], will develop a robust fictitious crack model that will be extensively used in the subsequent chapters were concrete cracks are to be modeled. It should be emphasized that the so-called discrete crack model (adopted here) is an alternative to the more widely used "smeared" crack model used in many finite element codes. The former is far superior if one knows the precise location of a crack (or a potential crack), or if there are few cracks (unreinforced concrete, interfaces between two

materials, or delamination). The second is more adapted to model reinforced concrete structures with multiple cracks.
Hence, one seeks to define relationships between normal and tangential stresses with opening and sliding displacements, Figure 15.11. The major premises upon which

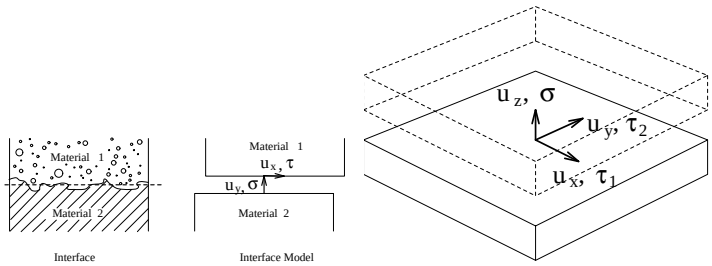

Fig. 15.11: Interface idealization and notations.

the model is developed are:

1. Shear strength depends on the normal stress.
2. Softening is present both in shear and tension.
3. There is a residual shear strength due to the friction along the interface, which depends on the compressive normal stress.
4. Reduction in strength, i.e. softening, is caused by crack formation.
5. There is a zero normal and shear stiffness when the interface is totally destroyed.
6. Under compressive normal stresses, neither the shear nor the normal stiffnesses decrease to zero. In addition, should a compressive stress be introduced in the normal direction following a full crack opening, two faces of the interface come into contact, and both tangential and normal stiffnesses become nonzero.
7. Irreversible relative displacements are caused by broken segments of the interface material and by friction between the two crack surfaces.
8. Roughness of the interface causes opening displacements (i.e. dilatancy) when subjected to sliding displacements.
9. The dilatancy vanishes with increasing sliding or opening displacements.

Figure 15.12 illustrates the probable character of the fracturing process along an interface.

15.3.2 Failure Function

In the proposed model the strength of an interface is described by a failure function:

$$F = (\tau_1^2 + \tau_2^2) - 2\,c\,\tan(\phi_f)(\sigma_t - \sigma) - \tan^2(\phi_f)(\sigma^2 - \sigma_t^2) = 0 \qquad (15.75)$$

where:

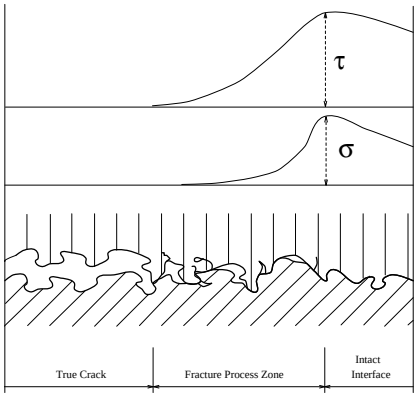

Fig. 15.12: Interface fracture

- c is the cohesion.
- ϕ_f is the angle of friction.
- σ_t is the tensile strength of the interface.
- τ_1 and τ_2 are the two tangential components of the interface traction vector.
- σ is the normal traction component.

The shape of the failure function in the two-dimensional case is shown in Figure 15.13, and it corresponds to the failure criterion first proposed by Carol, I. and Bažant, Z.P. and Prat, P.C. [166]. The general three-dimensional failure function is obtained by mere rotation around the σ-axis.

15.3.3 Evolution of the Failure Function

The evolution of the failure function is based on a softening parameter u^{ieff} which is the norm of the inelastic displacement vector $\boldsymbol{u}^i$. The inelastic displacement vector is obtained by decomposition of the displacement vector $\boldsymbol{u}$ into an elastic part $\boldsymbol{u}^e$ and an inelastic part $\boldsymbol{u}^i$. The inelastic part can subsequently be decomposed into plastic (i.e. irreversible) displacements $\boldsymbol{u}^p$ and fracturing displacements $\boldsymbol{u}^f$. The plastic displacements are assumed to be caused by friction between crack surfaces and the fracturing displacements by the formation of microcracks.

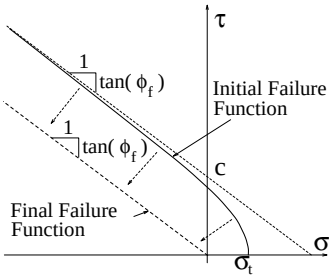

Fig. 15.13: Failure function

$$\begin{aligned} F = F(c, \sigma_t, \phi_f), \quad c = c(u^{\text{ieff}}), \quad \sigma_t = \sigma_t(u^{\text{ieff}}) \\ \boldsymbol{u} = \boldsymbol{u}^e + \boldsymbol{u}^i, \quad \boldsymbol{u}^i = \boldsymbol{u}^p + \boldsymbol{u}^f \\ u^{\text{ieff}} = ||\boldsymbol{u}^i|| = (u_x^{i\,2} + u_y^{i\,2} + u_z^{i\,2})^{1/2} \end{aligned} \tag{15.76}$$

In this work, both linear and bi-linear relationships are used for $c(u^{\text{ieff}})$ and $\sigma_t(u^{\text{ieff}})$.

$$\left.\begin{aligned} c(u^{\text{ieff}}) &= c_0(1 - \tfrac{u^{\text{ieff}}}{w_c}) \;\forall\; u^{\text{ieff}} < w_c \\ c(u^{\text{ieff}}) &= 0 \qquad\qquad \forall\; u^{\text{ieff}} \geq w_c \\ w_c &= \tfrac{2G_F^{IIa}}{c_0} \end{aligned}\right\} \text{ linear for cohesion}$$

$$\left.\begin{aligned} c(u^{\text{ieff}}) &= c_0 + u^{\text{ieff}} \tfrac{s_{1c} - c_0}{w_{1c}} \quad \forall\; u^{\text{ieff}} < w_{1c} \\ c(u^{\text{ieff}}) &= s_c(1 - \tfrac{u^{\text{ieff}} - w_{1c}}{w_c - w_{1c}}) \;\forall\; u^{\text{ieff}} \in \langle w_{1c}, w_c \rangle \\ c(u^{\text{ieff}}) &= 0 \qquad\qquad\qquad\quad \forall\; u^{\text{ieff}} > w_c \\ w_c &= \tfrac{2G_F^{IIa} - (s_{1c} + c_0) w_{1c}}{s_{1c}} \end{aligned}\right\} \text{ bi-linear for cohesion} \tag{15.77}$$

$$\left.\begin{aligned} \sigma_t(u^{\text{ieff}}) &= \sigma_{t0}(1 - \tfrac{u^{\text{ieff}}}{w_\sigma}) \;\forall\; u^{\text{ieff}} < w_\sigma \\ \sigma_t(u^{\text{ieff}}) &= 0 \qquad\qquad \forall\; u^{\text{ieff}} \geq w_{\sigma_t} \\ w_\sigma &= \tfrac{2G_F^I}{\sigma_{t0}} \end{aligned}\right\} \text{ linear for tensile strength}$$

$$\left.\begin{aligned} \sigma_t(u^{\text{ieff}}) &= \sigma_{t0} + u^{\text{ieff}} \tfrac{s_{1\sigma} - \sigma_{t0}}{w_{1\sigma}} \quad \forall\; u^{\text{ieff}} < w_{1\sigma} \\ \sigma_t(u^{\text{ieff}}) &= s_{1\sigma}(1 - \tfrac{u^{\text{ieff}} - w_{1\sigma}}{w_{\sigma_t} - w_{1\sigma}}) \;\forall\; u^{\text{ieff}} \in \langle w_{1\sigma}, w_\sigma \rangle \\ \sigma_t(u^{\text{ieff}}) &= 0 \qquad\qquad\qquad\quad \forall\; u^{\text{ieff}} > w_\sigma \\ w_\sigma &= \tfrac{2G_F^I - (s_{1\sigma} + \sigma_{t0}) w_{1\sigma}}{s_{1\sigma}} \end{aligned}\right\} \begin{array}{l}\text{bi-linear for} \\ \text{tensile strength}\end{array} \tag{15.78}$$

where G_F^I and G_F^{IIa} are mode I and II fracture energies. s_{1c}, w_{1c} and $s_{1\sigma}$, $w_{1\sigma}$ are the coordinates of the break-point in the bi-linear softening laws for cohesion and tensile strength, respectively. The critical opening and sliding corresponding to zero cohesion and tensile strength are denoted by w_σ and w_c, respectively, and they are determined from the condition that the area under the linear or bi-linear softening law must be equal to G_F^I and G_F^{IIa}, respectively. The significance of these symbols can be best explained through Figure 15.14. It should be noted that G_F^{IIa}

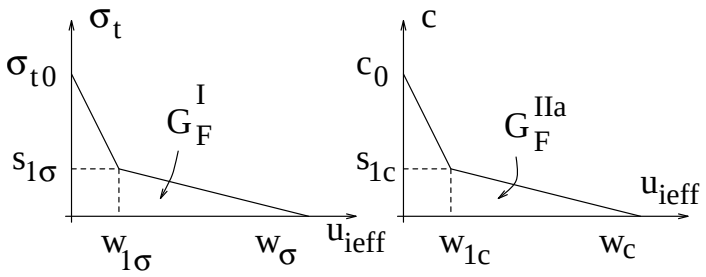

Fig. 15.14: Bi-linear softening laws

is not the pure mode II fracture energy (i.e. the area under a τ-u_x curve), but rather is the energy dissipated during a shear test with high confining normal stress. This parameter was first introduced by Carol, I. and Bažant, Z.P. and Prat, P.C. [166] in their microplane model. This representation seems to be more favorable to the pure mode II fracture energy G_F^{II}. The determination of G_F^{II} would require a pure shear test without confinement, which is extremely difficult to perform. Alternatively, a G_F^{IIa} test requires a large normal confinement and is therefore easier to accomplish. Furthermore, if G_F^{II} is used, the whole shear-compression region of the interface model would be an extrapolation from the observed behavior whereas the second approach represents an interpolation between the upper bound G_F^{IIa} and the lower bound G_F^I.
The residual shear strength is obtained from the failure function by setting both c and σ_t equal to 0, which corresponds to the final shape of the failure function in Figure 15.13 and is given by:

$$\tau_1^2 + \tau_2^2 \;=\; \tan^2(\phi_f)\,\sigma^2 \tag{15.79}$$

15.3.4 Stiffness Degradation

Stiffness degradation is modeled through a damage parameter, $D \in \langle 0, 1\rangle$, which is a relative measure of the fractured surface. Thus, D is related to the secant of the normal stiffness, K_{ns}, in the uniaxial case:

$$D = \frac{A_f}{A_o} = 1 - \frac{K_{ns}}{K_{no}} \tag{15.80}$$

where K_{no} is the initial normal stiffness of the interface; A_o and A_f are the total interface area and the fractured area, respectively. It is assumed, that the damage parameter D can be determined by converting the mixed mode problem into an equivalent uniaxial one (Figure 15.15). In the equivalent uniaxial problem, the normal inelastic displacement is set equal to u^{ieff}. Then, the secant normal stiffness can be determined from:

$$K_{ns} = \frac{\sigma}{u - u^p} = \frac{\sigma_t(u^{\text{ieff}})}{u^e + u^p + u^f - u^p} = \frac{\sigma_t(u^{\text{ieff}})}{\sigma_t(u^{\text{ieff}})/K_{no} + (1-\gamma)u^{\text{ieff}}} \quad (15.81)$$

where γ is the ratio of irreversible inelastic normal displacement to the total value of inelastic displacement. Experimentally, γ can be determined from a pure mode I test through:

$$\gamma = \frac{u_p}{u_i} \quad (15.82)$$

where u^p is the residual displacement after unloading and u^i is the inelastic displacement before unloading (Figure 15.15). For concrete, γ is usually assumed equal to

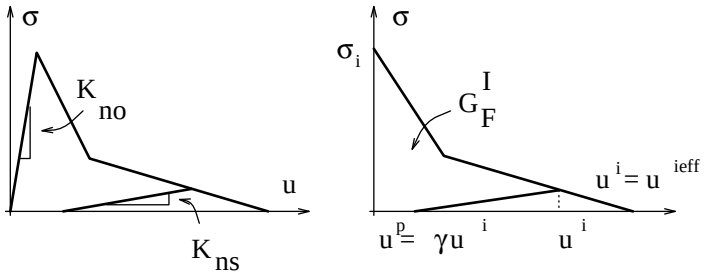

Fig. 15.15: Stiffness degradation in the equivalent uniaxial case

0.2 (Dahlblom and Ottosen 1990) or 0.3 (Alvaredo and Wittman 1992). Then, the evolution of the damage parameter D is defined by formula:

$$D = 1 - \frac{\sigma_t(u^{\text{ieff}})}{\sigma_t(u^{\text{ieff}}) + (1-\gamma)u^{\text{ieff}}K_{no}} \quad (15.83)$$

which is obtained by substituting Equation 15.81 into Eq. 15.80.
The stress-displacement relationship of the interface is expressed as:

$$\boldsymbol{\sigma} = \alpha \mathbf{E}(\boldsymbol{u} - \boldsymbol{u}^p) \quad (15.84)$$

where:
(a) $\boldsymbol{\sigma}$ is the vector of tangential and normal stress at the interface.

$$\boldsymbol{\sigma} = \{\tau_1, \tau_2, \sigma\}^T \quad (15.85)$$

(b) α is the integrity parameter defining the relative active area of the interface, and it is related to the damage parameter D.

$$\alpha = 1 - \frac{|\sigma|+\sigma}{2|\sigma|}D \tag{15.86}$$

It should be noted that α can be different from 1 only if the normal stress, σ, is positive (i.e. the interface is in tension). In other words, the damage parameter D is activated only if the interface is in tension. In compression, the crack is assumed to be closed, and there is full contact between the two crack surfaces. The activation of D is controlled through the fraction $\frac{|\sigma|+\sigma}{2|\sigma|}$, which is equal to one if σ is positive, and is zero otherwise.
(c) $\mathbf{E}$ is the elastic stiffness matrix of the interface:

$$\mathbf{E} = \begin{bmatrix} K_{to} & 0 & 0 \\ 0 & K_{to} & 0 \\ 0 & 0 & K_{no} \end{bmatrix} \tag{15.87}$$

It should be noted, that the off-diagonal terms in the elastic stiffness matrix, $\mathbf{E}$, of the interface are all equal to zero, which implies that no dilatancy is considered in the elastic range. The dilatancy is introduced later after the failure limit has been reached through the iterative solution process. The dilatancy of the interface is given by dilatancy angle ϕ_d, which is again assumed to be a function of u^{ieff}. In the proposed model, a linear relationship is assumed:

$$\begin{array}{ll} \phi_d(u^{\text{ieff}}) = \phi_{d0}(1 - \frac{u^{\text{ieff}}}{u_{dil}}) & \forall u^{\text{ieff}} \leq u_{dil} \\ \phi_d(u^{\text{ieff}}) = 0 & \forall u^{\text{ieff}} > u_{dil} \end{array} \tag{15.88}$$

where u_{dil} is the critical relative displacement after which the interface does not exhibit the dilatancy effect any more, and ϕ_{d0} is the initial value of the dilatancy angle.

Part IV
Engineering Models

Chapter 16
Soil Structure Interaction

Abstract
This chapter addresses the interaction between the structure and its foundation. It begins with a seldom covered problem: rocking of the structure on the foundation and possible "lift-off" that would act as stress reliever. Different techniques to model this problem are outlined. Then, deconvolution, the technique to apply a proper seismic excitation at the base of a model foundation as opposed to the accelerations recorded at the surface, is presented. It will be followed by the derivation of the wave equation which is essential to understanding the most commonly used soil structure interaction (SSI) model: the one by Lysmer. Then, the roles of both SSI and adjoining free field are discussed in a model developed by the first author along with a battery of simple validation problems highlighting the benefits of simple or complex SSI are presented. Finally, the chapter concludes with techniques to properly mesh a structure where the SSI is addressed.

16.1 Rocking

In a linear elastic analysis, one could perform a static analysis followed by an independent dynamic one (assuming that boundary conditions are preserved) and finally sum the results.
However, in the context of a nonlinear seismic analysis, a two step analysis must be performed. First a static one which takes into account the effects of all dead loads (gravity and others) and possible live loads likely to be present during an earthquake. In this case, the structure has to be vertically restrained by supports to prevent rigid body motion. Results would then have to be saved.
Then, prior to undertaking the subsequent dynamic analysis, the mesh will have to be modified to allow lateral displacements, and analysis will start by reading the internal state variables saved by the static analysis. At this point, it is recommended to reset all displacements to zero (without altering the initial state of stress) in order to facilitate visualization of the deformed shape. If vertical restraints are kept, then those will induce both compressive and tensile stresses. Those tensile stresses may very well exceed the tensile strength of the free field surrounding the foundation numerical model.

For nuclear structures, rocking may cause separation of the base-mat from the foundation [49, chap 11] [781]. For dams, three is already a weak interface with the rock, potentially an existing crack at the base (subjected to full uplift forces), and thus rocking will occur. This could have implications on the magnitude of the uplift pressure (see Section 17.1).

16.1.1 Rock Free-Field

If the foundation (finite size, non zero mass, zero gravity) is modeled, then the lateral inertial force will induce a "parasitic" alternating overturning moment which may not be negligible. Hence, in the context of a finite element model, the foundation support will restrain vertical displacement in both the upward (undesirable) and downward (desirable) directions. Hence, parasitic vertical elastic waves may result, Figure 16.1(a).
A solution to this problem is the twofold analysis described above. First static load is applied with vertical supports. Then prior to the restart of the dynamic analysis, all supports are removed and replaced by forces equal to the corresponding reactions (of the static analysis). Indeed, in the context of a dynamic analysis (and contrary to a static one), it is perfectly possible to omit all supports, Figure 16.1(b).

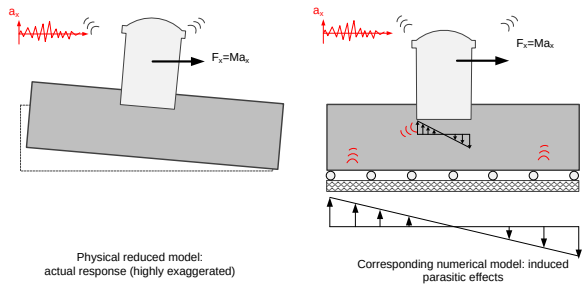

(a) The problem

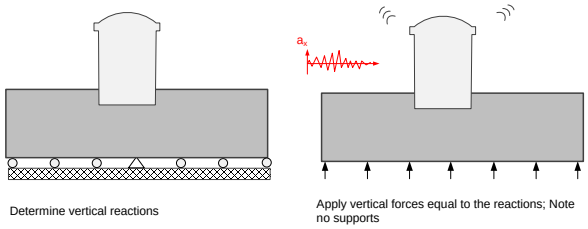

(b) Mitigation

Fig. 16.1: Rocking due to finite size foundation support

A number of approaches are possible to numerically inhibit this type of rocking; however those are best understood following soil structure interaction coverage in Section 16.4.

16.1.2 Concrete-Rock

Tensile stresses at the base of the structure are highly undesirable. When they occur, there is the potential for a separation between the structure and the foundation, Figure 16.2. This is often mitigated by anchoring the structure (dam most often) to the foundation (see example in Section29.1).

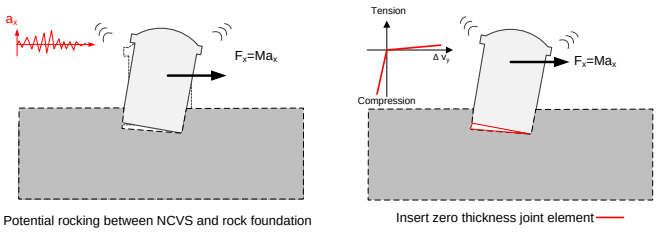

Fig. 16.2: Rocking due to concrete-rock interface

Numerically, this problem can be mitigated by insertion of zero thickness joint elements (as discussed in Section15.3). Alternatively, simple spring elements with a very large stiffness in compression, and a negligibly small one in tension could be used. However, this may induce results that are mesh size dependent if modeling a crack instead of an entire surface joint [99].

16.2 Deconvolution

Seismic events originate through tectonic slips and elastic (p- and s-) waves traveling through rock/soil foundation up to the surface. Hence, the seismographs (usually installed at the foot of the structure) record only the manifestation of the event.
On the other hand, modeling the foundation is essential for proper and comprehensive analysis of the dam, and as such the seismic excitation will have to be applied at the base of the foundation.
However, Figure 16.3, if we were to apply at the base the accelerogram recorded on the surface $I(t)$, the output signal $A(t)$ at the surface will be different than the one originally recorded (unless we have a rigid foundation). Hence, the accelerogram recorded on the surface must be de-convoluted into a new one, $I'(t)$, such that when the new signal is applied at the base of the foundation, the computed signal at the dam base matches the one recorded by the accelerogram.

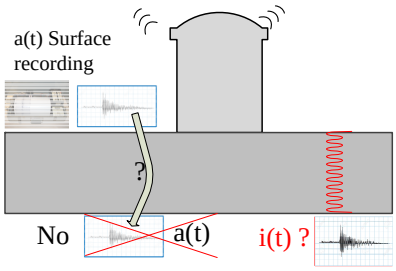

Fig. 16.3: Deconvolution

16.2.1 Preliminary Considerations

To facilitate understanding of the deconvolution process, one must first be familiarized with three key concepts: a) Fourier transform, b) filtering in the frequency domain, and c) transfer functions.
Fourier transforms enable us to transfer a signal from the time domain to the frequency domain through the following equation:

$$X(\omega) = \int_{-\infty}^{\infty} x(t) e^{-2i\pi\omega t} \mathrm{d}t \tag{16.1}$$

$$x(t) \overset{\mathrm{FFT}}{\longrightarrow} X(\omega) \tag{16.2}$$

while the inverse FFT takes us back from the frequency domain to the time domain through:

$$x(t) = \int_{-\infty}^{\infty} X(\omega) e^{2i\pi\omega t} \mathrm{d}\omega \tag{16.3}$$

$$X(\omega) \overset{\mathrm{FFT}^{-1}}{\longrightarrow} x(t) \tag{16.4}$$

Once we are in the frequency domain, special filters (especially the so-called Butterworth Filters), can be used before we come back to the time domain (with filtered data). Some of the most common Butterworth Filters include, Figure 16.4:

$$|H(j\omega)|^2 = \begin{cases} \text{Low pass} & \frac{1}{1+\left(\frac{\omega}{\omega_L}\right)^{2n}} \\ \text{High pass} & \frac{1}{1+\left(\frac{\omega_U}{\omega}\right)^{2n}} \\ \text{Band pass} & \frac{1}{1+\left(\frac{\omega}{\omega_L}\right)^{2n}} \frac{1}{1+\left(\frac{\omega_U}{\omega}\right)^{2n}} \\ \text{Band stop} & \frac{1}{1+\left(\frac{\omega_L}{\omega}\right)^{2n}} \frac{1}{1+\left(\frac{\omega}{\omega_U}\right)^{2n}} \end{cases} \tag{16.5}$$

where ω, ω_L, ω_U, and n are the frequency, the lower and upper filter frequencies, and the order of the filter, respectively.

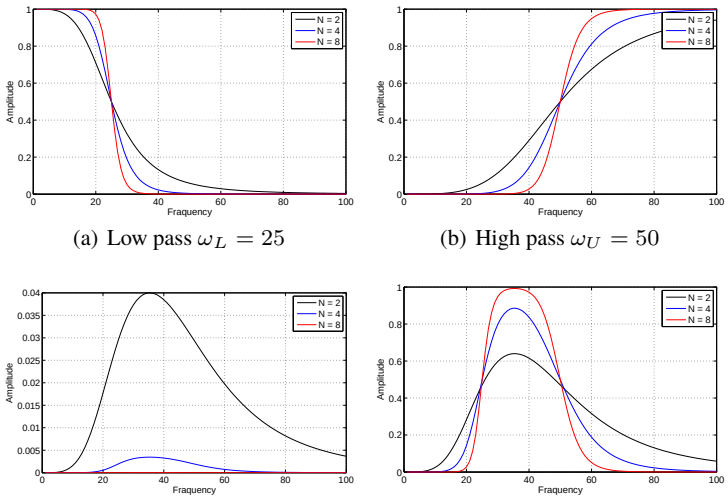

(a) Low pass $\omega_L = 25$ (b) High pass $\omega_U = 50$

(c) Band pass $(\omega_L = 25, \omega_U = 50)$ (d) Band stop $(\omega_L = 25, \omega_U = 50)$

Fig. 16.4: Comparison of Butterworth filters

Finally, transfer functions relate an input record, $i(t)$, and its amplification by $h(t)$ resulting in an output signal $o(t)$, Figure 16.5. Similarly, the operation can be defined in the frequency domain, and the output to input relationship is indeed of major importance in many disciplines. The transfer function is the "Laplace" transform of the output divided by the Laplace transform of the input. Hence, in 1D, we can determine the transfer function as follows:

1. $i(t) \xrightarrow{\text{FFT}} I(\omega)$
2. $o(t) \xrightarrow{\text{FFT}} O(\omega)$
3. Transfer Function is $TF_{I-O} = \frac{O(\omega)}{I(\omega)}$

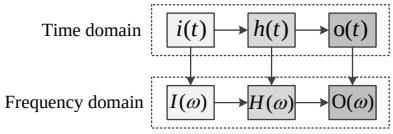

Fig. 16.5: Transfer function

16.2.2 Procedure

16.2.2.1 One-Dimensional

Extending our discussion one step further, we introduce the concept of deconvolution which addresses the dilemma posed in the introduction and will now require one (or more) finite element analyses. With reference to Figure 16.6:

1. Record the earthquake induced acceleration on the surface $a'(t)$, and apply it as $i'(t)$ at the base of the foundation.
2. Perform a transient finite element analysis.
3. Determine the surface acceleration $a(t)$ (which is obviously different from $i'(t)$).
4. Compute the following FFTs:

$$i'(t) \xrightarrow{\text{FFT}} I'(\omega) = A'(\omega) \tag{16.6}$$

$$a(t) \xrightarrow{\text{FFT}} A(\omega) \tag{16.7}$$

5. Compute transfer function from the base to surface as

$$TF_{I'-A} = A(\omega)/I'(\omega) \tag{16.8}$$

6. Compute the inverse transfer function $TF^{-1}_{I'-A}$.
7. Determine the updated excitation record in the frequency domain

$$I(\omega) = TF^{-1}_{I'-A} \times A'(\omega) = \frac{I'(\omega)}{A(\omega)} A'(\omega) \tag{16.9}$$

8. Determine the updated excitation in the time domain

$$I(\omega) \xrightarrow{\text{FFT}^{-1}} i(t) \tag{16.10}$$

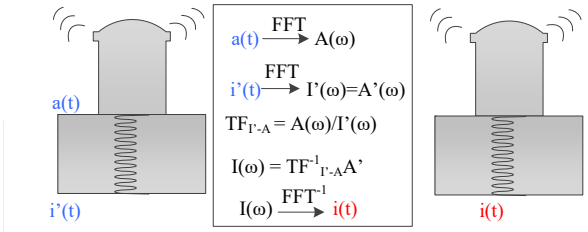

Fig. 16.6: Deconvolution applied in finite element analysis

16.2.2.2 Three-Dimensional

In 3D applications, the transfer function is a 3×3 matrix, each row corresponds to an excitation in a given direction, and each column corresponds to the response in a given direction. Hence, three separate analyses must be performed $\lfloor I'_x \; I'_y \; I'_z \rfloor$, and for each excitation, we must determine the three components of the surface acceleration. Then, we will compute the 3D transfer function:

$$[TF] = \underbrace{\begin{bmatrix} TF_{xx} & TF_{xy} & TF_{xz} \\ TF_{yx} & TF_{yy} & TF_{yz} \\ TF_{zx} & TF_{zy} & TF_{zz} \end{bmatrix}}_{TF_{I'-A}} = \begin{bmatrix} \frac{A_{xx}(\omega)}{I'_x(\omega)} & \frac{A_{xy}(\omega)}{I'_x(\omega)} & \frac{A_{xz}(\omega)}{I'_x(\omega)} \\ \frac{A_{yx}(\omega)}{I'_y(\omega)} & \frac{A_{yy}(\omega)}{I'_y(\omega)} & \frac{A_{yz}(\omega)}{I'_y(\omega)} \\ \frac{A_{zx}(\omega)}{I'_z(\omega)} & \frac{A_{zy}(\omega)}{I'_z(\omega)} & \frac{A_{zz}(\omega)}{I'_z(\omega)} \end{bmatrix} \tag{16.11}$$

Hence, the excitation to be applied in the frequency domain is given by:

$$\begin{Bmatrix} I_x(\omega) \\ I_y(\omega) \\ I_z(\omega) \end{Bmatrix} = [TF_{I'-A}]^{-1} \begin{Bmatrix} A'_x(\omega) \\ A'_y(\omega) \\ A'_z(\omega) \end{Bmatrix} \tag{16.12}$$

while in the time domain it is

$$\begin{Bmatrix} I_x(\omega) \\ I_y(\omega) \\ I_z(\omega) \end{Bmatrix} \overset{\text{FFT}^{-1}}{\longrightarrow} \begin{Bmatrix} i_x(t) \\ i_y(t) \\ i_z(t) \end{Bmatrix} \tag{16.13}$$

16.2.2.3 Simplification

The preceding 3D generalized procedure can be simplified by ignoring the off-diagonal terms

$$[TF] = \begin{bmatrix} TF_{xx} & 0 & 0 \\ 0 & TF_{yy} & 0 \\ 0 & 0 & TF_{zz} \end{bmatrix} = \begin{bmatrix} \frac{A_{xx}(\omega)}{I'_x(\omega)} & 0 & 0 \\ 0 & \frac{A_{yy}(\omega)}{I'_y(\omega)} & 0 \\ 0 & 0 & \frac{A_{zz}(\omega)}{I'_z(\omega)} \end{bmatrix} \tag{16.14}$$

which will greatly simplify the inversion of the transfer function.

$$\begin{aligned} \begin{Bmatrix} I_x(\omega) \\ I_y(\omega) \\ I_z(\omega) \end{Bmatrix} &= [TF_{I'-A}]^{-1} \begin{Bmatrix} A'_x(\omega) \\ A'_y(\omega) \\ A'_z(\omega) \end{Bmatrix} \\ &= \begin{bmatrix} \frac{I'_x(\omega)}{A_{xx}(\omega)} & 0 & 0 \\ 0 & \frac{I'_y(\omega)}{A_{yy}(\omega)} & 0 \\ 0 & 0 & \frac{I'_z(\omega)}{A_{zz}(\omega)} \end{bmatrix} \begin{Bmatrix} A'_x(\omega) \\ A'_y(\omega) \\ A'_z(\omega) \end{Bmatrix} \end{aligned} \tag{16.15}$$

and finally,

$$\left\{\begin{array}{c} I_x(\omega) \\ I_y(\omega) \\ I_z(\omega) \end{array}\right\} = \left[\begin{array}{ccc} \frac{I'_x(\omega)}{A_{xx}(\omega)} A'_x(\omega) & 0 & 0 \\ 0 & \frac{I'_y(\omega)}{A_{yy}(\omega)} A'_y(\omega) & 0 \\ 0 & 0 & \frac{I'_z(\omega)}{A_{zz}(\omega)} A'_z(\omega) \end{array}\right] \xrightarrow{\text{FFT}^{-1}} \left\{\begin{array}{c} I_x(t) \\ I_y(t) \\ I_z(t) \end{array}\right\} \tag{16.16}$$

16.3 Soil Structure Interaction

Nuclear structures operating in the United States must quantify the margin for beyond design basis events and take necessary actions to improve the margin if required. This would require a Seismic Probabilistic Risk Assessment (SPRA) requiring Soil-Structure Interaction (SSI) analysis as part of the overall analysis. Given the site profile data and the structural model developed as part of the Final Safety Analysis Report (FSAR) were generated many years ago, it is necessary to evaluate the SSI effects for structures founded on rock sites which were considered as fixed base condition during the original analysis.
Likewise for dams, SSI may be necessary for the probable maximum ground acceleration (PNGA) analyses.
It should be noted that for nuclear plants, it is often assumed that dynamic analysis for existing plants that are rock-founded (i.e. with shear wave velocity $>$ 3500 fps) (§sect:targetresponespectra) may be completed without consideration of soil structure interaction (SSI) effects [406].

16.3.1 Wave Equation

Before we introduce the SSI models, a review of the wave equation is necessary. Considering an infinitesimal element at rest, Figure 16.7, with elastic modulus E, and mass density ρ, we seek to determine the governing differential equation under dynamic condition.

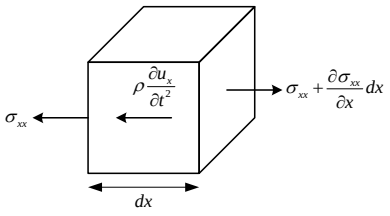

Fig. 16.7: Infinitesimal element subjected to elastic wave

Thinking in terms of equilibrium of forces, it is more appealing to invoke D'Alembert's principle of **dynamic equilibrium** rather than Newton's second law

of motion. This principle is based on the notion of a fictitious **inertia force**, equal to the product of mass times acceleration and acting in a direction opposite to the acceleration. Hence, the element force equilibrium requirements of a typical differential element are, using D'Alembert's principle which states that with inertia forces included, a system is in equilibrium at each time instant.

$$\frac{\partial \sigma_{xx}}{\partial x}\mathrm{d}x - \rho \frac{\partial^2 u_x}{\partial t^2}\mathrm{d}x = 0 \tag{16.17}$$

Since $\sigma_{xx} = \lambda \varepsilon_{xx} = \lambda \frac{\partial u_x}{\partial x}$, substituting, we obtain

$$\frac{\partial^2 u_x}{\partial t^2} - V_p^2 \frac{\partial^2 u_x}{\partial x^2} = 0 \tag{16.18}$$

where $V_p = \sqrt{\frac{\lambda}{\rho}}$
The solution of this equation, for harmonic wave propagation in the positive x-direction, is

$$u(t,x) = U\left[\sin(\omega t - \frac{\omega x}{V_p}) + \cos(\omega t - \frac{\omega x}{V_p})\right] \tag{16.19}$$

where ω is the arbitrary frequency of the harmonic motion. The velocity, $\frac{\partial u}{\partial t}$, of a particle at location x is

$$\dot{u}(t,x) = U\omega\left[\cos(\omega t - \frac{\omega x}{V_p}) - \sin(\omega t - \frac{\omega x}{V_p})\right] \tag{16.20}$$

and the strain in the x direction is

$$\varepsilon(x,t) = \frac{\partial u}{\partial x} = -\frac{\dot{u}(x,t)}{V_p} \tag{16.21}$$

The corresponding stress is now

$$\sigma(x,t) = \lambda \varepsilon(x,t) = -V_p \rho \dot{u}(x,t) \tag{16.22}$$

Thus, the compressive stress is equal to the force on a viscous damper with constant damping coefficient equal to ρV_p per unit area of boundary. It can be easily shown that the shear wave radiation boundary condition parallel to a free boundary, is satisfied if damping value is equal to ρV_s.
When modeling the wave motion in a spatial domain, it is essential to introduce artificial boundaries to limit the bounded domain to a reasonable size. The simple Dirichlet boundary condition, in which displacements are fixed, is unsuitable as substantial reflection (through Snell's law) will occur at the boundary and reflected waves will degrade the solution. A solution to this nagging problem could be to enlarge the numerical mesh, thus delaying the side reflections. Obviously this solution considerably increases the expense of computation and is not viable unless artificial damping can be introduced in the material near the far field [447]. Thus, a numerical

model (finite element in our case) should absorb the incoming waves just as they would be absorbed by the free field physically.

16.3.2 Lysmer Model

Lysmer and Kuhlemeyer [555] were the first to investigate the SSI problem. Their solution is simple, elegant and quite effective. It is based on the premises that one can surround the rock boundary by viscous boundaries (through energy absorbent dashpots) with

$$t_n = \rho V_P \dot{u}; \quad t_{s1} = \rho V_S \dot{v}; \quad t_{s2} = \rho V_S \dot{w}; \tag{16.23}$$

where t_n and t_s are the normal and shear tractions respectively; $\dot{u}$, $\dot{v}$ and $\dot{w}$ the normal and two tangential particle velocities at the boundary; ρ is the mass density; V_S and V_P are the shear and pressure waves velocities, respectively, given by

$$V_S = \sqrt{\frac{\mu}{\rho}} \quad \text{and} \quad V_P = \frac{1}{s} V_S \quad \text{where} \quad s^2 = \frac{1-2\nu}{2(1-\nu)} \tag{16.24}$$

where μ and ν are the shear modulus and the Poisson ratio, respectively.
Lysmer determined the ratio of the reflected energy to incident energy (of the P waves per unit time per unit area) as

$$\frac{E_r}{E_i} = A^2 + s\frac{\sin\beta}{\sin\alpha} B^2 \tag{16.25}$$

where a unit ratio corresponds to a perfect reflection (undesired), while a zero ratio corresponds to complete absorption (desired). A similar equation was determined for S waves. In both cases, it was found that a viscous boundary defined by $a = b = 1$ is: a) 95% effective in absorbing S waves and b) absorbs nearly all waves for $\alpha > 30^o$ (some reflection occurs at smaller angles), Figure 16.8.

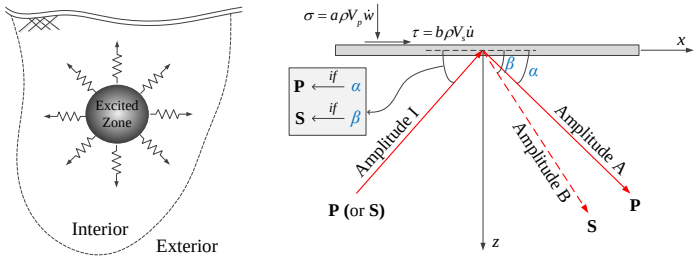

(a) Typical infinite system (b) Incident P- and S-waves at viscous boundary

Fig. 16.8: Elastic waves in an infinite medium

Strictly speaking, one must thus enforce the so-called Sommerfeld boundary condition [923], which is more casually referred to as Lysmer-Kuhlemeyer boundary condition. It is an exact solution if the P and S waves impinge at a right angle the artificial boundary. However they are only approximate solutions for inclined body waves where the reflected energy is only a small part of the total energy. In many cases, the farther one chooses the artificial boundary to be from a source which radiates waves, the more the angle of incidence with respect to the artificial boundary will approach 90°, and thus the better the viscous dampers will perform [888].
A major limitation of this approach is that the required damping coefficients are frequency dependent, and consequently they can (strictly speaking) only be used in frequency domain calculations though they are also often used in time domain analyses such as in [912].
From a practical point of view, in the context of a finite element simulation, Figure 16.9(a) illustrates the dashpot distribution for a mesh subjected to only lateral excitation. Should there be a vertical component, the vertical support at the base of the dashpots should also be removed (which would raise some problems in the presence of body forces). This model has been implemented in the SHAKE program for the frequency-domain analysis for shear-wave propagation in layered soils [775].
Whereas the viscous boundary model eliminated wave reflections, it did not necessarily account for the proper boundary conditions. This was addressed by Lysmer and Drake [553] in an *energy transmitting boundary* model. This model assumed a linear variation of shear strain, and those in turn are transformed into equivalent nodal forces to be applied on the numerical one. This model was implemented in the (frequency domain) program FLUSH [556]. Finally, Lysmer boundary conditions can modeled in Merlin using either one of two models, Figure 16.9: lumped or distributed.

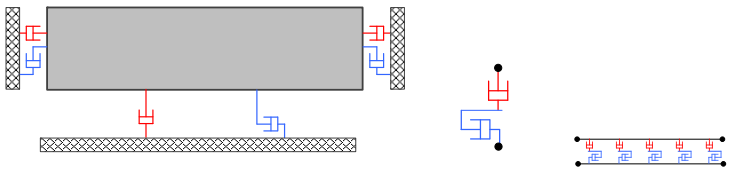

(a) Boundary conditions (b) Lumped (c) Distributed

Fig. 16.9: Lysmer Modeling for Lateral Excitation

16.3.3 Miura-Saouma Model

In an earlier publication (in Japanese) Miura and Toki [599] and [472] considered both viscous boundaries and energy transmitting boundaries. Those are divided into a) absorption of scattering wave energy on the sides and the bottom and b)

energy inflow from outer free fields. However, those references suffered from some limitations. First, there was no derivation of the matrices nor how the method could be actually implemented in a finite element analysis, and finally, it was limited to 2D homogeneous models (i.e. similar rock characteristics to the left/right of the foundation). A closer examination of the Japanese version of the model, [598], indicates that the free field is analyzed in parallel with the main body, and the principle of virtual work is invoked in the derivation. A 2D implementation of this model is reported in [497].
Hence, the first author has revisited the original model of Miura, systematically rederived all the equations, extended it to three dimensional non-homogeneous problems, and provided the reader with all necessary analytical expressions for the finite element implementation [769], and it is discussed below. The model seeks to concurrently account for

- Absorption of the outgoing scattered wave motion (or radiation damping).
- Input of the free field ground motion into the numerical model.

The former will be addressed by the classical Lysmer-Kuhlemeyer model. On the other hand, the input from the free field will be addressed through separate analysis, and resulting displacements and velocities will be transferred as discrete forces to the model. A key advantage of this method is the simplicity of the model and the fact that it is purely a pre- or post-processing operation which (contrary to some prevailing methods) does not require modification of the source code. All relevant equations (including 3D) are given, greatly facilitating implementation of the model with existing finite element codes [526].

16.3.3.1 Theory

The interaction between the free field and the foundation is examined first, Figure 16.10.

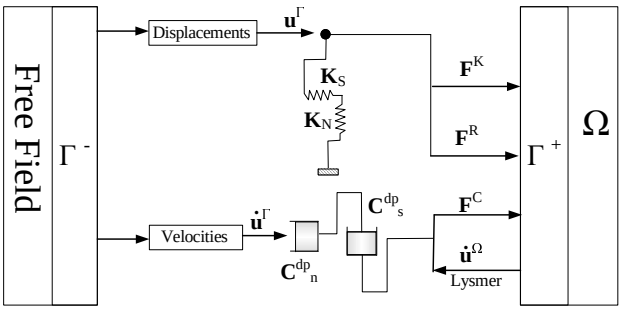

Fig. 16.10: Conceptual model

We identify four distinct parts: 1) the free field itself (F) without its contact surface Γ^-, 2) the contact surface of the free field Γ^-, 3) the contact surface of the model Γ^+, and 4) the model Ω without its contact surface Γ^+. Hence mass, damping, and stiffness matrices can each be decomposed into four parts as:

$$\left[\begin{array}{cc|cc} FF & F\Gamma^- & F\Gamma^+ & F\Omega \\ \Gamma^-F & \Gamma^-\Gamma^- & \Gamma^-\Gamma^+ & \Gamma^-\Omega \\ \hline \Gamma^+F & \Gamma^+\Gamma^- & \Gamma^+\Gamma^+ & \Gamma^+\Omega \\ \Omega F & \Omega\Gamma^- & \Omega\Gamma^+ & \Omega\Omega \end{array}\right] \tag{16.26}$$

where each term XY implies the effect of Y on X.
This is clearly a tightly coupled problem; should we neglect the influence of the model on the free field response, this reduces to

$$\left[\begin{array}{cc|cc} FF & F\Gamma^- & 0 & 0 \\ \Gamma^-F & \Gamma^-\Gamma^- & 0 & 0 \\ \hline 0 & 0 & \Gamma^+\Gamma^+ & \Gamma^+\Omega \\ 0 & 0 & \Omega\Gamma^+ & \Omega\Omega \end{array}\right] \rightarrow \left[\begin{array}{c|c} F & 0 \\ \hline 0 & \Omega^* \end{array}\right] \tag{16.27}$$

$\Gamma^-\Gamma^+$ becomes zero, and we now have a loosely coupled system through $\Gamma^+\Gamma^-$. Hence we can consider the equation of motion for the free field by itself, and will account for the interaction in the equation of motion in Ω by adding forces, stemming from $\Gamma^+\Gamma^-$, on the right hand side.
The first equation of motion for the free field is given by

$$\mathbf{M}^F\ddot{\mathbf{u}}^F + \mathbf{C}^F\dot{\mathbf{u}}^F + \mathbf{K}^F\mathbf{u}^F = \mathbf{t}^F \tag{16.28}$$

Solving this equation, we determine the displacements and velocities along Γ^-, and then solve for the equation of motion in the model:

$$\mathbf{M}^\Omega\ddot{\mathbf{u}}^\Omega + \mathbf{C}^\Omega\dot{\mathbf{u}}^\Omega + \mathbf{K}^\Omega\mathbf{u}^\Omega = \mathbf{t}^\Omega_{\text{bot}} - \underbrace{\left(\mathbf{C}^R_{\text{lft}}\dot{\mathbf{u}}^{\Gamma^-}_{\text{lft}} + \mathbf{K}_{\text{lft}}\mathbf{u}^{\Gamma^-}_{\text{lft}}\right)}_{\text{Left Virtual Interface}} - \underbrace{\left(\mathbf{C}^R_{\text{rgt}}\dot{\mathbf{u}}^{\Gamma^-}_{\text{rgt}} + \mathbf{K}_{\text{rgt}}\mathbf{u}^{\Gamma^-}_{\text{rgt}}\right)}_{\text{Right Virtual Interface}} \tag{16.29}$$

where $\mathbf{M}$, $\mathbf{C}$, and $\mathbf{K}$ are the usual mass, damping, and stiffness matrices, respectively; the subscripts $_{\text{lft}}$, $_{\text{rgt}}$, and $_{\text{bot}}$ correspond to left, right, and bottom; the superscript R corresponds to Rayleigh damping.
So far, we have not accounted for one of the premises of the model, that is absorption of the outgoing scattered wave. This is simply added through the inclusion of the dashpots in accordance with the Lysmer-Kuhlmeyer model. We note that the viscous forces should be expressed in terms of the relative displacements between Γ^+ and Γ^-.

$$\begin{aligned} \mathbf{M}^\Omega\ddot{\mathbf{u}}^\Omega + \mathbf{C}^\Omega\dot{\mathbf{u}}^\Omega + \mathbf{K}^\Omega\mathbf{u}^\Omega + \mathbf{C}^{dp}_{\text{lft}}\left(\dot{\mathbf{u}}^{\Gamma^+}_{\text{lft}} - \dot{\mathbf{u}}^{\Gamma^-}_{\text{lft}}\right) + \mathbf{C}^{dp}_{\text{rgt}}\left(\dot{\mathbf{u}}^{\Gamma^+}_{\text{rgt}} - \dot{\mathbf{u}}^{\Gamma^-}_{\text{rgt}}\right) + \mathbf{C}^{dp}_{\text{bot}}\dot{\mathbf{u}}^\Omega_{\text{bot}} \\ = \mathbf{t}^\Omega_{\text{bot}} - \left(\mathbf{C}^R_{\text{lft}}\dot{\mathbf{u}}^{\Gamma^-}_{\text{lft}} + \mathbf{K}_{\text{lft}}\mathbf{u}^{\Gamma^-}_{\text{lft}}\right) - \left(\mathbf{C}^R_{\text{rgt}}\dot{\mathbf{u}}^{\Gamma^-}_{\text{rgt}} + \mathbf{K}_{\text{rgt}}\mathbf{u}^{\Gamma^-}_{\text{rgt}}\right) \end{aligned} \tag{16.30}$$

This equation can be rewritten by separating known and unknown quantities and substituting the effects of the free field displacements and velocities by their corresponding nodal equivalent forces:

$$\begin{aligned}\left[\mathbf{M}^{\Omega}\ddot{\mathbf{u}}^{\Omega}+\mathbf{C}^{\Omega}\dot{\mathbf{u}}^{\Omega}+\mathbf{K}^{\Omega}\mathbf{u}^{\Omega}\right]+\left[\mathbf{C}^{dp}_{\text{lft}}\dot{\mathbf{u}}^{\Omega}_{\text{lft}}+\mathbf{C}^{dp}_{\text{rgt}}\dot{\mathbf{u}}^{\Omega}_{\text{rgt}}+\mathbf{C}^{dp}_{\text{bot}}\dot{\mathbf{u}}^{\Omega}_{B}\right]\\ =\mathbf{t}^{\Omega}_{\text{bot}}+\left[\mathbf{F}^{C}_{\text{lft}}+\mathbf{F}^{K}_{\text{lft}}+\mathbf{F}^{R}_{\text{lft}}\right]+\left[\mathbf{F}^{C}_{\text{rgt}}+\mathbf{F}^{K}_{\text{rgt}}+\mathbf{F}^{R}_{\text{rgt}}\right]\end{aligned}\tag{16.31}$$

where $\mathbf{F}^{C}$, $\mathbf{F}^{K}$, and $\mathbf{F}^{R}$ are the vectors of nodal equivalent forces caused by the free field velocities, stiffness, and damping, respectively. They will be separately derived later.
The corresponding three dimensional equation would be

$$\begin{aligned}&\left[\mathbf{M}^{\Omega}\ddot{\mathbf{u}}^{\Omega}+\mathbf{C}^{\Omega}\dot{\mathbf{u}}^{\Omega}+\mathbf{K}^{\Omega}\mathbf{u}^{\Omega}\right]+\left[\mathbf{C}^{dp}_{\text{lft}}\dot{\mathbf{u}}^{\Omega}_{\text{lft}}+\mathbf{C}^{dp}_{\text{rgt}}\dot{\mathbf{u}}^{\Omega}_{\text{rgt}}+\mathbf{C}^{dp}_{\text{bck}}\dot{\mathbf{u}}^{\Omega}_{\text{bck}}+\mathbf{C}^{dp}_{\text{fro}}\dot{\mathbf{u}}^{\Omega}_{\text{fro}}+\mathbf{C}^{dp}_{\text{bot}}\dot{\mathbf{u}}^{\Omega}_{B}\right]\\ &=\mathbf{t}^{\Omega}_{\text{bot}}+\left[\mathbf{F}^{C}_{\text{lft}}+\mathbf{F}^{K}_{\text{lft}}+\mathbf{F}^{R}_{\text{lft}}\right]+\left[\mathbf{F}^{C}_{\text{rgt}}+\mathbf{F}^{K}_{\text{rgt}}+\mathbf{F}^{R}_{\text{rgt}}\right]+\left[\mathbf{F}^{C}_{\text{bck}}+\mathbf{F}^{K}_{\text{bck}}+\mathbf{F}^{R}_{\text{bck}}\right]+\left[\mathbf{F}^{C}_{\text{fro}}+\mathbf{F}^{K}_{\text{fro}}+\mathbf{F}^{R}_{\text{fro}}\right]\end{aligned}\tag{16.32}$$

where bck and fro correspond to the back and front sides respectively.
To derive the expressions of the forces in the right hand side of Eq. 16.32, we apply the principle of virtual work to the *system*

$$\int_{\Omega}\delta\mathbf{u}.\left[\rho\ddot{\mathbf{u}}+\eta\dot{\mathbf{u}}+\mathbf{F}\right]\mathrm{d}\Omega=\int_{\Gamma}\delta\mathbf{u}.\left(\mathbf{t}^{\text{bot}}+\mathbf{t}^{\Gamma^{-}}\right)\mathrm{d}\Gamma\tag{16.33}$$

where ρ is the mass density, η the viscosity parameter, $\mathbf{F}$ the internal force, $\mathbf{u}$ the displacement vector, $\mathbf{t}^{\text{bot}}$ and $\mathbf{t}^{\Gamma^{-}}$ are the surface traction on the boundary Γ (base and free field). It can be readily shown that the left and right hand sides of Eq. 16.33 correspond to the integral form of the left and right hand sides of Eq. 16.32, respectively.

Internal Virtual Work Discretizing the continuum through shape functions, [925], it can be readily shown that the left hand side and the first right hand side term of Eq. 16.33 correspond to the classical form of the equation of motion

$$\mathbf{M}^{\Omega}\ddot{\mathbf{u}}^{\Omega}+\mathbf{C}^{\Omega}\dot{\mathbf{u}}^{\Omega}+\mathbf{K}\mathbf{u}^{\Omega}$$

In the context of the present analysis, this can be generalized to the right hand side of Eq. 16.32.

External Virtual Work Focusing on the remaining term, the external virtual force can be expressed as

$$\int_{\Gamma}\delta\mathbf{u}.\mathbf{t}^{\Gamma^{-}}\mathrm{d}\Gamma=\int_{0}^{t_y}\int_{0}^{t_z}\left[\delta u t_n+\delta v t_{s1}+\delta w t_{s2}\right]\mathrm{d}z\mathrm{d}y\tag{16.34}$$

In the next sections we will separately determine the tractions caused by presence of dashpots or the free field displacements.

Forces Caused by Velocity Due to the presence of the dashpots around the bounded model, we substitute Eq. 16.24 into Eq. 16.34. It should be noted that in the model, the velocities will actually correspond to the difference in velocities between the free field and the bounded model: $\dot{\mathbf{u}}_{\text{lft}}^{\Omega} - \dot{\mathbf{u}}_{\text{lft}}^{\Gamma^-}$ as in Eq. 16.30. The nodal displacements along the surface boundary can be expressed in terms of the known nodal ones through the shape functions (assuming a linear variation). Considering the x-plane, the finite element discretization yields

$$\begin{cases} u = \mathbf{N}_u \overline{\mathbf{u}}; \;\; \delta u = \mathbf{N}_u \delta \overline{\mathbf{u}}; \;\; V_p \dot{u} = V_p \mathbf{N}_u \dot{\overline{\mathbf{u}}} \\ v = \mathbf{N}_v \overline{\mathbf{u}}; \;\; \delta v = \mathbf{N}_v \delta \overline{\mathbf{u}}; \;\; V_s \dot{v} = V_s \mathbf{N}_v \dot{\overline{\mathbf{u}}} \\ w = \mathbf{N}_w \overline{\mathbf{u}}; \; \delta w = \mathbf{N}_w \delta \overline{\mathbf{u}}; \; V_s \dot{w} = V_s \mathbf{N}_w \dot{\overline{\mathbf{u}}} \end{cases} \tag{16.35}$$

where the shape functions, shown in Figure 16.11 for the bilinear element, are given by

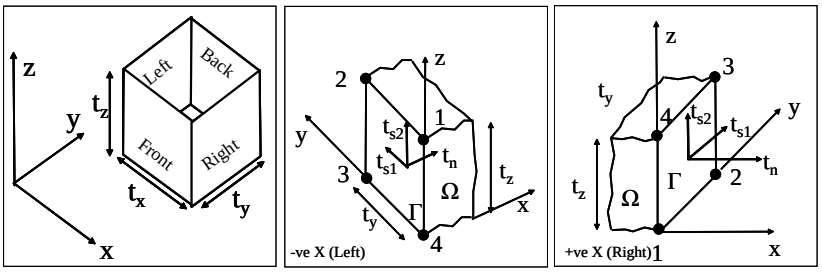

Fig. 16.11: 2D Idealization and Γ_i planes

$$\begin{aligned} \mathbf{N}_u &= \tfrac{1}{t_y t_z} \lfloor\, (t_y - y)(t_z - z)\; 0\; 0\; (t_z - z)y\; 0\; 0\; zy\; 0\; 0\; z(t_y - y)\; 0\; 0 \,\rfloor^T \\ \mathbf{N}_v &= \tfrac{1}{t_y t_z} \lfloor\, 0\; (t_y - y)(t_z - z)\; 0\; 0\; (t_z - z)y\; 0\; 0\; zy\; 0\; 0\; z(t_y - y)\; 0 \,\rfloor^T \\ \mathbf{N}_w &= \tfrac{1}{t_y t_z} \lfloor\, 0\; 0\; (t_y - y)(t_z - z)\; 0\; 0\; (t_z - z)y\; 0\; 0\; zy\; 0\; 0\; z(t_y - y) \,\rfloor^T \end{aligned} \tag{16.36}$$

and

$$\overline{\mathbf{u}} = \lfloor\, \overline{u}_1\; \overline{v}_1\; \overline{w}_1\; \overline{u}_2\; \overline{v}_2\; \overline{w}_2\; \overline{u}_3\; \overline{v}_3\; \overline{w}_3\; \overline{u}_4\; \overline{v}_4\; \overline{w}_4 \,\rfloor^T \tag{16.37}$$

Substituting[1] in Eq. 16.34,

$$\int_{\Gamma} \delta \mathbf{u}.\mathbf{t} \mathrm{d}\Gamma = \rho \int_0^{t_z} \int_0^{t_y} V_p \mathbf{N}_u.\mathbf{N}_u^T + V_s \left(\mathbf{N}_v.\mathbf{N}_v^T + \mathbf{N}_w.\mathbf{N}_w^T \right) \mathrm{d}y \mathrm{d}z \tag{16.38}$$

or $\mathbf{F}^C = \mathbf{C}_x^{dp} \dot{\mathbf{u}}$ where

[1] All operations were performed by *Mathematica*.

$$\mathbf{C}_x^L = \frac{\rho t_y t_z}{36}\begin{bmatrix} 4V_p & 0 & 0 & 2V_p & 0 & 0 & V_p & 0 & 0 & 2V_p & 0 & 0 \\ 0 & 4V_s & 0 & 0 & 2V_s & 0 & 0 & V_s & 0 & 0 & 2V_s & 0 \\ 0 & 0 & 4V_s & 0 & 0 & 2V_s & 0 & 0 & V_s & 0 & 0 & 2V_s \\ 2V_p & 0 & 0 & 4V_p & 0 & 0 & 2V_p & 0 & 0 & V_p & 0 & 0 \\ 0 & 2V_s & 0 & 0 & 4V_s & 0 & 0 & 2V_s & 0 & 0 & V_s & 0 \\ 0 & 0 & 2V_s & 0 & 0 & 4V_s & 0 & 0 & 2V_s & 0 & 0 & V_s \\ V_p & 0 & 0 & 2V_p & 0 & 0 & 4V_p & 0 & 0 & 2V_p & 0 & 0 \\ 0 & V_s & 0 & 0 & 2V_s & 0 & 0 & 4V_s & 0 & 0 & 2V_s & 0 \\ 0 & 0 & V_s & 0 & 0 & 2V_s & 0 & 0 & 4V_s & 0 & 0 & 2V_s \\ 2V_p & 0 & 0 & V_p & 0 & 0 & 2V_p & 0 & 0 & 4V_p & 0 & 0 \\ 0 & 2V_s & 0 & 0 & V_s & 0 & 0 & 2V_s & 0 & 0 & 4V_s & 0 \\ 0 & 0 & 2V_s & 0 & 0 & V_s & 0 & 0 & 2V_s & 0 & 0 & 4V_s \end{bmatrix} \tag{16.39}$$

The same expression applies on the positive and negative faces.
The two dimensional equivalent matrix is obtained by simply adding rows and columns 1-4, 3-6, 7-10, 9-12 (while dropping rows and columns 2, 5, 8 and 11) in Eq. 16.39. This reduces to

$$\mathbf{F}^C = \frac{\rho t_z}{6}\begin{bmatrix} 2V_p & 0 & V_p & 0 \\ 0 & 2V_s & 0 & V_s \\ V_p & 0 & 2V_p & 0 \\ 0 & V_s & 0 & 2V_s \end{bmatrix}\begin{Bmatrix} \dot{u}_1 \\ \dot{v}_1 \\ \dot{u}_2 \\ \dot{v}_2 \end{Bmatrix} \tag{16.40}$$

It should be noted that both the left and right sides will be subjected to the same $\mathbf{C}_x^L$ matrix.

Forces Caused by Displacements The lateral forces exerted on the bounded domain by the free field displacements are determined next. The free field will be modeled as a shear beam (where $\frac{\partial u}{\partial x} = 0$), and in the most general case, Figure 16.11, there will be displacements along the three axis x, y and z. Hence, unsymmetric and non-homogeneous boundaries could be accounted for. The traction terms to be substituted in Eq. 16.34 are thus:

$$\begin{cases} t_n = \sigma_{xx} = \lambda\left(\epsilon_{xx} + \epsilon_{yy} + \epsilon_{zz}\right) + 2\mu\epsilon_{xx} = \lambda\left(\frac{\partial v}{\partial y} + \frac{\partial w}{\partial z}\right) \\ t_{s1} = \tau_{xy} = \mu\gamma_{xy} = \mu\frac{\partial u}{\partial y} \\ t_{s2} = \tau_{xz} = \mu\gamma_{xz} = \mu\frac{\partial u}{\partial z} \end{cases} \tag{16.41}$$

where λ and μ are the classical Lame's parameters,

$$\lambda = \frac{\nu E}{(1+\nu)(1-2\nu)}; \qquad \mu = \frac{E}{2(1+\nu)} \tag{16.42}$$

The internal displacements can be expressed in terms of the known nodal ones through the shape functions, Eq. 16.36. Substituting into Eq. 16.34, we obtain:

$$\delta W_{ext} = \delta\overline{\mathbf{u}}\int_0^{t_z}\int_0^{t_y}\left[\mathbf{N}_u.\left[\lambda\left(\frac{\partial\mathbf{N}_v}{\partial y}+\frac{\partial\mathbf{N}_w}{\partial z}\right)\right]+\mathbf{N}_v.\left(\mu\frac{\partial\mathbf{N}_u}{\partial y}\right)+\mathbf{N}_w.\left(\mu\frac{\partial\mathbf{N}_u}{\partial z}\right)\right]\mathrm{d}y\mathrm{d}z\overline{\mathbf{u}} \tag{16.43}$$

Or

$$\mathbf{F}^K = \mathbf{K}_x^+\overline{\mathbf{u}} \tag{16.44}$$

where

$$\mathbf{F}^K = \lfloor\ F_{1,u}\ F_{1,v}\ F_{1,w}\ F_{2,u}\ F_{2,v}\ F_{2,w}\ F_{3,u}\ F_{3,v}\ F_{3,w}\ F_{4,u}\ F_{4,v}\ F_{4,w}\ \rfloor^T \tag{16.45}$$

and the corresponding stiffness matrix is given by

$$\mathbf{K}_x^+ = \frac{1}{12}\begin{bmatrix}
0 & -2t_z\lambda & -2t_y\lambda & 0 & 2t_z\lambda & -t_y\lambda & 0 & t_z\lambda & t_y\lambda & 0 & -t_z\lambda & 2t_y\lambda \\
-2t_z\mu & 0 & 0 & 2t_z\mu & 0 & 0 & t_z\mu & 0 & 0 & -t_z\mu & 0 & 0 \\
-2t_y\mu & 0 & 0 & -t_y\mu & 0 & 0 & t_y\mu & 0 & 0 & 2t_y\mu & 0 & 0 \\
0 & -2t_z\lambda & -t_y\lambda & 0 & 2t_z\lambda & -2t_y\lambda & 0 & t_z\lambda & 2t_y\lambda & 0 & -t_z\lambda & t_y\lambda \\
-2t_z\mu & 0 & 0 & 2t_z\mu & 0 & 0 & t_z\mu & 0 & 0 & -t_z\mu & 0 & 0 \\
-t_y\mu & 0 & 0 & -2t_y\mu & 0 & 0 & 2t_y\mu & 0 & 0 & t_y\mu & 0 & 0 \\
0 & -t_z\lambda & -t_y\lambda & 0 & t_z\lambda & -2t_y\lambda & 0 & 2t_z\lambda & 2t_y\lambda & 0 & -2t_z\lambda & t_y\lambda \\
-t_z\mu & 0 & 0 & t_z\mu & 0 & 0 & 2t_z\mu & 0 & 0 & -2t_z\mu & 0 & 0 \\
-t_y\mu & 0 & 0 & -2t_y\mu & 0 & 0 & 2t_y\mu & 0 & 0 & t_y\mu & 0 & 0 \\
0 & -t_z\lambda & -2t_y\lambda & 0 & t_z\lambda & -t_y\lambda & 0 & 2t_z\lambda & t_y\lambda & 0 & -2t_z\lambda & 2t_y\lambda \\
-t_z\mu & 0 & 0 & t_z\mu & 0 & 0 & 2t_z\mu & 0 & 0 & -2t_z\mu & 0 & 0 \\
-2t_y\mu & 0 & 0 & -t_y\mu & 0 & 0 & t_y\mu & 0 & 0 & 2t_y\mu & 0 & 0
\end{bmatrix} \tag{16.46}$$

Rayleigh Damping Rayleigh damping is introduced:

$$\left[\mathbf{F}^R\right] = \frac{\zeta}{\pi f}\left[\mathbf{K}\right] \tag{16.47}$$

where ζ is the damping factor at frequency f. We note that this is stiffness proportional only since we are dealing with a massless element. Again, the two dimensional equivalent matrix is obtained by simply adding rows and columns 1-4, 3-6, 7-10, 9-12 (while dropping rows and columns 2, 5, 8 and 11). This reduces to

$$\mathbf{K}_x^+ = \frac{t}{2}\begin{bmatrix} 0 & -\lambda & 0 & \lambda \\ -\mu & 0 & \mu & 0 \\ 0 & -\lambda & 0 & \lambda \\ -\mu & 0 & \mu & 0 \end{bmatrix} \tag{16.48}$$

16.3.3.2 Finite Element Implementation

Recognizing that in practice we do not have a rigid support for the foundation but rather a flexible one, we need to account for this added variability, Figure 16.12. The methodology adopted here is based on the work of [599]. The governing equation for a dam foundation system in an infinite flexible medium is given by

$$\begin{aligned}
&\left[\mathbf{M}\right]\left\{\ddot{\mathbf{x}}\right\} + \left(\left[\mathbf{C}\right] + \left[\mathbf{C}_B\right] + \left[\mathbf{C}_L\right] + \left[\mathbf{C}_R\right]\right)\left\{\dot{\mathbf{x}}\right\} + \left[\mathbf{K}\right]\left\{\mathbf{x}\right\} \\
&\quad = \left\{\mathbf{f}\right\} + \left[\mathbf{C}_L\right]\left\{\dot{\mathbf{x}}_L\right\} + \left[\mathbf{C}_R\right]\left\{\dot{\mathbf{x}}_R\right\} + \left[\mathbf{G}_{CL}\right]\left\{\dot{\mathbf{x}}_L\right\} \\
&\qquad + \left[\mathbf{G}_{CR}\right]\left\{\dot{\mathbf{x}}_R\right\} + \left[\mathbf{G}_L\right]\left\{\mathbf{x}_L\right\} + \left[\mathbf{G}_R\right]\left\{\mathbf{x}_R\right\}
\end{aligned} \tag{16.49}$$

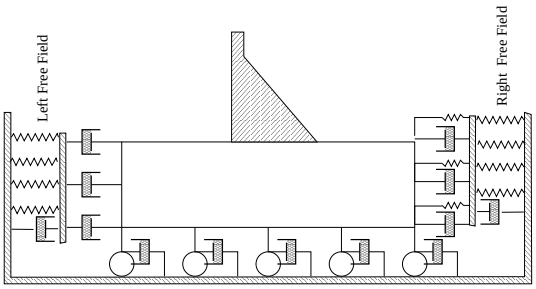

Fig. 16.12: Foundation boundary conditions for radiating flexible foundation

This equation can be rewritten as

$$\begin{aligned}
&\left[\begin{array}{cc|c|c} \mathbf{M}_{II} & \mathbf{M}_{IB} & \mathbf{M}_{IL} & \mathbf{M}_{IR} \\ \mathbf{M}_{BI} & \mathbf{M}_{BB} & \mathbf{M}_{BL} & \mathbf{M}_{BR} \\ \hline \mathbf{M}_{LI} & \mathbf{M}_{LB} & \mathbf{M}_{LL} & 0 \\ \hline \mathbf{M}_{RI} & \mathbf{M}_{RB} & 0 & \mathbf{M}_{RR} \end{array}\right] \left\{\begin{array}{c} \ddot{\mathbf{x}} \\ \ddot{\mathbf{x}}_B \\ \ddot{\mathbf{x}}_L \\ \ddot{\mathbf{x}}_R \end{array}\right\} + \left[\begin{array}{cc|c|c} \mathbf{C}_{II} & \mathbf{C}_{IB} & \mathbf{C}_{IL} & \mathbf{C}_{IR} \\ \mathbf{C}_{BI} & \mathbf{C}_{BB} & \mathbf{C}_{BL} & \mathbf{C}_{BR} \\ \hline \mathbf{C}_{LI} & \mathbf{C}_{LB} & \mathbf{C}_{LL} & 0 \\ \hline \mathbf{C}_{RI} & \mathbf{C}_{RB} & 0 & \mathbf{C}_{RR} \end{array}\right] \left\{\begin{array}{c} \dot{\mathbf{x}} \\ \dot{\mathbf{x}}_B \\ \dot{\mathbf{x}}_L \\ \dot{\mathbf{x}}_R \end{array}\right\} \\
&+ \left[\begin{array}{cc|c|c} \mathbf{K}_{II} & \mathbf{K}_{IB} & \mathbf{K}_{IL} & \mathbf{K}_{IR} \\ \mathbf{K}_{BI} & \mathbf{K}_{BB} & \mathbf{K}_{BL} & \mathbf{K}_{BR} \\ \hline \mathbf{K}_{LI} & \mathbf{K}_{LB} & \mathbf{K}_{LL} & 0 \\ \hline \mathbf{K}_{RI} & \mathbf{K}_{RB} & 0 & \mathbf{K}_{RR} \end{array}\right] \left\{\begin{array}{c} \mathbf{x} \\ \mathbf{x}_B \\ \mathbf{x}_L \\ \mathbf{x}_R \end{array}\right\} \\
&= \left\{\begin{array}{c} \mathbf{f} \\ \mathbf{f}_B \\ \mathbf{f}_L \\ \mathbf{f}_R \end{array}\right\} + \left[\begin{array}{cc|c|c} 0 & & & \\ 0 & & & \\ \hline & \mathbf{C}_{LL}+\mathbf{G}_{CL} & & \\ \hline & & & \mathbf{C}_{RR}+\mathbf{G}_{CR} \end{array}\right] \left\{\begin{array}{c} \dot{\mathbf{x}}_I \\ \dot{\mathbf{x}}_B \\ \dot{\mathbf{x}}_L \\ \dot{\mathbf{x}}_R \end{array}\right\} + \left[\begin{array}{cc|c|c} 0 & & & \\ 0 & & & \\ \hline & & \mathbf{G}_L & \\ \hline & & & \mathbf{G}_R \end{array}\right] \left\{\begin{array}{c} \mathbf{x} \\ \mathbf{x}_B \\ \mathbf{x}_L \\ \mathbf{x}_R \end{array}\right\}
\end{aligned} \tag{16.50}$$

where $[\mathbf{M}]$ is the mass matrix, $[\mathbf{C}]$ damping matrix, $[\mathbf{K}]$ stiffness matrix and subscripts I, B, L, R refer to interior, bottom, left, and right nodes; $\{\mathbf{x}\}, \{\dot{\mathbf{x}}\}, \{\ddot{\mathbf{x}}\}$ are the nodal displacements, velocities, and accelerations.
$[\mathbf{C}_B]$ is Lysmer (dashpot) viscous boundary conditions at the bottom (tuned to shear wave for lateral excitation and to pressure waves for vertical excitation).

$$[\mathbf{C}_B] = \frac{\rho L}{2} \begin{bmatrix} V_H & 0 & 0 & 0 \\ 0 & V_V & 0 & 0 \\ 0 & 0 & V_H & 0 \\ 0 & 0 & 0 & V_V \end{bmatrix}, \quad \begin{cases} V_H = V_S \cos\theta + V_P \sin\theta \\ V_V = V_P \cos\theta + V_S \sin\theta \end{cases} \tag{16.51}$$

$[\mathbf{C}_L], [\mathbf{C}_R]$ are Lysmer (dashpot) left and right boundary conditions tuned to pressure wave for lateral excitation and shear waves for vertical excitation. $[\mathbf{G}_L], [\mathbf{G}_R]$ are the boundary stiffness matrices associated with the displacement of the free field.

$$[\mathbf{G}] = \frac{1}{2} \begin{bmatrix} 0 & -\lambda & 0 & \lambda \\ -\mu & 0 & \mu & 0 \\ 0 & -\lambda & 0 & \lambda \\ -\mu & 0 & \mu 0 & \end{bmatrix} \tag{16.52}$$

where λ and μ are the Lame parameters, $\lambda = \frac{\nu E}{(1-2\nu)(1+\nu)} = K - \frac{2}{3}G$ and $\mu = \frac{E}{2(1+\nu)} = G$. For a symmetric foundation ($\mathbf{x}_L = -\mathbf{x}_R$) we can ignore this term. $[\mathbf{G}_{CL}], [\mathbf{G}_{CR}]$ are the boundary damping matrices associated with the free field. Their effects also cancel out for symmetric cases.
Hence, for symmetric boundary conditions, we can ignore
$[\mathbf{G}_R], [\mathbf{G}_L], [\mathbf{G}_{CR}], [\mathbf{G}_{CL}], \mathbf{x}_R, \mathbf{x}_L$, and the resulting governing partial differential equation to be solved is reduced to:

$$\begin{aligned}&[\mathbf{M}]\{\ddot{\mathbf{x}}\} + ([\mathbf{C}] + [\mathbf{C}_b] + [\mathbf{C}_L] + [\mathbf{C}_R])\{\dot{\mathbf{x}}\} + [\mathbf{K}]\{\mathbf{x}\} \\ &\quad = \{\mathbf{f}\} + [\mathbf{C}_L]\{\dot{\mathbf{x}}_L\} + [\mathbf{C}_R]\{\dot{\mathbf{x}}_R\}\end{aligned} \tag{16.53}$$

or

$$\begin{aligned}&\left[\begin{array}{cc|c|c} \mathbf{M}_{II} & \mathbf{M}_{IB} & \mathbf{M}_{IL} & \mathbf{M}_{IR} \\ \mathbf{M}_{BI} & \mathbf{M}_{BB} & \mathbf{M}_{BL} & \mathbf{M}_{BR} \\ \hline \mathbf{M}_{LI} & \mathbf{M}_{LB} & \mathbf{M}_{LL} & 0 \\ \hline \mathbf{M}_{RI} & \mathbf{M}_{RB} & 0 & \mathbf{M}_{RR} \end{array}\right] \left\{\begin{array}{c} \ddot{\mathbf{x}} \\ \ddot{\mathbf{x}}_B \\ \ddot{\mathbf{x}}_L \\ \ddot{\mathbf{x}}_R \end{array}\right\} + \left[\begin{array}{cc|c|c} \mathbf{C}_{II} & \mathbf{C}_{IB} & \mathbf{C}_{IL} & \mathbf{C}_{IR} \\ \mathbf{C}_{BI} & \mathbf{C}_{BB} & \mathbf{C}_{BL} & \mathbf{C}_{BR} \\ \hline \mathbf{C}_{LI} & \mathbf{C}_{LB} & \mathbf{C}_{LL} & 0 \\ \hline \mathbf{C}_{RI} & \mathbf{C}_{RB} & 0 & \mathbf{C}_{RR} \end{array}\right] \left\{\begin{array}{c} \dot{\mathbf{x}} \\ \dot{\mathbf{x}}_B \\ \dot{\mathbf{x}}_L \\ \dot{\mathbf{x}}_R \end{array}\right\} \\ &+ \left[\begin{array}{cc|c|c} \mathbf{K}_{II} & \mathbf{K}_{IB} & \mathbf{K}_{IL} & \mathbf{K}_{IR} \\ \mathbf{K}_{BI} & \mathbf{K}_{BB} & \mathbf{K}_{BL} & \mathbf{K}_{BR} \\ \hline \mathbf{K}_{LI} & \mathbf{K}_{LB} & \mathbf{K}_{LL} & 0 \\ \hline \mathbf{K}_{RI} & \mathbf{K}_{RB} & 0 & \mathbf{K}_{RR} \end{array}\right] \left\{\begin{array}{c} \mathbf{x} \\ \mathbf{x}_B \\ \mathbf{x}_L \\ \mathbf{x}_R \end{array}\right\} \\ &= \left\{\begin{array}{c} \mathbf{f} \\ \mathbf{f}_B \\ \mathbf{f}_L \\ \mathbf{f}_R \end{array}\right\} + \left[\begin{array}{cc|c|c} 0 & & & \\ & 0 & & \\ \hline & & \mathbf{C}_{LL} & \\ \hline & & & \mathbf{C}_{RR} \end{array}\right] \left\{\begin{array}{c} \dot{\mathbf{x}}_I \\ \dot{\mathbf{x}}_B \\ \dot{\mathbf{x}}_L \\ \dot{\mathbf{x}}_R \end{array}\right\}\end{aligned} \tag{16.54}$$

In order to solve this equation, we still need some quantities on the right hand side of the equation, namely $\dot{\mathbf{x}}_L$ and $\dot{\mathbf{x}}_R$. These can be obtained from two separate (one if we take advantage of symmetry) analyses of the free field which can be discretized as shown in Figure 16.13. We note the vertical restraint for lateral excitation and

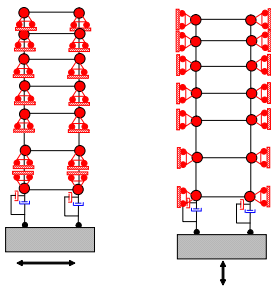

Fig. 16.13: Finite element discretization of the free field

the lateral restraint for vertical excitation in order to respect the far field boundary conditions. Thus the governing differential equations for these analyses are

$$[\mathbf{M}_L]\{\ddot{\mathbf{x}}_L?\} + [\mathbf{C}_L]\{\dot{\mathbf{x}}_L?\} + [\mathbf{K}_L]\{\mathbf{x}_L?\} = \{\mathbf{f}_L\surd\} \tag{16.55}$$

$$[\mathbf{M}_R]\{\ddot{\mathbf{x}}_R?\} + [\mathbf{C}_R]\{\dot{\mathbf{x}}_R?\} + [\mathbf{K}_R]\{\mathbf{x}_R?\} = \{\mathbf{f}_R\surd\} \tag{16.56}$$

from which we solve for $\dot{\mathbf{x}}_L$ and $\dot{\mathbf{x}}_R$.
Once the free field velocities have been obtained, they can in turn be used in the full 2D analysis of the dam/foundation discretization shown in Figure 16.14.

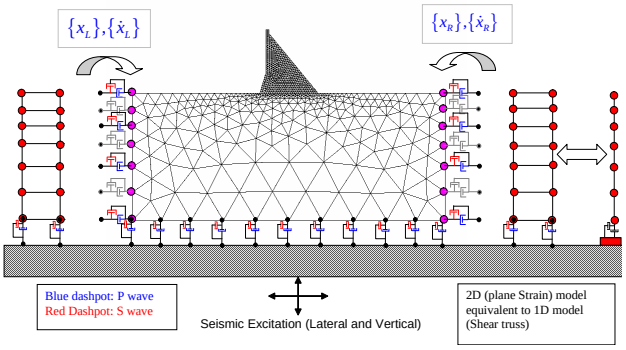

Fig. 16.14: Discretization of 2D dam foundation with free field velocities

$$\begin{bmatrix} \mathbf{M}_{II} & \mathbf{M}_{IB} & \mathbf{M}_{IL} & \mathbf{M}_{IR} \\ \mathbf{M}_{BI} & \mathbf{M}_{BB} & \mathbf{M}_{BL} & \mathbf{M}_{BR} \\ \mathbf{M}_{LI} & \mathbf{M}_{LB} & \mathbf{M}_{LL} & 0 \\ \mathbf{M}_{RI} & \mathbf{M}_{RB} & 0 & \mathbf{M}_{RR} \end{bmatrix} \begin{Bmatrix} \ddot{\mathbf{x}}? \\ \ddot{\mathbf{x}}_B? \\ \ddot{\mathbf{x}}_L? \\ \ddot{\mathbf{x}}_R? \end{Bmatrix} + \begin{bmatrix} \mathbf{C}_{II} & \mathbf{C}_{IB} & \mathbf{C}_{IL} & \mathbf{C}_{IR} \\ \mathbf{C}_{BI} & \mathbf{C}_{BB} & \mathbf{C}_{BL} & \mathbf{C}_{BR} \\ \mathbf{C}_{LI} & \mathbf{C}_{LB} & \mathbf{C}_{LL} & 0 \\ \mathbf{C}_{RI} & \mathbf{C}_{RB} & 0 & \mathbf{C}_{RR} \end{bmatrix} \begin{Bmatrix} \dot{\mathbf{x}}? \\ \dot{\mathbf{x}}_B? \\ \dot{\mathbf{x}}_L? \\ \dot{\mathbf{x}}_R? \end{Bmatrix}$$
$$+ \begin{bmatrix} \mathbf{K}_{II} & \mathbf{K}_{IB} & \mathbf{K}_{IL} & \mathbf{K}_{IR} \\ \mathbf{K}_{BI} & \mathbf{K}_{BB} & \mathbf{K}_{BL} & \mathbf{K}_{BR} \\ \mathbf{K}_{LI} & \mathbf{K}_{LB} & \mathbf{K}_{LL} & 0 \\ \mathbf{K}_{RI} & \mathbf{K}_{RB} & 0 & \mathbf{K}_{RR} \end{bmatrix} \begin{Bmatrix} \mathbf{x}? \\ \mathbf{x}_B? \\ \mathbf{x}_L? \\ \mathbf{x}_R? \end{Bmatrix} \tag{16.57}$$
$$= \begin{Bmatrix} \mathbf{f}\surd \\ \mathbf{f}_B\surd \\ \mathbf{f}_L\surd \\ \mathbf{f}_R\surd \end{Bmatrix} + \begin{bmatrix} 0 & & & \\ & \mathbf{C}_{LL} & & \\ & & \mathbf{C}_{RR} & \end{bmatrix} \begin{Bmatrix} \dot{\mathbf{x}}_I \\ \dot{\mathbf{x}}_B? \\ \dot{\mathbf{x}}_L\surd \\ \dot{\mathbf{x}}_R\surd \end{Bmatrix}$$

16.3.3.3 Finite Element Implementation

All the components of Eq. 16.32 having been defined, the analysis could then proceed as follows (for the 2D case), Figure 16.15:

1. Discretize the free field with an arbitrary mesh which is topologically consistent with the adjacent one in the bounded domain (that is, to each boundary node of the foundation mesh corresponds a node in the free field mesh). Place dashpots at the base of the mesh.
2. Constrain the vertical displacements of all the nodes (thus allowing only shear deformation), apply an horizontal excitation and analyze.

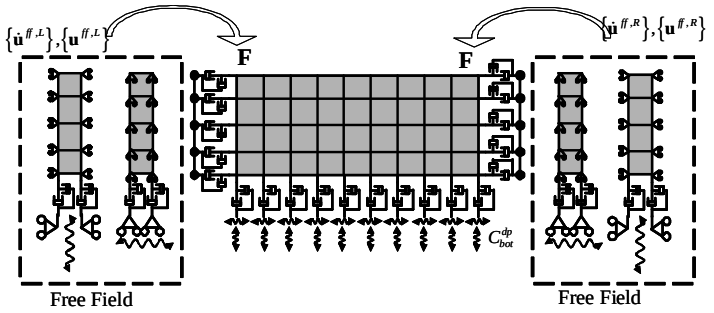

Fig. 16.15: 2D Finite Element Modeling

3. If the seismic record includes a vertical component, repeat the analysis by constraining all the horizontal displacements (thus allowing only axial deformation), apply the vertical component of the excitation and analyze.
4. Determine the nodal equivalent forces $\mathbf{F}^C$, $\mathbf{F}^K$, and $\mathbf{F}^R$ from Eqs. 16.40, 16.44, and 16.47, respectively.
5. Apply these as external (time dependent) boundary forces to the bounded domain (as in Eq. 16.31) and analyze.

In 3D, the model becomes more complex, Figure 16.16. We would have to perform

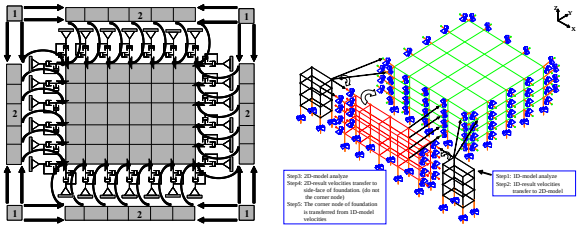

Fig. 16.16: 3D extension; procedure outline

three analyses (assuming that the earthquake record has x, y, and z components) of each of the corner blocks then transfer the nodal equivalent forces to the four side blocks using the procedure outlined above. Those in turn will be analyzed three times each, and finally nodal equivalent forces would again be transferred to the bounded domain. Thus, potentially twenty four analyses would have to be performed before the foundation can be analyzed. It should be noted that each one of those free field analyses is not computationally intensive, the major difficulty is "book-keeping" to properly determine the nodal forces and transfer them, at each time increment, to the correct corresponding node.

A major advantage of this method is that there is no need to modify existing finite element programs (as is the case in [125] and [87]). The entire operation is the

result of clever post- and pre-processing of analysis which can be performed on most existing finite element codes (only requirement: support dashpot elements).

16.3.4 Validation Problems

To assess the effectiveness of the method in dissipating elastic waves, an extensive parametric study is performed. We consider a soft foundation with E, ρ and ν equal to 1.563×10^3 MN/m^2, 2,500 kg/m^3 and 0.25, respectively. This corresponds to a shear wave velocity (V_S from Eq. 16.24) of 500 m/sec. Hence by exciting the base with a harmonic excitation with period of 0.4 sec, a full wave length develops over 200 m which is the height of the model. Length is set to 800 m, and the 3D model in turn is 200 by 800 by 800 m. Since the base excitation has a magnitude of 1 m/sec^2, ideally we should have a similar (though with a phase lag) response at the top of the bounded domain. In both cases element size was 25 m (except for a fine 2D mesh with half this size). Results are assessed by examining the acceleration at the top, distribution of accelerations at $h/8$ increments, deformed shapes, and velocity or acceleration contour lines. From this investigation we conclude that:

1. When the boundaries are left bare (for both 2D and 3D analyses), results are totally unacceptable, Figure 16.17(a).

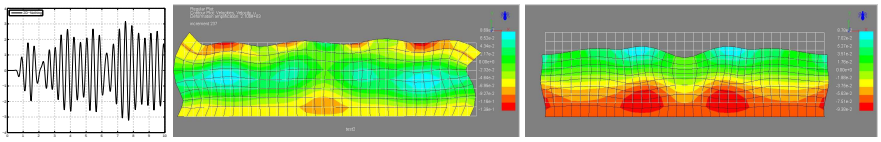

(a) Free boundaries

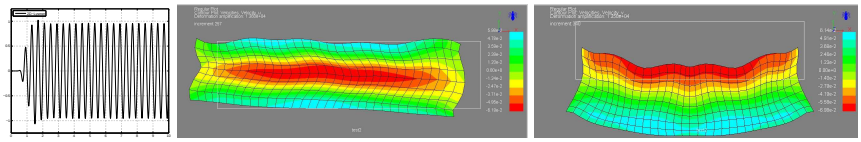

(b) 2D Lysmer

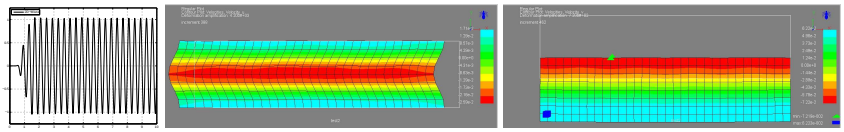

(c) Miura-Saouma

Fig. 16.17: Selected results for 2D analyses; Crest accelerations, deformed shapes with contour lines of V_X and V_Y

2. 2D Lysmer yields nearly perfect (0.9) acceleration at h, nearly zero accelerations at the knots ($h/4$ and $3h/4$), barely acceptable displacements for horizontal

excitation, and very bad ones for a vertical excitation. Top accelerations due to vertical excitation were slightly better than when a horizontal excitation was applied, Figure 16.17(b).

3. 2D present model gave excellent top acceleration ($\sim$ 1.0), nearly zero ones at the knots (half as large as those predicted by Lysmer), and a deformation which indeed is consistent with a shear beam. It should be noted that best results are achieved when both terms where included (C and K). Similarly, excellent results were obtained for vertical excitation (the importance of including both terms was more accentuated than for the horizontal acceleration), Figure 16.17(c).
4. The 3D analysis based on Lysmer's model yields top acceleration slightly higher than 1.0, a good deformation, and not quite a homogeneous velocity distribution, Figure 16.18(a).

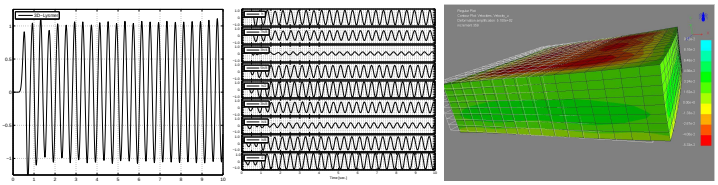

(a) Lysmer

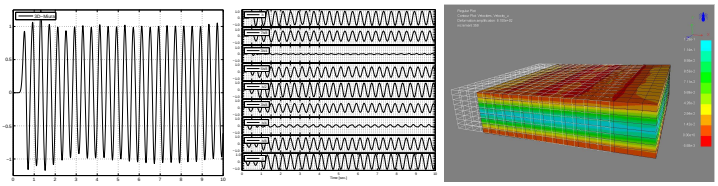

(b) Miura-Saouma

Fig. 16.18: Selected results for 3D analyses; Crest accelerations, accelerations at $h =$ 0, h/8, h/4, 3h/8, h/2, 5h/8, 3h/4, 7h/8 and h; deformed shapes with contour lines of V_X

5. The 3D analysis based on the present model yielded a nearly perfect acceleration distribution from bottom to top, a very smooth deformation and internal velocity distribution, Figure 16.18(b).

In summary, Lysmer's model performs better in 3D than in 2D, whereas the Miura-Saouma model yields excellent results in all analyses.

16.4 Modeling Aspects

Returning to the rocking consideration articulated in Section16.1.1 and the importance of free-field modeling (Section16.3.3), we now re-examine modeling the foundation in the context of a dynamic nonlinear analysis and associated problems.

16.4.1 Inhibition of Lateral Rigid Body Motion

Though this chapter addresses soil structure interactions, there would be problems in visualizing results since the corresponding analysis is dynamic.
The reason is because in a dynamic analysis there is no lateral restraint as excitation is applied along this direction. As a result, visualization of deformed shapes can be problematic as the mesh is likely to undertake a rigid body motion (without loss of fidelity as the internal stresses are a function of relative displacements). However, in a graphical post-processor, this makes it difficult to visualize the deformed shape as the rigid body motion is of such a magnitude to obliterate the relative displacements. A simple remedy to this is the insertion of lateral "soft" springs to greatly limit the rigid body motion.

16.4.2 Alternative Boundary Conditions for Dynamic Analysis

Based on the preceding, it is by now evident that there are up to eight different sets of boundary conditions that can be applied for the dynamic analysis of massive structures. Those are summarized in Table 16.1.

Table 16.1: Evaluation of Various Boundary Conditions

Criteria	1	2	3	4	5	6	7	8
Rocking	Y	Y	Y	N	N	Y	N	N
Radiation Damping	N	Y	Y	Y	Y	Y	Y	Y
Free Field	N	N	N	N	N	Y	Y	Y
Vertical Excitation	N	N	N	Y	Y	N	N	N
Gravity Load Transfer	N	N	N	Y	Y	N	Y	Y
Rigid Body Motion	Y	Y	N	Y	N	N	N	N
Figure	16.19(a)	16.19(b)	16.19(c)	16.19(d)	16.19(e)	16.19(f)	16.19(g)	16.19(h)

Ultimately, it will be left to the analyst to decide which approach is most feasible to follow.

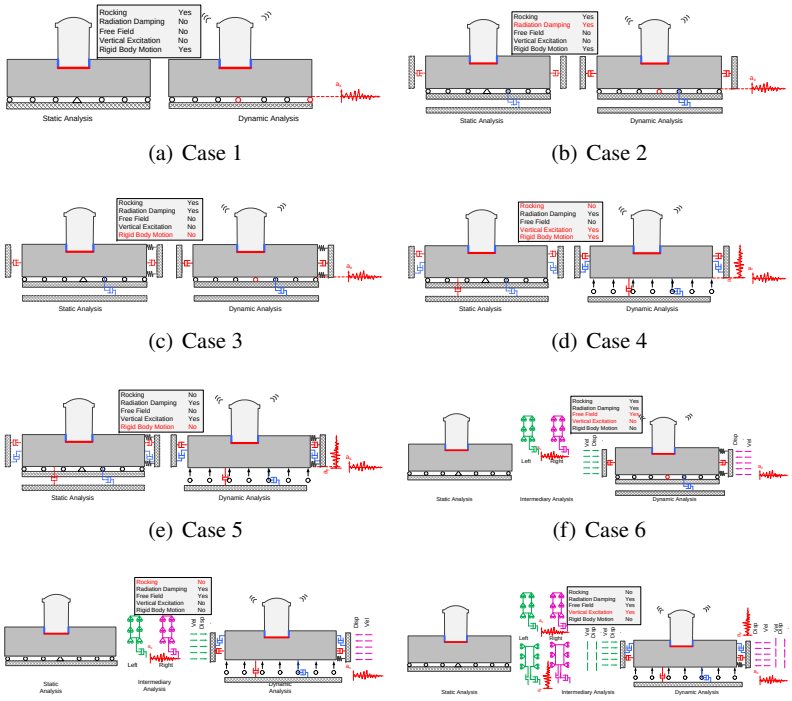

(a) Case 1 (b) Case 2

(c) Case 3 (d) Case 4

(e) Case 5 (f) Case 6

(g) Case 7 (h) Case 8

Fig. 16.19: Soil structure interaction models

Chapter 17
Fluid Structure Interactions

Abstract
Fluid-structure interaction (FSI) is the interaction of some movable or deformable structure with an internal or surrounding fluid flow. FSI is an interdisciplinary research field with several applications in structural engineering, e.g., interaction of reservoir water, dam, and the surrounding canyon, or dynamic interaction of wind with high-rise towers.
The focus of FSI in this book will be on dam engineering application in static and dynamic conditions.

17.1 Uplift

At first [133], the fluid-soil-interaction was investigated by Terzaghi and Rendulic [826] and his archival Filunger [315]. Eventually, this led to the investigation of the fluid-structure-interaction along cracks, or more prosaically uplift [827, 168]. The importance of uplift as an active force to be reckoned with in the stability of dams, Figure 17.1, was quickly acknowledged.

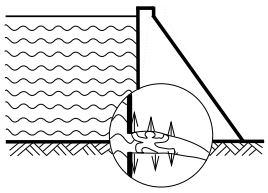

Fig. 17.1: Uplift pressures in a dam

By now, uplift models have been refined to account for upstream and downstream pool elevations, location (and elevation) of drains, as well as the drain effectiveness (clogged, partially clogged, or fully effective).
In the United States there are two major governmental (self-regulating) agencies that design dams: the U.S. Army Corps of Engineers [841] and the Bureau of Reclamation [725]. Most others (those that generate electricity) are regulated by

the Federal Energy Regulatory Committee (FERC) that has established its own guidelines [309].

17.1.1 Models for Rigid Body Equilibrium Analysis

All three agencies have similar guidance concerning uplift, Figure 17.2. Uplift pressures are considered in the static equilibrium analysis of a dam as a rigid body and the resultant stresses. The only major differences are the magnitude of reduction due to the site-specific drainage system and the computation of effective foundation pressures. The Bureau of Reclamation appears to use a greater reduction (67% for preliminary design) for drain effectiveness than the Corps of Engineers (25-50% based upon site evaluation). Neither the Bureau of Reclamation (for final design) nor FERC provides specific values but instead recommend that values be based upon a site evaluation. The Corps of Engineers uses a straight-line effective foundation pressure along the dam/foundation interface as determined from the resultant force based upon rigid-body analysis of the dam with all the forces, including uplift, acting on the dam. The Bureau of Reclamation and FERC subtract the uplift pressure from the foundation pressures along the dam-foundation interface based upon all the forces acting on the dam except uplift [244]. An excellent review of all three models was presented by Ebeling, Nuss, and Tracy [262] and Leclerc, M. and Léger, P. and Tinawi, R. [527].

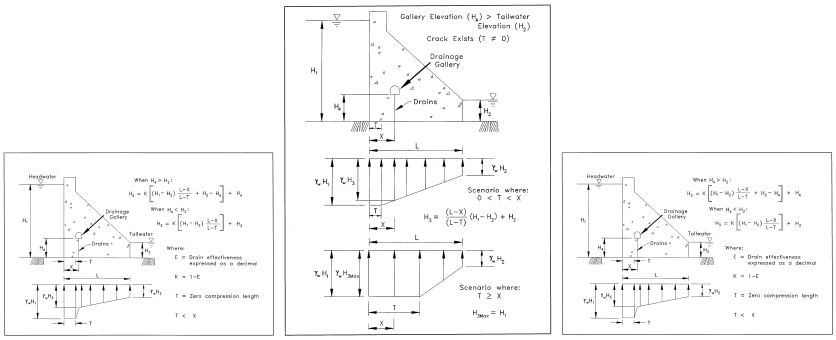

(a) Corps of Engineers (b) Bureau of Reclamation (c) Federal Energy Regulatory Commission

Fig. 17.2: Uplift models from three US agencies [262]

FERC's model is probably the most widely used and is addressed in some detail. Two cases are considered:

Crack does not extend beyond drain line then the following equations describe the uplift, Figure 17.3(a):

$$\begin{aligned} H4 > TW \Rightarrow H3 = K\left[(HW - TW)\tfrac{(L-X)}{(L-T)} + TW - H4\right] + H4 \\ H4 < TW \Rightarrow H3 = K\left[(HW - TW)\tfrac{(L-X)}{(L-T)}\right] + TW \end{aligned} \tag{17.1}$$

Crack extends beyond drain line Figure 17.3(b)

$$\begin{aligned} H4 > TW \Rightarrow H3 = K(HW - H4) + H4 \\ H4 < TW \Rightarrow H3 = K(HW - TW) + TW \end{aligned} \tag{17.2}$$

Where $K = (1 - E)$, and E is the drain effectiveness that must be verified by instrumentation (and is valid only for the reservoir loading at which the measurement was taken) and an effective maintenance plan.

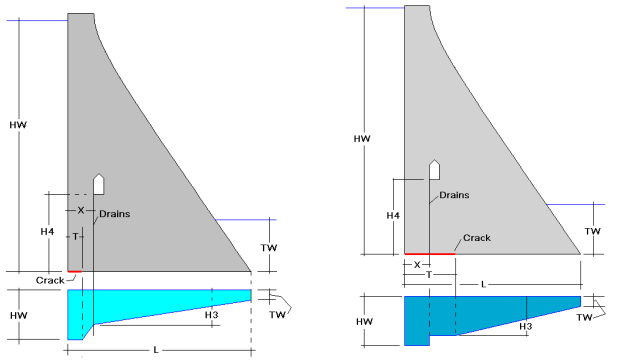

(a) Crack does not extend beyond drain line

(b) Crack extends beyond drain line

Fig. 17.3: Details of the FERC uplift model [309]

17.1.2 Finite Element Modeling of Uplift

Whereas the applicability of uplift models to rigid body equilibrium analysis is straightforward, their implementation in the context of a finite element simulation is more problematic. Among the three pre-cited agencies, only FERC [309, Fig. 11] provides some general guidance to finite element modeling of uplift, Figure 17.4:

> *The use of a thin interface layer of elements (standard Q4 elements) allows the uplift pressure to be applied to the bottom of the dam and the top of the foundation. ... The procedure also has the benefit of allowing interface elements to be systematically deleted so that a cracked base analysis may be performed in an iterative manner.*

Such an approach fails to recognize the singularity at the tip of the crack and the extent to which results will be mesh dependent [99]. Dewey, Reich, and Saouma [244] presented three different models for uplift modeling.

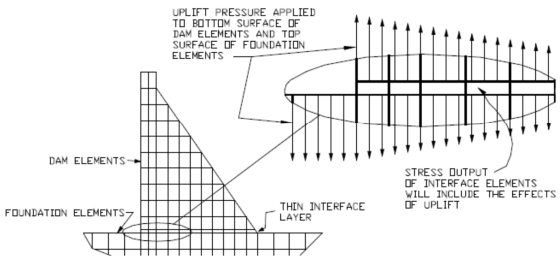

Fig. 17.4: FERC finite element model for uplift [309, Fig. 11]

Model 1: Fictitious crack elements, described in Section 15.3 are used along the concrete-rock interface, Figure 17.5(a). These (mesh-size insensitive) elements not only properly model the (unzipping) interface, but can be easily subjected to tractions on either side to model the uplift. Furthermore, uplift can be automatically adjusted to reflect the extent of cracking.

Model 2: The crack is inside an zone of elements with initial pore pressure (Section 1.4.4.4) adjusted to reflect the uplift pressure diagram. Those elements should be "isolated" from those elements above or below them through master-slave connections for the pore pressure effects not to diffuse into the rest of the mesh.

Model 3: A separate seepage (discussed separately) analysis must be performed for the foundation, Figure 17.5(c).

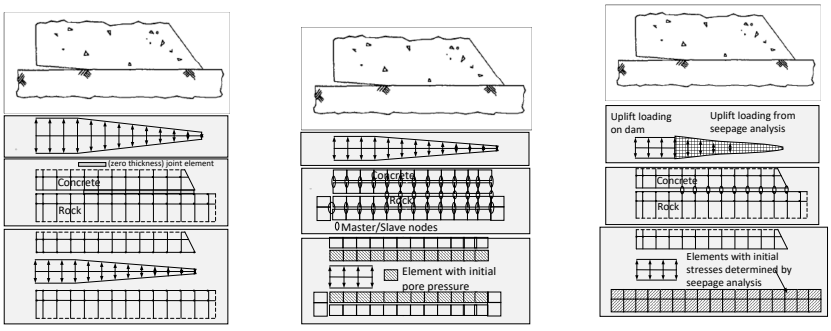

(a) Model 1 (b) Model 2 (c) Model 3

Fig. 17.5: Finite element models to model uplift; a) Dam; b) Assumed uplift loading; c) Finite element discretization; d) Loading on finite element model

Finally, a word of caution: Many reported (nonlinear) finite analyses of dam stability do not update the uplift profile as the crack extends, and the initially prescribed one remains constant. This will lead to un-conservative results.

17.1.3 Steady State Seepage Analysis

Steady state seepage analysis is governed by Darcy's law (Section 2.2.1) and will provide the best uplift profile as it will take into account drainage efficiencies and their spatial distribution. Whereas a seepage analysis with isotropic rock conductivity is likely to yield a linear steady state pressure distribution, such an analysis should be undertaken for orthotropic cases or three dimensional meshes, Figure 17.6.

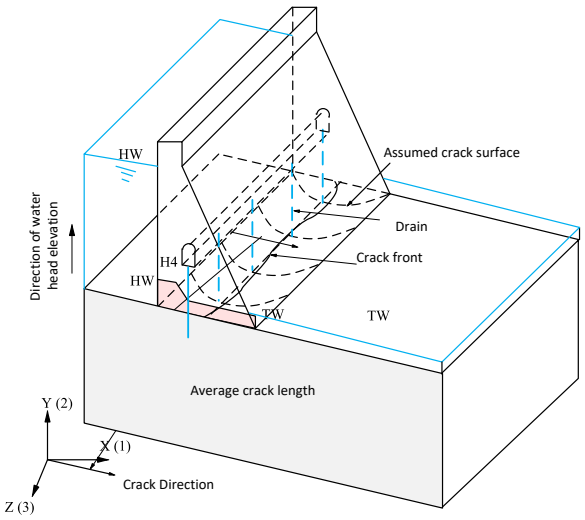

Fig. 17.6: Three-dimensional uplift model in Saouma, Červenka, and Reich [767]

Material properties required for a steady-state seepage flow analysis are summarized in Table 17.1. Note that for isotropic hydraulic conductivities the value of the permeability can be arbitrary.

Table 17.1: Required Material Properties for Seepage Analysis

Property	Isotropic	Orthotropic
Mass density	ρ	ρ
Permeability	k	θ, k_1, k_2

In most cases, individual joints are not modeled, and hence the permeability should be that of a homogeneous continuum equivalent to the jointed rock system. Alternatively, joints can be easily modeled (assuming that the joint permeability can be properly estimated).
In seepage problems, the primary field variable, Φ, is the hydraulic potential (or hydraulic/piezometric head), h; k_x and k_y are the permeabilities (m/day) and c the storativity. The fluid velocity (or fluxes) components are obtained from Darcy's law as:

$$v_x = -k_x \frac{\partial \Phi}{\partial x} \qquad v_y = -k_y \frac{\partial \Phi}{\partial y} \tag{17.3}$$

Lines of Φ = constant are called equipotential surfaces, across which flow occurs. Two types of boundary conditions are applicable, Figure 17.7:

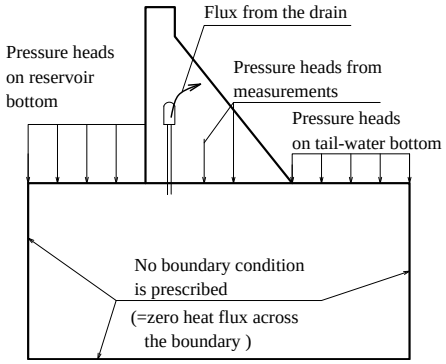

Fig. 17.7: Boundary Conditions for Seepage Analysis

Prescribed head: .

1. Caused by the known pressure head on the upstream and downstream sides.
2. Experimentally measured through piezometer readings.

Prescribed flux: .

1. Zero flux should be specified around the surface of the rock mass.
2. A point flux may be caused by a known flow through a drain.

Such an (uncoupled) steady state finite element analysis can be performed with many finite element codes, and results may have to be transferred to the code performing the subsequent stress analysis.

17.1.4 Dynamic Uplift

Whereas the static uplift pressures are well known, the same can not be said about the dynamic uplift that would occur during an earthquake. Indeed two distinct phenomena may occur. During crack closure, there can be a "wedge effect" where the water can not be expelled rapidly enough causing a spike in the uplift pressure. On the other hand, during rapid crack opening, there is undoubtedly a reduction in the uplift pressure and possibly cavitation (negative pressure), Figure 17.8. Few researchers have addressed this problem with notable exceptions [474].

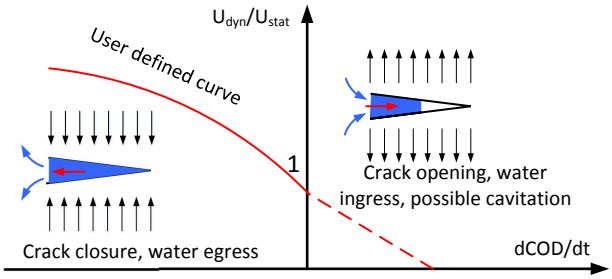

Fig. 17.8: Dynamic uplift

In this context, it should be noted that

> *'In a departure from the way the FERC has previously considered seismic loading, there is no longer any acceptance criteria for stability under earthquake loading. Factors of safety under earthquake loading will no longer be evaluated. Acceptance criteria is based on the dam's stability under post earthquake static loading considering damage likely to result from the earthquake.*

which makes considerations of dynamic uplift irrelevant unless one needs to predict the damaged state of a dam following an earthquake (as opposed to a *post-mortem* analysis based on *in-situ* damage assessment).

17.2 Hydro-Dynamic Pressures

Hydrodynamic forces can play an important role in the seismic response of a dam and hence must be accounted for. There are two distinct approaches. The first replaces the reservoir by added lumped masses, and the second explicitly models the reservoir. In this case there are two approaches: a) displacement based formulation and b) potential-based fluid finite elements. All these models are discussed below.

17.2.1 Lumped Mass Models

17.2.1.1 Westergaard

During an earthquake, the interaction between the gravity dam and the reservoir creates additional pressures on the upstream face of the dam. These hydrodynamic pressures may be approximated by the Westergaard [878] formula, which uses a parabolic approximation for the additional pressures due to earthquake motion. Westergaard defines the hydrodynamic pressure p and force q at depth z measured from base of the dam, with total reservoir height H_w, as:

$$p(z) = C_e \alpha \sqrt{H_w (H_w - z)} \tag{17.4}$$

$$q(z) = \frac{2}{3} C_e \alpha (H_w - z) \sqrt{H_w (H_w - z)} \tag{17.5}$$

where α measures the intensity of the earthquake by the relation $a = \alpha g$, where a is the maximum horizontal acceleration and g the acceleration of gravity. At the bottom of the reservoir, $z = 0$, the maximum hydrodynamic pressure, p_0, is:

$$p_0 = C_e \alpha H_w \tag{17.6}$$

and the total resultant force, q_0, is:

$$q_0 = \frac{2}{3} C_e \alpha H_w^2 \tag{17.7}$$

These parameters are illustrated in Figure 17.9.

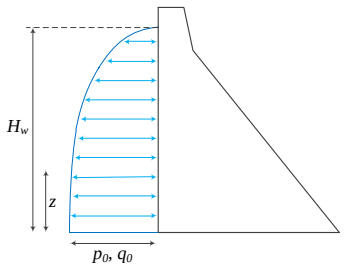

Fig. 17.9: Hydrodynamic water pressure and force

The coefficient C_e is a correction factor to account for water compressibility. Leclerc, M. and Léger, P. and Tinawi, R. [527] define this parameter as:

$$\begin{aligned} C_e &= 7.99 C_c \\ C_c &= \frac{1}{\sqrt{1-7.75\left(\frac{H_w}{1000T}\right)^2}} \end{aligned} \tag{17.8}$$

where T is the period to characterize the ground seismic acceleration imposed on the dam. In this relation, units are in kilonewtons, meters, and seconds.
If the upstream face of the dam is sloped, a correction factor K_θ should be applied to the p and q relations in Eqs. 17.4 and 17.5. For an angle of slope θ from the vertical, the correction factor is simply $K_\theta = \cos^2\theta$. The final expressions for the hydrodynamic pressure and force are then:

$$p(z) = C_e \alpha K_\theta \sqrt{H_w(H_w - z)} \tag{17.9}$$

$$q(z) = \frac{2}{3} C_e \alpha K_\theta (H_w - z)\sqrt{H_w(H_w - z)} \tag{17.10}$$

According to Westergaard [878], one can visualize the dynamic action of water on the upstream face of a dam by thinking of a certain body of water in the reservoir as moving with the dam while the remainder of the reservoir remains inactive. Westergaard has shown that the shape of this body of water is parabolic, with the vertex of the parabola located at the reservoir surface.
Westergaard states that at any depth, the corresponding added mass per unit area of the upstream face of the dam is:

$$\gamma_{lump}(z) = \frac{p(z)}{\alpha g} \tag{17.11}$$

The hydrodynamic pressure (which also assumes a parabolic distribution on the dam face) is defined by

$$p(z) = C\alpha\sqrt{H_w(H_w - z)} \tag{17.12}$$

where C is a constant:

$$C = \frac{K}{\sqrt{1 - \frac{16\rho_w H_w^2}{gkT^2}}} \tag{17.13}$$

where K is a constant defined by Westergaard as $K = 8,011.4$ N/m^3, k is the elastic modulus of water, and T is the period of ground horizontal vibration.
Combining these relations and canceling when possible results in the final relation to determine the lumped mass per unit area of the upstream dam face due to dynamic action of the water on the dam:

$$\gamma_{lump}(z) = \frac{K\sqrt{H_w(H_w - z)}}{g\sqrt{1 - \frac{16\rho_w H_w^2}{gkT^2}}} \tag{17.14}$$

It should be noted that in his original paper, Westergaard did go through an additional simplification of the preceding equation (removing the dependency on T) yielding:

$$\gamma_{lump}(z) = \frac{7}{8}\rho_w\sqrt{H_w(H_w - z)} \tag{17.15}$$

which is most often referenced in the literature, yet it is less exact than Eq. 17.14. Figure 17.10 shows the differences between the approximate and exact solutions based on the aforementioned equations for a hypothetical dam model in which the water level, H_w, is 100 m.

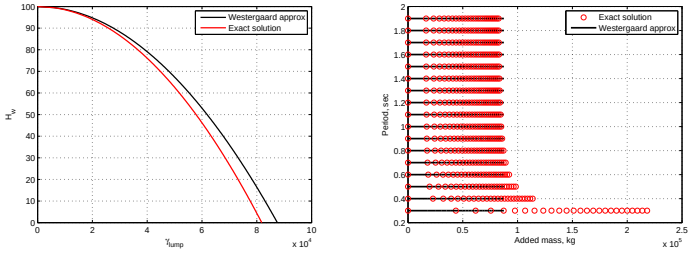

(a) Lumped mass per unit area versus the height

(b) Added mass versus the vibration period

Fig. 17.10: Comparison of the approximate and exact solutions for a hypothetical dam

17.2.1.2 Zangar

Using an electric analog, Figure 17.11, Zangar [904] determined experimentally the hydrodynamic effect of horizontal earthquake action on dams having upstream faces with either constant or compound slopes.
The pressure is given by

$$P_{hyd} = C\alpha\rho_w H_w \tag{17.16}$$

where P_{hyd} is the increase in pressure, α is the intensity of the horizontal earthquake (a/g), ρ_w is the mass density of water, H_w is the height of the water reservoir, and C is a coefficient given by:

$$C = \frac{C_m}{2}\left[\frac{z}{H_w}\left(2 - \frac{z}{H_w}\right) + \sqrt{\frac{z}{H_w}\left(2 - \frac{z}{H_w}\right)}\right] \tag{17.17}$$

and C_m is the maximum value of C given by Figure 17.12(a).
Finally, the lumped mass will be given by

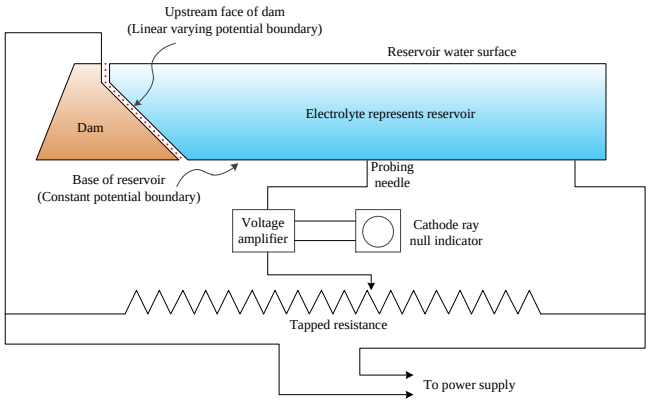

Fig. 17.11: Electric Analog Tray Model used by [904]

$$\gamma_{lump} = \frac{C\alpha\rho_w H_w}{\alpha g} \tag{17.18}$$

Figure 17.12(b) shows the values of the pressure coefficient with respect to the normalized height.

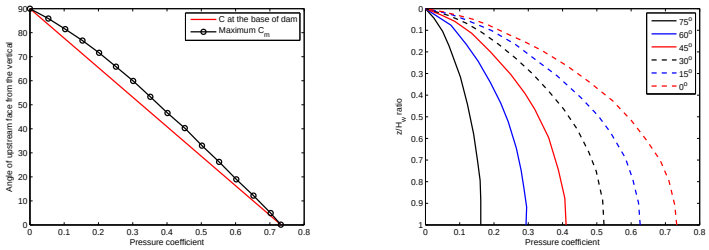

(a) Increase pressure coefficients for constant sloping faces

(b) Pressure coefficient distribution along the height

Fig. 17.12: Zangar [904] model

17.2.2 Continuum Model I: Displacement Based Formulation

From elasticity we have the following fundamental relations

$$\varepsilon_V = \frac{\mathrm{d}V}{V} = \varepsilon_{xx} + \varepsilon_{yy} + \varepsilon_{zz} \tag{17.19}$$

$$B = \frac{E}{3(1-2\nu)} \tag{17.20}$$

$$p = -B\varepsilon_V = -\frac{\sigma_{xx} + \sigma_{yy} + \sigma_{zz}}{3} \tag{17.21}$$

The stress strain relation is given by

$$\sigma_{ij} = \lambda u_{k,k} + 2G\varepsilon'_{ij} \tag{17.22}$$

where ε'_{ij} is the deviatoric strain:

$$\varepsilon'_{ij} = \varepsilon_{ij} - \frac{\varepsilon_V}{3}\delta_{ij} \tag{17.23}$$

As ν approaches 0.5 (water being incompressible), resistance to volume change greatly increases assuming that the shear resistance remains constant:

$$\frac{B}{G} = \frac{2(1+\nu)}{3(1-2\nu)} \tag{17.24}$$

Also since

$$\lambda = \frac{2\nu G}{1-2\nu} \tag{17.25}$$

it is clear that as ν approaches 0.5, the stress becomes unbounded and an alternative formulation will be needed:

$$\sigma_{ij} = \underbrace{-B\varepsilon_V}_{-p}\delta_{ij} + 2G\varepsilon'_{ij} \tag{17.26}$$

Now p becomes part of the solution as an additional unknown leading to a mixed formulation.

Water has an elastic and shear modulus of 0, a Poisson ratio of 0.5, and a bulk modulus of 2.1 GPa. However under dynamic loading, viscosity and boundary layer effects allow fluids to resist shear [54].

In light of the above, the traditional displacement based element formulation can be modified to model a "nearly" incompressible fluid (say $E = 6 \times 10^{-4}$ GPa and $\nu = 0.499995$) through simple modification of the element integration scheme.

The stiffness matrix is given by (Eq.13.42)

$$\mathbf{K} = \int_\Omega \mathbf{B}^T\mathbf{D}\mathbf{B}\mathrm{d}\Omega \tag{17.27}$$

In terms of G and B, the constitutive matrix (Section 1.4.4 and Eq. 13.29) is given by

$$\mathbf{D} = B \underbrace{\begin{bmatrix} 1&1&1&0&0&0 \\ 1&1&1&0&0&0 \\ 1&1&1&0&0&0 \\ 0&0&0&0&0&0 \\ 0&0&0&0&0&0 \\ 0&0&0&0&0&0 \end{bmatrix}}_{\mathbf{D}_B} + G \underbrace{\begin{bmatrix} 4/3 & -2/3 & -2/3 & 0&0&0 \\ -2/3 & 4/3 & -2/3 & 0&0&0 \\ -2/3 & -2/3 & 4/3 & 0&0&0 \\ 0 & 0 & 0 & 1&0&0 \\ 0 & 0 & 0 & 0&1&0 \\ 0 & 0 & 0 & 0&0&1 \end{bmatrix}}_{\mathbf{D}_G} \tag{17.28}$$

where the first term corresponds to the volumetric state and the second to the deviatoric one. Hence, we can rewrite

$$\mathbf{K} = B \int_{\Omega} \mathbf{B}^T \mathbf{D}_B \mathbf{B} \mathrm{d}\Omega + G \int_{\Omega} \mathbf{B}^T \mathbf{D}_G \mathbf{B} \mathrm{d}\Omega \tag{17.29}$$

or

$$(G\mathbf{K}_G + B\mathbf{K}_B)\overline{u} = \overline{\mathbf{p}} \tag{17.30}$$

As ν approaches 0.5, the bulk modulus B approaches infinity, and therefore $B\mathbf{K}_B$ acts as a penalty matrix that enforces the constraint of incompressibility. We will have numerical problems, and finally the mesh "locks" unless $\mathbf{K}_B$ is singular. The $\mathbf{K}_B$ is made singular by reducing the order of numerical quadrature employed to evaluate $\mathbf{K}_B$ below that "normal" used.
Hence a selective reduced numerical integration is performed, a regular one for $\mathbf{K}_G$ and reduced for $\mathbf{K}_B$. Because the linear triangular element uses a one point numerical integration scheme, it can not be used for fluid elements. Finally, we can have a viscous damping matrix $\mathbf{C}$

$$\mathbf{C} = \int_{\Omega} \mathbf{B}^T \mathbf{D}_G \mathbf{B} \mu \mathrm{d}\Omega \tag{17.31}$$

where μ is the dynamic coefficient of viscosity.

17.2.3 Continuum Model II: Pressure Based Formulation

17.2.3.1 Governing Equations

The governing equation of motion in the fluid is given by the Laplacian equation:

$$\bigtriangledown^2 P = 0 \tag{17.32}$$

where P is the hydrodynamic pressure developed within the fluid domain. In order to solve the above equation using the finite element technique, a set of appropriate boundary conditions are required as discussed in the following sections.

17.2.3.1.1 Boundary Condition at Fluid-Solid Interface On the interface of fluid and solid, there is no flow. The appropriate boundary condition on the interface is given as:

$$\frac{\partial P}{\partial n} = -\rho a_n^s \tag{17.33}$$

in which n and a_n^s are the outward normal direction to the solid and normal acceleration applied on the fluid on the interface, respectively, and ρ is the fluid density.

17.2.3.1.2 Boundary Condition at Free Surface Considering small amplitude gravity waves on the free surface of the fluid, the resulting boundary condition is given as:

$$\frac{1}{g}\frac{\partial^2 P}{\partial t^2} + \frac{\partial P}{\partial z} = 0 \tag{17.34}$$

in which z is the vertical direction and g is acceleration of gravity.

17.2.3.1.3 Discretized Equation of Fluid Domain Using Galerkin's technique, the discretized finite element governing equation of motion in fluid domain is given as:

$$[G]\{\ddot{P}\} + [C_f]\{\dot{P}\} + [K_f]\{P\} = \{F\} \tag{17.35}$$

in which

$$G_{ij}^e = \frac{1}{g}\int_{A_e} N_i N_j dA \tag{17.36}$$

$$H_{ij}^e = \int_{V_e}\left(\frac{\partial N_i}{\partial x}\frac{\partial N_j}{\partial x} + \frac{\partial N_i}{\partial y}\frac{\partial N_j}{\partial y} + \frac{\partial N_i}{\partial z}\frac{\partial N_j}{\partial z}\right)dV \tag{17.37}$$

$$\{F\} = \{F_i\} - \rho[Q]^T\left(\{\ddot{U}\} + \{\ddot{U}_g\}\right) \tag{17.38}$$

$$F_i^e = \int_{A_e} N_i \frac{\partial P}{\partial n} dA \tag{17.39}$$

where N_i, $\{\ddot{U}\}$, $\{\ddot{U}_g\}$, $[Q]$, and $[C_f]$ are the shape function of the ith node in the fluid element, acceleration vector of nodes in the structure domain, ground acceleration vector applied on the system, coupling matrix, and damping matrix of the fluid domain, respectively.

17.2.3.1.4 Coupling Matrix The coupling matrix, $[Q]$, transfers pressures applied on the fluid-solid interface as nodal forces to the solid domain. In the present formulation, this matrix is generated by proportional lumping method. For eight-node interface elements with x, y, and z translational DOF at each node on the face of the structure and corresponding four node interface elements with pressure DOF at each node attached to the fluid element, the coupling matrix is given as:

$$[Q] = \omega \int_{-1}^{+1} \int_{-1}^{+1} \begin{bmatrix} \alpha_1 N_1^s N_1^s N_1^f & & \alpha_1 N_1^s N_1^s N_4^f \\ \beta_1 N_1^s N_1^s N_1^f & \cdots & \beta_1 N_1^s N_1^s N_4^f \\ \gamma_1 N_1^s N_1^s N_1^f & & \gamma_1 N_1^s N_1^s N_4^f \\ \vdots & \ddots & \vdots \\ \alpha_8 N_8^s N_8^s N_1^f & & \alpha_8 N_8^s N_8^s N_4^f \\ \beta_8 N_8^s N_8^s N_1^f & \cdots & \beta_8 N_8^s N_8^s N_4^f \\ \gamma_8 N_8^s N_8^s N_1^f & & \gamma_8 N_8^s N_8^s N_4^f \end{bmatrix} \|t_\xi \times t_\eta\| \, d\xi d\eta \quad (17.40)$$

where

$$t_\xi = \left\{ \frac{\partial x}{\partial \xi}, \frac{\partial y}{\partial \xi}, \frac{\partial z}{\partial \xi} \right\}^T \quad (17.41)$$

$$t_\eta = \left\{ \frac{\partial x}{\partial \eta}, \frac{\partial y}{\partial \eta}, \frac{\partial z}{\partial \eta} \right\}^T \quad (17.42)$$

$$\omega = \frac{A}{\sum_{i=1}^{8} \int_{A_e} N_i^s N_j^s \, \|t_\xi \times t_\eta\| \, d\xi d\eta} \quad (17.43)$$

$$A = \int_{A_e} \|t_\xi \times t_\eta\| \, d\xi d\eta \quad (17.44)$$

and N_f and N_s are the shape functions in the fluid and solid domains, respectively.

17.2.3.1.5 Damping within the Fluid Domain The damping matrix within the fluid domain includes two terms, which are originated from impulsive and convective parts as follows:

$$[C_f] = a[G] + b[K_f] \quad (17.45)$$

in which a and b are computed based on Ryleigh damping. However, a is computed based on the fundamental vibration frequency of the free surface waves, and b is computed based on the fundamental frequency of the impulsive component.

17.2.3.2 Coupled Equations of the Solid and Fluid

The solid-fluid problem is a classical coupled problem which contains two second-order differential equations. The equations of the structure and the fluid are written in the following form:

$$\begin{cases} [M]\{\ddot{U}\} + [C]\{\dot{U}\} + [K]\{U\} = \{f_1\} - [M]\{\ddot{U}_g\} + [Q]\{P\} = \{F_1\} + [Q]\{P\} \\ [G]\{\ddot{P}\} + [C_f]\{\dot{P}\} + [K_f]\{P\} = \{F\} - \rho[Q]^T \left(\{\ddot{U}\} + \{\ddot{U}_g\} \right) = \{F_2\} - \rho[Q]^T \{\ddot{U}\} \end{cases} \quad (17.46)$$

17.2.3.2.1 Time-Stepping Scheme of the Coupled Equations In the present approach, direct integration scheme is used to find the displacement and hydrodynamic pressure at the end of the time increment $i+1$ given the displacement and hydrodynamic pressure at time i. The α-method is used for discretization of both equations

(implicit-implicit method). In this method $\{U\}_{i+1}$, $\{\dot{U}\}_{i+1}$, $\{P\}_{i+1}$, and $\{\dot{P}\}_{i+1}$ can be written as follows:

$$\begin{cases} \{\dot{U}\}_{i+1} = \{\dot{U}\}_{i+1}^{P} + \gamma\Delta t\{\ddot{U}\}_{i+1} \\ \{\dot{U}\}_{i+1}^{P} = \{\dot{U}\}_{i} + (1-\gamma)\Delta t\{\ddot{U}\}_{i} \end{cases} \tag{17.47}$$

$$\begin{cases} \{U\}_{i+1} = \{U\}_{i+1}^{P} + \beta\Delta t^2\{\ddot{U}\}_{i+1} \\ \{U\}_{i+1}^{P} = \{U\}_{i} + \Delta t\{\dot{U}\}_{i} + (1-\beta)\Delta t^2\{\ddot{U}\}_{i} \end{cases} \tag{17.48}$$

$$\begin{cases} \{\dot{P}\}_{i+1} = \{\dot{P}\}_{i+1}^{P} + \gamma\Delta t\{\ddot{P}\}_{i+1} \\ \{\dot{P}\}_{i+1}^{P} = \{\dot{P}\}_{i} + (1-\gamma)\Delta t\{\ddot{P}\}_{i} \end{cases} \tag{17.49}$$

$$\begin{cases} \{P\}_{i+1} = \{P\}_{i+1}^{P} + \beta\Delta t^2\{\ddot{P}\}_{i+1} \\ \{P\}_{i+1}^{P} = \{P\}_{i} + \Delta t\{\dot{P}\}_{i} + (1-\beta)\Delta t^2\{\ddot{P}\}_{i} \end{cases} \tag{17.50}$$

where γ and β are the integration parameters. The governing field equations at time $i+1$ can be written as follows:

$$\begin{cases} [M]\{\ddot{U}\}_{i+1} + [C]\{\dot{U}\}_{i+1} + (1+\alpha)[K]\{U\}_{i+1} = \{F_1\}_{i+1} + [Q]\{P\}_{i+1} + \alpha[K]\{U\}_{i} \\ [G]\{\ddot{P}\}_{i+1} + [C']\{\dot{P}\}_{i+1} + (1+\alpha)[K']\{P\}_{i+1} = \{F_2\}_{i+1} - \rho[Q]^T\{\ddot{U}\}_{i+1} + \alpha[K']\{P\}_{i} \end{cases} \tag{17.51}$$

These two coupled field equations can be solved using the staggered displacement solution scheme, in which the first equation is approximated as follows:

$$[M]\{\ddot{U}\}_{i+1}^{*} = \{F_1\}_{i+1} + [Q]\{P\}_{i+1}^{P} - [C]\{\dot{U}\}_{i+1}^{P} - (1+\alpha)[K]\{U\}_{i+1}^{P} + \alpha[K]\{U\}_{i} \tag{17.52}$$

then

$$[M]\{\ddot{U}\}_{i+1} = [M]\{\ddot{U}\}_{i+1}^{*} + \beta\Delta t^2[Q]\{\ddot{P}\}_{i+1} - \gamma\Delta t[C]\{\ddot{U}\}_{i+1} - (1+\alpha)\beta\Delta t^2[K]\{\ddot{U}\}_{i+1} \tag{17.53}$$

By neglecting higher order terms, the previous equation is modified as:

$$[M]\{\ddot{U}\}_{i+1} = [M]\{\ddot{U}\}_{i+1}^{*} + \beta\Delta t^2[Q]\{\ddot{P}\}_{i+1} \tag{17.54}$$

Substituting Eq. 17.54 into the second equation in 17.51, then:

$$\begin{aligned} &\left([G] + \rho\beta\Delta t^2[Q]^T[M]^{-1}[Q]\right)\{\ddot{P}\}_{i+1} + [C']\{\dot{P}\}_{i+1} + (1+\alpha)[K']\{P\}_{i+1} \\ &= \{F_2\}_{i+1} - \rho[Q]^T\{\ddot{U}\}_{i+1}^{*} + \alpha[K']\{P\}_{i} \end{aligned} \tag{17.55}$$

The right hand side terms are known; thus, $\{P\}_{i+1}$ is obtained. In order to correct the approximation made in Eq. 17.54, $\{P\}_{i+1}$ is substituted in the first equation of Eq. 17.51 to calculate $\{U\}_{i+1}$ and its derivatives. The procedure of the staggered displacement method can be summarized as:

- Solve Eq. 17.52 to calculate $\{\ddot{U}\}_{i+1}^{*}$
- Substitute $\{\ddot{U}\}_{i+1}^{*}$ in Eq. 17.55 and calculate $\{P\}_{i+1}$
- Substitute $\{P\}_{i+1}$ in the first equation of Eq. 17.51 to calculate $\{\ddot{U}\}_{i+1}$ and its derivatives

This method is unconditionally stable for the linear coupled equations whereas for the nonlinear systems, the numerical solution stability depends on the length of the time steps and the introduced numerical damping.

17.2.3.3 Dam-Reservoir Interaction Boundary Conditions

While the equations in the previous sections are general for any fluid-solid interaction, in the case of dam-reservoir interaction some specific boundary conditions might be used. This section presents the equation of the coupled fluid-solid interaction specifically for a dam-reservoir system based on the pressure-based formulation for the fluid domain. Let Ω_S be the solid domain with two sub-domains for dam, Ω_{S1}, and foundation, Ω_{S2}, Figure 17.13. The equation of the solid domain in displacement formulation is:

$$\rho_S \frac{\partial^2 u_i}{\partial t^2} - \frac{\partial \sigma_{ij}(\mathbf{u})}{\partial x_j} = 0, \quad in\ \Omega_S \tag{17.56}$$

where $\mathbf{u}$ is the displacement in solid domain, $\sigma(\mathbf{u})$ is the stress tensor, and ρ_S is the solid part density.

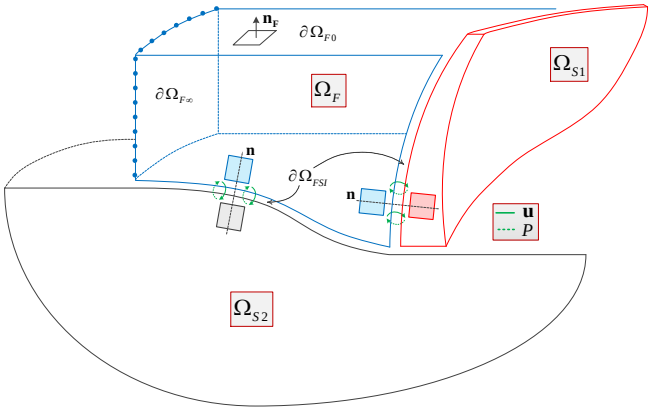

Fig. 17.13: Dam-reservoir-massed foundation coupled system and boundary conditions

On the other hand, Ω_F is the fluid domain with boundary $\partial\Omega_F = \partial\Omega_{F0} \bigcup \partial\Omega_{F\infty} \bigcup \partial\Omega_{FSI}$, where $\partial\Omega_{F0}$ is the fluid free face, $\partial\Omega_{F\infty}$ is the boundary part of the fluid which locates far from the solid-fluid interface boundary, and $\partial\Omega_{FSI}$ is the solid-fluid interface. $\mathbf{n}_F$ is the outward normal on $\partial\Omega_F$.
The equations of the fluid domain in pressure formulation can be written as follows, considering that the fluid is linearly compressible, inviscid, and having small-amplitude, convective term is neglected and irrotational motion:

$$\frac{1}{C_0^2}\frac{\partial^2 P}{\partial t^2} - \frac{\partial^2 P}{\partial x_i^2} = 0, \quad in\ \Omega_F \tag{17.57}$$

where C_0 is the sound speed of fluid and P is the pressure.
Considering small amplitude gravity waves on the free surface of the liquid, the resulting boundary condition is given as:

$$\frac{\partial^2 P}{\partial t^2} + g\frac{\partial P}{\partial x_j} n_{F\,j} = 0, \quad in\ \partial\,\Omega_{F0} \tag{17.58}$$

In practice, the effects of the surface sloshing can be neglected in high concrete dams, so the free surface boundary condition can be considered as a zero-pressure boundary. Assuming that there is no flow across the solid-fluid interface, the following boundary condition can be represented as:

$$\frac{\partial P}{\partial x_i} n_i - \frac{(1-\alpha_w)}{C_0\,(1+\alpha_w)}\frac{\partial P}{\partial t} + \rho_F \frac{\partial^2 u_i}{\partial t^2} n_i = 0, \quad in\ \partial\,\Omega_{FSI} \tag{17.59}$$

where ρ_F is mean fluid density, α_w is the wave reflection coefficient, and $\mathbf{n}$ is the inward normal on $\partial\,\Omega_{FSI}$.
It is assumed that the upstream face of concrete dams is mainly impermeable, so the second term can be neglected for the dam-reservoir interface. The wave reflection coefficient on the foundation-reservoir interface depends on the angle of incident pressure wave at the interface surface and varies between -1 and +1 for soft and hard materials, respectively.
For parts of the fluid domain that extend to infinity, it is possible to account for the infinite domain effects in the finite element formulations. In this book, the far-end truncated boundary of the reservoir is modeled using the simplified method proposed by Sommerfeld (1949):

$$\frac{1}{C_0}\frac{\partial P}{\partial t} + \frac{\partial P}{\partial x_j} n_j = 0, \quad in\ \partial\,\Omega_{F\infty} \tag{17.60}$$

17.2.3.4 Simplified Crack-Pressure Interaction

Hydrodynamic pressure effect in crack propagation and general stability of concrete dams is an important concern. Considering the opening/closing ability of the joints, it seems important to implement the water pressure at opened joints in order to make a realistic study on the behavior of dams during seismic action. Water pressure effect may be considered along the openings of the joints or in cracks of the mass concrete. Usually a discrete crack approach is used to model the contraction joints between the dam blocks. Figure 17.14 shows the general methodology for implementation of the water pressure inside the opened contraction joints. Under the static condition, only the hydrostatic pressure is applied on the upstream face. Considering that in current design practice for arch dams the effect of joint opening is ignored, no water pressure is applied inside the joints. However, under the severe seismic loading, opening of the joints due to arch tensile stresses may lead to penetration of the water inside the

joints which leads to additional pressure on inner walls of the dam blocks which could subsequently intensify the joint opening. Considering the joint opening, the total pressure is calculated at each level corresponding to the dam joint location. This pressure is applied as a resultant force perpendicular to the inner face of the blocks at the opened joint locations. Total pressure at each level and specific time is calculated as:

$$P_{tot}\left(\hat{t},h,r\right)=P_{st}\left(h\right)+P_{dyn}^{net}\left(\hat{t},h\right) \\ +\rho_F\frac{\partial^2 u_i\left(\hat{t},h,r\right)}{\partial t^2}n_i\cos\psi\overline{JOD}_r\left(\hat{t},h,r\right) \tag{17.61}$$

where $P_{tot}\left(\hat{t},h,r\right)$ is the total pressure at each specific time under dynamic loading $\hat{t}$, h is the distance from the free surface in the directional of gravitational force, r is the distance in the radial direction measured from the upstream face of the dam, $P_{st}\left(h\right)$ is the hydrostatic pressure which depends on only the level of the considered location and the water level which can be represented as $P_{st}\left(h\right)=\rho_F gh$. The parameter $P_{dyn}^{net}\left(\hat{t},h\right)$ is the net hydrodynamic pressure at the considered level at the specific time of ground shaking, ψ is the angle between the normal on $\partial\Omega_{FSI}$ and the horizontal plane, and $\overline{\mathrm{JOD}}_r\left(\hat{t},h,r\right)$ is joint opening displacement in the radial direction measured from joint mouth opening.

The equation is, in fact, the generalized model of the Zhang and Ohmachi (1998) relation for considering the hydrodynamic pressure at any node in the horizontal crack filled fully with water. The calculated total pressure then is applied as an effective force in each node of the affected element by multiplying it by effective area, A_{eff}, of that node as shown in Figure 17.14:

$$F_{eff}\left(\hat{t},h,r\right)=P_{tot}\left(\hat{t},h,r\right)\times A_{eff} \tag{17.62}$$

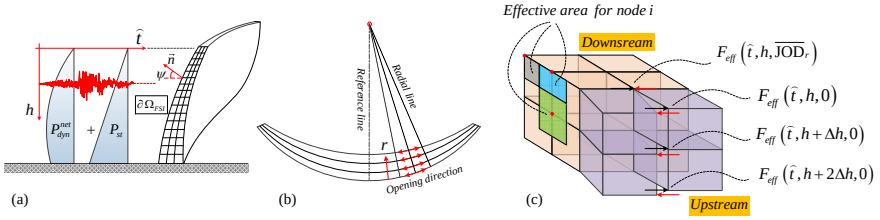

Fig. 17.14: Implementation of the water pressure inside the opened contraction joints, (a) calculation of hydrostatic and hydrodynamic pressure at considered level, (b) Joint opening direction on plane view of the dam body at considered level, (c) Calculation of effective area and force for each node

There are a set of assumptions made in this model as follows:

1. The presented model is only applicable to the discrete crack model. The effect of pressure in crack propagation of the models based on continuum crack approach is not considered.
2. No water stop (or damaged water stop) is assumed to be installed at the upstream face of the dam in the location of opened joints (this is a conservative assumption for older arch dams).
3. In practice, filling or emptying water is time dependent. However in the present model it is assumed that such a process is immediate and the time-dependency is ignored.
4. No residual water is present in the closed joint and consequently there is no water pressure.
5. Opening or closing mode can affect the distribution of the water pressure along the crack [475]. However, in the present model both opening and closing mode effects are neglected.
6. There is no interaction between crack wall motions and resulted water pressure.

Chapter 18
Uncertainty Quantification

Abstract
Uncertainty quantification (UQ) is "the science of quantitative characterization and reduction of uncertainties in both computational and real world applications." It tries to determine how likely certain outcomes are if some aspects of the system are not exactly known. This chapter discusses the fundamental concepts in UQ of structural systems, including different terminologies of risk-based assessment and failure probability.

There are two major types of UQ problems:

- Forward propagation of uncertainty: various uncertainty sources are propagated through the model to predict the overall uncertainty in the system output. Some techniques for this method are:
  - Simulation-based methods, e.g., Monte Carlo simulations.
  - Local expansion-based methods, e.g., Taylor series, and perturbation method.
  - Functional expansion-based methods, e.g., Neumann expansion, Karhunen-Loeve expansions (KLE), and polynomial chaos expansion (PCE).
  - Most probable point-based methods, e.g., first-order reliability method (FORM) and second-order reliability method (SORM).
  - Numerical integration-based methods, e.g., Full factorial numerical integration (FFNI) and dimension reduction (DR).
- Inverse assessment of model uncertainty and parameter uncertainty: the model parameters are calibrated simultaneously using test data. Examples are:
  - Frequentist
  - Bayesian

The chapter is mainly written based on Hariri-Ardebili [391], Hariri-Ardebili and Nuss [393] and Hariri-Ardebili and Pourkamali-Anaraki [395].

18.1 Uncertainty Quantification

18.1.1 Classification of Random Variables

The random variables (RVs) can be categorized as aleatory or epistemic [240]:

- Epistemic uncertainty is the scientific uncertainty in the model of the process and is due to limited data and knowledge. For continuous random variables, the epistemic uncertainty is modeled by alternative PDFs. It usually is addressed through use of a logic tree.
- Aleatory variability is the natural randomness in a process. For continuous variables, the randomness is parameterized by the PDF.
- Lexical uncertainty is due to subjective definition of parameters and hence, shows the lack of definite or sharp distinction [604].

The basic qualifier refers to directly observable quantities such as material properties (strength and stiffness), loads (earthquake magnitude and sea wave height), environmental phenomenons (temperature, alkali-aggregate reaction), and geometric dimensions (section size). Figure 18.1 show the comparison between the epistemic and aleatory universities applied to seismic hazard analysis.

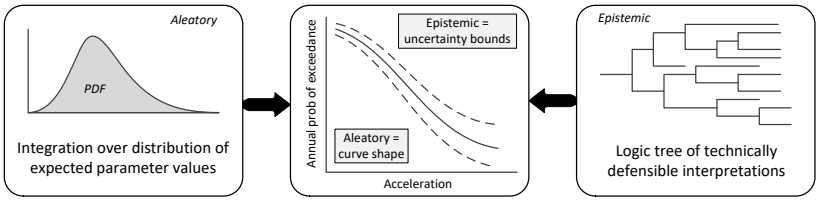

Fig. 18.1: Aleatory vs. epistemic uncertainty

18.1.2 Sensitivity Analysis

Sensitivity analysis determines the impact of a variation in an input parameter on output results. Mathematically, this corresponds to the partial derivative of the output function with respect to an input parameter at a given design point.
The procedure starts with the identification of the basic RVs, $\mathbf{X} = (X_1, \cdots, X_n)$, and their corresponding distributional model (e.g. normal, log-normal). Then, $2n+1$ analyses are performed [45] using mean (X_i^{mean}), minimum (X_i^{min}) and maximum (X_i^{max}) values of the RVs. The response can be mathematically expressed in terms of

$$\Theta = f\left(X_1, X_2, \cdots, X_i, \cdots, X_n\right) \tag{18.1}$$

A reference response Θ^{Ref} is first computed in terms of the n RVs in $S = \{1, 2, ..., n\}$ equal to their mean values

$$\Theta^{\text{Ref}} = f\left(X_i^{\text{mean}}\right), \ \forall\, i \in S \tag{18.2}$$

Then, $2n$ analyses are performed, each corresponding to a given maximum or minimum of a RV, while all others are set to their mean value

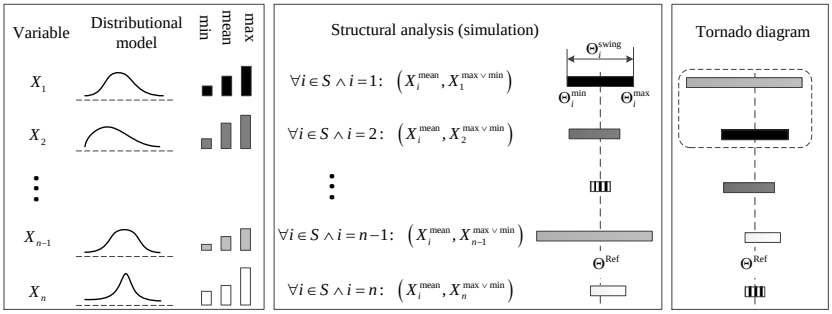

Fig. 18.2: Sensitivity analysis using Tornado diagram

$$\begin{aligned} \Theta_i^{\min} &= f\left(X_i^{\min}, X_j^{\text{mean}}\right),\ i = RV,\ \forall j \in S \wedge j \neq i \\ \Theta_i^{\max} &= f\left(X_i^{\max}, X_j^{\text{mean}}\right),\ i = RV,\ \forall j \in S \wedge j \neq i \end{aligned} \tag{18.3}$$

The swing for each of the n RVs is computed next

$$\Theta_i^{\text{swing}} = \left|\Theta_i^{\max} - \Theta_i^{\min}\right| \tag{18.4}$$

and are sorted in descending order. Finally, the Tornado diagram is plotted and one has to arbitrarily decide what are the most sensitive RVs, figure 18.2.

18.1.3 Uncertainty Analysis

The input factors of models are unfortunately not always known with a sufficient degree of certainty which can be caused by natural variations as well as by errors and uncertainties associated with measurements.
The uncertainty of input parameters is often expressed in terms of probability distributions; it can also be specified by samples of measured values, i.e. empirical probability distributions. The uncertainties of the different input parameters may have dependencies on each other, i.e. they may be correlated. Generally, the main reason for performing an uncertainty analysis is to assess the uncertainty in the model output that arises from uncertainty in the input RVs.

18.1.4 Sampling Techniques

The success and accuracy of a probabilistic based simulation hinges on the quality of its sampling techniques. Two approaches will be presented. In the first one, a finite number of simulations are performed on the basis of the standard deviations of each variable. In the second one, the user specifies the number of desired simulations (typically, but not necessarily, a “large” number).

18.1.4.1 Limited Number of Simulations

In this class of analysis, a fixed number of analyses must be performed based on the number of variables n. Two classical approaches are described below, and examples shown in Section 30.8.

18.1.4.1.1 Taylor's Series-Finite Difference Estimation This simplified approach starts with the first order Taylor series expansion about the mean and limited to linear terms, [116].

$$\mu_F = F(\mu_i) \tag{18.5}$$

where μ_i is the mean for all random variables. For independent random variables, the variance is given by

$$Var(F) = \sigma_F^2 = \sum \left(\frac{\partial F}{\partial x_i} \sigma_i \right)^2 \tag{18.6}$$

$$\frac{\partial F}{\partial x_i} \approx \frac{F_i^+ - F_i^-}{2\sigma_i} \tag{18.7}$$

$$F_i^+ = F(\mu_1, \cdots, \mu_i + \sigma_i, \cdots, \mu_n) \tag{18.8}$$

$$F_i^- = F(\mu_1, \cdots, \mu_i - \sigma_i, \cdots, \mu_n) \tag{18.9}$$

where σ_i are the standard deviations of the variables. Hence,

$$\sigma_F = \sum \left(\frac{F_i^+ - F_i^-}{2} \right) \tag{18.10}$$

Finally, the reliability index is given by Eq. 18.13.
The procedure [160] can be summarized as follows

- Perform an initial analysis in which all variables are set equal to their mean value. This analysis provides the mean μ.
- Perform $2n$ analyses, in which all variables are set equal to their mean values, except variable i, which assumes a value equal to $\mu_i + \sigma_i$, and then $\mu_i - \sigma_i$. Hence, this method requires $2n + 1$ analyses.
- For each pair of analyses in which variable x_i is modified, determine the standard deviation component associated with the specific variable i, which will provide an indication of the *sensitivity* of the results to variation of this particular variable. $\left(\frac{F_i^+ - F_i^-}{2} \right)$.
- The standard deviation of the entire structure is then determined by simply adding all the $\left(\frac{F_i^+ - F_i^-}{2} \right)$ terms.
- Having determined the mean and standard deviation of C/D, the corresponding values for the logarithm of C/D, $\mu_{\ln(C/D)}$ and $\sigma_{\ln(C/D)}$, and β are determined from Eq. 18.13.

18.1.4.1.2 Point Estimate Method In the Point Estimate Method, we select only a few points (in the design space) such that they match the mean, standard deviation, and coefficient of skewness of the distribution, [400, 889]. This is accomplished by limiting ourselves to all possible combinations of $\mu_i \pm \sigma_i$. For each analysis, we determine the ratio of capacity over demand, as well as its logarithm. Mean and standard deviation of the logarithmic values are determined from the 2^n analyses, and then β is the ratio of the mean to the standard deviation of these 2^n analyses, Eq. 18.13.

18.1.4.2 Variable Number of Simulations

Contrary to the previous section where a fixed number of simulations had to be performed on the basis of the standard deviation, this section presents an alternative where those simulations are randomly selected.
Sampling of the distributional model is indeed a key element of an uncertainty analysis.

- By far, the most widely used sampling method is the so-called Monte Carlo Simulation (MCS), described in more details in §18.3.4. Success of the crude MCS depends on a very large number of analyses. As a palliative to this handicap, an improved sampling method is achieved through the so-called Latin Hypercube Sampling (LHS) [459]. The method is explained in more details in §18.3.5.
- Pseudo-Random method: LHS guarantees samples to be drawn over the whole range of the distribution and proceeds as follows. Given a system with basic RVs, $\mathbf{X} = (X_1, ..., X_n)$ and corresponding distributions D_1, ..., D_n, first the range of each variable is split into m non-overlapping intervals of equal marginal probability $1/m$. Then, sampling starts with the random selection of an interval followed by another random selection of a point inside it. The procedure is repeated until all intervals have been accessed, and none of them more than once. This procedure is repeated for each of the n RVs.
- Quasi-Random method: Quasi-random sequences are those generated from a completely deterministic low-discrepancy process and have no inherent statistical properties. Two famous members in this group are Halton [362] (which is defined by bases of prime numbers. Each dimension is in need of a unique prime number as a base) and Sobol [797] (which benefits the base of two to construct finer uniform partitions of the unit interval and then reordering the coordinates in each dimension. It looks almost like a grid in lower dimensions, but forms a lower discrepancy pattern at higher dimensions). Figure 18.3 compares crude Monte Carlo vs. quasi Monte Carlo methods.

18.1.5 Correlation of Random Variables

It is possible to account for the correlation among the RVs. The correlation coefficient is bounded by $[-1, +1]$. It will have value of zero when the covariance (among the RVs) is zero and value of ± 1 when the RVs are perfectly correlated or anti-correlated.

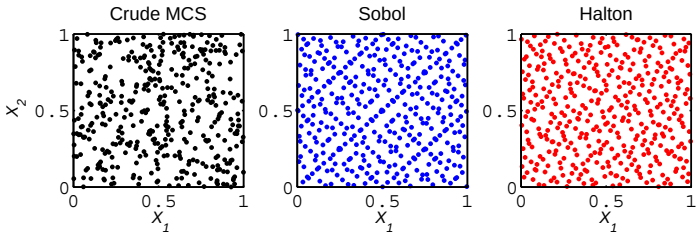

Fig. 18.3: Crude vs. quasi Monte Carlo methods

Figure 18.4 illustrated three cases with crude MCS, LHS and correlation effect, where only two RVs are assumed to exist.

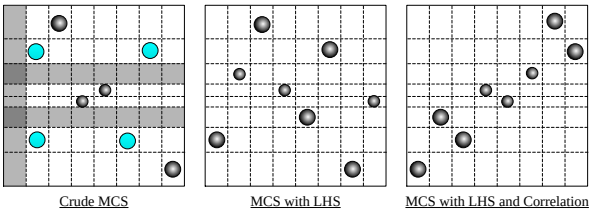

Fig. 18.4: Sampling of a system with two RVs

In general, it is possible to account for three types of correlations in engineering problems:

- Multivariate correlation: For the real world applications many of the material properties such as mass concrete, foundation rock, interface joint, etc. may be assumed as RVs. Usually there is partial correlation among these individual RVs (e.g. concrete modulus of elasticity and compressive strength). Figure 18.5 shows the correlation matrix for the concrete-rock interface joint element [385].
- Spatial correlation: Spatial variability of structural properties (i.e. material properties) is very important and can have substantial impact on the structural damage and failure (e.g. crack initiation and localization in homogeneous stress state region) [667]. Figure 18.6 shows three realizations based on LHS and "random fields" theory for the fracture energy, G_f, at the interface area.
- Temporal correlation: Temporal uncertainties are related to time-dependent variability and can be considered in two levels: 1) temporal prediction (uncertainty in future states) and 2) temporal retrodiction (uncertainty in past state) [641]. Figure 18.7 shows the temporal correlation in concrete elastic modulus of an AAR-affected structure over the 100 year time period. Time-dependent strength reduction is quantified for over 100 LHS-based simulations.

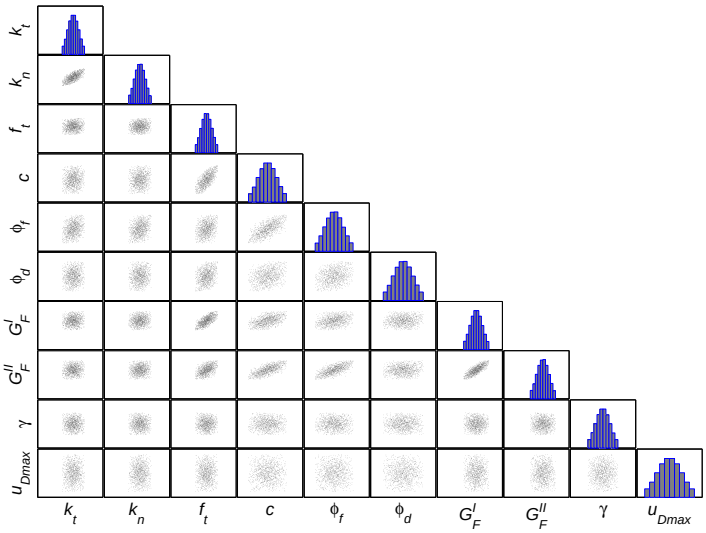

Fig. 18.5: A multivariate partial correlation matrix with 10,000 samples

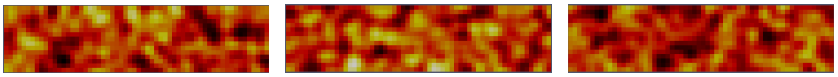

(a) 1st realization (b) 2nd realization (c) 3rd realization

Fig. 18.6: Three samples of spatial correlation of fracture energy

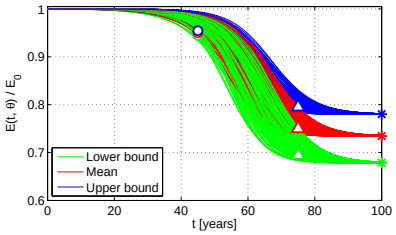

Fig. 18.7: Temporal correlation in concrete elastic modulus of an AAR-affected structure

18.2 Terminology of Risk-Based Assessment

18.2.1 Reliability

Structural reliability analysis deals with the quantitative assessment of the failure probability, P_f, given a model of the uncertainty in the structural, environmental and load parameters.

The "safety margin," Z, is defined as the difference between resistance, R, and stress, S [568]:

$$\begin{aligned} Z &= R - S \\ Z &= C - D \end{aligned} \tag{18.11}$$

or equivalently, in terms of capacity, C, and demand, D. Failure would occur if $Z < 0$.
Alternatively, C and D can be combined and the result expressed logarithmically:

$$X = \ln \frac{C}{D} \tag{18.12}$$

in which failure would occur for negative values of X.
Reliability index, β, is used as a relative measure of the reliability or confidence in the ability of a structure to perform its function in a satisfactory manner. Probabilistic methods are used to systematically evaluate uncertainties in parameters that affect structural performance, and there is a relation between the reliability index and risk [249].
In the case the demand and capacity are random variables and presented using the normal distributional models, an analytical solution can be found for reliability index. If X is assumed to follow a normal distribution then it has a mean value $\overline{X} = \left(\ln \frac{C}{D}\right)_{mean}$ and a standard deviation σ. Then, the reliability index is defined as the distance between mean performance value and the limit state normalized with respect to the standard deviation:

$$\beta = \frac{\mu_{\ln(\frac{C}{D})}}{\sigma_{\ln(\frac{C}{D})}} = \frac{\ln \mu_{(\frac{C}{D})} - \frac{\sigma^2_{\ln(\frac{C}{D})}}{2}}{\sqrt{\ln\left[1 + \left(\frac{\sigma_{(\frac{C}{D})}}{\mu_{(\frac{C}{D})}}\right)^2\right]}} \tag{18.13}$$

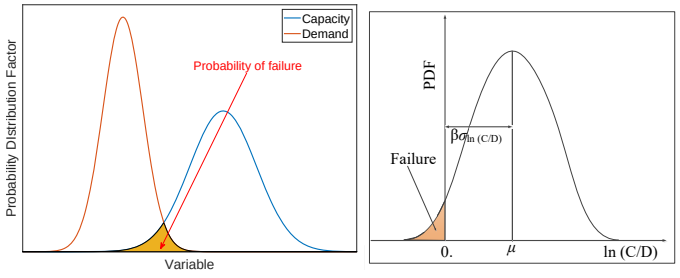

(a) Capacity and Demand (b) Reliability Index

Fig. 18.8: Capacity and demand reliability index

Alternatively, the reliability index can be expressed in terms of the individual means of C and D, and their respective coefficients of variation

$$\beta = \frac{\ln \frac{\mu_C}{\mu_D}}{\sqrt{COV_C^2 + COV_D^2}} \tag{18.14}$$

On the other hand, knowing the value of reliability index, the probability of failure, P_f, can be computed as follows which is, in fact, equal to the ratio of the shaded area to the total area under the curve in figure 19.8.

$$P_f = \Phi(-\beta) \tag{18.15}$$

where $\Phi(.)$ is the standard normal CDF (Matlab built-in function `normcdf` facilitates this operation).
Reliability indices for a number of components, or a number of modes of performance, may be used to estimate the overall reliability of a structure/system. Two extreme cases might be considered:

Series System: Such a system will perform poorly if any one component performs unsatisfactorily. If a system has n components in series, the probability of unsatisfactory performance of the ith component is p_i and its reliability $R_i = 1 - p_i$. Then the reliability of the system, or probability that all components will perform satisfactorily is

$$R = R_1 \times R_2 \times \cdots \times R_n \ = (1 - p_1)(1 - p_2) \cdots (1 - p_n)$$

Parallel Systems: Such a system will only perform unsatisfactorily if all component perform unsatisfactorily. Hence the reliability is

$$R = 1 - p_1 \times p_2 \times \cdots \times p_n \tag{18.16}$$

Reliability indices are a relative measure of the current condition and provide a qualitative estimate of the structural performance. Structures with relatively high reliability indices will be expected to perform well. If the value is too low, then the structure may be classified as a hazardous one. Target values for β are shown in Table 18.1. This is further illustrated by Fig. 18.9

18.2.1.1 Time-invariant Case

In "time-invariant" structural reliability problems, it is assumed that all the parameters are either deterministic or random variables. They are usually presented by probability distributional models showing the uncertainty over a given time interval. In addition, they can be combined to account for multiple effects on variables [588]. The limit state function takes the following form:

$$G(\boldsymbol{X}) = R(\boldsymbol{X}) - S(\boldsymbol{X}) \tag{18.17}$$

Expected Performance	β	Failure probability
High	5	3/10 million
Good	4	3/100,000
Above Average	3	1/1,000
Below Average	2.5	6/1,000
Poor	2.0	2.3/100
Unsatisfactory	1.5	7/100
Hazardous	1.0	16/100

Table 18.1: Reliability of steel and concrete structures

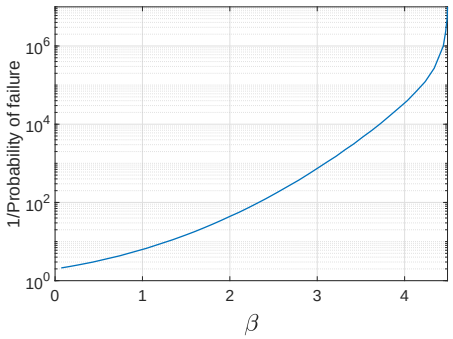

Fig. 18.9: Probability of failure in terms of reliability index β

where $\boldsymbol{X} \in \mathbb{R}^M$ is a random vector of N basic variables $\boldsymbol{X} = X_1, X_2, \cdots, X_N$.
In the time-invariant model, the resulting formulation seeks the probability that the uncertain demand exceeds the uncertain capacity at least once during the selected time period. The time-invariant failure probability, P_f, can be written as (the convolution integral), Fig 18.10(a):

$$\begin{aligned} P_f &= \mathbb{P}\left[R\left(\boldsymbol{X}\right) < S\left(\boldsymbol{X}\right)\right] \\ &= \int_{-\infty}^{\infty} F_R(\delta) f_S(\delta) d\delta = 1 - \int_{-\infty}^{\infty} F_S(\delta) f_R(\delta) d\delta \end{aligned} \tag{18.18}$$

where the randomness of R and S is expressed by probability density functions (PDFs) f_R and f_S, while F_R and F_S are the corresponding cumulative density functions (CDFs).
In the case that several random variables are contributing, the overall failure probability of the system is determined as $P_f = \int_{\{x\,:\,G(x)\leq 0\}} f_{\boldsymbol{X}}(\boldsymbol{x}) d\boldsymbol{x}$. Since the integration domain is only implicitly available, the direct estimation of P_f is very difficult (and impossible in many cases). Thus, P_f can be estimated by calculation of the expectation of a binary (safe/fail) classifier $\mathbf{I}_f$ as [568]:

$$P_f = \mathbb{E}\left[\boldsymbol{I}_f\left(\boldsymbol{X}\right)\right] \;; \quad \mathbf{I}_f\left(\boldsymbol{x}\right) = \begin{cases} 1 \text{ if } G(\boldsymbol{x}) \leq 0 \\ 0 \text{ if } G(\boldsymbol{x}) > 0 \end{cases} \tag{18.19}$$

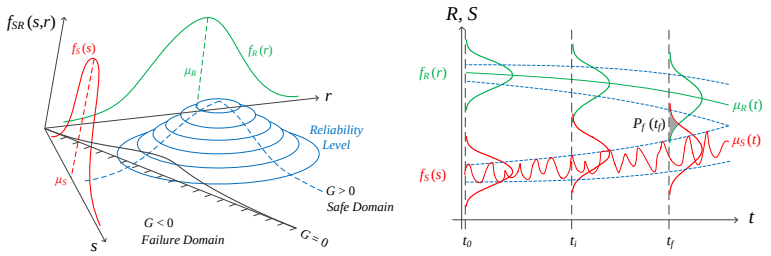

(a) Time-invariant model [589] (b) Time-variant model

Fig. 18.10: Concept of the reliability analysis with basic random variables

18.2.1.2 Time-variant Case

Demands on the structures as well as the structural capacity are often not constant, but they can change over time. It implies that the probabilistic analysis does not only include random variables, but also a random function of time. The limit state function can be written as:

$$G\left(\boldsymbol{X}(t)\right) = R\left(\boldsymbol{X}(t)\right) - S\left(\boldsymbol{X}(t)\right) \tag{18.20}$$

Figure 18.10(b) shows an example of a time-dependent system. At t_0 (construction time), the PDFs of demand and capacity models are far from each other with a (codified) safety factor. Structural resistance (capacity) often decreases as a function of time due to deterioration (e.g., alkali aggregate reaction), while the demand may increase over time (e.g., accumulated debris in the reservoir). Two PDFs are first crossing (assuming that they are truncated models) at t_i while the failure probability is practically zero. Further deterioration of the system or increase of the demand lead to overlapping PDFs (the overlapped area is interpreted as P_f). There are various methods to incorporate the temporal effects of both the demand and capacity in the reliability assessment (e.g., time-integrated and discrete approaches) [479]. In the present paper, the time-variant failure probability is written as:

$$P_f(t) = \mathbb{P}\left[R\left(\boldsymbol{X}(t)\right) < S\left(\boldsymbol{X}(t)\right)\right] = \int_0^\infty F_{R,t}(\delta) f_{S,t}(\delta) d\delta \tag{18.21}$$

where $F_{R,t}$ and $f_{S,t}$ are the instantaneous CDF of R and the instantaneous PDF of S at time t respectively, assuming that R and S are statistically independent [533]. Next, the time interval (t_0, t_f) (where $t_0 = 0$ is the initial or construction time and t_f refers to the final or expected life time of the structure) can be divided into n non-overlapping time instants, $t_1, t_2, \cdots t_n$ ($t_n = t_f$) and the probability of failure can be reported in two ways:

- Instant probability of failure, P_f^I, where the failure probability is calculated based on the instant status of both R and S, Eq. 18.18. This model only considers the system behavior at time $\tau = t_i$ and there is no condition on the previous failures.
- Cumulative probability of failure, P_f^C, in which the failure probability is calculated within the time interval $(0, \tau]$ as:

$$\begin{aligned} P_f^C(0,\tau] &= 1 - \mathbb{P}\left[\left(R\left(\boldsymbol{X}(t_1)\right) > S\left(\boldsymbol{X}(t_1)\right)\right) \cap \cdots \cap \left(R\left(\boldsymbol{X}(t_\kappa)\right) > S\left(\boldsymbol{X}(t_\kappa)\right)\right)\right] \\ &= 1 - \prod_{j=1}^{\kappa} \left(1 - P_f^I(t_j)\right) \end{aligned} \tag{18.22}$$

  In this model, the failure probability at any time instant is conditioned on all the previous times. The final simplified formula is, in fact, a generalized equation for a system with series components.

Time-dependency of the random variables is simply modeled using the initial state and a temporal degrading, $\psi(t)$. In the most general form, they can be written as:

$$\begin{cases} R(t) = R_0 \times \psi_R(t), & R_0 = R|_{t=0} \\ S(t) = S_0 \times \psi_S(t), & S_0 = S|_{t=0} \end{cases} \tag{18.23}$$

18.2.2 Hazard

Hazard analysis is the process of recognizing hazards that may arise from a system or its environment, documenting their unwanted consequences, and analyzing their potential causes. There are three objectives for a hazard analysis:

- Hazard identification: To determine the hazards and hazardous events of the equipment under control and the control system (in all modes of operation), for all reasonably foreseeable circumstances including fault conditions and misuse.
- Cause identification: To analyze the event sequences leading to the hazardous events identified.
- Risk determination: To analyze the risks associated with the hazardous events.

Hazards may be realized or unrealized. A realized hazard has happened in the past and can therefore be identified from experience. An unrealized hazard is a potential for a hazardous situation that has not happened in the past but can be recognized by analyzing the characteristics of an environment or failure modes of equipment items. The following is a review of the widely used hazard analysis techniques [5], [401]:

- Preliminary hazard analysis: This is a very broad technique and an initial study that focuses on 1) identifying apparent hazards, 2) assessing the severity of potential mishaps that could occur involving the hazards, and 3) identifying means for reducing the risks associated with the hazards. It focuses on identifying weaknesses early on in the life of a system, thus saving time and money, which might be required for a major redesign, if the hazards are discovered at a later date.

- Preliminary risk analysis: It is a streamlined mishap-based risk assessment approach. The primary objective of the technique is to characterize the risks associated with significant loss scenarios. This team-based approach relies on subject matter experts systematically examining the issues. The team postulates combinations of mishaps, most significant contributors to losses and safeguards. The analysis also characterizes the risk of the mishaps and identifies recommendations for reducing risk.
- What-if/checklist analysis: What-if analysis is a brainstorming approach that uses loosely structured questioning to 1) postulate potential upsets that may result in mishaps or system performance problems, and 2) ensure that appropriate safeguards against those problems are in place. Furthermore, checklist analysis is a systematic evaluation against pre-established criteria in the form of one or more checklists.
- Failure modes and effects analyses: It is an inductive reasoning approach that 1) considers how the failure modes of each component can result in system performance problems, and 2) ensures that appropriate safeguards against such problems are in place. A quantitative version of this model is known as Failure Modes, Effects and Criticality Analysis.
- Hazard and operability analysis: This technique is an inductive approach that uses a systematic process for 1) postulating deviations from design intents for sections of systems, and 2) ensuring that appropriate safeguards are in place to help prevent system performance problems.
- Fault tree analysis: This is a deductive analysis technique that graphically models how logical relationships between equipment failures, human errors and external events can combine to cause specific mishaps of interest. Sample application to the dams and appurtenant structures can be found in [402, 687].
- Event tree analysis: This is an inductive analysis technique that graphically models the possible outcomes of an initiating event capable of producing a mishap of interest. Sample application to the dams and appurtenant structures can be found in [142, 418, 802, 590, 403, 324].
- Relative ranking/risk indexing: It uses attributes of a vessel, shore facility, port, or waterway to calculate index numbers that are useful for making relative comparisons of various alternatives.
- Coarse risk analysis: It uses operations/evaluations and associated functions for accomplishing those operations/evaluations to describe the activities of a type of vessel or shore facility. Then, possible deviations in carrying out functions are postulated and evaluated to characterize the risk of possible mishaps.
- Pareto analysis: This is a prioritization technique based solely on historical data that identifies the most significant items among many. This technique employs the 80-20 rule, which states that $\sim 80\%$ of the problems (effects) are produced by $\sim 20\%$ of the causes.
- Root cause analysis: Root cause analysis uses one or a combination of analysis tools to systematically dissect how a mishap occurred (i.e., identifying specific equipment failures, human errors, and external events contributing to loss). Then, the analysis continues to discover the underlying root causes of the key con-

tributors to the mishap and to make recommendations for correcting the root causes.
- Change analysis: It systematically looks for possible risk impacts and appropriate risk management strategies in situations in which change is occurring.
- Common cause failure analysis: This is a specialized approach for systematically examining sequences of events stemming from the conduct of activities and/or operation of physical systems that cause multiple failures/errors to occur from the same root causes, thus defeating multiple layers of protection simultaneously.
- Human error analysis: It involves a range of methods from simple human factors checklists through more systematic analyses of human actions to more sophisticated human reliability analyses.

In structural engineering, seismic hazard refers to an uncertain relationship between some level of seismic intensity measure (IM) and the frequency or probability of a particular location experiencing at least that level of excitation. Usually, a probabilistic seismic hazard analysis (PSHA) is performed to derive the hazard curve. It expresses a plot where the horizontal axis is the IM at a site and the vertical one is annual frequency of exceedance, λ_{IM}, (inverse of the return period, T_R), Figure 18.11.

- Probability that the ground motion parameter exceeds a value y (note some books show it as y^*) from an earthquake of a given magnitude and distance, $P[Y > y|m, r]$ given by:

$$P[Y > y|m, r] = 1 - F_Y \left[\frac{\ln y - \overline{\ln y}}{\sigma_{\ln y}} \right] \tag{18.24}$$

  where F_Y is standard normal CDF.
- Assuming that the earthquake magnitude and distance are the only random variables (in most of the cases the uncertainty in these two is significantly larger that the others), the probability that the ground motion parameter Y exceed the particular value y when an earthquake occurs at the ith seismic source is given by:

$$P[Y > y] = \int_R \int_M P[Y > y|m, r] \; f_M(m) \; f_R(r) \; dm \, dr \tag{18.25}$$

  where f represents the PDF.

One of the applications of the PSHA is to develop seismic hazard maps. To produce the US national seismic hazard maps, hazard curves were calculated for several 5%-damped spectral acceleration ordinates at periods of 0.0 (PGA), 0.2, 0.3, 0.5, 0.75, 1.0 and 2.0 seconds. They are at annual recurrence rate of N = 0.00211, 0.00103 and 0.00040 per year, to obtain the corresponding values for 10%, 5% and 2% probability of exceedance in 50 years (based on Poisson model). Figure 18.12 illustrates a PGA-based US seismic hazard map for a 2% probability of exceedance in 50 years.

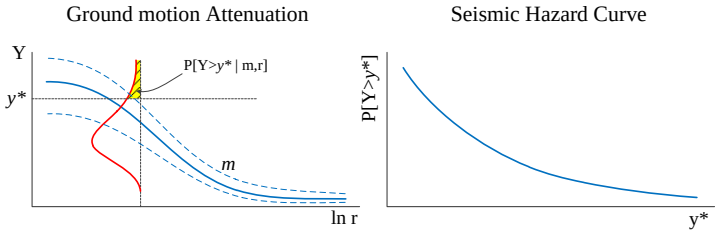

Fig. 18.11: Probabilistic Seismic Hazard

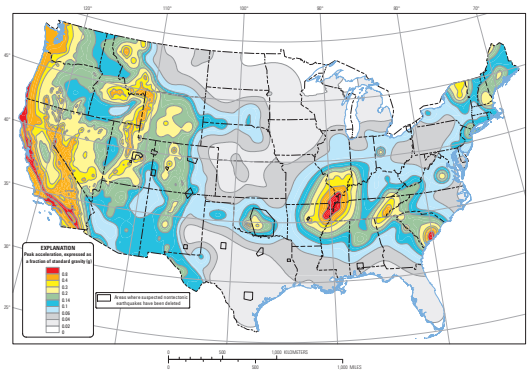

Fig. 18.12: 2% probability of exceedance in 50 years map of PGA [846]

18.2.3 Risk

In structural safety, risk can be defined as: "Measure of the probability and severity of an adverse effect to life, health, property, or environment. In the general case, risk is estimated by the combined impact of all triplets of scenario, probability of occurrence and the associated consequence". Risk can be quantified as [25]:

$$\text{Risk} = \int P\left[\text{Load Events}\right] \times P\left[\text{Responses} \mid \text{Loads}\right] \times C\left[\text{Loads, Responses}\right] \tag{18.26}$$

where $P\left[A|B\right]$ is the conditional probability that A is true given that B is true and C stands for the consequences.
Risk management encompasses activities related to making risk-informed decisions, prioritizing evaluations of risk, prioritizing risk reduction activities, and making program decisions associated with managing a portfolio of facilities. Risk management includes evaluating the environmental, social, cultural, ethical, political, and legal considerations of all parts of the decision process, Figure 18.13

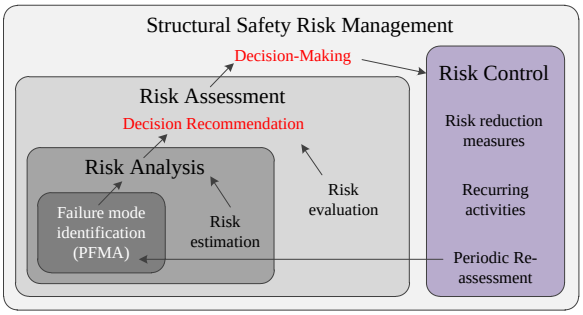

Fig. 18.13: Structural safety risk management

Risk assessment is the process of deciding whether existing risks are tolerable and present risk control measures are adequate and if not, whether alternative risk control measures are justified or will be implemented. Risk assessment incorporates the risk analysis and risk evaluation phases. Tolerable risk means different things to different people and organizations. Some focus on economic risks to their company or organization (e.g., insurance, offshore oil and gas) while others focus on loss of life. Most of the regularities use a so-called "risk curve" [326] (either in the form of f-N or F-N chart).

Bowles [141] defined the following factors as a metric for judging whether risks are ALARP (i.e., as low as reasonably practicable): 1) the level of risk in relation to the tolerable risk limits, 2) the disproportion between the cost of implementing the risk-reduction measures and the subsequent risk reduction achieved, 3) the cost-effectiveness of the risk-reduction measures, 4) compliance with good established practice, and 5) societal concerns as revealed by consultation with the community and other stakeholders.

The UK Health and Safety Executive (HSE) regulates the safety of all workplace activities in the UK. The HSE was a leader in developing the general tolerability of risk framework. The HSE proposes that F-N curves can be helpful for decision-making; however, it does not specifically promote one for water resources structures. Instead, HSE proposes Figure 18.14 for individual and societal risks. They are inverted triangles, in which the shape indicates the amount of attention and risk limits of a particular situation [432]. Except in extraordinary circumstances, unacceptable risks must be reduced regardless of the cost of these risk reduction measures.

ANCOLD [29] proposes a general framework for risk assessment of dams as illustrated in Figure 18.15. A majority of the research in risk analysis of dams is based on the hydrologic/flood hazard. Few of them account for the seismic and aging hazards as well. Additionally, nearly all the research papers dealing with the risk analysis include a section or chapter on the calculation of failure probability and probabilistic post-processing on the data.

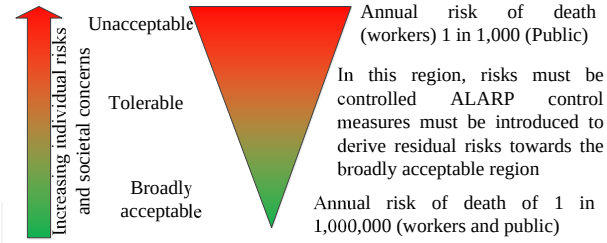

(a) Individual risk limits

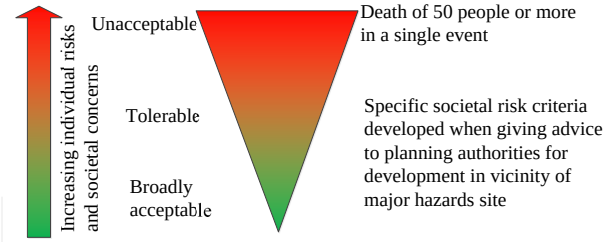

(b) Societal risk limits

Fig. 18.14: HSE tolerability of risk framework; adopted from HSE [432]

18.2.4 Fragility

A fragility curve is a continuous function showing the probability of exceedance of a certain limit state (LS) for specific level of ground motion intensity measure (IM), Figure 18.16(a) [269]:

$$\text{Fragility} = P\left[\text{LS}|\text{IM} = im\right] \tag{18.27}$$

where $P\left[A|B\right]$ is the conditional probability that A is true given that B is true. In addition, im refers to a particular value of IM, i.e., there is no uncertainty.
Alternatively, fragility can be defined as [470]:

$$\begin{aligned}\text{Fragility} &= P\left[D \geq C_{\text{LS}}|\text{IM} = im\right] = P\left[\frac{D}{C_{\text{LS}}} \geq 1|\text{IM} = im\right] \\ &= P\left[Y \geq 1|\text{IM} = im\right]\end{aligned} \tag{18.28}$$

where D is the demand parameter and C_{LS} is the capacity associated with the given LS. Note that Y may be in the component or structure level.
A fragility surface is a three-dimensional version of fragility curves [134]. A fragility surface can be presented with vectorized IM (double intensity measures). For such a system the fragility definition can be replaced by:

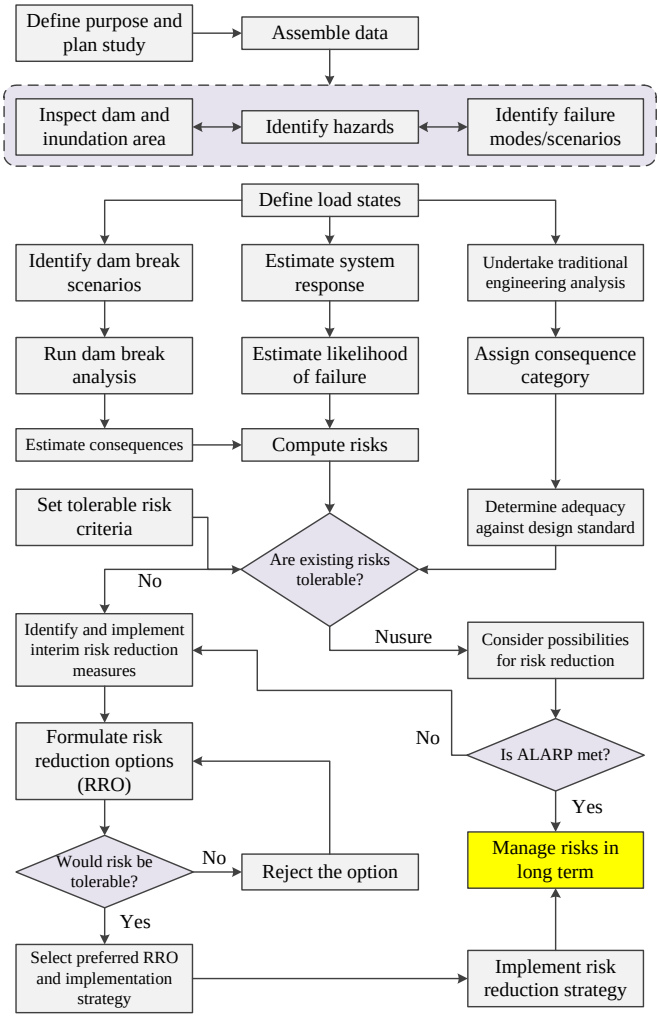

Fig. 18.15: Typical risk assessment process for a dam; adopted from ANCOLD [29]

$$\text{Fragility} = P\left[\text{LS}|\text{IM}_1 = im_1, \text{IM}_2 = im_2\right] \tag{18.29}$$

The two IMs can be among un-scalable parameters, e.g. $< M_w, R_{rup} >$ (earthquake magnitude and distance), or the scalable ones, e.g. $< S_a(T_1), I_A >$ (first-mode spectral acceleration and Arias intensity), figure 18.16(b).
A detailed discussion on the fragility function can be found in Section 25.

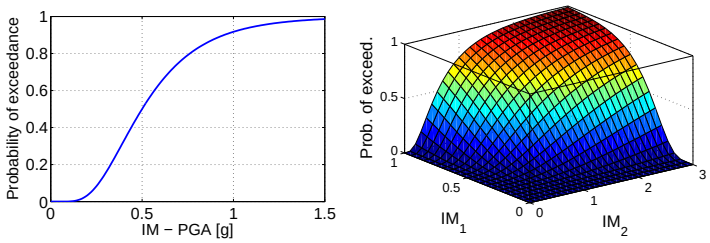

(a) Curve (b) Surface

Fig. 18.16: Fragility function

18.2.5 Vulnerability

Vulnerability originates from the Latin word *vulnerare*, which illustrates the potential to be harmed and the sensitivity to a perturbation or stress [258]. Lei et al. [531] collected a comprehensive list of definitions related to vulnerability. Some of those are reported here:

- Vulnerability means an environmental sensitivity. It is related to demographic, economic, social, and technical factors [258].
- When a social or ecological system loses resilience, it becomes vulnerable to change that previously could be absorbed. Thus, it is the flip side of resilience [492].
- Vulnerability is the degree to which a system is susceptible to, or unable to cope with, adverse effects of climate change [686].
- Vulnerability is the degree to which a system, subsystem, or system component is likely to experience harm due to hazardous exposures, either perturbations or stressors [837].
- Social vulnerability is a measure of both the sensitivity of a population to natural hazards and its ability to respond to and recover from the impacts of hazards [223].
- Vulnerability presents the characteristics of a group or individual in terms of its capacity to anticipate, cope with, resist, and recover from the impact of a hazard [127].
- Vulnerability places stress on a system's response to (potential) hazards, which determines the likelihood of loss. Exposure and sensitivity are two aspects of vulnerability [918].
- Vulnerability is the result of interactive change of both exposure and response, or the covariance between them [364].

In the field of earthquake engineering, vulnerability is different from fragility. The former measures loss (in terms of dollars, deaths, and downtime), while the latter measures probability [703]. A vulnerability curve expresses loss as a function of IM. Three major types of vulnerability curves are:

- Measuring repair cost: In such a case, the repair cost is normalized by the replacement cost of a new asset and is called a damage factor. The expected value of a damage factor conditioned on an IM parameter is called a mean damage factor, Figure 18.17.
- Measuring life safety: In such a case, the number of casualties is normalized by the number of indoor occupants and expressed as a function of IM parameter.
- Measuring downtime: It is measured in terms of the fraction of a year during which the structure cannot be used.

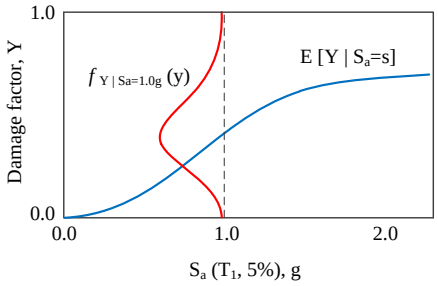

Fig. 18.17: Vulnerability function

In general, there are three approaches to developing a vulnerability function, i.e., empirical, analytical, and expert opinion [703]. An empirical vulnerability function is derived by regression analysis of observations of pairs of excitation and loss for specimens of an asset class [612]. This method is of interest by insurance companies as the data come directly from real world events.
Analytical vulnerability functions are useful in case there is not enough data from empirical sources. In this condition, having time and knowledge to create and analyze an analytical model, multiple numerical simulations are performed. This method involves defining one or more specimens to represent the class, creating and analyzing a structural model to estimate demand parameters as a function of ground motion intensity measure, estimating damage at the component level, and finally estimating loss given component damage.
Finally, in the case that the empirical data are missing and performing the analytical models is difficult (impossible or expensive), expert opinion can be used to develop vulnerability curves ATC-13 [66].

18.2.6 Resilience

The Presidential Policy Directive [708] defines the term resilience as "a structure's ability to prepare for and adapt to changing conditions while simultaneously being able to withstand and recover rapidly from functionality disruptions." There are several analytical studies that quantify the resiliency in civil infrastructures subjected

to an extreme event discussed in [158, 204, 132, 238, 783]. Resilience metrics for multi-hazard environments were defined by Ayyub [72]. The Task Committee (TC) on Infrastructure Impacts of Landscape-Driven Weather Change of the ASCE provided the following definition [427]: "A weather-climate resilient water infrastructure is defined as an infrastructure that can to a degree anticipate or adapt and recover from external disruptions due to severe weather and climate, and carry on providing the essential services the infrastructure is designed for with managed interruption to non-essential services, while balancing trade-offs among social (e.g., security), environmental, and economic factors."
Bruneau et al. [159] described one of the most comprehensive definitions of resilience that accounts for eleven aspects categorized in three groups [132]:

- Four dimensions:
  - Technical: includes all the technological aspects associated with the construction.
  - Organizational: includes all the management activities and plans, maintenance, and response to emergencies.
  - Social: includes societal effects and their mitigation.
  - Economic: includes all the indirect and direct costs due to the loss of functionality and the subsequent rehabilitation.
- Four properties:
  - Robustness: the ability to withstand a given extreme event and still deliver a service.
  - Rapidity: the speed with which a structure recovers from such an event to reach a high functionality level.
  - Redundancy: the extent to which components of the system are substitutable.
  - Resourcefulness: the capacity to make the appropriate budget available, identify problems, establish priorities, and mobilize resources after an extreme event.
- Three results:
  - More reliable: since it has a lower probability of reaching limit states.
  - Fast recovery: the rapidity of functionality restoration during a disaster is paramount to resilient systems.
  - Low socio-economic consequences: the reduced probability of significant service reductions and fast recovery decreases the impact of extreme events on a society.

Community resilience is the ability to prepare and plan for, absorb, recover from, and more successfully adapt to actual or potential adverse events [224]. Resilience is defined as a normalized function, indicating capability to sustain a level of functionality or performance, $Q(t)$, for a given building, lifeline, or community over a period of time, t_{LC}, (life cycle time) [205]. t_{LC} includes the structure recovery time, t_{RE}, and the business interruption time, t_{BI} (usually negligible). t_{RE} is the time

necessary to restore the functionality of a critical infrastructure system (and usually is a RV with high uncertainties). Resilience can be defined as [137]:

$$\text{Resilience } (\%) = \int_{t_0}^{t_{RE}} \frac{Q(t)}{t_{RE}} dt \tag{18.30}$$

where t_0 is the hazard (e.g., earthquake) occurrence time. Resilience and loss of resilience, its complement, are usually shown through a "recovery function", as shown in Figure 18.18.

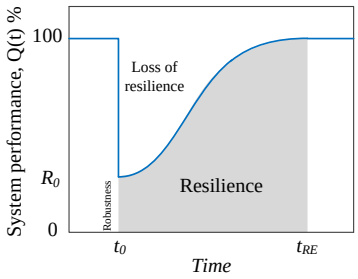

Fig. 18.18: Resilience curve

Furthermore, resilience and risk are connected to each other. Improving the resilience of a structural system constitutes an integral part of its risk management [358]. More specifically, the acceptable level of residual risk (e.g. recovery time and composite costs) in the system can be quantified, subjected to a particular threat scenario, and presented based on the associated PDFs. Manyena and Gordon [566] compared and contrasted the concept of resilience with fragility and stabilization. In the bigger picture, the major focus of resilience is on agencies, while it is the structures in fragility. The delivery of resilience is bottom-up, while it is top-down in fragility and stabilization. Similarly, Corotis [218] discusses the conceptual and analytical differences between resiliency and reliability.

The report published by National Research Council [622] might be the most comprehensive official source of dam/levee resilience. In the context of this report, "community" includes all persons and organizations exposed to direct and indirect consequences of dam or levee failure. The availability of hazard- and risk-related information is important for informed decision-making on the dam professionals community. Resilience-focused collaborations are a means of increasing understanding and communication of risks, shared needs, and opportunities. Social capital is necessary for community resilience. However, in a majority of the cases, the dam and levee safety programs operate independently of other community functions. Risk-informed approaches allow dam and levee professionals to improve their understandings of infrastructure-system operation, performance, vulnerability, and the consequences of potential failures. Finally, the dam safety program needs a cultural shift to be able to properly account for the community resilience.

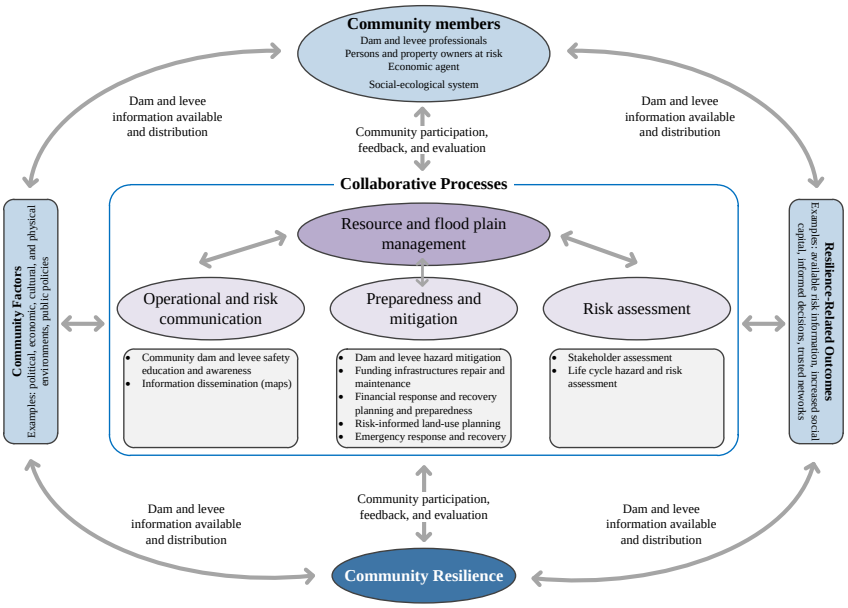

Fig. 18.19: Framework for resilience-based collaboration in dam/levee safety; adopted from National Research Council [622]

Figure 18.19 illustrates a conceptual framework for resilience-based collaboration in dam/levee safety. Enhancing resilience requires frequent and collaborative assessment of risk. The National Research Council [622] proposed a maturity matrix for assessing community engagement in dam safety programs. This is a general framework, which should be adjusted on a case-by-case basis. It uses a matrix to assess how advanced a program is with respect to a specific goal. The rows describe specific program or community processes, while columns refer to tools that are in place at given increased levels of community engagement related to that function. Table 18.2 shows a sample maturity matrix.

18.2.7 Sustainability

Sustainability is another concept which is similar to resilience but has its own definition. While resilience is presented as a metric to measure the ability of a structural system to withstand and recover from an unusual event, sustainability is a model that addresses simultaneously the current needs and impacts on future generations [157]. Sustainability combines three dimensions: economic, environmental, and social [132].

Different aspects of sustainability can be represented in four levels (associated with project management), as shown in Figure 18.20, where the lower levels influence

Table 18.2: Sample maturity matrix for assessing community engagement; adopted from National Research Council [622]

Elements	Level (I)	Level (II)	Level (III)	Level (IV)	Level (V)
Dam safety reviews	No activity	Standards-based only	Introduction of additional review criteria (e.g., failure mode analysis)	Application of quantitative risk assessment by using criteria developed by owner or regulator with input from community members and stakeholders	Application of quantitative risk assessment by using criteria that reflect the community's societal values
Emergency action plans	No activity	EAPs developed internally by owner	EAPs developed with input from emergency management agency	EAPs developed with input from community members and stakeholders and emergency management agency and shared with selected community representatives	Community collaboration with owners or operators to develop integrated EAPs that reflect community values
Floodplain management	No floodplain management plans	Floodplain management plans in place	Floodplain management plans accommodate shadow floodplain associated with catastrophic dam failure	Floodplain management plans integrated into community comprehensive or general plans	Floodplain management plans fully integrated into dam owners' planning processes

some goals associated with the higher ones. Usually sustainability is associated with words like "green design," "life cycle," and "social cost" whereas resilience is associated with "recovery," "extreme events," and " functionality." In spite of resilience (which is in the community and network level), most of the current applications in sustainability are limited to buildings and bridges [558, 535]. Furthermore, Marchese et al. [567] compared and contrasted the resilience and sustainability of environmental management applications. They considered three scenarios: 1) resilience as a component of sustainability, 2) sustainability as a component of resilience, and 3) resilience and sustainability as separate objectives.

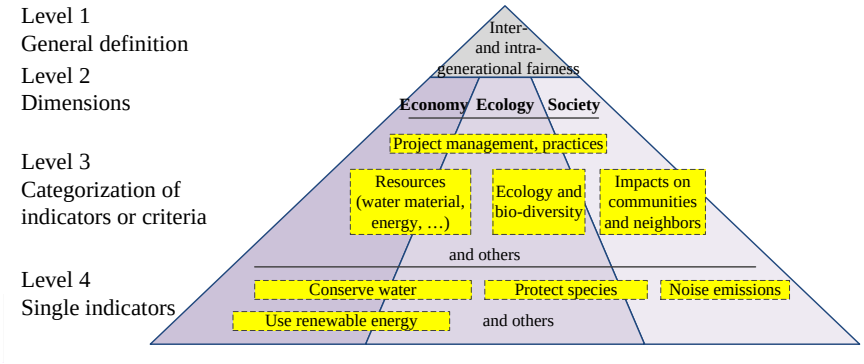

Fig. 18.20: Hierarchy levels in sustainability; adopted from Bocchini et al. [132]

18.3 Estimation of Failure Probability

18.3.1 Direct Integration

The probability of failure in terms of limit state function can be expressed as:

$$P_f = \mathbb{P}\left[G\left(\boldsymbol{X}\right) \leq 0\right] = \int_{G \leq 0} f_R(R) f_S(S) dR dS \tag{18.31}$$

where the randomness of R and S is expressed by probability density functions f_R and f_S.
It is possible to determine the failure probability in terms of the joint PDF of all contributing variables as:

$$P_f = \int_{\{x\,:\,G(x) \leq 0\}} f_{\boldsymbol{X}}(\boldsymbol{x}) d\boldsymbol{x} \tag{18.32}$$

Since the integration domain in this equation is only implicitly available, the direct estimation of the failure probability is very difficult (and usually impossible).

18.3.2 First order Reliability Method (FORM)

First order reliability method is based on the combination of 1) a local linear approximation of the LS function in a transformed space, and 2) an iterative search for the "design point" [407]. The first step to define the Hasofer-Lind reliability index, β_{HL}, is to normalize the basic RVs, $\boldsymbol{X}$, by transforming into a standard normal vector, $\boldsymbol{U}$, figure 18.21:

$$U_i = \frac{X_i - \mu_{X_i}}{\sigma_{X_i}} \tag{18.33}$$

where μ_{X_i} and σ_{X_i} are the mean and standard deviation of the random variable X_i. Note that in this new transformed space $\mu_{Z_i} = 0$ and $\sigma_{U_i} = 1$.

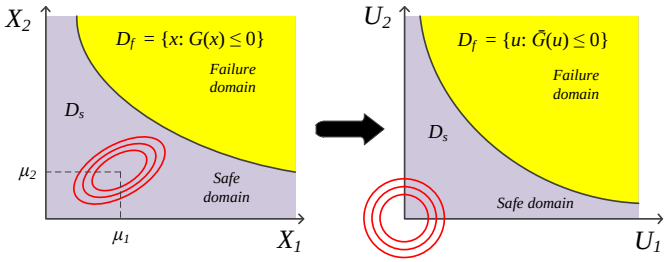

Fig. 18.21: FORM; Isoparametric transform from physical to standard normal space

Note that the LS function $G(\boldsymbol{X})$ in the original space will take the form $\bar{G}(\boldsymbol{U})$ in the standard normal space. The Hasofer-Lind reliability index is defined as the shortest distance from the origin in the standard normal space to the new transformed failure surface $\bar{G}(\boldsymbol{U})$, (this point is called design point, $\boldsymbol{U}^*$):

$$\boldsymbol{U}^* = \underset{\boldsymbol{u} \subset R^M}{\operatorname{argmin}} \left\{ \|\boldsymbol{u}\|, \bar{G}(\boldsymbol{u}) \leq 0 \right\} \tag{18.34}$$

and subsequently,

$$\beta_{HL} = \|\boldsymbol{U}^*\| = \min(\|\boldsymbol{U}\|) \tag{18.35}$$

and the "exact" FORM based failure probability for the linear LS functions can be computed as:

$$P_f^{\text{FORM}} = \Phi(-\beta_{HL}) \tag{18.36}$$

18.3.3 Second order Reliability Method (SORM)

Since the FORM linearly approximated the LS function at the design point, it may over- or underestimate the reliability index for the functions with significant curvature. In such a case, the second order reliability method may be used, where the LS function is approximated by a quadratic function at the design point (e.g., by a Tailor series expansion).
Different methods with different levels of complexity and accuracy were proposed for SORM; however, the following is a simple but practical formula on the basis of asymptotic analysis [153]:

$$P_f^{\text{SORM}} = \Phi(-\beta_{HL}) \prod_{i=1}^{N-1} (1 + \beta_{HL}\, \kappa_i)^{-1/2} \tag{18.37}$$

where κ_i are the principal curvatures of the paraboloid. This equation is asymptotically exact (as $\beta_{HL} \to \infty$ while $\beta_{HL}\, \kappa_i$ is kept constant) for any LS function having a single design point.
Figure 18.22 shows the conceptual comparison between FORM and SORM methods.

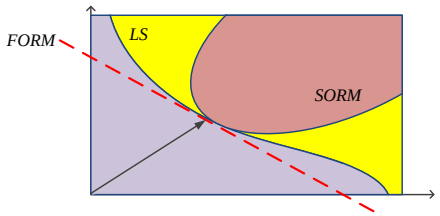

Fig. 18.22: FORM vs. SORM

18.3.4 Crude Monte Carlo Simulation

Monte Carlo simulation is used to directly calculate the failure probability based on a joint PDF of all the random variables. Since it is based on the theory of large numbers, $N_{\text{sim}} \to N_{\infty}$, an unbiased estimator of P_f is given by:

$$\hat{P}_f^{\text{MCS}} = \frac{1}{N_{\text{sim}}} \sum_{j=1}^{N_{\text{sim}}} \mathbf{I}_f\left(\boldsymbol{x}_j\right) = \frac{N_{\text{fail}}}{N_{\text{sim}}} \tag{18.38}$$

where N_{fail} is the number of failed samples, and the hat is the sign of estimation, and

$$\mathbf{I}_f\left(\boldsymbol{x}\right) = \begin{cases} 1 \text{ if } \; G(\boldsymbol{x}) \leq 0 \\ 0 \text{ if } \; G(\boldsymbol{x}) > 0 \end{cases} \tag{18.39}$$

The confidence intervals for $\hat{P}_f^{\text{MCS}}$ are:

$$\hat{P}_f^{\text{MCS}} \in \hat{P}_f^{\text{MCS}} \left[1 \pm \Phi^{-1}\left(\frac{\alpha}{2}\right) \left(\frac{1 - \hat{P}_f^{\text{MCS}}}{N_{\text{sim}} \times \hat{P}_f^{\text{MCS}}} \right)^{1/2} \right] \tag{18.40}$$

where $\Phi(.)$ is the standard normal CDF, and $\alpha \in [0, 1]$ is used to calculate the bounds with confidence level of $1 - \alpha$.
Finally, the associated generalized MCS based reliability index can be expressed as:

$$\beta_{\text{MCS}} = -\Phi^{-1}\left(\hat{P}_f^{\text{MCS}}\right) = \Phi^{-1}\left(1 - \hat{P}_f^{\text{MCS}}\right) \tag{18.41}$$

18.3.5 Latin Hypercube Sampling

LHS was developed with the idea to reduce the variance in the crude Monte Carlo estimate of the integrand [583]. LHS can be summarized as follows: Given the range $[0, 1]$ divided into N equal length intervals $1/N$, one point is randomly selected from each interval forming a sequence of N samples in H^1, $\left\{X_i^1\right\},\ i = 1, 2, ..., N$. Another sequence can be constructed independently by the same method as $\left\{X_i^2\right\},\ i = 1, 2, ..., N$. These two sequences can be paired to form a so-called bi-dimensional space. This method can be expanded until an m-dimensional sequence of N is formed [459], [667], [671], and [73].
Mathematically the algorithm can be presented as follows: Let $\{\pi_k\},\ k = 1, 2, ..., m$ be independent random permutations of $\{1, 2, ..., N\}$ each uniformly distributed over all $N!$ possible permutations. Set:

$$X_i^k = \frac{(\pi_k(i) - 1) + U_i^k}{N},\quad i = 1, 2, ..., N;\ k = 1, 2, ..., m \tag{18.42}$$

where U_i^k are the uniform independent sample points on the $[0, 1]$ interval.
So far, the maximum number of combinations for a LHS with N divisions and m RVs can be computed as:

$$N_{combo}^{LHS} = \left(\prod_{i=0}^{N-1} (N-i) \right)^{m-1} = (N!)^{m-1} \tag{18.43}$$

18.3.6 Importance Sampling

The crude MCS is in need of many samples as there is practically no control on the sampled point. A lot of methods have been proposed to reduce the number of sampling and consequently, reduce the variance of the responses. Importance sampling (IS) is one of these techniques [370].
The fundamental idea in IS is to concentrate the distribution of sampling in the most important region. A simple way is to move the sampling center from the origin in standard normal space to the design point on the failure function, Figure 18.23. In this method, a new sampling PDF, $h_{\boldsymbol{X}}(\boldsymbol{x})$ (known as sampling density function) is defined to obtain the samples in the desired region. Thus, the failure probability is reformulated as:

$$P_f^{\text{IS}} = \int_{\{x\,:\,G(x)\leq 0\}} \frac{f_{\boldsymbol{X}}(\boldsymbol{x})}{h_{\boldsymbol{X}}(\boldsymbol{x})} h_{\boldsymbol{X}}(\boldsymbol{x}) d\boldsymbol{x} \tag{18.44}$$

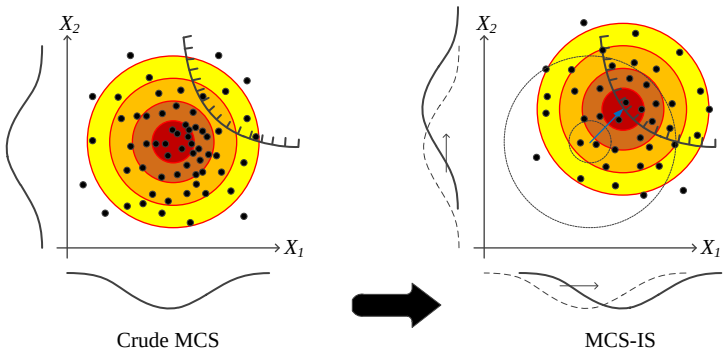

Fig. 18.23: Crude MCS vs. IS

With the similar analogy of Eq. 18.38, the failure probability can be approximated as:

$$\hat{P}_f^{\text{IS}} = \frac{1}{N_{\text{sim}}} \sum_{j=1}^{N_{\text{sim}}} \mathbf{I}_f\left(\boldsymbol{x}_j\right) \frac{f_{\boldsymbol{X}}(\boldsymbol{x}_j)}{h_{\boldsymbol{X}}(\boldsymbol{x}_j)} \tag{18.45}$$

An appropriate choice of $h_{\boldsymbol{X}}(\boldsymbol{x})$ is the key point in the successful implementation of IS method. Using the FORM results is one method to reach this goal.

Chapter 19
Probabilistic and Random FEM

Abstract
In general, the methods in structural analysis and design can be classified into two main groups: 1) deterministic simulations and 2) probabilistic simulations. In the case that the finite element method (FEM), used for discretization of the medium, is combined with statistics and reliability methods, the so-called probabilistic finite element method (PFEM) is developed and can be applied to both linear and non-linear systems.
Uncertainty can be propagated in both the finite element and applied load. Different sampling techniques based on crude MCS or more efficient techniques can be used. This chapter discusses three elements: (1) Mathematical review on sampling techniques, (2) Propagation of uncertainty in the response spectrum method (loading) and proposing the "random response spectrum method" (RRSM), and (3) Propagation of uncertainty directly in finite element and discussion on random finite element method (RFEM).

This chapter is written based on Hariri-Ardebili and Saouma [396], Hariri-Ardebili et al. [389] and Hariri-Ardebili et al. [399].

19.1 Uncertainty Propagation

19.1.1 Fundamentals

Based on the Der Kiureghian and Ke [241] definition, the term probabilistic or stochastic finite element method (SFEM) is used to refer to a method which accounts for the geometric or material uncertainties in the structure, as well as the applied loads.
The Monte Carlo Simulation (MCS) family is the basic method to perform a PFEM/SFEM analysis. It includes repetition of the simulation observed from a stochastic process in order to determine the probability of occurrence of a certain limit state (LS). Since it is based on the theory of large numbers, $N_{\text{sim}} \rightarrow N_{\infty}$, an unbiased estimator of P_{LS} is given by:

$$\hat{P}_{\text{LS}}^{\text{MCS}} = \frac{N_{\text{exc}}}{N_{\text{sim}}} \tag{19.1}$$

where N_{sim} and N_{exc} are the total number of simulations and the number of exceeded samples, respectively; and the hat is the sign of estimation.
MCS-based SFEM includes the following steps:

- A number of random variables or random fields are generated as input for the SFEM. Note that the term "random variable" is used for the probabilistic simulations in which the property has a constant value for the whole model, while in the case of "random field" the parameter has (time or space) variability within the model.
- Run the FEM for every random variable or random field.
- Extract the engineering demand parameter (EDP) as it is customarily called in Earthquake Engineering or quantity of interest (QoI) as it is called in uncertainty quantification (UQ). Then, perform a statistical analysis on the EDP/QoI to determine the appropriate distributional model.

By introducing a probabilistic method in Section 8, it becomes important to discuss the level of uncertainty propagation and, more importantly, the sampling techniques used for this method. In quantifying structural reliability and uncertainty, two major approaches are followed: 1) analytical techniques (e.g. first- and second-order reliability methods) and 2) simulation-based techniques (or random sampling methods). All such techniques belong (to some extent) to the Monte Carlo simulation family, depending on how the samples are generated.
In this paper, `Load_Generator.m` has been equipped with various sampling techniques that mostly belong to two key families: pseudo-random and quasi-random sequences.

- Truly random sequences are those exhibiting "true randomness," which is difficult (if not impossible) to generate through machines.
- Pseudo-random sequences are those appearing to show randomness yet nevertheless exhibit a specific, repeatable pattern. They have been generated by applying a set of rules.
  - Crude Monte Carlo Sampling (CMCS)
  - Latin Hypercube Sampling (LHS)
- Quasi-random (sub-random) sequences are generated from a completely deterministic, low-discrepancy process and possess no inherent statistical properties. Discrepancy is a metric for the degree of non-uniformity of numbers in a sequence.
  - Halton sequence
  - Sobol sequence

The following discussion will provide a brief review of the fundamental characteristics of each technique in a MATLAB [580] context:

19.1.2 Crude Monte Carlo Simulation

Consider the following integral over the n-dimensional unit hypercube H^n:

$$\theta = \int_{H^n} f(X)\mathrm{d}X \tag{19.2}$$

where $f(X)$ is an integrable function in H^n.
The Monte Carlo approach is based on a probabilistic interpretation of this integral. For a uniformly-distributed random variable X in H^n, the expectation is:

$$\theta = \mathrm{E}\left[f(X)\right] \ , \quad X \sim \mathrm{PDF}(X) \tag{19.3}$$

A Monte Carlo simulation generates N independent draws from the distribution $\mathrm{PDF}(X)$, $X_1, X_2, ..., X_N$ and approximates the integral as:

$$\hat{\theta}_N \equiv \frac{1}{N}\sum_{i=1}^{N} f(X_i) \tag{19.4}$$

In relying on the Law of "Large Numbers," the approximation $\hat{\theta}_N$ converges to θ with a probability of one. Although a Monte Carlo simulation can be very effective, the convergence rate is very slow with an error of $O(N^{-1/2})$.

19.1.3 Latin Hypercube Sampling (LHS)

LHS was developed by McKay, Beckman, and Conover [583] in the aim of reducing variance in the crude Monte Carlo estimate of the integrand. LHS can be summarized as follows: given a range $[0, 1]$ divided into N equal intervals $1/N$, a point is randomly selected from each interval, thus forming a sequence of N samples in H^1, $\left\{X_i^1\right\}$, $i = 1, 2, ..., N$. Another sequence can then be constructed independently but using the same method as $\left\{X_i^2\right\}$, $i = 1, 2, ..., N$. These two sequences can be paired to form a two-dimensional space. This method may be expanded until a m-dimensional sequence of N is formed.
Mathematically speaking, the algorithm can be presented as follows: Let $\{\pi_k\}$, $k = 1, 2, ..., m$ be independent random permutations of $\{1, 2, ..., N\}$, with each being uniformly distributed over all $N!$ possible permutations. Now, let's set:

$$X_i^k = \frac{(\pi_k(i) - 1) + U_i^k}{N} \ , \quad i = 1, 2, ..., N; \ k = 1, 2, ..., m \tag{19.5}$$

where U_i^k are the independent uniform sample points on the $[0, 1]$ interval.

19.1.4 Halton Sequence

This sequence was developed by Halton [362] and is defined by bases of prime numbers. Each dimension requires a unique prime number as its base. For example, a four-dimensional Halton set would have bases 2, 3, 5 and 7 (so as to better maintain order).
The nth term of the *van der Corput* sequence in base b, denoted by $\phi_b(n)$, is defined according to two steps: first, n is rewritten in its base b [666]:

$$n = (a_k ... a_1 a_0)_b = a_0 b^0 + a_1 b^1 + ... + a_k b^k \tag{19.6}$$

then, $\phi_b(n)$ is computed as

$$\phi_b(n) = (0.a_0 a_1 ... a_k)_b = \frac{a_0}{b^1} + \frac{a_1}{b^2} + ... + \frac{a_k}{b^{k+1}} \tag{19.7}$$

For example, the two-dimensional Halton sequence (with bases 2 and 3) contains the following points: $\left(\frac{1}{2}, \frac{1}{3}\right), \left(\frac{1}{4}, \frac{2}{3}\right), \left(\frac{3}{4}, \frac{1}{9}\right), \left(\frac{1}{8}, \frac{4}{9}\right), ...$ The fourth element in the second dimension (base 3) is computed as: $4 = (11)_3$, and $0.11_3 = \frac{1}{3} + \frac{1}{3^2} = \frac{4}{9}$. In MATLAB [580], the Halton sequence is created by the built-in function `haltonset`. To construct a `d`-dimensional point set `p` of the `haltonset` class with the ability to `Skip` the first `s` values and to `Leap` the algorithm discarding `l` values between each pick, `p = haltonset(d,'Skip',s,'Leap',l)` can be used. Moreover, the Halton sequence can be stored with the `net` generator that generates the first `q` points of the Halton sequence `p` in employing the command `pts = net(p,q)`.

19.1.5 Sobol Sequence

This sequence was developed by Sobol' [797] and utilizes a base of two to construct finer uniform partitions of the unit interval before reordering the coordinates in each dimension. This sequence almost appears like a grid in the lower dimensions, yet it forms a smaller discrepancy pattern at higher dimensions. Generating the jth component of the points in a Sobol sequence requires choosing a primitive polynomial of some degree s_j [481]:

$$X^{s_j} + a_{1,j} X^{s_j - 1} + a_{2,j} X^{s_j - 2} + \cdots + a_{s_j - 1, j} X^1 + 1 \tag{19.8}$$

where the $a_{1,j}$, $a_{2,j}$, ..., $a_{s_j-1,j}$ are either 0 or 1. A sequence of positive integers $\{m_{1,j}, m_{2,j}, \cdots\}$ is then defined using the recurrence relation:

$$\begin{aligned} m_{k,j} := {} & 2^1 a_{1,j} m_{k-1,j} \oplus 2^2 a_{2,j} m_{k-2,j} \oplus \cdots \oplus \\ & 2^{s_j - 1} a_{s_j - 1, j} m_{k - s_j + 1, j} \oplus 2^{s_j} m_{k - s_j, j} \oplus m_{k - s_j, j} \end{aligned} \tag{19.9}$$

where $\oplus$ is the bit-by-bit exclusive-or (XOR) operator. The initial values $m_{1,j}, m_{2,j}, \cdots$ may be freely chosen as long as each $m_{k,j}$ $(1 \leq k \leq s_j)$ is odd and less than 2^k, whereas the direction numbers are defined by:

$$v_{k,j} := \frac{m_{k,j}}{2^k} \tag{19.10}$$

Lastly, $X_{i,j}$, or the jth component of the ith point in a Sobol sequence, is:

$$X_{i,j} := i_1 v_{1,j} \oplus i_2 v_{2,j} \oplus \cdots \tag{19.11}$$

where i_k is the kth digit from the right when i is written in binary $i = (...i_3 i_2 i_1)_2$. Similar to the Holton sequence, MATLAB [580] includes a built-in function `sobolset`. To construct a `d`-dimensional point set `p` of the `sobolset` class with

the ability to `Skip` the first `s` values and `Leap` the algorithm discarding `l` values between each pick, $\mathtt{p} = \mathtt{sobolset}(\mathtt{d}, \text{`}\mathtt{Skip}\text{`}, \mathtt{s}, \text{`}\mathtt{Leap}\text{`}, \mathtt{l})$ can be used. Also, the Sobol sequence may be stored by exercising the command $\mathtt{pts} = \mathtt{net}(\mathtt{p}, \mathtt{q})$.

19.1.6 Comparison of Sampling Techniques

Figure 19.1 compares four sampling techniques (two from pseudo-random and two from quasi-random methods). Two sampling sizes were studied in order to reveal the impact of population on distribution uniformity. All the cases consist of two-dimensional random variables with a uniform distribution of zero mean and unit standard deviation. As can be observed, for a small number of samples (e.g. 100), both Sobol and Halton sequences are clearly advantageous compared to CMCS and even LHS. Increasing the number of samples (e.g. to 500) enhances the level of LHS uniformity, while CMCS retains considerable non-uniformity.

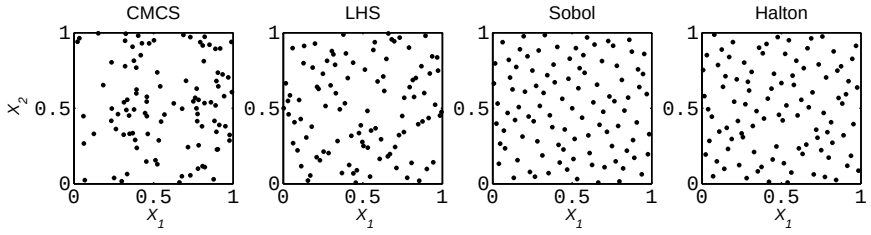

(a) Based on 100 samples

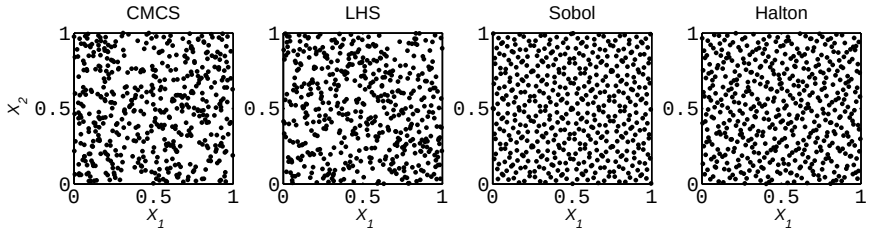

(b) Based on 500 sample

Fig. 19.1: Comparison of sampling techniques and impact of sample size

To avoid correlations in low-discrepancy sequences, it is customary to further "scramble" the sequence. A simple way is to introduce permutations of the original sequence. A built-in MATLAB [580] tool exists for the simple permutation (scrambling) of the first generated sequences.

19.2 Random Response Spectrum Method (RRSM)

In a series of publications [198], [305], [304], [306] and [301], UC Berkeley Professor Anil K. Chopra and his co-authors proposed a pseudo-dynamic method for computing the dynamic response of the dam-foundation-reservoir system at the fundamental period and higher modes.
The present section seeks to add a new dimension to this method by propagating uncertainties through the input parameters. The uncertainties that rise from material properties and modeling are mainly epistemic (since they are knowledge-based and can be reduced by investing resources to gain more precise information or build an advanced model), while the ground motion variability is aleatory (the reader should notice that the record-to-record randomness is not really applied in response spectrum method). Input parameter sensitivity is quantified and a step-by-step procedure is explained.
The following section explains the step-by-step procedure for the pilot model. The results of each step are quantified as subplots in Figure 19.2. Also, the standard values of Chopra's 4D model are graphically summarized in Figure 19.3.

1. Define the basic dam geometry including width at the base and crest (S_1 and S_2), height of the dam and neck (H_1 and H_2) and other dimensions, if necessary (slope and discontinuity at the upstream and downstream faces, slope of the base, etc.).
   Note that in the simplest case, the value of S_2 and H_2 can be defined as the ratios of S_1 and H_1, respectively. This outcome can be achieved using either an existing dam profile or an ICOLD benchmark model [456]. In such a case, the dam geometry can be described by the $\frac{H_1}{S_1}$ ratio and thus different dam classes can be compared.
2. Define the constant (deterministic) values as well as the random variables with their specific distributional model. The following MATLAB [580] built-in functions may be used: `makedist` defines any specific distributional model; `truncate` truncates the distribution using upper and lower bounds; and `random` is used for the crude sampling of N_{sim} simulations. Table 19.1 lists the assumed constants and variables in this illustrative pilot example. $N_{\text{sim}} = 1000$ has also been used herein. Since the computations are elastic, there is no need in the input model to define random variables for strength assessment (e.g., tensile strength, friction coefficient, cohesion). However, to interpret the results from a probabilistic point of view, this information is needed. The reader should notice that a log-normal distribution is often preferred for strength related parameters to avoid negative values (a truncated normal distribution can be used as well).
   Moreover, the reader should notice that the assumed damping ratio for the dam and foundation (Table 19.1) may increase the total damping ratio of the coupled system beyond 10% (this will be shown later). However, several forced vibration tests and earthquake measurements revealed a cap of $\sim 7\%$ for overall damping in the system [199], [724], [713] and [27].
3. Compute the depth ratio for reservoir water:

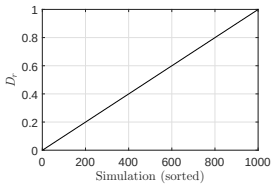

(a) Water depth ratio

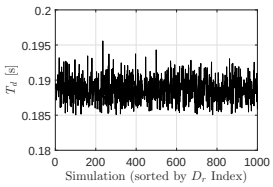

(b) Dam fundamental period

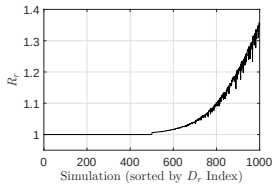

(c) Period elongation due to water

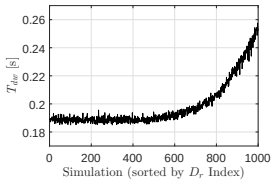

(d) Dam-reservoir period

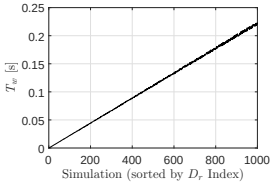

(e) Reservoir fundamental period

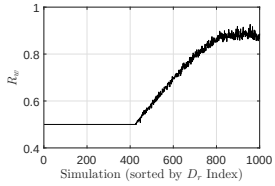

(f) Period ratio

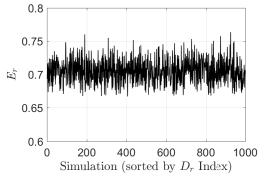

(g) Elasticity ratio

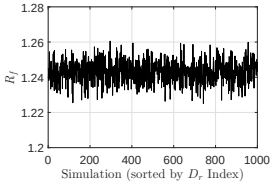

(h) Period elongation due to foundation

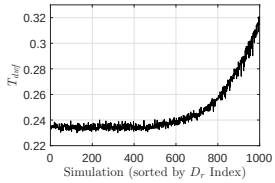

(i) Dam-reservoir-foundation period

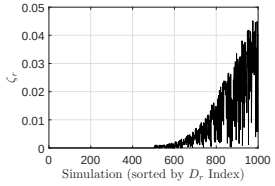

(j) Added damping due to water

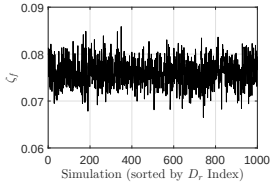

(k) Added damping due to foundation

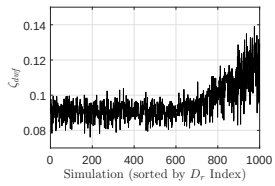

(l) Damping ratio of dam-reservoir-foundation

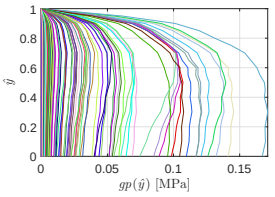

(m) Modified normalized hydrodynamic pressure

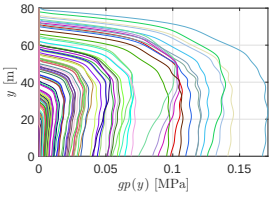

(n) Height-adjusted hydrodynamic pressure

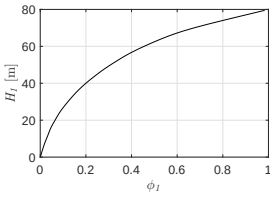

(o) Height-adjusted fundamental mode shape

$$D_r^i = \frac{H_w^i}{H_1} \; ; \quad i = 1, 2, ..., N_{\text{sim}} \tag{19.12}$$

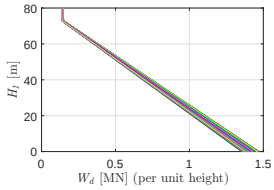

(a) Distribution of dam weight

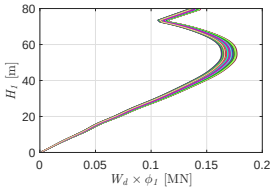

(b) Distribution of $W_d \times \phi_1$

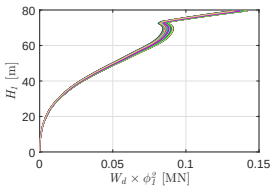

(c) Distribution of $W_d \times \phi_1^2$

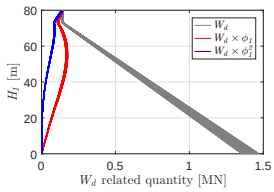

(d) Comparison of W_d related terms

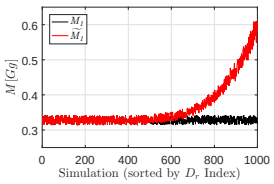

(e) Generalized mass

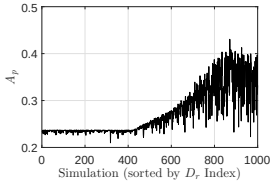

(f) Hydrodynamic force coefficient

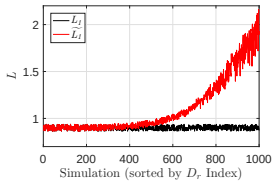

(g) Generalized earthquake force

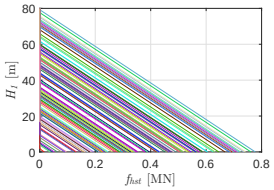

(h) Hydrostatic force

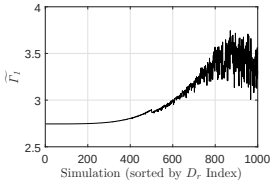

(i) Modal participation factor

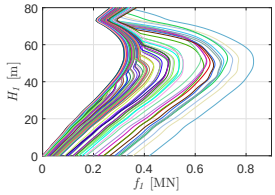

(j) Equivalent lateral force (1st mode)

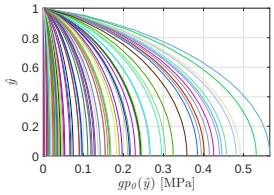

(k) Modified normalized hydrodynamic pressure (higher modes)

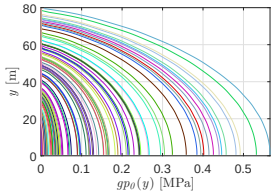

(l) Height-adjusted hydrodynamic pressure (higher modes)

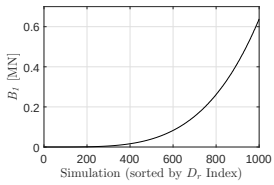

(m) Contribution of $p_0(y)$

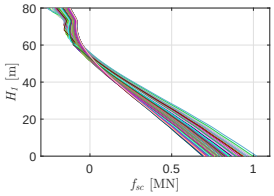

(n) Equivalent lateral force (higher modes)

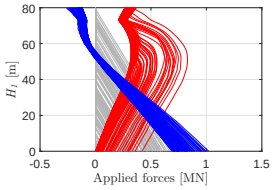

(o) Comparison of three applied forces

Fig. 19.2: Detailed random ESLF calculations for the gravity dams

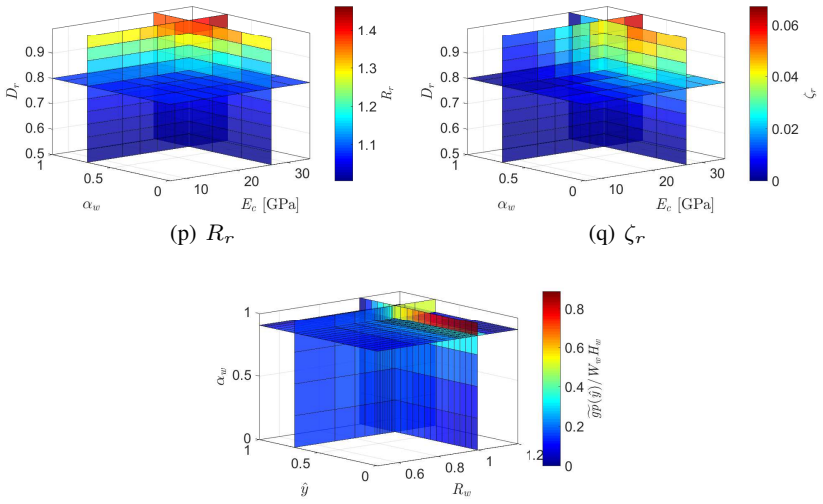

(p) R_r (q) ζ_r

(r) 1st mode $\tilde{gp}(\bar{y})/W_wH_w$

Fig. 19.3: Graphical representation of Chopra's 4D standard values for the ESLF method

Table 19.1: Parameters considered in the pilot example

Parameter	Symbol	Unit	Distributional model	Quantity	Bound
Width at the base	S_1	m	-	60	-
Width at the crest	S_2	m	-	6	-
Height of the dam	H_1	m	-	80	-
Height of the neck	H_2	m	-	7	-
Concrete mass density	ρ_c	kg/m^3	Normal	N(2400, 200)	(2300, 2500)
Water mass density	ρ_w	kg/m^3	-	1000	-
Concrete elastic modulus	E_c	MPa	Normal	N(26000, 500)	(24000, 27000)
Foundation elastic modulus	E_f	MPa	Normal	N(19000, 500)	(18000, 21000)
Damping ratio of dam alone	ζ_d	-	Normal	N(0.03, 0.01)	(0.01, 0.04)
Hysteretic damping coefficient of foundation	η_f	-	Normal	N(0.03, 0.02)	(0.01, 0.06)
Height of reservoir water	H_w	m	Uniform	U(0, H_1 =80)	-
Reservoir bottom wave reflection coefficient	α_w	-	Normal	N(0.8, 0.2)	(0, 1)
Velocity of pressure waves in water	C_w	m/s	Normal	N(1440, 15)	(1420, 1460)

Figure 19.2(a) shows the sorted value of the D_r^i for 1,000 simulations. This result should clearly vary between 0 (for $H_w = 0$) and 1 (for $H_w = 80$ m); however, values are sorted in ascending order and the index vector has been determined.

In all other plots in Figure 19.2, the considered quantity has been sorted based on the D_r index.

4. Estimate the fundamental period of a "standard" cross-section in the non-overflow monolith of the gravity dam (no foundation, no water) in seconds, see Figure 19.2(b):

$$T_d^i = 0.38 \frac{H_1}{\sqrt{E_c^i}} \; ; \quad i = 1, 2, ..., N_{\text{sim}} \tag{19.13}$$

5. Read the standard values for the period lengthening ratio due to hydrodynamic effects, R_r, from Appendix A in Løkke and Chopra [545]; this is a discrete function of the depth ratio, concrete modulus of elasticity and reservoir bottom wave reflection coefficient:

$$R_r = f(D_r, E_c, \alpha_w) \tag{19.14}$$

The original tables provide a value of R_r for six values of α_w, eight values of D_r and eleven values of E_c. These data are graphically presented by six subplots in Figure 19.4. Generally (but not always), R_r increases with increases in the three characterizing parameters. Let's also note that for $D_r < 0.5$, the dam-reservoir interaction is practically neglected ($R_r \approx 1.0$).

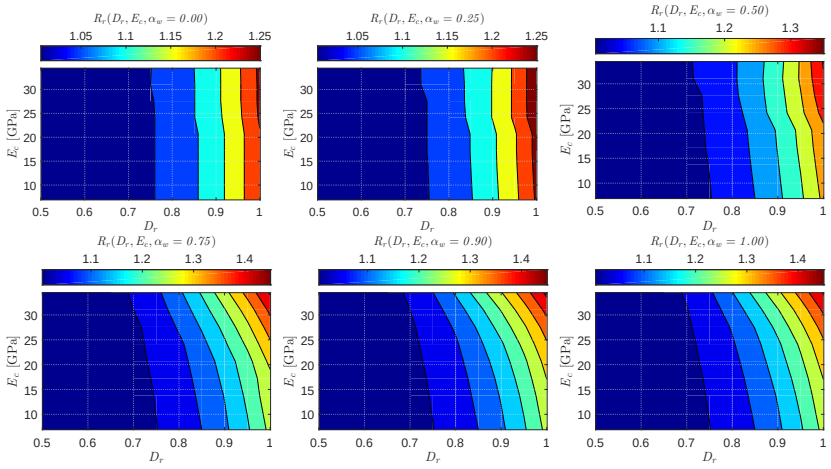

Fig. 19.4: Standard values for the period lengthening ratio due to hydrodynamic effects, R_r

The reservoir bottom wave reflection coefficient, α_w, is the ratio of the amplitude of the reflected hydrodynamic pressure wave to the vertically propagating wave. $\alpha_w = 1.00$ and 0.00 indicate a complete reflection of pressure waves and complete wave absorption, respectively. Løkke and Chopra [545] recommend that

interpolating α_w for intermediate values is not appropriate (for design purposes) and should be rounded up (i.e. 0.25, 0.5, 0.75, 0.9 and 1.0), based on the conservative assumption that the reservoir bottom is composed of various silt layers with different α_w values. This assumption however adds a level of uncertainty to the problem.
In this paper therefore, the values of R_r are computed by means of linear interpolation among three parameters (Eq. 19.14) using the MATLAB [580] built-in function `interp3`, Figure 19.3(p). The interpolated R_r values for the pilot model are shown in Figure 19.2(c).

6. Compute the natural vibration period of the equivalent SDOF system (representing the dam only), including the reservoir water, Figure 19.2(d):

$$T_{dw}^i = R_r^i T_d^i \; ; \quad i = 1, 2, ..., N_{\text{sim}} \tag{19.15}$$

7. Compute the fundamental vibration period of the reservoir water, Figure 19.2(e):

$$T_w^i = \frac{4H_w^i}{C_w^i} \; ; \quad i = 1, 2, ..., N_{\text{sim}} \tag{19.16}$$

8. Compute the period ratio of reservoir water to dam-reservoir period, Figure 19.2(f):

$$R_w^i = \frac{T_w^i}{T_{dw}^i} \; ; \quad i = 1, 2, ..., N_{\text{sim}} \tag{19.17}$$

9. Compute the elasticity ratio of the foundation rock to the dam concrete, Figure 19.2(g):

$$E_r^i = \frac{E_f^i}{E_c^i} \; ; \quad i = 1, 2, ..., N_{\text{sim}} \tag{19.18}$$

10. Read the standard values for the period elongation ratio due to foundation flexibility, R_f, from Appendix A in [545]; these are discrete values of the elasticity ratio:

$$R_f = f(E_r) \tag{19.19}$$

To facilitate implementation of this method and interpolation of the values, an analytical model is fitted to the discrete data points using a non-linear least-squares method:

$$R_f^i = 0.21(E_r^i)^{-0.75} + 0.98 \; ; \quad i = 1, 2, ..., N_{\text{sim}} \tag{19.20}$$

where the goodness-of-fit, as reflected by the coefficient of determination, is $R^2 > 0.999$. For $E_r > 5$, either the foundation effect can be neglected and R_f can be assumed to be unity (Chopra's recommendation) or Eq. 19.20 can be

used directly. The interpolated R_f values for the pilot model are shown in Figure 19.2(h).

11. Compute the fundamental vibration period of the equivalent SDOF system with reservoir water and a flexible foundation interaction, Figure 19.2(i):

$$T^i_{dwf} = R^i_r R^i_f T^i_d \; ; \quad i = 1, 2, ..., N_{\text{sim}} \tag{19.21}$$

12. Read the standard values for the added damping ratio due to hydrodynamic pressure, ζ_r, from Appendix A in Løkke and Chopra [545] which is a discrete function of depth ratio, concrete modulus of elasticity and reservoir bottom wave reflection coefficient (same as Eq. 19.14), Figure 19.5.
Interpolate the values of ζ_r among three parameters using the MATLAB [580] built-in function `interp3`, Figure 19.3(q). The interpolated ζ_r values for the pilot model are shown in Figure 19.2(j).

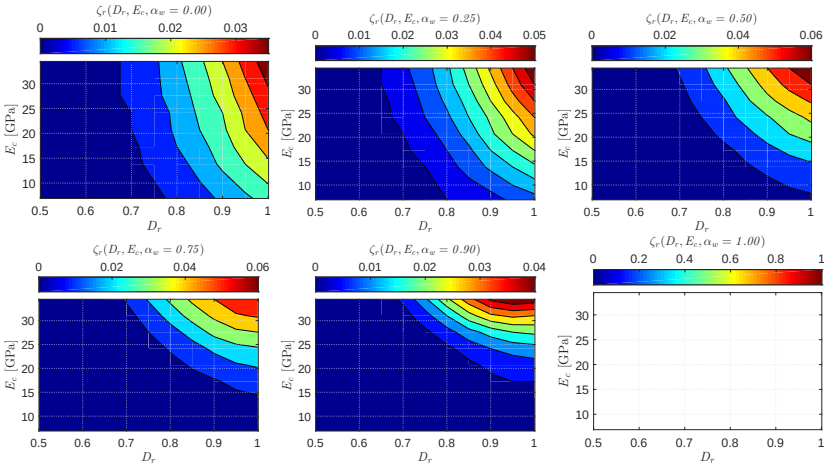

Fig. 19.5: Standard values for the period lengthening ratio due to hydrodynamic effects, ζ_r

13. Read the standard values for the added damping ratio due to foundation flexibility, ζ_f, from Appendix A in Løkke and Chopra [545]; this is a discrete function of the elasticity ratio and hysteretic damping coefficient of the foundation:

$$\zeta_f = f(E_r, \eta_f) \tag{19.22}$$

Interpolate any desired combination using the built-in MATLAB [580] function `interp2`. The interpolated ζ_f values for the pilot model are shown in Figure 19.2(k).
Alternatively, estimate the value of ζ_f using the analytical models derived based on the curve-fitting technique:

$$\zeta_f^i = C_1\left(\eta_f^i\right) \times {E_r^i}^{C_2\left(\eta_f^i\right)} + C_3\left(\eta_f^i\right) \;;\quad i = 1, 2, ..., N_{\text{sim}} \tag{19.23}$$

where η_f-dependent C_i coefficients are obtained with the non-linear least-squares method:

$$\begin{cases} C_1 = \;\; 0.159\eta_f^i + 0.0756 \\ C_2 = \quad\;\; -0.584 \\ C_3 = -0.026\eta_f^i - 0.0206 \end{cases} \quad \eta_f^i < 0.25$$
$$\begin{cases} C_1 = \;\; 0.063\eta_f^i + 0.0978 \\ C_2 = -0.269\eta_f^i - 0.5264 \\ C_3 = \;\; 0.02\eta_f^i - 0.03117 \end{cases} \quad \eta_f^i \geq 0.25 \tag{19.24}$$

14. Compute the damping ratio of the equivalent SDOF system, including water and foundation effects, Figure 19.2(l):

$$\zeta_{dwf}^i = \frac{1}{R_r^i}\frac{1}{{R_f^i}^3}\zeta_d^i + \zeta_r^i + \zeta_f^i \;;\quad i = 1, 2, ..., N_{\text{sim}} \tag{19.25}$$

15. Read the standard values of the normalized (first mode) hydrodynamic pressure for the full reservoir, $\tilde{gp}(\hat{y})/W_w H_w$, from Appendix A in Løkke and Chopra [545]; this is a discrete function of the period ratio, wave reflection coefficient and normalized reservoir height:

$$\{\tilde{gp}(\hat{y})/W_w H_w\} = f(R_w, \alpha_w, \hat{y} = \frac{y}{H_w}) \tag{19.26}$$

These standard values are shown in Figure 19.6. Note that for $\alpha_w = 1.00$, the values are only provided up to $R_w = 0.99$. Now, interpolate the values of $\tilde{gp}(\hat{y})$ from among three parameters using the built-in MATLAB [580] function `interp3`, Figure 19.3(r).

16. Modify the normalized hydrodynamic pressure values from the full reservoir for the specific water level, Figure 19.2(m) (for the sake of clarity, only 10% of the curves are shown):

$$\{gp(\hat{y})\}^i = \{\tilde{gp}(\hat{y})/W_w H_w\}^i \times \left(D_r^2\right)^i \times \left(g \times \rho_w \times H_w^i\right); i = 1, 2, ..., N_{\text{sim}} \tag{19.27}$$

Note that this equation has not yet been adjusted for the actual water height (only the hydrodynamic pressure magnitude is correct). Further adjust the pressure lines based on the actual (and not normalized) height of the water. The built-in MATLAB [580] function `interp2` can be used here to map the values from $\hat{y}$ to y. Consequently, the actual hydrodynamic pressure due to first-mode vibration along the height of the dam, $\{gp(y)\}^i$, is obtained, Figure 19.2(n).

17. Read the standard fundamental mode shape, $\phi_1(\hat{y})$ of the dam supported on a rigid foundation with an empty reservoir from Appendix A in [545]. Alternatively, the following analytical model can be adapted [323]:

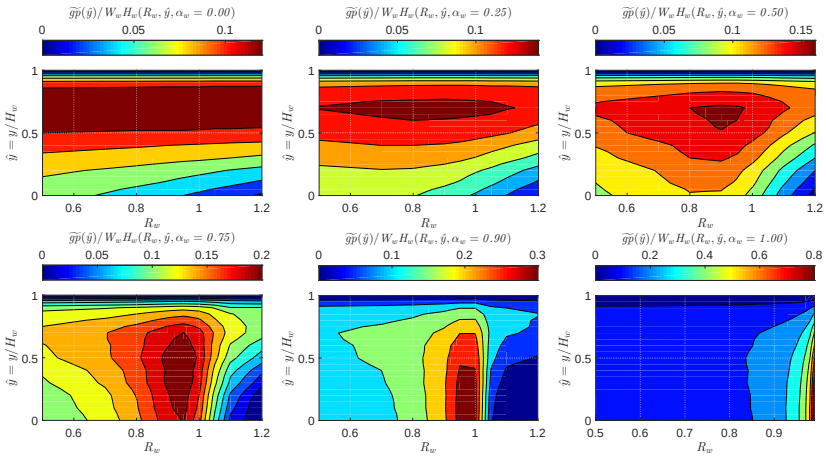

Fig. 19.6: Standard values for the normalized hydrodynamic pressure function with a full reservoir, $gp(\hat{y})/wH_w$

$$\phi_1(\hat{y}) = 1.25\hat{y}^4 - 1.33\hat{y}^3 + 1.02\hat{y}^2 + 0.06\hat{y}\ ; \quad \hat{y} = \frac{y}{H_1} \tag{19.28}$$

Then, adjust the values of $\phi_1(\hat{y})$ for the actual dam by mapping the values from $\hat{y}$ to H_1, Figure 19.2(o).

Note that one can compute the fundamental mode shape directly from finite element analysis and reduce the uncertainty in the pseudo-dynamic method. However, the advantageous of using analytical formulation is to make the entire calculation of "random ESLF" independent from numerical discretization.

18. Discretize the dam (to several trapezoidal and rectangular elements) along its height. In this paper, the discretization length has been set to unity (e.g. 1.00 m). For each block, find the centroid and compute the weight, W_d, of each block (per unit thickness) at this centroid, Figure 19.3(a).
19. Calculate two W_d-related quantities, namely: $W_d \times \phi_1$ (Figure 19.3(b)) and $W_d \times \phi_1^2$ (Figure 19.3(c)). The contribution of ϕ_1 changes both the magnitude and distribution of W_d along the height. Figure 19.3(d) compares three probabilistic W_d-related quantities.
20. Compute the generalized mass of the dam, M_1, and the generalized mass of the equivalent SDOF system, including hydrodynamic effects, $\tilde{M}_1$, see Figure 19.3(e):

$$M_1^i = \frac{1}{g}\int_0^{H_1} W_d^i(y)\phi_1^2(y)\mathrm{d}y\ ; \quad i = 1, 2, ..., N_{\text{sim}} \tag{19.29}$$

$$\tilde{M_1}^{\,i} = \left(R_r^i\right)^2 M_1^i\ ; \quad i = 1, 2, ..., N_{\text{sim}} \tag{19.30}$$

21. Read the values of the hydrodynamic force coefficient, A_p, from Appendix A in Løkke and Chopra [545]; this is a discrete function of the period ratio and wave reflection coefficient, Figure 19.7:

$$A_p = f(R_w, \alpha_w) \tag{19.31}$$

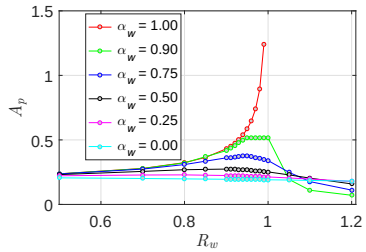

Fig. 19.7: Standard values for the hydrodynamic force coefficient, A_p

Interpolate any desired value using the built-in MATLAB [580] function `interp2`. Note that for $\alpha_w = 1.00$, the values of A_p are only available for $R_w < 1.00$. The interpolated A_p values for the pilot model are shown in Figure 19.3(f).
Alternatively, A_p can be calculated as the integral of $2\tilde{g}p(\hat{y})/W_w H_w$ over the depth of reservoir water for $\frac{H_w}{H_1} = 1$.

22. Compute the generalized earthquake force coefficient associated with both the dam, L_1, and equivalent SDOF system, $\tilde{L_1}$, see Figure 19.3(g):

$$L_1^i = \frac{1}{g}\int_0^{H_1} W_d^i(y)\phi_1(y)\mathrm{d}y \; ; \quad i = 1, 2, ..., N_{\text{sim}} \tag{19.32}$$

$$\tilde{L_1}^{\,i} = L_1^i + \frac{1}{g} f_{hst}^i \left(D_r^i\right)^2 A_p^i \; ; \quad i = 1, 2, ..., N_{\text{sim}} \tag{19.33}$$

where $f_{hst}^i = \frac{1}{2}(g\rho_w)\left(H_w^i\right)^2$ is the hydrostatic force on the upstream face, Figure 19.3(h).

23. Compute the modal participation factor, as shown in Figure 19.3(i):

$$\tilde{\Gamma_1}^{\,i} = \frac{\tilde{L_1}^{\,i}}{\tilde{M_1}^{\,i}} \; ; \quad i = 1, 2, ..., N_{\text{sim}} \tag{19.34}$$

24. Compute the equivalent static lateral forces acting on the upstream face of the dam over its fundamental vibration period, including the dam-water-foundation interaction:

$$f_1^i(y) = \tilde{\Gamma_1}^i \frac{S_a\left(T_{dwf}^i, \zeta_{dwf}^i\right)}{g}\left(W_d^i(y)\phi_1(y) + \{gp\,(y, T_{dw})\}^i\right) \quad (19.35)$$
$$i = 1, 2, ..., N_{\text{sim}}$$

where $S_a\left(T_{dwf}^i, \zeta_{dwf}^i\right)$ is the pseudo-acceleration ordinate of the design response spectrum at T_{dwf}^i and ζ_{dwf}^i of the equivalent SDOF system. All other terms have been previously defined. Assuming that $S_a\left(T_{dwf}^i, \zeta_{dwf}^i\right)$ is constant and equal to $0.7g$, the equivalent static lateral forces in the first mode are given in Figure 19.3(j). Note that this assumption is not quite correct; it has, however, been presented here for illustrative purposes.

25. All the previous steps have been conducted in order to compute the equivalent static force due solely to the first mode. On the other hand, this method is capable of accounting for the higher-mode effect by using the "static correction" concept whereby the ordinates of the pseudo-acceleration design spectrum at the higher modes are approximated by means of PGA. According to this simplified method, the dam-foundation dynamic interaction is neglected for higher modes. The remaining steps explain how to incorporate the equivalent static force due to the higher-mode effect.
26. Read the standard values for the hydrodynamic pressure, $g\tilde{p}_0(\hat{y})/W_w H_w$, from Appendix A in Løkke and Chopra [545]; this is a discrete function of the normalized reservoir height:

$$\{g\tilde{p}_0(\hat{y})/W_w H_w\} = f(\hat{y} = \frac{y}{H_w}) \quad (19.36)$$

Interpolate any intermediate values using the built-in MATLAB [580] function `interp1`.
Alternatively, the following exponential analytical model could be used, as obtained from a non-linear least-squares optimization with $R^2 > 0.999$:

$$\{g\tilde{p}_0(\hat{y})/W_w H_w\} = -0.033\exp(3.14\hat{y}) + 0.777\exp(-0.01\hat{y}) \quad (19.37)$$

Note that this is not a unique form and other analytical models, such as polynomial and Fourier, could also be used.

27. Modify the values of the normalized hydrodynamic pressure for higher modes from the full reservoir at the specific water level, Figure 19.3(k):

$$\{gp_0(\hat{y})\}^i = \{g\tilde{p}_0(\hat{y})/W_w H_w\}^i \times \left(D_r^2\right)^i \times \left(g \times \rho_w \times H_w^i\right); \quad (19.38)$$
$$i = 1, 2, ..., N_{\text{sim}}$$

28. Once again, Eq. 19.39 has not yet been adjusted for the actual water height (only the magnitudes are correct). Further adjust the pressure lines on the basis of the water level. The built-in MATLAB [580] function `interp1` can be used here to

map the values from $\hat{y}$ to y. Consequently, the actual hydrodynamic pressure due to higher modes along the height of the dam, $gp_0(y)$, is derived, Figure 19.3(l).

29. Calculate the value of B_1, which is a measurement that provides the contribution of $p_0(y)$ acting in the fundamental vibration mode along the height, Figure 19.3(m):

$$B_1^i = 0.2\,\frac{1}{g} f_{hst}^i \left(\frac{H_w^i}{H_1}\right)^2 \quad ; \quad i = 1, 2, ..., N_{\text{sim}} \tag{19.39}$$

30. Compute the equivalent lateral static forces associated with the higher vibration modes of dams, including the reservoir water effect (the foundation has already been neglected):

$$f_{sc}^i(y) = \frac{\text{PGA}}{g}\left[W_d^i(y)\left(1 - \frac{L_1^i}{M_1^i}\phi_1(y)\right) + \left(\{gp_0(y)\}^i - \frac{B_1^i}{M_1^i} W_d^i(y)\phi_1(y)\right)\right]; \quad i = 1, 2, \ldots, N_{\text{sim}} \tag{19.40}$$

Once again, in assuming that PGA is constant and equal to $0.5g$, the equivalent static lateral forces associated with higher modes are given in Figure 19.3(n). Let's note that in spite of $S_a\left(T_{dwf}^i, \zeta_{dwf}^i\right)$, PGA is still independent of both vibration period and damping; moreover, it is truly constant for a specific earthquake event recorded at a particular station.

Last but not least, Figure 19.3(o) shows the relative magnitude and direction (positive pushes the dam, negative pulls it) of the hydrostatic force, equivalent static lateral forces associated with the first mode ($S_a\left(T_{dwf}, \zeta_{dwf}\right) = 0.7g$), and higher modes (PGA=$0.5g$).

19.3 Random Fields

19.3.1 Random Fields Classifications

According to Vanmarcke [854], differences between types of random fields originated from the nature of the uncertainty in the studied stochastic environment. Uncertainty about the properties of a random medium is categorized in the passive type. However, a space-time process, $H(\mathbf{x}, \mathbf{t})$, is characterized by active and intrinsic uncertainty. On the other hand, depending on the locations of the observation points, the random field can be classified into the five groups:

- Random series: observations are made at discrete points on a time axis, Figure 19.8(a).
- Lattice process: observations are made at the sites of a lattice in space, Figure 19.8(b).
- Continuous random function: observations are made at all points along a spatial coordinate axes and/or time, Figure 19.8(c).

- Random partition of space: random discrete variable is observed at every point in space, Figure 19.8(d).
- Random point process: points are located in an random pattern in space, Figure 19.8(e).

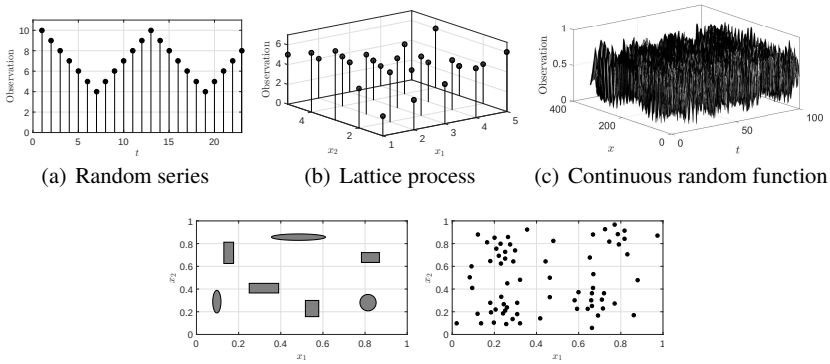

(a) Random series (b) Lattice process (c) Continuous random function

(d) Random partition of space (e) Random point process

Fig. 19.8: Classification of random field based on location of observation; adopted from [854]

19.3.2 Random Fields Generators

In an interesting classification, Van der Have [853] provided a comprehensive review on some of the widely used techniques to generate the random fields. Basically, two classes exist.

- Class I: This class consists of a spatially correlated random variable and a discretization method. For every point in the finite element domain, a random variable is generated which is correlated to other points in the random field domain. The evaluated points might be element integration points, nodes, or a representative point (e.g. element center).
  Discretization techniques can also be divided into three main categories:
  - Point discretization methods which result in a piecewise constant random field. They include MPM and IPM techniques.
  - Point discretization methods which result in a continuous random field. They include SFM and OLE techniques.
  - Average discretization methods which include SAM and WIM techniques.
- Class II: This class is based on series expansion methods where the random field is represented by a sum of functions which are multiplied by a random variable.

This class generates a continuous random field. To be applied in a finite element mesh, the continuous functions should be numerically integrated.

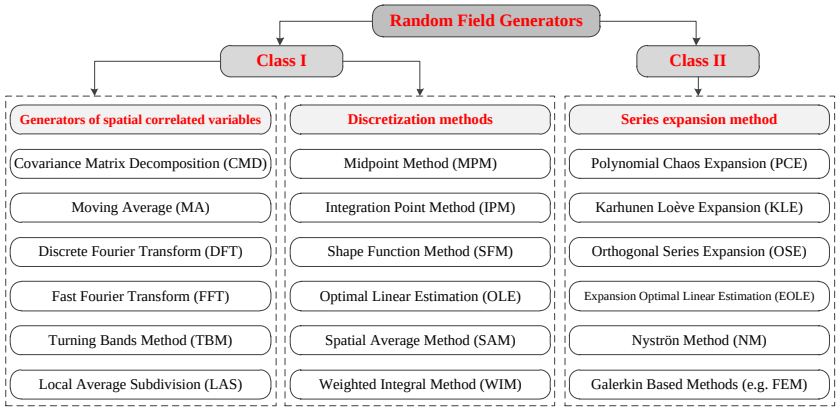

Fig. 19.9: Classification of random field based on generators; adopted from [853]

19.3.3 Efficient Random Field Generator

In this section, an efficient random field generator is explained based on covariance matrix decomposition and midpoint discretization technique. It is based on uniformly distributed random fields which are obtained by transformation from normally distributed, homogeneous and isotropic random fields [300]. It is used in the context of LHS to reduce the total number of simulations [667]:

- Assuming that the random field is time-independent, one can decompose $H(\mathbf{x})$ as:
$$H(\mathbf{x}) = \mu(\mathbf{x}) + \alpha(\mathbf{x}) \tag{19.41}$$
where $\mu(\mathbf{x})$ is mean value function, $\alpha(\mathbf{x})$ is fluctuating component, and $\mathbf{x}$ represents the position vector.
- $\mu(\mathbf{x})$ is a deterministic function, while $\alpha(\mathbf{x})$ is a random function with zero-mean and auto-covariance function of
$$C_{aa}(\xi, \sigma_0) = \sigma_0^2 \, \rho_{aa}(\xi) \tag{19.42}$$
where $\xi = |\mathbf{x} - \mathbf{x}'|$ is the distance of any two arbitrary locations, σ_0 is the (constant) standard deviation, and ρ_{aa} is the auto-correlation function.
- There are different expressions for the auto-correlation function [572]:

$$\rho_{aa}(\xi) = \begin{cases} \text{Exponential} & \exp\left(-\frac{\xi}{l_{corr}}\right) \\ \text{Isotropic Markov} & \exp\left(-\frac{2\xi}{l_{corr}}\right) \\ \text{Square exponential} & \exp\left(-\left(\frac{\xi}{l_{corr}}\right)^2\right) \\ \text{Sinusoidal} & \frac{\sin\left(-2.2\frac{\xi}{l_{corr}}\right)}{-2.2\frac{\xi}{l_{corr}}} \\ \text{Nugget-effect} & \begin{cases} 1 \text{ for } |\xi| = 0 \\ 0 \text{ for } |\xi| > 0 \end{cases} \end{cases} \tag{19.43}$$

Note that in some cases, higher-order exponential functions may be considered, i.e. $power > 2$. Figure 19.10(a) compares different models in Eq. 19.43. In all of them, the maximum ξ in the finite element domain is assumed to be unit and $l_{corr} = 0.5$. Moreover, Figure 19.10(b) shows dependency of ρ_{aa} to the correlation length and point distance (square exponential form is used).

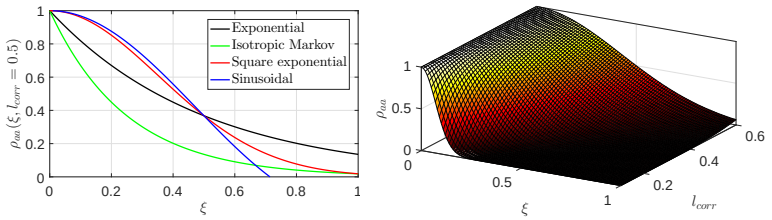

(a) Different correlation models (b) Different correlation length

Fig. 19.10: Comparison of auto-correlation functions with different length

- Midpoint method (MPM) is used to discretize the finite element domain [241]. Let us assume the objective is to generate a set of random fields for a square domain in which there are 25 nodes along each direction (there exist 625 nodes in total). Figure 19.11(a) shows the one-to-one ξ for all the nodes. Figures 19.11(b) and 19.11(c) show the correlation matrix assuming two l_{corr} as 0.25 and 0.50, respectively.
- The correlation matrix, $\mathbf{C}$, is constructed based on the discretized auto-correlation functions [77]

$$\mathbf{C} = \begin{bmatrix} \rho_{11} & \rho_{12} & \cdots & \rho_{1k} \\ \rho_{21} & \rho_{22} & \cdots & \rho_{2k} \\ \vdots & \vdots & \ddots & \vdots \\ \rho_{k1} & \rho_{k2} & \cdots & \rho_{kk} \end{bmatrix} = \begin{bmatrix} 1 & \rho_{12} & \cdots & \rho_{1k} \\ \rho_{21} & 1 & \cdots & \rho_{2k} \\ \vdots & \vdots & \ddots & \vdots \\ \rho_{k1} & \rho_{k2} & \cdots & 1 \end{bmatrix} \tag{19.44}$$

where if $i = j$, $\xi_{ij} = 0$ and $\rho_{ij} = 1$, and k is number of correlated random variables.

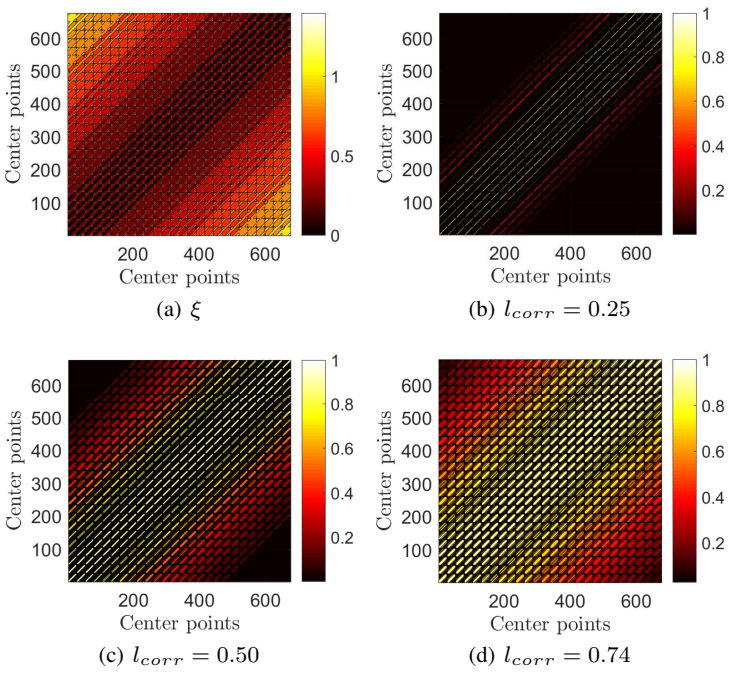

Fig. 19.11: Sample application of random field on a square with unit length and 25 nodes in each direction

- Replacing matrix $\mathbf{C}$ by a set of r uncorrelated random variables ($r \ll k$), the sum of the r largest eigenvalues is approximately equal to the trace of $\mathbf{D}$ (eigenvalue matrix of $\mathbf{C}$):

$$\mathbf{D} = \mathbf{Z}^T \mathbf{C} \mathbf{Z} \tag{19.45}$$

  where $\mathbf{Z}$ is eigenvector matrix of $\mathbf{C}$.
- If the r largest eigenvalues and eigenvectors are stored in an $r \times r$ matrix $\tilde{\mathbf{D}}$ and a $k \times r$ matrix $\tilde{\mathbf{Z}}$, the target covariance matrix is approximately equal to

$$\tilde{\mathbf{C}} = \tilde{\mathbf{Z}} \tilde{\mathbf{D}} \tilde{\mathbf{Z}}^T \tag{19.46}$$

  This important feature allows the application of Latin Hypercube sampling (LHS) in conjunction with random fields. Thus, the number of realization should be $n > r$ (and not $n > k$), where $r \ll k$.
- Generate an $n \times r$ matrix $\tilde{\mathbf{P}}$ in which each of r columns are a random permutation of $1, \ldots, n$.
- Generate matrix $\tilde{\mathbf{Y}}$ which is the normalized version of $\tilde{\mathbf{P}}$ and is mapped on a normal distribution:

$$\tilde{\mathbf{Y}} = \Phi^{-1}_{(0,1)}\left(\frac{\tilde{\mathbf{P}}}{n+1}\right) \tag{19.47}$$

- Estimate the covariance matrix of $\tilde{\mathbf{Y}}$ and factorize though the Cholesky decomposition
$$\tilde{\mathbf{L}}\tilde{\mathbf{L}}^T = \text{cov}(\tilde{\mathbf{Y}}) \tag{19.48}$$
where $\tilde{\mathbf{L}}$ is lower triangular.
- Compute a new matrix with sample covariance equal to the identity
$$\tilde{\mathbf{Y}}^* = \tilde{\mathbf{Y}}(\tilde{\mathbf{L}}^{-1})^T \tag{19.49}$$
- Construct another new matrix $\tilde{\mathbf{P}}^*$ using the ranks of the elements of the columns of $\tilde{\mathbf{Y}}^*$ (permutations of $1, \ldots, n$).
- Also, construct matrix $\mathbf{Q}$ (or Q_{ij}) which specifies the random component of variable $\tilde{\mathbf{Y}}$ in element i and realization j as
$$\mathbf{Q} = \bar{\mathbf{Q}}\tilde{\mathbf{D}}^{1/2}\tilde{\mathbf{Z}}^T \tag{19.50}$$
in which
$$\bar{\mathbf{Q}} = \Phi^{-1}_{(0,1)}\left(\frac{\tilde{\mathbf{P}}^* - \tilde{\mathbf{R}}}{n}\right) \tag{19.51}$$
where $\tilde{\mathbf{R}}$ is a random number uniformly distributed in $(0, 1)$.
- Finally, compute the sampling matrix
$$\tilde{\mathbf{V}} = F^{-1}\left[\Phi\left(\mathbf{Q}\right)\right] \tag{19.52}$$
where F^{-1} is a transformation with respect to a specified marginal statistics of the k variables. In the case of uniform distribution, the sampling matrix can be rewritten as
$$\tilde{\mathbf{V}} = \mathrm{L}_B + \left(\mathrm{U}_B - \mathrm{L}_B\right)\left[\Phi\left(\mathbf{Q}\right)\right] \tag{19.53}$$
where L_B and U_B refer to lower and upper bounds, respectively.

Figure 19.12 shows four realizations of the generated random fields assuming unit mean and standard deviation of 0.2. Five different correlation lengths are assumed: 0.025, 0.05, 0.1, 0.3 and 0.5, respectively.

19.3.4 FE Implementation of RF

The finite element (FE) implementation of the random fields is briefly explained in accordance to Figure 19.13. First, the shape and dimensions of the studied space (e.g. structural component in this plot) is identified, and an appropriate grid is formed all over it. Density of the grid should be proportional to the density of the FE mesh. It is possible to have a non-uniform mesh specially for the models in which the crack path is already (roughly) known.

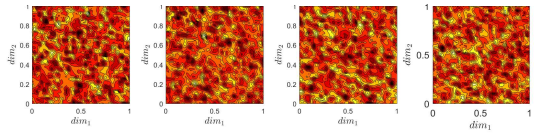

(a) $l_{corr} = 0.025$

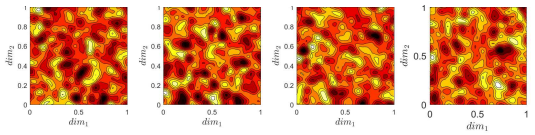

(b) $l_{corr} = 0.05$

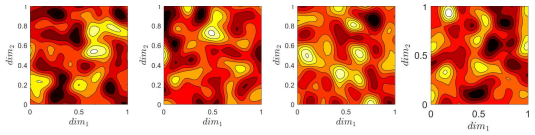

(c) $l_{corr} = 0.10$

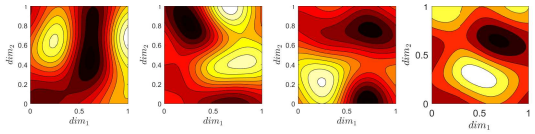

(d) $l_{corr} = 0.30$

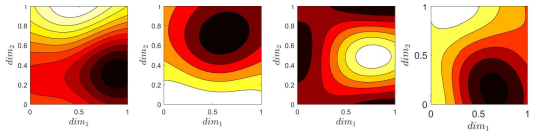

(e) $l_{corr} = 0.50$

Fig. 19.12: Four realizations of the generated two-dimensional random field with different correlation length

Next, several continuum RF realizations are generated over the domain using the mean and STD of the material property, lower and upper bounds, and the correlation length. The latter parameter is somehow unknown in most of the macro-scale analyses. One may use engineering judgment to draw a meaningful conclusion, or all the potential l_{corr} might be examined in a comprehensive study.
Midpoint of each element is determined, and then matched with the closest mesh grid point from RF. For very large elements, it is possible to take the average of the mesh grid points located inside it. Subsequently, the continuum nature of the RF is converted to a discrete form. Once those random properties are assigned to the elements, the model can be loaded and numerically analyzed with conventional

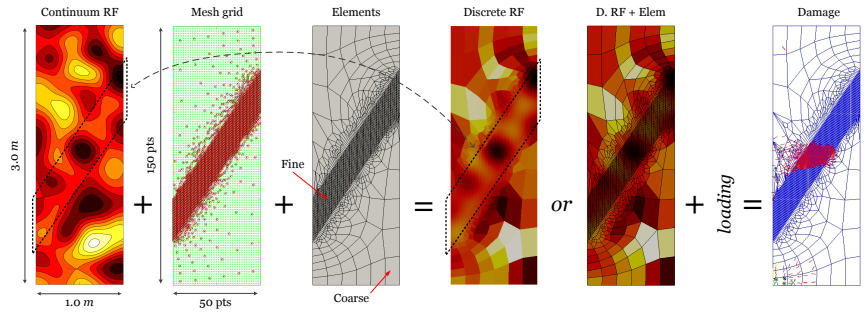

Fig. 19.13: Step-by-step RF generation by covariance matrix decomposition and midpoint discretization method; from left to right: 1) continuum RF with l_{corr}=0.2 m; 2) a uniform grid of 50×150 (green) points for RF, element (red) midpoint of irregular FE mesh, and closest matching (black) point from grid to mesh; 3) irregular FE mesh; 4) transfered continuum RF to discrete form; 5) discrete RF in the FE program; and 6) sample damage response of the model subjected to an arbitrary loading

techniques. Finally, the stress field and the potential crack propagation is computed. One may note that whole this procedure is only for a single realization, and it should be repeated (e.g. LHS technique) to propagate the uncertainty of spatial variability in macro-scale.

Chapter 20
Metamodeling and Machine Learning

Abstract
A metamodel, or surrogate model, is a model of a model. Metamodeling refers to a process of generating such metamodels which is based on analysis, construction and development of the frames, rules, constraints, models and theories applicable and useful for modeling a predefined class of problems. On the other hand, machine learning is an application of artificial intelligence that provides systems the ability to automatically learn and improve from experience without being explicitly programmed. This chapter provides a review on different design of experiment techniques, as well as various machine learning algorithms.

20.1 Introduction

According to the general framework of uncertainty quantification introduced by Sudret [809], for every type of uncertainty analysis, up to three ingredients can be identified, Figure 20.1:

- Step A: A computational model (in this book different infrastructures) used to compute several quantities of interest (QoIs) to the analyst. This model is (in a majority of cases) a black-box map of the form $Y = \mathcal{M}(\boldsymbol{X})$ that provides a set of responses Y for every combination of input parameters $\boldsymbol{X}$.
- Step B: A model of the uncertainty in the input parameters, $\boldsymbol{X}$, due to aleatory and/or epistemic nature of variability. It is usually presented in the form of probabilistic models.
- Step C: An uncertainty analysis that aims at combining the epistemic/aleatory uncertainties with the computational model, to quantify some property in the stochastic system (e.g., mean, variance).

The overall goal in this chapter is to investigate the application of different metamodels and machine learning techniques in uncertainty quantification. The provided materials are mainly based on Hariri-Ardebili [390], Hariri-Ardebili and Boodagh [379], Hariri-Ardebili and Barak [392], Hariri-Ardebili and Sudret [398].

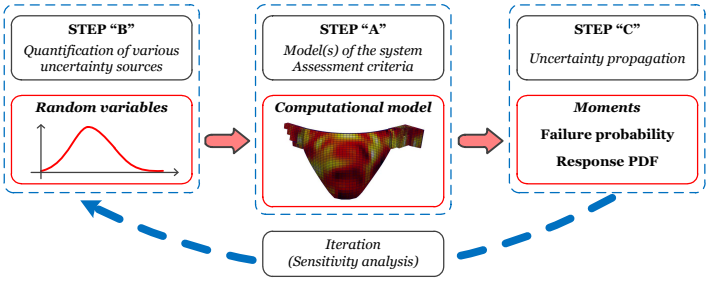

Fig. 20.1: The general uncertainty quantification framework; adapted from [570]

20.2 Concept of Metamodeling

Engineering analyses along with computer-based simulations are used extensively to obtain the outcome of a system given the input parameters. In most cases, an analytical or explicit solution does not exist between the input and output parameters. Many of the finite element packages act like a "black box" and provide the responses by spending extensive computational effort (especially for transient simulations) [721]. Metamodels provide the following support functions:

- Model approximation: simplified models are replaced by a computationally expensive one,
- Design space exploration: provide a comprehensive understanding of the problem in the whole design space,
- Optimization: can be coupled with different optimization techniques (e.g. global, multi-objective, probabilistic and etc.) to reduce the computational cost,
- Reliability based design: can be used to approximate the complex linear and nonlinear limit state functions.

A metamodel (or model of the model) is a mathematical approximation of the implicit simulation code. Outputs are presented in a closed-form function of input parameters. Let us assume that a true but unknown relationship exists between real output, y, and a vector of input variables, $\mathbf{u}$, in the form of:

$$y = g(\mathbf{u}) + \epsilon \tag{20.1}$$

where ϵ refers to noise with zero mean and variance σ^2. Then, a metamodel $\tilde{g}(\mathbf{u})$ is intend to approximate the true function $g(\mathbf{u})$ as well as possible. Thus, we want to minimize $(y - \tilde{g}(\mathbf{u}))^2$. It is well-accepted that whichever function $\tilde{g}(\mathbf{u})$ is selected, the expected error can be decomposed into bias and variance components:

$$\mathbb{E}\left[(y - \tilde{g}(\mathbf{u}))^2\right] = \underbrace{(E\left[\tilde{g}(u)\right] - g(u))^2}_{\text{Bias}^2} + \underbrace{E\left[(\tilde{g}(u) - E\left[\tilde{g}(u)\right])^2\right]}_{\text{Variance}} + \sigma^2 \tag{20.2}$$

The error due to bias is taken as the difference between the expected prediction of the metamodel and the correct value which is going to be predicted. However, the error due to variance is taken as the variability of a metamodel prediction for a given data point. There is a tradeoff between a metamodel's ability to minimize bias and variance.
Construction of a metamodel involves three main steps: 1) design of experiment, 2) metamodeling, and 3) model fitting. Figure 20.2 shows different choices for each of the above mentioned steps. Each combination of these three steps refers to a specific technique (some popular ones are mentioned inside the plot). Response surface method (RSM) is, in fact, a combination of DOE with polynomial-type functional form in which the least-squares regression is used for model fitting. The following section discusses RSM more in detail.

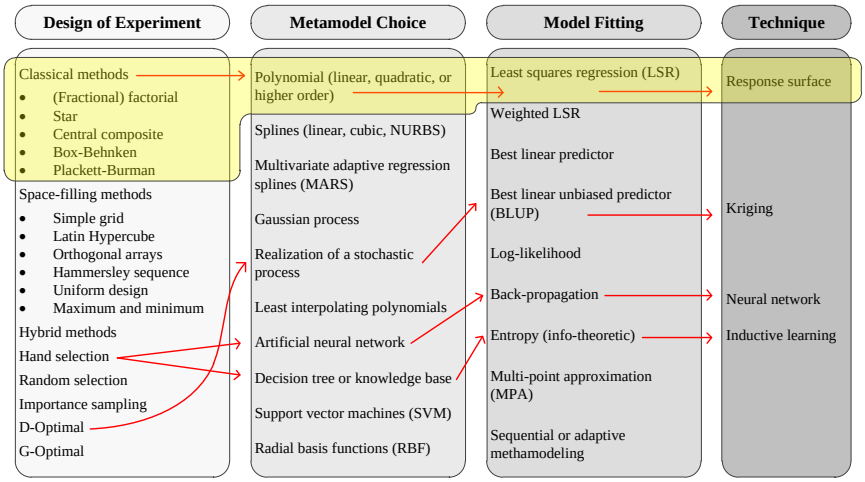

Fig. 20.2: Composition of commonly used metamodeling techniques, adapted from [792] and [865]

20.3 Design of Experiment

By definition, DOE refers to a statistical technique that systematically defines the minimum (or efficient) number of experimental sampling points to optimize the computed or observed responses [170]. There are three main terminologies dealing with a DOE:

- **Factor**: is a variable over which the designer has direct control in an experiment. There are different categories for a "factor." Among them *controllable* and *uncontrollable*; *primary* (their impact on the response is more relevant) and *nuisance* (can influence the response but they are not of interest for the designer).

- **Design space**: defines a range of variability and must be set for each variable.
- **Level**: is the number of different values a factor should be set to according to its discretization.

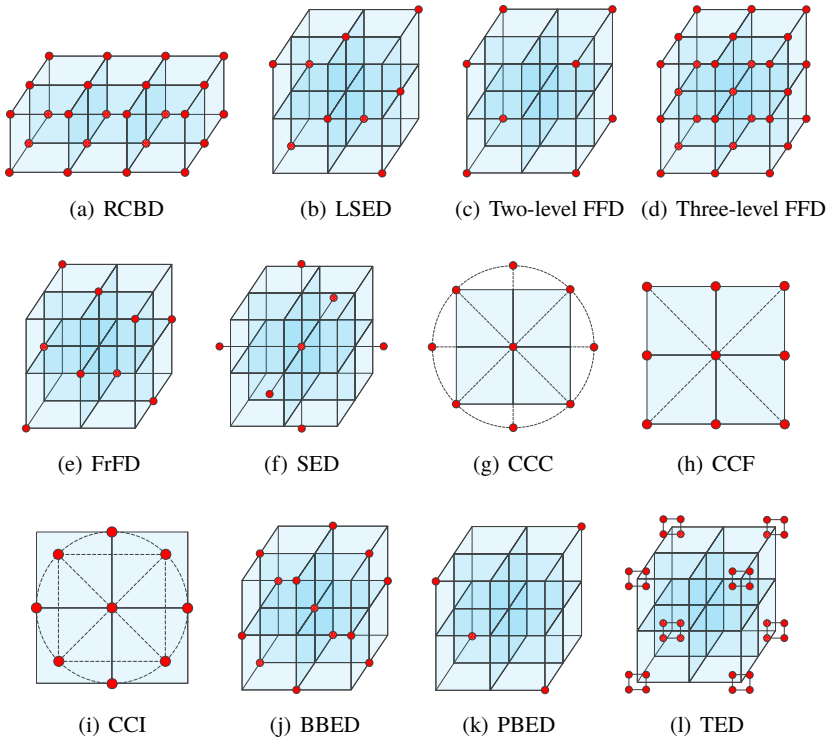

(a) RCBD (b) LSED (c) Two-level FFD (d) Three-level FFD

(e) FrFD (f) SED (g) CCC (h) CCF

(i) CCI (j) BBED (k) PBED (l) TED

Fig. 20.3: Three-factor DOE techniques with two, three and five levels

20.3.1 Randomized Complete Block Design (RCBD)

RCBD is a technique based on blocking and is used when the designer is interested in one or more particular (primary) factors. It means that the other (nuisance) factors are blocked by keeping them constant. Let us assume that in an experiment there are k controllable factors $X_1, X_2..., X_k$ and only one is a primary factor, X_k. Also, let us assume that the number of levels in each factor is $L_1, L_2, ..., L_k$. Thus, the number of required experiments for an RCBD will be $N_{DOE} = \prod_{i=1}^{k} L_i$. Figure 20.3(a) shows an RCBD with $k = 3$, $L_1 = 3$ (A, B, C), $L_2 = 4$ (α, β, γ, θ), $L_3 = 2$ (I, II), and $N_{DOE} = 24$.

20.3.2 Latin Square Experimental Design (LSED)

LSED is fundamentally similar to RCBD while it requires smaller set of samples. In fact, LSED performs a single experiment in each block, and it requires some conditions to be respected to be applicable. In this technique, k should be 3 with two nuisance factors (X_1 and X_2), one primary factor (X_3), and $L_1 = L_2 = L_3 = L$. The sample size is $N_{DOE} = L^2$. In LSED, X_1 and X_2 are discretized into an L-by-L grid. In each cell, a capital letter (i.e., A, B, C, $\cdots$) is written in a way that each row and column receive the first L letters of the alphabet once [170]. The row and the column numbers indicate the level of the nuisance factors, while the letters refer to the primary factor level. Figure 20.3(b) shows an LSED with $k = 3$, $L = 3$ and $N_{DOE} = 9$.

20.3.3 Higher Order LSED

The technique in Sec. 20.3.2 is only applicable for $k = 3$, but it can be extended for $k = 4$ and $k = 5$ which are called Graeco-Latin square (GLS) and Hyper-Graeco-Latin square (HGLS), respectively. In GLS and HGLS, additional nuisance factors should be used as Greek letters (and other symbols). Two rules should be respected: 1) in each row and column, the levels of the factors must not be repeated, and 2) each factor must follow a different letters/numbers pattern in the table. Note that for HGLS, L must be ≥ 4. In general, for a design with k and L, a table of L-by-L should be developed (thus the sample size is $N_{DOE} = L^2$) in which each cell contains $k-2$ letters/numbers. GLS and HGLS can not be shown graphically as they exceed 3D space.

20.3.4 Full Factorial Design (FFD)

FFD is the most common technique in experimental design which is usually performed as a two-level ($L = 2$) or three-level ($L = 3$) method. Since the samples are given by every possible combination of the factors (k), the sample size is $N_{DOE} = L^k$. FFD is an orthogonal design method in which the scalar product of the columns of any two factors becomes zero. This technique does not distinguish between the primary and nuisance factors. FFD is a suitable technique for polynomial response surface interpolation (this will be discussed later). Two-level FFD, Figure 20.3(c), can be interpolated with a complete bi-linear form, three-level FFD, Figure 20.3(d), with a complete bi-quadratic form, and four-level FFD with a complete bi-cubic [170].

It is convenient to use the "coded" (standardized) factors (x_i) instead of the actual values (u_i). In the case of two-level FFD they are referred to "± 1" and in the case of three-level FFD they are "-1," "0," and "+1." It is defined as:

$$x_i = \frac{u_i - (u_i^U + u_i^L)/2}{(u_i^U - u_i^L)/2} \tag{20.3}$$

where u_i^U and u_i^L are upper and lower bounds of the actual values, respectively.

20.3.5 Fractional Factorial Design (FrFD)

FrFD is, in fact, a subset of FFD to reduce the total number of experiments. The sample size in FrFD is usually one-half, one-third, or one-quarter of FFD. The key point in FrFD is to select the samples in a way that they be balanced (meaning that each factor has the same number of samples for each of its levels) and orthogonal. The sample size is $N_{DOE} = 2^{k-1}$ and $N_{DOE} = 2^{k-2}$ for one-half and one-quarter of two-level FFD and $N_{DOE} = 3^{k-1}$ for one-third of three-level FFD. For the general case, sample size is $N_{DOE} = L^{k-p}$, where p is related to the fraction of design.
The construction of one-half FrFD with k factors starts with a regular FFD with $k-1$ factors (2^{k-1} samples). Then, the levels of the additional factor are added as an interaction of the other parameters (e.g., $\pm X_1.X_2$). Figure 20.3(e) shows the one-half three-level FrFD with $k = 3$, $L = 3$ and $N_{DOE} = 9$.

20.3.6 Star Experimental Design (SED)

SED contains two axial points on the axis of each factor at a distance δ from the design center and one center point (with all factors in their mean - or 0 - value). Thus, the sample size is $N_{DOE} = 2k+1$. Selection of the star points location is important since it affects the rotatability properties (this will be discussed later). Figure 20.3(f) shows an SED with $k = 3$, $N_{DOE} = 7$ and $\delta > 1$.

20.3.7 Central Composite Design (CCD)

CCD is, in fact, a combination of a two-level FFD and an SED. Thus, the sample size is $N_{DOE} = k^2+2k+1$. Since there are more samples than those really necessary for a bilinear interpolation (i.e., $2k$), the curvature of the design space can be estimated as well. As discussed in Sec. 20.3.6, based on the location of star points (δ), different versions of CCD can be produced. First, the distance between the central point and the samples on FFD is normalized to unit (diagonal distance). Then, distance of the star points (from the center) can be chosen in one of the following ways (note that the concept of distance in this section is different from normalized coded values):

- Central Composite Circumscribed (CCC): If $\delta = 1$, all the samples are placed on a hyper-sphere centered on the central point and it requires five levels for each factor (i.e., -1, $-\frac{1}{\sqrt{k}}$, 0, $+\frac{1}{\sqrt{k}}$, +1). Figure 20.3(g) shows an example with $k = 2$, $L = 5$ and $N_{DOE} = 9$.
- Central Composite Faced (CCF): If $\delta = \frac{1}{\sqrt{k}}$, the star points remain on the same levels as the two-level FFD and thus, it requires only three levels for each factor (i.e., -1, 0, +1). Figure 20.3(h) shows an example with $k = 2$, $L = 3$ and $N_{DOE} = 9$.
- Central Composite Inscribed (CCI): This is a scaled down version of CCF, $\delta = \frac{1}{\sqrt{k}}$, and is used in the cases that the limits specified for the levels cannot be

violated. Again, it requires five levels for each factor (i.e., $-\frac{1}{\sqrt[4]{k^3}}$, $-\frac{1}{\sqrt{k}}$, 0, $+\frac{1}{\sqrt{k}}$, $+\frac{1}{\sqrt[4]{k^3}}$). Figure 20.3(i) shows an example with $k = 2$, $L = 5$ and $N_{DOE} = 9$.

- Central Composite Scaled (CCS): If δ is arbitrarily selected to be either > 1 or $< \frac{1}{\sqrt{k}}$, the star points fall outside or inside of the hypersphere. This method requires five levels for each factor.

20.3.8 Box-Behnken Experimental Design (BBED)

BBED is an incomplete three-levels factorial designs which is, in fact, a combination of two-level FFD and a special form of incomplete block designs. BBED is supposed to reduce the sample size as the number of parameters grow, but it is still sufficient to estimate the coefficients of a 2nd degree least-squares polynomial. Size of the factorial and number of the blocks have been selected in a way that it becomes rotatable. Specific tables are provided by Box and Behnken [143] for a wide range of factors. Figure 20.3(j) shows a BBED with $k = 3$ where the samples are at the center and middle of the edges. In general:

- $k = 3$, $N_{DOE} = 12 + 1 = 13$
- $k = 4$, $N_{DOE} = 24 + 1 = 25$
- $k = 5$, $N_{DOE} = 40 + 1 = 41$
- $k = 6$, $N_{DOE} = 48 + 1 = 49$

20.3.9 Plackett-Burman Experimental Design (PBED)

PBEDs are a set of economical designs with the run number a multiple of four and are appropriate for screening purposes and detecting the large effects because they are highly confounded with two-factor interactions. The experiment is constrained with the condition that $N_{DOE} = k + 1$. Sample size is then computed as $N_{DOE} = k+4-\text{MOD}(k, 4)$, in which MOD is the modulo operation which finds the remainder of the Euclidean division of k by 4. In PBED, the first row is provided by Plackett and Burman [697] and the second row to $N_{DOE} - 1$ are produced by shifting the elements of the previous row one place to the right. The last row is a 1-by-k vector of -1 (note that plus and minus signs refer to the two-level design). Some of the PBED patterns (for the first row only) are:

- $k = 3$, $N_{DOE} = 4$, Pattern: $+1\ +1\ -1$
- $k = 7$, $N_{DOE} = 8$, Pattern: $+1\ +1\ +1\ -1\ +1\ -1\ -1$
- $k = 11$, $N_{DOE} = 12$, Pattern: $+1\ +1\ -1\ +1\ +1\ +1\ -1\ -1\ -1\ +1\ -1$
- $k = 15$, $N_{DOE} = 16$, Pattern: $+1\ +1\ +1\ +1\ -1\ +1\ -1\ +1\ +1\ -1\ -1\ +1\ -1\ -1\ -1$

It is worthy to note that the cases $N_{DOE} = 4$, 8, 16, and 32 are equivalent to FrFD with 2^{3-1}, 2^{7-4}, 2^{15-11}, and 2^{31-26} [170]. In PBED, if $k < (N_{DOE} - 1)$, then only the first k columns are used. Figure 20.3(k) shows an example with $k = 3$ and $N_{DOE} = 4$.

20.3.10 Taguchi Experimental Design (TED)

TED is based on distinction between the controllable and noise factors to make the problem less sensitive to the variations in uncontrollable factors. Two orthogonal designs are selected: 1) inner array for the controllable variables and 2) outer array for the noise variables. Taguchi method is a combination of these two arrays. It means that a full set of outer array experiments are performed for each sample in the inner one (which provides valuable information about the interaction). Figure 20.3(l) shows an example with k = 5 ($k_i = 3$ and $k_o = 2$) and $L = 2$ based on FFD. The problem requires 2^2 factorial designs (outer array) for each of 2^3 samples in the inner array. At each of location the inner array ($i = 1, 2, \ldots, 2^3$), the total of 2^2 results are computed from the outer array and are referred to as $y_{i,j}$ ($j = 1, \ldots, 2^2$). Then, the expectation, $\mathbb{E}[y_i]$, and the standard deviation, $\mathbb{E}[(y_i - \mathbb{E}[y_i])^2]$, of entries with the fixed index i are evaluated.
Therefore, by adopting FFD for both the inner and outer arrays, TED requires $N_{DOE} = L^{k_i} \times L^{k_o}$ which is equivalent to FFD with $L^{k_i+k_o}$ samples. However, the main advantage of TED is that it allows one to estimate the statistics of the design point as noise enters the system. Cavazzuti [170] explains tables of the orthogonal arrays for TED along with some of the DOEs.

20.3.11 Comparison of DOE Techniques

Last but not least, Figure 20.4 compares different DOE techniques based on the required number of simulations for any desired factor, k. Some of them have a mushroom growth even at the medium k values (e.g., three-level FFD and RCBD); others have reasonable number of simulations for the systems with large factors (e.g., CCD and higher-order LSED).

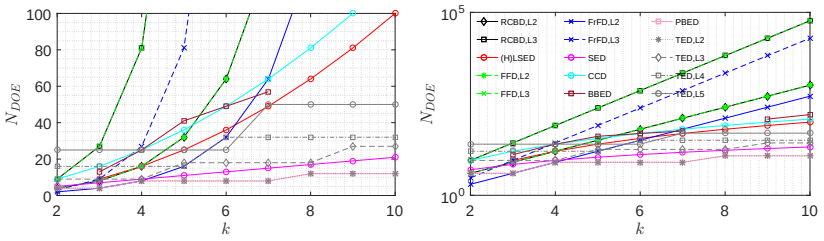

(a) Normal space for $N_{DOE} < 100$ (b) Logarithmic space for large N_{DOE}

Fig. 20.4: Relationship between number of simulations, technique type, number of factors and levels

20.4 Response Surface Method

Different versions of response surface method (RSM) with various capabilities and improvements are proposed for reliability analysis and design optimization. Some of the most relevant papers are [289], [718], [900], [890], [23], [914], [742], and [909] for the readers who want to explore this method more in detail. Khuri and Mukhopadhyay [502] provided a very comprehensive historical review on the development of RSM. In this section, an approach to construct a polynomial based response surface is explained. Next, the criteria to evaluate the accuracy of metamodels is summarized.

20.4.1 Polynomial Metamodel

Polynomial metamodels are among the widely used functions for RSM. The order of polynomial is limited to one or two for most of the practical applications. Also, accounting for the interaction terms increases the accuracy of the metamodel (although they are uneconomic for problems with many RVs). A quadratic polynomial with cross terms can be presented as:

$$y = \beta_0 + \sum_{i=1}^{k} \beta_i x_i + \sum_{i=1}^{k} \beta_{ii} x_i^2 + \sum_{i=1}^{k-1} \sum_{j=i+1}^{k} \beta_{ij} x_i x_j + \varepsilon \tag{20.4}$$

where y is the response variable, x_i and x_j are coded input variables (See Equation (20.3)), β_0, β_i, β_{ii}, β_{ij} are the unknown coefficients, ε refers to error term (in the regression context), and k is the number of factors.
Equation (20.4) has the ability to be written as a linear regression model with m parameters (total number of unknown coefficients to be estimated) as:

$$y = \beta_0 + \sum_{i=1}^{m-1} \beta_i z_i + \varepsilon \tag{20.5}$$

where $\mathbf{z}$ is a vector of dummy first-order variables which is replaced with the original input variable $\mathbf{x}$ that includes quadratic terms and m is obtained from Table 20.1. A general matrix form of the linear model in Equation (20.5) can be written as:

$$\mathbf{Y_{N\times 1}} = \mathbf{Z_{N\times m}} \boldsymbol{\beta}_{\mathbf{m}\times \mathbf{1}} + \boldsymbol{\varepsilon}_{\mathbf{N}\times \mathbf{1}} \tag{20.6}$$

where N is number of simulations or experimental designs, N_{DOE}.

Table 20.1: Relationship between m and k in polynomial form

Model type	Linear	Quadratic	Cubic	n^{th} degree
m	$k+1$	$\frac{(k+1)(k+2)}{2}$	$\frac{(k+1)(k+2)(k+3)}{6}$	$\frac{(k+n)!}{n!\,k!}$

The unknown parameters can be estimated by least-squares regression method which minimizes the sum of squares of the differences between the actual output, $\mathbf{Y}$, and the approximated one, $\hat{\mathbf{Y}}$. Box and Draper [144] showed that the coefficients can be estimated by:

$$\boldsymbol{\beta} = \left(\mathbf{Z}^{\boldsymbol{T}}\mathbf{Z}\right)^{-\mathbf{1}}\left(\mathbf{Z}^{\boldsymbol{T}}\mathbf{Y}\right) \tag{20.7}$$

20.4.2 Goodness-of-fit

Having the estimated coefficients from the previous section, the next step is to evaluate the adequacy of model fitting. Some of the widely used models to assess the goodness-of-fit (GOF) are:

- Normal regression parameter:

$$R^2 = 1 - \frac{\sum_{i=1}^{N}\left(y_i - \hat{y}_i\right)^2}{\sum_{i=1}^{N}\left(y_i - \bar{y}\right)^2}, \qquad \bar{y} = \frac{1}{N}\sum_{i=1}^{N} y_i \tag{20.8}$$

- Adjusted regression parameter:

$$R^2_{adj} = 1 - \left(1 - R^2\right)\left(\frac{N-1}{N-m}\right) \tag{20.9}$$

- Average absolute error:

$$Err_{avg} = \frac{\sum_{i=1}^{N}\left|y_i - \hat{y}_i\right|}{\sum_{i=1}^{N} y_i} \times 100\% \tag{20.10}$$

- Maximum absolute error:

$$Err_{max} = \max_i\left(\frac{\left|y_i - \hat{y}_i\right|}{\frac{1}{N}\sum_{i=1}^{N} y_i}\right) \times 100\% \tag{20.11}$$

- Root mean square error:

$$RMSE = \frac{\sqrt{\frac{1}{N}\sum_{i=1}^{N}\left(y_i - \hat{y}_i\right)^2}}{\frac{1}{N}\sum_{i=1}^{N} y_i} \tag{20.12}$$

20.5 Polynomial Chaos Expansions

20.5.1 Constructing the Polynomial Basis

Let us consider a system in which its computational model can be represented by $\mathcal{M}$ and is a function of M input parameters. Due to uncertainty, the parameters are modeled by an M dimensional vector $\boldsymbol{X} = \{X_1, X_2, ..., X_M\}$. The components are assumed to be statistically independent, with marginal probability density functions

$f_{X_i}, i = 1, ..., M$. The resulting joint distribution is denoted by $f_{\boldsymbol{X}}$. Thus, the scalar QoI which resulted from this system is also a random variable, denoted $Y = \mathcal{M}(\boldsymbol{X})$. Knowing that the response random variable Y has a finite variance, $\mathbb{E}\left[Y^2\right] < \infty$, it can be represented as a PCE [336]:

$$Y = \sum_{\boldsymbol{\alpha} \in \mathbb{N}^M} y_{\boldsymbol{\alpha}} \Psi_{\boldsymbol{\alpha}}(\boldsymbol{X}) \tag{20.13}$$

where $\Psi_{\boldsymbol{\alpha}}(\boldsymbol{X})$ are the multi-variate polynomials orthonormal with respect to $f_{\boldsymbol{X}}$, $y_{\boldsymbol{\alpha}} \in \mathbb{R}$ are the expansion coefficients to be determined, and $\boldsymbol{\alpha} \in \mathbb{N}^M$ are multi-indices that identify the components of the multi-variate polynomials.
The multi-variate polynomials are assembled as the tensor product of their univariate counterparts [810]:

$$\Psi_{\boldsymbol{\alpha}}(\mathbf{x}) = \prod_{i=1}^{M} \phi_{\alpha_i}^{(i)}(x_i) \tag{20.14}$$

where $\phi_{\alpha_i}^{(i)}$ is the univariate orthogonal polynomial in the ith variable of degree α_i, where orthogonality is meant with respect to the probability density function f_{X_i} of this i^{th} variable. A list of commonly-used classical univariate polynomial families can be found in Xiu and Karniadakis [893]. To be used in the context of real-world problems, the summation in Equation 20.13 should be limited to a finite sum:

$$Y^{PCE} = \mathcal{M}^{PCE}(\boldsymbol{X}) = \sum_{\boldsymbol{\alpha} \in \mathcal{A}} y_{\boldsymbol{\alpha}} \Psi_{\boldsymbol{\alpha}}(\boldsymbol{X}) \tag{20.15}$$

where $\mathcal{A}$ is the truncation set of multi-indices of cardinality P. There are two main truncation schemes, i.e. standard [286] and hyperbolic [129]. The former is based on selecting all polynomials in M input random variables of total degree not exceeding p:

$$\begin{aligned} &\mathcal{A}^{M,p} = \left\{\boldsymbol{\alpha} \in \mathbb{N}^M \ : \ |\boldsymbol{\alpha}| \leq p\right\}; \\ &\text{card}\, \mathcal{A}^{M,p} \equiv P = \binom{M+p}{p} = \frac{(M+p)!}{p!\ M!} \end{aligned} \tag{20.16}$$

The hyperbolic truncation is, in fact, a modification to the standard version, and uses the parametric q-norm to define the truncation:

$$\mathcal{A}^{M,p,q} = \left\{\boldsymbol{\alpha} \in \mathcal{A}^{M,p} \ : \ \|\boldsymbol{\alpha}\|_q \leq p\right\}, \quad \|\boldsymbol{\alpha}\|_q = \left(\sum_{i=1}^{M} \alpha_i^q\right)^{1/q} \tag{20.17}$$

For q=1, the hyperbolic truncation corresponds to the standard one. For $q < 1$, hyperbolic truncation includes all univariate polynomials up to degree p, yet for less polynomials that depend on many parameters. Figure 20.5 illustrates a set of 2D hyperbolic truncation with varying p and q. As seen, decreasing the value of q decreases the number of mixed order polynomials in the expansion.

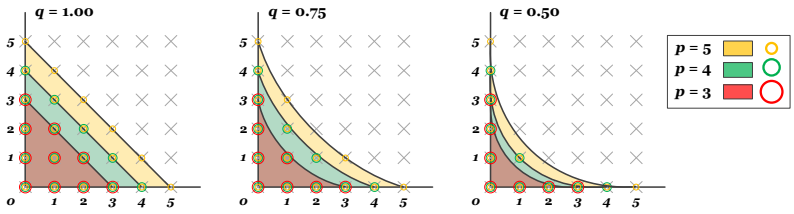

Fig. 20.5: Illustration of the hyperbolic truncation set with varying p (3 to 5) and q (0.5 to 1.0)

20.5.2 Computing the Expansion Coefficients

The expansion coefficients might be computed either using intrusive or non-intrusive approaches. The former is originally proposed in the context of the stochastic finite element method [335] to discretize the constitutive equations both in the physical and the random spaces. The latter relies on post-processing of the outputs from multiple simulations, so-called DOE [170], of the existing numerical model. There are multiple strategies to compute the expansion coefficients non-intrusively, among them the least-squares minimization is well-established [122]. Least-squares minimization adapts the candidate polynomial basis one after the other and computes the corresponding PCE. The least angle regression (LAR) leads to sparse PCE, where polynomials are selected from a candidate truncation scheme; only the polynomials that have the largest impact on the model response are retained (while the other coefficients are set to zero).
Based on Equations 20.13 and 20.15, one can write the infinite series as a sum of its truncated set and a residual:

$$\mathcal{M}(\boldsymbol{X}) = \mathcal{M}^{PCE}(\boldsymbol{X}) + \varepsilon_P = \sum_{j=0}^{P-1} y_i \Psi_j(\boldsymbol{X}) \equiv \boldsymbol{y}^T \Psi(\boldsymbol{X}) + \varepsilon_P \tag{20.18}$$

where ε_P is the truncation error, and superscript T means transpose.
The LAR method consists of finding a set of coefficients $\boldsymbol{y}$ which minimizes the mean square error including a penalty term of the form $\lambda \|\boldsymbol{y}\|_1$ as [264]:

$$\hat{\boldsymbol{y}} = \underset{\boldsymbol{y} \in R^P}{\arg\min}\, \mathbb{E}\left[\left(\boldsymbol{y}^T \Psi(\mathbf{X}) - \mathcal{M}(\mathbf{X})\right)^2\right] + \lambda \|\boldsymbol{y}\|_1 \tag{20.19}$$

where $\|\hat{\boldsymbol{y}}\|_1 = \sum_{\boldsymbol{\alpha} \in \boldsymbol{A}} |y_\alpha|$ is the regularization term that forces the minimization to favor sparse solutions. The LAR algorithm can be summarized by the following iterative procedure [129]:

1. Initialize the parameters: $y_{\boldsymbol{\alpha}} = 0\ ;\ \ \forall \boldsymbol{\alpha} \in \boldsymbol{A}$; candidate set of $\Psi_{\boldsymbol{\alpha}}$, active set of O, and set the residuals equal to the vector of observations $\boldsymbol{y}$.
2. Find the vector $\Psi_{\boldsymbol{\alpha}_j}$ which is most correlated with the current residual.

3. Move $y_{\boldsymbol{\alpha}}$ from zero towards their least-square value until their regressors $\Psi_{\boldsymbol{\alpha}_j}$ are equally correlated to the residual as some other regressor in the candidate set.
4. Compute the so-called leave-one-out error, Err^j_{LOO} for the current iteration (will be explained later), update all the active coefficients, and move $\Psi_{\boldsymbol{\alpha}_j}$ from candidate set to the active set.
5. Continue this step until the size of the active step becomes $\min(N-1, P)$.

The residual error, ε_P, in Equation 20.18 can be further computed using two techniques [569]:

- Normalized empirical error (NEE) is an estimator of the generalized error based on the response of the metamodel to the DOE points:

$$Err_{\text{NEE}} = \frac{\sum_{i=1}^{N} \left(\mathcal{M}\left(\boldsymbol{x}^{(i)}\right) - \mathcal{M}^{PCE}\left(\boldsymbol{x}^{(i)}\right)\right)^2}{\sum_{i=1}^{N} \left(\mathcal{M}\left(\boldsymbol{x}^{(i)}\right) - \frac{1}{N}\sum_{i=1}^{N} \mathcal{M}\left(\boldsymbol{x}^{(i)}\right)\right)^2} \tag{20.20}$$

- Leave-one-out (LOO) is intended to overcome the over-fitting limitation of NEE using cross validation technique. First, one DOE point is left out at a time, and then a polynomial chaos expansion $\mathcal{M}^{PCE\setminus i}$ is constructed using the remaining points [128]. Subsequently, the error is computed as follows after some algebraic simplifications:

$$Err_{\text{LOO}} = \frac{\sum_{i=1}^{N} \left(\frac{\mathcal{M}\left(\boldsymbol{x}^{(i)}\right) - \mathcal{M}^{PCE}\left(\boldsymbol{x}^{(i)}\right)}{1 - \text{diag}\left(\boldsymbol{A}\left(\boldsymbol{A}^T\boldsymbol{A}\right)^{-1}\boldsymbol{A}^T\right)}\right)^2}{\sum_{i=1}^{N} \left(\mathcal{M}\left(\boldsymbol{x}^{(i)}\right) - \frac{1}{N}\sum_{i=1}^{N} \mathcal{M}\left(\boldsymbol{x}^{(i)}\right)\right)^2} \tag{20.21}$$

  where $\boldsymbol{A}$ is the information matrix of size $N \times P$ which contains evaluations of all base polynomials at all points of the DOE, namely $A_{ij} = \Psi_j(\boldsymbol{x}^{(i)})$.

Over-fitting is a concept that stems from machine/statistical learning. When a model (e.g., neural network (NN), PCE, etc.) is built to approximate an input/output relationship from data (either a given data set in the usual machine learning setting, or the experimental design selected by the analyst in the context of PCE), there must be a trade-off between the number of data points and the "complexity" of the fitted model. The latter can be seen as the number of parameters used to compute (in our case, the number of PCE coefficients), which depends on the highest polynomial degree. If one tries to fit a large number of coefficients with a limited number of data points, one obtains a model that has little error on the data points used for its construction (possibly zero, think about an interpolating Lagrange polynomial), while it can have large errors for new input points. In other words, the model is over-fitted on the data points and has no predictive capabilities for other points.
One classical way to avoid this in machine learning (e.g., NN) is to split the data into training and validation sets: the model is fitted using only the points in the training set, and the error is judged on the validation set. In the case of surrogate modeling

and in particular PCE, one is interested in small data sets (i.e., small experimental designs), and it is of interest to avoid setting apart validation points. This is achieved by so-called LOO cross validation, Equation 20.21. More details can be found in Friedman, Hastie, and Tibshirani [320].

20.6 Concept of Machine Learning

Machine learning is a specific type of artificial intelligence that "learns" as it identifies new patterns in data and create strategies to improve decision making based on information hidden in huge data sets. Choosing the right algorithm is a key point in any machine learning application, and thus understanding the advantages and disadvantages of each technique is vital. Three major machine learning algorithms are Supervised, Unsupervised and Semi-supervised learning, Figure 20.6.

- Supervised learning is where the algorithm produces a function that maps inputs to outputs. The application can be found in classification and regression.
- Unsupervised learning in which the input data is not labeled and does not have a known result. The application can be found in clustering, dimensionality reduction, and association rule learning.
- Semi-supervised learning in which the input data is a mixture of labeled and unlabeled examples. The application can be found in classification and regression.

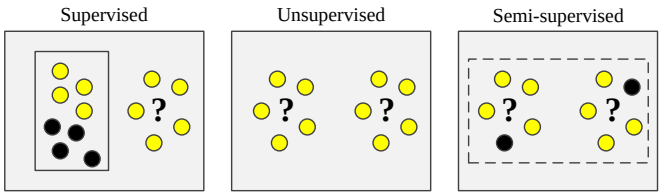

Fig. 20.6: Different learning styles in machine learning algorithms

Figure 20.7 highlights a number of diverse classes and sub-classes of algorithms and approaches applied in machine learning. In this book, only some of these techniques are briefly reviewed since their applications in concrete dam engineering will be explored later.

20.6.1 Hints on Machine Learning Modeling

Following there are several hints and terminologies to develop a successful machine learning model:

Variance vs. Bias: The goal of any machine learning algorithm is to have a model that is not biased (i.e., has high performance in training set), and is not over-fitted

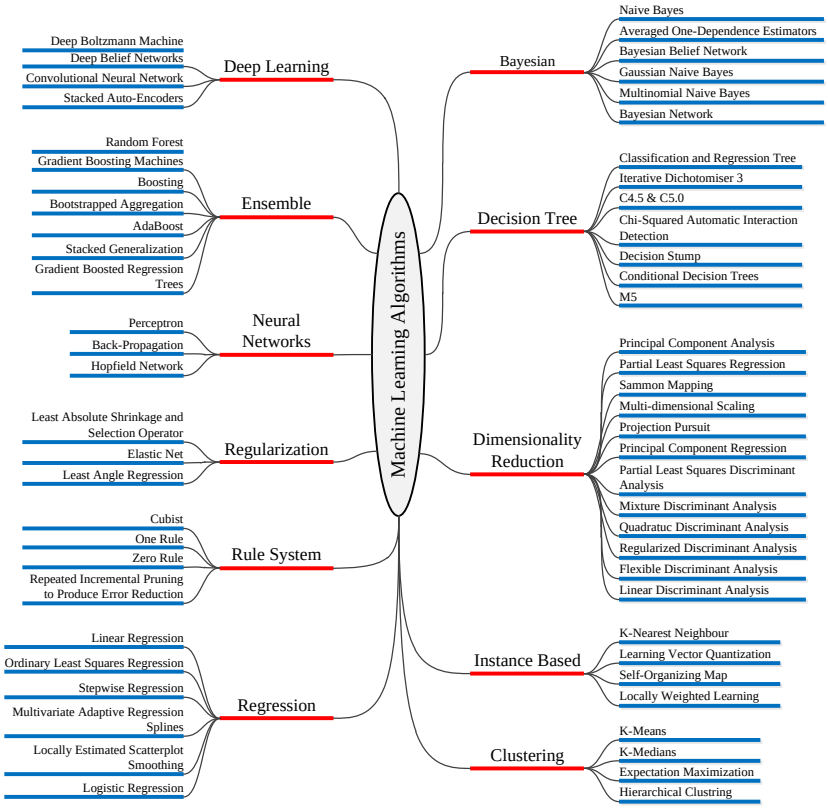

Fig. 20.7: Some of the important Machine Learning algorithms by Jason Brownlee

(i.e., has low variance across datasets), Figure 20.8(a). since achieving such an ideal model is difficult, there is a tradeoff between bias and variance. By increasing complexity of the model, its performance improves over the training set, while its variance increases.

Accuracy vs. Precision: They are two of the statistical measures to evaluate performance of machine learning models. Accuracy presents the number of correct predictions over total number of data points, while precision is the total number of correct predictions for positive class over total number of data points that are predicted to be positive, Figure 20.8(b). Again, the goal is to develop models as accurate and precise as possible.

Regularization: Developing a good/successful machine learning model is not only about low bias (i.e., high performance in training set) but also about low variance (i.e. high performance in validation set). Regularization is a method to avoid over-

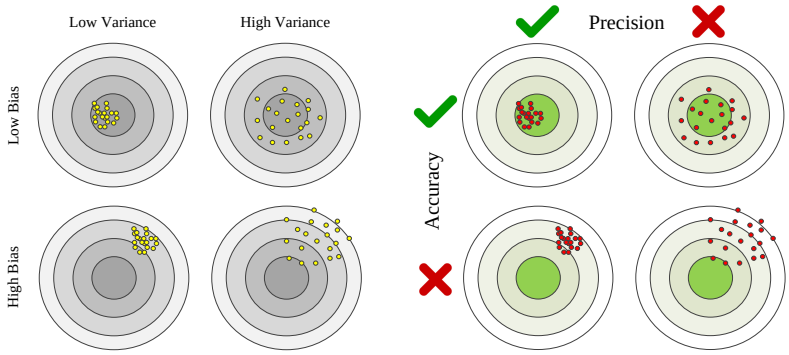

(a) Variance *vs.* bias (b) Precision *vs.* Accuracy

Fig. 20.8: Selection of right machine learning model

fitting. Applying a constraint on the parameter pace let the model to be as optimal as possible, while agreeing with the constraint. Lasso (least absolute shrinkage and selection operator), Ridge and elastic-net (combination of lasso and ridge) are three common regularization methods in linear models, Figure 20.9.

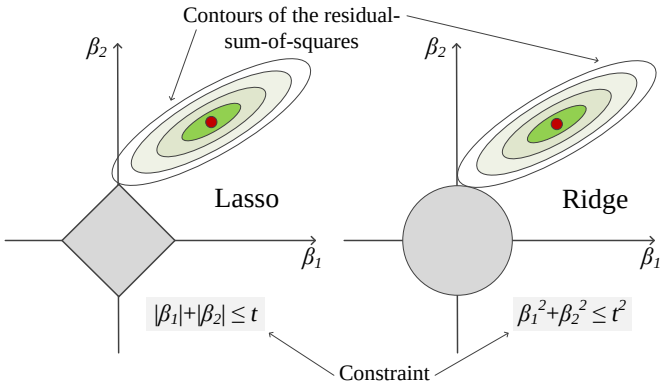

Fig. 20.9: Generalizability of machine learning models

Optimized Model Learning rate determines how fast the parameters should be changed in machine learning models. The direction of the change towards reaching minimum cost function (i.e., gradient descent process). However, depending on the learning rate, this process might be (1) slow (low learning rate), (1) bal-

anced/optimal rate, or (3) oscillatory (high learning rate), Figure 20.10. Learning rate may also varies from high to low during the training process.

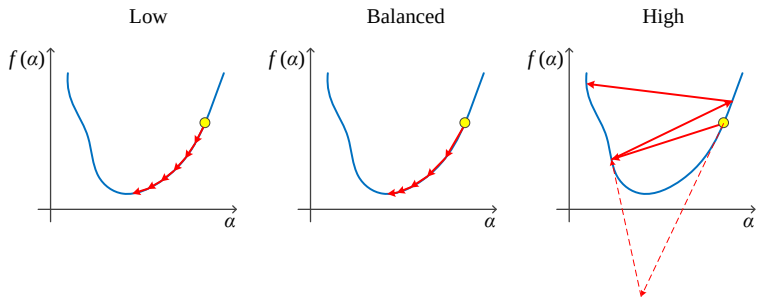

Fig. 20.10: Developing an optimized machine learning model

Model Stacking: It is a technique in which the outputs of multiple machine learning models, $\hat{y}_i$, are combined, and is used as the input for a secondary algorithm, $\hat{Y} = f(\hat{y}_i)$. The output of the second level algorithm is then interpreted as the final output of the system.

Entropy: It is a measure of purity of groups identified by machine learning methods. Entropy is measured between 0 and 1. Larger entropy corresponds to a high level of disorder, and low level of purity. The mathematical formula for Entropy is as follows:

$$\text{Entorpy} = -\sum_{i=1}^{C} P_i \log_2 (P_i)\,; \quad P_i = \frac{N_i}{\sum_{i=1}^{C} N_i} \tag{20.22}$$

where P_i is the frequentist probability of an element/class "i" in dataset, and C is the total number of classes.

Imbalanced Dataset: Many of the real-world datasets are imbalanced makes the process of training difficult. The model could learn more about the class with higher number of data points (majority class) and miss-classify minority class data points, Figure 20.11. Undersampling and Oversampling are two techniques used to adjust the class distribution of a data set. Both methods involve introducing a bias to select more samples from one class than from another, to compensate for an imbalance in the data.

Performance Metrics: Performance of machine learning models can be assessed using one of the following measures, where T: True, F: False, P: Positive, and N: Negative:

- Accuracy:

$$\text{Accuracy} = \frac{\text{Number of correct predictions}}{\text{Total number of data points}} \tag{20.23}$$

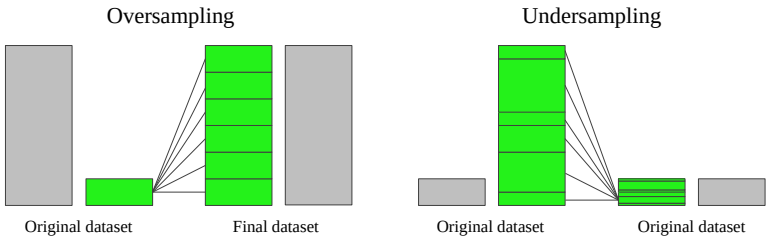

Fig. 20.11: Imbalance data set

- Accuracy for binary classification

$$\text{Accuracy} = \frac{TP + TN}{TP + TN + FP + FN} \tag{20.24}$$

- Precision:

$$\text{Precision} = \frac{TP}{TP + FP} \tag{20.25}$$

- Recall (or sensitivity):

$$\text{Recall} = \frac{TP}{TP + FN} \tag{20.26}$$

- Specificity (or selectivity):

$$\text{Specificity} = \frac{TN}{TN + FP} \tag{20.27}$$

- Balanced accuracy:

$$\text{Balanced accuracy} = \frac{\text{Recall} + \text{Specificity}}{2} \tag{20.28}$$

20.7 Classification Techniques

In machine learning, classification is the problem of assigning new observations to one of the discrete categories, of which there are a finite number. Therefore, the goal of classification is to learn a model that makes accurate predictions on new observations based on a set of training data points. To be formal, let $\mathbf{x}_1, \ldots, \mathbf{x}_n$ be a set of training observations in $\mathbb{R}^p$ with corresponding categories $y_1, \ldots, y_n$, where $y_i \in \{-1, +1\}$. Here, p denotes the number of features (random variables), and each category y_i is a binary variable such that $y_i = -1$ corresponds to class $\mathcal{C}_1$ (failure region) and $y_i = +1$ corresponds to class $\mathcal{C}_2$ (safe region). Using the learned classification rule in the training phase, a new observation $\mathbf{x} \in \mathbb{R}^p$ is assigned to one of these two categories.

In practice, the set of n training observations is used to form the training matrix $\mathbf{X}_{\text{trn}} = [\mathbf{x}_1, \ldots, \mathbf{x}_n]^T \in \mathbb{R}^{n \times p}$, where each row corresponds to one observation. Prior to the training phase, observations are often preprocessed since features or random variables might be measured in different units [408]. There are two main techniques to preprocess the training data: 1) rescaling and 2) standardization. In the first method, also known as Min-Max scaling, features or random variables are rescaled to be in the range $[0, 1]$ by computing the maximum and minimum values. However, the second method computes the sample mean and standard deviation of random variables. Then, the features in each column of $\mathbf{X}_{\text{trn}}$ are standardized by subtracting the mean and dividing them by the standard deviation. As a result, random variables will be rescaled so that they have the properties of a standard normal distribution with zero mean and unit standard deviation. The second method is employed in the present work since it has been shown to be crucial in clustering analyses [822].

In this paper, three popular classification algorithms are studied and contrasted: 1) K-Nearest Neighbor (KNN), 2) Support Vector Machine (SVM), and 3) Naive Bayes Classifier (NBC), Figure 20.12. These algorithms cover both deterministic and probabilistic classification approaches, and they are among the top ten data mining algorithms [891]. The training procedure, properties, and computational complexity of these three techniques are explained through Sec. 20.7.1, 20.7.2 and 20.7.3.

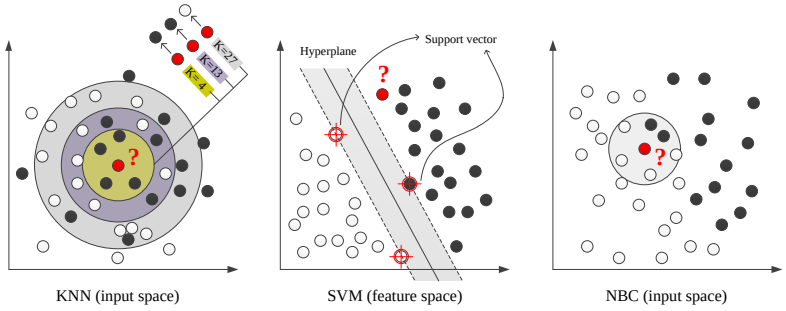

Fig. 20.12: Three classification techniques in machine learning. From left to right: K-Nearest Neighbor (KNN), Support Vector Machine (SVM), and Naive Bayes Classifier (NBC). In KNN, a new observation is classified based on the labels of K nearest neighbors. SVM solves an optimization problem to find a separating hyperplane with maximum margin and a new observation is classified based on its position. NBC is a probabilistic approach to find the most likely class for a new observation using Bayes theorem.

20.7.1 K-Nearest Neighbor

The K-Nearest Neighbor algorithm is one of the simplest classification techniques in machine learning. Given a new observation $\mathbf{x} \in \mathbb{R}^p$, K training observations from

the rows of $\mathbf{X}_{\text{trn}}$ closest in distance to $\mathbf{x}$ are found. Then, $\mathbf{x}$ is classified using the majority vote among these K nearest observations from the training set. Therefore, the KNN algorithm is sensitive to the local structure of the data, and its performance depends heavily on the choice of K.

To reduce the sensitivity of KNN, one possible approach is to weigh the contribution of each of the K nearest neighbors according to their distance to observation $\mathbf{x}$. For example, the class of each of the K nearest training observations is multiplied by a weight which is proportional to the inverse of the distance from $\mathbf{x}$. Thus, greater weight is given to closer neighbors. The classification rule of weighted KNN for a new observation $\mathbf{x}$ and its K nearest neighbors $\mathbf{x}_1, \ldots, \mathbf{x}_K$ with labels y_i, $i = 1, \ldots, K$, can be written as:

$$f(\mathbf{x}) = \text{sign}\left(\frac{\sum_{i=1}^{K} w_i y_i}{\sum_{i=1}^{K} w_i}\right), \quad w_i = \frac{1}{\|\mathbf{x} - \mathbf{x}_i\|} \tag{20.29}$$

where w_i is the distance weighting function.

20.7.2 Support Vector Machine

Support vector machine is one of the most popular classification algorithms. The determination of the model parameters can be written as a simple optimization problem by using the Lagrange multipliers method. Therefore, one can use standard off-the-shelf optimization softwares to find the required parameters.

The key idea of SVM is to map the training observations from $\mathbb{R}^p$ into a high (maybe infinite) dimensional feature space so that the mapped data is linearly separable. Therefore, there exists at least one separating hyperplane of the form (because of linear separability assumption [776]):

$$f(\mathbf{x}) = \mathbf{w}^T \varphi(\mathbf{x}) + b \tag{20.30}$$

where the operator $\varphi : \mathbb{R}^p \to \mathbb{R}^H$ represents the transformation; $\mathbf{w} \in \mathbb{R}^H$ is the coefficient vector that determines the orientation of the hyperplane, and $b \in \mathbb{R}$ is the bias term. Among all possible hyperplanes, the one with the largest margin is selected, where margin is defined as the smallest distance between the hyperplane and any of the training observations. After determination of the model parameters $\mathbf{w}$ and b, a new test data point $\mathbf{x}$ is classified according to the sign of $f(\mathbf{x})$ (recall that the corresponding target for each observation is either -1 or $+1$).

Now, we explain the problem formulation and optimization to find the separating hyperplane in SVM. Since the mapped data is linearly separable, all the training observations $\mathbf{x}_1, \ldots, \mathbf{x}_n$ satisfy the following constraints:

$$\begin{cases} \mathbf{w}^T \varphi(\mathbf{x}_i) + b \geq +1 \text{ for } y_i = +1 \\ \mathbf{w}^T \varphi(\mathbf{x}_i) + b \leq -1 \text{ for } y_i = -1 \end{cases} \tag{20.31}$$

and these two constraints can be combined into one set of inequalities:

$$y_i \left(\mathbf{w}^T \varphi(\mathbf{x}_i) + b\right) - 1 \geq 0 \text{ for all } \quad i = 1, \ldots, n \tag{20.32}$$

Under this setup, the points that are closest to the separating hyperplane, known as "support vectors," lie on the following hyperplane:

$$y_i \left(\mathbf{w}^T \varphi(\mathbf{x}_i) + b\right) = 1 \tag{20.33}$$

This hyperplane and the separating hyperplane in Eq. 20.30 are parallel (they have the same orientation or coefficient vector $\mathbf{w}$), and the distance between them is $1/\|\mathbf{w}\|$, where $\|\mathbf{w}\|$ is the Euclidean norm of $\mathbf{w}$. Thus, the hyperplane which gives the maximum margin is obtained by maximizing $\|\mathbf{w}\|^{-1}$, which is equivalent to minimizing $\|\mathbf{w}\|^2$, subject to the constraints given in Eq. 20.32.

To solve the above constrained optimization problem, the Lagrange multipliers method is often used which results in maximizing the following term with respect to $\mathbf{a}$ [126]:

$$\tilde{\mathcal{L}}(\mathbf{a}) = \sum_{i=1}^{n} a_i - \frac{1}{2} \sum_{i=1}^{n} \sum_{j=1}^{n} a_i a_j y_i y_j k(\mathbf{x}_i, \mathbf{x}_j) \tag{20.34}$$

subject to the constraints:

$$\begin{cases} a_i \geq 0, \ i = 1, \ldots, n \\ \sum_{i=1}^{n} a_i y_i = 0 \end{cases} \tag{20.35}$$

Here, the "kernel function" is defined by $k(\mathbf{x}_i, \mathbf{x}_j) = \varphi(\mathbf{x}_i)^T \varphi(\mathbf{x}_j)$, which represents the dot product between two mapped data points $\varphi(\mathbf{x}_i)$ and $\varphi(\mathbf{x}_j)$. Given the optimal solution $\mathbf{a}^* = [a_1^*, \ldots, a_n^*]^T$ in the training procedure, a new data point $\mathbf{x}_{\text{test}}$ is classified according to the sign of $f(\mathbf{x}_{\text{test}})$:

$$f(\mathbf{x}_{\text{test}}) = \sum_{i=1}^{n} a_i^* y_i k(\mathbf{x}_{\text{test}}, \mathbf{x}_i) + b^* \tag{20.36}$$

where b^* can be found by substituting the optimal value $\mathbf{w}^* = \sum_{i=1}^{n} a_i^* y_i \varphi(\mathbf{x}_i)$ in Eq. 20.33 and can be expressed in terms of the kernel function.

Note that the separating hyperplane is optimized without ever having to explicitly compute the coordinates of data points $\varphi(\mathbf{x}_i)$ in feature space. Thus, employing kernel functions is an efficient approach to perform nonlinear classification by "implicitly" mapping training observations into feature space. The two commonly used families of kernels are polynomial kernels and radial basis functions (RBF) [705], [704]. The polynomial kernel function is of the form $k(\mathbf{x}_i, \mathbf{x}_j) = (\mathbf{x}_i^T \mathbf{x}_j + 1)^d$ with parameter $d \in \mathbb{N}$. On the other hand, RBF (also known as Gaussian kernel) takes the form $k(\mathbf{x}_i, \mathbf{x}_j) = \exp(-\gamma \|\mathbf{x}_i - \mathbf{x}_j\|^2)$ with parameter $\gamma \in \mathbb{R}^+$.

In the derivation of SVM as presented so far, it is assumed that the mapped data points $\varphi(\mathbf{x}_1), \ldots, \varphi(\mathbf{x}_n)$ are linearly separable. However, in practice, it is often not possible to find exact separation of the training data. For example, noise and outliers might be present in the training data [408]. To make the algorithm work for these

cases, the optimization problem that finds the maximum margin classifier must be reformulated. Consider a set of n variables $\xi_1, \ldots, \xi_n$, then the constraints in Eq. 20.32 are modified:

$$\begin{cases} y_i \left(\mathbf{w}^T \varphi(\mathbf{x}_i) + b \right) \geq 1 - \xi_i & \text{for all } i = 1, \ldots, n \\ \xi_i \geq 0 & \text{for all } i = 1, \ldots, n \end{cases} \tag{20.37}$$

In this case, the goal is to minimize $\frac{1}{2}\|\mathbf{w}\|^2 + \lambda \sum_{i=1}^{n} \xi_i$, where the parameter $\lambda > 0$ controls the relative weighting between two objectives: 1) making $\|\mathbf{w}\|^2$ small to find maximum margin classifier and 2) ensuring that most of the training data points have margin at least 1. To solve this problem as explained before, a Lagrangian function is constructed to find the dual representation. Consequently, the following term should be maximized with respect to the vector $\mathbf{a}$:

$$\tilde{\mathcal{L}}(\mathbf{a}) = \sum_{i=1}^{n} a_i - \frac{1}{2} \sum_{i=1}^{n} \sum_{j=1}^{n} a_i a_j y_i y_j k(\mathbf{x}_i, \mathbf{x}_j) \tag{20.38}$$

subject to the constraints:

$$\begin{cases} 0 \leq a_i \leq \lambda, \ i = 1, \ldots, n \\ \sum_{i=1}^{n} a_i y_i = 0 \end{cases} \tag{20.39}$$

This optimization problem is identical to the separable case, except that the constraint set is different.

20.7.3 Naive Bayes Classifier

Naive Bayes Classifier is a probabilistic classification algorithm which is based on Bayes theorem. In the training phase, this method estimates the parameters of a probability distribution which is often assumed to be the normal distribution for continuous variables. Then, a new observation $\mathbf{x}$ is classified based on the probability that $\mathbf{x}$ belongs to each class. To explain this classification technique, Bayes theorem is adapted.

Given a new observation $\mathbf{x}$, the main idea behind Naive Bayes Classifier is to find the following probability for each of two classes known as posterior probability:

$$P(\mathcal{C}_j|\mathbf{x}), \quad j = 1, 2. \tag{20.40}$$

where $P(\mathcal{C}_j|\mathbf{x})$ is the probability of observing $\mathcal{C}_j$ given that $\mathbf{x}$ is true.

Then, $\mathbf{x}$ is assigned to the class that has the maximum posterior probability:

$$\hat{\mathcal{C}} = \underset{j \in \{1,2\}}{\operatorname{argmax}} P(\mathcal{C}_j|\mathbf{x}). \tag{20.41}$$

To find the posterior probability in Eq. (20.40), Bayes theorem is used to get the following reformulation:

$$P\left(\mathcal{C}_j|\mathbf{x}\right) = \frac{P\left(\mathbf{x}|\mathcal{C}_j\right)P\left(\mathcal{C}_j\right)}{P\left(\mathbf{x}\right)}. \tag{20.42}$$

In this equation, the denominator does not depend on the class $\mathcal{C}_j$, which means that the denominator is effectively constant. Therefore, the main difficulty in finding the posterior probability is to calculate the term $P\left(\mathbf{x}|\mathcal{C}_j\right)$ in the numerator. To solve this problem, a "naive" assumption is considered: the p features of the new observation $\mathbf{x} \in \mathbb{R}^p$ are conditionally independent given the class. Thus, the classification rule for the new observation vector $\mathbf{x} = [x_1, \ldots, x_p]^T$ is given as:

$$\hat{\mathcal{C}} = \underset{j\in\{1,2\}}{\operatorname{argmax}} P\left(\mathcal{C}_j\right) \prod_{i=1}^{p} P\left(x_i|\mathcal{C}_j\right). \tag{20.43}$$

20.8 Regression Techniques

Although there are many machine learning based regression techniques, only few of them are discussed in this book.

20.8.1 Support Vector Regression

Regression is used to predict continuous values compared with classification, which is used to predict classes or labels (discrete values). To be formal, a training data set consisting of n data points $\mathbf{x}_1, \ldots, \mathbf{x}_n$, with observed response values $y_i \in \mathbb{R}$ are given. Here, the goal is to find a linear model of the form:

$$f\left(\mathbf{x}\right) = \mathbf{w}^T\varphi\left(\mathbf{x}\right) + b \tag{20.44}$$

which is used to predict the response values. Hence, the following term should be minimized:

$$\frac{1}{2}\|\mathbf{w}\|^2 + \lambda\sum_{i=1}^{n} E_\epsilon\left(f(\mathbf{x}_i) - y_i\right) \tag{20.45}$$

where the parameter $\lambda > 0$ controls the weighting between $\|\mathbf{w}\|^2$ and the error term, known as ϵ-insensitive error function, which is defined as:

$$E_\epsilon\left(f(\mathbf{x}) - y\right) = \begin{cases} 0 & \text{if } |f(\mathbf{x}) - y| < \epsilon \\ |f(\mathbf{x}) - y| - \epsilon & \text{otherwise} \end{cases} \tag{20.46}$$

As shown before, the above optimization problem can be reformulated by introducing two variables $\xi_i \geq 0$ and $\xi_i' \geq 0$. The modified constraints are:

$$\begin{cases} y_i \geq f(\mathbf{x}_i) - \epsilon - \xi_i' \\ y_i \leq f(\mathbf{x}_i) + \epsilon + \xi_i \end{cases} \tag{20.47}$$

for all $i = 1, \ldots, n$ and the objective function in Eq. 20.45 should be modified as well:

$$\frac{1}{2}\|\mathbf{w}\|^2 + \lambda \sum_{i=1}^{n} \left(\xi_i + \xi_i'\right). \tag{20.48}$$

This optimization problem involves maximizing the following term with respect to $\mathbf{a} = [a_1, \ldots, a_n]^T \in \mathbb{R}^n$ and $\mathbf{a}' = [a_1', \ldots, a_n']^T \in \mathbb{R}^n$ [126]:

$$\begin{aligned} \tilde{\mathcal{L}}\left(\mathbf{a}, \mathbf{a}'\right) = -\frac{1}{2} \sum_{i=1}^{n} \sum_{j=1}^{n} \left(a_i - a_i'\right)\left(a_j - a_j'\right) k\left(\mathbf{x}_i, \mathbf{x}_j\right) \\ -\epsilon \sum_{i=1}^{n} \left(a_i + a_i'\right) + \sum_{i=1}^{n} y_i \left(a_i - a_i'\right) \end{aligned} \tag{20.49}$$

subject to the constraints: $0 \leq a_i \leq \lambda,\ 0 \leq a_i' \leq \lambda$ for all $i = 1, \ldots, n$ and $\sum_{i=1}^{n} \left(a_i - a_i'\right) = 0$
Given the optimal solution of the dual representation, the response value for a new test point $\mathbf{x}$ is estimated via the following expression:

$$f\left(\mathbf{x}\right) = \sum_{i=1}^{n} \left(a_i - a_i'\right) k\left(\mathbf{x}, \mathbf{x}_i\right) + b \tag{20.50}$$

This equation only requires finding the values of the kernel function $k(\mathbf{x}, \mathbf{x}_i)$ for $i = 1, \ldots, n$ where the commonly used kernels are linear, polynomial, and radial basis kernel functions.

20.8.2 Decision Tree Regression

Decision tree regression (DTR) is a non-parametric and nonlinear machine learning technique. It takes advantage of a hierarchical structure for recursively segmenting training data, and therefore, it has a great flexibility and interpretability in data analysis. The most common strategy to induct a decision tree is greedy top-down construction which recursively partitions the data into subsets until the stopping criterion has been met. The stopping criterion is crucial so that it can prevent growing branches that do not affect the tree quality [616]. Some of the stopping rules are:

1. The number of observations in a node is less than a pre-specified threshold.
2. All observations assigned to a node belong to the same class.
3. Depth of the node is more than some pre-specified limit.
4. Nodes purity are more than a specified threshold [281].

Decision trees are often prone to over-fitting according to high variance, and hence, methods are proposed to find the right sized tree. The most famous method is pruning trees [735]; in order to have a high quality tree, first a complete tree is built, and

then inefficient sub-trees, that do not influence the cost function significantly, are removed.
The evaluation function used for splitting classification trees in CART (classification and regression tree) method is the Gini index, which describes the chance of coming up with a false node for the data if the node was chosen randomly from the nodes' distribution. The Gini index can be stated as:

$$\text{Gini}(t) = 1 - \sum \left[P\left(K|t\right)\right]^2 \tag{20.51}$$

where $P\left(K|t\right)$ is the proportion of finding the data class K in the node t (node purity). The objective is to minimize the Gini index. From the formula it can be inferred that if the classification is done in a perfect way, the Gini index would be zero [320, 515].

20.8.3 Random Forest

Random forest (RF) is a kind of ensemble classifier, made by a combination of decision trees which are created by recursive partitioning. The idea behind RF is to combine the results of many different decision trees to overcome the vulnerabilities of the individual one. In order to construct an RF model, with the help of bootstrapping, new sets of training data are created, and then, RF randomly chooses the variable for each set (for better diversity in results). Next, RF starts creating decision trees for each group with respective variables. Finally, the outcome forest of trees is combined and the average of the predictions is considered as the result [872].
For testing the accuracy of an RF, Out-of-Bag (OOB) data (which are the samples that were not selected in bootstrapping in the RF procedure) can be used. An error will be assigned by applying the RF model to the OOB data, and hence, the performance of the RF model can be examined. One key parameter in the RF algorithm is the importance score (IS) which is described as:

$$\text{IS} = \frac{1}{N_{tree}} \sum_{i=1}^{B} \left(Err_i - Err_i^*\right) \tag{20.52}$$

Where N_{tree} is the number of trees in the RF model, and Err_i and Err_i^* are the errors of each tree applied on OOB and perturbed OOB data, respectively. More details can be found in Thakur and Kumar [829]. The benefit of using RF is to have a reduced variance in comparison to a single tree so that over-fitting will not happen [320].

20.8.4 Tree Bagging

Bagging, a short term for "Bootstrap Aggregation," is an ensemble technique that uses bootstrap to generate samples of the original data. In prediction problems, this algorithm averages the prediction over a collection of bootstrap samples and the class of a new observation is the most selected class among the number of trees

constructed on bootstrap samples [152]. In this algorithm, trees are grown deep without pruning. However, by building sufficient trees, the over-fitting is less likely to happen. A pseudo-code for tree bagging is shown in algorithm 1. In this method, similar to the RF, the OOB data can be used to justify the performance of the model [512].

Algorithm 1 Tree Bagging pseudo-code

```
for i = 1:N_tree do
    Generate bootstrapped sample of the data
    Create un-pruned decision trees on the samples
    Average on all the outcomes
end for
```

20.8.5 Extreme Gradient Boosting

Extreme gradient boosting (XGBoost) is a statistical nonlinear machine learning algorithm used for functions such as classification, regression, and ranking [186]. Scalability and speed of XGBoost in comparison to other solutions have made it very popular among data scientists [185]. XGBoost is an implementation of the gradient boosted trees algorithm [832]. In order to combine a set of weak learners to develop a strong learner, two ways are proposed. Either first build a set of learners and then average the result like RF and TB methods, or sequentially add learners in order to optimize the cost function in a step-wise manner as in boosting methods [621].
In additive learning of XGBoost, the first learner is fitted on the whole data, and the next learners are fitted to the residuals of the former ones. In fact, each learner is fitted using information from previously fitted learners. The general function for the prediction at each step is presented as follows:

$$\hat{f}_j^t = \sum_{i=1}^{t} f^i(x_j) = \hat{f}_j^{t-1} + f^t(x_j) \tag{20.53}$$

where $f^i(x_j)$ is the learner at step i, $\hat{f}_j^t$ is prediction at step t, and x_j is the input variable.
Unlike RF and TB, gradient boosting methods are prone to over-fitting if the number of trees is too large. Computation procedure for preventing over-fitting can be found in Fan et al. [287]. More information about computation of XGBoost in R Core Team [716] can be found in Chen and Guestrin [185].

20.8.6 Artificial Neural Networks

Artificial neural networks (NN) are used to map an input to a desired output like a mathematical function. It is inspired by the behavior of neurons located in the brain [709]. NNs are non-parametric estimators that can be used for several kinds of tasks

such as forecasting, clustering, function approximation and optimization [587]. The inputs for a neural network are vectors of variables corresponding to an observation. These vectors are weighted and combined by linear filters and become the inputs of the hidden layers where the nonlinear computation is performed on the inputs. Network output will be calculated by an activation function which receives output of hidden layers and calculates the output of the network [328].
The mathematical explanation of a multilayer perception, which is one of the most favored models of NN, can be presented as [910]:

$$F_t = \beta_0 + \sum_{n=1}^{N} \beta_n W \left(\theta_{0i} + \sum_{j=1}^{m} \theta_{nj} x_j \right) \tag{20.54}$$

Where m is the number of input parameters (x_j), N is the number of nodes in the hidden layer, θ_{nj} is the weight of the output layer, and β_n is the weight of the hidden layer. Here the zeroth indices in the weight coefficients refer to the bias nodes in each layer.
One may use either sigmoid or hyperbolic tangent functions as a transfer function, W. The whole process of learning is achieved by adjusting the weight parameters and the network is updated each time it has been fed by a new dataset. After the parameters are updated, the desired outcome will be the classification of data. More on this can be found in Ragg, Braun, and Landsberg [717].

20.8.7 Extreme Learning Machine

Extreme learning machine (ELM) is a single-hidden layer feed-forward network (SLFN) algorithm used for regression, classification and clustering, where the parameters of hidden nodes need not be tuned [436]. Compared to the traditional artificial NN using the gradient descent learning algorithm, the ELM randomly assigns the input weights and the hidden layer biases, and then it is fixed without need to iteratively tuning. The training speed of ELM is then significantly improved and its generalized performance is better [246]. The outputs of a standard ELM with N hidden nodes can be described as:

$$F_t = \sum_{i=1}^{N} \beta_i f \left(a_i . x_j + b_i \right)_j ; \quad j = 1, ..., N \tag{20.55}$$

Where a_i denotes the weight vector linking the ith hidden node and the input nodes, β_i is the weight vector connecting the jth hidden node and the output nodes, b_i is the threshold of the ith hidden node, and f refers to the activation functions.
Several activation functions can be used in the ELM, including sigmoid, hyperbolic tangent, and Gaussian function. Different variations and extensions of this method including the bidirectional extreme learning machine, the kernel extreme learning machine, and the online sequential extreme learning machine can be found in Huang et al. [435].

20.8.8 Gaussian Process Regression

Gaussian process regression (GPR) is a non-parametric Bayesian model that directly defines a prior probability distribution over a latent function. This approach can be used to solve nonlinear regression and classification problems. From the function space perspective, a Gaussian Process is a set of random variables, any finite subset of which has a joint Gaussian distribution, i.e., the joint probability distribution of any random variable set $\{\mathbf{x}_i \in \mathbf{X},\ i = 1, ..., n\}$ and the corresponding process states $\{f(\mathbf{x}_1), ..., f(\mathbf{x}_n)\}$ are subject to an n-dimensional Gaussian distribution. The statistical characteristics of the Gaussian process can be fully specified by the corresponding mean function $m(\mathbf{x})$ and covariance function $k(\mathbf{x}, \mathbf{x}')$ [722]:

$$\begin{cases} m(\mathbf{x}) &= E\left[f(\mathbf{x})\right] \\ k(\mathbf{x}, \mathbf{x}') &= E\left[\left(f(\mathbf{x}) - m(\mathbf{x})\right)\left(f(\mathbf{x}') - m(\mathbf{x}')\right)^T\right] \end{cases} \tag{20.56}$$

where $\mathbf{x}, \mathbf{x}' \in \mathbf{X}$ are d-dimensional input vectors.
A Gaussian process can be written as follows:

$$f(\mathbf{x}) \sim GP\left(m(\mathbf{x}), k(\mathbf{x}, \mathbf{x}')\right) \tag{20.57}$$

It is found that the covariance function parameterized by a set of hyper-parameters affects the prediction results of GPR. Therefore, the choice of covariance function is quite important for GPR modeling. Maximum likelihood estimation is the commonly used method for the parameter estimation. Computation procedure and the implementation algorithm can be found in Rasmussen and Nickisch [723].

20.8.9 Multi Adaptive Regression Splines

Multi Adaptive Regression Splines (MARS) is an adaptive technique proposed by Friedman [321] and Friedman and Roosen [322] whose outcome is computed as the combination of piecewise linear functions. These are defined in *reflected pairs* which take the form $\max(0, X_i - t)$ and $\max(t - X_i, 0)$, where X_i is one of the input variables, and t is a constant often called *knot*. All functions of this kind are defined as candidate functions, being t all observed values for each X_i in the training set. The function which results in greater minimization of the residual error is chosen and progressively added until the model includes some pre-defined amount of terms. This typically results in over-fitting, therefore the final model is obtained after some terms are pruned using generalized cross-validation (GCV) criterion: a version of the residual sum of squares which considers the number of terms in the ensemble [320].

Chapter 21
Performance Based Earthquake Engineering

Abstract
Over the past years there have been two concomitant developments: 1) performance based earthquake engineering (PBEE) which is a proposed new paradigm for the seismic safety investigation of a building and 2) potential failure mode analysis (PFMA) which is a generally accepted methodology to assess dam safety. Though similar, and written by different communities, much can be gained through an attempt to bring together those two paradigms. Figure 21.1 highlights the similarities between the two approaches in general. Each one will be discussed later in detail.

	Potential Failure Mode Analysis	Performance Based Earthquake Engineering
Step 1	Define the failure criteria (i.e. uncontrolled release of the water)	Perform seismic hazard analysis at the facility site, produce target response spectrum and select ground motions
Step 2	Define the initiator, and identify the potential failure modes (i.e. sliding due to an earthquake)	Perform a set of nonlinear dynamic structural analyses and determine the response of the facility
Step 3	Develop a sequence of events for a failure to transpire (event tree and if needed fault tree)	Perform damage analysis on the facility and determine the fragility curves in term of structural responses
Step 4	Select a path with the most likely chance to failure, perform the structural analysis, and quantify the uncertainties	Evaluate the repair efforts to determine repair costs, operability, repair duration, and the potential for casualities
Step 5	Quantify the risk and import the results on an f-N curve, and final decision making	Final decision making based on contribution of all the previous steps

Fig. 21.1: Comparison of general methodologies in PFMA and PBEE

21.1 Basic Definitions

21.1.1 Performance Based Engineering (PBE)

PBE is defined as consisting of the selection of design criteria, appropriate structural systems, layout, proportioning, and detailing for a structure and its non-structural components and contents, and the assurance and control of construction quality and long-term maintenance, such that at specified levels of all the excitation and with defined levels of reliability, the structure or facility will not be damaged beyond

certain limit states. PBE is a process that begins with the first concepts of a project and lasts throughout the life of the structure [120].

21.1.2 Performance Based Earthquake Engineering (PBEE)

PBEE is defined as the application of PBE to the case that seismic hazard controls the design. Therefore, PBEE involves the complete design, construction, and control (monitoring) of the maintenance and function of the structure to assure that the constructed structures will resist the effects of earthquake ground motions of different severity within specified limiting levels of damage [121].

21.1.3 Performance Based Seismic Design (PBSD)

PBSD is the subset of activities of PBEE that focus on the design process. Therefore, it includes identification of seismic hazards, selection of the performance levels and performance design objectives, determination of site suitability, conceptual design, numerical preliminary design, final design, acceptability checks during design, design review, specification of quality assurance during the construction, and monitoring of the maintenance and occupancy (function) during the life of the structure [120].

21.1.4 Performance Based Assessment (PBA)

PBA is the implementation of the PBEE in quantitative evaluation of the performance of a given structure (even an existing structure or a completed design of a new structure). PBA provides stakeholders with information about the structure (usually expressed in probabilistic terms) that facilitates informed decision making for risk management [905].

21.2 PBEE Predecessors

In the U.S., interest in PBSD initiated in the 1980s among engineers engaged in seismic retrofit of existing buildings. Owners of existing buildings would not commit to investing in retrofit construction unless they had an understanding of the probable performance of their buildings in future earthquakes, decided that this performance was undesirable, and that acceptable performance could be obtained at a reasonable cost. Engineers quickly found that evaluations of buildings to the current editions of the building code provided information on the building's conformance to current design practice but did not provide direct information on the way a building was likely to behave in an earthquake. Thus, engineers began to develop rudimentary procedures for assessing the likely earthquake performance of existing buildings so that they could evaluate whether collapse or other life-threatening damage was likely, and if not to assess the severity and likely consequences of damage that would occur [363].

Several documents were credited with laying the basis of PBE concepts. The following section describes each of these codes and documents in detail. It should be mentioned that all of these documents attempted to develop procedures that can be used as seismic provisions in building codes.

21.2.1 ATC-13 (1985) and ATC-14 (1987)

In the mid-1980s, the Applied Technology Council (ATC) published several documents. The ATC-13 report provided statistical data on the probable repair costs for buildings of different types, based on the opinions of earthquake engineering experts [66]. The ATC-14 report provided a standardized methodology for evaluating life safety hazards in buildings [67].

21.2.2 SEAOC Vision 2000 (1995)

Based on Structural Engineers Association of California (SEAOC) Vision 2000, the first step in PBEE is the definition and selection of the performance objectives (PO). A PO is a coupling of expected performance levels with levels of seismic ground motions. A performance level represents a distinct band in the spectrum of damage to the structural and non-structural components and contents, and also considers the consequences of the damage to the occupants and functions of the facility [120]. The four discrete performance levels in this document are: 1) fully operational, 2) operational, 3) life safety, and 4) near collapse in terms of damage to structural and non-structural components and consequences to the occupants and functions carried on within the facility as shown in Figure 21.2 [780]. Also SEAOC Vision 2000 describes various hazard levels as: 1) frequent intensity level with a 50% exceedance probability in 30 years, 2) the occasional intensity level with a 50% exceedance probability in 50 years, 3) the rare intensity level with a 10% exceedance probability in 50 years, and 4) the very rare intensity level with a 10% exceedance probability in 100 years. It should be noted that the earthquake design levels were shown as an earthquake with specific return period in Figure 21.2. In this figure, the diagonal lines represent different *objectives* which correspond to different facility types.

21.2.3 ATC-40 (1996)

In 1996, the ATC published a document entitled: "*Seismic Evaluation and Retrofit of Concrete Buildings*" in which the performance based design refers to the methodology that structural criteria are expressed in terms of achieving a performance objective. The document is limited to concrete buildings and emphasizes the use of the capacity spectrum method [68].

21.2.4 FEMA 273 (1997) and FEMA 274 (1997)

In 1997, the Federal Emergency Management Agency (FEMA) published the National Earthquake Hazards Reduction Program (NEHRP) guidelines for the seismic

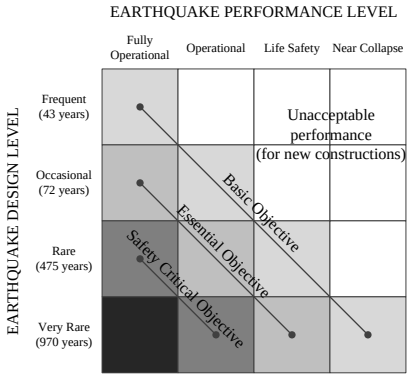

Fig. 21.2: Recommended minimum seismic performance design objectives for buildings

rehabilitation of buildings [295] and associated commentary documents [294]. The FEMA 273 document presents a variety of performance objectives with associated probabilistic ground motions. Analysis and design methods for the multiple-level performance range from linear static to inelastic time history analysis. The document defines performance levels for non-structural elements and systems and proposes drift limits for various lateral-load-resisting structural systems at different performance levels.

21.2.5 FEMA 356 (2000)

FEMA 365 is one of the most comprehensive guidelines for PBEE entitled: "*Prestandard and Commentary for the Seismic Rehabilitation of Buildings*." FEMA 356 was written to provide professional engineers nationwide a tool for designing seismic rehabilitation measures for existing structures [296]. The document defines various target building performance levels and earthquake hazard levels similar to those presented in SEAOC Vision 2000. The performance levels and descriptions of corresponding physical damage are shown in Table 21.1.

21.2.6 Global Framework for PBEE

As mentioned before, there are several conceptual frameworks for PBEE (SEAOC Vision 2000, FEMA 273, ATC-40) which differ in details but not in concepts [337]. Figure 21.3 is proposed by Krawinkler [509] as a global framework which identifies processes, concepts, and major issues that need to be addressed. The issues include seismological, geotechnical, structural, architectural, and socio-economic considerations.

Some other authors were more emphasized on developing a deep understanding and appreciation of the multi-disciplinary aspects of PBEE. They proposed that

Table 21.1: The range of damage of structural and non-structural components for various target building performance levels (Table C1-2) [296]

Performance levels	Collapse prevention	Life safety	Immediate occupancy	Operational
Overall damage	Severe	Moderate	Light	Very light
Structural components	Little residual stiffness and strength, but load-bearing columns and walls function. Large permanent drifts. Some exits blocked. Infills and unbraced parapets failed or at incipient failure. Building is near collapse.	Some residual strength and stiffness left in all stories. Gravity-load-bearing elements function. No out-of plane failure of walls or tipping of parapets. Some permanent drift. Damage to partitions. Building may be beyond economical repair.	No permanent drift. Structure substantially retains original strength and stiffness. Minor cracking of facades, partitions, and ceilings as well as structural elements. Elevators can be restarted. Fire protection operable.	No permanent drift. Structure substantially retains original strength and stiffness. Minor cracking of facades, partitions, and ceilings as well as structural elements. All systems important to normal operation are functional.
Non-structural components	Extensive damage.	Falling hazards mitigated but many architectural, mechanical, and electrical systems are damaged.	Equipment and contents are generally secure, but may not operate due to mechanical failure or lack of utilities.	Negligible damage occurs. Power and other utilities are available, possibly from standby sources.

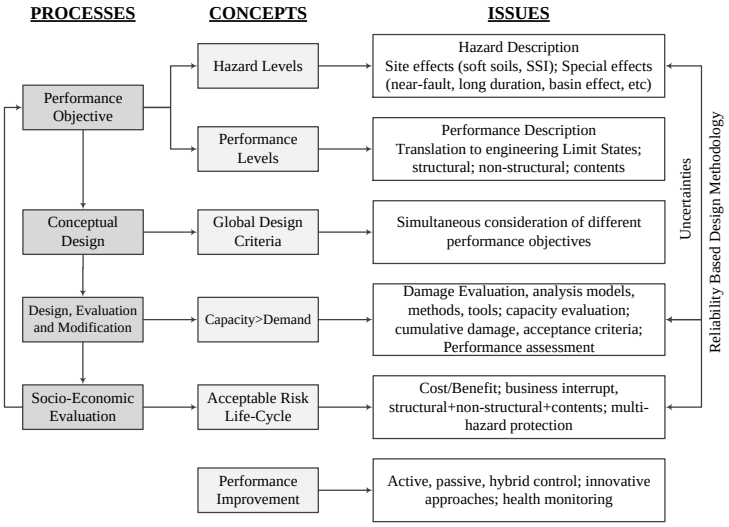

Fig. 21.3: Global framework for performance based earthquake engineering

any new conceptual developments in existing researches (downstream nodal point at the Figure 21.4) should be accompanied by updating the upstream nodal point accordingly [182].

21.3 First Generation of PBEE

All the documents discussed in the previous section are categorized as part of the first generation of PBEE which presents assessment and design procedures for buildings [602]. This procedure is also shown in Figure 21.5 conceptually, [882] and it is assumed that a structure is loaded by earthquake-induced lateral forces that produce a nonlinear response in structural components. Relations were established between

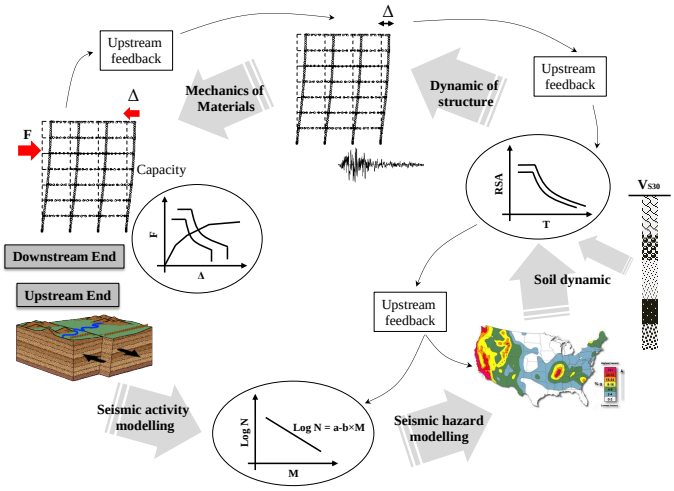

Fig. 21.4: The disciplines contribute in global framework of performance based earthquake engineering

structural responses (inter-story drift ratio, inelastic member deformation, and member force) and performance-oriented descriptions (such as immediate occupancy, life safety and collapse prevention, Table 21.1).

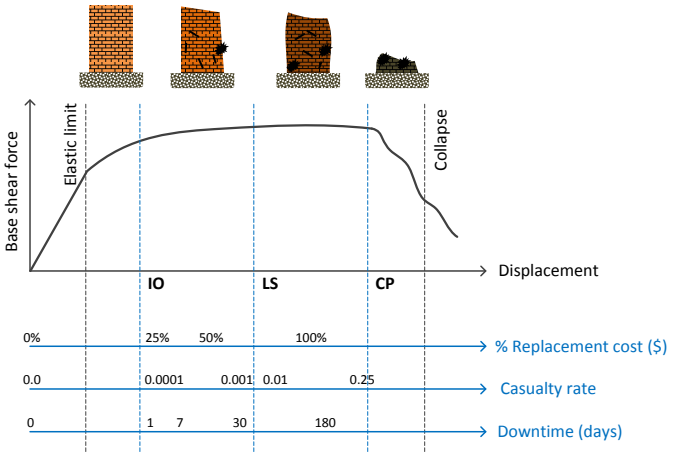

Fig. 21.5: Conceptual description of first generation of PBEE

The first generation of PBEE (also called as PBEE-1) represents a significant improvement over past practice. It includes standard methods of defining performance in terms of quantified performance levels that relate to calculated seismic response parameters and incorporate a formal methodology for simulating building response to earthquake motions and assessing performance capability based on the predicted magnitude of a series of structural response parameters [363]. Considering all these developments, they also had shortcomings which needed to be improved:

- PBEE-1 evaluated performance on the basis of the demands and capacities of individual components, rather than global building behavior. So the weakest or the least ductile elements in a structure controlled the estimation of overall structural performance (even if these elements had relatively little significance to the structure's overall seismic resistance).
- The reliability of PBEE-1 is questionable because many of the acceptance criteria contained in the documents are based on the judgment of those who developed the method, rather than laboratory data or other direct substantiating evidence.
- Considering that much of the losses experienced by structures in past earthquakes can be attributed to the performance of non-structural components and systems, the procedures that evaluate these elements in PBEE-1 are limited almost entirely to consideration of their ability to remain structurally stable and do not address well either the damageability or post-earthquake functionality of these components and systems comprised of these components.
- The reliability of the procedures in PBEE-1 and their ability to achieve the desired performance has never been established, and many engineers believe that the procedures are excessively conservative and may not result in adequate performance capability. The standard performance levels do not directly address some primary stakeholder concerns, that is probable repair costs and time of occupancy loss in the building, due to earthquake induced damage.
- The basic process of performance based engineering carries with it significant potential liability as many building owners may perceive that the design professional has provided a warranty on the design's performance capability.

21.4 Second Generation of PBEE

PBEE implies design, evaluation, and construction of engineered facilities whose performance under common and extreme loads responds to the diverse needs and objectives of owners, users, and society. In 1997 the Pacific Earthquake Engineering Research Center (PEER) decided to develop a more robust methodology for performance based earthquake engineering, called next generation PBEE (also called PBEE-2 or PEER PBEE). The PEER PBEE framework developed by PEER facilitates direct calculation of the effects of uncertainty and randomness on each step in the performance based procedure [700].

The general framework for PEER PBEE is shown in Figure 21.6. It breaks the seismic performance assessment into four primary steps: 1) ground motion hazard characterization, 2) structural response analysis, 3) damage analysis, and 4) loss

assessment [405]. The results of each of these steps are represented as generalized variable: Intensity Measure (IM), Engineering Demand Parameter (EDP), Damage Measure (DM), and Decision Variable (DV). This process can be expressed in terms of a triple integral that is an application of the total probability theorem [700]:

$$g\left[\mathrm{DV}|\mathrm{D}\right] = \int\int\int p\left[\mathrm{DV}|\mathrm{DM,D}\right] p\left[\mathrm{DM}|\mathrm{EDP,D}\right] \\ p\left[\mathrm{EDP}|\mathrm{IM,D}\right] g\left[\mathrm{IM}|\mathrm{D}\right] d\mathrm{IM}.d\mathrm{EDP}.d\mathrm{DM} \tag{21.1}$$

where $p\left[\mathrm{X}|\mathrm{Y}\right]$ denotes the complementary cumulative distribution function of X conditioned on Y, $g\left[\mathrm{X}|\mathrm{Y}\right]$ denotes the mean annual occurrence rate of X given Y, and D denotes facility location, structural, non-structural, and other features. Note that in future we omit conditioning on D for simplicity.

IM: describes the characteristics of the earthquake ground motion quantitatively. This parameter is expressed typically as a function of mean annual probability of exceedance, $g\left[\mathrm{IM}\right]$.

EDP: describes the response of the structural and the non-structural components and contents to earthquake shaking. The products of this step are conditional probabilities, $p\left[\mathrm{EDP}|\mathrm{IM}\right]$.

DM: describes the physical condition of structural and non-structural components. DMs include effective descriptions of damage to characterize the functionality, occupancy-ready, life safety and necessary repairs of the building. The products of this step are conditional probabilities, $p\left[\mathrm{DM}|\mathrm{EDP}\right]$.

DV: serves to translate damage estimates into quantities that are useful to those tasked with making risk-related decisions. Currently used DVs which are identified as decision metrics are direct dollar losses, downtime (or restoration time), and deaths (casualties). The products of this step are conditional probabilities, $p\left[\mathrm{DV}|\mathrm{DM}\right]$.

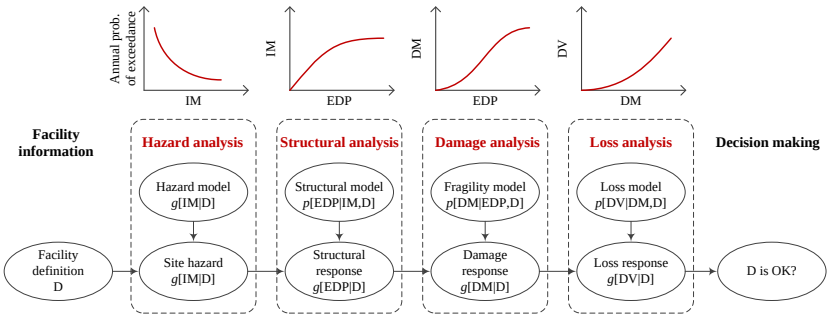

Fig. 21.6: General framework of PEER PBEE methodology [700]

As mentioned before, direct dollar losses, downtime, and casualties are used as decision variables in PBEE-2 methodology for the performance assessment of structures.

Applied Technology Council [41] uses three types of performance assessments: 1) intensity-based, 2) scenario-based, and 3) time-based.

21.4.1 Intensity-Based Performance Assessments (IBPA)

This method evaluates a structure's performance assuming that it is subjected to a specific intensity of shaking. In the case of frame structures, shaking intensity is defined by a 5% damped elastic acceleration response spectra. This assessment is usually used when the structure is subjected to the earthquake shaking with a specific response spectrum (such as design response spectrum) [41], Figure 21.7.

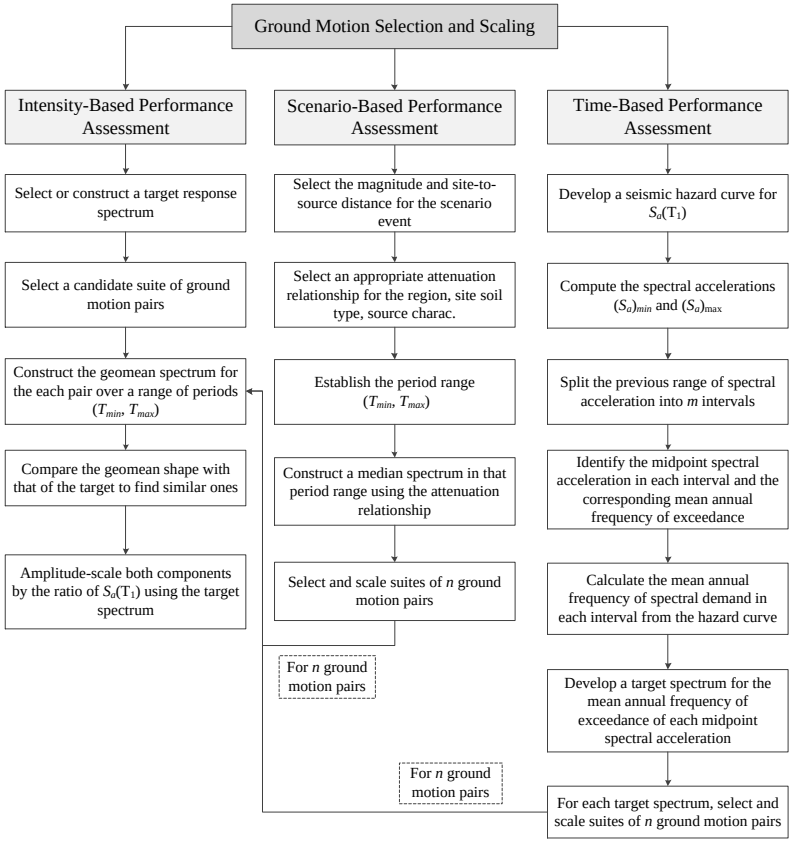

Fig. 21.7: Comparison of ground motion selection and scaling for IBPA, SBPA and TBPA

21.4.2 Scenario-Based Performance Assessments (SBPA)

This method evaluates a structure's performance assuming that it is subjected to the effects of a specific magnitude earthquake occurring at a specific location relative to the structure site. Scenario assessments may be useful for decision makers with structures located close to one or more known active faults. Scenario-based assessments are very similar to intensity-based assessments except that uncertainty in the earthquake intensity, given the scenario, is considered [41], Figure 21.7.

21.4.3 Time Based Performance Assessments (TBPA)

This method evaluates a structure's performance over a period of time considering all earthquakes that may occur in that period of time and the probability that each will occur. Time-based assessments consider uncertainty in the magnitude and location of future earthquakes as well as the intensity of motion resulting from these earthquakes. Assessments based on a single year are useful for cost-benefit evaluations used to decide between alternative performance criteria [41].
Figure 21.7 compares the step-by-step procedure for ground motion selection and scaling based on the three above mentioned methods. It is noteworthy that in TBPA, the recommended values for the parameters introduced in Figure 21.7 are as follows: $(S_a)_{min}$ = 0.05 g, and $(S_a)_{max}$ is associated with the annual frequency of exceedance of $0.00002/yr$ (that is, 1 occurrence in 50,000 years). The number of intervals m is usually recommended to be 8.

Chapter 22
Ground Motion Intensity Measures

Abstract
Ground motion is the movement of the earth's surface from earthquakes or explosions. The earthquake ground motion is produced by waves that are generated by a sudden slip on a fault and travel through the earth and along its surface. Typical the ground motion records, such as acceleration time histories, contain a tremendous amount of information. For engineering purposes, the three main characteristics of ground motions are: 1) amplitude, 2) frequency content, 3) duration.
The ground motions are recorded by different types of instruments. A seismograph is used to measure relatively weak ground motions. The records they produce are called "seismograms." On the other hand, an accelerograph is used to measure strong ground motions. The records they produce are called "accelerograms." An "accelerograph" can be referred to as a strong motion "seismograph" or simply an earthquake "accelerometer."

22.1 Ground Motion Records

22.1.1 Sources

Ground motion records can be obtained from a number of sources, among them the following two are the most useful:

- PEER Strong Ground Motion Database
- COSMOS Virtual Data Center

The web-based Pacific Earthquake Engineering Research Center (PEER) ground motion database provides tools for searching, selecting, and downloading ground motion data. ALL downloaded records are UNSCALED and as-recorded (UNROTATED).

22.1.2 Time Histories

Acceleration is recorded at discrete points and is shown as $a(t)$ or $\ddot{x}(t)$, Figure 22.1(a). The maximum absolute value of a acceleration time history is called peak ground acceleration (PGA).

Mathematically, the velocity time history can be obtained by integration of the acceleration time history in the time domain. It is shown as $v(t)$ or $\dot{x}(t)$. The integration produces a smoothing or filtering effect. The velocity time history displays substantially less high-frequency motion than the acceleration time history, Figure 22.1(b), and its absolute peak value is called peak ground velocity (PGV). In some instances, a large peak velocity may be associated with a so-called fling step displacement pulse. These types of ground motions are called "pulse-like motions." They are very important because of their potential to cause severe damage to structures.
Finally, displacement time history can be obtained by double integration of the acceleration time history in the time domain. It is shown as $x(t)$. The displacement time history obtained by another round of integration (with respect to velocity) is dominated by relatively low frequency motion, Figure 22.1(c). Its peak value is called peak ground displacement (PGD).

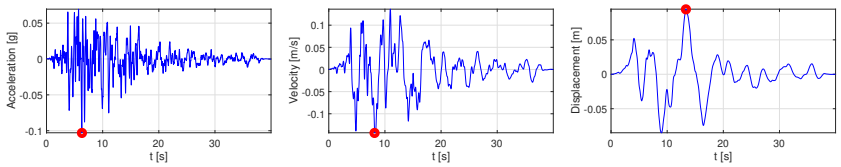

(a) $\ddot{x}(t)$ (b) $\dot{x}(t)$ (c) $x(t)$

Fig. 22.1: Time history of acceleration, velocity, and displacement for a sample ground motion record

22.2 Frequency Content Parameters

Any periodic function can be expressed using Fourier analysis as the sum of a series of simple harmonic terms of different frequency (ω_n), amplitude (c_n), and phase (ϕ_n) as:

$$x(t) = c_0 + \sum_{n=1}^{\infty} c_n \ \sin\left(\omega_n t + \phi_n\right) \tag{22.1}$$

22.2.1 Fourier Spectra

Fourier spectrum is a way to characterize the frequency content of a ground motion in the frequency domain. The Fourier transform of the ground acceleration time series, $a(t)$, is defined as:

$$A\left(\omega\right) = \int_0^{t_{tot}} a(t)\ e^{-i\omega t}\ dt \tag{22.2}$$

where $A(\omega)$ is the Fourier transform of the ground acceleration, ω is circular frequency [rad/s], and t_{tot} is total time duration.
Given the Fourier spectrum, $A(\omega)$, the time series $a(t)$ can be recovered through the inverse Fourier transform:

$$a(t) = \frac{1}{2\pi} \int_{-\infty}^{\infty} A(\omega)\ e^{i\omega t}\ d\omega \tag{22.3}$$

Equation 22.2 can be rewritten as:

$$A(\omega) = \int_0^{t_{tot}} a(t)\cos(\omega t)\ dt - i \int_0^{t_{tot}} a(t)\sin(\omega t)\ dt = C(\omega) - i\ S(\omega) \tag{22.4}$$

The amplitude of $A(\omega)$ is called the Fourier amplitude spectrum (FAS) and is defined as:

$$\text{FAS}(\omega) = \sqrt{C^2(\omega) + S^2(\omega)} \tag{22.5}$$

Figures 22.2(a) and 22.2(b) show the FAS for ground motion record in Figure 22.1. If the FAS is smoothed and plotted on a logarithmic scale, its characteristic shape can be seen easily, Figure 22.2(c). The Fourier amplitude tends to be larger over an intermediate range of frequencies bounded by the corner frequency, f_C, (from the left side) and the cut-off frequency, f_{max}, (from the right side). The corner frequency is inversely proportional to the cube root of the seismic moment. For example, for a ground motion with seismic moment about 7, f_C is about 0.5 Hz.

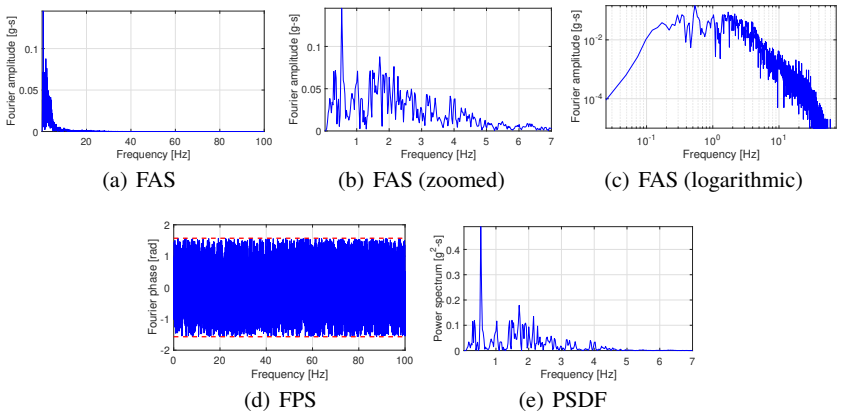

(a) FAS (b) FAS (zoomed) (c) FAS (logarithmic)

(d) FPS (e) PSDF

Fig. 22.2: Frequency dependent parameters of a sample ground motion record

The largest frequency that can be represented by the Fourier spectrum (due to symmetry of data) is referred to as the "Nyquist frequency." For a ground motion sampled with a sampling rate, f_s, (or time step $\Delta t = \frac{1}{f_s}$), the Nyquist frequency,

f_{Nq}, is:

$$f_{\text{Nq}} = \frac{f_s}{2} = \frac{1}{2\Delta t} \tag{22.6}$$

For example, for a ground motion with $\Delta t = 0.005s$, f_{Nq} is 100 Hz.
The phase of $A(\omega)$ is called the Fourier phase spectrum (FPS) and is defined as:

$$\text{FPS}(\omega) = -\tan^{-1}\left(\frac{S(\omega)}{C(\omega)}\right) \tag{22.7}$$

The FPS is bounded between $[-\pi/2, \pi/2]$. Given a digitally recorded ground acceleration time series, the computation of the Fourier spectrum is usually performed by a discrete Fourier transform (DFT) and fast Fourier transform (FFT) techniques. In the computation of the FAS using the DFT, the frequency resolution (the shortest frequency interval at which the FAS can be computed) is inversely proportional to the record length.

22.2.2 Power Spectral Density Function

The power spectral density function (PSDF) is used to describe the frequency content of a ground motion. It can also be used to estimate the statistical properties of a ground motion and to compute stochastic response using random vibration techniques, Figure 22.2(e).

$$\text{PSDF}(\omega) = \frac{\text{FAS}^2(\omega)}{t_{tot}} \tag{22.8}$$

22.3 Response Spectrum

22.3.1 Elastic Response Spectra

Seismic response spectra for a given accelerogram $a(t)$ are evaluated by subjecting a series of viscously damped SDOF systems (with variable fundamental periods but a common damping ratio ζ) to a support excitation equal to $a(t)$ and determining their maximum response quantity (e.g. the acceleration, displacement, or velocity). Recall the solution for the equation of motion (EOM) in an SDOF system as:

$$x_{SDOF}(t) = -\frac{1}{\omega_D}\int_0^t \ddot{x_g}(\tau) e^{-\zeta\omega_n(t-\tau)} \sin\omega_D(t-\tau)\, d\tau \tag{22.9}$$

The maximum response of the system with period T_n (or frequency ω_n) and damping ratio of ζ is:

$$S_d(T_n, \zeta) = |x_{SDOF}(t)|_{max} = \left| \frac{1}{\omega_D} \int_0^t \ddot{x}_g(\tau) e^{-\zeta \omega_n (t-\tau)} \sin \omega_D (t-\tau)\, d\tau \right|_{max} \tag{22.10}$$

where $S_d(T_n, \zeta)$ is the relative displacement spectrum of the earthquake ground motion for the parameters of T_n and ζ.
Similarly, the relative velocity spectrum, $S_v(T_n, \zeta)$, and absolute acceleration response spectrum, $S_a(T_n, \zeta)$, are expressed as:

$$S_v(T_n, \zeta) = |\dot{x}_{SDOF}(t)|_{max} \tag{22.11}$$

$$S_a(T_n, \zeta) = |\ddot{x}_{SDOF}(t) + \ddot{x}(t)|_{max} \tag{22.12}$$

where $\ddot{x}(t)$ is actually ground acceleration, $\ddot{x}_g(t)$.
Elastic response spectrum assumes a linear relationship between force and displacement. The sample response spectra for the ground motion in Figure 22.1 are shown in Figure 22.3 (note arithmetic and logarithmic scales). Note that $S_a(T = 0, \zeta)$ corresponds to PGA. The response spectrum can be divided into three regions:

- Acceleration-controlled: High frequency
- Velocity-controlled: Intermediate frequency
- Displacement-controlled: Low frequency

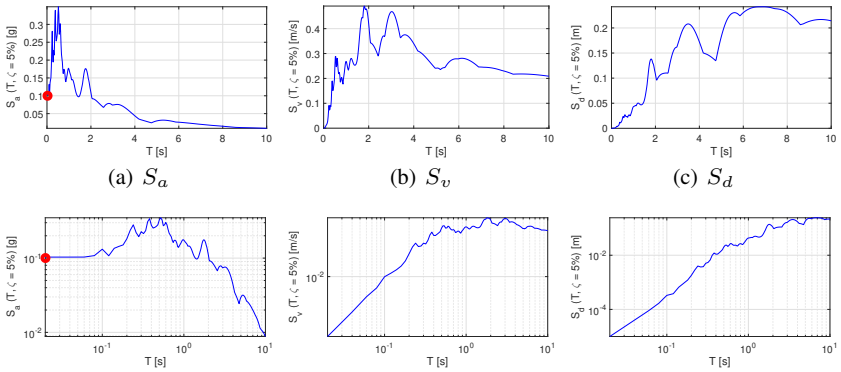

(a) S_a (b) S_v (c) S_d

(d) S_a (logarithmic) (e) S_v (logarithmic) (f) S_d (logarithmic)

Fig. 22.3: Response spectra for a sample ground motion record

22.3.2 Pseudo Response Spectra

The pseudo velocity and acceleration response spectra, S_{pv}, S_{pa} for the system are defined as:

$$S_{pv}(T_n,\zeta) = \omega_n \; S_d(T_n,\zeta) = \frac{2\pi}{T} \; S_d(T_n,\zeta) = \sqrt{\frac{k}{m}} \; S_d(T_n,\zeta) \quad (22.13)$$

$$S_{pa}(T_n,\zeta) = \omega_n^2 \; S_d(T_n,\zeta) = \frac{4\pi^2}{T^2} \; S_d(T_n,\zeta) = \frac{k}{m} \; S_d(T_n,\zeta) \quad (22.14)$$

Recall from SDOF system, for an undamped system under seismic loading, the EOM can be written as:

$$\ddot{x}_{SDOF}(t) + \omega_n^2 x_{SDOF}(t) = -\ddot{x}_g(t) \quad (22.15)$$

Substitution in Equation 22.12, yields:

$$\begin{aligned} S_a(T_n,\zeta) = & \quad \left|\ddot{x}_{SDOF}(t) + \ddot{x}_g(t)\right|_{max} = \left|-\omega_n^2 x_{SDOF}(t)\right|_{max} \\ = & \quad \omega_n^2 \left|x_{SDOF}(t)\right|_{max} = \omega_n^2 S_d(T_n,\zeta) = S_{pa}(T_n,\zeta) \end{aligned} \quad (22.16)$$

This means that for an undamped system the acceleration response spectrum corresponds to the pseudo acceleration response spectrum. The plots in Figure 22.4 compare $S_{pa}(T_n, \zeta = 5\%)$ *vs.* $S_a(T_n, \zeta = 5\%)$ and also $S_{pv}(T_n, \zeta = 5\%)$ *vs.* $S_v(T_n, \zeta = 5\%)$. As seen for $\zeta = 5\%$, acceleration responses are nearly identical, while there are some differences between velocity responses.

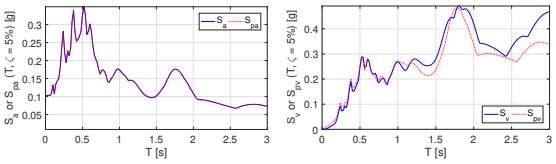

(a) S_a (b) S_v

Fig. 22.4: Comparison of response spectra and pseudo response spectra for a sample ground motion record

22.3.3 Damping Effects

Damping is one of the most important parameters in the determination of the response spectra. A higher damping value reduces the spectral responses, Figure 22.5.

22.4 Ground Motion Duration

22.4.1 Fundamentals

Ground motion duration can have a strong influence on the earthquake damage and some physical processes, such as:

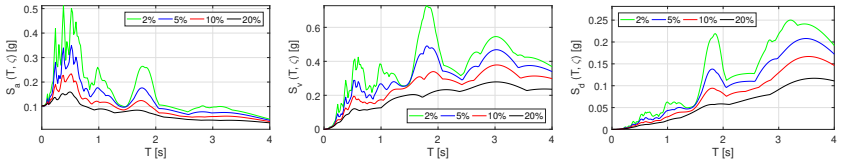

(a) S_a (b) S_v (c) S_v

Fig. 22.5: Damping effects on response spectra

- Degradation of stiffness and strength of certain types of structures (e.g., concrete dams),
- Buildup of pore-water pressure in loose, saturated sands

Short duration ground motions may not have enough load reversals for a damaging response, even if the amplitude is high. The ground motion duration has a direct relation with the time required for release of the accumulated strain energy by rupture along the fault. As the length, or area, of fault rupture increases, the time required for rupture increases. Thus, the ground motion duration increases with increasing earthquake magnitude. For a particular rock site, the shaking duration is a regression function of earthquake (moment) magnitude [136]:

$$\log D_E = 0.69 M_W - 3.70 \tag{22.17}$$

where D_E is called effective duration in [sec].
Arias intensity, I_A, is a ground motion parameter related to the spectrum of the energy demanded by a strong-motion record:

$$I_A = \frac{\pi}{2g} \int_0^{t_{tot}} [\ddot{u}_g(t)]^2 \, dt \tag{22.18}$$

where t_{tot} is total ground motion duration (from when the accelerogram starts to record the earthquake motion, until the time the motion has returned to the level of background noise). In some cases, the Arias intensity is presented in percentage.

22.4.2 Classification

There are four different definitions associated with a ground motion record:

- Total ground motion duration, t_{tot}.
- Significant duration, t_{sig}, is a measure of strong ground motion part and usually refers to a portion of ground motion which includes about 90% of the energy, Figure 22.6(a).

$$D_{5-95} = t_{sig} = t_{0.95 I_A} - t_{0.05 I_A} \tag{22.19}$$

- Seismological duration, D_{5-75}, is another intensity measure that seismologists often adopt.

$$D_{5-75} = t_{0.75I_A} - t_{0.05I_A} \tag{22.20}$$

- Bracketed duration [135] is the elapsed time between the first and last acceleration excursions greater than a given level (usually 0.05g), Figure 22.6(b).

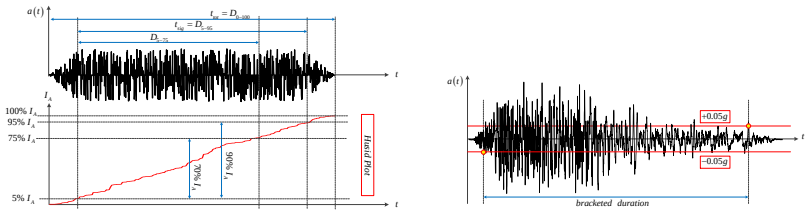

(a) Significant duration (b) Bracketed duration

Fig. 22.6: Determination of different ground motion durations

22.5 Time-Dependent IM Functions

Ground motion intensity measures (IM) are parameters that synthetically describe the intensity of ground motions (with particular reference on their effects on structures). General formulas have been proposed to represent the intensity of a time-dependent function, $f(t)$, $t \subseteq [0, t_{tot}]$ where t_{tot} refers to the total duration of the function. The $f(t)$ is defined to be either: 1) a time-dependent ground motion characteristic (such as acceleration, velocity, and displacement), or 2) a frequency-dependent ground motion characteristics (such as acceleration, velocity and displacement response spectra). The intensity measure relations for a raw function are given by:

$$\begin{aligned} f_{peak} &= max(|f(t)|) \\ f_{sum} &= \int_{t_1}^{t_2} f(t)dt \\ f_{sum}^{abs} &= \int_{t_1}^{t_2} |f(t)|\, dt \\ f_{avg} &= \frac{1}{t_2 - t_1} \int_{t_1}^{t_2} f(t)dt \end{aligned} \tag{22.21}$$

where t_1 and t_2 refer to specific duration ($t_2 > t_1$).
For oscillatory $f(t)$ we define

$$
\begin{aligned}
f_{sum}^{sqr} &= \int_{t_1}^{t_2} (f(t))^2 dt \\
f_{avg}^{sqr} &= \frac{1}{t_2 - t_1} \int_{t_1}^{t_2} (f(t))^2 dt
\end{aligned}
\tag{22.22}
$$

When Equations 22.21 and 22.22 are integrated from t_0 to t_{tot} they yield a single scalar quantity (this is generally the case when the full ground motion record is used). On the other hand, if integration is carried between t_0 and an arbitrary t_i then a vector results. This is the case when an artificial function is used. The sample variation of those functions for an intensifying acceleration function are shown in Figure 22.7.

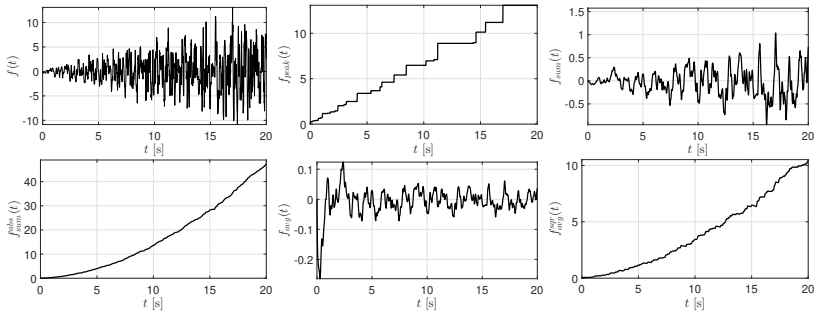

Fig. 22.7: Characterization of a time-dependent function $f(t)$

22.6 Ground Motion IMs

22.6.1 Category I: Unscalable IMs

In this case, the IMs are independent from both the ground motion scaling methods and the characteristics of the target structure. These are: earthquake magnitude, M, epicentral distance, R_{epi}, hypocentral distance, R_{hypo}, ground motion duration, t_{tot}, significant duration, t_{sig}, and seismological duration.

22.6.2 Category II: Ground Motion Dependent Scalar IMs

Peak Values The most widely used IM is the PGA. Not only is it used in hazard maps, but attenuation relations are usually available in terms of PGA. The PGV and PGD are other typical single-parameter scalar IMs. Hao, Xie, and Xu [369] found that PGV correlates to damage better than PGA [212].

$$\begin{aligned} \text{PGA} &= max\left(|\ddot{u}(t)|\right) \\ \text{PGV} &= max\left(|\dot{u}(t)|\right) \\ \text{PGD} &= max\left(|u(t)|\right) \end{aligned} \tag{22.23}$$

where $\ddot{u}(t)$, $\dot{u}(t)$, and $u(t)$ refer to the acceleration, velocity, and displacement time history of the ground motion record, respectively.

Root-mean-square $(.)_{RMS}$ of acceleration, a_{RMS}, velocity, v_{RMS}, and displacement, u_{RMS}, are used as a measure of effective $F(t)$ acceleration (or velocity or displacement) of a ground motion time-history

$$(..)_{RMS} = \left(\frac{1}{t_{tot}}\int_0^{t_{tot}} ((.)(t))^2 dt\right)^{1/2} \tag{22.24}$$

A set of intensity measures similar to Eq. 22.24, which do not account for the average values (shown in the denominator of the previous equation) and neglecting the damping ratio, was also proposed by Nau and Hall [623]

$$\begin{aligned} a_{rs} = \left(\underbrace{\int_0^{t_{tot}} (\ddot{u}(t))^2 dt}_{E_a}\right)^{1/2} \quad ; \quad v_{rs} = \left(\underbrace{\int_0^{t_{tot}} (\dot{u}(t))^2 dt}_{E_v}\right)^{1/2} \\ u_{rs} = \left(\underbrace{\int_0^{t_{tot}} (u(t))^2 dt}_{E_d}\right)^{1/2} \end{aligned} \tag{22.25}$$

Arias Intensity is a measure of dissipated energy per unit mass in an elasto-plastic system [44]

$$I_A(\zeta) = \frac{\cos^{-1}\zeta}{g\sqrt{1-\zeta^2}}\int_0^{t_{tot}} (\ddot{u}(t))^2 dt \tag{22.26}$$

where ζ is the damping ratio of a structure and g the gravitational acceleration. In the standardized form, I_A with zero damping yields Eq. 22.18.

Destructiveness Potential Although the original (and standardized) I_A accounts for the ground motion peak and duration, the frequency characteristics are somehow neglected. Araya and Saragoni [42] proposed a factor that measures the destructiveness potential, P_D, or capacity to induce structural damage.

$$P_D = \frac{I_A}{\upsilon_0^2} \tag{22.27}$$

where υ_0 is the number of zero-crossings occurrence of the ground motion record per unit time.

Specific Energy Density, SED, measures the total energy of the ground motion:

$$SED = \int_0^{t_{tot}} (\dot{u}(t))^2 dt \tag{22.28}$$

Since SED is calculated from the velocity time history, the general trend of mean values is not as smooth as the other parameters.

Cumulative Absolute Velocity, CAV, is defined as the integral of the absolute value of the acceleration time series [277]

$$CAV = \int_0^{t_{tot}} |\ddot{u}(t)|\, dt \tag{22.29}$$

CAV is the IM that best correlates with the onset of damage. However it should be noted that CAV does not account for the mismatch of arrival time for different energy phases. This is the case for a large velocity pulse [164]. The Electrical Power Research Institute (EPRI) introduced a standardized version of CAV_{STD} that prevents contribution of the low-amplitude, non-damaging ground motions [276]

$$CAV_{STD} = \sum_{i=1}^{N} \left(H(PGA_i - \ddot{u}_{min}) \int_{i-1}^{i} |a(t)|\, dt \right) \tag{22.30}$$

$$H(\delta) = \begin{cases} 0 & \delta < 0 \\ 1 & \delta \geq 0 \end{cases}$$

where N is the number of non-overlapping one-second time intervals, PGA_i is the peak ground acceleration (in term of g) in i^{th} time interval (inclusive of the first and last points), $\ddot{u}_{min}$ is an acceleration threshold (user-defined, but usually taken as $0.025g$) to exclude low amplitude motions contributing to the sum, and $H(x)$ is the Heaviside step function.

Cumulative Absolute Displacement, CAD, is defined in a similar way to CAV [557]

$$CAD = \int_0^{t_{tot}} |\dot{u}(t)|\, dt \tag{22.31}$$

Sustained Values The absolute values of highest accelerations that sustained for 3 and 5 cycles in acceleration time history are defined as 3-cycle sustained and 5-cycle sustained maximum accelerations, SMA, respectively. A similar concept is applicable to the velocity time history which results in sustained maximum velocity, SMV [664].

22.6.3 Category III: Ground Motion Dependent Compound IMs

A generalization of the previously addressed scalar IM, is one which considers the IM to be a vectorial quantity.

$$\begin{aligned} IM_{com} = C_{com}\, (\text{PGA})^{\beta_1}\, (\text{PGV})^{\beta_2}\, (\text{PGD})^{\beta_3}\, (a_{RMS})^{\beta_4} \\ (v_{RMS})^{\beta_5}\, (u_{RMS})^{\beta_6}\, (I_A)^{\beta_7}\, (t_{sig})^{\beta_8} \end{aligned} \tag{22.32}$$

where β_i, i = 1, ..., 8 are effectively weight coefficients associated with each of the IMs, and C_{com} a pre-multiplying factor.
Some of the most commonly representations for IM_{com} include the following:
Velocity to Acceleration Ratio is probably the most commonly used and is expressed in terms of PGV and PGA. It is the simplest method to categorize near-fault pulse-like ground motions.

$$\begin{aligned} I_{v/a} &= (PGA)^{-1}(PGV)^{+1} \\ I_{v^2/a} &= (PGA)^{-1}(PGV)^{+2} \end{aligned} \tag{22.33}$$

Characteristic Intensity, I_C, is defined by Park, AH-S., and Wen [684]

$$I_C = (a_{RMS})^{+3/2}(t_{sig})^{+1/2} \tag{22.34}$$

Riddell-Garcia Intensity is a set of compound IMs that minimize dispersion of hysteretic energy-dissipation spectra of inelastic systems proposed by Riddell and Garcia [734]

$$\begin{aligned} I_a &= (PGA)^{+1}(t_{sig})^{+1/3} \\ I_v &= (PGV)^{+2/3}(t_{sig})^{+1/3} \\ I_d &= (PGD)^{+1}(t_{sig})^{+1/3} \end{aligned} \tag{22.35}$$

Fajfar Intensity is a compound IM that takes into account the damage capacity of medium-period structures Fajfar, Vidic, and Fischinger [285]

$$I_F = (PGV)^{+1}(t_{sig})^{+1/4} \tag{22.36}$$

Cosenza-Manfredi Intensity, I_D, accounts for the number of plastic cycles or, equivalently, the energy content of the earthquake Cosenza and Manfredi [219]. This is a dimensionless IM defined by

$$I_D = \frac{2g}{\pi}(PGA)^{-1}(PGV)^{-1}(I_A)^{+1} \tag{22.37}$$

Shaking Intensity Rate, SIR, is applicable for liquefaction-induced building settlements [229]. It represents the rate of earthquake energy buildup:

$$SIR = \frac{I_{A5-75}}{D_{5-75}} \tag{22.38}$$

where I_{A5-75} is the change in Arias intensity from 5 to 75% of its total value, and D_{5-75} is its corresponding time duration.

22.6.4 Category IV: Structure-Independent Spectral IMs

Bounded Spectrum Intensities These IMs are determined from the ground motion response spectra. In some cases, a specific period range is considered. Acceleration, ASI, velocity, VSI, and displacement DSI spectrum intensities are defined by [148]:

$$\begin{aligned} ASI &= \int_{0.1}^{0.5} S_a\left(T, \xi = 5\%\right) dT \\ VSI &= \int_{0.1}^{2.5} S_v\left(T, \xi = 5\%\right) dT \\ DSI &= \int_{2.0}^{5.0} S_d\left(T, \xi = 5\%\right) dT \end{aligned} \tag{22.39}$$

where S_a, S_v, and S_d are the acceleration, velocity, and displacement response spectra, T the vibration period, and ξ the damping ratio.
Housner Intensity, HI, is similar to VSI; however, the pseudo velocity spectrum, PS_v, is used instead of S_v [428]:

$$HI = \int_{0.1}^{2.5} PS_v\left(T, \xi = 5\%\right) dT \tag{22.40}$$

Effective Peak Values Effective peak acceleration, EPA, and effective peak velocity, EPV first defined in ATC [65] and modified in Kurama and Farrow [519] are as follows (note that the factor 2.5 is an empirical value):

$$\begin{aligned} EPA &= \frac{1}{2.5} \times \frac{\int_{0.1}^{0.5} S_a\left(T, \xi = 5\%\right) dT}{0.4} \\ EPV &= \frac{1}{2.5} \times \frac{\int_{0.8}^{1.2} S_v\left(T, \xi = 5\%\right) dT}{0.4} \end{aligned} \tag{22.41}$$

Improved Effective Peak Values Since the fixed period range for EPA and EPV does not account for the ground motion frequency content, and since the dominant period, T_P, of a response spectrum implicitly accounts for the frequency characteristics of the ground motions, the following expressions were proposed by Yang, Pan, and Li [897]

$$\begin{aligned} IEPA &= \frac{1}{2.5} \times \frac{\int_{T_P^a - 0.2}^{T_P^a + 0.2} S_a\left(T, \xi = 5\%\right) dT}{0.4} \\ IEPV &= \frac{1}{2.5} \times \frac{\int_{T_P^v - 0.2}^{T_P^v + 0.2} S_v\left(T, \xi = 5\%\right) dT}{0.4} \end{aligned} \tag{22.42}$$

where T_P^a and T_P^v are the periods where the spectral acceleration, S_a, and spectral velocity, S_v, reach the maximum value, respectively.

22.6.5 Category V: Structure-Dependent Spectral IMs

This set of IM parameters are derived from response spectrum of the ground motion while accounting for the natural periods of the target structure.

Single-Period Intensities are the most commonly used structure-dependent spectral IMs. They are expressed in terms of $S_a(T_1, \xi = 5\%)$, $S_v(T_1, \xi = 5\%)$, and $S_d(T_1, \xi = 5\%)$ in which T_1 is the first-natural period of the structure. Moreover, spectral acceleration of some specific modes are of interest such as: $S_a(T = T_P, \xi = 5\%)$, $S_a(T = 0.2, \xi = 5\%)$,and $S_a(T = 1.0, \xi = 5\%)$. Critical T values are 0.2 and 1.0 s as they are often used in design codes.

Cordova Intensity A limitation of the previous case is the significant variability in the level of structural response in an MDOF system [791]. $S_a(T_1, \xi = 5\%)$ does not account for the higher-order vibration modes and so is not appropriate for structures sensitive to higher modes. Hence, an improved two-parameter scalar IM that accounts for the period lengthening is given by Cordova et al. [213]

$$S_a^* = \left(S_a\left(T_1, \xi\right)\right)^{1-\alpha} \left(S_a\left(c.T_1, \xi\right)\right)^{\alpha} \tag{22.43}$$

where c and α are two parameters to be calibrated; however, they are usually taken to be 2.0 and 0.5, respectively.

Vamvatsikos Intensity Vamvatsikos and Cornell [851] proposed an IM which considers the participation of higher-order vibration modes as:

$$\begin{aligned} \overline{S_a} = &\quad \left(S_a\left(T_a, \xi = 5\%\right)\right)^{1-\alpha} \left(S_a\left(T_b, \xi = 5\%\right)\right)^{\alpha} \\ \overline{\overline{S_a}} = &\quad \left(S_a\left(T_a, \xi = 5\%\right)\right)^{1-\beta-\gamma} \left(S_a\left(T_b, \xi = 5\%\right)\right)^{\beta} \\ &\qquad \left(S_a\left(T_c, \xi = 5\%\right)\right)^{\gamma} \end{aligned} \tag{22.44}$$

where T_a, T_b and T_c are arbitrary periods and $\alpha, \beta, \gamma \in [0, 1]$ are obtained by system identification with $\beta + \gamma \leq 1$.

Multiple-Period Intensities is primarily used for high-rise building structures [919] and accounts for both the higher-order modes and the effective mass at each mode. Considering the first two vibration modes, the combined intensity measures can be expressed as:

$$\begin{aligned} S_a^{1\&2} &= \left(S_a\left(T_1, \xi\right)\right)^{\alpha'} \left(S_a\left(T_2, \xi\right)\right)^{\beta'} \\ \alpha' &= \frac{m_1^{eff}}{m_1^{eff} + m_2^{eff}}; \quad \beta' = \frac{m_2^{eff}}{m_1^{eff} + m_2^{eff}} \end{aligned} \tag{22.45}$$

where α' and β' are the ratios of effective mass and m_i^{eff}, $i = 1, 2, 3$ is the effective mass for the ith mode.

Hariri-Saouma Intensity (Modified Multiple-period Intensity) In the case that multiple vibration modes contribute in the general vibration behavior of the structural system, the effects of all those modes can be considered in the combined spectral value-based IM [386]:

$$S_a^{1-to-N} = \sum_{i=1}^{N} \left(S_a\left(T_i, \xi\right)\right)^{\alpha_i} \quad , \quad \alpha_i = \frac{m_i^{eff}}{\sum_{j=1}^{N} m_i^{eff}} \tag{22.46}$$

where N is the number of the effective modes, T_i is the period of the ith mode, and α_i is the ratio of effective masses. Note that in the case that N=1, S_a^{1-to-N} yields to $S_a\left(T_i, \xi\right)$.

Relative Average Spectral Acceleration, ASA_R, De Biasio et al. [231] proposed an IM as:

$$ASA_R\left(T_1\right) = \frac{T_1}{\left(1 - X_f\right)} \int_{T_1}^{\frac{T_1}{X_f}} \frac{S_{pa}\left(T, \xi\right)}{T^2} \mathrm{d}T \tag{22.47}$$

where $X_f = 1 - R/100$ is a factor that accounts for the drop in T_1, R indicates the amount of drop in T_1, and S_{pa} is the spectral pseudo-acceleration.

22.6.6 Category VI: Vector-Based IMs

Vector-based IMs are defined in terms of two or more parameters [134].

Vamvatsikos Vector-Based Intensity uses a combination of one scalable and one scaling-independent IM, Vamvatsikos and Cornell [851]. The scalable component is $S_a\left(T_1, \xi\right)$, while the spectral ratio, $R_{sa}\left(\kappa, T_1, \xi\right)$, is the non-scalable one.

$$\left\langle S_a\left(T_1, \xi\right), R_{sa}\left(\kappa, T_1, \xi\right)\right\rangle = \left\langle S_a\left(T_1, \xi\right), \frac{S_a\left(\kappa T_1, \xi\right)}{S_a\left(T_1, \xi\right)} \right\rangle \tag{22.48}$$

where κ is a constant factor, usually 1.5.

Baker Intensity has a scalable parameter given by $S_a(T_1)$ and a scaling-independent one that is typically the magnitude, M_w, distance, R, or epsilon, ϵ, Baker and Cornell [78]. It is found that $\left\langle S_a\left(T_1, \xi\right), \epsilon\right\rangle$ is significantly superior to $S_a(T_1)$ alone. ϵ is defined as the number of standard deviations by which an observed logarithmic spectral acceleration, $\ln S_a(T)$, differs from the mean logarithmic spectral acceleration, $\overline{\ln S_a(T)}$, of a ground-motion prediction equation.

Bojorquez Intensity uses a combination of $S_a\left(T_1, \xi\right)$ with other scalar IMs in order to determine the optimal vector IM, Bojorquez et al. [134]. $\left\langle S_a\left(T_1, \xi\right), PGA\right\rangle$ and $\left\langle S_a\left(T_1, \xi\right), PGV\right\rangle$ are used as indicators of the peak responses of the structural system. $\left\langle S_a\left(T_1, \xi\right), t_{sig}\right\rangle$ and $\left\langle S_a\left(T_1, \xi\right), I_D\right\rangle$ are used as indicators of combination of peaks and cumulative damage potential of ground motions.

$$\begin{gathered} \left\langle S_a\left(T_1, \xi\right), R_{T_1,T_2}\right\rangle \quad , \quad R_{T_1,T_2} = \frac{S_a(T_2)}{S_a(T_1)} \\ \left\langle S_a\left(T_1, \xi\right), N_p\right\rangle \quad , \quad N_p = \frac{S_a\left(\left(\prod_{i=1}^{N} T_i\right)^{1/N}, \xi\right)}{S_a(T_1, \xi)} \end{gathered} \tag{22.49}$$

22.6.7 Category VII: IM for Multiple-Component Ground Motions

All the scalar or vector-based IM parameters introduced so far were determined for a single-component ground motion record. In multiple-component ground motions, one determines an IM for each one of them. Subsequently those values are averaged [507].

$$\begin{aligned} \text{IM}_{\text{art}} &= \frac{1}{2}\sum_{i=1}^{2}\text{IM}_i \\ \text{IM}_{\text{geo}} &= \left(\prod_{i=1}^{2}\text{IM}_i\right)^{1/2} \\ \text{IM}_{\text{srss}} &= \left(\sum_{i=1}^{2}\text{IM}_i^2\right)^{1/2} \\ \text{IM}_{\text{max}} &= max(\text{IM}_i), i = 1, 2 \end{aligned} \tag{22.50}$$

22.7 Optimal IM Selection

Selection of an optimal IM parameter requires one to perform multiple nonlinear transient analyses based on Cloud analysis technique. The outputs (i.e. EDP) are plotted versus the IM parameters in logarithmic scale. These scatter data points have a linear trend implying a power curve in the arithmetic scale.

$$\ln\left(\eta_{\text{EDP|IM}}(\text{IM})\right) = b.\ln(\text{IM}) + \ln(a) \tag{22.51}$$

where $\ln(a)$ and b are the linear regression constants and $\eta_{\text{EDP|IM}}$ is the median value of EDP given IM.

Cloud analysis results can then be used to develop a probabilistic seismic demand model (PSDM) [216]. The logarithmic standard deviation (also called dispersion) of the EDP conditioned on the IM are also computed, $\beta_{\text{EDP|IM}}$ (assuming a lognormal distribution).

Next, selection of an optimal IM parameter is based on the following criteria, Padgett, Nielson, and DesRoches [674] and Tothong and Luco [833]:

Efficiency: Efficient IM parameters will reduce the EDP variability for a given IM [342]. In other words, efficiency will simply lower the dispersion, $\beta_{\text{EDP|IM}}$ with respect to the estimated median for a set of nonlinear transient analyses. Dispersion is inversely proportional to efficiency.

Practicality: is an indicator of the correlation between an IM and the EDP [674]. Practicality can be measured by b in Eq. 22.51 (high values being indicative of increased practicality).

Proficiency: is a composite measure of efficiency and practicality. A more proficient IM would have lower modified dispersion, ζ [674].

Sufficiency: A sufficient IM is one in which the conditional probability distribution of EDP (for a given IM) is independent of seismic hazard parameters such as M_w, R_{rup}, ε, and T_p [833]

$$P\left[\text{EDP} \geq edp|\text{IM}\right] \cong P\left[\text{EDP} \geq edp|\text{IM}, \varepsilon, M_w, R_{rup}, T_p\right] \tag{22.52}$$

Sufficiency is quantified by the p-value which is the probability of rejecting the null hypothesis and thus proves independency of the IM from other seismic hazard characteristics (M_w, R_{rup}, and ε). A higher p-value is a sign of a sufficient IM. Numerically p-values are obtained from linear regression of the residuals, $\epsilon^{\text{EDP}}|\text{IM}$:

$$\begin{aligned} \epsilon^{\text{EDP}}|\text{IM} = &\quad a_M + b_M(M_w) \\ \epsilon^{\text{EDP}}|\text{IM} = &\quad a_R + b_R(R_{rup}) \\ \epsilon^{\text{EDP}}|\text{IM} = &\quad a_\varepsilon + b_\varepsilon(\varepsilon) \end{aligned} \tag{22.53}$$

where a_i and b_i are the linear regression coefficients.

Hazard compatibility: Corresponds to the computational complexity in determining the hazard curve for a candidate IM [342]. Currently, hazard curves are available in terms of PGA or $S_a(T)$, while the other IMs require more effort to be determined.

The first four criteria in PSDA can be holistically represented by Figure 22.8.

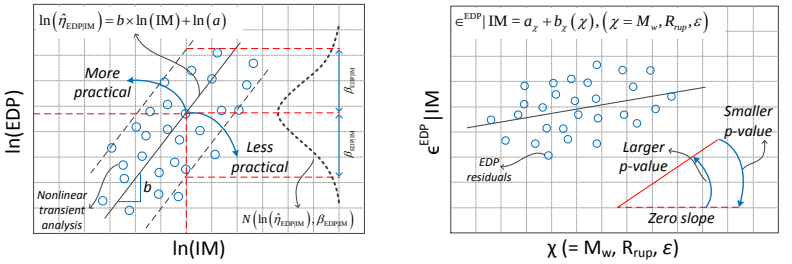

(a) Efficiency, practicality, proficiency (b) EDP residuals, p-value and sufficiency

Fig. 22.8: PSDM and criteria for optimal IM selection

Chapter 23
Seismic Hazard Analysis

Abstract
This section explains the fundamentals of seismic hazard analysis as part of earthquake engineering. According to Elnashai and Di Sarno [271], Earthquake Engineering is a branch of engineering concerned with the estimation of earthquake consequences and the mitigation of these consequences. It is an interdisciplinary subject involving seismologists, structural and geotechnical engineers, architects, urban planners, information technologists, and social scientists.

The seismic risk associated to a region depends on 1) probability of occurrence of an earthquake causing a certain level of ground shaking (seismic hazard) and 2) structural vulnerability of the constructions. Seismic hazard analysis requires two separate models:

- Seismicity model (recurrence relation/law): describes geographical distribution of potential active source zones (seismotectonic sources) and distribution of magnitudes in each source.
- Attenuation model: describes effect of an earthquake originating from a specific seismotectonic source, at any given site, as a function of magnitude and source-to-site distance.

23.1 Recurrence Relationship

Recurrence relationships express the likelihood of an earthquake of a given size occurring in the given source during a specific period of time, e.g. one year. The Gutenberg and Richter [354] frequency-magnitude relationship is expressed as Figure 23.1:

$$\begin{aligned} \ln N_M &= a - b\,M \\ \log N_M &= a' - b'\,M \end{aligned} \tag{23.1}$$

where a and b are model constants that can be evaluated from seismological observational data through least-square fitting. N_M is the number of earthquakes of magnitude greater or equal to M per units of time and units of area. The relation between a and a' and also b and b' is:

$$a = 2.3025a', \qquad b = 2.3025b' \tag{23.2}$$

Typical values for a' and b' [487]:

- Western Canada: $a' = 5.05$; $b' = 1.09$
- Japan: $a' = 6.86$; $b' = 1.22$
- Western United States: $a' = 5.94$; $b' = 1.14$
- Eastern United States: $a' = 5.79$; $b' = 1.38$

One may note that the $\frac{1}{N_M}$ represents the return period in units of time.

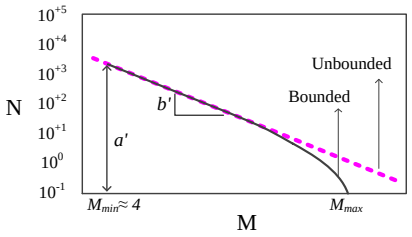

Fig. 23.1: The (bounded) Gutenberg-Richter recurrence law

Records of events with $M < 4$, although quite numerous, go back only a few years. These data are usually excluded when calculating the magnitude-recurrence relation as they may give a misleading bias. Thus, $M_{min} \approx 4$. On the other hand, for any fault line, there is a maximum achievable magnitude. M_{max} arises because of physical constraints limiting maximum size of an event. Thus, the recurrence law should be modified to capture M_{max}.
The bounded (modified) Gutenberg-Richter recurrence law may be written as a quadratic relationship, Figure 23.1:

$$N_M = N_{M_{min}} e^{-b(M-M_{min})} \; ; \quad M > M_{min} \tag{23.3}$$

where $N_{M_{min}} = e^{a-b_{M_{min}}}$.
Considering that probability may be interpreted as a relative frequency, the cumulative probability distribution (shown with capital F) of earthquake magnitude may be then expressed as:

$$\begin{aligned} F_{\mathfrak{M}}(M) &= P\left[\mathfrak{M} < M | \mathfrak{M} > M_{min}\right] \\ &= \frac{N_{M_{min}} - N_M}{N_{M_{min}}} = 1 - e^{-b(M-M_{min})} \end{aligned} \tag{23.4}$$

and its corresponding probability density function (shown with small f) will be:

$$f_{\mathfrak{M}}(M) = \frac{d}{dM} F_{\mathfrak{M}}(M) = be^{-b(M-M_{min})} \tag{23.5}$$

Therefore, the bounded Gutenberg-Richter is further modified by applying an upper bound:

$$N_M = N_{M_{min}} \frac{e^{-b(M-M_{min})} - e^{-b(M_{max}-M_{min})}}{1 - e^{-b(M_{max}-M_{min})}};\ M_{min} \leq M \leq M_{max} \tag{23.6}$$

The corresponding cumulative distribution function becomes

$$F_{\mathfrak{M}}(M) = P\left[\mathfrak{M} < M | M_{min} \leq M \leq M_{max}\right] = \frac{1 - e^{-b(M-M_{min})}}{1 - e^{-b(M_{max}-M_{min})}} \tag{23.7}$$

and finally, the corresponding probability density function is

$$f_{\mathfrak{M}}(M) = \frac{be^{-b(M-M_{min})}}{1 - e^{-b(M_{max}-M_{min})}} \tag{23.8}$$

The recurrence law applies over the geometrical area of a given earthquake source. Therefore, definition of the geometry of the earthquake sources becomes critical in seismic hazard analysis. In general, a seismic source can be classified as one of the following models [314], Figure 23.2:

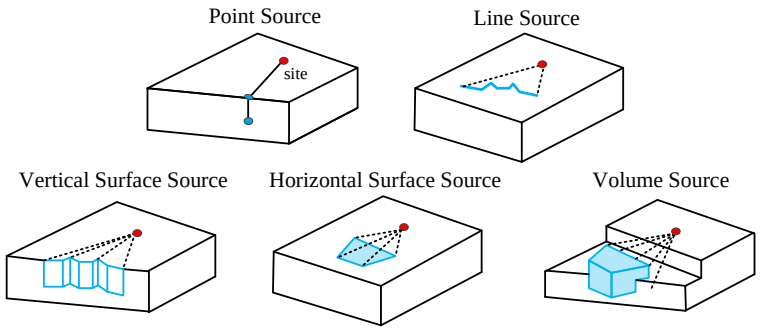

Fig. 23.2: Classification of seismic sources

- Point sources: Earthquakes originating from volcanic activity typically occur in areas that are small enough to be characterized as point sources. The faults with short rupture length also can be considered as point source.
- Line source: Fault planes propagating to the surface are usually well-defined and generate shallow earthquakes on or near the surface. These sources can be considered as one-dimensional line sources.
- Vertical surface source: can be used to to model regions with well-defined but deeper earthquakes.
- Horizontal surface source: In regions where earthquake faulting is poorly defined (e.g. north east America), individual faults are not easily identified. If shallow

earthquakes occur in these regions, they can be categorized as horizontal surface sources.
- Volume source: In regions where earthquake faulting is poorly defined and deep earthquakes occur, they are characterized by large volume sources. The focal depth can vary.

23.2 Attenuation Model

23.2.1 Fundamentals

An attenuation relationship is a function that is used to estimate different measures of ground motion intensity as a function of magnitude and distance [70, 798, 901].

$$\text{IM} = f\left(M, R\right) \tag{23.9}$$

where IM is intensity measure, e.g. PGA, $S_a(0.2s)$, etc.
In reality, many variables are involved which are also difficult to evaluate correctly. Thus, a high level of uncertainty is associated with attenuation relations. Attenuation relations are sometimes called ground motion prediction equations (GMPE). The most famous functional form for Equation 23.9 is:

$$\begin{aligned}\log\left(\text{IM}\right) = \log(b_1) + \log\left[f_1(M)\right] + \log\left[f_2(R)\right] \\ + \log\left[f_3(M,R)\right] + \log\left[f_4(E_i)\right] + \log(\varepsilon)\end{aligned} \tag{23.10}$$

where E_i is possible source, site, and geologic and geotechnical structures effects; ε is a parameter which represents the uncertainty and errors.

23.2.2 Boore, Joyner, and Fumel (1997)

There have been proposed hundreds of GMPEs for different regions and accounting for various complexity levels. Douglas [257] summarized all those relations from 1964-2010. For example, the following equation was proposed by Boore, Joyner, and Fumal [139] for spectral ordinates at rock sites:

$$\ln\left(\text{Y}\right) = b_1 + b_2(M-6) + b_3(M-6)^2 + b_5 \ln(r) + b_V \ln\left(\frac{V_S}{V_A}\right) \tag{23.11}$$

where

$$r = \sqrt{r_{jb}^2 + h^2} \tag{23.12}$$

and

$$b_1 = \begin{cases} b_{1SS} & \text{for strike-slip earthquakes} \\ b_{1RV} & \text{for reverse-slip earthquakes} \\ b_{1ALL} & \text{if mechanism is not specified} \end{cases} \tag{23.13}$$

The variable Y is spectral acceleration (5% damping) in [g]; M is moment magnitude, V_S is the average shear wave velocity in [m/s] in the upper 30 m of the profile under consideration, and V_A is reference shear wave velocity in [m/s].
The r_{jb} is the closest horizontal distance in [km] from the site to the surface projection of the source, and h is depth. All the coefficients are in [km] and listed in Table 23.1.

Table 23.1: Period-dependent coefficients of Boore, Joyner, and Fumal [139] model

Period	b_{1ss}	b_{1RV}	b_{1ALL}	b_2	b_3	b_5	b_V	V_A	h	$\sigma_{\ln(Y)}$
0	-0.313	-0.117	-0.242	0.527	0	-0.778	-0.371	1396	5.57	0.52
0.1	1.006	1.087	1.059	0.753	-0.226	-0.934	-0.212	1112	6.27	0.479
0.12	1.109	1.215	1.174	0.721	-0.233	-0.939	-0.215	1452	6.91	0.485
0.14	1.135	1.261	1.208	0.707	-0.23	-0.938	-0.228	1718	7.18	0.489
0.16	1.112	1.257	1.192	0.702	-0.226	-0.935	-0.248	1910	7.24	0.495
0.18	1.063	1.222	1.151	0.705	-0.216	-0.93	-0.27	2037	7.16	0.499
0.2	0.999	1.17	1.089	0.711	-0.207	-0.924	-0.292	2118	7.02	0.502
0.22	0.925	1.104	1.019	0.721	-0.198	-0.918	-0.315	2158	6.83	0.508
0.24	0.847	1.033	0.941	0.732	-0.189	-0.912	-0.338	2178	6.62	0.511
0.26	0.764	0.958	0.861	0.744	-0.18	-0.906	-0.36	2173	6.39	0.514
0.28	0.681	0.881	0.78	0.758	-0.168	-0.899	-0.381	2158	6.17	0.518
0.3	0.598	0.803	0.7	0.769	-0.161	-0.893	-0.401	2133	5.94	0.522
0.4	0.212	0.423	0.311	0.831	-0.12	-0.867	-0.487	1954	4.91	0.538
0.5	-0.122	0.087	-0.025	0.884	-0.09	-0.846	-0.553	1782	4.13	0.556
0.6	-0.401	-0.203	-0.314	0.928	-0.069	-0.83	-0.602	1644	3.57	0.569
0.7	-0.634	-0.452	-0.555	0.962	-0.053	-0.818	-0.639	1545	3.2	0.582
0.8	-0.829	-0.666	-0.76	0.992	-0.041	-0.809	-0.666	1476	2.98	0.593
0.9	-0.993	-0.848	-0.933	1.018	-0.035	-0.802	-0.685	1432	2.89	0.604
1	-1.133	-1.009	-1.08	1.036	-0.032	-0.798	-0.698	1406	2.9	0.613
1.1	-1.249	-1.145	-1.208	1.052	-0.03	-0.795	-0.706	1396	2.99	0.622
1.2	-1.345	-1.265	-1.315	1.064	-0.032	-0.794	-0.71	1400	3.14	0.629
1.3	-1.428	-1.37	-1.407	1.073	-0.035	-0.793	-0.711	1416	3.36	0.637
1.4	-1.495	-1.46	-1.483	1.08	-0.039	-0.794	-0.709	1442	3.62	0.643
1.5	-1.552	-1.538	-1.55	1.085	-0.044	-0.796	-0.704	1479	3.92	0.649
1.6	-1.598	-1.608	-1.605	1.087	-0.051	-0.798	-0.697	1524	4.26	0.654
1.7	-1.634	-1.668	-1.652	1.089	-0.058	-0.801	-0.689	1581	4.62	0.66
1.8	-1.663	-1.718	-1.689	1.087	-0.067	-0.804	-0.679	1644	5.01	0.664
1.9	-1.685	-1.763	-1.72	1.087	-0.074	-0.808	-0.667	1714	5.42	0.669
2	-1.699	-1.801	-1.743	1.085	-0.085	-0.812	-0.655	1795	5.85	0.672

The V_S can be simply estimated from Table 23.2. One may note that Y is the median value of the spectral acceleration. Therefore, ln (Y) will be the predicted mean value. Moreover, $\sigma_{\ln(Y)}$ is the standard deviation of ln (Y).
Different definitions of the site-to-source distance are, Figure 23.3:

- Rupture distance: the shortest distance from the station to the rupture surface
- Joyner-Boore distance: the shortest horizontal distance to the vertical projection of the rupture
- Seismogenic distance: the shortest distance from a site to a point on a rupture surface that is deeper than some minimum seismogenic depth

Table 23.2: Estimated V_S based on site class

NEHRP site class B	1070 m/s
NEHRP site class C	520 m/s
NEHRP site class D	250 m/s
Rock	620 m/s
Soil	310 m/s

- Seismogenic depth: depth of the surface materials (assumes that near-surface rupture in sediments is non-seismogenic)
- Hypocentral distance: the distance from the station to the hypocenter

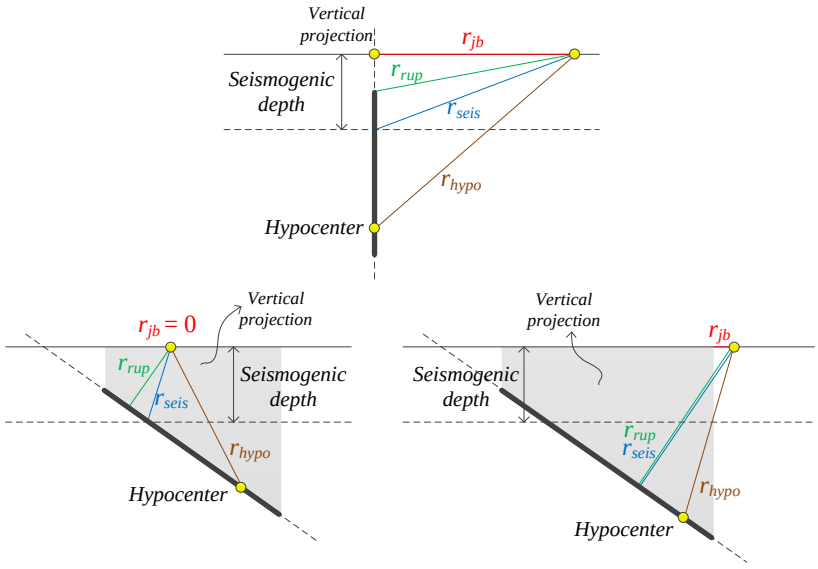

Fig. 23.3: Classification of site-to-source distances

23.2.3 Parametric Evaluation

One may derive the following generalized observations for the GMPEs, Figure 23.4:

- Increasing distance decreases intensity measure (Y).
- Increasing magnitude increases intensity measure (Y).
- Magnitude and distance affect not only the intensity but also the spectral shape.

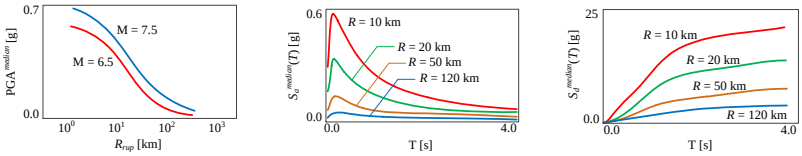

(a) R and M effects (b) Period-dependent spectral evolution

Fig. 23.4: Parametric investigation on GMPEs

23.3 Deterministic Seismic Hazard Analysis

Deterministic seismic hazard analysis (DSHA) uses geology and historical seismicity to identify earthquake sources and interpret the strongest earthquake (worst case) that each source is capable of producing regardless of time. The procedure involves development of a seismic scenario and characterization of that scenario. Application of DSHA requires four separate steps, Figure 23.5:

- STEP 1: Identify and characterize (geometry and maximum magnitude) all earthquake sources capable of generating significant shaking at the site.
- STEP 2: Calculate the source-to-site distance for each source identified in step 1 (depending on attenuation relationship, epicentral or hypocentral distance can be used).
- STEP 3: Select the controlling earthquake. This is the earthquake that will generate the greatest shaking at the site using an appropriate attenuation relationship.
- STEP 4: Define the hazard at the site based on the controlling earthquake. The hazard can be expressed by spectral ordinates, maximum ground acceleration, maximum ground velocity, maximum ground displacement, etc.

- Advantages:
  - Simple to apply,
  - Conservative procedure where tectonic features are well defined (line sources).
- Disadvantages:
  - Difficult to apply to distributed sources close to the site,
  - Uncertainty is not treated well,
  - No information is provided on the likelihood of the controlling earthquake,
  - No information is provided on the level of shaking that might be experienced in the lifespan of the structure at the site.

23.4 Probabilistic Seismic Hazard Analysis

Probabilistic seismic hazard analysis (PSHA), proposed by C.A. Cornell (1968), used to determine the design earthquake for all locations in the USA. It gives a

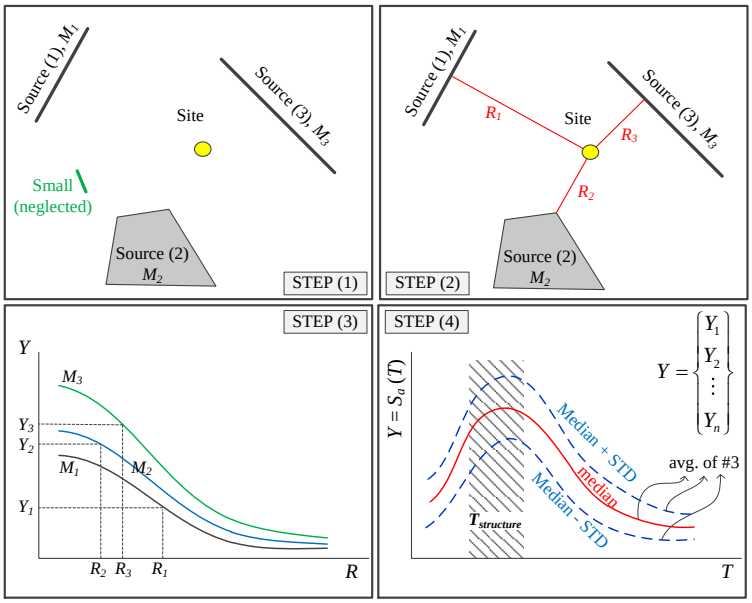

Fig. 23.5: Deterministic Seismic Hazard Analysis

relative quantification of the design earthquake, for a given site, in terms of seismic parameters (PGA, PGV, $S_a(T_i)$). PSHA takes into account uncertainties associated with occurrence and effects of important earthquakes. It cannot predict the date, magnitude, location, or effects of future earthquakes in active seismic zones.
The PSHA approach uses the elements of the DSHA and adds an assessment of the likelihood that ground motions of a given magnitude would occur. The probability or frequency of occurrence of different magnitude earthquakes on each significant seismic source and inherent uncertainties are directly accounted for in the analysis. The possible occurrence of each magnitude earthquake at any part of a source is directly incorporated in a PSHA. Results from the PSHA approach can also be used to identify which combinations of magnitude and distance is the largest contributor to hazard. Application of PSHA requires four separate steps, Figure 23.6:

- STEP 1: Definition of the seismogenic sources: For a given site, geographic zones representing seismotectonic sources are drawn. For each zone, it is assumed that the probability of earthquake occurrence is the same for the entire surface area (seismogenic source).
- STEP 2: Definition of a seismicity model: For each source, a magnitude-recurrence relation of the type $\ln N_M = a - b\,M$ is defined. Historical seismicity is used to establish the parameters of this relation. A cut-off magnitude, M_{max}, is also defined for each source.

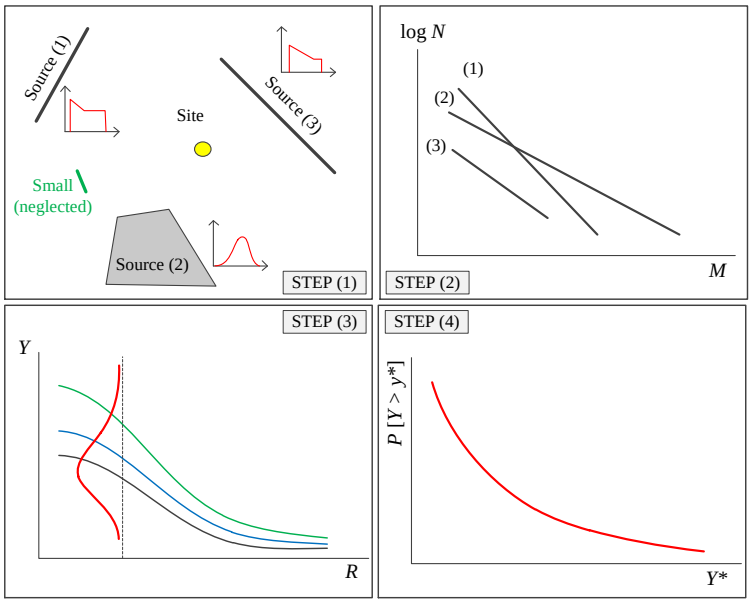

Fig. 23.6: Probabilistic Seismic Hazard Analysis

- STEP 3: Definition of an attenuation model: An attenuation relation is determined between each source and a given site. Usually the same attenuation relation is used for the entire region.
- STEP 4: Calculation of hazard curve for the site:
  - STEP 4-1: Calculation of the recurrence rate of a given ground motion level: The attenuation relations are combined with the magnitude-recurrence relations to find the annual number of earthquakes causing a chosen ground motion level at any given site.
  - STEP 4-2: Calculation of the annual probability of exceeding a chosen ground motion level: A theoretical probability distribution is used to calculate the annual probability of exceeding a chosen ground motion level at any given site. The calculation is based on the recurrence rate calculated in Step 4-1.
  - STEP 4-3: Plotting of contour lines having a constant annual probability of exceedence: All previous steps (1 to 4-2) are repeated for each given site. Contour lines are then plotted for the chosen ground motion parameter. These contour lines are based on the same annual probability of exceedence for the entire surface area.

23.5 Occurrence Time

The recurrence rate, N, and the return period, T_R, are obtained from the historical seismicity of a region. Predictions can be obtained by assuming that the sequence of earthquake occurrence follows a theoretical probability distribution model.
In PSHA, Poisson's probability model, which assumes that earthquakes are space and time independent (seismogenic model), is usually considered. The probability, $P_n(y)_t$, of having n earthquakes producing a value of the seismic parameter of interest greater or equal to y at a given site over a certain time t is given by:

$$P_n(y)_{t|N} = \frac{(Nt)^n \, e^{-Nt}}{n!} \tag{23.14}$$

where N is number of annual earthquakes (recurrence rate) producing a value of the seismic parameter of interest greater than or equal to y at the site.
The probability, $P_n(y)_{t|N}$, of having at least one earthquake causing a value of the seismic parameter of interest greater than or equal to y at the site during a given time t is then equal to 1 minus the probability, $P_n(y)_{t|N}$, of having no earthquake causing a value of the seismic parameter of interest greater than or equal to y at the site, Figure 23.7(a).

$$P(y)_{t|N} = 1 - e^{-Nt} \tag{23.15}$$

Considering the annual probability (t = 1 year), the equation yields to, Figure 23.7(b).

$$P(y)_{1|N} = 1 - e^{-N} \tag{23.16}$$

For small values of N, the simplified model is

$$P(y)_{1|N} = N \tag{23.17}$$

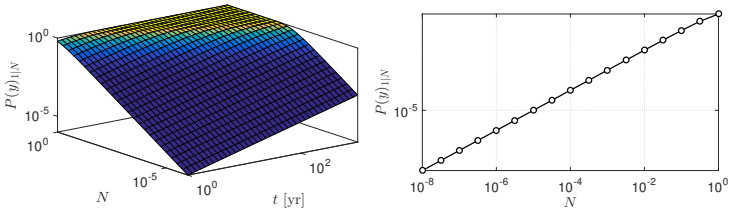

(a) Equation 23.15 (b) Equation 23.16

Fig. 23.7: Poisson's probability model

23.6 Seismic Hazard Curves

The fundamental outcome of a PSHA is the seismic hazard curve, which shows the annual rate or probability at which a specific ground motion level will be exceeded at the dam site. In any hazard curve, the vertical axis presents annual probability of exceedence (or return period), and the horizontal axis is intensity measure (IM) parameter. Seismic hazard curves are usually an important and useful tool in risk analysis of dams and nuclear structures. Figure 23.8 shows typical seismic hazard curves at the Pine Flat Dam site.

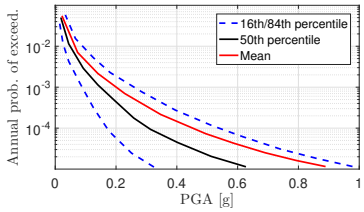

Fig. 23.8: Sample of mean and fractile seismic hazard curves

There are different computer codes in order to produce a seismic hazard curve. For example, *OpenSHA Hazard Curve Calculator* at `www.opensha.org/apps` is one of the most famous online codes.
Based on USBR recommendations [845], the most common intensity measure in the generation of hazard curves for dams is PGA; however, $S_a(T = 1sec)$ is typically used for embankment dams, and shorter periods like $S_a(T = 0.2sec)$ or $S_a(T = 0.4sec)$ curves are often used for concrete dams.
Having access to the earthquake rupture forecast and ground motion prediction equations, the seismic hazard curve is estimated as follows [40]:

$$\lambda\left(Y \geq y\right) = \sum_{f=1}^{N_f} \sum_{m=M_{min}}^{M_{max,f}} \sum_{\varrho=1}^{N_{\varrho,f,m}} \left(\lambda\left(f, m, \varrho\right) - \lambda\left(f, m + \Delta m, \varrho\right)\right) \times \left(1 - F_{Y|f,m,\varrho}\left(y\right)\right) \tag{23.18}$$

where,

$$F_{Y|f,m,\varrho}\left(y\right) = \frac{1}{N_a} \sum_{a=1}^{N_a} \Phi\left(\frac{\ln\left(\frac{y}{exp(\mu_{\ln Y,a})}\right)}{\sigma_{\ln Y,a}}\right) \tag{23.19}$$

- Y is site shaking IM parameter, usually $S_a(T_1, \xi = 5\%)$,
- y is a particular value of Y,
- $\lambda\left(Y \geq y\right)$ is mean rate at which the site can experience shaking of intensity y or greater, referred to here as the seismic hazard,

- f is an index to faults in the earthquake rupture forecast, $f = 1, 2, ..., N_f$,
- N_f is number of faults in the earthquake rupture forecast,
- m is moment magnitude, in Δm = 0.1-magnitude increments; $m = M_{min}$, $M_{min} + \Delta m$, $M_{min} + 2\Delta m$, ..., $M_{max,f}$,
- M_{min} is minimum magnitude considered, such as 5.0,
- $M_{max,f}$ is maximum magnitude that fault f is believed to be capable of producing, according to the earthquake rupture forecast,
- ϱ is an index to discrete locations along a fault trace at which earthquake epicenters are discretized, $\varrho = 1, 2, ..., N_{\varrho,f,m}$,
- $N_{\varrho,f,m}$ is number of discrete locations along fault f at which an earthquake of magnitude m can be centered,
- $\lambda(f, m, \varrho)$ is mean frequency with which fault f can produce earthquakes of magnitude m or greater at location ϱ, according to the earthquake rupture forecast,
- $F_{Y|f,m,\varrho}(y)$ is probability that shaking intensity $Y \leq y$ given an earthquake on fault f of magnitude m with epicenter located at ϱ,
- a is an index to the ground motion prediction equations used here, $a = 1, 2, ..., N_a$,
- N_a is number of ground motion prediction equations used,
- Φ is standard normal cumulative distribution function evaluated at the term in parentheses. This thesis assumes that all ground motion prediction equations assume that Y is log-normally distributed conditioned on magnitude, distance, mechanism, etc.
- $\mu_{\ln Y,a}$ is expected value of the natural logarithm of Y under ground motion prediction equation a.
- $\sigma_{\ln Y,a}$ is total standard deviation of the natural logarithm of Y under ground motion prediction equation a.

23.7 Seismic Hazard Maps

The national seismic hazard maps are usually produced using the hazard curves with several 5%-damped spectral acceleration ordinates at periods of 0.0 (PGA), 0.2, 0.3, 0.5, 0.75, 1.0 and 2.0 seconds. The annual recurrence rate of N = 0.00211, 0.00103 and 0.00040 per year are used to obtain the corresponding values for 10%, 5% and 2% probability of exceedance in 50 years. The probability of exceedance is usually calculated using the Poisson (time-independent) probabilistic model. For the U.S. hazard maps, the uniform firm-rock site conditions with the average shear wave velocity of 760 m/s in the upper 30 m of the crust was assumed.
Sample seismic hazard maps for the U.S. are shown in Figure 23.9. United States Geological Survey (USGS) National Hazard Maps show the distribution of earthquake shaking levels that have a certain probability of occurring in the United States. One can create a customized hazard map using online USGS application[1]

[1] USGS Custom Hazard Map

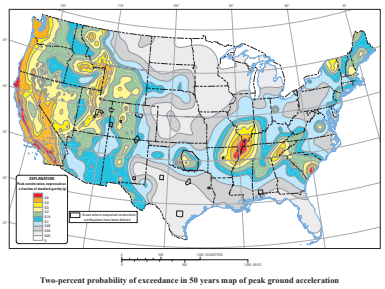

(a) 2%/50yr; PGA

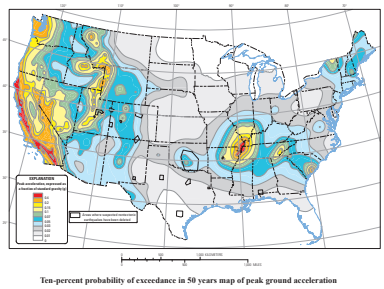

(b) 10%/50yr; PGA

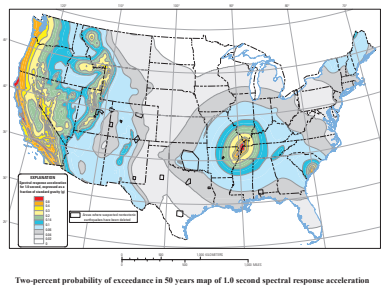

(c) 2%/50yr; $S_a(T = 1.0s)$

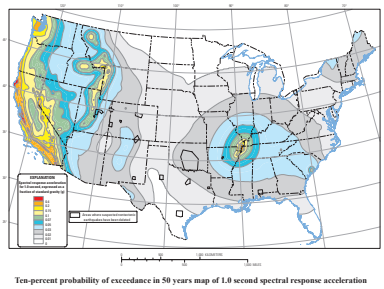

(d) 10%/50yr; $S_a(T = 1.0s)$

Fig. 23.9: Samples of US hazard maps

23.8 Seismic Hazard Deaggregation

Seismic hazard deaggregation plots are useful since they can provide a clear vision on contribution of the different parameters in the record selection process. Also they can be used for identification of the source controlling the hazard at the dam site. A deaggregation plot shows the combinations of magnitude and distance that contribute most to a hazard curve. It is useful used for selecting earthquake time histories for response history analysis. A deaggregation plot depends on intensity of interest and probability of exceedance. In practice, the deaggregation is obtained numerically over small increments of magnitude, Δm, and distance, Δr.

$$C(M,R) = \frac{N(m \leq M < m + \Delta m\,;\; r \leq R < r + \Delta r)}{N_{total}} \tag{23.20}$$

where $N(M,R)$ is recurrence rate of earthquakes having a magnitude and distance around m and r, and N_{total} is total recurrence rate at the site.

Figure 23.10 shows the seismic deaggregation plots for University of Colorado Boulder with different intensity measures and return periods on rock medium [846]. The modal distance, magnitude, and inter-event term can be found in each case.

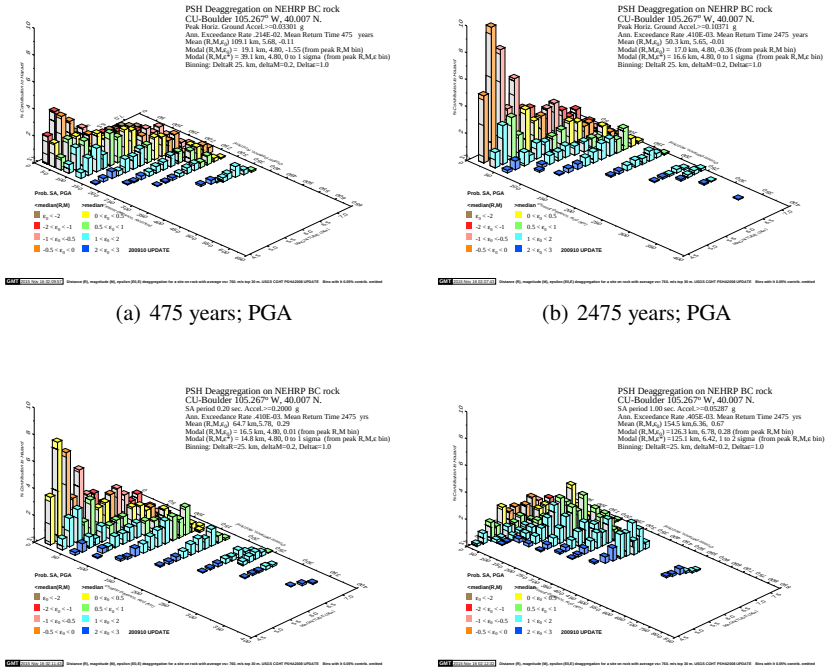

(a) 475 years; PGA (b) 2475 years; PGA

(c) 2475 years; $S_a(T = 0.2s)$ (d) 2475 years; $S_a(T = 1.0s)$

Fig. 23.10: Samples of seismic deaggregation plots for the University of Colorado Boulder

23.9 Target Response Spectra

One spectrum is required for each of the several seismic hazard intervals used for analysis which are selected from the site seismic hazard curve. Three types of common spectra are:

- Uniform Hazard Spectra (UHS)
- Conditional Spectra (CS)
- Conditional Mean Spectra (CMS)

UHS are computed from the seismic hazard curves. This is done by developing hazard curves for several vibration periods to define the response spectra. Then,

for a given exceedance probability or return period, the ordinates are taken from the hazard curves for each spectral acceleration, and an "equal hazard response spectrum" is generated. Thus, the response spectra curves are generated for specified return periods of interest, usually 10,000 and 50,000 years, but often at either lower, intermediate, or even higher return periods. Figure 23.11(a) shows the UHS for only the horizontal direction at the hypothetical dam site.

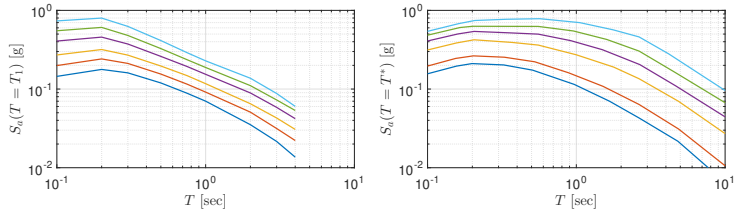

(a) UHS ($T_1 = 0.3$ s) (b) CMS ($T^* = 2.5$ s)

Fig. 23.11: Comparison of different response spectra

On the other hand, the CS is a response spectrum that specifies the probability distribution of different spectral accelerations over a period range conditioned on spectral acceleration at a particular (conditioning) period, T^* [542]. The conditional spectrum accounts for the correlations between spectral accelerations at various periods to calculate the expected spectrum and its variability [81]. Figure 23.11(b) presents sample CMS at different hazard levels for a structure with $T^* = 2.5$ s.
For frequent events, the UHS and CMS should have similar shapes. For infrequent events, the amplitude of a CMS will be smaller at some periods than the UHS as the conditional mean spectrum quantifies a less conservative and more realistic spectrum for a single earthquake. The CS differs from the CMS only in that it considers uncertainty in spectral values. The use of either CMS or CS will provide more accurate estimates of response for a given intensity of earthquake shaking than the UHS, but additional effort is required to generate these types of spectra.
The extended version of CMS, which considers other ground motion parameters than response spectra, is the generalized conditional intensity measure (GCIM) [149]. This method is mainly based on construction of the multivariate distribution of any set of ground motion IMs conditioned on the occurrence of a specific ground motion IM (usually obtained from PSHA).
The fundamental steps in order to compute a CMS, which is adopted from [542], can be summarized as follows:

- Determine the input parameters for earthquake including target spectral acceleration, $S_a(T^*)$, at the conditioning period, T^*, using PSHA and the associated mean causal earthquake magnitude, M, distance, R, rupture mechanism, and site condition, θ.

- Compute the logarithmic mean, $\mu_{\ln S_a}(M, R, \theta, T_i)$, and standard deviation, $\sigma_{\ln S_a}(M, \theta, T_i)$, of spectral acceleration at all periods, T_i, using the GMPE models.
- Compute epsilon, $\varepsilon(T_i)$, (the number of standard deviations by which $\ln S_a(T_i)$ differs from the mean spectral ordinate predicted by a given GMPE) for any $S_a(T_i)$ value:

$$\varepsilon(T_i) = \frac{\ln S_a(T_i) - \mu_{\ln S_a}(M, R, \theta, T_i)}{\sigma_{\ln S_a}(M, \theta, T_i)} \tag{23.21}$$

- Compute the conditional mean logarithmic spectral acceleration, $\mu_{\ln S_a(T_i)|\ln S_a(T^*)}$, using the correlation model [81] that specifies the correlation coefficient between pairs of epsilon values at two periods, $\rho\left(\varepsilon(T_i), \varepsilon(T^*)\right)$, as:

$$\begin{aligned}\mu_{\ln S_a(T_i)|\ln S_a(T^*)} &= \mu_{\ln S_a}(M, R, \theta, T_i) \\ &+ \rho\left(\varepsilon(T_i), \varepsilon(T^*)\right) \sigma_{\ln S_a}(M, \theta, T_i)\end{aligned} \tag{23.22}$$

- Compute conditional standard deviation, $\sigma_{\ln S_a(T_i)|\ln S_a(T^*)}$, as:

$$\sigma_{\ln S_a(T_i)|\ln S_a(T^*)} = \sigma_{\ln S_a}(M, \theta, T_i)\sqrt{1 - \rho^2\left(\varepsilon(T_i), \varepsilon(T^*)\right)} \tag{23.23}$$

- The combination of conditional standard deviation and conditional mean value specifies a complete distribution of logarithmic spectral acceleration values at all periods. The resulting spectrum distribution is termed the CS, to be distinguished from the CMS that does not consider the variability.

For intensity-based performance assessment (IBPA), any spectrum of the user's choice can be used. The spectral shape should be consistent with the site's geologic characteristics. For scenario-based performance assessment (SBPA), the target spectrum should be derived directly from appropriate attenuation relationships. For time-based performance assessment (TBPA), one spectrum is required for each of the several seismic hazard intervals, selected from the seismic hazard curve for the site [40].

23.10 Stochastic Ground Motion Simulation

Although the use of real ground motion records is a standard method in the seismic evaluation of the structures, it may suffer from having a limited number of recorded ground motions (which might cover a narrow and discrete range of seismic hazard) and may necessitate simulation of extra ground motion records to be used in the context of PBEE.

Most ground motion simulation techniques are capable of generating an acceleration time-series based on a particular seismic hazard scenario which makes them an excellent option for use in SBPA [731], [896]. In general, these techniques can be divided into two groups [895, 812, 732]:

- Physics-based models simulate the ground motion by explicitly modeling the fault rupture, wave propagation, and the near-surface site amplification. They

require precise information to provide good estimation of real ground motions. This approach is, in general, expensive to implement and not very accurate for high-frequency motions [695, 812].

- Stochastic models directly simulate the ground motion time-series and are empirically calibrated based on the existing dataset. This approach is, in general, computationally inexpensive. Stochastic models can be constructed using one of the following methods [731]: 1) passing a white noise through a filter [789], 2) passing a train of Poisson pulses through a linear filter [217], 3) autoregressive moving average model [426], and 4) evolutionary spectral models [710]. To obtain a good estimation of real ground motions, both the temporal non-stationarity (the amplitude change with time) and the spectral non-stationarity (the frequency change with time) should be accounted for in the model.

In this section, two recently developed and widely used stochastic ground motion models are explained.

23.10.1 Rezaeian and Der Kiureghian (R-D) Modal

Rezaeian and Der Kiureghian developed a fully non-stationary stochastic ground motion model based on a modulated filtered white-noise process with time-varying parameters [730], [731]. In this model the temporal and spectral non-stationary characteristics are completely decoupled which facilitates easy identification of the model parameters. The model has a small number of parameters with physical interpretations. The discretized acceleration time-series of the ground motion can be expressed as:

$$\hat{x}\left(t|\boldsymbol{\theta},\mathbf{W}\right)=\beta\left(t,\boldsymbol{\theta}\right)\sum_{i=1}^{k}\frac{h\left[t-t_i,\boldsymbol{\theta}(t_i)\right]}{\sqrt{\sum_{j=1}^{k}h\left[t-t_j,\boldsymbol{\theta}(t_j)\right]^2}}w\left(i\Delta t\right), \qquad k\Delta t<t<(k+1)\Delta t \tag{23.24}$$

where $\mathbf{W}=\left[w\left(i\Delta t\right);i=1,2,...,N_T\right]$ is a Gaussian white noise sequence, Δt is the chosen discretization interval, $\boldsymbol{\theta}$ is an n_θ-dimensional model parameter vector (i.e. $\boldsymbol{\theta}=[\theta_1,\theta_2,...,\theta_{n_\theta}]$), $\beta\left(t,\boldsymbol{\theta}\right)$ is the time-modulating function, and $h\left[t-\tau,\boldsymbol{\theta}(\tau)\right]$ is a unit impulse function due to pseudo-acceleration response of an SDOF linear oscillator with time-dependent natural frequency $\omega_f(\tau)$ and damping ratio $\zeta_f(\tau)$, in which τ denotes the time of the pulse.

$$h\left[t-\tau,\boldsymbol{\theta}(t)\right]=\begin{cases}\dfrac{\omega_f(\tau)}{\sqrt{1-\zeta_f^2(\tau)}}\exp\left[-\omega_f(\tau)\zeta_f(\tau)(t-\tau)\right] & \\ \qquad\sin\left[\omega_f(\tau)\sqrt{1-\zeta_f^2(\tau)}(t-\tau)\right] & \tau\le t \\ 0 & \text{otherwise}\end{cases} \tag{23.25}$$

The time-dependent frequency function takes a linear form, while the damping function is assumed to be constant:

$$\omega_f(\tau) = \omega_{mid} + \omega' (\tau - t_{mid}) \; ; \quad \zeta_f(\tau) = \zeta_f \tag{23.26}$$

where ω_{mid} refers to central frequency, ω' is the frequency variation, and t_{mid} is the mid-time of the strong motion duration (the time in which Arias intensity achieves 45% of its final value).
For the modulating function, a gamma-type function is selected which is controlled by three parameters:

$$\beta(t, I_A, \alpha_2, \alpha_3) = \underbrace{\sqrt{I_A \frac{(2\alpha_3)^{2\alpha_2-1}}{\Gamma(2\alpha_2-1)}}}_{\text{intensity}} \underbrace{t^{\alpha_2-1}}_{\text{shape}} \underbrace{e^{-\alpha_3 t}}_{\text{duration}} \tag{23.27}$$

where $\Gamma(.)$ is the gamma function, I_A is the scaled Arias intensity, and α_2 and α_3 are the shape and duration controlling parameters and can be connected to the physics of the problem through the effective duration, $D_{5-95} = I_A^{95\%} - I_A^{5\%}$, and t_{mid}, respectively. Finally, the simulated function is high-pass filtered to assure zero residual velocity.
The ground motion model parameter vector can be summarized as
$\boldsymbol{\theta} = \{I_A, D_{5-95}, t_{mid}, \omega_{mid}, \omega', \zeta_f\}$. Predictive relationships have been developed for each model parameter by fitting the stochastic model to a subset of the next generation attenuation (NGA) strong motion database. These predictive models describe $\boldsymbol{\theta}$ in terms of the following earthquake and site characteristics: 1) moment magnitude (M_w), 2) closest distance to rupture (R_{rup}) in [km], 3) shear wave velocity of the top 30 m of soil (V_{S30}) in [m/s], and 4) fault mechanism (F_{mech}), either srtike-slip or reverse. The empirical equations take the following generic form:

$$\Phi^{-1}[F_\theta(\theta)] = \mu(M_w, R_{rup}, V_{S30}, F_{mech}, \mathbf{c}) + \eta + \sigma \tag{23.28}$$

where θ is a model parameter, $\Phi[.]$ is the standard Gaussian cumulative distribution function (CDF), and F_θ is the CDF of θ (which is empirically determined). Subsequently, $\Phi^{-1}[F_\theta(\theta)]$ transforms a model parameter from the physical space to the standard normal space. μ is the predicted mean as a function of the earthquake and site characteristics and $\mathbf{c}$ represents the vector of regression coefficients. Moreover, η and σ are normally distributed zero-mean random variables and refer to the inter-event and the intra-event errors, respectively. The regression coefficients, the variances of the error terms, and the correlations between the model parameters can be found in [731].

23.10.2 Yamamoto and Baker (Y-B) Model

Yamamoto and Baker employed the wavelet packet transform (WPT) (which is the extended version of the discrete wavelet transform, DWT) in order to quantify the time and frequency characteristics of time-series for generating stochastic ground motions [895], [896]. WPT increases the flexibility in controlling the resolution in

time and frequency domains. Moreover, the basis functions are orthogonal, which enables the easy reconstruction of time-series.
The forward and inverse WPT are defined as:

$$c_{j,k}^{i} = \int_{-\infty}^{+\infty} x(t)\psi_{j,k}^{i}(t)dt \; ; \quad x(t) = \sum_{i=1}^{2^{j}} \sum_{k=1}^{2^{N-j}} c_{j,k}^{i}\psi_{j,k}^{i}(t) \tag{23.29}$$

where $x(t)$ is the time-series, 2^N is the number of data points in the time-series, $c_{j,k}^{i}$ denotes the ith set of wavelet packets at the jth scale parameter and k is the translation parameter, and $\psi_{j,k}^{i}$ is WPT function.
WPT results in time-series with few large-amplitude wavelet packet coefficients and many small-amplitude ones. Yamamoto and Baker used this advantage and defined two groups of major (which contains about 70% of the total energy in the ground motion) and minor (which contains the remaining 30% of the energy) wavelet packet coefficients. As a result, the total wavelet packet coefficients are a combination of these two groups:

$$\left|c_{j,k}^{i}\right|^{2} = \left|c_{j,k,maj}^{i}\right|^{2} + \left|c_{j,k,min}^{i}\right|^{2} \tag{23.30}$$

in which $c_{j,k,maj}^{i}$ and $c_{j,k,min}^{i}$ are the major and minor wavelet packet coefficients. This model requires 13 parameters to fully quantify the time and frequency characteristics of the acceleration time-series. These parameters are categorized here, however, for the detailed formulation the readers are referred to [896].

- For the major group: 1) temporal centroid $E(t)_{maj}$, 2) temporal variance $S^2(t)_{maj}$, 3) spectral centroid $E(f)_{maj}$, 4) spectral variance $S^2(f)_{maj}$, 5) correlation between time and frequency of coefficients $\rho(t,f)_{maj}$, 6) mean of squared amplitudes the wavelet packet coefficients $E(a)_{maj}$,
- For the minor group: 7) temporal centroid $E(t)_{min}$, 8) temporal variance $S^2(t)_{min}$, 9) spectral centroid $E(f)_{min}$, 10) spectral variance $S^2(f)_{min}$, 11) correlation between time and frequency coefficients $\rho(t,f)_{min}$,
- 12) randomness of amplitude of wavelet packets $S(\xi)$, and 13) cumulative squared acceleration E_{acc}.

The wavelet packets in the major group are strongly random in comparison with those in the minor group. Thus, the squared amplitudes and time-frequency locations of wavelet packets are modeled separately

$$\begin{aligned} a_{maj} &\sim \text{Exponential}\left[E\left(\left|c_{j,k,maj}^{i}\right|^{2}\right)\right] \\ [t_{k,maj}, f_{i,maj}] &\sim \text{Lognormal}\left[M_{maj}, \Sigma_{maj}\right] \end{aligned} \tag{23.31}$$

where a_{maj} is the squared amplitudes of the wavelet packet coefficient in the major group, $t_{k,maj}$ and $f_{i,maj}$ are the center of the time and frequency location of the major wavelet coefficients, and M_{maj} and Σ_{maj} are defined as:

$$M_{maj} = \left[E\left(\ln t_{k,maj}\right)\ E\left(\ln f_{i,maj}\right)\right]$$
$$\Sigma_{maj} = \begin{bmatrix} S^2\left(\ln t_{k,maj}\right) & Cov\left(\ln t_{k,maj}, \ln f_{i,maj}\right) \\ Cov\left(\ln t_{k,maj}, \ln f_{i,maj}\right) & S^2\left(\ln f_{i,maj}\right) \end{bmatrix} \tag{23.32}$$

On the other hand, the wavelet packets in the minor group can be estimated by the bivariate lognormal functions of the time, frequency, and residuals (which requires only five parameters to control):

$$\left|c^i_{j,k,min}\right|^2 = \frac{1}{2\pi S\left(\ln t_{k,min}\right) S\left(\ln f_{i,min}\right)\sqrt{1-\rho^2\left(\ln t_{k,min}, \ln f_{i,min}\right)}}$$
$$\times \frac{1}{\ln t_{k,min}.\ln f_{i,min}} \exp\left[-\frac{W_1^2 - 2\rho\left(\ln t_{k,min}, \ln f_{i,min}\right) W_1 W_2 + W_2^2}{2\left(1-\rho^2\left(\ln t_{k,min}, \ln f_{i,min}\right)\right)}\right] \times \xi_{k,i} \tag{23.33}$$

where $t_{k,min}$ and $f_{i,min}$ are the center of the time and frequency location of the minor wavelet coefficients, ρ is the correlation coefficient, $\xi_{k,i}$ is a lognormal random variable used for calibration, and two intermediate variables are defined as $W_1 = \frac{\ln t_{k,min} - E(\ln t_{k,min})}{S(\ln t_{k,min})}$ and $W_2 = \frac{\ln f_{i,min} - E(\ln f_{i,min})}{S(\ln f_{i,min})}$.
Finally, in order to generate a ground motion for a particular earthquake scenario, the 13 parameters are connected to those scenario parameters using the two-stage regression analysis. A large set of recorded ground motions from the NGA database were used to estimate the parameters using maximum likelihood estimation and the following functional form:

$$Y = \alpha + \beta_1 M_w + \beta_2 \ln M_w + \beta_3 \exp M_w + \beta_4\left(R_{hyp} - R_{rup}\right)$$
$$+\beta_5 \ln\sqrt{R_{rup}^2 + h^2} + \beta_6 \ln V_{S30} + \eta + \sigma \tag{23.34}$$

where Y is the natural logarithm of a model parameter, and σ and η are intra- and inter-event residuals, respectively. The parameter h is assigned to avoid predicting extremely large values of Y for small values of R_{hyp} (hypocenteral distance), and the parameters α and β_i are regression coefficients that can be found in [895] and [896].

23.11 Endurance Time Excitation Functions

Practical use of the endurance time (ET) method requires appropriate endurance time excitation functions (ETEFs) that lead to consistent analysis results. This section highlights different ETEF generations, as well as their producing objective functions[2]. In the endurance time method, ETEFs are used as dynamic load input functions. In the ET method, all intensity levels are covered in a single excitation function. In other words, each time in an endurance time excitation corresponds to a particular intensity level. ETEFs are normally generated so that they are compatible with desired design spectra or sets of ground motions and intensities which increase with time. Compatibility with ground motions and intensification are two major features of ETEFs that must be considered in simulating these artificial functions. The

[2] This section is written in collaboration with Prof. H.E. Estekanchi and Dr. M.R. Mashayekhi.

intensification property of ETEFs is obtained by applying an amplitude increase profile. The amplitude increase profile can take various forms. In initial endurance time excitations, a linear profile (in which maximum acceleration is directly proportional to time) was adopted. Exponential forms are also considered to simulate cumulative absolute velocity consistent endurance time excitations [577].
Compatibility with ground motions is another important feature of endurance time excitation. Ground motions have three major characteristics: intensity, frequency content, and duration. In order to simulate an efficient endurance time excitation, these three features have to be considered. Since frequency content and amplitude of motions are adequately reflected in response spectra, considering response spectra in the simulation process implies that amplitude and frequency content are suitably considered.
The above-mentioned requirements are known as simulating constraints. The number of simulating constraints are usually much more than the number of variables, regardless of which variable definition method is used, Mashayekhi, Estekanchi, and Vafai [574] and Mashayekhi, Estekanchi, and Vafai [575]. Since analytical methods do not provide a practical procedure to simulate ETEFs, the optimization approaches are then employed.
In this section, the generation of ETEFs are explained. Existing acceleration load functions differ in terms of the target spectrum, periods range, objective functions, time step, duration length, and optimization algorithm. These excitations are available online through the Endurance Time Method website. In the progress path of ETEF production, five generations of endurance time excitations can be distinguished.

23.11.1 First Generation of ETEFs

First generation excitations were only generated to introduce the basic concept of ET method. ETEFs of this generation are not suitable for practical use. In the simulation of first-generation excitations, the concept of non-stationary random patterns in amplitude and frequency content were used. In this method, excitation functions are expressed by summing a finite number of harmonic functions as:

$$a(t) = \sum_{i=1}^{N} A_i \sin(\omega_i t + \phi_i) \tag{23.35}$$

where N is the number of harmonic functions, ω_i and ϕ_i are the angular frequency and phase angel of ith sine function, and A_i is the frequency amplitude.
A random excitation with Gaussian distribution with zero mean and standard deviation of one was considered. The number of acceleration data points was chosen to be 2048, with the maximum acceleration of 1.0 g. An appropriate modulating function was adopted. In order to remove undesirable frequency ranges, the excitations were filtered by inverse Fourier transform technique. The objective was to simulate an excitation that matches a particular spectrum. The target spectrum was a typical seismic code design spectrum. The signal was modified to match the spectral

acceleration function by adjusting its Fourier spectral amplitudes. This procedure was repeated until the acceptable correspondence was achieved. The resulting stationary accelerogram was then modified by applying a linear profile function that made it intensifying, with respect to peak accelerations, at different time intervals. These accelerograms served well for the purpose of demonstrating the concept of endurance time analysis. A sample acceleration time history of the first generation is shown in Figure 23.12(a).

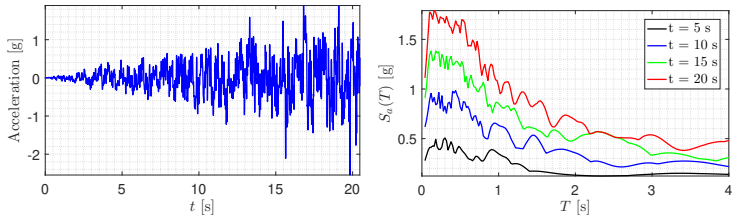

(a) Acceleration time history; ETA20ac01 (1st generation)

(b) Response spectra; ETA20a01 (2nd generation)

Fig. 23.12: Sample ETEF

23.11.2 Second Generation of ETEFs

In the second generation, acceleration and displacement spectra are considered in the simulation process. Target spectrum can be the average spectra of a set of ground motions, or a code-conforming spectrum. In the second generation, optimization techniques were employed for the first time to simulate new ETEFs. In the optimization context, equations are expressed in terms of objective functions. The objective function for this series is shown in Equation 23.37. Acceleration and displacement spectra are considered in the objective function.

$$F(a_g) = \sum_{T_j=0}^{T_j=T_{max}} \sum_{t_i=0}^{t_i=t_{max}} \{[S_a(T_j,t_i) - S_{aC}(T_j,t_i)]^2 + \alpha\,[S_u(T_j,t_i) - S_{uC}(T_j,t_i)]^2\} \tag{23.36}$$

where a_g is the endurance time excitation being sought, and α is the relative weight parameter that can adjust the effective penalty attributed to displacement deviation as compared to acceleration deviations from target values. High values of α make the target function more sensitive to displacement response differences and low value of α makes the target function more sensitive to acceleration spectra differences. $S_{aC}(T,t)$ is the target acceleration response spectra at time t, and period T which can be codified design acceleration spectrum or average spectrum of a suite of ground motions. $S_{uC}(T,t)$ is the target displacement response spectra at time t, and period T. $S_u(T,\tau)$ and $S_a(T,\tau)$ are displacement and acceleration response spectra of endurance time excitation at period T, and time τ. t_{target} is target time that is the

time in which endurance time excitations produce target spectrum. The choice of an appropriate target time should also be given consideration. In the general nonlinear case, if the target time is too low, the structure may not have time to go through a reasonable number of nonlinear cycles. On the other hand, if the target time is too high, the number of cycles will become unrealistically large.
Nonlinear response matching is not included in generating second-generation endurance time excitations. However, by including long periods in the simulation of second-generation excitations, they can be used in nonlinear dynamic analysis with reasonable accuracy. Acceleration spectra of ETA20a01, which is the first series generated in the second generation, is shown in Figure 23.12(b). It can be seen that acceleration spectra of this excitation is linearly increased.

23.11.3 Third Generation of ETEFs

In the simulation of third generation, compatibility of nonlinear responses was also considered. Similar to the formulation of simulating second generation endurance time excitations, third generation is simulated by defining strength factor R is formulated as follows:

$$S_u(T,t,R) = \max\left(|u(\tau)|\right); \quad \tau \in [0,t] \tag{23.37}$$

$$S_{uT}(T,t,R) = \frac{t}{t_{target}} \times S_{uT}(T,R) \times \frac{T^2}{4\pi^2}; \quad \tau \in [0,t] \tag{23.38}$$

$$F(a_g) = \sum_{T_k=0}^{T_k=T_{max}} \sum_{R_j=0}^{R_j=R_{max}} \sum_{t_i=0}^{t_i=t_{max}} \left[S_u(T_k,R_j,t_i) - S_{uT}(T_k,R_j,t_i)\right]^2 \tag{23.39}$$

In contrast to the second generation where the computing objective function at each period required a single dynamic analysis for all times, the computing objective function of third generation at each period requires a separate dynamic analysis for each time. This fact complicates simulating third-generation endurance time excitations.

23.11.4 Fourth Generation of ETEFs

In the fourth generation, duration related parameters are also included in simulation procedure. Although acceleration and displacement spectra are good representatives of intensity and frequency contents of ground motions, in order to properly quantify the ground motions, it is necessary to consider not only the intensity and frequency content, but also the duration characteristics. Even though a variety of definitions have been proposed for duration in the literature of earthquake engineering [665, 866, 136, 135], the cumulative absolute velocity (CAV) has been included in simulation of the fourth-generation ETEFs. Campbell and Bozorgnia [163] suggest that CAV might be used to rapidly assess potential damage to a general class of conventional

structures. CAV is mathematically represented as $CAV = \int_0^{t_{max}} |a(t)|\, dt$, where $a(t)$ is acceleration time history, and t_{max} is duration.
Objective functions of Equation 23.40 were used to simulate the "ETA40lc" series. The first three terms compute the residuals in a relative way, and the other three compute the residuals in an absolute way. Mashayekhi et al. [577] showed that the combination of absolute and relative terms yields to a more efficient endurance time excitation. These objective functions integrate residuals over entire time and period ranges. It should be noted that acceleration spectra, linear displacement spectra, and CAV are considered in these objective functions.

$$F_{CAV-M}(a_g) = \sum_{T_j=0}^{T_j=T_{max}} \sum_{t_i=0}^{t_i=t_{max}} \left\{ \begin{array}{c} \left[\frac{S_a(T_j,t_i)-S_{aC}(T_j,t_i)}{S_{aC}(T_j,t_i)}\right]^2 \\ + \left[\frac{S_u(T_j,t_i)-S_{uC}(T_j,t_i)}{S_{uC}(T_j,t_i)}\right]^2 \\ + \left[\frac{CAV(t_i)-CAV_C(t_i)}{CAV_C(t_i)}\right]^2 \\ + \left[S_a(T_j,t_i) - S_{aC}(T_j,t_i)\right]^2 \\ + \alpha_{S_u} \left[S_u(T_j,t_i) - S_{uC}(T_j,t_i)\right]^2 \\ \alpha_{CAV} \left[CAV(t_i) - CAV_C(t_i)\right]^2 \end{array} \right\} \quad (23.40)$$

where a_g is the acceleration time history.
These objective functions take a_g as the input; α_{S_u} and α_{CAV} are weight factors which control the contribution of residuals associated with displacement spectra and CAV, respectively.
The intensifying profile which controls the shape of increasing acceleration spectra in time does not need to be linear. An exponential profile was used for this series. CAV of ETA40lc01 is compared with the target in Figure 23.13 and a considerable match between them is observed.

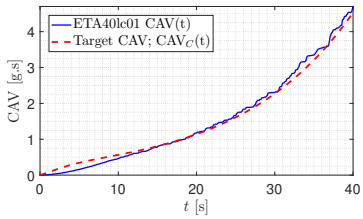

Fig. 23.13: CAV of ETA40lc01 versus target

23.11.5 Fifth Generation of ETEFs

In fifth generation, absorbed hysteretic energy is also included in the generating process. It should be mentioned that absorbed hysteretic energy demand is used as an indicator of the cumulative damage related parameter. A linear increasing function

for acceleration spectra is adopted and a corresponding increasing function of nonlinear displacement spectra and hysteretic energy are mathematically computed. A detailed procedure for computing increasing functions of nonlinear displacement and hysteretic energy demand can be found in Mashayekhi et al. [576]. Equation 23.42 is the objective function which calculates squared discrepancies between dynamic characteristics of endurance time excitations and target ground motions:

$$F_{ETEF}(a_g) = \sum_{T_j=0}^{T_j=T_{max}} \sum_{t_i=0}^{t_i=t_{max}} \left[S_a(T_j,t_i) - S_{aC}(T_j,t_i)\right]^2 \tag{23.41}$$

$$+ \sum_{\mu_k=1}^{\mu_k=\mu_{max}} \sum_{T_j=0}^{T_j=T_{max}} \sum_{t_i=0}^{t_i=t_{max}} \left\{ \begin{array}{c} \alpha_{u_m}\left[u_m(\mu_k,T_j,t_i) - u_{mC}(\mu_k,T_j,t_i)\right] \\ +\alpha_{E_H}\left[E_H(\mu_k,T_j,t_i) - E_{HC}(\mu_k,T_j,t_i)\right] \end{array} \right\}$$

where $a_g(t)$ is acceleration time history, $S_a(t,T)$, $u_m(t,T,\mu)$ and $E_H(t,T,\mu)$ are dynamic characteristics of endurance time excitations, and $S_{aC}(t,T)$, $u_{mC}(t,T,\mu)$ and $E_{HC}(t,T,\mu)$ are dynamic characteristics of ground motions. E_H is hysteretic energy, and u_m is nonlinear response displacement. Figure 23.14 compares the hysteretic energy of ETA20kd01 with the target at four different periods.

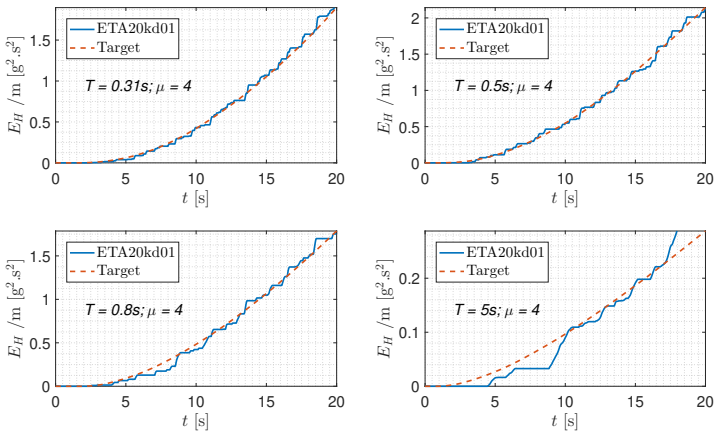

Fig. 23.14: Hysteretic energy of ETA20kd01 versus target

Chapter 24
Capacity Functions

Abstract
Structural analyses are an important part of safety assessment. In this chapter, the concept of a "capacity function" is explained in the context of existing structural analysis techniques. Loading due to seismic, hydrologic, and aging hazard are studied from a probabilistic point of view. Single, multiple, and combined capacity functions are derived. Moreover, the summarized capacity functions and their confidence intervals are presented.

24.1 Fundamentals

The safety of infrastructure (e.g. concrete dams and nuclear containment vessels) is affected by many events. A comprehensive safety evaluation methodology should take into account all potential events. Ultimate decision-making can be based on either the critical event or on the result of all events with their respective contributions. A safety assessment can be performed within the framework of performance based engineering (PBE); this process begins with a project's initial concepts and extends throughout the life cycle of the structure [120].
The PBE of buildings and infrastructure has been indirectly undertaken since the introduction of strength in concrete structural design in the 1960's [882]. It has included force-based analysis and the design verification of components using:

$$\sum \alpha_i \, L_i \leq \phi \, C \tag{24.1}$$

where α_i is the load factor, L_i the load effects (dead load, live load, etc.), ϕ a capacity reduction factor, and C the component capacity.
In concrete dams, "failure" refers to the uncontrolled release of the reservoir water. This may or may not always be the case, and many other definitions are acceptable for failure depending on the project's purpose [308]. The initiating events leading to dam failure include [388]: 1) hydrological events, such as flooding and increased flow through the spillway; 2) static events, such as reservoir water load, ice load, and equipment malfunction; 3) material deterioration, such as erosion and alkali-aggregate reaction (AAR) in the concrete; 4) increased seepage, clogging of drains, degradation of the grout curtain; 5) seismic events, such as earthquake load; and

6) other initiators, such as human operating error, fire, landslides into the reservoir, vehicular impact, underwater explosion, sabotage, and vandalism.
Considering just the most probable events, i.e. seismic, hydrological, and material degradation, the structural capacity should be evaluated in the context of PBE. This concept has already been developed for various events, e.g. performance based earthquake engineering (PBEE) [700], performancebased fire engineering (PBFE) [871], performance based hurricane engineering (PBHE) [84], performance based blast engineering (PBBE) [882], and performance based wind engineering (PBWE) [203]. One commonality among all these events is to evaluate the capacity of the structure subjected to the specific event using varying amplitudes. Such a step yields the system response at different structural levels (i.e. linear, nonlinear, collapse).
Figure 24.1 shows the role of the capacity function within the global framework for performance-based assessment. This chapter is heavily written based on Hariri-Ardebili and Saouma [387].

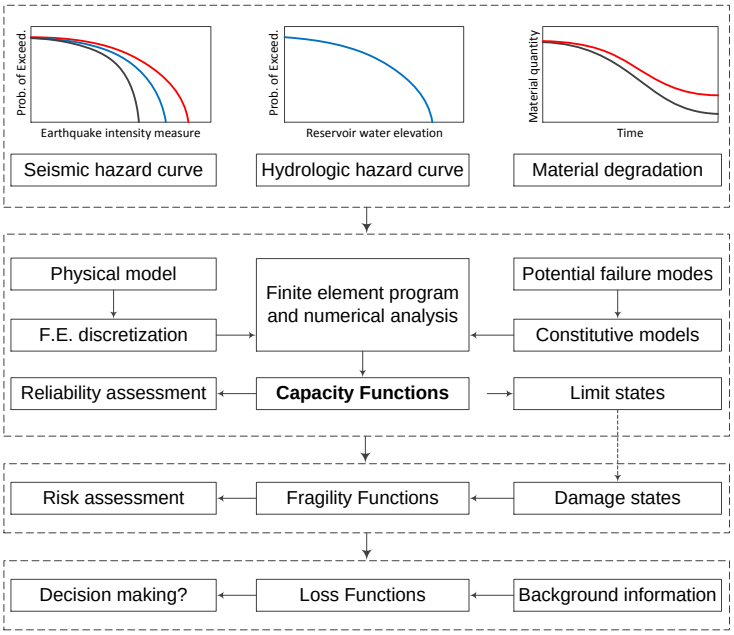

Fig. 24.1: Global framework for PBE and the role of capacity function

24.2 Generalized Capacity Functions

24.2.1 Basic Definitions

Let's begin by distinguishing the various terms related to the "capacity" of the structural system.

Capacity Curve: In its original definition, this notion refers to a nonlinear force-displacement curve [318]; it is determined by statically loading the structure in order to calculate the roof displacement *vs.* base shear. This curve also refers to the *pushover curve* [319]. In the laboratory, the load-displacement curve may be recorded by setting up either load control or displacement control protocols, depending on the availability of facilities. However, using the displacement control test, the post-failure can be captured. The conventional capacity curve may also be plotted in terms of dissipated energy, referred to as the *energy-based capacity curve* [227].

Capacity Diagram: This notion refers to the pseudo-acceleration *vs.* deformation spectrum ordinate [196]; it is computed by dividing both the base shear by the effective modal mass at the fundamental vibration mode and the peak displacement by the mass participation factor. This diagram is also called the *capacity spectrum*.

Capacity Function: This notion is defined as the relationship between an external (or internal) parameter affecting the capacity of the structure, also referred to as a "stressor" (S) and "response" (R) of the system at the macro level. As opposed to the conventional capacity curve, the capacity function is a more general concept and can be generated by any of the initiators explained in the introduction; moreover, it is not limited to just seismic action.

Stressor: can be 1) an incrementally-increasing monotonic, cyclic, or time-dependent load (or displacement, acceleration, pressure); 2) an incrementally-decreasing resistance parameter or degradation in strength properties; or 3) a discrete increasing/decreasing critical parameter in a system leading to failure. In PBEE, S is typically called an intensity measurement (IM) parameter [700]. In the present paper however, S is more generally defined and refers to any quantity whose variation (continuous or discrete) may lead to progressive system failure and its ultimate collapse.

Response: is representative of the system behavior under the varying stressor. It is depicted in either an absolute or relative sense. R may be: 1) a single damage variable (DV), such as drift or energy dissipation; 2) a combination of several DVs in terms of damage index (DI); or 3) any safety monitoring index [870]. In the field of earthquake engineering, R is typically called an engineering demand parameter (EDP) [850].

24.2.2 Mathematical model

Figure 24.2(a) shows a sample capacity function normalized in both axes for the sake of simplicity. Three parts can be detected in this curve: 1) linear, 2) nonlinear, and 3) asymptotic to the horizon. The linear part refers to the elastic behavior of the structure; the nonlinear part refers to an elastic-to-plastic transient (or any other nonlinear model); and the horizontal part represents the system failure/collapse. In

addition, Figure 24.2(b) shows the derivation of the vertical axis with respect to the horizontal axis $\frac{\partial \mathrm{S}}{\partial \mathrm{R}}$. In the first part, the slope remains constant, while in the last part it equals zero. In the transient part, the slope decreases either regularly or in an irregular pattern. Three important assumptions/key points are inherent in the ideal capacity functions:

1. Some capacity estimation methods are capable of capturing the post-failure behavior, as will be discussed in Section 24.3.5. This implies the existence of another part (i.e. a fourth part) in the capacity function, which displays a decreasing nature (linear or nonlinear pattern). However, in the present study, we have only considered the concrete dam behavior up to failure.
2. Depending on the progressive failure methodology (see Section 24.3) used to derive the capacity function, only one, two or all three parts may be involved. From a mathematical standpoint, the absence of each part is modeled by considering a very small variation for the given part ($\mathrm{R}_i \longrightarrow 0$).
3. The capacity function shown in Figure 24.2(a) and its subsequent mathematical representation in this section have been idealized (and smoothed). In reality, a single capacity curve has no uniform trend (especially in the nonlinear phase) mainly due to specific characteristics of the model and analysis. It is common practice however to quantify the epistemic and aleatory uncertainties in using the mean or median curve, which is smoother [852].

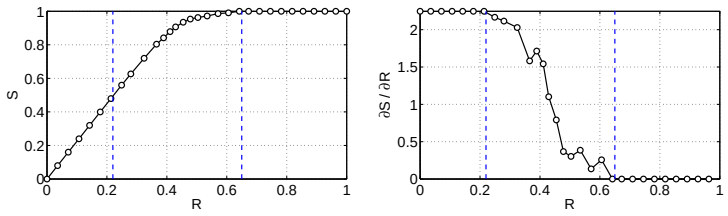

(a) Capacity function (b) Derivative of the capacity function

Fig. 24.2: A sample idealized capacity function (normalized form)

The capacity function can be expressed through analytical models. The analytical solution may have the following general form in its simplest expression:

$$\begin{cases} \mathrm{S}_1 = a.\mathrm{R} + b & \text{for} \quad 0 \leq \mathrm{R} < \mathrm{R}_e \\ \mathrm{S}_2 = f_N(\mathrm{R}) & \text{for} \quad \mathrm{R}_e \leq \mathrm{R} < \mathrm{R}_u \\ \mathrm{S}_3 = c & \text{for} \quad \mathrm{R} \geq \mathrm{R}_u \end{cases} \tag{24.2}$$

where a, b and c are constants, f_N is a nonlinear function representing the transition part, R_e and R_u are the limits for the elastic and ultimate responses. The following boundary conditions should also be satisfied when the three parts are connected to form a unified function:

$$\begin{cases} f_N(\mathrm{R}_e) - a.\mathrm{R}_e - b = 0 & \text{for} \quad \mathrm{R} = \mathrm{R}_e \\ f_N(\mathrm{R}_u) - c = 0 & \text{for} \quad \mathrm{R} = \mathrm{R}_u \\ \frac{\partial}{\partial \mathrm{S}} f_N(\mathrm{R}_e) - a = 0 & \text{for} \quad \mathrm{R} = \mathrm{R}_e \\ \frac{\partial}{\partial \mathrm{S}} f_N(\mathrm{R}_u) = 0 & \text{for} \quad \mathrm{R} = \mathrm{R}_u \end{cases} \tag{24.3}$$

It is possible to find a closed-form solution to the nonlinear function, f_N, by curve-fitting to data obtained from numerical analyses or experimental tests. Figure 24.3(a) shows an attempt to fit a three-part function to the original data points. The nonlinear least-squares method is used for curve-fitting [580]. The residuals of this fitting step are also shown in Figure 24.3(b). As can be remarked, the residuals are around 1% in this case. Moreover, all residuals stem from the second part of the curve (i.e. the nonlinear transient part). For this specific example, the following function has been selected:

$$f_N(\mathrm{R}) = \alpha_1 + \alpha_2 . \frac{1 - e^{\alpha_3 . \mathrm{R} + \alpha_4}}{1 + e^{\alpha_5 . \mathrm{R} + \alpha_6}}, \qquad \mathrm{R}_e < \mathrm{R} < \mathrm{R}_u \tag{24.4}$$

where α_i (i=1, 2, ..., 6) are the model constants obtained from nonlinear least-squares curve-fitting.

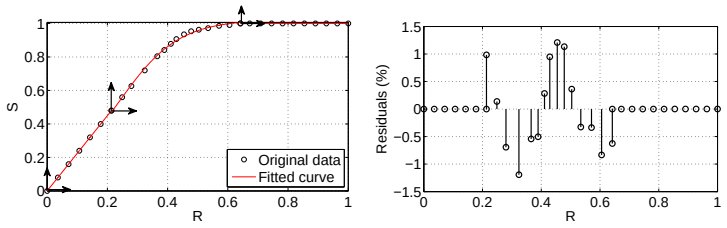

(a) Curve fitting (b) Residual assessment

Fig. 24.3: Fitting an analytical capacity function

Figure 24.4 displays some of the likely forms of Equation 24.4, all of which are increasing. The first two exhibit downward and upward concavity, respectively; while the third one has an inflection point. It should be noted that f_N is not limited to a specific form and can be represented in other forms as well. Recently, Pujades et al. [715] showed that the nonlinear part of a conventional capacity curve can be simulated by either cumulative lognormal or Beta functions.

As discussed above, the capacity functions are used to determine the capacity of structures from linear phase to nonlinear phase and ultimately to failure. Knowing the composition and general form of the capacity functions, it now becomes important to discuss the different failure analysis methodologies capable of producing the capacity functions.

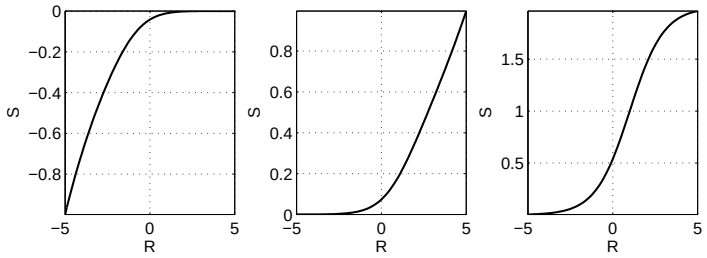

Fig. 24.4: Various forms of the nonlinear function f_N based on Eq. 24.4

24.3 Single-Hazard Capacity Functions

In general, static mechanics-based, hydraulic-based, quasi-static, pseudo-dynamic, and dynamic methods can all be used for capacity estimation purposes. The selection of an appropriate method depends on both the application and desired level of accuracy. The failure analysis and capacity function derivation methods will be summarized in this section.

24.3.1 Strength Reserve Factor (SRF)

This method is usually employed to study the ultimate bearing resistance (capacity) of the dam and its foundation. It is capable of emphasizing the uncertainty and possible weakening effect of material strength, thus making it possible to study the strength reserve degree of a structure [874].
Let κ_{SRF} be the strength reserve factor ($\kappa_{SRF} > 1.0$), and M_O the original material property of the dam with the capacity to deteriorate (tensile strength of concrete, modulus of elasticity, cohesion, etc.). Strength reduction can then be calculated as M_O/κ_{SRF}. In an iterative procedure, the new properties are replaced by the previous ones. It is worth noting that the loading condition (static loads) is kept unchanged, and the system is analyzed under the new conditions. A gradually increasing κ_{SRF} leads to progressive failure from the local to global scale and finally system failure. Consequently, R can be recorded for each of the analyses up to failure. The κ_{SRF} *vs.* R plot can be derived, yielding the actual capacity function. Figure 24.5(a) shows this procedure schematically.

24.3.2 Time-dependent Strength Degradation (TSD)

This method is usually applied to uncertainty in time-dependent problems. The underlying phenomenon tends to be observed under special environmental conditions. Examples are: alkali-aggregate reaction (AAR), alkali-silica reaction (ASR) [751], and creep [111]. AAR, creep, and shrinkage are typically related to one another. An external display (expansion) of AAR may be hidden by creep and shrinkage (contraction). Figure 24.6 shows strain variation in a dam, in assuming that the elastic strain

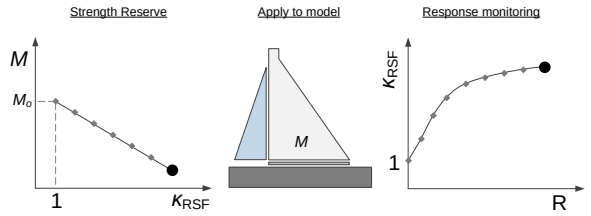

(a) Strength reserve factor

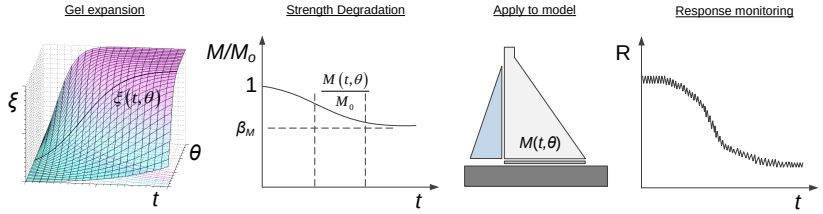

(b) Time-dependent strength degradation; AAR

Fig. 24.5: Capacity estimation using mechanics-based methods

is ε_{el} = 0.0003, creep strain is ε_{crp} = 0.001 and the AAR strain is $\varepsilon^{\infty}_{AAR}$ = 0.005. It is apparent that the external appearance of AAR has been substantially delayed by shrinkage/creep; great care should thus be exercised in discerning shrinkage/creep contraction strains from AAR expansion strains.

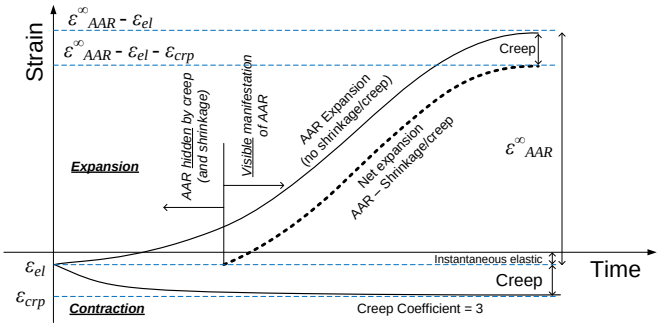

Fig. 24.6: AAR and creep interaction [772]

AAR is a chemical reaction that leads to expansion of the gel and a reduction in material strength and stiffness, thus generating microcracks and, consequently, reducing the bearing capacity of the dam concrete [750].
TSD-AAR is used to assess the capacity of concrete dams affected by AAR during their life cycle and defines the residual strength relative to existing loads. This AAR process results in time-dependent material deterioration:

$$\frac{M(t,\theta)}{M_0} = 1 - (1-\beta_M)\frac{1 - e^{-\frac{t}{\tau_c(\theta)}}}{1 + e^{-\frac{t-\tau_l(\theta)}{\tau_c(\theta)}}} \tag{24.5}$$

where $\tau_l(\theta)$ and $\tau_c(\theta)$ are the temperature-dependent latency and characteristic times, respectively. M is either the modulus of elasticity, E, or tensile strength, $f_t{}'$, M_0 is the original material property, and β_M is a residual fractional value as strain tends to $\varepsilon^{\infty}_{AAR}$.
Once the time-dependent material degradation has been applied in the numerical model, the system can be analyzed under the current load condition to determine the capacity function. The time history of the desired R is recorded. This procedure is diagrammed in Figure 24.5(b).

24.3.3 Hydro-pressure Overload Factor (HPOF)

This method mainly targets the uncertainty of the applied load in determining the bearing capability of the structure. It is also called the "triangle overloading method," featuring a progressive overloading of the upstream water pressure, which is assumed equivalent to the increase in water density. In the meantime, all other dam and foundation properties are kept unchanged [532].
Let κ_{HPOF} be the overload factor ($\kappa_{HPOF} > 1.0$) and P_0 denote the total hydrostatic load at the normal reservoir level. Overloading can then be calculated as $\kappa_{HPOF} \times P_0$ [544]. According to this method, the shape of the loading vector is the same for all increments. Therefore, the finite element model can be overloaded by multiplying the mass density of water by an overload factor, i.e. $\kappa_{HPOF} \times \rho_w$.
The hydro-pressure overload factor method is a suitable means to calibrating the structural physical model experiments [921], in which hydrostatic pressure is applied by servo-controlled hydraulic jacks on the upstream face. This method usually requires a large κ_{HPOF} to induce collapse of the system. Consequently, the κ_{HPOF} *vs.* R plot can be derived for the system, as shown in Figure 24.7(a).

24.3.4 Flood Overload Factor (FOF)

This method primarily focuses on the uncertainty of a potential flood on the dam and the resultant applied pressure in order to determine the capability of the structure. According to this method, the dam is overloaded by continuously increasing the water head. A sample application is explained in Comi, Fedele, and Perego [210]. This method is similar to HPOF; in FOF however, the applied load is technically more uniform in height, while in HPOF, the main overload is handled by the base of

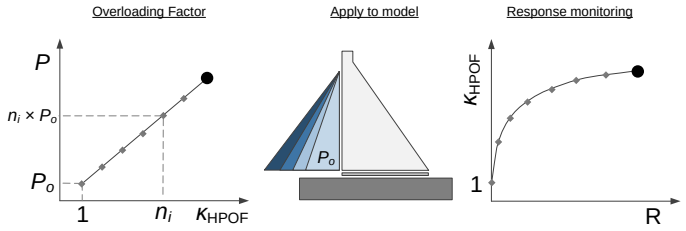

(a) Hydro-pressure overload factor

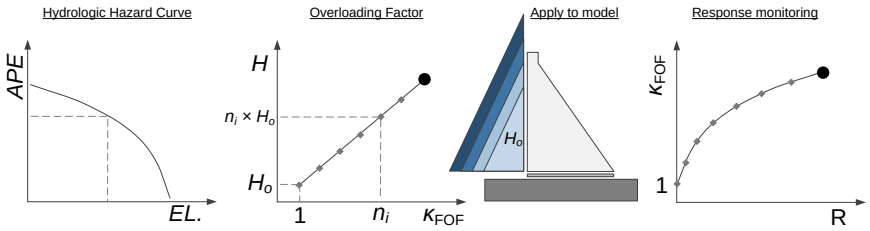

(b) Flood overload factor

Fig. 24.7: Capacity estimation by hydraulic-based methods

the dam. In 2D gravity dams, both the HPOF and FOF methods may ultimately yield similar capacity functions because the gravity dam only stands on its base. In 3D arch dams, the structure is supported by both the base and the abutments (support along the height). Thus, HPOF and FOF may lead to different failure modes and, consequently, different capacity functions.

A hydrological hazard curve must first be derived for the reservoir [811]; it is a graph of peak flow (or volume or maximum reservoir elevation - El.) *vs.* annual probability of exceedance (APE). The head of the water is then increased based on a linear protocol. Let κ_{FOF} be the flood overload factor ($\kappa_{FOF} > 1.0$) and H_0 denote the normal reservoir level. Flood overloading can now be calculated for a new water level as: $\kappa_{FOF} \times H_0$. The shape of the loading vector in FOF is different than in HPOF. Figure 24.7(b) shows the step-by-step procedure.

24.3.5 Pushover-based Analysis (POA)

This method is mainly used to determine the load-displacement curve in structural systems. Although it is popular in seismic assessment of buildings, there are few papers which discuss the applicability of POA for concrete dams [31], [32], [33]. With this method, the magnitude of applied load (or displacement) is increased incrementally according to a predefined protocol up to failure. Extracting the capacity curve is normally one of the steps involved in POA. Various versions of the full POA

for the framed structures already investigated have been published by: Freeman [318], Chopra and Goel [196], Fajfar [284], Chopra and Goel [197], Antoniou and Pinho [39], Casarotti and Pinho [169], and Giorgi and Scotta [341]. These are different classifications for POA and have been based on the type of load vector (varying quantity):

- Forced-based Pushover Analysis (FPA): According to this method, a scaled force vector is applied along the structure. At each step, the index point displacement is plotted *vs.* base shear.
- Displacement-based Pushover Analysis (DPA): According to this method, a displacement vector is applied incrementally to the structure, and the corresponding base shear is recorded. Subsequently, the base shear *vs.* maximum displacement is plotted for the structure [39].
- Energy-based Pushover Analysis (EPA): According to this method, the displacement is applied based on the energy (area under the force-displacement curve) increments [413]. Figure 24.8(a) compares the three POA methods indicated above for a sample frame.

In another classification, the POA is based on the applied load distribution pattern:

- Conventional POA (CPOA): CPOA is the nonlinear incremental-iterative solution to the equilibrium equation $\mathbf{KU} = \mathbf{P}$ in a finite element formulation, where $\mathbf{K}$, $\mathbf{U}$, and $\mathbf{P}$ are the nonlinear stiffness matrix, displacement, and applied load vectors, respectively. According to this method, the lateral load may be a set of forces or displacements that must maintain a constant ratio throughout the analysis (fixed pattern) [680]. The critical parameters in CPOA are: 1) type of lateral load, 2) load distribution pattern along the height, 3) load magnitude, 4) number of applied load steps, 5) iterative strategy, and 6) convergence criteria.
- Adaptive POA (APOA): In APOA, the analysis begins by assuming an initial lateral load distribution, whereas the additional loads imposed during subsequent increments are calculated from the previous load step [38]. The applied load is updated based on both the instantaneous dynamic characteristics of the structure and a site-specific spectrum. Figure 24.8(b) shows the two capacity functions for CPOA and APOA, along with the load distributions at different levels of elasticity, yield, and collapse.

The following subsections classify the POA on the basis of the lateral load distribution pattern on concrete dams:

24.3.5.1 Invariant single-load vectors

This method, which has been recommended by FEMA [296], includes two sets of lateral load distributions, i.e.:

1. The load vector consists of a vertical distribution proportional to:
   - The pseudo lateral load, which is governed by: $f_i^* = m_i(h_i)^k$ at the height of the structure, where f_i^* is the lateral force, m_i the mass of the ith lumped

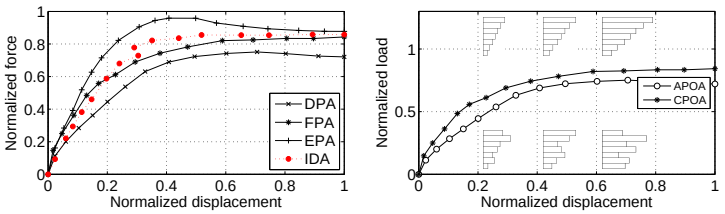

(a) Based on load vector (b) Based on load distribution

Fig. 24.8: Classification of the pushover-based capacity functions

mass, h_i the height of the ith lumped mass above the datum, and the exponent k=1 is used for structures with $T_1 \leq 0.5$ s (which is the case for most concrete gravity dams).

- The elastic first mode shape, which is governed by: $f_i^* = m_i \phi_{i1}$ at the height of the structure. In this load vector, ϕ_{i1} is the fundamental mode shape component at the ith lumped mass.
- The story shear distribution computed by response spectrum analysis, in which f^* is defined by the lateral force back-calculated from the story shear, as determined by a linear response spectrum analysis of the structural system including at least 90% of the total mass. For gravity dams, the story shear is computed along the lift joints.

2. The load vector consists of a mass-proportional uniform load pattern, $f_i^* = m_i$, or adaptive load patterns that change as the structure is displaced. This distribution should be modified from the original one by considering the properties of the yielded structure.

24.3.5.2 Invariant multi-mode vectors

1. Modal Pushover Analysis (MPOA): In MPOA, the seismic demand due to individual terms in the modal expansion of the effective earthquake forces is determined by a POA, using the inertial force distribution for each mode. Combining these modal demands provides an estimate of the total seismic demand on inelastic systems [197]. In MPOA, the lateral force distribution in each mode is expressed as:

$$f_n^{\text{MPOA}} = \underbrace{\frac{\{\phi_n\}^T [m] \{i\}}{\{\phi_n\}^T [m] \{\phi_n\}}}_{\Gamma_n} [m] \{\phi_n\} \underbrace{\omega_n^2 D_n}_{A_n} \tag{24.6}$$

where $[m]$ is the mass matrix of the structure, $\{\phi_n\}$ the corresponding mode shape, ω_n the frequency, and D_n the modal displacement. Γ_n is the modal participation factor of the nth mode and $\{i\}$ is the unit vector.

2. Modified Modal Pushover Analysis (MMPOA): MMPOA is an extension of MPOA; it combines the elastic influence of higher modes with the inelastic

response of a first-mode pushover analysis using modal combination rules. The underlying procedure involves conducting a nonlinear (mass concrete smeared cracking and/or discrete joint opening/sliding) time history analysis of the first-mode SDOF system unless an inelastic response spectrum is available for the target (design) ground motion [197].

3. Upper-bound Pushover Analysis (UBPOA): UBPOA is based on utilizing a single load vector, obtained as the combination of the first-mode shape and a factored second-mode shape. The spectral displacements corresponding to the first and second periods are estimated from the elastic spectrum of the considered ground motion; moreover, the upper-bound contribution of the second mode is established using modal participation factors [197].

24.3.5.3 Hybrid load vector

As mentioned previously, the lateral load vector should be applied to the structural system with the same (or as close as possible) pattern of imposed seismic lateral loads in an earthquake event. As opposed to conventional framed structures, in which the load vector is mainly composed of the inertial loads due to the frame self-weight, concrete dams experience an additional load vector due to the reservoir water pressure, i.e. the hydrodynamic load. Thus, a hybrid load vector needs to be applied incrementally.

For concrete gravity dams, obviously a non-uniform mass distribution exists along the height. Typical medium-rise gravity dams have small vibration periods and are known as first-mode predominant structures. Figure 24.9(a) shows the variation in natural period of the Koyna gravity dam (on rigid foundation and empty reservoir), as well as some of the selected mode shapes based on the finite element technique. In assuming that the dynamic behavior of a gravity dam mainly originates from its first vibration mode, the inertial load vector can thus be represented as:

$$f_{inr}(z) = m_c(z)\ \phi_1(z) \tag{24.7}$$

where $f_{inr}(z)$ is the lateral load vector due to inertial loads, $m_c(z)$ represents the mass distribution along the height of the dam, $\phi_1(z)$ is the normalized fundamental model shape of the dam, and z is measured from the dam base. Considering the homogeneous concrete in a dam body, the mass distribution is proportional to the dam width along its height. Therefore, for equal increments of the dam height, $m_c(z) = \rho_c b(z)$, where ρ_c is the concrete mass density and $b(z)$ the height-dependent dam width.

It is worth mentioning that accounting for the reservoir water and foundation flexibility increases the fundamental period of the coupled system, as shown in Figure 24.9(b), where $L_2 = 0.75L_1$, $L_3 = 0.10L_1$, and $L_4 = 0.075L_1$. The elastic modulus of dam concrete is assumed to be 25 GPa. For large dams ($L_1 > 100$ m), the impact of higher-modes should be also considered in determination of $f_{inr}(z)$ [386]. Subsequently, the hydrostatic pressure and total force depend on the water height and are represented as:

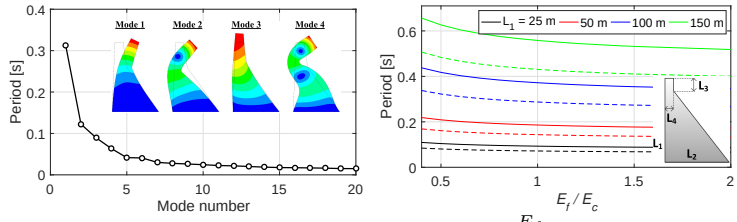

(a) Period *vs. mode number for typical medium-rise dam on rigid foundation and no reservoir*

(b) Period *vs.* $\frac{E_f}{E_c}$ *for dam on flexible foundation; solid line = full reservoir, dashed line = half reservoir*

Fig. 24.9: Modal analysis of concrete gravity dams

$$p_{hst}(z) = \rho_w \, g \, (H_w - z), \quad f_{hst}(z) = \frac{1}{2}\rho_w \, g \, (H_w - z)^2 \tag{24.8}$$

where ρ_w is the water mass density, and H_w the reservoir water height.
During an earthquake, the interaction between the dam and the reservoir creates additional pressures on the upstream face of the dam. These hydrodynamic pressures may be approximated either by the Westergaard (§17.2.1.1)formula or by Zangar (§17.2.1.2) [747].

- Westergaard [879] used a parabolic approximation for the additional pressures due to earthquake motion on a rigid dam with a vertical upstream face. The modified version of this equation which also accounts for the upstream constant inclination can be simplified as [202], [201]:

$$p^w_{hdy}(z) = \frac{7.99 \, \alpha_{GM} \, K_\theta}{\sqrt{1 - 7.75 \left(\frac{H_w}{1000T}\right)^2}} \sqrt{H_w(H_w - z)} \tag{24.9}$$

  where α_{GM} measures the intensity of the ground motion by the relation $a_g = \alpha_{GM} g$, where a_g is the maximum horizontal acceleration. For the sloped upstream face, a correction factor K_θ should be applied. For an angle of slope θ from the vertical, the correction factor is $K_\theta = \cos^2 \theta$, and T is the period for characterizing the ground seismic acceleration imposed on the dam. In this relation, units are expressed in kilo-Newton, meter, and seconds.
- Using an electric analog, Zangar [904] determined experimentally that the hydrodynamic effect of horizontal earthquake action on dams with upstream faces of either constant or compound slopes. The pressure is given by:

$$p^z_{hyd} = \underbrace{\frac{C_m}{2}\left[\frac{z}{H_w}\left(2 - \frac{z}{H_w}\right) + \sqrt{\frac{z}{H_w}\left(2 - \frac{z}{H_w}\right)}\right]}_{C_z} \alpha_{GM} \rho_w H_w \tag{24.10}$$

where z, H_w, ρ_w and α_{GM} are identical to those in the Westergaard model, and C_z is a coefficient with a maximum value of C_m.

All the inertial, hydrostatic, and hydrodynamic forces should be combined to form the final lateral load vector on the dam. The total lateral load vector can be composed as follows:

$$f_{hybrid}(z) = \delta_1 f_{inr}(z) + \delta_2 f_{hst}(z) + \delta_3 f_{hdy}(z) \tag{24.11}$$

where δ_i (i=1, 2, 3) are the proportional weight factors among the load vectors and should be obtained for the considered dam by comparison with the total base shear of the dam for both the full and empty reservoirs. Some preliminary recommendations have been furnished by Alembagheri and Ghaemian [21] for a specific gravity dam (Pine Flat dam).

It should be noted that the hydrostatic force is independent of the earthquake and remains unchanged while incrementally increasing the inertial and hydrodynamic loads. Another important point in finding the correct derivation of a capacity function for a dam-reservoir-foundation system based on POA is to account for the uplift pressure at the dam-foundation interface. Uplift pressure decreases the capacity of the dam [796], [475], [842]. Let's also note that the uplift is not affected by the earthquake (it merely depends on the head water and the crack length, l_{cr}, at the dam-foundation interface). Figure 24.10 shows a flowchart for applying a hybrid load vector on the coupled dam-reservoir-foundation system.

It is worth noting that due to the unbiased nature of concrete dams, the computed lateral load needs to be applied twice monotonically and in separate analyses, i.e. on the upstream face towards the downstream direction and on the downstream face towards the upstream direction. The final function is the one with less capacity.

24.3.6 Cyclic Pushover Procedure (CPP)

For the POA, the loads are statically applied to the structure, thus making the strain rate negligible. However, when a concrete structure is subjected to cyclic loading, cumulative damage occurs under repeated loads, resulting in stiffness degradation and strength deterioration [678]. Research has shown that monotonic loading provides greater strength than cyclic loading for RC frame structures [508]. When considering that mass concrete structures (concrete dams in general as brittle structures) follow the same rules, it would be more appropriate to apply a cyclic load to capture the capacity function. The lateral force vector can be derived for a CPP, as suggested in Panyakapo [678]:

$$f_n^{\text{CPP}} = \lambda_j \Gamma_n [m] \{\phi_n\} A_n \tag{24.12}$$

where f_n^{CPP} is the lateral force distribution for cyclic pushover in each mode, j defines the sequence numbers of peak displacement for the specified displacement history, and $\lambda_j = (-1)^{j+1}$ is a factor defining the force direction.

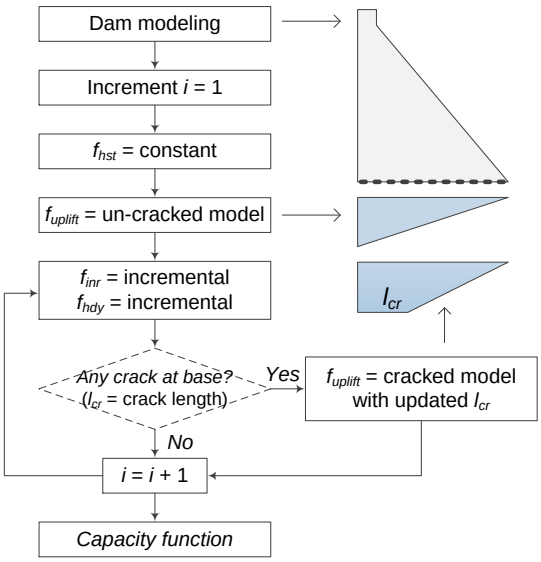

Fig. 24.10: Algorithm to find the derivation of a capacity function using the hybrid load vector

A key to the successful implementation of CPP is to use the appropriate displacement time history. Different displacement time histories were proposed for experimental studies; they may be distinguished by: 1) total number of cycles, 2) number of initiation cycles, 3) number of primary cycles, 4) inclusion of trailing cycles, 5) inclusion of repeating cycles, 6) sequence of primary cycle amplitudes, 7) a reference parameter, and 8) loading symmetry [313].
To the best of the authors' knowledge, no specific recommendation has been issued for the appropriate selection of the cyclic loading protocol on concrete dams; however, some applications have been explained in Ghobarah and Ghaemian [338] and Alembagheri and Ghaemian [21]. In the present paper, the following protocols are recommended for concrete dams:
Experimental Cyclic Test Protocol: Displacement histories can be categorized based on the type of the structure as:

- Concrete structures: New Zealand protocol [190]
- Steel structures: ATC-24 protocol [221], SAC protocol [207].
- Wood structures: FCC protocol [491], ASTM E72 protocol (1995), ASTM E564 protocols (1995), CEN protocol (1995), ISO protocol (1998), CUREE-Caltech protocol (2000)
- Masonry structures: Sequential Phase Displacement (SPD) protocol

The New Zealand protocol [190], which has basically been developed for concrete structures, may be a good choice for concrete dams. SPD can also be used, in considering that the cracking pattern of masonry material is similar to that of mass concrete.

The New Zealand protocol is based on a yield displacement, Δ_y, obtained by extrapolating the test specimen displacement at 75% of the theoretical strength, V_i, as measured during the third cycle of the loading sequence ($\Delta_y = 1.33\Delta_{0.75V_i}$). Although this protocol does not require a preliminary monotonic test, the theoretical strength of the test specimen should be defined first. The displacement history for this protocol is shown in Figure 24.11(a). The first three cycles are all load-controlled. The first two cycles impose a lateral force corresponding to 50% of V_i. The first yield displacement is determined during the third cycle. The other cycles are displacement-controlled based on the displacement-ductility ratio ($\mu_\Delta = \Delta/\Delta_y$).

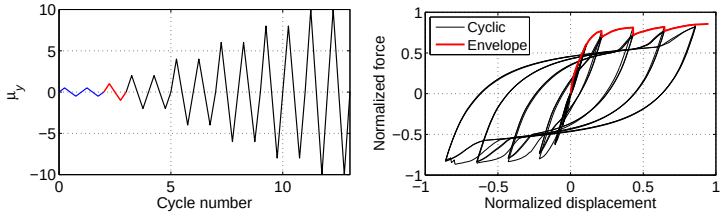

(a) Displacement history (b) Cyclic/envelope capacity functions

Fig. 24.11: Cyclic pushover procedure for the New Zealand protocol

It is apparent that in this method, the capacity function will have a cyclic nature. The envelope of this loop should be determined in order to obtain a capacity function similar to the monotonic loading. For this purpose, ASCE/SEI-41-13 [50] criterion can be used; it takes both the strength and stiffness deterioration into account. The capacity function is obtained using the points given by the intersection of an unloading branch and the loading curve of the next load cycle, which moves to a higher level of displacement. Figure 24.11(b) shows the cyclic pushover function and its envelope (capacity function) for a sample frame. The envelope curve may be smoothed even more for use in conjunction with the analytical solution provided in Section 24.2.2.

Numerical Cyclic Loading Protocol: Filiatrault, Wanitkorkul, and Constantinou [313] proposed a numerical cyclic protocol derived by taking into account the general properties of all experimental protocols. This two-step process includes both the monotonic and cyclic analyses:

1. Monotonic POA: Perform a preliminary POA, and derive the capacity curve. Identify the failure displacement, Δ_y. The expected failure displacement corresponds to a fraction, α_y, of the maximum base shear. α_y is either calibrated based on the results of IDA or set equal to approximately 0.80 [313].

2. Cyclic POA: Perform a CPP as discussed in the previous case. The only difference here is a new displacement history. The new protocol includes 7 cycle groups with 3 cycles in each (i.e. a total of 21 cycles). The amplitudes for the 7 groups are: $\mu_\Delta = \Delta/\Delta_y$ = 0.1, 0.2, 0.3, 0.4, 0.6, 0.8, and 1.0.

The control point (target point) for a framed structure is typically located at the center of mass at the roof level. Due to the unique shape of concrete dams (especially the 3D arch dam model), the displacement distribution pattern tends to be non-uniform in both height and cross-stream directions. The control point for concrete dams may be highly affected by local failure modes or partial dam failure, though it does not represent a global failure mode. The control point should thus be selected in considering the global failure mode of the dam. It is possible to track the capacity curve for more than one control point at the start of the assessment process, while the final capacity curve should be chosen based on overall dam failure. For the 2D gravity dam model with a standard body topology, the target point can be selected as the crest node on the upstream face, though the node located at the point of slope discontinuity on the downstream face can also be a good target point candidate. For the 3D arch dam model, further investigations are required to reveal the location of the target point in both height and cross-stream directions for both the symmetrical case and asymmetrical typologies.

24.3.7 Equivalent Static Lateral Force (ESLF)

The Response Spectrum Analysis (RSA) estimates peak responses directly from the earthquake design spectrum and is normally used for preliminary design and safety evaluation of concrete gravity dams. In a series of publications, Fenves and Chopra [303], Fenves and Chopra [301], and Løkke and Chopra [546] developed an analytical solution for the RSA of a gravity dam-foundation-reservoir system using ESLF. It is possible to adapt this equivalent lateral force vector and apply it incrementally to the dam.

In considering just the fundamental vibration mode and neglecting the vertical component of ground motion, the dam alone may be subjected to ESLF acting on the upstream face, e.g. [546]:

$$
\begin{aligned}
f^{\text{ESLF}}(z) &= \frac{\tilde{L}_1}{\tilde{M}_1} \frac{A\left(\tilde{T}_1, \tilde{\zeta}_1\right)}{g} \left[w_s(z)\phi_1(z) + g\, p(z, \tilde{T}_r) \right] \\
\tilde{M}_1 &= (R_r)^2 \frac{1}{g} \int_0^{H_s} w_s(z)\, \phi_1^2(z)\, dz \\
\tilde{L}_1 &= \frac{1}{g} \left(\frac{w_r H_w^2}{2} \right) \left(\frac{H_w}{H_s} \right)^2 A_p + \frac{1}{g} \int_0^{H_s} w_s(z)\, \phi_1(z)\, dz
\end{aligned}
\tag{24.13}
$$

where $\phi_1(z)$ is the horizontal component of displacement at the upstream face of the dam in the fundamental mode supported on a rigid foundation with an empty reservoir; $w_s(z)$ is the weight per unit height of the dam; g is the ground acceleration; $\tilde{L}_1$ is the generalized mass; $\tilde{M}_1$ is the generalized earthquake force coefficient; H_w

and H_s are the height of water and dam in meters, respectively; w_r is the unit weight of the reservoir; R_r is the period-lengthening ratio and depends on the wave reflection coefficient, α_w, H_w/H_s and the mass concrete modulus of elasticity (in MPa); E_s. A_p is the hydrodynamic force coefficient corresponding to the period ratio, $R_w = \frac{4H_w}{C_w}\frac{1}{\tilde{T}_r}$, and α_w where C_w denotes the pressure wave velocity in water. The fundamental period of the dam-reservoir, $\tilde{T}_r$, dam-reservoir-foundation, $\tilde{T}_1$, and the damping ratio of the equivalent SDOF system of the dam-reservoir-foundation, $\tilde{\zeta}_1$ are [546]:

$$\begin{aligned} T_1 &= 0.38 H_s {E_s}^{-1/2} \\ \tilde{T}_r &= R_r T_1 \\ \tilde{T}_1 &= R_r R_f T_1 \\ \tilde{\zeta}_1 &= {R_r}^{-1} {R_f}^{-3}\, \zeta_1 + \zeta_r + \zeta_f \end{aligned} \tag{24.14}$$

where T_1 is the fundamental period of the dam body itself on a rigid foundation; R_f is the period-lengthening ratio, which depends on E_f/E_s, where E_f is the foundation modulus of elasticity; ζ_1 is the viscous damping ratio of the dam body itself, ζ_r is the added damping due to dam-reservoir interaction and reservoir bottom absorption, and ζ_f is the added radiation and material damping due to dam-foundation interaction and the constant hysteretic damping factor for the foundation rock, η_f. Figures 24.12 and 24.13 show the standard values of R_r, ζ_r, R_f, and ζ_f for concrete gravity dams.

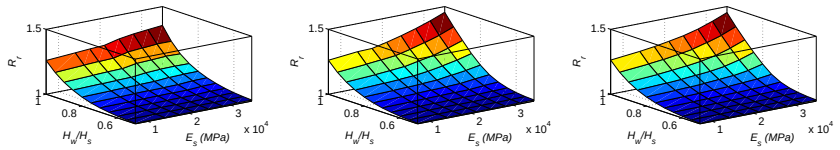

(a) R_r for α_w=0.50 (b) R_r for α_w=0.75 (c) R_r for α_w=1.00

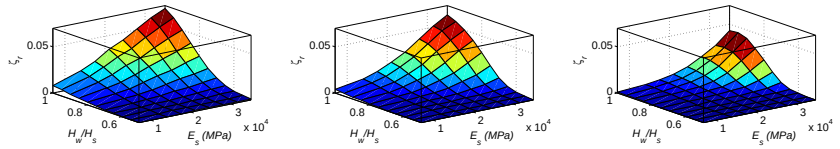

(d) ζ_r for α_w=0.50 (e) ζ_r for α_w=0.75 (f) ζ_r for α_w=0.90

Fig. 24.12: Standard contribution factors for the dam-reservoir interaction [546]

$A\left(\tilde{T}_1, \tilde{\zeta}_1\right)$ is the pseudo-acceleration ordinate of the earthquake design spectrum, evaluated over vibration period $\tilde{T}_1$ and for damping ratio $\tilde{\zeta}_1$ of the equivalent SDOF

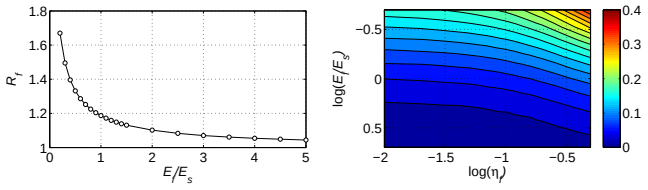

(a) R_f (b) ζ_f

Fig. 24.13: Standard contribution factors for the dam-foundation interaction [546]

system representing the dam-reservoir-foundation system. Note that in the incremental format of ESLF, $A\left(\tilde{T}_1, \tilde{\zeta}_1\right)$ should be increased incrementally.

The function $p(z, \tilde{T}_r)$ is the real-valued component of the complex-valued function representing the hydrodynamic pressure on the upstream face. Normalized $gp(z, \tilde{T}_r)$ can be computed based on Figure 24.14 as corresponding to the values of R_w, α_w, and assuming $H_w/H_s = 1$. Finally, the result is multiplied by $(H/H_s)^2$.

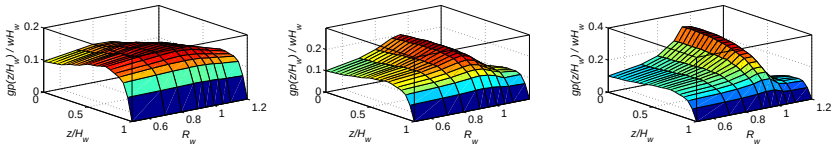

(a) α_w=0.50 (b) α_w=0.75 (c) α_w=0.90

Fig. 24.14: Standard values of the hydrodynamic pressure for a full reservoir [546]

24.3.8 Incremental Dynamic Analysis (IDA)

24.3.8.1 Single-Record IDA (SR-IDA)

The seismic capacity function can be obtained using real ground motion. In the SR-IDA, single ground motion is used for the nonlinear time history analysis of the coupled system. Ground motion can be obtained from a hazard analysis. This method however is mainly used for structures (or their small-scale models in the laboratory) already damaged by a certain amount of ground motion. The examples cited are: the 1967 Koynanagar earthquake for analysis of the Koyna gravity dam [383] and the 1990 Manjil earthquake for analysis of the Sefidrud buttress dam [329]. A special format of SR-IDA using the artificial accelerogram has been reported by Pan, Xu, and Jin [675] for concrete arch dams.

Let $\ddot{\mathbf{x}}_g$ be the "as-recorded" (unscaled) acceleration time history (it may already be filtered, rotated or baseline-corrected). The vector elements are $\ddot{x}_g(t_i)$, t_i= $0, t_1, t_{n-1}$. To consider both the stronger and weaker scenarios, ground motion can be scaled uniformly using a factor $\lambda_{SF} \in [0, +\infty)$ [849]. The scaled ground motion will be: $\ddot{\mathbf{x}}_g^{\lambda} = \lambda_{SF}\ddot{\mathbf{x}}_g$. Note that (at least) one of the following three methods may be used for scaling: 1) time domain direct scaling of the acceleration time history, 2) scaling of the elastic acceleration response spectrum, and 3) frequency domain scaling by applying λ_{SF} to all Fourier amplitudes while keeping the phase unchanged. The scaled ground motion should be represented by a monotonic scalable intensity measure (usually referred to as Intensity Measure - IM) in the form of Eq. 24.15. Note that IM in SR-IDA corresponds to the load vector (Section 24.3.5) in POA and a response quantity, R, (Section 24.2.1) in the general definition of capacity function.

$$\text{IM} = \Psi(\ddot{\mathbf{x}}_g^{\lambda}); \text{IM} \in [0, +\infty) \tag{24.15}$$

where Ψ is any scalar monotonic representation of the scaled ground motion, such as peak ground acceleration (PGA) or the 5% damped Spectral Acceleration at the first-mode period ($S_a(T_1, \xi = 5\%)$). A comprehensive list of ground motion IMs is provided in [733]. The application of optimal IMs in dam engineering has already been studied by Hariri-Ardebili and Kianoush [375] and Hariri-Ardebili, Saouma, and Porter [388].

With these scaled ground motions, the nonlinear time history analysis should be performed in each case. Let's assume that the response of the nonlinear system to the scaled signal is $\mathbf{R}^{\lambda}$, where the response vector elements are: $R^{\lambda}(t_i)$, $t_i = 0, t_1, t_{n-1}$. The response parameter can be any general monitoring item in dams, such as deformation, stress, uplift or even DIs. It is usually worthwhile to record the maximum absolute value of $\mathbf{R}^{\lambda}$ for each scaled ground motion, see Eq. 24.16. In the language of earthquake engineering, R is referred to as the engineering demand parameter (EDP).

$$\text{EDP} = \Omega(\mathbf{R}^{\lambda}) = \max\left\{\text{Abs}\left(R^{\lambda}(\tau) : \tau \in [0, t_{n-1}]\right)\right\}; \quad \text{EDP} \in [0, +\infty) \tag{24.16}$$

where Ω is the maximum absolute function.

Single-IM SR-IDA (SIM-SR-IDA): This is a plot of different pairs of (IM, EDP) from linear elastic to the nonlinear phase and including system failure. The m discrete points (which means m nonlinear time history analyses) are then connected to one another using either: 1) piecewise linear interpolation, 2) spline interpolation, or 3) the Ramberg-Osgood equation to form the capacity function.

- Spline interpolation: The spline comes in m cubic polynomial pieces, with m being the number of convergent runs plus one for the $(0, 0)$ point; it is parameterized on a single non-negative parameter, $\tau \in [0, \tau_1] \cup ... \cup [\tau_{n-1}, \tau_n]$. For each value of the parameter τ and depending on the interval $[\tau_{i-1}, \tau_i]$ where it lies, one polynomial for IM and another for EDP can be derived [850]:

$$\begin{cases} x_i(\tau) = (a_1)_{xi}\tau^3 + (a_2)_{xi}\tau^2 + (a_3)_{xi}\tau + (a_4)_{xi} \\ y_i(\tau) = (a_1)_{yi}\tau^3 + (a_2)_{yi}\tau^2 + (a_3)_{yi}\tau + (a_4)_{yi} \end{cases} \tag{24.17}$$

where $\tau \in [\tau_{i-1}, \tau_i], i = 1, 2, ..., n$.
Using the above equation, it is now possible to approximate the EDP value for an arbitrary level of IM and vice versa:

$$\begin{aligned} \text{EDP} &= y\left(x^{-1}(\text{IM})\right) \\ \text{IM} &= x\left(y^{-1}(\text{EDP})\right) \end{aligned} \tag{24.18}$$

- Ramberg-Osgood (R-O) equation: Considering that the spline interpolation is cumbersome in some cases, the R-O equation may be used [565]:

$$\frac{\text{EDP}}{\text{EDP}_c} = \frac{\text{IM}}{\text{IM}_c} + \left(\frac{\text{IM}}{\text{IM}_c}\right)^r = \frac{\text{IM}}{K.\text{EDP}_c}\left(1 + \left|\frac{\text{IM}}{\text{IM}_c}\right|^{r-1}\right) \tag{24.19}$$

where K is the initial slope of the IDA curve in the proportional range; IM_c is the critical IM occurring at the onset of large EDPs that subsequently lead to collapse; $\text{EDP}_c = \text{IM}_c/K$ is the critical value of EDP; and r is a constant parameter.
In order to use the R-O equation, the median IDA curve must first be derived by interpolation from the actual IDA data, then the R-O equation needs to be fitted to the observed median IDA curve. The value of the r parameter may be set at a reasonable number, while the other parameters K and IM_c can be estimated using least squares analyses.

Anatomy of SIM-SR-IDA: For a simple framed structure, four types of capacity curves can be distinguished: 1) capacity curve with a fully softening response, 2) capacity curve including some minor hardening, 3) capacity curve including severe hardening, and 4) capacity curve with a fully wavy behavior. In concrete gravity dams, only the first three types can be observed, Figure 24.15(a). Both options (1) and (2) have the capability of being represented in the form of Eqs. 24.2 and 24.3, as explained in Section 24.2.2. However, due to the heavy dependence on ground motion in option (3), no analytical form is available.
Multi-IM SR-IDA (MIM-SR-IDA): As mentioned above, the capacity function based on SIM-SR-IDA is a flatter curve of IM *vs.* EDP. Choosing an appropriate IM parameter is always a challenging task as it differs by type of structure. For conventional framed structures $S_a(T_1, \xi = 5\%)$ is usually the best choice [851]. For a concrete arch dam, Acceleration Spectrum Intensity (ASI) and PGA are the most optimal ones [388]. It is helpful therefore to have a three-dimensional curve, where the vertical axis is EDP and the horizontal axes are two IMs. Note that similar to SIM-SR-IDA, in MIM-SR-IDA again one of the IMs has been scaled while the other one is computed externally using simple calculations on the scaled ground motion. Figure 24.15(b) shows a 3D capacity function as EDP-IM_1-IM_2. The projections of this curve are also given so as to represent the conventional SIM-SR-IDA as EDP-IM_1 and EDP-IM_2.

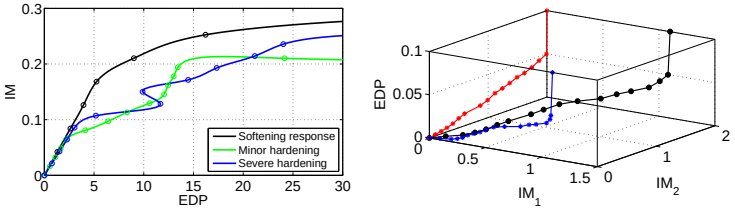

(a) SIM-SR-IDA (b) MIM-SR-IDA

Fig. 24.15: Single-Record IDA capacity functions

24.3.8.2 Multi-Record IDA (MR-IDA)

MR-IDA is a collection of several, n, SR-IDA for the same structural system. The required ground motion records are usually obtained from a Probabilistic Seismic Hazard Analysis (PSHA) conducted at the site [581]. The number of required records typically varies given the dispersion among them. The order of n for framed structures (with less computational effort) is about 30 [851], while for concrete dams (with high computational effort), it is around 12 [21]. Let's note that some approximate methods have been proposed in order to reduce the number of required records when estimating the median response of structures [74], [75]. Other applications of MR-IDA in concrete dam engineering (including the seismic fragility curves) can be found in Alembagheri and Ghaemian [21, 19, 20], Hariri-Ardebili and Saouma [384], and Soysal, Binici, and Arici [800].

Single-IM MR-IDA (SIM-MR-IDA): This is the most common format of an IDA plot in the IM-EDP coordinate system. Figure 24.16 presents the raw data obtained from MR-IDA. This figure also shows the capacity functions resulting from n=40 ground motion based on the piecewise linear interpolation and spline interpolation techniques discussed in Section 24.3.8.1 for SR-IDA.

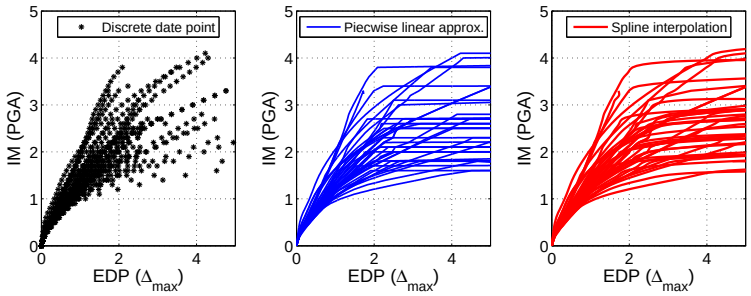

Fig. 24.16: Multi-Record IDA capacity functions using different interpolation techniques

Considering the record-to-record variance in the capacity functions in SIM-MR-IDA, they should be summarized using some central values like mean, median, 16% and 84% fractiles. Two methods can be introduced: 1) first, find the parametric model for each SIM-SR-IDA (using Eq. 24.2 or any other model), then identify the parameter statistics and 2) use of non-parametric methods such as a running mean, running median, LOESS, or the smoothing spline [409, 849]. The resulting summary capacity curves tend to be smoother than the SIM-SR-IDA curve, Figure 24.15(a), and more easily fitted to the analytical model (Eq. 24.2).

Vector-IM MR-IDA (VIM-MR-IDA): MR-IDA curves are plotted in $< \text{IM}_{SC}, \text{IM}_{NSC}, \text{EDP} >$ coordinates, with one scalable and one non-scalable IM. The previously proposed vector-valued IMs for frame structures are:

- Vamvatsikos and Cornell [851] proposed $S_a(T_1)$ as the scalable component, while the spectral ratio, $R_{sa}(\kappa, T_1)$, is the non-scalable one:

$$\langle S_a(T_1), R_{sa}(\kappa, T_1)\rangle = \left\langle S_a(T_1), \frac{S_a(\kappa T_1)}{S_a(T_1)} \right\rangle \tag{24.20}$$

  where κ is a constant factor, typically 1.5.
- Baker and Cornell [78] proposed $S_a(T_1)$ as a scalable component and epsilon, ϵ as a scaling-independent component. It has been found that $\langle S_a(T_1), \epsilon\rangle$ is significantly greater than $S_a(T_1)$ alone. ϵ is defined as the number of standard deviations by which an observed logarithmic spectral acceleration, $\ln S_a(T)$, differs from the mean logarithmic spectral acceleration, $\overline{\ln S_a(T)}$, for a ground-motion prediction equation.
- Bojorquez et al. [134] proposed the following two vector-valued IMs:

$$\begin{aligned} \langle S_a(T_1), R_{T_1,T_2}\rangle \;,\quad R_{T_1,T_2} &= \frac{S_a(T_2)}{S_a(T_1)} \\ \langle S_a(T_1), N_p\rangle \;,\quad N_p &= \frac{S_a\left(\left(\prod_{i=1}^{N_m} T_i\right)^{1/N_m}\right)}{S_a(T_1)} \end{aligned} \tag{24.21}$$

  where N_m is the number of contributing modes.

Figure 24.17(a) shows the MR-IDA for Pine Flat dam. The next step consists of summarizing the discrete 3D curve and generating a "surface" [851]. The resulting so-called IDA surface can then be used for 16%, 50%, and 84% capacity lines for a given limit state.

Multi-IM MR-IDA (MIM-MR-IDA): The IDA curves are plotted in $< \text{IM}_{SC}, \text{IM}_{SC}, \text{EDP} >$ coordinates, with two scalable IMs. Bojorquez et al. [134] used a combination of $S_a(T_1)$ with other scalar IMs in order to determine the optimal vector IM. $\langle S_a(T_1), PGA\rangle$ and $\langle S_a(T_1), PGV\rangle$ were used to indicate the peak responses of the structural system. $\langle S_a(T_1), t_{sig}\rangle$ and $\langle S_a(T_1), I_D\rangle$ were used to indicate the combination of peaks and cumulative damage potential of ground motions. Figure 24.17(b) shows 3D MR-IDA curves, where $S_a(T_1)$ and ASI are two

scalable IMs. ASI is selected because it results in relatively low dispersion. Hariri-Ardebili, Saouma, and Porter [388] used $\langle PGA, ASI \rangle$ for arch dams in conjunction with the multiple-stripe analysis (MSA). They found that using a vectorized IM slightly improves the linear regression of responses with respect to ground motion IM.

Multi-EDP MR-IDA (MEDP-MR-IDA): The IDA curves are plotted in $< \text{EDP}_1, \text{EDP}_2, \text{IM}_{SC} >$ coordinates with two EDPs. This type of 3D plot is useful when the two EDPs have a strong dependency, i.e. joint opening and sliding in mixed-mode fracture mechanics problems, Figure 24.17(c). The summary curves can be viewed in the format of "curved capacity surfaces" (not shown here).

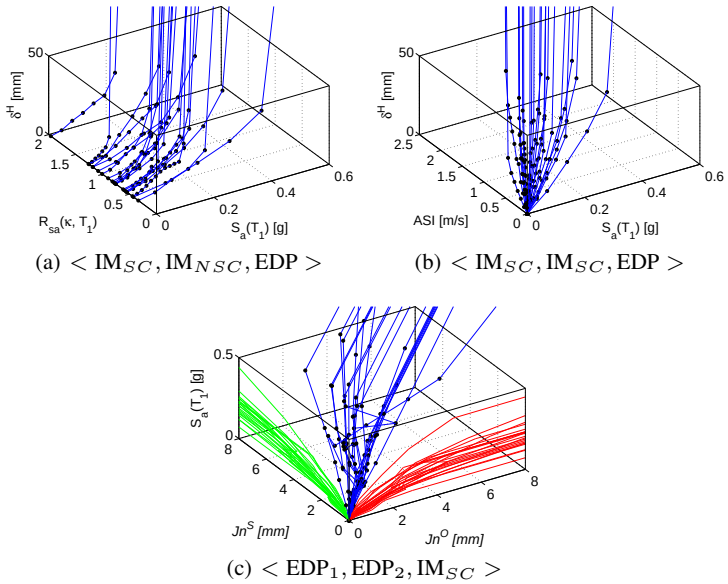

(a) $< \text{IM}_{SC}, \text{IM}_{NSC}, \text{EDP} >$ (b) $< \text{IM}_{SC}, \text{IM}_{SC}, \text{EDP} >$

(c) $< \text{EDP}_1, \text{EDP}_2, \text{IM}_{SC} >$

Fig. 24.17: Comparison of various 3D MR-IDA capacity functions

24.3.9 Cloud Analysis (CLA)

CLA is a numerical procedure in which a structure is first subjected to a set of (un-scaled or as-recorded) ground motions and analyzed numerically. If the ground motion records are extracted from a bin, they can represent an earthquake scenario defined by (M_{bin}, R_{bin}), i.e. the magnitude and distance representative of the bin [468]. From these results, EDP *vs.* IM are then determined and form the so-called cloud response. The CLA method is normally used in conjunction with probabilistic seismic demand analysis (PSDA) [790]. It is now well accepted that the discrete data points resulting from CLA have a linear trend on the logarithmic scale, thus

implying a power curve on the arithmetic scale [674, 471, 720].

$$\begin{aligned} \eta_{\text{EDP|IM}}(\text{IM}) &= a.(\text{IM})^b \\ \ln\left(\eta_{\text{EDP|IM}}(\text{IM})\right) &= b.\ln(\text{IM}) + \ln(a) \end{aligned} \tag{24.22}$$

where $\ln(a)$ and b are the linear regression constants and $\eta_{\text{EDP|IM}}$ is the median value of EDP given IM.

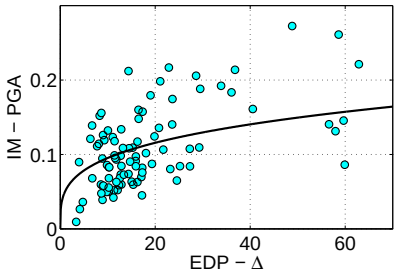

Fig. 24.18: Cloud-based data power-form capacity function

Application of CLA and PSDA for concrete gravity dams was discussed by Hariri-Ardebili and Saouma [386].

24.3.10 Endurance Time Analysis (ETA)

ETA is a dynamic pushover procedure used to estimate the seismic performance of structures when subjected to pre-designed intensifying excitation [283]. The simulated acceleration functions are intended to shake the structure from a low excitation level - with a structural response in the elastic range - to a medium excitation level - where the structure experiences some nonlinearity - and ultimately to a high excitation level causing failure. All these response ranges are experienced in a single time history analysis.
The challenging part of this method lies in generating the endurance time acceleration functions (ETAF). Different versions of ETAFs have been generated by Nozari and Estekanchi [643] and further optimized by Mashayekhi and Estekanchi [573]. The major steps for producing ETAFs are:

- Generate a stationary random acceleration function, $Z(t)$ (using $\delta t = 0.01$, $N_{pnt} = 2^{11}$ node, and PGA= 1.0 g). Note that N_{pnt} is optional.
- Transfer this function to the frequency domain, $Z(i\omega) = \mathcal{F}(Z(t))$, where i is an imaginary unit and ω is frequency.
- Apply an appropriate filter function in order to resemble real ground motions [208]:

$$A(i\omega) = \frac{1 + 2i\xi_1 \frac{\omega}{\omega_1}}{1 - \left(\frac{\omega}{\omega_1}\right)^2 + 2i\xi_1 \frac{\omega}{\omega_1}} \frac{\left(\frac{\omega}{\omega_2}\right)^2}{1 - \left(\frac{\omega}{\omega_2}\right)^2 + 2i\xi_2 \frac{\omega}{\omega_2}} Z(i\omega) \tag{24.23}$$

where the first and second terms are low-pass and high-pass filter functions, respectively; ω_1 and ξ_1 are frequency and damping coefficients for the low-pass filter function, and ω_2 and ξ_2 are frequency and damping coefficients for the high-pass filter function.

- Use several cycles of stepwise modifications on frequency content of the filtered acceleration functions, $A(i\omega)$, in order to make the resulting response spectrum compatible with the target.

$$A^{new}(i\omega) = A^{old}(i\omega) \frac{S_a^{\text{trg}}(\omega)}{S_a^{\text{gen}}(\omega)} \tag{24.24}$$

where $A^{new}(i\omega)$ is the modified frequency content being replaced with the previous content in each modification cycle. $S_a^{\text{trg}}(\omega)$ is the target spectrum (code-based spectrum or from a probabilistic seismic hazard analysis), and $S_a^{\text{gen}}(\omega)$ is the generated response spectrum.

- Modify the acceleration time history by a linear profile function, $l(t) = t/t_{trg}$, that makes the resulting one intensifying at various time intervals. Note that t_{trg} is optional, though it is usually considered to be 10 seconds.
- Modify both the acceleration and displacement response spectra by applying a linear profile function. An unconstrained optimization technique in the time domain may be used, such as:

$$\min_{a_g} F(a_g) = \int_0^{T_{max}} \int_0^{t_{max}} \left\{ \left[S_a(T,t) - \frac{t}{t_{\text{trg}}} S_a^{\text{trg}}(T) \right]^2 + \chi_0 \left[S_d(T,t) - \frac{t}{t_{\text{trg}}} \left(\frac{T}{2\pi}\right)^2 S_a^{\text{trg}}(T) \right]^2 \right\} \tag{24.25}$$

where a_g is the ETAF being sought, χ_0 a weight parameter, t_{max} and T_{max} are the maximum time and period in the optimization process, respectively. Figure 24.19(a) shows a sample ETAF.

In order to retrieve a capacity function in the form of Figure 24.2(a), the "ETA curve" should first be derived, see Figure 24.19(b). This curve is a diagram, whose vertical axis refers to the maximum absolute values of EDP during the time interval from 0 to t (see Eq. 24.26) and whose horizontal axis is time.

$$\Omega(\text{EDP}(t)) \equiv \max\{\text{Abs}(\text{EDP}(\tau) : \tau \in [0,t])\} \tag{24.26}$$

Finally, the "time" parameter is converted to IM (this can be easily performed due to the direct relation between time and acceleration, Figure 24.19(a)), and the EDP-IM coordinate is changed to IM-EDP. The resulting stepwise capacity function can be smoothed later, Figure 24.19(c). Note that although this procedure is applicable only with a single ETAF, in order to reduce the uncertainty (due to its random nature) of ETAFs, the mean of three is typically used [381] [383].

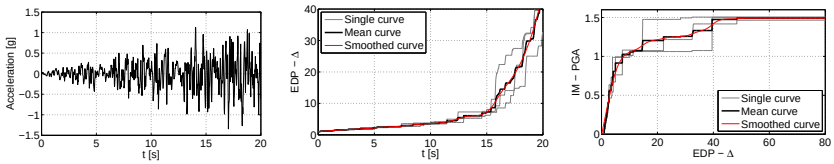

(a) Sample ETAF (b) ETA curve (c) Capacity function

Fig. 24.19: ETA-based capacity function generation

24.4 Multi-Hazard Capacity Functions

As explained in Section 24.3 and shown in Figure 24.1, seismic, hydrological, and time-dependent characteristics are three sources of uncertainties during capacity function derivation. It is possible to either: 1) extend the capacity function or 2) combine two capacity functions.

24.4.1 Extended Capacity Function

An extended capacity function refers to what was previously explained in Section 24.3, in considering one more uncertainty source (usually material uncertainty). This procedure is explained for two events.

- Seismic + Material uncertainty: Different approaches are available to consider both the material (epistemic) and seismic record-to-record (aleatory) uncertainties in the analysis of structures [673, 538, 852, 174, 254, 173, 494]. However, a method with limited computational demands (compared to Monte Carlo Simulation - MCS) is explained. This method accounts for epistemic uncertainty along with MR-IDA. The original method was described in Dolšek [252, 253] and is called an extended-IDA. We have therefore called the capacity curves resulting from this method as extended capacity functions.
  - Perform a sensitivity analysis on N_{RV} random variables (RV) and select the N_{Var} that are the most sensitive.
  - Perform N_{Sim} sampling for each RV, where N_{Sim} is the number of structural models.
  - Construct $\mathbf{X}_{N_{Sim} \times N_{Var}}$, which includes N_{Sim} realizations for N_{Var} RVs:

$$x_{j,i} = F_i^{-1}\left(\frac{\pi_i(j) - 0.5}{N_{Sim}}\right), \quad i = 1, ..., N_{Var}, \; j = 1, ..., N_{Sim} \tag{24.27}$$

    where $\pi_i(1)$, ..., $\pi_i(N_{Sim})$ is a random permutation of 1,...,N_{Sim}; F_i^{-1} is the inverse of the cumulative distribution function of the ith RV.
  - Modify the correlation matrix of $\mathbf{X}$, $\mathbf{C}$ with respect to the target correlation matrix, $\mathbf{T}$. For this purpose, the Simulated Annealing method can be used

[857] to minimize the norm, E, which is a measure of the difference between the generated and target correlation matrices.
– The optimized sample matrix $\mathbf{Y}_{N_{Sim} \times N_{Var}}$ has the arrays of $\mathbf{X}$ with the correlation matrix close to $\mathbf{T}$.

Figure 24.20(a) shows an example of a system with three sensitive RVs, N_{Var}=3, (M_1, M_2, and M_3), where M_2 and M_3 are partially correlated. For each RV, N_{Sim}=100 realizations have been sampled. Note that all RVs follow a normal distribution.
Figure 24.20(b) presents $N_{IDA} = 1 \times 20 = 20$ curves resulting from $N_{GM} = 20$ ground motions and $N_{Sim} = 1$ structural model. This set of capacity functions only account for the record-to-record variability, and this method yields approximately $N_{Anlz} = 20 \times 10 = 200$ nonlinear transient analyses.
Figure 24.20(c) shows $N_{IDA} = 100 \times 20 = 2{,}000$ curves resulting from $N_{GM} = 20$ ground motions and $N_{Sim} = 100$ structural models. This set of capacity functions accounts for both the record-to-record variability and material uncertainty. This method yields approximately $N_{Anlz} = 2000 \times 10 = 20{,}000$ nonlinear transient analyses.

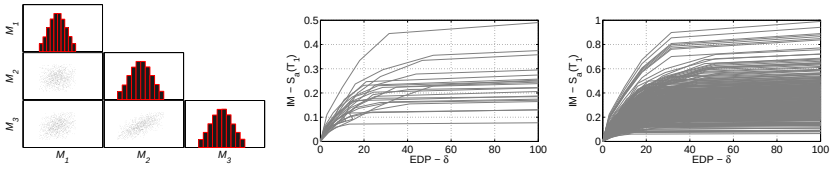

(a) Sampling three RVs (b) Capacity functions (c) Extended capacity functions

Fig. 24.20: IDA-based extended capacity function generation

- AAR + Material uncertainty: According to this condition, the material uncertainty is considered along with material degradation (e.g. AAR). First, the time-dependent RV (material property) is sampled based on a pre-defined distributional model, Figure 24.21(a), at time t=0. The material uncertainty is then propagated into strength reduction functions using Eq. 24.5, Figure 24.21(b). Finally, the finite element analyses are performed using the time-dependent uncertain material and the responses are determined, Figure 24.21(c). To be used within the PBE concept, the median, 16% and 84% fractiles should all be extracted.

24.4.2 Combined Capacity Function

Combined capacity functions pertain to time-dependent seismic or hydrological events. They mainly account for aging and deterioration effects on the capacity function (and later on the fragility functions) of structures. Several studies have shown the importance of aging on the probability of structural failure especially in

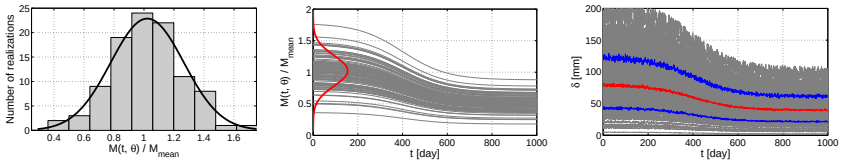

(a) Sampling RV (b) Strength degradation functions (c) Extended capacity functions

Fig. 24.21: Time-dependent strength degradation with material uncertainty

harsh environments. Among these studies, let's cite Ghosh and Padgett [339], Dong, Frangopol, and Saydam [256], Pitilakis, Karapetrou, and Fotopoulou [696], and Guo et al. [353].

Figure 24.22(a) shows a POA on a hypothetical dam system with aging concrete. The original pushover curves along with the bilinear idealizations are depicted. Both the yield displacement and yield force are reduced with time (again). Similar results were reported by Ghosh and Padgett [339] on the time-dependent corrosion of an RC column. They found that due to corrosion and subsequent losses of reinforcing steel, the load-carrying capacity and yield curvature of the RC columns underwent a significant reduction (about 20% in 50 years).

Figure 24.22(b) shows the median IDA capacity function for a deteriorating system. A nearly identical conclusion can be drawn for the IDA-based capacity functions. Aging reduces both the load-carrying capacity and collapse displacement; it also lowers the dispersion of the SR-IDA curves. The median and dispersion of the resulting fragility curves will thus be reduced by aging.

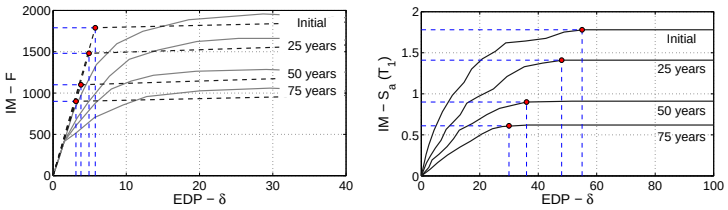

(a) POA (b) IDA

Fig. 24.22: Combination of time-dependent and seismic capacity functions

Chapter 25
Fragility Functions

Abstract
Fragility functions are resulted from a structural assessment of the system (in the case of analytical form). In simple language, the fragility can be defined as "the quality of being easily broken or damaged" Porter [703]. The seismic fragility functions are first introduced by Kennedy et al. [499] as a probabilistic relationship between frequency of component failure in a nuclear power plant and peak ground acceleration. Fragility functions are not specific to earthquake events and can be developed for any "stressor" (i.e., flood, hurricane, wind).

25.1 Fundamentals

First it is important to distinguish among some terms, their definitions and their relationship. In general, a "fragility function," as described by Porter [703], *expresses the probability that an undesirable event will occur as a function of the value of some (potentially uncertain) environmental excitation*.

25.1.1 Fragility Curve *vs.* Surface

Fragility function is a general term and may be referred to 2D "fragility curve" or 3D "fragility surface":

- Fragility curve is a continuous function showing the probability of exceedance of a certain limit state (LS) for a specific level of ground motion intensity measure (IM) [269], Figure 25.1(a):

$$\text{Fragility} = P\left[\text{LS}|\text{IM} = im\right] \tag{25.1}$$

  where $P\left[A|B\right]$ is the conditional probability that A is true given that B is true. In addition, im refers to a particular value of IM, i.e., there is no uncertainty. Alternatively, fragility can be defined as [470]:

$$\begin{aligned} \text{Fragility} &= P\left[D \geq C_{\text{LS}}|\text{IM} = im\right] \\ &= P\left[\frac{D}{C_{\text{LS}}} \geq 1|\text{IM} = im\right] = P\left[Y \geq 1|\text{IM} = im\right] \end{aligned} \tag{25.2}$$

where D is the demand parameter and C_{LS} is the capacity associated with the given LS. Note that Y may be in the component or structure level.
In the context of performance based earthquake engineering (PBEE), where the structural responses are expressed as engineering demand parameters (EDP), the fragility can be defined as:

$$\text{Fragility} = P\left[\text{EDP} \geq edp | \text{IM} = im\right] \tag{25.3}$$

where edp is a specific threshold value of EDP.

- Fragility surface is a three-dimensional version of a fragility curve and can be expressed in one of the following ways:
  - Fragility surface with vectorized IM is a continuous function showing the probability of exceedance of a certain LS conditioned on two IM parameters. For such a system the fragility definition in Eq. 25.1 should be replaced with [134]:

$$\text{Fragility} = P\left[\text{LS} | \text{IM}_1 = im_1, \text{IM}_2 = im_2\right] \tag{25.4}$$

    The two IMs can be among un-scalable parameters, e.g. $< M_w, R_{rup} >$ (earthquake magnitude and distance), or the scalable ones, e.g. $< S_a(T_1), I_A >$ (first-mode spectral acceleration and Arias intensity) [601], Figure 25.2(a).
  - Fragility surface which is a function of an external parameter (or variable). Usually this parameter is time. The resulted fragility surface showing the time-dependent seismic behavior (aging, deterioration, creep) of the structural system. For such a system the fragility is defined as [340]:

$$\text{Fragility} = P\left[\text{LS}(t) | \text{IM} = im\right] \tag{25.5}$$

    A sample of a fragility surface for a system with the capability of aging in 30 years is plotted in Figure 25.2(b). As seen, aging reduces the capacity and increases probability of exceedance of a certain LS.
  - Fragility surface with scalar IM but for a range of LS $\in [\text{LS}_{min}, \text{LS}_{max}]$ as a continuous function. This can be used when there is a no established criterion for the LS in a new structure. Note that the governing equation in this case is again similar to Eq. 25.1 while a "*for loop*" is required on LS from LS_{min} to LS_{max}. Figure 25.2(c) shows a sample of fragility surface with varying LS that normalized based on $\frac{\text{LS}-\text{LS}_{min}}{\text{LS}_{max}-\text{LS}_{min}}$.

25.1.2 Fragility *vs.* Vulnerability *vs.* Hazard

Although the main focus of this chapter is on fragility curves, two other terms need to be clearly defined and distinguished, i.e. vulnerability curves and hazard curves:

- Vulnerability curves: Vulnerability is different from fragility [703]. The former measures loss (in terms dollars, deaths, and downtime) whereas the latter measures probability. A vulnerability curve expresses the loss as a function of the IM parameter. Three major types of vulnerability curves are:

  - Measuring repair cost: In such a case the repair cost is normalized by the replacement cost and is called damage factor. The expected value of the damage factor conditioned on IM parameter is called mean damage factor, Figure 25.1(b).
  - Measuring life-safety: In such a case the number of casualties is normalized by the number of indoor occupants and expressed as a function of the IM parameter.
  - Measuring downtime: It is measured in terms of fraction of a year during which the structure cannot be used.

- Hazard curves: It expresses a plot where the horizontal axis is the IM at a site and the vertical one is annual frequency of exceedance, λ, (inverse of the return period, T_R), Figure 25.1(c). Hazard curves are usually obtained by performing a probabilistic seismic hazard analysis (PSHA).

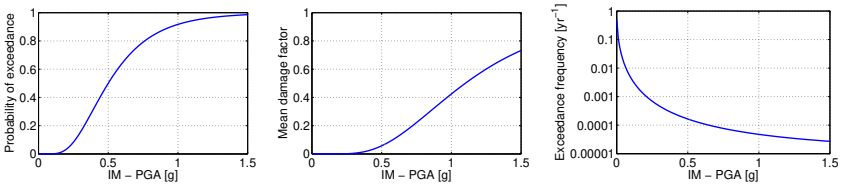

(a) Fragility curve (b) Vulnerability curve (c) Hazard curve

Fig. 25.1: Comparison of seismic fragility, vulnerability and hazard curves

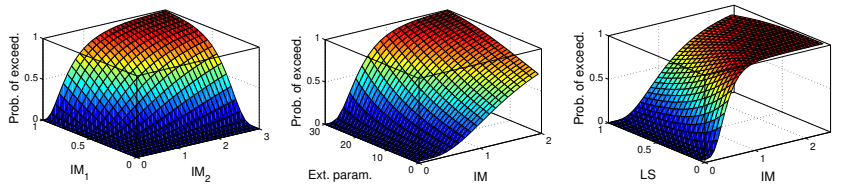

(a) Two IM parameter (b) IM + External parameter (c) IM + LS variation

Fig. 25.2: Different aspects of seismic fragility surfaces

Note that the seismic hazard curve for an IM, λ_{IM}, (result of PSHA) can be combined with the seismic fragility curve (the result of structural analysis) to obtain the mean annual frequency of exceeding a specified EDP value, λ_{EDP}, as [833]:

$$\lambda_{\text{EDP}}(edp) = \int_{im} P\left[\text{EDP} \geq edp | \text{IM} = im\right] . \left|\text{d}\lambda_{\text{IM}}(im)\right| \tag{25.6}$$

where $\mathrm{d}\lambda_{\mathrm{IM}}(im)$ is the slope of the hazard curve and the absolute value is used because the slope is negative.

25.1.3 Continuous Function *vs.* Discrete Matrix

Based on another classification, the results of a fragility analysis can be represented either as a continuous function, i.e. fragility curve or a table of discrete values, i.e. damage probability matrix (DPM) [278]:

- Single *vs.* multiple fragility curves: So far Figure 25.1(a) presented a single fragility curve based on a certain LS in Eq. 25.1 or a certain edp in Eq. 25.3. However, it is also possible to define the fragility of a structural system using multiple LSs or EDP threshold values.
  LSs are the borders between different damage states (DS) in a structure. DS has a (mainly) qualitative definition, e.g. slight damage, moderate damage, etc. However, it can be presented quantitatively using the damage index (DI) concept. For a system with N_{LS} limit states ($N_{\mathrm{LS}} = 1, 2, ...$), there are $N_{\mathrm{DS}} = N_{\mathrm{LS}} + 1$ damage states ($N_{\mathrm{DS}} = 0, 1, 2, ...$). DS_0 corresponds to the "undamaged state" and there is a one-to-one correspondence between the other LSs and DSs, i.e. LS_i and DS_i ($i = 1, 2, ...$). Figure 25.3(a) shows a set of fragility curves for a structural system with five DSs and four LSs.
  In such a condition, one of the following situations may occur:

  – DSs are in series (Sequential): In this condition, DS_i should be reached before DS_{i+1} and so on. The order does matter. The probability of being in a specific DS can be computed as:

$$P[\mathrm{DS} = ds_i|\mathrm{IM} = im] = \begin{cases} 1 - P[\mathrm{LS}_1|\mathrm{IM} = im] & i = 0 \\ P[\mathrm{LS}_i|\mathrm{IM} = im] - P[\mathrm{LS}_{i+1}|\mathrm{IM} = im] & 1 \leq i < N_{\mathrm{DS}} \\ P[\mathrm{LS}_i|\mathrm{IM} = im] & i = N_{\mathrm{DS}} \end{cases} \tag{25.7}$$

  – DSs are parallel (Simultaneous): In this condition, probability of being in one DS can be evaluated independently from the others. The order does not matter. The probability of being in a specific DS can be computed as:

$$P[\mathrm{DS} = ds_i|\mathrm{IM} = im] = \begin{cases} 1 - P[\mathrm{LS}_1|\mathrm{IM} = im] & i = 0 \\ P[\mathrm{LS}_1|\mathrm{IM} = im].P[\mathrm{DS} = ds_i|\mathrm{LS}_1] & 1 \leq i \leq N_{\mathrm{DS}} \end{cases} \tag{25.8}$$

    where $P[\mathrm{DS} = ds_i|\mathrm{LS}_1]$ is the probability that, if damaged, it is in ds_i (or others as well) [703]. Note that since the damage states are simultaneous it is possible to have $\left(\sum_{i=1}^{N_{\mathrm{DS}}} P[\mathrm{DS} = ds_i|\mathrm{LS}_1]\right) > 1.0$.

- DPM is a matrix of data showing the discrete values of DS probabilities at some specified seismic intensity levels (SIL). The columns represent the discrete SILs

and the rows are different DSs, Figure 25.3(b). Note that this DPM corresponds to the multiple fragility curves shown in Figure 25.3(a) which is extracted only for four SILs.

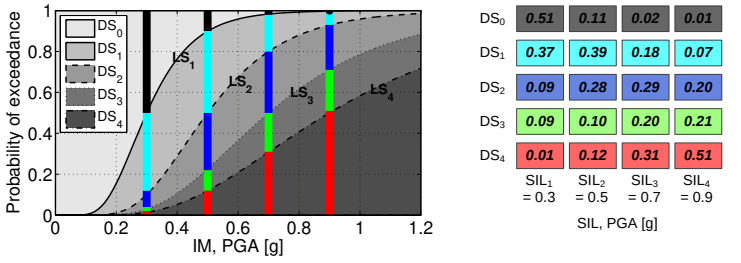

(a) Fragility curve (b) Damage probability matrix

Fig. 25.3: Relationship between fragility curve and damage probability matrix

25.1.4 Classification Based on Data Type

Fragility curves can also be classified according to the data type used in their determination [741]:

- **Empirical fragility curves** are constructed based on post-earthquake surveys which are usually the most reliable source for this purpose. The reason is that they are real world damage observations accounting for all the details of ground motion and structure characteristics. However, they lack generality and usually there is large uncertainty in their determination mainly due to inconsistency in DS definitions and different inspection techniques [612].
- **Heuristic fragility curves** are based on expert elicitation and are useful where the empirical information about damage data is very limited or when the analytical approach is difficult or impossible to practically perform. The ATC-13 [66] report is one of the most practical examples of the expert opinion-based fragility curves (in fact DPM) for the California infrastructure system (including concrete dams).
- **Analytical fragility curves** are constructed based on structural simulations and numerical analyses. Depending on the application and required accuracy of the fragility curves, different techniques may be used: 1) static or dynamic analysis, 2) linear or nonlinear, 3) with or without uncertainties in material and modeling.
- **Experimental fragility curves** can be constructed based on large- or small-scale experimental tests; however, this method is not common because it is expensive and the required data is limited [858].
- **Hybrid fragility curves** are based on a combination of the above sources. The objective is to reduce the computational effort of the analytical simulations and to compensate for the subjective bias of the expert elicitation approach [490].

25.1.5 Fragility in the Context of PBEE

The explicit determination of the performance measures (e.g. monetary losses, casualties, downtime) in a probabilistic manner accounting for all sources of uncertainty (e.g. earthquake ground motion, structural properties, damage, and loss) can be performed in the context of the Pacific Earthquake Engineering Research Center (PEER) PBEE (also known as PBEE-2). The primary steps in PEER PBEE are [700]: 1) seismic hazard analysis, 2) structural response analysis, 3) damage analysis, and 4) loss assessment. The results of each of these steps are represented as generalized variables: IM, EDP, damage measure (DM), and decision variable (DV). Based on total probability theorem, the mean annual frequency of exceedance of a DV is [80, 239]:

$$\lambda_{\text{DV}}(dv) = \int_{dm}\int_{edp}\int_{im} G_{\text{DV}|\text{DM}}[dv|dm] \left|\text{d}G_{\text{DM}|\text{EDP}}[dm|edp]\right| \left|\text{d}G_{\text{EDP}|\text{IM}}[edp|im]\right| \left|\text{d}\lambda_{\text{IM}}(im)\right| \tag{25.9}$$

where $G_{\text{X}|\text{Y}}[x|y] = P[\text{X} > x|\text{Y} = y]$ denotes the conditional complementary cumulative distribution function (CCDF) of random variable X given $\text{Y} = y$. Thus Eq. 25.9 can be rephrased as:

$$\lambda_{\text{DV}}(dv) = \int_{dm}\int_{edp}\int_{im} P[\text{DV} \geq dv|\text{DM} = dm] \text{d}P[\text{DM} \geq dm|\text{EDP} = edp] \text{d}P[\text{EDP} \geq edp|\text{IM} = im] \left|\text{d}\lambda_{\text{IM}}(im)\right| \tag{25.10}$$

As mentioned already in Eq. 25.3, the conditional probability $P[\text{EDP} \geq edp|\text{IM} = im]$ is called fragility or "demand fragility" [559]. However, to be used in the context of the PEER PBEE the fragility is defined as [702, 352]:

$$\text{Fragility} = P[\text{DM} \geq dm|\text{EDP} = edp] \tag{25.11}$$

Note that both the Eqs. 25.8 and 25.9 can be converted to a format of Eq. 25.11.

25.1.6 Treatment of Collapse (Large Data Point)

All the Eqs. 25.1, 25.2, and 25.3 were written assuming that there is no collapse or structural instability among the data points (usually resulted from analytical procedures). Should there be real collapse or numerical instability in analyses, the fragility has an alternative expression [470]:

$$P[\text{EDP} \geq edp|\text{IM} = im] = P[\text{EDP} \geq edp|\text{IM} = im, \text{NLg}] \cdot (1 - P[\text{Lg}|\text{IM} = im]) + P[\text{Lg}|\text{IM} = im] \tag{25.12}$$

where Lg and NLg are referred to "very large" and "not very large" EDPs. In some references, they corresponds to "collapse" and "non collapse" data points and are shown with C and $\bar{C}$, respectively, [719]. $P[\text{Lg}|\text{IM} = im]$ is the probability of

having a "very large" EDP for a given IM and can be computed based on the relative frequency method (RFM):

$$P\left[\text{Lg}|\text{IM}=im\right]=P\left[\text{C}|\text{IM}=im\right]=\frac{N_C}{N_T} \tag{25.13}$$

where N_C and N_T are number of demands causing collapse and total number of realizations, respectively.
Note that similar to Eq. 25.6, the mean annual frequency of collapse, $\lambda_{\text{collapse}}$, can be computed as [79]:

$$\lambda_{\text{collapse}}=\int_{im} P\left[C|\text{IM}=im\right].\left|\text{d}\lambda_{\text{IM}}\left(im\right)\right| \tag{25.14}$$

25.2 Analytical Models Based on Generalized Linear Models

In statistics, the generalized linear model (GLM) is a generalization of the linear model (linear regression) and consists of three components:

- A *random component*, specifying the conditional distribution of the response variable, y, given the values of the explanatory variables in the model. The distribution of response variable is one of the exponential family members, e.g. Gaussian, binomial, Poisson, gamma, or inverse-Gaussian.
- A *linear predictor*, γ, is a linear function of regressors.
- A smooth and invertible linearizing *link function*, $g()$, which transforms the expectation of the response variable, $\mu\equiv E(Y)$, (also mean of the distribution) to the linear predictor.

$$g(\mu)=\gamma=\theta_0+\sum_{i=1}^{n}\theta_i x_i \tag{25.15}$$

where x_i are independent variables and θ_i are coefficients.

Commonly used link functions for seismic fragility curves are summarized in Eq. 25.16. These functions are used because they are for binomial data where the LS status can be defined as 0 or 1.

$$g(\mu)=\begin{cases}\text{Probit} & \Phi^{-1}\left(\mu\right)\\ \text{Logit} & \ln\left(\mu\right)-\ln\left(1-\mu\right)\\ \text{log-log} & -\ln\left(-\ln\left(\mu\right)\right)\\ \text{Complementary log-log} & \ln\left(-\ln\left(1-\mu\right)\right)\end{cases} \tag{25.16}$$

where Φ is the cumulative distribution function (CDF) of the standard-normal distribution.
The link function is invertible, and the inverse link $g^{-1}()$ is called the *mean function*:

$$\mu = g^{-1}(\gamma) = g^{-1}\left(\theta_0 + \sum_{i=1}^{n} \theta_i X_i\right) \tag{25.17}$$

Subsequently, the inverse of the functions in Eq. 25.16 are:

$$g^{-1}(\gamma) = \begin{cases} \text{Probit} & \Phi(\gamma) \\ \text{Logit} & 1/(1+\exp(-\gamma)) \\ \text{log-log} & \exp(-\exp(-\gamma)) \\ \text{Complementary log-log} & 1-\exp(-\exp(\gamma)) \end{cases} \tag{25.18}$$

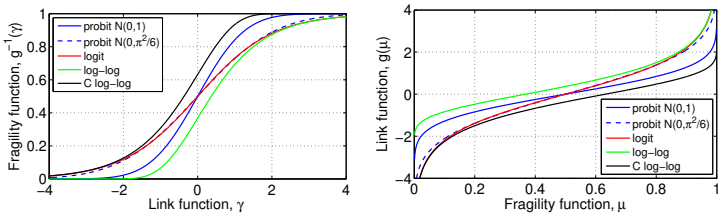

(a) $g^{-1}(\gamma)$ (b) $g(\mu)$

Fig. 25.4: Link functions for binomial data and their relationship

Note that in the context of seismic fragility curves, a single independent variable, x_1, is used with two coefficients which represent the slope and the intercept of the linear model. The independent variable, x_1, is assumed to be an IM parameter, and μ is the probability of the LS exceeding (fragility itself). The two common forms of Eq. 25.15 for the seismic fragility curves are: $\theta_0 + \theta_1 \text{IM}$ (simple linear form) and $\theta_0 + \theta_1 \ln(\text{IM})$ (Logarithmic form) [465]. Combining these two forms with those four link functions in Eq. 25.16 provides at least eight possible seismic fragility curve representations. Four out of eight representations (which are mentioned already in the literature [520]) in the form of Eq. 25.3 are summarized here:

- Probit GLM with logarithmic IM form [183]:

$$\begin{aligned} \Phi^{-1}\left(P\left[\text{EDP} \geq edp | \text{IM} = im\right]\right) &= \theta_0 + \theta_1 \ln(im) \Rightarrow \\ P\left[\text{EDP} \geq edp | \text{IM} = im\right] &= \Phi\left(\theta_0 + \theta_1 \ln(im)\right) \end{aligned} \tag{25.19}$$

- Logit GLM with linear IM form [668]:

$$\begin{aligned} \ln\left(\frac{P\left[\text{EDP} \geq edp | \text{IM} = im\right]}{1 - P\left[\text{EDP} \geq edp | \text{IM} = im\right]}\right) &= \theta_0 + \theta_1(im) \Rightarrow \\ P\left[\text{EDP} \geq edp | \text{IM} = im\right] &= \frac{\exp\left(\theta_0 + \theta_1(im)\right)}{1 + \exp\left(\theta_0 + \theta_1(im)\right)} \end{aligned} \tag{25.20}$$

- Logit GLM with logarithmic IM form:

$$\ln\left(\frac{P\left[\text{EDP} \geq edp|\text{IM} = im\right]}{1 - P\left[\text{EDP} \geq edp|\text{IM} = im\right]}\right) = \theta_0 + \theta_1 \ln\left(im\right) \Rightarrow$$
$$P\left[\text{EDP} \geq edp|\text{IM} = im\right] = \frac{\exp\left(\theta_0 + \theta_1 \ln\left(im\right)\right)}{1 + \exp\left(\theta_0 + \theta_1 \ln\left(im\right)\right)} = \frac{e^{\theta_0} im^{\theta_1}}{1 + e^{\theta_0} im^{\theta_1}} \tag{25.21}$$

- Complementary log-log GLM with logarithmic IM form:

$$\ln\left(-\ln\left(1 - P\left[\text{EDP} \geq edp|\text{IM} = im\right]\right)\right) = \theta_0 + \theta_1 \ln\left(im\right) \Rightarrow$$
$$P\left[\text{EDP} \geq edp|\text{IM} = im\right] = 1 - \exp\left(-\exp(\theta_0 + \theta_1 \ln\left(im\right))\right) = 1 - e^{-e^{\theta_0} im^{\theta_1}} \tag{25.22}$$

25.3 Analytical Models Based on Lognormality Assumption

Among different models, lognormal CDF is the form most often used to define a fragility function. There are two rules to present the fragility curves based on the lognormal model, i.e. 1) IM-based rule and 2) EDP-based rule.

25.3.1 IM-based Rule

In this condition, Eq. 25.1 can take the following form [255]:

$$P\left[\text{LS}|\text{IM} = im\right] = \Phi\left(\frac{\ln(im) - \ln(\eta_{im_{\text{LS}}})}{\beta_{im_{\text{LS}}}}\right) \tag{25.23}$$

where $\eta_{im_{\text{LS}}}$ and $\beta_{im_{\text{LS}}}$ are the median LS intensity and the corresponding logarithmic standard deviation (also called dispersion), respectively. Note that $\beta_{im_{\text{LS}}}$ is also shown as $\sigma_{\ln(im_{\text{LS}})}$ which is the standard deviation of the natural logarithms of the LS intensity.
Mathematically, the standard-normal CDF is represented in one of the following forms:

$$\Phi\left(t\right) = \frac{1}{\sqrt{2\pi}} \int_{-\infty}^{t} \mathrm{e}^{-u^2/2} \mathrm{d}u$$
$$\Phi\left(t\right) = \frac{1}{2}\left(1 + \text{erf}\left(\frac{t}{\sqrt{2}}\right)\right) \tag{25.24}$$

where $\text{erf}\left(t\right) = \frac{1}{\sqrt{\pi}} \int_{-t}^{+t} \mathrm{e}^{-u^2} \mathrm{d}u$ is the error function and is defined as the probability of a random variable with normal distribution of mean 0 and variance 1/2 falling in the range $[-t, t]$.

Combination of Eqs. 25.23 and 25.24 gives:

$$P\left[\text{LS}|\text{IM}=im\right]=\int_{0}^{im}\frac{1}{\sqrt{2\pi}\,.\,\beta_{im_{\text{LS}}}\,.\,im}\exp\left[-\frac{(\ln(im)-\eta_{im_{\text{LS}}})^{2}}{2\beta_{im_{\text{LS}}}^{2}}\right]\text{d}\,im \tag{25.25}$$

In the same way, the lognormal-based fragility curve for Eq. 25.3 can be written as:

$$P\left[\text{EDP}\geq edp|\text{IM}=im\right]=\Phi\left(\frac{\ln(im)-\ln(\eta_{im_{edp}})}{\beta_{im_{edp}}}\right) \tag{25.26}$$

Finally, note that Eq. 25.26 is the other form of Eq. 25.19 assuming $\theta_0=-\frac{\ln(\eta)}{\beta}$ and $\theta_1=\frac{1}{\beta}$.

25.3.2 EDP-based Rule

In this condition, Eq. 25.3 can take the following form [468]:

$$P\left[\text{EDP}\geq edp|\text{IM}=im\right]=1-\Phi\left(\frac{\ln(edp)-\ln(\eta_{\text{EDP}|\text{IM}=im})}{\beta_{\text{EDP}|\text{IM}=im}}\right) \tag{25.27}$$

where $\eta_{\text{EDP}|\text{IM}=im}$ and $\beta_{\text{EDP}|\text{IM}=im}$ are the median value and the logarithmic standard deviation of EDP given IM.
Combination of Eqs. 25.27 and 25.24 gives:

$$P\left[\text{EDP}\geq edp|\text{IM}=im\right]=1-\int_{0}^{edp}\frac{1}{\sqrt{2\pi}\,.\,\beta_{\text{EDP}|\text{IM}=im}\,.\,edp}\exp\left[-\frac{1}{2}\left(\frac{\ln(edp)-\ln(\eta_{\text{EDP}|\text{IM}=im})}{\beta_{\text{EDP}|\text{IM}=im}}\right)^{2}\right]\text{d}\,edp \tag{25.28}$$

Last but not least, two questions arise: 1) how can one obtain the empirical data points to be used for fragility analysis? and 2) how can one estimate the parameters in Eqs. 25.26 and 25.27 properly? The next section will discuss different nonlinear analysis techniques to get the data points and also data fitting.

25.4 Analysis Techniques and Data Fitting

25.4.1 Incremental Dynamic Analysis (IDA)

In this method, each ground motion is scaled successively to multiple IM levels and the maximum EDP is computed at each scale level [849]. The IDA curve connects the resulting EDPs corresponding to each ground motion, usually based on the spline fitting [850]. Using IDA results, the percentiles of response can be calculated as continuous curves, e.g., the median IDA curve or the 16th and 84th fractile IDA curves.

This is a famous method because the researchers are usually interested in collapse probability of structures and IDA guarantees the collapse of the structures at higher intensities. However, scaling the ground motions may lead to generating records with a non-realistic shape, which in turn implies that the shape of the records should be considered Haselton et al. [404].
Thus, the focus will be on calculating $P\,[\text{C}|\text{IM} = im]$. Three approaches can be used: 1) EDP capacity based with full IDA results, 2) IM capacity based with full IDA results, and 3) IM capacity based with truncated IDA results. The only difference between the full and truncated IDA methods is that in the former, all the ground motions are incrementally scaled up to collapse of the structure, while in the latter there is a limitation in scaling ground motion to no more than IM_{trunc}. Thus, some of the scaled ground motions may not lead to collapse.

- EDP capacity based with full IDA: First, a full IDA is performed and the IDA curves are plotted, Figure 25.5(a). In this approach, the structure is assumed to be collapsed when the EDP demand, EDP_d, exceeds the EDP capacity, EDP_c [906]:

$$P[\text{C}|\text{IM} = im] = P[\text{EDP}_d \geq \text{EDP}_c|\text{IM} = im] = \sum_{\text{all } edp_c} P[\text{EDP}_d \geq \text{EDP}_c|\text{EDP}_c = edp_c, \text{IM} = im]P[\text{EDP}_c = edp_c] \tag{25.29}$$

  where the first term inside the summation sign is the probability that the demand exceeds a specific capacity value, edp_c, at IM = im and the second term is the probability that capacity is equal to edp_c.
  Figure 25.5(a) shows the EDP capacity points for different records, as well as the EDP demand at two specific IM levels. Then, for each IM (low to high) the probability of collapse is computed, Eq. 25.29, and plotted as a cumulative histogram. A log-normal CDF can be fitted to the empirical collapse points.
- IM capacity based with full IDA: After performing IDA, the approximate IM collapse capacity, IM_{cap}, is tagged as an asymptotic point on each IDA curve, Figure 25.5(b). The probability of collapse is:

$$P[\text{C}|\text{IM} = im] = P[\text{IM}_{cap} < \text{IM} = im] \tag{25.30}$$

  The empirical fragility is computed simply by Eq. 25.13 at each IM_{cap} level. A log-normal CDF, Eq. 25.23, can be fitted to the collapse data point. Subsequently, the median and logarithmic standard deviation can be estimated by one of the following methods:

  – Method of Moments (MM) seeks $\hat{\eta}$ and $\hat{\beta}$ in a way that the resulting log-normal distribution has the same moments (mean and standard deviation) as the collapse data points:

$$\hat{\eta} = \exp\left(\frac{\sum_{i=1}^{N_T} \ln(\text{IM}_{cap_i})}{N_T}\right),$$
$$\hat{\beta} = \sqrt{\frac{\sum_{i=1}^{N_T} \left(\ln\left(\text{IM}_{cap_i}\right) - \ln\left(\hat{\eta}\right)\right)^2}{N_T - 1}} \tag{25.31}$$

where N_T is total number of ground motions and superscript $\hat{-}$ refers to an estimated value.

– Maximum Likelihood Estimation (MLE) seeks the parameters in a way to maximize a "likelihood function." For the readers not familiar with the MLE concept, assume a generic form of an n-dimensional random vector, $\mathbf{U}$, with probability density function (PDF) $f\left(\mathbf{u} \mid \theta\right)$. Assuming $\mathbf{U}$ is independent and identically distributed (iid) observations, the PDF can be written as $f\left(\mathbf{u} \mid \theta\right) = f\left(u_1 \mid \theta\right) \times f\left(u_2 \mid \theta\right) \times ... \times f\left(u_n \mid \theta\right)$. Further, it is assumed that θ is a fixed and unknown constant. The "complete-data likelihood function" of θ is defined as:

$$\mathcal{L}(\theta\,;\,\mathbf{u}) = f(\mathbf{u} \mid \theta) = \prod_{i=1}^{n} f(u_i \mid \theta) \tag{25.32}$$

where $\mathbf{u}$ is assumed to be fixed and θ is the variable for $\mathcal{L}$. In practice, it is convenient to work with the logarithmic version of 25.32. The "average log-likelihood function" is then $\ell = \frac{1}{n} \ln \mathcal{L}$. The MLE method estimates $\hat{\theta}$ by maximizing $\ell(\theta\,;\,\mathbf{u})$:

$$\{\hat{\theta}\} = \underset{\hat{\theta}}{argmax}\ \ell(\theta\,;\,\mathbf{u}) = \underset{\hat{\theta}}{argmax}\ \frac{1}{n}\sum_{i=1}^{n} \ln\left(f(u_i \mid \theta)\right) \tag{25.33}$$

In the case of N_T seismic data, it is assumed that the observation of each ground motion is either collapsed or safe and also is independent of the other ground motions. Thus, Eq. 25.33 takes the following form:

$$\left\{\hat{\eta}, \hat{\beta}\right\} = \underset{\hat{\eta},\hat{\beta}}{argmax}\ \ell(\eta, \beta\,;\,\mathbf{IM}_{cap}) =$$
$$\underset{\hat{\eta},\hat{\beta}}{argmax} \sum_{i=1}^{N_T} \ln\left\{\phi\left(\frac{\ln(\text{IM}_{cap_i}) - \ln(\eta)}{\beta}\right)\right\} \tag{25.34}$$

Note that Eq. 25.34 has an analytical solution, where the $\hat{\eta}$ is exactly same as Eq. 25.31, while for the $\hat{\beta}$, the $(N_T - 1)$ should be replaced with N_T.

- IM capacity based with truncated IDA: First IM_{trunc} is selected and then the truncated IDA is performed. The IM_{cap} and the number of ground motions leading to failure, N_C, are defined, Figure 25.5(c). The probability of collapse can be computed based on Eq. 25.30. Considering that the collapse data are

incomplete (censored), the method of moments, Eq. 25.31, can not be used for data fitting. The alternative method is:

– Maximum Likelihood Estimation with Censored Data (MLECD) can be used for fitting the type I censored data. Assume during the T hours of a test with n samples, there are r observed failures with the (exact) failure times as $t_1, t_2, ..., t_r$. Thus, there are $(n - r)$ samples that survived the entire T-hour test without failing. This type of censoring is also called "right censored data" since the failure times to the right are missing. The "censored likelihood function" for such a system is defined as:

$$\mathcal{L}(\theta\,;\,\mathbf{t}\,,T) = c_0 \left(\prod_{i=1}^{r} f(t_i \mid \theta) \right) (1 - F(T \mid \theta))^{n-r} \tag{25.35}$$

where $F(t)$ is the CDF of $f(t)$ and c_0 is a constant that has no effect in MLE process.
In the same way, the "censored likelihood function" for truncated IDA can be written as:

$$\mathcal{L}(\eta\,,\beta\,;\,\mathbf{IM}_{cap}\,,\mathrm{IM}_{trunc}) = \left(\prod_{i=1}^{N_C} \phi \left(\frac{\ln(\mathrm{IM}_{cap_i}) - \ln(\eta)}{\beta} \right) \right) \tag{25.36}$$

$$\left(1 - \Phi \left(\frac{\ln(\mathrm{IM}_{trunc}) - \ln(\eta)}{\beta} \right) \right)^{N_T - N_C} \tag{25.37}$$

Again, similar to Eqs. 25.33 and 25.34 it is easier to maximize the logarithm of the censored likelihood function. The estimated parameters will be [79]:

$$\begin{aligned} \left\{ \hat{\eta}, \hat{\beta} \right\} = \underset{\hat{\eta},\hat{\beta}}{argmax} \sum_{i=1}^{N_C} \left\{ \ln \phi \left(\frac{\ln(\mathrm{IM}_{cap_i}) - \ln(\eta)}{\beta} \right) \right\} \\ + (N_T - N_C) \ln \left(1 - \Phi \left(\frac{\ln(\mathrm{IM}_{trunc}) - \ln(\eta)}{\beta} \right) \right) \end{aligned} \tag{25.38}$$

25.4.2 Multiple Stripe Analysis (MSA)

Instead of selecting a fixed set of ground motions and scaling them (i.e., IDA), the analyses can be performed in several discrete SILs. Having three or more SILs in this new method is called multiple stripe analysis (MSA) [215]. If the analyses are performed for one or two stripes, the method is called single stripe analysis (SSA) and double stripe analysis (DSA), respectively. Some important points in MSA are:

- The intervals between two sequential SILs are not necessarily identical. For example in Figure 25.6(a), the distance between SIL_2 and SIL_3 and also between SIL_6 and SIL_7 is more than others. The reason can be attributed to the desired frequency of exceedance for the project/analyzer.

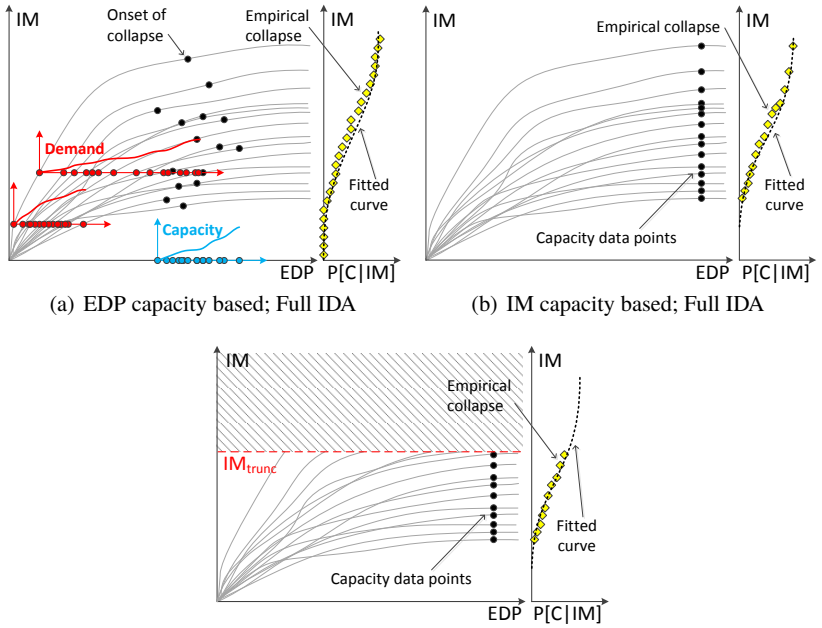

(a) EDP capacity based; Full IDA

(b) IM capacity based; Full IDA

(c) IM capacity based; Truncated IDA

Fig. 25.5: Conceptual collapse fragility curves based on IDA method

- The number of ground motions in each stripe can be different from the others.
- The selected ground motions in each stripe may be different from other stripes, especially when the conditional spectrum is used to select the ground motions.
- The number of selected SILs is optional. Increasing the number of SILs, increases the accuracy of future curve fitting. In Figure 25.6(a), the analyses are performed only for 8 SIL, while it can be extended up to collapse of all ground motions (this is computationally demanding).
- The empirical collapse in each SIL can be obtained using Eq. 25.13.
- Considering different ground motions in each stripe, the empirical collapse for SIL_i may be equal to or more than SIL_{i+1}. In Figure 25.6(a), SIL_4 leads to a higher empirical collapse than SIL_5. Also, the number of collapse data points in SIL_7 and SIL_8 are equal.

One of the following three methods can be used to estimate the median and logarithmic standard deviation:

- Sum of Squared Error (SSE) tries to minimize the sum of squared error between the observed fractions of collapse data and probabilities predicted by the fragility function:

$$\left\{\hat{\eta},\hat{\beta}\right\} = \underset{\hat{\eta},\hat{\beta}}{argmin} \sum_{i=1}^{m} \left(\frac{N_{C_i}}{N_{T_i}} - \Phi\left(\frac{\ln(im_i) - \ln(\eta)}{\beta}\right)\right)^2 \tag{25.39}$$

where N_{C_i} and N_{T_i} are number of collapsed data and total ground motions at level IM $= im_i$, and m is the number of IM levels. Note that $\frac{N_{C_i}}{N_{T_i}}$ is similar to that showed in Eq. 25.13.

- Maximum Likelihood Estimation (MLE) can be used assuming that the collapse and non-collapse data at each SIL are independent. In such a case the binomial distribution assumption is valid. Recall that the PDF for the binomial distribution with parameter p is $\binom{u}{v} p^v (1-p)^{u-v}$ where v is successes in u trials. Substituting in Eq. 25.32, the "likelihood function" for this system is defined as:

$$\mathcal{L}(p\,;\,\mathbf{u}\,,\,\mathbf{v}) = \prod_{i=1}^{m} \binom{u_i}{v_i} p_i^{v_i} (1-p_i)^{u_i - v_i} \tag{25.40}$$

In the same way, the "likelihood function" for the MSA can be written in the form of Eq. 25.41 considering that p (in Eq. 25.40) is the probability of collapse for a ground motion at IM = im_i.

$$\mathcal{L}(\eta\,,\beta\,;\,\mathbf{IM}\,,\,\mathbf{N_T}\,,\,\mathbf{N_C}) = \prod_{i=1}^{m} \binom{N_{T_i}}{N_{C_i}} \Phi\left(\frac{\ln(im_i) - \ln(\eta)}{\beta}\right)^{N_{C_i}} \left(1 - \Phi\left(\frac{\ln(im_i) - \ln(\eta)}{\beta}\right)\right)^{N_{T_i} - N_{C_i}} \tag{25.41}$$

Again, similar to Eq. 25.33 it is easier to maximize the logarithm of the likelihood function. The estimated parameters will be [79]:

$$\left\{\hat{\eta},\hat{\beta}\right\} = \underset{\hat{\eta},\hat{\beta}}{argmax} \sum_{i=1}^{m} (\ln\binom{N_{T_i}}{N_{C_i}} + N_{C_i} \ln\left(\Phi\left(\frac{\ln(im_i) - \ln(\eta)}{\beta}\right)\right) + (N_{T_i} - N_{C_i}) \ln\left(1 - \Phi\left(\frac{\ln(im_i) - \ln(\eta)}{\beta}\right)\right)) \tag{25.42}$$

- Linear Regression in Transferred Space (LRTS) or Method B in Porter, Kennedy, and Bachman [702]: As it is stated already, in MSA the ground motions are selected in stripes to have (almost) identical IM, Figure 25.6(a). The primary option for IM in different structures is $S_a(T_1)$. However, sometimes it is required to present the results based on an alternative IM called IM′. In such a case, the data points do not rest on the specific stripes and they spread in the space, Figure 25.6(b). Thus, SSE and MLE are not applicable any more. In this case, LRTS can be used as summarized in the following steps:
  - For all the data points (i.e. collapse and non-collapse), O_i, identify the corresponding IM'_i value.

- Assuming the total number of data points to be M, divide them into N bins, where $N = \left\lfloor \sqrt{M} \right\rfloor$. Each bin should have an approximately equal number of data points. Porter, Kennedy, and Bachman [702] recommend the minimum M to be 25.
- For each bin j determine the exact number of data points, M_j, the mean intensity measure, $\overline{\text{IM}'}_j$, and the number of collapse data points, m_j. Thus,

$$\overline{\text{IM}'}_j = \frac{1}{M_j} \sum_{k=1}^{M_j} \text{IM}'_j \; ; \quad M = \sum_{i=1}^{N} M_j \tag{25.43}$$

- Determine the X and Y coordinates as:

$$X_j = \ln\left(\overline{\text{IM}'}_j\right) \; ; \quad Y_j = \Phi^{-1}\left(\frac{m_j + 1}{M_j + 1}\right) \tag{25.44}$$

- Fit a line, $\hat{Y} = A_1 X + A_0$, to the data points, $\langle X_j, Y_j \rangle$, using the least-squares approach, and estimate the slope, A_1, and the intercept, A_0.
- Determine the random logarithmic standard deviation, β, and the median, η, as:

$$\beta = \frac{1}{A_1} \; ; \quad \eta = \exp\left(-\frac{A_0}{A_1}\right) \tag{25.45}$$

  Having these two parameters, a lognormal fragility curve can be plotted, Figure 25.6(b).

25.4.3 Cloud Analysis (CLA)

CLA is a procedure in which the structure is subjected to a (relatively large) set of (unscaled or as-recorded) ground motions and is analyzed numerically. If the ground motion records are taken from a bin, they can represent an earthquake scenario defined by (M_{bin}, R_{bin}), the magnitude and distance representative of the bin [468]. Then from the results, EDP *vs.* IM are determined and form the so-called cloud response. CLA method is usually used in conjunction with probabilistic seismic demand analysis (PSDA). It is a well-accepted assumption that the discrete data points resulted from CLA have a linear trend in the logarithmic scale implying a power form in the arithmetic scale [674, 471, 720]:

$$\eta_{\text{EDP|IM}} = a.\text{IM}^b \tag{25.46}$$

where a and b are the regression constants and $\eta_{\text{EDP|IM}}$ is the median value of EDP given IM. Also, the logarithmic standard deviation is:

$$\beta_{\text{EDP|IM}} = \sigma_{\ln(\text{EDP|IM})} \cong \sqrt{\frac{\sum \left(\ln(edp_i) - \ln\left(a.\text{IM}^b\right)\right)^2}{n-2}} \tag{25.47}$$

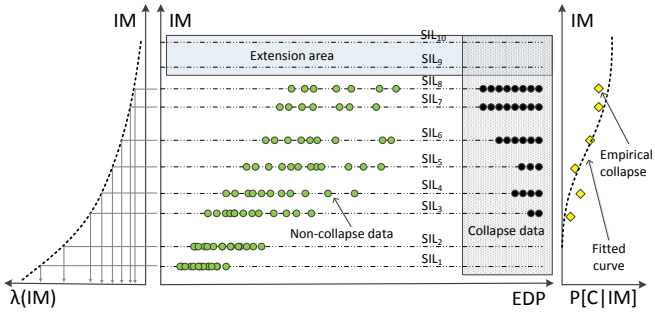

(a) Based on primary IM

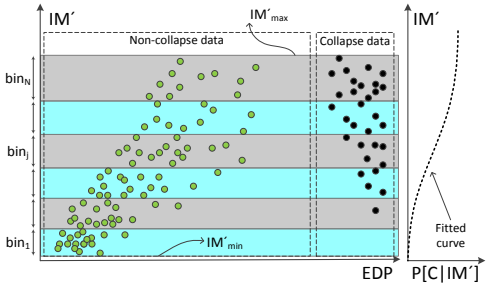

(b) Based on alternative IM′

Fig. 25.6: Conceptual collapse fragility curves based on MSA method

where n is the number of nonlinear transient analyses.

Chapter 26
Damage Index

Abstract
The performance of the infrastructures subjected to internal or external loading should be a property quantified to be used in the context of performance based engineering. Quantification of the potential damage due to earthquakes has the utmost importance. Seismic damage indices (DI) are widely used for this purpose. Having a comprehensive list of DIs, one may derive any type of fragility function. The objective of this chapter is to propose a series of mass and reinforced concrete structure-related damage indices and the corresponding damage states.

26.1 Damage Index for RC Structures

Given the lead taken by the building industry in spearheading PBEE [352], this section will start by reviewing work done in this field.

26.1.1 Damage Index vs. Damage Variable

In general, damage in concrete or reinforced concrete can be attributed to irrecoverable (inelastic) deformations. First one differentiates between *damage variable* (DV) and *damage index*. Any structural response that can be used as an indicator of damage is designated DV. Examples include: plastic deformation, energy dissipation, low cycle fatigue of element, and changes in vibrational parameter of structure. On the other hand, damage index is a quantity set to zero in the absence of any damage and unity when failure or collapse occurs. A DI can be combination of one or several DVs [489]. Figure 26.1(a) illustrates the DI as a function of only one DV. DI is zero at $DV \leq DV_0$, and its value is one at $DV = DV_u$ where the structure has failed. In fact, DV_0 and DV_u are the lower and upper boundaries (threshold) of the damage variable. Once the initial and the end points are determined, an appropriate function should be derived between the damage index and damage variable. The shape of this function should be defined based on experimental tests. The general format of this function can be [489]:

$$DI = \left(\frac{DV - DV_0}{DV - DV_u} \right)^{\kappa} \tag{26.1}$$

where κ is an exponent related to the rate of the changes in damage index at different stages of the damage variable.
If the DI is a function of more than one DV, e.g. two variables as DV^1 and DV^2, it can be shown that the DI function will be given by:

$$DI = \left(\frac{DV^1 - DV_0^1}{DV^1 - DV_u^1}\right)^{\kappa_1} \times \left(\frac{DV^2 - DV_0^2}{DV^2 - DV_u^2}\right)^{\kappa_2} \tag{26.2}$$

where κ_1 and κ_2 are the exponents associated with the rate of the changes of the respective damage indices. Figures 26.1(b) and 26.1(c) show the relationship between the DI and two DVs where κ_1 and κ_2 are both larger than one or both smaller than one.

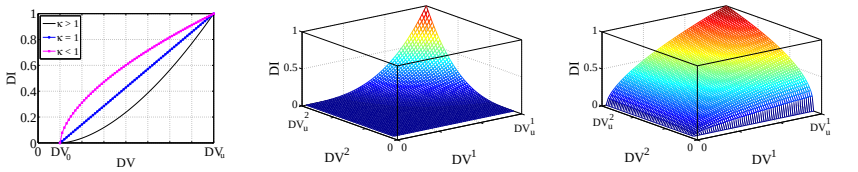

(a) $DI = f(DV)$ (b) $DI = f(DV^1, DV^2)$, κ_1, $\kappa_2 > 1$ (c) $DI = f(DV^1, DV^2)$, κ_1, $\kappa_2 < 1$

Fig. 26.1: Relationship between damage variable and damage index

26.1.2 Classification of Damage Index

The following is a review and summary of damage indices for reinforced concrete structures.

- Deformation-based, non-cumulative, local index [706]:

$$DI_\mu = \frac{\Delta_{max} - \Delta_y}{\Delta_{mon} - \Delta_y} = \frac{\mu - 1}{\mu_{mon} - 1} \tag{26.3}$$

  where Δ_{max} = maimum deformation, Δ_y = yield deformation, Δ_{mon} = maximum deformation under monotonically increasing lateral deformation, $\mu = \Delta_{max}/\Delta_y$, and $\mu_{mon} = \Delta_{mon}/\Delta_y$.
- Drift-based, non-cumulative, global index:

$$DI_\Delta = \frac{\Delta_{max}^t}{H^t} \tag{26.4}$$

  where Δ_{max}^t = maximum drift at the target point and H^t = corresponding structural height.
- Displacement-based, cumulative index [82]:

$$DI_{NCR} = \frac{\sum_{i=1}^{n} |(\theta_{max})_i - \theta_y|}{\theta_y} \tag{26.5}$$

where $(\theta_{max})_i$ = maximum rotation in cycle i, θ_y = yield value, and n = number of cycles.

- Force-based, cumulative index [869]:

$$DI_D = 1 - \frac{F_y}{F_{max}} \tag{26.6}$$

where F_y = failure force during a loading cycles, and F_{max} = maximum force during previous cycle.

- Hysteretic energy-based index [220]:

$$DI_{E_H} = \frac{E_H}{E_{H\,mon}} \tag{26.7}$$

where E_H = non-recoverable dissipated hysteretic energy and $E_{H\,mon}$ = hysteretic energy capacity of the structure obtained from pushover analysis.

- Multi-variable Park-Ang index [683]:

$$DI_{P-A} = \frac{\Delta_{max}}{\Delta_{mon}} + \beta \frac{E_H}{F_y \Delta_{mon}} \tag{26.8}$$

where F_y = yield strength and $\beta \geq 0$ is a constant that depends on the structural characteristics and history of inelastic response and is obtained by experimental test.

- Multi-variable modified Park-Ang index [517]:

$$DI_{P-A}^{modified} = \frac{\varphi_{max} - \varphi_y}{\varphi_u - \varphi_y} + \beta \frac{\int dE}{M_y \varphi_u} \tag{26.9}$$

where φ_u = ultimate curvature, φ_y = curvature at failure point, φ_{max} = curvature corresponding to the maximum bending moment, M_y = bending moment at failure, and dE = incremental dissipated hysteretic energy.

- Global index based on the modal parameters of the structure [247, 248]:

$$\begin{cases} DI_{max} = 1 - \frac{T_{UD}}{T_{max}} & \text{maximum softening} \\ DI_{pl} = 1 - \frac{T_D^2}{T_{max}^2} & \text{plastic softening} \\ DI_F = 1 - \frac{T_{UD}^2}{T_D^2} & \text{final softening} \end{cases} \tag{26.10}$$

where T_{UD} = period of the undamaged structure, T_D = period of the damaged structure, and T_{max} = natural period corresponding to the maximum softening.

- Damage spectra [146]:

$$\begin{cases} DI^1_{B-B} = \left[\frac{(1-\alpha_1)(\mu-\mu_e)}{(\mu_{mon}-1)}\right] + \alpha_1 \left(\frac{E_H}{E_{H\,mon}}\right) \\ DI^2_{B-B} = \left[\frac{(1-\alpha_2)(\mu-\mu_e)}{(\mu_{mon}-1)}\right] + \alpha_2 \sqrt{\left(\frac{E_H}{E_{H\,mon}}\right)} \end{cases} \tag{26.11}$$

where $\mu_e = \Delta_{elastic}/\Delta_y$ = elastic ductility, $\mu_e = 1$ for inelastic behavior, $\mu_e = \mu$ if the response remains elastic, and $0 \leq \alpha_1 \leq 1$ and $0 \leq \alpha_2 \leq 1$ are two constant coefficients.

Damage indices can be classified based on different applications as:

- Local vs. Global: Local DI is an indicator of damage in an element, member, or limited part of the structure. The global DI on the other hand captures damage state in an entire structure. The global DI can be computed by weighted summation of the local DIs.
- Single-variable vs. Multi-variable: As shown in Figure 26.1, the DI can be computed either from a single variable or from a combination of several ones. Usually a combined DI takes into account different parameters and provides a more comprehensive indicator of the damage progress.
- Cumulative vs. Non-cumulative: A cumulative DI is capable of capturing the accumulation of the damage during the transient analysis whereas a non-cumulative one can only capture the end state.
- Deterministic vs. Stochastic: As all materials are heterogeneous, the DI may or may not capture this heterogeneity through stochastic or deterministic expressions.
- Damage index vs. Damage spectrum: Damage spectrum represents variation of the damage index versus the structural period for a series of single-degree-of-freedom systems subjected to a ground motion record [146].
- Structural vs. Economical: A structural DI captures the damage in terms of structural parameters. On the other hand, an economical DI would introduce concepts of cost such as the ratio of repair cost to corresponding replacement cost.

26.2 Damage Index for Gravity Dams

In order to define a damage index for gravity dams, first the failure mechanism should be investigated, Figure 26.2. As seen, under normal water level and imposed ground motion, there are some critical locations in a dam where cracking may start. They are: (A) neck area at the change of downstream face slope; (B) along lift joints at various elevations; (C) along dam-foundation interface at the toe and heel of dam; and (D) horizontal, vertical or inclined cracking at the foundation in near-field of the dam. It should be emphasized the main source of nonlinearity stems from the rock-concrete interface. Hence, in practice there is no need to consider the far-field of the foundation in potential failure mode analysis of the dam body.
Based on the summary of the damage indices reviewed in the previous section, a cumulative multi-variable damage index is introduced for concrete gravity dams. This DI will handle local, intermediate, and global states. The controlling variables

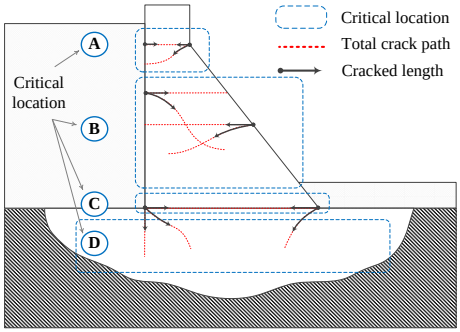

Fig. 26.2: Potential failure mechanism of a typical gravity dam, critical locations and crack paths

in the proposed damage index are crack length L^C, dissipated energy E_H, and maximum drift u_{max}.

$$DI = f\left(L^C, E_H, u_{max}\right) \tag{26.12}$$

The dam structural integrity will be assumed to reach unity (critical) when a thorough crack (connecting upstream and downstream faces) occurs. Hence, a micro damage index for each of the critical locations shown in Figure 26.2 is defined as the weighed ratio of cracked length over the estimated total crack path:

$$DI_i^j = \beta_\Delta \times \frac{L_i^C}{L_i^T} \tag{26.13}$$

where $DI_i^j \in [0,1]$ is a micro damage index where i and j refer to the ith crack path in the jth critical location and $j = A, B, C, D$ shown in Figure 26.2. The L^C and L^T are the cracked and total lengths, respectively. The β_Δ is the controlling coefficient which is computed based on the index point's displacement.

It is noteworthy that the DI is a post-analysis quantity which is determined from the controlling damage variables obtained from nonlinear analysis. Definition of the L^T deserves special attention. There are two possibilities, i.e. either the thorough crack pre-exists or the section is initially partially cracked. In the former case, the length of L^T is deterministic as it can be accurately quantified. In the latter, it is estimated based on Figure 26.2 and accounting for the fact that a crack will always propagate such that there is minimum energy dissipation. In those cases where the crack abruptly changes its path, then Eq. 26.13 would lead to conservative results.

Moreover, the case of a thorough crack across the concrete dam deserves special attention. Whereas at first one may conclude that a thorough crack (upstream-downstream) is indeed synonymous with failure, this is not necessarily the case. Indeed a thorough crack where the upper segment did not overturn is indicative of severe damage but not failure. Conceptually, this is akin to a dam resting on a con-

crete foundation with a contact surface providing shear resistance through friction exclusively.

For example, the 109 m high Sefidrud concrete buttress dam suffered a thorough crack during the devastating 1990 Manjil earthquake, and the dam was subsequently repaired and strengthened [330]. Examples of seismic analysis of a dam with concrete thorough crack include Ghaemmaghami and Ghaemian [329] and Malla and Wieland [562]. In both cases, analysis starts with a fully developed crack from upstream to downstream. Accordingly, a dam may have a thorough crack ($\frac{L^C}{L^T} = 1$), yet there is no (or minimal) sliding, u_{max}, compared to what may be perceived as an unacceptable one, u_{ult}, which is selected based on the location of the index point and the type of the predicted failure. This is addressed through the coefficient β_Δ,

$$\beta_\Delta = \begin{cases} \Gamma & |DR| < DR_{limit} \\ 1.00 & |DR| \geq DR_{limit} \end{cases} \tag{26.14}$$

where $0.9 < \Gamma < 1.0$ is the reduction factor, and the drift ratio (DR) is simply defined as

$$DR = \frac{u_{max}}{H_{dam}} \times 100\% \tag{26.15}$$

In RC structures, the limit drift ratio is usually around 5% [52]. Based on the authors' experience, it is estimated that for gravity dams this ratio should not exceed $\simeq 0.1\%$ (DR of 0.188% and 0.088% have been reported by Ellingwood and Tekie [266] and Zhong et al. [915] respectively). It is determined by simply subtracting the linear response from the nonlinear one under near-collapse intensity earthquake.

Next, this DI is expanded based on the dissipated energy at the system during the damage process. The dissipated energy due to inelastic action and damage, E_H, can be evaluated [838]:

$$E_H = E_I - E_K - E_D - E_E \tag{26.16}$$

where E_I is the energy imparted to the system by the dynamic motion of the ground, E_K the stored kinetic energy, E_D the energy dissipated by damping, and E_E elastic strain energy. Those are given by

$$E_I = \int \mathbf{U}_t^T \cdot \mathbf{M} \cdot d\mathbf{U}_g + \int \mathbf{S} \cdot \mathbf{P} \cdot d\mathbf{U} + \int \mathbf{f}_{ext}^T \cdot d\mathbf{U} \tag{26.17}$$

$$E_K = \frac{1}{2}\dot{\mathbf{U}}_t^T \cdot \mathbf{M} \cdot \dot{\mathbf{U}}_t \tag{26.18}$$

$$E_D = \int \dot{\mathbf{U}}_t^T \cdot \mathbf{C} \cdot d\mathbf{U} \tag{26.19}$$

$$E_E = \frac{1}{2}\mathbf{U}_t^T \cdot \mathbf{K}_e \cdot \mathbf{U}_t \tag{26.20}$$

$$\tag{26.21}$$

where $\mathbf{M}$, $\mathbf{K}_e$, and $\mathbf{C}$ are mass, elastic stiffness, and damping matrices of the structure, respectively. $\mathbf{P}$ and $\mathbf{U}$ are the vectors of hydraulic pressure and displacement.

The subscripts t and g refer to total and ground displacements, respectively. $\mathbf{S}$ is the coupling matrix of fluid-structure. $\mathbf{f}_{ext}$ is vector of body forces.
The ratio of dissipated energy along a crack path with respect to total dissipated energy is:

$$\zeta_i^j = \frac{(E_H)_i}{E_H} \tag{26.22}$$

where $(E_H)_i$ is the dissipated energy along the discrete joint elements (if discrete cohesive cracks are used) or inside surrounding solid elements (if a smeared crack model is adopted).
The previously defined micro DI and the dissipated energy can then be combined to define a meta DI, corresponding to each critical location in Figure 26.2

$$\overline{DI}^j = \sum_{i=1}^{n} DI_i^j \times \zeta_i^j \tag{26.23}$$

where n is the total number of cracks.
Finally, one can define a macro DI for the entire dam or the dam-foundation coupled system as:

$$\overline{\overline{DI}} = \sum_{j=A}^{D} \overline{DI}^j \tag{26.24}$$

where m is the identifier of critical locations. The coupled system can be divided into four main locations as shown in Figure 26.2 (for instance the dam would correspond to $m = A, B, C$, while the foundation to $m = D$).
Usually concrete dams are designed with relatively high safety factor against seismic excitation; hence their performance is expected to be in the serviceability range. The performance of a concrete gravity dam under the earthquake excitation can be categorized as one of six possibilities (as shown also in Figure 26.3):

- Type (I): There is no thorough crack between the upstream and downstream faces. In this case the micro, meta, and macro DIs are computed from Eqs. 26.13, 26.23, and 26.24.
- Type (II): There is one thorough crack at the critical locations A or B (Figure 26.2) but the upper segment does not overturn. Maximum displacement of the index point (shown as a circle) is less than the ultimate displacement (or $|DR| < DR_{limit}$). DI will be assigned a value of Γ, and the dam will be considered to be damaged but not failed.
- Type (III): There is one thorough crack at the critical locations C or D but the dam body has no or limited displacement. Maximum displacement of the index point is less than the ultimate displacement. Here, DI$= \Gamma$. The dam is considered to be severely damaged but not failed. Damage type (III) is worse than type (II), as it may lead to a larger flood downstream should there be full failure.
- Type (IV): There is one thorough crack at critical locations A or B and the upper segment slides or overturns freely with respect to the lower stable part. Maximum displacement of the index point is excessive and so the instability coefficient is

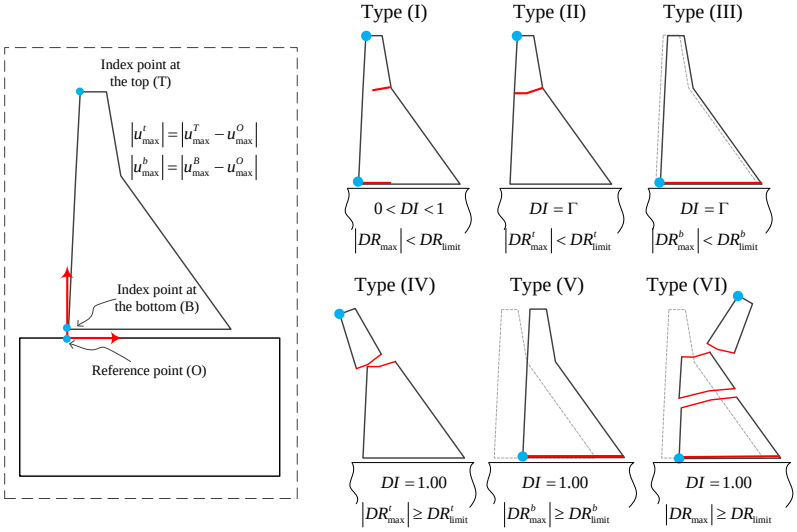

Fig. 26.3: Different cracking scenarios for gravity dams under earthquake excitation

set to unit. Under this scenario $DI = 1.00$. The dam is assumed to have failed (reach to limit).

- Type (V): There is one thorough crack at critical locations C or D and the dam body slides excessively. Maximum drift or rotation of the index point is excessive and hence DI$= 1.00$. The dam is assumed to have failed (reach to limit).
- Type (VI): There is more than one thorough crack and the cracked segments slide and overturn with respect to each other. Maximum drift or rotation of the index points are excessive. DI$= 1.00$ with catastrophic failure.

In summary, performance of a gravity dam can be quantitatively evaluated using those proposed micro, meta, and macro damage indices prior to full damage. Finally, damage severity and judgment on failure can be assessed from the location of cracking and magnitude of the cracked segment movement. It should be noted that the proposed DI is independent of the seismic analysis model for crack propagation. The effects of hydrodynamic pressure, pore water pressure, etc. are implicitly taken into account and the dam stability during seismic analysis is controlled by Fig. 26.3. However, post-seismic stability of a dam (in terms of stable or unstable crack) is not the subject of this paper.

Finally, for qualitative assessment and decision making, it is desirable to identify a damage state. Following a similar approach to the one espoused by the RC seismic design community [34], the damage states shown in Table 26.1 are proposed. The quantitative numbers are based on the expert opinions of the authors.

Table 26.1: Definition of the proposed damage states for gravity dams

Symbol	Damage State	Damage index range
DS1	Intact	$\overline{\overline{DI}} = 0.00$
DS2	Slight	$0.00 < \overline{\overline{DI}} \leq 0.10$
DS3	Moderate	$0.10 < \overline{\overline{DI}} \leq 0.30$
DS4	Severe	$0.30 < \overline{\overline{DI}} \leq 0.60$
DS5	Near collapse	$0.60 < \overline{\overline{DI}} \leq 0.99$
DS6	Collapse	$\overline{\overline{DI}} = 1.00$

In addition to the proposed DI, several other researchers have also tried to quantify the damage evolution in concrete dams, among them Alembagheri and Ghaemian [21, 19, 20], Zhang et al. [911], and Amirpour and Mirzabozorg [28]. For example, Ansari and Agarwal [35] proposed the following two DIs for gravity dams:

- DI based on crest displacement and cumulative damage energy dissipation from nonlinear analysis:

$$\mathrm{DI}_d = \frac{\left(d_y E_y^{\mathrm{dsp}}\right)_i - \left(d_y E_y^{\mathrm{dsp}}\right)_0}{\left(d_y E_y^{\mathrm{dsp}}\right)_f - \left(d_y E_y^{\mathrm{dsp}}\right)_0} \qquad d_{y0} \leq d_{yi} \leq d_{yf} \tag{26.25}$$

  where d_{y_0} and d_{y_f} are maximum crest displacement at initial and final yield points, respectively; ${E_y^{\mathrm{dsp}}}_0$ and ${E_y^{\mathrm{dsp}}}_f$ are cumulative energy dissipated up to initial and final yield points, respectively. Note that for d_{y_i} less than d_{y_0} or more than d_{y_f}, DI is zero or one, respectively.
- DI based on factor of safety against sliding (FSS) is computed as:

$$\mathrm{DI}_{FSS} = \frac{\sum_{i=1}^{n} \left(1 - \frac{FSS_i}{FSS_f}\right)^{1/2}_{\text{base-body}} + \frac{1}{2}\left(1 - \frac{FSS_i}{FSS_f}\right)^{1/2}_{\text{neck}}}{n+1} \tag{26.26}$$

  where FSS_i is the factor of safety against sliding at any intermediate crack length; FSS_f is the total factor of safety against sliding at no damage state and n is the number of crack paths in the dam excluding neck crack. Note that the static loading condition is used for calculation of FSS_i. Finally, four DSs are considered: 1) Slight, 2) Moderate, 3) Extensive, and 4) Severe, Figure 26.4.

26.3 Damage Index for Arch Dams

One needs to know the "anatomy of the dam capacity function" to properly determine the Limit States (LS). Figure 26.5(a) schematically shows a capacity function for a U-shape arch dam based on ETA method where the EDP is assumed to be crest horizontal displacement and IM is PGA. Four LS are defined as follows:

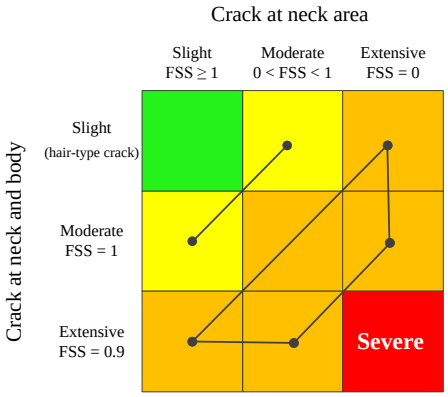

Fig. 26.4: FSS-based DS matrix [35]

- Joint local yielding: is associated with the first significant joint opening or sliding in a dam body. Though a user-defined value, it is recommended to be set at 1-3 mm based on the height of the dam or twice the static value.
- Material local yielding: is associated with the first concrete cracking/crushing on the upstream or downstream face of the dam.
- Global yielding: is associated with the significant slope change on the capacity curve and considerable joint opening/sliding and concrete cracking ($\sim$ 20-30 % damage).
- Ultimate damage: is associated with the point where the capacity curve becomes nearly horizontal and is assumed to correspond to the dam failure.

Figure 26.5(b) shows the capacity functions for six (equally-spaced) points along the central cantilever of an arch dam. As noted, moving from crest to the base increases the IM-capacity while the EDP-capacity decreases. From this figure, one can determine the ultimate damage line for the dam instead of a single point. Note that under some ground motions (with specific frequency content), displacement of the crest may be less than its lower elevation.
Single-variable DIs can be categorized into three broad groups for concrete arch dams, i.e. 1) Displacement-dependent, 2) Crack-dependent, and 3) Energy-dependent DIs. Each one is capable of recognizing one or more LSs.

26.3.1 Displacement-dependent DIs

In this category, damage evolution is assessed based on the displacement response. This approach is the simplest and most effective way to quantify damage. The displacement-dependent DIs are only derived for the central block (which is usually the most critical one); however it can be extended to consider the effects of the other blocks also.

- Non-cumulative global displacement-based DI:

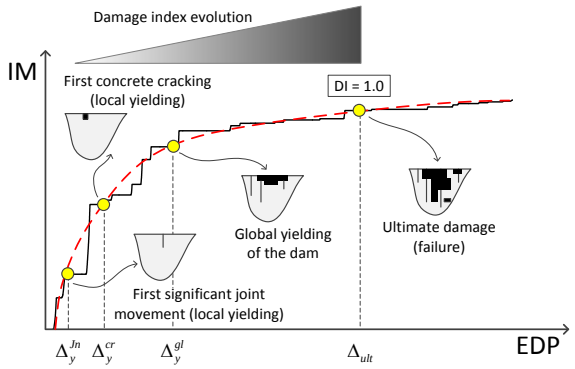

(a) Crest capacity function

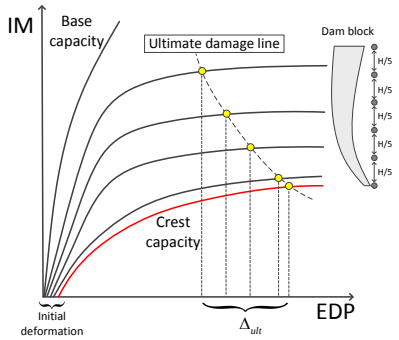

(b) Central block capacity functions

Fig. 26.5: ETA-based capacity functions for a generic arch dam (no scale)

$$\mathrm{DI}_{\mathrm{I}}(t) = \left(\frac{\Omega\left(\Delta(t)\right)}{\Delta_{ult}} \right)_{cn} \tag{26.27}$$

where $\Omega\left(\Delta(t)\right)$ refers to the maximum absolute displacement up to t, and Δ_{ult} is the ultimate horizontal displacement, Figure 26.5(a). Note that based on this definition, the initial displacement effect is also considered at $t = 0$. One may use the following alternative form to account for the seismic response only:

$$\mathrm{DI}_{\mathrm{I}}(t) = \left(\frac{\Omega\left(\Delta(t)\right) - \Delta_{ini}}{\Delta_{ult} - \Delta_{ini}} \right)_{cn} \tag{26.28}$$

where Δ_{ini} is the initial (self-weight + hydrostatic + thermal) response.

- Non-cumulative linear local-global displacement-based DI, Figure 26.6(a):

$$\mathrm{DI_{II}}(t) = \begin{cases} 0 & \Omega\left(\Delta(t)\right) < \Delta_y \\ \left(\frac{\Omega(\Delta(t)) - \Delta_y}{\Delta_{ult} - \Delta_y}\right)_{cn} & \Omega\left(\Delta(t)\right) \geq \Delta_y \end{cases} \tag{26.29}$$

where Δ_y is the yield displacement and can be considered as one of the three options in Figure 26.5(a). This index, in fact, bounds the damage between [Δ_y, Δ_{ult}]. This DI is similar to the one proposed by [706] for framed structures.

- Non-cumulative non-linear local-global displacement-based DI, Figure 26.6(a):

$$\begin{aligned} \mathrm{DI_{III}}(t) &= \begin{cases} 0 & \Omega\left(\Delta(t)\right) < \Delta_y \\ \left(\frac{\Delta_{ult}}{\Omega(\Delta(t))} \times \frac{\Omega(\Delta(t)) - \Delta_y}{\Delta_{ult} - \Delta_y}\right)_{cn} & \Omega\left(\Delta(t)\right) \geq \Delta_y \end{cases} \\ \mathrm{DI_{IV}}(t) &= \begin{cases} 0 & \Omega\left(\Delta(t)\right) < \Delta_y \\ \left(\frac{\Omega(\Delta(t))}{\Delta_{ult}} \times \frac{\Omega(\Delta(t)) - \Delta_y}{\Delta_{ult} - \Delta_y}\right)_{cn} & \Omega\left(\Delta(t)\right) \geq \Delta_y \end{cases} \end{aligned} \tag{26.30}$$

$\mathrm{DI_{III}}(t)$ (concave downward) and $\mathrm{DI_{IV}}(t)$ (concave upward) are non-linear versions of $\mathrm{DI_{II}}(t)$ (linear).

- Non-cumulative exponential-form local-global displacement-based DI, Figure 26.6(b):

$$\mathrm{DI_{V}}(t) = \begin{cases} 0 & \Omega\left(\Delta(t)\right) < \Delta_y \\ \left(\frac{\Omega(\Delta(t)) - \Delta_y}{\Delta_{ult} - \Delta_y}\right)^{\beta}_{cn} & \Omega\left(\Delta(t)\right) \geq \Delta_y \end{cases} \tag{26.31}$$

where $\beta \in (0, +\infty)$ is an exponent related to the rate of the change in DI at different stages. For $\beta < 1$, DI has downward concavity while for $\beta > 1$, it has upward concavity.

- Non-cumulative sigmoid-type local-global displacement-based DI, Figure 26.6(c):

$$\mathrm{DI_{VI}}(t) = \begin{cases} 0 & \Omega\left(\Delta(t)\right) < \Delta_y \\ \left(\frac{1 - e^{-\frac{\Omega(\Delta(t)) - \Delta_y}{\Delta_1}}}{1 + e^{-\frac{\Omega(\Delta(t)) - \Delta_y - \Delta_2}{\Delta_1}}}\right)_{cn} & \Omega\left(\Delta(t)\right) \geq \Delta_y \end{cases} \tag{26.32}$$

where,

$$\begin{aligned} \Delta_1 &= \beta_1 \left(\Delta_{ult} - \Delta_y\right) \\ \Delta_2 &= \beta_2 \left(\Delta_{ult} - \Delta_y\right) \end{aligned} \tag{26.33}$$

where β_1 controls the curvature and β_2 controls the inflection point; they are assumed to be 0.1 and 0.5 in this study.

- Cumulative global displacement-based DI:

$$\mathrm{DI_{VII}}(t) = \left(\frac{\sum_{j=1}^{N(t)} \left|\Delta_j^{abs} - \Delta_{ult}\right|}{\sum_{j=1}^{N(t_{ult})} \left|\Delta_j^{abs} - \Delta_{ult}\right|}\right)_{cn} \tag{26.34}$$

where Δ_j^{abs} is the absolute deformation in cycle j, $N(t)$ is number of cycles up to time t, and $N(t_{ult})$ is number of cycles up to ultimate time. This DI is similar to the one proposed by [82] for reinforced concrete members in term of element rotation.

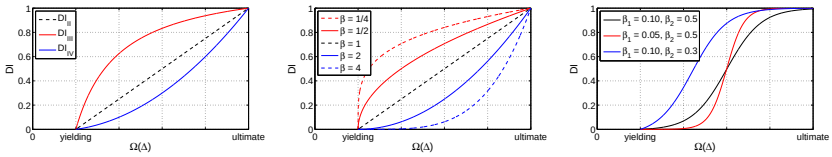

(a) $\mathrm{DI_{II}}$, $\mathrm{DI_{III}}$ and $\mathrm{DI_{IV}}$ (b) $\mathrm{DI_{V}}$ (c) $\mathrm{DI_{VI}}$

Fig. 26.6: Direct relation between DI and $\Omega(\Delta)$

26.3.2 Crack-dependent DIs

Crack-dependent DIs are divided into two groups: 1) DI from discrete joints in terms of opening and sliding and 2) DI from continuum crack (damage plasticity or smeared crack) in term of material cracking/crushing.

- Global joint opening/sliding DI:

$$\mathrm{DI_{VIII}}(t) = \frac{\Omega\left(\delta^{Jn}(t)\right)}{\delta^{Jn}_{ult}} \tag{26.35}$$

  where $\delta^{Jn}(t)$ refers to both joint opening and sliding and δ^{Jn}_{ult} is the maximum joint opening/sliding up to the ultimate time.
- Global-local joint opening/sliding DI:

$$\mathrm{DI_{IX}}(t) = \begin{cases} 0 & \Omega\left(\delta^{Jn}(t)\right) < \delta^{Jn}_{y} \\ \frac{\Omega\left(\delta^{Jn}(t)\right) - \delta^{Jn}_{y}}{\delta^{Jn}_{ult} - \delta^{Jn}_{y}} & \Omega\left(\delta^{Jn}(t)\right) \geq \delta^{Jn}_{y} \end{cases} \tag{26.36}$$

  where δ^{Jn}_{y} is the yielding on the capacity curve, Figure 26.5(a), usually can be assumed to a very small value, e.g. 1-3 mm.
- Non-normalized crack ratio DI:

$$\mathrm{DI_{X}}(t) = \begin{cases} 0 & t < t^{cr}_{y} \\ \frac{A^{cr}(t)}{A^{T}} & t^{cr}_{y} \leq t \leq t_{ult} \\ 1 & t > t_{ult} \end{cases} \tag{26.37}$$

  where $A^{cr}(t)$ is the cracked area at time t and A^{T} is the total area of dam. This DI can be calculated for both the upstream and downstream faces. Note that this DI only explicitly accounts for the final ultimate condition of the dam by shifting the DI to unit.
- Normalized crack ratio DI:

$$\mathrm{DI_{XI}}(t) = \frac{A^{cr}(t)}{A^{cr}_{ult}} \tag{26.38}$$

where $A^{cr}(t)$ is the cracked area at time t and A^{cr}_{ult} is the ultimate cracked area at the time of failure. This DI effectively considers the ultimate condition of dam.

26.3.3 Energy-dependent DIs

In order to properly define the energy-dependent DIs, it is necessary to determine the effective terms in the damage-related energy balance equation of system. In the most general form, the conservation of energy by the first law of thermodynamic can be expressed as [175] (note that the terms related to heat are neglected):

$$\underbrace{\frac{\mathrm{d}}{\mathrm{d}t}\int_V \rho U \mathrm{d}V}_{\text{Internal Energy}} + \underbrace{\frac{\mathrm{d}}{\mathrm{d}t}\int_V \frac{1}{2}\rho \mathbf{v}.\mathbf{v}\mathrm{d}V}_{\text{Kinetic Energy}} = \underbrace{\int_V \mathbf{f}.\mathbf{v}\mathrm{d}V}_{\text{Body Forces}} + \underbrace{\int_S \mathbf{T}.\mathbf{v}\mathrm{d}S}_{\text{Surface Forces}} + \underbrace{\cancelto{0}{\int_V \dot{Q}\mathrm{d}V}}_{\text{Heat Generation}} + \underbrace{\cancelto{0}{\int_S \mathbf{q}.\mathbf{n}\mathrm{d}S}}_{\text{Heat Flux}} \tag{26.39}$$

where ρ is density, U internal energy, $\mathbf{v}$ velocity vector, $\mathbf{f}$ body force vector, $\mathbf{T}$ surface traction vector, $\dot{Q}$ the heat generation rate per unit volume, $\mathbf{n}$ the unit normal vector to the control volume surface, $\mathrm{d}V$ the differential volume element of the control volume, $\mathrm{d}S$ the differential surface element of the control volume, and $\mathrm{d}t$ the differential time increment.
The simplified energy balance equation for dam system can be stated as [3]:

$$E_{\mathrm{T}} = E_{\mathrm{K}} + E_{\mathrm{E}} + E_{\mathrm{P}} + E_{\mathrm{D}} + E_{\mathrm{V}} + E_{\mathrm{F}} - E_{\mathrm{W}} + E_{err} \tag{26.40}$$

where E_{T} is total energy, E_{K} kinetic energy, E_{E} recoverable strain energy, E_{P} energy dissipated by rate-dependent and rate-independent plasticity, E_{D} energy dissipated by damage, E_{V} energy dissipated by viscous damping, E_{F} energy dissipated by frictional damping, E_{W} is work done by external work, and E_{err} is the error term due to neglecting some other energy parameters (mainly due to numerical computations such as work by constraint and contact penalties or energy dissipation by distortion control). Each of the energy terms can be mathematically expressed as:

$$
\begin{aligned}
E_{\mathrm{K}} &= \frac{1}{2}\int_V \rho \mathbf{v}.\mathbf{v}\,\mathrm{d}V \\
E_{\mathrm{E}} &= \int_0^t \left(\int_V \frac{1-d_t}{1-d}\boldsymbol{\sigma}^c : \dot{\boldsymbol{\varepsilon}}^{el}\,\mathrm{d}V\right)\mathrm{d}\tau \\
E_{\mathrm{P}} &= \int_0^t \left(\int_V \boldsymbol{\sigma}^c : \dot{\boldsymbol{\varepsilon}}^{pl}\,\mathrm{d}V\right)\mathrm{d}\tau \\
E_{\mathrm{D}} &= \int_0^t \left(\int_V \frac{d_t-d}{1-d}\boldsymbol{\sigma}^c : \dot{\boldsymbol{\varepsilon}}^{el}\,\mathrm{d}V\right)\mathrm{d}\tau \\
E_{\mathrm{V}} &= \int_0^t \left(\int_V \boldsymbol{\sigma}^v : \dot{\boldsymbol{\varepsilon}}\,\mathrm{d}V\right)\mathrm{d}\tau \\
E_{\mathrm{F}} &= \int_0^t \left(\int_S \mathbf{T}^f.\mathbf{v}\,\mathrm{d}S\right)\mathrm{d}\tau \\
E_{\mathrm{W}} &= \int_0^t \left(\int_S \mathbf{T}^l.\mathbf{v}\,\mathrm{d}S + \int_V \mathbf{f}.\mathbf{v}\,\mathrm{d}V\right)\mathrm{d}\tau
\end{aligned}
\tag{26.41}
$$

where $\boldsymbol{\sigma}$ is the total stress tensor, $\boldsymbol{\sigma}^v$ viscous stress, $\boldsymbol{\sigma}^c$ non-viscous stress, $\dot{\boldsymbol{\varepsilon}}$ strain rate tensor, $d \in [0,1]$ is damage parameter and d_t is damage parameter associated with unloading which remains fixed at time t. The superscripts el and pl refer to elastic and plastic, while f and l refer to frictional traction and surface distributed traction, respectively.

Figure 26.7 shows the variation of all seven energy terms in Eq. 26.40 for ETA of an arch dam. The arithmetic scale, Figure 26.7(a), is useful for long-duration analyses, while the logarithmic one, 26.7(b), is useful to compare the short-duration energy responses. The following observations can be drawn:

- E_{W} and E_{V} are two dominant energy terms compared to others.
- E_{V}, E_{P}, E_{F}, and E_{D} are the terms corresponding to energy dissipation in the system and they always have a cumulative nature.
- At the start of the dynamic analysis, all the energy terms are zero except recoverable strain energy, E_{E}.
- Rate of the energy change is slower for E_{E} and E_{K} compared to others.

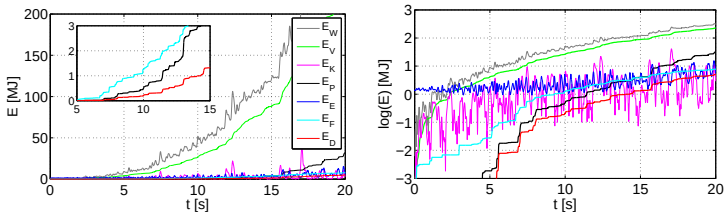

(a) Arithmetic scale (b) Logarithmic scale

Fig. 26.7: Evolution of energy terms under the ETA method

Considering that the damage evolution in the dam corresponds to the dissipation of energy, only E_{P}, E_{D}, E_{F}, E_{V} are of importance. However, only E_{P}, E_{D}, E_{F} have direct contribution to failure of the dam in terms of damage to mass concrete or the joints.

- Energy-dissipation DI:

$$\mathrm{DI}_{\mathrm{XII}}(t) = \frac{E^{\mathrm{dsp}}(t)}{E^{\mathrm{dsp}}_{ult}}\ , \quad E^{\mathrm{dsp}}(t) = E_{\mathrm{P}}(t) + E_{\mathrm{D}}(t) + E_{\mathrm{F}}(t) \tag{26.42}$$

  where E^{dsp}_{ult} is the ultimate dissipated energy due to concrete damage, plasticity, and joint movement.

Energy dissipation in brittle material (e.g. concrete) is a function of not only intensity of applied dynamic load but also the duration of excitation. Thus a new DI can be defined to account for both the "dissipated energy" and "time period." In physics, the integral of energy over time (taken along the path of the system between the initial and the final time) is called "action" [883].

$$\Lambda(t) = \int_{t_1}^{t_2} E(t)\mathrm{d}t \tag{26.43}$$

where the dimension is [energy].[time] and its SI unit is joule-second. Dimensionally, it has the same unit as angular momentum.

- Action-dissipation DI:

$$\mathrm{DI}_{\mathrm{XIII}}(t) = \frac{\Lambda^{\mathrm{dsp}}(t)}{\Lambda^{\mathrm{dsp}}_{ult}}\ , \quad \Lambda^{\mathrm{dsp}}(t) = \int_0^t E^{\mathrm{dsp}}(t)\mathrm{d}t \tag{26.44}$$

  where E^{dsp}_{ult} is the ultimate dissipated energy due to concrete damage, plasticity, and joint movement.

Part V
Applications; Dams

Chapter 27
Potential Failure Mode Analysis

Abstract
Identification, description, and evaluation of site-specific potential failure modes (PFMs) are the most important steps towards a risk analysis. Potential failure mode analysis (PFMA) is a standard and state-of-the-practice technique in dam engineering and forms the basis for risk evaluations and event tree development. Figure 27.1 illustrates the key steps of a PFMA. It should be noted that it is purely qualitative. This chapter presents both the qualitative and quantitative failure metrics for a variety of concrete dams.

27.1 Historical Seismic Damage in Concrete Dams

Since there have been few reported earthquake-induced failures or major damages in concrete dams, this section will review some of the most important cases reported in the literature. They can assist in the identification of PFM below.

Koyna Dam (India) was a rubble concrete gravity dam of 853 m length and 103 m height. The 1967 Koyna earthquake induced horizontal cracks on both faces of the tallest non-overflow blocks at the elevation of the downstream change of slope. However, the dam did not breach and no flooding occurred. Subsequently, the dam was strengthened by the addition of buttresses on the downstream face of the non-overflow blocks [195]. This observed performance clearly points to the type of overstressing failure that could occur in a gravity dam.

Shih Kang Dam (Taiwan) was 21.4 m gravity dam and 357 m long. The dam was located directly over a branch of the fault caused by the M7.6 Chi Chi earthquake on September 1999. The fault rupture extended both upstream and downstream of the dam and caused extensive damage to bays 16 to 18. The ground movement led to a vertical differential movement of about 9 m in these bays. There was also a diagonal horizontal offset through the dam of about 7 m, and the dam collapsed with uncontrolled release of water [663].

Uh Dam (Japan) is a 14 m high concrete gravity dam. The dam is located about 1.0 km from the epicenter of the 2,000 Western Tottori Earthquake (M7.3). The only damage to the dam was cracking 10 mm to 30 mm wide on the spillway channel near the base of the downstream face, and there was no uncontrolled release of water [663].

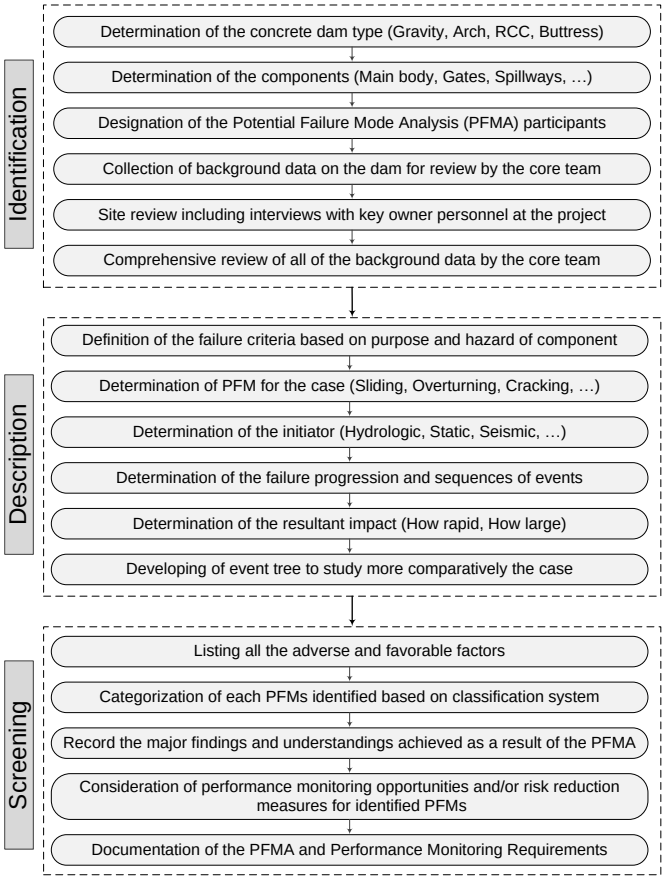

Fig. 27.1: Steps towards PFMA of concrete dams based on qualitative approach; adapted from FERC [308] and USBR-manual [845]

Pacoima Dam (USA) is a 111 m high arch dam with a crest length of 180 m. Abutment rock movements and contraction joint openings were observed following the 1971 San Fernando earthquake and the 1994 Northridge earthquake. In 1994, the contraction joint between the arch dam and thrust block on the left abutment opened 5 cm at the crest level. The opening continued downward, tapering to 0.64 cm 18.3 m below the crest level. Also a crack diagonally crossed two lift joints and reached the abutment rock. Other contraction joints did also moderately open [331].
Hsinfengkiang Dam (China) is a 105 m buttress dam with a 440 m crest length. The dam has 19 diamond-head buttresses in the central portion with gravity sections located on either side. In 1962, the dam was shaken by an M6.1 earthquake located

very close to the dam (it is widely believed that it may have been triggered by the infill of the reservoir) resulting in horizontal cracks [785].
Sefid-rud Dam (Iran) is a 106 m gravity buttress dam with 7 gravity monoliths and 23 massive head buttress units. In 1990 it was damaged by the M7.3 Manjil earthquake with the epicenter at about 32 km, however the fault rupture was much closer. The main damage to the central monoliths was cracks at lift joints extending from the dam face through the buttress face and web. These occurred close to the change in slope near the crest and resulted in a 2 cm shear displacement. Although no catastrophic release of the reservoir occurred, the overall stability of the dam was not perceived to be of major concern. Subsequently the dam was repaired using epoxy-grouting for water tightness with post tensioning strands to restore shear strength in the cracked sections [16].

27.2 Potential Failure Mode Analysis

A dam potential failure mode (PFM) is a chain of events leading to unsatisfactory performance of the dam which could lead to uncontrolled release of the reservoir water [308].
Identifying, fully describing, and evaluating site-specific potential failure modes and sequences leading to failure are arguably the most important initial steps in conducting a structural analysis of a dam, assessing the dam safety assessment, developing an instrumentation plan, budgeting funds for modifications, and scheduling maintenance [299]. The process can clearly show why certain activities are undertaken or why certain decisions are made. This process lays out potential problems with a facility, develops the sequence of events required to adversely affect the facility, and finally helps all involved to better understand the facility.
A facilitated multi-discipline team (rather than an individual person) is best for developing potential failure modes for a concrete dam since concrete dams are complex structures and synergy develops within a group. A complete understanding of the structure would involve team members with specialties in seismology, concrete construction, concrete materials, structural stability, foundation materials, rock mechanics, foundation stability, and dam operations. The team would consist minimally of a structural engineer, a geotechnical engineer, and a geologist. The team is greatly enhanced when field personnel are included. Materials engineers are included when there are issues with the concrete or foundation. Specialists in seismology are included to develop seismic hazard curves.
If the analysis is of an existing dam, the team should review initial designs and assumptions, construction records, historic inspections, as-built drawings, material testing, field investigations, rehabilitations, instrumentation data, structural and stability analyses, and current operations. The team brainstorms potential failure modes after reviewing historic data and before visiting the site. The potential failure modes are then reviewed after a site visit. Site inspections could identify new misalignments, deterioration, seepage, plugged drains, and cracking that may not be in the historic records.

There are two basic methods of developing potential failure modes. The first method starts with initiating events and then determines possible adverse effects. The second method identifies potentially adverse effects and then determines possible mechanisms that could lead to them. Both should be used to make sure all modes are captured. After the potential failure modes are identified, they should be developed further by describing the sequence of events leading to failure that occur from an initiating event.

27.3 Initiators

Failures of dams start with some initiating event (initiator) that causes an adverse change in the structure. This paper focuses on seismic events, but initiating events can occur from loads or changing conditions during normal loading conditions such as flooding, human interaction, or landslides. During an earthquake, inertial forces on the structure might lead to overstressing and cracking of the dam or concrete members in an appurtenant structure, or displacement of the foundation under the dam could cause overstressing or misalignment of the dam, finally a long-duration seismic event might cause a sliding instability.
Safety is assessed in terms of the probability of deaths due to an uncontrolled release of water. Since it is impossible to completely assure life safety, some low probability of deaths is deemed to be tolerable, and since more deaths are generally less tolerable than fewer deaths, we offer acceptance criteria that tolerate more earthquake-related deaths albeit with lower probability.
Figure 27.2 illustrates the initiators for gravity and arch dams. Once all PFMs have been determined, they must be ranked to identify the most critical one which should be described in great detail.

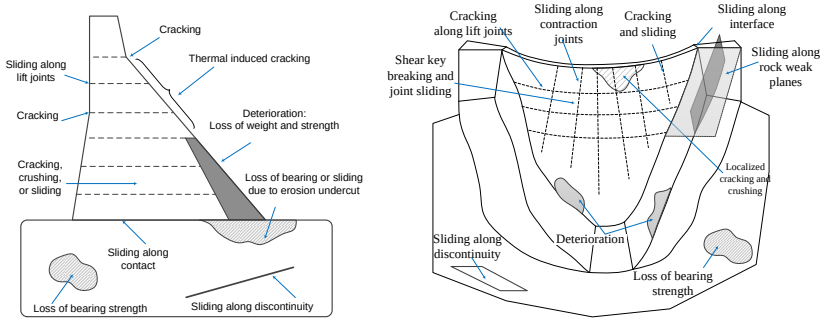

(a) Gravity dam (b) Arch dam

Fig. 27.2: Initiators in concrete dams

27.4 Determination of PFMs

27.4.1 Gravity Dams

Ghanaat [331] reported three major potential failure modes in gravity dams, i.e. overstressing, sliding (either along cracked surfaces in the dam body or along the weak planes in the dam-foundation interface), and sliding accompanied by rotation in the downstream direction. The damage response of a typical gravity dam due to earthquake ground motions is shown in Figure 27.3(a). Different damages will result from the cyclic excitation. Under upstream direction acceleration, cracking may occur at the heel of the dam, and for downstream acceleration, it is most likely to affect the slope discontinuity especially when the pool level is low [842].
When a crack nucleates at the slope discontinuity, it is subjected to a mixed mode loading condition (shear and normal stresses) that will cause the crack to propagate along an inclined direction toward the heel; this was indeed observed in Koyna dam [195]. As a result of this cracking, sliding and/or rotational instability may occur [562], as illustrated in Figure 27.3(b).

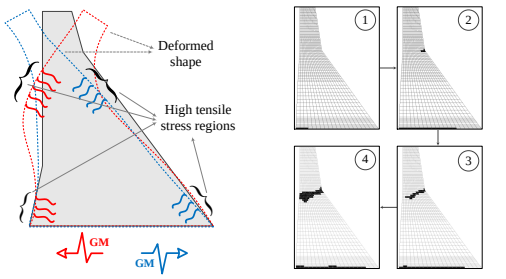

(a) Typical crack pattern under cyclic motion (b) Crack propagation process

Fig. 27.3: Damage response of gravity dam under earthquake ground motion

27.4.2 Arch Dams

Though, by design, arch dams are thin walled hyperstatic structures composed of intersecting arches and cantilevers, this added strength does not completely eliminate the likelihood of failure. Those are: 1) excessive contraction joint opening combined with tensile cracking of the cantilevers (and not in arches), 2) buckling, 3) crushing of concrete, and 4) global instability [331]. Since contraction joints have practically no tensile resistance, repeated cyclic loads are likely to break the weak bond between the grout and the concrete. This, in turn, will relieve arch tensile stresses but drastically increasing those in the cantilevers [842], which may ultimately crack (possibly at the lift joints). Finally, the breakdown of the dam integrity may lead to failure, as shown

in Figure 27.4(a). This process is illustrated by the progressive chain of localized failures in Dez dam (subject of the subsequent case study in this paper), Figure 27.4(b). However, it should be noted that most of these effects can be mitigated by the presence of shear keys.

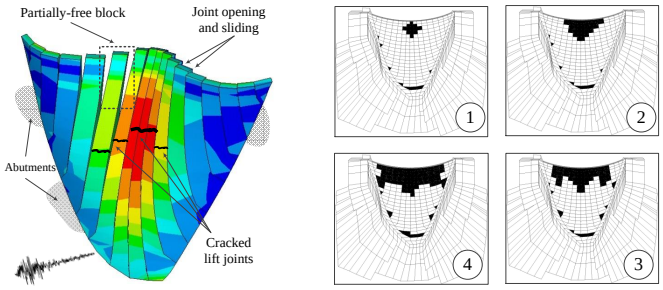

(a) Typical joint openings and cracking under cyclic motion

(b) Crack propagation process

Fig. 27.4: Damage response of arch dam under earthquake ground motion

In some cases, it is found more convenient to analyze the cantilever by itself. In this case, one can assume to have the adjacent contraction joints to be a) fully opened or b) partially opened. In the first case, a stability analysis could be performed to assess its integrity [307]. A numerical procedure for such a simplified analysis was recently undertaken by [561] and [374]. This is possible by applying the dynamic moment equilibrium equation to the partially-free block:

$$\begin{aligned} M_{hdy}(t) + M_{hst}(t) + M_{upl}(t) - mgRcos(\theta+\varphi) \\ -mR\ddot{u}_i(t)sin(\theta+\varphi) + \rho I_P \frac{\partial^2 \varphi}{\partial t^2} = 0 \end{aligned} \tag{27.1}$$

where $M_{hdy}(t)$, $M_{hst}(t)$, and $M_{upl}(t)$ are the moment due to hydrodynamic pressure, hydrostatic pressure, and uplift pressure, respectively, about the pivot point. m is the mass of the portion of the block suspected to overturn. ρ is the mass density of the detached section. R is the distance from pivot point to block center of mass. I_P is the polar moment of inertia about the pivot point. θ is the angle between the line connecting center of mass to the pivot point and the horizon in the pre-cracked condition. φ is the rotation angle of the detached part with respect to the horizon. $\ddot{u}_i(t)$ is the horizontal acceleration at the location of cracking. This is the ground acceleration if the block is sitting on the ground.

This equation can be derived for any partially-free blocks and then solved numerically. This equation assumes that there is no bond between the detached part and the rest of the block, so it is very conservative. Recently, Malla [561] proposed a

simple numerical methodology for stability analysis of the detached concrete blocks in 2D and 3D spaces. They modeled possible lift joints explicitly using the contact elements and employed the gap elements at the downstream face to prevent rigid body motion. It is noteworthy that in the case of high free-cantilevers, the large deformation effects should also be added to the above mentioned equation [374].

27.4.3 Buttress Dams

Buttress dams are reinforced concrete structures composed of an upstream water barrier (flat slab, large domes, cylindrical arches, massive heads) and buttresses. Whereas hydrostatic pressure is transferred to the foundation through the slab and buttresses (analogous to gravity dams), resistance to lateral seismic forces (stream direction) is more akin to arch dams; it is a three-dimensional hyperstatic problem. On the other hand, buttress dams are very sensitive to cross stream excitation.
Failure modes for such a dam include: 1) sliding of the weak planes (stream and cross stream), 2) racking (resulting from inelastic accumulated displacements) in cross-stream cases, 3) slab or buttress localized failures (cracking or crushing), and 4) buckling of buttress, as illustrated in Figure 27.5.

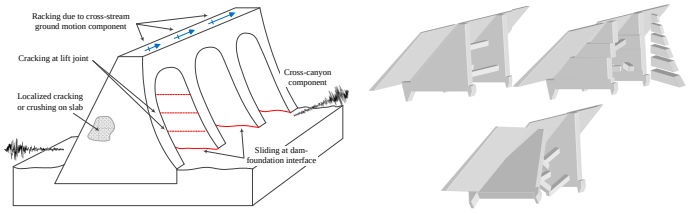

(a) Damage under two-component in-plane cyclic excitation

(b) Progressive failure

Fig. 27.5: Damage response of buttress dam under earthquake ground motion

27.4.4 Foundation-related PFMs

It is reported that about 70% of concrete dam failures can be attributed to dam foundation issues (geological or geotechnical) [455]. Whereas dams have generic PFM, foundation failures modes are very specific to a dam. The major ones are tabulated in Table 27.1 [145].

27.5 Classification of PFMs

The identified PFMs should be categorized based on their importance. The importance of the PFM is a function of what types of issues are deemed important to

Table 27.1: Common foundation-related PFMs for concrete dams

Initiator	Foundation-related PFM
Static	Piping of foundation materials
	Sliding stability of foundation materials
	Sliding stability of reservoir rim materials
	Irregular settlement/deformation of foundation materials
	Dissolution of foundation materials
	Landslide-induced waves
Hydrologic	Overtopping of dam leading to erosion of the foundation
	Stability of foundation/reservoir rim materials
	Landslide-induced waves
Seismic	Deformation of foundation materials
	Sliding stability of foundation/reservoir rim materials
	Landslide-induced waves

management, the client, society, etc. This could include statements concerning the potential loss of life, economic, environmental, political, etc. The present research focuses mainly on life safety, though they could be extended using PBEE principles to repair costs and environmental impacts.

The first step is to briefly describe the adverse impact of the PFM. This will help categorize the PFMs in subsequent steps. For example, long duration seismic loads might cause enough sliding along the dam to foundation contact to cause a rapid release of the reservoir well beyond the safe downstream channel capacity and potentially induce significant loss of life. Yielding of the reinforcement within a spillway pier might cause significant deflections causing spillway gates to collapse and result in an unexpected flow downstream, endangering fisherman but not causing flow outside the river banks. Rupture of the outlet works pipe during a seismic event would be an economic loss, but the upstream bulkhead can be closed under flow and stop the release of water in a short period of time resulting in no loss of life or significant property damage. Toppling of the intake tower would not cause any immediate loss of life because in interior gates might be closed, but the dam would be in danger from overtopping from subsequent flooding during the upcoming rainy season.

At this point, an initial screening should take place to identify the more important potential failure modes to carry into the next step. Less important potential failure modes are documented but set aside. Each important PFM is developed further and hopefully a better understanding develops. Tables are made for each PFM listing what is known, the aspects making the PFM more likely or less likely, and the estimated consequences. Sometimes the PFM will emerge even more important than the others or sometimes less important. Each PFM is categorized according to the classification system shown in Table 27.2. This table gives definitions for categories to rank PFMA by FERC [308] and USBR-manual [845]. It does not provide quantitative likelihood estimates for the identified PFMs.

Table 27.2: Categories used to rank identified PFMs

ID	Code	Identifier	Definition
I	USBR-USACE	*Failure is in progress or imminent*	The PFM has initiated and is in progress, in which case emergency actions may be warranted, or the situation appears to be so dangerous that increased monitoring or other interim risk reduction actions may be warranted while risk estimates and documentation are being completed.
	FERC	*Highlighted PFM*	Those PFMs of greatest significance considering need for awareness, potential for occurrence, magnitude of consequence and likelihood of adverse response are highlighted.
II	USBR-USACE	*Failure mode is credible*	These PFMs are significant enough that they should be carried forward into a risk analysis, but do not appear to require immediate action based on the available information. Monitoring may be an appropriate risk management activity.
	FERC	*PFM considered but not highlighted*	These are judged to be of lesser significance considering need for awareness, potential for occurrence, magnitude of consequence and likelihood of adverse response. They are still described and included with reasons for and against the occurrence of the PFM.
III	USBR-USACE	*Insufficient information to determine credibility of failure mode*	There is insufficient information to make a judgment on whether these PFMs should be carried forward for risk analysis. Increased monitoring may be an appropriate interim risk management activity while information is being collected.
	FERC	*More information or analyses are needed in order to classify*	These PFMs to some degree lacked information to allow a confident judgment of significance and thus a dam safety investigative action or analyses can be recommended. Because action is required before resolution, the need for this action may also be highlighted.
IV	USBR-USACE	*Failure mode is not credible*	These PFMs are clearly so remote that the likelihood of failure is negligible, and hence do not need to be carried forward for risk estimates. However, they still need to be documented along with the reasons they are considered to be negligible risk contributors. Monitoring is likely not warranted for these PFMs.
	FERC	*Failure mode ruled out or is considered not viable*	The candidate PFM is ruled out as a PFM because the team discovers that the physical possibility for the failure mode does not exist. Or the candidate PFM is considered as not a viable one because it is found to clearly be so remote as to be non-credible or not reasonable to postulate based on information available at this time.

27.6 Event Tree and Fault Tree

By definition “Event Tree Analysis” is a technique that is used to identify the possible outcomes given the occurrence of an initiating event while “Fault Tree Analysis” is a

technique by which conditions and factors that can contribute to a specified undesired event are identified and organized in a logical manner and represented pictorially. Event tree analysis is a commonly-used approach for understanding, analyzing ,and communicating dam safety risk and for supporting decision making [142, 402].
In dam safety applications, event tree analysis can also be extended to the representation of a possible series of events that link the occurrence of a dam failure (or accident) or even normal operations, especially in the case of flood operation, to the realization of consequences [142]. Given the occurrence of an initiating event, event tree analysis also serves as a logical method to quantify the consequences resulting from a given initiator.

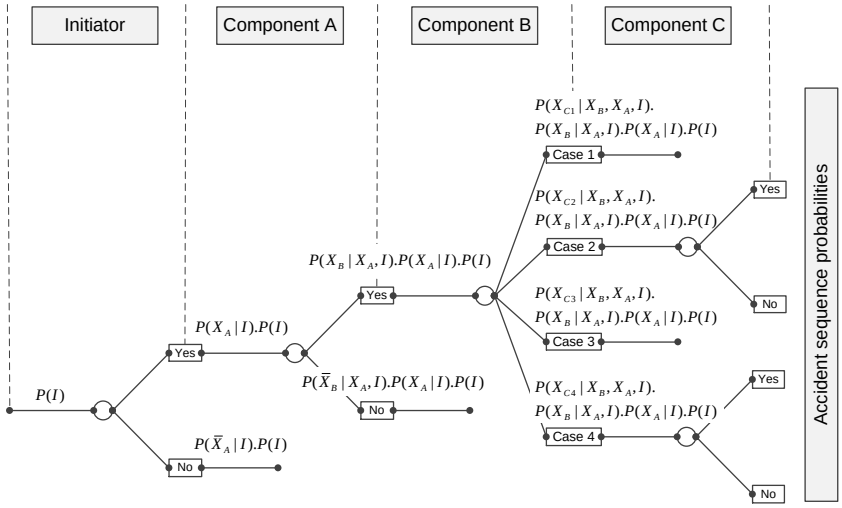

Fig. 27.6: Event tree for an independent three-component system indicating accident sequences; $P(X_A|I) = P(X_A)$, $P(X_B|X_A,I) = P(X_B)$, and $P(X_{Ci}|X_B,X_A,I) = P(X_{Ci})$

On the other hand, Hartford and Baecher [402] define fault tree analysis as a quantitative or qualitative technique to deductively identify the conditions and factors that can contribute to a specified undesired event. Fault tree analysis can also be defined as "a top-down approach to failure analysis starting with an undesirable called a top event, such as a failure or malfunction and then determining all the ways it can happen" [402].
In event tree analysis, each identified PFM is decomposed into a sequence of component events and conditions that all must occur for the failure to develop. The event tree depicts the sequence or progression of events and conditions in a branching fashion, with one or more paths leading to failure of the dam and the rest leading to no failure. Event trees consist of a series of linked nodes and branches. Each node represents an uncertain event or condition. Each branch represents one possible outcome of the

event or condition, and it is assigned a probability. The Event Tree is constructed from left to right, usually starting with an initiator and proceeding through PFM development to a dam breach and its consequences. Branch probabilities at each node must sum exactly to 1.0. They are estimated by the judgment of knowledgeable people, guided when possible by numerical modeling, statistical analysis, case histories, and theory. When estimating likelihood for each branch in an event tree, it is assumed the event represented by the previous branch has occurred (regardless of its likelihood) [299].

An example of an event tree is shown in Figure 27.6. The overall annual probability of a breach is found by multiplying the branch probabilities along each path that leads to breach and summing the branches. The loading is typically (but not necessarily) put into the event tree near the beginning of the tree. When loads are represented with annual probabilities, the results are annualized, representing the probability of that failure mode in any random year. In most cases, it is necessary to partition earthquake or flood loading into ranges, and evaluate the remainder of the tree for each load range. The branch probabilities following the loading are referred to as conditional probabilities because they are based on the assumed condition that the specified loading and any other previous events have occurred [802]. Moreover, Figure 27.7 illustrates some of the failure modes of a gravity dam system using a fault tree approach.

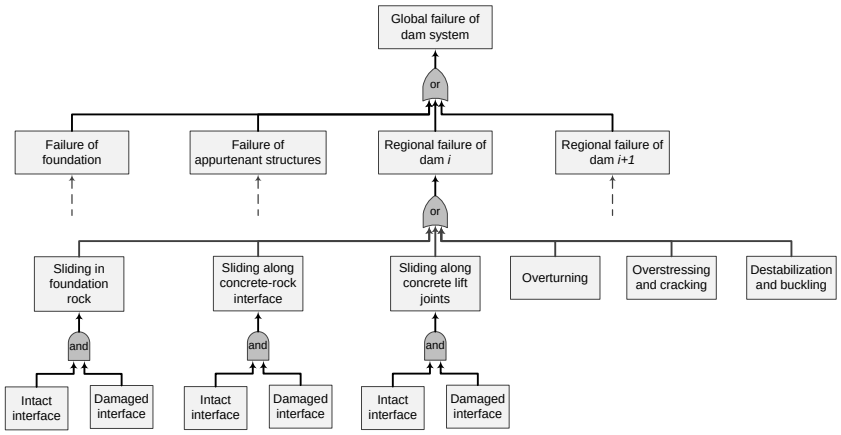

Fig. 27.7: Failure modes of a gravity dam using fault tree approach

Failure modes may be independent or correlated. Assuming independent k modes, the total reliability probability of the dam in series (P_R^s) and parallel (P_R^p) is given by [434]:

$$P_R^s = \prod_{i=1}^{k} P_R\left(X_i\right) \tag{27.2}$$

$$P_R^p = 1 - \prod_{i=1}^{k} \left(1 - P_R\left(X_i\right)\right) \tag{27.3}$$

where $P_R\left(X_i\right)$ is the reliability probability of the ith failure mode.
In addition, it is possible to transform the event tree and fault tree into each other as can be seen in Figure 27.8. Finally, it can be concluded that both methods are complementary to each other in problem solving even though each can be used separately under different situations.

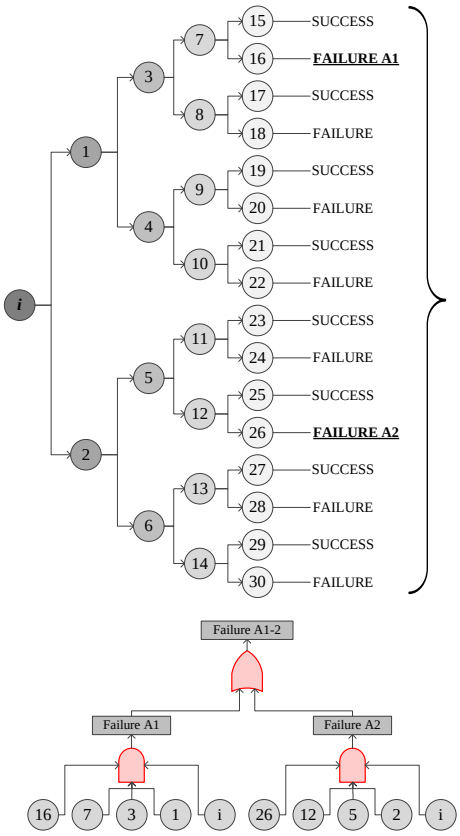

Fig. 27.8: Transformation of event tree to fault tree and vice versa

27.7 Quantitative Assessment of PFMs

Finite element analysis of dams is either linear or nonlinear. It is suggested that the former be undertaken for small dam heights in low seismicity regions. Nonlinear analysis on the other hand should be undertaken for: I) high dams (> 100 m), II) those with large reservoir capacity ($> 1,000$ Mm^3), or III) thin arch and buttressed dams. In either case, one needs a quantification of the PFM using elements from PBEE-2.

The slenderness coefficient of an arch dam can be computed roughly using the relations proposed by Fanelli and Lombardi [288] or Ren and Wang [728], respectively, as:

$$C_l = \frac{F^2}{V \times H} \tag{27.4}$$

$$C_r = \frac{3.4 f_c'}{\rho_w g H} \tag{27.5}$$

where F is the dam surface, V the concrete volume, H the height of the dam, f_c' compressive strength of concrete, and ρ_w mass density of the water.

For the arch dams, the Lombardi slenderness coefficient (C_l) times H should remain below 2500. It is an empirical rule derived from experience and as such is only an indicative value. Dams with higher slenderness (as shown in Figure 27.9(a)) have an above-average susceptibility to damage. Ren and Wang [728] modified this coefficient by taking into account the concrete strength. As seen in Figure 27.9(b), they are susceptible to more damage.

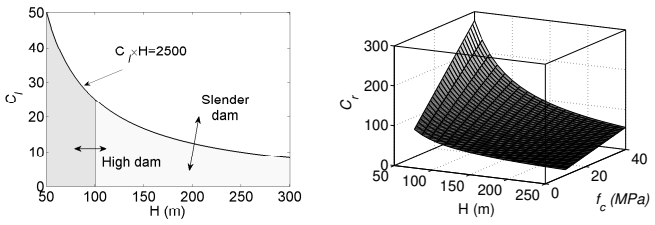

(a) Lombardi slenderness curve (b) Ren slenderness surface

Fig. 27.9: Slenderness of concrete arch dams and susceptibility to damage

In the linear case, quantification of the PFM has already been addressed by some and will be revisited next. In the nonlinear case, the methods introduced in Chapter 24 should be applied.

27.7.1 Linear System

Quantification of PFM in linear analysis can be addressed through indices and corresponding criteria. The indices are dam type independent whereas the criteria are not. Note that a linear analysis is indeed a simplified model of the dam as a homogeneous structures with no contraction or lift joints (where the tensile strength is usually not well known).

27.7.1.1 Indices

Indices are essentially metrics for damage, and the recommended ones are an extension of those proposed by Ghanaat [331] and later adopted by USACE [842]. Among the three original criteria, two are extended and a fourth proposed as follows:

27.7.1.1.1 Demand capacity ratio (DCR): In addition to the standard stress-based criterion, an alternative strain-based criterion is proposed. Indeed, though stress and strain are linearly dependent (in the context of a linear elastic analysis), they can yield different criteria due to the triaxiality of the stress and strain tensors (and the non-zero Poisson ratio),

$$\varepsilon_{ij} = \frac{1+\nu}{E}\sigma_{ij} - \frac{\nu}{E}\delta_{ij}\sigma_{kk} \tag{27.6}$$

not to mention the possible presence of thermal, creep, or chemically induced (alkali aggregate reaction) strains.

$$\begin{cases} \text{Stress DCR}^{\sigma} = \frac{\sigma}{f_t'} \\ \text{Strain DCR}^{\varepsilon} = \frac{\varepsilon}{\varepsilon_{cr}} \end{cases} \tag{27.7}$$

In either case, the compared stress or strain should correspond to the major principal one for gravity dams ($\varepsilon_{(1)}$) and the arch (ε_{arch}) or cantilever (ε_{cant}) quantities for arch dams.

27.7.1.1.2 Cumulative inelastic duration (CID): refers to the total duration of stress or strain excursions above a stress (or strain) level associated with a certain DCR. In the context of a linear elastic analysis with dynamic elastic properties, it is not surprising that stress or strain-based criteria are being violated. However, since stress redistribution (known to occur in hyperstatic structures) is not accounted for (as they would be in a nonlinear analysis), a single exceedance does not inevitably lead to failure. Accordingly, this index establishes a heuristic rule, which simply counts the exceedance (stress or strain) duration during the seismic excitation at two levels ($1.0 \leq \text{DCR} \leq 2.0$), as shown in Figures 27.10.

27.7.1.1.3 Cumulative inelastic area (CIA): The previous index does not account for the magnitude of the exceedance. This one seeks to account for it by measuring

the sum of shaded areas in Figure 27.10. If a stress-based index is adopted, then the CIA has units of FTL^{-2}.

27.7.1.1.4 Damage spatial distribution ratio (DSDR): Whereas previous criteria were evaluated pointwise, this one seeks to measure the topological extent of computed damage (which may not match the one stemming from a nonlinear analysis). Hence, the ratio of the overstressed (or as stated above, overstrained) region to total dam area (cross-section area in gravity dams and upstream or downstream faces in arch dams) at the specific DCR is the DSDR.

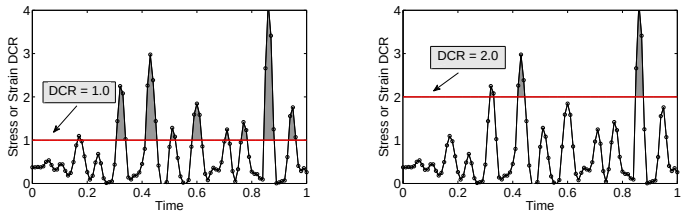

(a) Lower bound, DCR=1.0 (b) Upper bound, DCR=2.0

Fig. 27.10: Calculation of the CID and CIA for two DCRs using stress (or strain) time histories

27.7.1.2 Criteria

To each of the preceding indices, one must specify limiting individual criteria. Those will be addressed first. Then criteria for coupled indices will be presented. For individual criteria, those shown in Table 27.3 are based on the authors' judgment and the proposed ones in the literature [842]. As to CIA_{cr}, it was derived from an assumption of a hypothetical harmonic excitation with a DCR of 2.0, oscillation period of 0.25 s and limited to 5 cycles. This would give CIA_{cr}=0.275 and given the approximate nature of the derivation is bracketed by 0.2 and 0.4.

Table 27.3: Proposed index criteria for linear analysis

Index	Quantity			Note
	Arch	Gravity	Buttressed	
DCR_{cr}	[1, 2]			[376]
CID_{cr}	0.4 s	0.3 s	0.4 s	[842]
CIA_{cr}	[0.2, 0.4]			Refer to text
DSDR_{cr}	20%	15%	15%	[842]

A more comprehensive approach must account for the combined criteria and their possible coupling. This is accomplished by pairing the following indices: DCR-CID

and DCR-DSDR, Figure 27.11. In zone "A," stresses (or strains) are below their critical values, the structure is safe, and there is no need for further evaluation. Stresses (or strains) exceed their acceptable values in "B" and "C." Assessment through DSDR and CID is performed through "B" and "C" respectively. Finally, "D" is unacceptable as it is outside the failure surface. Linear analysis in zone "A" is enough, in "B" and "C" is acceptable, and in "D" is unacceptable.

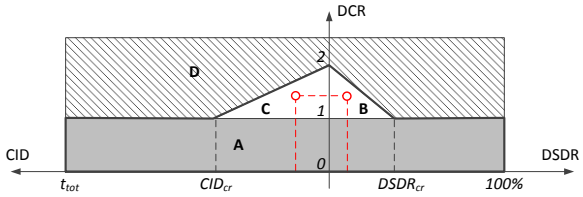

Fig. 27.11: Failure surface for concrete dams under linear analysis (no scale); t_{tot} is total ground motion duration

27.7.2 Nonlinear System

Should a linear analysis of the dam indicate potential severe damage, as shown in Figure 27.11, one should perform a nonlinear structural analysis. Furthermore, should there be initial macro/structural cracks (thermal cracks, poor construction, previous earthquake, etc.), a nonlinear analysis is always warranted. On the other hand, micro-cracks, indicative of material (as opposed to structural) damage, are ignored. There are a number of factors that should be considered in nonlinear structural analysis of concrete dams:

- Staged construction process
- Fluid-structure interaction, fluid fracture interaction, and soil-structure interaction
- Environmental effects such as thermal loads and ice loads
- Aging of concrete, alkali-aggregate reaction, and creep
- Concrete fracture and joint modeling (concrete-concrete and concrete-rock)
- Spatial variation of the ground motion and near-fault ground motion

Whereas sensitivity analyses should be performed to assess the relevance of the aforementioned sources of nonlinearities, the first two authors personal experience indicates that dam-reservoir interaction, joints, and concrete cracking are predominant.

Because a nonlinear analysis attempts to capture the real response of a dam as much as possible, failure can not be as explicitly assessed as in the linear analysis (such as with reference to Figure 27.11). As such, the authors have introduced the notion of damage index (DI) in [383].

Methodology

Different methodologies are introduced in Chapter 24.

Indices

Different indices are introduced in Chapter 26.

Chapter 28
Risk-Informed Decision Making

Abstract
This chapter is, in fact, a summary of the Federal Energy Regulatory Commission (FERC) Risk-Informed Decision Making Guidelines to identify, analyze, assess, and manage the risks in dams. The concept of risk and its differences with other similar topics (e.g. hazard, vulnerability, fragility) are already discussed in Section 18.2.3.

According to FERC [310], there are two general approaches for dam safety assessment:

- The standards-based approach (SBA): is a traditional approach in dam safety assessment by following established rules for design events and loads, structural capacity, safety coefficients, and defensive design measures. Although the SBA is still a necessary component of dam safety management, it is not the best assessment method for some issues such as internal erosion and gate reliability.
- The risk-informed decision making (RIDM): is the process of safety decision making by asking this important question: "Are the existing risks tolerable and present risk measures adequate?" and "if not, are alternative risk reduction measures are justified?"
- It is noteworthy that the authors introduced another (relatively) different technique which has its root in performance based earthquake engineering (PBEE). This hybrid technique of PBEE and PFMA considers the elements from both methods. The decision making in this approach is based on developed fragility and vulnerability functions.

28.1 Basic Terminology

The basic definitions are adopted from "Risk Assessment in Dam Safety Management" by ICOLD [457], Figure 28.1:

- Risk: a measure of the probability and severity of an adverse effect to life, health, property, or the environment.
- Risk Analysis: is the use of available information to estimate the risk to individuals or populations, property, or the environment from hazards. It contains: scope definition, hazard identification, and risk estimation. Moreover, it is based on quantification of knowns and uncertainties about the present and future performance of the dam.

- Risk Evaluation: is the process of examining and judging the significance of risk. It involves incorporating the "values" (societal, regulatory, legal, and owners) in the decision making process.
- Risk Assessment: is the actual decision making process and answering this question: "whether existing risks are tolerable and present risk measures are adequate, and if not, whether alternative risk reduction measures are justified or will be implemented".
- Risk Management (Control): is the systematic application of management policies, procedures, and practices to the tasks of identifying, analyzing, assessing, communicating, mitigating, and monitoring risk.
- Risk Communication: is, in fact, a critical component of an effective RIDM. It is not a separate component, and it must be integrated into all aspects of the process.

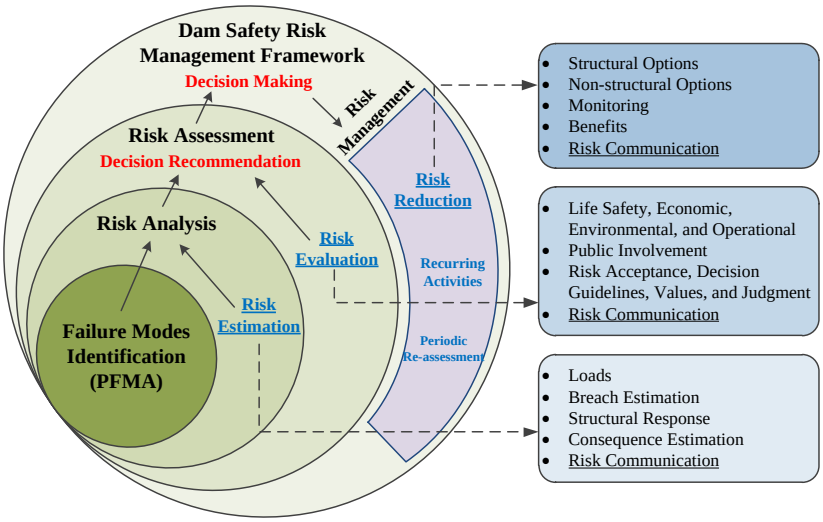

Fig. 28.1: General framework of risk-based dam safety; [310]

In the context of dam safety, the risk concept is composed of three elements:

- The likelihood of occurrence of a load (e.g. flood, earthquake),
- The likelihood of an adverse structural response (e.g., dam failure) given the load, and
- The magnitude of the consequences resulting from that adverse event (e.g., loss of life, money loss, environmental damages) given that it occurs.
  - Direct consequences are always estimated.
  - Indirect consequences (e.g. downtime, destruction of property, and the displacement of people) are also estimated, where possible, and can be incorporated into the risk estimates.

Although the risk estimates reflect the risk at a given site (i.e. dam) and particular time frame, it may be developed for future increase in consequences.

28.2 Risk Analysis

28.2.1 Risk Types

The first step is to identify different inundation scenarios, Figure 28.2:

- (a) Breach prior to over-topping,
- (b) Over-topping with breach,
- (c) Inundation resulting from partial or complete release of the reservoir due to the malfunction of dam components or mis-operation,
- (d) Spillway flow without breach of the dam or over-topping without breach (non-breach).

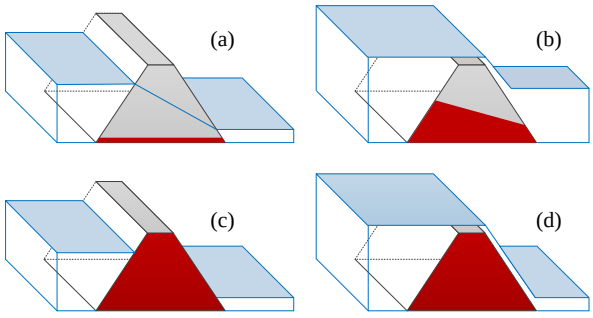

Fig. 28.2: The Four Inundation Scenarios; [843]

Using these inundation scenarios, three different types of risk are estimated:

- **Incremental risk:** is the risk to the reservoir area and downstream floodplain occupants that can be attributed to the presence of the dam should the dam breach prior or subsequent to over-topping, or undergo component malfunction or mis-operation where the consequences considered are over and above those that would occur without dam breach [843]. The incremental consequence is, in fact, the difference between the consequences associated with the estimated performance of the project with and without breach, component malfunction, or mis-operation.
- **Non-breach risk:** Even if the dam does not fail, the reservoir area and the downstream affected floodplains may be in a state of high risk due to "normal" operation or "over-topping without breach".

- **Residual risk:** is the risk in the reservoir area and downstream of the dam at any point in time (i.e. prior to, during, or after implementation of risk reduction measures). It simply refers to the risk that remains.

28.2.2 Risk Measures

Four types of risk measures are to be estimated (1, 3 and 4 include incremental and non-breach risk/consequences):

- Life safety risk
- Annual probability of failure (APF)
- Economic considerations
- Environment and other non-monetary consequences

28.2.2.1 Life Safety Risk

The following incremental life safety risks are to be evaluated:

- Individual incremental life safety risk: using probability of life loss for the identifiable person or group by location that is most at risk of loss of life due to dam breach. It is computed from all exposure conditions and all PFMs associated with all loading or initiating events.
- Societal incremental life safety risk:
  - Probability distribution of potential life loss: is represented by a probability distribution of the estimated annual probability of potential life loss from dam failure or breach for all loading types and conditions, all PFMs, and all population exposure scenarios.
    It is displayed in an F-N chart which is a plot of the cumulative frequency of incremental life loss of N or more lives, F, *vs.* incremental loss of life, N, associated with the incremental flood risk.
  - Average annual life loss (AALL): The value of this metric for a dam should be estimated from all PFMs associated with all loading or initiating event types and considering all exposure conditions associated with life loss.
    AALL is presented in an f-N chart. The estimated life loss plotted on the horizontal scale is the weighted average incremental life loss, $\bar{N}$.

The non-breach life safety risk is also considered and plotted on the cumulative frequency distribution of potential life loss (F-N) chart with the x-axis showing Life Loss, N, from non-breach flood.

28.2.2.2 Annual Probability of Failure

Annual probability of failure (APF) is estimated for those PFMs associated with the incremental risk. APF is estimated from all PFMs associated with all loading or initiating event types.

28.2.2.3 Economic Considerations

Economic considerations accounts for both the direct losses of the dam failure, and other economic impacts on the regional or national economy [843].

- **Direct cost/loss**: can be categorized in several groups.
  - Damage to property located downstream due to dam failure such as: damage to private and public buildings, contents of buildings, vehicles, public infrastructure (e.g. roads and bridges), public utility infrastructure, agricultural crops, agricultural capital, and erosion losses to land.
  - The value from the loss in services provided by the dam such as: hydropower, water supply, flood damage reduction, navigation, and recreation.
  - The costs associated with the emergency response for evacuation and rescue, and the additional travel costs associated with closures of roads and bridges.
  - The cost of repairing the damage to the dam (depends on the damage extent). If the dam can be repaired, these repair costs may or may not be counted as a direct economic cost (loss). In the case of catastrophic failure, these rebuilding costs are typically not included in the direct costs.
- **Indirect cost**: are those associated with the destruction of property and the displacement of people due to the failure.
  - The destruction due to the failure flood can have significant impacts on the local and regional economy as businesses at least temporarily close resulting in loss of employment and income.
  - Economic activity linked to the services provided by the dam will also have consequences, such as: business that provide goods/services for the recreation activities associated with the reservoir.
  - Regional and national effects due to the resulting reduction in spending on goods and services in the region.
  - The dam owner should also consider the financial losses and (both direct and indirect) impacts from a dam failure.

28.2.2.4 Environment Consequences

A dam failure usually has both direct and indirect consequences that cannot be measured in monetary terms, such as impacts to environmental, cultural, and historic resources. More specifically,

- Area and type of habitat impacted, habitat of threatened and endangered species impacted, number and type of historic sites impacted, and the number and type of culturally significant areas impacted.
- The exposure of people and the ecosystem to hazardous and toxic material released from landfills, warehouses, and other facilities.
- The sediment accumulated behind the dam is another source of hazardous material.

- Intangible consequences are also important. They don't have directly observable physical dimensions but exist in the minds.
  - The grief and loss suffered by relatives and friends of those who die,
  - The impact of multiple deaths on the psyche of the community in which they lived,
  - The stress involved in arranging alternative accommodations and income,
  - The sense of loss by those who enjoyed the natural landscape destroyed,
  - The fear of lost status and reputation of the dam owning/regulating organization(s) and their technical staff.

28.2.3 Levels of Risk Analysis

More detailed risk analyses require more detailed engineering analyses and studies resulting in a better understand of the problem, reduced uncertainty, and increased confidence in the risk estimates. In general, there are four broad categories in dam safety risk analyses, Figure 28.3:

- Level 1: Screening Level Risk Analyses
- Level 2: Periodic Risk Analyses
- Level 3: Semi-Quantitative Risk Analyses (SQRA)
- Level 4: Quantitative Risk Analyses (QRA)

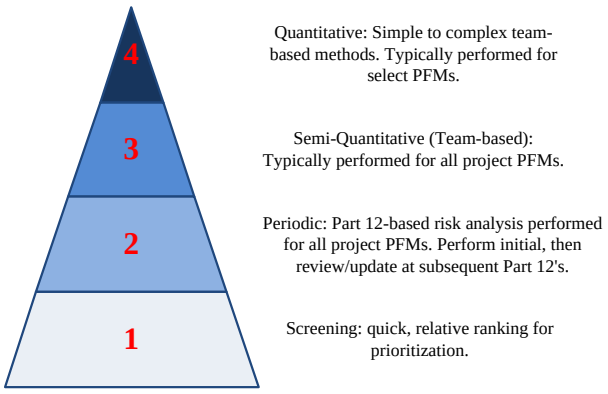

Fig. 28.3: Level of Risk Framework; [310]

28.2.3.1 Screening Level Risk Analyses

The screening level risk analysis can be summarized as follows:

- Purpose/outcome: 1) initial prioritization of inventory, 2) identify dams that are potentially very high risk that require immediate attention, and 3) not appropriate for decisions.
- Type of risk: Incremental life safety economic (in very general terms).
- Typical level of effort: Minimal effort. Lead by a single individual or small team.
- Loading: Rapid assessment using simple, readily available tools.
- Consequences: Simplified methods.
- System response: Common PFMs using simplified tools.
- Uncertainty: Qualitative to none.

All the major agencies such as USACE, USBR, and FERC have their own tools for screening level risk analysis. For example, screening level portfolio risk analysis (SLPRA) was developed by FERC (2010) which uses a qualitative approach. The PFMs are subdivided into four categories (i.e. static, flood, seismic, and operational). The results for each dam (in the form of PFMs) are plotted in a risk matrix, Figure 28.4. A numerical value might be assigned to each cell which facilitates the comparison of dams within an inventory.

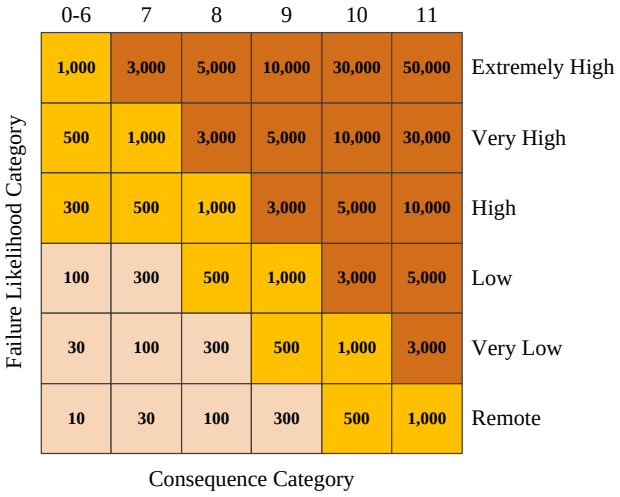

Fig. 28.4: SLPRA risk index scoring matrix; [310]

The USBR Risk Based Profile System (RBPS) was developed in 1997 and could be used to characterize the risk associated with individual loading conditions or sum the total risk imposed by a given structure [225]. The "Failure Index" (FI) is the foundation of RBPS, in which the dam is assessed by assigning a maximum of 1,000 points based on four categories: static (300 points), hydrologic (300 points), seismic (300 points), operation, maintenance and safety (100 points). The higher the point total, the greater the potential risk. To determine the FI, a series of worksheets need

to be completed which address the full range of loading and physical conditions of the dam.
The FI is further multiplied by a loss of life factor (LoLF) to characterize the consequences associated with a failure and is called the "Risk Index" (RI). The LoLF is determined based on several factors including the total population at risk, the location of this population below the dam, the severity of the flooding, and the severity of the failure mode. The RI is calculated separately for each category of FI and then summed to represent the total RI [225].
The final scoring for any particular dam is calculated by comparing its score to the highest score found for all the dams in Reclamation's inventory, expressed as a percentage. This is a deterministic method based on qualitative assessment and heavily depends on the failure modes analysis. It falls under the index prioritization approach category because the ranking is based on the calculated indices from a combination of weights, which are assigned to capture various attributes of dam safety deficiencies [401].

28.2.3.2 Periodic Risk Analyses

The periodic risk analysis can be summarized as follows:

- Purpose/outcome: 1) identification of all PFMs, 2) prioritization of additional studies, 3) lowest level of risk analysis for decisions, 4) prioritization of inventory, 5) tolerable risk evaluation for existing conditions.
- Type of risk: Incremental life safety economic.
- Typical level of effort: Low to moderate effort. Lead by a single individual (Independent Consultant) or a small team.
- Loading: Basic tools/methods to estimate annual exceedance probability (AEP).
- Consequences: Simplified methods.
- System response: Common PFMs using simplified approach.
- Uncertainty: Qualitative.

28.2.3.3 Semi-Quantitative Risk Analyses

The semi-quantitative risk analysis can be summarized as follows [393]:

- Purpose/outcome: 1) project-wide assessment of risks and 2) identification of PFMs needing further study.
- Type of risk: Incremental life safety economic.
- Typical level of effort: Effort can vary greatly depending on PFMs and issues. Team-based, facilitated.
- Loading: Basic tools/methods to estimate AEP.
- Consequences: Simple to intermediate methods.
- System response: Comprehensive evaluation of PFMs using semi-quantitative approach.
- Uncertainty: Qualitative.

The SQRA was a joint effort by USACE and USBR to establish a methodology for some projects at the beginning of an Issue Evaluation Study (IES) to re-evaluate the incremental risk and urgency of action [844]. This approach is mainly built on four concepts: 1) failure likelihood, 2) consequences, 3) confidence level, and 4) risk matrix. First each of those four is briefly described, then the step-by-step procedure for SQRA is explained.

28.2.3.3.1 Failure Likelihood Categories The following failure likelihood categories and descriptors were proposed for SQRA in dam safety [844]:

- Remote: The annual failure likelihood is more remote than 10^{-6}. Several events (with negligible likelihood) must occur in series or parallel to cause failure.
- Low: The annual failure likelihood is between 10^{-5} and 10^{-6}. The possibility cannot be ruled out, but there is no compelling evidence to suggest it has occurred.
- Moderate: The annual failure likelihood is between 10^{-4} and 10^{-5}. The fundamental condition or defect exists; indirect evidence suggests it is probable; and key evidence is weighted more heavily toward "less likely."
- High: The annual failure likelihood is between 10^{-3} and 10^{-4}. The fundamental condition or defect exists; indirect evidence suggests it is plausible; and key evidence is weighted more heavily toward "more likely."
- Very High: The annual failure likelihood is greater than 10^{-3}. There is direct evidence to suggest it has initiated or is likely to occur in near future.

28.2.3.3.2 Consequences Categories In the USACE-USBR SQRA, the failure consequences are typically evaluated using potential life loss, with the idea that the broader socio-economic, environmental, and property damages would be generally commensurate. The following broad consequence categories are used for SQRA [844]:

- Level 0: No significant impacts to the downstream population other than temporary minor flooding of roads or land adjacent to the river.
- Level 1: Downstream discharge results in limited property and/or environmental damage. Direct loss of life is unlikely due to severity or location of the flooding.
- Level 2: Downstream discharge results in moderate property and/or environmental damage. Incremental life loss in the range of 1 to 10.
- Level 3: Downstream discharge results in significant property and/or environmental damage. Incremental life loss in the range of 10 to 100.
- Level 4: Downstream discharge results in extensive property and/or environmental damage. Incremental life loss in the range of 100 to 1,000.
- Level 5: Downstream discharge results in extremely high property and/or environmental damage. Extremely high direct loss of life can be expected. Incremental life loss greater than 1,000.

28.2.3.3.3 Confidence Level The confidence level that the evaluating team has in the previous categories, should be determined using the following qualitative descriptors [844]:

- High: The team is confident in the order of magnitude for the assigned category.
- Moderate: The team is relatively confident in the order of magnitude for the assigned category.
- Low: The team is not confident in the order of magnitude for the assigned category, and it is entirely possible that additional information would change the estimate.

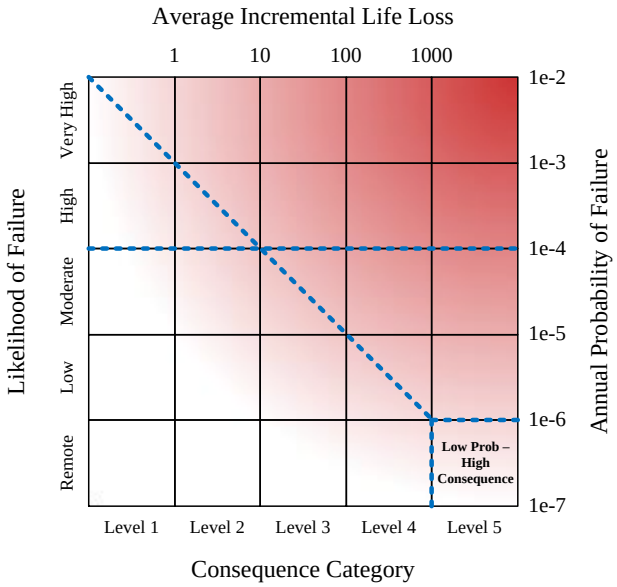

Fig. 28.5: USACE-USBR incremental risk matrix; [844]

28.2.3.3.4 Risk Matrix The risk matrix simply represents the relationship between the failure likelihood and incremental consequences, Figure 28.5. The "Annualized Life Loss" (i.e. social risk) is represented by the diagonal dashed line, while the "Annual Probability of Failure" (i.e. individual risk) is represented by the horizontal dashed line. The identified PFMs are supposed to fill a particular cell, or even cross several cells.

28.2.3.3.5 SQRA Procedure The following steps summarize SQRA [844]:

1. Review basic statistics and key features of the dam.
2. Review normal operating condition loadings.
3. Review available seismic hazard curves, more specifically the ground motions associated with 10^{-4}/yr earthquake, the approximate return period of the maximum credible earthquake.
4. Review inundation studies including probable impacts to downstream dams, roads and bridges, etc.

5. Develop the PFM.
6. Develop the factors making the PFM more likely and less likely to occur.
7. Elicit failure likelihood categories from each team member, along with the reasoning behind their estimate.
8. The facilitator or designated recorder captures the information, including the likelihood category and the rationale for its assignment (including the confidences).
9. A similar elicitation process is repeated to arrive at a consequence category for each PFM.

28.2.3.4 Quantitative Risk Analyses

A QRA provides the estimated risk in terms of probability and consequences of all the involved items in a quantitative fashion. In a mathematical form, the risk of failure can be presented as:

$$\text{Risk} = \int P[l] \,.\, P[f|l] \,.\, C[l, f] \tag{28.1}$$

where $P\,[A|B]$ is the conditional probability that A is true given that B is true and C stands for the consequences; l presents the load event, and f is the system failure. Moreover, the integral accounts for all the events under study.
In the context of risk analysis, Equation 28.1 can be transformed into other forms as well:

- Structural failure probability, P_f, can be computed using the first two elements of the main equation,

$$P_f = \int P[l] \,.\, P[f|L] \tag{28.2}$$

- Individual risk: is a risk imposed on an individual because of the existence of the dam. It can be estimated by the probability of death of the most exposed person living downstream due to dam failure.
- Societal risk: is computed though combining the social consequences of dam failure, C_S, (e.g. loss of life) on the affected population and the dam failure probability,

$$\text{Risk}_S = \int P[l] \,.\, P[f|l] \,.\, C_S[l, f] \tag{28.3}$$

- Economical risk: is computed though combining the economic consequences of dam failure, C_E, (e.g. loss of money) and the dam failure probability,

$$\text{Risk}_E = \int P[l] \,.\, P[f|l] \,.\, C_E[l, f] \tag{28.4}$$

On the other hand, the incremental and total risk are formulated as:

- Incremental risk: is the risk exclusively produced by the dam failure:

$$\text{Risk}_{S/E}^{inc} = \int P[l] \,.\, P[f|l] \,.\, C_{S/E}^{inc}; \tag{28.5}$$
$$C_{S/E}^{inc} = C_{S/E}[l, f] - C_{S/E}[l, \bar{f}]$$

where $\bar{f}$ refers to non-failure cases.

- Total risk: is the total flooding risk in the downstream are resulted from both the failure and non-failure conditions:

$$\text{Risk}_{S/E}^{tot} = \int P[l] \,.\, P[f|l] \,.\, C_{S/E}[l, f] \tag{28.6}$$
$$+ \int (1 - P[l] \,.\, P[f|l]) \,.\, C_{S/E}[l, \bar{f}]$$

According to FERC [310], three sub-levels in quantitative risk analysis can be summarized as follows:

- Purpose/outcome:
  - Sub-level A: Lowest level of issue-specific risk analyses to determine if risks are tolerable or unacceptable.
  - Sub-level B: Intermediate level of issue-specific risk analyses.
  - Sub-level C: Highest level of issue-specific risk analyses to determine if risks are tolerable or unacceptable.
- Type of risk:
  - Sub-level A, B and C: Individual life safety; incremental life safety; non-breach life safety; annual probability of failure; economic.
- Typical level of effort:
  - Sub-level A: Relatively simple/routine models. Team-based, facilitated.
  - Sub-level B: Moderate to high level of effort. Team-based, facilitated.
  - Sub-level C: Intense level of effort. Sophisticated/detailed models. Team-based, facilitated.
- Loading:
  - Sub-level A: Simple loadings with no challenging technical issues.
  - Sub-level B: Intermediate difficulty. Use of additional experts may be required.
  - Sub-level C: Complex, difficult loadings. Use of additional experts likely to be required.
- Consequences:
  - Sub-level A: Relatively simple to estimate. Straightforward.
  - Sub-level B: Intermediate difficulty. Use of additional experts may be required.
  - Sub-level C: Challenging and difficult. Use of additional experts likely to be required.
- System response:

  - Sub-level A: Simple, common PFMs.
  - Sub-level B: Intermediate difficulty.
  - Sub-level C: Complex, multiple PFMs with multidisciplinary teams.
- Uncertainty:
  - Sub-level A: Simple approach to quantify.
  - Sub-level B: Moderate approach to quantify.
  - Sub-level C: Detailed approach to quantify.

Level 4 risk analyses (i.e. QRA) are typically focused on those PFMs that have been identified as credible and significant from the results of the Level 3 risk analysis (i.e. SQRA). The scope of the Level 4 risk analysis is more rigorous and is intended to achieve a defensible, risk-informed basis for initiating permanent risk reduction studies. Level 4 risk analyses have three sub-levels with increasing robustness and effort (from A to C). Level 4C risk analysis often requires probabilistic seismic and hydrologic loadings.

28.3 Risk Assessment

Risk assessment is the process of considering the results from a quantitative or qualitative estimated risk analysis of an existing dam, along with all other factors related to a safety decision [297]. Quantitative results provide three measures related to risk:

- Likelihood of a failure occurrence or adverse consequence in terms of annual probability.
- Estimated life loss given failure or adverse consequence presented as the total estimated loss for a given annual probability of failure, or the product of those two values which is called the "average annual life loss" (f-N and F-N charts).
- The economic damages (F-$ chart).

28.3.1 Tolerable Risk

The concept of tolerable risk is tied with different conditions [310]:

- Risks that society is willing to live with so as to secure certain benefits,
- Risks that society does not regard as negligible (broadly acceptable) or something it might ignore,
- Risks that society is confident are being properly managed by the owner,
- Risks that the owner keeps under review and reduces still further if and as practicable [417, 611].

Two fundamental principles, from which tolerable risk guidelines are derived, are: 1) equity and 2) efficiency [457]. Often there is a conflict in achieving equity and efficiency. Therefore, balancing between these two is important to develop a tolerable risk guideline. The tolerable risk should consider both societal and individual risks in managing risks.

The "as-low-as-reasonably-practicable" (ALARP) concept provides a way to address efficiency aspects in both individual and societal tolerable risk guidelines. Different agencies and organizations developed tolerable risk guidelines for dam safety, such as: ANCOLD, NSW, DSC, CDA, USACE.

28.3.2 Risk Guidelines

As listed in Section 28.2.2, there are four risk measures. Risk guidelines for life safety and APF are explained below. All the numbers provided below are based on FERC requirements, and they might be different for other agencies/organizations. The FERC has no tolerable risk guideline for economic and environmental consequences.

28.3.2.1 Life Safety

For three types of incremental life safety risk guidelines:

- Individual incremental life safety: The individual risk (IR) should meet the following criteria:
  - If IR $\geq$ 1E-4 per year: risks are unacceptable except in extraordinary circumstances.
  - If 1E-6 $\leq$ IR $<$ 1E-4 per year: risks are intolerable unless ALARP conditions are satisfied.
  - If IR $<$ 1E-6 per year: risks are generally tolerable; however, ALARP considerations should be employed.
- Societal incremental life safety:
  - Probability distribution of potential incremental life loss: The social incremental risk (SIR) should meet the following criteria and is evaluated based on the F-N chart, Figure 28.6:
    - If SIR $\geq$ 1E-3 lives per year: SIR above the tolerable risk reference line is unacceptable except in extraordinary circumstances.
    - If 1E-5 $\leq$ IR $<$ 1E-3 lives per year: SIR in this range will be considered intolerable unless ALARP considerations are satisfied.
    - If SIR $<$ 1E-5 per year: SIR in this range will be considered tolerable; however, the ALARP considerations should be employed.
    - Low Probability / High Consequence region: If the estimated social risk falls into the gray zone in Figure 28.6, the evaluation of the tolerability of risk must be based on a thorough review of the project benefits and risks.
  - Average Annual Life Loss (AALL): The AALL should meet the following criteria in accordance with f-$\bar{N}$, Figure 28.6:
    - If AALL $\geq$ 1E-3 lives per year: AALL in this range is unacceptable except in extraordinary circumstances.
    - If 1E-5 $\leq$ AALL $<$ 1E-3 lives per year: AALL in this range will be considered intolerable unless ALARP considerations are satisfied.

- If AALL < 1E-5 per year: AALL in this range will be considered tolerable; however, the ALARP considerations should be employed.
- Low Probability / High Consequence region: If the estimated social risk falls into the gray zone in Figure 28.6, the evaluation of the tolerability of risk must be based on a thorough review of the project benefits and risks.

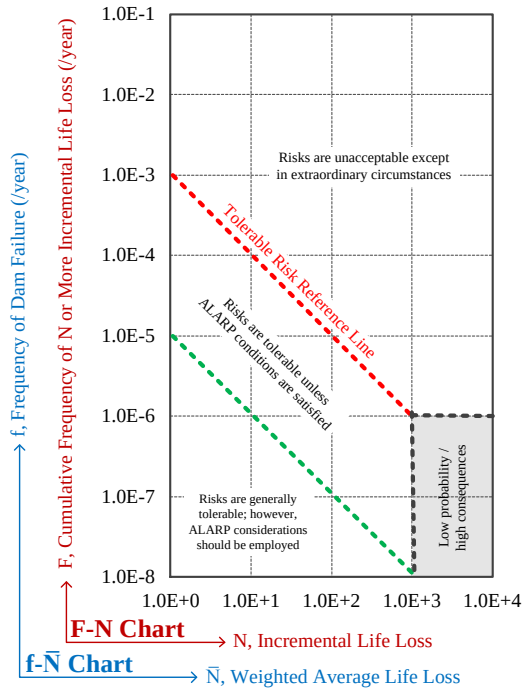

Fig. 28.6: SIR (F-N chart) and AALL (f-N̄ chart); [310]

28.3.2.2 Annual Probability of Failure

FERC uses the equity principal to estimate the APF:

- APF $\geq$ 1E-4 per year: APF in this range is unacceptable except in extraordinary circumstances.
- APF < 1E-4 per year: APF in this range will be considered tolerable provided the other risk guidelines and the ALARP considerations are met.

28.3.3 Comparison of Different Guidelines

Figure 28.7 shows the F-N or f-N charts from different agencies/organizations.

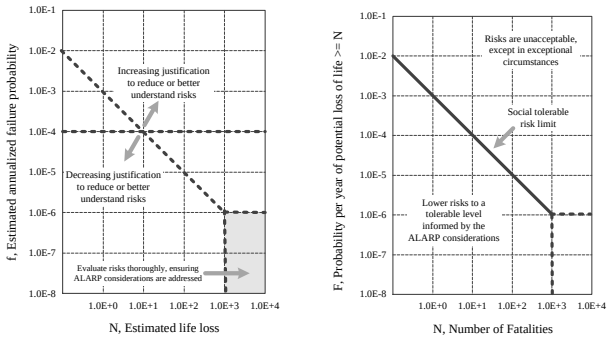

(a) USBR (b) USACE

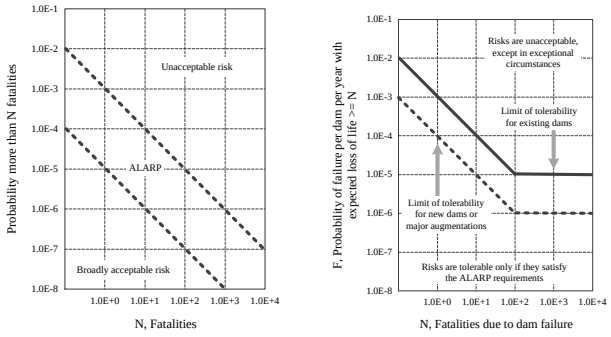

(c) CDA (d) ANCOLD

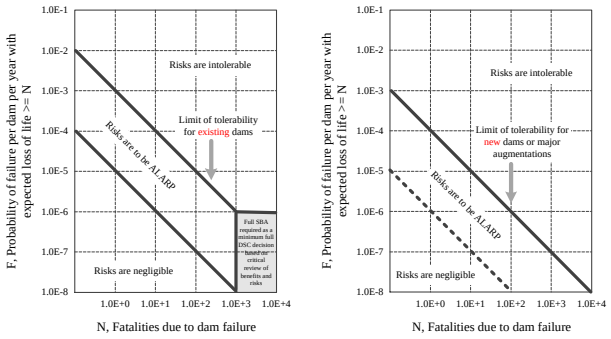

(e) NSW

Fig. 28.7: F-N or f-N charts by different agencies/organizations

Chapter 29
Deterministic Analyses of Concrete Dams: Examples

Abstract
Six examples of deterministic nonlinear analyses of dams are presented in this chapter. The first is a potential failure mode analysis that relies on nonlinear joint elements to capture potential sliding. The next two examples are nonlinear AAR analyses of an arch gravity dam and a hollow buttress dam. The next two report the seismic safety evaluation analysis of dams, and the last example addresses the impact of SSI modeling on a dam.

29.1 Potential Failure Mode Analysis

At times, the rigid body limit equilibrium model (LEM) of a gravity dam yields factors of safety below the acceptable values. Since such an analysis relies on a number of assumptions, a proper finite element analysis is warranted before the dam is indeed deemed to be unsafe for the corresponding probable maximum flood.
Such an analysis was performed for Gilboa dam. The dam, completed in 1927, is a 180-foot-high dam that consists of a 700-foot-long earth embankment and a 1,324-foot-long cyclopean concrete spillway [922]. The spillway was built on nearly horizontally interbedded layers of sandstone, mudstone, siltstone, and shale, with shale being the predominantly weak rock unit. The spillway is composed of cyclopean concrete and has a stepped downstream face. A cutoff wall of varying depth was constructed near the upstream face. It was determined that sliding stability of the spillway structure may not meet current New York State dam safety criteria and was marginal for the record flood. Given the critical nature of the reservoir, an interim stability improvement project was implemented for completion prior to anticipated major reconstruction, Figure 29.1.
The finite element study was confronted by a number of challenges. The dam model had dimensions spanning two orders of magnitudes and had a complex geometry at its "underbelly," in particular its cutoff, and variable geometry from East to West. Furthermore, part of the downstream face is buried under rock foundation. This resulted in a complex network of uplift.

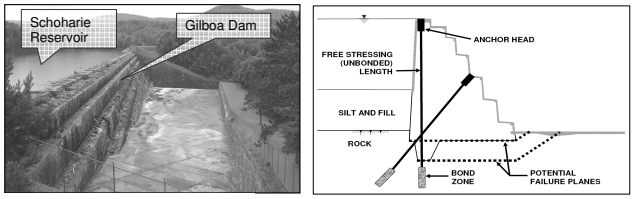

(a) Aerial view (b) Interim stability improvement

Fig. 29.1: Gilboa dam, [922]

29.1.1 Model

The first step consists of identifying the potential failure mode (PFM) [309] and then preparing accordingly a finite element mesh where joint elements will be inserted in-between otherwise "rigid" blocks. For each PFM, cohesive cracks (or joints) are placed along the potential failure planes making sure that a sliding/overturning mechanism could eventually develop. Those joints would have different properties depending on their locations (concrete-concrete, concrete-rock, or rock-rock). The zero-thickness cohesive joint element (described in Section15.3) will be characterized (among others) by cohesion, angle of fraction, fracture energy, dilatancy angle, and a yield surface. Hence, during the analysis, individual segments of the interface may fail (by traction and/or shear) resulting in a localized degradation (up to complete loss) of cohesion and tensile strength. Finally, should failure occur, the nonlinear analysis would fail to converge within reasonably assigned convergence criteria, and the post-processor will display the failure mode (rigid body translation/rotation of an un-deformed structure). Typically, the previous increment will display anticipated displacements.

To facilitate interpretation of results, the analysis Saouma, Červenka, and Reich [767] will also output for each joint/crack: summation of normal and shear forces, total cohesive forces, average angle of friction, and FSS Value. In addition, it will display the location of each of the resultant forces in the Cartesian coordinate system. These results can then be readily merged (if more than one crack segment defined the failure mode) in an excel file for final post-processing.

We identify three types of joints, Figure 29.2(a): a) concrete-concrete (dam and shear key; red), b) rock-concrete (blue), and c) rock-rock (green). These joints are defined for the purpose of assessing SSF along discrete postulated failure planes and do not necessarily represent joints as applied during construction. Cracks (numbered) and loads (lettered) are shown in Figure 29.2(b) where:

A. Hydrostatic on the upstream, governed by pool elevation. Note that A' will be acting on both sides of the cutoff (slightly unconservative as the pressure on the downstream side is likely to be slightly less than the one on the upstream).
B. Silt pressure (applied only on a portion of the upstream face).

C. Uplift along joint 4 (not extending beyond the toe of the dam). Uplift is full along that portion of the dam which may be cracked, trapezoidal otherwise extending from the upstream to the downstream pool elevations. Note that all uplift pressures are applied on the two opposite faces of the joints.
D. Constant uplift along joint 5. Uplift is equal to the downstream pool elevation acting on the second portion of the crack (the one beyond the dam).
E. Uplift along joint 2 (not extending beyond the toe of the dam). Uplift is full along that portion of the dam which may be cracked, trapezoidal otherwise extending from the upstream to the downstream pool elevations.
F. Constant uplift along joint 3. Uplift is equal to the downstream pool elevation acting on the second portion of the crack.
G. Downstream hydrostatic pressure acting against the portion of the dam under the rock. Pressure depends on the downstream pool elevation.
H. Upstream and downstream hydrostatic load applied over the foundation; H' hydrostatic pressure acting over the concrete slab.
I. Hydrostatic pressure acting over the crest based on the full head water.
J. Additional weight of concrete steps.
K. Post tensioning force at the crest.
L. Post tensioning force on the downstream face.
M. Self weight of the dam.
N. Self weight of the rock.

The 3D conceptual model of the dam is shown in Figure 29.2(c). Finally, a verification of the ability of the mesh to capture the potential failure modes was tested by a pushover analysis in which the upstream pool elevation was increased until failure, Figure 29.2(d). The adopted 3D finite element mesh is shown in Figure 29.2(e). Incidentally, such an analysis would determine the Imminent Failure Mode (IMF). The sliding safety factor (SSF) is defined as the ratio of the resisting forces over the applied forces. Using a photographic analogy, this value can be defined through:

- "Coarse grain" by simply adding all the three sets of forces acting along the three joints.
- "Fine grain" by determining the safety factor point wise (at each Gauss point) along each of the three joints.
- "Medium grain" by determining the average for each joint separately.

It is by now evident that for a direct comparison with the prevalent guidelines, a coarse grain approach is most appropriate. However, one ought not to entirely overlook the fine grain view also. Indeed it is quite possible that localized "failures" may be captured by the fine grains expression of FSS. Finally, we should keep in mind that passive activation may occur without failure, and similarly localized dam failure may occur with or without passive activation. .

29.1.2 Finite Element Analysis

Focusing on block 6 (perceived to be the most critical one), the principal stresses are shown in Figures 29.3(b) and 29.3(c). The smallest compressive stress in the

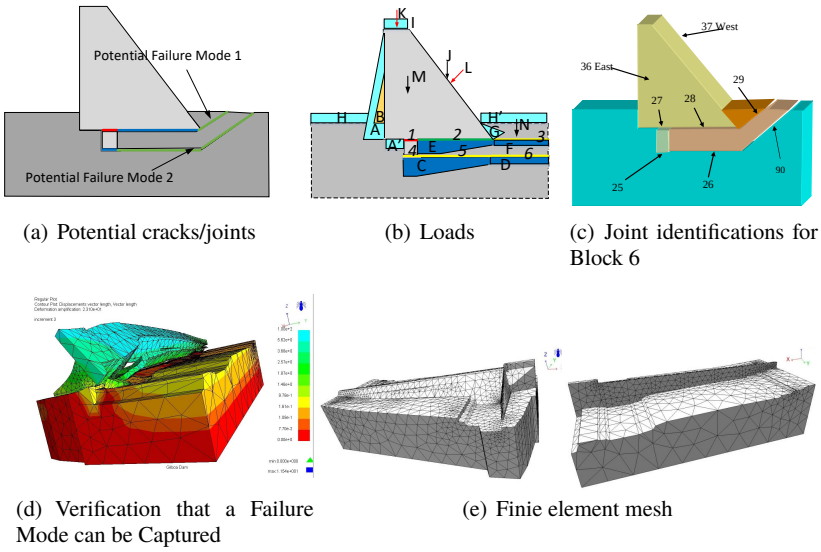

(a) Potential cracks/joints

(b) Loads

(c) Joint identifications for Block 6

(d) Verification that a Failure Mode can be Captured

(e) Finie element mesh

Fig. 29.2: Modeling considerations

concrete is 77 ksf (540 psi), and the largest one (tension) is 10.77 ksf (75 psi). Those are small values. The tensile stress occurs along the West wall base at a point where the complexity of the geometry (and thus discretization) is likely to cause some numerical singularities. Nevertheless, the kinematics of the structure can explain tensile stresses at that portion of the wall. This detail may require further focused and detailed investigation but should not affect the results of this analysis. With regard to the vertical transverse joint displacements (not to be confused with the horizontal joints connecting dam to rock), Figure 29.3(a), we distinguish between the translation of the joint (with respect to the original mesh) and the joint opening. The former, joint translation, is in the downstream direction as expected and is larger around block 6 than in others. As to the joint opening displacement, we note that it is entirely closed.

In this regard, further insight is achieved through examination of joint 36 (between blocks 5 and 6) relative sliding and opening in Figure 29.4(a) and Figure 29.4(b), respectively. The relative displacements (crack sliding and opening displacements) increase with elevation (Z) and decrease from the upstream to the downstream (in other words, most of the displacements occur close to the upstream side and taper down as we go downstream). Again those values are quite small. It should be noted that those (so-called) carpet colored plots are generated by GNUPLOT on the basis of unstructured (not with equal x and y spacing, and not within a rectangular bounding box) data coming from the finite element analysis. The program in turn performs an internal interpolation to display results on a regular grid and extrapolates if necessary to fill up a rectangular bounding box. The effect is that a portion of the rectangular

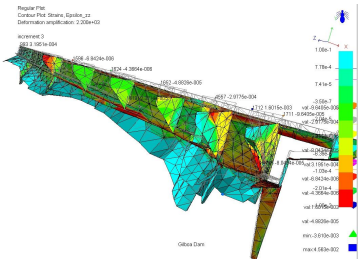

(a) Vertical Transverse Joint Opening Displacements due to hydrostatic loads (Contour maps of Crack Sliding/relative Displacements in ft.)

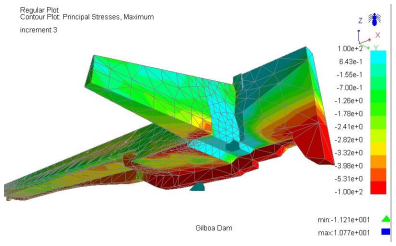

(b) Dam

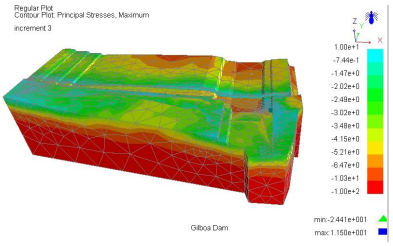

(c) Foundation

Fig. 29.3: Selected results

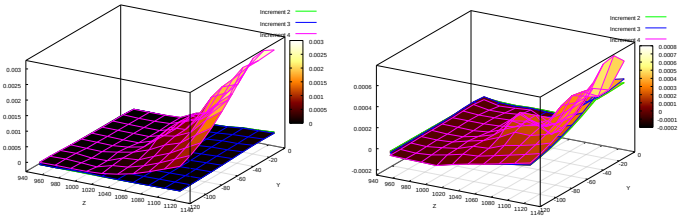

(a) Relative Sliding (ft) due to hydrostatic load only

(b) Relative Opening (ft) due to hydrostatic load only

Fig. 29.4: Joint 36 (between Block 5 and 6)

color plot surface has been extrapolated outside of the physical bounds of the model and has no physical meaning.

The minimum and maximum stresses were equal to -56.7 ksf (390 psi) and 11.5 ksf (80 psi), respectively. Those are small localized values which are well within the range of stresses that can be realistically accommodated by the average allowable bearing stress for the bulk foundation.

29.1.3 Safety Factors against Sliding

Undoubtedly, the most important factor to consider for the dam safety is the FSS. It is defined as

$$FSS = \frac{cA_{unc} + \sum F_N \tan \Phi}{\sum F_S} \tag{29.1}$$

where c, A_{unc}, F_N, Φ, and F_S are the cohesion, uncracked area, normal force, angle of friction, and shear force.

The PFM is composed of two or more segments, and throughout the analysis, the finite element code will print for each one the data required to evaluate the FSS. Hence, in our calculation, the FSS will be first evaluated for each crack segment and the forces added together to obtain a single representative FSS. This assessment can be performed for each of the blocks. Results of the FSS calculations for block 6, which is of most concern, is shown in Table 29.1.

Table 29.1: FSS Calculation for the upper crack of block 6

Top Crack			
	27	28	29
	C-C	C-R	R-R
	Cutoff	Base of Dam	Passive Wedge
Average Friction Angle	47.6	29.4	55
Total Cohesion Force	100,100.	0	982.8
Total Normal Force	-50,040.	-59,400.	0.2
Total Shear Force	3,680.	13,300.	437.4
Global FSS	42.1	2.5	2.2
Total Area	2,861.	10,318.	679.2
FSS Computed	42.1	2.5	2.2
Total resultant F_Z	-50,070.	-59,601.	-27
Resultant F_Z loc. y	-10.3	-80.2	-159.6
For Blocks	27-28	27-28-29	
Total Cohesive Force	100,100.	101,100.	
$\sum F_N \tan \Phi$	88,280.	88,280.	
Resistance	188,400.	189,400.	
Horizontal Force	16,980.	17,417.	
FSS	**11.1**	**10.9**	
Y Location of F_Z (Vert.)	**-48.3**	**-48.3**	
Length of base of dam (not rock)	153	214	
1/3 length	51	71.3	
2/3 length	102	142.7	
Angle of Resultant	**-89.6**	degrees wrt horizontal	

We note that:

1. The FSS of each segment taken individually is quite high. FSS values of 42.1 for joint 27 (concrete-concrete), 2.5 for a segment along the horizontal concrete-rock interface (28), and 2.2 for the inclined rock-rock segment (29) were determined.
2. The upper passive wedge is subjected to a small tension. It should be noted that the bulk of the horizontal hydrostatic load is transferred through the cutoff

to the lower failure plane (which puts interface 90 under high normal stresses) whereas a much smaller portion of that load is transferred along the upper failure plane. This is compounded with the relatively high uplift (at PMF) in the upper passive wedge, and thus explains the small tensile normal stress (as opposed to a compressive stress which would have been intuitively expected).

3. If we consider the joint to be composed of all three segments, then the FSS is 10.9; if we consider only the segments right under the dam, then the FSS is 11.1.
4. The resultant force (considering only the first two segments which are under the dam) is about 109,672 kips (50,070+59,601) and is at 48.3 ft from the upstream side of the cutoff (which is at 12 ft from the upstream face of the dam) whereas the middle third of the interface is at 51 ft.

29.1.4 Summary

This example first highlighted the surmountable challenges of a very complex geometry with complex PFM, but also the complexity of uniquely defining the factor of safety against sliding in a finite element analysis.

29.2 AAR in an Arch Gravity Dam; Isola

This section reports on a highly detailed analysis of an arch gravity dam (see Figure 29.5) and is intended to serve as a reference for the steps required to perform a diagnosis of major infrastructure adversely affected by AAR. The data preparation for such an analysis may prove to be complex and will be reported first, followed by a discussion of results.

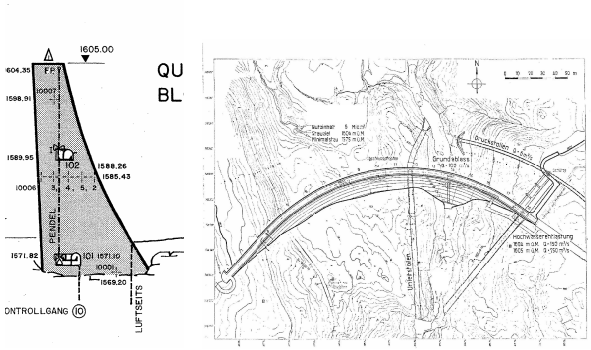

(a) Section (b) Internal stresses

Fig. 29.5: Arch gravity dam geometry

29.2.1 Data Preparation

The comprehensive incremental AAR analysis of a concrete dam is relatively complex, regardless of the selected AAR model, given that data preparation for the load can be as cumbersome as it is voluminous (see Figure 29.6(a)).
The seasonal pool elevation variation (for both the thermal and stress analyses) must first be identified (Figure 29.6(b)); moreover, the stress-free temperature, T_{ref} (typically either the grouting temperature or the average annual temperature), needs to be identified along with the external temperature (Figure 29.6(d)). The pool elevation will affect the internal state of stress, which in turn will alter AAR expansion (through Eq. 11.11, 11.13 and 11.18). This situation is more relevant for high Alpine dams (where the annual pool variation is greater than for low-head, low-altitude dams). This variation will then be replicated over n years for the duration of the analysis (Figure 29.6(c)). External air and water temperatures will be considered next (Figure 29.6(d)). In the absence of precise field data, the air temperature may be obtained from NOAA [640].

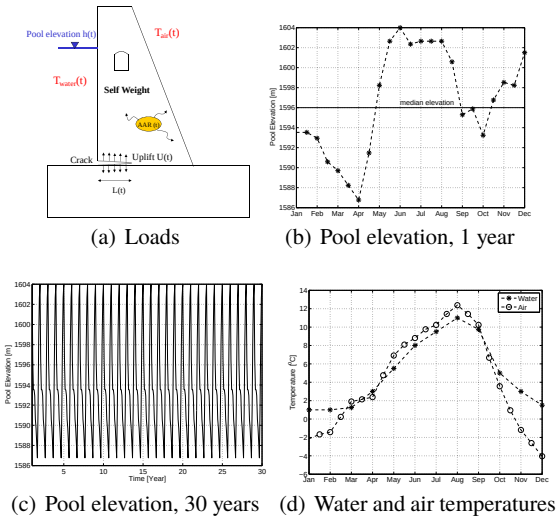

(a) Loads (b) Pool elevation, 1 year

(c) Pool elevation, 30 years (d) Water and air temperatures

Fig. 29.6: Preliminary load data to be collected for the AAR analysis of a dam

The units adopted are MN and Gg for F and M, respectively. For time, the ATU (Analysis Time Unit) has been adopted, corresponding to 4.35 weeks or 30.42 days (i.e. 12 ATU span one year).
The next step calls for conducting a transient thermal analysis since the reaction is thermodynamically activated. Consequently, the total temperature is included as part of the constitutive model. Heat transfer by both conduction and convection are taken into account whereas radiation is implicitly incorporated (Figure 29.7(a)). The

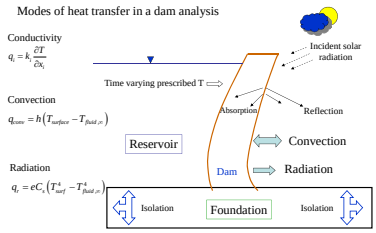

(a) Governing equations for the thermal analysis

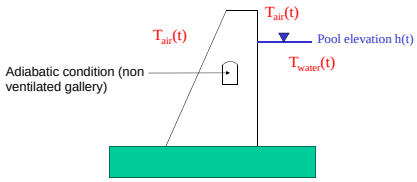

(b) Thermal boundary conditions

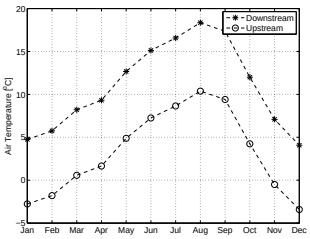

(c) Upstream and downstream air temperatures with inclusion of radiation

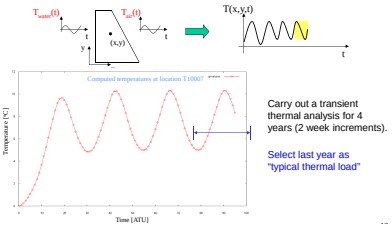

(d) Preliminary transient analysis

Fig. 29.7: Data preparation for thermal analysis of a dam subjected to AAR

thermal analysis is conducted using the parameters listed in Table 29.2.

Table 29.2: Thermal properties found in an arch gravity dam

Reference temperature	T_{ref}	°C	7.0
Conductivity	k	MN.m/(m.ATU.°C	7.738
Specific heat	c	MN.m/(Gg,°C)	887
Density	r	Gg/m^3	2.510^{-3}

Radiation is implicitly included by means of a simplified procedure whereby ambient air temperature is modified [563]:

$$\begin{aligned} T_{us} &= 0.905T_{air} - 0.4°\text{C} \quad \text{Upstream} \\ T_{us} &= 0.937T_{air} + 7.2°\text{C} \ \text{Downstream} \end{aligned} \tag{29.2}$$

resulting in the temperature distribution shown in Figure 29.7(c).
Even though the external boundary conditions can be readily determined, the condition associated with the gallery is of primary importance for potential internal cracking (Figure 29.7(b)). More specifically, it is important to know whether during

construction the gallery is closed or open to the outside air. The precise thermal analysis should be performed in accordance with Figure 29.7(a).
Next, the transient thermal analysis is to be performed for at least 3-5 years, until the annual variation appears to converge (Figure 29.7(d)). These analyses enable deriving, among other things, the spatial and temporal variations of temperature ($T(x, y, z, t)$).
The dam, however, must first be discretized. As is the case with most dams, a set of analytical parametric curves defining the arches (in general, circular segments in the U.S. and parabolic or elliptical segments elsewhere) is (typically) given. These curves are plotted in Figure 29.8(a).

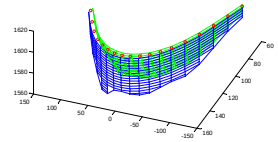

(a) Mathematical model of the dam

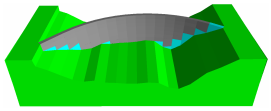

(b) Dam and foundation outlines

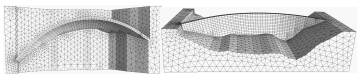

(c) Full 3D mesh for initial load increments

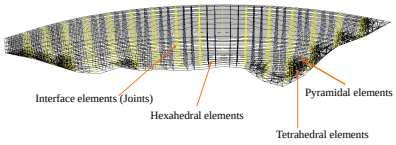

(d) Simplified 3D mesh for AAR expansion

Fig. 29.8: 3D Finite element mesh for the stress analysis

Using a special program (e.g. Beaver, developed by the author), the surface can be discretized. The boundary representation of the dam is then entered into a preprocessor, such as Saouma [753], in order to generate the finite element mesh. Figure 29.8(c) shows the resulting full 3D mesh used for the stress analysis. Joint elements are placed at both the joints and the rock-concrete interface (Figure 29.8(d)). Let us point out that a different mesh was required for the thermal analysis since the interface elements needed to be removed.
As previously indicated, the time increment of one ATU corresponds to 4.35 weeks, and the initial reference temperature was set to zero. Given the external air temperature, both the pool elevation and water temperature boundary conditions were input into this initial boundary value problem. The analysis was performed using [767], making it possible to examine the temperature fields. It was found that after four years, the temperature field was harmonic with a one-year frequency. At this point, the analysis was interrupted and $T_{thermal}(x, y, z, t)$ recorded. The computed temperature distribution is shown in Figure 29.9. Note that these temperatures are to be used to evaluate the thermal strains, given that for the AAR analysis the total

(i.e. absolute) temperature is needed (and is simply obtained by adding the reference temperature of 7°C).

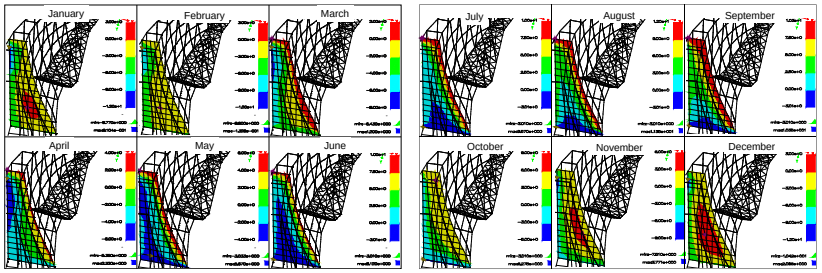

(a) January-June (b) July-December

Fig. 29.9: Computed internal temperature distribution variation

Subsequent to the thermal analysis, $T_{thermal}(x, y, t)$ must be transferred to $T_{stress}(x, y, t)$ since, in general, the same finite element mesh is not available (the foundations, joints, and cracks are not typically modeled as part of the thermal analysis).
Lastly, a comprehensive input data file must be prepared for the stress analysis; this file includes:

1. Gravity load (first increment only).
2. $\Delta\dot{T}(x, y, t) = \dot{T}_{stress}(x, y, t) - T_{ref}$ in an incremental format. This is a subtle step that must not be overlooked. The stress analysis is in fact based on the difference between the actual and stress-free temperatures. In addition, an incremental analysis requires this set of data to be provided in an incremental format.
3. Stress-free referenced temperature which is to be added to the temperature data in order to determine the total absolute temperature needed for AAR.
4. Cantilever and dam/foundation joint characteristics. The former must be included in any arch dam since expansion may lead to an upstream joint opening while the latter must be taken into account given that AAR-induced swelling may result in a separation of the dam from the foundation in the central portion of the foundation.
5. Uplift load characteristics (typically matching the upstream hydrostatic load).
6. AAR data, which has been described above.

Moreover, the compiled set of data must be looped over at least 50 years in order to provide a complete and correct set of natural and essential boundary conditions (Figure 29.10).
The dead load is applied during the first increment. Following this step, displacements are reset to zero while maintaining the internal strains/stresses. During increments two through five, the hydrostatic (and uplift) load is applied, and the AAR expansion only initiates at increment six.

		January		February		March		April		May		June	
Incr.		6.00	7.00	7.00	8.00	9.00	10.00	11.00	12.00	13.00	14.00	15.00	16.00
Body force		dam											
Hydrostatic	Pool Elevation	1596.47	1593.53	1593.53	1592.94	1590.59	1589.71	1588.24	1586.76	1591.47	1598.24	1602.65	1604.00
	Incremental Elevation	-5.03	-2.94	0.00	-0.59	-2.35	-0.88	-1.47	-1.47	4.71	6.76	4.41	1.35
Uplift	Pool Elevation	1596.47	1593.53	1593.53	1592.94	1590.59	1589.71	1588.24	1586.76	1591.47	1598.24	1602.65	1604.00
	Incremental Elevation	-5.03	-2.94	0.00	-0.59	-2.35	-0.88	-1.47	-1.47	4.71	6.76	4.41	1.35
Temperature [°C]	Air	-3.10	-2.14	-1.67	-1.43	0.24	1.90	2.14	2.38	4.76	6.90	8.10	8.81
	Water	1.00	1.00	1.00	1.00	1.00	1.50	3.00	3.00	5.00	6.00	8.00	8.00

		July		August		September		October		November		December	
Incr.		17.00	18.00	19.00	20.00	21.00	22.00	23.00	24.00	25.00	26.00	27.00	28.00
Body force		dam											
Hydrostatic	Pool Elevation	1602.35	1602.65	1602.65	1602.65	1600.59	1595.29	1595.88	1593.24	1596.76	1598.53	1598.24	1601.50
	Incremental Elevation	-1.65	0.29	0.00	0.00	-2.06	-5.29	0.59	-2.65	3.53	1.76	-0.29	3.26
Uplift	Pool Elevation	1602.35	1602.65	1602.65	1602.65	1600.59	1595.29	1595.88	1593.24	1596.76	1598.53	1598.24	1601.50
	Incremental Elevation	-1.65	0.29	0.00	0.00	-2.06	-5.29	0.59	-2.65	3.53	1.76	-0.29	3.26
Temperature [oC]	Air	9.76	10.24	11.43	12.38	11.43	10.24	6.67	3.57	0.95	-1.19	-2.62	-4.05
	Water	9.00	10.00	11.00	11.00	11.00	8.50	6.00	4.00	3.00	3.00	2.00	1.00
AAR	AAR	Activated											

Fig. 29.10: Data preparation, cyclic load

29.2.2 Stress Analysis

Following completion of the transient thermal analysis, the stress analysis may be performed. It should be noted however that the finite element mesh for the stress analysis of a dam affected by AAR must differ from the mesh used for the thermal analysis and moreover includes joints, the interface between dam and rock foundation, and the rock foundation. These components are not required in the thermal analysis but are very important to capturing the real behavior of a dam affected by AAR (and thus capturing the real crest displacements on which parameter identification is based, as will be explained in the following section). AAR expansion can indeed result in: 1) opening of the downstream vertical joints and closure of the upstream vertical joints in an arch dam, 2) possible movement of the various buttresses on a gravity dam along the joints, and 3) sliding of the dam when subjected to a compressive state of stress on the foundation joint.
With regard to the temporal and spatial variations of temperature, it should be kept in mind that the stress analysis requires a temperature difference with respect to the stress-free temperature (namely the grouting temperature $T(x, y, z) - T_{grout}$) whereas AAR evolution depends on the total absolute temperature inside the dam $T(x, y, z)$.

29.2.3 Results

Since the "proper" AAR parameters were not known *a priori*, the system identification process described in Section 11.5 was adopted with the initial and final values shown in Table 29.3. Figure 29.11 illustrates the real-time graphical display of the evolution of the three key parameters as well as the comparison between computed and actual crest displacements. Each data point, constituting a full 30-year analysis (or about 360 increments), is thus a CPU-intensive operation (requiring a few days of CPU time).

Table 29.3: Initial and final parameter values in system identification study; Reference temperature 60°C

Parameter	Initial	Final	Unit
$\varepsilon^{\infty} \times 10^3$	3.8947	3.5500	-
τ_C	1.564	1.453	ATU
τ_L	3.279	4.072	ATU

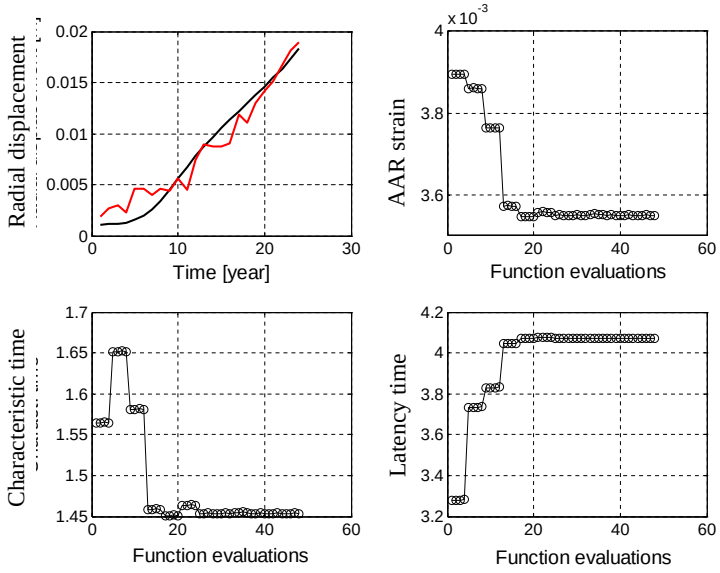

Fig. 29.11: System identification process for the AAR analysis of an arch gravity dam

The final results are shown in Figure 29.12(a), where the field measurement of crest displacements are plotted along with the first and last numerical simulations. These results are "sharper" upon examination of Figure 29.12(c). In either case, given the complexity of the simulation and the randomness of actual material properties (as "smoothed" through the system identification process), the results can be qualified as "good" and then used for prediction purposes.

The stress and strain comparisons are shown in Figure 29.13. A zone of high tensile stresses can be noted at the center of block 10.

Of special interest herein are the stresses and displacements along the base, as indicated in Figure 29.14(a). Let's note the positive crack opening displacement of the joint with confirmation provided by the deformed shape (Figure 29.14(b)). The zone of high tensile stresses at the center of block 10 is indicative of a potential

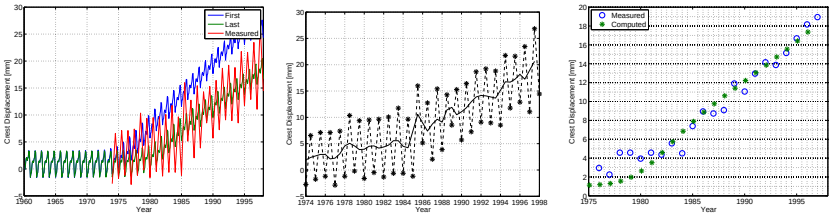

(a) System identification and results with seasonal variation

(b) Field-recorded crest displacements

(c) Final annual comparison

Fig. 29.12: Crest displacement comparison

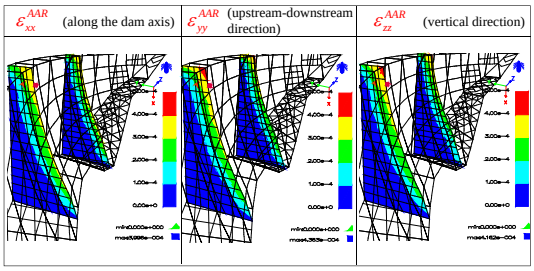

(a) Internal strains caused by AAR

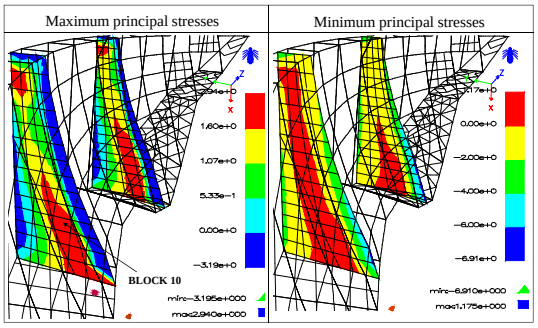

(b) Internal stresses

Fig. 29.13: Internal AAR and stresses

internal crack. Such a crack was actually observed in the gallery though it appears to be confined (for now) inside the dam and has not yet "daylighted" on the downstream face (Figure 29.15).

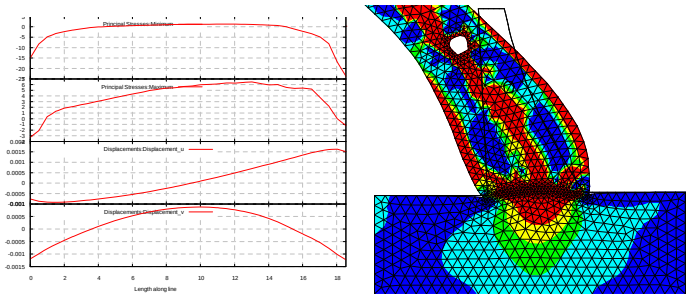

(a) Minimum/maximum stresses (MPa) and displacements (m) along the rigid rock/concrete interface; maximum principal stresses (MPa)

(b) Deformed shape of dam section

Fig. 29.14: "Lift-off" of central portion of dam due to AAR



(a) Internal crack

(b) Internal crack

Fig. 29.15: Observed internal crack

29.3 AAR in a Hollow Buttress Dam; Poglia

This example has been drawn from the contribution by the authors to the 8th ICOLD Benchmark Workshop on the Numerical Analysis of Dams (held in Wuhan, Hubei, China on Oct. 23-30, 2005), during which the contributors were asked to assess the safety of Poglia Dam [762]. The dam in Figure 29.16 is a hollow gravity dam composed of two lateral gravity dams and four hollow central diamond-head buttress elements.

This dam is characterized by a 137.1 m crest length, a 50 m height, two 14 m wide spillways, and a 22 m joint spacing. The concrete volume equals 34,600 m^3 while the reservoir volume is 500,000 m^3. The base, maximum, and operating pool elevations are 628.1, 632, and 625-628 m, respectively. The concrete properties are: a mass density of 2,400 kg/m^3, an elastic modulus of 18,000 MPa, a Poisson's ratio of 0.2, and compressive and tensile strengths of 32 and 1.5 MPa, respectively. Accelerated expansion tests were conducted on cores extracted from Poglia Dam at both 38

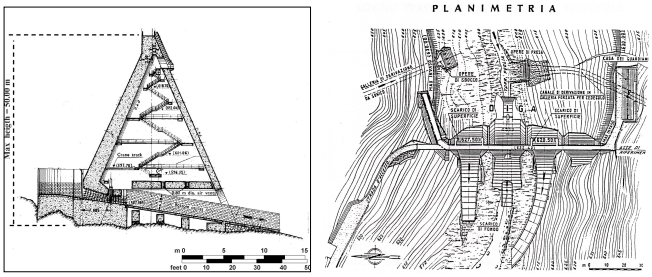

(a) Section (b) Plan

Fig. 29.16: Section (central element) and layout of Poglia Dam

and 80°C. From these tests, it was determined that the residual expansion equals approximately 0.095%. Rock has an elastic modulus of 10,000 MPa and a Poisson's ratio equal to 0.1. The compressive and tensile strengths amount to 32 and 0.15 MPa, respectively. Let's also closely observe the rock/concrete joint, with a friction angle of 37 degrees and a cohesion of 1.0 MPa.

The dam monitoring system is essentially based on: 1) 12 monitoring points along the dam for recording vertical displacements, 2) 6 targets for recording horizontal crest displacements in the stream direction, and 3) 2 pendulums for recording both longitudinal and lateral displacements. The targets have been placed on either side of the vertical joints. Additional instrumentation consists of extensometers and piezometers.

Though no chart exists to plot crest displacement vs. time, it is understood that the crest vertical drift (which started in 1970) reached 8 mm in 1982 and then a total value of 30 mm in 2000. This increase is quasi-linear with a slightly greater rate during the later years (Figure 29.17). In addition, irreversible displacements of

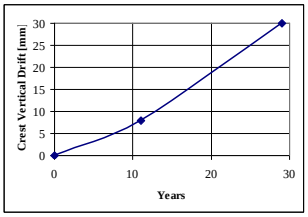

Fig. 29.17: Measured crest vertical displacement

about 0.1 mm/year and 0.2 mm/year were recorded in the cross-valley direction (i.e. toward the right side) and along the stream direction, respectively. A downstream

displacement recorded on the right-hand corner may prove to be the most worrisome finding (due to lateral expansion of the two adjacent blocks).

29.3.1 Transient Thermal Analysis

Since our AAR model is highly dependent on temperature, a preliminary transient thermal analysis needs to be performed. In this analysis, only the dam is considered. Half the central element was modeled, and due to symmetry, adiabatic boundary conditions could be applied on the plane of symmetry. Convection was neglected, and the recorded temperatures were assigned on the faces exposed to air (both outside and inside) and to water (Figure 29.18). Conductivity, k, was set to 44.67

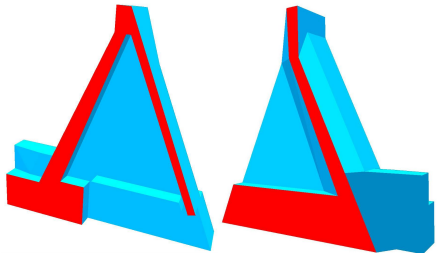

Fig. 29.18: Adiabatic boundary conditions for the thermal analysis

MN.m/(mATU.°C) and the mass density to 2.4310^{-3} Gg/m^3. In the context of our analysis, one ATU (Analysis Time Unit) corresponded to 6 months; hence 2 time increments per year were used. The temperatures are listed in Table 29.4. It

Table 29.4: Temperatures used for the Poglia Dam analysis

Season	Inside	Outside	Water
Winter	4.4	0.1	2.9
Summer	19.2	29	12.6

should be noted that the average (stress-free condition) temperature was subtracted from these values when conducting the thermal analysis. This average temperature was subsequently added to the nodal temperature for the AAR analysis (given that expansion depends on the total temperature and not on the temperature differential). The transient analysis was performed for five years; since results stabilized after four years, the Year 5 results were considered to be representative of the annual temperature variation. Figure 29.19 displays the internal dam temperature.

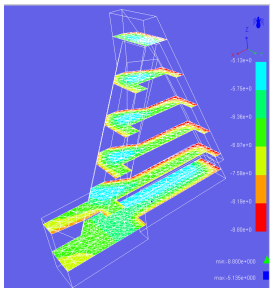

Fig. 29.19: Internal temperature of Poglia Dam

29.3.2 Stress Analysis

Following the thermal analysis, a stress analysis was conducted using a mesh that included the dam, its foundation, and the rock/concrete interface joints.
The material properties adopted for the analysis are those specified by the Benchmark with one notable exception. The tensile strength and cohesion of the dam/foundation interface were increased to 1.5 and 1.0 MPa (rather than the specified 0.15 and 0.10 MPa) because the preliminary analysis had indicated that these specified values were too small to resist the pool elevation. It should be noted that only initial guesses were introduced for the maximum volumetric strain latency and characteristic time since these values were to be determined subsequently from an automated system identification procedure (see Section 11.5). Following convergence of this minimization (of the error between computed and measured crest displacements), "fine-tuning" was manually performed to further reduce this error. The final (numerically obtained) volumetric strain was $3.50\text{x}10^{-3}$ whereas the experimentally obtained value (from laboratory tests) was $0.95\text{x}10^{-3}$. Total dam expansion however could only be justifiably determined from the numerical calculation.
The gravity load (for the dam only) was applied in the first increment, and the displacements (but not the stresses) were subsequently reset to zero (to remove self-weight displacements from the results). The pool elevation was then raised from the base elevation (582.10 m) to the maximum elevation (628.09 m) in four increments of 11.5 m each. It should be noted that as the pool elevation was increased, not only did the hydrostatic pressure rise, but so did the uplift pressure distribution under the dam. This pressure distribution will be automatically adjusted from triangular to trapezoidal should the dam base crack. From the sixth increment forward, pool elevation was kept constant and the AAR was active (increments 6 and 7 correspond to winter and summer of the first year). An analysis corresponding to 55 years of dam operations was carried out, and the resulting crest displacements were compared with measurements from the inverse analysis.

29.3.3 Analysis and Results

The 3D finite element mesh contained 6,145 nodes and 24,133 elements. The 3D nonlinear analysis employed the Tangent Stiffness method along with a Line Search and comprised 115 increments. The convergence criteria were set to 0.01, 0.02, 0.05, and 0.02 for the Energy, Relative Residual (ratio of the Euclidian norm of the current to the initial residual load vectors), Absolute Residual (ratio of the infinity norm of the current to the initial residual load vectors), and Displacement Error, respectively. A 50-iteration maximum was allowed. Each analysis lasted roughly 7 hours on a 3.00-GHz Xeon processor with 1.5 GB of RAM.

Figure 29.20(a) shows the crest displacements for the first seven increments, thus highlighting the crest displacement resulting from gravity and resetting the displacements to zero, followed by the four increments associated with impounding. Crest displacements over the entire analysis are provided in Figure 29.20(b); let's note that while the measured crest displacement has not been captured, all later displacements have been (accounting for about 3 cm). This situation may be partially due to the scarcity of field observations (moreover, indication is lacking as to whether they were taken during the summer or winter) as well as to the fact that the lateral and significant dam displacement/sliding has been neglected. Figures 29.20(c) and

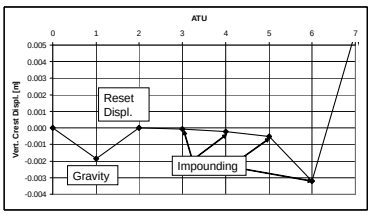

(a) Initial crest displacement during first seven increments

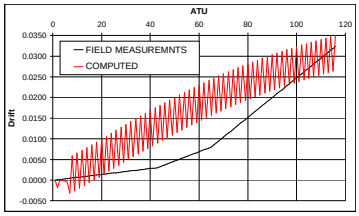

(b) Drift

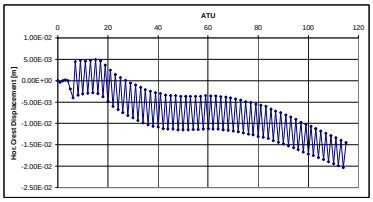

(c) Horizontal crest displacement

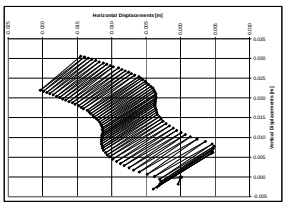

(d) Horizontal vs. vertical displacements

Fig. 29.20: Analysis results for the Poglia Dam

29.20(d) show both the vertical and horizontal crest displacements. Let's note that the seasonal variations are not negligible (possibly due to the thermal gradient between air trapped inside the dam and outside air) as compared to the total irreversible

AAR variation. As expected (due to lateral stresses), the horizontal displacements are substantially smaller than vertical displacements.
The overall deformed shape, however, is somewhat puzzling (Figure 29.21). It ap-

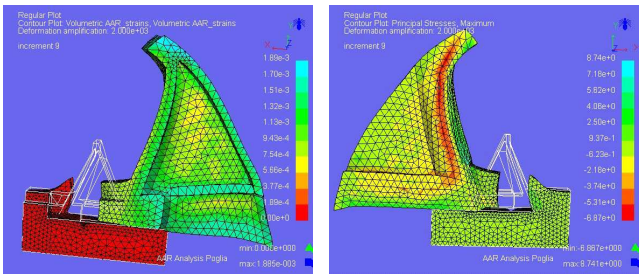

(a) Volumetric AAR strain (b) Maximum principal stresses (MPA)

Fig. 29.21: Deformed shape of the Poglia Dam

pears that for the given numerical assumptions, most of which have been stipulated by the Benchmark organizers, the dam is failing because of sliding. The sharp curvature of the top deformation corresponds to the pool elevation, which indeed lies 2 m below the crest.
Figure 29.22 illustrates various contour lines for the main rock/concrete joint. It is interesting to note that the crack opening displacements are maximum in the middle and then minimum on the upstream/downstream side. This finding had already been observed in the arch gravity dam analyzed previously. The normal stresses are mostly zero, and full uplift develops over most of the joint. The joint sliding displacement is linear and equals at most to 4.5 cm (note that adopting the Line Search method may have constrained overall sliding to such a "small" value). The shear distribution over the joint can also be visualized in this figure. According to these indications, the global safety factor relative to sliding remains below 1.
The overall AAR expansion at the end of the analysis ε^{∞} was 1.65 x 10^{-3} whereas the actual AAR expansion inside the dam was about 4 x 10^{-4}; this difference is due to the various model reduction factors. Furthermore, this expansion is on average equivalent to 40°C, i.e. just slightly lower than the 42°C determined in a previous study, which did not model the interface or assume thermal expansion to be uniform.
A second analysis was conducted using the lateral faces of the dam unconstrained in the lateral (Z) direction. Figure 29.23 shows that with the lateral faces of the dam now free to expand, the vertical displacement is reduced in accordance with the premises of our model. The deformed shape of the dam is depicted in Figure 29.24, where the lateral swelling is quite obvious. Despite the extensive effort for this analysis, the authors are not convinced that the structural model adopted actually reflects the current state of the dam. According to the numerical model, the dam has,

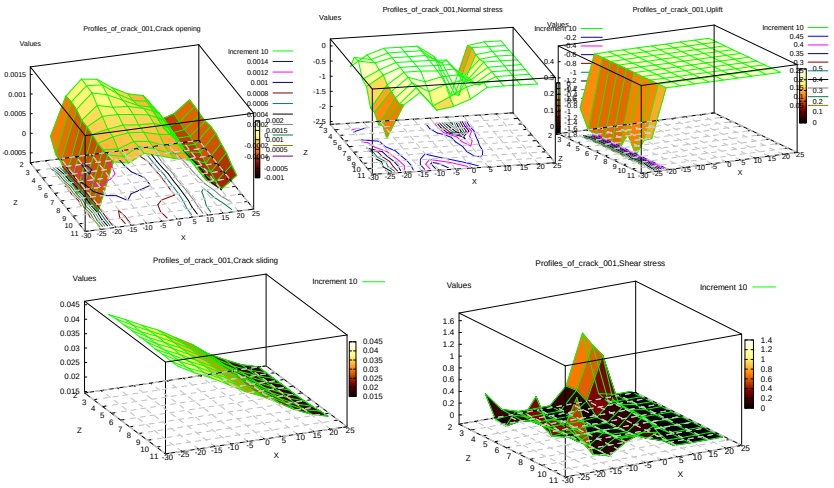

Fig. 29.22: Contour plots of the main rock/concrete joint, joint opening displacements (m), normal stresses (MPa), uplift pressures (MPa), joint sliding displacements (m) and joint shear stresses (MPa)

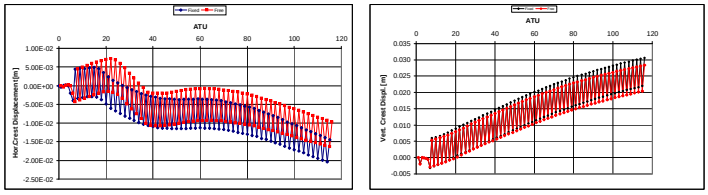

(a) Horizontal (b) Vertical

Fig. 29.23: Effects of lateral constraints on AAR expansion

at the very least, partially failed (though we know it is still “alive and well”). This perspective has rendered any subsequent evaluation of the failure pool elevation redundant, especially given the model’s limited scope. Let’s emphasize that the concern here is not the selected AAR constitutive model, but rather some of the physical assumptions, including:

- Rock/concrete interface properties. The cohesion was specified to be 0.15 MPa by the Benchmark organizers, which is a very low value. Moreover, preliminary analysis has indicated that the dam could not even sustain the hydrostatic load, let alone AAR expansion. The cohesion and tensile strength values were thus arbitrarily increased by a factor of 10.

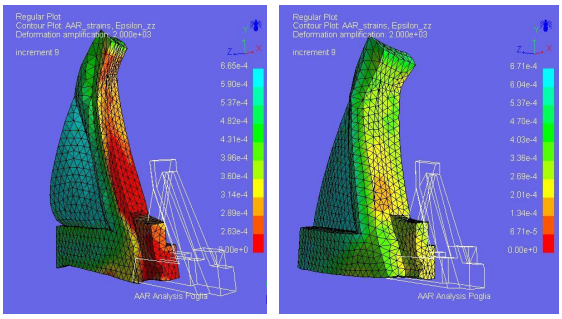

(a) Fixed (b) Free

Fig. 29.24: Deformed mesh and AAR strains in the lateral directions for both free and fixed boundary conditions

- The "2D" plane strain assumption may not actually reflect the complex stress state in this oddly shaped dam.
- This dam appears to be overly sensitive to thermal loads; hence an accurate long-term prediction of the dam would have required smaller time steps than what was adopted (6 months due to computational and "human" constraints).
- The benefit of a complete model is further justified by the most likely failure mechanism shown.

In light of the above assumptions and for a more accurate long-term prediction of this dam, the author would suggest that any future analysis considers the following:

1. Modeling of the entire dam since opening of the joint connecting the dam to the lateral gravity dams may be the primary concern (Figure 29.25), which in turn could cause overall structural failure.
2. Smaller time steps for the thermal and AAR analyses accompanied by a better grasp of the temperature boundary conditions.
3. Improved investigation of the rock/concrete interfaces through core extractions and testing in addition to piezometer readings of the uplift pressures.
4. Possibly, but not necessarily, accelerated tests of concrete cores at either 38°C or 70°C.
5. Again possibly, but not necessarily, "calibration" of the dam response by carefully monitoring crest displacements and the internal stress state using flat jacks (an appropriate step given the relatively small thickness of the structural components) during dam drainage and impounding.

Only with these considerations can the failure pool elevation be realistically determined, as any competing approach would serve as a mere academic exercise useful for comparing models but not for performing an accurate evaluation. Conducting a full 3D analysis of this dam would simply offer speculation on the likely mode of failure mechanism. The sharp corner between the two dam segments constitutes,

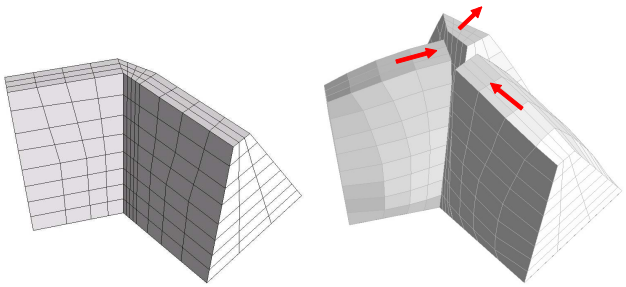

(a) Initial

(b) Localized failure due to AAR expansion

Fig. 29.25: Possible failure mechanism at a joint connecting two parts of the dam

in this case, the dam's "Achilles' heel," a worrisome feature that warrants further investigation.

29.4 Seismic Analysis of High Arch Dam: Dez

29.4.1 Dam Description

Dez Dam is a 203 m high double curvature arch dam with a peripheral joint separating the dam body from a concrete saddle structure called Pulvino. The dam is located in a narrow gorge at the Dez River in the Khuzestan Province in Iran. The dam was commissioned in 1963, and since then, sediments have accumulated in the reservoir up to an elevation of approximately 15 m below the intake of the power tunnel. General characteristics of Dez Dam are summarized in Table 29.5.

Table 29.5: Main characteristics of Dez Dam

Characteristics	Quantity
Maximum height above the foundation	203.5m
Crest length	240m
Crest thickness	4.5m
Base thickness at body/pulvino	21m/28m
Concrete volume (dam only)	328,000m^3
Concrete volume (dam and pulvino)	142,000m^3
Crest height	354m-asl
Normal operational level	350m-asl
Minimum operational level	290m-asl
Full reservoir capacity	3,350 Mm^3

At every level, the configuration of the upstream face is a constant radius arc, having a common center with the constant radius arc of the central portion of the downstream face. This results in a constant thickness, at each level, for the central portion of the arch. Towards the abutments, the downstream face follows smaller radii arcs, thereby increasing the arch thickness as the abutments are approached. The central angles of the arches increase gradually from the roadway over the top of the dam to approximately six-tenths of the top of the plug, which is located approximately nine-tenths of the distance down from the top of the roadway. The radii of the arches decrease from top to bottom. The centers of horizontal arches also move upstream. This results in a pronounced downstream overhang of the roadway in the central portion of the dam and a general concave appearance when viewed from downstream.

29.4.2 Finite Element Model

Three types of finite element models were provided in the present study for: thermal calibration (FE1), static structural calibration (FE2), and nonlinear seismic analysis (FE3) of the arch dam. The configurations of all three models are the same, and only element type and the element numbers are changed based on their usage and application. The thermal model of Dez Dam consists of 792 elements and has three layers in thickness. Also, all joints have been modeled using 956 contact elements in four layers. Mainly eight-node cubed solid-thermal elements with one degree of thermal freedom were used for modeling while some prism elements were used in the body-Pulvino connection. The reservoir and foundation were not modeled in the transient thermal analysis of the dam because their thermal effects are modeled as external thermal loads.

The ANSYS [37] finite element software was used as the main platform for modeling and analysis. For the preparation of the structural model for calibration, eight-node solid-structural elements were used in the dam body and Pulvino which have three translational degrees of freedom at each node. Similar to the thermal model, 792 elements were used for the dam and 956 contact elements were used for modeling contraction and peripheral joints using as-built drawings. The peripheral joint was modeled in such a way that completely separates the main body from the Pulvino while the contraction joints are continuous up to near the peripheral joint but never cut it.

Foundation medium was modeled using 3,770 twenty-node solid-structural elements while infinite elements were used for the outer boundary of the foundation medium. It should be noticed that the foundation dimensions were chosen to be large enough with respect to the dam body to properly model the soil-structure interaction effects. Eight-node Eulerian-fluid elements with three translational degrees of freedom and one pressure degree of freedom were used for modeling the reservoir water. Totally, 3,660 elements were used in the reservoir domain which extended about five times the dam height in the upstream direction. Based on a topographic map of the dam site and also a general view of the dam position in the valley, it can be seen that there is no opening in the valley shape for a distance up to 600 m from the dam center. So

it is an acceptable assumption for simulation of the reservoir with uniform section (like as dam upstream face).
The third finite element model, FE3 which is used for nonlinear seismic analysis, is mainly similar to the second model while 6,336 (792 × 8 = 6,336, each element was divided into 8 sub-elements) solid-structural elements were used in the dam body to properly capture the nonlinear behavior under the dynamic load condition. Figure 29.26 shows the finite element model of the dam, reservoir, foundation, and joints.

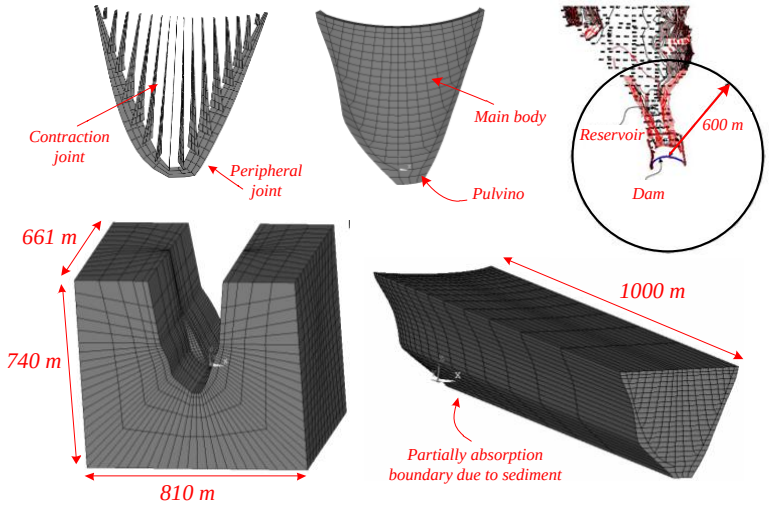

Fig. 29.26: Finite element model of dam, reservoir, foundation and used elements

29.4.3 Thermal Analysis

29.4.3.1 Applied Initial Temperature

In order to perform a valid thermal analysis, it is required to know the initial temperature (reference temperature) at the system. Considering that Dez Dam is very old with limited instrumentation within the dam body, there is no reliable information about initial temperature distribution within the body. Therefore, a heuristic method is used in the current study for determination of the initial temperature.
In the first step, a constant temperature of 23°C is applied to the nodes, which is defined by tracking similar dams and engineering judgment. Then, thermal transient analysis is performed for one year considering the imposed boundary conditions. Results of the thermal distribution on the nodes at the end of this step are applied

to the model again as the new initial conditions for the next step, and this loop is repeated for several years until the results approach the stable responses. The results of the thermal distribution at the end of the last step can be interpreted as the real initial temperature of the model after several years. Figure 29.27 illustrates the proposed algorithm for calculating the initial temperature distribution on the dam body.

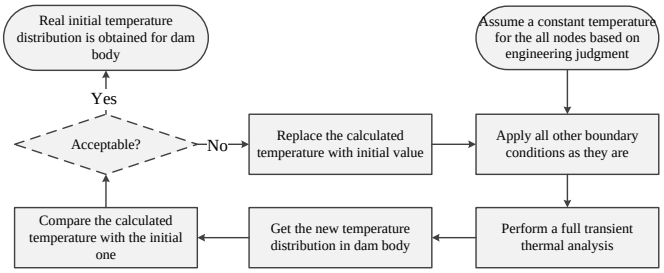

Fig. 29.27: Proposed algorithm for calculation of the real initial temperature distribution

Figure 29.28 compares the results obtained from numerical analysis with the data collected from thermometers installed in block 9 corresponding to year 1973. Results indicate that the responses from thermal analysis are in good compliance with the actual values. It should be mentioned that there is no middle point in the numerical model, and the results for this point are the average of two side nodes; some differences between the actual and theoretical data are expected.

29.4.3.2 Determination of Meteorological Parameters

29.4.3.2.1 Air Temperature Both the recorded data and the simplified sinusoidal function could be used for determination of the air temperature at the dam site. Considering that the nearest meteorological station to the dam site is station No.21-144, those results are used as reference. Air temperature is recorded monthly in this station, so it is required to use linear interpolation in order to extract daily air temperatures. Figure 29.29 shows the sample air temperature variation for the period of six years in this station.

29.4.3.2.2 Reservoir Water Temperature The empirical-analytical Bofang's relations are used to calculate the temperature of the reservoir water. Using equations in Section 2.3.1.1.2 and considering d=2.15 and f=1.30, it is possible to simulate the water temperature at different elevations. A sample of computational results in comparison with values recorded by the water temperature thermometers, T_w, at the upstream face in block 9 are shown in Figure 29.30. According to these plots, the

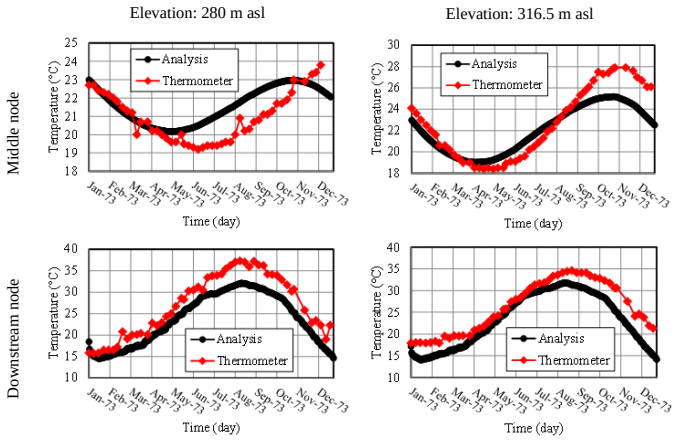

Fig. 29.28: Comparison of the results obtained from thermal analysis and thermometers

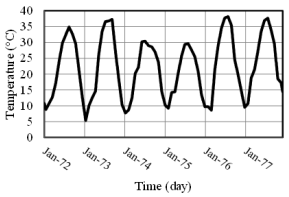

Fig. 29.29: Variation of the air temperature recorded in Dez Dam site

calculated values show good agreement with the real values. The differences between analysis and thermometer data for level 328 m are due to decreasing reservoir water in some months to lower than this level, and therefore, this part of the dam is in exposure of the air temperature instead of the water.

29.4.3.2.3 Effect of Solar Radiation In order to implement the solar radiation, the direct and indirect values of daily radiation on a horizontal plane should be determined. Due to the lack of the required instruments for measuring radiation near the dam site, its amount is determined according to the recorded daily sunshine hours at the Dez station for several years. Direct, indirect, and total radiation calculated for the six years are shown in Figure 29.31(a).

The reflection coefficient is assumed to be 0.2 for the region surrounding the site and 0.3 for the water surface. Estimated values for the coefficient of the surface reflectance and variation of reflection coefficient from water surface are shown in Table 29.6 and Figure 29.31(b), respectively. Also, the absorption coefficient for the body concrete is considered to be 0.7.

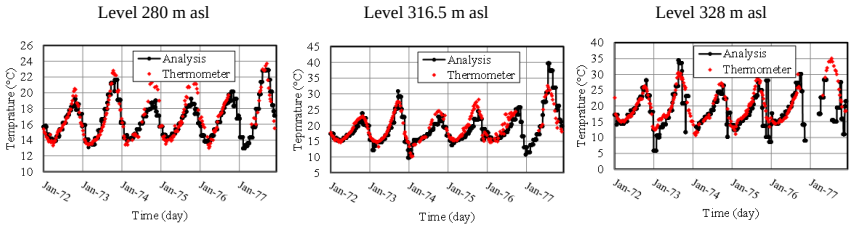

Fig. 29.30: Comparison of the results obtained from thermal analysis and thermometers at upstream face of block number 9

Table 29.6: Recommended values of n for different months (average day of the month) [596]

Month	n value for ith day of month	nth day of month	nth day of year
January	i	17	17
February	31+i	16	47
March	59+i	16	75
April	90+i	15	105
May	120+i	15	135
June	151+i	11	162
July	181+i	17	198
August	212+i	16	228
September	243+i	15	258
October	273+i	15	288
November	304+i	14	318
December	334+i	10	344

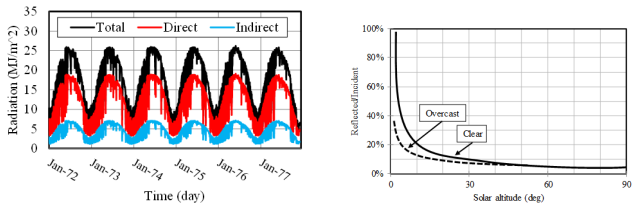

(a) Estimated values for the direct, indirect, and total radiation

(b) Ratio of the total reflected radiation to the total radiation at the water surface according to sun height and smooth/cloudy sky

Fig. 29.31: Solar radiation at Dez Dam site

29.4.3.2.4 Reservoir Water Level Changes In order to properly investigate the environmental temperature effects on the thermal distribution of the dam body, the reservoir water level was tracked carefully corresponding to reservoir operation regime. To do so, the upper part of the upstream face, which is not in contact with

water, is detected based on reservoir daily water level. At each step of the thermal transient analysis, the lower part of the upstream face, immersed in water, is affected only by reservoir temperature while the part out of the water is affected by the air temperature and solar radiation. Figure 29.32 shows the variation in water level for the period of six years.

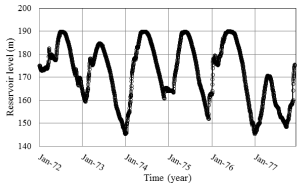

Fig. 29.32: Variation of the reservoir level in Dez Dam site

29.4.3.3 Thermal Calibration of Model

The model calibration was performed comparing the calculated data with the actual values recorded by thermometers at block 9, which is the only instrumented block in the Dez Dam. The calibration process was conducted for six years, 1972 to 1977, because only the data for these years were available. To do so, the initial thermal condition was determined for January 1972, and thermal transient analysis was performed using a daily time step. In other words, there were 2190 load steps in the thermal transient analysis.

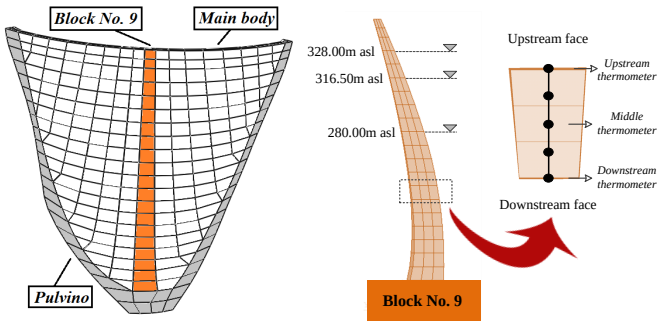

Fig. 29.33: Variation of the reservoir level in Dez Dam site

Figure 29.33 shows the location of block 9 in the dam and also the position of the thermometers at various levels and sections. Table 29.7 represents the initial and final values of important parameters on which the calibration of the finite element

model is based. All of these parameters were obtained after almost wide range sensitivity analysis on the responses. Finally, Figure 29.34 shows the comparison of the results of the calibrated model at various levels and sections with those recorded by thermometers for the considered time period at the reference block. Results confirmed that the provided thermal model considering the solar radiation effects is able to model the real conditions and, therefore, can be used for predicting the thermal behavior of the dam body.

Table 29.7: Thermal properties of dam-environmental system

Parameter	Unit	Proposed range	Final
Thermal conductivity coefficient of concrete	$W/m^\circ K$	(1, 4)	1.7
Specific heat coefficient of concrete	$W/hr.kg^\circ C$	(0.1, 0.4)	0.25
Solar absorptivity coefficient of concrete	-	(0.6, 0.85)	0.7
Emissivity coefficient of concrete surface	-	(0.3, 0.9)	0.8
Diffuse reflectance coefficient (upstream face)	-	-	0.3
Diffuse reflectance coefficient (downstream face)	-	-	0.2
Convection coefficient of air	$W/m^{2\circ} K$	(5, 60)	60
Convection coefficient of water	$W/m^{2\circ} K$	-	6000

29.4.3.4 Thermal Analysis Considering Solar Radiation Effects

According to Figure 29.35, solar radiation has an undeniable role in the creation of the non-uniform temperature distribution on the dam surfaces. It means that the temperature difference between some coincident nodes highly affected by solar radiation is about 6°C to 10°C for the hottest and coldest month, respectively. Also, the reservoir water fluctuation is effective on temperature controlling of the parts under water level on the upstream face. In arch dams, their own special geometry leads to heat concentration at some areas even at the same level. Due to the location of Dez Dam, which is in the northern hemisphere of the earth, and considering that the axis of the dam has a slight angle (about 6°) to the geographic south, the sun (which is located in the south) shines on the downstream face and leads to more heat concentration near the abutments and middle elevations.

The effect of direct solar radiation is almost negligible on the upstream face because it is fully behind the sun. This distribution is affected by indirect radiation reflected from environmental surfaces, which is almost insignificant. The contours depicted in Figure 29.35 also show the effects of reservoir water level and temperature on thermal distribution of the upstream face. Based on this, temperature variation is not considerable in the lower part of the dam, especially along the same level, because the concrete in these regions is affected mostly by the reservoir temperature instead of the air temperature and solar radiation.

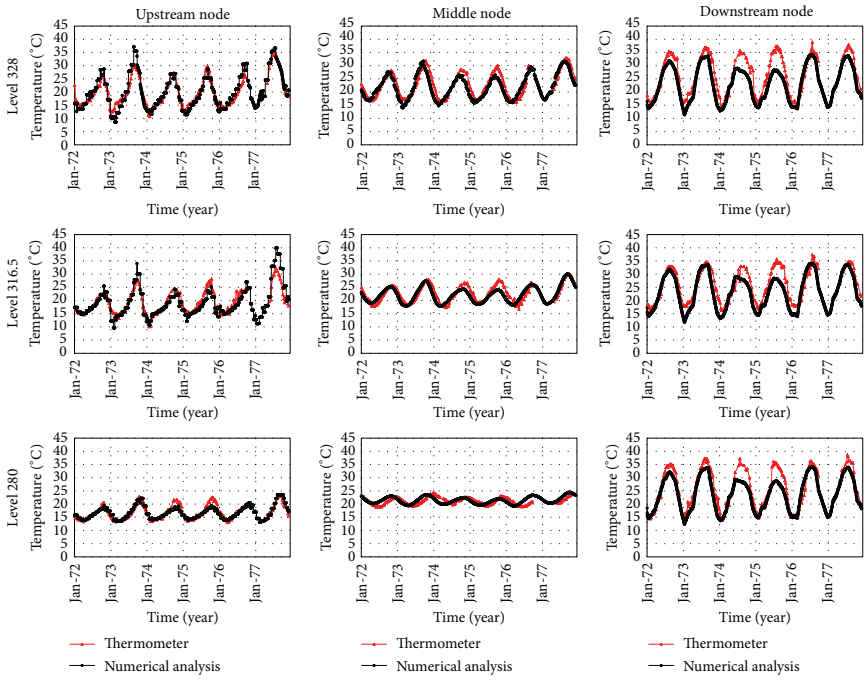

Fig. 29.34: Comparison of the results from thermal calibration analysis with thermometers data

29.4.3.5 Thermal Analysis Neglecting Solar Radiation Effects

Figure 29.36 shows the temperature distribution in the dam body neglecting the solar radiation effect. It can be clearly seen that the solar radiation had a large effect on temperature distribution. Neglecting solar radiation effects at the downstream face leads to a completely uniform temperature distribution because only the air temperature acts as the thermal boundary condition. On the other hand, the same trend is shown on the upstream face in which temperature distribution changes only by changing reservoir levels, and there is no non-uniform temperature at the nodes located at the same level.

29.4.4 Structural Calibration

Considering the reliability and accuracy of the available 16 series of geodetic data obtained from micro geodesies measurements conducted on the dam site, the series numbered 9th, 10th, 11th, and 15th were selected for calibrating the numerical model. The structural calibration procedure made during the current study starts with thermal transient analysis for determining the temperature distribution and then follows by static structural analysis applying thermal, self-weight, and hydrostatic

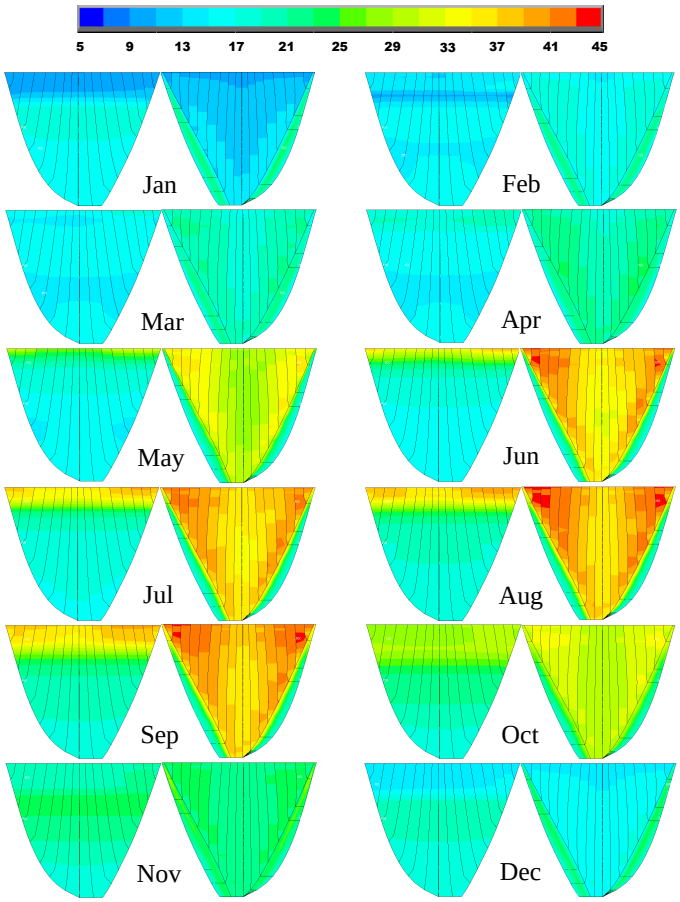

Fig. 29.35: Temperature distribution on the upstream and downstream surfaces of the dam for the year 1973 considering solar radiation effects (°C)

loads on the model. Silt pressure was modeled as equivalent fluid with higher density. A set of sensitivity analyses are required in order to determine the thermal expansion coefficient of concrete, elastic modulus of concrete, and deformation modulus of foundation rock. Figure 29.37 shows the results obtained from the last set of sensitivity analyses on the reference block for 20 years. As seen, the responses of the numerical model are in good agreement with those obtained using geodetic measurement.

This is a typical parameter optimization procedure, which is usually done by comparing the results of numerical analysis and the geodetic measurements. Another set of sensitivity analyses are performed in order to determine the normal and tangential stiffness of contact elements in joints. Consequently, the values of the normal and

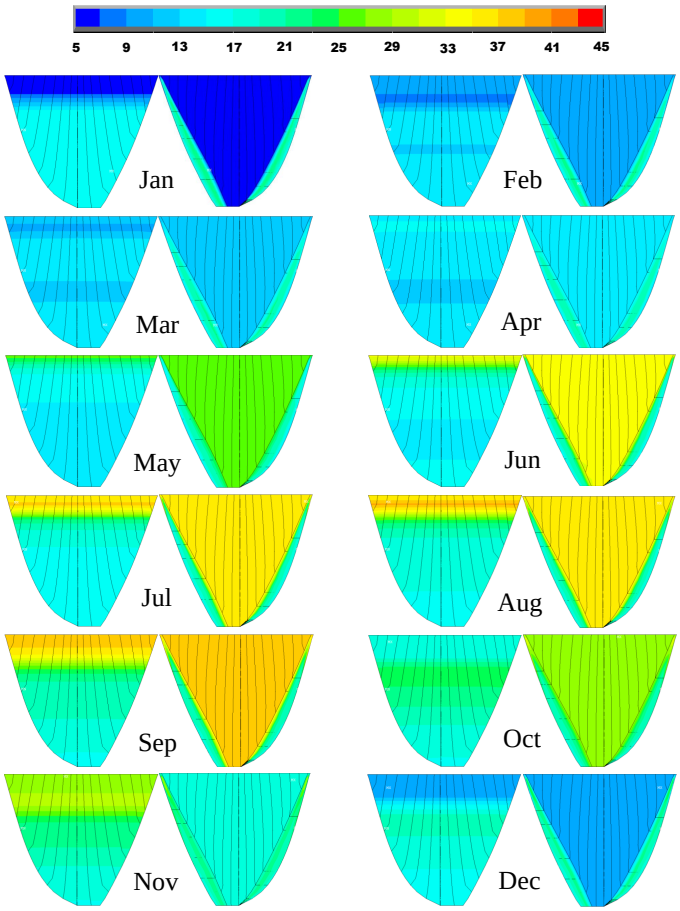

Fig. 29.36: Temperature distribution on the upstream and downstream surfaces of the dam for the year 1973 neglecting solar radiation effects (°C)

tangential stiffness are computed as 240 GPa/m and 24 GPa/m which are reasonable for high arch dams. It is noteworthy that the normal and tangential stiffness for peripheral joints were considered as 210 GPa/m and 16.8 GPa/m, respectively. Final material properties for mass concrete, foundation rock, and reservoir water are given in Table 29.8. It is noteworthy that there is no ambient dynamic test on Dez Dam. The only way to calibrate the finite element model is to use the geodesic measurements.

29.4.5 Modal Analysis

Determination of the modal responses of the arch dam-reservoir-foundation system is an important step in dynamic analysis of the coupled system. Also, determination

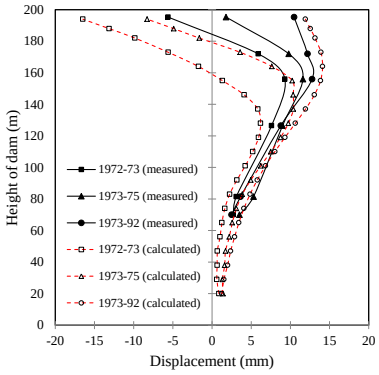

Fig. 29.37: Comparison of the calculated results and the geodetic measurement for the reference block

Table 29.8: Mechanical properties of materials based on calibration

Property	Symbol	Quantity
Modulus of elasticity (concrete)	E_c (GPa)	40
Mass density (concrete)	ρ_c (kg/m^3)	2400
Poisson's ratio (concrete)	ν_c	0.20
Thermal expansion coefficient (concrete)	α_V (°C)	6×10^{-6}
Grouting temperature (concrete)	T_0 (°C)	23
Deformation modulus, saturated region (rock)	E_F^{Sat} (GPa)	13
Deformation modulus, dry region (rock)	E_F^{Dry} (GPa)	15
Mass density, saturated region (rock)	ρ_F^{Sat} (kg/m^3)	2500
Mass density, dry region (rock)	ρ_F^{Dry} (kg/m^3)	2400
Poisson's ratio (rock)	ν_F	0.25
Mass density (water)	ρ_w (kg/m^3)	1000
Wave velocity (water)	C_0 (m/s)	1440
Bottom wave reflection coefficient	α_0	0.8
Mass density (sediment/silt)	ρ_s (kg/m^3)	1360

of the appropriate structural damping in terms of critical damping is necessary. For the direct time integration, it is necessary to specify viscous damping in terms of the Rayleigh damping with the mass and stiffness proportional damping coefficients α_M and β_K, respectively. These parameters are chosen for two characteristic frequencies. Generally structural damping has nonlinear properties and increases as deformation increases. Thus, using a constant damping ratio cannot accurately reflect the damping characteristics of these structures. The guidelines of FEMA and USACE suggest that an effective damping of 5% of the critical provides a reasonable estimate of the dynamic response of concrete hydraulic structures at or near yield and cracking. In situations where such nonlinear responses could develop, a damping value as high as 10% can be justified in performing linear response analyses. However, after

increasing the damping to 10%, if the structure is still showing further nonlinear behavior, then a nonlinear response analysis should be performed.
Figure 29.38 shows the first four mode shapes of the linear elastic model and the model considering the joints. The mode shapes are extracted for the models with the reservoir at normal water level. Material properties are assumed to be linear elastic during modal analysis in both cases, but the stiffness of the second model is lower than the first one due to consideration of the weak planes between the blocks. Also the frequencies of the first 20 modes are shows in this figure. As seen, the frequency of the model with joints is less than that of the monolith model due to low initial stiffness. Based on the results of analyses, the dam experiences 0.5 mm joint opening and 1.5 mm sliding under the static condition. This leads to a reduction in the total stiffness matrix of the coupled system and, consequently, a reduction in frequency values. The mass and stiffness proportional damping was applied to the dam-foundation system, and the first and tenth natural vibration modes were considered as the effective range. The reason for selecting the 10th mode is that there is no meaningful change in frequencies after 10th mode. $\overline{\xi}$=5% was assumed for the linear elastic model, and $\overline{\xi}$=8% was assumed for the nonlinear models.

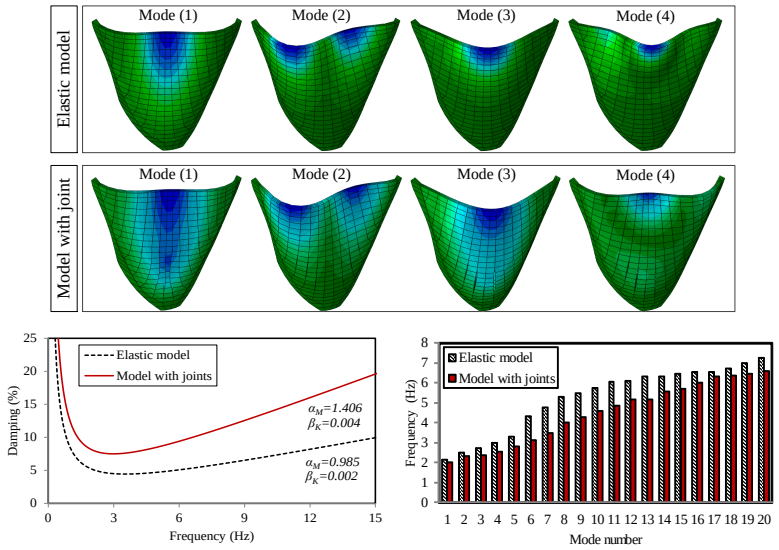

Fig. 29.38: Modal analysis of dam and calculation of Rayleigh damping coefficients

29.4.6 Seismic Safety Evaluation

Seismic safety of arch dams should be evaluated using the maximum credible earthquake on a linear elastic finite element model of the dam. In the case with extensive over-stressed areas in the upstream and downstream faces, detailed nonlinear dynamic analysis is required in order to obtain the real-life behavior of the dam for future decisions. Based on the analyses conducted previously on a linear elastic finite element model of Dez Dam at maximum credible level, the dam experiences high nonlinearities in term of cracking and joint opening.

Hence, the main objective in this section is to evaluate the dam safety and the stability of the blocks considering all possible failure modes. One of the main steps in seismic analysis of engineering structures is the hazard analysis of the site. Figure 29.39 shows the site spectra at maximum credible level. The dam is founded on rock having a shear wave velocity of more than 760 m/s and is considered to be located in near-field range of the ground motions with $M_S \sim 6.7$ and in far-field range of the ground motions with $7.0 < M_S < 7.4$.

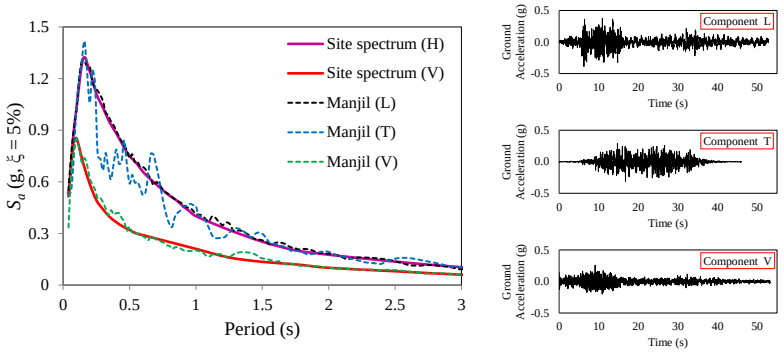

Fig. 29.39: Dynamic inputs at MCL: (left) acceleration response spectra and, (right) acceleration time histories of the scaled main shock, Manjil ground motion

Manjil ground motion recorded at Abbar Station (Figure 29.39) was selected as the main shock and scaled in both horizontal and vertical components at MCL. The total length of the ground motion was about 53 s while the first 42 s was selected for dynamic analysis of the system, which corresponds to 95% of the total energy. It is noteworthy that all the three components of the selected ground motion are applied simultaneously at the base of the foundation rock.

Applied loads on the model and their sequences are: the dam body self-weight (considering staged construction effect), hydrostatic pressure (considering gradual impounding of the reservoir), thermal loads (based on the summer condition obtained from thermal transient analysis), and the earthquake loading. Figure 29.40 shows the distribution of the hydrostatic pressure on the upstream face of the dam and

Pulvino. Also, the time histories of the hydrostatic and net hydrodynamic pressures are shown in the index point which is the lower node on the main dam body. This node is located on the interface of the main body and Pulvino and shows the hydrodynamic pressure which is applied to the peripheral joint when it is open. The Newmark-β time integration method was utilized to solve the coupled nonlinear problem of the dam-reservoir-foundation system, and the displacement and flow characteristics were chosen as the convergence criteria in each load step of the conducted dynamic analysis. Due to rate dependence of the mechanical and strength properties of mass concrete, based on FERC and USACE engineering manuals, Table 29.9 presents the dynamic properties used in seismic analyses of the coupled system.

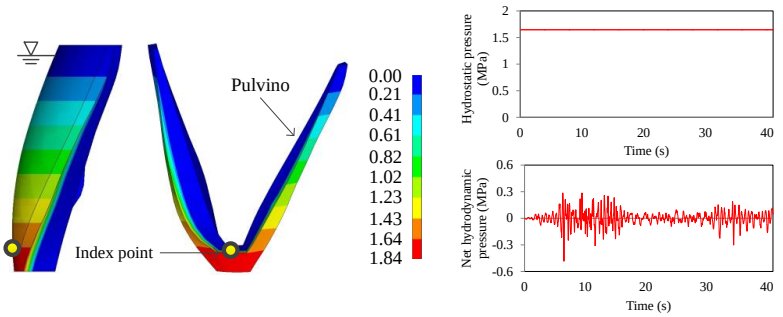

Fig. 29.40: Water pressure (left) hydrostatic pressure distribution (MPa) and (right) time history of the pressure at the index point

Table 29.9: Mechanical and strength properties of concrete in static and dynamic conditions

Property	Symbol	Static quantity	Dynamic quantity
Modulus of elasticity (concrete)	E_c (GPa)	40	46
Poisson's ratio (concrete)	ν_c	0.20	0.14
Compressive strength (concrete)	f'_c (MPa)	35	36.5
Tensile strength (concrete)	f'_t (MPa)	3.4	5.1
Bi-axial compressive strength (concrete)	f_{cb}	$1.2f'_c$	$1.2f'_c$

The finite element model, FE3, is used as the base model for dynamic analyses. Four different scenarios are assumed for the seismic analyses as follows:

- DYN1: Concrete dam is assumed to be linear elastic.
- DYN2: Joint nonlinearity in terms of contraction and peripheral joints is considered. Geometric nonlinearity of the potential free-cantilevers is taken into account.

- DYN3: Material nonlinearity in terms of concrete cracking is taken into account. Considering or neglecting the geometric nonlinearity is not important in this case because there is no risk for free-cantilever formation.
- DYN4: All sources of nonlinearities are considered, i.e. joint opening/sliding, concrete cracking, and large deformation.

Figure 29.41 shows the time history of the crest displacement in the stream direction for all four scenarios. The linear elastic model, DYN1, was provided as benchmark model. Modeling the joints lead to an initial displacement of about 32 mm in the downstream direction due to hydrostatic pressure while in the linear elastic model, where there is no joint, the initial displacement is only 3 mm. Analysis of the DYN2 model shows a similar trend to the linear model, but there is a jump in crest displacement at $t = 6.4$ s due to joint instability at this level. This means that the joints are open, and the central blocks slide with respect to each other. The DYN3 model shows a similar behavior to DYN1 with some higher values of displacement response. Higher response in this model corresponds to the development of cracking of mass concrete and a reduction in the total stiffness matrix of the coupled system. However, there is no sudden jump in displacement time history or any sign of instability.

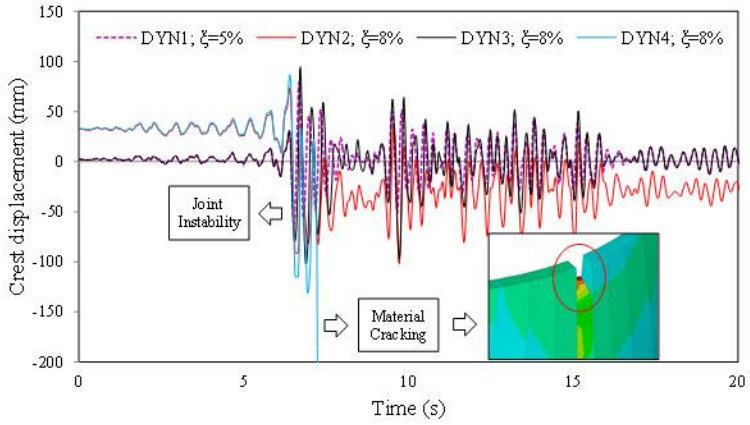

Fig. 29.41: Comparison of the displacement time histories (first 20s) under the main shock

Analysis of the dam with all three sources of nonlinearities, DYN4, shows a large displacement after the block instability, and finally the model fails at $t = 7.2$ s. The failure of the upper section of the central block under the combination of the nonlinearity sources is shown in Figure 29.41. Comparing all three nonlinear models, i.e. DYN2, DYN3, and DYN4, reveals that modeling the joints is the most important source of nonlinearity in arch dams. Also, considering the coupled effect

of all nonlinearity sources makes the finite element model more sensitive for failure compared to the effect of each parameter individually.
Figure 29.42 shows the non-concurrent envelope of the first principal stresses on upstream and downstream faces of the dam body. In the first model, DYN1, the stresses are allowed to increase without any limitation. The stress reaches 17.0 MPa on upper parts of the upstream face. The second model, DYN2, considers the joint and geometry nonlinearities in the finite element model. In this model, the areas with high tensile stresses are concentrated in the central part of the downstream face and also some areas near the abutments in the upstream face. Modeling the contraction and peripheral joints reduces the maximum first principal stresses to about 10.5 MPa which are mainly cantilever-type stresses in upper parts of the dam due to large openings in the joints. Modeling only the material nonlinearity and neglecting the effect of joints, DYN3, lead to propagation of high tension areas in most of the upper parts of the dam body in both upstream and downstream faces. Finally, the DYN4 model with all sources of nonlinearities shows the extensive stress concentration area in upper parts of both upstream and downstream faces. As can be seen, modeling the integrative behavior of the concrete arch dams leads to more damage to the structure under the main shock.

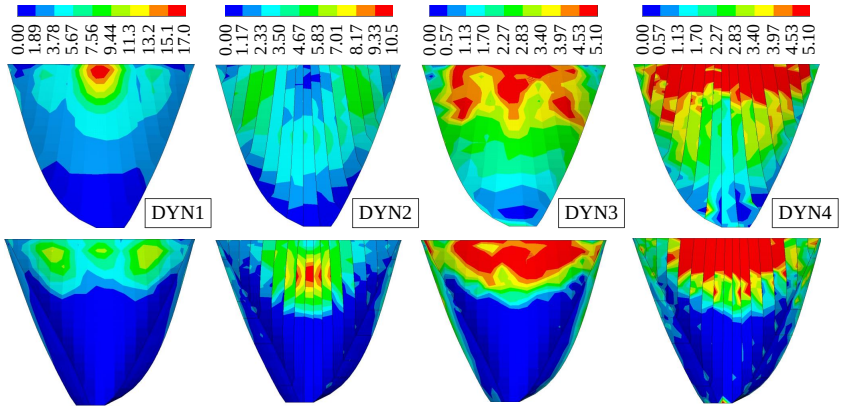

Fig. 29.42: Comparison of the non-concurrent maximum first principal stresses (MPa)

The real-life seismic safety assessment of Dez arch dam is further studied only based on the DYN4 model. Figure 29.43 (left) shows the central block displacement in the stream direction for the DYN1 and DYN4 models. For the lower 1/4 part of the block, both the linear and full nonlinear models have the same results whereas in the upper 1/4 part, the nonlinear model shows very high displacements due to concrete cracking and free-cantilever movement. Also, Figure 29.43 (right) shows the envelope of the joint opening and joint sliding along the height of the central

blocks. Based on this figure, there is a sudden change in joint opening and sliding at level 115 m and 135 m, respectively. It shows that there is instability in higher levels due to a change in the load carrying method of the dam from 3D continuous (arch + cantilever actions) to cantilever beams which increases the probability of the global failure of the dam due to concrete brittle cracking. Also, improper performance of the joints in levels higher than 155 m (and the free-cantilever formation) leads to extensive displacement in blocks due to both material cracking and geometry nonlinearity effects.

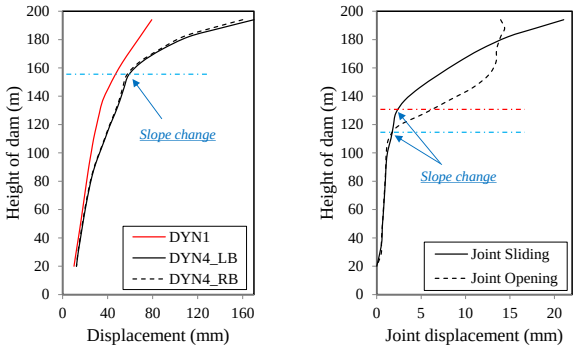

Fig. 29.43: Response of the central block (left) maximum displacement and (right) maximum joint opening and sliding

Figure 29.44 shows the cracked elements (1st, 2nd, and 3rd cracks) on the upstream and downstream faces of the full nonlinear model (DYN4) up to 7.2 s where the crest level is failed. In this model, cracking at the upstream face starts earlier than at the downstream face. As mentioned before, in the current model, any Gaussian point is able to crack in three principal directions. Generation of the 3rd crack in a Gaussian point depends on the formation of both the 1st and 2nd cracks. Due to 1) non-convergence of the numerical model after about 7.0 s of the applied main shock, 2) fast propagation of the cracked area on both faces, 3) dramatic displacement in the crest point, and 4) high potential for separation of the central blocks especially in upper parts, the dam is supposed to be failed under a main shock with MCL scenario.

29.4.7 Post-Earthquake Safety Evaluation

If the predicted performance of the concrete dam under the postulated MCL scenario indicates substantial damage, a post-earthquake safety evaluation is usually required. Also, the extent of damages that may have resulted due to another intense earthquake should be examined. Detailed inspections are required from the dam body, galleries, abutments, and the appurtenances. In addition, measurements from the position

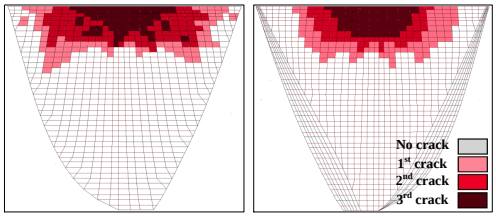

Fig. 29.44: Cracked elements in the full nonlinear model, DYN4, under the main shock

indicating system should be carefully studied for possible evidence of permanent displacements caused by earthquake.

In numerical safety evaluation of an existing dam, the postulated damage should not weaken the dam to a point where its capacity to resist static loads and aftershocks is threatened. In the case of Dez Dam, the full nonlinear model, DYN4, shows failure of the dam (at least at the crest level), and thus post-earthquake safety evaluation is not required. In such a case, pre-earthquake retrofitting is necessary. However, the dam is survived using either DYN2 or DYN3 models. Therefore, these two models are evaluated for the post-earthquake events.

Figure 29.45 illustrates a proposed methodology for comprehensive seismic safety evaluation of existing concrete dams. First, the finite element model is defined and all the nonlinearity sources as well as interactions are applied in the model. Coupled or uncoupled thermo-mechanical analysis is implemented to realize the performance of the dam at the pre-earthquake condition. Pre-earthquake safety assessment of the concrete dams may be conducted for a relatively long period of time (based on the seismicity condition of the site). In such a case, safety evaluation analysis should include the aging constitutive models, e.g. creep and alkali-aggregate reaction. The typical time period used for pre-earthquake analysis varies from several months to some decades.

Second, seismic analysis is performed considering the calibrated parameters obtained from the previous step. An appropriate main shock is selected based on the event that has the most contribution on ground-motion exceedance hazard in terms of moment magnitude and source-to-site distance. The selected ground motion can then be scaled using the uniform hazard response spectra. Seismic safety evaluation should include the damage response of the dam in terms of joint opening/sliding and crack propagation. The typical time period used for earthquake analysis is on the order of seconds or minutes.

Third, post-seismic analysis is performed taking into account the condition of the dam at the end of main shock. Static stability analysis and seismic analysis using the aftershock event(s) are required to ensure the safety of the dam. In general, three types of aftershock events may be considered: 1) as-recorded aftershock, 2) repeated aftershock (which is similar to the main shock with a reduced scale factor), and 3)

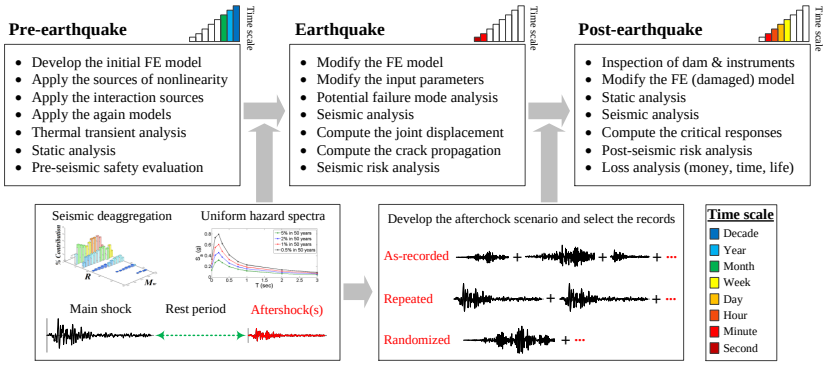

Fig. 29.45: A comprehensive methodology for seismic safety evaluation of the existing concrete dams

randomized aftershock (which uses another ground motion record compatible with the dam site). This step usually ends up with loss analysis of the dam system in terms of loss of life, downtime, and economic losses. The typical time period used for post-earthquake analysis varies from a couple of minutes to several weeks.

In the present study, the randomized aftershock approach is used because there is no information about the aftershock events of the Manjil earthquake. The 1997 Qaen earthquake recorded at Qaen station is used as the aftershock event. Its magnitude is 6.4, and the source-to-site distance is 10 km. The horizontal and vertical components are then scaled to 0.75 of the MCL response spectra shown in Figure 29.39. The reason is that the aftershocks are usually less intense than the main shock. Based on the Båth [88] Law, the difference in magnitude between a main shock and its largest aftershock is approximately constant and independent of the main shock magnitude, typically 1.2. Another assumption in this study is that there is only one intense aftershock event; however, in reality, the rate of aftershock occurrence is proportional to the inverse of time since the main shock.

Static analysis of the partially damaged dam for both DYN2 and DYN3 models satisfies the structural stability of the dam. Seismic analysis is then performed using the aftershock ground motion. Again, the results of the linear elastic analysis are provided as a reference case. Figure 29.46 shows the displacement time history of the crest point in the stream direction for the main shock and aftershock events. A rest period of 30 s is added between earthquake events to recreate the real world situation, in which the dam comes to rest but is not repaired. In both nonlinear models, i.e. DYN2 and DYN3, there is a permanent displacement at the end of both main shock and aftershock events. In DYN1,the dam has a 2.5 mm displacement in the downstream direction at the end of pre-earthquake analysis. Crest displacement reaches 2.7 mm and 2.8 mm at the end of seismic and post-seismic analyses, respectively. Hence, they do not have an important role on the linear elastic system.

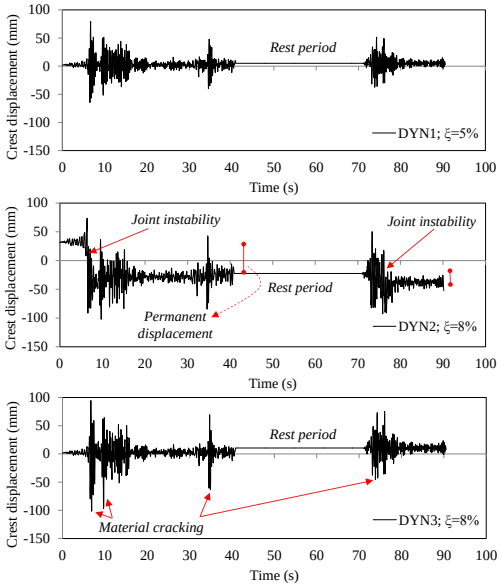

Fig. 29.46: Displacement time histories under the main shock and after shock events

In the DYN2 model, joint instability can be seen clearly in the main shock and aftershock events. However, the continuity of the displacement time history shows that there is no global failure in this model at the end of post-seismic analysis. The dam experienced a 32 mm displacement in the downstream direction at the end of pre-earthquake analysis. It reaches 22.3 mm displacement in the upstream direction at the end of seismic analysis. Thus, there is a large permanent displacement in this condition. The cumulative permanent displacement is increased at the end of the aftershock event. In the DYN3 model, material cracking (softening) can be recognized in several points on the displacement time history in comparison with the DYN1 model. Permanent displacement at the end of main shock is 10.5 mm which is about ¼ of the DYN2 model. The cumulative permanent displacement at the end of the aftershock event is 13.5 mm which shows that there is no extensive damage under this scenario. It is noteworthy that the stresses, especially at the critical locations in the vicinity of the crest, are less than those experienced by the dam under the main shock.

The results of the post-earthquake analysis can be used for classification of the dam condition. The following classification system is adopted from FERC with some changes:

- Safe: No apparent hazard found although repairs may be required. Cracking is primarily surficial and confined to small regions of the dam and abutments.

Contraction joints may open and close during the earthquake excitation, but they are closed with minimal offsets after the shaking stops.
- Limited usage: Hazardous condition believed to be present due to damage resulting from relatively significant cracking and permanent joint separation of the dam. If necessary, reservoir water level should be lowered to reduce the possible major aftershock hazard.
- Unsafe: Extreme hazard condition with imminent danger of collapse from an aftershock. The damage is expected to be widespread with major cracking, joint opening with offsets, and possible sliding originating along the cracked sections within the dam, at the dam-foundation interface, or along the planes of weakness within the abutments. The reservoir water should be lowered and a warning issued for immediate evacuation of the population living downstream.
- Failed: The dam has collapsed (local or global failure) under the main shock or the major aftershock event. There are extensive joint openings, cracking of concrete from lift joints, and separation of some parts of the dam. The dam is not able to maintain the reservoir water, and the potential flood is expected at the downstream.

Based on this classification, the seismic behavior of the dam is evaluated to be unsafe under the main shock and a major aftershock event in the case of the DYN2 and DYN3 models. The dam is expected to fail under the main shock in the case of the DYN4 model. As seen, using a more advanced numerical model is effective on the decision making for seismic safety of the considered dam.

29.4.8 Impact of Water Level Variation

In this section, the effects of reservoir water in four different levels are investigated on the seismic performance of Dez arch dam. Dynamic equilibrium equations of the dam-reservoir-massless foundation coupled system are solved by Newmark's time integration algorithm. Several three-component ground motions are used for excitation of the finite element model. Seismic performance is evaluated based on the criteria introduced in Section 27.7.
For the linear elastic analysis, no contraction joint or smeared crack is modeled. Water levels in the reservoir are considered as 56, 101, 155 and 188 m that correspond to level I, level II, level III and level IV. The results are discussed for Tabas ground motion at MCL and generalized further for Manjil and Duzce ground motions.

29.4.8.1 Detailed Single Ground Motion

Time histories of the crest displacement at the central cantilever as well as the static and maximum dynamic responses are shown in Figure 29.47. Considering that the positive direction of the axis is toward downstream, it becomes evident from static results that in low levels of the reservoir, the dam body tends to move in the upstream direction. Static displacement of the dam toward downstream increases intensively by increasing the reservoir level. As it becomes evident from dynamic analyses results, increase of the reservoir level from I to IV leads to an increase in maximum

displacement at the crest towards the downstream direction, and generally, movement of the crest in the upstream direction decreases except in level I in comparison with level II.

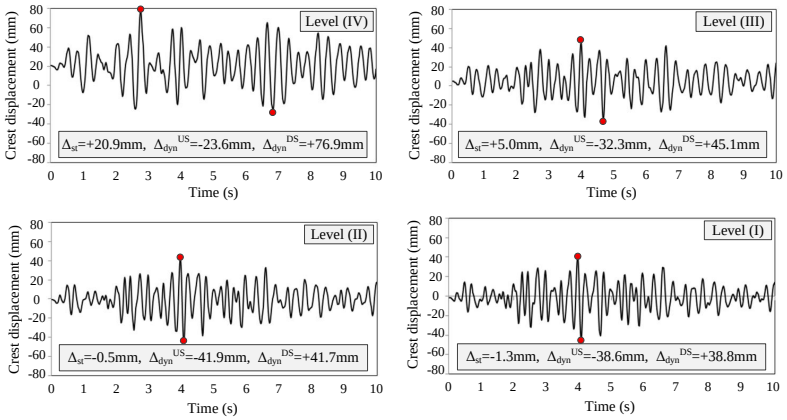

Fig. 29.47: Time history of the crest displacement in stream direction for Tabas ground motion

Non-concurrent envelope of the maximum and minimum principal stresses on the upstream and downstream faces of the dam body are shown in Figure 29.48. As seen, dewatering the reservoir increases maximum principal stresses within the dam body, especially in upper parts and in the vicinity of the crest. On the other hand, impounding the reservoir increases the area with high compressive stresses in the central upper part of the upstream face and in upper parts in the vicinity of the foundation on the downstream face.
Figure 29.49 shows the extension of the overstressed areas on upstream and downstream faces. As can be seen, dewatering the reservoir increases overstressed areas on both faces. Differences of the overstressed area between levels II and I are negligible for both faces. Although the areas on upstream face for lower water levels are completely overlapped with those corresponding with higher levels, this is not true for the downstream face.

29.4.8.2 Generalized Findings

Figure 29.50 represents a non-concurrent displacement envelope for upstream nodes of the central cantilever based on three selected ground motions and the average of them in each reservoir level. As it was shown, the displacement envelope is critical when the reservoir is in level IV (full reservoir), and dewatering the reservoir lead to decreasing displacements, especially in lower parts of the cantilever. Maximum displacement always occurs in level IV.

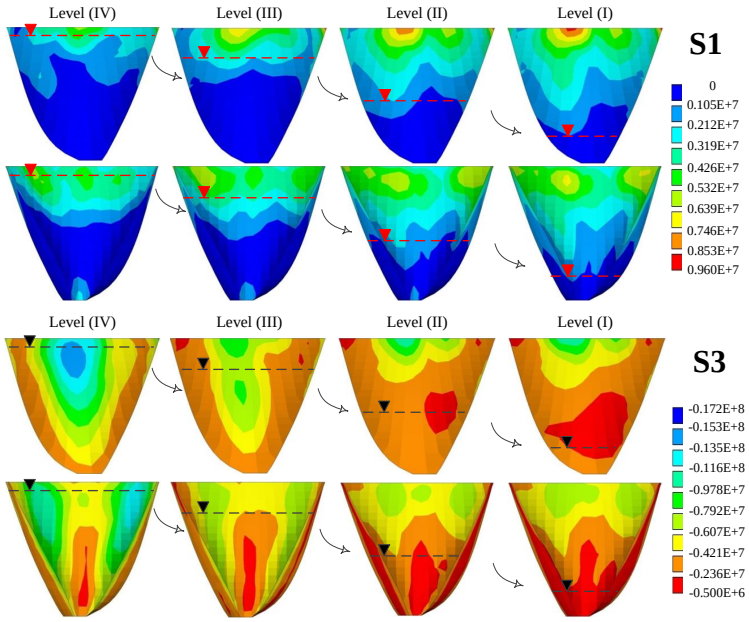

Fig. 29.48: Non-concurrent envelope of the maximum and minimum principal stresses on US and DS faces (Pa) for Tabas ground motion

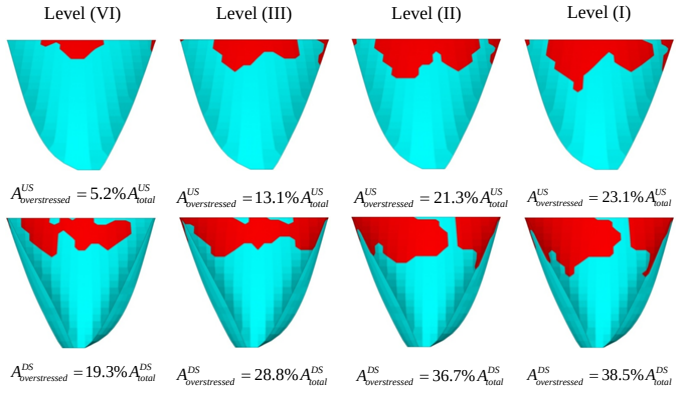

Fig. 29.49: Extension of the overstressed areas on upstream and downstream faces for Tabas ground motion

Figure 29.51 displays envelopes of the maximum first principal stress (S1) and minimum third principal stress (S3) along the height of the central cantilever. It

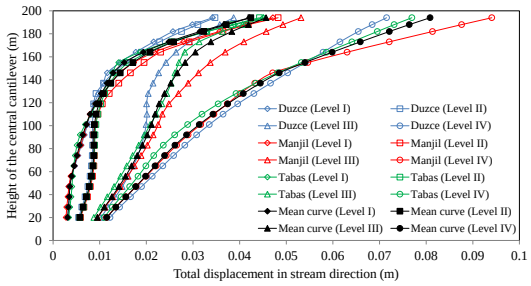

Fig. 29.50: Comparison of the non-concurrent displacement envelope of the central cantilever in stream direction for the three scaled ground motions

is clear the generally dams experience a higher S1 when the reservoir is in low levels. Also, resemblance of curves decreases for upper reservoir levels. In addition, increasing the water level increases the absolute value of S3, especially for upper parts of the dam body.

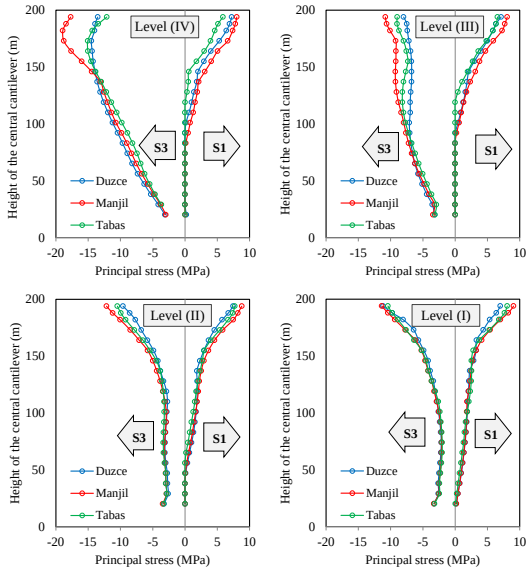

Fig. 29.51: Non-concurrent envelope of the maximum first principal stress and minimum third principal stress along the height of the central cantilever

Figure 29.52 shows the status of the most representative nodes on upstream and downstream faces of the dam body based on the demand/capacity ratio and also cumulative inelastic duration. As seen, for all ground motions, the performance curves

are below the predefined threshold in level IV. Performance curves of upstream nodes in level III exceed from PTC partially. For reservoir levels II and I, both upstream and downstream nodes' performance curves exceed from PTC, but generally it is more critical for level I than level II.

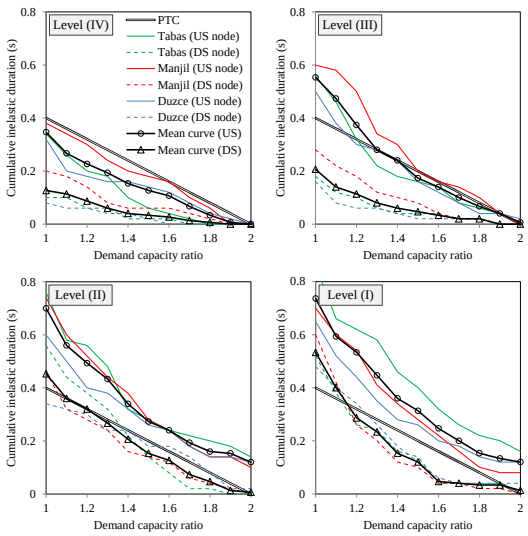

Fig. 29.52: Non-concurrent envelope of the maximum first principal stress and minimum third principal stress along the height of the central cantilever

29.4.9 Endurance Time Analysis Method

In this chapter, the nonlinear behavior of mass concrete (based on a smeared crack approach) is combined with the Endurance Time Analysis (ETA) method for the estimation of probable damages in Dez arch dam.

29.4.9.1 ETAFs and Equivalent Target Time

The so-called e-series of ETAFs are used. The finite element model is excited at the foundation boundaries. A structural damping of 5% of critical damping is assumed. All seismic inputs are applied to the system only in upstream/downstream direction considering two possible permutations (zero and 180 phases). On the other hand, for the conventional time history analyses (THA), a total of nine ground motions, all scaled to maximum credible level, are used.
Response of the dam at each time window is corresponding to a certain seismic performance level. Smaller target times correspond to the lower performance levels, and vice versa. In the present study, a statistical method is used to determine an

appropriate equivalent target time. In this technique, the 10th second of ETAF is selected as base target time, and therefore, the average response spectrum resulted up to the 10th second of ETAFs is interpreted as the base response spectrum. Subsequently, the equivalent target time for various seismic performance levels is calculated by multiplying ETAF's base response spectrum in the factor ψ (spectrum ratio), $t_{eq}^{EQGM} = \psi \times t_{eq0}$. A simple optimization is needed to minimize the area enclosed between the two curves of $\psi \times S_a^{ETAF}$ and S_a^{EQGM} (which is the response spectrum at the desired performance level) weighted by a percentage of the effective mass. Mathematically, this can be presented as:

$$\min \left| \left\{ \sum_{i=T_1}^{T_2} (m_{\text{eff}})_i \left(\psi \times (S_a^{ETAF})_i - (S_a^{EQGM})_i \right) \right\} \right| \tag{29.3}$$

in which $(S_a^{EQGM})_i$ and $(S_a^{ETAF})_i$ are spectral accelerations in the ith mode and $[T_1, T_2]$ is period interval including 90% of total mass of the system; $(m_{\text{eff}})_i$ is effective mass of the system in the vibration direction. This method is based on the arithmetic mean weight concept.

Calculations show that the equivalent target time is 6.36 s for MCL. This means that according to ETA, the crack profile (or any other response) up to time t = 6.36 s should have close schema to those obtained from averaging the maximum values resulted from nonlinear time history analyses under real ground motions in MCL. In the other words, ETA estimates THA results in MCL based on a target time of 6.36 s.

29.4.9.2 Response Prediction

Figure 29.53(a) shows time history of the crest displacement in the stream direction for Manjil and Tabas ground motions (as samples of real ground motions in MCL). Figure 29.53(b) represents the same plots for three ETAFs resulted from the linear and nonlinear models. As seen in Figure 29.53(a), there is a complete consistency between the results of linear and nonlinear analyses while nonlinear models lead to higher values for displacement in both cases. None of the nonlinear THAs leads to instability. On the other hand, although there is good consistency between the results of linear and nonlinear models based on ETAFs up to time about t =7.0 s, nonlinear analyses lead to very large results for the time interval [7.0 - 9.0], and global instability in analyses is shown at times greater than t = 9.0 s.

ETA curves for the crest displacement in linear and nonlinear models are depicted in Figure 29.54. Also, the results of real ground motions and their average are shown at the equivalent target time calculated in the previous section. For the linear system, the average value obtained from the nine real ground motions is 81.9 mm while the estimated values using three ETAFs and their average are 70.3, 70.1, 92.3, and 77.6 mm, respectively. Therefore, using the average of three ETAFs underestimates the results by about 5.2% for the linear model. Moreover, using a linear trend line for the ETA average curve leads to a value of about 83 mm, which overestimates the crest displacement by about 1.3%. On the other hand, the average value obtained

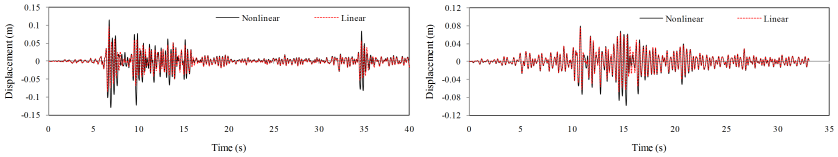

(a) Real ground motions

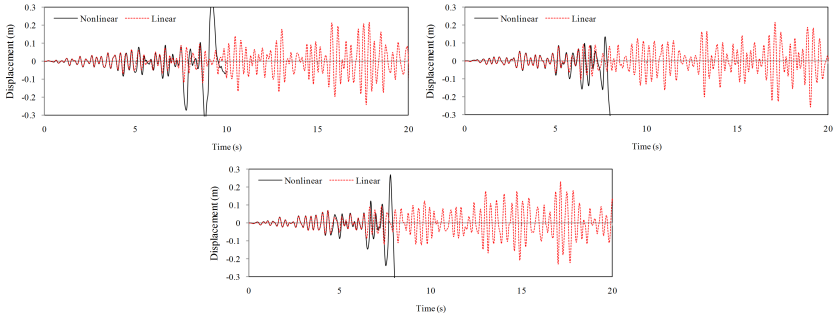

(b) ETAFs

Fig. 29.53: Displacement time history at crest point in stream direction

from THAs in nonlinear analyses is 107 mm, and the estimated values by three ETAFs and their average are 102.3, 87.2, 123.1, and 104.2 mm, respectively. Using the average of ETAFs underestimates results by about 2.6% for the nonlinear model. In the nonlinear model, the system shows instabilities for times larger than t = 7.0 s. Standard deviations of the extreme values resulted from THAs for linear and nonlinear analyses are 7.6 mm and 11.3 mm, respectively.

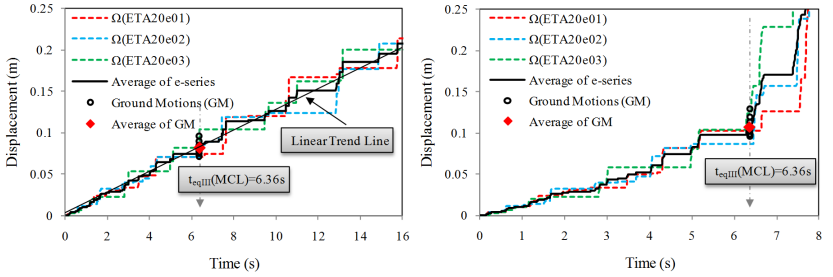

Fig. 29.54: ETA curves for the crest displacement, left: linear, right: nonlinear

Figure 29.55 presents the crack profiles resulted from two ground motions and three ETAFs. All dynamic excitations are applied twice considering the possible

permutations; the first one in the zero phases, and the second one in 180 phases. As seen, the damage (the number of cracked elements) when using real ground motions is more intense for Manjil earthquake than Tabas. In addition, among ETAFs, ETAF-3 leads to more damage than the two others. Although there are some differences in crack profiles resulted from ETAFs in opposite directions, their profiles are closer compared to real ground motions.
Figure 29.56 presents the total number of cracked elements for the critical direction for real ground motions and ETAFs. The average of cracked elements based on real motions for the first, second, and third cracks are 21.7%, 8.6%, and 4.1%, respectively. In addition, the same percentages for ETAFs are 23.4%, 10.9%, and 6.4%. It can be concluded that the ETAFs can predict the average crack profiles and the number of cracked elements resulted from the real ground motions with acceptable accuracy.

29.5 Dam Foundation Interaction: Karaj

The impact of input ground motion mechanism on the seismic response of a typical symmetry concrete arch dam is investigated by relying on the foundation numerical model. For this purpose, six ground motions, including near-fault and far-field recordings with various characteristics in the acceleration response spectrum, have been used to analyze the coupled system. Three different options have been introduced for the dam-foundation interaction: 1) the foundation rock is assumed to be rigid; 2) the foundation rock is modeled as a massless medium; and 3) a massed foundation is assumed with the inclusion of infinite elements at the far-end boundaries. The reservoir medium is assumed to be compressible and has been modeled according to the Eulerian approach. It has also been observed that modeling the foundation as a massed element decreases stresses relative to the massless model while use of a rigid foundation model leads to a stress concentration at the dam-foundation interface. In all these foundation types, near-fault ground motions have led to higher responses than far-field motions, especially for upper parts of the dam body, with less scattering of results in far-field ground motion.

29.5.1 Modeling the Dam-Foundation Interaction

Three types of foundations with different characteristics and boundary conditions have been examined:

- The rigid foundation model, which neglects the dam-foundation interaction as well as both the foundation material stiffness and mass, is introduced into the overall coupled equation of motion.
- In the conventional massless foundation model, only flexibility (stiffness) of the foundation finite element model is taken into account in setting up the coupled system equation. An appropriate volume of foundation rock must be included in the dam model so as to account for the effects of foundation flexibility [307]. Also, the foundation model should extend out to a distance beyond which its

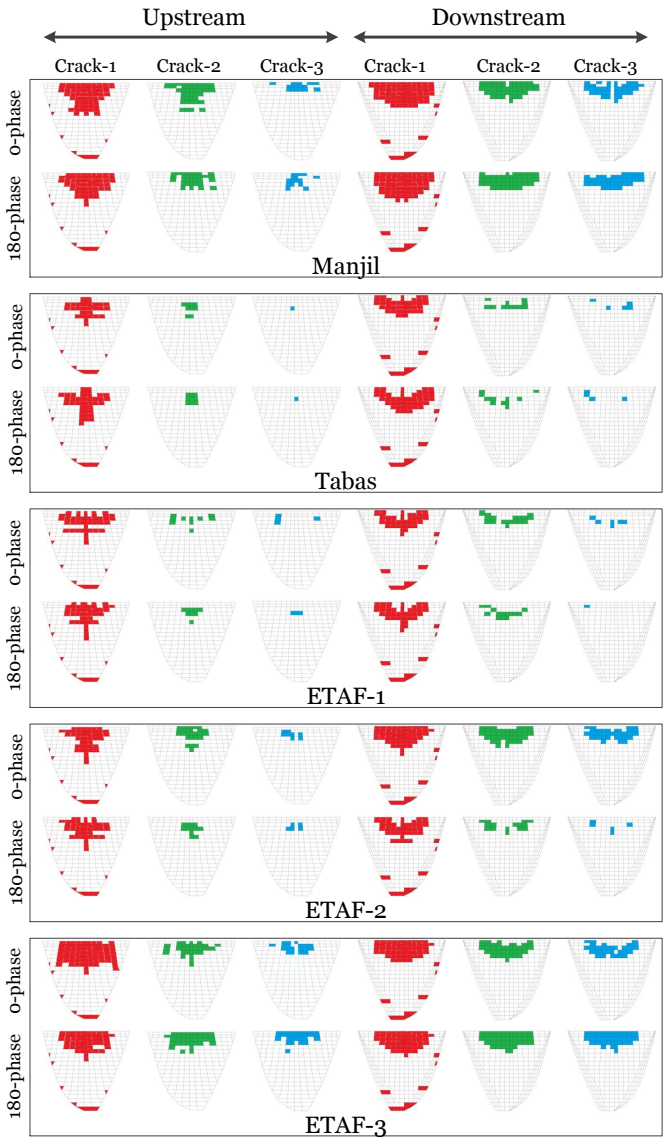

Fig. 29.55: Crack profiles from real ground motions and ETAFs

effects on dam deflections and stresses become negligible. A prismatic foundation mesh constructed on semi-circular planes can typically be employed [307] along with smaller elements near the dam-foundation contact region where the largest deformations and stresses occur. In contrast, larger elements are used away from

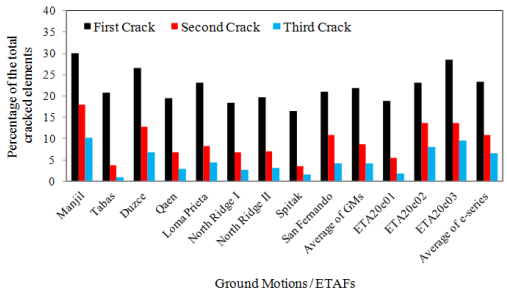

Fig. 29.56: Summary of cracked elements from real ground motions and ETAFs

the dam where interactions with the dam are reduced. According to the standard massless foundation model, the volume of the foundation rock region extends a distance equal to one or two dam heights in the upstream, downstream, and downward directions. Since wave propagation is neglected in this model, all nodes on exterior surfaces of the foundation mesh are fixed in space, as shown in Figure 29.57(a).

- The last type of foundation is massed and includes appropriate boundary conditions at the far-end in order to absorb outgoing waves. The most famous artificial boundary condition at the far-end boundaries of a foundation medium is known to be the viscous boundary (Figure 29.57(b)), which generally uses three orthogonal dampers in all exterior nodes of the foundation model for energy absorption [554].
- The other way to prevent wave reflection at the artificial boundary is by introducing infinite elements at the foundation exterior (Figure 29.57(c)). The use of infinite elements, stiffness, and damping pertinent to the semi-infinite medium via the artificial boundary of the structure has been incorporated into these analyses. The basic idea behind infinite elements is to allow use of elements with special shape functions for the geometry at the far-end truncated boundary. Two sets of shape functions will therefore be applied: the standard shape function, N_i, and a growth shape function, M_i, which grows without a bound as the coordinate of the ith node approaches infinity. The N_i functions are applied to field variables [380] while M_i is applied to the geometry. These M_i shape functions and their derivatives are presented in Table hl1 for a 20-node solid element with a face in infinity (Figure 29.57(c)). The effect of a semi-infinite medium via the far-end boundary of the foundation is taken into account once the resultant stiffness matrices and their related proportional damping matrices have been assembled into both the global stiffness matrix and global damping matrix of the system.

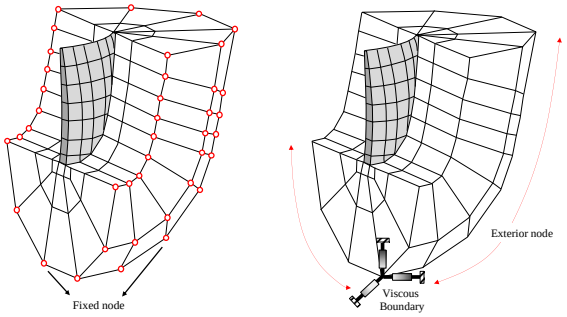

(a) Standard massless foundation model

(b) Massed foundation with viscous boundaries

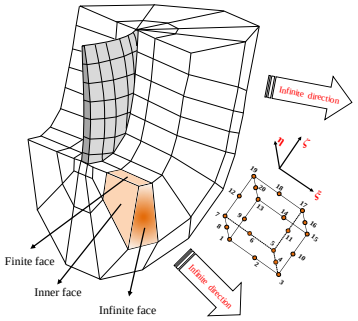

(c) Massed foundation with infinite elements

Fig. 29.57: Different foundation models

29.5.2 Numerical Model of the Coupled System

Karaj Dam offers a symmetric double curvature; its crest is 390 m long, and it extends a height of 168 m above the foundation. A general view of Karaj Dam is displayed in Figure 29.58(a). The dam structure and foundation medium have been modeled using 20-node isoparametric elements. The radius of the foundation region, which was modeled in a semi-spherical shape, was set at 330 m with the center of the semi-spherical body located at the middle of the dam body crest. The reservoir was simulated using 8-node isoparametric fluid elements extending roughly twice the height of the dam body in the upstream direction.

The finite element model of the dam-reservoir-foundation system is shown in Figure 29.58(b). Due to the inherent rate dependence of the mechanical and strength properties of mass concrete [842], the dynamic properties differ from the static properties as follows: the modulus of elasticity, Poisson's ratio, tensile and compressive strength of mass concrete under static and dynamic conditions are equal to 26 GPa, 32 GPa,

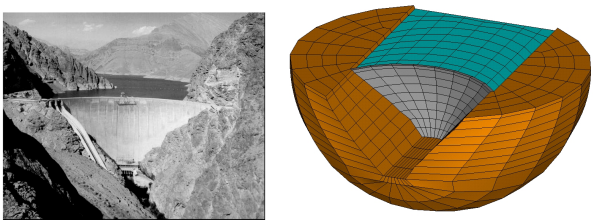

(a) General view

(b) Finite element model of the dam-reservoir-massless foundation system

Fig. 29.58: Karaj Dam

0.17, 0.13, 3.66 MPa, 5.00 MPa, 37.0 MPa and 50.0 MPa, respectively. In addition, the mass concrete density is 2,450 kg/m^3.
The static and dynamic modulus of deformation of the foundation is set at 16.3 GPa, and the Poisson's ratio equals 0.15. The pressure wave propagation velocity and density of water equal 1,436 m/s and 1,000 kg/m^3, respectively. The mass and stiffness proportional damping is applied on the structure whose damping ratio for the fundamental mode has been selected to be 5%. For the nonlinear failure analysis of concrete dams, it is possible to use the quasi-linear damping mechanism, which may be updated during the seismic analysis based on the instantaneous stiffness matrix of the dam body.
Figure 29.59 shows vibration periods for the first 30 modes of the dam-reservoir system in considering foundation effects. In addition, this figure depicts some of the selected dam mode shapes on a rigid foundation. As observed in this figure, the massed foundation model leads to higher periods than the massless foundation, and both models produce higher values for the period than the rigid foundation model. Let's note that based on this figure, the influence of foundation on the period covering the first ten modes (T $>$ 0.15 s) is more significant than the subsequent modes.

29.5.3 Loading of the Coupled System

The loads applied on the system are: dam self-weight, hydrostatic pressure at normal water level, earthquake loading, and resulting hydrodynamic pressure on the upstream face. To investigate both the near-fault and far-field ground motion effects on the seismic safety performance of concrete dams, three ground motions have been selected for each group. Acceleration and velocity time histories are depicted in Figure 29.60; in addition, Figure 29.61 shows the horizontal acceleration response spectrum of the Karaj Dam site (as a target spectrum) with a maximum credible level (MCL). The ground motions have been scaled in order to provide acceptable consistency to the target spectrum over a range of structural periods, T_{min} to T_{max}, as defined below. The dam's small-amplitude fundamental period of vibration is denoted here by T_1. T_{max} is set at $2T_1$, and T_{min} should typically be set at $0.2T_1$.

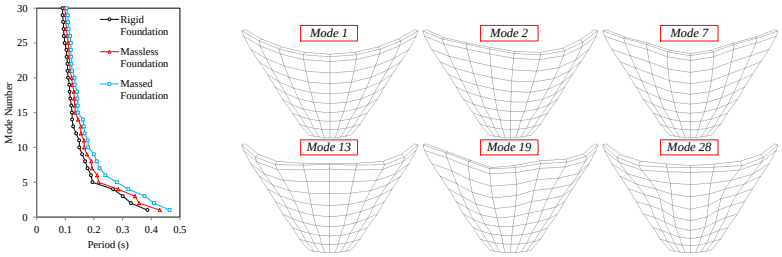

(a) Comparison of the undamped coupled dam modes

(b) sample of key dam mode shapes

Fig. 29.59: Mode shapes

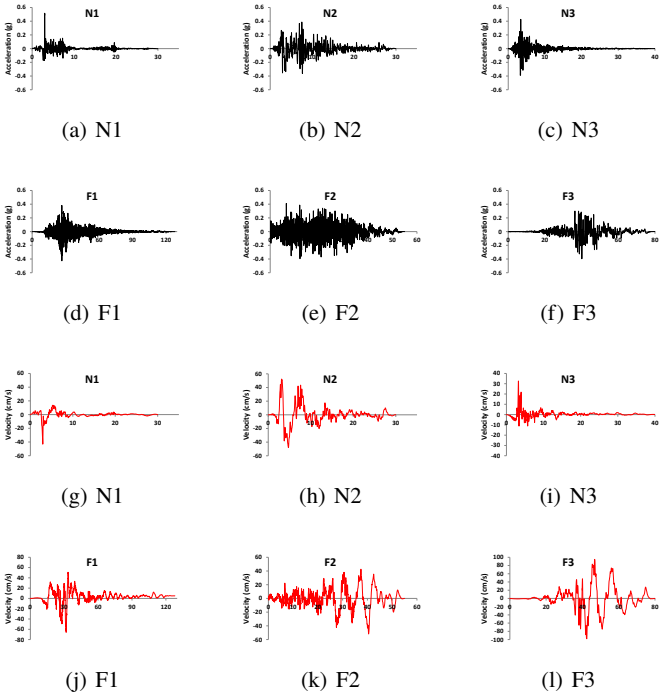

(a) N1 (b) N2 (c) N3

(d) F1 (e) F2 (f) F3

(g) N1 (h) N2 (i) N3

(j) F1 (k) F2 (l) F3

Fig. 29.60: Scaled acceleration and velocity time-histories for near-fault and far-field ground motions

In time history analysis, it may be necessary to identify the stronger horizontal component in order to obtain the highest-magnitude system response. The orthogonal

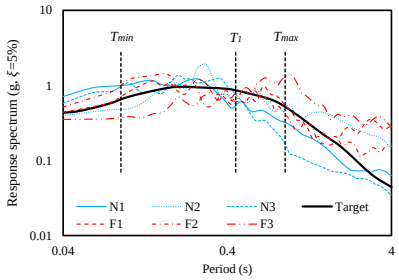

Fig. 29.61: Scaled acceleration response spectra of selected records based on the target spectrum

components of earthquake ground motion are commonly applied along the principal axes of the structure while the maximum response may occur in any direction other than the principal axes. This effect can be determined from component rotation and may be significant in some cases, especially when the second ground motion component is not as strong as the first and when the arch dam is not symmetric along the dam axis. This effect is shown schematically in Figure 29.62(b), which also displays the maximum first principal stress of Karaj Dam under an N1 ground motion for the massless foundation case with the rotation of horizontal components. In this case, applying the orthogonal components along the principal dam axes (x and y) leads to generating a maximum first principal stress in the dam body equal to 3.96 MPa whereas applying ground motion at an angle of $\theta = 45°$ with respect to the principal axes (x45 and y45) leads to a higher maximum first principal stress of approximately 4.59 MPa. A $\theta = 315°$ angle of application with respect to the principal axes (x315 and y315) yields a lower maximum first principal stress (i.e. about 3.01 MPa).

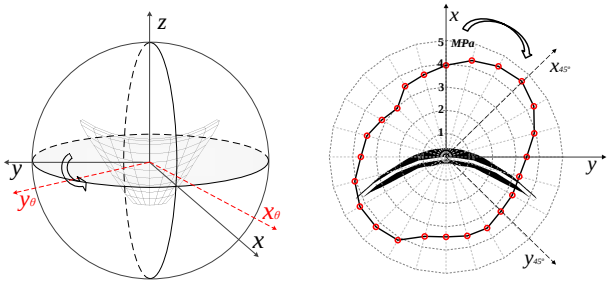

(a) The rotational effect of horizontal ground motion components

(b) Variation in maximum first principal stress due to N1 with respect to component rotation

Fig. 29.62: Rotational effect

For the 3D time-history analysis of arch dams, a complete permutation of all three components with positive and negative signs may be required to obtain the most critical directions causing the greatest structural response. Figure 29.63 shows the effects of considering all eight permutations of N1 ground motion on the massless foundation for both stress and displacement responses. As can be observed, despite some differences between results, these responses are negligible for the current case due to a completely symmetric dam. In this figure, the displacement response differs for all load combinations, while the stress response no longer seems to be sensitive to the direction of the second horizontal ground motion component. This finding suggests that the load combinations are reduced to four different cases under this condition.

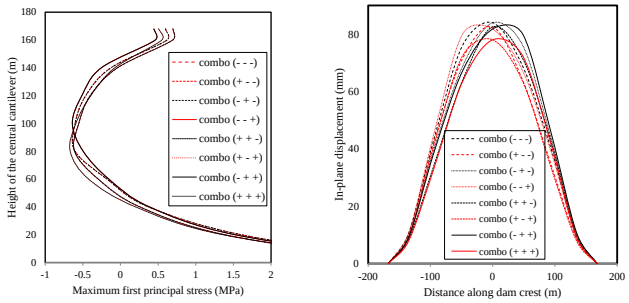

(a) maximum first principal stress (b) displacement along the crest

Fig. 29.63: The effects of considering permutations of all three earthquake components

29.5.4 Near- vs. Far-Field Responses

The comparisons of displacement time histories for the crest point have been omitted, but the non-concurrent envelope of displacement in the stream direction for the central cantilever is shown in Figure 29.64. Based on this figure, the massless foundation leads to higher displacement values than the massed foundation, with both of these values exceeding the rigid foundation displacement. An analysis of the coupled system using the massless foundation model thus yields a more conservative response than the actual massed foundation model. The rigid foundation model, considering no relative displacement at the dam-foundation interfaces, would be expected to output lower displacement values than the other two models. In all cases, near-fault ground motions generate greater responses than the far-field motions, especially over the upper half of the cantilever. The scaled near- and far-field ground motion differences for the rigid foundation model are wider than either the massed or massless foundation model. Figure 29.64(d) shows the average displacement

response for two types of ground motions. The percentage difference at the crest point equals 57%, 38% and 31% for the rigid, massed and massless foundation models, respectively. Generally speaking, far-field ground motions produce results closer to each other than near-fault ground motions. The scattering of results in near-fault motion is greater than that for far-field motion, yet still lies within an acceptable range. For both massless and massed foundation models, N3 provides a greater response than either N1 or N2 while in the rigid model (even though all ground motions exhibit nearly the same crest point response), N1 leads to higher values than N3 or N2 over the middle part of the cantilever.

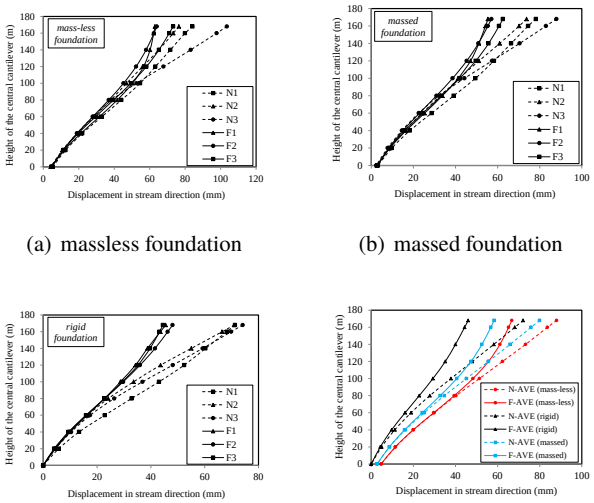

(a) massless foundation (b) massed foundation

(c) rigid foundation (d) shows the average results

Fig. 29.64: Non-concurrent envelope of displacement in the stream direction at the central cantilever for the

Figure 29.65 presents the percentage of overstressed area of the dam under various conditions with respect to the predefined threshold curve proposed by USACE. Even though the demand curves for all models lie below the threshold curve, the rigid foundation generally produces a greater overstressed area than either the massless or massed foundation at various DCR values. Moreover, Figure 29.65(d) compares these curves for near- and far-ground motion recordings. It is clearly apparent that the difference between these two types remains small for massless and massed foundation models; nonetheless, near-fault motions show a bigger jump than far-field motions for the rigid foundation model.

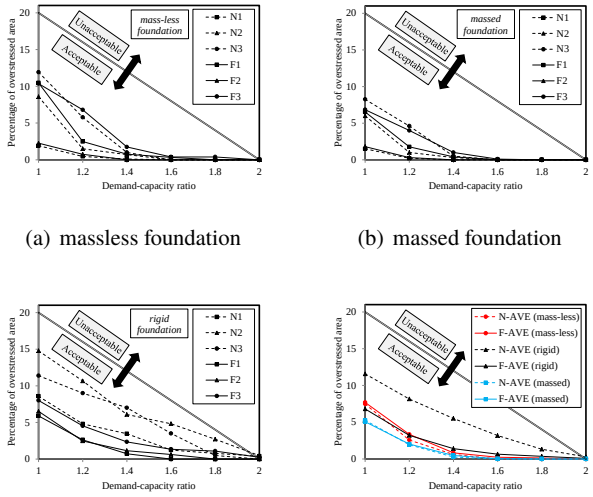

(a) massless foundation (b) massed foundation

(c) rigid foundation (d) shows the average results

Fig. 29.65: Percentage of overstressed area on the dam face at various DCR values

29.6 Soil Structure Interaction: Folsom Dam

Mills-Bria, B. and Nuss, L. and Dixon, L. and Powell, C. and Harris, D. and O'Connell, D. [593] state that when dynamic linear elastic finite element analysis was first applied to dam/foundation systems in the 1960s, it was found that varying the extent of the foundation modeled changed the response and the stresses found in the dam. Because the foundation was given mass and there were no infinite boundaries being used at the foundation outer edges, seismic energy was being trapped and reflected back into the dam. Changing the extent of the foundation modeled changed the frequency of the foundation "box." This in turn affected the dam/foundation interaction. The concept of a massless foundation, although not realistic, eliminated these problems by removing the inertia from the foundation. Only the stiffness of the foundation was included. Because the inertia force (Force = mass $\times$ acceleration) is only applied to portions of the model that have mass, the frequencies and response of the dam only are computed, and they are independent of the size of the foundation modeled. Ground motions applied at the foundation boundaries do not vary through the massless foundation mesh and are, therefore, independent of the size of the foundation modeled. However, when a massless foundation is used, important inertia effects and radiation damping are ignored. Ignoring radiation damping may lead to unrealistically high stresses in the dam.

This section will thus provide verification examples to the model discussed in Chapter 16.

29.6.1 Dam Description

The reference dam for this investigation is a 2D model of Folsom Dam Figure 29.66. This dam was selected because its analysis has been widely reported in the literature, [261, 579, 46].

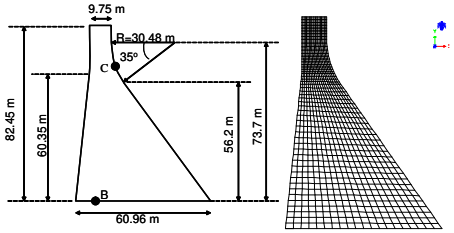

Fig. 29.66: Folsom Dam Geometry and Corresponding Finite Element Mesh

Concrete elastic modulus, Poisson ratio, and mass density were set to 40,679 MPa, 0.19, and 2,500 kg/m^3 respectively. Rock and foundation properties (including size) are given in Table 29.10. We note the various sizes of foundations selected. The dam is discretized by linear quadrilateral elements. A preliminary assessment of the model is based on the comparison of computed eigenvalues and their comparison with those reported by Matheu and Garner [579], Figure 29.67.

Table 29.10: Foundation Sizes and Properties

Foundation	$L \times H$ (m)	Density (kg/m^3)	Young modulus (GPa)	Poisson's ratio
A	800x200	2,500	1.563	0.25
B	800x200	2,400	39.07	0.20
C	400x100	2,400	39.07	0.20
D	24,000x200	2,500	1.563	0.25
E	24,000x2,000	2,500	1.563	0.25

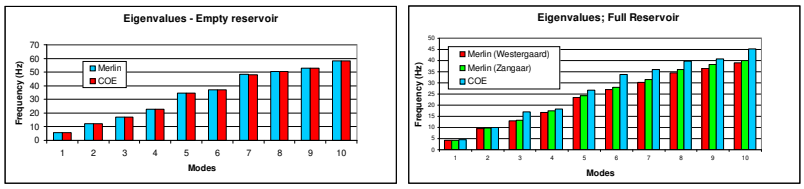

Fig. 29.67: Folsom Dam Eigenvalues

Satisfied with the correlation, the ground motion is examined next. This investigation considered both a harmonic excitation with different frequencies and the 1971 San Fernando Earthquake, recorded at Pacoima dam (Component: 254°, 0.30 peak ground acceleration) shown in Figure 29.68.

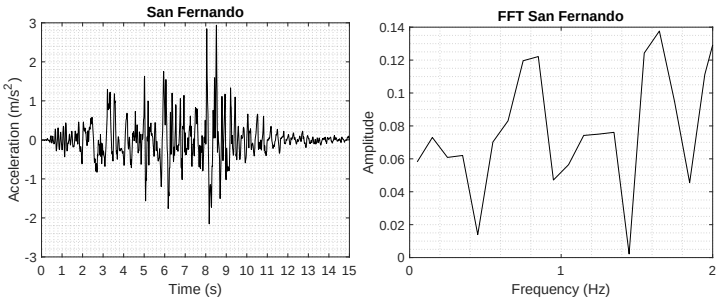

Fig. 29.68: San Fernando Earthquake

All analyses were performed with the time integration scheme of [416] with time step values Δt, α, β and γ of 10^{-2} sec., -1.0, 0.3 and 0.6 respectively. To facilitate comparison, mass and stiffness proportional damping were set to zero unless specified otherwise. Finally, in all the analyses we consider both the dam and the foundation; however for the investigation of the effect of mesh size and extent of foundation, we limited the analysis to the foundation only.

29.6.2 Analyses

This study required many analyses which are schematically described in Figure 29.69. The results of each analysis were entered into a database, and then a Matlab code was used to generate the various plots.
Table 29.11 summarizes the cases considered.

Case	1	2	3	4	5	6
Radiation Damping	No		Lysmer		Miura	
Rocking	Yes	Yes	No	No	Yes	No
Gravity Load Transfer	Yes	Yes	No	Yes	No	Yes
Figure	16.19(a)	16.19(b)	16.19(c)	16.19(d)	16.19(f)	16.19(h)

Table 29.11: Evaluation of Various Boundary Conditions

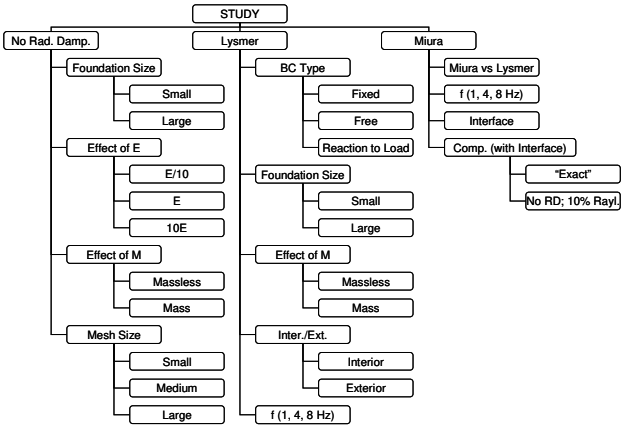

Fig. 29.69: Analyses Performed

29.6.2.1 No Absorbing Boundary Conditions

In this first series, the dam boundary conditions correspond to case 1 which is the most "simplistic" model, yet one which is likely to be adopted by many inexperienced analysts. In all cases, we consider only the foundation (no dam).

First we examine the effect of foundation size for both harmonic and the San Fernando ground motion. As anticipated for such a model lacking radiation damping, the top foundation acceleration depends on the size of the model. Response of dam B (twice as large as C) is quite different. Hence we do not not have an "objective" model if only the foundation is modeled, Figure 29.70.

In Figure 29.71, we again consider the foundation only but with different models and all subjected to San Fernando ground motion. Whereas model E has the smallest acceleration (and largest foundation), the top of the foundation has an acceleration almost nil. This is because of the excessive height of the foundation (the elastic waves do not reach the top of the foundation as in model D). It should be noted that models D and E drastically increase the computational cost of the analysis.

The effect of the foundation stiffness is investigated next, again with the San Fernando record on foundation (model C) only, Figure 29.72. For "soft" rock, the accelerations are highly amplified, and additional frequencies are exacerbated. On the other hand for "hard" rock, some very high frequencies are amplified, yet the peak accelerations are very close to the ground excitation.

The effect of mass is examined in Figure 29.73 where we now consider both the foundation and the dam using model C. If the ground acceleration is applied through a massless foundation, accelerations will be much smaller than through a massed foundation (and no radiation damping is present). We further note that in a massless foundation (3 and 5), the maximum amplitudes are almost identical to the ones of Figure 29.72; however toward the end of the time history, the acceleration at the top of the foundations remain high.

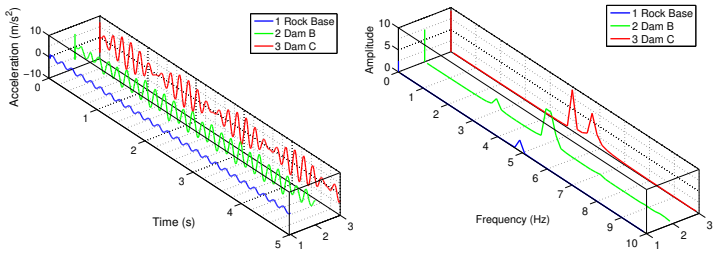

Fig. 29.70: Size effect on foundation analysis (no dam), 5hz

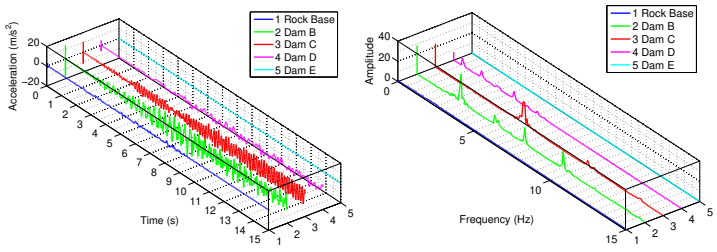

Fig. 29.71: Size effect on foundation analysis (no dam), San Fernando

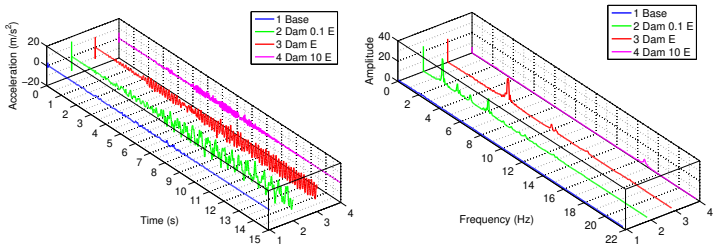

Fig. 29.72: Effect of E on crest acceleration, model C, foundation only

Finally, we examine the effect of the finite element mesh size on the foundation only (model C). Since the analysis is implicit, element sizes should not affect the results. Figure 29.74, shows the response for different average element sizes (5, 10, and 20 m). It is evident that in this particular case, finite element mesh size bears no influence.

29.6.2.2 Lysmer Boundary Condition

This second series of investigations will provide radiation damping in its simplest form through the model of Lysmer and Kuhlemeyer [555].

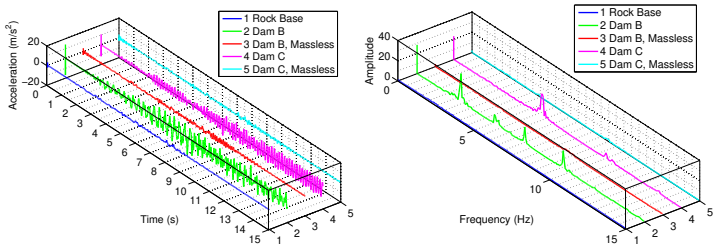

Fig. 29.73: Effect of mass modeling on foundation and dam using foundation model C, San Fernando; Dam base accelerations

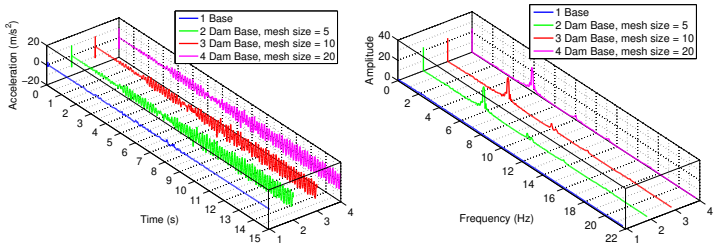

Fig. 29.74: Effect of finite element mesh size, Dam Foundation only, San Fernando

The results of this study are summarized in Figure 29.75 where 2, 3, and 4 correspond to the boundary condition cases 1, 2, and 4. We observe that the presence of a vertical support (curve 2) highly amplifies the accelerations as a result of the reflection of the elastic waves. On the other hand, practically identical results are obtained if we have no displacement or traction boundary conditions (curve 3) as the case in which we replace the reactions with equivalent forces (curve 4). However, the deformed shape in the former is erroneous since the dam will be "sinking" under its own weight in the absence of vertical forces to counteract the statically defined gravity load.

The effect of foundation mass modeling, with foundation model C, dam and foundation is next illustrated in Figure 29.76. When the foundation mass is modeled, the inertia is larger, and hence the crest accelerations are lower. However, it should be noted that a deconvolution of the input signal will eliminate this effect.

The effect of foundation size is explored in Figure 29.77 (foundation and dam). We note that using Lysmer's model, as expected, we greatly reduce the size dependency, and only a narrow band of frequencies is amplified.

Finally, the ground motion frequency is examined in Figure 29.78.

Here we observe a strong dependency on the excitation frequency. Which is the reason one should carefully select the height of the foundation to correspond to a multiple of the shear elastic wave length. This is easily determined from

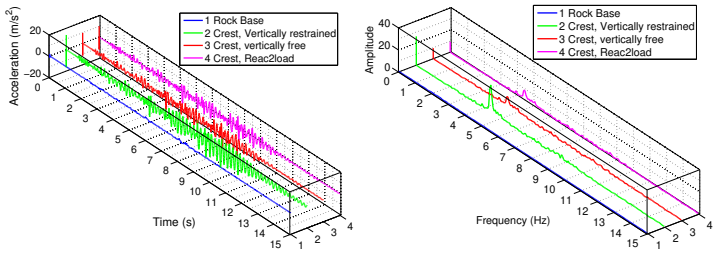

Fig. 29.75: Effect of Lysmer boundary conditions, dam crest accelerations, foundation model C, San Fernando

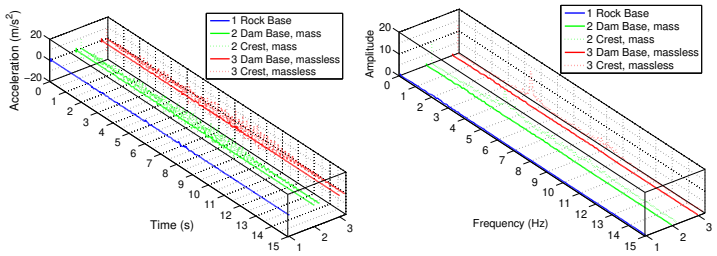

Fig. 29.76: Effect of mass modeling in Lysmer with foundation model C, foundation and dam, San Fernando

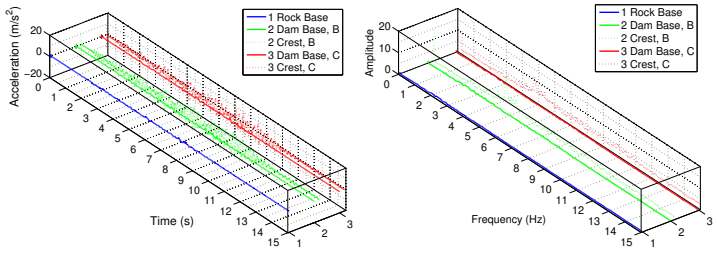

Fig. 29.77: Effect of foundation size, Model C, foundation and dam, San Fernando

$$V_s = \sqrt{\frac{E}{2\,(1+\nu) * \rho}} = 266.4\ \mathrm{m.s}^{-1} \tag{29.4}$$

and (for model C) $H = V_s T$. For such an "optimized" foundation height, we obtain Figure 29.79. Henceforth, the dominant frequency of the San Fernando ground excitation being 22 Hz, and for the given shear velocity of 266.4 m/s, the height of the foundation should be 118.4 m which would be a reasonable height to assume

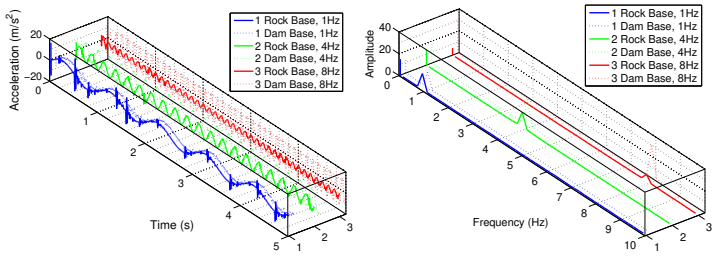

Fig. 29.78: Effect of frequency

in the context of a finite element discretization. We note that in this case, the top foundation acceleration is now practically the same as the one applied at the base.

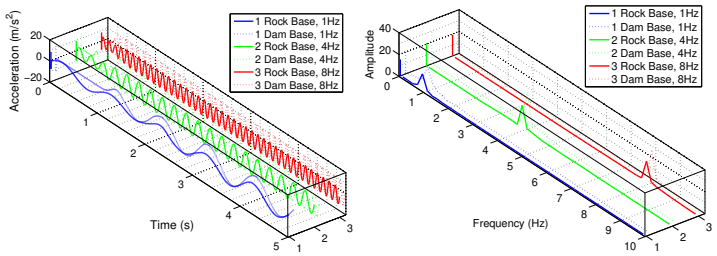

Fig. 29.79: Effect of frequency, foundation (model C) and dam, optimized height

29.6.2.3 Miura Model

Comparing Lysmer with Miura, Figure 29.80, it would appear that both approaches yield the same results, yet close examination of the response in the frequency domain shows that crest accelerations with Miura are slightly smaller.

We examine the model dependency on the frequency, Figure 29.81, next. For an "optimized" foundation height, we observe the improved transfer function (base to top) in Miura's model as opposed to the one of Lysmer.

So far, it has been assumed that there was a perfect bond between the concrete dam and the rock foundation. This assumption was made in order to facilitate comparison amongst various models. If we now model the interface through joint elements [177] we obtain the results shown in Figure 29.82. In this particular study, the excitation was strong enough to induce joint openings. We note that whereas both responses appear to be identical, the frequency domain response indicates a sharp amplification. Furthermore, the joints dissipate some of the energy, thus reducing the stress field, Figure 29.83.

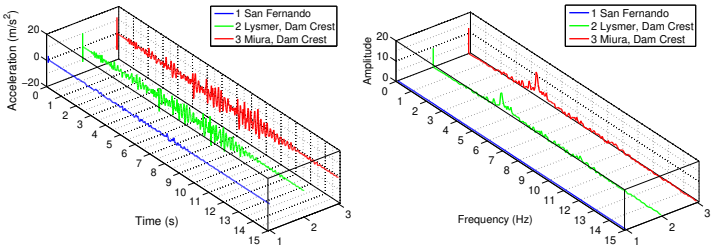

Fig. 29.80: Comparaison Miura/Lysmer San Fernando

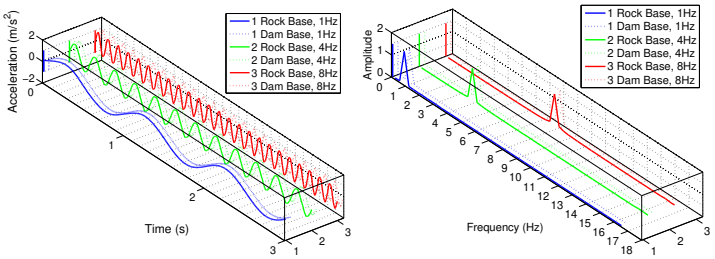

Fig. 29.81: Effect of frequency, Optimized Height

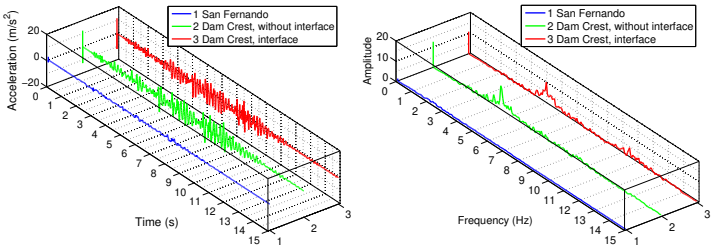

Fig. 29.82: Effect of Rock-Concrete Interface on Acceleration

Often times, engineers combine a simplified finite element model (no radiation damping, massless) with an arbitrarily "high" Rayleigh damping coefficient which is assumed (implicitly) to account for the model deficiencies. For a 10% damping, Figures 29.84 and 29.85 compare crest accelerations and maximum stresses, respectively, between the "simplified" model and the more refined one based on Miura (without damping). We note that despite the large Rayleigh damping coefficient, the acceleration and the stresses remain particularly high. Another way to express this difference is to say that an accurate model can drastically reduce accelerations and stresses. Preliminary studies show that one would have to use damping of $\sim 20\%$ in order to achieve accelerations approaching those based on Miura's model.

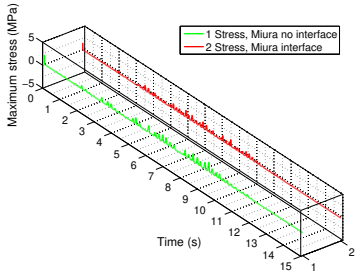

Fig. 29.83: Effect of Rock-Concrete Interface on Stresses

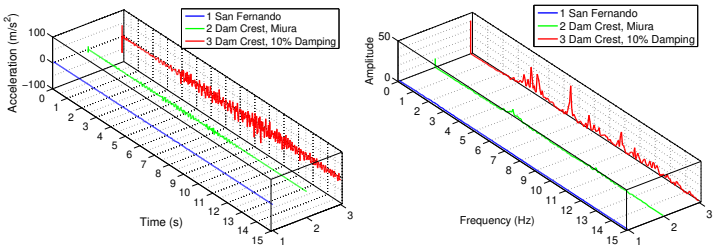

Fig. 29.84: Acceleration Comparison of a refined model (no damping) and a Simplified model (massless foundation) at 10% Damping

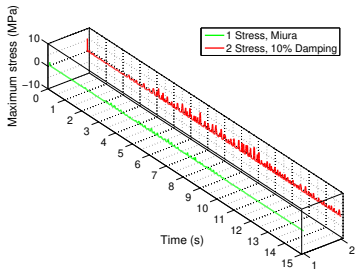

Fig. 29.85: Stress Comparison of a refined model (no damping) and a Simplified model (massless foundation) at 10% Damping

29.6.3 Observations

Through a parametric investigation of the foundation model of Folsom Dam, this paper attempted to shed some light on the relative importance of finite element modeling. Major conclusions, drawn for this particular dam/foundation earthquake records but likely to be generalized to others, are:

1. Structural response can have a strong dependency on the size of the foundation if the mass is modeled.
2. If no radiation damping is present, "very large" foundations should be used. However whereas the length along the direction of the excitation can be as large as desired, the height should be carefully selected. In either case, computational cost of such an analysis can be prohibitive.
3. The foundation rock stiffness plays an important role. For "soft" rock, the mass of the foundation should be modeled as we can have substantial amplification of the input signal.
4. When the mass is modeled, we have a larger inertia and thus slightly reduced dam accelerations. However this effect is mitigated by deconvolution of the input signal which should be performed.
5. A massless foundation will a generate larger response than a massed foundation.
6. In an implicit transient analysis, the size of the elements in the foundations plays a very minor role. Henceforth, one could decrease computational cost of a model without radiation damping by using relatively large elements.
7. One should not apply vertical support in a seismic analysis of a massive concrete structures with its foundation as rocking will induce additional accelerations (and stresses).
8. Practically identical results are obtained in the absence of vertical supports or inclusion of vertical forces equal to the static vertical reactions. However the second solution is preferred for graphical post-processing (otherwise the vertical forces not being in equilibrium will "sink").
9. When radiation damping is present, we greatly reduce the dependency on the size of the foundation.
10. Even when radiation damping is present, the height of the foundation should be carefully selected to correspond to a multiplier (one should be enough) of the shear wave length.
11. Accounting for free field (as in Miura's model) can further reduce the accelerations.
12. Interface (or joint) elements between the dam and the foundation may not substantially reduce the accelerations but will reduce the stresses.
13. A model based on Miura with interface elements is equivalent to a "simpler" model (with no interfaces, no radiation damping) with a Rayleigh damping of about 15%.

We have highlighted the advantages of adopting a proper (although complex) model for the foundation. It is by now amply evident that some of the simpler models advocated can be over-conservative, which is probably why the corresponding factors of safety are quite "heuristic" (such as the tensile stresses can not exceed the dynamic tensile stress more than x times).

Modern computational tools (hardware and software) enable us to perform sophisticated transient nonlinear finite element analysis of massive concrete structures which could not have been performed until recently. However, one should carefully revisit the corresponding criteria to evaluate the safety factors.

Finally, if the "potential failure mode" approach [309, Chapter 14] is indeed to be used, it is of paramount importance that the detailed nonlinear computational model does also properly model the foundation as shown in this paper.

Chapter 30
Probabilistic Analysis of Dams; Examples

Abstract
This chapter will present two classes of advanced analysis of dams. In the first one, thirteen case studies based on probabilistic concepts are presented. They are followed by four additional ones based on machine learning. Uncertainties considered are material properties, dam geometry and ground motion record-to-record variability.

This chapter begins by detailing illustratively, Figure 30.1, the major considerations to be accounted for in a modern probabilistic based safety assessment of concrete dams [393] and have been previously addressed in related chapters as shown in Table 30.1.

Table 30.1: Safety assessment examples and cross-referencing to corresponding theory

Topic	Chapter	Examples
Seismic Hazard	22, 23	30.1, 30.2, 30.15
Aging Hazard	11	
Numerical Modeling	12, 14	30.1, 30.2, 30.8
Reservoir Special Features	17	30.13
Foundation Special Features	16	
Dam Body Special Features	4, 3, 30.3	30.1, 30.2, 30.8
Thermal Simulations	2	
Uncertainty Quantification	8, 18	30.1, 30.2, 30.3, 30.5, 30.6, 30.11, 30.12, 30.13, 30.15, 30.16, 30.17
Seismic Analyses	24	30.1, 30.2, 30.4, 30.9, 30.12, 30.13, 30.14, 30.15
Performance Criteria	25	30.1, 30.2, 30.4, 30.10
Damage Assessment	26	30.1, 30.2, 30.3, 30.4, 30.6, 30.7, 30.10, 30.13, 30.14
Dam Safety Objectives	27	30.8, 30.9, 30.10, 30.16, 30.17
Meta-modeling and Machine Learning	20	30.5, 30.6, 30.7, 30.14, 30.15, 30.16, 30.17
Decision tools	28	

30.1 Probabilistic Seismic Demand Model Analysis of a Gravity Dam

This section which is adapted from Hariri-Ardebili and Saouma [386] presents a probabilistic seismic demand model for concrete gravity dams. This approach is performed within the context of a cloud analysis (i.e. a multitude of probabilistically defined input data). From such an analysis, an optimal IM (in terms of efficiency,

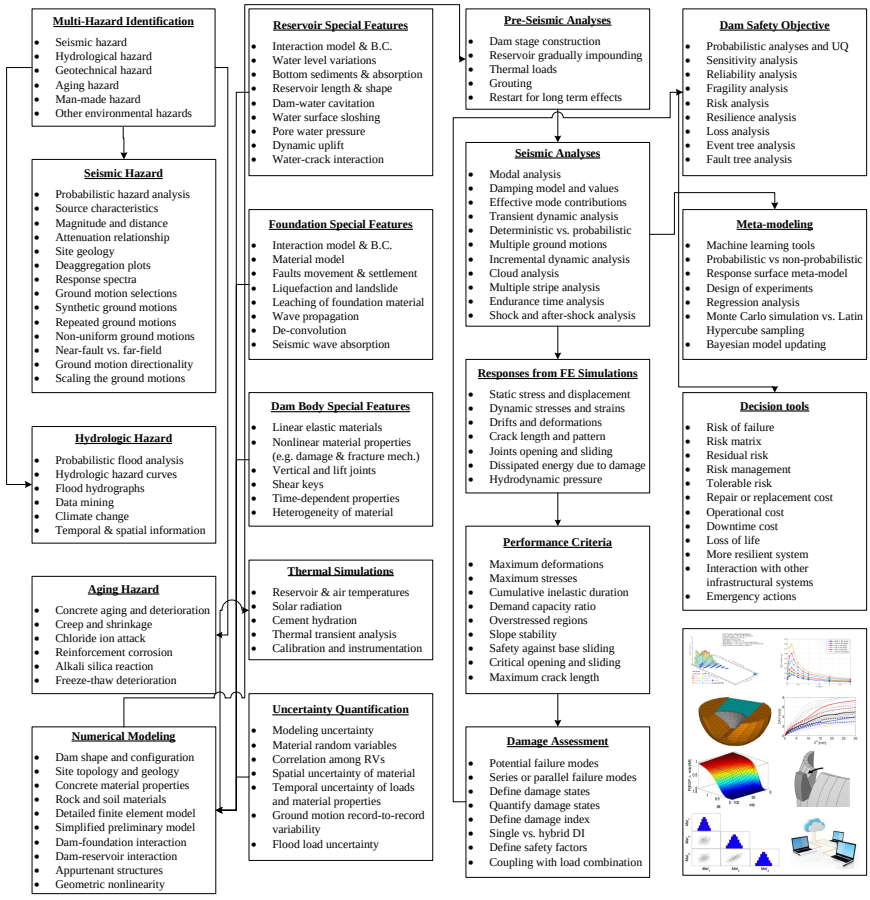

Fig. 30.1: Big picture and the elements of the next-generation dam safety framework

practicality, proficiency, sufficiency, and hazard compatibility) is selected, and the seismic fragility curves are built.

30.1.1 Case Study Dam

Pine Flat concrete gravity dam is used as a case study. Figure 30.2 shows the cross section of the tallest non-overflow monolith. The finite element code Merlin is used for analysis [767]. Two-dimensional plain strain elements are used for modeling the dam body and the foundation. Nonlinearity stems from the use of zero-thickness interface elements for modeling the discrete joints at the base only [177]. Though one could potentially have upper cracks (with crack trajectory not *a priori* known) [332, 333], this paper considers only what is perceived as the most relevant failure

mode: base cracking. Applied loads to the system are: 1) self-weight, 2) hydrostatic pressure, 3) uplift which is automatically updated with crack propagation, and 4) seismic loads.

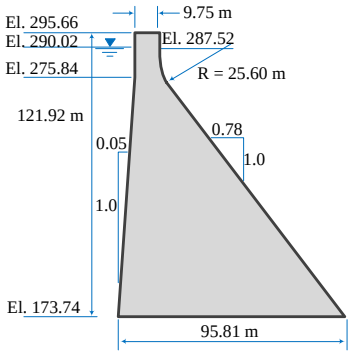

Fig. 30.2: Tallest non-overflow monolith of Pine Flat dam

30.1.2 Ground motion Characteristics

In order to develop a probabilistic seismic demand model (PSDM) a large group of un-scaled ground motions are required. The detailed concept of PSDM and Cloud analysis (CLA), Section 24.3.9, and optimal selection of intensity measures (IM), Section 22.7, were already explained. The unconditional (not dependent on structure natural periods) ground motion selection is adopted [476] to select $n = 100$ records based on the following criteria:

- Site-to-source distance, $0 < R < 250$ km
- Magnitude, $4.5 < M_w < 8.0$
- Fault mechanism: Strike-slip
- Shear wave velocity, 100 m/s $< V_{S30} <$ 1500 m/s

Acceleration response spectra of the 100 ground motions, their mean, median and 95% confident intervals are shown in Figure 30.3(a). Further characteristics are shown in Figure 30.3(b). As in most cases, there is no statistical relationship between V_{S30} and M or R_{hypo}.

30.1.3 IM Distribution Models for Selected GMs

Section 22.6 of Chapter 22 defined seven broad categories of IMs; however, only the first five are considered. As a result, a total of 70 IMs are being considered for the 100 ground motions. For each one, a histogram is plotted, and the most appropriate distribution model is fitted to the observed/computed data. For nearly all the IM parameters in categories II, III, IV, and V, the lognormal model is the best option.

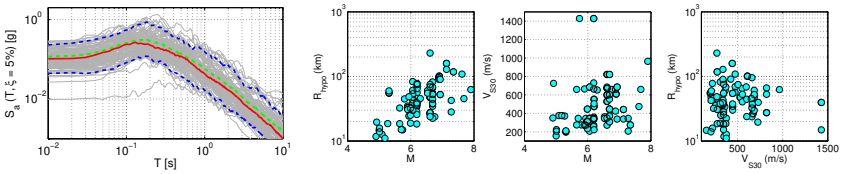

(a) Response spectra (b) M, R_{hypo} and V_{S30} relations

Fig. 30.3: General characteristics of the selected ground motions; mean = green solid line, median = red solid line, 95% confidence interval = blue dashed lines

In category I, the normal distribution is found to be the best fit for M, Weibull for D_{5-75}, and lognormal distribution for the others. Figure 30.4 shows some of the fitted models for the ground motion dependent scalar IMs Section 22.6.2.

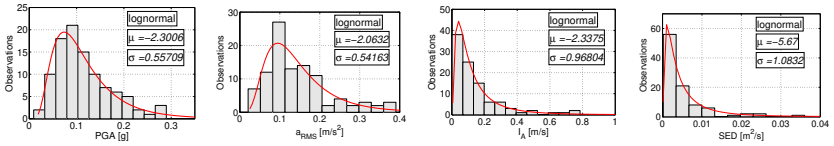

(a) PGA (b) a_{RMS} (c) I_A (d) SED

Fig. 30.4: Histograms and distributional models for some IMs

30.1.4 Cloud Analysis

One hundred nonlinear dynamic analyses are performed in the context of CLA, Section 24.3.9. Seventeen out of 100 are failed through large sliding. Four EDPs were considered: 1) horizontal crest displacement, 2) ratio of crack length over total base length, 3) crack mouth opening, and 4) sliding. Results in IM-EDP coordinates take a form similar to the one in Figure 24.18.

30.1.5 Optimal IM, (EDP = Displacement)

The optimal IM selection is based on the procedure in Section 22.7. For argument's sake, the displacement is considered as EDP. The optimal selection parameters for some IMs are tabulated in Table 30.2. Detailed interpretation of each criteria can be found in Hariri-Ardebili and Saouma [386]. However, the major conclusions are:

- None of the unscalable IMs (Category I) are suitable for probabilistic seismic analyses.
- Among the ground motion-dependent scalar IM parameters (Category II), PGV is the best option.

- Among the ground motion-dependent compound IMs (Category III), I_F has the efficiency, practicality, and proficiency but does not reject the null hypothesis for earthquake distance. Overall, I_F is the most suitable IM for this category.
- Among the structure-independent spectral IMs (Category IV), both the ASI and EPA lead to similar condition.
- Among the structure-dependent spectral IMs (Category V), $S_a(T_1)$, $S_v(T_1)$, and $S_d(T_1)$ lead to nearly identical conditions. Among the acceleration response spectra, the fundamental mode is far better than higher modes. Combined acceleration response spectra, including the effective mass, S_a^{1-to-N}, are the most practical and proficient in the whole set.

Table 30.2: Demand models and IM comparisons for displacement response

IM	b	β	ζ	R^2	p-value (M)	p-value (R_{hypo})
PGA	0.66	0.43	0.65	0.42	0.00	0.38
PGV	0.85	0.32	0.38	0.67	0.93	0.61
PGD	0.27	0.53	1.94	0.13	0.04	0.00
a_{RMS}	0.68	0.43	0.64	0.42	0.75	0.68
I_A	0.42	0.39	0.94	0.52	0.84	0.66
SED	0.35	0.42	1.22	0.44	0.00	0.00
CAV	0.64	0.46	0.72	0.34	0.03	0.00
ASI	0.84	0.32	0.39	0.67	0.00	0.06
VSI	0.84	0.34	0.41	0.64	0.74	0.48
DSI	0.31	0.53	1.74	0.13	0.10	0.00
$S_a(T_1)$	0.84	0.21	0.24	0.87	0.93	0.46
$S_v(T_1)$	0.86	0.22	0.26	0.85	0.32	0.77
$S_d(T_1)$	0.84	0.21	0.25	0.87	0.93	0.46
S_a^{1-to-2}	1.74	0.22	0.12	0.85	0.37	0.98
S_a^{1-to-3}	2.56	0.23	0.09	0.84	0.30	0.90

30.1.6 Fragility Curves

Fragility curves are derived based on the procedure in Section 25.4.3. The collapsed data is also treated as explained in Section 25.1.6.

Figure 30.5(a) presents the fragility curves for a particular EDP value using different IM parameters. Both PGA and $S_a(T_2)$ generates wider curves than $S_a(T_1)$. In addition, S_a^{1-to-2} is similar to the $S_a(T_1)$ shifted by about 0.1 g. The impact of variable EDP is shown in Figure 30.5(b) in terms of fragility surface.

Figure 30.5(c) shows the fragility curves based on joint opening and sliding at the dam-rock interface. Three different LS are considered as initiation of opening/sliding, propagation of the opening/sliding, and near collapse condition. In all cases, joint sliding has the highest probability of exceedance.

Finally, the fragility curves can be defined in a more generic way in terms of damage index (DI), Chapter 26. The damage and limit states in Table 26.1 are used. Figure 30.5(d) shows the fragility curves in terms of the LS. The last curve (LS = 0.99) corresponds to the the probability of failure (collapse).

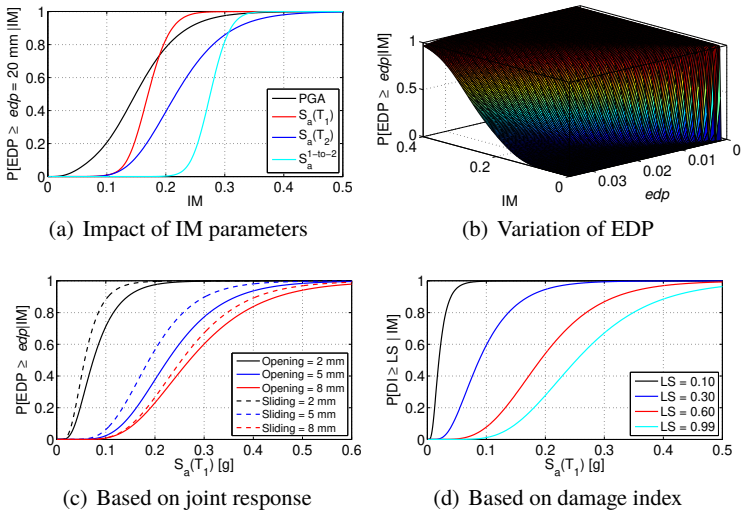

(a) Impact of IM parameters (b) Variation of EDP

(c) Based on joint response (d) Based on damage index

Fig. 30.5: Different versions of cloud-based fragility functions for a gravity dam

30.2 Incremental Dynamic Analysis of a Gravity Dam

This section which is adapted from Hariri-Ardebili and Saouma [384] presents the application of PBEE for concrete dams. The IDA method is applied to a gravity dam with and without the vertical ground motion component. Single-IDA and multiple-IDA methods are discussed, and the Resurrection phenomenon is identified. The optimal IM parameters are determined for gravity dams under scaled ground motion records, and the collapse fragility curves are derived based on dominant failure mode. Finally, the impact of pool elevation on the collapse fragility curves are investigated.

30.2.1 Case Study Dam

Pine Flat Dam is used as case study. The modeling procedure is identical to the one in Section 30.1.1.

30.2.2 Ground motion Characteristics

Probabilistic seismic hazard analysis (PSHA), Section 23, is used for ground motion selection (both the horizontal and vertical components), according to the following conditions:

- Site-to-source distance, $1 < R_{rup} < 120$ km
- Magnitude, $5.5 < M_w < 7.5$
- Fault mechanism: Strike-slip
- Shear wave velocity, 600 m/s $< V_{S30} <$ 1500 m/s; preferably $V_{S30} \approx 760 m/s$

- No pulse-like record

Figure 30.6 shows the horizontal (H) and vertical (V) components of $n = 21$ un-scaled acceleration response spectra, as well as the V/H ratio as a function of period. The mean ratio is less than unit.

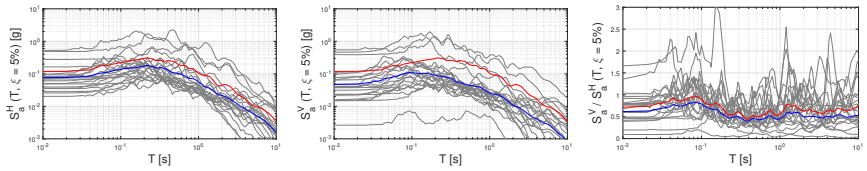

(a) Horizontal component (b) Vertical component (c) V/H ratio

Fig. 30.6: Response spectra for 21 un-scaled ground motions (Gray: individual ground motions, red: arithmetic mean, blue: geometric mean)

30.2.3 Capacity Curves

30.2.3.1 Single Record IDA

All 21 records were subjected to the SR-IDA, Section 24.3.8.1, and three forms were identified for the IM in terms of the EDP (crest displacement) and four types for IM in terms of DI (crack ratio), Figures 30.7(a) and 30.7(b), respectively. Whereas the softening response of the concrete dam is expected, the hardening one is enigmatic. This is attributed to the fact that two scaled ground accelerations at a given time t may result in damages in two different locations [849]. In gravity dams, cracking tends to initiate at the heel, and depending on the ground motion amplitude, different cracking patterns may follow.

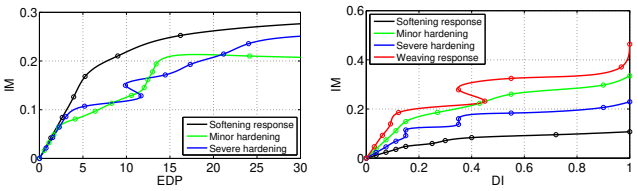

(a) EDP-based (b) DI-based

Fig. 30.7: SR-IDA curves for gravity dams

30.2.3.2 Resurrection Phenomenon

In the classical PBEE literature associated with buildings, it is shown that in an IDA a first failure triggered by an IM_j may be followed by a non-failure at IM_{j+1} and failure again at IM_{j+2}. The transition from j to $j+1$ has been labeled as "resurrection" [849]. It was determined that to capture such a phenomena in concrete dams one must model the concrete nonlinearity (using smeared cracks) in addition to the discrete nonlinear rock/concrete interface (multiple source of failure modes). This is shown in Figure 30.8 and resurrection occurs only for "H + V" between IM 4 and 6 (Figures 30.8(i), 30.8(j), and 30.8(k)). Moreover, the overall failure is at a lower amplitude in "H + V" than "H only."

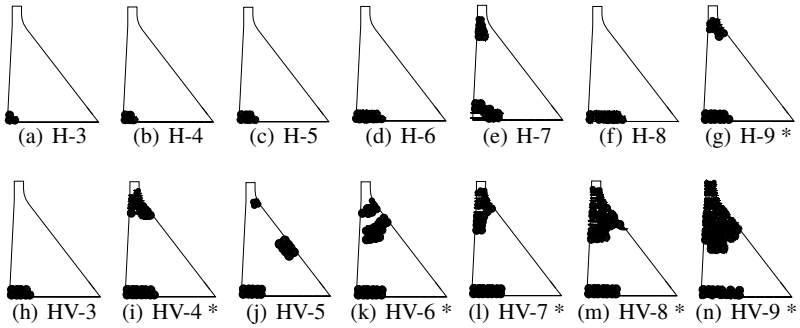

Fig. 30.8: Progressive failure with single record IDA; * means failure; number refers to intensity level

30.2.3.3 Multiple Record IDA

Results of multiple record IDA, Section 24.3.8.2, for three different IM parameters (i.e. PGA, ASI and S_a^{1-to-2}) are shown in Figure 30.9, while the EDP is the horizontal crest displacement. In all cases, the "H + V" has a lower IM capacity than "H only," and the dispersion for S_a^{1-to-2} is smaller than the other two (a desirable effect).

30.2.4 Collapse Fragility Curves

Benefiting from the MR-IDA results, one can next determine the collapse fragility curves. The procedure can be found in Section 25.4.1. For the current case study, the fragility curves are plotted in Figure 30.10(a) where three different methods were used for curve fitting. The worst fit was achieved through the simplest moment method (MM) as it underestimated the probability of collapse. The Lilliefors test is used to measure the goodness-of-fitting [539]. This is consistent with the essence

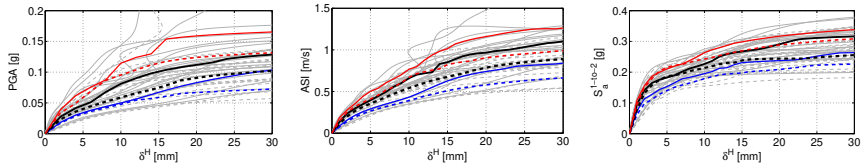

(a) IM = PGA (b) IM = ASI (c) IM = S_a^{1-to-2}

Fig. 30.9: Impact of IM on the MR-IDA curves and their summary

of this simplified method which seeks to match the central parameters (median and standard deviation) rather than the entire distribution as also determined in [520]. Figure 30.10(b) shows the impact of a vertical ground motion component on the fragility curves. Accounting for the vertical component reduces the median of the probability of collapse by 22%.

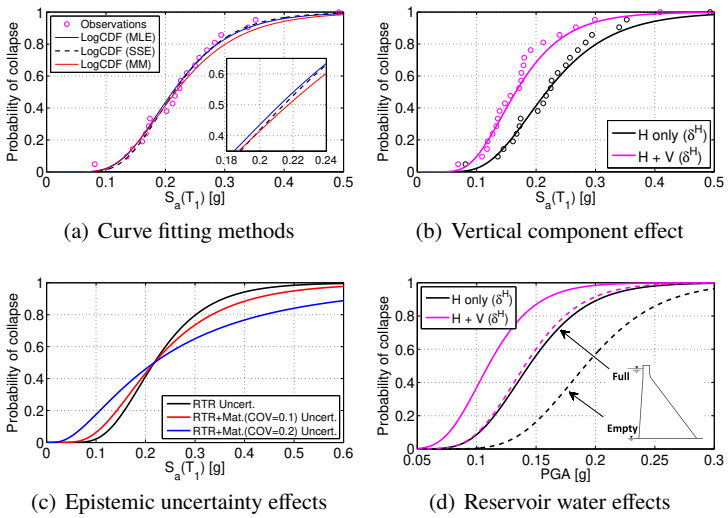

(a) Curve fitting methods (b) Vertical component effect

(c) Epistemic uncertainty effects (d) Reservoir water effects

Fig. 30.10: Comparison of different methods for collapse fragility curves fitting

One may want to add the epistemic uncertainty on top of the record-to-record (aleatory) variability. Ideally one would perform Monte Carlo simulation family with direct sampling which accounts for both uncertainties [173]; however, this can be very computationally demanding. An alternative and simplified method combines analytically the two uncertainties through [216]: $\beta_{RU} = \sqrt{\beta_R^2 + \beta_U^2}$, where β_R and β_U are the uncertainties associated with the record-to-record and material randomness, respectively. Major underlying assumptions are: 1) the two sources of

uncertainties are independent, and 2) median values remain constant while the dispersion is altered. The resulting collapse fragility curves with both uncertainties are shown in Figure 30.10(c). The epistemic uncertainty increases the total dispersion and makes the curves wider.
Finally, the impact of the reservoir water on the collapse fragility curves is shown in Figure 30.10(d) for the full and empty dams. For this dam, $\frac{\eta^{\text{Full}}}{\eta^{\text{Empty}}}$ is 0.75 and 0.78 for the "H only" and "H + V" cases, respectively. Also, $\frac{\beta^{\text{Full}}}{\beta^{\text{Empty}}}$ is 1.08 in both cases, i.e. the dispersion is not affected. Note that PGA is used as the IM to avoid dependency on the vibration period.

30.3 Epistemic Uncertainty Quantification in a Gravity Dam

This section which is adapted from Hariri-Ardebili and Saouma [385] investigates pushover analysis of a simple interface element under modes I and II and dynamic analysis of a dam with joint elements subjected to mixed-mode fracture. This investigation leads to a probabilistic-based safety assessment of structures whose responses are primarily governed by cohesive cracking. LHS-based technique is used for sampling, and the sensitivity analysis is performed with a Tornado diagram. Finally, results are presented in the format of fragility curves.

30.3.1 Case Study Dam

Pine Flat Dam is used as the case study. The modeling procedure is identical to the one in Section 30.1.1. Since the dam-foundation interface under dynamic excitation is a mixed-mode fracture mechanics, two other simple examples are also studied for mode I and II fracture mechanics. Both of the simplified examples include two blocks on top of each other. One of them is subjected to monotonically increased displacement, while the second one is subjected to incremental sliding displacement.

30.3.2 Material Properties

Only very few of the parameters in the joint constitutive model can be experimentally measured, such as tensile strength f'_t, the cohesion c, the angle of friction ϕ_f, and the fracture energy G_F^I. For the present study, the fracture parameters shown in Table 30.3 are used. In all the cases, normal distributions are assumed and are truncated to [0.5 mean, 1.5 mean]. Indeed, since many of the joint parameters have to be estimated by the analyst, the purpose of this study is precisely to assess their impact on the results.

Table 30.3: Parameters defining the zero thickness joint element

Characteristics	Symbol	Unit	Mean	COV	[Lower, Upper]
Tangential stiffness	k_t	GPa	224	0.2	[112, 336]
Normal stiffness	k_n	GPa	224	0.2	[112, 336]
Tensile strength	f_t'	MPa	2.24	0.2	[1.12, 3.36]
Cohesion	c	MPa	1.90	0.2	[0.95, 2.85]
Friction angle	ϕ_f	Deg.	38	0.2	[19, 57]
Dilatancy angle	ϕ_d	Deg.	20	0.2	[10, 30]
Specific mode I fracture energy	G_F^I	N/m	252	0.2	[126, 378]
Specific mode II fracture energy	G_F^{II}	N/m	2520	0.2	[1260, 3780]
Relative irreversible deformation	γ	-	0.3	0.1	[0.15, 0.45]
Max. displacement for dilatancy	$u_{D_{max}}$	m	0.01	0.1	[0.005, 0.015]
Tensile stress at break-point	$s_{1\sigma}$	MPa	0.56	-	-
COD at break-point	$w_{1\sigma}$	m	1.12e-4	-	-
Cohesion at break-point	s_{1c}	MPa	0.475	-	-
CSD at break-point	w_{1c}	m	1.89E-3	-	-

30.3.3 Uncertainty of Mode I and II Fracture Mechanics

In this study, 10 of the parameters are assumed to be RVs. A total of 1,000 analyses are performed for each of the most sensitive RVs based on LHS. Moreover, two extra cases are studied: correlated RVs and un-correlated RVs. The sampling matrix for the cases with and without correlation are shown in Figure 30.11.

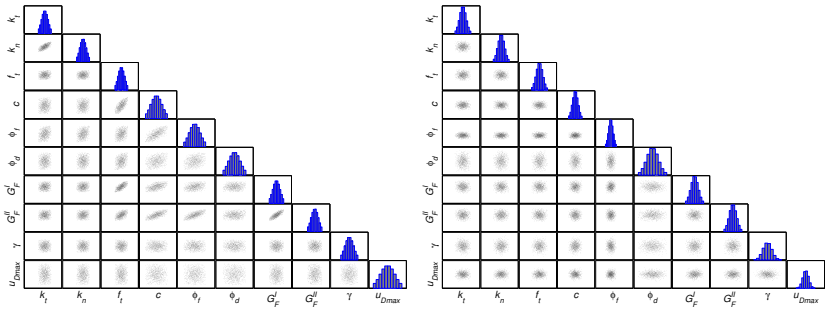

(a) With correlation (b) Without correlation

Fig. 30.11: Sampling of the RVs for mode I and II fracture mechanics (no scale)

Figure 30.12 compares all the individual, correlated and un-correlated fragility curves for mode I and II fracture. Considering the uncertainty in all RVs without any correlation leads to the widest fragility curve. In mode II fracture, all the curves are nearly passing from the 50% probability while this is not the case in mode I fracture. These plots clearly show that the most influencing RV in mode I and II are k_n and c, respectively.

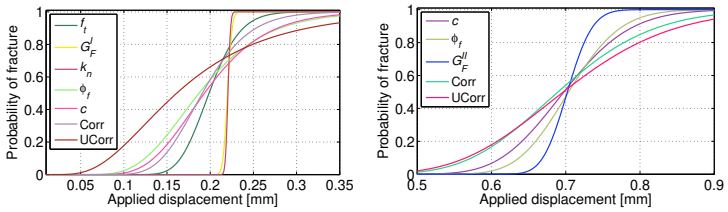

(a) Mode I fracture (b) Mode II fracture

Fig. 30.12: Comparison of fragility curves for mode I and II fracture

30.3.4 Sensitivity Analysis of Dam (Mixed-Mode Fracture)

Having examined two highly idealized cases, attention is now turned to a mixed mode crack propagation in a real structure: a concrete dam subjected to seismic loading. Additional variables associated with concrete and rock are introduced in Table 30.4.

Table 30.4: Characteristics of concrete and rock

Characteristics	Symbol	Unit	Mean	COV	[Lower, Upper]
Concrete modulus of elasticity	E_c	GPa	22.4	0.15	[15.6, 29.1]
Concrete Poisson's ratio	ν_c	-	0.2	0.15	[0.14, 0.26]
Concrete tensile strength	f'_{t_c}	MPa	2.24	0.20	[1.12, 3.36]
Concrete mass density	ρ_c	kg/m^3	2500	0.10	[2000, 3000]
Foundation modulus of elasticity	E_f	GPa	24.0	0.15	[16.8, 31.2]
Foundation Poisson's ratio	ν_f	-	0.25	0.15	[0.18, 0.32]

Sensitivity analysis is performed for 12 RVs for the joint ($u_{D_{max}}$ and γ were left out in light of their limited contribution) and the four elastic proprieties of the concrete and rock. Thus, $2 \times 16 + 1 = 33$ observations are required. Endurance time analysis (ETA) [383] technique is used for simulations, Section 24.3.10. This method uses 3 dynamic analyses for each case and then takes the mean response. Hence, there are 99 analyses in total.
Based on the mean response of the three analyses, the tornado diagram is developed as shown in Figure 30.13. As seen, nearly all parameters are equally important. This implies that there are no redundant parameters in the examined model.

30.3.5 Quantification of Uncertainties in Dam

Since the preceding sensitivity analysis has determined that all RVs are nearly equally relevant, the uncertainty quantification will retain them all. For each set of uncertainties, 100 simulations are performed. The randomness in the target variable is sampled though LHS, Tables 30.3 and 30.4. Contrary to the sensitivity analysis, the ETA method is limited to a single acceleration function in order to avoid aleatory uncertainties to be mixed with epistemic ones. Again, two sets of analyses are reported,

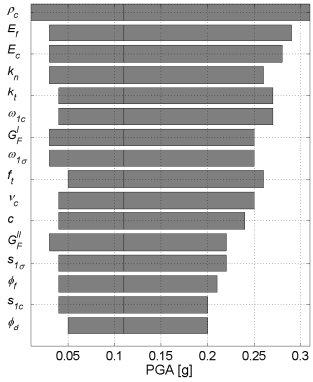

Fig. 30.13: Tornado diagram for the mixed-mode fracture

i.e. correlated and un-correlated. Furthermore, four limit states are considered. They correspond to crack length over the total base. Four distinct ones are selected as 10%, 30%, 60%, and 99% [383].

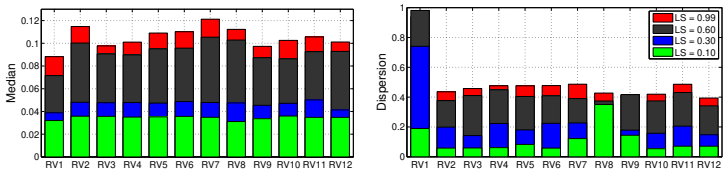

(a) Median (b) Dispersion

Fig. 30.14: Comparison of all RVs for four LSs under mixed-mode fracture condition

Single RV: It was determined that nearly all the fragility curves corresponding to a given LS_i $(i = 1, 2, 3, 4)$ are identical. This confirms the results of sensitivity analysis in Figure 30.13. To better quantify the results, the median and dispersion are separately shown in Figure 30.14. It is noted that the medians at LS=0.10 and LS=0.30 are almost identical for all RVs. The medians at LS=0.60 and LS=0.99 vary for different RVs yet have the same trend. Another notable observation is that the dispersion of $RV1 = \rho_c$ is about twice the next highest one. This can be explained by the fact that in the context of the seismic analysis, proper evaluation of the mass is essential.

Multiple RVs: Correlated and uncorrelated RVs, when they are all modified simultaneously, are shown in Figure 30.15. It is clear that in this process, the range of capacity curves go from nearly zero to a maximum. The former is induced

by a random selection of unfavorable RVs across the board. Examination of the damage index reveals that higher PGAs are needed to trigger larger limit states. Results for correlated an uncorrelated values are nearly identical. The fragility curves confirm the brittle nature of the problem, where the difference between LS=0.10 and 0.30 is small; however the one between 0.30 and 0.60 is substantially larger. Accounting for correlation reduces the dispersion of fragility curves.

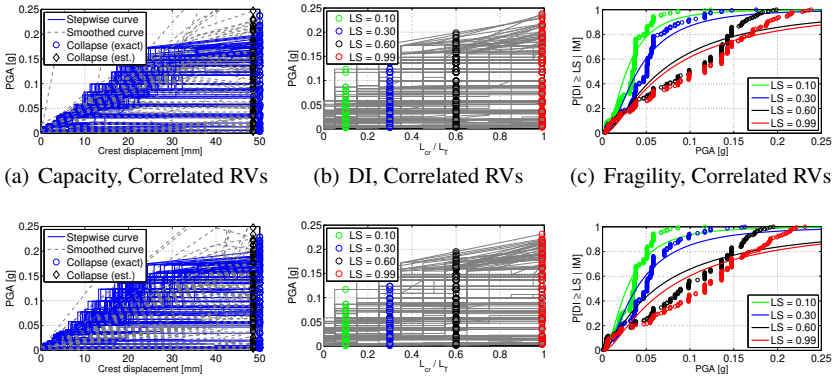

(a) Capacity, Correlated RVs (b) DI, Correlated RVs (c) Fragility, Correlated RVs

(d) Capacity, Uncorrelated RVs (e) DI, Uncorrelated RVs (f) Fragility, Uncorrelated RVs

Fig. 30.15: Impact of RV correlation on the uncertainty quantification of the mixed-mode fracture

30.4 Comprehensive Fragility Analysis of Concrete Dams

This section which is adapted from [377] focuses exclusively on surveying the reported fragility analysis for concrete dams. First, the fundamental underpinnings of the concept will be presented to facilitate subsequent comprehension of the extensive and comparative survey. Finally, tables summarizing the various publications will be presented.

30.4.1 Contextual Framework

The steps towards generating seismic fragility curves for concrete dams are conceptually showed in Figure 30.16. Each step is briefly explained:

1. **Site Characteristics:** Determine dam site seismicity map which can be obtained from US Geological Survey (USGS) web-site or similar studies in other countries.

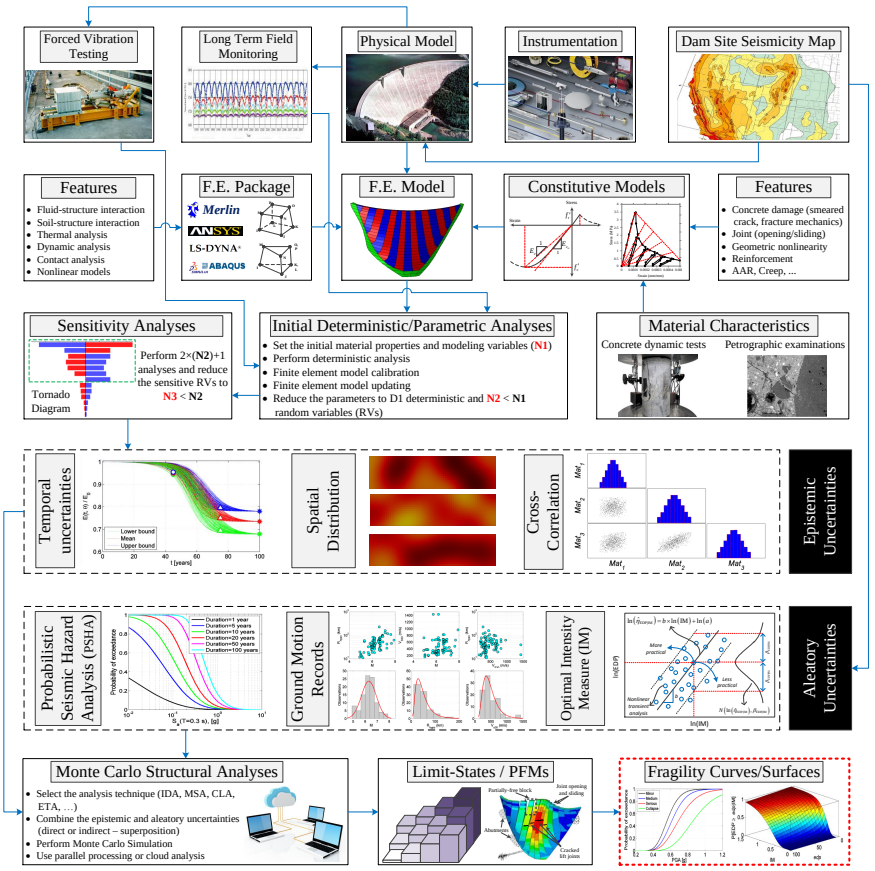

Fig. 30.16: Outline of the concrete dams fragility analysis

2. **Experimental Tests:** Examine the dam physical model using appropriate instrumentation, record the long term field monitoring data, and possibly perform a forced vibration test to obtain the most reliable initial material properties.
3. **Finite Element (FE) Model:** Develop the initial finite element model based on the previous data and material characteristics. Decide on required features (e.g., fluid-soil-structure interaction, thermal loads, nonlinearity) for the numerical analyses and determine the constitutive models. Finally, select an appropriate FE Package.
4. **Initial Deterministic Analysis:** Perform the initial FE deterministic analysis to ensure the accuracy of model. This is followed by a set of parametric analyses with initially *N1* identifiable unknown parameters, which may be reduced to *N2* through calibration with forced vibration testing and long term field monitoring.
5. **Analysis Recheck:** Double check the FE analysis in terms of numerical methods used for time integration, number and size of increments, explicit/implicit solution scheme, convergence criteria, etc.

6. **Sensitivity Analysis:** Assuming that each of the remaining *N2* variables has a minimum and maximum value, then $2\times N2$+1 sensitivity analyses are performed. The first has all variables set to their mean value, and then each variable is assigned the minimum or maximum, one at a time. Results are then displayed though a "Tornado Diagram" from which the most sensitive *N3* random variables are selected and kept in further studies.
7. **Epistemic Uncertainties:** These types of uncertainties are those associated with quantities that should be known but are practically impossible to quantify, such as material property spatial distribution or temporal uncertainties (e.g. time-dependent material degradation). Either one of those two may have two or more random variables (such as tensile strength and fracture energy) and a possible cross-correlation matrix (which is used to define the dependency between multiple variables at the same time).
8. **Aleatory Uncertainties:** These types of uncertainties are those due to insurmountable lack of knowledge such as seismicity at a given site and at a given time. First, a "probabilistic seismic hazard analysis" (PSHA) is performed to determine the hazard curves. Then, corresponding ground motion records are selected (e.g. PEER center web-site), and finally the optimal IM parameter is determined (e.g. PGA or $S_a(T_1)$).
9. **Combined Uncertainties:** Outcomes of both epistemic and aleatory uncertainties are combined by performing Monte Carlo simulations (MCS). Advanced methods such as Latin Hypercube Sampling (LHS), Halton, or Sobel can be used to reduce the number of analyses. One of the following three approaches can be used when both aleatory and epistemic uncertainties are present, Figure 30.17:

    - **Method I:** This is a simultaneous method where the number of ground motion records in each seismic intensity level (SIL), *n*, should be equal to the number of models (already sampled and prepared based on LHS). Then, each of the ground motions are randomly paired with one of the models, and *n* nonlinear transient analyses are performed for a specific SIL. Thus, a total of $n \times k$ analyses are required, where k is the number of SILs. In the resulting fragility curves, the median and the logarithmic standard deviation have the combined nature.
    - **Method II:** This is a simultaneous method, where the number of ground motion records, n, is independent from the number of models, m. Thus, for each SIL, $n \times m$ analyses are required which results a total of $n \times m \times k$ analyses.
    - **Method III:** This is a non-simultaneous method, where uncertainties are treated separately and then combined. Ground motion record-to-record (RTR) variability is computed assuming $m = 1$ in "Method II" (it means a deterministic model with all RVs at the mean values). Performing the nonlinear analyses lead to β_{RTR}. On the other hand, the logarithmic standard deviation due to material/modeling (MM) uncertainty, β_{MM}, can be obtained from a set of nonlinear analyses, literature survey, or engineering judgment. Finally, the combined dispersion can be obtained as $\beta_{comb} = \sqrt{\beta_{RTR}^2 + \beta_{MM}^2}$.

10. **Fragility Analysis:** Limit States and Potential Failure Modes (PFMs) are then extracted through data mining. Examples of LSs include crest displacements and joint opening/sliding. In the last step, fragility curves/surfaces are derived from the previous through a statistical interpretation and a cumulative distribution function.

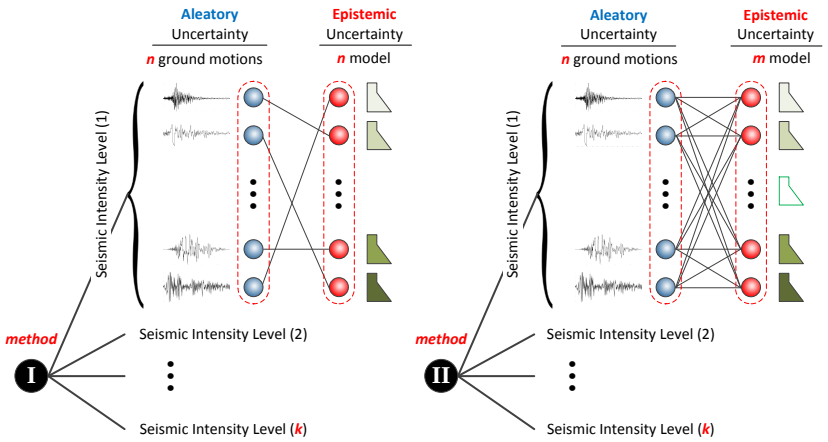

Fig. 30.17: Outline of the concrete dams fragility analysis

30.4.2 Review of Current Applications

This section aims to address some of the current applications of the seismic fragility analysis of concrete dams. Table 30.5 summarizes the major features of each case followed by Figure 30.18 which shows a sample plot. For each paper, an ID is assigned as written in the footnote.

30.5 Response Surface Meta-Model for a Linear Gravity Dam

This section which is adapted from Hariri-Ardebili [390] is an application of response surface meta-model on concrete dams. Originally, eleven DOE techniques are compared and contrasted for a real-world engineering problem subjected to seismic excitation (with 120,000 seismic finite element simulations). The CMCS is compared with other pseudo- and quasi-random methods. The concept of "dam classes" is introduced, and its impact on the accuracy of meta-models is studied. Last but not least, a scenario-based meta-model for dams is proposed which accounts for time and frequency domain ground motion features.

Table 30.5: Summary of the fragility analysis of concrete dams, adopted from [391]

ID	Year	Dam	Software	Joint	Mat. NL	FSI	SSI	Uplift	LE or NL	Technique	Mat uncert.	Un-	Sampling	Total Sim.	Fragility
1	1998	Gravity	Not specified	No	Yes	Yes	Yes	No	NL	Random	Yes		MCS	50	Gussian CDF
2	2003	Gravity	Abaqus	Yes	No	Yes	Yes	Yes	NL	IDA	Yes		LHS	72	LN CDF
3	2007-8	All	-	No	No	No	No	No	-	Empirical	No		-	-	LN CDF
4	2009	Gravity	NSAG-DRI	No	Yes	Yes	Yes	No	NL	IDA	No		-	42	LN CDF
5	2011-2	Gravity	FEAP	No	No	Yes	Yes	Yes	LE	Random	Yes		MCS	60	Empirical
6	2012	Arch	Abaqus	Yes	No	Yes	Yes	No	NL	MSA-IDA	No		-	48	-
7	2013	Gravity	EAGD-84	No	No	Yes	Yes	No	LE	Single dynamic	Yes		Parametric	2700	Weibull dist.
8	2013	Arch	Not specified	No	Yes	Yes	Yes	No	NL	Random	Yes		MCS	Not specified	LN CDF
9	2013	Gravity	Not specified	Yes	No	Yes	Yes	No	NL	Random	Yes		LHS	60	LN CDF
10	2015	Overflow weir	Abaqus	No	No	Yes	Yes	Yes	LE	IDA	No		-	420	LN CDF
11	2011	Turbine blg.	LS-Dyna	Yes	No	Yes	Yes	Yes	NL	Truncated IDA	Yes		LHS	150	LN CDF
12	2012	Gravity	LS-Dyna	Yes	No	Yes	Yes	Yes	NL	Truncated IDA	Yes		LHS	100	Weibull dist.
13	2015	Overflow Sec.	LS-Dyna	Yes	Yes	Yes	Yes	Yes	NL	Truncated IDA	Yes		LHS	300	LN CDF
14	2015	Arch	Ansys	Yes	No	Yes	Yes	No	NL	IDA	No		-	80	N CDF
15	2016	Arch	Ansys	Yes	Yes	Yes	Yes	No	LE, NL	MSA	No		-	54	LN CDF
16	2016	Gravity	Merlin	Yes	No	Yes	Yes	Yes	NL	CLA	No		-	100	LN CDF
17	2016	Gravity	Merlin	Yes	Yes	Yes	Yes	Yes	NL	Full IDA	No		-	1200	LN CDF
18	2016	Gravity	Merlin	Yes	No	Yes	Yes	Yes	NL	ETA	Yes		LHS	200	LN CDF
19	2015	Gravity	LS-Dyna	Yes	Yes	Yes	Yes	Yes	NL	Truncated IDA	Yes		LHS	160	N/LN/Weibull
20	2016	Gravity	LS-Dyna	Yes	Yes	Yes	Yes	Yes	NL	MSA / IDA	Yes		LHS	140	LN CDF
21	2016	Gravity	Abaqus	No	Yes	Yes	Yes	Yes	NL	IDA	No		-	170	LN CDF
22	-	-	-	-	-	-	-	-	-	-	-		-	-	-
23	2016	Gravity	-	No	No	No	No	No	LE	Random	Yes		LHS	∞	Empirical
24	2017	Gravity	Abaqus	Yes	Yes	Yes	No	No	NL	CLA	No		-	135	LN CDF
25	2018	CFRD	GEODYNA	No	Yes	No	Yes	No	NL	IDA	No		-	~ 100	LN CDF
26	2018	Gravity	Abaqus	Yes	Yes	Yes	No	No	NL	CLA	No		-	200	LN CDF
27	2018	Gravity	Merlin	No	No	Yes	Yes	No	LE	Spectrum	Yes		LHS, Sobol,	10,000	LN CDF
28	2018	Arch	Abaqus	Yes	Yes	Yes	Yes	No	NL	IDA	Yes		LHS	100	LN CDF , Spline
29	2018	Arch	Ansys	No	Yes	Yes	Yes	No	NL	BBED	Yes		LHS	275	LN CDF Empirical

Notes: IDA: incremental dynamic analysis; MSA: multiple stripe analysis; CLA: cloud analysis; NL: nonlinear; LE: linear elastic; BBED: Box-Behnken experimental design; MCS: Monte Carlo Simulation; LHS: Latin Hypercube Sampling; CDF: cumulative distribution function; LN: Log-normal
1: de Araújo and Awruch [230]; 2: Tekie and Ellingwood [825]; 3: Lin and Adams [540, 541]; 4: Mirzahosseinkashani and Ghaemian [597]; 5: Lupoi and Callari [549, 550]; 6: Yao, Elnashai, and Jiang [898]; 7: Yücel [903]; 8: Zhong, Wang, and Lin [916]; 9: Abdelhamid, Mahmoud, and Hussein [4]; 10: Ju and Jung [484]; 11: Ghanaat et al. [334]; 12: Ghanaat, Patev, and Chudgar [332]; 13: Ghanaat, Patev, and Chudgar [333]; 14: Kadkhodayan, Aghajanzadeh, and Mirzabozorg [486]; 15: Hariri-Ardebili, Saouma, and Porter [388]; 16: Hariri-Ardebili and Saouma [386]; 17: Hariri-Ardebili and Saouma [384]; 18: Hariri-Ardebili and Saouma [385]; 19: Bernier et al. [119]; 20: Bernier, Monteiro, and Paultre [118]; 21: Ansari and Agarwal [35]; 22: Ansari, Saqib, and Agarwal [36]; 23: Morales-Torres et al. [606]; 24: Yazdani and Alembagheri [899]; 25: Pang et al. [677]; 26: Alembagheri [22]; 27: Hariri-Ardebili and Saouma [396]; 28: Wang et al. [868]; 29: Hariri-Ardebili, Seyed-Kolbadi, and Noori [397].

30.5.1 Case Study Dam

Pine Flat gravity dam is selected as the case study in this paper. The finite element code EAGD [302] is used to perform linear transient analyses. Applied loads on the system are: 1) self-weight, 2) hydrostatic pressure, and 3) seismic loads (both in horizontal and vertical directions). The objective is to develop a meta-model for material and ground motion uncertainty. Two series of separate simulations are performed:

- **Material uncertainty**: This is addressed though a series of design of experiments (DOE) models in conjunction with MCS technique. Originally, nine properties are affecting the seismic response of the gravity dam on flexible foundation with reservoir water interaction [303]. They are listed in Table 30.6 along with their mean values (corresponds to coded "0" factor in DOE).
- **Seismic uncertainty**: This is briefly addressed through ground motion record-to-record variability.

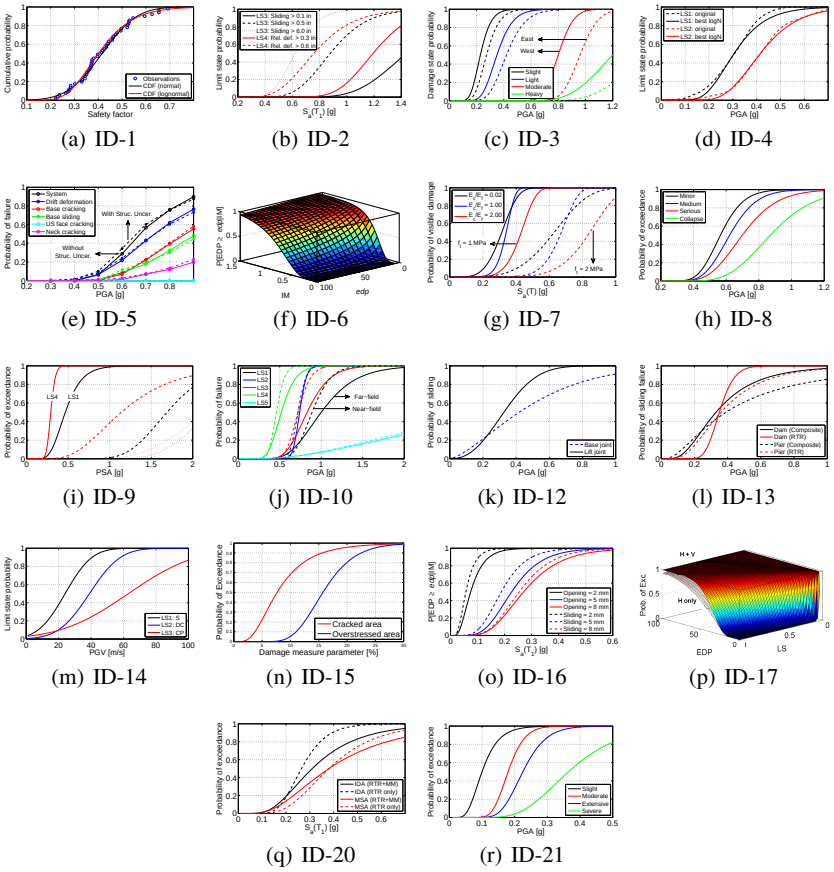

(a) ID-1 (b) ID-2 (c) ID-3 (d) ID-4

(e) ID-5 (f) ID-6 (g) ID-7 (h) ID-8

(i) ID-9 (j) ID-10 (k) ID-12 (l) ID-13

(m) ID-14 (n) ID-15 (o) ID-16 (p) ID-17

(q) ID-20 (r) ID-21

Fig. 30.18: Samples of seismic fragility curves and surfaces for concrete dams

30.5.2 Material Uncertainty Quantification

Four major techniques are studied for material uncertainty quantification (UQ):

- Pseudo-random sequences: CMCS and LHS.
- Quasi-random sequences: Halton and Sobol.

For CMCS $N_{sim} = 100,000$, and for the three others (i.e., LHS, Sobol and Halton) $N_{sim} = 1,000$ samples are drawn. Figure 30.19(a) presents the dependency of the mean and 95% confidence intervals of CMCS to the sample size. In this technique, the displacement response reaches relative stability after about 20,000 simulations. On the other hand, LHS, Sobol and Halton show acceptable stability with 1,000 simulations, Figure 30.19(b). Moreover, Figure 30.19(c) compares the four techniques in terms of median of the response, interquartile (25% to 75%) range, and the outliers.

Table 30.6: Material properties and modeling parameters

Quantity	Symbol	Unit	DA	DOE		UQ		
			Mean (0)	L (-1)	U (+1)	Model	COV	Truncation
Concrete modulus of elasticity	E_c	MPa	23,950	21,550	26,330	Normal	0.10	[19,100 28,800]
Concrete Poisson's ratio	ν_c	-	0.2	-	-	-	-	-
Concrete mass density	ρ_c	kg/m^3	2,470	-	-	-	-	-
Concrete constant hysteretic damping	η_c	-	0.06	0.02	0.10	Normal	0.33	[0.02 0.10]
Foundation modulus of elasticity	E_f	MPa	21,550	19,150	23,950	Normal	0.10	[17,700 25,400]
Foundation Poisson's ratio	ν_f	-	0.33	-	-	-	-	-
Foundation mass density	ρ_f	kg/m^3	2,680	-	-	-	-	-
Foundation constant hysteretic damping	η_f	-	0.05	0.03	0.07	Normal	0.40	[0.02 0.08]
Wave reflection coefficient for the reservoir bottom materials	α	-	0.50	0.25	0.75	Normal	0.50	[0.05 0.95]

DA: Deterministic Analysis UQ: Uncertainty Quantification
COV: Coefficient of Variation

In all cases, the median and interquartile range are nearly identical, while CMCS has more outliers.

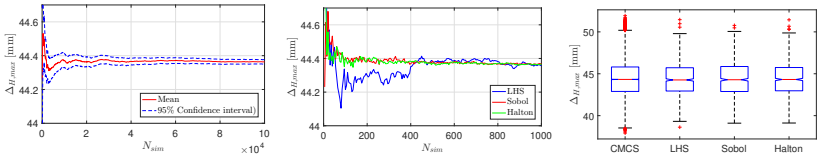

(a) CMCS technique (b) Refined techniques (c) Median and interquartile range

Fig. 30.19: Comparison of convergence rate and statistics of four UQ techniques

30.5.3 Meta-Model for Material Uncertainty

Five RVs (i.e., E_c, η_c, E_f, η_f and α) are used in DOE. Following is the step-by-step procedure to implement a DOE and evaluate its accuracy:

1. Select a DOE technique from Section 20.3.
2. Develop the DOE "coded" table. Since $k = 5$, these tables are developed and reported in Hariri-Ardebili [390].
3. Map the material properties of five RVs based on these tables, Equation (20.3). Keep the other parameters at their mean value.
4. Perform N_{DOE} analyses and record the required outputs, $\mathbf{Y}$.

5. Develop the $\mathbf{Z}$ matrix. Note that a quadratic polynomial is going to be used in this paper with all interacting terms. It means that $m = 21$, Table 20.1. This requires that $N_{DOE} > 21$.
   For those DOE techniques in which $11 < N_{DOE} < 21$, the interaction terms are neglected and thus, $m = 2 \times k + 1 = 11$. For those DOE techniques in which $6 < N_{DOE} < 11$, the second-order terms are also neglected and thus, $m = k + 1 = 6$.
6. Estimate β from Equation 20.7. An alternative and efficient method in MATLAB [580] is $\beta = \texttt{mldivide}(\mathbf{Z}, \mathbf{Y})$.
7. Use one of the UQ methods (CMCS with 100,000 samples or LHS, Sobol, Halton with 1,000 samples) and β from previous step to estimate the response parameter, Equation 20.6. Note that the error term is neglected. Hereafter, these DOE-estimated values are refereed to $\mathbf{Y}_{DOE}$.
8. Compare $\mathbf{Y}_{DOE}$ with those already calculated from FEM, $\mathbf{Y}_{FEM}$. Evaluate GOF based on Section 20.4.2.

Figure 30.19 compares three techniques of DOE with FEM. Each sub-plot includes 100,000 samples directly from FEM-CMCS *vs.* DOE along with the equity line. Shown in these plots are estimated β_i values (21 for full case, 11 for models without interaction, and 6 for those with only first-order terms).
Figures 30.20(a) and 30.20(b) are based on FFD with three-levels. It requires a total of $N_{DOE} = 243$ simulations and is the most high-demanding technique among the others. Accuracy of prediction is excellent and all 21 coefficients of the linear regression model are obtained. Intercept, β_0, is very large compared to other coefficients.
Figures 30.20(c) and 30.20(d) are based on SED techniques with only 11 simulations. The interaction coefficients do not exist. Displacement points have a crescent-type distribution, while stress points have a propeller-like pattern with minimum dispersion at the center of the distribution and larger towards the tails.
Figures 30.20(e) and 30.20(f) are developed based on fractional factorial design with one-half of the two-level FFD model. They don't have second-order and interaction coefficients. They provide a relatively poor estimation of the responses compared to others.

30.5.4 Meta-Model for Ground motion Uncertainty

PSHA of the dam site is performed using *OpenSHA Hazard Curve Calculator (local)* (www.opensha.org). A total of 340 records are selected and used in dynamic analysis according to cloud analysis technique [468]. Nine ground motion IM parameters are extracted for each record. They are chosen since they reflect the peak intensity in time and frequency domain as well as the time- and frequency-dependent cumulative intensities of the applied signals.
Next, these nine IMs are used to develop a response surface meta-model which accounts for the ground motion uncertainties. Again, a quadratic form is adopted for the polynomial including the interaction terms. Having $k = 9$ IM parameters, the minimum number of required simulations can be obtained as $m = 55$ using Table

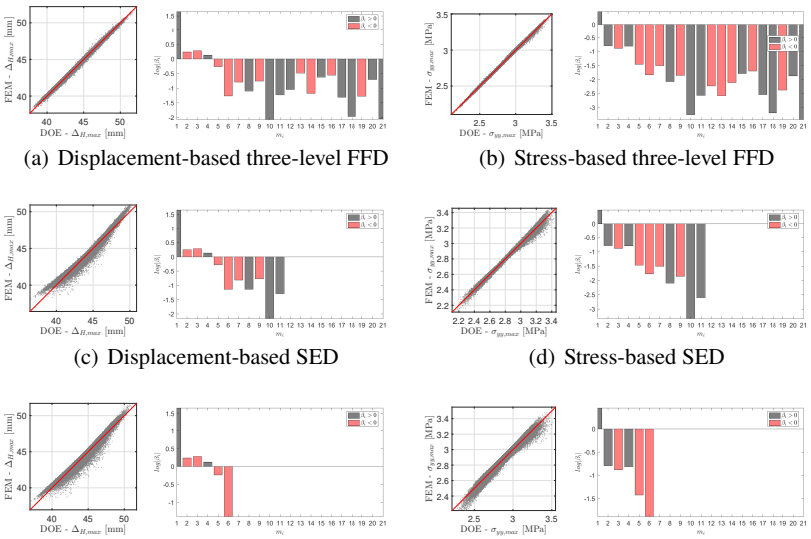

(a) Displacement-based three-level FFD (b) Stress-based three-level FFD

(c) Displacement-based SED (d) Stress-based SED

(e) Displacement-based one-half FeFD (f) Stress-based one-half FeFD

Fig. 30.19: Comparing CMCS-based seismic analyses results computed from FEM and estimated from DOE

20.1. Subsequently, a polynomial meta-model with $m = 55$ terms is developed based on Eq. 20.5. For the ground motion uncertainty quantification, the polynomial takes the following form:

$$\begin{aligned}\hat{y}^{GM}_{quad} = {} & \beta_1 + \beta_2(PGA) + \beta_3(PGV) + \beta_4(S_a(T_1)) + \beta_5(S_v(T_1)) + \beta_6(a_{RMS}) + \beta_7(v_{RMS}) \\ & + \beta_8(ASI) + \beta_9(VSI) + \beta_{10}(I_A) + \beta_{11}(PGA)^2 + \beta_{12}(PGV)^2 + \beta_{13}(S_a(T_1))^2 \\ & + \beta_{14}(S_v(T_1))^2 + \beta_{15}(a_{RMS})^2 + \beta_{16}(v_{RMS})^2 + \beta_{17}(ASI)^2 + \beta_{18}(VSI)^2 + \beta_{19}(I_A)^2 \\ & + \beta_{20}(PGA)(PGV) + \beta_{21}(PGA)(S_a(T_1)) + \beta_{22}(PGA)(S_v(T_1)) + \beta_{23}(PGA)(a_{RMS}) \\ & + \beta_{24}(PGA)(v_{RMS}) + \beta_{25}(PGA)(ASI) + \beta_{26}(PGA)(VSI) + \beta_{27}(PGA)(I_A) \\ & + \beta_{28}(PGV)(S_a(T_1)) + \beta_{29}(PGV)(S_v(T_1)) + \beta_{30}(PGV)(a_{RMS}) + \beta_{31}(PGV)(v_{RMS}) \\ & + \beta_{32}(PGV)(ASI) + \beta_{33}(PGV)(VSI) + \beta_{34}(PGV)(I_A) + \beta_{35}(S_a(T_1))(S_v(T_1)) \\ & + \beta_{36}(S_a(T_1))(a_{RMS}) + \beta_{37}(S_a(T_1))(v_{RMS}) + \beta_{38}(S_a(T_1))(ASI) + \beta_{39}(S_a(T_1))(VSI) \\ & + \beta_{40}(S_a(T_1))(I_A) + \beta_{41}(S_v(T_1))(a_{RMS}) + \beta_{42}(S_v(T_1))(v_{RMS}) + \beta_{43}(S_v(T_1))(ASI) \\ & + \beta_{44}(S_v(T_1))(VSI) + \beta_{45}(S_v(T_1))(I_A) + \beta_{46}(a_{RMS})(v_{RMS}) + \beta_{47}(a_{RMS})(ASI) \\ & + \beta_{48}(a_{RMS})(VSI) + \beta_{49}(a_{RMS})(I_A) + \beta_{50}(v_{RMS})(ASI) + \beta_{51}(v_{RMS})(VSI) \\ & + \beta_{52}(v_{RMS})(I_A)\beta_{53}(ASI)(VSI) + \beta_{54}(ASI)(I_A) + \beta_{55}(VSI)(I_A)\end{aligned} \tag{30.1}$$

The estimated β_i values in Equation 30.1 for displacement are shown in Figure 30.20. As seen, all the single and combined IM parameters incorporate in overall response of the dam. In addition, most of the β_i coefficients exhibit similar trends and relative magnitudes.

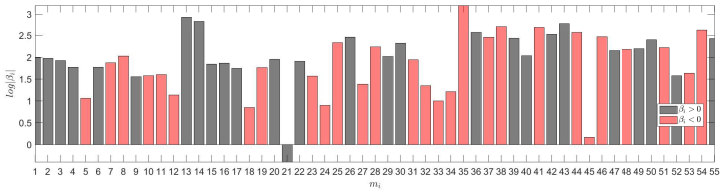

Fig. 30.20: Estimation of 55 polynomial coefficients to develop a meta-model for seismic uncertainty

30.6 Response Surface Meta-Model for a Nonlinear Arch Dam

This section which is adapted from Hariri-Ardebili, Seyed-Kolbadi, and Noori [397] presents the concept of response surface meta-model for nonlinear analysis of an arch dam with epistemic random variables. A second-order polynomial meta-model is developed and the associated fragility curves are built.

30.6.1 Case Study Dam

Dez double curvature arch dam is selected as the case study. The finite element model is identical to the one discussed in Section 29.4.1. Nonlinearity stems only from the concrete cracking (smeared crack model), and the contraction joints are not modeled in this study. This is to keep the number of overall variables in a reasonable range to perform the response surface meta-modeling.
Table 30.7 lists the material properties. Four of them are assumed to be RVs. A full correlation is assumed among the concrete tensile and compressive strength through a deterministic relationship $f'_t = 0.1 f'_c$.
The coupled system is excited with a 25 s ground motion record selected based on PSHA to match the maximum design level (MDL) of the site. Its PGA is about 0.4g.

30.6.2 Selection of DOE Model

Having four RVs, many of the DOE techniques in Section 20.3 can be adopted. For example, a two-level and three-level FFD require 16 and 81 simulations, respectively. However in the present study, the BBED technique is used which can capture the potential curvature of the response surface. Box and Behnken [143] determines the required number of simulations as:

- $k = 3$, $N_{DOE} = 12 + 1 = 13$
- $k = 4$, $N_{DOE} = 24 + 1 = 25$
- $k = 5$, $N_{DOE} = 40 + 1 = 41$
- $k = 6$, $N_{DOE} = 48 + 1 = 49$

Table 30.7: Material properties for the finite element model

Quantity	Symbol	Unit	DOE				UQ		
			Mean (0)	Variation	Lower (-1)	Upper (+1)	Model	COV	Truncation
Concrete modulus of elasticity	E_c	MPa	40,000	15%	34,000	46,000	Normal	0.08	[34,000 46,000]
Concrete Poisson's ratio	ν_c	-	0.2	-	-	-	-	-	-
Concrete mass density	ρ_c	kg/m^3	2,400	10%	2,160	2,640	Normal	0.06	[2,160 2,600]
Concrete compressive strength	f'_c	MPa	35.0	20%	28.0	42.0	Normal	0.10	[25.0 40.0]
Concrete tensile strength	f'_f	MPa	3.5	20%	2.8	4.2	Normal	0.10	[2.5 4.0]
Foundation modulus of elasticity	E_f	MPa	20,000	25%	15,000	25,000	Normal	0.10	[15,000 25,000]
Foundation Poisson's ratio	ν_f	-	0.25	-	-	-	-	-	-
Foundation mass density	ρ_f	kg/m^3	2,500	-	-	-	-	-	-
Water mass density	ρ_w	kg/m^3	1,000	-	-	-	-	-	-
Wave velocity in water	C_w	m/s	1,440	-	-	-	-	-	-
Wave reflection coefficient at the bottom	α_w	-	0.80	-	-	-	-	-	-
Sediment/silt mass density	ρ_s	kg/m^3	1,360	-	-	-	-	-	-

DOE: Design of Experiment UQ: Uncertainty Quantification COV: Coefficient of Variation

The BBED-based simulations can be presented in the form of Table 30.8. In this table, x_1 to x_4 correspond to E_c, ρ_c, f'_c, and E_f, respectively. The lower bound (-1), mean (0), and the upper bound (+1) for each RV can be found in Table 30.7.

Table 30.8: Tabulated simulations in a BBED with $k = 4$

Simulations	Coded values			
	x_1	x_2	x_3	x_4
1-4	± 1	± 1	0	0
5-8	± 1	0	± 1	0
9-12	± 1	0	0	± 1
13-16	0	± 1	± 1	0
17-20	0	± 1	0	± 1
21-24	0	0	± 1	± 1
25	0	0	0	0

30.6.3 Nonlinear Transient Analyses

Following the material combinations, 25 nonlinear transient analyses are performed. Results are extracted in terms of crest maximum horizontal displacement, cracking in three directions, and crushing. Except the displacement, the results are presented in term of the volumetric damage index, DI:

$$DI_{vol} = \frac{\text{Damaged volume}}{\text{Total volume}} \tag{30.2}$$

The solid elements in the present formulation may crack in three directions. Therefore, $DI_{vol}^{cr3} \subset DI_{vol}^{cr2} \subset DI_{vol}^{cr1}$. The raw results of BBED are presented in Table

30.9. Furthermore, Figure 30.21 shows the damage distribution results from first cracks on the upstream (US) face of the dam.

Table 30.9: Summary of the BBED simulations

Sim	E_c	ρ_c	f'_c	E_f	Δ^{sta}_{max} [mm]	Δ^{dyn}_{max} [mm]	DI^{cr1}_{vol}[%]	DI^{cr2}_{vol}[%]	DI^{cr3}_{vol}[%]	DI^{crush}_{vol}[%]
1	46	2640	35	20	19.7	117.6	17.6	6.3	3.2	0.1
2	46	2160	35	20	19.8	95.1	11.5	2.1	0.7	0.0
3	34	2640	35	20	25.4	168.7	14.2	5.8	3.7	0.3
4	34	2160	35	20	25.4	137.6	11.6	3.0	1.2	0.0
5	46	2400	42	20	19.8	99.5	8.4	1.0	0.3	0.0
6	46	2400	28	20	19.8	99.5	8.4	1.0	0.3	0.0
7	34	2400	42	20	25.4	141.6	8.9	1.3	0.3	0.0
8	34	2400	28	20	25.4	177.0	16.8	7.8	5.6	1.0
9	46	2400	35	25	19.0	98.2	13.5	3.3	1.3	0.0
10	46	2400	35	15	21.1	113.7	19.8	4.3	1.7	0.1
11	34	2400	35	25	24.7	146.8	12.3	4.4	1.9	0.0
12	34	2400	35	15	26.7	159.5	15.0	5.2	2.1	0.1
13	40	2640	42	20	22.1	130.2	0.8	0.0	0.0	0.0
14	40	2640	28	20	22.1	149.0	22.4	9.5	6.5	1.9
15	40	2160	42	20	22.2	108.8	5.5	0.3	0.1	0.0
16	40	2160	28	20	22.2	151.0	18.7	9.2	7.0	2.4
17	40	2640	35	25	21.4	133.0	14.4	5.8	2.7	0.0
18	40	2640	35	15	23.3	151.0	19.1	6.3	3.2	0.2
19	40	2160	35	25	21.4	109.1	10.2	1.9	0.8	0.0
20	40	2160	35	15	23.5	122.4	14.1	3.1	1.0	0.1
21	40	2400	42	25	21.4	114.8	7.8	1.3	0.4	0.0
22	40	2400	42	15	23.4	127.0	10.9	1.4	0.2	0.0
23	40	2400	28	25	21.4	145.0	17.4	8.4	5.9	1.3
24	40	2400	28	15	23.4	168.0	24.4	8.8	6.1	1.7
25	40	2400	35	20	22.2	126.3	14.7	4.5	1.9	0.0

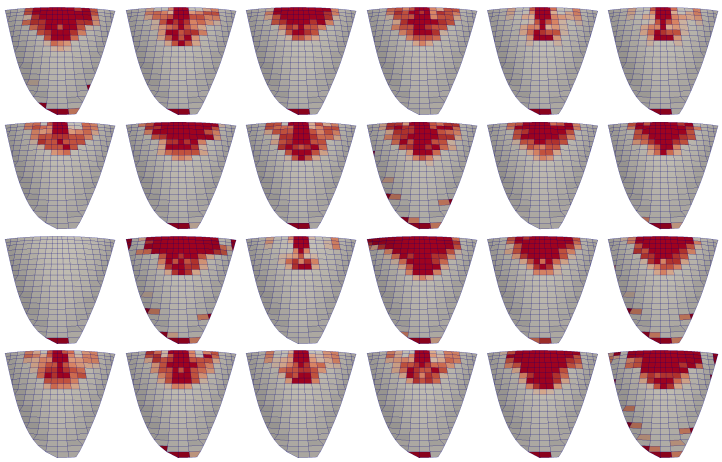

Fig. 30.21: Distribution of first crack on upstream face; top left: Sim-1; first row: 1 to 6; bottom right: Sim-24

30.6.4 Develop a Meta-Model

In order to derive a response surface meta-model, a second order polynomial including the interaction terms is used:

$$\begin{aligned} E\hat{D}P = \beta_1 + \beta_2 E_c + \beta_3 \rho_c + \beta_4 f_c' + \beta_5 E_f + \beta_6 E_c^2 + \beta_7 \rho_c^2 + \beta_8 f_c'^2 + \beta_9 E_f^2 \\ + \beta_{10} E_c \rho_c + \beta_{11} E_c f_c' + \beta_{12} E_c E_f + \beta_{13} \rho_c f_c' + \beta_{14} \rho_c E_f + \beta_{15} f_c' E_f \end{aligned} \tag{30.3}$$

where the hat sign represents the estimated EDP.
The meta-models are drived and validated with 250 independent analyses. The predicted β_i values are shown in Figure 30.22 (only displacement and first cracks). The probability of exceedance of response parameters are shown in the last column. The empirical cumulative distribution function (CDF) of the FEM and BBED are plotted, as well as the fitted curves using the lognormal (LN) distributional model.

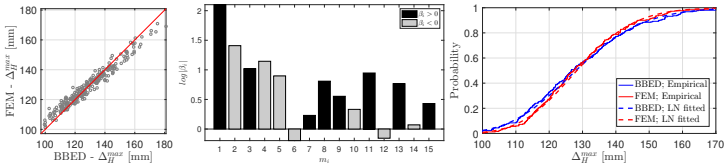

(a) Dynamic displacement

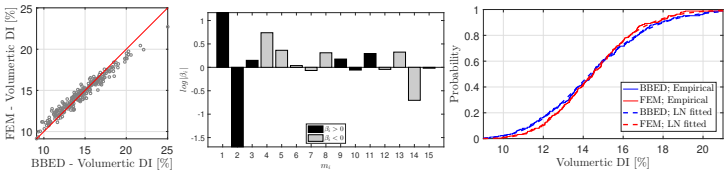

(b) First crack

Fig. 30.22: Validation of the predicted response surface using LHS method

30.7 Meta-Model based Reliability Analysis of a Gravity Dam

This section which is adapted from Hariri-Ardebili and Boodagh [379] presents the concept of meta-modeling based on the Taguchi design of experiments. Different Taguchi combinations are contrasted and applied to a gravity dam. Six RVs will be incorporated in the construction of the meta-models, and more than 40,000 seismic finite element simulations will be performed on the dam model. An optimal method is proposed to combine the aleatory and epistemic uncertainties. Finally, the ground motion-dependent (dynamic) sensitivity analysis is discussed.

30.7.1 Case Study Dam

Koyna Dam is selected as a vehicle for numerical simulations [124, 378]. The finite element code EAGD [302] is used to perform transient analyses. Applied loads on the system are: self-weight, hydrostatic pressure (water level is at 91.75 m), bottom sediment, and seismic loads (only the horizontal component). Six material properties are assumed to be RVs: modulus of elasticity, hysteretic damping, and mass density for both concrete and foundation rock. The properties and their ranges are similar (not identical) to those reported in Table 30.6. Taguchi DOE, Section 20.3.10, is used for meta-modeling in the context of polynomial response surface model.

30.7.2 Dynamic Sensitivity

A suite of 101 ground motions are selected based on PSHA [581] and a specific earthquake scenario $< M_w, R_{rup} >$ [69]. Since there are six RVs in the model, $2 \times 6 + 1 = 13$ finite element models are prepared and one reference model (see Section 18.1.2 for sensitivity analysis). Next, each of 13 finite element groups are subjected to 101 ground motions and the results are recorded (totally 1,313 dynamic simulations).
Figure 30.23 quantifies the impact of "dynamic sensitivity" on the finite element model. In each sub-plot the histogram of 101 simulations from lower bound material is compared to that from upper bound. Furthermore, a normal distribution is fitted in each case. The major findings are:

- The normalized pairs of <mean, STD> for 6 RVs based on the "reference" model can be summarized as:
  - Decreasing E_c increases the mean responses and STD.
  - Increasing ρ_c increases the mean responses but does not have an impact on the STD.
  - Increasing η_c decreases responses and STD.
  - Increasing E_f statistically has very small impact on decreasing the response. STDs are nearly identical.
  - Increasing ρ_f has nearly no impact on the mean and STD.
  - Increasing η_f decreases mean but does not have an impact on the STD.
- Among three material properties (i.e., E, ρ and η), E has the highest impact on the response and larger STD.
- Among the concrete material properties, E_c and ρ_c have highest impact.
- Among the foundation material properties, E_f has highest impact on distribution of responses but not on the mean response.
- Impact of ρ_f might be neglected in probabilistic dynamic analyses.

30.7.3 Reliability Assessment

The application on Taguchi design in seismic reliability assessment of dams is discussed in this section. Figure 30.24 proposes a methodology to perform a cost-

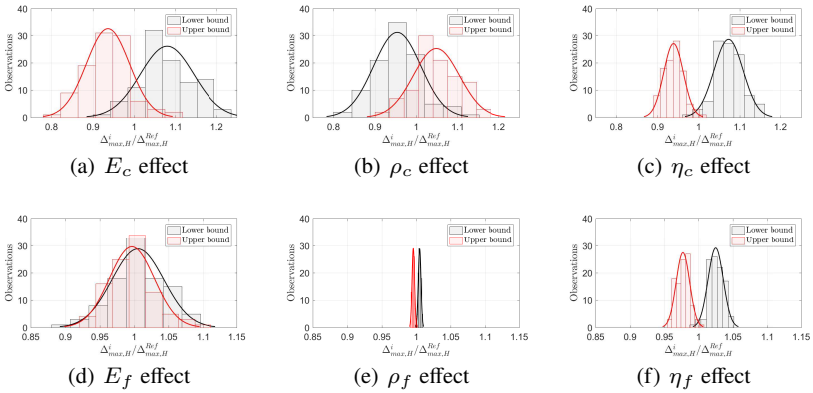

(a) E_c effect (b) ρ_c effect (c) η_c effect

(d) E_f effect (e) ρ_f effect (f) η_f effect

Fig. 30.23: Dynamic sensitivity of material RVs

effective seismic reliability assessment for large systems. The major steps can be summarized as:

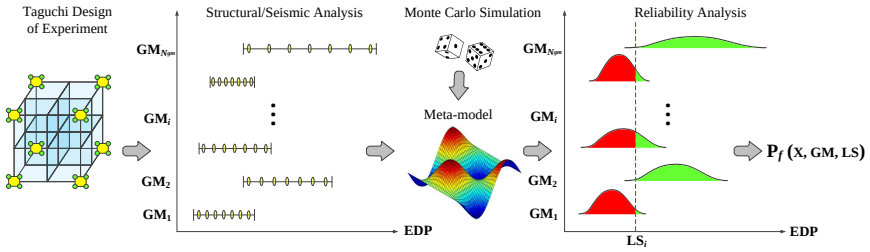

Fig. 30.24: Proposed Taguchi based meta-modeling for seismic reliability analysis

- Select N_{RV} basic RVs for material properties.
- Select an appropriate DOE (Taguchi in this study) with N_{DOE} simulations.
- Select a suite of N_{gm} ground motions based on PSHA. In the context of PBEE, one may use 1) intensity-based, 2) scenario-based, or 3) time-based performance assessment [41] (see Figure 21.7).
- Perform a total of $N_{DOE} \times N_{gm}$ seismic analyses using "Cloud" analysis technique (See Section 24.3.9).
- Develop N_{gm} meta-models (i.e. one meta-model for each of the N_{gm} ground motions) based on the recommendations in Section 20.3.10.
- Perform the following tasks for each of N_{gm} ground motions:

- Perform $N_\infty \sim 10e6$ MCS on each meta-model. Note that from now on, all the operations will be on the meta-model and not the initial FEM. Alternatively, use LHS, Sobol or Halton with a smaller number of samples.
- Extract the required outputs.
- Develop and fit an appropriate distributional model (e.g. normal or lognormal) for N_∞ data points for each meta-model.
- Determine the ith limit state, LS_i, of the problem. Different types of LS functions can be found in Tekie and Ellingwood [825], Lupoi and Callari [549], and Hariri-Ardebili and Saouma [383].
- Compute the individual probability of failure (or probability of exceeding any specific LS) by conditional assessment of the responses from a particular ground motion j and all range of material uncertainty:

$$P_{f_i}^{j} = f\left(\boldsymbol{X}, GM_j, LS_i\right) \tag{30.4}$$

- Compute the total failure probability of the system. The selected ground motion sets are assumed to be mutually exclusive events. Since all the ground motions are equally weighted, the total failure probability for a particular LS will be:

$$P_{f_i} = f\left(\boldsymbol{X}, \boldsymbol{GM}, LS_i\right) = \sum_{j=1}^{N_{gm}} \frac{1}{N_{gm}} P_{f_i}^{j} \tag{30.5}$$

- All the above mentioned procedure should be repeated for the next limit state, LS_{i+1}.
- Finally, the generalized reliability index can be computed using

$$\beta_{\text{GRI}} = \Phi^{-1}\left(1 - \hat{P}_f\right) \tag{30.6}$$

where $\Phi(.)$ is the standard normal cumulative distribution function (CDF).

Figure 30.25(a) shows the impact of four sample ground motions on the displacement response and their statistics. Figure 30.25(b) shows the cumulative CDF of all 101 ground motions which is presented as probability of exceedance of any specific LS. Three LSs are selected in this paper. LS_2 is adopted from Hariri-Ardebili and Saouma [383] which is based on using $\simeq 0.1\%$ of total dam height as "drift ratio." Note that similar values of 0.188% and 0.088% have been reported by Ellingwood and Tekie [266] and Zhong et al. [915], respectively. The other two LSs are simply assumed to be $\simeq 0.05\%$ and $\simeq 0.2\%$ of the dam height, respectively. Based on the calculations, the probability of exceedance of three LSs are 31.2%, 10.6%, and 3.9%. If the value and number of LSs are not known *priori*, it is possible to perform an iterative procedure and compute the probability of exceedance (and consequently the reliability index) for a wide range of LS values. Such a plot is shown in Figure 30.25(c).

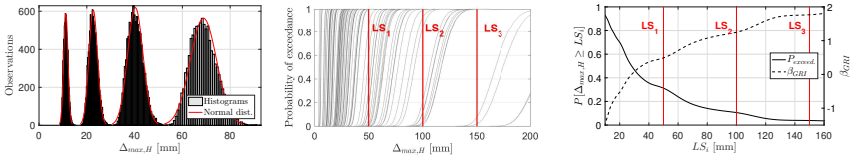

(a) Sample ground motion effect on the responses (b) Probability of exceedance of all ground motions (c) Conditional probability of exceedance and reliability index

Fig. 30.25: Seismic reliability assessment of the cases study example including material uncertainties

30.8 Fracture Mechanics based Reliability Analysis of a Gravity Dam

This section which is adapted from Saouma [752] reports a reliability based safety assessment of a dam which has been targeted for major rehabilitation. This dam was built in the thirties and based on recent hydrological data can no longer sustain its probable maximum flood. The approach considered is one based on fracture mechanics. Two reliability analysis methods (point estimate method and Taylor's Series-Finite Difference Estimation) are applied and compared to each other.

30.8.1 Dam Description

The dam, built in the thirties, is 176 ft high, has 53 monoliths, and a crest elevation of 1,535 ft, Figure 30.26(a). Based on recent hydrologic studies, it was determined (using classical analysis) that the Probable Maximum Flood (PMF) elevation is at 1,555.8 ft. However, its computed Imminent Failure Flood (IFF), which is the pool elevation which would trigger failure (through failure of the rock concrete interface and ensuing sliding), is at 1,533 ft or 22 ft below the PMF. Hence, this dam has been targeted for major rehabilitation. Whereas numerous remediation schemes have been investigated, the one retained for this study entails pre-stressing the dam from crest to foundation using high-strength steel anchors and mass concrete thrust blocks to be added at the toe of the dam, Figure 30.26(b).

A two-dimensional analysis (justified by the U shape of the valley) focuses on monolith 12 which was recognized as the most critical one. The performance function (limit state) is based on sliding safety factor (SSF):

$$\text{SSF} = \frac{\text{Capacity}}{\text{Demand}} = \frac{\sum F_V \tan\phi + cL_{uncr}}{\sum F_H} \tag{30.7}$$

where ϕ, c, and L_{uncr} are the friction angle, the cohesion, and the length of the un-cracked ligament respectively. The "Demand" is governed by the PMF (which is considered as a constant). Hence we seek $P[Z = C/D \leq 1]$ or $P[Z = SSF - 1 \leq 0]$.

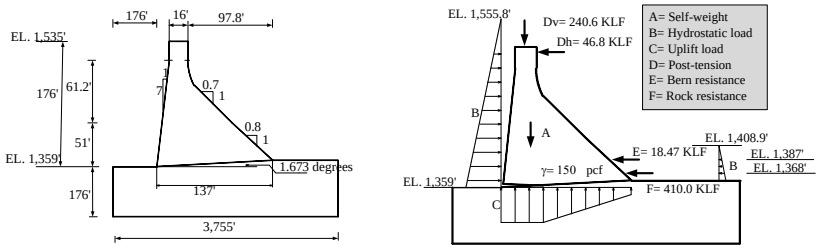

(a) Dam dimensions (b) Proposed Retrofit

Fig. 30.26: Case study dam for reliability analysis and rehabilitation

30.8.2 Analysis

A nonlinear analysis using the fictitious crack model described in Section 15.3 is performed. The preliminary one is not reported as it was clearly unsafe ($\beta < 1$); only details of the nonlinear analysis of the retrofitted one is presented. The assumed constants are: density of concrete and elastic moduli, whereas the assumed variables are four: a) the pool elevation μ = 1,532.5 ft, σ = 5 ft, b) the fracture energy G_F^I μ = 0.35 lbs/in, σ = 0.1 lbs/in, c) cohesion c μ = 42 psi, σ = 5 psi, and d) angle of friction μ = 51°, σ = 5°. In this analysis, the tensile strength is determined from the cohesion c and angle of friction ϕ

$$\sigma_t = \frac{2c}{\cos\phi_f + \tan\phi_f(1+\sin\phi_f)} \tag{30.8}$$

and the mode II fracture energy G_F^{II} is set to three times the mode I fracture energy G_F^I. Since this investigation was completed, there has been new evidence that the ratio should be closer to ten than to three.

30.8.2.1 Point Estimate Method

For this first method, $2^4 = 16$ analyses were performed with results tabulated in Table 30.10, where h is the pool elevation and L_c the cracked ligament length. Two sets of SSF were determined. In the first, it is based on global rigid body equilibrium, and in the other it is determined from a weighted average of values computed at each interface element.

As anticipated, both β values are in the acceptable range, however the one associated with the more accurate element-wise evaluation of SSF (6.62) is higher than the other (3.04). This discrepancy results from the simplifying (and conservative) assumption that the shear stress is constant along the base.

	Variables											Global		Pointwise	
	1	2	3		4										
ID	h ft.	c psi	ϕ deg.	σ_t psi	G_F^I lbs/in	G_F^{II} lbs/in	L_c ft.	$\sum V$ kips	Uplift kips	$\sum H$ kips	Capacity kips	SSF	ln SSF	SSF'	ln SSF'
μ	196.8	42.	51.	29.7	0.35	1.05									
σ	5.	0.5	5.		0.1										
1	**201.8**	**42.5**	**56.**	*26.0*	**0.45**	*1.35*	69.3	-72.4	109.0	55.7	141.8	2.55	0.935	3.56	1.269
2	**201.8**	**42.5**	**56.**	*26.0*	0.25	*0.75*	80.5	-85.7	114.8	73.5	155.7	2.12	0.752	3.48	1.248
3	**201.8**	**42.5**	46.	*34.3*	**0.45**	*1.35*	54.2	-94.1	102.2	64.1	139.6	2.18	0.779	3.65	1.295
4	**201.8**	**42.5**	46.	*34.3*	0.25	*0.75*	52.4	-128.3	100.1	95.4	176.0	1.85	0.613	3.24	1.177
5	**201.8**	41.5	**56.**	*25.4*	**0.45**	*1.35*	59.9	-80.8	103.3	60.8	158.2	3.11	1.135	4.09	1.409
6	**201.8**	41.5	**56.**	*25.4*	0.25	*0.75*	39.2	-108.6	95.4	65.2	209.6	3.21	1.167	4.30	1.458
7	**201.8**	41.5	46.	*33.5*	**0.45**	*1.35*	80.5	-149.9	114.1	135.8	183.3	1.35	0.300	2.73	1.005
8	**201.8**	41.5	46,	*33.5*	0.25	*0.75*	84.3	-69.3	116.1	50.8	97.9	1.93	0.656	2.61	0.960
9	191.8	**42.5**	**56.**	*26.0*	**0.45**	*1.35*	24.2	-98.8	83.1	48.1	204.0	4.25	1.446	4.96	1.601
10	191.8	**42.5**	**56.**	*26.0*	0.25	*0.75*	27.9	-96.8	82.2	50.8	199.0	3.92	1.366	5.09	1.627
11	191.8	**42.5**	46.	*34.3*	**0.45**	*1.35*	10.4	-110.7	73.5	46.1	179.1	3.89	1.358	4.55	1.515
12	191.8	**42.5**	46.	*34.3*	0.25	*0.75*	10.4	-110.8	73.5	45.9	179.2	3.90	1.361	4.55	1.514
13	191.8	41.5	**56.**	*25.4*	**0.45**	*1.35*	29.8	-97.3	83.2	49.5	197.5	3.99	1.384	5.29	1.665
14	191.8	41.5	**56.**	*25.4*	0.25	*0.75*	16.7	-104	3	78	214.6	4.82	1,572	5.17	1.643
15	191.8	41.5	46.	*35.5*	**0.45**	*1.35*	27.9	-95.4	82.2	48.1	153.1	3.19	1.159	4.10	1.412
16	191.8	41.5	46	*33.5*	0.25	*0.75*	41.1	-89.8	89.5	51.3	140.8	2.74	1.008	3.77	1.328
											$\mu_{\ln(C/D)}$	-	**1.062**	-	**1.383**
											$\sigma_{\ln(C/D)}$	-	**0.349**	-	**0.209**
											β	-	**3.04**	-	**6.62**

Note: $f_t' = \frac{2c}{\cos\phi + \tan\phi(1+\sin\phi)}$; $G_F^{II} = 3G_F^I$

Table 30.10: Tabulation of Point Estimate Method; Nonlinear Analysis; Retrofitted Dam.

30.8.2.2 Taylor's Series-Finite Difference Estimation

For this second method, $2 \times 4 = 8$ analyses were performed. As in the previous case, two sets of SSF are computed. Results are tabulated in Table 30.11.

		Variables											Global		Pointwise	
		1	2	3		4										
ID		h ft.	c psi	ϕ deg.	f_t' psi	G_F^I lbs/in	G_F^{II} lbs/in	L_c ft.	$\sum V$ kips	Uplift kips	$\sum H$ kips	Capacity Kips	SSF A	B	SSF' A	B
	μ	196.8	42.	51.	29.7	0.35	1.05									
	σ	5.	0.5	5.		0.1										
0	**	196.8	42.0	*51.*	29.7	0.35	*1.05*	14.6	-109.7	77.5	46.7	197.1	**4.22**		**4.78**	
1	F_h^+	**201.8**	42.0	51.	29.7	0.35	*1.05*	14.6	-110.9	79.5	49.7	198.7	4.00		4.51	
2	F_h^-	**191.8**	42.0	51.	29.7	0.35	*1.05*	14.6	-107.7	75.6	44.8	194.7	4.35	.175	4.95	.22
3	F_c^+	196.8	**42.5**	51.	30.1	0.35	*1.05*	29.8	-99.6	85.3	47.6	177.6	3.73		4.66	
4	F_c^-	196.8	**41.5**	51.	29.4	0.35	*1,05*	44.9	-92.8	93.0	58.8	160.5	2.73	.5	3.99	.33
5	F_ϕ^+	196.8	42.0	**56.**	25.7	0.35	*1.05*	26.1	-104.3	83.4	53.2	210.5	3.96		5.32	
6	F_ϕ^-	196.8	42.0	**46.**	33.9	0.35	*1.05*	12.5	-109.7	77.3	47.7	176.3	3.70	.13	4.01	.65
7	$F_{G_F^I}^+$	196.8	42.0	51.	29.7	**0.45**	*1.35*	18.5	-105.8	79.6	48.5	190.3	3.92		4.79	
8	$F_{G_F^I}^-$	196.8	42.0	51.	29.7	**0.25**	*0.75*	18.5	-108.2	79.6	50.1	193.3	3.86	.03	4.82	.015
												$\boldsymbol{\sigma}_{(C/D)}$	-	**.835**	-	**1.215**
												β	-	**7.2**	-	**6.1**

A: $|\frac{F_i^+ - F_i^-}{2}|$
B: $\sigma_{(C/D)}$

Table 30.11: Tabulation of Taylor's Series Finite Difference Estimate Method; Nonlinear Analysis; Retrofitted Dam.

For the first case, we have $\mu_{C/D}$= 4.22 and $\sigma_{C/D} = 0.835$. Substituting in Eq. 18.13, this results in $\beta = 7.2$ which is indicative of a very safe structure. In terms of sensitivity, results are most sensitive to pool elevation, cohesion, angle of friction, and fracture energy (in this order).
For the second case, we have $\mu_{C/D}$= 4.78 and $\sigma_{C/D} = 1.215$. Substituting in Eq. 18.13, this results in $\beta = 6.1$. Not so surprisingly, this analysis shows that the safety is most sensitive to the angle of friction, cohesion, pool elevation, and finally fracture energy. The change in relative importance is attributed to the fact that the SSF is determined point-wise along the base.
When compared with the point estimate method, there is a large discrepancy in β when the calculations are based on SSF (7.2 versus 3.04), but a smaller one for those based on SSF' (6.1 versus 6.62). Clearly, this discrepancy is indicative of some limitations of the reliability of the methods. Indeed misleading or erroneous results can be obtained when dealing with probabilities of rare events or when the failure design space is not sufficiently represented (as in this case). Nevertheless in all cases, we have evidence of a very safe structure.

30.9 Classical Reliability Analysis of a Gravity Dam with LEM

This section which is adapted from Hariri-Ardebili and Pourkamali-Anaraki [395] investigates the classical reliability analysis of a typical gravity dam and is explained based on limit equilibrium method (LEM). In this method, the dam is assumed to be a rigid body and the loads are applied in a static fashion. Thus, only the magnitude and the moment arm of the resultant loads are important. Several classical reliability analysis methods such as FORM, SORM, crude MCS, importance sampling, and LHS are compared.

30.9.1 Case Study Dam

The applied loads are: 1) self-weight, 2) static uplift pressure, 3) hydrostatic (based on normal or flood water levels) pressure, 4) silt pressure, 5) ice pressure, 6) wind load, and 7) surface wave load. The uplift pressure is shown in detail in Figure 30.27. Furthermore, Table 30.12 shows the parameters considered in this analytical showcase and their distributional models. Sliding at the dam-foundation interface is considered to be the explicit LS function.

30.9.2 Classical Reliability Methods

All the classical reliability analysis techniques in Section 18.3 are implemented which include FORM, SORM, crude MCS, MCS-LHS, MCS-IS. Table 30.13 shows the failure probability and reliability index obtained from classical methods. As seen, all the methods provide a good estimation of the failure probability (compared to the reference method: crude MCS). FORM and SORM overestimate P_f; however, the

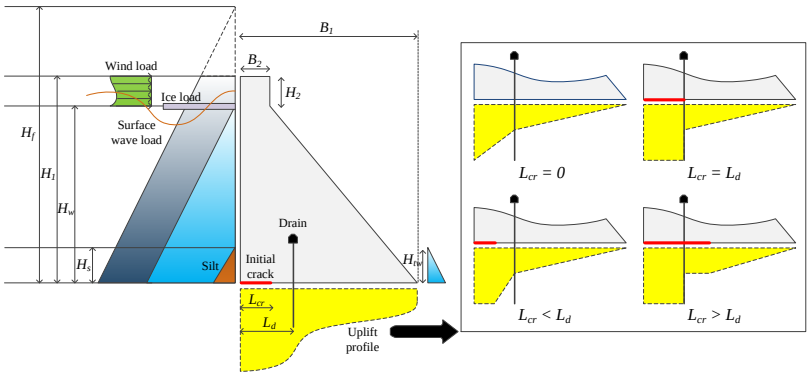

Fig. 30.27: LEM based model description (loads and geometry)

Table 30.12: Parameters considered for the LEM analytical limit state function

Parameter	Symbol	Unit	Distributional model	Quantity	Bound
Width at the base	B_1	m	-	60	-
Width at the crest	B_2	m	-	5	-
Height of the dam	H_1	m	-	80	-
Height of the neck	H_2	m	-	5	-
Location of drainage	L_d	m	Uniform	$U(5, 15)$	-
Pre-existing crack at the base	L_{cr}	m	Lognormal	$LN(13, 0.4)$	(0, 30)
Pre-existing crack at the neck	L_{cr}^n	m	Lognormal	$LN(0.5, 0.4)$	(0, 1)
Height of the water	H_w	m	Lognormal	$LN(67, 18)$	(30, 100)
Height of the silt layer	H_s	m	Normal	$N(10, 7)$	(1, 30)
Height of the surface wave	H_{sw}	m	Normal	$N(1, 0.5)$	(0.1, 2)
Concrete mass density	ρ_c	kg/m^3	Normal	$N(2400, 100)$	(2200, 2600)
Water mass density	ρ_w	kg/m^3	-	1000	-
Silt mass density	ρ_s	kg/m^3	Normal	$N(1850, 50)$	(1750, 2000)
Rock-concrete cohesion	c_{rc}	MPa	Lognormal	$LN(0.62, 0.17)$	(0.2, 2)
Rock-concrete friction angle	ϕ_{rc}	deg.	Normal	$N(30, 7)$	(15, 45)
Concrete-concrete cohesion	c_{cc}	MPa	Lognormal	$LN(0.71, 0.13)$	(0.5, 2)
Concrete-concrete friction angle	ϕ_{cc}	deg.	Normal	$N(34, 6)$	(20, 45)
Drain efficiency	eff_D	-	Uniform	$U(0.01, 0.99)$	-
Silt internal friction angle	ϕ_s	deg.	Normal	$N(30, 8)$	(15, 45)
Wind pressure	P_{wind}	Pa	Uniform	$U(100, 150)$	-
Ice pressure	P_{ice}	Pa	Normal	$N(300, 150)$	(100, 1500)
Ice thickness	t_{ice}	m	Normal	$N(0.4, 0.3)$	(0.01, 1)

reliability indices are only 4.9% and 1.9% less than crude MCS, respectively. All three simulation-based methods lead to nearly identical results; however, the number of required simulations, N_{sim}, for the crude MCS, MCS-LHS, and MCS-IS decreases from 1e6 to 1e5 and 1e4, respectively. Figure 30.28 compares the convergence of these three methods. In each plot, the failure probability and the confidence intervals are shown versus the number of simulations. Based on this figure, MCS-LHS and MCS-IS reach enough stability even with 50,000 and 5,000 simulations, respectively. It is also possible to calculate the local sensitivity of the parameters. Based on the FORM results, the following RVs contribute 99.99% of the total results: 1) $H_w =$

Table 30.13: Comparison of classical reliability methods

Method	FORM	SORM	Crude MCS	MCS-LHS	MCS-IS
Failure probability (P_f)	2.27e-2	1.95e-2	1.77e-2	1.78e-2	1.79e-2
Reliability index (β)	2.000	2.065	2.104	2.102	2.099
$Err(\%) = \frac{\beta - \beta_{\text{MCS}}}{\beta_{\text{MCS}}} \times 100\%$	-4.9%	-1.9%	0.0	-0.1%	-0.2%

56.55%; 2) $c_{rc} = 14.03\%$; 3) $L_{cr} = 12.84\%$; 4) $\phi_{rc} = 10.51\%$; 5) $\text{eff}_D = 5.37\%$; 6) $\rho_c = 0.51\%$; 7) $L_d = 0.10\%$; 8) $H_s = 0.08\%$; and other RVs nearly zero.

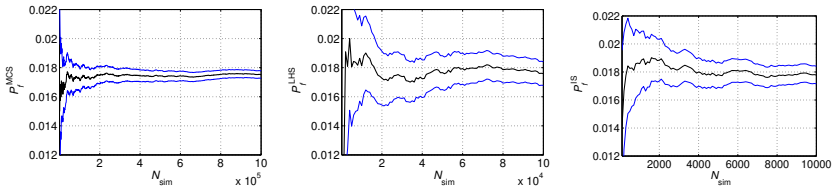

(a) Crude MCS; $N_{\text{sim}} = 1e6$ (b) MCS-LHS; $N_{\text{sim}} = 1e5$ (c) MCS-IS; $N_{\text{sim}} = 1e4$

Fig. 30.28: Estimated failure probability and the confidence intervals for three simulation-based methods; full analytical model

30.9.3 Reduced Model Reliability

Section 30.9.2 presented the results of the classical reliability for a full analytical model. However for most of the existing dams, part of the parameters introduced as RV are already known (e.g., location of drainage, mass density, etc). Thus, it is possible to reduce the dimension of the uncertainty in the problem to only "sensitive unknown" RVs. Thus, only three parameters are assumed to be RVs: c_{rc}, ϕ_{rc}, and H_w (others are kept constant).

Furthermore, the impact of correlation between the two RVs (e.g., c_{rc} and ϕ_{rc}) is investigated on the failure probability. Figure 30.29(a) shows the sampling pattern of the two RVs with different correlation coefficients, ρ_{1-2} (note that both RVs are truncated, one is normal and the other lognormal). Figure 30.29(b) shows the reliability index as a function of water level and correlation coefficient. Crude MCS with $N_{sim} = 1e6$ simulations is used. As seen, increasing both H_w and ρ_{1-2} reduces the reliability index; however, the variation of β is more intense with respect to H_w. Moreover, under the lower water levels, the impact of ρ_{1-2} is higher.

30.10 Failure Probability of Gravity Dam Classes

This section which is adapted from Hariri-Ardebili [373] establishes an analytical failure model and quantifies the failure probability of dams. An analytical model

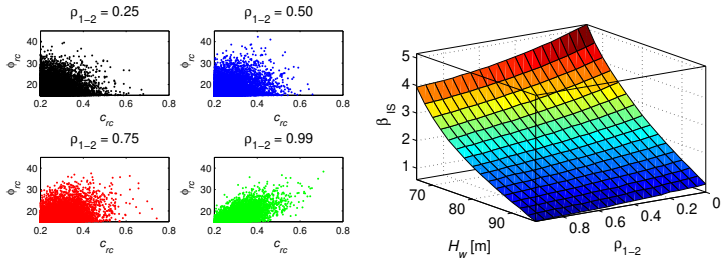

(a) Correlation between c_{rc} and ϕ_{rc} (b) Impact of H_w and ρ_{1-2}

Fig. 30.29: Impact of correlation on the reliability index in reduced model

is proposed using a parametric-probabilistic approach, which allows estimation of failure probability for different dam classes. The analytical model is calibrated using data from finite element analyses.

30.10.1 Case Study Dam

In classical reliability analysis of gravity dams, the probability of failure is computed against the hydrological hazard (i.e., increasing water level in the dam reservoir) [877]. The finite element approach is used to simulate the failure response of concrete dams. Different classes of gravity dams are modeled based on the upstream height and base width (other dimensions are proportional). Only the global failure mode (in terms of sliding along the base joint) is considered. The tangential contact between the concrete and rock is modeled by Coulomb friction law.
Magnitude and distribution of the uplift pressure is computed based on the drainage location, pre-defined base crack length, and elevation of the reservoir water in upstream face (headwater). The model parameters and material properties are summarized in Table 30.14. Only a limited number of parameters are assumed to be RVs (i.e., those highly affect the demand and capacity).

30.10.2 Step by Step Procedure

The step-by-step strategy to perform the combined parametric-probabilistic simulations can be summarized as:

- A total of 11 (50:5:100 divisions on B_1) $\times$ 21 (50:5:150 divisions on H_1) = 231 different generic gravity dam models are constructed.
- Five parameters are taken to be the most effective/sensitive RVs in calculation of the failure probability: L_{cr}, H_w, c_{rc}, ϕ_{rc}, and eff_D, Table 30.14.
- These five parameters are varying in both a parametric and probabilistic manner. It means that the possible range of these parameters is divided into some finite sub-spaces and then, samples are drawn randomly from each of these specific sub-spaces.

Table 30.14: Model and material parameters for probabilistic finite element simulations (Note: for the lognormal distribution in the form of $LogN(\mu, \sigma)$, the mean and standard deviations are: $e^{\mu+\sigma^2/2}$ and $\sqrt{(e^{\sigma^2-1})e^{2\mu+\sigma^2}}$, respectively.)

Parameter	Symbol	Unit	Distributional model	Quantity
Width at the base	B_1	m	Parametric	50:5:100
Width at the crest	B_2	m	$0.08 \times B_1$	4:0.4:8
Height of the dam	H_1	m	Parametric	50:5:150
Height of the neck	H_2	m	$0.06 \times H_1$	3:0.3:9
Location of drainage	L_d	m	$0.15 \times B_1$	7.5:0.75:15
Base crack ratio	L_{cr}	m	Uniform $B_1 \times (\alpha_1, \alpha_1 + 0.1)$	$\alpha_1 = 0 : 0.1 : 0.5$
Height of the water	H_w	m	Lognormal $(\log(\alpha_2 H_1), \log(1.3))$	$\alpha_2 = 0.6 : 0.1 : 1.1$
Height of the silt layer	H_s	m	Normal $(0.1H_1, 0.06H_1)$	(5:0.5:15, 3:0.3:9)
Concrete mass density	ρ_c	kg/m^3	Deterministic	2400
Water mass density	ρ_w	kg/m^3	Deterministic	1000
Silt mass density	ρ_s	kg/m^3	Deterministic	1850
Base joint cohesion	c_{rc}	MPa	Lognormal $(\log(\alpha_3), \log(1.3))$	$\alpha_3 = 0.1 : 0.2 : 0.9$
Base joint friction angle	ϕ_{rc}	deg.	Normal $(\alpha_4, 0.2\alpha_4)$	$\alpha_4 = 10 : 10 : 50$
Drain efficiency	eff_D	-	Uniform $(\alpha_5, \alpha_5 + 0.1)$	$\alpha_5 = 0 : 0.2 : 0.8$
Silt internal friction angle	ϕ_s	deg.	Normal	(30, 7.5)

- All other parameters (beside those five most effective RVs) are deterministic.
- Impact of those five major RVs is studied independent of each other. For example, when α_1 in Table 30.14 takes 6 different values, the quantity of α_2 to α_5 are assumed to be at "reference value." The same analogy is applied to the other four major RVs.
- The "reference value" for those five major RVs are: $\alpha_1 = 0$, $\alpha_2 = 0.9$, $\alpha_3 = 0.5$, $\alpha_4 = 30$, and $\alpha_5 = 0.8$.
- Thus, in general, there are $6 + 6 + 5 + 5 + 5 = 27$ ($N_{RV_1} + N_{RV_2} + N_{RV_3} + N_{RV_4} + N_{RV_5}$) parametric models.
- Each of these 27 parametric models is combined with one of the 231 dam classes, resulting in 6,237 groups.
- For each of these 6,237 groups, 1,000 samples are drawn based on LHS technique and consequently 6,237,000 nonlinear finite element simulations are performed.
- Probability of failure is computed in each group as the ratio of the failed simulations to 1,000 (total number of simulations in each group).
- Finally, results are presented for each of those five major RVs as "multiple 3D surfaces," where the vertical axis represents P_f and the two horizontal ones are dam height and width (dam class).

30.10.3 Dam Class Failure Probability

Detailed failure probability of the dam classes as a function of dam height, dam width, and one of the five base RVs is shown in Figure 30.30. In each case, statistics of the data points are presented using box plots including the upper and lower quartiles and the outliers.

The summarized plots are shown in Figure 30.31. Variation of each "mean failure surface" is a function of dam height, dam width, and the targeted base RV with its own properties (i.e. mean, standard deviation and distributional model):

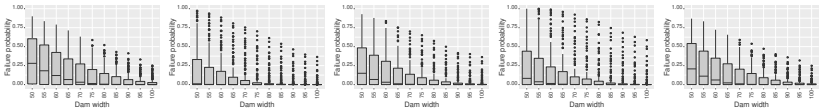

(a) Function of dam width

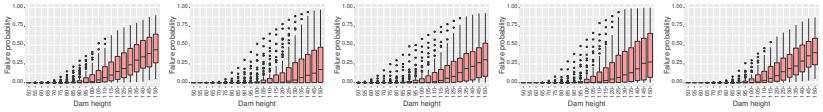

(b) Function of dam height

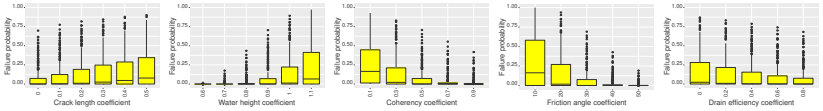

(c) Function of random variable

Fig. 30.30: Box-plots showing dependency of failure probability on dam class and varying parameters (Left to right: crack length, water height, coherency, friction angle, and drain efficiency)

$$P_f^{\text{mean}} = G\left(H_1, B_1, \text{PDF}\left(RV; \mu, \sigma\right)\right) \tag{30.9}$$

where PDF presents probability density function of random variable, RV, with parameters of the distribution μ and σ.
Based on Figure 30.31, increasing the crack length ratio and the reservoir water elevation increases the mean failure probability for all dam classes. Coherency, friction angle and drain efficiency have an inverse effect. On the other hand, based on this figure, variation of different failure surfaces is considerable by variation of H_w and ϕ_{rc}, while it is minor by variation of L_{cr} and eff_D. These surfaces can be directly used to predict the failure probability in the similar cases.

30.11 Random Field Vibration Anatomy of Arch Dams

This section which is adapted from Hariri-Ardebili et al. [399] investigates the vibration characteristics (e.g., natural frequencies and mode shapes) of old concrete arch dams by applying random field theory. The impact of correlation length is studied on the frequency response dispersion and inter-correlation among vibrational modes. Six different arch dams are studied and an analytical model is proposed for dam frequency. Finally, an iterative random field-based system identification technique is proposed for arch dams.

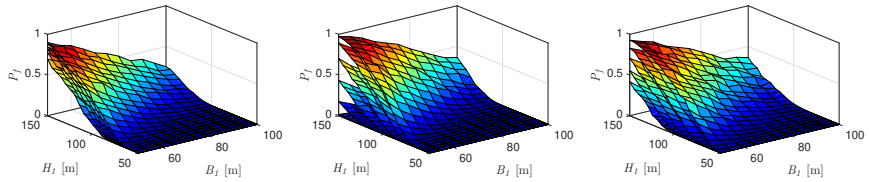

(a) L_{cr}; (0.0, 0.1, 0.2, 0.3, 0.4, 0.5) (b) H_w; (0.6, 0.7, 0.8, 0.9, 1.0, 1.1) (c) c_{rc}; (0.9, 0.7, 0.5, 0.3, 0.1)

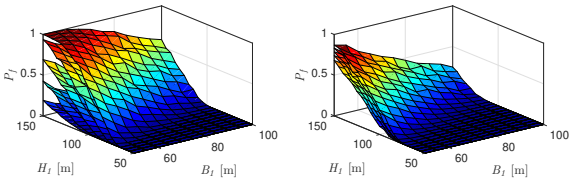

(d) ϕ_{rc}; (50, 40, 30, 20, 10) (e) eff_D; (0.8, 0.6, 0.4, 0.2, 0.0)

Fig. 30.31: Parametric computed failure probabilities for different dam classes based on finite element simulations; in each plot, the provided range is the bottom-to-top order of the surfaces

30.11.1 Case Study Dams

Six large arch dams were studied, Table 30.15. All dams are considered to be high dams (between 140 and 224 m in height). Three heterogeneous models with correlation length l_{corr} = 20, 40, 80 m and one homogeneously random model (based on LHS) have thus been considered. Random material is only affected by the modulus of elasticity, E_c, and mass density is assumed to be deterministic. The number of samples depends on dam size, number of dam elements, and correlation length in the random field. The number of samples varies from 100 to 1,200 based on different scenarios. Figure 30.32 shows the finite element models with one sample of l_{corr} = 20 m.

Table 30.15: Basic characteristics and material properties of concrete arch dams

ID	1	2	3	4	5	6
Dam name	Karaj	Dez	Karun-I	Karun-III	Morrow Point	Luzzone
Max. height above found. [m]	168.0	203.5	200.0	205.0	143.0	225.0
Crest length [m]	384.0	240.0	380.0	462.0	221.0	510.0
Crest thickness [m]	7.85	4.50	6.00	5.50	3.75	4.51
Base thickness [m]	32.00	21-28	33.50	29.00	15.60	35.71
Concrete volume [Mm^3]	0.657	0.318	1.137	0.896	0.187	1.252
Slenderness coefficient [-]	9.9	11.2	14.6	14.7	14.2	13.8
Modulus of elasticity, E_c [GPa]	25	40	21	30	33	19
Mass density, ρ_c [kg/m^3]	2450	2400	2500	2400	2400	2450
Poisson's ratio ν_c [-]	0.17	0.20	0.20	0.20	0.15	0.18
Height in FE model [m]	168.0	174.0	200.0	205.0	140.0	224.0
Number of FE nodes	4,592	956	3,093	5,623	8,229	552
Number of FE elements	3,240	648	2,197	3,946	34,681	316

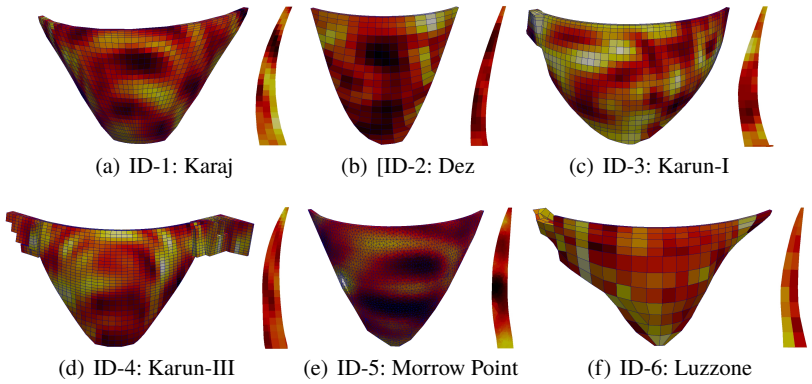

(a) ID-1: Karaj (b) [ID-2: Dez (c) ID-3: Karun-I

(d) ID-4: Karun-III (e) ID-5: Morrow Point (f) ID-6: Luzzone

Fig. 30.32: Geometry and finite element mesh of the studied arch dams; no scale; with one sample random fields of E_c

30.11.2 Vibration Response for Homogeneous Pilot Dam

Figure 30.33 reveals the anatomy of a set of probabilistic analyses on the homogeneous model of the Karun-I Dam. As seen in Figure 30.33(a), frequency response varies with mode number. Figure 30.33(b) shows the variation in the normalized participation factor (PF) for translational modes. Dominant vibration modes can be detected in these plots for each direction. Figure 30.33(c) shows the cumulative normalized effective mass for six directions.

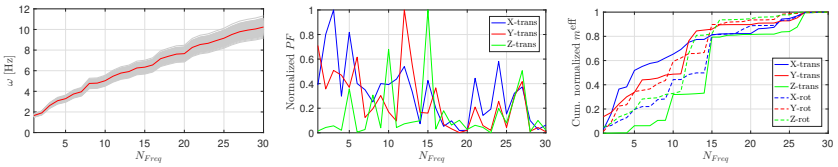

(a) Frequencies (b) Translational PFs (c) Effective mass

Fig. 30.33: Detailed vibration anatomy of the homogeneous pilot dam

30.11.3 Vibration Response of Heterogeneous Pilot Dam

Both the PFs and effective masses in the heterogeneous model are not deterministic, and their variation depends on correlation length, Figure 30.34. Note that this figure only shows the participation factor in the x-direction (as a sample) and moreover the cumulative normalized effective mass is plotted in three translational directions.

In general, the participation factor dispersion increases with correlation length. Also, since some of the closer modes change at higher frequencies, the variation is unpredictable in any single model. A similar trend can be observed for the cumulative effective mass, i.e. greater dispersion for higher correlation lengths.

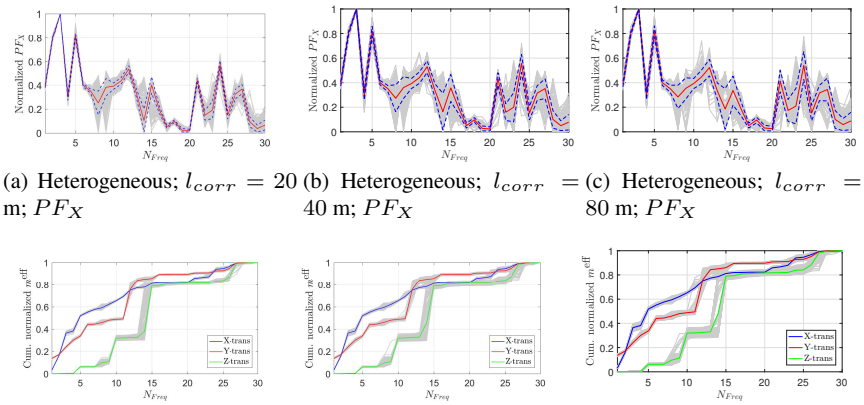

(a) Heterogeneous; $l_{corr} = 20$ m; PF_X (b) Heterogeneous; $l_{corr} = 40$ m; PF_X (c) Heterogeneous; $l_{corr} = 80$ m; PF_X

(d) Heterogeneous; $l_{corr} = 20$ m; m^{eff} (e) Heterogeneous; $l_{corr} = 40$ m; m^{eff} (f) Heterogeneous; $l_{corr} = 80$ m; m^{eff}

Fig. 30.34: Detailed vibration anatomy of the heterogeneous pilot dam

30.11.4 Generalized Model

The findings are then generalized for all six arch dams. The random field does not alter the mean response obtained with different l_{corr}. It merely depends on dam shape and base material properties (i.e. E_c and ρ_c). The variation in mean frequency, ω_{mean}, is shown in Figure 30.35(a) for all dams. Figure 30.35(b) presents the variation in standard deviation for each dam and each model. Increasing the l_{corr} clearly increases the standard deviation of the frequency response, ω_{STD}. In order to quantify the relative importance of mean and STD, the coefficient of variation, ω_{COV}, is obtained for all cases, Figure 30.35(c). The individual COV plots fluctuate slightly along a horizontal line. The mean plot for each l_{corr} is quite linear (straight line for the homogeneous case). The following empirical equation can be derived for the mean variation of ω_{COV} as a function of correlation length:

$$\mu_{\omega_{COV}} = -0.13\, l_{corr}^{-1/4} + 0.07 + \varepsilon_{\omega_{COV}} \tag{30.10}$$

where $\varepsilon_{\omega_{COV}}$ is the regression error.

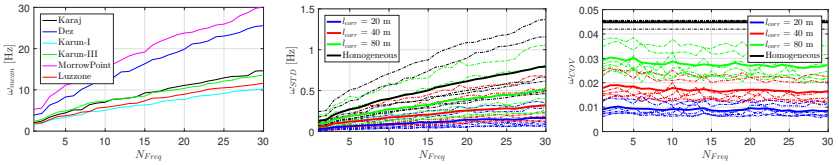

(a) Mean frequency of all dams (b) STD of each class and their mean (c) COV of each class and their mean

Fig. 30.35: Summary of frequency variation for all six dams

30.11.5 DOE-Based Analytical Model

Since six different dams are being studied in this paper, it is important to identify an analytical model for the dam vibration response as a function of shape and material uncertainty. Such a parametric analysis can be constructed using the design of experiment (DOE) technique.
The dam frequency response is proposed to be:

$$\omega_{rand} = \omega_1 \times (\alpha_1 \times N_{Freq}^{\alpha_2} + \alpha_3) \times (\beta_0 + \beta_1 \bar{E}_c + \beta_2 \bar{\rho}_c + \beta_3 {\bar{E}_c}^2 + \beta_4 {\bar{\rho}_c}^2 + \beta_5 \bar{E}_c \bar{\rho}_c) \tag{30.11}$$

where the coefficients α_i and β_j are based on Table 30.16. The N_{Freq} is the frequency number, $\bar{E}_c$ and $\bar{\rho}_c$ are the coded (normalized between minimum and maximum values) modulus of elasticity and mass density, and ω_1 is the first mode frequency.
Moreover, it is important to find a relationship between the dam shape and the first frequency, ω_1. A new correlation is developed and called the Hariri Shape Coefficient (HSC):

$$\text{HSC} = H_{max}^{\delta_1} \times L_{crest}^{\delta_2} \times V_{body}^{\delta_3} \times t_{ave}^{\delta_4} \tag{30.12}$$

where H_{max} is the maximum dam height, L_{crest} the crest length, V_{body} the body concrete volume, t_{ave} the average dam thickness, and δ_i are the coefficients to be optimized. Based on a large set of parametric analyses, it is found that the best coefficients (based on the six current dams) are: $\delta_1 = 2, \delta_2 = 0.5$, and $\delta_3 = \delta_4 = -1$. Let's assume that such a model leads to a semi-linear relation between HSC and ω_1. Subsequently, ω_1 can be written as a function of either HSC or the dam shape directly as:

$$\omega_1 = 23\,\text{HSC} + 1.23 = 23 \times \frac{H_{max}^2 \times L_{crest}^{0.5}}{V_{body} \times t_{ave}} + 1.23 \tag{30.13}$$

30.12 Random Field Linear Seismic Analysis of a Gravity Dam

This section which is adapted from Hariri-Ardebili et al. [389] formulates the random field theory for the time history elastic properties of gravity dams. The correlation length effect on response dispersion is evaluated, along with single- and double-

Table 30.16: Coefficients of the analytical model for a shape-dependent frequency analysis

Dam	ω_1	α_1	α_2	α_3	β_0	β_1	β_2	β_3	β_4	β_5
ID-1	2.286	0.6566	0.6819	0.3340						
ID-2	3.384	0.5431	0.7185	0.4494						
ID-3	2.037	0.5235	0.7063	0.4693	1	0.1694	-0.0414	-0.0144	0.0026	-0.0071
ID-4	2.411	0.5550	0.6604	0.4434						
ID-5	5.057	0.6260	0.6271	0.3668						
ID-6	2.423	0.4464	0.7421	0.5482						

random field distributions. The impact of ground motion intensity on response dispersion is also assessed. The impact of dam class (e.g. shape and size) on response pattern is studied.

30.12.1 Case Study Dams

Koyna gravity dam is used as the case study. Figure 30.36 shows the finite element model including the reservoir and the foundation. Two-dimensional plane strain transient simulations are performed using ANSYS [37]. Pressure-based fluid elements are placed in the reservoir domain. The fluid-structure interaction (FSI) is applied according to the Eulerian-Lagrangian approach. Both domains, the (massless) foundation and the reservoir, extend three times the dam height [307]. Loads consist of: self-weight, hydrostatic pressure (full reservoir), bottom sediment, and seismic loads.

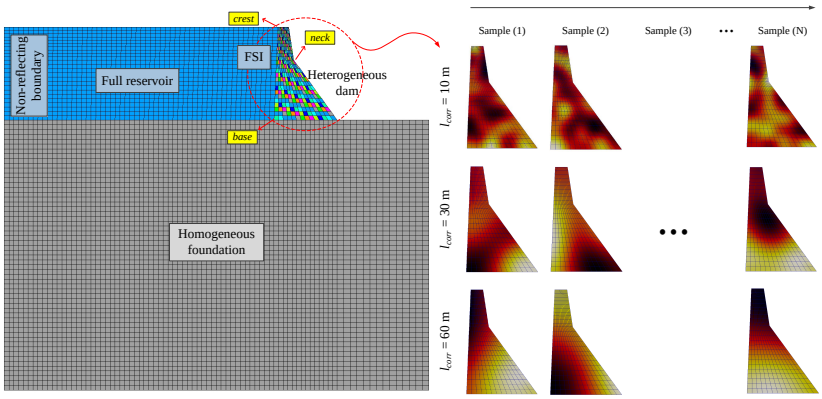

Fig. 30.36: Finite element model of the coupled dam-reservoir-foundation system, including three realizations of a heterogeneous dam with different correlation lengths

The foundation is assumed to be a homogeneous material with E_f = 17 GPa, ν_f = 0.18, and ρ_f = 2700 kg/m^3. The mean concrete properties are: E_c = 30 GPa, ν_c =

0.20, ρ_c = 2643 kg/m^3, and f'_t = 2.2 MPa. In all heterogeneous models, the standard deviation, σ_0, is assumed to equal 0.5. For the modulus of elasticity, the bound is limited to [22, 38] GPa. Two models have been studied, namely:

- Heterogeneous concrete: E_c is treated as a random field with three different correlation lengths, i.e. l_{corr} = 10, 30, and 60 m.
- Homogeneous concrete: E_c is treated as a random variable and sampled based on LHS.

The seismic performance is then evaluated using: demand capacity ratio (DCR), cumulative inelastic duration (CID), cumulative inelastic area (CIA), and damage spatial distribution ratio (DSDR) [842, 331].

30.12.2 Anatomy of Random Field Responses

In the pilot model, l_{corr} equals 30 m. The concrete modulus of elasticity, E_c, is assumed to be the only variable and is distributed randomly within the dam section. A total of 100 samples are drawn and, subsequently, 100 seismic analyses performed. Figure 30.37 shows the anatomy of these results. Each subplot can be explained as follows:

- Figure 30.37(a) shows 100 individual horizontal displacement time histories (at the dam crest).
- Figure 30.37(b) shows maximum horizontal displacements (three at the crest level, three at the neck discontinuity, and three at the base). More uniform relative response corresponds to more homogeneous (less heterogeneous) model. For a homogeneous model (E_c treated as a random variable), these data should not reveal any dispersion.
- Figure 30.37(c) shows the normal distribution fitted to the normalized displacements. For all the static, dynamic, and total displacements, the response at the crest exhibits greater dispersion than that at the neck. Among the three displacement components, total response is the most highly dispersed.
- Figure 30.37(d) shows the first (maximum) principal stress time history at the dam base (i.e. heel of the dam). Two sets of horizontal lines (corresponding to DCR) have also been drawn. One DCR^{mean} = 1.0 (using f_t^{mean} = 2.2 MPa) is shown with a dashed line, while the 100 DCR^{rand} = 1.0 lines are obtained using random sampling from a truncated normal distribution (with COV of 0.1 and bounds set at 0.25 of the mean).
- Figures 30.37(e) and 30.37(f) exhibit the CID-DCR curves for the dam base (thus far the most critical point of the dam). The former curve is based on a deterministic f_t while the latter has been computed based on random f_t.
- Figures 30.37(g), 30.37(h), and 30.37(i) show the DSDR-DCR curves with deterministic, random, and random field assumptions, respectively. Two important points need to be highlighted: 1) the DSDR values are calculated based on element stresses and areas and thus some approximation is introduced into element stresses based on the contribution of each node, and 2) in practically no cases

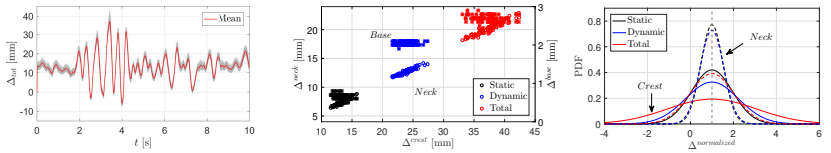

(a) Crest horizontal displacement (b) Maximum displacements (c) Displacement dispersion; solid = crest, dashed = neck

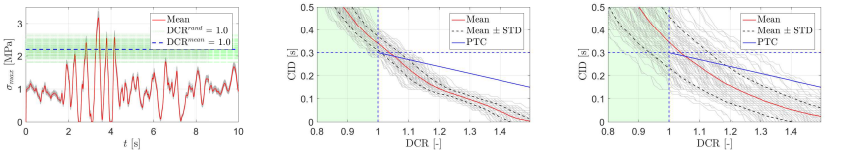

(d) Maximum principal stress at dam base (e) CID-DCR with deterministic f_t (f) CID-DCR with random f_t

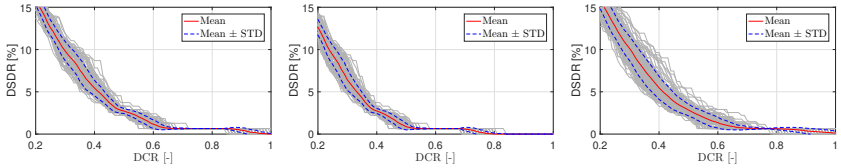

(g) DSDR-DCR with deterministic f_t (h) DSDR-DCR with random f_t (i) DSDR-DCR with random field f_t

Fig. 30.37: Anatomy of outputs from the random field simulation of a gravity dam

does DSDR exceed DCR = 1.0. This is because the nodal stresses are averaged in the elemental level. Hence, the results between DCR (0.2, 1.0) can be presented.

30.12.3 Impact of Spatial Correlation Length

In this section, the analyses are performed with three heterogeneous models (l_{corr} = 10, 30, and 60 m) and a homogeneous model. In all, four models are run and 100 samples drawn for each. The comparative findings are summarized in Figure 30.38. Each subplot can be explained as follows:

- Figure 30.38(a) shows the COV in displacement time history of the crest point. The spikes correspond to the peak displacement in the response history analyses. In the heterogeneous models, increasing the correlation length increases the COV. In the homogeneous model, the COV is nearly identical to the model with $l_{corr} = 60$ m.
- Figures 30.38(b) and 30.38(c) display the mean and STD of the maximum displacement results at the crest and neck. Note that the black/white bars belong to

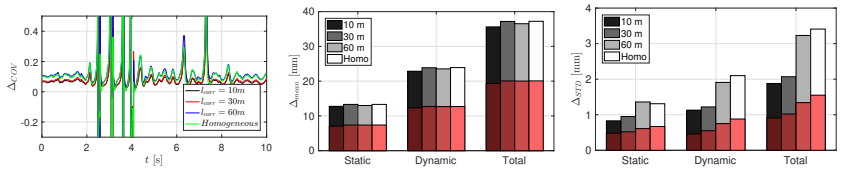

(a) COV of total crest displacement

(b) Mean of the extreme displacements; B/W = crest; Colored = Neck

(c) STD of the extreme displacements; B/W = crest; Colored = Neck

Fig. 30.38: Impact of spatial correlation length on the variability of results

the crest (higher value) and the colored bars represent the neck area (lower values). Concrete heterogeneity has minimal effect on the mean displacement responses. Increasing the correlation length however increases the STD. The homogeneous model exhibits the highest STD (because it is assumed that its correlation length is infinity). A jump in STD occurs from l_{corr} 30 to 60 m.

30.12.4 Impact of the Double Random Field Distribution

Thus far, all the models discussed have been based on just one random field model in the finite element simulation process (i.e. E_c). In this section, the impact of two simultaneous random fields will be investigated. The second random field is assumed to be the concrete mass density, ρ_c. Figure 30.39 compares the pilot model with the double random field model (both have a $l_{corr} = 30$ m). Each subplot can be explained as follows:

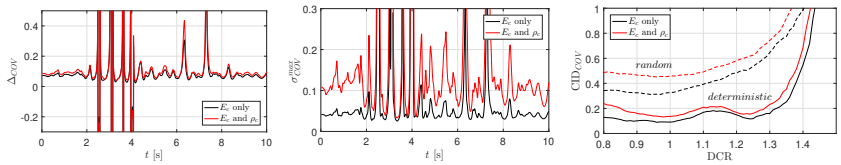

(a) COV of total crest displacement

(b) COV of maximum principal stress at the base

(c) COV of CID-DCR curves

Fig. 30.39: Impact of a single- or double-random field assumption

- Figure 30.39(a) compares the displacement COV at the crest point. The double random field model exhibits a higher COV for nearly the entire time history. Under the spikes, the double random field model yields a much higher COV value.
- Based on Figure 30.39(b), the double random field model has a higher COV. When averaged, the COV in the double random field model is twice that of the single random field model.

- Figure 30.39(c) compares the COV resulting from the CID-DCR curves. In both, the deterministic and random assumptions of f_t, the double random field distribution leads to a higher COV. Moreover, the random f_t model has a higher COV compared to the deterministic model.

30.13 Random Field Damage Assessment of a Gravity Dam

This section combines the concept of random field theory with nonlinear dynamic analysis to quantify uncertainties in potential failure modes of a gravity dam. Different random parameters are studied, as well as various correlation lengths, and the damage index is computed for each case. Finally, different crack patterns are contrasted.

30.13.1 Case Study Dams

Koyna Dam is used as a case study, Figure 30.40(a), with concrete material being heterogeneous in macro-scale. The numerical model includes the reservoir and the foundation. The mesh is refined around the neck and dam-foundation interface to capture all the potential failure modes precisely. All other conditions and loads are similar to Section 30.12.1.

The foundation is isotropic, homogeneous, and linear elastic. E_f = 17 GPa, ν_f = 0.18, and ρ_f = 2700 kg/m^3. Concrete is isotropic, homogeneous/heterogeneous, and nonlinear. Three concrete properties are assumed to be independently random, i.e. E_c, ρ_c, and f_c. All the other parameters are deterministically related to those three. Since Koyna is an old dam, and considering the potential deterioration, the following mean values are assumed for the concrete: E_c = 31$\times$0.85=26.35 GPa, ρ_c = 2640 kg/m^3, and f_c = 24*0.85=20.40 MPa. The reduction factor 0.85 accounts for 15% deterioration (overall). A standard deviation, σ_0, of 0.5 is assumed.

Three heterogeneous concrete models are considered with correlation lengths, l_{corr}, of 5, 10, and 30 m. These values correspond to 4%, 8%, and 25% of the maximum length in the FE model. Moreover, a set of homogeneous models is studied which technically corresponds to RV theory. Figures 30.40(b), 30.40(c), 30.40(d), and 30.40(e) show four samples for each correlation length. Twenty four realizations are generated for each of the heterogeneous models as well as the homogeneous one.

In order to study the progressive failure of the dam, an artificially generated acceleration function is used. Both the acceleration time history and its time-dependent response spectra linearly increase with time, Figure 30.40(a)-left. This technique is called Endurance Time Analysis (ETA), See Section 24.3.10. The intensifying acceleration function pushes the structure all the way from linear elastic range to nonlinear phase, and finally leads to failure. Theoretically, the larger failure (or endurance) time, t_f, corresponds to the stronger structure.

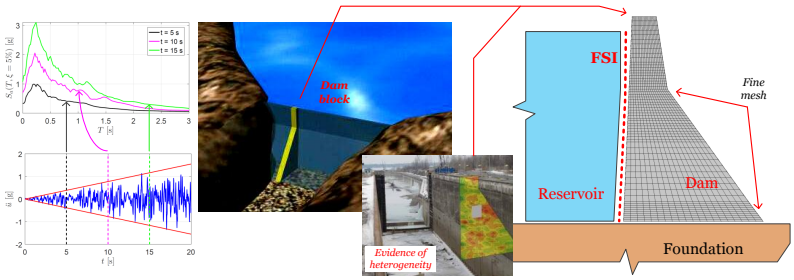

(a) Transfering the dam-reservoir-foundation from physical to FE model accounting for the macro-scale heterogenity, and input synamic excitation

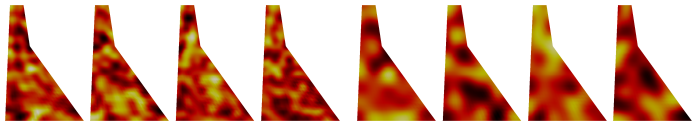

(b) Realizations with $l_{corr}/l_{max} = 0.04$

(c) Realizations with $l_{corr}/l_{max} = 0.08$

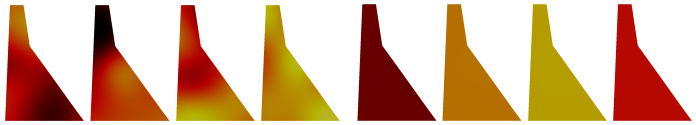

(d) Realizations with $l_{corr}/l_{max} = 0.25$

(e) Homogenous samples

Fig. 30.40: Preparing the numerical models with concrete heterogeneity and different correlation length

30.13.2 Anatomy of Pilot Model

A dam with heterogeneous modulus of elasticity of l_{corr}/l_{max} = 0.04 is selected as the pilot model. Twenty four realizations are randomly generated and mapped into the FE model. Transient analyses are performed with intensifying acceleration function, and the raw outputs are data-mined. Summary of the findings are illustrated in Figure 30.41 and elaborated in detail as follows:

Figure 30.41(a) illustrates the dynamic displacement of the crest in stream direction. Up to time about 8.0 s in which all the models are nearly in the linear (with some minor nonlinearity) range, all the displacement curves are very close to each other. Nonlinear behavior leads to a considerable dispersion among the time histories. Next, the ETA capacity functions are derived as shown in Figure 30.41(b). In these curves, failure corresponds to a vertical line. Those failure points are shown with black circles.

Individual values of the t_f are shown in Figure 30.41(c) along with the deterministic model (red dashed line). The reference model is failed at about $t_f = 13.7$ s. Only six of the random models exceed this value. Ten of them are less than 13.7 s (varying

from 10.2 to 13.0 s); the nine others do not fail up to t = 15.0 s (which was the duration of the applied excitation to reduce the computational time).

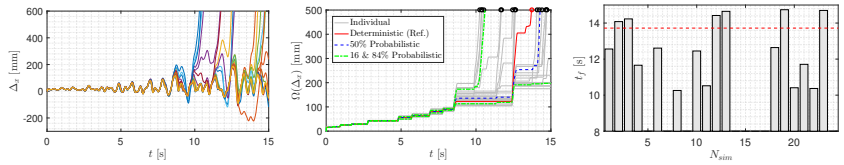

(a) Dynamic horizontal displacement (b) ETA function of horizontal displacement (c) Failure time

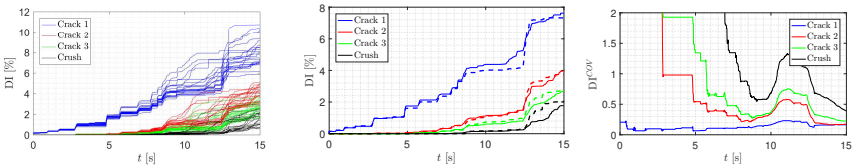

(d) Individual DI evolution (e) Meadian vs. deterministic DI (f) COV of DI evolution

Fig. 30.41: Response summary of the pilot dam model; E_c as random field with correlation length ratio of 0.04

Nonlinearity in this dam is originated from a smeared crack model in Ansys. Each integration point is capable of cracking in three orthogonal directions (referred to as crack 1, 2 and 3), as well as crushing. To be used in the context of this paper, the damage in the integration points are transferred to the elemental level. Zero means no damage, and one represents a fully damaged element in that particular direction. This elemental damage is referred to as the damage variable (DV) and shows the degree of local damage.
Next, this local DV needs to be transferred to the global level. Thus, the concept of damage index (DI) is adopted:

$$\mathrm{DI}^j(t) = \frac{\sum_{i=1}^{N_{el}} \mathrm{Vol}_i \times \mathrm{DV}_i^j(t)}{\sum_{i=1}^{N_{el}} \mathrm{Vol}_i} \tag{30.14}$$

where $j = 1, 2, 3$ presents the cracking in three directions and $j = 4$ is the crushing. N_{el} is the number of elements, Vol_i is the elemental volume, and $\mathrm{DV}_i^j(t)$ is the time-dependent DV for element i at direction j.
Resulted DIs for cracking and crushing of the 24 models are shown in Figure 30.41(d). Clearly crack 1 is more than others and crushing has the minimum percentage. For crack 1, the percentage of cracking at t = 15 s is about [6, 11]% for different models. Furthermore, Figure 30.41(e) compares exclusively the median (i.e. 50% fractile) of DI in random models (solid lines) with those obtained from the deterministic reference model (dashed lines). There is a very good consistency among different

cracking and crushing models. Last but not least, Figure 30.41(f) illustrates the COV of DI curves from random models. For crack 1, COV has nearly a constant value from 0.1-0.2. Crack 2, crack 3, and crushing start at about time 5, 7, and 9 s, respectively. All of them have a peak at about t = 12 s, which more or less corresponds to the failure time. In addition, crushing has higher COV compared to crack 3, then crack 2 and finally crack 1.

30.13.3 Crack Pattern

Next, the damage pattern is studied. Figure 30.42 show the DV^1 distribution in all 24 models at t = 15 s. As seen, there are lots of diverse failure modes and crack propagation. In several cases, secondary (and higher-order) crack paths are generated in addition to the main one observed in the deterministic model.

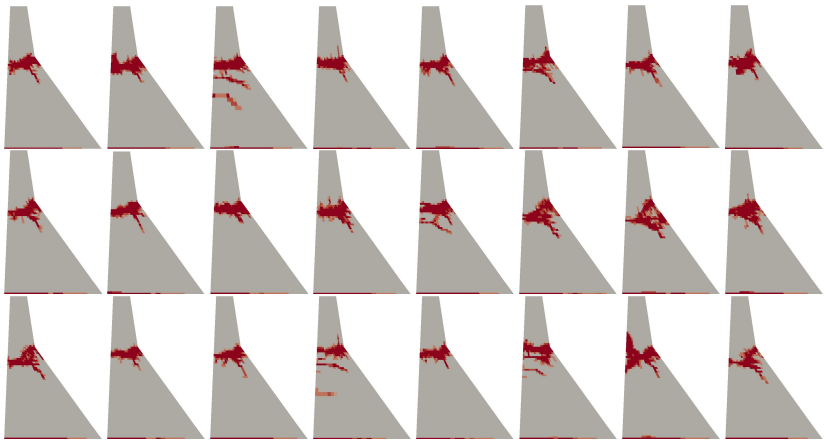

Fig. 30.42: DV^1 (crack 1) profile of all 24 E_c RF models with normalized correlation length of 0.04; all the plots are at t=15 s

30.14 SVM for Nonlinear Seismic Analysis of a Gravity Dam

This section which is adapted from Hariri-Ardebili and Pourkamali-Anaraki [395] proposes the application of support vector machine in response classification and prediction of a nonlinear dam-foundation-reservoir coupled system. Different response quantities (displacements and damage index) are classified either based on failed/safe or damage index value, and an algorithm is proposed for hybrid FEM-SVM analysis of dams.

30.14.1 Case Study Dam

Pine Flat gravity dam is used as the case study. The model preparation and loading is essentially similar to the one discussed in Section 30.1.1. The finite element code "Merlin" is used for dynamic analyses [767]. Applied loads on the system are: 1) self-weight, 2) hydrostatic pressure, 3) dynamic uplift which is automatically updated with crack propagation, and 4) seismic loads, Figure 30.43.

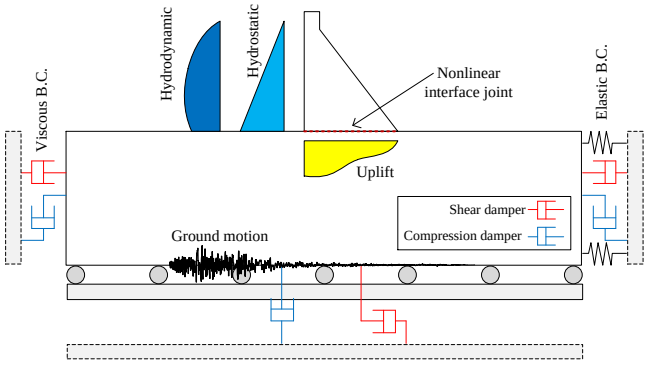

Fig. 30.43: FEM based model description (loads and boundary conditions)

All the material properties, geometry, and loading (except ground motion) are kept constant (no epistemic uncertainty). Material properties for concrete are: mass density (ρ_c) 2250 kg/m^3, modulus of elasticity (E_c) 22.4 GPa, Poisson's ratio (ν_c) 0.20, and tensile strength (f'_t) 2.24 MPa. Foundation material properties are: mass density (ρ_f) 2600 kg/m^3, modulus of elasticity (E_f) 24 GPa, and Poisson's ratio (ν_f) 0.25. Interface joint properties are: tangential stiffness (k_t) 224 GPa, normal stiffness (k_n) 224 GPa, cohesion (c) 1.9 MPa, friction angle (ϕ_f) 38°, dilatancy angle (ϕ_d) 20°, specific mode I and II fracture energies (G_F^I, G_F^{II}) 252/2520 N/m, relative irreversible deformation (γ) 0.3, maximum displacement for dilatancy (u_{Dmax}) 0.01 m, tensile stress and opening displacement at break point $< s_{1\sigma}, COD >$ is $< 0.56MPa, 1.12E-4m >$, and cohesion and sliding displacement at break point $< s_{1c}, CSD >$ is $< 0.375MPa, 1.26E-3m >$.
The system is excited only in the horizontal direction (aleatory uncertainty) using the list in Hariri-Ardebili and Saouma [386]. Several intensity measures are computed for each ground motion record, Table 30.17. These IMs are calculated for one hundred ground motions and in each case an appropriate distributional model is fitted to the raw data histograms.

30.14.2 Hybrid FEM-SVM

Figure 30.44 proposes a step-by-step hybrid methodology based on SVM and FEM for seismic analysis of concrete dams. This technique uses all three main charac-

Table 30.17: Summary of the ground motion IMs for gravity dam

Description	Symbol	Unit	Fitted model	Quantity
Moment magnitude	M_w	-	Normal	$N(6.31, 0.62)$
Rapture distance	R_{rup}	km	Lognormal	$LN(38.6, 25.6)$
Significant duration	t_{sig}	s	Lognormal	$LN(14, 8.8)$
Peak ground acceleration	PGA	g	Lognormal	$LN(0.12, 0.07)$
Peak ground velocity	PGV	m/s	Lognormal	$LN(0.062, 0.036)$
Peak ground displacement	PGD	m	Lognormal	$LN(0.019, 0.016)$
Root-mean-square of acceleration	a_{RMS}	m/s^2	Lognormal	$LN(0.147, 0.086)$
Root-mean-square of velocity	v_{RMS}	m/s	Lognormal	$LN(0.011, 0.007)$
Root-mean-square of displacement	u_{RMS}	m	Lognormal	$LN(0.006, 0.007)$
Arias intensity	I_A	m/s	Lognormal	$LN(0.114, 0.07)$
First-mode spectral acceleration	$S_a(T_1)$	g	Lognormal	$LN(0.124, 0.087)$
First-mode spectral velocity	$S_v(T_1)$	m/s	Lognormal	$LN(0.114, 0.076)$
First-mode spectral displacement	$S_d(T_1)$	m	Lognormal	$LN(0.009, 0.007)$
Combined (1 to 2) spectral acceleration	S_a^{1-to-2}	g	Lognormal	$LN(0.223, 0.07)$
Combined (1 to 3) spectral acceleration	S_a^{1-to-3}	g	Lognormal	$LN(0.325, 0.066)$

teristics of the SVM (regression, binary- and multi-class prediction) along with probabilistic seismic hazard and structural analysis adopted from performance based earthquake engineering (PBEE).

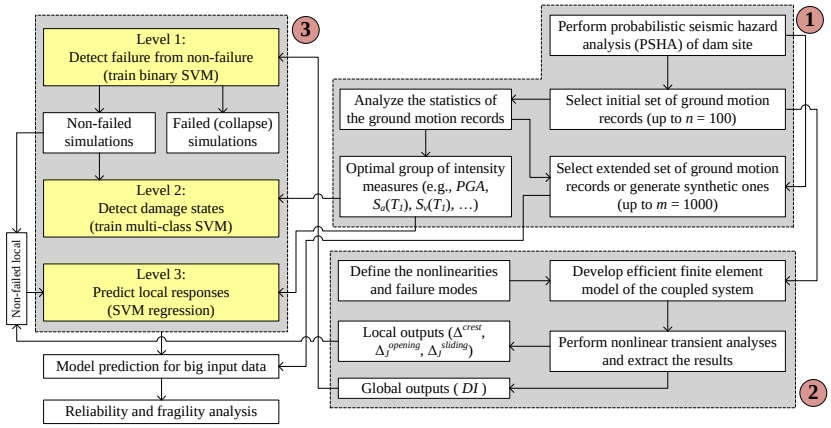

Fig. 30.44: Proposed hybrid FEM-SVM methodology for seismic analysis of concrete dams

1. **PSHA** First, probabilistic seismic hazard analysis is performed and two sets of ground motions are selected based on seismicity of the dam site.
   - A small group with up to 100 ground motions and a large set with up to 1000 ground motions.
   - The smaller group may includes only the real ground motions which reflect the actual characteristics of earthquake records.

- The statistics of the small set is analyzed and the optimal intensity measure parameters are selected. These are later used for the larger set as well.
- Since the number of recorded ground motions are limited in the PEER [688] website, the large set of ground motions might be combination of real ground motions and the generated ones [731, 896].

2. **FEM** An efficient finite element model is developed, and the potential failure modes are implemented by introducing appropriate nonlinearities (discrete or smeared crack). The small set of selected ground motions are applied to the numerical model, and the results are extracted in two levels: local outputs (crest displacement and joint response) and global damage index.
3. **SVM** Support vector machine families are used to post-process the results, classification, training, and regression in three levels:

- Level 1: Detecting the failed from non-failed simulations based on global damage index and binary SVM training.
- Level 2: Categorizing the non-failure simulations in different pre-defined damage states employing optimal intensity measure parameters.
- Level 3: Predicting the contentious local responses for the non-failure simulations and developing a meta-model for future reliability and fragility assessment of the dam with any desired set of input ground motions (the large earthquake set).

30.14.3 Detecting Failure from Non-Failure

Support vector machines are employed to learn a classifier that allows prediction of the output (failure/non-failure) for a set of ground motion IMs. This set contains 15 RVs that can be viewed as data points in $\mathbb{R}^{15}$, Table 30.17. To measure the accuracy of learned classifier, 100 simulations are divided into two subsets: 1) training set and 2) test set. The training set is used to fit the SVM classifier, and the test set is used for assessment of the generalization error of the final chosen model. From 83 non-failure cases, 73 data points are used for training and the remaining 10 data points are used for testing. Also, 12 out of 17 failure cases are chosen for training and the remaining 5 data points are used for testing.

The accuracy of trained SVM classifier is investigated for various kernel function types. Based on simulations, the trained SVM using a polynomial kernel function classifies 15 test cases successfully. Thus, the learned SVM model using the polynomial function is able to detect outputs for all 15 test cases.

A set of experiments are performed on 2 RVs, instead of the 15 initial ones, to get some intuition and visualize the decision boundary. In each case, one of the RVs is set to be $S_a(T_1)$ and the other RV is selected from PGA, I_A, $S_v(T_1)$. Next, an SVM classifier in conjunction with the polynomial kernel function is trained on 100 data points in $\mathbb{R}^2$. Recall that 83 of these data points belong to the "non-failure" class and the rest belong to the "failure" one. In Figure 30.45, these 100 data points as well as decision boundary and support vectors obtained from the SVM training are plotted. Note that the nonlinear decision boundary corresponds to a separating hyperplane

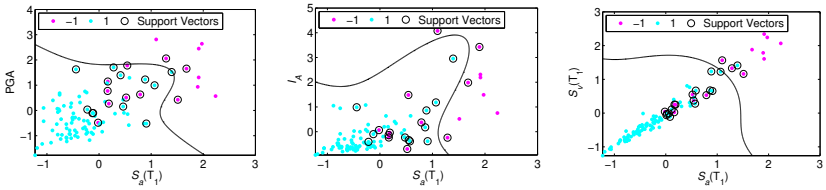

(a) PGA vs. $S_a(T_1)$ (b) I_A vs. $S_a(T_1)$ (c) $S_v(T_1)$ vs. $S_a(T_1)$

Fig. 30.45: Binary classification of seismic responses with two RVs

in the feature space induced by the nonlinear polynomial kernel function. It is found that all three cases show reasonable classification of two classes (failure/non-failure).

30.14.4 Regression of Non-Failure Results

In this section, the performance of SVM regression on estimating values of three local output quantities will be investigated. The goal is to learn a regression model based on a training set that allows us to predict values of these three quantities for new test data points. The values of SVM-based responses are plotted versus the FEM-based ones in Figure 30.46 for crest displacement. Based on the previous observation, a polynomial kernel function is used to train SVM regression on all 83 non-failure simulations. It is observed that all these points are close to the so-called "line of equality" showing the accuracy of SVM regression.

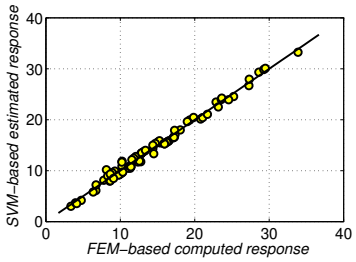

Fig. 30.46: SVM regression for non-failure crest displacement [mm]

30.15 Ground motions Meta-Features for Dam Response Prediction

This section which is adapted from Hariri-Ardebili and Barak [392] proposes a series of biometric-like ground motion unique signatures. Next, six forecasting techniques are compared in response prediction of finite element models. A general framework

is proposed to reduce computational cost in seismic risk assessment. Finally, the concept of feature selection is examined in the context of seismic response of dams.

30.15.1 Case Study Dam

Pine Flat gravity dam is selected as a case study. The finite element model and loading are similar to those explained in Section 30.5.1. Applied loads on the system are: 1) self-weight, 2) hydrostatic pressure, and 3) seismic loads. Standard deterministic material properties are assumed for the mass concrete and the foundation rock. The main objective in this section is to establish a model for the ground motion record-to-record (RTR) variability. The crest horizontal displacement and vertical stress at the vicinity of the dam's heel are used as QoIs.
The applied ground motions are downloaded from the PEER [688] website. A total of 1,929 ground motion records are used. Ground motions are applied to the system as-recorded (Cloud analysis). For each input ground motion, the resulted QoI parameters are recorded in an array. Figure 30.47 illustrates the correlation among the IM parameters. For more accurate prediction, some of the large data QoIs are eliminated. Statistical summary of the response parameters (from all data) are as follows:

- Δ^{H}_{max}: minimum = 1.08, lower adjacent = 1.08, 25th percentile = 7.14, median = 14.82, mean = 23.50, 75th percentile = 28.74, upper adjacent = 61.04, maximum = 224.74.
- σ^{yy}_{max}: minimum = -0.09, lower adjacent = -0.09, 25th percentile = 0.15, median = 0.45, mean = 0.77, 75th percentile = 0.99, upper adjacent = 2.24, maximum = 8.70.

Results of forecasting are presented in two parts: 1) with all features (IM parameters) and 2) with subset of features.

30.15.2 Employing All the Features

This section investigates the quality of prediction based on different techniques. All the ground motion-dependent features are employed. Tables 30.18 and 30.19 provide a general overview on the Goodness-of-fit (GOF) by comparing the error functions resulted from six techniques. The machine learning techniques are: Decision Tree Regression (DTR), Random Forest (RF), Tree Bagging (TB), Extreme Gradient Boosting (XGBoost), Artificial Neural Networks (ANN), and Support Vector Regression (SVR). For each response, the GOF is provided for the train and test data separately. The major observations are:

- For displacement response:
  - For the training data set, the order of models from lowest to highest error functions is:
    - Based on RMSE (or SMAPE): XGB, RF, SVR, ANN, TB, DTR.

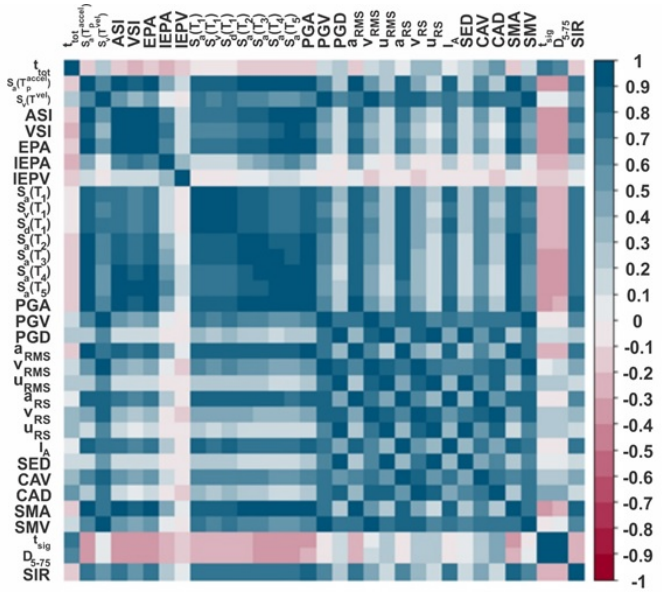

Fig. 30.47: Correlation map between input IM parameters

Table 30.18: GOF for the displacement with all the features

	Train		Test	
	RMSE	SMAPE	RMSE	SMAPE
Decision Tree Regression	34.45	0.198	36.72	0.209
Tree Bagging	30.25	0.188	32.48	0.194
Random Forest	11.22	0.052	26.51	0.121
XG-Boost	1.72	0.014	27.88	0.126
Neural Network	23.35	0.143	25.53	0.139
SVR	21.58	0.103	29.02	0.128

Table 30.19: GOF for the stress with all the features

	Train		Test	
	RMSE	SMAPE	RMSE	SMAPE
Decision Tree Regression	1.306	0.614	1.513	0.540
Tree Bagging	1.119	0.497	1.229	0.430
Random Forest	0.434	0.125	1.115	0.237
XG-Boost	0.068	0.062	1.199	0.249
Neural Network	0.933	0.278	1.202	0.278
SVR	0.893	0.243	1.241	0.274

  - For the test data set, the order of models from lowest to highest error functions is:
    - Based on RMSE: ANN, RF, XGB, SVR, TB, DTR.
    - Based on SMAPE: RF, XGB, SVR, ANN, TB, DTR.

- For stress response:

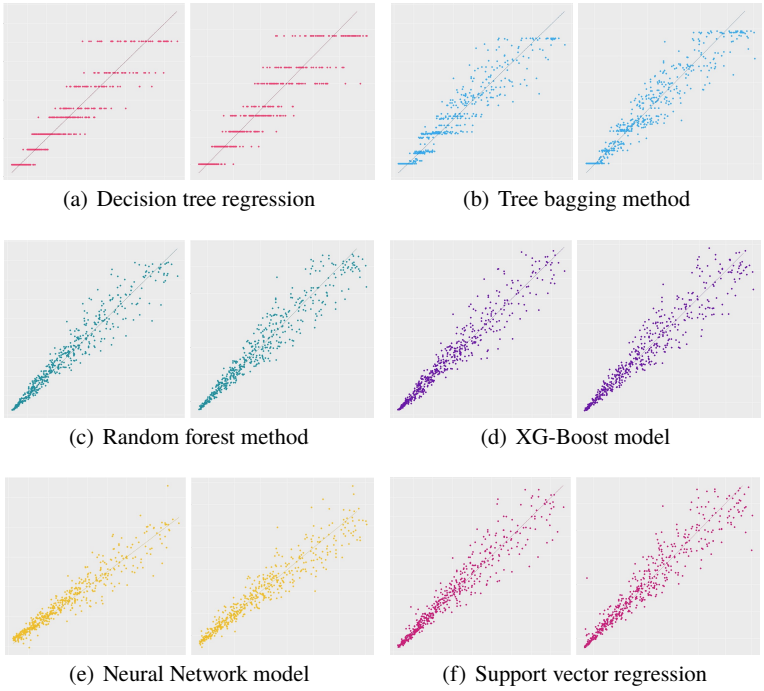

(a) Decision tree regression (b) Tree bagging method

(c) Random forest method (d) XG-Boost model

(e) Neural Network model (f) Support vector regression

Fig. 30.48: Quality of prediction based on different forecasting techniques and QoIs.

  - For the training data set, the order of models from lowest to highest error functions is:
    - Based on RMSE (or SMAPE): identical to the displacement.
  - For the test data set, the order of models from lowest to highest error functions is:
    - Based on RMSE: RF, XGB, ANN, TB, SVR, DTR.
    - Based on SMAPE: RF, XGB, SVR, ANN, TB, DTR.

- The order of models for the training data set is identical for displacement and stress (either RMSE or SMAPE).
- For all the data sets and error functions, the Decision Tree Regression provides the worst prediction.
- For the training data set and any error function, XGBoost is the best model.
- For the test data set, the Random Forest is the best model. Again, the second rank belongs to XGBoost.
- Figure 30.48 illustrates the quality of the prediction for all six models and two QoIs. Deficiency of Decision Tree Regression and to some extend Tree Bagging is obvious. On the other hand, Random Forest has a uniform trend along the equality

axis. In each sub-figure, the left plot belongs to the displacement, and the right one shows the stress variation. In each plot, the horizontal axis is the computed finite element model (i.e. true value) and the vertical axis is the predicted one based on machine learning. The solid black line presents the equality line.

30.15.3 Employing the Selective Features

In this section, the feature weighting methods are used to select a subset of features and label them as more significant ones. Six filtering methods have been applied from "FSelector" library [738] including: 1) Information Gain, 2) Information Gain Ratio, 3) Chi-square, 4) OneR, 5) Relief, and 6) Symmetrical Uncertainty. A brief summary of these techniques is presented in 20 for those readers interested in mathematical theories behind those names [83].

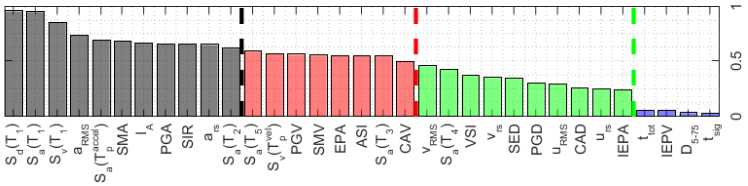

(a) Displacements

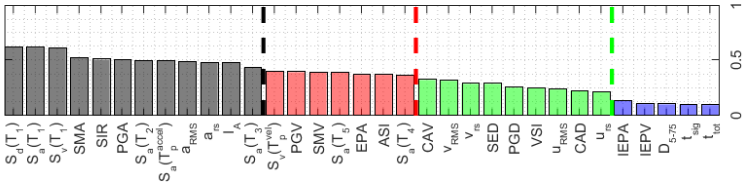

(b) Stress

Fig. 30.49: Feature selection using different subsets for two response quantities.

The outcome of the feature selection is shown in Figure 30.49 in which three subsets with 28, 19, and 12 features are chosen for displacement, and three subsets of 29, 19, and 11 features are defined for stress response. We simply selected N top features where there was a sudden slope change in the weight factors between the feature N and $N+1$. This can be easily visualized from Figure 30.49 in which the selected features have darker color. In this figure, black bars (all IMs left of the black line) = subset 3; black + red bars (all the IMs left of the red line) = subset 2; green + red + black bars (all IMs left of the green line) = subset 1.

30.16 Machine Learning based Multi Hazard Reliability of Gravity Dams

This section which is adapted from Hariri-Ardebili and Pourkamali-Anaraki [394] aims to provide a simplified probabilistic framework in order to determine the failure probability for gravity dams subjected to multi-hazard risk. Aging hazards of gravity dams are studied with up to six degrading/increasing models for random variables. A comprehensive study on the temporal reliability of gravity dams are performed considering both instant and cumulative failure probabilities. The results are presented in the form of a fragility function. Three machine learning techniques are compared for estimation of structural failure probability. Finally, the estimated failure probability is generalized for a class of dams, and a sigmoid-type analytical model is presented for dam failure probability.

30.16.1 Case Study Dam

Three main examples are studied in this section corresponding to three natural hazards, i.e., hydrological, aging, and seismic. All examples are based on limited equilibrium method (LEM). The model and loading are essentially similar to that of Section 30.9. The model parameters are listed in Table 30.20. Depending on the analysis type, the natural hazard, and the potential risk these parameters may take deterministic or probabilistic values. Moreover, the class of gravity dams studied are where the $\frac{B_1}{H_1}$ ratio varies 0.5:0.1:1:0. The one with $\frac{B_1}{H_1} = 0.7$ is considered as the standard shape.

Table 30.20: Model parameters for analytical limit state function

Parameter	Symbol	Unit	Distributional model
Width at the base	B_1	m	Parametric (Dam classes)
Width at the crest	B_2	m	$0.08 \times B_1$
Height of the dam	H_1	m	Parametric (Dam classes)
Height of the neck	H_2	m	$0.06 \times H_1$
Location of drainage	L_d	m	$0.15 \times B_1$
Crack at the base	L_{cr}	m	Uniform (depends on B_1)
Height of the water	H_w^*	m	Lognormal (depends on H_1)
Height of the silt layer	H_s	m	Normal (depends on H_1)
Concrete mass density	ρ_c	kg/m^3	Normal
Water mass density	ρ_w	kg/m^3	Deterministic
Silt mass density	ρ_s	kg/m^3	Deterministic
Rock-concrete cohesion	c_{rc}	MPa	Lognormal
Rock-concrete friction angle	ϕ_{rc}	deg.	Normal
Drain efficiency	eff_D	-	Uniform (0, 1)
Silt internal friction angle	ϕ_s	deg.	Deterministic
Aging time	t_{age}	year	$t_0 : t_f$
Seismic coefficient	α_{gm}	-	$0 : \alpha_{max}$
Earthquake vibration period	t_e	sec	Uniform

* Height of the water, H_w, is equal to H_f (flooding height) when it exceeds H_1 (dam height).

30.16.2 Methodology of Machine Learning

This section investigates the application of three machine learning based classification techniques, i.e. KNN, SVM, and NBC, to estimate the failure probability of gravity dam classes. In each classification technique, a set of N_{trn} training data points in $\mathbb{R}^6$ (for hydrological and aging hazards and later $\mathbb{R}^8$ for seismic hazard) and their corresponding labels are given as the input. These training data points can be viewed as the rows of the matrix $\mathbf{X}_{\text{trn}} \in \mathbb{R}^{N_{\text{trn}} \times 6}$, where each column represents one of the six random variables used in the analyses. The labels are also stored in the column vector $\mathbf{y}_{\text{trn}} \in \mathbb{R}^{\text{trn}}$, where each entry is either $+1$ (for safe) or -1 (for fail).
Three classification techniques are used to learn a classifier from the training data that allows us to predict responses (safe/fail) for a new set of test data points. Thus, the learned classification rules can be used to estimate the failure probability. Similar to the training phase, test data points are stored as the rows of matrix $\mathbf{X}_{\text{test}} \in \mathbb{R}^{N_{\text{test}} \times 6}$. The goal is to predict the response vector $\hat{\mathbf{y}}_{\text{test}} \in \mathbb{R}^{N_{\text{test}}}$ by using three classification techniques. Finally, the failure probability can be estimated as the number of failed cases, i.e., number of entries of $\hat{\mathbf{y}}_{\text{test}}$ that are equal to -1, normalized by the total number of cases, N_{test}. Given the estimate of failure probability $\hat{P}_f$, the normalized estimation error is used to measure the accuracy which is defined as $|\hat{P}_f - P_f|/P_f$. The overall training and estimation procedure is summarized in Algorithm 2. In order to make the implementation of the proposed method easier for interested readers, MATLAB's built-in functions are used in the given algorithm [580]. Here, $\mathbf{X}_{\text{trn}}(:, i)$ denotes the ith column of matrix $\mathbf{X}_{\text{trn}}$. The three classification methods can be implemented in MATLAB using FITCKNN(), FITCSVM(), and FITCNB(). The learned classification rule is then used in PREDICT() to estimate the responses for a set of standardized test data points.

30.16.3 Hydrological Hazard

This example deals with hydrological hazard on the standard dam ($\frac{B_1}{H_1} = 0.7$). Material and modeling are selected based on Table 30.20. The performance of three classification methods are studied for various numbers of training data points. The value of N_{trn} varies from $1e3$ to $1e4$ and from $1e2$ to $1e3$ in crude MCS and MCS-IS, respectively. A set of $1e6$ test data points are used to estimate the failure probability, which is compared with true value of P_f. Figure 30.50 reports the mean and standard deviation of the normalized estimation error over 50 trials. In each trial, N_{trn} data points are chosen randomly from the total number of $1e6$ data points for crude MCS and $1e4$ data points for MCS-IS. The normalized estimation error for each trial is defined as $|P\widehat{P}_f - P_f|/P_f$, where $P\widehat{P}_f$ and P_f are the estimated and true values of the failure probability, respectively. We compute the mean and standard deviation of 50 normalized estimation errors.
It is observed that the KNN classification method has much higher accuracy on crude MCS compared to MCS-IS. This is mainly due to the fact that KNN depends heavily on the local structure of the data which may not be preserved under Importance

Algorithm 2 Estimation of P_f via Machine Learning Techniques

Input: $\mathbf{X}_{\text{trn}} \in \mathbb{R}^{N_{\text{trn}} \times 6}$, $\mathbf{y}_{\text{trn}} \in \mathbb{R}^{N_{\text{trn}}}$, $\mathbf{X}_{\text{test}} \in \mathbb{R}^{N_{\text{test}} \times 6}$, `classification-method`
Output: estimated failure probability $\hat{P}_f$
Training classifier:

for $i = 1, \ldots, 6$ **do**
  $\mu_i = \text{MEAN}(\mathbf{X}_{\text{trn}}(:, i))$
  $\sigma_i = \text{STD}(\mathbf{X}_{\text{trn}}(:, i))$
  $\tilde{\mathbf{X}}_{\text{trn}}(:, i) \leftarrow (\mathbf{X}_{\text{trn}}(:, i) - \mu_i)/\sigma_i$
end for
if `classification-method=KNN` **then** model $\leftarrow$FITCKNN($\tilde{\mathbf{X}}_{\text{trn}}$, $\mathbf{y}_{\text{trn}}$)
end if
if `classification-method=SVM` **then** model $\leftarrow$FITCSVM($\tilde{\mathbf{X}}_{\text{trn}}$, $\mathbf{y}_{\text{trn}}$)
end if
if `classification-method=NBC` **then** model $\leftarrow$FITCNB($\tilde{\mathbf{X}}_{\text{trn}}$, $\mathbf{y}_{\text{trn}}$)
end if

Estimation via trained classifier:

for $i = 1, \ldots, 6$ **do**
  $\tilde{\mathbf{X}}_{\text{test}}(:, i) \leftarrow (\mathbf{X}_{\text{test}}(:, i) - \mu_i)/\sigma_i$
end for
$\hat{\mathbf{y}}_{\text{test}} \leftarrow$PREDICT(model, $\tilde{\mathbf{X}}_{\text{test}}$)
$\hat{P}_f = |\{i : \hat{\mathbf{y}}_{\text{test}}(i) = -1\}|/N_{\text{test}}$

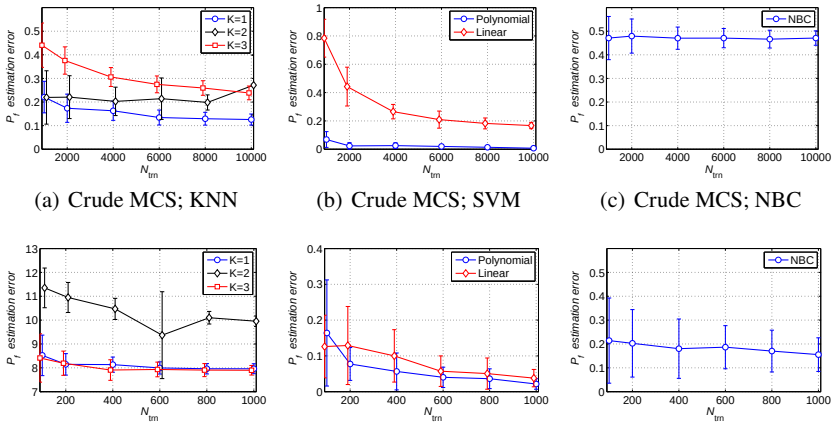

(a) Crude MCS; KNN (b) Crude MCS; SVM (c) Crude MCS; NBC

(d) MCS-IS; KNN (e) MCS-IS; SVM (f) MCS-IS; NBC

Fig. 30.50: Failure probability estimation error using various machine learning techniques for the pilot hydrological hazard model

Sampling assumptions. Moreover, based on Figure 30.50(a), KNN method with $K = 1$ performs more accurately compared to $K = 2, 3$.
The accuracy of SVM classification technique using both linear and polynomial kernel functions is reported in Figures 30.50(b) and 30.50(e). It is shown that the polynomial kernel function leads to more accurate estimates of P_f for both crude

MCS and MCS-IS. This means that the polynomial kernel function is capable of dealing with the nonlinearity in the structure of the data in this example.
Finally, the accuracy of NBC is investigated for both crude MCS and MCS-IS in Figures 30.50(c) and 30.50(f). It is observed that the Naive Bayes Classifier using MCS-IS has higher accuracy than crude MCS. In fact, the estimation error is reduced by a factor of 2 using MCS-IS.

30.16.4 Aging Hazard

In this section, four sets of experiments are performed to investigate the estimation of failure probability under the aging condition: 1) SVM using crude MCS, 2) SVM using MCS-IS, 3) KNN using crude MCS, and 4) NBC using MCS-IS. In Figure 30.51(a), the mean and standard deviation of the estimated P_f is reported and compared with the reference value of P_f^{MCS} using $1e6$ simulations. It is observed that all four classification strategies lead to accurate estimates of P_f (i.e., the differences between estimated and true values are negligible). However, in the small scales, SVM family underestimates the failure probability while KNN and NBC overestimate P_f. To further investigate the performance of these methods, a plot of estimation error in log scale is provided in Figure 30.51(b). In general, the estimation error is reduced when time passes (therefore, increasing the failure probability). Among four methods, SVM using crude MCS has the best performance. Furthermore, SVM using MCS-IS has the most stable condition as the estimation error has a smaller reduction rate. Finally, the P_f estimation error in NBC using MCS-IS is higher than SVM using crude MCS by one order of magnitude.

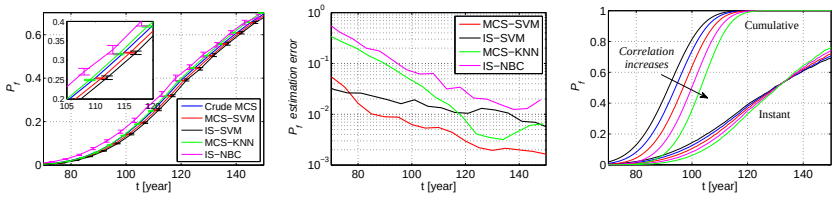

(a) Instant P_f comparison (Uncorrelated) (b) Instant P_f estimation error (Uncorrelated) (c) Instant *vs.* cumulative P_f (Correlation varies 0.0:0.25:1.0)

Fig. 30.51: Estimated failure probability under aging risk

Figure 30.51(c) investigates the impact of correlation between c_{rc} and ϕ_{rc} on the failure probability. Also shown in this figure is the comparison between instant and cumulative failure probabilities. Correlation varies 0.0:0.25:1.0 (zero means two variables are independent and one means they are fully correlated).

30.16.5 Seismic Hazard

Seismic hazard is modeled using seismic coefficient method by adding the inertia force of the dam itself and hydrodynamic pressure to demands. Figure 30.52(a) shows the failure probability as a function of seismic coefficient, α_{gm}. Two broad models are considered: 1) uncorrelated random variables (zero) and 2) fully correlated random variables (unit) between friction angle and cohesion.

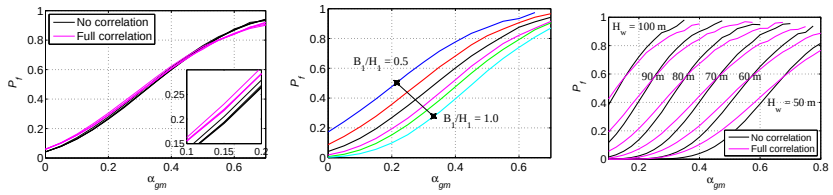

(a) t_e varies; Corr *vs.* Uncorr RVs (b) $\frac{B_1}{H_1}$ varies; Uncorr mode (c) H_w varies; Corr *vs.* Uncorr RVs

Fig. 30.52: Estimated failure probability for different dam classes, correlation and water level subjected to seismic hazard

Figure 30.52(b) shows the failure probability of different dams classes. In all cases, the uncorrelated random variable assumption is considered and t_e is one. As expected, decreasing the $\frac{B_1}{H_1}$ ratio, increases the failure probability. For example, comparing P_f for $\frac{B_1}{H_1} = 0.5$ and $\frac{B_1}{H_1} = 1.0$ shows that the former is about five times the latter at $\alpha_{gm} = 0.2$ and twice at $\alpha_{gm} = 0.5$. Based on this figure, even under very small α_{gm} values, there is a jump in P_f value.
Next, the simultaneous impact of seismic loading and reservoir water levels are studied on the failure probability, Figure 30.52(c). Again the fully correlated and uncorrelated modes are contrasted. As in Figure 30.52(a), the curves are crossing at $P_f = 0.6$. Increasing H_w increases P_f. For the half reservoir (i.e., $H_w = 50$ m), the probability of failure is not unit even for a large value of seismic coefficient (i.e., $\alpha_{gm} = 0.8$). For the full reservoir (i.e., $H_w = 100$ m), the probability of failure under relatively small α_{gm} values (i.e., 0.1) is already 40%.

30.17 Soft Computing based Material and Modeling Uncertainty Quantification in Gravity Dams

This section which adapted from Hariri-Ardebili and salazar [382] presents a comparative study of the predictive capacity of five soft computing algorithms in the frame of probabilistic analysis of dams. Both the material and modeling uncertainties are accounted for including 14 random variables. The effects of the RVs in the displacement and stress responses of the system are identified. Finally, a geometry-

based meta-model is proposed for the initial sketch out of gravity dams in an optimal way.

30.17.1 Case Study Dam

Koyna Dam is used as the pilot case study for numerical simulations. The height of the central non-overflow monolith is 103 m, the thickness at the base and at the crest are 70.2 m and 14.8 m, respectively. Figure 30.53(a) shows the 3D slice view of the geometry model for the dam (including the base dimensions) prepared in ANSYS [37]. In the current paper, a 2D plane strain model is used to reduce the computational cost. The finite element mesh for the dam-reservoir-foundation system is shown in Figure 30.53(b). Four-node, linear elastic elements are used in the dam and foundation domain while the water is modeled using pressure-based elements. Solid and fluid elements are in interaction at the dam-water interface as well as the foundation-water interface.

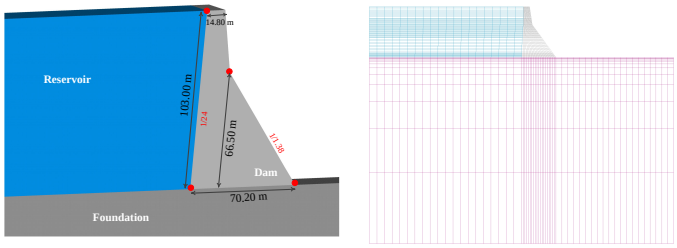

(a) Geometry and dimensions (b) Finite element mesh

Fig. 30.53: Description of case study, Koyna Dam, including the dam body, foundation, and reservoir

Table 30.21 represents the material properties for mass concrete and the foundation rock. It includes the mean, coefficient of variation (COV), and the truncation bound. Normal distribution is assumed in all cases. Applied loads on the system are: self-weight, hydrostatic pressure (normal water level (NWL) is at 91.75 m for the pilot model), bottom sediment (wave reflection coefficient for the reservoir bottom materials is assumed to be 0.75), and earthquake induced loads (both inertia and hydrodynamic).

30.17.2 Prediction Tasks

Maximum crest displacement and maximum vertical stress at heel are chosen as two QoIs. The objective is to compare different soft computing (SC) techniques in prediction of structural response, as well as their relative performance:

Table 30.21: Material properties for the concrete and foundation

ID	Quantity	Symbol	Unit	Mean	COV	Truncation
M_1	Concrete modulus of elasticity	E_c	GPa	24	0.10	[19.1 28.8]
-	Concrete Poisson's ratio	ν_c	-	0.2	-	-
M_2	Concrete mass density	ρ_c	kg/m^3	2,470	0.1	[2,160 2,790]
M_3	Concrete hysteretic damping	η_c	-	0.06	0.33	[0.02 0.10]
M_4	Foundation modulus of elasticity	E_f	GPa	21.5	0.10	[17.7 25.4]
-	Foundation Poisson's ratio	ν_f	-	0.33	-	-
M_5	Foundation mass density	ρ_f	kg/m^3	2,680	0.1	[2,320 3,040]
M_6	Foundation hysteretic damping	η_f	-	0.05	0.40	[0.02 0.08]

$$
\begin{aligned}
MAE &= \frac{\sum_{i=1}^{N}\left|QoI_i^{FE}-QoI_i^{SC}\right|}{N}\\
MAPE &= \frac{100}{N}\sum_{i=1}^{N}\left|\frac{QoI_i^{FE}-QoI_i^{SC}}{QoI_i^{FE}}\right|\\
ARV &= \frac{\sum_{i=1}^{N}\left(QoI_i^{FE}-QoI_i^{SC}\right)^2}{\sum_{i=1}^{N}\left(QoI_i^{FE}-\bar{QoI}^{FE}\right)^2}
\end{aligned}
\tag{30.15}
$$

where N is the size of the test set, QoI_i^{FE} are the observed outputs from finite element, $\bar{QoI}^{FE}$ is the mean value, and QoI_i^{SC} are the predicted values by SC. Prediction tasks (PT) can be summarized as follows with increasing complexities, Figure 30.54:

PT-1 : The pilot dam with fixed reservoir at NWL and six material properties as RVs; 10,000 realizations were used for algorithm comparison.
PT-2 : Scaled pilot dam with fixed reservoir at NWL and six material RVS. Eight different scale factors (SF) are used for scaling the dam size up and down.
PT-3 : The pilot dam with variable water level (simulating the flooding conditions) and also six material properties as RVs.
PT-4 : A class of different dam shapes (with seven RVs controlling the geometry), variable water level, and six random material properties.
PT-5 : The pilot dam is analyzed to assess the sensitivity of the predictive models on multiple points along the height of the dam (and not a single-targeted task).

Results of PT-1 and PT-4 is presented in this book.

30.17.3 PT-1: Pilot Model

The first prediction task (i.e. PT-1) is the full analysis of the Koyna Dam. Assumptions and procedure are summarized as follows:

- The geometry of the dam and the water level is fixed.
- Initially, 10,000 simulations are performed in which only the six material properties are RVs.

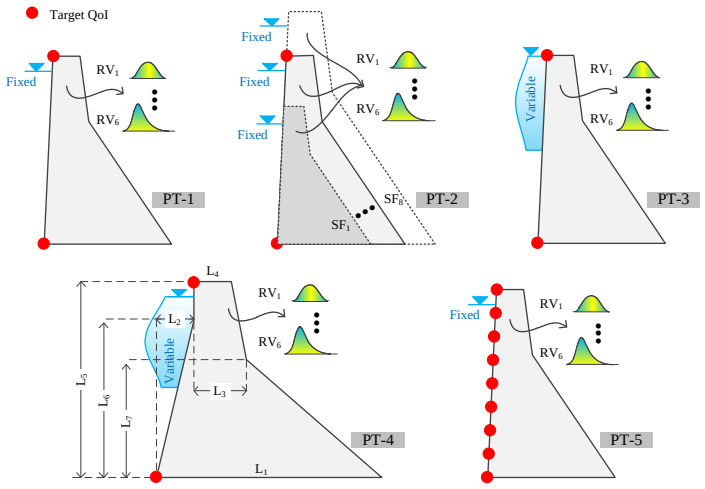

Fig. 30.54: Schematic presentation of different prediction tasks

- Five different SC methods are used for prediction.
- Two QoIs are studied, i.e. crest displacement and heel stress.
- Three metrics are used to evaluate the accuracy of prediction, Equation 30.15.
- Different sample sizes are used for training, namely 50, 100, 200, 300, 500, 1,000 and 2,000.
- The rest of the simulations (8,000) are taken as external validation to control the accuracy.
- Evaluation is based on the validation set.
- For each training set, 100 iterations are repeated to account for the randomness in realizations of the RVs, as well as in the training process of the algorithms. Results are presented as mean and mean $\pm$ standard deviation (STD).
- To prevent poor performance of the SC models when extrapolating, the maximum and minimum value of each RV are always included in the training set.

Figure 30.55 presents the variation of the prediction accuracy for different training sets, SC algorithms, QoIs and metrics. Major observations are:

- In general (as expected), increasing the number of training samples reduces the mean and STD of the error for all metrics and SC techniques.
- NN provides the highest accuracy for both outputs, followed by SVM. The RF is the worst case, especially for the smaller N_{train}.
- The NN, SVM, and BRT reach stability after about $N_{train} = 500$. However, similar results are obtained with $N_{train} = 300$, which can be useful for practical/engineering purposes.

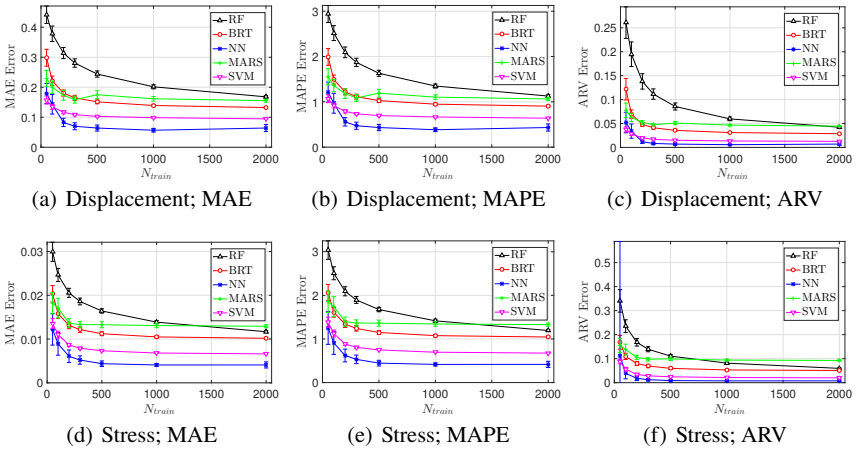

(a) Displacement; MAE (b) Displacement; MAPE (c) Displacement; ARV

(d) Stress; MAE (e) Stress; MAPE (f) Stress; ARV

Fig. 30.55: Prediction accuracy of the algorithms in PT-1 considered for the validation set (8,000 cases) and 100 iterations

- Results are similar for both displacement and stress in relative terms (MAPE and ARV). The differences of displacement and stress in MAE is due to the range of variation of both variables.

30.17.4 PT-4: Material and Modeling Effect

Finally, the shape of the gravity dam is also assumed to be unknown (i.e. variable) in addition to the material randomness and water level. This is, in fact, a very important topic for users dealing with a diverse portfolio of dams. Developing a general approach which can be used for different dam shapes is of interest for many big dam owners (e.g. USBR). There are several evidences that dam design companies try to correlate the response of dams in different size and shape.
To account for different dam shapes (note that this is different from SF used in PT-2), a generic form for the gravity dam is proposed with 7 variable lengths as shown in Figure 30.54 (L_1 to L_7). The following relations are used in order to generate a random dam shape, Figure 30.56:

- L_1 = rand (50, 150) m.
- $L_2 = L_1 \times \alpha_1$; $\alpha_1 = \texttt{rand}(0.00, 0.03)$
- $L_3 = L_4 \times \alpha_3$; $\alpha_3 = \texttt{rand}(1.00, 1.15)$
- $L_4 = L_1 \times \alpha_2$; $\alpha_2 = \texttt{rand}(0.12, 0.24)$
- $L_5 = L_1 \times \alpha_4$; $\alpha_4 = \texttt{rand}(1.20, 1.50)$
- $L_6 = L_5 \times \alpha_5$; $\alpha_5 = \texttt{rand}(0.30, 0.70)$
- $L_7 = L_5 \times \alpha_6$; $\alpha_6 = \texttt{rand}(0.75, 0.90)$
- $WL = L_5 \times \alpha_7$; $\alpha_7 = \texttt{rand}(0.50, 1.00)$

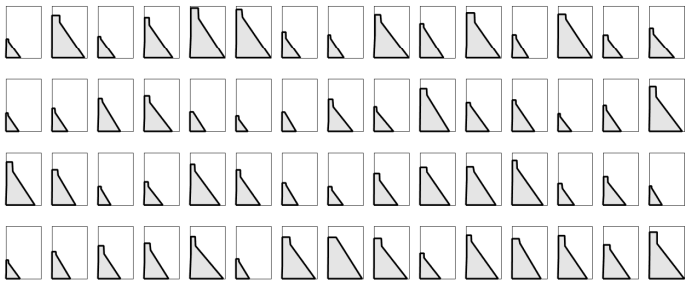

Fig. 30.56: The first 60 random gravity dam shapes generated based on a Matlab code; the box size is 150 $\times$ 225 m in all cases

Figure 30.57 shows the comparison of the algorithms in terms of prediction accuracy. A similar pattern is observed, with the NN model featuring highest accuracy. With so much uncertainty, prediction accuracy decreases compared to previous tasks. The results suggest that the training set size should be enlarged for stable results (in particular for heel stress). However, the NN model was capable of predicting both outputs with around 6% error. The displacement-based error variation for different SC algorithms are well-separated compared to stress-based errors.

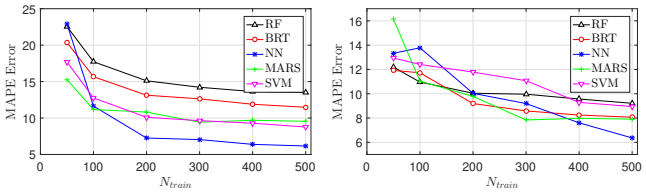

(a) Displacement-based (b) Stress-based

Fig. 30.57: Prediction accuracy for the algorithms in PT-4 (only based on MAPE)

Next, the results of the sensitivity analysis of the 6+1+7=14 RVs and the NN model are shown in Figure 30.58 for both displacement and stress QoIs. The results are based on the model trained with 500 samples and 100 iterations. The major observations are:

- The impact of material randomness is overshadowed with modeling/geometry uncertainty.
- The most influencing RV is L_5 (dam height) for both QoIs, followed by L_7 (neck height) for displacements and by L_1 (base length) for heel stress.
- The water level, WL, has positive effect on both QoIs, with higher impact on stress. However, it has lower relevance than the mentioned geometrical parameters.

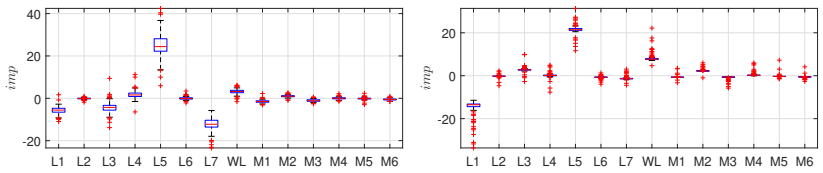

(a) Displacement-based (b) Stress-based

Fig. 30.58: Relative influence of the predictors for 100 training repetitions; and partial dependence on WL and shape

- The impact of each geometry is next discussed which is consistent with the physics of the problem in all cases:
  - L_1 (base length) has negative impact on both QoIs (mainly dominates stress).
  - L_2 and L_6 (location of upstream slope) have practically no impact on the response quantities.
  - L_3 (width of the lower neck) has negative impact on displacement as increasing it increases the stiffness and thus, reduces the displacement. On the other hand, it has a positive impact on stress as it increases the weight.
  - L_4 (width of the upper neck) has practically no impact on the base stress and a slight positive impact on the crest displacement.
  - L_5 (dam height) is the most effective parameter and has a positive correlation with both QoIs.
  - L_7 (neck height) has a negative impact on displacement, as increasing it makes the neck shorter (and stiffer) and reduces the displacement. It does not have practically any impact on base stress.
- The relative importance of 6 material RVs is qualitatively similar to those obtained in the pilot model, though lower as compared to the geometrical parameters.

The findings in Figure 30.58 are further supported by detailed dependence plots in Figure 30.59. General observations are similar to those explained for the sensitivity plots. However, the dependence plots show the linear or nonlinear trend of the QoIs with respect to input parameters. Of more importance is the sigmoid shape of the L_5 (so far the most important parameter) with respect to QoIs. The narrow upper/lower bound of water level also confirms the direct and strong correlation of this external load on the dam response.

30.18 Polynomial Chaos Expansion for Uncertainty Quantification in Dam Engineering

This section which adapted from Hariri-Ardebili and Sudret [398] aims to investigate the application of Polynomial Chaos Expansion (PCE) in concrete dams. The main objective of this paper is to answer the following questions: 1) How to properly

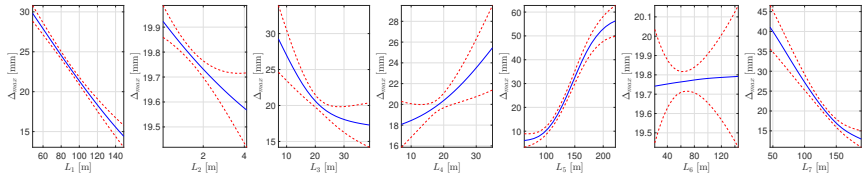

(a) Displacement-based; (geometry)

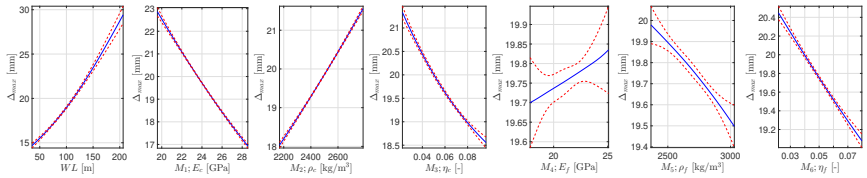

(b) Displacement-based; (WL and material)

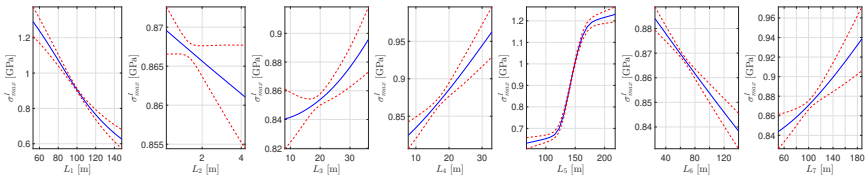

(c) Stress-based; (geometry)

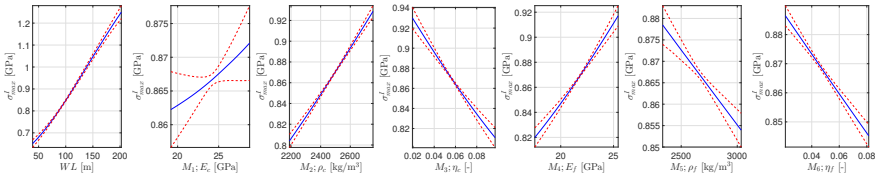

(d) Stress-based; (WL and material)

Fig. 30.59: Partial dependence plots for 14 RVs in PT-4

employ the PCE meta-models in practical dam engineering problems?, 2) How to interpret the results from meta-modeling?, 3) How to use the PCE for uncertainty quantification?, and 4) What are the main advantages and potential limitations of the PCE in dam engineering applications?

30.18.1 Case Study Dam

Four examples of concrete dams with different complexities are explained in this section. They are: 1) analytical model of a gravity dam, 2) simplified finite element analysis of a gravity dam, 3) detailed coupled analysis of an arch dam-foundation-reservoir system, and 4) frequency analysis of an arch dam with stage construction. Each of these problems includes different features and complexities and seek different

QoIs related to the concrete dam safety assessment. Figure 30.60 summarizes all these problems with a representative plot including the loading and sample results.

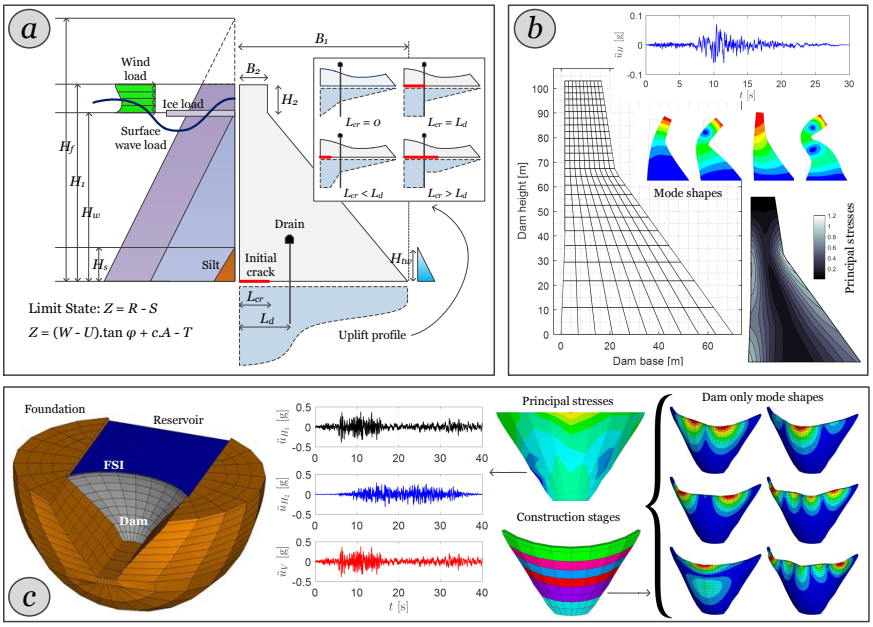

Fig. 30.60: Model description of four case studies in this paper including geometry, loads, and sample QoIs; (a) analytical gravity dam; (b) 2D simplified finite element gravity dam model for seismic analysis; (c) 3D reservoir-foundation-arch-dam for both seismic analysis and free vibration

30.18.2 Analytical Gravity Dam Model

This case study is a classical reliability analysis of a gravity dam based on limit equilibrium method. The applied loads are: 1) self-weight W, 2) static uplift pressure U, 3) hydrostatic (based on normal or flood water levels) pressure P_{hyd}, 4) silt pressure P_{silt}, 5) ice pressure P_{ice}, 6) wind load P_{wind}, and 7) surface wave load P_{wave}. The uplift pressure is updated (as a function $g(.)$) based on the crack length L_{cr}, drain location L_d, the head water H_w, and tail water H_{tw}, pressures. Figure 30.60(a) illustrates all the effective loads as well as the dam dimensions. In this showcase, the LS function is presented explicitly and the material properties and the static loads are all assumed to be random variables. A global LS is used in this example which accounts for the sliding at the dam-foundation interface.

PCE models are developed based on LAR method with q set to 0.75. Different DOEs (with 50 to 400 points) are used to evaluate the sensitivity and accuracy of the prediction. Figure 30.61 shows a sample prediction (in the first row) and corresponding

expansion coefficients (the second row). Four initial (and deterministic) DOE values are considered, i.e. 50, 100, 200 and 400. Obviously, increasing the initial sample size, increases the accuracy of the PCE model. Also it increases the number of expansion coefficients required for the meta-modeling.
In Figures 30.61(a) to 30.61(c) (and in general, in all the similar plots in this paper), the estimated QoIs are shown in the vertical axis, Y^{PCE}, while the analytical (or FEM) results are in the horizontal axis, $Y^{Analytical}$ (or Y^{FEM}). In this first example, Y equals to Z (i.e., limit state). In Figures 30.61(e) to 30.61(g), the expansion coefficients, y_α, are shown in a logarithmic form. Since the coefficients might be positive or negative, a "black dot" (inside the circle) is used to distinguish the positive ones. Results are also categorized by color and size for different degrees, p. All the degrees up to three are shown separately, while the higher order ones are collected under $p > 3$. Note that not all the α have value. For example, there are only 16 coefficients in Figure 30.61(e).

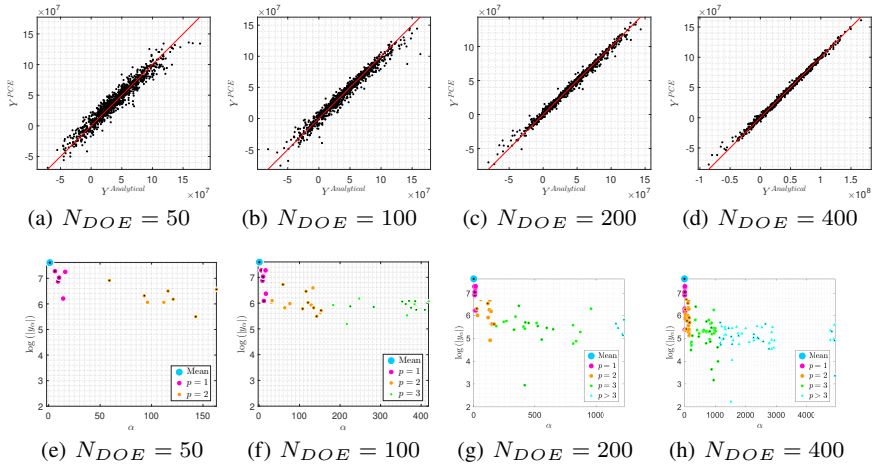

(a) $N_{DOE} = 50$ (b) $N_{DOE} = 100$ (c) $N_{DOE} = 200$ (d) $N_{DOE} = 400$

(e) $N_{DOE} = 50$ (f) $N_{DOE} = 100$ (g) $N_{DOE} = 200$ (h) $N_{DOE} = 400$

Fig. 30.61: Example 1; PCE meta-model; LAR technique; Reference model $N_{LHS} = 1000$; N_{DOE} is variable; meta-modeling is based on Z

Since deterministic DOE values, used in Figure 30.61, cannot quantify the uncertainty in meta-modeling (due to the random sampling of the experimental design), a probabilistic version (with 100 replications) is presented in Figure 30.62. This figure, in fact, summarizes the mean and standard deviation (STD) of different metrics related to the meta-model as a function of N_{DOE}. The following observations can be drawn:

- Mean value is stable after $N_{DOE} = 100$, Figure 30.62(a). There is a large STD for the meta-models with N_{DOE} = 50.
- Variance of the meta-model output is increased by increasing the N_{DOE}, but its STD yields to a small value, Figure 30.62(b).

- The mean and STD of the number of non-zero coefficients is also increased by N_{DOE}, Figure 30.62(c). On average, a meta-model based on 200 DOE points has three times more expansion coefficients than the one based on 50 DOE points.
- Both the LOO and NEE residual errors decrease with increasing N_{DOE}, Figures 30.62(d) and 30.62(e). STD of the meta-model predictions with N_{DOE} equal to or greater than 200 is practically zero. This means that the obtained results do not depend anymore on the sampling of the DOE when its size is greater than 200.

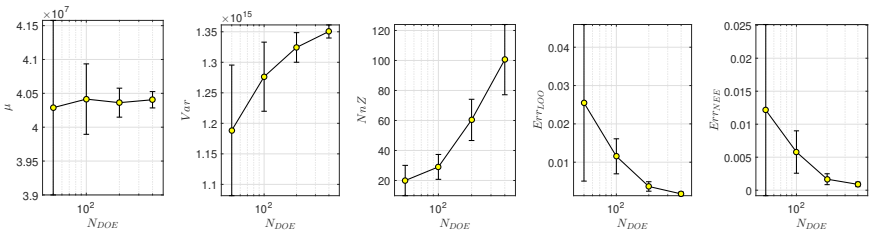

(a) Mean (b) Variance (c) Number of non-zero coefficients (d) LOO error (e) NEE error

Fig. 30.62: Example 1; Uncertainty quantification of PCE meta-model based on 100 replications of the analyses; N_{DOE} is variable; meta-modeling is based on Z

30.18.3 Simplified Gravity Dam Finite Element Model

This second example deals with simplified seismic analysis of a gravity dam. Figure 30.60 (b) shows the cross section of the dam including a relatively coarse mesh. The dam is modeled as a 2D finite element system, and the water is idealized by a fluid domain of constant depth and infinite length. The foundation rock is also idealized as a homogeneous, isotropic, viscoelastic half-plane. The applied loads are: dam self-weight, hydrostatic pressure, bottom sediment, and the (horizontal component of) ground motion excitation (Loma Prieta earthquake of 1989 at San Francisco 1295 Shafter station with 6.9 magnitude).

In this example, the material properties and the vibration characteristics for the concrete and rock are assumed to be uncertain. MCS is performed using Latin Hypercube Sampling (LHS) with N_{sim} = 1,000 dynamic analyses. No correlation is assumed among the RVs. QoIs are extracted in terms of the displacement and principal stresses. The results of these 1,000 simulations are later used in PCE meta-models.

A statistical method is used to quantify the meta-models with different DOE values, Figure 30.63. One hundred samples are taken for each N_{DOE}, and the mean and STD of different metrics are evaluated. Two QoIs are used (i.e. displacement and

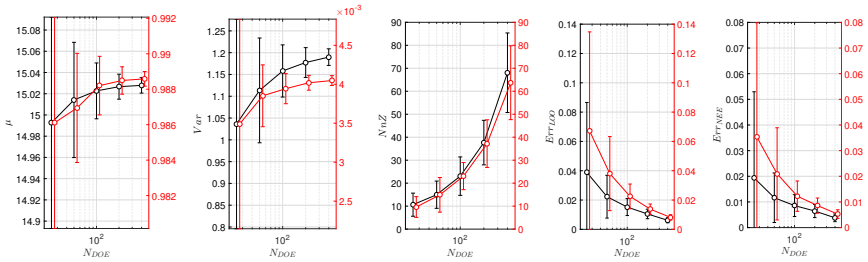

(a) Mean (b) Variance (c) Number of non-zero coefficients (d) LOO error (e) NEE error

Fig. 30.63: Example 2; Uncertainty quantification of PCE meta-model; N_{DOE} is variable; black line: crest displacement in [mm]; red line: heel vertical stress in [MPa]; Note: the red curves are shifted a bit right to avoid overlapping with black ones

stress) to contrast suitability of various outputs during surrogating. The following observations can be drawn:

- Mean value is nearly stable after $N_{DOE} = 100$, Figure 30.63(a). The STD of its variation is also reduced for both displacement and stress QoIs. There is no meaningful difference between the two QoIs.
- Variance of the meta-model is increased by increasing the N_{DOE}, while its STD yields a small value, Figure 30.63(b). The rate of increase is lower for the stress response.
- Although not surprising, the mean and STD of the non-zero coefficients is also increased by N_{DOE}, Figure 30.63(c).
- Both the LOO and NEE residual errors decrease with increasing N_{DOE}, Figures 30.63(d) and 30.63(e). For smaller N_{DOE} values, the stress QoI leads to higher error; however, both the QoIs yield to nearly same value at $N_{DOE} = 400$, i.e. less than 1% error, which is more than sufficient for an engineering purpose.

30.18.4 Coupled Arch Dam-Reservoir-Foundation Model

Two previous examples included 2D analysis of gravity dams. This third example addresses the seismic analysis of a 3D arch dam-reservoir-foundation coupled system. The foundation is assumed to be massless. The reservoir was simulated using 8-node isoparametric fluid elements. Fluid-structure interaction is modeled based on Eulerian-Lagrangian approach. The finite element model of the dam-reservoir-foundation system is shown in Figure 30.60 (c). Only three material properties are assumed to be uncertain, and the coupled system is excited using a three component ground motion record. QoIs are extracted in terms of displacement time histories and principals stresses.

Since the stress distribution in arch dams is the governing factor in safety assessment of these infra-structures, it is important to evaluate the capability of the PCE in prediction of spatial QoIs with the body. Figure 30.64 illustrates the main metrics for the first (S1) and third (S3) principal stresses within the dam body. A coarse mesh is used for this academic example; however, one can simply refine the element size. Moreover, only half of the dam is shown due to its symmetry. The following conclusions can be drawn:

- For S1, the higher values of the mean are observed close to the base and also in the vicinity of the crest. However for S3, the crest level next to abutment has the highest (absolute) mean stress value.
- In term of variance, moving upward (along the height) decreases the variance for S1. In the case of S3, the variance takes higher values at the bottom and crest while it is minimum in mid-height.
- The residual errors have, in general, a uniform pattern within the body. There are some localized areas in which the element's error is higher than the neighboring ones. This is limited to one element at the base of dam for S1, and one element next to the abutment in S3.

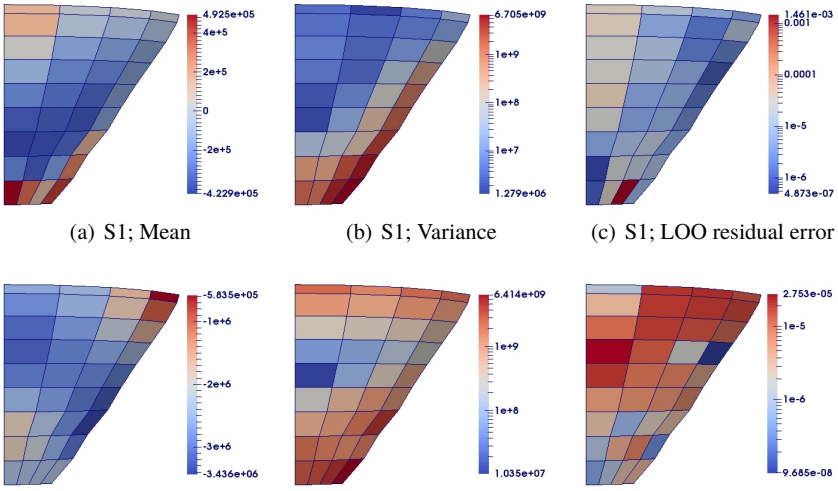

(a) S1; Mean (b) S1; Variance (c) S1; LOO residual error

(d) S3; Mean (e) S3; Variance (f) S3; LOO residual error

Fig. 30.64: Example 3; Coupled arch dam; PCE meta-model; LHS-based $N_{DOE} = 50$; elemental principal stresses over dam body; Unit = [Pa]

30.18.5 Layered Arch Dams Vibration Characteristics

The final case study deals with frequency analysis of the previous arch dam. As opposed to the third example, the concrete is not considered homogeneous anymore, and different values of moduli of elasticity are assumed for various layers. Overall, six stages of construction are assumed, and the random modulus of elasticity is assigned based on a uniform distribution in the range of (17.5, 32.5) GPa. All the other material properties are kept constant. QoIs are extracted in the form of vibration frequencies, participation factors and effective masses in six (translational and rotational) directions, and the mode shapes.

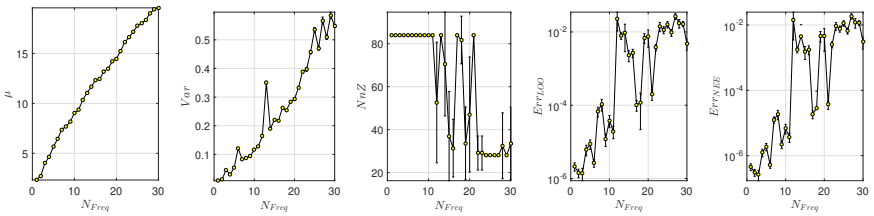

(a) Mean (b) Variance (c) Non-zero coefficients (d) LOO error (e) NEE error

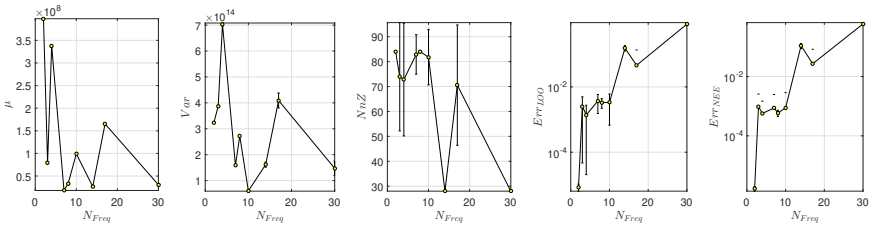

(f) Mean (g) Variance (h) Non-zero coefficients (i) LOO error (j) NEE error

Fig. 30.65: Example 4; Layered arch dam; $N_{LHS} = 1000$; $N_{DOE} = 200$; two QoIs

A batch with 200 initial DOEs is selected using LHS technique and considered to be the pilot model. Figure 30.65 summarizes the results of probabilistic PCE meta-model for different QoIs and directions. Two sets of results are studied:

- General frequency response, Figures 30.65(a) to 30.65(e).
  - The mean and variance both increase as a function of frequency. The mean is quite uniform, while there are some nonlinear variations for the variance.
  - The NnZ is constant and equal to 80 for the first 11 modes (without any dispersion).
  - Both the residual errors have similar and increasing trend, with relatively large variation and small dispersion.

- Effective mass in X direction, Figures 30.65(f) to 30.65(j).
  - These results represent all six directions. For other translational and rotational directions, one may drive similar conclusions.
  - The results are shown only for 9 effective modes.
  - There is no general observation for mean and variance.
  - In general, smaller frequencies have higher NnZ.
  - In general, both the residual errors are increased by frequency.

Part VI
Applications; Nuclear Structures

Chapter 31
Analysis of Nuclear Containment Structures; I Introduction

Abstract
This is the first of four chapters dedicated to the analysis of nuclear structures, or Containment Enclosure Building (CEB) more precisely. It constitutes an attempt to contextualize the complex, and seldom fully addressed, problematic of the safety of nuclear reactor enclosure buildings.
This chapter will begin with some general remarks associated with seismic analysis of nuclear structures. Then, a broad review of the literature related (primarily but not exclusively) to the probabilistic risk assessment of nuclear structures is presented. Finally, the third section will revisit the summary report of (what the authors consider) a landmark report by Sandia. This report [415] contains many recommendation for the nonlinear finite element analysis (many of which have not "'aged") that could be invaluable for the modern analyst.

31.1 Introduction

Given that seismic load is probably the most critical load in containment enclosure buildings (CEB), this, and following two, chapter is best introduced by quoting ASCE 4-16 [49]

> *Regulatory government agencies are frequently faced with decisions related to the seismic design of operating nuclear facilities... As new information becomes available, the design basis may be challenged. ... Because of its pervasive nature, an earthquake will"seek out" facility vulnerabilities... At issue is whether the changes can be accommodated within the inherent capacity of the original design or whether facility modifications are required.... current design practice does not provide a picture of the actual margin to failure, nor does it provide enough information to make realistic estimates of seismic risk... The seismic probabilistic risk assessment (SPRA) is an integrated process that includes consideration of the uncertainty and randomness of the seismic hazard, structural response, and material capacity parameters to give a probabilistic assessment of risk.*

Until fairly recently, the only imaginable new information was increased ground motion records resulting in increased demand (or stressors). On the other hand, there is increasingly concern of diminished capacity through concrete degradation resulting from ASR.

These concerns have been amplified by two major events: the Fukushima Daiichi Accident and the discovery of ASR in a nuclear power plant (Seabrook).
Hence, there is increased need to properly address the structural safety of nuclear power plants subjected to what is termed beyond design basis loads. Whereas there may be limited need to revisit seismic evaluations of CEB, the absence of regulatory provisions to handle ASR is of major concern. In its presence, industry and regulatory agencies enter uncharted territory. Based on recent evidence, the research/academic community has had practically no influence on related major decisions.

31.1.1 Guidelines

The integrity of a NPP is ensured by many guidelines. All of them have been written for the design of new structures, and only those related to SPRA address the existing NPPs.
General design principles are enunciated in ASME III [56]. ASCE/SEI 43-05 [51] stipulates that the seismic demand and structural capacity evaluations should have enough conservatism to achieve less than 1% probability of unacceptable performance for the design base earthquake (DBE) and that than 10% probability of unacceptable performance for a ground motion equal to 150% of DBE. These demands will necessitate the elaboration of fragility curves. Analysis guidelines can be found in ASCE 4-16 [49] where a "non-mandatory" evaluation beyond the design basis SPRA is suggested. A similar (but less explicit) set of guidelines is given by IAEA [454].

31.1.2 Challenges

In the spirit of ASCE 4-16 [49], the nuclear industry is confronted with mounting challenges to the design basis of existing NCVS:

Beyond Design Basis Loads Though severe accident management guidelines have long been in place prior to the Fukushima accident, the Tohoku earthquake[1] highlighted the fact that for some operating nuclear power plants, available seismic data and models show increased seismic hazard estimates [592]. As a result, orders were issued by the NRC to develop mitigation strategies for beyond design-basis external events [651].

Accidental and unanticipated damage. A perfect example is the delamination (or splitting crack along post-tensioning sleeves) resulting from the cable detensioning of Crystal-River 3 [712]. The reactor was ultimately decommissioned for financial reasons.

ASR Induced Ageing which has already affected an NCVS. Accordingly, the NRC has issued notices alerting NPP operators of this potential problem [645].

Second License Renewal Beyond 60 Years As of February 2018, the NRC has renewed the operating licenses of 89 commercial nuclear reactors through the

[1] It should be emphasized that despite its magnitude M_w=9.0-9.1, the earthquake did not directly cause substantial damage. Failure was caused by the ensuing tsunami.

process described in NRC [646] (from 40 to 60 years). The NRC and the industry are currently focusing on "subsequent license renewals" which would authorize plants to operate up to 80 years. The NRC has developed guidance for staff and licensees specifically for the subsequent renewal period. The first subsequent license renewal application, for the Turkey Point Units 3 and 4 reactors, was submitted to the NRC in January 2018 [657]. In anticipation for this requirement a joint NRC-DOE (Department of Energy) effort objectively ranked the safety significance of materials degradation issues, particularly as they relate to subsequent license renewal. Using a Phenomena Identification and Ranking Table (PIRT), ASR, acid attack and creep emerged as secondarily important mechanisms (following impact of irradiation) [348].

Design Safety Issues May be a major challenge as one may be applying modern safety issues (i.e. accounting for increased regional seismicity or concrete deterioration) not fully grasped at the time of the design.

These challenges beg for modern solutions suitable that can yield quantifiable safety assessment indicators such as fragility curves. At best, this will require at a dynamic analysis. This can be carried out through anyone of the following methods: a) static equivalent load; b) static pushover (linear or nonlinear, monotonic or cyclic); c) response spectrum analysis (RSA); and d) time history: linear or nonlinear analyses. Historically, engineers have favored RSM as it was not CPU intensive. However, one must recognize that the RSA is a very approximate method which only produces positive values of displacements and member forces which are not in equilibrium; thus demand/capacity ratios have very large errors. Interestingly, Prof. Wilson is reported to have said:

> *Ray Clough and I regret we created the approximate response spectrum method for seismic analysis of structures in 1962.... At that time many members of the profession were using the sum of the absolute values of the modal values to estimate the maximum member forces. Ray suggested we use the SRSS method to combine the modal values. However, I am the one who put the approximate method in many dynamic analysis programs which allowed engineers to produce meaningless positive numbers of little or no value... After working with the RSM for over 50 years, I recommend it not be used for seismic analysis.*
>
> [885]

In the context of design, demand in seismic assessment has traditionally been determined through an RSA and results linearly superimposed to those obtained from a static analysis with factored loads. Capacity in turn is assessed element by element in accordance with the provisions of **aci318**, Fig. 31.1(a). The dichotomy of a linear elastic analysis and a plastic design should be noted as it may cause the violation of the consistency condition of plasticity. Finally, some convoluted (heuristic and approximate) adjustments are made for the stress redistribution caused by cracking. The true structural safety factor remains unknown, even more so when localized concrete damage impact has not been properly accounted for.

Contrarily to the previous approach, a fragility analysis assesses the entire structure through multiple nonlinear transient analyses that will track the response throughout its load history. Ultimately probability of localized failure will be quantified. In some

types of analysis, the full capacity curve of the structure (as opposed to element in the preceding approach) can be determined if needed, Fig. 31.1(b).
Strength is not the only criteria, the so-called serviceability (unfactored or service loads) is equally if not more important for NCVS. In this context, this will govern the formation of concrete cracks that may constitute a pathway for radioactive gas (in case of core damage, and liner failure). However, cracks can not be estimated from a linear elastic RSA-based analysis (neither the corresponding displacements), but can only be captured from a nonlinear analysis where the large inelastic displacements can be indeed captured.

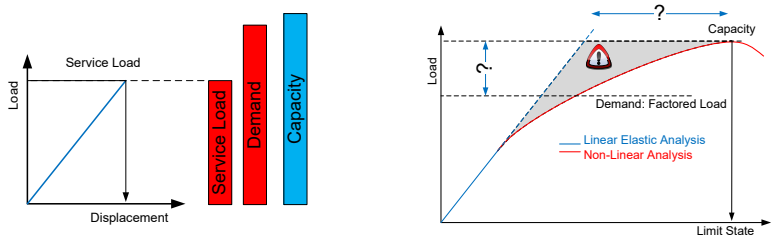

(a) Safety assessment of one elment (b) Fragility Analysis of a structure

Fig. 31.1: Concerns with nonlinear analysis

Hessheimer, M.F. and Dameron, R.A. [415] provided an excellent set of guidelines for the nonlinear analysis of NCVS; however, it seems to have been seldom consulted by published documents, and is by now mostly obsolete. More recently a short EPRI report [275] addressed concrete degradation, beyond-design basis analysis, forensic analysis of concrete structures, and structural modeling. A comprehensive set of guidelines were submitted to the NRC by the authors [756].

31.2 Contextual Framework

To place the subsequent studies in context, it is important that the literature be properly reviewed. Hence this section will begin with an overview of historical development followed by seismic assessment of NCVS in terms of seismic hazard analysis, numerical simulations, and probabilistic risk assessment. Then, the analyses of concrete structures (NCVS in particular) affected by ASR will be reviewed.

31.2.1 Historical Development

Whereas the emphasis of this book is on seismic capacity and fragility analysis, it is important to contextualize their role inside the broader scope of a seismic probabilistic risk assessment (SPRA) which is a well-established methodology within the nuclear industry.

Probabilistic risk (or safety) assessment (PRA) consists of an analysis of the operations of a particular nuclear power plant (NPP), which focuses on the failures or faults that can occur to components, systems or structures, and that can lead to damage and ultimately to the release of radioactive material, especially the fission products and actinides within the reactor fuel [112]. Hence, the analysis seeks to identify the initiating events and the sequence of possible events that can lead to various levels of damage.

The first attempt to categorize accidents levels was the seminal paper of Farmer [290]. Drawing on this early work, in 1972 the US Atomic Energy Commission initiated the first comprehensive assessment of the risks associated with nuclear power plants by examining the system design and operating practices at two specific plants and using composite models to represent site meteorology and population density. The results were published in WASH-1400 [873]. This document concluded that for plants analyzed, the risk of nuclear reactor accidents is much smaller than other man-made and natural events to which society is generally already exposed. Another important outcome of this document was an extension of the work of Farmer [290] to structure NPP's PRAs in three levels. Level 1: models the risk of damage of the reactor cored (*severe accident*); Level 2: analyzes the progression of an accident by considering how the containment structures and systems respond to the accident, which varies based on the initial status of the structure or system and its ability to withstand the harsh accident environment; Finally, Level 3: PRA is the *consequence analysis* resulting from radioactive material released in a severe accident. Hence, the safety philosophy of NPP design is built around the concept of defense-in-depth, which includes the concept of multiple barriers [53]. The NCVS being the final barrier against the release of radioactive material to the environment.

The 1979 accident at Three Mile Island substantially changed the character of the analysis of severe accidents worldwide. Kemeny [496] and Rogovin and Grampton [737] (the major investigations of that accident) recommended that PRA be used to complement the traditional deterministic methods of analyzing NPP safety and that probabilistic safety goals be developed for nuclear plants. The first PRA studies were limited to the assessment of events initiated by internal plant faults but were later extended to include external event initiators such as seismic leading to an SPRA [659]. In common practice today, the principal outputs of an SPRA are core damage frequency (CDF) and large early release frequency (LERF) [661]. In general for regulatory purposes it is adequate to only calculate CDF and LERF and no detailed Level 3 are required.

ASME [55] and EPRI [273] have developed guidelines and training for the performance of SPRA that are used by virtually all utilities in the U.S. for the analysis of their plants. Furthermore, prior to the Fukushima accident, all U.S. NPPs were required to perform an analysis of the risk of external events, including seismic through an Individual Plant Examination for External Events (IPEEE) [644] [272]. These assessments either used SPRA or a simplified-SPRA approaches.

It should be emphasized that an SPRA is not performed for the Operating Basis Earthquake (OBE) or Safe Shutdown Earthquake (SSE) ground motions but only for

the very low probability high intensity ones (frequency on the order of 1×10^{-6} per year or lower).
Finally, after Fukushima, plants were required to reevaluate the potential impact of external events on their structures [274] as in some cases the seismic stressor may have been underestimated [371].
In response to severe unanticipated seismic loads: a) the NCVS may fail to perform its function in maintaining leak tightness (liner damage and concrete cracking); and b) an internal structure supporting vital equipment (such as pumps, valves, pipes, or electrical cabinets) could lead to severe fuel damage. It should be emphasized that should there be no severe fuel damage (Level 1 above), it does not matter whether or not the NCVS maintains its integrity. Thus, the principal risk measure, CDF, is unaffected by NCVS integrity.
Whereas an SPRA study should include: 1) seismic hazard analysis; 2) structure/equipment fragility assessment; 3) accident sequence analysis; and 4) consequence (risk) evaluation analogies with subsequently developed Performance Based Earthquake Engineering (PBEE) for buildings is highlighted in Table 31.1

Table 31.1: Analogy between nuclear and building safety guidelines

Nuclear **SPRA**	Building **PBEE**
Relevant Documents	
Kennedy and Ravindra [498]	
ASME III [56]	FEMA P-750 [298]
ASCE/SEI 43-05 [51]	Applied Technology Council [40]
ASCE 4-16 [49]	Deierlein, Reinhorn, and Willford [234]
Steps	
1. Seismic hazard evaluation	1. Hazard Analysis → Intensity measure (IM) 2. Structural Analysis → Engineering demand parameter (EDP)
2. Component fragility evaluation	3.Damage analysis → Damage measure (DM); fragility curves
3. Plant system and accident sequence analysis	4. Loss analysis → Decision variable (DV)
4. consequence analysis	

31.2.2 Literature Survey

31.2.2.1 Seismic Hazard Analysis

A seismic risk analysis has to start with a crisp identification of the site seismic hazard parameters [856]. For nuclear sites, many analyses have been reported in the literature in terms of both deterministic and probabilistic seismic hazard analyses (PSHA). Ares and Fatehi [43] provided an excellent introduction to the problematic of seismic hazard analysis.

Lapajne and Fajfar [522] performed seismic hazard assessment for an existing NCVS in Slovenia that included multiple models to handle uncertainties in the data. Desai and Choudhury [242] performed PSHA, one-dimensional equivalent linear ground response analysis, and developed the design uniform hazard response spectra (UHRS) of critical sites in Mumbai, India. Mohanty and Verma [603] implemented a similar research on Kakrapar NCVS in western India. Choi, Choun, and Seo [193] developed a probability-based scenario earthquakes for the Korean NCVS site using PSHA data. The response spectra were further modified by a factor correction to incorporate the near-fault earthquake effects. Similar study was performed by Nakajima et al. [617]. Klügel [505] addressed the large scale PSHA of a Swiss NCVS and the corresponding potential overestimation of the seismic hazard in low seismic activity zones due to the inherent possibilities of unconstrained accumulation of uncertainties. Similar research was reported by Renault [729].

31.2.2.2 Numerical Simulations

Broadly speaking, there are two models for the FE analysis of NCVS: a) simplified LMSM approach; and b) detailed continuum model (using either solid or shell elements). The latter may include structural components [317, 642, 781] and non-structural ones (i.e. reactor vessel and steam generator). However, it is a CPU intensive endeavor, specially in the nonlinear regime [619]. The former is a much simplified one that consists of several lumped masses which form a column or tree as a numerical equivalent substitute to the actual structure [617, 528, 682].
Modeling of foundation was addressed by Xu et al. [894] who performed FE simulation of deeply embedded and/or buried NCVS structures. Simplified *vs* detailed soil-structure interaction (SSI) was investigated, and the seismic-induced earth pressures on the buried structures was quantified. Nakamura [618] performed seismic response analyses of a nuclear reactor building deeply embedded in inhomogeneous soil considering frequency-dependent soil impedance in the time domain. Coleman, Bolisetti, and Whittaker [209] developed a nonlinear SSI model for NCVS which could be easily implemented in time-domain numerical codes. Kumar, Raychowdhury, and Gundlapalli [516] investigated the seismic response of a NCVS modeled with both nonlinear Winkler springs, dashpots and gap elements in the context of bi-directional ground motions. Kabanda, Kwon, and Kwon [485] performed a nonlinear time domain analysis focusing on the SSI in a nuclear power facility by first comparing the response through time and (simpler) frequency domains. They determined that the equivalent-linear frequency domain analysis amplifies some frequencies and results in higher structural acceleration than the nonlinear time domain analysis method which should be the preferred method. Ryu et al. [743] proposed a 3D radial-shaped dynamic infinite elements fully coupled to finite elements for SSI analysis of NCVS system in a horizontally layered medium. Nakamura et al. [620] studied the impact the irregular ground shape and adjacent buildings on the 3D nonlinear seismic response of NCVS buildings and highlighted its influence.
Joint elements to model the soil structure interface was investigated by Saxena, Paul, and Kumar [774]. Base-isolation for NCVS has been numerically explored by

various researchers [263, 441, 444, 913, 690, 184, 514, 513]. In particular, Medel-Vera and Ji [586] performed an extensive comparative study of various seismic protection systems. Multiple adjacent NCVS require special attention. This potential interaction was studied by [359, 360, 525, 777].

31.2.2.3 Probabilistic Risk Evaluation

In seismic reliability analysis the total failure probability is determined by combining the fragility curve – representing the response of the structure to seismic excitation – with the seismic hazard curve (Chapter 23). The determination of fragility curves has a long tradition in the nuclear industry and reaches back to the 1970s [908].
There has been a gradual shift toward probabilistic risk evaluations in recent years. Kennedy and Ravindra [498] were the first to introduce the concept of seismic fragility for NCVS. Fragility curves are conditional failure frequency curves plotted against peak ground acceleration (PGA). This general framework accounted for both aleatory and epistemic uncertainties. This first study was based on available data combined with judicious extrapolation of design information from plant structures and equipment. Medel-Vera and Ji [585] proposed a very comprehensive framework for seismic probabilistic risk analysis of NCVS based on simulated accelerograms. This method neither used ground motion prediction equations nor Monte Carlo simulation (MCS). However, it demands longer use of computer resources as it is based on large number of nonlinear dynamic analyses. Huang, Whittaker, and Luco [442, 443] proposed a new procedure for probabilistic seismic risk assessment of NCVS using elements adopted from performance-based earthquake engineering of buildings. Seismic fragility of both structural and non-structural components were studied using nonlinear response history analysis combined with MCS. Zentner et al. [907] presented the application of probabilistic analyses on a NCVS component based on MCS and fragility curves. They also discussed methods for statistical estimation of fragility curves.
Choi et al. [194] performed nonlinear LMSM seismic simulation of a CANDU containment structure subjected to 30 near-fault earthquakes. Fragility analyses were performed for both linear and nonlinear analyses. Hoseyni et al. [425] developed seismic fragility curves for a typical containment structure considering the SSI effect.
Aging and time-dependent response was first introduced by Ellingwood [270] within a probabilistic framework. Age-related degradation of structures and passive components critical to the the safe operation of NCVS was investigated by Braverman et al. [151] through the development of fragility curves. Guimarães, Cabral, and Lapa [350] further proposed the application of an adaptive neural fuzzy inference system to determine the fragility curves in degraded NCVS passive components. Huang et al. [440] investigated the long-term performance (caused by shrinkage, creep, and relaxation of pre-stressing tendons) of a typical NCVS structure using a nonlinear FE model.
Sensitivities and uncertainties of FE model were quantified by Baušys et al. [90]. Response surfaces was used by De Grandis, Domaneschi, and Perotti [233] in de-

termining seismic fragility functions for equipment components in NCVS. System fragility, determined through combination of component ones accounting for both aleatory and epistemic uncertainties, was performed by Kim, Choi, and Park [503]. Finally, and most recently [908] presented an excellent review of existing approaches and applications of fragility analysis methods.
A complete probabilistic study of a nuclear power plant component based on Monte Carlo simulation and evaluation of fragility curves was presented by Zentner et al. [907]. Also discussed are different methods for statistical estimation of fragility curves and comment on the choice of the ground motion parameter. It was shown that appropriate ground motion parameter can reduce uncertainty.

31.2.3 Anatomy of a Probabilistic Seismic Analysis

With reference to the outcome of an SPRA mentioned above, this study is limited to the first two components and four steps are defined and then used, Fig. 31.2:

Aleatory Uncertainties represent variability that cannot be reduced but can be characterized. In this study, it is associated with ground motion selection. This starts with the hazard curves, site identifications, deaggregation model, and site specific acceleration response spectra. Finally, a set of real ground motions are selected and scaled to be consistent in the aggregate with the design response spectrum [522, 476, 254, 150]. Alternatively, one may generate synthetic ground motion or even intensifying acceleration functions [576, 730].

Epistemic Uncertainties represent variability that can be reduced by data collection or experimentation. In this study, it is associated with material and modeling and is best accomplished through Monte Carlo Simulation (MCS) Family [852, 385]. The finite element model preparation is included in this block.

Finite Element Simulations where the preceding two uncertainties are combined and dynamic analyses performed. Again, whereas response spectrum method (RSM) was adequate early on [53], time history is now strongly recommended. The analyses should be nonlinear so as to capture the various levels of engineering demand parameters (EDP). Different techniques exist for multiple dynamic analyses [849, 468, 469, 907, 440].

Post-Processing of the results to extract EDPs, construct capacity functions [387], and finally compare the results with multiple limit states (LS) functions and drive fragility curves or surfaces Baker [79], Porter [701], and Huang, Whittaker, and Luco [442, 443].

Finally, it should be noted that not all SPRA encompass the epistemic uncertainties, and few of them perform a nonlinear time history analysis.

31.3 Revisit of Sandia's Report

A landmark document was written by the Sandia Laboratory Hessheimer, M.F. and Dameron, R.A. [415] and given the paucity of guidelines for the finite element

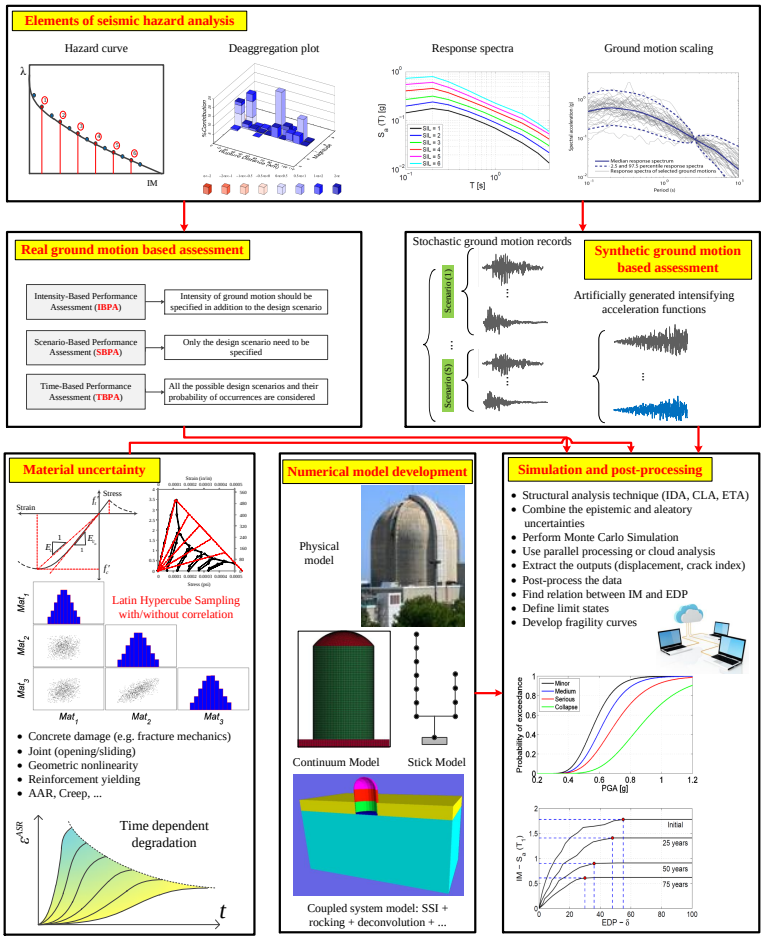

Fig. 31.2: Anatomy of a Seismic Probability Risk Assessment in Nuclear structures

analysis of CEB, this document will be summarized in here. A more extensive review of this document has been published by Saouma [748].

31.3.1 Background

31.3.1.1 Historical Context

Following World War II, safety concern associated with the emergence of commercial reactors, imposed a residence exclusion distance residence exclusion distance R

$$R(\text{miles}) = 0.01\sqrt{P(\text{KWt})} \tag{31.1}$$

thus for a 3,000 MWt plant, the exclusion distance is 17.3 m or 28 km. However, such an exclusion distance could not be imposed on nuclear powered submarine, often anchored in heavily populated cities, thus the Navy relied on rigorous accident prevention strategies along with the containment capability provided by the hull. Hence, in the early fifties, new commercial power reactors were built within the exclusion distance, and hence they were provided with a containment building. This was a major and decisive step allowing the construction of new plants close to populated cities as containments provided a barrier to the release of radionuclides. They were originally designed to provide safeguards against Design Basis Accident (DBA) by being able to withstand the peak pressure associated with the reactor coolant system blowdown and remain intact. They were not designed to withstand the loads associated with gross rupture of the vessel (not considered to be a credible event).

In the mid sixties there was much concerns about what was called euphemistically the "China syndrome". In 1974, the Advisory Committee on Reactor Safeguards (ACRS) concluded that the possibility of a Reactor Pressure Vessel (RPV) failure was less than 10^{-6} per vessel year and that a loss of coolant could indeed lead to the molten core breaching the lower head of the Reactor Pressure Vessel (RPV), penetrating the concrete containment basemat and coming into contact with the earth ("China Syndrome"). As a result, emphasis shifted from containment to prevention. Following a congressional request for a comprehensive assessment of reactor safety, a major probabilistic study was initiated in 1972 known as the Rasmussen report after the study director, Professor Norman Rasmussen of MIT, this study used a methodology pioneered by the Department of Defense (DOD) and NASA, called Probabilistic Risk Assessment (PRA) to predict the effects of component failures on large, complex systems. One of the tasks "...was to determine the thresholds and modes of failure of reactor buildings (containments)... when subjected to internal pressures and temperatures greater than the design values" for two prototypical plants. It was concluded that, while the risks of a core melt accident were small, they were more likely than previously thought, approximately 5×10^{-5} per reactor year. At 4:00 AM on March 28, 1979, the most severe accident in US nuclear history occurred at the Three Mile Island-2 plant. During the course of the accident, the containment building was subjected to a peak pressure spike (recorded by one sensor as 28 psig) when hydrogen, released when a Pressure Operated Relief Valve (PORV) was opened, ignited and burned with oxygen in the reactor building atmosphere. This accident put to rest the notion that severe nuclear power accidents were not credible. It also led to significant changes in the NRC and the industry and increased emphasis on the importance of containment survival during severe accidents. Following this accident the Nuclear Regulatory Commission (NRC) established both qualitative and quantitative safety goals, aand accelerated the NRC effort to study containment systems with the Sandia National Laboratory.

The first Sandia study had concluded that the few experiments on containment integrity had been either of too small a scale or lacked sufficient details of actual

plants to be of reliable use for understanding containment response to *beyond design basis* accidents. Based on this study, the program, which is summarized in this chapter report, was formulated to investigate containment systems subjected to beyond-design-basis loads for Light Water Reactor (LWR) containment systems subjected to loads beyond those specified in the design codes and not to determine the pressure carrying capacity of actual containments by testing scale models.

31.3.1.2 Containment Design

As of 2006, there were 103 US commercial light-water nuclear reactors (LWR) with operating licenses at 64 sites in 31 states, 69 pressurized water reactors (PWR) and 34 boiling water reactors (BWR). There are six basic containment types in the fleet. Four of these designs primarily use the passive pressure suppression concept, and two rely primarily on large, strong volumes and all of these containments erre constructed of either steel or concrete with a steel liner for leak tightness. Many containers have a large, thick basemat that provides seismic capability, supports the structures, and, while not designed for this, may serve to contain molten material during a severe accident.
The containment consists not only the structural concrete and/or steel shell surrounding the nuclear steam supply system, but also all of the penetrations (fixed and operable) and any other component which completes the pressure boundary. Any evaluation of containment integrity must also include an evaluation of these penetrations. The containment system is thus primarily designed to:

1. Contain any radioactive material that may be released from the primary system in case of an accident.
2. Protect the nuclear system from weather and other external threats such as missiles produced by earthquakes, tornadoes, wind, and in some cases aircraft impact.
3. Act as a supporting structure for operational equipment, e.g. cranes.

Historically, design practices for steel containments were developed solely by ASME which treats them as pressure vessels and specifies allowable stresses for the prescribed loads. Design practices for concrete containments, which were developed primarily by ACI and ASME, treats them as a structure. This approach combines the ACI practice of applying Load Factors to the design loads in consideration of their importance to safety, while retaining the concept of allowable stresses used by ASME.

31.3.1.3 Toward Containment Testing at Sandia

Given the importance of the containment as one of the cornerstones of the NRC "defense-indepth" strategy coupled with the lack of data and analysis tools to characterize containment performance to "beyond design basis" loads, the NRC commissioned Sandia to perform a "background" study, completed in 1981, to *develop a methodology for reliably predicting the ultimate capacity of steel and concrete containment structures under loadings caused by accidents and severe environments.* [130].

The review concluded that the *pressure tests of concrete containments indicate(d) that the models behave(d), in a gross sense, as predicted*. The concrete tests indicated, however, the importance of the behavior of the liner and penetrations which were not accurately represented in the models. The tests of actual containments were limited to small overpressures and provided little information on large deformation non-linear response.
Based on this review, an ambitious program was proposed to conduct tests of models of containment structures to failure and determine the suitability of existing analytical methods to predict failure by comparison with the test results.

31.3.2 Preliminary Considerations

31.3.2.1 Failure

Two types of failures were identified:

Functional Failure denote a loss of containment function, i.e. a leak rate in excess of the specified minimum leak rate of the containment, usually associated with a loss of liner integrity of loss of penetration sealing. Functional failure typically occurs when global deformations and strains exceed the elastic limit and/or local strains exceed the material strain limits.

Structural Failure includes the concept of "catastrophic rupture" in NUREG-1 150, or the occurrence of such large deformations (strains) of the liner or of a containment structural element, that a breach of the containment pressure boundary is predicted.

Practically, functional failure criteria are not particularly useful for conducting tests to determine the structural capacity of a containment vessel model, especially when the objectives are 1) to generate large inelastic response modes for comparison with analytical predictions, which may be well beyond the levels required to cause functional failure, and 2) to gain some insight into design margins, i.e. the functional and structural capacity beyond the specified design load conditions. It should be noted that the pressurization system is typically designed to allow the model to be pressurized to levels significantly above those expected to cause local strains in the model to exceed the ultimate strain limits of the materials.

31.3.3 Tests

Keeping in mind that the primary considerations in the tests was the impact of internal over-pressurization, two major tests were conducted:

A 1:6-scale Reinforced Concrete Model tested in by Sandia Laboratories in July 1987. It represented a nominal 1:6-scale model of a reinforced concrete PWR containment and was designed according to the ASME code for a design pressure of 0.32 MPa (46 psig). The model, shown in cross-section in Fig. 31.3(a), consisted of a reinforced concrete shell with steel liner and included functional models of equipment hatches, an airlock and smaller penetrations. Eight layers of primary

reinforcing were included in the cylinder wall and the steel liner was anchored to the concrete using headed studs, as in similar prototype containments. The model was tested pneumatically to failure.

A series of independent pretest calculations predicted failure by various mechanisms including hatch leakage, liner tearing and base shear failures at pressures ranging from 0.90 to 1.31 MPa. The model was slowly pressurized using nitrogen gas and after 32 hours the test was concluded due to excessive leakage. At 0.96 MPa (140 psig) the leak rate was estimated to be approximately 10 scfm. The leak rate grew to 50 scfm at 0.98 MPa (143 psig) and to over 5000% mass/day or 4000 scfm at 1.0 MPa (145 psig). At this point the pressurization system could not compensate for the leakage of gas through the liner tear and cracked concrete and the test was terminated.

The major source of leakage was a 22 inch long tear in the liner plate at a row of studs adjacent to a thickened insert plate assembly, shown in Fig. 31.3(c). After the test, further inspection revealed a number of smaller (1/8 to 12 inch long) liner tears and incipient tears in highly distressed areas. All of these tears were adjacent to liner anchor studs near penetrations.

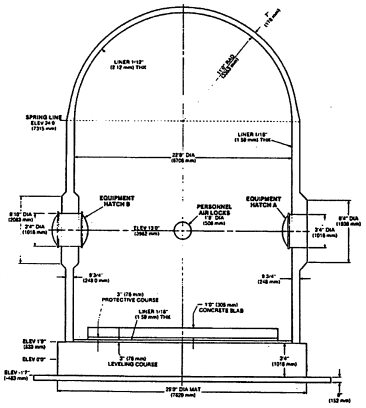

(a) Cross-section

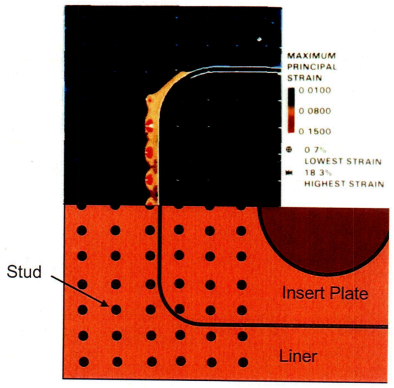

(b) Posttest analysis model liner at 1.0 MPa (145 psig)

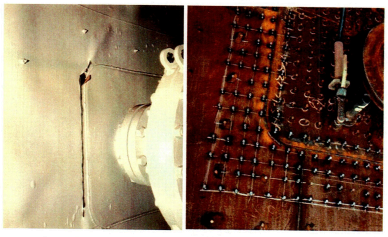

(c) major liner tear

Fig. 31.3: 1:6 scale model reinforced containment vessels

Prestressed Concrete Containment Vessel Model Test performed as part of a Co-operative Containment Research Program that was co-sponsored and jointly funded by the Nuclear Power Engineering Corporation (NUPEC) of Japan and the U.S. Nuclear Regulatory Commission (NRC). This was a 1:4-scale model of a large, dry PWR prestressed concrete containment vessel. The design pressure, P_d, for the model and the prototype was 0.39 MPa. The features and scale of the PCCV model were chosen so that the response of the model would mimic the global behavior of the prototype and local details, particularly those around penetrations, would be represented.

The model includes a steel liner anchored to the concrete shell by semi-continuous structural shapes (T's). Conventional reinforcing ratios match the prototype and prestressing tendons match 1-to-1 with the prototype. The un-bonded prestressing system consists of three, seven-wire strands per hairpin tendon, anchored in the basemat and identical, 360° hoop tendons anchored in opposing vertical buttresses. The overall geometry and dimensions of the PCCV model are shown in Fig. 31.4(a).

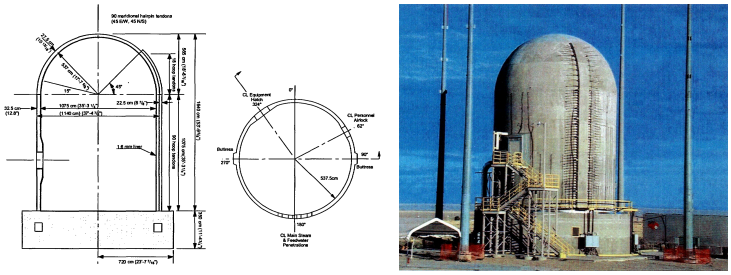

(a) Tear #12 at equiment hatch (b) Structural failure model test

Fig. 31.4: PCCV Model

31.3.4 Containment Capacity Analysis Guidelines

31.3.4.1 Introduction

This section provides guidelines which analysts may use in performing analysis to determine the capacity of containment structures to withstand loads beyond their design basis. These guidelines address only overpressurization in combination with elevated temperature, i.e. the scenarios associated with severe accidents. These guidelines come directly out of experience and lessons learned from the Sandia containment research program, both direct experience from Sandia (and contractor) analysis, and the shared experience of international participants in roundrobin analyses.

In general, containment structural analysts need to develop a model that represents the geometry, structural details and material properties which are "important" to the

response regime being analyzed and to the goals of the analysis. With continuing advances in computational power, the trend (and temptation of analysts) may be to model containments with more elements, more detail, and more comprehensiveness than ever before. But there remain real limits on what the state-of-the-art in material models can simulate and, generally, very real limits on the experimental data which is needed for interpreting and verifying the quality of complex model representations.

Everything should be made as simple as possible, but no simpler!

Albert Einstein

Though cliche, this is still probably the best philosophy, but also the biggest challenge, for containment analysis. Any analysis effort should include at least the following four steps:

1. Planning and identifying the goals of the analysis;
2. Developing model(s);
3. Calculating the response;
4. Interpreting and checking the results.

This section is structured around these four key steps. And although the topics presented here are discussed separately, these overall tasks must also be well integrated. Failure criteria must be consistent with the geometric details in the model(s) and the physical phenomena (i.e., plasticity, large deformations, etc.) accounted for in the calculations. Failure criteria have been proposed, and calculation methods are described here, as well as the geometric details that should be considered to be consistent with the proposed criteria. It also must be decided how predictions for containment performance will be used, because this strongly influences choices of methods and modeling details.

31.3.4.2 Analysis Goals and Planning

The first step in choosing an analysis method is to ask how the results will be used, i.e. what question the analysis will answer or what decisions will be made based on the results. For most containment capacity analyses, the results will be used to answer questions regarding safety margins and may be used in Level 2 PRA analyses and risk-informed licensing decisions.
The answer to this question affects selection of the tools and methods, which are important features of the work. For example, analysis of containments for the specified design loads can usually be done with elastic or mildly nonlinear analysis since the code-specified design limits on stresses are usually constrain the response to the elastic regime. But predictions of containment response to severe accidents or ultimate capacity typically require capabilities for simulation far into the nonlinear range of response. Both the load limits, in terms of pressure and temperature, and the modes of response or failure are important for severe accident risk assessments and emergency preparedness planning.
Analysis planning and goals should be established as follows.

1. Identify the loads to be applied.

- Typically, severe accident containment loads consist of both transient pressure and thermal loading.
- In some cases, the pressure transient may be considered independent of the thermal load because the peak pressure may not occur simultaneously with significant thermal loading.
- The transient nature of the pressure and thermal loading is usually ignored since the duration of the loading is usually longer than the period of the structure. As a result, static analysis methods are usually adequate.
- While these simplifications are usually valid, the analyst should review their validity in planning the analysis approach.

2. Conduct an initial "failure/vulnerability review"[2].

- Identify potential failure locations and modes and the types of models needed to simulate them.
- It is helpful to discriminate between functional failure modes, i.e. loss of containment integrity or leakage, which is generally progressive and structural failure modes which can occur rapidly. The primary value of discriminating between these modes of failure is in determining the risk significance of any given mode. Usually, this is beyond the scope of the structural analysis, but is important to the interpretation and application of the analysis results.
- Failure modes and thresholds of "engineered components" such as penetration assemblies, may rely on some level of analysis, but are typically determined by testing. This section focuses on recommendations for the analysis of the structure that comprises the primary containment boundary.

3. Define the engineering significance of the failure prediction. For example, is the goal to determine the margin of safety between the design pressure and the pressure at which a loss of containment integrity occurs.
4. Determine if the focus the analysis is on making a best estimate prediction or on a "conservative" lower bound estimate. Typically, containment analyses have been deterministic due to the complexity of performing detailed non-linear structural analyses. Estimates of uncertainty or probability of failure have been based on engineering judgment or multiple simplified analyses which are usually restricted to considering model parameter uncertainty.

This last item has consequences on choices of material properties (i.e., using actual properties, when available, rather than design-spec properties, etc.), and choices on modeling parameters, such as friction, foundation spring stiffness, etc.
It is crucial to not underestimate the importance of planning the analysis. The obvious, but often overlooked, fact is that only those features of the structure or modes of response/failure that are included in the model will be represented in the results. Experience has shown that the critical response or failure modes of the real structure are often not considered important or overlooked and not included in

[2] Refer to Sect. 12.1.1. Anticipated failure modes should be identified prior to any finite element analysis.

the model. As a result, analysis planning should also make use of judgment and experience on containment behavior.
For example for a prestressed concrete containment, since it appears likely that measurable leakage will not occur prior to the onset of general yielding; simplified methods can be used to predict containment performance. A failure criterion based on an average hoop strain of 1 to 2 % appears reasonable based on the (limited) experimental data. Simple axisymmetric models, either finite element or closed form formulations, could be used in conjunction with such a failure criteria. While this method may tend to underestimate the rupture pressure, yet, it could be acceptable if it can be demonstrated that significant leakage occurs (past penetration seals, bellows, or isolation valves, for example) at a lower pressure. If leakage does not occur before general yielding, a method based on a simple model and failure criteria like that described above is not adequate. This is due to it not allowing for the possibility of leakage which can occur at a local tear, and preclude the occurrence of rupture.

31.3.4.3 Simulation Code Selection

Containment capacity analyses require the use of a robust, general-purpose finite element code. There are a large number of code that meet the basic requirements and the selection of a particular code often depends on features that make the development of the model, the definition of the material constitutive models and the analysis of the results more efficient and convenient for the analyst.
It is not appropriate to recommend or endorse any particular finite element code in this report, however, the required or desirable features should include the following:

- Solution algorithm appropriate for simulating nonlinear response
- Suitable element library (including rebar for concrete containments)
- Appropriate material models that work for all needed element types (either resident in the program, or having an interface for user-supplied models)
- Capability to apply prestress (for a PCCV)
- Numerically robust Contact Simulation (only for some specific modeling procedures)
- Track record of performance for this class of problems

More specific requirements on element types and material modeling are provided later in this section. The last item, "track record of performance," is included to stress the need to test finite element programs for new applications (at least new to the user). Sometimes, while a program may have theoretically sound published capabilities, in practice, it may prove difficult to advance solutions far into the nonlinear response range.

31.3.4.4 Model Development

31.3.4.4.1 Geometric Considerations One of the primary modeling decisions to be made is to determine the scope or extent of the simulation model and which elements of the real structure can be ignored or simplified without affecting the analysis goals. Decisions made in this step are a continuation of the model planning and goal

setting, particularly the "failure/vulnerability review". The geometric considerations which enter into this step include:

1. Global versus Local models

   - Probably the most fundamental decision to be made is whether to construct a detailed global model which incorporates all of the relevant features of structure or a simplified global model which captures the global behavior combined with submodels to capture the local behavior. With ongoing increases in computing capacities and simulation codes that can take advantage of these capacities, there may be (is) a tendency or temptation to construct the most detailed, three-dimensional model possible. If these modeling capabilities are used judiciously this can provide a very accurate simulation, however, the potential complexities can often mask the underlying mechanisms and can also introduce model artifacts.
   - This decision is tightly coupled with the choice of a global or local failure criterion. It should be obvious that all failures initiate at the local level, but experience has shown it is much more difficult to identify and simulate local response, which is often driven or influenced by as-built conditions, than the global response of the structure.

2. What structure "idealizations" can be made without loss of achieving analysis goals?

   - Typically small penetrations can reasonably be ignored in terms of their effect on overall containment response.
   - Typically basemat irregularities, such as reactor cavities or access tunnels for control mechanisms, can be ignored.
   - Typically, the gravity effects of containment internal structures and adjacent external structures can be ignored due to the high stiffness of the basemat.

   These last two simplifications should be carefully reviewed if a relatively flexible basemat is encountered.

3. What symmetries in the structure can be exploited? If existing symmetries can be exploited, a finer mesh can usually be used than would be possible in a full, 3D model.

   - Bi-symmetric about one plane or Quarter-symmetry about two orthogonal planes?
   - Wedge or Sector symmetry, i.e. can a 'slice' or repeating sector (e.g. 300) of the structure represent the response of the entire structure
   - Axisymmetric? A majority of the containment structures currently in use or proposed can be fairly represented by an axisymmetric model. This makes sense since a uniform shell is more efficient in resisting internal pressure than an irregular structure. The axi-symmetry of the containment is usually compromised, however, by constructability and operational considerations. Nevertheless, idealizing the structure as axisymmetric is usually possible and reasonable. Sources of nonaxisymmetric behavior include

- Major openings (usually the Equipment Hatch and Personnel Airlocks)
- Hoop tendon buttresses
- Dome tendon layout (part of which is often rectilinear)
- Basemat rebar layout (part of which is often rectilinear)

It should be noted that apparent geometric symmetries can often mask underlying asymmetries in the structure, such as changes in stiffness associated with variations in reinforcing in concrete containments or local thickening or stiffeners in steel structures.

4. Interaction with adjacent structures or components.

   - Is there a shield structure or other adjacent structure that could restrict containment "growth"?
   - Can the pipe penetrations and equipment supports accommodate differential movement (both radial and vertical)?

   As discussed in section 31.3.4.4.1, there are two major issues involved in developing the finite element models: determining what geometric detail of a containment need to be represented and establishing proper mesh discretization. As part of the last two decades of Sandia containment research, many containments have been analyzed, and for the Sandia large scale model tests, many analyses were conducted by round-robin participants. In most cases, to complete a thorough set of predictions of behavior to overpressure, several different model types are developed and analyzed for each containment.

31.3.4.4.1.1 Element Types for Concrete Containments

1. Concrete is typically modeled with continuum elements. In 2D planar or axisymmetry, 8-node (quadratic edge) continuum elements, but reasonable accuracy can also beobtained with a finer mesh using 4-node (linear edge) continuum elements. In 3D, 20-node (quadratic edge) or 8-node “brick” elements are recommended.
2. In concrete elements which crack at the finite element integration points, it is best to select elements with reduced integration, as long as appropriate care is taken as to meshsize and to control of numerical issues such as “hour-glass.” (These issues are beyond the scope of this guidelines, but are usually well covered by the theory manuals of finite element programs.) The reason for this is improved convergence characteristics once cracking begin to develop.
3. An axisymmetric liner should be modeled with two-node or three-node shell elements (whatever is compatible with the adjoining concrete elements), and beam elements can be used for representing liner angle anchors or stiffeners. In most models except for those studying very localized effects of liner/concrete interaction, the liner is considered to be fully bonded to the concrete. In 3D models, the liner should be modeled with 3D shell elements. (It should be noted that for the original designs, the liner was generally ignored in analysis.)

4. Smeared rebar sub-elements should be used to model reinforcement. Such elements assume strain compatibility between rebar and concrete[3].
5. Smeared rebar sub-elements can be used to model tendons for global axisymmetric analysis of a P/C containment. (In an axisymmetric analysis, strain compatibility of hoop tendons is automatic, but with meridional tendons, the analyst has a choice of modeling tendons as ordinary rebar, or as separate truss elements external to the grid and attached to the grid with linkage elements. (Extensive study of axisymmetric analysis for the 1:4 PCCV did not show good "return on invested labor" (in terms of improved accuracy) for modeling vertical tendons with explicit elements that could slide relative to the concrete. A different conclusion was reached, however, for 3D local models targeting circumferential variations related to hoop tendon behavior; such analytical goals require special treatment of prestressing tendons with separate elements tied to the concrete, but also allowed to slip and have different hoop strain than the neighboring concrete.)

31.3.4.4.2 Constitutive Modeling of Concrete Containment After selecting or defining a set of material properties, the next choice is the selection of an appropriate constitutive model. For linear-elastic analysis, this choice is straight forward, but for non-linear, quasi-static or dynamic analysis, this is more difficult and requires experienced judgment. This is further complicated by the fact that constitutive models are often dependent on the code and solution strategy used. It is not possible to specify a particular constitutive model that is applicable in all cases, but the considerations given below may help guide the analysis of containment structures.

1. Concrete constitutive models should include tensile cracking (normally treated as occurring in the principal stress directions at the integration points). Alternatively, the concrete can be treated as a no-tension material in analyses aimed at predicting global response[4].
2. There is a wide range of opinion within the industry as to the proper simulation of the concrete post-cracking stress-strain curve. From the many years of analysis during the Sandia containment research program it has been concluded that while it is the most theoretically robust to implement an experimentally-verified tension stiffening curve, it is not absolutely necessary to achieve reasonable failure predictions for containments. What is more important is to caution against using overly "strong" tension-stiffening curves, which is often tempting to analysts, because their use can significantly improve convergence characteristics. For failure prediction, it is better (and conservative!) to assign little or no tension stiffening to post-cracked concrete than to assign too much. c. Some method for simulating post-cracking shear retention should also be included. Shear retention is particularly important at the wall base junction, and numerical solutions in this region are found to be sensitive to the shear retention algorithm used. Description of these methods, and a reasonable assessment of the current "state of the prac-

[3] Careful, in seismic analysis, it may be important to model the bond between next to the matt.

[4] Again, fracture mechanics of concrete should be used.

tice" in concrete modeling are available in the report on the Round-Robin Pretest Analyses of the 1:4 Scale PCCV Model.

3. While most of the concrete elements in a computational grid will probably experience no compressive stress at high pressures, a few elements at the outer wall base and along the top of the basemat will experience compression, sometimes large enough to exceed the concrete compressive strength, f'_c. Thus, it is important to properly model concrete crushing. An elastic/perfectly plastic stress-strain curve has shown reasonable results in most cases, but inclusion of strain-softening is preferred for completeness. (Although, the associated plasticity algorithm is more complex.) As complex behavior is to be expected at the wall base, it is important that the concrete compressive yield algorithm properly treat the effective stress and strain calculation. Compressive yield is more likely to be reached by the combination of vertical compressive stress and shear stress rather than any one component stress reaching f'_c. This condition is essential for predicting potential wall-base shear failure[5] .
4. Geometric Nonlinearities. Though not a constitutive modeling issue, it is still a nonlinearity. Contrary to the recommendations for steel containment analysis in which geometric nonlinearity formulation is required to predict failure, it has been found that second order and large rotation terms need not be included in the strain-displacement relations for concrete containment analyses. The stiffness matrix need not be updated to reflect the changes in geometry or thinning of the wall, as it is in steel shells. This recommendation carries with it some practical advantages, especially for modeling such complexities as prestressing tendons. Restricting the solution to small-displacement theory provides some options as to approximate formulations for friction and other effects.

Most finite element programs handle the mechanical analysis of thermal expansion well, and it is generally adequate to assign a linear thermal expansion coefficient. But the analyses of coupled pressure and temperature accident scenarios become exceedingly more complex when temperatures reach high enough to cause significant material property degradation. These thresholds are approximately 150°C (300°F) for concrete and 427°C (800°F) for steels; these are the temperatures at which material strengths degrade by about 10%. And degradation curves become much steeper beyond these temperatures.

31.3.4.5 Interpretation and Evaluation of Results

31.3.4.5.1 Basic Model Checks Conducting basic quality and "sanity"[6] checks are essential to completing a containment analytical study. And although many such checks are part of the "skills of the trade" learned through experience, for containment global analysis, at a minimum, the analyst should conduct basic hand calculation of approximate event milestones (in terms of pressure) for the radial expansion of the containment cylinder. The calculations are not overly complex, and a detailed

[5] Refer to Cervenka and Papanikolaou [178] for a modern treatment of the subject.

[6] as addressed in Sect. 12.1.1

example of such a calculations (conducted for the 1:4 Scale PCCV) is provided below

31.3.4.5.2 Failure Criteria and Interpreting Analytic Solution The importance of defining failure criteria to the implementation of finite element results cannot be overstated. Is it a performance-based criteria that requires prediction of actual release of containment contents, or is it a criteria which predicts the onset of a material failure. Until very recently, nearly all containment analysis in the Sandia research program has invoked the latter.

But even with the ductility-based criteria (which predicts failure when steel strains are in the range of 15%-25%), engineering judgment is needed to interpret finite element analysis results. It is only with the very finest of meshes and detailed modeling approaches that such high strains can be reliably predicted, and even with very fine meshes, some measure of mesh-size sensitivity[7] will always be present near structural discontinuities. This means that for most analysis, judgment will be required to extrapolate from global model predicted strains of 1%-2% to high strains likely to exist near structural discontinuities. And though a comprehensive database of strain concentration factors is still lacking, there is substantial evidence (found in test and analysis reports cited herein) to support such engineering judgment and failure prediction based on global analysis.

Investigation and validation of methods for evaluating other potential failure modes is still needed. Shear failure is particularly[8] difficult to evaluate; there is no generally recognized method of determining shear capacity of a reinforced concrete section under simultaneous application of tensile load and bending moment. Failure of large rebars where they are bent around penetrations, as occurred in an EPRI test are also of some concern. The effects of cold working on the available ductility to these bars should be studied further. Rates of pressurization and effects of temperature must be considered in more detail. At high rates of pressurization, there is a possibility that sequential failure modes could occur; that is, for very high rates of pressurization, liner tearing may not arrest the pressure buildup within the containment, and another failure mode could occur at slightly higher pressure. This is the basic reason for emphasizing the development and validation of analysis methods. A reliable evaluation of containment performance must be based on careful, detailed analysis of the specific containment geometry and loading of interest.

[7] This was first documented in [99].

[8] As pointed above, it remains a complex problem as it often results in brittle size-dependent failure, [902].

Chapter 32
Analysis of Nuclear Containment Structures; II Reported Analyses

Abstract
This chapter focuses on reported (finite element) studies/investigation in four NPP that have received much attention lately: Gentilly 2, Ikata, and Crystal River. The first two are the only ones reported to have suffered from ASR, and the last has notoriously delaminated following detensioning for steam generator replacement.
Each case is treated separately (and not all with the same level of details) in a section itself composed of two parts. First attempt is made to summarize findings on the basis of open literature, and then the authors provide a critical review. In writing the second part (review), the authors have exercised the same "zeal" that they would have used by a University researcher reviewing a manuscript being considered for publication. Undoubtedly, in many cases reviews by industry or some governmental agencies tend to be less strict. We do not necessarily agree with this presupposition if the consequence of an accident can be too severe.
Again, the authors acknowledge that in some cases they may be limited in either their description of the facts or in their assessment. This is simply due to a lack of full documentation, and they do apologize for possible mis-representations.
It should be noted that, given the sensitivity of the subject (specially in the last case study), all information are exclusively extracted from publicly available documents.

32.1 AAR: Gentilly

Adapted from [188] and [344].

32.1.1 Reported Analyses/Investigation

The Nuclear Power Plant of Gentilly-2 (G2) owned by Hydro-Quebec (HQ), was approaching the end of its first life cycle of 30 years, in accordance with the initial design. Before the decommissioning of the plant, G2 was poised for a major refurbishment project with the aim of extending its service life for another cycle of 25-30 years. The G2 containment structure was constructed using concrete and mild carbon reinforcing steel. It was also pre-stressed using three different types of tendon anchorage arrangements. The ring beam accommodates tendon anchorage for the ellipsoidal dome and the vertical containment walls. Four vertical buttresses accommodate horizontal tendon anchorage for the walls, Figure 32.1.

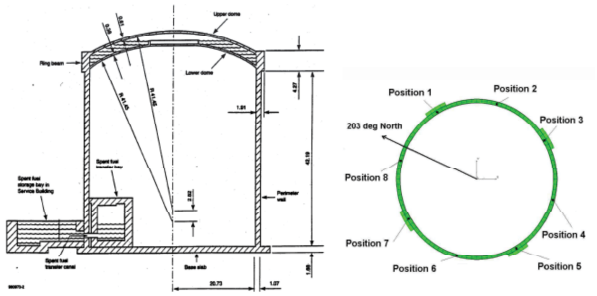

Fig. 32.1: Containment structure (reactor building envelope), vertical and horizontal sections [344]

Given the restrictions imposed on sample extraction from an operating NPP, an extensive numerical analysis was conducted. This was the first, and insofar the most extensive reported study on the impact of ASR on a NPP.
These studies included evaluation of various aging/degradation mechanisms. The numerical simulations included a transient thermal analysis over the period of construction, a series of static analyses together with simulation of a continuing AAR effect, and a dynamic analysis simulating a seismic event.
HQ defined a number of degradation mechanisms relevant to G-2 NPP. In general, the degradation mechanisms affecting concrete structures have been extensively studied and are relatively well known. Some of these mechanisms are listed below in groups according to the severity of the damage that they may produce in the affected structures:

1. Mechanisms referred to as “Primary Degradation Mechanisms” which are expected to cause significant damage:
   - Alkali-Aggregate Reaction
   - loss of pre-stressing (stress relaxation)
   - corrosion of reinforcing and prestressing steel
   - chemical attack
2. Mechanisms referred to as “Secondary Degradation Mechanisms” which are not expected to cause significant damage:
   - construction deficiencies (initial hydration cracking)
   - differential settlement
   - shrinkage
   - creep
   - normal degradation over time
   - frequent leakage-rate testing, accelerating the degradation over time
   - freeze/thaw cycles (important for Canadian climate) thermal exposure
   - radiation

32.1.1.1 Material Aspects and Laboratory Testing

Hydro-Québec owns and operates more than 656 dams and 60 hydroelectric power plants. As of today, there are 36 hydraulic structures in these installations in which the ASR has been confirmed with only 7 are considered severely affected, 15 moderately affected, while a mild effect was found in the remaining 14 structures. G2, the only Nuclear Power Plant owned by Hydro-Quebec, is affected by ASR in concrete (severely affected if based on the free expansion rate of concrete but moderately if based on the in-situ measured expansions). Therefore, the ASR is the major concrete degradation mechanism at G2.

In 1985, it was found that the aggregate in the region of Trois-Riviéres - used in the construction of G2 is reactive. The average alkali content in the cement was estimated to be 0.820 %; therefore, the alkali content in the concrete varied between 2.05 kg/m^3 and 3.69 kg/m^3. Based on test results, it can be stated that the concrete used in the construction of G2 NPP is the most reactive when compared to the concrete used in the construction of any of the other ASR-affected structures in HQ's hydroelectric power plants. For example, the maximum free expansion rate of concrete at Beauharnois hydroelectric power plant, as obtained from in-situ measurements, is 95 μm/m/yr, at 100% RH. On the other hand, the maximum free expansion rate of the concrete at G2 NPP is estimated to be 150 μm/m/yr at 100% RH. Lower concrete expansion rates were observed at lower RH values. It has been observed also that concrete expansion is affected or slowed down, due to internal or external confinement. Most NPPs structures are heavily reinforced and/or post-tensioned and the RH is usually low. In fact, the internal confinement and the lower relative humidity are the two main factors which may reduce concrete expansion rate considerably. The expansion rate of concrete at G2 is reduced to an average of 9 μm/m/y in the walls of the containment building, under bi-axial state of stress.

From the long-term monitoring of ASR-affected structures at HQ, it was concluded that the structures where the alkali content is less than 1.6 kg/m^3 may be considered mildly affected and, therefore, giving a special attention to these structures is not required. The same applies to the structures where the concrete growth is inferior to 20 μm/m/yr. Indeed, at this rate of expansion, only limited adjustments to the affected equipment is occasionally performed.

Early on, initial research was conducted to understand the phenomenon: the chemical reaction and the consequential concrete swelling. This led to attempt to judge the behavior of ASR-affected concrete in real structure based on information extracted from standardized testing procedures - carried out on samples with relatively small size. They proved to be unproductive. Hence, HQ investigated the following:

- Mechanical properties of concrete at G2 NPP and hydroelectric power plants,
- The expansion rate of concrete (small concrete samples - accelerated tests),
- Effect of relative humidity and temperature on concrete expansion (small cylindrical samples),
- Effect of the state of stress in the ASR-affected concrete (uniaxial versus multiaxial tests),

- Effect of one-dimensional (1D) confinement on concrete expansion (small cylindrical samples),
- Effect of two-dimensional (2D) confinement on concrete expansion for 350 x 350 x 350 mm cubes,
- Effect of 2D confinement on concrete expansion for 600 x 600 x 600 mm cubes,
- The expansion rate of concrete on real structures as obtained from in-situ measurements,
- The effect of uniaxial and biaxial confinement on full scale structures.

and test results on the 600 mm $\times$ 600 mm $\times$ 600 mm concrete blocks as well as in-situ material testing and taking measurements of the deformed structure proved more useful.

32.1.1.2 Material Modeling

HQ performed some material modeling and laboratory-testing. However, the former was not intended to simulate the tests. Cylinder and block tests were perceived as material tests that define the rate of free expansion under different conditions, and provide valuable information that may be employed to identify the parameters entering the law of reaction kinetics. Hence, it was considered that they could not be simulated numerically unless a multi-scale approach (i.e., micro/meso-scale) that, even though conceptually attractive, cannot be employed in the context of analysis of large-scale structures.
HQ attempted to use a mesoscale approaches that distinguishes between the concrete matrix and pores occupied by gel and water with limited success (only for small element), and failed to capture the structural response of large-scale structures due to limitations of the model.

32.1.1.3 Structural Modeling

HQ carried out extensive numerical studies for the containment structure of G2 NPP and for the other concrete structures affected by ASR in the plant. These numerical simulations included the implementation of a transient thermal analysis for the period of construction and for the freeze-thaw cycles occurring during a fifty-year period. The numerical simulations included as well static analyses for simulating the continuing ASR and dynamic analyses simulating seismic events. An in-depth study of the consequences of an assumed crash of a fast flying commercial aircraft upon the containment building was also carried out for assessing, in particular, the potential damage to the ASR-affected concrete structure. The study, which was prompted by the September 11, 2001 terrorist attacks in the USA, has also incorporated the assessment of the damage due to the subsequent fire that to follow the crash (due to about 92,000 liters of spilled aircraft fuel).
It was determined that commercial finite element codes then available were not suitable to adequately address some complex problems involving ASR-related swelling. In particular, most of these codes lacked material models with constitutive relations

that are suitable for the description and the evolution of complex material properties related to ASR.
HQ determined that the essential requirements of the concrete/reinforced concrete constitutive model accounting for the chemo-mechanical interaction, which should be incorporated in advanced Finite Element (FE) codes, are as follow:

- Adequate description of the kinetics of the reaction
- General failure criterion, provision for the development of irreversible deformations, general criterion for the onset of macro-cracking in both compression and tension regimes
- Degradation law for strength and deformation characteristics
- Proper description of propagation of damage in both tension and compression regimes (viz. homogenization incorporating a characteristic dimension, XFEM or similar)
- Constitutive relation for the interface material relating the velocity discontinuity to the traction vector

Hence, HQ has developed constitutive relations [694] for ASR-affected reinforced concrete that satisfy the aforementioned requirements and has incorporated them in the main algorithms of the commercially available finite element codes: COSMOS/M and ABAQUS, and they were properly calibrated prior to deployment to ensure appropriate nonlinear static or dynamic predictions. The procedure is outlined in the following:

Step 1

- Evaluate material properties based on laboratory reports:
  - results from tests on cylinders at 28 days
  - results from periodic tests conducted on extracted cores (from the time of construction until the present time)
- Evaluate the rate of free expansion
  - based on a non-confined direction (vertical) and the distribution of RH
  - based on periodic reports: surveying results of the benchmarks installed in the structure and the instrumentation data (winter and summer readings, measurements for a period of at least 8 to 10 years)
- Define the parameters used in the numerical formulation
  - The material properties required to define the model parameters are as follows (for COSMOS/M software):
    - Modulus of elasticity of concrete
    - Poisson's ratio
    - Density of concrete
    - Initial compressive strength of concrete
    - Confinement stress at which the ASR expansion rate reduces
    - Confinement stress at which the ASR expansion rate is zero
    - Strain softening parameter
    - Material constant that controls the rate of strain softening

- Material constant for brittle-ductile transition value of confinement stress
- Material constant that defines the form of residual strength envelope
- Initiation time of ASR
- End time of ASR
- Time increment corresponding to real time for ASR (EX: 1 time step = 1 month)
- Maximum free expansion rate due to ASR
- Correction parameters to allow the degradation of strength properties during the length of ASR

– Define the time step to be used

Step 2: Run Preliminary Analyses: runs for 20, 30, 40... years, calibration of the input properties

- Comparison of calculated and measured displacements at 20, 30, 40 years.
- Comparison of damaged regions (predicted versus observed), if possible
- If the compared results are satisfactory, go to step 3, if not, make corrections in step1 and restart the analysis from the beginning
- Repeat the abovementioned steps until acceptable results are obtained

Step 3: Run Final Structural Analyses for present time evaluation: from the end of construction time until present time

- Comparison of calculated and measured displacements at present.
- Comparison of damaged regions (predicted versus observed) at present
- Seismic evaluation (nonlinear dynamic analysis of the cracked structure) based on the calculated structural safety indicator

Step 4: Run Structural Analyses for future time assessment: evaluation of the structural behavior in the future; service life expectations or service life extension and studies of the cracked infrastructure

32.1.1.4 Non-Destructive Testing and *in-situ* Condition Assessment

Two sets of non destructive testing were performed: a) periodic integrated leakage-rate testing every three years at 124 kPa(g). Generally speaking, these high pressure air-tightness safety testing cause the widening and the propagation of existing cracks, during and after each performed test; and b) *in-situ* condition assessment. Only the later is described here.

HQ recognized that ASR was the "Primary Degradation Mechanism" resulting in (a) cracking of concrete, which may or may not have an effect on the air-tightness of the containment building or on the rate of leakage of water (if any) from the reactor vault, spent fuel exchange room, spent fuel storage pool, dousing tank; and (b) degradation over time of the mechanical characteristics of the concrete that may have effects on the local or overall structural behavior, and on the capacity of the anchor bolts fixing the power plant equipment to the ASR affected concrete floors, walls. It was deemed that in any ASR-affected concrete structure of a NPP, almost

all of the other known degradation mechanisms are influenced by the deterioration effects associated with the ASR. For example: the loss of pre-stressing depends on whether the concrete is affected by ASR. The same applies to the effects of creep, freeze/thaw cycles, degradation due to leakage-rate testing, corrosion of reinforcing and prestressing steel, thermal exposure following an accident.
The following was investigated.

Change of post-tensioning due to ASR and Creep: The changes from the original values that were developed until the time when the study was carried out in 2010 and the further anticipated changes which should take place until the year 2035, were assessed taking into consideration the combined ASR and creep effects. The estimated changes of strain due to the combined ASR and Creep effects in the horizontal (tangential) and the vertical directions were obtained from a number of sampling points where instruments were installed. These points were placed in selected locations of the containment building wall in order to avoid the effects of boundaries at the extremities of the building. Deformation values were obtained numerically and then were used to evaluate the post-tensioning forces in the cables at the time of study and in future. It was concluded that the effects of ASR in concrete (with the exception of the degradation of mechanical properties) are "beneficial" for the post-tensioning long term behavior. It may be expected that in year 2035 the gradual increase of the initial post-tensioning force will be about 4% and 2.8% in the horizontal and the vertical cables, respectively. The variation of the post-tensioning losses/gains is influenced mainly by the non-uniformity of the walls (increased wall thickness at the closed openings initially used for entering the equipment or the existence of permanent wall openings).

Micro-cracking due to Creep and/or ASR: The numerical analysis of creep effects in the post-tensioned concrete of the G2 containment building has shown that an extensive micro-cracking propagates throughout the concrete sections due to the elevated effects of creep (with diminishing ASR expansion effects due to the high post-tensioning stresses). The ducts and the post-tensioning cables create a non-homogeneous concrete section. The stress fields due to the positioning of the cables are also non uniform. The RH throughout the thickness of the walls is not uniform; therefore, the Creep is not uniform as well. These factors are minor and may not be important if there is no requirement of air-tightness of the containment building under internal pressure. More elaborate study revealed that the magnitudes of the slightly non-uniform compressive stresses in the concrete (induced by the 2D prestressing) which are affecting the creep should not be high. A parametric study has demonstrated that the post-tensioning stress in the concrete section should not be higher than 6.0 to 6.5 MPa in each direction in order to avoid the creation of micro-cracking throughout the walls of G2 reactor building envelope under the combined effects of ASR and Creep. These values are expected to be slightly lower if only Creep effects are present. The damage due to the propagation of micro-cracks is not uniform in the structure. The main reason is the non-uniform expansion of concrete due to the uneven distribution of the humidity in the entire structure. Based on the magnitude of the evaluated humidity distribution, forty-two different concrete expansion rates were

defined in the calibration process and were employed in the analysis. Moreover, the deterioration of the mechanical properties of concrete over time has great importance on the effect of this degradation mechanism. The results obtained from the parametric studies have demonstrated the significant effect that the predicted tensile strength of concrete has on the time of commencement and the subsequent development of structural cracking.

Impact of differential expansion on junction of perimeter wall and base slab: The results of the analysis have revealed that the early cracking, in the areas close to the bottom of the walls, was affected largely by the expansion of the base slab. This is even without subjecting the containment building to internal pressure.

Concrete splitting in duct plane: The FE analysis results reveal that there are areas of the containment where there is a relatively high tensile stresses perpendicular to the planes of the post tensioning cables. The continuous loss of tensile strength of the concrete as a result of ASR may provoke concrete splitting parallel to these planes as it was the case with another massive structure that was constructed using the same concrete aggregate used at G2 NPP. The splitting of concrete may occur also in a containment concrete structure not affected by ASR if the prestressing is relatively high. A study in which the prestressing force in both directions was doubled indicated that there would be a high probability of concrete splitting. It is suggested that this may have been a possible cause of Crystal River delamination. It was also determined that the tensile stresses of the concrete in the areas where splitting may occur, were between 0.5 MPa and 1.0 MPa for the year 2010, and between 1.0 MPa to 1.5 MPa for the year 2020. The reduction of the tensile concrete strength, as a result of the degradation of concrete properties due to ASR, was obtained by laboratory tests conducted on extracted concrete cores. Based on the test results, the tensile concrete strength was determined to be equal to 2.5 MPa for 2010 and it was conservatively estimated to be equal to 2.0 MPa for 2035.

Impact of water on ASR in non-prestressed reinforced concrete: In general, non-prestressed reinforced concrete structures such as: the spent fuel storage pool, the spent fuel exchange room, the reactor vault, are affected by the ASR-induced concrete swelling more than the prestressed structures. For G2 NPP, The concrete growth rate in these structures varies between 60 to 100 μm/m/yr. As a result of these elevated rates of expansion, extensive cracking and large deformations have developed and have been observed in many of these structures. Many consequent complications have taken place and have disturbed the normal operation of the NPP, including: water leakage, distortion of the bases of the equipment serving to manipulate (exchange or store) the spent fuel rods, jamming of doors. Moreover, in some cases, the degradation of concrete strength is affecting the capacity of steel anchors attaching equipment and pipes to the concrete floors and walls.

Impact of ASR on Turbo-Generator foundation: Like almost all of the other structures at G2 NPP, the foundation is affected by the ASR-induced concrete swelling. Based on the measurements obtained from the instruments (invar wires) which were installed after the presence of ASR had been detected, the concrete growth rate of the foundation varies between 40 and 60 μm/m/yr. This elevated growth

rate has resulted in the extensive cracking and the large deformations which were observed in the structure and which are expected to continue in the future. The concrete expansion induces uneven displacements, which are much larger than the prescribed tolerances. These differential displacements have to be frequently adjusted in order to maintain normal operating conditions. The accumulated periods of intervention time required for executing the repetitive adjustments represent a considerable power production loss for HQ as this generator has an installed capacity of 670 MW. In order to optimize the intervention time required to counter the effects of future expansion and the subsequent differential displacements of the turbo-generator's supports, an elaborate numerical analysis was performed where the model was calibrated using the results of the installed instruments. Based on the results of the study, a proposal for the adjustment of the turbo-generator supports was submitted to the manufacturer of the unit. In addition, a dynamic analysis of the cracked foundation was performed in order to investigate the possibility of having a future increase in the vibration level of the turbo-generator, considering that the unit is supported on a cracked and a continuously deteriorating foundation. It is to be noted that a higher level of vibration of hydroelectric generating units was observed in some of the ASR-affected hydroelectric powerhouses.

Impact of seismic excitation on the structural integrity: The structural behavior of G2 NPP containment building which has already been weakened by the progressive ASR effects - was examined under seismic excitations. Two separate analyses were conducted where the continuous effects of ASR were simulated up to the end of the planned life extension; namely, up to the year 2035; then seismic excitations were simulated. Two slightly different values of concrete tensile strength were assigned to the concrete in the two analyses. The assumed values of concrete tensile strength were $f_{t,2035} \sim 2.0$ MPa and 2.25 MPa. The structure was analyzed using dynamic procedures and using an ASR material model containing inelastic constitutive relations defining the mechanical behavior of concrete affected by swelling due to ASR and exposed to the other prescribed loads. Concrete reinforcement was modeled using two different approaches: (a) as elements in the FE model; i.e., in a discrete manner and (b) as fractions of the concrete volume in a homogenization technique. The effect of concrete confinement was accounted for directly in the evolution law of the program.

The time histories for the seismic excitations used in the nonlinear analyses were developed on the basis of 6 records of ground motion time histories to match the target spectrum for G2 NPP site and were based on a probability of exceedance of 1/10 000 p.a., for hard rock ground condition and for the 84% confidence level. Three sets were obtained from seismological simulations and three others were obtained using a spectral matching technique where the frequency contents of certain historical ground motions were modified. The effects of the assumed earthquake - taking place in the region of G2 site during the year 2010 - on the propagation of damage in concrete are shown in Figure 32.2. It was shown that during an earthquake, even though the structural integrity is not affected, the cracked regions extend at the junction of the wall and the base slab. According

to these results, the probability of enduring a considerable loss of air-tightness after an earthquake is considerable. This probability will be even higher in the following years (years 2011-2035) since the concrete cracking will gradually increase. This latter conclusion was made based on the results obtained from the analysis simulating expansion of the concrete followed by an earthquake in 2035.

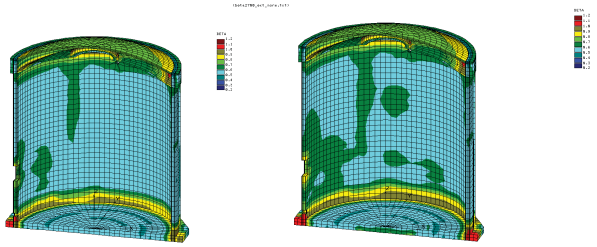

Fig. 32.2: Distribution of coefficient of deterioration β due to own weight, post-tensioning and after 25 years of combined ASR and creep effects (a) before an earthquake and (b) after an earthquake (Analysis of structural state in 2010; Interior view) [344]

32.1.1.5 Conclusions

HQ drew a number of conclusions, the most relevant of which (in the context of this book) being:

1. Regardless of how elaborate these tests are; however, they cannot provide answers to the most important question which is as follows: at what level of safety and operational reliability this ASR-affected structure stands? In fact, after 40 years of research, the approach of conducting typical material tests is still the most common tool of investigation. However, from a structural engineering point of view, the question can be answered mainly by performing adequate structural analysis.
2. In an existing and operating NPP, many areas are inaccessible, while only a restricted access is available to many other locations in the plant. Conducting an analytical study may be the "only feasible" evaluation method to assess the state of degradation and the safety level of the NPP. In this case, an adequate elaborate numerical analysis is essential to evaluate the state of the NPP. High level of confidence in the conclusions based on such analysis can be achieved when there is a good agreement between the obtained analysis results and the measured and observed signs of deteriorations.
3. Many of the commercially available software packages can be used to perform an adequate and an elaborate structural analysis for concrete structures which are not affected by ASR. To the contrary, it is not the case when it comes to analyzing ASR-affected concrete structures. This is due to the fact that these codes are usually

lacking material models with adequate constitutive formulation that is particularly suitable for simulating the behavior of ASR-affected concrete structures. In many cases, the software can be used to arrive to some reasonable "displacements" solutions, however; the associated results may not be representative to the state of the analyzed structure in terms of the severity of damage, state of stress, crack locations and predicted behavior. Therefore, many of these solutions should be re-examined carefully.

4. The essential requirements of the concrete/reinforced concrete constitutive model accounting for the chemo-mechanical interaction in ASR-affected concrete are as listed below. Advanced Finite Element (FE) codes should incorporate material models that satisfy these requirements in order to provide an adequate tool to analyze ASR-affected structures:

   - Adequate description of the kinetics of the reaction
   - General failure criterion, provision for the development of irreversible deformations, general criterion for the onset of macro-cracking in both compression and tension regimes
   - Degradation law for strength and deformation characteristics
   - Proper description of propagation of damage in both tension and compression regimes (viz. homogenization incorporating a characteristic dimension, XFEM or similar)
   - Constitutive relation for the interface material relating the velocity discontinuity to the traction vector.

5. The conclusions of the in-situ condition assessment can be summarized as follow:

   - The long term post-tensioning losses or gains in the cables can be predicted with reasonable accuracy by numerical analysis and from the in-situ tests considering the combined actions of creep and the ASR swelling effects.
   - Micro-cracks may propagate throughout the concrete envelope of the containment building due to creep effect, elevated prestressing or the combined effects of creep and ASR swelling.
   - Local disorders, such as cracking and loss of air-tightness, may occur due to uneven expansion of structural components (wall and base slab junction; wall and dome junction).
   - High prestressing - whether alone or combined with the ASR effects - may cause concrete splitting in the planes which are parallel to the wall surfaces.

32.1.2 Critical Review

This reported investigation is most impressive. Close collaboration with three research institutions has yielded a comprehensive scientifically sound report. The authors will add a few comments:

1. Failure of the meso-scale model to properly capture the structural response of large structure remain a major challenge. Some recent advanced such models have yet to report analyses of structures [24].

2. The *in-situ* assessment show that nearly all degradation mechanisms are influenced (if not overshadowed) by ASR.
3. Delamination due to splitting along a plane of weakness is a real possibility. In G@ the ducts provided a plane of weakness (as in Crystal-River), however even in non-prestressed concrete structures the micrro cracks in the center (unreinforced) may cause such a delamination due to the compounding effects of ASR, creep, and crep fracture.
4. Seismic excitation may not necessarily cause structural failure but sufficient cracking so as to render the structure inoperable.
5. Discontinuities or unevenness can be very pernicious. They can be easily overlooked but may cause great problems (or localized "disorder") in ASR affected structures.

32.2 AAR: Ikata

32.2.1 Reported Analyses/Investigation

Ikata No.1 nuclear power station is the PWR Plant with 566 MW capacity is constructed by Shikoku Electric Power Company [816]. The Turbine Generator foundation (TG) of Unit 1 is the reinforced concrete structure that supports turbine and generator which are located inside of the turbine building. Construction of this TG foundation was completed in 1975. Commercial operation of turbine generator started in 1977.The TG foundation is 50.0m long, 15.0 m wide, 18.7m high; typical beam sizes are 3.19m wide and 4.0m deeep. Concrete strength was 20.6 Mpa (moderate heat Portland cement), washed fine aggregate of sea origin, crushed aggregate. The TG is resting on bedrock, Figure 32.3(a)

As early as 1979, and Alkali-silica reaction cracks were observed Figure 32.3(b) and 32.3(d) on TG foundation. This was confirmed by various tests. It was later determined that the TG foundation had been expanded in the longitudinal direction due to the affect of ASR, and that the maximum expanded rate was about 500 mm Figure 32.3(b). Yet, it was determined that the TG foundation had sufficient bearing capacity to resist seismic load.

Accelerated expansion tests on recovered cored were performed [815] in accordance with JCI-DD2. 1986 tests indicated an expansion of 1.0%[1]. When the same test was repeated in 1989 the expansion had dropped to less than 0.04% implying that the final expansion due to AAR has been reached, Figure 32.3(d).

This occurrence of ASR has given rise to numerous studies by the Japanese research/academic community.

Takatura et al. [817] reports on the field investigation work: location, extent of cracking, variation in concrete elastic modulus and compressive strength, expansion in sufficient detail to adequately understand the extent of damage.

The influence of ASR on mechanical properties (in particular, the influence of rebar) and on structural behavior has been discussed by Murazumi et al. [614] and

[1] The authors refer to "after-expansion rate" which is unfortunately not defined.

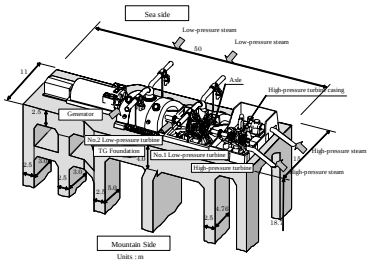

(a) Turbine generator foundation

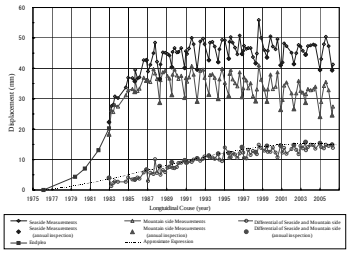

(b) Axial expansion of the TG foundation

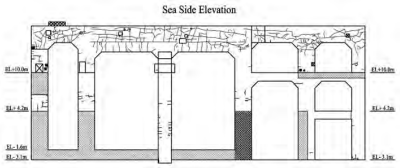

(c) Sketches of cracks on the "sea side"

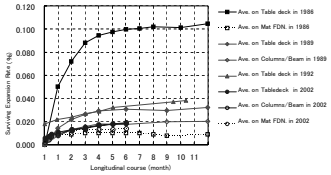

(d) Test Result of After-Expansion Rate

Fig. 32.3: Ikata Turbine generator foundation [816]

Murazumi et al. [615], respectively. In the latter study, beams made from reactive concrete were tested for shear and flexure. These beams were cured at 40°C and 100% relative humidity for about six weeks. Some doubt remains, however, as to how representative such a beam is for those NPP where ASR has been occurring for over 30 years.

A study of the material properties introduced in the structural analysis was first reported by Shimizu et al. [788].

An investigation of the safety margin for the turbine generator foundation has also been conducted modeling the structure by a series of beam element (i.e. not continuum ones) [787]. It appears that impact of ASR was accounted for by simply reducing the compressive strength from 30.4 to 28.8 MPa, and the elastic modulus from 24.9 GPa to 16.7 GPa (based on core tests). It was concluded that the structure is seismically "safe".

Later, vibration measurements and simulation analyses have been performed [818]. Takagkura et al. [814] has recently reported on an update of the safety assessment at this NPP.

Presently monitoring includes:

Impact of ASR on TG: foundation:

1. Table deck expansions 4 times/year (1 during annual inspection, 3 during operation) in longitudinal direction.
2. Reinforcement strain 3 times/year (1 during annual inspection, 2 during operation) at 9 locations: hoops, stirrups and main bars at table deck, columns and mat foundation.

3. Cracks condition at exterior surface of the TG foundation 1 time/year during annual inspection.
4. Continuous measurement of TG foundation vibration characteristics at 9 locations and recorded monthly
5. Continuous measurement of temperature and humidity at 4 locations under th table deck and recorded monthly.

Safe operation of turbine generator against ASR development. Should any value exceed threshold values, then alarm and/or automatic tripping will occur to ensure f turbine generator safe operation:

6. Continuous monitoring of shaft vibration
7. Continuous monitoring of bearing metal temperature

Planned additional monitoring

6. Nondestructive concrete tests
7. Deformation measurements of the TG

32.2.2 Critical Review

As there was no publicly available report on a finite element simulation of the impact of ASR on Ikata, we can not comment. However, it should be mentioned that this ASR occurrence has given rise to what appears to be a close interaction between the operator and the research community (as manifested in numerous papers at SMIRT conferences). Furthermore, the monitoring (a.k.a. Ageing Management Program) seems to be comprehensive.

32.3 Crystal River Delamination

32.3.1 Introduction

Inside nuclear reactors, the release of high-energy neutrons causes long-term degradation of material, including neutron embrittlement which will result in reduced toughness and cracking [200]. When this becomes unmanageable, then replacement of units must be undertaken. This is indeed a major problem for the massive heat exchange units (also known as steam generator) that may have to be replaced to ensure safe (crack free) continuous operation of the plant [138].
Progress Energy Florida (PEF) had to replace the heat exchanger in Crystal River 3. Given the size, PEF had to cut a 27-by-27-foot hole in the 187-foot-tall containment enclosure building (CEB) to extract the unit. However, since the CEB was post-tensioned, cables had to be judiciously detensioned, a task successfully accomplished in other sites. In this case, PEF opted to self manage the operation despite internal studies warning it of “huge” risk [819].
Initially, 97 tendons were to be detensioned (per calculations by Sargent & Lundy). Given the high cost, PEF reduced the number to 65 which was considered “adequate” by Bechtel. Even then, PEF decided to loosen a total of just 27 tendons. Additionally,

they hired a company to cut into the nuclear containment wall that had never done that type of work.

After detensioning and during concrete removal, it was found that the CEB had delaminated. There was an initial attempt to repair the CEB by fully detensioning it[2]. However, this only aggravated the problem, and additional delamination occurred. Ultimately, this operation resulted in extensive cracking that made any further repair impractical, and CR-3 had to be decommissioned [658] at a cost of approximately $700 million by 2027. Hence, an attempt to save $15 million resulted in a $3 million loss.

Gregory Jaczko, a former chairman of the U.S. Nuclear Regulatory Commission, blamed the disaster on a utility that didn't understand a job that should have been "routine." "That's a multibillion dollar asset that had to be shut down because of improper work planning, improper understanding of how to properly do this containment retrofit," said Jaczko.

Most shocking, yet not to the surprise of the author, the Nuclear Regulatory Commission stated that "Analysis has shown that the 2009 delamination (cracking) could not have been predicted" [711].

Ironically, this is not the only shut-down of a nuclear reactor due to problems associated with steam generator replacement [548] (a $2 billion loss was incurred by the decommissioning of San Onofre nuclear power plant).

Given the international attention that this accident has generated, and taking advantage of the wealth of publicly available documentation provided by the NRC (which should be commended for its transparency) through "NRC-ADAMS" [647], this report is an attempt to cast a critical light on the root cause investigation[3].

Hence, this document is composed of three parts. First, relying on publicly available documents, the root cause investigation of Crystal River 3 (CR) will be described in great detail. In the second part, the author reviews the finite element analysis and finally provides an alternate solution.

32.3.2 Reported Analyses/Investigation

This section will review [649] and [712]; that is, the non-proprietary version of the root cause investigation of the unanticipated delamination of Crystal River Unit 3.

In a pressurized water reactor plant, there are three main barriers that protect the public from the radiation hazards associated with nuclear operations, Figure 32.4(a). One of those barriers is known as the containment, which houses the fuel, the reactor, and the reactor cooling system. The Crystal River containment structure is a steel

[2] **Disclaimer:** The author was retained by Structural Integrity Associates to be one of the reviewers of the MPR calculations for the detensioning sequence.

[3] **Disclaimer:** The first author was retained as a consultant to PII for the root cause investigation. As such, he was privy to some confidential information, none of which will be reported directly or indirectly here. Furthermore, the author did perform a fracture mechanics based analysis of CR-3 that was not retained by PII, and at his request his name was not included in the final report. The author was subsequently retained as consultant by Structural Integrity Associates, Inc. to provide technical support for third party review of CR-3 containment detensioning evaluation and related documents. Again, the confidentiality of those documents is fully respected.

lined, post-tensioned, cylindrical concrete structure of about 157 feet in height with an outside diameter of about 138 feet. The containment has 42 inch thick concrete walls and has a flat foundation mat and a shallow torispherical dome. Post-tensioning is achieved by utilizing an outer array of horizontal tendons immediately adjacent to an inner array of vertical tendons that are embedded in the walls about 15 inches from the outside surface [482]. Tendons are also provided in the dome. In addition, steel rebar is embedded in the concrete walls at the outside surface and at other locations.

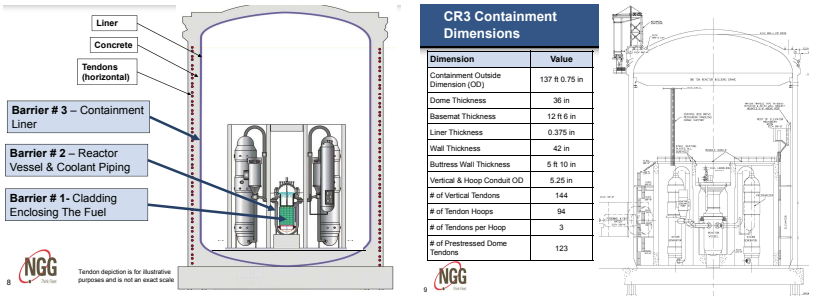

(a) Fission product barriers (b) Crystal River Unit 3 Dimensions

Fig. 32.4: Crystal River Unit 3 characteristics [712]

The containment is lined with a continuous 3/8-inch-thick carbon steel liner which acts as a vapor barrier for leak-tightness and also as an inner form for the concrete. The dome is post-tensioned by 123 tendons that are arranged in a three-way (layer) configuration and are anchored to a ring girder. The containment walls include 282 horizontal (Figure 32.5(a)) and 144 vertical (Figure 32.5(c)) tendons.

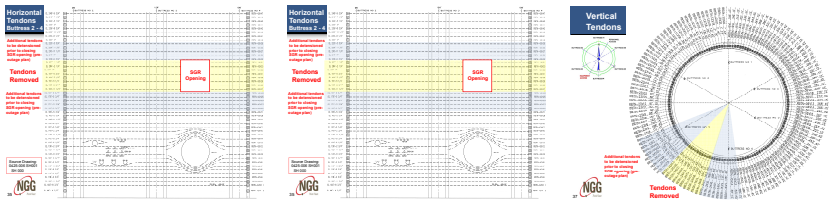

(a) Horizontal tendons, Buttress 2-4 (b) Horizontal tendons, Buttress 3-6 (c) Vertical tendons

Fig. 32.5: Post-tensioning cables [712]

Tendons are anchored to 6 vertical buttresses equally spaced circumferentially around the containment (Figure 32.6) and were designed to cross one buttress between the

end anchor ones (for the opening, tendons in 2-4 and 3-5 were released). Each tendon consists of numerous small diameter wires, which are greased and housed inside a conduit. The conduit for each tendon is about five inches in diameter and is made of galvanized steel, Figure 32.7.

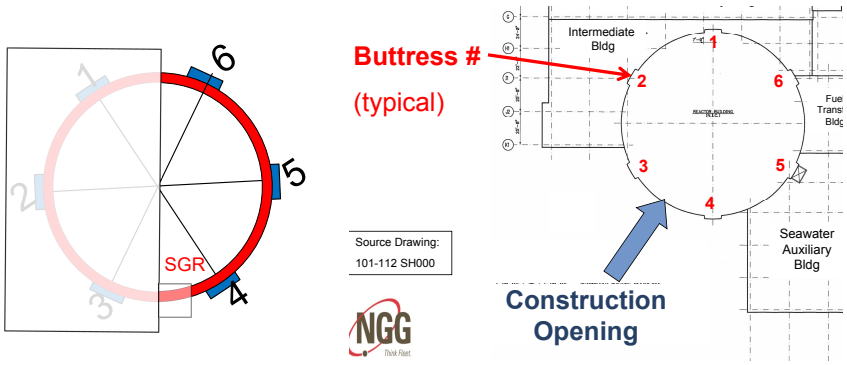

Fig. 32.6: Six anchoring buttresses [712]



Fig. 32.7: Five inch tendon conduits [712]

In nuclear power plants, and in Crystal River in particular, steam generator tubes are commonly fabricated from plain carbon steels, as well as low and high alloy steels; these components often fail catastrophically due to hydrogen embrittlement. At some point, continuous repairs may become prohibitively expensive, and the entire unit must be replaced. Though an equipment hatch is present in all containments, it was not large enough for the steam generators to be removed or replaced intact, and an alternative 25 by 27 foot opening through the 42 inch thick containment unit was envisioned, Figure 32.10(d).

Prior to cutting (through hydro-demolition with pressure as high as 25,000 psi), post-tensioned tendons crossing the opening were properly released, Figure 32.9(a), then the concrete was "excavated" according to the sequence shown in Figure 32.8.

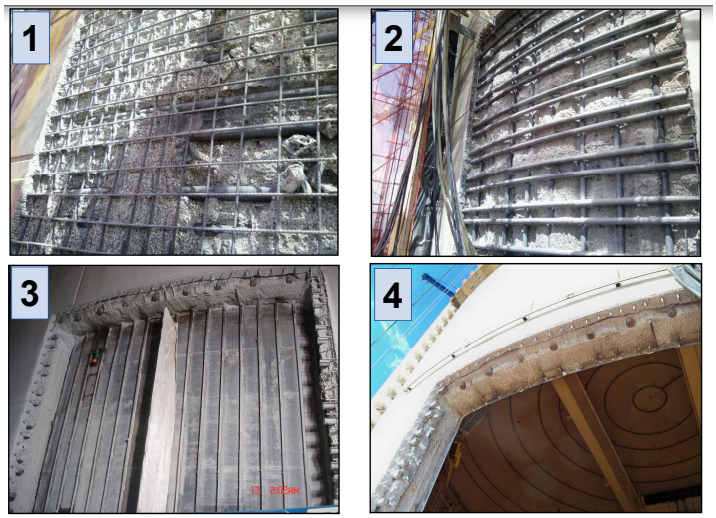

Fig. 32.8: Concrete and liner removal sequence [712]

In the process of cutting such an opening in the concrete containment wall, a concrete separation condition was discovered, Figure 32.10(a). It was located approximately in the cylindrical plane of the centerline of the hoop tendons, approximately nine to twelve inches from the exterior surface of the containment building, and had the shape of a butterfly, Figure 32.9(b).

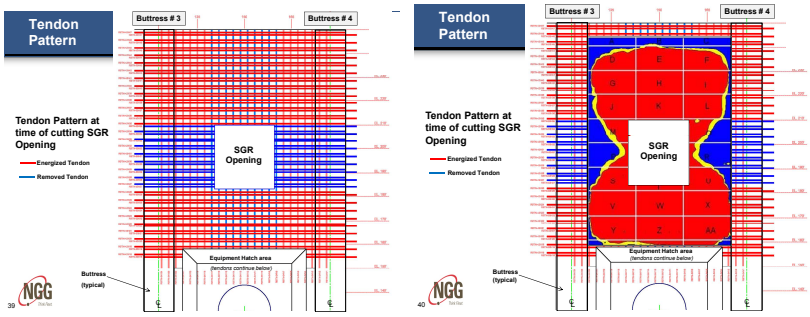

(a) Active and passive tendons (b) Buterfly defect

Fig. 32.9: Tendon pattern [712]

Approximately 30 inches of concrete remained in apparent good condition all the way to the liner plate. The hydro-demolition of the concrete continued until all concrete had been removed down to the liner and the containment building liner was exposed, Figure 32.10(b).



(a) Delamination

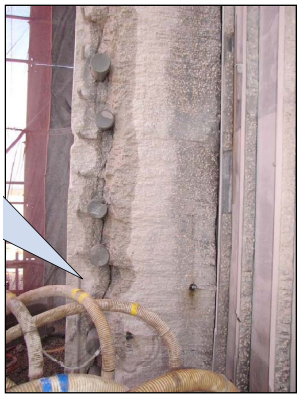

(b) Exposed liner

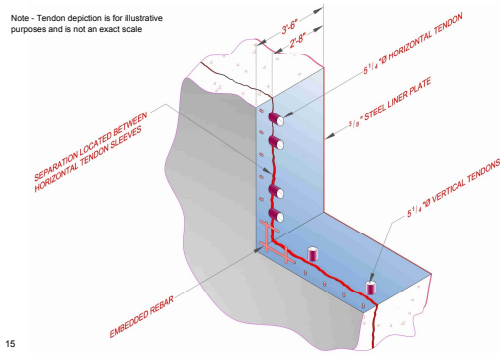

(c) Delamination explained



(d) Steam Generator Replacement opening (between buttresses 3 and 4)

Fig. 32.10: Delamination of Crystal River [712]

As a result of the unanticipated delamination, PEF engaged Performance Improvement International (PII) to perform a comprehensive root cause assessment to identify the cause or causes of the delamination. A total of 75 potential failure modes (FM) in nine general groups were identified to encompass the scope of possible contributors to the delamination event; eight of them were confirmed. Those have been lumped into the following groups:

Group 1: Containment Design: Excessive vertical and hoop stress; Excessive radial tensile stresses/no radial reinforcement; and Inadequate design analysis methods of radial tensile stresses (near sleeves, no radial reinforcement).
Group 2: Concrete Construction: Inadequate strength properties.
Group 3: Use of Materials: Inadequate aggregates.
Group 7: SGR Activities: Inadequate detensioning sequence and scope; Added stress due to removing concrete at the opening.

Finite element analyses were reported in association with Groups 1 and 7 only, thus only those two will be separately reviewed.
In the end, the licensee's investigation concluded that the delamination was caused during the creation of the opening in containment, Figure 32.10(c). As part of preparations for making the opening, tendons in the containment building wall were detensioned. The main cause of the delamination was attributed to the scope and sequence of this tendon detensioning. Tendon detensioning began after the plant was shut down in Operating Mode 5 when containment operability was not required.
The licensee found that the delamination was centered on the steam generator opening and formed the shape of an hour-glass. The delamination was limited to the containment bay between buttresses 3 and 4 and did not affect other bays of containment. The licensees repair plan to remove and replace the delaminated condition included: (1) additional detensioning of containment, (2) removal of delaminated concrete, (3) installation of reinforcement, including radial reinforcement through the delamination plane, (4) placing of new concrete, (5) retensioning containment, and (6) post-repair confirmatory system pressure testing. The licensee developed new finite element analysis models to predict stresses in the repaired containment wall under design basis loads. Using these and other supporting new analysis models, the licensee planned and implemented additional containment detensioning without causing further delamination. Subsequent to removal of the delaminated concrete, vertical cracks were observed along the vertical tendon lines.
Ultimately, when the cost of fixing the broken containment rose too high, the owner opted to permanently shut down the facility before its original operating license expired.

32.3.2.1 Finite Element Models

This section will attempt to present three important topics covered in the report[4] in the following sequence:

1. Attachment 1 Computer Modeling.
2. Failure modes associates with Group 1.
3. Failure modes associated with Group 7.

Though not clearly stated, PII developed two models:

[4] Note that many segments of this section were copied *verbatim* from [712]. For the sake of clarity, those were not italicized.

Global Model of the entire Nuclear Containment Structure (NCS). It is a linear elastic model which seeks to capture creep through a visco-elastic fracture model. It uses the implicit version of Abaqus. This model was used to provide boundary condition displacements for the next, more refined model.

Detailed Model of a wall panel which encompasses 6 horizontal and 3 vertical tendons. Meshing is identical to the global model with two major differences: a) A concrete layer immediately surrounding the tendon sleeves is modeled by the Lee-Fenves concrete damaged plasticity model [529]; and b) the explicit version of Abaqus is used.

There are four input values which can be adjusted to make the computer model output match the benchmark data, Table 32.1. Though the Global/Detailed values are redacted (i.e. blackened), they are identified as the two subjected to adjustments to reflect the analysis mesh size used.

Table 32.1: Input values adjusted for matching

Parameter	Typical Value	Abaqus Global/Detailed	Impact
Tensile Capacity	500 psi	Redacted	Onset of Cracking
Fracture Energy	0.40 lbf/in	Redacted	Onset of Cracking
Elastic Modulus	3.45×10^6 psi	Redacted	Radial Displacement
Creep Coefficient	2.2	Redacted	Radial Displacement

PII reports to have reduced the level of uncertainty by developing a *linear elastic super model*[5], but this model still suffered from the limitations of linear elastic modeling such as difficulty dealing with creep in concrete. The creep effect makes concrete respond more like a viscous fluid than an elastic solid in very particular conditions, and unless the model is capable of applying the different properties selectively as appropriate to the situation, one set of properties must be applied throughout the model, which leads to non-physical material properties being used.
In response to these limitations, PII developed a *Global Visco-elastic Abaqus model* that selectively applies the appropriate creep response for the local conditions. The result is appropriate calculation of delamination with realistic material parameters and radial displacements that agree well with benchmark data. The model uses the Lee-Fenves concrete damaged plasticity properties [529]. The model includes individual tendons and specifically models the steel properties of the liner, conduits, and rebar... The Abaqus global model is run using the sparse solver in Abaqus/Standard and the various sub-models are run in both Abaqus/Standard and Abaqus/Explicit. The global model provides displacement data to the edges of the panel sub-models and other sub-models, which further provide higher resolution of localized behavior. The driven sub-models include stress models and concrete damaged plasticity models, all within Abaqus.

[5] Underlines were inserted by the authors for emphasis.

Each and every curved tendon in the containment was explicitly modeled using embedded beam elements in the global model. The tendons were assigned the cross-sectional stiffness of the sleeves, and loads were applied.
The global displacements, stress state, creep law, and the concrete damaged plasticity parameters are all implemented into the *sub-models*. This results in two technical barriers: 1) Abaqus does not normally allow both mapping of the stress state and sub-modeling to be used simultaneously; and 2) Abaqus does not normally allow the creep law and the concrete damaged plasticity parameters to be used simultaneously. In order to overcome these hurdles: **redacted** approach was followed.
The Abaqus Global model has four sections in the containment wall: a steel liner plate, an inner concrete cylinder, a hoop tendon sleeve layer, and an outer concrete cylinder. Curved sections of tendon sleeves are matched to the mesh. The average value of tensile stress is about 23 psi. It increases to 31 psi due to concrete displacement.
Until recently, the resolution was to adjust the tensile capacity of the concrete to compensate for this. That is why a capacity of **redacted** psi was assumed in global calculations. It does not affect radial displacement, but it does facilitate the delamination evaluation. With the creation of the detailed sub-model, the peak stresses become more visible, and a tensile capacity of **redacted** becomes appropriate. Note that even at a **redacted** inch mesh size, there is still significant averaging of peak stresses occurring.
Applying that factor to the assumed tensile capacity of **redacted** for an infinitely small mesh, that corresponds to the measured tensile capacity of CR-3 concrete. The average direct tensile capacity measured in 9 samples was 448 ± 73 psi. The average split tensile capacity measured in 10 samples was 594 ± 59 psi. It is generally accepted that tensile capacity is 90% of the tested split tensile capacity, which gives 535 psi. Fracture energy is similarly impacted.
There are a number of ways to address the mesh issue. For radial displacements or general stress calculations, **redacted** mesh is sufficient to obtain realistic values. For scenarios which depend heavily on peak stress values, one approach is to use a stress concentration factor. Recent comparisons indicate that for global Abaqus, that factor would be about **redacted**. For the detailed sub-model, it would be about **redacted**. Another way to achieve exactly the same result is to adjust the tensile capacity of the concrete. For events such as the onset of delamination, the details of the process are very sensitive to the peak stresses involved, and fine mesh analysis is the best approach. Once initiated, delamination is less sensitive to peak parameters, so the overall extent and width of cracking can be well described by a detailed sub-model or even the normal sub-model.

Global Model The report identifies the global model as composed of the following subparts:

Liner: Thick conventional shell elements with elements located on the inner surface of the concrete, Figure 32.11(a).

Inner Cylinder: Goes from the liner 29 inches to the outer edge of the vertical sleeves. It is modeled by two layers of continuum shell elements, each with 5 integration points through the thickness for bending accuracy, Figure 32.11(b).

Hoop Conduits: All hoop conduits are explicitly modeled as beams with pipe sections. Only curved sections are modeled on which a radial line load is applied, Figure 32.11(c).

Hoop Layer A 5.25" thick layer which encompasses the vertical and horizontal sleeves. It is modeled by solid elements with damaged plasticity material properties based on the Lee-Fenves model [529]. These regions are allowed to crack and potentially to delaminate. The green regions are not allowed to crack since those regions are reinforced with steel, Figure 32.11(d).

Outer Cylinder: A 7.125" layer of concrete from the edge of the horizontal sleeves to the outer concrete, modeled by one layer of continuum shell elements with 5 integration points for accurate bending representation, Figure 32.11(e).

Damage Material Regions Regions of the hoop layer which have the concrete damage plasticity material properties. These regions are allowed to crack and may result in delamination of the outer cylinder from the inner cylinder, Figure 32.11(f).

Driven Regions: The region is driven by the displacements from the global model. The displacements are synchronized with the loadings in the delamination model. Hence, the global effects due to tensioning, creep, and SGR detensioning (including the unloading of the 10 vertical tendons) are accounted for, Figure 32.11(g).

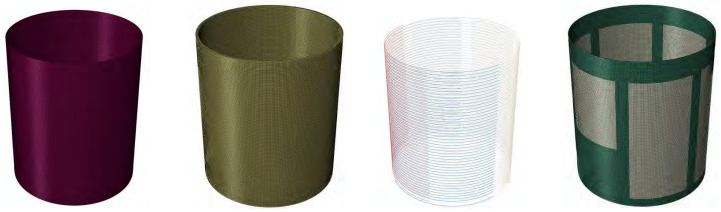

(a) Liner (b) Inner Cylinder (c) Hoop Conduits (d) Hoop Layers



(e) Outer Cylinder (f) Damage Material Regions (g) Driven Regions

Fig. 32.11: Group 7 Finite element analyses; global sub-model [649]

Detailed Model The detailed model includes 6 horizontal and 3 vertical tendons as shown in Figure 32.12. Radially, it matches the global mesh for ease of boundary condition transfers. Again, contrary to the global one, the inner cylinder is modeled by a nonlinear constitutive relationship, and it is analyzed by the explicit version of Abaqus.

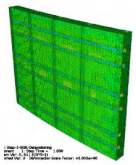

Fig. 32.12: Detailed model [649]

32.3.2.2 Failure Modes in Group 1: Containment Design

In this first set of reported analyses, PII alleges that high stress concentrations played a partial (but not decisive) role in the delamination.
Some of the relevant quotes include:

1. FM 1.1 determines that CR-3's containment design results in high vertical and hoop compression stresses and radial tensile stresses when compared to the designs of other plants. FM 1.15 determines *that stress concentration factors (SCFs) were not explicitly considered in the original design* of the containment building. FM 1.2 determines that radial stresses in the containment structure are high and that no radial reinforcement is currently in place. As with all the confirmed Failure Modes, the conclusions reached indicate that these issues did not individually cause the delamination, but rather contributed to the conditions that resulted in delamination.
2. The large diameter tendons have another impact as well. They are located at a depth of 10 inches from the outer containment wall with a set of tendons about every 39 inches. *At that depth, 27% of the cross-sectional area has the concrete displaced by tendon sleeves*.
3. A horizontal tendon provides the radial compressive stress of about 340 psi averaged over the diameter of the tendon sleeve. The average over the entire cross-section of concrete being radially compressed by that horizontal tendon is about 100 psi. Normally the average radial tensile stress would be 23 psi, but *due to concrete displacement*, it is 31 psi at the centerline of the horizontal tendons.

The analysis used to support this finding is also reported later on in conjunction with the Group 2 analysis.
To support the allegation, PII reports not to use NASTRAN to quantify concrete fracture so fracture parameters are not applicable. Abaqus applies creep correction only for long time period intervals such as the time step of 30 years of operation

with the containment tensioned. Material properties are reported in Table 32.2. E_0 is the elasticity modulus, and E_1 is the creep adjusted elasticity modulus. The average modulus measured on 22 CR-3 containment cores is 3.45×10^6 psi. f'_t is tensile capacity, and G_t is the fracture energy. Fracture energy was measured to be 0.40 lbf/in.

Table 32.2: Material properties for Group 1 Analyses

Figure	Model	E_0	E_1	$f't$	G'_t	Creep
32.13(a)	Abaqus Detail	3.45×10^6	3.45×10^6	360	0.08	2.2
32.13(b)	Abaqus Detail	3.45×10^6	3.45×10^6	360	0.08	2.2
32.13(c)	Nastran	4.29×10^6	4.29×10^6	NA	NA	o

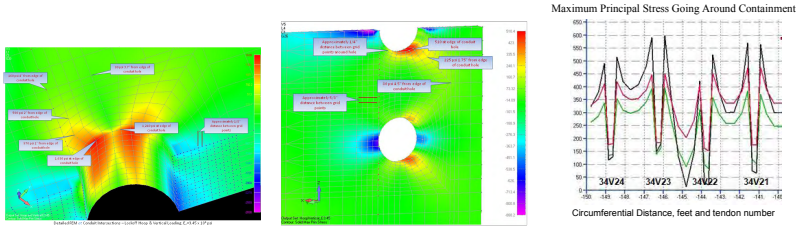

(a) Stress contours for normally tensioned conditions at the intersection of a vertical wall. and horizontal tendon. (Three dimensional effect looking through a hoop tendon hole)

(b) Sketch of the delamination cracking in the bay 34

(c) Plot of maximum principal stress as a function of distance around the containment circumference. (Black is pre-SGR, Green is post SGR detensioning, Red is post SGR concrete removal).

Fig. 32.13: Group 1 Finite Element Analyses [649]

On the basis of Figure 32.13(a), PII points to the peak tensile stress at the edge of the horizontal tendon hole near a vertical tendon is well in excess of the tensile capacity of the CR-3 concrete. It is likely that small cracks formed at these intersections but then stopped propagating when they reached a location where the stress was too low to continue. This is further illustrated by Figure 32.13(c).
PII concludes that:

- CR-3's containment design results in a somewhat higher potential for delamination than other similar designs on the basis of Compressive-Tensile Stress Interaction.
- Radial tensile stresses are high, and there is no radial reinforcement. Large tendons lead to high peak stresses.
- Stress concentration factors were not explicitly considered in the original design of the containment building. As with all the confirmed failure modes, they conclude

that these issues did not individually cause the delamination but contributed to the conditions that resulted in delamination.

Considered alone, the stresses involved in the CR-3 containment design are well within the capability of the concrete material used. However, when stresses occur for other reasons, such as local stresses resulting from de-tensioning of tendons and cutting the opening, these additional stresses at CR-3 contribute to the overall stress condition.

32.3.2.3 Failure Modes in Group 7: SGR Activities

This second group addresses a separate set of failure modes: a) Inadequate de-tensioning sequence and scope; and b) Added stress due to removing concrete at the opening[6].
The computer model and its validation were presented in attachments 1 and 2 in the report. However for increased clarity, and given their importance, they were presented above in this one.

32.3.2.3.1 Discussions The report starts by discussing the inadequacy of the de-tensioning sequence and the added stress due to removing concrete at the opening. It points out the impact of the change from a symmetric load and deformation to an unsymmetric one on stresses and strains that may exceed the containment's capacity. Also mentioned is the potential for excessive stresses and/or strains to develop when transitioning between two symmetric states because of the sharp local transition from a series of tensioned tendons and a series of de-tensioned tendons. Reference is made to Figure 32.15(d) which shows the radial displacement that occurred during the SGR de-tensioning. Delamination occurs where radial stress is high which occurs at sharp bends in the wall. Note in Figure 32.15(d) that the radial displacement associated with de-tensioning is linear. This means that the stress that develops is monotonically increasing, and other sequences of de-tensioning the same number of tendons would not change the end-point which is the highest stress condition.
The report does also mention that in an area as large as bay 34 and with the large stress concentration factors on a detailed scale, it is probable that cracking began in isolated points of highest stress. As the stresses increased (due to the growing number of de-tensioned tendons) and shifted (due to the various tendons de-tensioned), small cracks grew and joined until they eventually covered the entire delaminated area.
It is clear from the finite element analysis that the localized de-tensioning in bay 34 led to curvature which contributed to the delamination. The March, 2010 analysis and subsequent de-tensioning for repair found that use of more symmetrical de-tensioning of the entire circumference was required to avoid delamination in other bays, and the building was successfully de-tensioned.

[6] Presentation of the failure modes associated with this group was deemed to be very convoluted by the author. As such, headings and order of coverage were modified, but the content strictly adheres to what the report has presented. No comments were interjected, these will be presented later in Sect. 32.3.3

32.3.2.3.2 Global Radial Response The tendon de-tensioning simulation, using the previously described model, was simplified by not relaxing the tendons in order but instead relaxing all the tendons partially at the same time. Thus 25% through the de-tensioning means all tendons are stressed to 75% of their lock-off value.
The sequence was as follows:

1. The containment is initially constructed with straight vertical walls. Radial displacement is 0 inches since this is the measurement baseline, Figure 32.14(a).
2. Upon completion of tendon tensioning the building is mostly symmetrical and each bay has an inwardly curved wall with a maximum deflection of -0.5 inches, Figure 32.14(b).
3. Over the next three decades, the concrete creeps and radial displacement grows to a maximum of -1 inch, Figure 32.14(c).
4. As SGR de-tensioning proceeds, bay 34 begins to move radially outward. Bays 23 and 45 also begin to move radially outward at half the rate of bay 34 because bay 34 has shared tendons with each of bays 23 and 45. The other bays begin to move inward in response to the buttresses having unbalanced side loads. The building develops an overall vertical curvature, Figure 32.14(d).

Table 32.3: Material properties used in the detensioning simulations

Figure	Model	E_0 psi	E_1 psi	f'_t psi	G'_t lbf/in	Creep
32.14(a), 32.14(b), 32.14(d), 32.14(e), 32.14(f), 32.15(a), 32.15(c)	Abaqus Global	3.45×10^6	3.45×10^6	NA	NA	2.2
32.15(e), 32.15(f) 32.13(b),	Abaqus Global Bay sub model	3.45×10^6	3.45×10^6	108	0.08	2.2
32.14(c), 32.15(b), 32.15(d)	Abaqus Global	3.45×10^6	1.1×10^6	NA	NA	2.2
32.13(b), 32.18(a), 32.18(b), 32.18(c), 32.19	Abaqus Global Bay sub model	3.45×10^6	3.45×10^6	360	0.08	2.2

The global response of the container in terms of displacement is captured by Figures 32.14(a) to 32.14(d), and they show the progression of containment shape over time. It was originally a cylinder but it became concave with the tensioning of the tendons. The SGR de-tensioning sequence resulted in a building-wide change in shape as bay 34 moved out close to its original tensioned position prior to creep, Figure 32.15(d). The report does provide qualitative support for the observed radial displacement.

32.3.2.3.3 Delamination Explained To explain the observed delamination, focus is placed on the details of the local wall-radial displacement response based on the global model first and then on the detailed one.

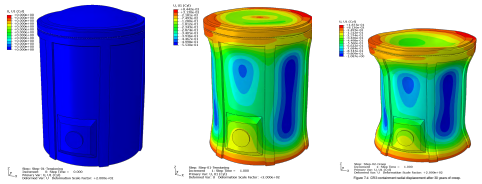

(a) Untensioned (b) Fully tensioned (c) After 30 years of creep

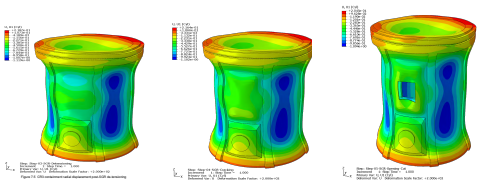

(d) Post SGR de-tensioning (e) Post SGR de-tensioning (f) After SGR opening completion

Fig. 32.14: CR-3 Containment radial displacements [649]

Global Model Using the model previously described, the report states that it was indeed capable of capturing the field observed delamination from the global model. Figures 32.15(a) to 32.15(c) show the (displacement) contour lines of the global model (subjected to a linear elastic analysis) at various stages. Figure 32.15(d) is a plot of bay 34 midline profile at various stages. Delamination is observed in Figures 32.15(e) and 32.15(f) right before concrete removal and after concrete removal. Displacement contour lines in Figure 32.15(e) are compared to the field observed extent of cracking shown in Figure 32.16.
Local stresses increased since the rest of the bay was still restrained by tensioned tendons, Figures 32.17(a) to 32.17(h).

Detailed Model It is shown that the detailed model was also capable of capturing the delamination. This is observed in the panel, and the situation ultimately led to localized cracking that propagated over most of bay 34, Figures 32.18(a) and 32.18(c). The maximum stresses in the delaminated area are shown separately in Figure 32.19.

32.3.3 Critical Review

Undoubtedly, a very detailed (numerical) investigation was performed. There was a recognition of the complexity of the problem, and as a result, advanced nonlinear analyses were performed. However, the authors found the report difficult to follow (and not only for the many redacted portions).

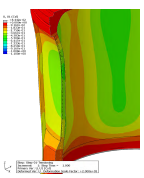

(a) Post initial tensioning in 1975

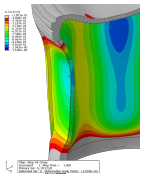

(b) After 30 years of creep

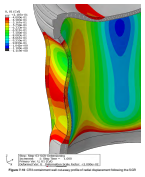

(c) After the SGR

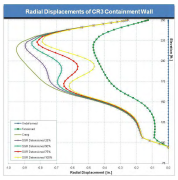

(d) Bay 34 midline profile for progressive SGR detensioning

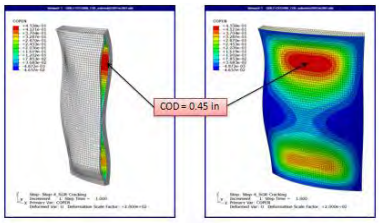

(e) Step 4

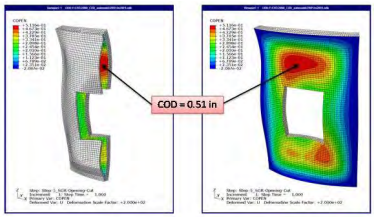

(f) Step 5 (after concrete removal)

Fig. 32.15: CR-3 bay 34, cracking and crack opening displacement [649]

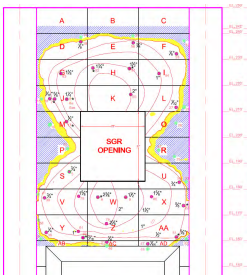

Fig. 32.16: Plot of delamination damage in Bay 34. Shown are the measurements of the delamination gap both by impulse response test and by core bores [649]

32.3.3.1 Analysts/Analysis

NRC-ML 102861026 [649] provides the *curriculum vitae* of those involved in the reported analysis. Surprisingly, none of them seem to have any experience in the analysis of reinforced concrete, let alone in nonlinear analysis. Having experience with a tool such as Abaqus for mechanical design does not qualify someone to perform the investigation of a multi-million dollar accident. Regretfully, this lack of expertise transpires throughout the report where technical terms are often misused, repeated, or out of context; confusion seems to prevail, and results are highly questionable. For example on page 32, the report says, “Abaqus Global does not calculate fracture so those parameters are not applicable for it”.

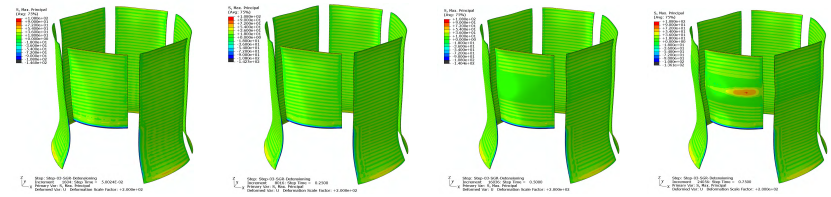

(a) Step 1/20 (b) Step 5/20 (c) Step 10/20 (d) Step 15/20

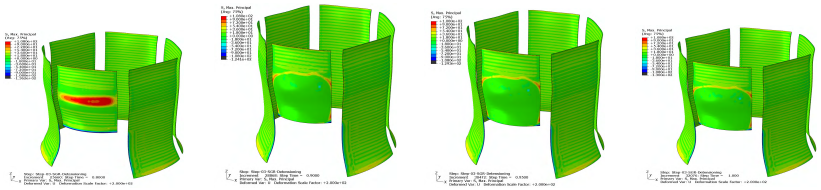

(e) Step 16/20 (f) Step 18/20 (g) Step 19/20 (h) Step 20/20

Fig. 32.17: Maximum principal stresses (psi) [649]

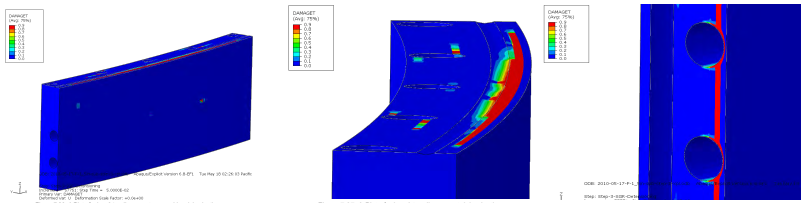

(a) Bay 34 wall segment approaching delamination (b) Bay 34 wall segment delaminating (c) f'_t= 360 psi

Fig. 32.18: Bay 34 wall segment delamination

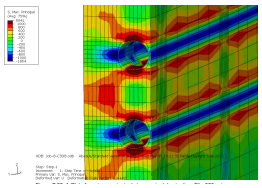

Fig. 32.19: Plot of maximum principal stresses in delamination. f'_t =360 psi. [649]

32.3.3.2 Validation

"Benchmarking" of the code results are inconclusive at best. Structural integrity test (SIT) (in theory) should not have induced any nonlinearity (cracking or otherwise);

hence excellent correlation between measurements and computations should be expected. Indeed adequate correlation is reported; however this does not necessarily validate the code for nonlinear analyses.
Validation with the 2010 detensioning is inconclusive as there are too many variations in laser readings, and errors bars are not included for either of the two reported values (experimental or numerical). The use of the term "benchmarking" is unfortunate; a more traditional term would have been "validation" or possibly "calibration" (as it is reported later that elastic properties have been modified to yield adequate correlation between numerical findings and field observations).
The nonlinear constitutive model used for the detailed model [529] is far from simple. Some of the key input parameters include:

$\overline{D}_c$, $\overline{D}_t$	formatting: Measured elastic stiffness degradation for uniaxial compression and tension, respectively.
G_c G_t	Compressive and tensile fracture energies, respectively.
l_c, l_t	Compressive and tensile characteristic length parameters, respectively.
α, β	Coefficients of the yield function.

Except for G_t, none of the other parameters are provided. Hence, one can easily fine-tune the model to obtain desired results, but such an approach is highly circumspect. The selected parameter should have been first validated independently and then tabulated in the report (as they were in the original paper by Lee and Fenves).

32.3.3.3 Elastic Modulus and Visco-Elasticity

The report addresses the finite element model used for Group 1. We find it confusing. The authors of the report start by professing not to use NASTRAN to quantify fracture, and as such fracture parameters are not applicable. Yet ever since the pioneering work of Hillerborg, Modéer, and Petersson [420], any modern investigation of concrete fracture would have to use fracture mechanics. The website of the International Association of Fracture Mechanics of Concrete and Concrete Structures (IA-FraMCoS), with over a thousand indexed papers, is a testimony to the rich and relevant literature associated to the fracture mechanics of concrete.
In the document, reference to creep is made in conjunction with G'_t, the tensile fracture energy. It is assumed that the authors meant G'_F which is the concrete fracture energy and is completely unrelated to creep[7]. Furthermore the table entry labeled "Creep" may be misleading; it is assumed that the authors meant "Creep Coefficient."
A particularly troublesome approach taken by the authors is the liberty with which material properties are at times modified to match intended results. In Table 32.2, E_0 is equal to 3.45×10^6 in the Abaqus analyses and 4.29 in the NATRAN analyses. The global model used is labeled visco-elastic fracture, yet there is no fracture modeled whatsoever. Furthermore, visco-elasticity is a term usually reserved for those models where creep and linear response are separable (that is, the model

[7] Disclaimer: The fracture energy tests were performed under contract from PII by the author.

is expressed by a relaxation function). In the reported analysis, the so-called visco-elasticity (which Abaqus has implemented) is instead modeled by reducing the elastic modulus through the creep coefficient.
Whereas the reported assumed value of $E = 1.1 \times 10^6$ psi allowed the model to predict the onset of delamination with significant uncertainty, it is not clear how it correlates with the earlier reported value of 3.45×10^6 psi. It is not at all clear if this reported value of 1.1×10^6 psi is E_0 which will then be reduced by creep, or if it is the creep reduced value. Coincidentally, this value may be acceptable on the basis of an assumed creep coefficient of 2.2 (not supported by referenced laboratory tests):

$$E' = \frac{E}{1+\xi} = \frac{3.45 \times 10^6}{1+2.2} = 1.07 \times 10^6 \text{psi} \tag{32.1}$$

Though the compressive strength is not provided, it can be inferred from

$$E = 57,000\sqrt{f'_c} \Rightarrow f'c = \left(\frac{E}{57,000}\right)^2 = \left(\frac{3.45 \times 10^6}{57,000}\right)^2 = 3,600\text{psi} \tag{32.2}$$

which is a reasonable value to which corresponds a creep coefficient ξ of 2.98
This creep coefficient is applicable in the absence of reinforcement which is known to drastically reduce creep. Indeed, Equation 9.5.2.5 of ACI 349 [11] states that unless values are obtained by a more comprehensive analysis, additional long term deflection resulting from creep and shrinkage of flexural members shall be determined by multiplying the immediate deflection caused by the sustained load considered by the factor λ_Δ

$$\lambda_\Delta = \frac{\xi}{1+50\rho'} \tag{32.3}$$

where ρ' shall be the value at midspan for simple and continuous spans.... It shall be permitted to assume ξ, the time dependent factor for sustained loads, to be equal to 2.0 for 5 years or more. A commonly accepted reinforcement ratio for an NCS can vary from 0.5 to 1%, thus

$$\lambda_\Delta = \frac{\xi}{1+50\rho'} = \frac{2.}{1+50 \times [0.005|0.01]} = [2.3|1.98] \tag{32.4}$$

These values correspond to the reported one used in Eq. 32.1, but unfortunately, the document is not at all clear which E is used. The finally selected values are redacted.

32.3.3.4 Tensile Strength

There is a "mystery" surrounding the actual value of the tensile strength used with references to "adjusting its value." Much of the critical information, of what should be a laboratory measured value, is redacted.

32.3.3.5 Modeling

To better understand and visualize the model adopted by PII, Figure 32.20 was prepared by the author. Further explanation is provided later.

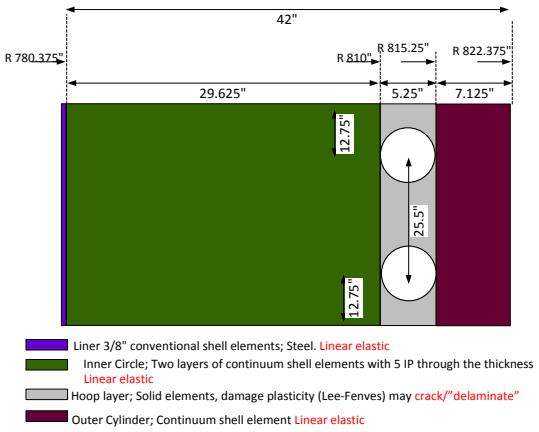

(a) PII global & refined model

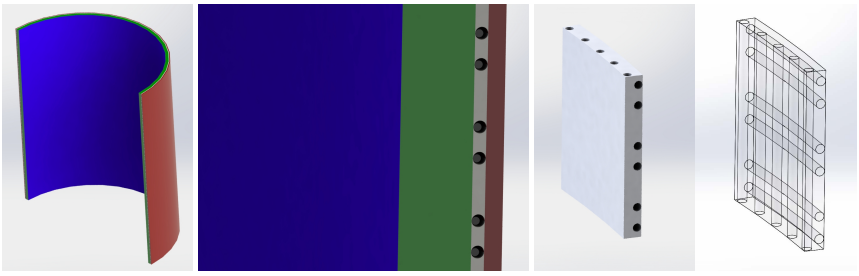

(b) Global model (c) Closeup of global model (d) Refined model

Fig. 32.20: Models

Point Loads in the Sleeves Tendon loads in the sleeves were applied as line loads. This induced a stress singularity which may have been interpreted as cracking. This is clearly visible in both Figure 32.13(a) and 32.19. Those are "distractions" from the actual stress field which may have caused cracking/delamination. Modeling the stiffness of the sleeve is very unlikely to have sufficiently smoothed or distributed the point load into a traction wide enough to avoid stress singularity.
Finally, the reader should consult [7] for a good coverage of this delicate topic.

Reinforcements In a structure as complex as CR-3, clearly there are zones with heavier reinforcement than others (around the hatch for instance). Yet the reinforcement modeling is not explicitly addressed. It is not expected that reinforcement should be modeled explicitly, but as a minimum, the elastic properties of concrete should be replaced by a "weighted modulus" based on the reinforcement ratio, ρ:

$$E_{eq} = E_c + \rho_s E_s \tag{32.5}$$

From Global to Detailed A two tier analysis for complex structures is not unusual (this is commonly referred as "substructuring" in finite element parlance). It is not clear how the boundary conditions are transferred from the global to the detailed model, especially as the report mentions a so-called "driven region" (Figure 32.11(g)). Finally, the panel (detailed model) should be subjected to high vertical compressive forces caused not only by the post-tensioning but also the self weight of the structure. There is no indication that this was accounted for.

How is it all put together? This is possibly the major concern for this author:

1. There is no indication in the report on how the various constituents of the global or detailed models are connected. Is there a full connection; are nodes master-slaved, or are they assumed to act independently as a parallel system (as opposed to a single one)?
2. In the absence of such information, and in view of the observed "delamination" (Figures 32.15(e), 32.15(f) and 32.11), indications are that the constituents were not all tied together, and as such, of course a "delamination" will be observed. As discussed in the next section, the analyst should have tied the damage material region, Figure 32.11(f) to the adjacent ones by joint/interface, zero-thickness elements commonly found in most finite element codes. These can range from the simplest ones [345] to the more advanced fracture mechanics based one [177].

Keeping in mind that there is a one way coupling (that is from global to the detailed model) and that the simplified linear elastic global model was able to capture delamination (Figure 32.15(e), 32.15(f)), why was there a need to perform the detailed analysis and then capture the delamination in Figure 32.11?
The delamination in the global model is captured as a separation of nodes (implying that no interface elements were used), and in the detailed model, is conjectured that the delamination occurred in light of the damage zone showed through the continuum elements in Figure 32.11.

Explicit Analysis An explicit model will always yield some result. However, because equilibrium is not checked at the end of each increment, one has to be extremely careful in accepting the results of such an analysis. Indeed the Lee and Fenves [529] model adopted is known to be extremely unstable in implicit analysis, but will always yield results in an explicit one. A remedy to this concern is to ensure balance of energy throughout the analysis.

Weak and Strong Links There is an imbalance in modeling effort. On the one hand, "strong links" are present in modeling the sleeves of the tendons, which is not needed; neither model would have needed to have such a fine mesh. On the other hand, there are "weak links" as the reinforcement does not seem to be modeled, and the various components of the mesh were not "glued" together.

32.4 Saint Laurent

adapted from [749]
Built between 1965 and 1970, he Saint-Laurent nuclear power station (France) is a GCR Prestressed Concrete Pressure Vessels (PCPV) with internal diameters ranging from 10 to 24 meters, internal height between 15 and 40 meters, and wall and cap thickness from 3 to 6 meters. The service pressure inside the PCPV ranged between 1.5 to 4.6 MPa in operation. In 1990 it ceased operation, was given 50 years time period to reduce radioactivity before decommission. Nevertheless, the structure must remain impervious to the internal radioactive material.
However, starting 1974, concrete started to swell resulting in increased prestressing. At first, swelling was attributed to creep, however after a few years of operation, both PCPV exhibited an increased "swelling" strain trend, attributed to AAR [560]. This led to an increase of the prestressing force, Figure 32.21(a) and Figure 32.21(b).

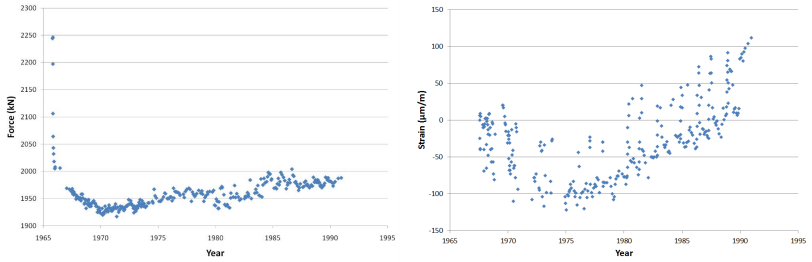

(a) Time history of force readings

(b) Strain readings (scatter due to temperature variation, and operation cycles)

Fig. 32.21: Impact of AAR on the Saint-Laurent nuclear power station

32.5 Tihange 2

Tihange is a double containment with annular space (analogous to Seabrook). In 2008, during in-service inspection, it was determined that there was spalling of concrete above the corroded rebars on the external face of the containment building. Causes of Tihange 2 (observed during in-service inspection, 2008) Possible identified causes included:

- Insufficient concrete cover above the rebars
- Advanced carbonation front with rebars corrosion followed by spalling of concrete surfaceParticularly along cracks
- Alkali-silica reaction (ASR)
- Reduced mechanical properties of the concrete, with white traces and presence of alkaline silica gel

A three phases repairs initiated in 2010. First non-reinforced shotcrete was applied, but it was found that it had poor adherence. In the second phase, concrete was scrapped shotcrete and steel grids were applied. Finally phase 3 will address zones not too severely affected.
A 2012 assessment concluded that [692] [821], Figure 32.22:

- Unexpected size of the degraded surface and the affected depth, 50% of the surface wWith a maximum depth of 30 cm on 5% of the surface.
- New analyses confirmed the predominance of ASR. The ASR is mainly observed at the top of the containment (upper 6 m). ASR and carbonation are two degradation mechanisms mutually exclusive.
- Measured porosity of the concrete: between 6 and 9%. Target value is 5%.
- New assessment of the structural integrity performed by the operator.
- ASR was one of the main issue:
  - Presence of reactive chalcedony (SiO2 am) in the river sand used as fine aggregate
  - Water infiltrations from the top of the containment building due to standing water and privileged exposure to poor meteorological conditions that could have favoured ASR
  - Secondary ettringite formation also observed in air bubbles in cement and thus there may be a possible concomitant occurrence of delayed ettringite formation (DEF).

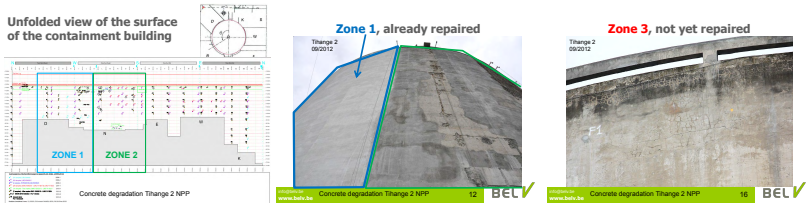

Fig. 32.22: Reported impact of ASR on Tihange nuclear power plant [821]

Complementary tests are planned:

- Residual swelling capacity (ASR)
- Uranyl acetate test (ASR)
- Sensitivity check on the aggregates

- More detailed compression and traction tests
- Scanning electron microscopy (SEM)
- Ultrasonic analysis of the concrete
- Petrographic analysis of the limestone aggregates to determine their origin
- Search for delayed ettringite formation (DEF)

Chapter 33
Analysis of Nuclear Containment Structures; III Analyses by the Authors

Abstract
Whereas in the previous chapter we have detailed, and commented on, reported analyses of NPP by others, this one will provide an alternative numerical solution to these case studies using methods covered in this book.

33.1 Crystal River Delamination

As indicated earlier, based on [192] [649] and [712], a renewed analysis of Crystal River was undertaken by the first author [757]. This section will detail a fracture mechanics based analysis to explain CR-3 delamination.

33.1.1 Assumption and Model

Finite element modeling of the Crystal River containment structure, detensioning sequence, staged "excavation" of the concrete cover, and finally ensuing delamination is a challenging task. Ultimately, a finite element model is an engineering compromise between accuracy, representativeness, simplicity, elegance, computational cost, and most importantly a good understanding of the physics governing the problem being solved. In this case, given that delamination is a manifestation of cracking, the solution has to be rooted in fracture mechanics. After all, one is trying to capture cracking of a brittle material, and plasticity is of little relevance in this case.
A particularity of this analysis, is that the crack trajectory is known; it is a (curvilinear) plane connecting the sleeves where delamination occurred. Since there is no indication that concrete crushed as a result of compressive stresses exceeding approximately half the compressive strength, all the nonlinearity would stem from cracking. As such, a discrete/cohesive crack model (Section 15.3) would better capture the nonlinearity than a smeared (diffuse) crack model. In CR-3, delamination occurred (in the duct plane) in an unreinforced direction (gray zone in Figure 33.1(a)).
Accordingly, a suitable model is one that:

- Takes advantage of geometrical symmetry (180°), Figure 33.2(a). It should be noted that post-tensioning cable layouts violate symmetry; however this was a sensible compromise to ensure reasonable computational cost.
- Restricts the nonlinearity (i.e. cracking) to the delamination plane.

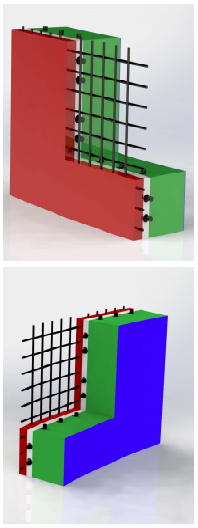

(a) Cut through conceptual model (viewed from extrados and intrados)

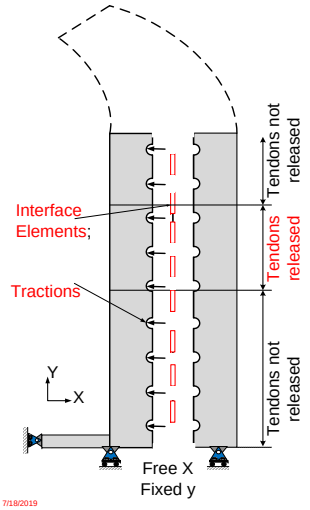

(b) Structural idealization for finite element mode

Fig. 33.1: CR Idealization

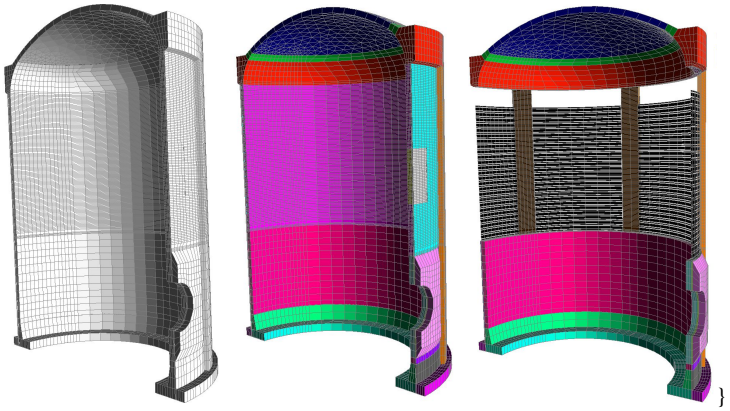

(a) Final finite element mesh

(b) Individual groups

(c) Peeled concrete showing interface elements

Fig. 33.2: Finite element mesh

- Models sleeve holes individually, and an inward traction models the hoop post-tensioning (which are ungrouted) as individual radial forces, Figure 33.1(b).

- Uses reinforcement either smeared over the elements (reinforcement mat), or adopts an effective elastic modulus (in terms of E_c and E_s) (around the batch) as described in Section14.7.
- Models vertical prestressing as a set of point forces.
- Models prestressing in dome as a uniform (downward) radial traction.

Hence, a total of 19 material groups were used; some had identical properties, but were separately defined in order to model the "peeling" of the concrete in the Steam Generator Replacement opening (SGRO), Figure 33.2(b).
The load sequence leading to delamination is modeled in 17 increments, Table 33.1.

Table 33.1: Load increment in CR analysis by authors

Incr.	Load	Incr.	Load
1	Gravity	2-3	Post-tensioning
4-5	Creep	6-9	Cyclic temperature (inside/outside)
10-16	Cable detensioning in SGR zone	17	concrete removal
	Delamination occurs		

33.1.2 Results

Figure 33.3(a) shows the global response (with highly amplified deformation) of the CEB whereas closeups on the captured delamination are shown in Figure33.3(b). We note the impact of the individual hoop tendons. Though they have been detensioned, elastic recovery reduced the impact of the forces. However, creep recovery is still taking place (Figure 5.1), and its impact clearly shown.
It is noteworthy that delamination was a brittle failure and not a progressive one. This is indeed characteristic of concrete shear/tension failure in the absence of reinforcement.

33.1.3 Conclusion

It is the author's opinion that delamination was caused by the abrupt change in curvature due to the detensioning of the cables inside the SGRO, i.e. not enough cables were detensioned as reported by Tampa Bay Times [819]. This could have been prevented if the tendons right outside the SGRO had been detensioned also in order to minimize abrupt curvature changes.
The simple, yet elegant, fracture mechanics based approach was capable of fully capturing the delamination of Crystal-River.

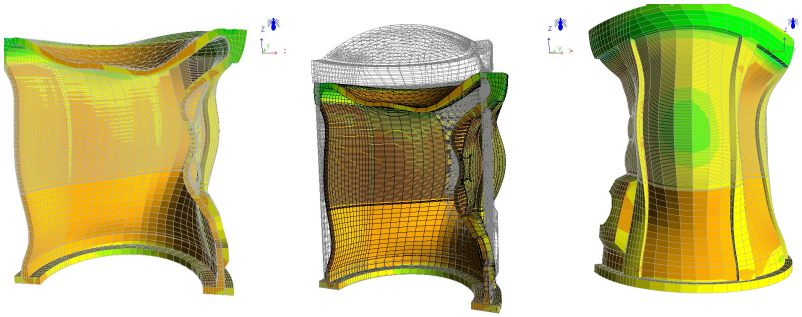

(a) Global response

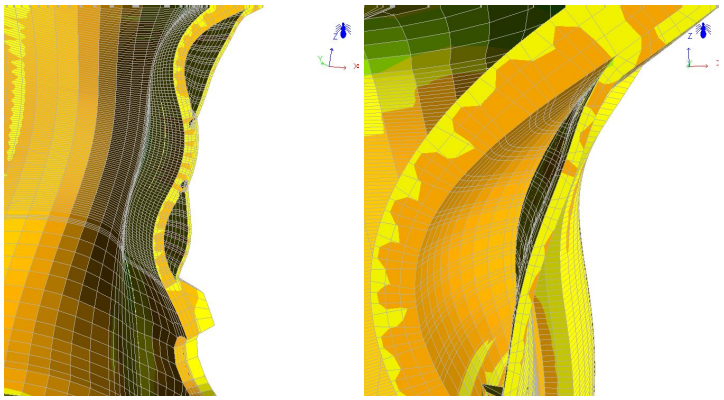

(b) Delamination details

Fig. 33.3: Delamination of CR captured by a fracture mechanics based approach

33.2 CEB Subjected to ASR and Seismic Loads

Contrarily to CR-3, this section will not attempt to reanalyze Seabrook *per-se*. Instead, analysis of a generic (but similar) CEB subjected to 40 years of ASR followed by a seismic excitation is reported. The sequence of two non-linear analyses will be cast ina probabilistic context resulting in fragility curves. This analysis was first reported in [771].
The major steps can be summarized as:

1. Prepare a detailed nonlinear finite element model including rock-containment interaction, concrete material nonlinearity, and interface joint around the CEB.
2. Apply a pre-defined ASR expansion to the CEB.
3. Develop two types of seismic excitations:
   - Scenario-based stochastic ground motions
   - Endurance time intensifying acceleration functions.
4. Determine the local and global failure modes.

5. Perform a set of nonlinear transient analyses using cloud computing and data mine the results.
6. Develop appropriate capacity and fragility curves for sound and ASR-affected CEB.

33.2.1 Finite Element Mesh

The NVCS has dimensions inspired from NUREG/CR-6706 [662]. The structure will be first subjected to 40 years of ASR expansion followed by multiple seismic excitations (with or without ASR induced damage), and results will be compared with the response of the CEB subjected to the same seismic excitations but without prior ASR expansion (Figure 33.4 B, C, and A respectively).

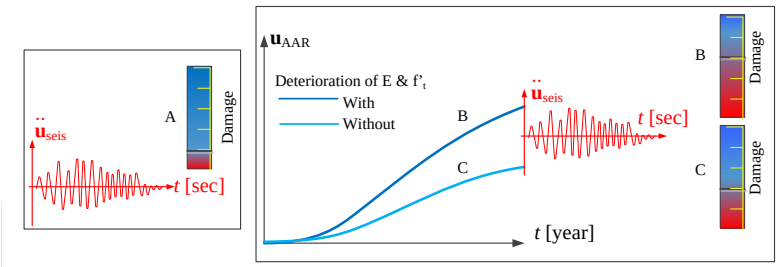

Fig. 33.4: Three scenarios of investigation: A: No ASR; B: ASR with 40% damage; and C: ASR without Damage.

Outline of the analysis procedure is partially shown in Figure 31.2 where after identification of the physical model site characteristics, probabilistic seismic hazard analysis and seismic hazard de-aggregation are performed. Then, ASR properties are identified, and dynamic excitations are generated through: a) ETAF, and b) scenario-based stochastic ground motions. Then, the FE analysis is performed in the cloud (i.e. using multiple CPU's) and finally capacity and fragility curves are derived for ETA and stochastic models, respectively. In each case, three analyses were performed, Figure 33.4.

The selected and partially buried CEB is schematically shown in Figure 33.5(a). Note that only the concrete underneath the soil level will be subjected to ASR (as a result of the high relative humidity likely to be present in the surrounding foundation). Material properties are separately shown in 33.2, 33.3 and 33.4.

The potential secondary stresses induced by the uplift forces (caused by the eccentricity of the resulting inertial force), Figure 33.5(b), will be mitigated by the insertion of cohesive based joint elements [177] where necessary. A 3D continuum model, Figure 33.5(c) is prepared. Reinforcement is modeled as "smeared" by altering the stiffness matrices of those continuum elements they cross. A 0.5% reinforcement was assumed in both directions, resulting in the reinforcement shown in Figure 33.6(b).

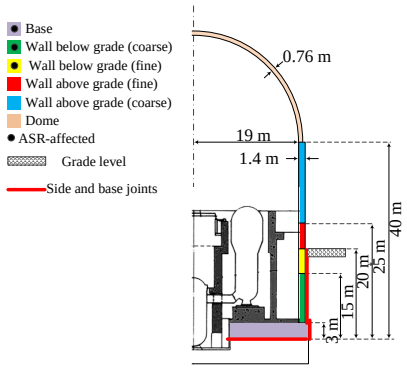

(a) Geometry and dimensions

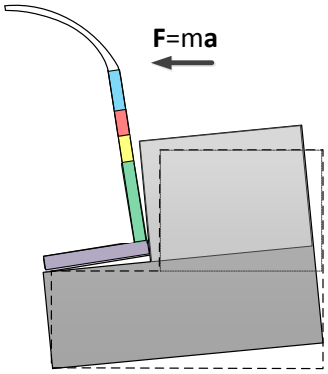

(b) Potential uplift modeled by joint elements

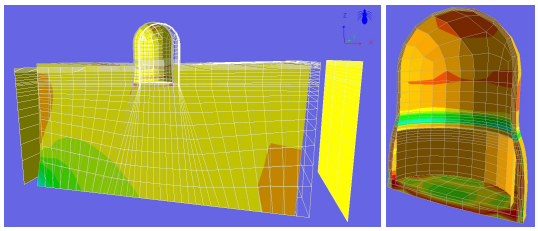

(c) Half 3D model with lateral viscous dampers and container mesh (with ASR expansion)

Fig. 33.5: Geometry, material groups, role of joint elements, and finite element mesh

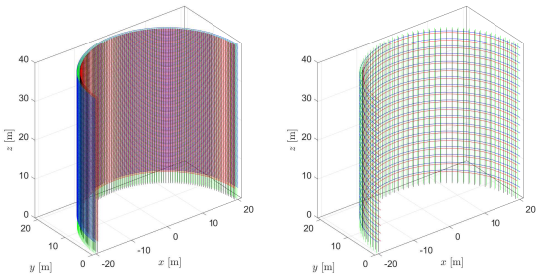

(a) Actual reinforcement in the CEB

(b) Adopted reinforcement in the model

Fig. 33.6: Reinforcement details

Different material groups are defined in the FE model. Concrete was modeled by four distinct groups according to location, mesh densities, and whether it is reactive, Figure 33.5(a). The dome is assumed to be linear elastic, whereas the wall and the base are modeled as nonlinear using the well-tested smeared crack model [178] of the FE code ATENA [179].

ASR is captured by the constitutive model described above, [761]. It is assumed that the CEB operates for 40 years during which it undergoes a relatively mild total expansion of 0.3% uniformly distributed over the "contaminated" zone as an additional internal strain. In actuality, ASR is not so uniform and is more likely to be "spotty" to reflect the usage of reactive aggregates in some, but not all the pours. This stochastic process is not accounted for in this study, however a separate study indicates that a sparsely distributed ASR expansion may be more detrimental than a uniformly distributed one (due to the induced strain discontinuities) [372]. Accompanying this expansion are two levels of concrete degradation zero and 30% reduction of E and f_t' after 40 years. The 40 years expansion is simulated in two weeks increments assuming a constant temperature and RH. The external average temperature at the site is estimated to be 11^oC (external face of CEB), the internal temperature is in turn estimated to be 25^oC. Hence, an average mean yearly temperature of $(25+11)/2 = 18\ ^oC$ is assumed. Note that in a more refined analysis, the temperature distribution across the wall should be considered, and monthly average temperatures should also be refined.

Rock (both the foundation and lateral) is assumed to be linear elastic. Interface joints are placed around and below the CEB to capture potential uplift of lateral separation of the container from the adjacent rock.

Table 33.2: Concrete mechanical properties

Characteristics	Symbol	Unit	Base	Wall below	Wall above	Dome
Mass density	ρ	Gg/m^3	0.002250	0.002250	0.002250	0.002250
Modulus of elasticity	E	MPa	39,000	39,000	39,000	39,000
Poisson's ratio	ν	-	0.2	0.2	0.2	0.2
Tensile strength	f_t	MPa	3.1	3.1	3.1	3.1
Fracture energy (Exponential softening)	G_F	MN/m	1.2e-4	1.2e-4	1.2e-4	1.2e-4
Compressive strength	f_c	MPa	-31.0	-31.0	-31.0	-31.0
Critical displacement in compression	w_d	m	-0.0005	-0.0005	-0.0005	-0.0005
Factor beta for return direction	β	-	0.0	0.0	0.0	0.0
Factor e for roundness of failure surface	e	-	0.55	0.55	0.55	0.55
Onset of nonlinearity in compression	f_{c_0}	MPa	-20.0	-20.0	-20.0	-20.0
Plastic strain at compressive strength	ϵ_{cp}	-	-1e-3	-1e-3	-1e-3	-1e-3

Table 33.3: Characteristics of the ASR model

Characteristics	Symbol	Unit	Base	Wall
Reference temperature	T_0	-	18	18
Maximum volumetric expansion at T_0^{test}	$\varepsilon_{ASR}^{\infty}$	-	0.3%	0.3%
Characteristic time at T_0^{test}	τ_C	ATU	64	64
Latency time at T_0^{test}	τ_L	ATU	160	160
Activation energy for τ_C	U_C	-	5,400	5,400
Activation energy for τ_L	U_L	-	9,400	9,400
Residual reduction factor	Γ_r	-	0.5	0.5
Fraction of ε_t prior to reduction of ASR expansion due to macro cracking	γ_t	-	0.5	0.5
ASR expansion annealing stress	σ_U	MPa	-8	-8
Post-ASR residual relative Young modulus	β_E	-	70%	70%
Post-ASR residual tensile strength	β_{f_t}	-	70%	70%

Table 33.4: Rebar mechanical properties

Characteristics	Symbol	Unit	Vertical	Horizontal
reinforcement ratio	ρ	-	0.01	0.005
Modulus of elasticity	E	MPa	200,000	200,000
Poisson's ratio	ν	-	0.3	0.3
Yield stress	σ_Y	MPa	248	248

33.2.2 Stochastic Seismic Excitation

Selection of the "right" earthquake records is a critical (and often underestimated) task. A multi-step approach is followed:

1. Site Characteristics are first determined assuming that the CEB is located in New Hampshire, USA (coordinates $42^o53'56''N$ and $70^o51'03''W$). The corresponding site conditions are then estimated from the *opensha* code [312] which requires V_{S30} (shear wave velocity 30 m below the surface) determined from the topographic slope site classification map method [860], Figure 33.7(a).
2. The seismic hazard de-aggregation (probability of occurrence in terms of distance and magnitude of earthquake) is determined next. Using the USGS 2008 *Interactive Deaggregations service* [846], the modal distance (R), magnitude (M), and inter-event term (ϵ_0) contributing to the 50%/50yr shaking are computed. Figure 33.7(b) shows a de-aggregation seismic hazard plot where peaks correspond to magnitude-distance combinations that contribute more to the hazard. This was determined from[1] USGS [847].
3. Collecting a set of ground motion records is the last step. Ground motions are either selected (PEER ground-motion database is used in most of the cases [689]) or artificially generated. As already stated, two stochastic techniques are used in this paper:

[1] The site was being upgraded in the Fall 2017, and subsequent results are not exactly the corresponding ones.

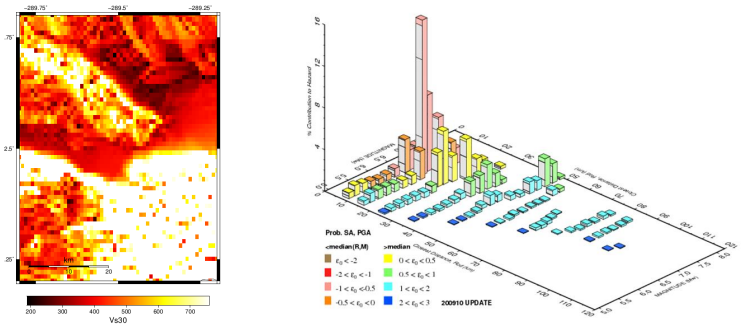

(a) Map of estimated V_{S30} (b) Seismi de-aggregation

Fig. 33.7: Seismic hazard characterization around the nuclear site

a. ETAFs: Six different randomly generated ETAFs, with main characteristics previously explained were used. Schematically, all the ETAFs are analogous Figure 33.8 as the base of all of them is a random white noise.

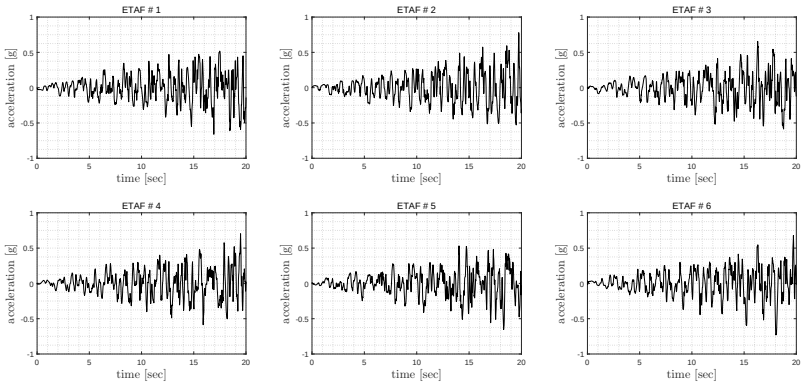

Fig. 33.8: Six adopted ETF

b. Stochastic Ground motions: Two scenarios, based on Figure 33.7(b), were considered: a) S1: $< M = 7.0, R = 10 >$, Figure 33.9(a); and b) S2: $< M = 5.5, R = 50 >$, Figure 33.9(b); where M refers to the magnitude, and R the distance. In both cases a total of N_{sim} = 25 samples are selected to properly address the record-to-record (RTR) variability. S1 scenario is stronger than S2, and thus, more damage is expected for that. All generated [730] ground motions were far-field resulting from a strike-slip fault, and a shear wave velocity V_{S30} of 760 m/s.

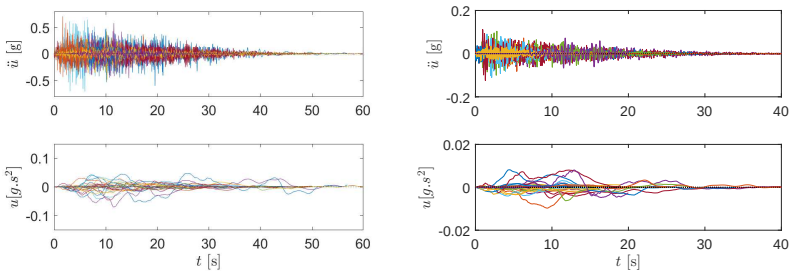

(a) S1 $< M = 7.0, R = 10 >$ (b) S2 $< M = 5.5, R = 50 >$

Fig. 33.9: Acceleration and displacement time history of 25 random signals for each scenario

33.2.3 Results

Analysis was performed by the code Merlin [767]. Three sets of analyses were performed: 1) Static + ASR, 2) Static + Dynamic, and 3) Static + ASR + Dynamic (100 for the stochastic ground motions, and three for each of the six ETA).

33.2.3.1 Static + ASR Analyses

In this first analysis, 40 years of ASR in the CEB is simulated. Figure 33.10(a) shows swelling of the container along with a closeup on the concrete-rock separation. Clearly ASR expansion interacts with the structure in what may be *a priori* counter-intuitive: a) the mat expands in a concave shape due to the structural constraints of the cylindrical vessel, Figure 33.10(b)-1; b) the wall pushes against the adjacent rock, but is constrained by both the base mat and the upper portion of the enclosure not subjected to expansion, Figure 33.10(b)-2, causing strong curvature, joint opening, and ensuing stress discontinuities; and c) sliding of the CEB itself, Figure 33.10(b)-3. Furthermore, the evolution of concrete cracks is shown in Figure 33.10(c). It should be noted that cracking starts at the central region of the mat base and along a ring on the wall next to soil level.

33.2.3.2 Impact of ASR on Capacity Curves: ETA Method

Impact of ASR on the structural response of the CEB can now be ascertained by comparing "Static + Seismic" with "Static + ASR + Seismic" for displacement and stresses for six different ETA functions. Three sets of simulations are compared: a) Static + dynamic analysis (Referred to Dyn. in the plots); b) Static + ASR with degradation of f'_t and E over time + dynamic analysis; and c) Static + ASR (without material degradation) + dynamic analysis.

Displacements: The absolute value of the (horizontal) displacements corresponding to peaks in (the six) ETAFs is first extracted. The mean of those six ETAFs

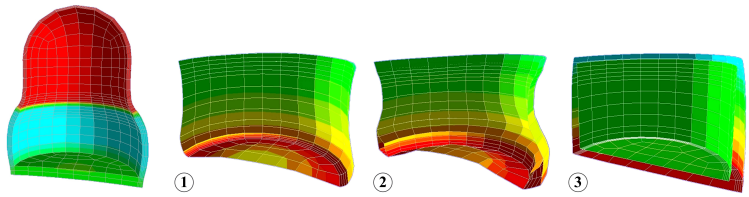

(a) Swelling of contaminated zone

(b) Evolution of joint opening/sliding due to ASR

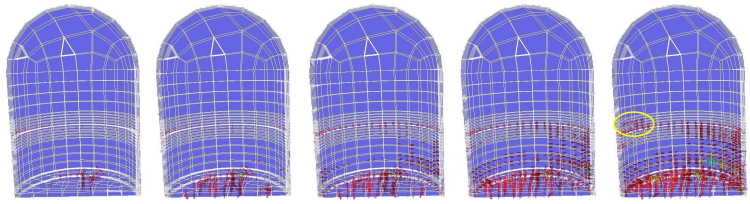

(c) Internal crack propagation (left to right)

Fig. 33.10: Response of CEB under static + ASR analysis after 40 years

for each of three assumptions are computed, Figure 33.11(a). These are ramping curves as the dynamic acceleration is indeed defined as a linearly increasing one (Figure 33.8). To better grasp the impact of ASR, results are normalized with respect to the one without ASR (dynamic only), Figure 33.11(b). The deviations are time-dependent and, as expected, model with ASR degradation is much more impacted than the one without. On average, and for this case study, ASR with degradation results in $\sim$20% change, whereas the one without has $\sim$8% variation with respect to the "Dyn. only" model. If material degradation is ignored (which is an erroneous abstraction) displacements are still lower than those cases without ASR, but greater than ASR with degradation. Note that discrepancy with respect to the case without ASR starts at around 9 s (i.e., until this point the ASR had little impact on deformation). The impact of ASR (with and without degradation) is time-dependent due to the complexities of the internal stress states induced by it or resulting from the seismic excitation, Figure 33.11(b).

Stresses: Time history of maximum principal stresses are recorded. The ASR affected responses result in higher stresses than those without degradation, and additional substantial damages will be induced by the ASR (with internal damage accounted for). At the base, Figure 33.12(a), maximum principal stresses are positive (cracking) and attenuate with time. Stresses are at first low when ASR dominates, but then suddenly increase with a localized damage at time $\simeq$ 17 sec. At the grade elevation, Figure 33.12(b), stresses are much higher without ASR, and then gradually decrease with no indication of failure. Note that the tensile strength is 3.1 MPa. On the other hand, in the presence of prior ASR expansion, the stresses are negative, and a sudden localized failure appears at t= 14 sec. For

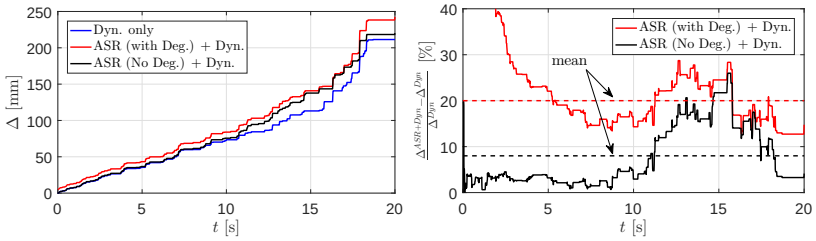

(a) Displacement profile at the top

(b) Displacements normalized and mean differences

Fig. 33.11: ETA-based displacements and the mean differences

a point above grade, Figure 33.12(c), stresses are higher in the absence of ASR and there is indication of a localized failure at $t = 15$ s. In the presence of ASR, the failure is delayed to about 17 sec. Finally, at the base of the dome, Figure 33.12(d), the ASR stresses are substantially higher than without and localized failure occurs around 17 s. For this case, ASR has reduced the stresses at the base, but substantially increased them at the base of the dome. Indeed, stress attenuation with time is the direct result of a nonlinear analysis where upon cracking there is a substantial stress redistribution resulting in localized stress reduction.

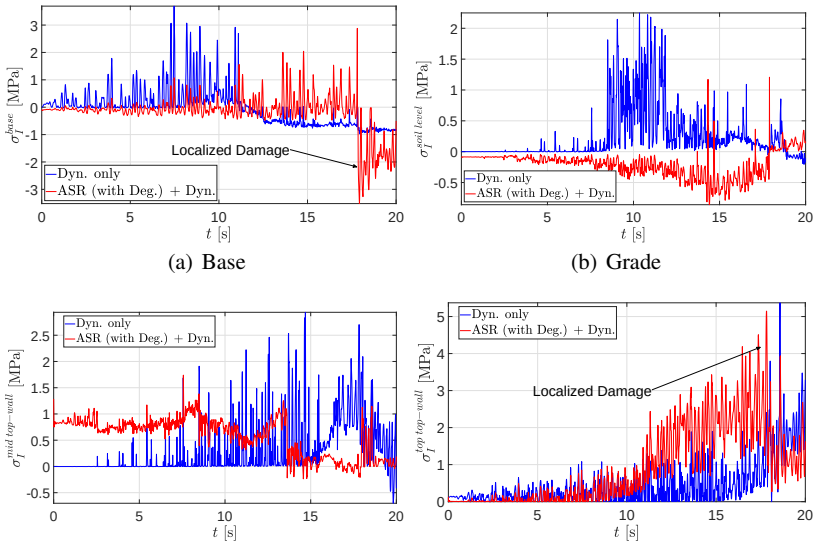

(a) Base

(b) Grade

(c) Above grade

(d) Base of dome

Fig. 33.12: Principal stresses capacity curves

Cracking: of the structure is shown Figure 33.13 at different times. In general, the crack pattern of ASR affected models are different and the previous observations are qualitatively confirmed by the crack profiles. Indeed, the damage index (DI), ratio of the cracked sections to the total area, is highest when ASR (with damage) preceded the seismic excitation. The ASR has a much higher impact of that portion of the CEB below grade than above (where no ASR is modeled).
The sound CEB experiences the major cracks at the soil level at about 12.8 s, while at the corresponding time the ASR-affect CEB had already some major cracks though all the top-wall. Results of ETA analysis prove that "endurance" of the CEB is reduced when it is subjected to initial ASR.

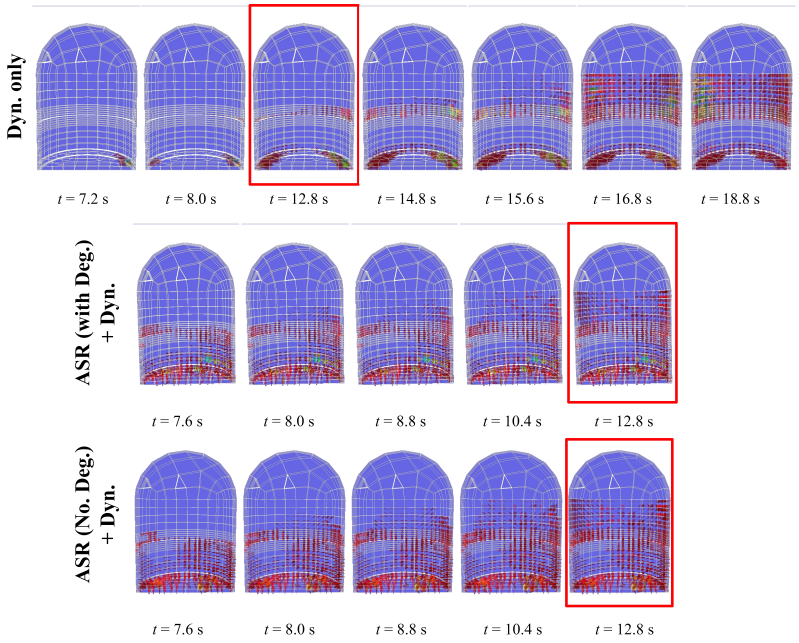

Fig. 33.13: Crack profile from a sample ETA simulation at identical time steps

33.2.3.3 Impact of ASR on Fragility Curves: Stochastic Analysis

As previously mentioned, two scenarios are selected, S1 and S2 and for each one, 25 random ground motions are generated. Then, each set is applied to the virgin CEB (i.e. without ASR) and then to the ASR affected one (with material degradation). Thus, a total of $4 \times 25 = 100$ simulations are performed.
Although it is possible to perform the fragility analysis based on various QoIs, the displacement response is selected as: 1) it is a global metric capturing the structural response; and 2) it is simple and straightforward to use in the probabilistic model.

Figures 33.14(a) and 33.14(c) show the peak displacements for each of the 25 stochastic ground motions versus the PGA for scenario S1 ($< M = 7.0, R = 10 >$) and S2 ($< M = 5.5, R = 50 >$), respectively. These figures call for the following observations: a) The minimum intensity of the records in S1 group (PGA $\sim$ 0.13 g) is nearly identical to the maximum PGA in S2; b) Relative displacements (with respect to the base) Δ_{max} in S1 is distributed between 5 and 55 mm, while in S2 they range from 1 to 10 mm (with only one exception at about 16 mm); and c) For the lower intensity case (S2), displacements of ASR affected CEB are consistently higher than sound ones, however for the higher intensity (S1), 5 out of 25 models show lower displacements for ASR-affected CEB.

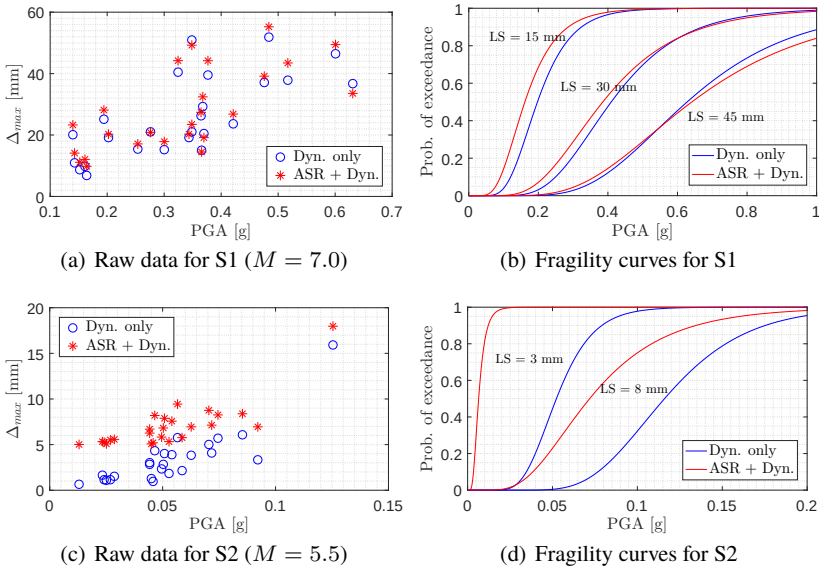

(a) Raw data for S1 ($M = 7.0$)

(b) Fragility curves for S1

(c) Raw data for S2 ($M = 5.5$)

(d) Fragility curves for S2

Fig. 33.14: Displacement-based fragility curves

Fragility curves require a limit state (LS) value (by QoI in the equation). Ideally, this should be a concrete crack opening. Should the steel liner leak tightness be also jeopradized, then and only then there could be leakage. However, such LS are not codified in nuclear engineering (as opposed to relative drifts for instance for buildings). Hence, and due to software current limitation, a displacement based LS at the top of the dome was adopted and values arbitrarily assumed (and shown in the respective figures). Resulting fragility curves are shown in Figures 33.14(b) and 33.14(d). For scenario S2, the probability of exceedance of a specific LS function is always higher for ASR-affected CEB. On the other hand, under scenario S1, the impact of ASR on the probability of exceedance is much smaller than under scenario S2. This would imply that ASR has a higher impact for low intensity earthquake

events (such as design based earthquakes) than for high ones (associated with the low probability events used in an SPRA).

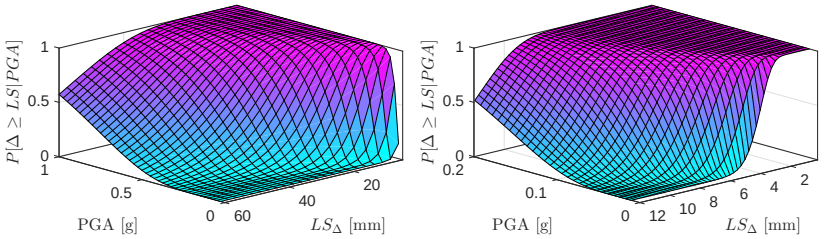

(a) Scenario S1 (b) Scenario S2

Fig. 33.15: Displacement-based fragility surfaces

Finally, when both the ground motion intensity and the LS threshold are not known, then a corresponding fragility surface combining the two parameters can be generated to address the increased uncertainties, Figure 33.15.

Part VII

Applications; Others & Case Study

Chapter 34
Massive Reinforced Concrete Structures

Abstract
Though the title of this book implies exclusive focus on concrete dams and nuclear structures, coverage (most of it) applies also to other types. By way of example, this chapter will use two distinct illustrative examples: a) a massively reinforced concrete supporting structure and b) a landmark bridge.
Each one of those two examples will provide a different set of methods wrapped around the central issue of ASR.

34.1 Introduction

With the aging of infrastructure, Alkali Aggregate Reactions (AAR) are increasingly burgeoning as most of them were built at a time when the nature of the reaction was poorly understood, and standards for the detection of potential AAR in concrete mixes were not well established. Whereas the problem has been traditionally associated with dams, it has also affected massive reinforced concrete structures and bridges worldwide [876]. In an early study, [699] it was reported that in *Denmark, 600 bridges (roads and railways) and an unknown number of municipal ones are potentially AAR dangerous*.
This chapter will give analysis examples of ASR affected structures other than dams or nuclear structures, and two case studies will be presented: a) a heavily reinforced massive concrete girder and b) a long-span bridge.

34.2 Massive Reinforced Concrete Structure

Analysis performed by Y. Yagome, H. Noguchi (Tokyo Electric Power Company) with V. Saouma; reproduced here with permission.

34.2.1 Description

AAR makes no distinction with respect to the type of structure it will affect; its effects however are most drastic in massive (in terms of volume) concrete structures that are regularly subject to monitoring, e.g. dams. Other unmonitored structures

may also be adversely affected by AAR expansion, but only the most strategically important structures receive proper attention from their owners. Such is the case for the massive reinforced concrete support of a high-voltage transmission tower with 1.5 m by 1.5 m cross-girders (13.7 m span) and 2.0 m by 2.0 m columns. The girders are heavily reinforced both longitudinally (14 H 29 and 14 H 22) and vertically (H 16 spaced at 250 mm).
An unusual crack pattern, within a localized section, was observed with AAR expansion being suspected (Figure 34.1). This pattern was later confirmed through laboratory tests.

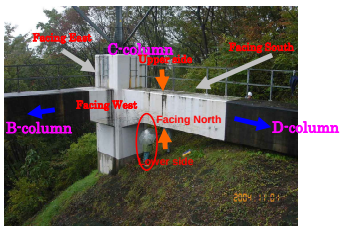

(a) Location of the zone affected by AAR



(b) Close-up

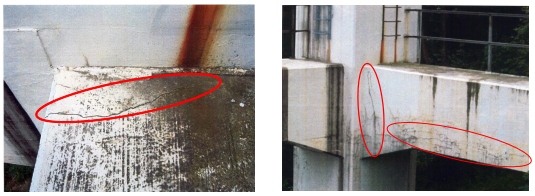

(c) Structural cracks along with FE simulation results

Fig. 34.1: Heavily reinforced transmission tower foundation partially affected by AAR

Figures 34.2(a) and 34.2(b) show the geometry, loading, and dimensions of this massive structure. The corner transmission tower exerts both tensile and compressive loads on its supports.
Of particular concern herein is girder CD, where AAR had been observed at one end. Figure 34.3(a) illustrates the field-recorded cracks on the four faces, while Figure 34.3(b) shows the AAR strain measurements based on crack index. This massive structure is also heavily reinforced (Figure 34.4).

34.2.2 Model

Four finite element models have been considered:

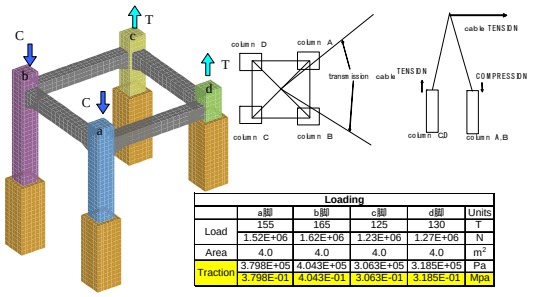

Loading					
	a節	b節	c節	d節	Units
	155	165	125	130	T
Load	1.52E+06	1.62E+06	1.23E+06	1.27E+06	N
Area	4.0	4.0	4.0	4.0	m^2
Traction	3.798E+05	4.043E+05	3.063E+05	3.185E+05	Pa
	3.798E-01	4.043E-01	3.063E-01	3.185E-01	Mpa

(a) Geometry

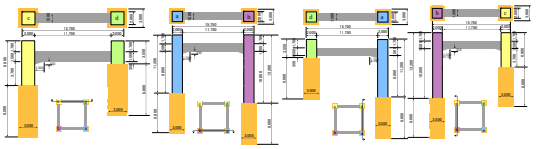

(b) Dimensions

Fig. 34.2: Geometry of the massive reinforced concrete structure

Model	Model	Extent of Expansion
1	Frame C-D	Entire Girder C-D
2	Entire	Entire Girder C-D
3	Frame C-D	Localized in Girder C-D
4	Entire	Localized in Girder C-D

and the finite element mesh (6,271 elements and 3,176 nodes) associated with the 3D model is shown in Figure 34.5. Let's point out the heavy internal reinforcement that has been explicitly modeled along with the Winkler springs surrounding a portion of the columns buried below ground. This becomes an important consideration in the presence of a large lateral load.

34.2.3 Results

The results for each of the four analyses will be presented separately.
For case 1, Figure 34.6(a): No cracks are observed in girder C-D or column D. On the other hand, an unreasonably large crack is found in column C. For case 2, Figure 34.6(b): A few cracks are observed in C-D, no cracks in column D, and large cracking in column C. As for case 3, Figure 34.6(c): Excessive cracking is noted in girder C-D and in column C. Lastly, for case 4, Figure 34.6(d): The cracking is finally close to the observed pattern, and only a few cracks are computed in column C.
The computed crack opening displacement can now be compared with the measured displacement (through the crack index) in Figure 34.7; this comparison confirms the earlier qualitative assessment that case 4 indeed yields the closest values. This

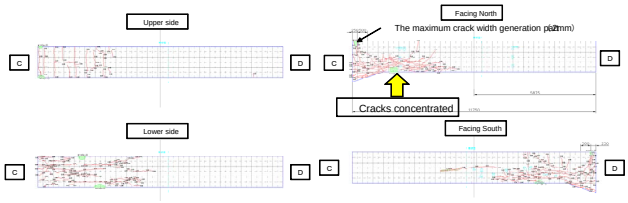

(a) Girder C-D

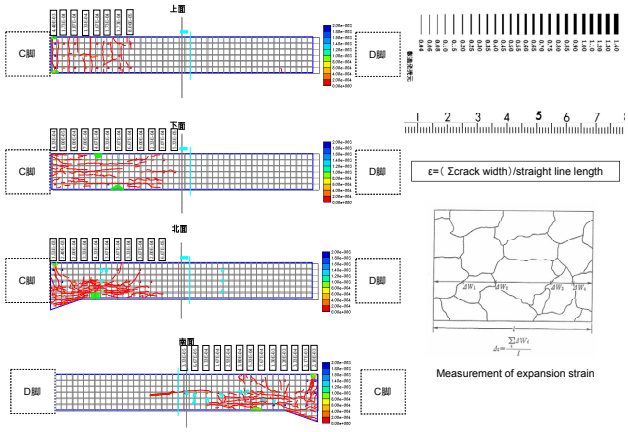

(b) Field strain in CD

Fig. 34.3: Field strain measurements

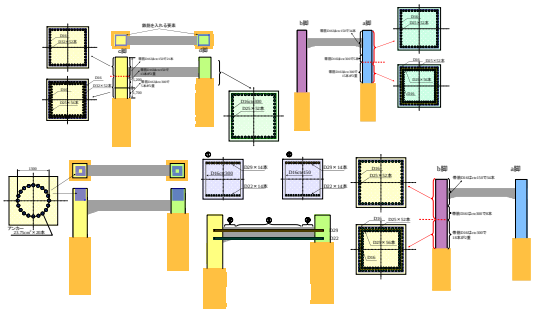

Fig. 34.4: Reinforcement

finding has further been confirmed by a closer examination of the damaged zone in analysis 4, Figure 34.8, where the strains are in fact very close. The temporal evolution of strains is shown in Figure 34.9.

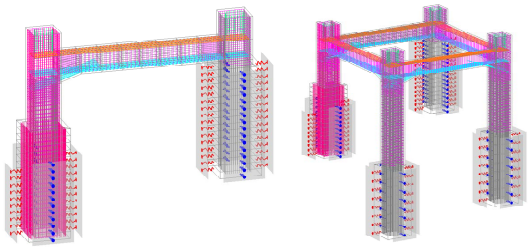

Fig. 34.5: Finite element mesh

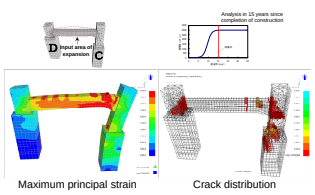

(a) 1. Frame C-D; AAR over the entire C-D

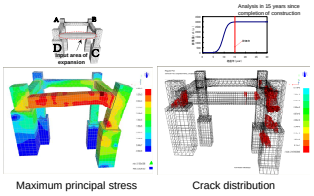

(b) 2. Entire Frame; AAR over the entire C-D

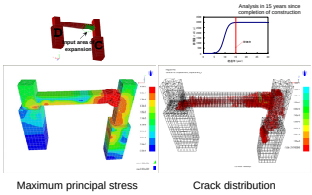

(c) 3. Frame C-D; AAR in the localized part of C-D

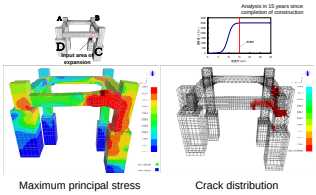

(d) 4. Entire Frame; AAR in the localized part of C-D

Fig. 34.6: Finite element analysis of various cases

34.2.3.1 Seismic Analysis Following AAR Expansion

Following a static analysis of the structure, which has more or less captured both the observed crack pattern and strain recordings in the field, a seismic analysis was performed.

It would be erroneous to undertake such an analysis simply with the degraded tensile strength and Young's modulus since the "locked-in" stresses caused by AAR and existing cracking would not be taken into account. Instead, the analysis was performed via a "restart" feature in the Merlin finite element code. Per the owner's request however, these results cannot be published..

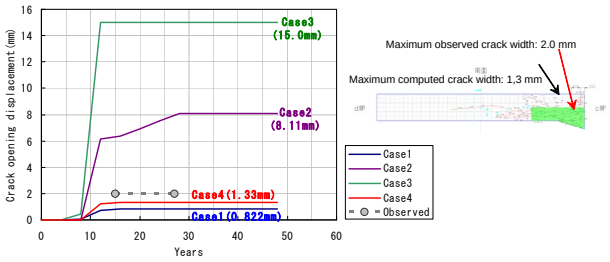

Fig. 34.7: Finite Element Analysis summary; COD

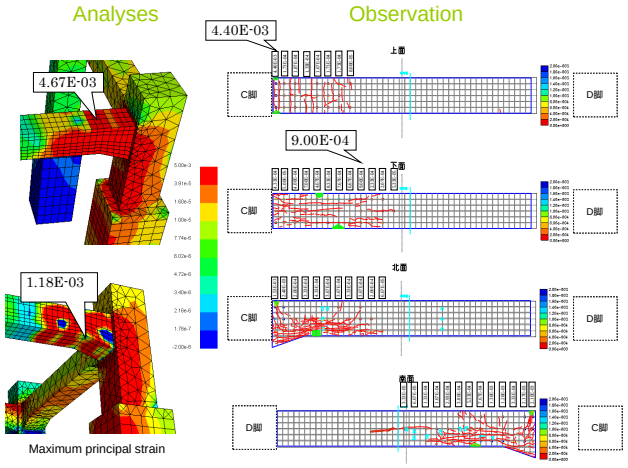

Fig. 34.8: Close-up of analysis 4: Strains

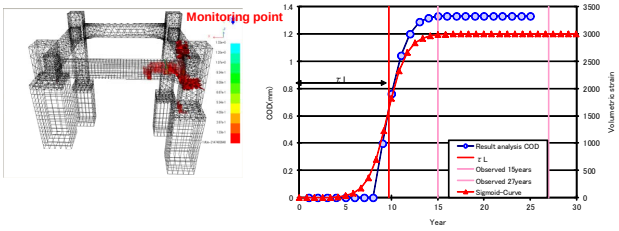

Fig. 34.9: Kinetics of analysis 4

34.3 Segmental Bridge

Adapted from [372]

34.3.1 Description of the Viaduct

The *Viaduct de Chillon* is a precast post-tensioned bridge spanning between 92 m and 104 m over a total length of 2,120 m. The French double-cantilever construction system was used with precast voussoirs. It was opened to traffic in 1969 and is a well-known, widely recognized innovative and iconic structure [744], Figure 34.10.



Fig. 34.10: General view of the viaduct [511]

34.3.2 Concrete Conditions

Scheduled inspections have revealed a significant increase in reinforcement corrosion due to chloride diffusion through cracks. Ensuing preliminary investigations of the deck (concrete compressive strength, mild and pre-stressing steel tensile strength) were performed and repairs conducted in 2012-2013. However, poor adhesion of the repair overlay mortar to the subjacent concrete was observed. Should the concrete have been sound, this would not have occurred, and as such AAR was strongly suspected. In 2012, many samples were extracted along the nearly 2 km in order to properly account for the inherent and inevitable variabilities encountered in such a structure. Cores were extracted from the slabs and webs but not from the inclined segments as their structural role was perceived as minimal. Tests included: microscopic analysis (composition and micro-structure, state of degradation), residual expansion measurements, compressive strength of cores, direct tensile strength, tensile axial splitting, static elastic modulus in compression, and hardened concrete mass density. Findings [511] led to the following observations.

Concrete Degradation:

The aggregates used come from a mixture of silica and silicate metamorphic rocks of sedimentary and crystalline nature, with a slow/late reaction potential. The Portland cement content of the deck ranged from 350 to 400 kg/m^3 (350 kg/m^3 specified).

So far, concrete has undergone relatively small expansions as it has been in a relatively dry condition (there were no visible signs of micro cracks), and the potential for expansion is intact. It is estimated that present (45 years after construction) expansion is less that 0.1% and that future expansion (after an additional 45 years) should be between approximately 0.4 and 0.9%.
Expansion tests have not revealed a "plateau;" this is often the case when aggregates do also contain alkali. It was estimated that the laboratory maximum rate of expansion is 0.7-0.8 mm/m/year. Based on Arrhenius law, it is estimated that at 11°C, expansion is about 5 (units?) slower than at 38°C, yielding a guesstimate 0.1-0.2 mm/m/year in the worst case scenario. This in turn will result in 0.45-0.9% future expansion *in the most unfavorable conditions*, that is wet surfaces without protection. Indeed, this concrete was labeled as one of the most reactive concretes known in Switzerland.

Mechanical Properties

were obtained from 100 mm diameter cores and maximum aggregate size of 32 mm. Values are shown in Table 34.1, and corresponding percentage losses (determined from concrete in unaffected zones) are also shown. The mechanical properties of the inclined members were not tested as they play a relatively minor structural role, and the concrete used in these components is likely to have been quite different than the one used in the main box girder. Finally, in anticipation of a possible strengthening, a crude estimate of the possible evolution of mechanical strength in the next 30 years has been attempted [511], Table 34.1.

Table 34.1: Mean and minimum values of concrete properties [511]

Property	Intact	Mean values degraded				Minimum values degraded			
	Bottom	CT	Loss %	BS	Loss %	CT	Loss %	BS	Loss %
Current (year 2015, age 45 years)									
f'_c[MPa]	90± 10	75 ± 10	5-20	90 ± 10	0	65	30	80	10
f'_t [MPa]	4.5 ± 0.5	2.5 ± 0.7	40-45	3.7 ± 0.7	15-20	1.8	60	3.0	30
E [GPa]	40 ± 4	32 ± 4	15-20	38 ± 4	0-5	28	30	30	15
Projected (year 2045, age 75 years)									
f'_c [MPa]	90 ± 10	55 ± 10	35-40	70 ± 10	20-25	40	30	55	10
f'_t [MPa]	4.5 ± 0.5	2.0 ± 1.0	50-60	2.0 ± 1.0	30-35	1.0	60	2.0	30
E [GPa]	40 ± 4	25 ± 5	30-35	30 ± 5	20-25	21	30	25	15

CT: Center top; BS; Bottom Side.

34.3.3 Finite Element Model

Analysis was undertaken with the computer code Saouma, Červenka, and Reich [767] based on the model presented in Section11.2.
Based on the engineering report [511], three zones were identified, Figure 34.11(a). The top deck layer (T) is the warmest and has the maximum exposure to water, and

hence it is assigned the largest volumetric expansion $\varepsilon^{i}nfty$. The other two zones, C and B/S (center and bottom/side), are better protected from both the water and the radiant heat and are thus assigned 80% and 70% of the deck value.

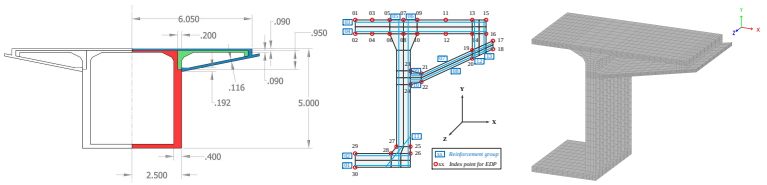

(a) Modeled section identifying the T, C and B/S regions (blue, green and red)

(b) Location of index points and rebar groups

(c) Mesh

Fig. 34.11: Finite element mesh

Thirteen reinforcement groups are identified, Figure 34.11(b): 8 mm reinforcement for the lateral reinforcement (x direction) spaced at @100 mm and at 125 mm from the external faces and 7 mm @125 mm for the rest. Also shown in the figure are the "index" points for which the finite element analyses will be recording the engineering demand parameters (EDP) such as deformations and displacements.

Since the computational cost load for a probabilistic based nonlinear finite element analysis of the viaduct will be prohibitive, and as this is the first attempt to provide such a solution, only one (half, by virtue of symmetry) segment is modeled, and it is assumed to be fully supported at the base, Figure 34.11(c).

The model has 6,380 nodes and 4,820 eight-node brick elements. Longitudinal displacements are constrained on the front and rear faces (z axis), whereas free expansion is allowed along the lateral and vertical directions (x and y axis) except along the plane of symmetry (constrained in the x direction) and along the base (in the y direction) as the model assumed to be supported vertically. There are 10 layers in the longitudinal direction. The self weight is applied in the first increment, but is rapidly overwhelmed by the response to concrete swelling due to the subsequent AAR increments.

Coupled with the previously described AAR model is a nonlinear damage-fracture constitutive model for the concrete [178], both implemented in the code Merlin [767].

Given that the viaduct is 45 years old, the analyses seek to predict the incremental response over a total of 100 years. A time increment that is too short will be computationally prohibitive but too long will result in gross imprecision. Hence, and following some parametric studies, a time increment (known as Analysis Time Unit - ATU - in the model) of 40.56 days was selected, and 900 increments will be needed for each of the (implicit) analyses.

The average yearly temperature at the viaduct location is 11°C and will be used. Hence laboratory values for τ_L and τ_C (measured at 38°C) are adjusted per Equation 11.4.
As to the reinforcement, only the yield stress (in an elastic-perflectly plastic model) is considered variable and is assigned a normal distribution function with a mean of 248 MPa and a range of $[225,\ 250]$.

34.3.4 Preliminary Deterministic Analysis

A preliminary deterministic set of analyses were performed to assess the impact of the spatial distribution of the concrete properties and the corresponding computational time. As reported earlier, three distinct zones of AAR exposure were identified, Figure 34.11(a). Hence the same (arbitrarily selected) high ultimate volumetric AAR strain of 1.0% was assigned to three analyses (identified as uniform, partial and full nonuniform). In the first, identical properties were uniformly assigned to all regions. In the second and third, 1.0, 0.8, and 0.7 percent expansion were assigned to the three regions; however the latency and characteristic times were kept constant in the second and varied in the last.
It was quickly noticed that the CPU time was commensurate with the model heterogeneity: 6.1, 7.7, and 19 hours, respectively. Indeed, the first model with uniform property assignment gave no sign of cracking; minor and extensive cracking were observed in the last two.
Deformed shape, crack pattern, horizontal and vertical displacements of three index points (1, 7 and 15 in Figure 34.11(b)) were scrutinized for all three analyses to better understand the impact of the non-uniform assignment of AAR properties, Figure 34.12.
As expected, the more heterogeneous are the concrete properties assigned, the more convoluted (and un-predictive) is the deformed shape from which one can identify zones of tensile and compressive stresses (Figures 34.12(a), 34.12(b) 34.12(c) where the shaded surfaces correspond to the vertical displacement). In these analyses, the web undergoes relatively small flexure, and the inclined deck support appears to play an important role in the expansion. Induced (smeared) cracks at the end of the 900 increments (100 years, 0.1% volumetric strain) are shown in Figures 34.12(d), 34.12(e) and 34.12(f). Consistent with the previous figures, the most realistic model (full non-uniformity) exhibits most cracks in the deck and the web-deck connection. Figures 34.12(g) and 34.12(h) show the stress distribution along the center lateral top reinforcement (group #4 shown in Figure 34.11(b)) in terms of time (as measured from the centerline). As one would expect, the stress increases with time until it reaches the rebar yield stress. Of concern is that the yield stress is reached within the 45 years (i.e. presently). This finding must be tempered by the high assumed final volumetric strain of 0.1%. The uniform case has only a small discontinuity, while the full nonuniform case exhibits strong stress jumps at the deck intersection with the supporting components.
Finally, Figures 34.12(i) and 34.12(j) show the lateral (x) and vertical (y) displacements of three index points, i.e. Loc.01, Loc.07 and Loc.15 (Figure 34.11(b)). The

displacement trend of the partial uniform case is very similar to the uniform one (not shown) but with smaller values. On the other hand, the displacement curves for the non-uniform case are slightly different. Whereas the lateral displacements follow the same smooth sigmoid shape, the vertical displacements exhibit a peak and then a "softening". *A priori*, this could be attributed to a phase shift caused by the differences in the characteristic and latency times.

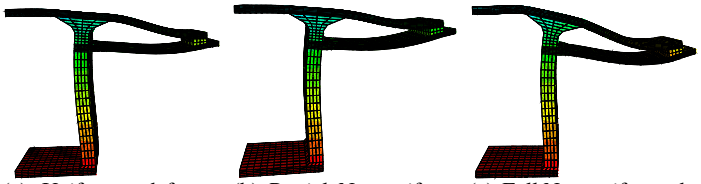

(a) Uniform; deformation (b) Partial Non-uniform; deformation (c) Full Non-uniform; deformation

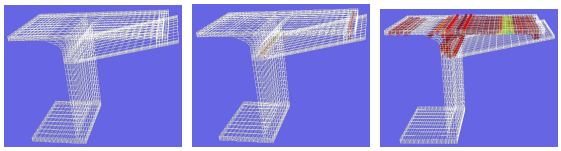

(d) Uniform; damage (e) Partial Non-uniform; damage (f) Full Non-uniform; damage

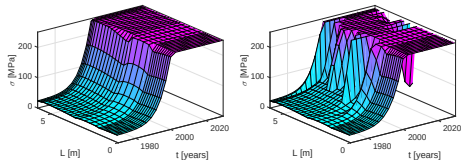

(g) Uniform; Reinf # 4 (h) Full Non-uniform; Reinf # 4

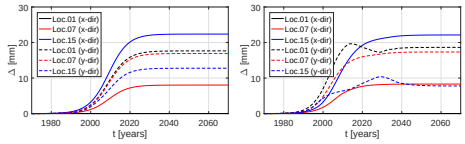

(i) Partial Non-uniform; displacement (j) Full Non-uniform; displacement

Fig. 34.12: Comparison of the uniform, partial and fully non-uniform models

34.3.5 Uncertainty Quantification Framework

To perform a deterministic analysis of this bridge would be too presumptuous as there are so many poorly quantified variables. Those are either aleatory in nature such as

random distribution of pockets of high reactivity in the bridge, or they are epistemic since we do not fully know the concrete characteristics. In light of the above, a probabilistic investigation is undertaken. For the finite element investigation to be properly carried out, a mathematical representation of the kinetics should be given. Consistent with the model presented earlier, the maximum volumetric strain ε^{∞} (Eq. 11.1) and the degradations of the elastic modulus and tensile strength β_E, and β_{ft} (Eq. 11.20 and 11.21) must be determined in a manner consistent with the findings of the laboratory observations (Table 34.1).

Starting with ε^{∞}, and as previously mentioned, the estimated present expansion is less than 0.1%, and the future expansion at age 90 years is expected to be in the range of 0.45-0.9%. Hence, for the sake of the analysis, it is assumed that the range of current expansion (after 45 years) is 10% of those values or 0.045-0.09%. As to the estimate of total expansion in the subsequent 35 (45+45-10) years (under most unfavorable conditions), it will be 0.45-0.9%. Finally, guesstimating for a total of 100 (45+45+10) years, the lower bound is maintained at 0.45% and the upper bound is 2.0% (again based on the reported 0.2 mm/m/year estimated from laboratory tests). Hence, the domain of uncertainties is illustrated by Figure 34.13 and is broken into three zones: present, near and far future.

Finally, having two points from current uncertainty and four points from future uncertainty, eight potential expansion curves (marked as corner curves) are fitted, which is shown in Figure 34.13.

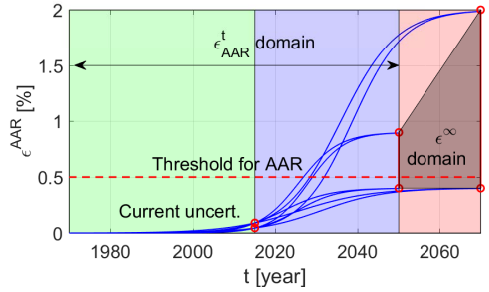

Fig. 34.13: Domain of investigation for AAR expansion (1970-2015: dry and 2016-2070: wet condition)

At this point, a strategy must be devised on how to generate the random expansion curves for the Monte-Carlo simulation (MCS). The curves can be defined by three points: 1) the origin, 2) a random point at the current time (2015), and 3) a random point bounded by the time interval of 2050-2070, and expansion intervals of 0.45-0.9% and 0.45-2.0%. The approach taken is heavily inspired by the LHS-wised technique of MCS [459].

First, n_{sim} points are orderly identified within the (trapezoidal) domain of future uncertainly, and another n_{sim} are randomly located within the axis of present uncertainty. The end point providing the time of reaction saturation and the maximum

volumetric expansion ε^{∞}, a curve (based on Equation 11.1(a)) is then passed through those points and τ_l, τ_c are determined, Figure 34.14(a).

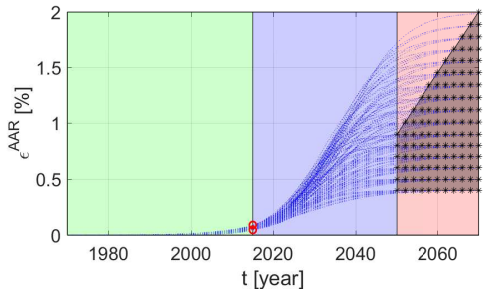

(a) LHS-wised sampling approach

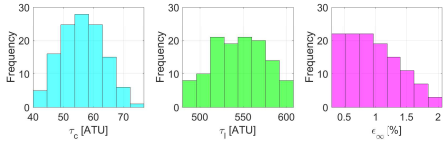

(b) Determined variable histograms

Fig. 34.14: Latin Hypercube based sampling method

Then, the corresponding distributions of the degradations must be defined as a set of random variables. Starting with f_t and E, the degradation model is given by Eq. 11.20 and 11.21 and must be calibrated with estimated material degradations shown in Table 34.1 defined as $M \pm m$. Hence, three sets of nonlinear least-squares optimizations are run to obtain the β values. Results are shown in Figure 34.15.
Finally, a simple approach was adopted for the degradation of the compressive strength f_c as the constitutive model does not currently account for its degradation. The average values of 67 and 78 MPa (from Table 34.1, for top-center and bottom/side, respectively) are taken as a mean with a range of $\pm$ 10 MPa.
So far, variables have been independently defined; however there is a strong correlation amongst some of them. Unfortunately, there is no literature on what should be the correlation of key concrete parameters; hence "engineering judgment" was exercised in assigning those coefficients, ρ: $\rho_{(G_F \leftrightarrow f_t)} = 0.5$, $\rho_{(G_F \leftrightarrow f_c)} = 0.6$, $\rho_{(f_c \leftrightarrow f_t)} = 0.6$, $\rho_{(E \leftrightarrow f_c)} = 0.6$, $\rho_{(U_l \leftrightarrow U_c)} = 0.6$, $\rho_{(\beta_E \leftrightarrow \beta_{f_t})} = 0.7$ and $\rho = 0.0$ for the rest.

34.3.6 Analyses Results

An initial attempt to interpret results brought up an unanticipated set of two responses that resulted in two drastically different deformation shapes of this complex structure.

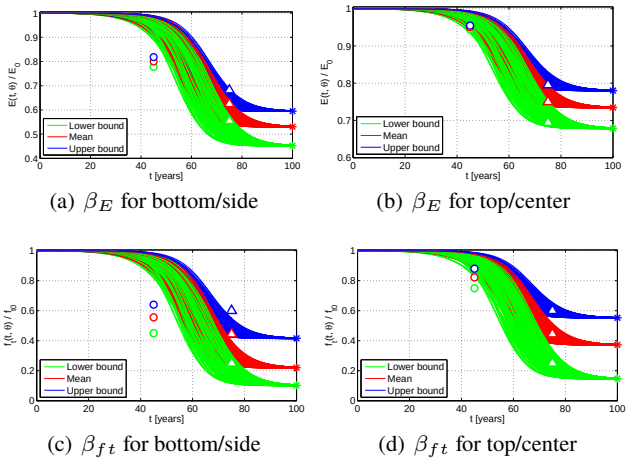

(a) β_E for bottom/side (b) β_E for top/center

(c) β_{ft} for bottom/side (d) β_{ft} for top/center

Fig. 34.15: Predicting degradation of E and f_t based on optimization of experimental tests

Hence, the next section will examine the peculiar idiosyncracy of the problem, and results of the 121 analyses will be addressed next.

34.3.6.1 Effect of Kinetics (classification)

Scanning all 121 analyses results, two major deformation trends emerged, Figures 34.16(a) and 34.16(b) (with colored shaded contour corresponding to the volumetric AAR expansion), tagged as Class I and II, respectively. The first one notes the great "distortion" of the section with much flexure in both the flanges and the web. In Class II, the vertical elongation of the web is clearly dominant, resulting in smaller curvatures in the web. Examining the corresponding (randomly generated) input data for each class of response, the cause was immediately attributed to the set of latency and characteristic times and the corresponding activation energies rather than with the values of ε^{∞} associated with different regions. From this set of analyses, the importance of differential kinetics properties (used in Eq. 11.4) was highlighted.
This cause was confirmed by Figures 34.16(c) and 34.16(d) where the time lag in expansion amongst components is much more accentuated in the second, hence prioritizing the vertical expansion of the web in Class II. The displacements of the deck centerline (Loc01) and edges (Loc15) in the y and x directions further illustrate this response, Figure 34.16(e). Time-wise, the vertical displacement of the deck centerline in Class I moves downward for the first 25 years, and then with the stress release caused by cracking (Figure 34.17(c)), it reverses and displaces upward.
The rebar (located at the bottom and across the deck) stresses in Class I yield entirely after about 30 years, Figure 34.17(a). Again, locations are from the deck centerline. However, in Class II, reinforcement only partially yields in vicinity of

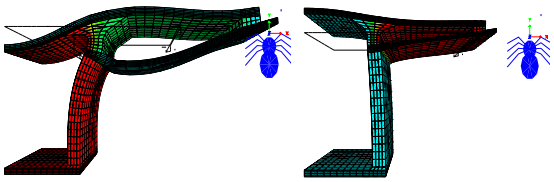

(a) Class I; deformation (b) Class II; deformation

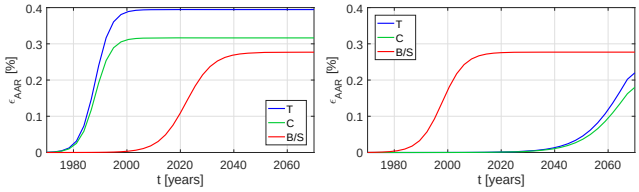

(c) Class I; expansion (d) Class II; expansion

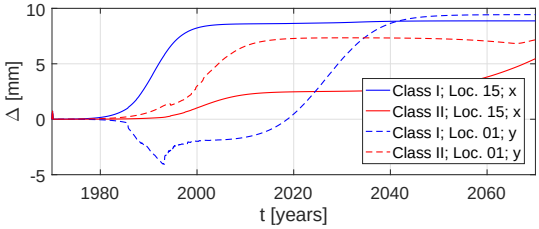

(e) Horizontal and vertical displacements

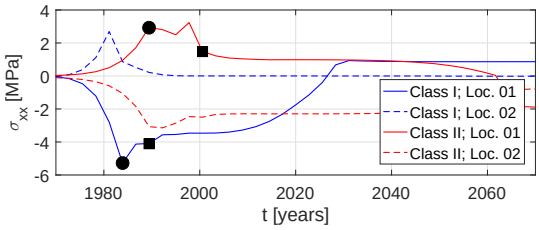

(f) Stress σ_{xx}

Fig. 34.16: Identification of two distinct structural responses attributed to delayed AAR expansion

the centerline. This is confirmed by the high curvature in the center part of the deck in Figure 34.16(b). On the other hand, throughout most of the life span of the structure, the bottom reinforcement stress away from the centerline is very small for Class II, Figure 34.17(b). This finding is further supported by the absence of cracking in the corresponding part in Figure 34.17(c), where in addition, the crack initiation corresponds to discontinuity in the stress diagram. In this figure, the crack initiation and propagation correspond to the solid circle and square points shown in the stress-time history curve, Figure 34.16(f).

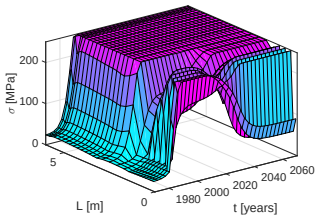

(a) Class I; rebar #4

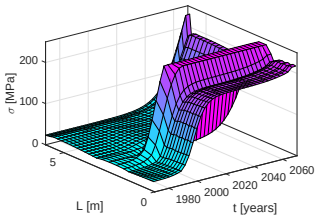

(b) Class II; rebar #4

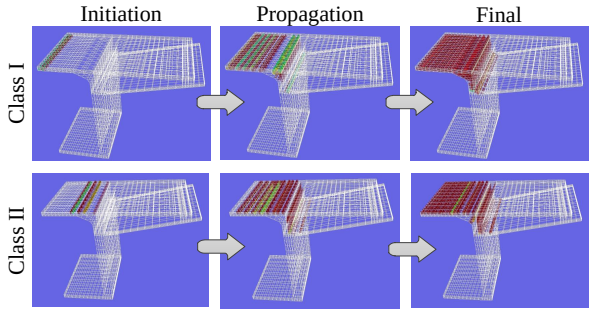

(c) Crack profile

Fig. 34.17: Rebar spatial and temporal stress distributions and cracking for two identified structural responses

34.3.6.2 Probabilistic Based Assessment

The initial batch of 121 simulations yielded a set of 13 ($\sim 10\%$) nonlinear analyses which terminated prematurely due to lack of convergence. This was attributed to a pathological combination of variables which stretched the capabilities of the models. Otherwise, CPU times ranged from 4 to 187 hours each, with a mean of 15.2 hours. Thus, the complete set of analyses required about 2 months of computations on a Dell Precision Tower (dual Intel Xeon Processor E5-2687W, 3.5GHz Turbo, 32 GB RAM).

Following the earlier classification of analyses into two classes (I and II), 59 fell into the first and 49 into the second. Out of the 30 index points with identifiable results (Figure 34.11(b)), only three EDPs are reported (Figure 34.18(a)): the lateral (x) displacement of the edge deck (Loc.15), vertical displacement at the deck centerline (Loc.01), and the corresponding σ_{xx} stress. The maximum anticipated horizontal and vertical displacements are 43 and 30 mm and remain relatively small compared to the dimensions of the voussoir. The corresponding median, 16th and 84th fractiles for each set of curves is shown as well. Again, consistent with previous observations, the vertical displacements are higher for Class II and lower for the lateral one. Finally, the stress reversal for Class II is worth noting. In all cases, the maximum tensile stress is capped by the $\simeq 4$ MPa tensile strength specified. On the other hand, the

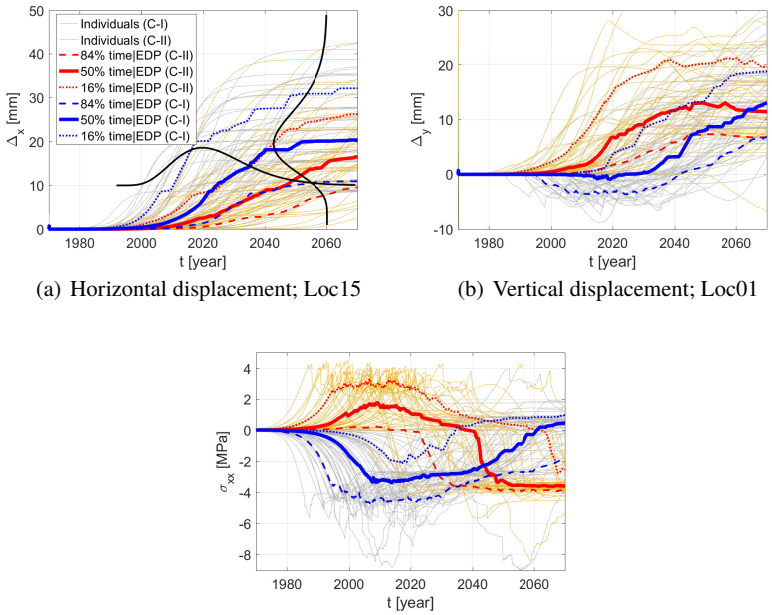

(a) Horizontal displacement; Loc15

(b) Vertical displacement; Loc01

(c) σ_{xx} stresses; Loc01

Fig. 34.18: Individual probabilistic-based simulations and the 16, 50 and 84% fractiles

compressive stresses are nearly negligible compared with the compressive strength of 67 MPa.

34.3.7 Risk Informed Conditional Assessment

This probabilistic based analysis of a major infrastructure suffering from AAR can now serve as a vehicle to finally define the risk informed conditional assessment (RICA) of similar structures. Though this paradigm is not entirely new, [268] it has seldom been used in the context of evaluation of structures suffering from AAR. First a few terms commonly used in earthquake engineering will be introduced.
Figure 34.19(a) illustrates this concept as typically used in earthquake engineering: What is the probability of an LS exceeding a certain value in terms of the seismic excitation, and what would be the corresponding level of damages. Similarly, for structures affected by AAR, Figure 34.19(b) would be a corollary that gives the probability of a volumetric expansion exceeding a value in terms of time.
Following these brief introductory remarks, attention is returned to the problem previously analyzed. The DV is considered to be the vertical displacement (Figure 34.18(a)), and an LS of 50 mm is assumed (that is, should the vertical displacement exceed 50 mm, then the structure is considered to have locally failed). Then, per

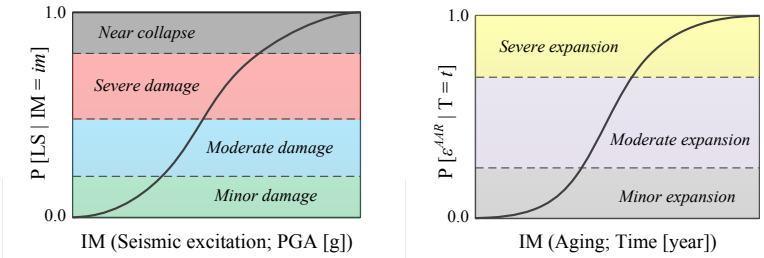

(a) Earthquake (b) AAR

Fig. 34.19: Fragility curves

Figure 34.20(a), the temporal distribution of the DI is shown in Figure 34.20(b) where 6 points are identified: the intersection of the 16th, median, and 84th fractiles with: A) a vertical line corresponding to the year 2040 and B) a horizontal one corresponding to a DI=0.2 (or displacement of 10 mm).

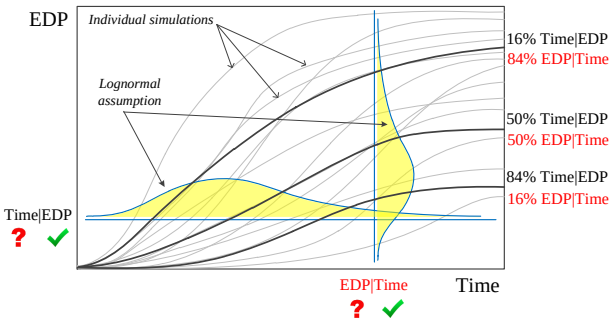

(a) Interpretation of the results based on summarized curves

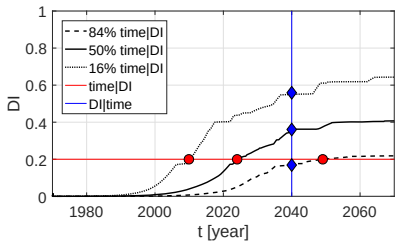

(b) 16, 50 and 86th Percentile temporal evolution of the DI

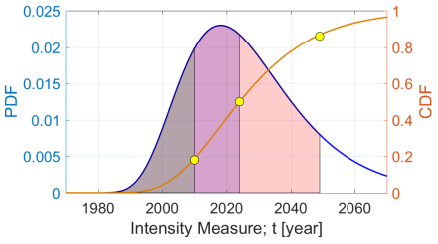

(c) PDF and CDF for the DI

Fig. 34.20: Engineering interpretation of results

Two conditional assessments are then extracted: 1) time|DI and 2) DI|time. The former is associated with the time needed for a given DI to occur (horizontal line), and the second with the likelihood of a given DI occurrence at a given time (vertical line), Table 34.2.

Table 34.2: Central fractiles for the two conditional assessments of Class I case; number inside the parentheses represents absolute date

Conditional Assessment	Central Fractiles		
	16th	50th	84th
time|DI [years]	40 (2010)	54 (2024)	79 (2049)
DI|time [-]	0.17	0.36	0.56

From three fractiles, one can estimate the mean μ and the log-normal standard deviation β, [605]

$$\mu_{\text{time|DI}} = \ln(\text{time}^{50\%}) \tag{34.1}$$

$$\beta_{\text{time|DI}} \approx \frac{1}{2}\left(\ln(\text{time}^{84\%}) - \ln(\text{time}^{16\%})\right) \tag{34.2}$$

which result in $\mu_{\text{time|DI}} = 3.99$ and $\beta_{\text{time|DI}} = 0.34$. From these values, the lognormal probability density function (PDF) and corresponding cumulative distribution function (CDF) are determined, Figure 34.20(c). This last curve, for all practical purposes, is the fragility curve of the bridge assessed in terms of the DI of a potentially excessive displacement.

Similar curves could then be determined from other sets of quantities, and engineers could meaningfully and rationally answer such basic and important questions as: A) how long would it take for a certain degradation to occur? or B) what is the degradation likely to occur at a given time. This is the essence of RICA presented in this AAR analysis.

Chapter 35
Case Study: Seabrook Station Unit 1 ASR Problem

Abstract
In this chapter, we examine a particularly complex case-study, one that brings together multiple issues separately addressed in this book and is thus a fitting last chapter.
More specifically. we examine the response by a single nuclear reactor's private owner and the governmental regulator to aging and cracking issues due to ASR. The reactor, Seabrook Station Unit 1 in New Hampshire, owned and operated by NextEra Energy Seabrook LLC, is the first and only United States reactor where ASR has been discovered. ASR affects significant safety structures at Seabrook, including the containment enclosure building (CEB) which surrounds the reactor containment and protects against radiation releases from the reactor core. Because the adequacy of NextEra's program for detection and monitoring of ASR at Seabrook was subject to an investigation and licensing process by the regulator, the U.S. Nuclear Regulatory Commission (NRC), the response to ASR at Seabrook is relatively well-documented. As previously discussed, ASR is a highly complex problem that poses significant challenges in any attempt to assess it. In the case of a nuclear reactor, the stakes are particularly high, given the increase in seismic vulnerability that may be induced by ASR. In the case of Seabrook, both the private licensee and the government regulator pursued a code-based engineering heuristic approach. While that approach is standard and often acceptable for addressing nuclear reactor engineering problems, it is not sufficiently sophisticated to account for the complexities of ASR. From the authors'[1] point of view, the most critical concerns are the licensee's inability to detect internal potential delamination, and the reduced shear capacity of the CEB in resisting seismic excitation. This is a serious deficiency, given the importance of the CEB in protecting public health and safety against the inadvertent release of radioactivity during an earthquake.

This chapter will provide detailed information on Seabrook Station Unit 1, the first reported nuclear power plant in the U.S. known to suffer from ASR. This detailed information was yielded by private and government investigations into ASR since its discovery in 2009, as well as a license amendment request (LAR) submitted by NextEra to the NRC in 2016. The LAR, which was approved by the NRC technical

[1] Though this chapter will make multiple references to the "authors", it was entirely written by the first author of the book: V. Saouma.

staff in 2019, sought approval of NextEra's ASR assessment and its proposed ASR monitoring program, and has been used to justify extended operation of Seabrook beyond its current 2030 operating deadline until 2050[2].

Whereas the previous chapter addressed some aging or cracking issues at four nuclear reactors, this chapter will be dedicated exclusively to a single reactor which suffers from ASR. Seabrook is appropriate for separate coverage within this book, for two reasons. First, ASR at Seabrook has been studied for ten years, and thus it provides a good test-case for how aging/shaking and cracking issues, the subject of this book, are addressed in practical terms. Second, the investigations of ASR at Seabrook are relatively well-documented and publicly available in the NRC's Agency wide Documents Access and Management System (ADAMS) the official record-keeping system through which the NRC provides access to publicly available documents [42]. In this context, the NRC should be complimented for the high level of transparency to the public as practically all (non-confidential) information are available for examination.

Naturally, ASR is a very complex issue that has been scrutinized at Seabrook for over 10 years, and relevant information is disseminated in multiple reports. Hence, to increase comprehension/readability, the authors have not hesitated to logically subdivide this chapter in up to five levels of sub sectioning. In addition, the reader will find multiple cross-referencing to topics covered in the first part of the book (Theory).

The authors wish to point out that not all factual information relevant to the Seabrook investigation is publicly available, for two reasons. First, some information has been redacted, i.e., withheld from public disclosure, by NextEra Energy, on the ground that it is proprietary. Second, some information inevitably is unavailable because it simply has not been developed.

To the extent that information has been redacted from publicly available documents and is not available from any other source, it is not discussed in this chapter. The authors note, however, that some information that has been redacted from documents that are publicly available on ADAMS appears in other publicly available documents such as academic research papers. In that case, the authors cite those research papers. The authors apologize for any possible misrepresentations resulting from lack of documentation. On the other hand, the authors make no apologies for reviewing the publicly available documents with the same, if not more (given what is potentially at stake) zeal and scrutiny they would have exercised in reviewing a manuscript submitted for journal publications.

Regarding organization: this chapter will be broken into two parts. First the underpinnings of the LAR will be described, primarily based on public information available through ADAMS,. Then, the authors will provide their own assessment (or

[2] Disclaimer: In 2014, the first author received a grant from NRC to evaluate ASR, and prepared three detailed reports for the agency that were submitted in 2017. After finishing that work, he served as an expert witness for a small "citizens" group (C-10 Research and Education Foundation) that has challenged the reliability of the LAR in the NRC's license amendment proceeding. As such, he reviewed many documents (including confidential ones), wrote numerous others, and was a witness during a four-day administrative hearing.

critical review of the process). Again, it should be noted that all reported details of Seabrook are taken from publicly available documents.

35.1 Reported Analyses/Investigation

35.1.1 Background

First, it should be noted that the design of Seabrook unit 1 is somewhat unusual, Figure 35.1(b). Unlike many other pressurized water reactors, it has a 30 inch thick CEB "wrapped around" a containment structure (48 inches). The CEB serves to collect any fission products that may leak from the primary containment structure following a loss of coolant accident (LOCA). The area between the two containment structures is maintained at a negative pressure ($\sim$ 0.25" water gauge) to ensure that any leakage into the area is 1) collected; 2) filtered; and 3) released from an elevated location in a controlled and monitored fashion [650].

In 2010, NextEra [629] submitted an application for renewal of the Seabrook Station NPP Unit 1 operating license for another 20 years beyond the current licensing date of May 15, 2030. This renewal process consisted of two concurrent reviews: a technical review of safety issues and an environmental review. For the safety review, the NRC's license renewal rule process and application requirements for commercial power reactors are based on two key principles: a) that the current regulatory process, continued into the extended period of operation, is adequate to ensure that the continuing license basis of all currently operating plants provides an acceptable level of safety, with the possible exception of the detrimental effects of aging on certain passive systems, structures, and components (SSCs), and possibly a few other issues related to safety only during the period of extended operation; and b) each plant's continuing license basis is required to be maintained [653]. Hence, as part of the license renewal process, an aging management program (AMP) is to be identified that is determined to be acceptable to manage potential problems such as ASR on passive safety components such as the CEB.

ASR was first discovered in 2010 in a tunnel (Bravo-1) that is supposed to provide intake and discharge cooling water to the ocean (ultimate heat sink). Later on, it was determined that ASR was much more pervasive and affected numerous structures including the concrete CEB. This was clearly highlighted by the NRC's safety evaluation report (SER) [653], Figure 35.1(c).

Consequentially, the NRC informed NextEra that in order to gain approval of its license extension application, it must provide a reasonably accurate assessment of ASR at Seabrook, as well as a monitoring program for the 20-year license extension period.

Moreover, the NRC made it clear that a final decision on the license renewal application would not be announced until concrete degradation issues identified at the plant had been satisfactorily addressed, [356].

In 2013, a root cause investigation [632] determined that ASR developed because the concrete mix designs unknowingly utilized a coarse aggregate that, in the long term, would contribute to the Alkali Silica Reaction. Although testing at the time

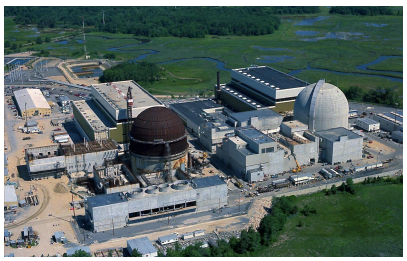

(a) Seabrook. Unit 1 (right) and "mothballed" Unit 2 (left) in the background

https://www.telegram.com/news/20180706/criticism-of-seabrook-nuclear-power-plant-finds-new-momentum

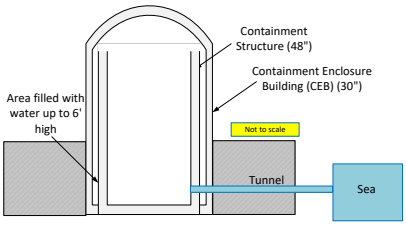

(b) Schematic of the reactor (based on [652]

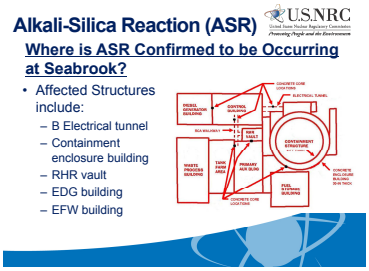

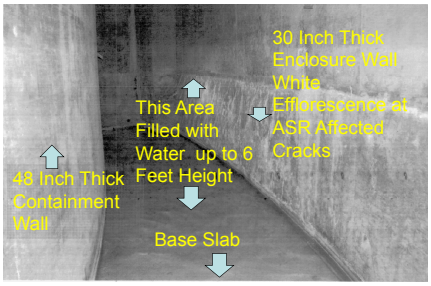

(c) Identification of damage [652] [654]

Fig. 35.1: Cracking at Seabrook

of construction was conducted in accordance with ASTM standards, these standards were subsequently found to be limited in their ability to predict the presence of slow reactive aggregates that produce ASR in the long term. Furthermore, based on the long-standing belief that ASR is not a credible failure mode due to the concrete mix design, the original operating license did not require any consideration of conditions related to ASR in the licensee's reports involving groundwater intrusion or concrete degradation, or in the structural health monitoring program. Hence, NextEra's LAR was the first licensing document to address ASR.

35.1.2 The Process

The discovery of ASR at Seabrook constituted the first time that the NRC was confronted with a nuclear reactor infected by ASR. Unfortunately, rather than issuing regulations for NextEra to utilize in assessing the safety of Seabrook, the Agency for all practical purposes delegated this task to NextEra. This was an iterative process, during which the NRC initially asked NextEra to provide the necessary information and analyses, then requested additional details or explanation.

In turn, NextEra contracted with a major reputable consulting company Simpson Gumpertz & Heger (SGH) to lead the task. SGH oversaw the overall project and took the lead in the finite element analysis and monitoring program. It also solicited the assistance of MPR Associates (MPR) a company with extensive expertise in the nuclear engineering field. MPR in turn oversaw laboratory testing at the Ferguson Structural Engineering Laboratory (FESL) at the University of Texas in Austin.
As will be discussed below, the authors do not question the qualifications of these companies to address well-understood nuclear engineering problems. However, they showed a lack of understanding of the complex challenges posed by ASR, or even an appreciation of the skill level that would be needed to address it adequately.

35.1.3 License Amendment Request

In 2016, NextEra submitter the LAR [633]. The major technical arguments of this document will first be reported, and in a subsequent section they will be commented on by the authors. The LAR was essentially based on three major and inter-related components, Figure 35.2:

Large-Scale Testing Program (LSTP): at the Ferguson Structural Engineering Laboratory (FSEL) in which large beams were tested for shear strength, flexural stiffness, and anchor capacity (Only the first will be reviewed). In addition, there was an instrumentation testing component to this task.

Building Deformation Aging Management (BDAM): to monitor and measure the *in-situ* total volumetric ASR expansion since construction.

Building Deformation Assessment (BDA): to assess numerically the integrity of the structures (primarily through the finite element analysis).

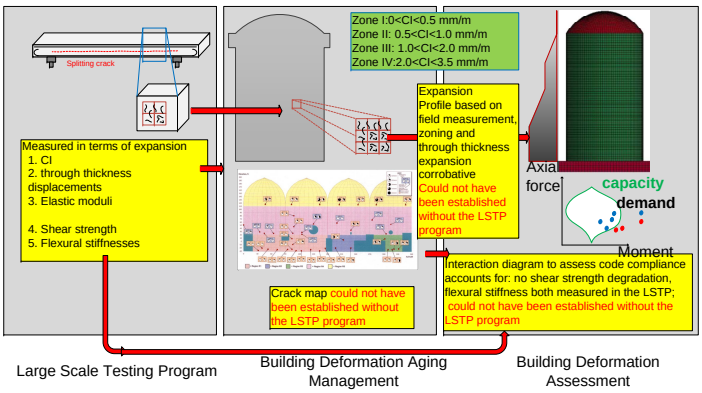

Fig. 35.2: Integration of the three major components of the LAR, adapted from [794]

To the extent possible, this section will describe each of those components. The authors note that much of the key information described in this section can be found in publicly available redacted versions of the LAR and/or reports by NextEra's consultants that are available on ADAMS. Some other key information discussed in this chapter appears in publicly available academic theses, technical reports or papers (such as [106] [859] [861]), although it has been redacted from the LAR and/or NextEra's consultants' reports. Information that has been redacted from the LAR and consultant reports, and that is not available in any other publicly available document, is not discussed.

35.1.3.1 Ferguson Structural Engineering Laboratory

35.1.3.1.1 In/out-of-plane Shear Transfer The LSTP did not test for the in-plane shear mode. As the NRC stated

> the LSTP did not test for the in-plane shear mode. This was because the out-of-plane shear failure mode was judged to be more critical than in-plane shear mode (note: nominal permissible out-of-plane shear stress in concrete per the ACI 318-71 code is $2\sqrt{f'_c}$ versus allowable total shear stress of $10\sqrt{f'_c}$ for in-plane shear.
>
> NRC-ML19261A762 [655]

35.1.3.1.2 Concrete Mix One of the first tasks of the LSTP was the design of the concrete mix for the test beam and expansion measurement block. The LSTP concrete mix included high reactive fine aggregate as well as reactive coarse aggregates and cement with high alkali content to accelerate the reaction [635]. Furthermore, MPR claimed that "to the extent practical, concrete constituents were obtained from sources that were consistent with concrete at Seabrook Station" [607]. The mix was used for anchor block, anchorage, the 24-inch shear and instrument specimens, Figure 35.3(b). However, as noted in the figure, all details are regretfully redacted.

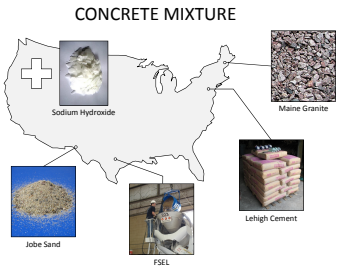

(a) Concrete mix design [106]

Parameter	Anchor Block Specimens	Reinforcement Anchorage Specimens	24-inch Shear Specimens	Instrument Specimen
Height				
Width				
Length				
Presence of Lap Splice	No	Yes	No	No
Vertical Rebar Size & Spacing				
Horizontal Rebar Size & Spacing				
Stirrups Size & Spacing				

*Two half-length specimens were fabricated in a single placement

(b) Specimens tested [607]

Fig. 35.3: Concrete and specimens

35.1.3.1.3 Beam Tests This review will limit itself to the shear tests of the FSEL beam (and will not include anchorage). In the absence of reported explicit dimensions of the beam, one could rely on technical reports [106] or on the PhD thesis of Wald [859] as the best alternative sources of information. While it is not certain that the tests described in these reports are identical to the FSEL tests, their general description so closely fits the LSTP as described in publicly available documents that the authors would be very surprised if they differed much if at all.

35.1.3.1.3.1 Dimensions and Loading Dimensions of the LSTP test specimens are assumed to be comparable to those described in Figures 35.4(a) and 35.4(b). LSTP reinforcement is thought to be similar to the one shown by Wald, Martinez, and Bayrak [859] in Figure 35.4(c) and 35.4(d). As described in [861] the specimens were cleverly partitioned into three wetting zones: A (away from stirrups and with periodic moist conditions), B (close to stirrups and periodic moist conditioning) and C (close to stirrups Figure and constant wet conditioning) to assess impact of relative humidity (RH). Figure 35.4(e) illustrates the conditioning process. Finally, all specimens were stored in an environmental conditioning facility where specimens were

> exposed to temperatures on the order of 5–10°C greater than seasonal ambient outdoor temperatures. In central Texas, ambient temperatures typically ranged between 5 and 40°C from winter to summer. The entire specimen was subjected to alternating, week-long wet and dry conditioning cycles using mist foggers to produce a periodic state of 90–100% relative humidity within the storage space.
>
> Wald, Martinez, and Bayrak [859].

35.1.3.1.3.2 Structural Crack The shear tests were "bruised" by

> the formation and subsequent growth of large cracks on the side (x-z) surfaces of the specimen perpendicular to the mats of reinforcement, Figure 35.5. The cracks were located midway between the mats of reinforcement and oriented parallel to the x direction reinforcement. The cracks were located only in the biaxially reinforced part of the beam; they did not extend into the beam ends where stirrups were present.
>
> The cracks on the x-z faces of the specimens were identified to be caused largely by a mechanical boundary effect rather than purely due to ASR expansion perpendicular to the cracks (i.e., in the z direction). It was suggested that the cracks formed due to tension induced in the outer fibers of the specimen from nonuniform restraint to expansion provided locally by the two discretely placed mats of reinforcement. The concrete between these reinforcing layers, separated by more than 350 mm, was freer to expand. The net effect was a concentrated deformation of concrete near the reinforced surfaces with the interior concrete outwardly "bending" between reinforcement locations, which acted as supports.
>
> Wald, Martinez, and Bayrak [859]

On the other hand, [607] indicates that this was confined to the specimen edges and penetrated only a few inches into the specimen height. NextEra also states that

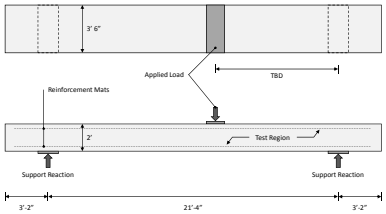

(a) Dimensions [106]

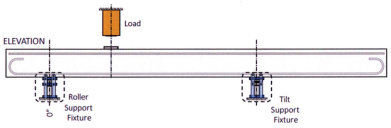

(b) Shear loading [607]

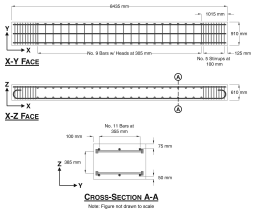

(c) Reinforcement [859]

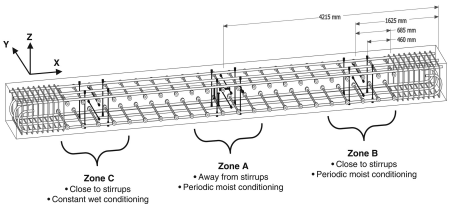

(d) Wetting zones [859]



(e) Conditioning [106]



(f) Environmental conditioning facility [859]

Fig. 35.4: Shear beam tests

This large crack is not representative of expansion behavior of structures at Seabrook Station, which have a network of members that are either cast together or integrally cast with special joint reinforcing details. In an actual structure, a vertical wall with two-dimensional reinforcement will be confined in the through-thickness direction at its intersection with neighboring members (i.e., at the top and bottom with floor and ceiling slabs, at the sides with perpendicular walls, and uniformly along the wall face by the subgrade for below grade external walls). The confinement provided by the network of members in a structure is likely sufficient to preclude large cracks like those seen in the FSEL test specimens.

MPR-ML16216A242 [607]

35.1.3.1.3.3 Shear Failure Per [607], shear capacity was based on the ACI 318 definition: onset of diagonal cracking which was identified visually. In addition there was a slight reduction in load carrying capacity shown on the load-deflection curve. Yet, per [106] testing continued until failure of the specimen, as identified by a rapid loss in load carrying capacity, Figures 35.6(a) and 35.6(b).
As expected and widely reported in the literature [181] [17] [243] [867], an increase in shear capacity was reported in conjunction with the ASR expansion. All shear

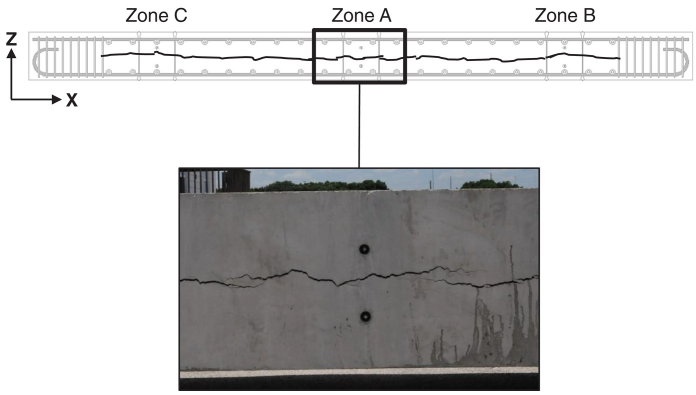

(a) Splitting crack [859]

Fig. 35.5: Splitting structural crack

test results exceed the theoretical shear capacity calculated per ACI 318-71, which is a normalized shear capacity of 2.0. The large number of tests and the repeatability of the data provide strong confidence in the conclusion that there was no adverse effect on shear capacity at the expansion levels tested. Likewise, the stiffness in ASR-affected test specimens is reported to be clearly greater than the control test specimen and that there was an increasing trend with respect to through-thickness expansion [607].

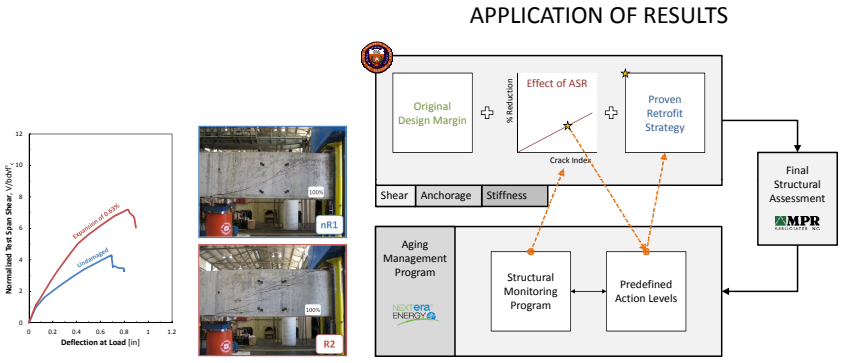

(a) Representative results [106] (b) Application of results [106]

Fig. 35.6: Shear test results

35.1.3.2 Building Deformation Aging Management

The Building Deformation Aging Management Program (BDAM) uses visual inspections of cracking associated with the Structures Monitoring Program and out-of-plane expansion measurements associated with the ASR to identify buildings that are experiencing deformation. Cracks are measured by the classical crack index (CI) approach to measure in-plane expansion. The second method is an innovative one (never noted by the authors in the context of ASR measurements) that measures the through thickness expansion. Through thickness expansion measurements are expected to be much higher than the former [859] as evidenced in Figure 35.9.

35.1.3.2.1 Crack Index Crack indices, Figure 35.7, will be correlated to measured expansions as well as structural tests results for use in Seabrook Station [106]. The

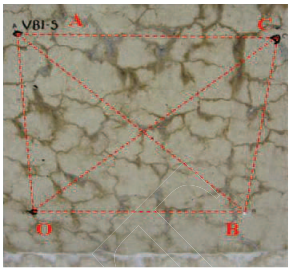

(a) Crack Index grid [311]

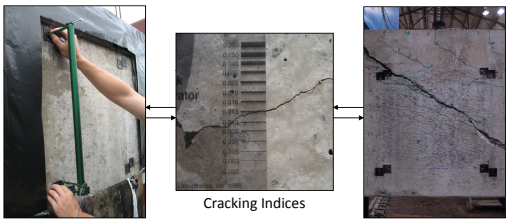

(b) Expansion monitoring by the FSEL [106]

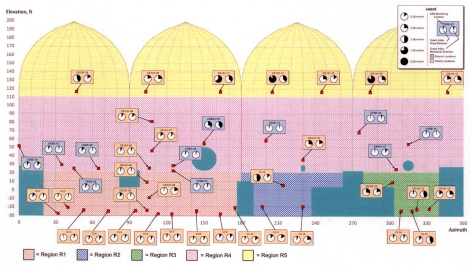

(c) ASR regions and crack index measurement locations [794]

Fig. 35.7: Crack index measurements

CEB was subdivided into four regions selected to contain Cl values that are generally within the limits of an ASR Severity Zone defined as [794], Table 35.1.
CI readings in turns are subdivided in three tiers, as shown in Table 35.2.

35.1.3.2.2 out-of-plane Expansion For Tier 1, it is recommended that a through-wall expansion monitoring system be installed. This consists in installing a com-

Table 35.1: Severity zones [794]

Zone	CI [mm/m] Min	Max
I	0	0.5
II	0.5	1.0
Ill	1.0	2.0
IV	2.0	3.5

mercial snap ring borehole extensometer (SRBE), Figure 35.8(a) [607]. A so-called "corroborative modulus expansion" is performed to determine the through thickness expansion. It is based on the observation that the decrease in elastic modulus can be correlated to the expansion. Hence, based on a calibration curve obtained in the laboratory, Figure 35.8(b), the assumption is that one can compute the normalized elastic modulus from

$$E_n = \frac{E_{present}}{E_{28days}} \tag{35.1}$$

where $E_{present}$ is the current elastic modulus measured from a recovered core based on ASTM test, and E_{28days} is the elastic modulus around 28 days after casting computed from the ACI-318 equation

Table 35.2: Acceptance criteria for CI measurements [635]

Tier	Structures Monitoring Program	Recommendation for Individual Concrete Components	Criteria
3	Unacceptable (requires further evaluation)	• Structural Evaluation • Implement enhanced ASR monitoring such as through-wall expansion monitoring using Extensometers	1.0 mm/m (0.1%) or greater strain measurement (CCI or pin-pin)
2	Acceptable with deficiencies	Quantitative Monitoring and Trending	• 0.5 mm/m (0.05%) or greater strain measurement (CCI or pin-pin) • CI or pin-pin measurement of greater than 0.5mm/m (0.05%) in the vertical and horizontal direction
		Qualitative Monitoring	Any area with visual presence of ASR (as defined in [830] accompanied by a CI of less than 0.5 mm/m (0.05%) in the vertical and horizontal directions.
1	Acceptable	Routine inspection as prescribed by the Structural Monitoring Program	Area has no indication of pattern cracking or water ingress; No visual symptoms of ASR

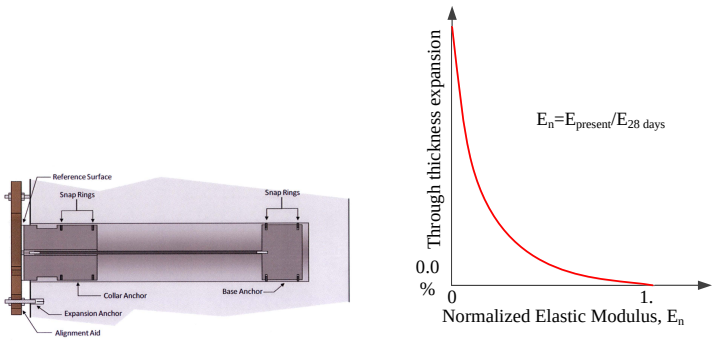

(a) Snap ring borehole extensometer [607]

(b) Correlation between ASR expansion and volumetric expansion

Fig. 35.8: Determination of volumetric ASR expansion

$$E = 57,000\sqrt{f'_c} \tag{35.2}$$

And where f'_c is the recorded 28 days strength (in psi units) measured on selected cores during construction (around 1977). Finally, the volumetric total ASR strain is the sum of the through thickness (by far the largest) and the two in-plane expansions measured by CI.

To confirm that expansion behavior at Seabrook Station is similar to the FSEL test specimens, NextEra-ML18141A785 [635] recommends that checks identified in table 35.3 be conducted.

35.1.3.2.3 Recorded Expansion Finally, with regard to the directional expansions for the three zones

> each biaxially restrained portion of the beam exhibited a similar expansion response. At all times, expansions in the unreinforced direction (z) were greater than those in the reinforced directions (x and y). Despite differences in gross reinforcing ratios for the x and y directions, the beam expanded nearly identically in the two directions. At approximately 90-100 days after casting, there was a relatively abrupt shift in expansion behavior. The data, [Figure 35.9] indicate that the expansions in the reinforced directions effectively stopped while the beam continued to expand in the unreinforced direction. The expansions in the X and Y directions reached maxima of approximately 0.1-0.15%. These expansions were less than an approximate yielding strain of 0.2% for the reinforcement. Continued expansion of the beam in the z direction was sensitive to thermal fluctuations with less additional expansion occurring during colder months. The rate of this expansion in the z direction was increased in Zone C, which was under constant wet conditioning.
>
> Wald, Martinez, and Bayrak [859]

Table 35.3: Recommendations for confirming expansion behavior at Seabrook Station is similar to test programs [635]

Objective	Recommended Approach	When
Ongoing Monitoring		
Expansion within limits from test programs	Compare measured in-plane expansion (ε_{xy}), through-thickness expansion (ε_z), and volumetric expansion (ε_v) at the plant to limits from test programs ($\varepsilon_{xy} \leq$ [redacted]%, $\varepsilon_z \leq$ [redacted]%, and $\varepsilon_v <$ [redacted]%)	Intervals as specified in Structures Monitoring Program (SMP) or Aging Management Program (AMP)
Lack of mid-plane crack	Inspect cores removed from ASR-affected structures (and boreholes) for evidence of mid-plane cracks	When cores are removed to install extensometers or for other reasons.
Periodic Confirmation of Expansion Behavior		
Lack of mid-plane crack	Review of records for cores removed to date or since last assessment	Periodic assessments • At least 5 years prior to the Period of Extended Operations (PEO) • Every 10 years thereafter
Expansion initially similar in all directions but becomes preferential in z-direction	Compare ε_{xy} to ε_z using a plot of ε_z versus in-plane expansion	
Expansions within range observed in test programs	Compare measured ε_{xy}, ε_z, and ε_v at the plant to limits from test programs ($\varepsilon_{xy} \leq$ [redacted]%, $\varepsilon_z \leq$ [redacted]%, and $\varepsilon_v <$ [redacted]%) to check margin for future expansion	
Corroborate modulus-expansion correlation with plant data	For 20% of the extensometer locations: • Remove cores for modulus testing. • Compare ε_z determined from the modulus-expansion correlation with ε_z determined from the extensometer and the original modulus result. A detailed explanation of this approach is provided in Appendix C.	At least 5 years prior to PEO (initial study) and 10 years thereafter (follow-up study).

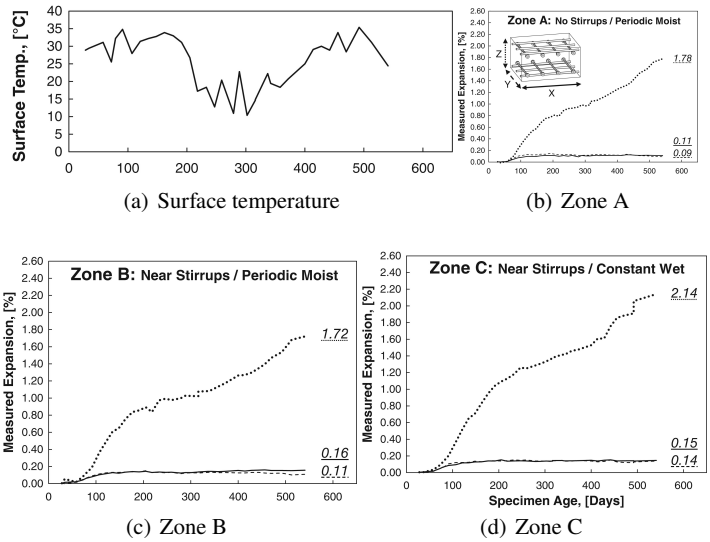

(a) Surface temperature (b) Zone A

(c) Zone B (d) Zone C

Fig. 35.9: Directional expansion measurements [859]

35.1.3.3 Building Deformation Assessment

35.1.3.3.1 Screening Evaluations The LAR [634] defines self-straining loads as a term that encompasses ASR expansion (largest contributor), creep, and shrinkage

as those contribute to the observed deformations and were not included in the original analysis.

A three-stage screening analysis is applied to Seismic category I structure [3], Figure 35.1(c) although the inner containment is assessed separately. All three stages of the evaluation process use the original design acceptance criteria given in Seabrook's Updated Final Safety Analysis Report (UFSAR) [630]. In applying the three-stage process to each structure, the original design loads are combined with the self-straining.

> Each stage of the analysis applies more sophisticated methods and uses additional field data to improve the accuracy of the results.
>
> Stage One, Screening Evaluation: Each of the seismic Category I structures is screened for susceptibility to structural deformation caused by ASR using existing field data and conservative calculations.
>
> Stage Two, Analytical Evaluation: An analytical evaluation is performed for each structure that the Stage One Screening Evaluation identifies as susceptible to deformation but does not satisfy ACI 318-71 acceptance criteria. A finite element model of the structure is used to estimate structural demands due to self-straining loads, while all other demands are taken from existing design calculations. Additional field data are obtained to use in the analysis. The evaluation verifies compliance with ACI 318-71 using the same criteria as the original design.
>
> Stage Three, Detailed Evaluation: A detailed design confirmation calculation is performed when the Stage Two Analytical Evaluation concludes that some area of a structure does not satisfy ACI 318-71 acceptance criteria or when the structure has sufficient deformation that may impact demands computed in the original design. The detailed evaluation uses the Stage Two finite element model to compute demands due to self-straining loads as well as all other design loads. In the Stage Three evaluation, consideration is given to cracked section properties, self-limiting secondary stresses, and the redistribution of structural demands when sufficient ductility is available.
>
> NextEra-ML16216A240 [634]

As shown in Figure 35.1(c), the inner containment structure is protected from the outside elements by the CEB. Thus, NextEra considers it to be less susceptible to deleterious effects of ASR. While NextEra states on the one hand that assessment will be performed using the three stage process discussed above, on the other it states that it is expected that the Containment will be screened as only Stage 1 evaluation. Each analysis stage will determine threshold monitoring limits to define the criteria for re-evaluating structures with deformation. The threshold monitoring limits are specific to each structure and will be included in the Structural Monitoring Program. Monitoring and acceptance criteria for ASR cracking and deformation of structures are shown in Table 35.4.

35.1.3.3.2 Factored Self-Straining Loads In accordance with the load and resistance factor design (LRFD) method of [10], factored load combinations are used,

[3] Defined by the NRC as "Structures, systems, and components that are designed and built to withstand the maximum potential earthquake stresses for the particular region where a nuclear plant is sited (https://www.nrc.gov/reading-rm/basic-ref/glossary/seismic-category-i.html)."

Table 35.4: ASR Expansion Limits For Structural Limit States

Structural Limit State	ASR Expansion Limit
Shear	[redacted]% through-thickness
Flexure	[redacted]% through-thickness
Reinforcement Anchorage	[redacted]% through-thickness
Anchors	[redacted]% in-plane

Table 35.5. The factored self-straining loads are combined with the original design load combination for the screening and analytical evaluations discussed above. The load factors for dead load are used for the shrinkage, creep, and swelling loads in accordance with ACI 318-71. However, since the code does not have load factors applied to ASR, those were developed to yield reliability index values (§18.2.1) similar to load factors specified in ACI 318-71 [793]. The ASR load factors account for the uncertainty in ASR expansion by considering the variability in crack index measurements from all ASR monitoring grids in Seabrook Station structures. For unusual load combinations, such as SSE and tornado wind combinations, all load factors are taken as 1.0 [794].

35.1.3.3.3 Finite Element Analysis The reported finite element analysis [794] is composed of the following:

Static Analysis: All analyses are linear elastic and use shell elements. ASR expansion is simulated by applying an isotropic thermal expansion to the elements representing the CEB concrete. Steel reinforcement membrane elements are included in the model and are given thicknesses based on the total area of reinforcement provided. The expansion of the concrete creates tension in the steel membrane elements, which also causes a corresponding compression force in the concrete elements.

Applied ASR expansion magnitude and distribution are adjusted to match field measurements in two ways: First, strain in the finite element model caused by unfactored ASR expansion of the CEB wall is compared with field measurements of CI. In general there is a match. Second, deformations due to unfactored sustained loads plus unfactored self-straining loads are compared to field measurements of seismic gap (the structural gap between the CEB and adjoining concrete structures). There is recognition that abrupt transitions in ASR expansion can cause stress concentration, hence an artificial taper (about 60 ft long) is used between regions.

For the CEB analysis, factored (to account for uncertainty) ASR loads are amplified by an additional threshold factor (1.2) to account for additional ASR expansion that may occur in the future. This factor applies only to the CEB.

Dynamic Analysis: A finite element model of the most limiting area was developed to address the potential of an adverse dynamic response associated with the apparent modulus of elasticity tests conducted on the extracted core samples.

Table 35.5: Load combinations [794]

Label[1]	Combination
N0_1	(2.0× k_{th})S_a + 1.4S_w + 1.40 + 1. 7L + 1. 7H
N0_2	(1.5× k_{th})S_a + 1.4S_w + 1.050 + 1.28L + 1.28H
N0_3	(1.0× k_{th})S_a + 1.4S_w + 1.00 + 1.0L + 1.0H + 1.5P_a
OBE_1	(1.3× k_{th})S_a + 1.4S_w + 1.40 + 1.7L + 1.9Eo + 1.7H + 1.9H_e
OBE_2	(1.0× k_{th})S_a + 1.4S_w + 1.050 + 1.28L + 1.43Eo + 1.28H + 1.43H_e
OBE_3	(1.3× k_{th})S_a + 1.4S_w + 1.20 + 1.9Eo + 1. 7H + 1.9H_e
OBE_4	(1.0× k_{th})S_a + 1.4S_w + 1.00 + 1.0L + 1.25Eo + 1.0H + 1.25H_e + 1.25P_a
SSE_1	(1.0× k_{th})S_a + 1.4S_w + 1.00 + 1.0L + 1.0Ess + 1.0H + 1.0H_s
SSE_2	(1.0× k_{th})S_a + 1.4S_w + 1.00 + 1.0L + 1.0Ess + 1.0H + 1.0H_s + 1.0P_a
W_1	(1.× k_{th})S_a + 1.4S_w + 1.40 + 1.7L + 1.7W + 1.7H
W_2	(1.28× k_{th})S_a + 1.4S_w + 1.050 + 1.28L + 1.3W + 1.28H
W_3	(1.?× k_{th})S_a + 1.4S_w+ 1.20+1.7W+ 1.7H
W_4	(1.0× k_{th})S_a + 1.4S_w + 1.00 + 1.0L + 1.0Wt + 1.0H
W_5	(1.0× k_{th})S_a + 1.4S_w + 1.00 + 1.0L + 1.0W + 1.0ls
W_6	(1.0× k_{th})S_a + 1.4S_w + 1.00 + 1.0L + 1.0W + 1.0ls + 1.0F

1 NO: Normal load comb1nations (non-se1sm1c and non-wind)
QBE Load combinations including operating basis earthquake E_a
SSE Load combinations including safe shutdown earthquake E_ss
W Load combinations including wind, W, and tornado wind, W_t
2 OBE and SSE combinations are performed for each of the directional combinations

D Dead load (includes hydrostatic pressure)
H Lateral static soil pressure
E_a Operating basis earthquake (OBE)
H_e Dynamic earth pressure due to OBE
W_t Tornado wind load
L_s Unusual snow load
S_a ASR expansion of wall and backfill concrete
S_h Shrinkage (self-straining force)
L Live load
w Wind load
E_{ss} Safe shutdown earthquake (SSE)
$H-s$ Dynamic earth pressure due to SSE
P_a Accidental Pressure load
F Design basis flood load
S_c Creep (self-straining force)
S_w Concrete swelling (self-straining force)

According to this model, a differential analysis of the structure with various modulus changes could be performed [632]. This analysis concluded that

> Finite Element Model Results:
>
> - Maximum acceleration profiles and In Structure Response Spectrum not significantly impacted by ASR affected properties
> - Distribution of forces and moments are not significantly impacted by ASR affected properties.
>
> NextEra-ML121160422 [631]

Structural Evaluation: Analyses are conducted for multiple load cases using an element by element approach as well as section cut approach. Evaluation criteria are based on strength according to [10]. Maximum displacements are are compared against clearances with adjacent structures.
Finally, it is argued that

> Evaluating a structure on an element-by-element basis is considered a conservative approach because it does not allow for concentrations of high demands to be distributed locally within the structure. Factored demand exceeding capacity in the element-by-element evaluation does not necessarily indicate a structural deficiency. Since a relatively small finite element size is used in the analyses, stress concentrations can cause localized capacity exceedances in the element by element evaluation which may not have any real structural impact. If an element's capacity is exceeded in the element-by-element evaluation, the area is evaluated again using a section cut approach. If the element-by-element capacity exceedance is identified as insignificant (i.e., a stress concentration that will not impact structural performance), then further analysis/evaluation is not performed.
>
> Simpson Gumpertz & Heger-ML16279A049 [794]

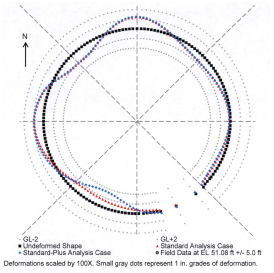

(a) Comparison between as-deformed condition simulations and field measurements [794]

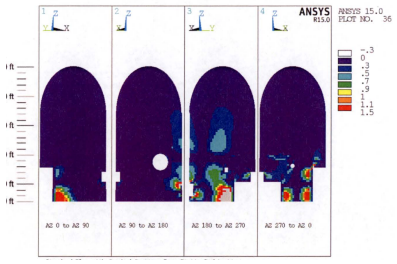

(b) Representative finite element analysis model using shell elements [794]

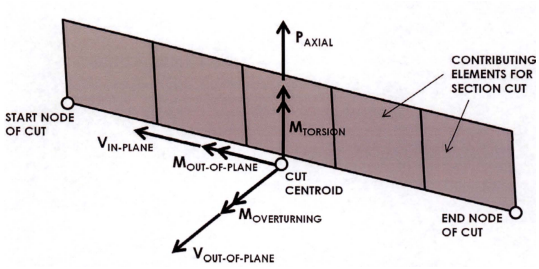

(c) Section cut resultant forces and moments at cut centroid [794]

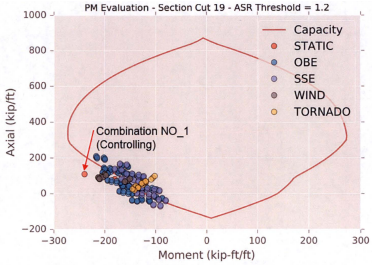

(d) Interaction diagram check [794]

Fig. 35.10: Representative plots of the finite element analyses

35.2 Critical Review

At issue here is how to make a prediction of remaining service life. And of course, service life must be reasonably safe as required by federal law (the Atomic Energy

Act). In pursuing this important (if not vital) task, NextEra was confronted with a common problem plaguing engineers who pursue similar objectives. First, there is a glaring absence of codes for the assessment of existing structures[4]. This is particularly troublesome when the aging of our infrastructure is widely recognized. The second is the danger of entrusting engineers, reared in the design of new structures, with the safety assessment of older ones. Those two tasks require two very different skill sets; simply put, the former may be performed by an engineer with minimum training (as one would "simply" have to follow the myriad of code provisions), but the latter would require one to have had some graduate education. And this was blatantly clear throughout our review. As stated by the drafters of ASCE 4-16 [49]

> Regulatory government agencies are frequently faced with decisions related to the seismic design of operating nuclear facilities... As new information becomes available, the design basis may be challenged. ... Because of its pervasive nature, an earthquake will"seek out" facility vulnerabilities... At issue is whether the changes can be accommodated within the inherent capacity of the original design or whether facility modifications are required.... current design practice does not provide a picture of the actual margin to failure, nor does it provide enough information to make realistic estimates of seismic risk.
>
> ASCE 4-16 [49]

Unfortunately, however such recommendations[5] were mostly ignored.
Hence, guided by this spirit, and ultimately concerned by the lack of a rigor scientific study, this section will now "dissect" the LAR using basic principles of scientific/engineering examination. While the authors acknowledge that the NRC technical staff has approved the LAR, they have applied their own independent analysis.

35.2.1 The Process and Concepts for Development and Review of LAR

Having reported to the best of our ability the complex technical underpinning of the LAR, this section will review it. By now it is quite evident that a code-based engineering heuristic approach was followed by NextEra and approved by the NRC. Under normal circumstances, this would be perfectly acceptable. However, in this case of ASR we are dealing with an exceedingly complex and challenging problem, one with which the the industry annd the NRC have been confronted for the first time, and one where an erroneous safety assessment could lead to a nonconservative response and perhaps devastating consequences. The authors see a disturbing dichotomy between the relatively simplistic engineering approach taken by NextEra and the NRC, and the much more rigorous "first principle" based analytical approach used in the numerous analyses reported throughout this book.

---

[4] The ACI 365 code "Service-Life-Prediction; State-of-the-Art Report" [12] has 10 lines under §4.3 focusing on *Prediction of remaining service life*.

[5] Though written for challenges caused by seismic considerations, one could easily substitute "seismic" with "ASR" without loss of relevance

In-fine it is hoped that this section will be ultimately perceived by all as constructive criticisms driven by a thirst for scientific rigor.

35.2.1.1 Role of NRC

It is evident that rather than *regulating* ASR, the NRC instead subcontracted the work of determining how to assess the extent and gravity f ASR at Seabrook to the very same corporation it is supposed to oversee. While the NRC posed a number of questions to NextEra during its technical review, the agency did not exercise due diligence in scrutinizing the scientific validity of NextEra's response. Unfortunately, this is reminiscent of the problem that came to plague the Boeing 737 MAX. As stated by the Boeing 737 MAX flight Control System Joint Authorities Technical Review (JATR)

> 1. A complicated system is characterized by a linear relationship between cause and effect, whereas a complex system is characterized by a non-linear relationship between cause and effect, such that small causes could lead to very large effects.
> 2. The Federal Aviation Administration (FAA) failed to provide an independent assessment of the adequacy of the Boeing proposed certification activities...
> 3. The BASOO [FAA's Boeing Aviation Safety Oversight Office] delegated a high percentage of approvals and findings of compliance to the Boeing ODA for the B737 MAX program.
> 4. [FAA should] conduct a workforce review of the BASOO engineer staffing level to ensure there is a sufficient number of experienced specialists to adequately perform certification and oversight duties, commensurate with the extent of work being performed by Boeing. The workforce levels should be such that decisions to retain responsibility for finding compliance are not constrained by a lack of experienced engineers.
> 5. [FAA should encourage applicants to] have a system safety function that is independent from the design organization, with the authority to impartially assess aircraft safety and influence the aircraft/system design details.
> 6. The FAA and applicants should develop, validate, and implement analytical tools appropriate for the analysis of complex systems.
>
> JATR [473]

Each one of those quotes would be applicable to the approach taken by NextEra and the NRC:

1. As Boeing, NextEra erroneously assumed that it was dealing with merely a complicated system, whereas it is actually dealing with a complex one.
2. There was no *independent assessment of the adequacy* of the LAR.
3. The NRC *delegated a high percentage of approvals and findings of* the LAR to NextEra.
4. The NRC should have had *a workforce review* and *engineer staffing level to ensure there is a sufficient number of experienced specialists to adequately perform certification and oversight duties, commensurate with the extent of work being performed by* NextEra.
5. The NRC should *have a system safety function that is independent from the design organization, with the authority to impartially assess* nuclear power plant safety.

6. The NRC and NextEra *should develop, validate, and implement analytical tools appropriate for the analysis of complex systems*.

35.2.1.2 Competence and Independence of LAR Preparation and Reviewers

Regretfully, the LAR was not prepared by persons who were competent in the complexity of ASR, nor was it peer-reviewed by an independent panel of experts. In addition, while the LAR was reviewed by two layers of government reviewers, none of them had the requisite competence to evaluate the LAR. More specifically:

- Neither NextEra nor the SGH and MPR consulting firms used engineers with significant and broad experience in ASR.
- While NextEra claimed to have support from the Brookhaven National Laboratory, the focus of the Brookhaven support was mainly on the [linear elastic!] analysis methodology, and the Brookhaven scientists did not have any ASR expertise [656, pg. 269, l. 9].
- The only external academic expert consulted by NextEra was Prof. Ellingwood, an eminent researcher. However, Dr. Ellingwood reviewed only the load amplification factor for ASR, Table [656, pg. 799, l. 14]. He was not retained to review the entire LAR or NextEra's overall solution strategy.
- The head internal reviewer at the NRC is a senior geotechnical engineer, with no expertise whatsoever in ASR. The closest link he has to expertise in concrete is that "he looks at the performance of concrete structures and vaults for housing low-level waste" [656, pg. 799, l. 14].
- Neither NextEra nor the NRC staff sought to apply the current state of knowledge regarding ASR to obtain independent review of their work [656, pg. 285, l. 18]
- The NRC staff did not even consult research that it had contracted for. When the NRC staff was asked if they have seen the report written by the first author under the NRC's grant [648][6], the NRC's reply was "No. We, we have only seen the, the summary report that's part of the exhibit here" [656, pg. 875, l. 1].
- The NRC stated that their regional office did get an independent review of the ASR, the ASR issue at Seabrook by a faculty at the University of Pittsburgh.

> [H]e helped the NRC staff to, to do our initial assessments of the safety of the ASR issue and its effect on structures. He accompanied us on, on a couple of inspections and also assisted the NRC in forming its confirmatory action letter which was an enforcement interaction where, where the licensee was required To do corrective actions. And, that was, that was with the help of, of Prof. [xxx] who is a professor of structural engineering and mechanics from the University of Pittsburgh, and also had expertise in, in ASR.
>
> NRC-ML19312B609 [656, p. 801, l. 19]

To the best of the authors' knowledge, the faculty mentioned has never undertaken any research on ASR, nor had he published any peer reviewed journal article on said topic at the time he was retained.

[6] Grant No. NRC-HQ-60-14-G-0010, [756] [755] [765] [770].

- While NextEra claimed to have support from the Brookhaven National Laboratory, the focus of the Brookhaven support was mainly on the [linear elastic!] analysis methodology, and the Brookhaven scientists did not have any ASR expertise [656, pg. 269, l. 9].
- As required by the Atomic Energy Act, NRC's independent watchdog, the Advisory Committee on Reactor Safeguard (ACRS) reviewed the LAR and also the NRC's review process. The ACRS found both were satisfactory. But none of the ACRS officials involved in these reviews was specifically familiar with ASR. Nor was any of these individuals a structural engineer [656, pg. 267, l. 21].
- A number of former NRC/DOE employees would have been eminently qualified to perform a peer review. Inexplicably, their technical advise was not solicited.

35.2.1.3 Code approach

As discussed above, NextEra took a strictly code-based approach to evaluating ASR at Seabrook. In this context, the licensee carries a burden to demonstrate that the structures will remain safe and operable. The structures must also continue to stay within their design and licensing bases. Despite the complexity and potential gravity of the problem at hand, NextEra (with the consent of the NRC) opted to simply demonstrate that the "design codes and original licensing basis remains intact" [656, pg 574 l. 17]. In fact, however, applying the code was not a simple matter, given that ASR was not (for obvious reasons) addressed by ACI 318-71 [10]. Thus, NextEra followed a very convoluted approach to propose modifications to the code that would –according to NextEra– address ASR. Hence, for NextEra looking beyond the codes was outside of the scope of the requirement for the structures to remain operable and to stay within the bounds of their licensing basis [656, pg. 574, l. 12].
It is most regretful that the NRC has endorsed this simplistic approach, because it lacks the level of sophistication needed to address the extremely complex problem of ASR in a CEB. It is the authors' understanding that the Atomic Energy Act gives the NRC full statutory authority to take all measures needed to protect public health and safety, including requiring a stricter and more sophisticated science-based approach to ASR (as opposed to the inadequately sophisticated engineering code). It is however unacceptable to wait for accidents to happen for a forensic investigation to finally perform proper nonlinear analyses.

35.2.1.4 Tests Based on Tunnel not CEB

All the tests at the FSEL were driven by considerations of the Bravo electrical tunnel, which was deemed to be the most critical component. Indeed, SGH states that: "The hydrostatic load is significantly larger ... than seismic load. It varies with structure" [656, pg. 1048, l. 25]. And the NRC stated that

> So, well, when we looked at the – when we were reviewing the LAR, we looked at what the licensee proposed and that was to use the same geometric configurations and dimensions and reinforcement of the worst area that we were aware of, which was the bravo electrical tunnel. So there was we agreed that that – that it would be reasonable to use that area to model considering that that was the worst ASR area.

NRC-ML19312B609 [656, pg. 1047, l. 14]

For this reason, no scaling was performed.

35.2.1.5 Scaling and Boundary Conditions

Ultimately, a test (FSEL) is a model of a prototype (Seabrook), and Buckingham's law [161] of similitude must be respected to the extent possible. In other words, all prototypes' dimensions must be scaled by the same factor λ in order to correctly model the prototype, Table 35.6

Quantity	Prototype	Model at λ–g
Length	1	$1/\lambda$
Time	1	$1/\lambda$
Mass	1	$1/\lambda^3$
Force	1	$1/\lambda^2$
Energy	1	$1/\lambda^3$
Fracture Energy	1	$1/\lambda$
Pressure	1	1
Stress	1	1
Strain	1	1
Density	1	1

Table 35.6: Some commonly used scale factors [778].

So, when asked whether models have been the results of a proper scaling analysis, NextEra's reply was

> In terms of a specific scaling analysis, we didn't perform one, but we did note that the containment enclosure building was different in that up to a certain height it's got triaxial reinforcement. The amount of ASR was much – was different and less severe than the bravo electrical tunnel. And so we didn't – we weren't presented with a large-scale test that was specific to the containment enclosure building, but we found it acceptable, what the licensee proposed because it modeled the worst location for ASR.

NRC-ML19312B609 [656, pg. 1047, l. 19]

Hence, the representativeness of the tests in properly modeling the CEB is open to legitimate question.

Another critical requirement for a model test, is that it be subjected to representative boundary conditions. Should the beam model the tunnel, then conceivably the beam was sufficiently long to assume that the simply supported boundary conditions were adequate.

However, should the beam pretend to be representative of the CEB, the boundary conditions are not correct. The CEB walls are subjected an axial compressive force resulting from weight of the container itself. This compressive force, is ignored in the tests. Likewise, shear would be caused by inertial forces distributed equally all along the model and point loads may not necessarily capture this effect.

At the very minimum, this should have been addressed, and convincing arguments made to ignore the misrepresentation of the boundary conditions.

35.2.1.6 Box Limits not Applicable for Applications to Seabrook Site

NextEra's establishment of and reliance on conceptual "box" limits to assess the gravity of ASR at the Seabrook site is one of the authors' most serious concern about the LAR.
The box concept is described at length, and with approval, in the NRC staff's hearing testimony on the ASR. The Staff's testimony established that staying with the "box" established by NextEra is the key measure agreed on by NextEra and the Staff for ensuring that ASR remains at safe levels. For instance, the NRC staff stated

> At a very high level, the staff determined that, one, since the test specimens were representative of structures at Seabrook, and two, since they showed no adverse structural impacts from ASR expansion and cracking in the concrete, there is reasonable assurance that the existing Seabrook structures can continue to carry the loads imposed upon them as provided by their licensing basis building codes, as long as the level of expansion in those structures is less than the level of expansion in the test specimens. In order to provide additional assurance for this finding, the staff conditioned it in part on NextEra performing assessments of expansion behavior at Seabrook to confirm that future in situ expansion is comparable to what was observed in the test specimens.
>
> Moreover, because of the uniqueness of the issue, the staff office with the responsibility for the review of the license amendment request, the Office of Nuclear Reactor Regulation, or NRR, had a separate staff office, the Office of Nuclear Regulatory Research, or Research, provide its opinion of NextEra's method. Research agreed with NRR that NextEra's method was reasonable.
>
> The staff also presented NextEra's method to the Advisory Committee on Reactor Safeguards, or ACRS, which is a body separate from the staff that is composed of highly qualified professionals. The ACRS found that NextEra's method was acceptable because, in part, it used highly representative test specimens and used a similar approach and produced similar results as a large body of ongoing ASR research. Based in part on these findings, the staff granted the license amendment request in March 2019.
>
> NRC-ML19312B609 [656, pg 253]

Similarly, the staff stated

> Right, the whole point, remember, of this entire project, is to know where we are, and stay inside that box that's defined by the testing program that shows that we're still inside that design basis.
>
> NRC-ML19312B609 [656, pg. 331]

> But what we're kind of seeing here, the reason we didn't, gets to the crux of what we've been talking about for the last probably hour is the fundamental approach. We're not trying to understand where we may go in the future and what the effects might be. The fundamental piece of trying to stay within the design basis and the law that governs it is to see where we are now and within a reasonable amount of growth – that's exactly what the LSTP was designed to do – to define that box where we understand the properties of the concrete, we understand what's happening, and then we make sure that we stay within that box.
>
> NRC-ML19312B609 [656, pg. 376]

In other words, as long as expansions measured at Seabrook are within the values measured in the FSEL (the "box"), then both NextEra and the NRC assume that everything is fine. This assumption is wrong on multiple levels.

First and foremost, one can not assume that a highly complex three dimensional 30+ years old structure (Seabrook), will responds structurally the same way as one-dimensional beam tested in ideal conditions: a) on-site, there is a complex stress redistribution mechanism which is not necessarily conservative; b) ASR is not uniformly occurring; c) there are gradients of ASR that can cause localized failures; and d) often failure occurs when and where least expected due to an oversight of secondary stresses. For reference, te authors' study of a CEB affected by ASR expansion of only 0.3% resulted in substantial cracking and damage (Figure 33.13).

Although the reported values of ASR expansion in the tests are redacted, one could easily infer that those values were significant from the measurements of [1.72-2.14]% expansion reported by Wald, Martinez, and Bayrak [859] in Figure 35.9. If the box limits are anything close to (or even half of) those values[7] they are dangerously high.

In our professional/scientific opinion, should the NRC allow for an ASR expansion to get anywhere close to this limit, there would be major structural damage (and not all of it visible on the surface) such as delamination. Again, to assume that a CEB will respond to ASR the same way as a beam in a laboratory is a very gross, simplistic, and hugely unconservative assumption. At the very least, NextEra should have performed proper finite element studies to support the validity (or limitations) of such an assumption.

Last, but not least, the authors find numerous reasons of concern regarding the beam tests relied upon to define the "box". Those are described below in §35.2.2.1.

35.2.2 License Amendment Request

35.2.2.1 Ferguson Structural Engineering Laboratory

35.2.2.1.1 In/out-of-plane Shear Transfer Mechanisms The FSEL beam tests modeled only the out-of-plane shear and not the in-plane shear(§35.1.3.1.1). This concern can be visualized by holding a can in one's hand and pushing in one direction. Along that direction the can must provide an out-of-plane shear resistance, but at 90 degrees, the can will be in in-plane shear mode. The latter mode was neither tested, Figure 35.11 nor was its role numerically investigated.

The fact that the ACI 318-71 code allows 10 times the square root of the compressive strength for in-plane shear, as opposed to only two times for out-of-plane, is irrelevant. In both cases, the relative loss in strength will be equal to the square root of the fraction of the loss (because the 2 and the 10 cancel out). For instance, if the original compressive strength is 100 (never mind the units), and due to ASR the compressive drops to 70, the loss in shear strength for both in-plane and out-of-plane will be equal to the square root of 70 divided by 100 (0.83).

[7] The authors reasonably infer that the work reported in Wald, Martinez, and Bayrak [859] and [861], is similar/identical to the work performed for MPR (which financial support is explicitly acknowledged.) most possibly on behalf of NextEra.

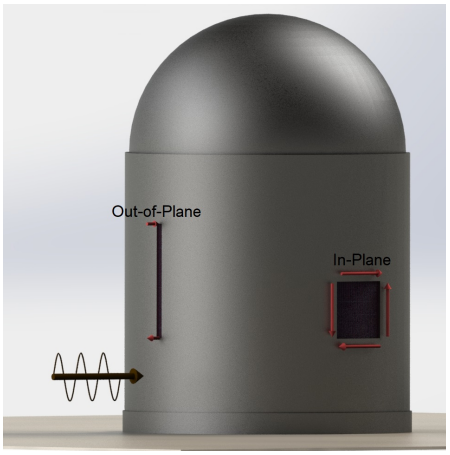

Fig. 35.11: in-plane and out-of-plane shear in a CEB

Furthermore, NextEra assumes that

> Cracked section properties do not affect the global seismic response of the CEB. This assumption is justified because the global response of the CEB to seismic motion primarily causes in-plane shear and overturning stresses; both are resisted by the membrane stiffnesses of the CEB wall that are not impacted by cracking.
>
> Simpson Gumpertz & Heger-ML16279A049 [794, pg 215]

This is clearly wrong, because the lateral load is equally resisted by in-plane and out-of-plane shear, Figure 35.11.

35.2.2.1.2 Concrete representativeness Ideally, the FSEL test beam concrete would be (nearly) identical to the concrete used at Seabrook (§35.1.3.1.2), i.e. the same aggregates, sand and cement. The FSEL used aggregates with physical properties (shape, hardness, strength, and size distribution) that were similar to the physical properties of Seabrook concrete (but not with the same mineralogical composition). However, the FSEL did not use identical sand. Instead it used a highly reactive sand in order to accelerate the development of ASR for purposes of conducting the test. It should be noted that usage of the so-called "jobe" sand to accelerate laboratory expansion is not uncommon if one is simply trying to induce expansion.
However, the problem is that the same laboratory mix design was used to establish the correlations for the CI and out-of-plane expansion, Figure 35.8(b). In this instance, having reactive concrete is not sufficient; there has to be a mineralogical similarity. Indeed:

- It is well established [707] that fine aggregates (sand) will yield a faster reaction (by virtue of their high volume to-surface ratio which facilitates diffusion) than coarse ones. However, the coarse aggregates will ultimately yield larger total

expansion than the expansion yielded by the sand. Hence, expansion testing on fine aggregates will under-estimate total expansion in the long run.
- Expansion is highly dependent on mineralogical types of aggregates. Some are so called early-expansion, others are late-expansion. Overlooking the geological nature of the aggregate and sand will fatally compromise the outcome of any investigation [749].

Additional related concerns are addressed in §35.2.2.2.3.1.
As a result, the key feature of ASR internal micro-cracking and surface manifestations of cracking may greatly differ depending on the mineralogy of the aggregates/sand/ used.

35.2.2.1.3 Beam Tests Tests were conducted on flexural beams designed to fail in shear (§35.1.3.1.3.1); yet the actual failure mode of the CEB due to ASR and seismic load is not determined. It is assumed to be in shear, but could also very well be in flexure for certain load combinations (Table 35.5). Indeed, Wang and Morikawa [867] performed tests on beams subjected to AAR for up to three years. Specifically designed to assess the impact of AAR on shear strength, a relatively low span to depth ratio of 5 was selected. As expected, failure load increased due to ASR, due to the well known prestressing effect of the reinforcement on the concrete swelling. However, what is noteworthy is that only the control specimen had the intended shear failure, and "all others failed through flexure".
Nevertheless, there are five major concerns in regard to the tests. Each will be addressed separately.

35.2.2.1.3.1 Splitting crack As noted above (§35.1.3.1.3.2), a splitting crack occurred in all specimens prior to testing. The cause of the crack is pretty straightforward. ASR expansion being "opportunistic", it redirected the expansion along the two restrained directions to the one which is un-reinforced, Figure 35.12(a).
This was too rapidly dismissed by NextEra as an "edge effect" (not a technical term), because there were no visible cracks when the specimen was cored. Visual examination does not provide a sufficient basis to dismiss the splitting crack, however, FSEL should have performed petrographic studies to determine whether there were microcracks (see below). Indeed as noted in §4.3.7.2.1 when inspecting for cracks, it is customary to assume the presence of a crack equal to the smallest detectable size. To better understand what may have happened, a nonlinear 3D fracture mechanics based finite element analysis [**chap:fracfembook**] of the tested beam was conducted (Figure 35.12(b)) by the authors. As the location of the splitting crack was sharply defined, the discrete joint element discussed in §15.3 was used.
Results are summarized below :

1. Because of unconstrained vertical expansion, indeed a crack formed in the portion of the beam that is not resisted by shear reinforcement (stirrups) as shown in Figure 35.12(c). This matches the crack observed in the LSTP, Figure 35.5.
2. At midspan, the computed crack profile is shown in Figure 35.12(d). It matches what has been reported by NextEra, that is the crack opening is largest on the

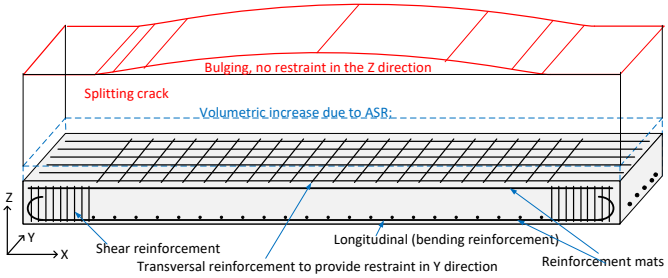

(a) Possible explanation for splitting cracks based on figures in [859]

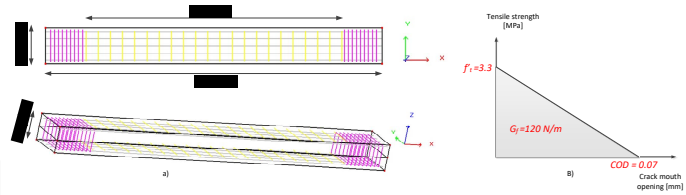

(b) Nonlinear fracture mechanics based finite element model adapted from [859]

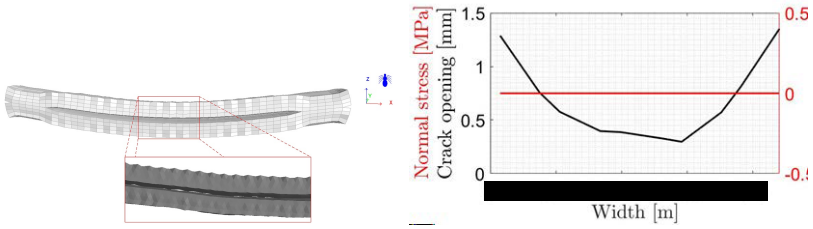

(c) Highly amplified deformation showing crack opening in between the stirrups

(d) Crack opening profile across the beam (along y axis)

Fig. 35.12: Finite element simulation of specimen splitting

edge. We estimated it to be 1.4 mm (this may be less than what was determined, but again in the absence of tests we had to estimate the fracture energy G_F).

3. The close-up showing an "oscillation" in the vertical displacements is due to the confinement provided by the transverse rebars (along the Y-axis). In other words, displacements are constrained by the bars, but in between, we have small spikes.
4. We also have the crack profile showing a minimum in the center (about 0.3 mm crack width). Again, this (to some extent) matches what NextEra has "dubbed" an inconsequential edge crack.
5. Note that whereas a 0.3 mm may not necessarily be visible by the naked eye, it is enough to inhibit transfer of tensile stresses per the model (§9.1.2).

It is not surprising that NextEra did not detect a crack when they examined the specimen visually, because the crack was too small for the naked eye.
Again, it should be emphasized that this analysis does not pretend to be quantitatively exact; however, it is most certainly qualitatively correct and based on sound, established, fracture mechanics models. Hence, we can safely assert that the observed splitting crack is far more serious than asserted by NextEra.
NextEra also asserts that delamination will not occur in the CEB. This statement is unfounded. Given the lack of reinforcement across the thickness of the CEB, a delamination crack (similar to Crystal River) is in the realm of possibilities.
The relevance of such an (unanticipated) crack, one which inhibits tensile stress transfer, can not be discarded. They simply were not anticipated during planning purposes, caught NextEra by surprise (though any basic understanding of ASR expansion would have anticipated them) and should disqualify test results. An biological analogy would be if a Petri dish had been contaminated by an external agent, thus rendering results questionable. Similarly, a basic tenant of experimental mechanics is to avoid any secondary source of uncertainty. Indeed, one can not discard the likelihood that the presence of the splitting crack has not affected the trajectory of the shear-flexural crack in Figure 35.5.
Most importantly, and contraily to NextEra's assessment, such a crack (delamination) may form inside the walls of Seabrook. Currently, it may not be detected with the naked eye, but with microscopic (i.e., petrographic) examination.

35.2.2.1.3.2 Chemical Prestressing Side Effects Chemical prestressing is not a panacea to solve ASR problems. While MPR states that "the beneficial effects of confinement are recognized in the structural engineering community" [636], the potentially adverse effects of chemical prestressing are also recognized in [243] (summarizing work conducted for the Texas Department of Transportation at the FSEL and which indicated that thirty cases of "fractured reinforcements" have been found in bridges and other structures).
The phenomenon is simply illustrated in Figure 35.13(a) based on the classical free body diagram of flexurally-cracked reinforced concrete beams [228].
Unfortunately, no strain gauges were installed to quantify the additional steel and compressive strains (and thus stresses). Hence, the effects of prestressing had to be numerically estimated by NextEra.

35.2.2.1.3.3 Fracturing of stirrups Another possible "side effect" of restrained expansion is that it may either yield or fracture the stirrups that provide both shear reinforcement as well as confinement for the concrete (thus increasing its strength) [500]. Such a failure did occur [600], Figure 35.13(b).
The reported rupture has triggered much research in Japan[8].

[8] Inoue et al. [462] states: "In recent years, it is reported in Japan that stirrups, as well as longitudinal steels, in T-shaped beams of bridge piers were ruptured at the bent corner or butt joints. In order to make clear the causes of this rupture, vigorous research works has been done after the finding of the rupture in existing reinforced concrete structures. Up to the present, it is recognized that this phenomenon occurred not only due to excessive ASR expansion but also under complex

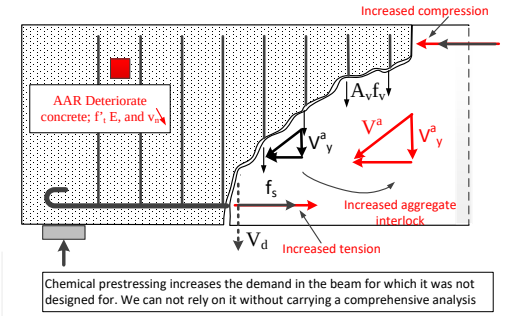

(a) Side effects to "chemical prestressing"



(b) Fractured reinforcement due to ASR [600]

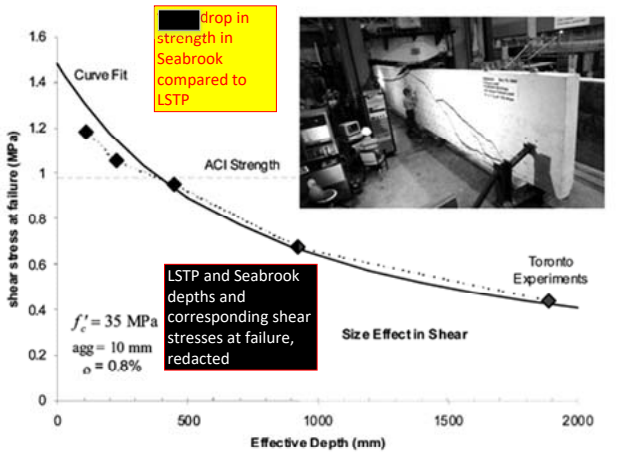

Fig. 1—Example of size effect in shear for reinforced concrete members without stirrups.[1]

(c) Size Effect Bentz [117]

Fig. 35.13: Issues about shear tests

35.2.2.1.3.4 Size Effect Simply put, size effect is the reduction in strength with increase in size (§9.1.6). This has an impact in the reported study because the beam itself was about [[redacted value]] scale [[redacted value]] depth whereas the wall of a CEB and the containment structure are 30 and 48 inches respectively. This is not unusual in component testing. However, given the brittle nature of shear failure

---

combinations of several factors, such as mechanical properties and surface shape of reinforcing bars, bending or welding methods of reinforcing bars, corrosive atmospheres and so on."

and associated size effect, the shear strength in the CEB will be lower than the one from the LSTP. This very well-known phenomenon of size effect, first highlighted by Bažant [93] [92] (and later generalized by the author [758]) was experimentally validated for large size shear unreinforced beams by Bentz [117], Figure 35.13(c).
Size effect is relevant to NextEra's reliance on the B tunnel (allegedly prototype) to *model* the ASR in the CEB. Indeed, the beam may have been a proper model for the tunnel, however, it was not an appropriate model for the more critical CEB prototype.
Hence, failure to account for the size effect may lead to an overestimation of the shear carrying capacity.

35.2.2.1.3.5 Creep was addressed in Chapter 5, or more precisely its corollary relaxation will reduce in time the beneficial effect of chemical prestressing (§5.6.2). Indeed estimating prestress loss due to creep is the dedicated subject of an ACI publication [15] and it is unequivocally clear that prestressing will diminish with time. Likewise chemical prestressing will decrease with time.
The phenomenon of creep or relaxation was completely ignored by NextEra. As a result, the LAR fails to account for the fact that the full beneficial effect of chemical prestressing is only temporary, and will be reduced with time.
Had the tests at the FSEL lasted longer (which could have been prohibitively expensive), the full impact of creep would have been assessed. But NextEra had other feasible means for assessing creep. A simple numerical calculation could have provided a reasonable estimate for that nefarious effect.

35.2.2.2 Building Deformation Aging Management

35.2.2.2.1 Crack Index Determination of the CI (§35.1.3.2.1) is NextEra's "first line of defense" in detecting ASR induced expansion. But *in-fine*, CI readings are only a small fraction of the total volumetric expansion, Figure 35.9. Thus they are extremely misleading.
NextEra's reliance on CI also fails to account for the critical role played by relative humidity (RH) in the expansion of concrete. As mentioned previously, a RH less than 80% will not result in any expansion [165] [804]. This has very strong implication for the reliability of surface measurements of cracks to ascertain the presence/extension of ASR. In other words, due to shrinkage and external exposure, the surface of the wall most certainly has a relative humidity less than 80% . As such, one would only capture severe cracks emanating from the center and reaching the surface. Those are what we will refer to as ASR cracks, not to be confused with internal structural cracks that we will address separately. The result is (and this will be again discussed in the next question) that the CI will not be reliable.
However, it is important to observe that, unlike the consistent temperature and humidity conditions created for the beams in the LSTP, neither the relative humidity nor the temperature is constant across the 30-48" containment structure walls. This is schematically illustrated by Figure 35.14(a).
Table 35.7 highlights the different environmental conditions: "The internal humidity

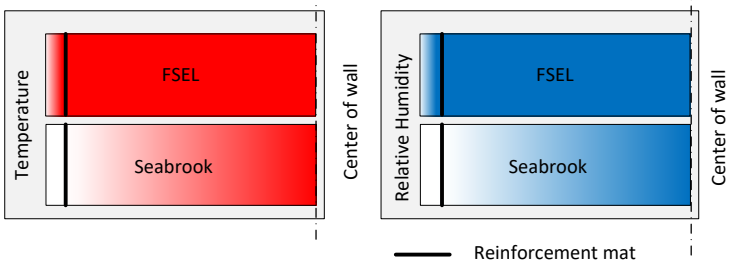

(a) Temperature and elative humidity distributions across the wall

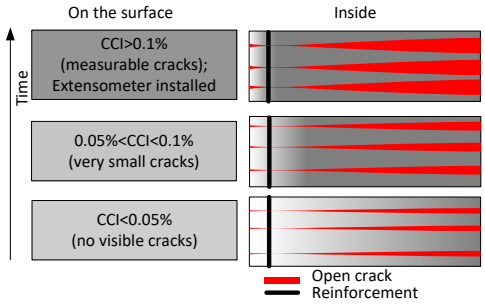

(b) Impact of reinforcement mat on the "pinching" of ASR cracks

Fig. 35.14: Impacts of temperature, relative humidity, and reinforcement on limited surface CI measurements

of the concrete and the atmospheric conditions in the ECF were sufficient to drive progression of ASR uniformly throughout the test specimens"[608].
Hence, the ideal conditions in the LSTP which were intended to validate the CI measurements' reliability for Seabrook are not representative of *in-situ* conditions at Seabrook.
This has strong negative implications for NextEra's ability to capture internal cracks by surface measurements.
The low RH on the surface of the wall, compounded with the proximity of the large mat reinforcement (presumably number 11 bars [861]) clearly inhibit the formation of surface material ASR cracks (in other words the reinforcement will "pinch" the crack and the opening on the surface will be much smaller than on the inside). This is further illustrated in Figure 35.14(b) (where the crack opening is in red).
Finally, it should be noted that the applicability of the crack index method has been the subject of internal discussion at the NRC. In one NRC document, it is indeed stated that

> ... using the method of combined crack indexing alone to characterize the extent of ASR damage to-date and monitor the progression is not adequate, and that additional measures

Table 35.7: Comparison between FSEL test conditions and Seabrook Station

FSEL	Seabrook
Temperature kept high to simulate ASR expansion. Given the dimensions of the beam, and the internal heat of hydration, one can reasonably state that the temperature was uniform (no gradient) across the beam.	There is always a temperature gradient across the 30-48" CEB, the containment structure will have a constant (higher) temperature. wall.
The relative humidity was kept high in the FSEL (by covering the specimen with burlap, Figure 35.4(e). Because of the continuously wetted burlap and the high water to cement ratio, it is safe to state that in the FSEL the relative humidity was constant across the specimen. ∗	The surface of the CEB wall has dried, and is not prone to expansion whereas the expansion will take place inside the wall where the relative humidity is much higher. The expansion of the containment structure is the one likely to be uniform.
The FHWA report stipulates that for CI measurements, the "most severely cracked" components "generally correspond to those exposed to moisture and severe environmental conditions, as well as those where ASR should normally have developed to the largest extent." [311, pg 12].	The surface of the CEB is certainly no longer moist, it has dried. The surface of the containment structures is likely to be within a higher relative humidity

> should be taken to provide a baseline understanding of the ASR affect on structures before crack indexing measurements can be correlated to anticipated structural performance. Surface cracking may not be indicative of the conditions of the concrete through the full section of the concrete member, and crack indexing measurements may not consistently indicate the level of ASR severity from one structure to another.
>
> [162]

Those were very correct statements, however they were subsequently deemed

> not to be an official NRC position on the topic, but rather was prepared by an individual staff member to facilitate internal technical discussion and inform staff review of an issue. The NRC's current position on the role of visual inspections in identifying ASR is set forth in this document. The referenced position paper does not state that visual examination is insufficient to identify indications of ASR. However, it does note that surface cracking or crack mapping, alone, may not indicate the severity of ASR degradation and is not adequate to determine structural effects of ASR. The NRC agrees that surface crack mapping alone is not adequate to monitor ASR progression and to address its structural effects. In addition, petrographic examination provides very limited information to evaluate the structural effects of ASR.
>
> Federal Register [291]

In light of the above, we continue to insist that the expansion inside Seabrook CEB is almost certain to be much higher than what can be recorded by CI.

35.2.2.2.2 out-of-plane Expansion As shown in Figure 35.9 the bulk of the volumetric strain is along the unreinforced out-of-plane expansion. This value is to be measured when CI exceed certain threshold values (Figure 35.2, §35.1.3.2.2).
The method has been calibrated with measurements from the FSEL (Figure 35.8(b)). Yet this method is most unreliable for the following reasons:

- As described above, the difference in mineralogy will result in different expansion characteristics (due to the microcracking).
- Values of the 28 days compressive strength measured in mid 1970's are likely to be: relatively few, not accurate enough to be applied with Equation 35.2, Figure 35.16(b) (20% strength increase will result in $\sim$ 14% increase in E) .
- Concrete gains in strength the first two years (about 20%) [228], Figure 35.15 ignoring this will result in an underestimate of the ASR.

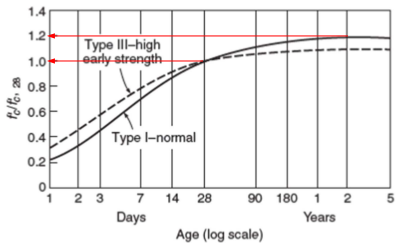

Fig. 35.15: Early age compressive strength increase in concrete [228]

- A most critical component of the process is the determination of the ASR induced deterioration. This hinges first on Eq. 35.2, but also on data collected at the FSEL, resulting in a highly approximate phenomenological model[9] that estimates expansion in terms of normalized elastic modulus, Figure 35.8(b). As shown in Figure 35.16(a) two experimental errors are compounded:
  - Horizontal axis: the normalized elastic modulus is most approximate. Let us not forget that it hinges on determining the elastic modulus *during construction* based on cylinder tests collected for quality assurance. Again two sources of errors here:
    - The volume of concrete in a CEB is very large, and though hundreds of cores may have been tested *in-situ*, the concerns are that the testing method (back then) were neither reliable, nor sufficient. Indeed, it is very likely that

[9] A phenomenological model is one "that describes the empirical relationship of phenomena to each other, in a way which is consistent with fundamental theory, but is not directly derived from theory. In other words, a phenomenological model is not derived from first principles. A phenomenological model foregoes any attempt to explain why the variables interact the way they do, and simply attempts to describe the relationship, with the assumption that the relationship extends past the measured values." (Wikipedia).

the measurement density (number of tests per cubic yard) will be too low to accommodate the one needed to capture the elastic modulus at various locations 30+ years later. As such, it is very possible that ASR will be taking place in a location not tested for compressive strength.

- Equation 35.2 is known to be very approximate by itself, and is only a substitute for the direct measurement of the concrete elastic modulus per ASTM C469 [61].

– Vertical axis: expansion is determined in the laboratory under ideal conditions, with concrete whose representativeness *vis à a vis* of the one at Seabrook given that "mineralogically" speaking they are different (§35.2.2.1.2). Even if the mineralogy was indeed correct, any time precise and critical measurements are to be taken, margin of errors must be reported.

With so many potential errors, ultimately errors bars are not provided[10] [656, pg 473, l. 18]. This is particularly problematic, as one can not develop a heuristic model, based on laboratory testing without also providing an indication of the experimental errors. [448].

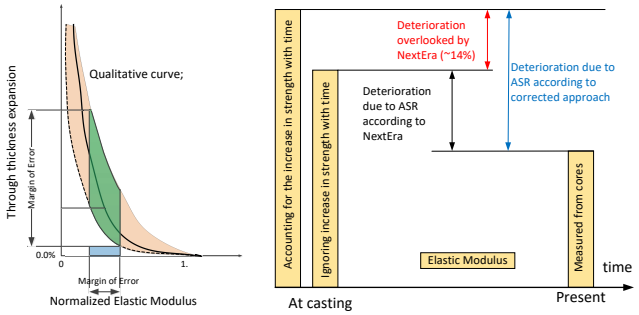

(a) Procedural margins of error

(b) Impact of early strength gain on out-of-plane expansion determination

Fig. 35.16: Concerns about out-of-plane expansion measurements

The authors would argue that a far more reliable approach to the determination of the past expansion is the one presented in §11.6 (Figure 11.13).

35.2.2.2.3 Unaddressed Concerns

35.2.2.2.3.1 Internal Cracks There is ample evidence that ASR will cause internal micro-cracking (Figure 9.18(c)) [463]. Furthermore, sand and gravel will cause

[10] Such omission, would only be permitted when the equation has been vetted/verified/validated by multiple researchers before they are typically enshrined in a code (such as Eq. 35.2).

drastically different internal crack patterns, Figures 35.17(a) and 35.17(b) [311]. This is further evidenced by Figures 35.17(c) and 35.17(d) which show images of concrete with reactive sand (cracks run thorough the paste, impregnated and polished sample in UV light) and an image of reactive gravel (diameter 5 cm, impregnated and polished sample for SEM) courtesy of Leemann [530].

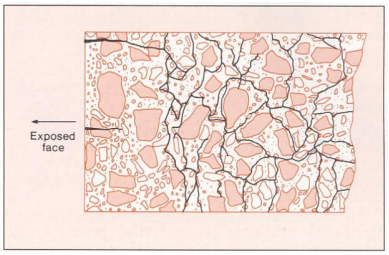

(a) Internal crack pattern which can be caused by ASR: reactive silica in the sand fraction [311]

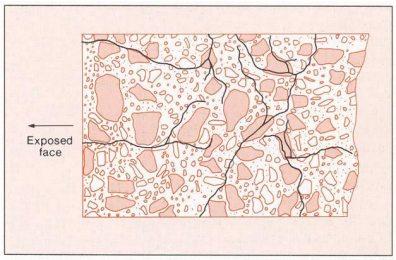

(b) Internal crack pattern which can be caused by ASR: reactive silica in the coarse aggregate [311]

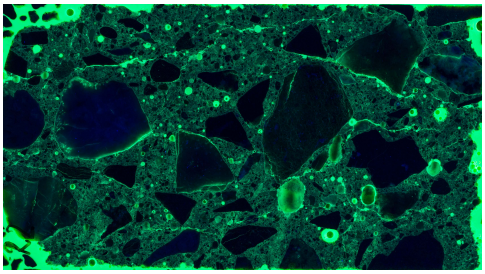

(c) Reactive Sand [530]

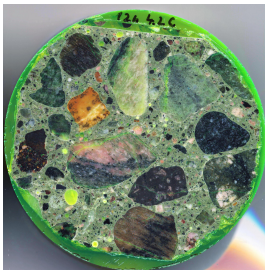

(d) Reactive Aggregate [530]

Fig. 35.17: Crack patterns caused by reactive sand and aggregates

NextEra has repeatedly indicated that no cracks were observed when cores were extracted

> [i]n the prior session regarding the taking of the core. Not only do we take the cores and do the compression and modulus testing. We actually do, a visual examination of those cores as they're taken. We validate that there's no – that the core is coming out solid. That it's not crumbling within its – when it's removed from its confinement. We're validating there's no midline cracks. We actually inspect the bore hole and verify there's no voids. No cracking. No deterioration of the aggregate.
>
> NRC-ML19312B609 [656, pg 532]

Yet, throughout the documents, indications are micro-cracks are present,

> Micro-cracking due to ASR is generated through forces applied by the expanding aggregate particles and/or swelling of the alkali silica gel within and around the boundaries of reacting aggregate particles.
>
> NextEra-ML16216A240 [633]

> It was determined that ASR caused this additional aging effect through cumulative micro-cracking in ASR-affected structures. In addition, there was discrete large cracks and the effects were not anticipated. They were identified by the NRC as a different consequence of ASR.
>
> NRC-ML19312B609 [656, pg 204]

The key takeaway is that NextEra has conducted *visual examination* to detect cracking, with the expectation that cracking may mean crumbling. This will be a false-negative reading of the situation because NextEra is looking for macro-cracks (visible with the naked eye), when it should be scrutinizing all the cores through petrographic analysis for unusual micro-cracking, and understanding that those micro-cracks are ominous and are likely to grow, coalesce and ultimately delaminate the CEB.

35.2.2.2.3.2 Potential Delamination The internal cracks, previously addressed, will

Propagate as a result of increased ASR with time, and as a result of creep fracture discussed in §9.2.3.

Coalesce as the crack density is at first high, and some of those micro-cracks will eventually coalesce (as discussed in §9.2.4).

Again, ASR induced delamination will occur when swelling is constrained in two directions (in-plane) and unconstrained in the third (out-of-plane). Indeed, given all the swelling potential being now channeled along the weak direction, this could be problematic.

With reference to Figure 35.18(a) a segment of the wall is subjected to compressive stresses, and is reinforced only in the periphery vertically and radially. Micro-cracks are likely to coalesce in the center where the temperature and the relative humidity are highest, and this would be an in-plane crack. Due to ASR, expansion will be as indicated.

When the whole wall is considered, Figure 35.18(b), we consider four stages corresponding to different times. At first, expansion affects the center zone, and ASR would be localized in the middle where temperature and relative humidity are high. With time, the zone affected by ASR will expand but cracks are unlikely to "daylight" in significant way as a) the surface is likely to have dried over time; and b) and the reinforcement will pinch the crack. As such, the cracks will remain confined to the center, and will eventually fully coalesce into a major internal in-plane crack.

One cannot rely on visual inspection to determine whether there is internal cracking. Such a crude approach could be valid only once there has been a major crack, and this may be too late.

Such a delamination did occur in the FSEL, Figure 35.5 (§35.2.2.1.3.1), and at Seabrook, there is a very strong likelihood that micro-cracks already exist.

Indeed, such cracks have been reported in topologically similar structures (retaining walls with no shear reinforcement) in Switzerland 35.18.

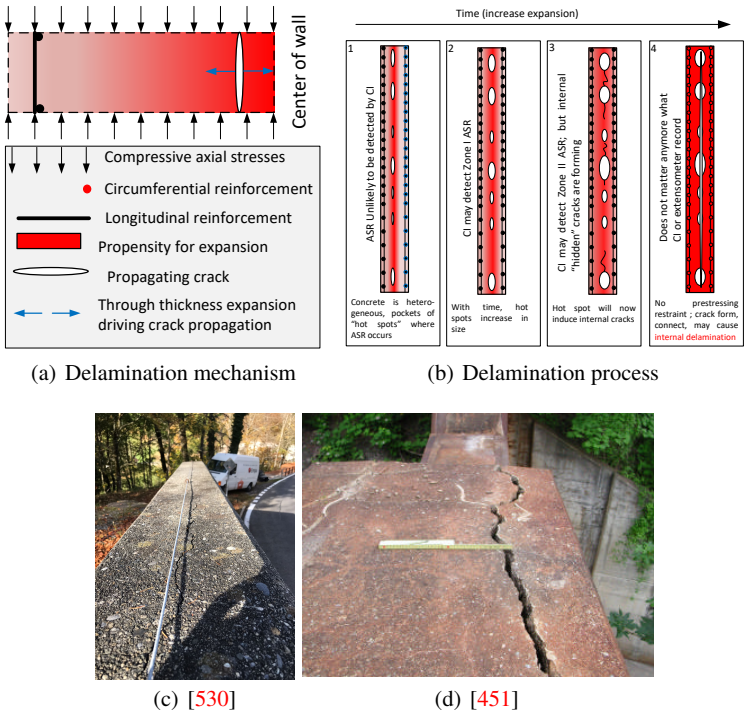

(a) Delamination mechanism (b) Delamination process

(c) [530] (d) [451]

Fig. 35.18: Causes and examples of delamination in walls without out-of-plane reinforcement

35.2.2.2.3.3 Uncertainty in Future Expansion; Threshold Factors As mentioned in §35.1.3.3.3, Simpson Gumpertz & Heger-ML16279A049 [794] defined a threshold factor K_{th} of 20% (to the CEB only) to account for "additional ASR load that may occur in the future".

This is symptomatic of many aspects of the LAR: when confronted with what could be determined (experimentally or numerically), NextEra simply considers it an unknown and defines (yet another) "safety factor". The problem is that we do not know how reliable is that safety factor, i.e. could it be too low?

In this particular instance, it is reasonable to ask on which basis was the 20% value selected? And why not 10% or 40%? Short of a study similar to that described in §11.6, one can not assume that 20% would be appropriate.

35.2.2.2.3.4 "Elastic" Margin for Future Expansion NextEra also made allowances for "margin for future expansion" [608]. More specifically, based on "expansion rate", NextEra acknowledged the potential for future expansion to exceed the anticipated limits. In that event, NextEra plans to consider relaxation of the limits

> NextEra's review should include consideration of the uncertainty associated with extensometer readings and with in-plane expansion measurements. Assessments of "expansion rate" for the purpose of projecting future expansion should rely on trends comprised of multiple data points. If such projections indicate that the limits may be exceeded prior to the next periodic check, NextEra should include consideration of the uncertainty associated with extensometer readings and with in-plane expansion measurements. if such projections indicate that the limits may be exceeded prior to the next periodic check, then NextEra should further investigate the location(s) in question or develop contingency plans for extending the expansion limit (e.g., supplemental testing).
>
> MPR-ML19170A332 [608]

By setting such an elastic "margin for future expansion" raises a significant concern about the scientific credibility of its approach. In addition, the "moving target" paradigm for establishing regulatory compliance raises questions about the rigor of NextEra's program for protecting public health and safety. It is hard to understand the rationale (if not the ethics) of NextEra's approach to regulatory compliance, i.e. to first establish allowable limits for code compliance, to then assessing the code compliance of a structure, and finally – should the expansion rate be found to exceed allowable limits–, to then *extend those limits*. The authors are not aware of any organization that would allow for such an elastic interpretation of a safety code.

35.2.2.3 Building Deformation Assessment

35.2.2.3.1 Screening Evaluation was addressed in §35.1.3.3.3. A finite element analysis would result in Gauss point stresses at the Gauss points (§13.3.3), and indeed the most natural approach would be to perform a stress-based failure assessment based on failure criterion (§3). However, the approach taken by NextEra is to determine equivalent forces (axial and moments) from nodal values (themselves not ideal for evaluation), and then perform a force-based failure assessment based on ACI code interaction diagrams.

The authors recognize that this is not an uncommon approach for some structural components, such as beams and columns subjected to loads covered by the ACI code. However, in the case of ASR we are dealing with an exceedingly complex and challenging problem, one with which the NRC has been confronted for the first time, and one where an erroneous safety assessment could lead to a nonconservative response and perhaps devastating consequences. The authors see adisturbing dichotomy between the relatively simplistic engineering approach taken by NextEra and the much more rigorous "standards" with which the authors are accustomed by virtue of their (academic/researcher) background.

NextEra's approach reduces the CEB to a series of parallel columns with no interaction among them. Furthermore, the model relies heavily on the conclusion of the FSEL beam tests (showing an increase in shear strength and flexural stiffness). But

the limitation of these tests have been previously highlighted §35.2.2.1.3.5. Furthermore, NextEra's approach allows the analysis to ignore any material deterioration in the CEB [794, pg 18].
NextEra claims that

> Evaluating a structure on an element-by-element basis is considered a conservative approach because it does not allow for concentrations of high demands to be distributed locally within the structure. Factored demand exceeding capacity in the element-by-element evaluation does not necessarily indicate a structural deficiency.
>
> [794, pg 53]

This assertion is purely speculative however, and no supporting argument is made.

35.2.2.3.2 Factored Self-Straining Loads The so-called Load Resistance Factor Design (LRFD), used in [10] hinges on the concept of Reliability Index (§18.2.1 Figure 18.8) and was addressed in the seminal paper of [267]. Simply put, load will be multiplied by a factor λ [52] and we reduce the ultimate capacity by Φ.

$$\Phi C_n \geq \Sigma \lambda_i D_i \tag{35.3}$$

where C_n and D are the nominal capacity and demands (or nominal resistance and load), and limit states are generally determined from the plastic capacity *without* a nonlinear analysis. LRFD will assign α and Φ such that the probability of failure does not exceed a certain value. In practical terms this implies seeking to have a Reliability Index β (Equation 18.13) such that $\beta >\sim 3.5$. The Reliability Index is a "universal" indicator on the adequacy of a structure, and can be used as a metric to 1) assess the health of a structure, and 2) compare different structures targeted for possible remediation. For instance in [9] Φ is 0.9 in flexure and 0.7 in shear; likewise α for dead load and live loads are 1.4 and 1.7 respectively. The difference in the numerical value of the factors reflects different consequences of failure (shear failure being sudden and brittle, while flexural failure is ductile), as well as the uncertainly associated with the load (larger uncertainties are associated with the live load than with the dead load).
Irrespective of the code, load factors are developed following statistical analysis of numerous sources, .e. as many sources as possible

> The sources for statistics and distributions for individual loads are primarily the load subcommittees within ANSI Committee A58 that have expertise in and responsibility for the loads in the current version and projected revisions of the A58 Standard. Similarly, data on resistance of structural members and components is obtained from the numerous research reports and papers published by individual researchers, industrial groups and trade associations.
>
> Ellingwood et al. [267]

Now, for the LAR, the challenge was to develop load factors for ASR (Sa or λ_{AAR}), from a very limited data set (i.e. sufficient reliable, trustworthy experiments). This was for all practical purposes an impossible task, and thus

> The load factors applied to ASR loads (Sa) are developed to yield reliability index values similar to load factors specified in ACI 318-71 (Reference 17). The ASR load factors account for the uncertainty in ASR expansion by considering the variability in crack index measurements from all ASR monitoring grids in Seabrook Station structures.
>
> NextEra-ML16216A240 [634]

Thus, the load amplification factors are based on the crack index measurements at Seabrook. But those are very poor indicators of the ASR expansion (§35.2.2.2.1). Thus, while NextEra's procedure is most certainly correct, given that it was reviewed by a highly respected researcher (indeed, the only external faculty/expert consulted) the reliability of the raw data used to develop the load amplification factors is very questionable.
Furthermore, as shown in Fig. 35.9 the in-plane strain measurements, upon which the load factors are built, are negligibly small compared to the out-of-plane strain. Hence those amplifications factors can-not be representative.
Yet, despite the large margins of errors associated with λ_{AAR}, this factor is 1.45. In comparison, the very well-known factor for dead load is 1.4 and the highly uncertain factor for live load is 1.7, Table 35.5.
Hence, whereas we do not dispute the procedure to determine the (relatively low) amplification factors associated with ASR, we believe that they are based on incomplete, and erroneous data, and are consequently both unrepresentative and unconservative.

35.2.2.3.3 Finite Element modeling

35.2.2.3.3.1 Lack of Verification and Validation The very first concern is: How reliable is the finite element code used by NextEra in capturing ASR? And the corollary concern: Have those capabilities been verified and validated? The importance of these preliminary tasks was addressed in §12.2.5. Indeed, verification is needed to [806]

- Reduce risk of high-consequence code errors;
- Reduce development and maintenance costs by finding code implementation errors sooner;
- Quantify numerical errors as part of validation and predictions;
- Reduce numerical errors through mesh adaptivity; and
- Assist the NRC licensing process by providing application-driven evidence of code and solution quality.

Regulations [726, Appendix K Part 50] explicitly defines acceptable and required features of the Emergency Core Cooling Systems evaluation models as described in §50.46, including:

- Code documentation;
- Spatial and temporal convergence studies;
- Code validation;
- Sensitivity Studies; and

- Uncertainty Quantification.

One could argue that the same requirements should be applicable to ASR (especially when it is the very first time that it is addressed by the NRC).
Some software quality assurances procedures for the NRC are already in place and available to licensees like NextEra

> Software quality assurance (SQA) is the planned and systematic actions to provide confidence that the software product meets established technical requirements. Quality assurance procedures ensure that software correctly performs all intended functions and does not perform any unintended function. SQA activities can be categorized as follows:
>
> 1. documentation of the software or software modules as they are developed,
> 2. verification and validation activities and their documentation,
> 3. nonconformance (error) reporting and corrective actions and their documentation,
> 4. acceptance testing and installation of the software and upgrading of code manuals,
> 5. configuration management, and
> 6. quality assessment and improvement.
>
> NUREG-1737 [660]

It is thus puzzling that the software used for the ASR analysis was not subjected to any scrutiny. Guidelines for ASR finite element code validation are given in [749, chapter 21].

35.2.2.3.3.2 Shell Elements "The CEB walls and dome concrete consist of four-node shell elements ... modeled using centerline geometry" [794, pg 32]. The shell elements used in the finite element study (`SHELL181` in ANSYS Release 15) would have been a reasonable *approximation* had there not been a need to capture the through-the-thickness impact of factors affecting ASR expansion. Each shell element is a four-noded element with six degrees of freedom at each node: translations/rotations in the x, y, and z directions. However, a shell element can not capture the through thickness expansion which is lower on the surfaces and higher in the center (different RH). Given the nature of the problem, one would have thought that solid 3D elements would be used for a more accurate modeling. On the other hand, if NextEra insisted on using shell elements, then a minimum of 2-4 elements would have to be used as *overlayed* elements, Figure 35.19. Yet a thorough search in all available documents failed to show that any overlayed elements were used [656, pg 953]. .

35.2.2.3.3.3 Nonlinear Analysis About twenty years ago, the drafters of the ASME code for concrete reactor vessels and containments wrote

> In recent years, detailed two- and three-dimensional finite element modeling of these discontinuity regions to include the effects of cracking and nonlinear concrete behavior have significantly reduced the uncertainty of structural response in these regions.
>
> It has been said that in the late 1960s it took two days to design a containment and two weeks to analyze it before the release of the design for construction. Today it would still take

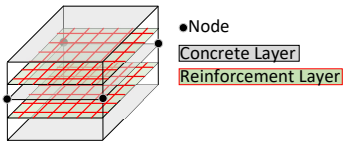

Fig. 35.19: Example of overlayed four noded shell element

> about two days to design a containment but about two years to analyze it. This is particularly interesting, for the actual amounts of concrete and deformed-bar or prestressing reinforcing steel have changed little in location and quantity over the past 35 years.
>
> Ashar et al. [53]

The need for nonlinear analysis is even more acute for Seabrook where *additional* nonlinearity is caused by the time dependent (thus incremental) swelling with accompanying cracking, degradation of the concrete mechanical properties (tensile, shear and compressive strength along with elastic modulus), possible yielding of the steel, stress redistribution. This non linearity has been recognized in the analysis of Gentilly (§32.1) and all ASR analyses reported in this book.

Another concern is the idiosyncrasy embedded in ACI codes: determine capacity from a plastic analysis, and demand from *amplified* loads (Equation 35.3) with a linear elastic analysis. Whereas this may be acceptable for well understood structures (such as buildings) with adequate reliability indexes (β Equation 18.13), it is not necessarily correct for a CEB.

Finally, ACI-318 does not concern itself solely with strength (factored load), but also serviceability (service load). This results in code requirements for minimum crack width. In the context of the CEB analysis, capturing the impact of cracks on possible gas leakage (in the absence of liners and notwithstanding the presence of the two containment walls, Figure 35.1(b)) is critical. A linear elastic analysis will underestimate cracking, Figure 14.1.

Guidelines have indeed been written for the nonlinear analysis of nuclear structures (reviewed in Chapter 31), Hessheimer, M.F. and Dameron, R.A. [415][275] and most recently [756].

35.2.2.3.3.4 Demand and Capacity NextEra's safety assessment determines demand from a linear elastic analysis, but capacity is determined at either the element or section level. This is much different from the common finite element procedure of first determining the computed stresses at the Gauss Points (§13.3.3), and then applying a failure criterion to assess localized failure (§3).

NextEra's approach may very well be a commonly-followed procedure for the linear elastic analysis of nuclear structures, but can not be defended when the ASR itself is inherently so nonlinear, and most importantly when miscalculations may be as consequential as they would be for a nuclear structure compromised by ASR..

35.2.2.3.3.5 ASR Model None of the minimum requirements for ASR modeling addressed in 14.8 have been considered. In addition the reported finite element modeling of ASR suffers from many flaws.
Most glaring, is the modeling of ASR as an isotropic thermal load. Indeed, a compressive stress greater than about 8 MPa will either limit or entirely prevent expansion in the corresponding direction [410]. Thus, under complex triaxial state of stress, expansion will redirect in the other directions (thus inducing an anisotropic expansion) [610] [537], Fig. 35.20. NextEra's isotropic model of ASR at Seabrook would assign only one-third of that expansion to the out-of-plane direction [772]. This is clearly

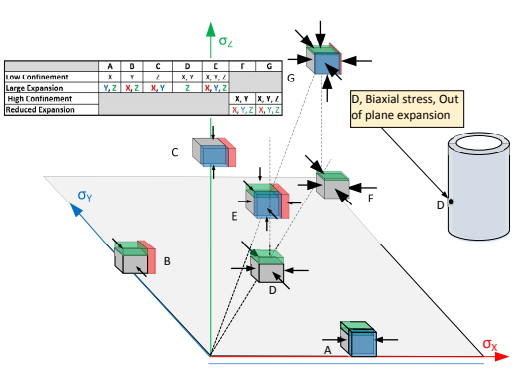

Fig. 35.20: Stress induced anisotropy during volumetric ASR expansion

unconservative, because it is anticipated (lack of radial confinement) and verified (Fig. 35.9) that by far, most of the expansion occurs radially, i.e. out-of-plane.
In addition, such a thermal equivalent load does not account for the relative humidity or temperature gradients across the CEB wall. These gradients may be sharp, i.e. far more critical than the absolute ones.
NextEra has attempted to avoid sharp gradients in the ASR expansion by "smoothing" its distribution across zones of different measured expansion. But that is not a realistic or conservative approach. In reality, there is potentially a significant gradient of expansion across the thickness that should be modeled (Figure 35.14(a)).
Finally, it is well established that ASR will reduce the tensile strength and the elastic modulus of concrete [311] by as much as 60%. In addition, there is a recent evidence [282] that compressive strength is reduced also by ASR, thus contradicting the long-held assumption that compressive strength is not affected by ASR. None of these types of degradation was modeled by NextEra, based on the justification that ASR was found in the FSEL to increase the shear strength and flexural stiffness as a result of "chemical prestressing". This argumentation was partially refuted in §35.2.2.1.3.

35.2.2.3.3.6 ASR Demand NextEra determined the ASR load as follows

> Alkali-silica reaction (ASR) demands are selected based on extensive field measurements of strain on the CEB and are increased by a load factor to account for uncertainty in the demands and a threshold factor to account for limited future ASR expansion.
>
> The strains due to ASR expansion simulated by the finite element model (FEM) reasonably approximate crack index measurements.
>
> [794, pg 14-15]

Field measurement of both the CI and the out-of-plane ASR strains are prone to much criticism (§35.2.2.2.3.1 and 35.2.2.2.3.4). (The authors note, however, that consideration of out-of-plane ASR strains is unlikely to be captured by the use of a single shell element). Hence, they may not provide an accurate picture for purposes of assessing the structural safety of the CEB.
Furthermore, this procedure is akin to a glorified "curve fitting". And these field measurement are not necessary, given that it is indeed expected that the finite element analysis would be able to capture the *essential* boundary conditions (§1.4.4.4), otherwise a wrong FEA program is used. What is lost on NextEra, is that "capturing" the response of few selected points (where the ASR expansion is imposed) does not make the analysis correct. This is illustrated by Figure 35.21 where one is able to fit a curve through a few data points. While this is an easy task, there is a near certainty that the model (curve in this case) will give erroneous values for the intermediary points.

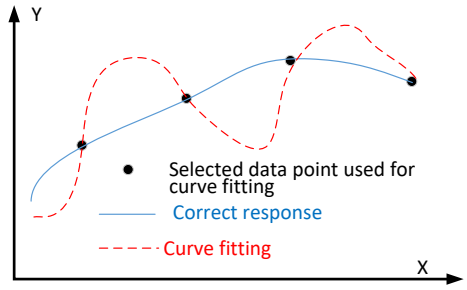

Fig. 35.21: Problems arising from fitting $y = f(x)$ through interpolation

35.2.2.3.3.7 Modeling chemical prestressing is addressed by NextEra as follows

> ASR expansion is simulated by applying a thermal expansion to the elements representing the CEB concrete. Steel reinforcement membrane elements are included in the model and are given thickness based on the total area of reinforcement provided. The expansion of the concrete creates tension in the steel membrane elements, which also causes a corresponding compression force in the concrete elements.

- In the absence of external restraint, the steel tensile force due to ASR and the concrete compressive force due to ASR will sum to zero. However, external boundary conditions, applied loading, and restraint from other portions of the structure can restrict the concrete from expansion and cause a net force or moment to be developed.
- The steel membrane elements are only included in the model when applying ASR expansion of the CEB wall and concrete swelling.

[794, pg 41]

Thus, steel is modeled only to capture the negative impact of the chemical prestressing (Figure 35.13(a)). However, this approach is not only convoluted, but also unconservative and erroneous. Chemical prestressing is a deleterious additional parasitic stress added to the pre-existing stress due to other loads. The combined stresses (reportedly not computed) could possibly result in the yielding (if not fracturing) of the reinforcement.

35.2.2.3.3.8 Static Soil Structure Interaction Generally, in non-ASR related engineering analyses, one would not have to worry about the static soil structure interaction. In the presence of a swelling concrete, however, there may be unanticipated and large deformation that could cause separation of the structure from the surrounding soil. This may occur both laterally and along the foundation, figure 33.5(b) and 33.10(b).
Yet, allowance for such detachment was not made for Seabrook: "The base of the CEB foundation is restrained vertically... Since ASR expansion of the wall is largest below-grade" [794]. This omission could result in an erroneous stress field.

35.2.2.3.3.9 Dynamic Analysis Model As discussed above, about twenty years ago, the authors of the ASME code for concrete reactor vessels and containments wrote

> The dynamic analysis of containment structures for earthquake loads have progressed from a few two-dimensional lumped three or four mass stick models employing response spectrum modal analysis (in the late 1960s) to complex three-dimensional hundreds to thousands of degrees of freedom finite element models (in the 1970s and 1980s).
>
> Ashar et al. [53]

Hence, we were surprised that for such an important structure as Seabrook+ASR, it is reported that [794, pg 45] "Response spectra analysis was performed using a simplified "stick" model. For lateral analyses, the model was fully fixed below EI. 0 ft. For vertical analyses, the model was fixed at the base at El. (-)30 ft."
The stick model is a model of the past when computers did not have sufficient capability to handle the time history analysis of a 3D model. The model cannot capture the seismic contact between the (ASR induced wall expanded wall) with the adjacent soil unless joint elements are inserted, Fig. 33.5(b).

> The dynamic analysis of containment structures for earthquake loads have progressed from a few two-dimensional lumped three or four mass stick models employing response spectrum

> modal analysis (in the late 1960s) to complex three-dimensional hundreds to thousands of degrees of freedom finite element models(in the 1970s and 1980s). The dynamic modeling of containment has generally included Soil-Structure Interaction (SSI) effects.
>
> Ashar et al. [53].

35.2.2.3.3.10 Dynamic Analysis Time Integration Historically, engineers have favored modal analysis in conjunction with the response spectrum method (RSM) as it was not computationally expensive. However, one must recognize that the RSM is a very approximate method which only produces positive values of displacements and member forces which are not in equilibrium; thus demand/capacity ratios have very large errors.

> Seismic loads are applied using a static equivalent method utilizing the design-basis maximum acceleration profiles, which were computed during original design from response spectra analysis. Amplify ASR loads by a threshold factor to account for potential future ASR expansion. Evaluate capacity based on ACI 318-71 criteria with combined demands from all design loads, including the self-straining loads associated with the as deformed condition.
>
> [794, pg 2]

This oversimplified method brings to mind what Prof. Wilson is reported to have said

> Ray Clough and I regret we created the approximate response spectrum method for seismic analysis of structures in 1962.... At that time many members of the profession were using the sum of the absolute values of the modal values to estimate the maximum member forces. Ray suggested we use the SRSS method to combine the modal values. However, I am the one who put the approximate method in many dynamic analysis programs which allowed engineers to produce meaningless positive numbers of little or no value... After working with the RSM for over 50 years, I recommend it not be used for seismic analysis.
>
> Wilson [885]

We conclude that using the combination of RSM and static equivalent load is an oversimplification for such a critical analysis.

35.2.2.3.3.11 Nonlinear Analysis

> The seismic analysis of safety-related structures is typically performed by analysis of linearly elastic mathematical models. Nonlinear analysis may be performed in some cases, especially for beyond design basis calculations or evaluation of existing facilities.
>
> ASCE 4-16 [49]

In this case, a linear analysis was conducted to assess the effects of ASR at an existing facility (Seabrook). While the analysis addressed compliance with the design basis (not beyond design basis accidents), ASR has not previously been included in the design basis for NPPs. Thus, in some respects, the analysis went beyond the design basis. Under the circumstances, a linear analysis was not appropriate.

A reasonably accurate determination of the appropriate margin of safety is critical where a potential leak may occur as a result of concrete degradation. The authors submit that in these circumstanaces, it can only be achieved through a nonlinear analysis.

35.2.2.3.3.12 Dynamic Uplift/Rocking Fixing the mat to the foundation is not good as it restricts ASR expansion of the mat, and most importantly, it can not capture rocking (or uplift) as suggested by [49, chap 11] and discussed in chapter 16. Hence, the dynamic analysis in or opinion was flawed.

35.3 Conclusion

The authors examined the response by a private industry licensee (NextEra) and the responsible federal regulatory agency (NRC) to the presence of ASR in the CEB, a major safety structure at the Seabrook nuclear power plant. ASR was not discovered in a U.S. nuclear plant until 2009, when it was found at Seabrook. Thus, ASR is not addressed in the original licensing regulations or building codes for Seabrook, nor is it addressed in current operating regulations or codes. Nevertheless, the NRC had full statutory authority to develop all requirements needed to protect public health and safety, including requiring an adequately strict and sophisticated science-based approach to ASR.
The authors found that:

- The Seabrook case illustrates the importance of a rigorously scientific and sophisticated approach to ASR in a regulatory setting. ASR is a dangerous phenomenon because it compromises the integrity of concrete during seismic events, and thus challenges the design basis by which the NRC assures the protection of public health and safety. An erroneous safety assessment could lead to a nonconservative response and perhaps devastating consequences.
- The LAR was not prepared, nor was it internally or externally reviewed, by competent persons with a solid understanding of ASR and its nefarious impact on a structure as complex as a CEB.
- While NextEra relied on reputable engineering firms to assess ASR at Seabrook, they nevertheless lacked sufficient expertise in the complexities and challenges that ASR poses in a structure as complex as a CEB. As a result, rather than applying modern understanding of ASR, they adopted a simplistic and heuristic approach rooted in a 1971 design code. The authors see a disturbing dichotomy between the relatively simplistic engineering approach taken by NextEra and the much more rigorous approach with which the authors are accustomed by virtue of their (academic/researcher) backgrounds.
- NextEra did not avail itself of widely available modern computational tools that have been used internationally with success. Nor did NextEra consult experts with broad ASR experience.
- NextEra's consultants relied heavily on laboratory beam tests and calibration methodologies that were deficient in multiple respects. They also made the grossly

simplistic and hugely consequential assumption that a CEB will respond to ASR the same way as a simply supported beam with in a laboratory.
- The authors are particularly concerned about NextEra's effective dismissal of the potential for the formation, propagation, and coalescence of microcracks inside the CEB that could result in a delamination of the walls; or the likelihood that this delamination would be undetectable in a timely fashion by the proposed monitoring program.
- NextEra also devised a "box" concept based on the beam tests to establish acceptable limits for ASR expansion in the CEB. However, the parameters of the box were set arbitrarily, and were not scientifically established. NextEra further undermined the scientific credibility of its approach by setting an elastic "margin for future expansion", allowing relaxation of the box limits if they were exceeded or even approached. This raises questions about the rigor of NextEra's program for protecting public health and safety. The authors are not aware of any organization that would allow for such an elastic interpretation of a safety code.
- Whereas one may reasonably use a code-based approach for the design of new structures, the safety assessment of a swelling and cracking structure, that is required to resist seismic load, can only be assessed by a proper nonlinear analysis. Such a nonlinear analysis was not performed.
- The NRC, as regulator, had a significant responsibility for assuring that its own review was competent and independent. Yet, none of the NRC reviewers had any ASR expertise.
- Nor did the NRC's watchdog agency, the Advisory Committee on Reactor Safeguards – which conducted an additional review and gave approval to the LAR – have any ASR expertise.

The authors find it particularly disturbing that the NRC, as the regulator with ultimate responsibility for ensuring the protection of public health and safety, lacked sufficient expertise or independence to make an objective and scientifically accurate assessment. Most troublesome was the glaring absence of an independent review panel. As a result, a private industry licensee with no experience in addressing ASR and was essentially left to regulate itself. The seriously inadequate LAR now stands as the NRC's model for an adequate program for addressing ASR at nuclear facilities. The Seabrook case constitutes a warning sign that the U.S. government's systems for regulating facilities may lack sufficient systems and controls to ensure the application of sound scientific methods to address emerging risks. While sophisticated methods for addressing ASR were most certainly available in the scientific literature, the NRC seemed unaware of them. Instead, the NRC stuck to the well-trodden path of standard engineering expertise, which was grossly insufficient. The lack of awareness of attention to modern methods for addressing emerging problems is a matter of particular concern for the NRC, given that it is now in the process of renewing nuclear reactor licenses to operate for as long as 80 years – twice the term originally anticipated when the reactors were first licensed. ASR is one of numerous phenomena emerging in aging reactors for which the construction codes used in original licensing are far from adequate to address. The authors recommend that the NRC undertake a rigorous scientific evaluation of ASR and establish a rigorous regulatory system in

consultation with knowledgeable scientists. The NRC should also take measures to ensure that programs for addressing ASR at U.S. nuclear facilities receive thorough reviews by independent expert panels. If the ACRS performs that function, it should obtain the necessary expertise from consulting experts.

In summary, NextEra thought ASR was a complicated problem that could be handled with the engineering skills it already knew well; however, it was a complex one requiring a complementary skill set that it lacked. Thus the solution was bungled and the regulatory system failed to correct the mistakes.
Seabrook could and should provide a test case for improving NRC's regulatory program for emerging safety and service problems.

References

[1] A. C. 209-Creep and V. C. in Concrete. "Prediction of creep, shrinkage, and temperature effects in concrete structures". In: American Concrete Institute. 1982.

[2] A. Ababneh, F. Benboudjema, and Y. Xi. "Chloride Penetration in Non-Saturated Concrete". In: *ASCE Journal of Materials in Civil Engineering* 15 (2003), pp. 183–191.

[3] ABAQUS. *Abaqus Theory Manual*. Version6.7. ABAQUS, Inc. Providence, RI, USA, 2007.

[4] H. Abdelhamid, B. Mahmoud, and M. Hussein. "Seismic Fragility and uncertainty Analysis of Concrete Gravity Dams under Near-Fault Ground Motions". In: *Civil and Environmental Research* 5 (2013), pp. 123–129.

[5] ABS. *Risk Assessment Application for the Marine and Offshore Oil and Gas Industries*. Tech. rep. Houston, USA: American Bureau of Shipping, 2000.

[6] M. Abuhaikal et al. "Le Châtelier's conjecture: Measurement of colloidal eigenstresses in chemically reactive materials". In: *Journal of the Mechanics and Physics of Solids* 112 (2018), pp. 334–344.

[7] S. Acharya and D. Menon. "Prediction of Radial Stresses due to Prestressing in PSC Shells". In: *Nuclear Engineering and Design* 225 (2003), pp. 109–125.

[8] ACI. *Prediction of Creep, Shrinkage, and Temperature Effects in Concrete Structures*. Tech. rep. American Concrete Institute, 2008.

[9] ACI 318. "Building code requirements for structural concrete (ACI 318-19) and commentary". In: American Concrete Institute. 2019.

[10] ACI 318-71. "Building code requirements for structural concrete (ACI 318-71) and commentary". In: American Concrete Institute. 1971.

[11] ACI 349. *Code Requirements for Nuclear Safety-Related Concrete Structures (ACI 349 M-06) and Commentary*. Tech. rep. American Concrete Institute, Farmington Hills, 2006.

[12] ACI 365. *Service Life Prediction; State of the Art Report*. Tech. rep. American Concrete Institute, 2010.

[13] ACI 446.1R-91. *Fracture Mechanics of Concrete: Concepts, Models and Deformation of Material Properties (Reapproved 1999)*. Tech. rep. ACI 446.1R-91. Detroit, MI: American Concrete Institute, 2002.

[14] ACI 446.3R-97. *Finite element analysis of fracture in concrete structures*. Tech. rep. ACI 446.3R-97. Detroit, MI: American Concrete Institute, 2002.

[15] ACI-ASCE 423.10R-16. "Guide to Estimating Prestress Loss". In: American Concrete Institute. 2016.

[16] M. Ahmadi et al. "Behavior of a large concrete dam to an actual maximum credible earthquake". In: *Proceeding of the 10th World Conferance on Earthquake Engineering*. Vol. 7. 1992, pp. 3995–4000.

[17] T. Ahmed, E. Burley, and S. Rigden. "The state and fatigue strength of reinforced concrete beams affected by alkali-silica reaction". In: *Materials Journal* 95.4 (1998), pp. 376–388.

[18] S. Alekseev, F. Ivanov, and S. Modry. *Durability of Reinforced Concrete in Aggressive Media*. Brookfield, VT: A.A. Balkema Publishers, 1993.

[19] M. Alembagheri and M. Ghaemian. "Damage assessment of a concrete arch dam through nonlinear incremental dynamic analysis". In: *Soil Dynamics and Earthquake Engineering* 44 (2013), pp. 127–137.

[20] M. Alembagheri and M. Ghaemian. "Incremental dynamic analysis of concrete gravity dams including base and lift joints". In: *Earthquake Engineering and Engineering Vibration* 12.1 (2013), pp. 119–134.

[21] M. Alembagheri and M. Ghaemian. "Seismic assessment of concrete gravity dams using capacity estimation and damage indexes". In: *Earthquake Engineering and Structural Dynamics* 42 (2013), pp. 123–144.

[22] M. Alembagheri. "Investigating Efficiency of Vector-Valued Intensity Measures in Seismic Demand Assessment of Concrete Dams". In: *Advances in Civil Engineering* 2018 (2018).

[23] D. L. Allaix and V. I. Carbone. "An improvement of the response surface method". In: *Structural Safety* 33.2 (2011), pp. 165–172.

[24] M. Alnaggar, G. Cusatis, and G. Di Luzio. "Lattice discrete particle modeling (LDPM) of alkali silica reaction (ASR) deterioration of concrete structures". In: *Cement and Concrete Composites* 41 (2013), pp. 45–59.

[25] L. Altarejos-Garcia et al. "Methodology for estimating the probability of failure by sliding in concrete gravity dams in the context of risk analysis". In: *Structural Safety* 36–37 (2012), pp. 1–13.

[26] A. Alvaredo and F. Wittman. "Crack Formation Due to Hygral Gradients". In: *Third International Workshop on Behaviour of Concrete Elements Under Thermal and Hygral Gradients*. Weimar, Germany, 1992.

[27] S. Alves and J. Hall. "System identification of a concrete arch dam and calibration of its finite element model". In: *Earthquake engineering & structural dynamics* 35.11 (2006), pp. 1321–1337.

[28] A. Amirpour and H. Mirzabozorg. "Quantifying the qualitative limit-states using IDA approach in concrete arch dams". In: *Arabian Journal for Science and Engineering* 39.11 (2014), pp. 7729–7740.

[29] ANCOLD. *Guidelines on risk assessment*. Tech. rep. Sydney, New South Wales, Australia: Australian National Committee on Large Dams, 2003.

[30] T. Anderson. *Fracture Mechanics, Fundamentals and Applications*. CRC Press, 1995.

[31] A Andonov and K Apostolov. "Displacement-Based Seismic Capacity Assessment of Concrete Dams". In: *Proceedings of the 15th World Conference on Earthquake Engineering*. Lisbon, Portugal, 2012.

[32] A Andonov and K Apostolov. "Displacement-Based Seismic Capacity Assessment of Concrete Dams". In: *Proceedings of the 15th World Conference on Earthquake Engineering*. Lisbon, Portugal, 2012.

[33] A. G. Andonov, A. Iliev, and K. S. Apostolov. "Towards Displacement-Based Seismic Assessment of Concrete Dams Using Non-linear Static and Dynamic Procedures". In: *Structural Engineering International* 23.2 (2013), pp. 132–140.

[34] A. Ang. “Seismic damage assessment and basis for damage-limiting design”. In: *Probabilistic Engineering Mechanics* 3 (1988), pp. 146–150.

[35] M. I. Ansari and P. Agarwal. “Categorization of Damage Index of Concrete Gravity Dam for the Health Monitoring after Earthquake”. In: *Journal of Earthquake Engineering* 0.ja (2016), null.

[36] M. I. Ansari, M. Saqib, and P. Agarwal. “Geometric Configuration Effects on Nonlinear Seismic Behavior of Concrete Gravity Dam”. In: *Journal of Earthquake and Tsunami* (2018), p. 1850003.

[37] ANSYS. *ANSYS software reference manuals, release notes, mechanical APDL, elements reference, commands reference and theory reference, version Release 11*. Canonsburg, PA, 2007.

[38] S. Antoniou and R. Pinho. “Advantages And Limitations Of Adaptive And Non-Adaptive Force-Based Pushover Procedures”. In: *Journal of Earthquake Engineering* 8 (2004), pp. 497–522.

[39] S. Antoniou and R. Pinho. “Development And Verification Of A Displacement-Based Adaptive Pushover Procedure”. In: *Journal of Earthquake Engineering* 8 (2004), pp. 643–661.

[40] Applied Technology Council. *Seismic Performance Assessment of Buildings Volume 1 - Methodology*. Tech. rep. FEMA P-58-1. Federal Emergency Management Agency, 2012.

[41] Applied Technology Council. *Seismic performance assessment of buildings, Volume 1: Methodology*. Tech. rep. ATC-58-1. Redwood City, CA: Federal Emergency Management Agency, 2012.

[42] R. Araya and R. Saragoni. “Earthquake accelerogram destructiveness potential factor”. In: *Proceedings of the 8th World Conference of Earthquake Engineering*. San Francisco, USA, 1984, pp. 835–841.

[43] A. F. Ares and A. Fatehi. “Development of probabilistic seismic hazard analysis for international sites, challenges and guidelines”. In: *Nuclear Engineering and Design* 259 (2013), pp. 222–229.

[44] Arias A. *A measure of earthquake intensity, Seismic Design for Nuclear Power Plants*. Cambridge, UK: MIT Press, 1970, pp. 438–483.

[45] Army Corps of Engineers. *Reliability Assessment of Navigation Structures*. ETL 1110-2-532. Washington, D.C.: Department of the Army, US Army Corps of Engineers, 1992.

[46] Army Corps of Engineers. *Time-History Dynamic Analysis of Concrete Hydraulic Structures*. Engineering Manual 1110-2-6051. Washington, D.C.: Department of the Army, US Army Corps of Engineers, 2003.

[47] A Arnstein and M Reiner. “Creep of cement, cement mortar, and concrete”. In: *Civil Engineering and Public Works Review* 40.9 (1945), pp. 198–202.

[48] S. Arrhenius. “On the Reaction Velocity of the Inversion of Cane Sugar by Acids”. In: *Zeitschrift für physikalische Chemie* 4 (1889), p. 226.

[49] ASCE 4-16. *Seismic Analysis of Safety-Related Nuclear Structures*. Tech. rep. American Society of Civil Engineers, 2016.

[50] ASCE/SEI-41-13. *Seismic Evaluation and Retrofit of Existing Buildings*. Tech. rep. Reston, VA: American Society of Civil Engineers, 2014.

[51] ASCE/SEI 43-05. "Seismic Design Criteria for Structures, Systems, and Components in Nuclear Facilities". In: *American Society of Civil Engineers, Reston, VA* (2005).

[52] ASCE/SEI 7. *Minimum Design Loads For Buildings and Other Structures*. Tech. rep. American Society of Civil Engineers, 2010.

[53] H. Ashar et al. "Code for concrete reactor Vessels and containments". In: *ASME Boiler & Pressure Vessel Code, Sec. III* 504.2 (2001).

[54] M. Aslam et al. "Earthquake Analysis of Radial Gates/Dam Including Fluid-Structure Interaction". In: *Proceedings, Third U.S.-Japan Workshop on Advanced Research on Earthquake Engineering for Dams*. San Diego, CA., 2002.

[55] ASME. "Standard for Level 1/Large Early Release Frequency Probabilistic Risk Assessment for Nuclear Power Plant Applications". In: *American Society of Mechanical Engineers* (2008).

[56] B. ASME III. *BPVC Section III-Rules for Construction of Nuclear Facility Components-Division 2-Code for Concrete Containments*. Tech. rep. American Society of Mechanical Engineering, 2015.

[57] ASTM C192. "Standard Practice for Making and Curing Concrete Test Specimens in the Laboratory". In: *Annual book of ASTM standards* 04.02 (2016).

[58] ASTM C31. "Standard Practice for Making and Curing Concrete Test Specimens in the Field". In: *Annual book of ASTM standards* 04.02 (2016).

[59] ASTM, C39. "39, Standard test method for compressive strength of cylindrical concrete specimens". In: *Annual book of ASTM standards* 04.02 (2016).

[60] ASTM C42. "Standard Test Method for Obtaining and Testing Drilled Cores and Sawed Beams of Concrete". In: *Annual book of ASTM standards* C09.61 (2016).

[61] ASTM C469. "469, Standard test method for static modulus of elasticity and Poisson's ratio of concrete in compression". In: *Annual book of ASTM standards* 04.02 (2016).

[62] ASTM C496. "496, Standard test method for splitting tensile strength of cylindrical concrete specimens". In: *Annual book of ASTM standards* 04.02 (2016).

[63] ASTM C512. "469, Standard Test Method for Creep of Concrete in Compression". In: *Annual book of ASTM standards* 04.02 (2016).

[64] ASTM E4. "Standard Practices for Force Verification of Testing Machines". In: *Annual book of ASTM standards* 03.01 (2016).

[65] ATC. *Tentative provisions for the development of seismic regulations for buildings, Report No. ATC 3-06*. Tech. rep. Palo Alto, CA: Applied Technology Council, 1978.

[66] ATC-13. *Earthquake damage evaluation data for California. Report No.ATC-13*. Tech. rep. Redwood City, CA: Applied Technology Council, 1985.

[67] ATC-14. *Evaluating the seismic resistance of existing buildings. Report No.ATC-14*. Tech. rep. Redwood City, CA: Applied Technology Council, 1987.

[68] ATC-40. *Seismic evaluation and retrofit of concrete buildings. Report No.ATC-40*. Tech. rep. Redwood City, CA: Applied Technology Council, 1996.

[69] ATC-58. *Engineering demand parameters for structural framing systems*. Tech. rep. Redwood City, CA: Applied Technology Council, 2004.

[70] G. M. Atkinson and D. M. Boore. "Ground-motion relations for eastern North America". In: *Bulletin of the Seismological Society of America* 85.1 (1995), pp. 17–30.

[71] E. K. Attiogbe and D. Darwin. "Submicrocracking in cement paste and mortar". In: *Materials Journal* 84.6 (1987), pp. 491–500.

[72] B. M. Ayyub. "Resilience metrics for multi-hazard environments". In: *Vulnerability, Uncertainty, and Risk: Quantification, Mitigation, and Management*. American Society of Civil Engineers, 2014, pp. 925–936.

[73] B. M. Ayyub and K.-L. Lai. "Structural reliability assessment using latin hypercube sampling". In: *Structural Safety and Reliability*. ASCE. 1989, pp. 1177–1184.

[74] A. Azarbakht and M. Dolšek. "Prediction of the median IDA curve by employing a limited number of ground motion records". In: *Earthquake Engineering and Structural Dynamics* 36 (2007), pp. 2401–2421.

[75] A. Azarbakht and M. Dolšek. "Progressive Incremental Dynamic Analysis for First-Mode Dominated Structures". In: *Journal of Structural Engineering* 137 (2011), pp. 445–455.

[76] I. Babuska and A. Miller. "The Post-Processing Approach to Finite Element Method– Part II". In: *Int. J. Num. Meth. Engrg.* 20 (1984), pp. 1111–1129.

[77] G. B. Baecher and J. T. Christian. *Reliability and statistics in geotechnical engineering*. John Wiley & Sons, 2005.

[78] J. Baker and C. Cornell. "A vector-valued ground motion intensity measure consisting of spectral acceleration and epsilon". In: *Earthquake Engineering and Structural Dynamics* 34 (2005), pp. 1193–1217.

[79] J. Baker. "Efficient analytical fragility function fitting using dynamic structural analysis". In: *Earthquake Spectra* 31.1 (2015), pp. 579–599.

[80] J. Baker and C. Cornell. "Uncertainty propagation in probabilistic seismic loss estimation". In: *Structural Safety* 30.3 (2008), pp. 236–252.

[81] J. Baker and N. Jayaram. "Correlation of spectral acceleration values from NGA ground motion models". In: *Earthquake Spectra* 24 (2008), pp. 299–317.

[82] H. Banon and D. Veneziano. "Seismic safety of reinforced members and structures". In: *Earthquake Engineering and Structural Dynamics* 10 (1982), pp. 179–193.

[83] S. Barak and M. Modarres. "Developing an approach to evaluate stocks by forecasting effective features with data mining methods". In: *Expert Systems with Applications* 42.3 (2015), pp. 1325–1339.

[84] M. Barbato et al. "Performance-based hurricane engineering (PBHE) framework". In: *Structural Safety* 45 (2013), pp. 24–35.

[85] G. Barenblatt. “The Mathematical Theory of Equilibrium Crack in the Brittle Fracture”. In: *Advances in Applied Mechanics* 7 (1962), pp. 55–125.
[86] R. Barsoum. “Application of Quadratic Isoparametric Finite Elements in Linear Fracture Mechanics”. In: *Int. J. Fract.* 10 (1974), pp. 603–605.
[87] U. Basu. “Explicit finite element perfectly matched layer for transient three-dimensional elastic waves”. In: *International Journal for Numerical Methods in Engineering* 77 (2009), pp. 151–176.
[88] M. Båth. “Lateral inhomogeneities of the upper mantle”. In: *Tectonophysics* 2.6 (1965), pp. 483–514.
[89] K. Bathe. *Finite Element Procedures*. Prentice-Hall Inc., 1996.
[90] R. Baušys et al. “Sensitivity of dynamic behaviour of the FE model: case study for the Ignalina NPP reactor building”. In: *Journal of Civil Engineering and Management* 14.2 (2008), pp. 121–129.
[91] Z. Bažant and Y. Li. “Cohesive crack with rate-dependent opening and viscoelasticity: I. mathematical model and scaling”. In: *International Journal of Fracture* 86 (1997), pp. 247–265.
[92] Z. Bažant and J. Planas. *Fracture and Size Effect in Concrete and Other Quasibrittle Materials*. CRC Press, 1998.
[93] Z. Bažant. “Instability, Ductility and Size Effect in Strain Softening Concrete”. In: *Journal of Engng. Mech., ASCE* 102.2 (1976), pp. 331–344.
[94] Z. Bažant. “Size effect in blunt fracture: Concrete, rock, metal”. In: *J.of Engng.Mechanics, ASCE* 110 (1984), pp. 518–535.
[95] Z. Bažant. Personal Communication, Dec. 8 2009. 2009.
[96] Z. Bažant and S. Baweja. “Creep and shrinkage prediction model for analysis and design of concrete structures - model B3.” In: *Materials and Structures* 28.1 (1995), pp. 357–365.
[97] Z. Bažant and S. Baweja. “Creep and shrinkage prediction model for analysis and design of concrete structures-model B3”. In: *Mater Struct* 28 (1995), pp. 357–65.
[98] Z. Bažant and E. Becq-Giraudon. “Estimation of fracture energy from basic characteristics of concrete”. In: *Fracture Mechanics of Concrete Structures (Proc., FraMCoS-4 Int. Conf., Paris)*. Ed. by R. de Borst et al. Balkema, 2001, pp. 491–495.
[99] Z. Bažant and L. Cedolin. “Blunt Crack Propagation in Finite Element Analysis”. In: *J. of the Engineering Mechanics Division, ASCE* 105 (1979), pp. 297–315.
[100] Z. Bažant and J. C. Chern. “Concrete creep at variable humidty: constitutive law and mechanism”. In: *Materials and Structures* 18.1 (1985), p. 1.
[101] Z. Bažant and L. Najjar. “Nonlinear Water Diffusion in Nonsaturated Concrete”. In: *Materials and Structures* 5 (1972), pp. 3–20.
[102] Z. Bažant and P. Pfeiffer. “Determination of Fracture Energy Properties from Size Effect and Brittleness Number”. In: *ACI Material Journal* 84.6 (1987), pp. 463–480.

[103] Z. Bažant, G. Zi, and C. Meyer. "Fracture Mechanics of AAR in Concretes with Waste Glass Particles of Different Sizes". In: *J. of Engineering Mechanics, ASCE* 126.3 (2000), pp. 226–232.

[104] Bažant, Ž. and Gettu, R. "Rate Effects and Load Relaxation in Static Fracture of Concrete". In: *ACI Materials Journal* 89.5 (1992), pp. 456–468.

[105] Bažant, Ž and Xiang, Y. "Crack growth and lifetime of concrete under long time loading". In: *ASCE J. of Engineering Mechanics* 123 (1997), pp. 350–358.

[106] O. Bayrak. *Structural Assessment of Seabrook Station; Findings and Structural Testing Plan*. Tech. rep. Online; accessed 2018-07-11. University of Texas, Austin, 2012.

[107] Z. P. Bazant. "Physical Model for Steel Corrosion in Concrete Sea Structures-Theory". In: *Journal of the Structural Division* 105.ST6 (1979), pp. 1137–1153.

[108] Z. P. Bazant and S. Baweja. "Creep and shrinkage prediction model for analysis and design of concrete structures: Model B3". In: *ACI Special Publications* 194 (2000), pp. 1–84.

[109] Z. P. Bažant and M. Jirásek. *Creep and hygrothermal effects in concrete structures*. Vol. 225. Springer, 2018.

[110] Z. Bažant, M. H. Hubler, and Q. Yu. "Excessive creep deflections: An awakening". In: *Concrete international* 33.8 (2011), pp. 44–46.

[111] Bazant, Z.P. *Mathematical modeling of creep and shrinkage of concrete*. John Wiley and Sons, New York, 1988.

[112] E. S. Beckjord, M. A. Cunningham, and J. A. Murphy. "Probabilistic safety assessment development in the United States 1972–1990". In: *Reliability Engineering & System Safety* 39.2 (1993), pp. 159–170.

[113] A. W. Beeby and R. Narayanan. *Designers' Guide to EN 1992-1-1 and EN 1992-1-2. Eurocode 2: Design of Concrete Structures: General Rules and Rules for Buildings and Structural Fire Design*. Thomas Telford, 2005.

[114] T. Belytschko, W. Liu, and B. Moran. *Nonlinear Finite Elements for Continua and Structures*. Wiley & Sons, Ltd., 2000.

[115] M. Ben-Ftima, H. Sadouki, and E. Bruhwiler. "Development of a computational multi-physical framework for the use of nonlinear explicit approach in the assessment of concrete structures affected by alklai-aggregate reaction". In: *9th International Conference on Fracture Mechanics of Concrete and Concrete Structures; FraMCoS-9*. Ed. by V. Saouma, J. Bolander, and E. Landis. Berkeley, CA, 2016.

[116] J. Benjamin and C. Cornell. *Probability, Statistics, and Decision for Civil Engineers*. New York: McGraw Hill, 1970.

[117] E. Bentz. "Empirical modeling of reinforced concrete shear strength size effect for members without stirrups". In: *ACI structural journal* 102.2 (2005), p. 232.

[118] C. Bernier, R. Monteiro, and P. Paultre. "Using the Conditional Spectrum Method for Improved Fragility Assessment of Concrete Gravity Dams in Eastern Canada". In: *Earthquake Spectra* 0.0 (2016), null.

[119] C. Bernier et al. “Seismic Fragility of Concrete Gravity Dams with Spatial Variation of Angle of Friction: Case Study”. In: *Journal of Structural Engineering* (2015), p. 05015002.

[120] R. Bertero and V. Bertero. “Performance-based seismic engineering: the need for a reliable conceptual comprehensive approach”. In: *Earthquake Engineering and Structural Dynamics* 31 (2002), pp. 627–652.

[121] R. Bertero and B. V.V. “Application of a comprehensive approach for the performance-based earthquake-resistant design of buildings”. In: *Proceeding of the 12th World Conferance on Earthquake Engineering*. 2000.

[122] M. Berveiller, B. Sudret, and M. Lemaire. “Stochastic finite element: a non intrusive approach by regression”. In: *European Journal of Computational Mechanics/Revue Européenne de Mécanique Numérique* 15.1-3 (2006), pp. 81–92.

[123] F. internationale du béton. *fib model code for concrete structures 2010*. Berlin: Ernst & Sohn, 2013.

[124] S. Bhattacharjee and P. Leger. “Application of NLFM models to predict cracking in concrete gravity dams”. In: *ASCE Structural Engineering* 120 (1994), pp. 1255–1271.

[125] J. Bielak and P. Christiano. “On the Effective Seismic Input for Non-Linear Soil-Structure Interaction Systems”. In: *Earthquake Engineering and Structural Dynamics* 12 (1984), pp. 107–119.

[126] C. M. Bishop. “Pattern recognition”. In: *Machine Learning* 128 (2006).

[127] P. Blaikie et al. *At risk: natural hazards, people’s vulnerability and disasters*. Routledge, 2014.

[128] G. Blatman and B. Sudret. “An adaptive algorithm to build up sparse polynomial chaos expansions for stochastic finite element analysis”. In: *Probabilistic Engineering Mechanics* 25.2 (2010), pp. 183–197.

[129] G. Blatman and B. Sudret. “Adaptive sparse polynomial chaos expansion based on least angle regression”. In: *Journal of Computational Physics* 230.6 (2011), pp. 2345–2367.

[130] T. Blejwas et al. *Background study and preliminary plans for a program on the safety margins of containments*. Tech. rep. Sandia National Labs., Albuquerque, NM (USA), 1982.

[131] G. Blight. “A study of four waterproofing systems for concrete”. In: *Magazine of Concrete Research* 43.156 (1991), pp. 197–203.

[132] P. Bocchini et al. “Resilience and sustainability of civil infrastructure: Toward a unified approach”. In: *Journal of Infrastructure Systems* 20.2 (2013), p. 04014004.

[133] R. Boer, R. Schiffman, and R. Gibson. “The origins of the theory of consolidation: the Terzaghi—Fillunger dispute”. In: *Geotechnique* 46.2 (1996), pp. 175–186.

[134] E. Bojorquez et al. “Comparing vector-valued intensity measures for fragility analysis of steel frames in the case of narrow-band ground motions”. In: *Engineering Structures* 45 (2012), pp. 472–480.

[135] B. A. Bolt. "Duration of strong ground motion". In: *Proceedings of the 5th World Conference on Earthquake Engineering*. Vol. 1. 1973, pp. 1304–1313.

[136] J. J. Bommer and A. Martinez-Pereira. "The effective duration of earthquake strong motion". In: *Journal of earthquake engineering* 3.02 (1999), pp. 127–172.

[137] H. Bonstrom and R. B. Corotis. "First-order reliability approach to quantify and improve building portfolio resilience". In: *Journal of Structural Engineering* 142.8 (2016), p. C4014001.

[138] S. Booker et al. *Aging management guideline for commercial nuclear power plants-heat exchangers*. Tech. rep. Sandia Report SAND933-7070, 1994.

[139] D. M. Boore, W. B. Joyner, and T. E. Fumal. "Equations for estimating horizontal response spectra and peak acceleration from western North American earthquakes: A summary of recent work". In: *Seismological research letters* 68.1 (1997), pp. 128–153.

[140] J. Boussinesq. *Application des potentiels à l'étude de l'équilibre et du mouvement des solides élastiques: principalement au calcul des déformations et des pressions que produisent, dans ces solides, des efforts quelconques exercés sur une petite partie de leur surface ou de leur intérieur: mémoire suivi de notes étendues sur divers points de physique, mathematique et d'analyse*. Vol. 4. Gauthier-Villars, 1885.

[141] D. S. Bowles. "What is ALARP and how can it improve dam safety decisions?" In: *ASDSO conference On Dams*. 2013.

[142] D. Bowles and D. McClelland. *Event tree analysis*. Tech. rep. Logan, Utah: Working paper prepared for the Canadian Electricity Association Dam Safety Interest Group. Institute for Dam Safety Risk Management, Utah State University, 2000.

[143] G. E. Box and D. W. Behnken. "Some new three level designs for the study of quantitative variables". In: *Technometrics* 2.4 (1960), pp. 455–475.

[144] G. E. Box and N. R. Draper. *Empirical model-building and response surfaces*. Vol. 424. Wiley New York, 1987.

[145] D. Boyer. "Geologic factors influencing dam foundation failure modes". In: *Proceedings of the 26th Annual USSD Conference*. San Antonio, Texas, USA, 2006.

[146] Y. Bozorgnia and V. Bertero. "Damage spectra: characteristics and applications to seismic risk reduction". In: *Structural Engineering, ASCE* 129 (2003), pp. 1330–1340.

[147] Y. Bozorgnia and V. V. Bertero. *Earthquake engineering: from engineering seismology to performance-based engineering*. CRC press, 2004.

[148] B. Bradley. "Empirical equations for the prediction of displacement spectrum intensity and its correlation with other intensity measures". In: *Soil Dynamics and Earthquake Engineering* 31 (2011), pp. 1182–1191.

[149] B. A. Bradley. "A generalized conditional intensity measure approach and holistic ground-motion selection". In: *Earthquake Engineering & Structural Dynamics* 39.12 (2010), pp. 1321–1342.

[150] B. A. Bradley et al. “Guidance on the Utilization of Earthquake-Induced Ground Motion Simulations in Engineering Practice”. In: *Earthquake Spectra* 33.3 (2017), pp. 809–835.

[151] J. Braverman et al. “Degradation assessment of structures and passive components at nuclear power plants”. In: *Nuclear engineering and design* 228.1 (2004), pp. 283–304.

[152] L. Breiman. “Bagging predictors”. In: *Machine learning* 24.2 (1996), pp. 123–140.

[153] K. Breitung. “Asymptotic approximations for multinormal integrals”. In: *Journal of Engineering Mechanics* 110.3 (1984), pp. 357–366.

[154] D. Broek. *Elementary Engineering Fracture Mechanics, 4th Edition*. Martinus Nijhoff Publishers, 1986.

[155] E. Brühwiler and F. Wittmann. “Failure of Dam Concrete Subjected to Seismic Loading Conditions”. In: *Engineering Fracture Mechanics* 35.3 (1990), pp. 565–572.

[156] Brühwiler, E. “The Wedge Splitting Test for the determination of fracture properties”. In: *Numerical Models in Fracture Mechanics of Concrete, Proceedings of the 1st Bolomey Workshop on Numerical Models in Fracture Mechanics of Concrete*. Ed. by F. Wittmann. Zurich, Switzerland: Balkema, 1992, pp. 19–27.

[157] G. H. Brundtland. “Our common future—Call for action”. In: *Environmental Conservation* 14.4 (1987), pp. 291–294.

[158] M. Bruneau and A. Reinhorn. “Exploring the concept of seismic resilience for acute care facilities”. In: *Earthquake Spectra* 23.1 (2007), pp. 41–62.

[159] M. Bruneau et al. “A framework to quantitatively assess and enhance the seismic resilience of communities”. In: *Earthquake spectra* 19.4 (2003), pp. 733–752.

[160] L. Bryant, J. Brokaw, and P. Mlakar. *Reliability Modeling of Concrete Overstressing*. Tech. rep. Report Submitted to U.S. Army Engineer Waterways Experiment Station. JAYCOR, Vicksburg Mississippi, 1993.

[161] Buckingham, E. “The principle of similitude”. In: *Nature* 96 (1915), pp. 396–397.

[162] A. Buford. *Position Paper: In Situ Monitoring Of Alkali-Silica Reaction (ASR) Affected Concrete: A Study On Crack Indexing And Damage Rating Index To Assess The Severity Of ASR And To Monitor ASR Progression*. 2013.

[163] K. W. Campbell and Y. Bozorgnia. “Cumulative absolute velocity (CAV) and seismic intensity based on the PEER-NGA database”. In: *Earthquake Spectra* 28.2 (2012), pp. 457–485.

[164] K. Campbell and Y. Bozorgnia. “A ground motion prediction equation for the horizontal component of cumulative absolute velocity (CAV) based on the PEER-NGA strong motion database”. In: *Earthquake Spectra* 26.3 (2010), pp. 635–650.

[165] B. Capra and J. Bournazel. "Modeling of induced mechanical effects of alkali-aggregate reactions". In: *Cement and Concrete Research* 28.2 (1998), pp. 251–260.

[166] Carol, I. and Bažant, Z.P. and Prat, P.C. "Microplane Type Constitutive Models for Distributed Damage and Localized Cracking in Concrete Structures". In: *Proc. Fracture Mechanics of Concrete Structures*. Breckenridge, CO: Elsevier, 1992, pp. 299–304.

[167] A. Carpinteri et al. "Tensile and flexural creep rupture tests on partially damaged concrete specimens". In: *Materials and Structures* 30 (1997), pp. 269–276.

[168] A. Casagrande. "Seepage through dams". In: *J. New England Water Works Ass.* (1937).

[169] C. Casarotti and R. Pinho. "An adaptive capacity spectrum method for assessment of bridges subjected to earthquake action". In: *Bulletin of Earthquake Engineering* 5 (2007), pp. 377–390.

[170] M. Cavazzuti. *Optimization methods: from theory to design scientific and technological aspects in mechanics*. Springer Science & Business Media, 2012.

[171] CEB. *Concrete under Multiaxial States of Stress Constitutive Equations for Practical Design*. Tech. rep. Bulletin d'Information 156. Comité Euro-International du Béton, 1983.

[172] L. Cedolin, S. Dei Poli, and I. Iori. "Tensile Behavior of Concrete". In: *J. of Engineering Mechanics, ASCE* 113.3 (1987).

[173] D. Celarec and M. Dolšek. "The impact of modelling uncertainties on the seismic performance assessment of reinforced concrete frame buildings". In: *Engineering Structures* 52 (2013), pp. 340–354.

[174] O. Celik and B. Ellingwood. "Seismic fragilities for non-ductile reinforced concrete frames–Role of aleatoric and epistemic uncertainties". In: *Structural Safety* 32 (2010), pp. 1–12.

[175] Y. A. Cengel, M. A. Boles, and M. Kanoglu. *Thermodynamics: an engineering approach*. Vol. 1056. McGraw-Hill New York, 1998.

[176] J. Cervenka. Personal Communication. 2009.

[177] J. Cervenka, J. Chandra, and V. Saouma. "Mixed Mode Fracture of Cementitious Bimaterial Interfaces; Part II: Numerical Simulation". In: *Engineering Fracture Mechanics* 60.1 (1998), pp. 95–107.

[178] J. Cervenka and V. Papanikolaou. "Three Dimensional Combined Fracture-Plastic Material Model for Concrete". In: *International Journal of Plasticity* 24.12 (2008), pp. 2192–2220.

[179] V. Červenka and L. Jendele. *ATENA Program Documentation Part*. 2016.

[180] Červenka, J. *Verification of Containment Design in Nuclear Power Plants*. Cervenka Consulting. Prague, Czech Republic, 2008.

[181] P. Chana and G. Korobokis. *The structural performance of reinforced concrete affected by alkali silica reaction: Phase I*. Tech. rep. British and Cement Association, 1992.

[182] A. Chandler and N. Lam. “Performance-based design in earthquake engineering: A multidisciplinary review”. In: *Engineering Structures* 23 (2001), pp. 1525–1543.

[183] I. Charvet et al. “Empirical fragility assessment of buildings affected by the 2011 Great East Japan tsunami using improved statistical models”. In: *Natural Hazards* 73.2 (2014), pp. 951–973.

[184] J. Chen et al. “Seismic analysis and evaluation of the base isolation system in AP1000 NI under SSE loading”. In: *Nuclear engineering and design* 278 (2014), pp. 117–133.

[185] T. Chen and C. Guestrin. “Xgboost: A scalable tree boosting system”. In: *Proceedings of the 22nd acm sigkdd international conference on knowledge discovery and data mining*. ACM. 2016, pp. 785–794.

[186] T. Chen, T. He, M. Benesty, et al. “Xgboost: extreme gradient boosting”. In: *R package version 0.4-2* (2015), pp. 1–4.

[187] W. Chen and H. Zhang. *Structural Plasticity*. Springer-Verlag, 1990.

[188] J. Chénier et al. “An approach regarding aging management program for concrete containment structure at the gentilly-2 nuclear power plant”. In: *Proceedings of 33rd Annual Conference of the Canadian Nuclear Society, TCU Place, Saskatoon, Saskatchewan, Canada*. Vol. 1013. 2012, p. 126.

[189] G. Cherepanov. *Mechanics of Brittle Fracture*. McGraw-Hill, 1979.

[190] P. Cheung, T. Pauley, and R. Park. “New Zealand Tests on Full-Scale Reinforced Concrete Beam-Column-Slab Sub-assemblages Designed for Earthquake Resistance”. In: *ACI Special Publication SP-123, Design of Beam-Column Joints for Seismic Resistance*. Detroit, MI, USA, 1991, pp. 1–37.

[191] M. Chiorino et al. “CEB design manual on structural effects of time-dependent behaviour of concrete”. In: (1984).

[192] C. Chiu et al. *Root Cause Assessment Crystal River Unit 3 Containment Concrete Delamination*. Tech. rep. Non Proprietary Version. ML102861026. Performance Improvement International, 2010.

[193] I.-K. Choi, Y.-S. Choun, and J.-M. Seo. “Scenario earthquakes for Korean nuclear power plant site considering active faults”. In: *XVII International Conference on Structural Mechanics in reactor technology, Prague, Czech Republic, August*. 2003, pp. 17–22.

[194] I.-K. Choi et al. “Probabilistic seismic risk analysis of CANDU containment structure for near-fault earthquakes”. In: *Nuclear Engineering and Design* 238.6 (2008), pp. 1382–1391.

[195] A. Chopra and P. Chakrabarti. “The Koyna Earthquake and the damage to Koyna Dam”. In: *Bulletin of the Seismological Society of America* 63.2 (1973), pp. 381–397.

[196] A. Chopra and R. Goel. “Capacity-Demand-Diagram Methods Based on Inelastic Design Spectrum”. In: *Earthquake Spectra* 15 (1999), pp. 637–656.

[197] A. Chopra and R. Goel. “A modal pushover analysis procedure for estimating seismic demands for buildings”. In: *Earthquake Engineering and Structural Dynamics* 31 (2002), pp. 561–582.

[198] A. K. Chopra. “Earthquake resistant design of concrete gravity dams”. In: *Journal of the Structural Division* 104.6 (1978), pp. 953–971.

[199] A. K. Chopra. “Earthquake analysis of arch dams: factors to be considered”. In: *Journal of Structural Engineering* 138.2 (2012), pp. 205–214.

[200] O. Chopra. *Effects of Thermal Aging and Neutron Irradiation on Crack Growth Rate and Fracture Toughness of Cast Stainless Steels and Austenitic Stainless Steel Welds*. Tech. rep. NUREG/CR-7185. U.S. Nuclear Regulatory Commission, 2015.

[201] A. T. Chwang. “Hydrodynamic pressures on sloping dams during earthquakes. Part 2. Exact theory”. In: *Journal of Fluid Mechanics* 87.02 (1978), pp. 343–348.

[202] A. T. Chwang and G. W. Housner. “Hydrodynamic pressures on sloping dams during earthquakes. Part 1. Momentum method”. In: *Journal of Fluid Mechanics* 87.02 (1978), pp. 335–341.

[203] M. Ciampoli, F. Petrini, and G. Augusti. “Performance-based wind engineering: towards a general procedure”. In: *Structural Safety* 33.6 (2011), pp. 367–378.

[204] G. P. Cimellaro, A. M. Reinhorn, and M. Bruneau. “Framework for analytical quantification of disaster resilience”. In: *Engineering Structures* 32.11 (2010), pp. 3639–3649.

[205] G. Cimellaro, A. Reinhorn, and M. Bruneau. “Quantification of seismic resilience”. In: *Proceedings of the 8th US National conference on Earthquake Engineering*. 2006, pp. 18–22.

[206] J. J. S. of Civil Engineers). “Standard specification for concrete structures”. In: JSCE Tokyo. 2002.

[207] P. Clark et al. *Protocol for Fabrication, Inspection, Testing and Documentation of Beam-Column Connection and Other Experimental Specimens*. Tech. rep. SAC/BD-97/02. Sacramento, CA, USA: SAC Joint Venture, 1997.

[208] Clough, R.W. and Penzien, J. *Dynamics of Structures*. McGraw-Hill Inc., London, UK, 1993.

[209] J. L. Coleman, C. Bolisetti, and A. S. Whittaker. “Time-domain soil-structure interaction analysis of nuclear facilities”. In: *Nuclear Engineering and Design* 298 (2016), pp. 264–270.

[210] C. Comi, R. Fedele, and U. Perego. “A chemo-thermo-damage model for the analysis of concrete dams affected by alkali-silica reaction”. In: *Mechanics of Materials* 41 (2009), pp. 210–230.

[211] A. Committee and I. O. for Standardization. “Building code requirements for structural concrete (ACI 318-08) and commentary”. In: American Concrete Institute. 2008.

[212] J.-M. of Construction. *Japanese Building Code*. Tech. rep. Japan: Japanese Ministry of Construction, 2000.

[213] P. Cordova et al. “Development of a two-parameter seismic intensity measure and probabilistic assessment procedure”. In: *Proceedings of the 2nd US-Japan workshop on performance-based earthquake engineering methodology for RC building structures*. Japan, 2001, pp. 187–206.

[214] H. Cornelissen, D. Hordijk, and H. Reinhardt. "Experimental determination of crack softening characteristics of normalweight and lightweight". In: *Heron* 31.2 (1986), p. 45.

[215] A. Cornell and F. Jalayer. "Factored nonlinear displacement demand estimation methods for probability-based safety assessment". In: *Annual Meeting Research Digest No. 2002-7, A publication of the Pacific Earthquake Engineering Research Center*. 2002.

[216] A. Cornell, F. Jalayer, and R. Hamburger. "Probabilistic basis for 2000 SAC federal emergency management agency steel moment frame guidelines". In: *Journal of Structural Engineering* 128 (2002), pp. 526–532.

[217] C. A. Cornell. *Stochastic process models in structural engineering*. Department of Civil Engineering, Stanford University, 1964.

[218] R. B. Corotis. "Conceptual and analytical differences between resiliency and reliability for seismic hazards". In: *Structures Congress 2011*. 2011, pp. 2010–2020.

[219] E. Cosenza and G. Manfredi. "The improvement of the seismic-resistant design for existing and new structures using damage criteria". In: *Seismic design methodologies for the next generation of codes*. Ed. by P. Fajfar and H. Krawinkler. Roterdam: Balkema, 1997, pp. 119–130.

[220] E. Cosenza and G. Manfredi. "Damage indices and damage measures". In: *Progress in Structural Engineering and Materials* 2 (2000), pp. 50–59.

[221] A. T. Council. *Guidelines for Cyclic Seismic Testing of Components for Steel Structures*. Tech. rep. Redwood City, CA, USA: Applied Technology Council, 1992.

[222] R. Courant, K. Friedrichs, and H. Lewy. "On the partial difference equations of mathematical physics". In: *IBM Journal of Research and Development* 11.2 (1967), pp. 215–234.

[223] S. L. Cutter, B. J. Boruff, and W. L. Shirley. "Social vulnerability to environmental hazards". In: *Social science quarterly* 84.2 (2003), pp. 242–261.

[224] S. L. Cutter et al. "Disaster resilience: A national imperative". In: *Environment: Science and Policy for Sustainable Development* 55.2 (2013), pp. 25–29.

[225] J. Cyganiewicz et al. *Risk Based Profiling System*. Tech. rep. Denver, CO, USA: U.S. Bureau of Reclamation, 2001.

[226] O. Dahlblom and N. S. Ottosen. "Smeared Crack Analysis Using a Generalized Fictitious Crack Model". In: *Journal of Engineering Mechanics* 116.1 (1990), pp. 55–76.

[227] A. D'Ambrisi and M. Mezzi. "An energy-based approach for nonlinear static analysis of structures". In: *Bulletin of Earthquake Engineering* 13.5 (2015), pp. 1513–1530.

[228] D. Darwin, C. Dolan, and A. Nilson. *Design of Concrete Structures*. 15th Ed. McGraw-Hill, 2014.

[229] S. Dashti et al. “Centrifuge testing to evaluate and mitigate liquefaction-induced building settlement mechanisms”. In: *Journal of geotechnical and geoenvironmental engineering* 136 (2009), pp. 918–929.

[230] J. de Araújo and A. Awruch. “Probabilistic finite element analysis of concrete gravity dams”. In: *Advances in Engineering Software* 29 (1998), pp. 97–104.

[231] M. De Biasio et al. “A simple and efficient intensity measure to account for nonlinear structural behavior”. In: *Earthquake Spectra* 30.4 (2014), pp. 1403–1426.

[232] L. De Ceukelaire and D. Van Nieuwenburg. “Accelerated carbonation of a blast-furnace cement concrete”. In: *Cement and Concrete Research* 23 (1993), pp. 442–452.

[233] S. De Grandis, M. Domaneschi, and F. Perotti. “A numerical procedure for computing the fragility of NPP components under random seismic excitation”. In: *Nuclear Engineering and Design* 239.11 (2009), pp. 2491–2499.

[234] G. G. Deierlein, A. M. Reinhorn, and M. R. Willford. *Nonlinear structural analysis for seismic design; A Guide for Practicing Engineers*. National Institute of Science and Technology (NIST) report GCR 10-917-5. 2010.

[235] deLorenzi, H.G. “Energy Release Rate Calculations by the Finite Element Method”. In: *Engineering Fracture Mechanics* 21 (1985), pp. 103–110.

[236] Denarié, E. and Saouma, V.E. and Iocco, A. and Varelas, D. “Concrete Fracture Process Zone Characterization; Part I Experimentallly with Internal Fiber Bragg Grating Sensors”. In: *Journal of Engineering Mechanics* 127.5 (1999), pp. 494–502.

[237] J. Dennis and R. Schnabel. *Numerical Methods for Unconstrained Optimization and Nonlinear Equations*. Englewood Cliffs, 1983.

[238] G. Deodatis, B. R. Ellingwood, and D. M. Frangopol. *Safety, reliability, risk and life-cycle performance of structures and infrastructures*. CRC Press, 2014.

[239] A. Der Kiureghian. “Non-ergodicity and PEER’s framework formula”. In: *Earthquake Engineering and Structural Dynamics* 34.13 (2005), pp. 1643–1652.

[240] A. Der-Kiureghian and O. Ditlevsen. “Aleatory or epistemic? Does it matter?” In: *Structural Safety* 31 (2009), pp. 105–112.

[241] A. Der Kiureghian and J.-B. Ke. “The stochastic finite element method in structural reliability”. In: *Probabilistic Engineering Mechanics* 3.2 (1988), pp. 83–91.

[242] S. S. Desai and D. Choudhury. “Site-specific seismic ground response study for nuclear power plants and ports in Mumbai”. In: *Natural Hazards Review* 16.4 (2015), p. 04015002.

[243] D. J. Deschenes, O. Bayrak, K. J. Folliard, et al. *ASR/DEF-damaged bent caps: shear tests and field implications*. Tech. rep. Austin, TX: Ferguson Structural Engineering Laboratory, The University of Texas, 2009.

[244] R. Dewey, R. Reich, and V. Saouma. “Uplift Modelling for Fracture Mechanics Analysis of Concrete Dams”. In: *ASCE J. of Structural Division* 120.10 (1994), pp. 3025–3044.

[245] T. Diana. “DIANA Finite Element Analysis User’s Manual Release 9.4. 4”. In: *Delft, The Netherlands* (2012).

[246] S. Ding et al. “Extreme learning machine: algorithm, theory and applications”. In: *Artificial Intelligence Review* 44.1 (2015), pp. 103–115.

[247] E. Dipasquale and A. Cakmak. *Identification of the serviceability limit state and detection of seismic structural damage, Report NCEER-88-0022*. Tech. rep. State University of New York, Buffalo NY: National Center for Earthquake Engineering Research, 1988.

[248] E. Dipasquale and A. Cakmak. *On the relation between local and global damage indices, Technical Report NCEER-89-0034*. Tech. rep. State University of New York, Buffalo NY: National Center for Earthquake Engineering Research, 1989.

[249] O. Ditlevsen and H. O. Madsen. *Structural reliability methods*. Vol. 178. Wiley New York, 1996.

[250] T. Dolen. *Materials Properties Model of Aging Concrete*. Tech. rep. Report DSO-05-05. U.S. Department of the Interior, Bureau of Reclamation, Materials Engineering and Research Laboratory, 86-68180, 2005.

[251] T. Dolen. “Selecting Strength Input Parameters for Structural Analysis of Aging Concrete Dams”. In: *21st Century Dam Design; Advances and Adaptations*. 31st Annual USSD Conference. San Diego, California, 2011, pp. 227–243.

[252] M. Dolšek. “Incremental dynamic analysis with consideration of modeling uncertainties”. In: *Earthquake Engineering and Structural Dynamics* 38 (2009), pp. 805–825.

[253] M. Dolšek. “Estimation of Seismic Response Parameters Through Extended Incremental Dynamic Analysis”. In: *Computational Methods in Earthquake Engineering*. Ed. by M. Papadrakakis, M. Fragiadakis, and N. D. Lagaros. Vol. 21. Computational Methods in Applied Sciences. Springer Netherlands, 2011, pp. 285–304.

[254] M. Dolšek. “Simplified method for seismic risk assessment of buildings with consideration of aleatory and epistemic uncertainty”. In: *Structure and infrastructure engineering* 8 (2012), pp. 939–953.

[255] M. Dolšek. “” In: *Encyclopedia of Earthquake Engineering*. Ed. by M. Beer et al. Springer Berlin Heidelberg, 2015, pp. 1–19.

[256] Y. Dong, D. Frangopol, and D. Saydam. “Time-variant sustainability assessment of seismically vulnerable bridges subjected to multiple hazards”. In: *Earthquake Engineering and Structural Dynamics* 42 (2013), pp. 1451–1467.

[257] J Douglas. *Ground Motion Estimation Equations 1964–2010*. 2011.

[258] T. E. Downing et al. “Adapting to climate change in Africa”. In: *Mitigation and adaptation strategies for global change* 2.1 (1997), pp. 19–44.

[259] H. Duda. “Stress-Crack-Opening Relation and Size Effect in High-Strength Concrete”. In: *Darmastad Concrete* 5 (1990), pp. 35–46.

[260] D. Dugdale. “Yielding of Steel Sheets Containing Slits”. In: *J. Mech. Phys. Sol.* 8 (1960), pp. 100–108.

[261] Z. Duron et al. *Dynamic Testing and Numerical Correlation Studies for Folsom Dam*. Tech. rep. ERDC/GSL TR-05-22. US Army Corps of Engineers, Engineer Research and Development Center, 2005.

[262] R. Ebeling, L. Nuss, and F. Tracy. *Evaluation and comparison of stability analysis and uplift criteria for concrete gravity dams by three federal agencies*. Tech. rep. ERDC/ITLL TR-00-1. Army Engineer Waterways Experiment Station Vicksburg Ms Engineer Research . . ., 2000.

[263] K Ebisawa, K Ando, and K Shibata. "Progress of a research program on seismic base isolation of nuclear components". In: *Nuclear Engineering and Design* 198.1-2 (2000), pp. 61–74.

[264] B. Efron et al. "Least angle regression". In: *The Annals of statistics* 32.2 (2004), pp. 407–499.

[265] F. El Mohandes and F. Vecchio. *VecTor3: A. User's Manual; B. Sample Coupled Thermal and Structural Analysis*. Dept. of Civil Engineering, University of Toronto. Toronto, Canada, 2013.

[266] B. Ellingwood and P. Tekie. "Fragility analysis of concrete gravity dams". In: *ASCE Journal of Infrastructure Systems* 7 (2001), pp. 41–48.

[267] B. Ellingwood et al. *Development of a probability based load criterion for American National Standard A58: Building code requirements for minimum design loads in buildings and other structures*. Vol. 13. US Department of Commerce, National Bureau of Standards, 1980.

[268] B. Ellingwood. "Risk-informed condition assessment of civil infrastructure: state of practice and research issues". In: *Structure and infrastructure engineering* 1.1 (2005), pp. 7–18.

[269] B. Ellingwood and K. Kinali. "Quantifying and communicating uncertainty in seismic risk assessment". In: *Structural Safety* 31.2 (2009). Risk Acceptance and Risk CommunicationRisk Acceptance and Risk Communication, pp. 179–187.

[270] B. R. Ellingwood. "Issues related to structural aging in probabilistic risk assessment of nuclear power plants". In: *Reliability Engineering & System Safety* 62.3 (1998), pp. 171–183.

[271] A. S. Elnashai and L. Di Sarno. *Fundamentals of earthquake engineering: from source to fragility*. John Wiley & Sons, 2015.

[272] EPRI. *Individual Plant Examination for External Events (IPEEE) Seismic Insights*. Tech. rep. 1000895. Electric Power Research Institute, 2000.

[273] EPRI. *Seismic Probabilistic Risk Assessment Implementation Guide*. Tech. rep. 3002000709. Electric Power Research Institute, 2003.

[274] EPRI. *Seismic Evaluation Guidance: Augmented Approach for the Resolution of Fukushima Near-Term Task Force Recommendation 2.1 - Seismic*. Tech. rep. 3002000704. Palo-Alto, CA: Electric Power Research Institute, 2013.

[275] EPRI. *Modeling Existing Concrete Containment Structures: Lessons Learned*. Tech. rep. 58 pages. Electric Power Research Company, 2017.

[276] EPRI-1014099. *Program on Technology Innovation: Use of Cumulative Absolute Velocity (CAV) in Determining Effects of Small Magnitude Earth-*

quakes on Seismic Hazard Analyses. Tech. rep. Palo Alto, CA: Electrical Power Research Institute (EPRI), 2006.

[277] EPRI-NP-5930. *A Criterion for Determining Exceedance of the Operating Basis Earthquake*. Tech. rep. Palo Alto, CA: Electrical Power Research Institute (EPRI), 1988.

[278] M. Erberik. "" In: *Encyclopedia of Earthquake Engineering*. Ed. by M. Beer et al. Springer Berlin Heidelberg, 2015, pp. 1–10.

[279] Erdogan, F. and Sih, G.C. "On the Crack Extension in Plates Under Plane Loading and Transverse Shear". In: *Journal of Basic Engineering* 85 (1963), pp. 519–527.

[280] J. Eshelby. "Calculation of energy release rate". In: *Prospect of Fracture Mechanics Nordhoff* (1974), pp. 69–84.

[281] F. Esposito et al. "A comparative analysis of methods for pruning decision trees". In: *IEEE transactions on pattern analysis and machine intelligence* 19.5 (1997), pp. 476–491.

[282] R. Esposito et al. "Influence of the alkali-silica reaction on the mechanical degradation of concrete". In: *Journal of Materials in Civil Engineering* 28.6 (2016), p. 04016007.

[283] H. Estekanchi, A. Vafai, and M. Sadeghazar. "Endurance time method for seismic analysis and design of structures". In: *Scientia Iranica* 11 (2004), pp. 361–370.

[284] P. Fajfar. "A nonlinear analysis method for performance based seismic design". In: *Earthquake Spectra* 16 (2000), pp. 573–592.

[285] P. Fajfar, T. Vidic, and M. Fischinger. "A measure of earthquake motion capacity to damage medium-period structures". In: *Soil Dynamics and Earthquake Engineering* 9 (1990), pp. 236–242.

[286] N. Fajraoui, S. Marelli, and B. Sudret. "Sequential Design of Experiment for Sparse Polynomial Chaos Expansions". In: *SIAM/ASA Journal on Uncertainty Quantification* 5.1 (2017), pp. 1061–1085.

[287] J. Fan et al. "Comparison of Support Vector Machine and Extreme Gradient Boosting for predicting daily global solar radiation using temperature and precipitation in humid subtropical climates: A case study in China". In: *Energy Conversion and Management* 164 (2018), pp. 102–111.

[288] M. Fanelli and G. Lombardi. "On the Lombardi slenderness coefficient for assessing the cracking potential of arch dams". In: *Proceedings of the International Symposium on Arch Dams*. Nanjing, China, 1997.

[289] L. Faravelli. "Response-surface approach for reliability analysis". In: *Journal of Engineering Mechanics* 115.12 (1989), pp. 2763–2781.

[290] F. R. Farmer. *Reactor Safety And Siting: A Proposed Risk Criterion*. Tech. rep. United Kingdom Atomic Energy Authority, Risley, Eng., 1967.

[291] Federal Register. "Improved Identification Techniques Against Alkali-Silica Reaction (ASR) Concrete Degradation at Nuclear Power Plants". In: *Federal Register* 84.228 (2019), pp. 65024–65032.

[292] C. Felippa. *Finite Element Lecture Notes*. Tech. rep. Dept. of Aerospace Engineering, University of Colorado, Boulder, 1999.

[293] C. Felippa. *Lecture Notes in Advanced Finite Element Methods (ASEN 5367)*. Tech. rep. Dept. of Aerospace Engineering, University of Colorado, Boulder, 2000.

[294] FEMA. *NEHRP commentary on the guidelines for seismic rehabilitation of buildings*. Tech. rep. Washington, DC: Federal Emergency Management Agency, 1997.

[295] FEMA. *NEHRP guidelines for seismic rehabilitation of buildings*. Tech. rep. Washington, DC: Federal Emergency Management Agency, 1997.

[296] FEMA. *Prestandard and commentary for the seismic rehabilitation of buildings*. Tech. rep. Washington, DC: Federal Emergency Management Agency, 2000.

[297] FEMA. *Federal guidelines for dam safety risk management*. Tech. rep. Washington, DC: Federal Emergency Management Agency, 2015.

[298] FEMA P-750. "NEHRP recommended seismic provisions for new buildings and other structures (FEMA P-750)". In: *Federal Emergency Management Agency, Washington, DC* (2009).

[299] FEMA-PFM. *Selecting analytic tools for concrete dams to address key events along potential failure mode paths*. Tech. rep. Denver, Colorado: Federal Emergency Management Agency, 2011.

[300] G. A. Fenton and D. V. Griffiths. *Risk assessment in geotechnical engineering*. Vol. 461. Wiley Online Library, 2008.

[301] G. Fenves and A. K. Chopra. "Simplified earthquake analysis of concrete gravity dams". In: *Journal of Structural Engineering* 113.8 (1987), pp. 1688–1708.

[302] G. Fenves and A. Chopra. *EAGD-84: A computer program for earthquake analysis of concrete gravity dams*. University of California, Earthquake Engineering Research Center, 1984.

[303] G. Fenves and A. Chopra. "Earthquake analysis of concrete gravity dams including reservoir bottom absorption and dam-water-foundation rock interaction". In: *Earthquake Engineering and Structural Dynamics* 12 (1984), pp. 663–680.

[304] G. Fenves and A. K. Chopra. "Simplified earthquake analysis of concrete gravity dams: Combined hydrodynamic and foundation interaction effects". In: *Journal of engineering mechanics* 111.6 (1985), pp. 736–756.

[305] G. Fenves and A. K. Chopra. "Simplified earthquake analysis of concrete gravity dams: Separate hydrodynamic and foundation interaction effects". In: *Journal of engineering mechanics* 111.6 (1985), pp. 715–735.

[306] Fenves, Gregory and Chopra, Anil K. *Simplified analysis for earthquake resistant design of concrete gravity dams*. Tech. rep. UCB/EERC-85/10. Berkeley, CA: Earthquake Engineering Research Center, 1986.

[307] FERC. *Engineering guidelines for the evaluation of hydropower projects: Chapter 11: Arch dams*. Tech. rep. Washington, DC, USA: Federal Energy Regulatory Commission, 1999.

[308] FERC. *FERC guidance document: Potential failure mode analysis*. Tech. rep. Federal Energy Regulatory Committee, 2005.

[309] FERC. *Engineering Guidelines for the Evaluation of Hydropower Projects*. Tech. rep. Federal Energy Regulatory Commission, Office of Energy Projects, 2016.

[310] FERC. *Risk-Informed Decision-Making (RIDM), Risk Guidelines For Dam Safety*. Tech. rep. Washington, DC: Federal Energy Regulatory Commission, 2016.

[311] FHWA. *Report on the Diagnostis, Prognosis, and Mitigation of Alkali-Silica Reaction (ASR) in Transportation Structures*. Tech. rep. FHWA-HIF-09-004. Federal Highway Administration, 2010.

[312] E. Field, T. Jordan, and C. Cornel. "OpenSHA: A Developing Community-Modeling Environment for Seismic Hazard Analysis". In: *Seismological Research Letters* 74 (2003), pp. 406–419.

[313] A. Filiatrault, A. Wanitkorkul, and M. Constantinou. *Development and Appraisal of a Numerical Cyclic Loading Protocol for Quantifying Building System Performance*. Tech. rep. MCEER-08-0013. University at Buffalo, State University of New York, 2008.

[314] A. Filiatrault. *Elements of earthquake engineering and structural dynamics*. Presses inter Polytechnique, 2013.

[315] P. Filunger. "*Der Auftrieb in Talsperren*". In: *Österr Wochenschrift für den öffentl. Baudienst* (1913).

[316] R. Foreman, V. Kearney, and R. Engle. "Numerical Analysis of Crack Propagation in Cyclic-Loaded Structures". In: *J. of Basic Engineering* 89 (1967), pp. 459–464.

[317] R. L. Frano, G Pugliese, and G Forasassi. "Preliminary seismic analysis of an innovative near term reactor: Methodology and application". In: *Nuclear Engineering and Design* 240.6 (2010), pp. 1671–1678.

[318] S. Freeman. "Prediction of response of concrete buildings to severe earthquake motion". In: *Proceedings of Douglas McHenry international symposium on concrete and concrete structures*. Ed. by A. C. Institute. Detroit, MI, USA, 1978.

[319] S. Freeman. "The capacity spectrum method". In: *Proceedings of the 11th European conference on earthquake engineering*. Paris, France, 1998.

[320] J. Friedman, T. Hastie, and R. Tibshirani. *The elements of statistical learning*. Vol. 1. Springer series in statistics New York, 2001.

[321] J. H. Friedman. "Multivariate adaptive regression splines". In: *The annals of statistics* (1991), pp. 1–67.

[322] J. H. Friedman and C. B. Roosen. "An introduction to multivariate adaptive regression splines". In: *Statistical Methods in Medical Research* 4.3 (1995), pp. 197–217.

[323] L. Furgani, M. Basili, and C. Nuti. "Base sliding methods for seismic assessment of concrete gravity dams". In: *Proceeding of the 4th ECCOMAS Thematic Conference on Computational Methods in Structural Dynamics and Earthquake Engineering (COMPDYN 2013)*. Kos Island, Greece, 2013.

[324] I. Gabriel-Martin et al. “Influence of initial reservoir level and gate failure in dam safety analysis. Stochastic approach”. In: *Journal of hydrology* 550 (2017), pp. 669–684.

[325] R. Gallagher. *Finite Element Analysis Fundamentals*. Prentice Hall, Englewood Cliffs, N.J., 1975.

[326] P. Gardoni and C. Murphy. “A scale of risk”. In: *Risk analysis* 34.7 (2014), pp. 1208–1227.

[327] E. Gdoutos. *Fracture Mechanics; An Introduction*. Kluwer Academic Press, 1993.

[328] N. A. Gershenfeld and N. Gershenfeld. *The nature of mathematical modeling*. Cambridge university press, 1999.

[329] A. Ghaemmaghami and M. Ghaemian. “Experimental seismic investigation of Sefid-rud concrete buttress dam model on shaking table”. In: *Earthquake Engineering and Structural Dynamics* 37 (2008), pp. 809–823.

[330] A. Ghaemmaghami and M. Ghaemian. “Shaking table test on small-scale retrofitted model of Sefid-rud concrete buttress dam”. In: *Earthquake Engineering and Structural Dynamics* 39 (2009), pp. 109–118.

[331] Y. Ghanaat. “Failure modes approach to safety evaluation of dams”. In: *Proceedings of the 13th World Conference on Earthquake Engineering*. Vancouver, BC, Canada, 2004.

[332] Y. Ghanaat, R. Patev, and A. Chudgar. “Seismic Fragility Analysis of Concrete Gravity Dams”. In: *Proceedings of the 15th World Conference on Earthquake Engineering*. Lisbon, Portugal, 2012.

[333] Y. Ghanaat, R. Patev, and A. Chudgar. “Seismic Fragility For Risk Assessment of Concrete Gravity Dams”. In: *Proceeding of the 2015 USSD Annual Conference*. 2015, pp. 645–660.

[334] Y. Ghanaat et al. “Seismic Fragility of Mühleberg Dam using Nonlinear Analysis with Latin Hypercube Simulation”. In: *Proceeding of the 2011 USSD Annual Conference*. 2011, pp. 1197–1212.

[335] R. G. Ghanem and P. D. Spanos. “Stochastic Finite Element Method: Response Statistics”. In: *Stochastic finite elements: a spectral approach*. Springer, 1991, pp. 101–119.

[336] R. G. Ghanem and P. D. Spanos. *Stochastic finite elements: a spectral approach*. Dover Publications, 2003.

[337] A. Ghobarah. “Performance-based design in earthquake engineering: State of development”. In: *Engineering Structures* 23 (2001), pp. 878–884.

[338] A. Ghobarah and M. Ghaemian. “Experimental Study of Small Scale Dam Models”. In: *Journal of Engineering Mechanics - ASCE* 124 (1998), pp. 1241–1248.

[339] J. Ghosh and J. Padgett. “Aging Considerations in the Development of Time-Dependent Seismic Fragility Curves”. In: *Journal of Structural Engineering* 136 (2010), pp. 1497–1511.

[340] J. Ghosh and J. Padgett. “Aging considerations in the development of time-dependent seismic fragility curves”. In: *Journal of Structural Engineering* 136.12 (2010), pp. 1497–1511.

[341] P. Giorgi and R. Scotta. "Validation and improvement of {N1} method for pushover analysis". In: *Soil Dynamics and Earthquake Engineering* 55 (2013), pp. 140–147.

[342] P. Giovenale, A. Cornell, and L. Esteva. "Comparing the adequacy of alternative ground motion intensity measures for the estimation of structural responses". In: *Earthquake Engineering and Structural Dynamics* 33 (2004), pp. 951–979.

[343] E. Giuriani and G. P. Rosati. "Behaviour of Concrete Elements under Tension After Cracking". In: *Studi e Ricerche, Corso di Perfezionamento per le Costruzioni in Cemento Armato* 8 (1986). (in Italian), pp. 65–82.

[344] V. Gocevski. *Pathologies/Degradation Mechanisms Experienced by Hydro-Quebec During the Evaluation of Gentilly-2 NPP*. Tech. rep. Report submitted to ASCET. Hydro-Quebec, *Equipement et services partagés*, 2015.

[345] Goodman, R.E. and Taylor, R.C. and Brekke, T.C. "A Model for the Mechanics of Jointed Rocks". In: *J. of the Soil Mechanics and FOundations Division ASCE* 94 (1968), pp. 637–659.

[346] V. S. Gopalaratnam and P. S. Shah. "Softening Response of Plain Concrete in Direct Tension". In: *ACI Journal* 82 (1985), pp. 310–323.

[347] V. Gouda. "Corrosion and corrosion inhibition of reinforcing steel". In: *British Corrosion Journal* 5.4 (1970), pp. 198–203.

[348] H. Graves et al. *Expanded Materials Degradation Assessment (EMDA), Volume 4: Aging of Concrete*. Tech. rep. NUREG/CR-ORNL/TM-2011/545. U.S. Nuclear Regulatory Commission, 2013.

[349] A. Griffith. "The Phenomena of Rupture and Flow in Solids". In: *Phil. Trans. Roy. Soc. London* A221 (1921), pp. 163–197.

[350] A. C. F. Guimarães, D. C. Cabral, and C. M. F. Lapa. "Adaptive fuzzy system for degradation study in nuclear power plants' passive components". In: *Progress in Nuclear energy* 48.7 (2006), pp. 655–663.

[351] J. Gulikers. "Experimental investigations on macrocell corrosion in chloride-contaminated concrete". In: *HERON* 41.2 (1996), pp. 107–123.

[352] S. Gunay and K. Mosalam. "PEER performance-based earthquake engineering methodology, revisited". In: *Journal of Earthquake Engineering* 17.6 (2013), pp. 829–858.

[353] A. Guo et al. "Time-dependent seismic demand and fragility of deteriorating bridges for their residual service life". In: *Bulletin of Earthquake Engineering* (2015), pp. 1–21.

[354] B. Gutenberg and C. F. Richter. "Frequency and energy of earthquakes". In: *Seismicity of the Earth and Associated Phenomena* (1954), pp. 17–19.

[355] B. Gutenberg and C. F. Richter. "Earthquake magnitude, intensity, energy, and acceleration". In: *Bulletin of the Seismological Society of America* 32.3 (1942), pp. 163–191.

[356] S. Haberman. "Seabrook Station nuclear plant license advancing". In: *Seacoast On-Line* (2013).

[357] M. Ben Haha. "Mechanical effects of alkali silica reaction in concrete studied by SEM-image analysis". Thèse EPFL 3516. PhD thesis. Ecole Polytechnique Federale de Lausanne, 2006.

[358] Y. Y. Haimes. "On the definition of resilience in systems". In: *Risk Analysis* 29.4 (2009), pp. 498–501.

[359] T Hakata. "Computer model for coincidental failure of nuclear power plants due to seismic events in a multi-unit site". In: *Probabilistic Safety Assessment and Management*. Springer. 2004, pp. 1245–1251.

[360] T. Hakata. "Seismic PSA method for multiple nuclear power plants in a site". In: *Reliability Engineering & System Safety* 92.7 (2007), pp. 883–894.

[361] J. Hallquist. "Livermore Software Technology Corporation". In: *Livermore, Ca* (1998).

[362] J. H. Halton. "Algorithm 247: Radical-inverse quasi-random point sequence". In: *Communications of the ACM* 7.12 (1964), pp. 701–702.

[363] R. Hamburger et al. "The ATC-58 Project: Development of next-generation reformance-based earthquake engineering design criteria for buildings". In: *Proceeding of the 13th World Conferance on Earthquake Engineering*. Vancouver, Canada, 2004.

[364] G. Han. "Understanding regional dynamics of vulnerability: a historical approach to the flood problem in China". PhD thesis. Clark University, Graduate School of Geography, 2011.

[365] E. Hansen and V. Saouma. "Numerical Simulation of Concrete Deterioration; Part I: Chloride Diffusion". In: *ACI Material Journal* 96.2 (1999), pp. 173–180.

[366] E. Hansen and V. Saouma. "Numerical Simulation of Concrete Deterioration; Part II: Steel Corrosion and Concrete Fracture". In: *ACI Material Journal* 96.3 (1999), pp. 331–339.

[367] E. J. Hansen. "Rate Deterioration Investigation of Bridge Decks Based on Diffusion/Fracture Mechanics Numerical Studies". MA thesis. Boulder, CO, U.S.A.: University of Colorado, Dept. Civ. Eng., 1997.

[368] W. Hansen. "Drying shrinkage mechanisms in Portland cement paste". In: *Journal of the American Ceramic society* 70.5 (1987), pp. 323–328.

[369] M. Hao, L. Xie, and L. Xu. "Some considerations on the physical measure of seismic intensity". In: *Acta Seismologica Sinica* 27 (2005), pp. 230–234.

[370] A. Harbitz. "An efficient sampling method for probability of failure calculation". In: *Structural safety* 3.2 (1986), pp. 109–115.

[371] G. Hardy et al. "US Nuclear power industry post-Fukushima seismic response initiatives". In: *Proceedings of the 23rd conference on structural mechanics in reactor technology, Manchester, United Kingdom*. 2015.

[372] M. Hariri-Ardebili, V. Saouma, and C. Merz. "Risk-Informed Conditional Assessment of a Bridge with Alkali Aggregate Reaction". In: *ACI Structural Journal* 115.2 (2018), pp. 475–487.

[373] M. A. Hariri-Ardebili. "Analytical failure probability model for generic gravity dam classes". In: *Proceedings of the Institution of Mechanical Engineers, Part O: Journal of Risk and Reliability* 231.5 (2017), pp. 546–557.

[374] M. A. Hariri-Ardebili and M. R. Kianoush. "Integrative seismic safety evaluation of a high concrete arch dam". In: *Soil Dynamics and Earthquake Engineering* 67 (2014), pp. 85–101.

[375] M. A. Hariri-Ardebili and M. R. Kianoush. "Seismic analysis of a coupled dam-reservoir foundation system considering pressure effects at opened joints". In: *Structure and Infrastructure Engineering* 11 (2015), pp. 833–850.

[376] M. A. Hariri-Ardebili, H. Mirzabozorg, and A. Ghasemi. "Strain-based seismic failure evaluation of coupled dam-reservoir-foundation system". In: *Coupled Systems Mechanics* 2.1 (2013), pp. 85–110.

[377] M. A. Hariri-Ardebili and V. E. Saouma. "Seismic Fragility Analysis of Concrete Dams: A State-of-the-Art Review". In: *Engineering Structures* 128 (2016), pp. 374–399.

[378] M. A. Hariri-Ardebili, S. M. Seyed-Kolbadi, and M. R. Kianoush. "FEM-based parametric analysis of a typical gravity dam considering input excitation mechanism". In: *Soil Dynamics and Earthquake Engineering* 84 (2016), pp. 22–43.

[379] M. Hariri-Ardebili and P Boodagh. "Taguchi design-based seismic reliability analysis of geostructures". In: *Georisk: Assessment and Management of Risk for Engineered Systems and Geohazards* (2018), pp. 1–19.

[380] M. Hariri-Ardebili and H. Mirzabozorg. "A comparative study of the seismic stability of coupled arch dam-foundation-reservoir systems using infinite elements and viscous boundary models". In: *International Journal of Structural Stability and Dynamic* 13 (2013).

[381] M. Hariri-Ardebili and H. Mirzabozorg. "Estimation of probable damages in arch dams subjected to strong ground motions using endurance time acceleration functions". In: *KSCE Journal of Civil Engineering* 18 (2014), pp. 574–586.

[382] M. Hariri-Ardebili and F salazar. "Engaging Soft Computing in Material and Modeling Uncertainty Quantification of Dam Engineering Problems". In: *Soft Computing* 111 (2020), pp. 111–111.

[383] M. Hariri-Ardebili and V. Saouma. "Quantitative failure metric for gravity dams". In: *Earthquake Engineering and Structural Dynamics* 44 (2015), pp. 461–480.

[384] M. Hariri-Ardebili and V. Saouma. "Collapse Fragility Curves for Concrete Dams: Comprehensive Study". In: *ASCE Journal of Structural Engineering* 142.10 (2016), p. 04016075.

[385] M. Hariri-Ardebili and V. Saouma. "Sensitivity and Uncertainty Quantification of the Cohesive Crack Model". In: *Engineering Fracture Mechanics* 155 (2016), pp. 18–35.

[386] M. Hariri-Ardebili and V. Saouma. "Probabilistic seismic demand model and optimal intensity measure for concrete dams". In: *Structural Safety* 59 (2016), pp. 67–85.

[387] M. Hariri-Ardebili and V. Saouma. "Single and multi-hazard capacity functions for concrete dams". In: *Soil Dynamics and Earthquake Engineering* 101 (2017), pp. 234–249.

[388] M. Hariri-Ardebili, V. Saouma, and K. Porter. "Quantification of Seismic Potential Failure Modes in Concrete Dams". In: *Earthquake Engineering and Structural Dynamics* (2016).

[389] M. Hariri-Ardebili et al. "Random finite element method for the seismic analysis of gravity dams". In: *Engineering Structures* 171 (2018), pp. 405–420.

[390] M. A. Hariri-Ardebili. "MCS-based response surface metamodels and optimal design of experiments for gravity dams". In: *Structure and Infrastructure Engineering* (2018), pp. 1–23.

[391] M. A. Hariri-Ardebili. "Risk, Reliability, Resilience (R3) and beyond in dam engineering: A state-of-the-art review". In: *International journal of disaster risk reduction* 31 (2018), pp. 806–831.

[392] M. A. Hariri-Ardebili and S. Barak. "A series of forecasting models for seismic evaluation of dams based on ground motion meta-features". In: *Engineering Structures* (2020), p. 109657.

[393] M. A. Hariri-Ardebili and L. K. Nuss. "Seismic risk prioritization of a large portfolio of dams: Revisited". In: *Advances in Mechanical Engineering* 10.9 (2018), p. 1687814018802531.

[394] M. A. Hariri-Ardebili and F. Pourkamali-Anaraki. "Simplified reliability analysis of multi hazard risk in gravity dams via machine learning techniques". In: *Archives of Civil and Mechanical Engineering* 18.2 (2018), pp. 592–610.

[395] M. A. Hariri-Ardebili and F. Pourkamali-Anaraki. "Support vector machine based reliability analysis of concrete dams". In: *Soil Dynamics and Earthquake Engineering* 104 (2018), pp. 276–295.

[396] M. A. Hariri-Ardebili and V. E. Saouma. "Random Response Spectrum Analysis of Gravity Dam Classes: Simplified, Practical and Fast Approach". In: *Earthquake Spectra* (2018).

[397] M. A. Hariri-Ardebili, S. M. Seyed-Kolbadi, and M. Noori. "Response Surface Method for Material Uncertainty Quantification of Infrastructures". In: *Shock and Vibration* 2018 (2018).

[398] M. A. Hariri-Ardebili and B. Sudret. "Polynomial chaos expansion for uncertainty quantification of dam engineering problems". In: *Engineering Structures* (2020), p. 109631.

[399] M. A. Hariri-Ardebili et al. "Anatomy of the vibration characteristics in old arch dams by random field theory". In: *Engineering Structures* 179 (2019), pp. 460–475.

[400] M. Harr. *Reliability Based Design in Civil Engineering*. New York: McGraw Hill, 1987.

[401] J. R. Harrald et al. *Review of risk based prioritization/decision making methodologies for dams*. Tech. rep. Washington, DC: US army corps for engineers, The George Washington University, Institute for Crisis, Disaster, and Risk Management, 2004.

[402] D. Hartford and G. Baecher. *Risk and uncertainty in dam safety*. Tech. rep. London, UK: Thomas Telford, Ltd, 2004.

[403] D. Hartford et al. “Operational Safety of Dams and Reservoirs - Understanding the Reliability of Flow-Control Systems”. In: *ICE Publishing, London* (2016).

[404] C. Haselton et al. “Accounting for ground-motion spectral shape characteristics in structural collapse assessment through an adjustment for epsilon”. In: *Structural Engineering* 137.3 (2011), pp. 332–344.

[405] C. Haselton et al. *An assessment to benchmark the seismic performance of a code-conforming reinforced concrete moment-frame building, PEER report 2007/12*. Tech. rep. Berkeley, Califprnia: Pacific Earthquake Engineering Research Center, University of California, 2008.

[406] A. Hashemi. *Soil Structure Interaction Effects on a Nuclear Containment Structure*. Tech. rep. Redacted Report. Bechtel National, Inc., 2012.

[407] A. M. Hasofer and N. C. Lind. “Exact and invariant second-moment code format(for reliability analysis in multivariate problems)”. In: *American Society of Civil Engineers, Engineering Mechanics Division, Journal* 100 (1974), pp. 111–121.

[408] T. Hastie, R. J. Tibshirani, and J. H. Friedman. *The elements of statistical learning: data mining, inference, and prediction*. Springer, 2011.

[409] Hastie, T.J. and Tibshirani, R.J. *Generalized Additive Models*. Chapman and Hall: New York, 1990.

[410] D. Hayward et al. “Engineering and Construction Options for the Management of Slow/Late Alkali-Aggregate Reactive Concrete”. In: *16th International Congress of Large Dams, Q62?C R33?* San Francisco, 1988.

[411] T. Hellen and W. Blackburn. “The calculation of stress intensity factor for combined tensile and shear loading”. In: *Int. J. Fract.* 11 (1975), pp. 605–617.

[412] R. D. Henshell and K. G. Shaw. “Crack Tip Elements Are Unnecessary”. In: *International Journal of Numerical Methods in Engineering* 9.3 (1975), pp. 495–509.

[413] E. Hernandez-Montes, O. Kwon, and M. Aschheim. “An Energy-Based Formulation For First-And Multiple-Mode Nonlinear Static (Pushover) Analyses”. In: *Journal of Earthquake Engineering* 8 (2004), pp. 69–88.

[414] B. H. Hertlein. “Assessing the role of steel corrosion in the deterioration of concrete in the national infrastructure: A review of the causes of corrosion and current diagnostic techniques”. In: *Corrosion Forms & Control for Infrastructure*. San Diego, CA, 1992.

[415] Hessheimer, M.F. and Dameron, R.A. *NUREG/CR-6906 SAND2006-2274P: Containment Integrity Research at Sandia National Laboratories; An Overview*. 2006.

[416] H Hilber, T. Hughes, and R. Taylor. “Improved Numerical Dissipation for Time Integration Algorithms in Structural Dynamics”. In: *Earthquake Engineering and Structral Dynamics* 5 (1977), pp. 283–292.

[417] P. Hill et al. “Estimating overall risk of dam failure: practical considerations in combining failure probabilities”. In: *ANCOLD 2003 Risk Workshop*. 2003.

[418] P. Hill et al. “On the art of event tree modeling for portfolio risk analyses”. In: *NZSOLD/ANCOLD 2001 Conference on Dams*. 2001.

[419] A. Hillerborg, M. Modéer, and P. Petersson. “Analysis of Crack Formation and Crack Growth in Concrete by Means of Fracture Mechanics and Finite Elements”. In: *Cement and Concrete Research* 6.6 (1976), pp. 773–782.

[420] A. Hillerborg, M. Modéer, and P. Petersson. “Analysis of Crack Formation and Crack Growth in Concrete by Means of Fracture Mechanics and Finite Elements”. In: *Cement and Concrete Research* 6.6 (1976), pp. 773–782.

[421] D. Ho and R. Lewis. “Carbonation of concrete and its prediction”. In: *Cement and Concrete Research* 17 (1987), pp. 489–504.

[422] D. Ho and R. Lewis. “The specification of concrete for reinforcement protection-performance criteria and compliance by strength”. In: *Cement and Concrete Research* 18.4 (1988), pp. 584–594.

[423] D. Hobbs. “Influence of aggregate restraint on the shrinkage of concrete”. In: *Journal Proceedings*. Vol. 71. 9. 1974, pp. 445–450.

[424] M. Hori and S. Nemat-Nasser. “Interacting micro-cracks near the tip in the process zone of a macro-crack”. In: *Journal of the Mechanics and Physics of Solids* 35.5 (1987), pp. 601–629.

[425] S. M. Hoseyni et al. “Effects of soil-structure interaction on fragility and seismic risk; a case study of power plant containment”. In: *Journal of Loss Prevention in the Process industries* 32 (2014), pp. 276–285.

[426] M Hoshiya and Z Hasgur. “AR and MA models of nonstationary ground motion”. In: *Bull. Int. Inst. Seismol. Earthq. Eng.* 16 (1978), pp. 55–68.

[427] F. Hossain et al. “Local-to-regional landscape drivers of extreme weather and climate: implications for water infrastructure resilience”. In: *Journal of Hydrologic Engineering* 20.7 (2015), p. 02515002.

[428] G. Housner. “Measures of severity of earthquake ground shaking”. In: *Proceedings of the U.S. National Conference on Earthquake Engineering*. Ann Arbor, MI., 1975, pp. 25–33.

[429] Y. Houst. “Microstructural Changes of Hydrated Cement Paste Due to Carbonisation”. In: *Mechanisms of Chemical Degradation of Cement-Based Systems*. Ed. by K. Scrivener, J. Young, and L. E & FN Spon. 1997.

[430] Y. Houst, P. Roelfstra, and F. Wittmann. “A model to predict service life of concrete structures”. In: *Proceedings of International Colloquim on Material Science and Restoration*. Filderstadt, 1983.

[431] COMSOL. 2019.

[432] HSE. *Reducing risks, protecting people: HSE’s Decisionmaking process, Risk assessment policy unit*. Tech. rep. London, England: Health and Safety Executive (HSE), 2001.

[433] T. Hsu et al. “Micro cracking of Plain Concrete and the Shape of the Stress-Strain Curve”. In: *Journal of the American Concrete Institute* 60 (1963), pp. 209–224.

[434] S. Huaizhi, H. Jiang, and Z. Wen. “Service Life Predicting of Dam Systems with Correlated Failure Modes”. In: *ASCE Journal of Performance of Constructed Facilities* 27 (2013), pp. 252–269.

[435] G. Huang et al. “Trends in extreme learning machines: A review”. In: *Neural Networks* 61 (2015), pp. 32–48.

[436] G.-B. Huang, Q.-Y. Zhu, and C.-K. Siew. “Extreme learning machine: theory and applications”. In: *Neurocomputing* 70.1-3 (2006), pp. 489–501.

[437] H. Huang and B. Spencer. “Grizzly model for fully coupled heat transfer, moisture, diffusion, alkali-silica reaction and fractureing process in concrete”. In: 9th *International Conference on Fracture Mechanics of Concrete and Concrete Structures; FraMCoS-9*. Ed. by V. Saouma, J. Bolander, and E. Landis. Berkeley, CA, 2016.

[438] H. Huang, B. Spencer, and G. Cai. *GRIZZLY Model of Multi-Reactive Species Diffusion, Moisture/Heat Transfer and Alkali-Silica Reaction for Simulating Concrete Aging and Degradation*. Tech. rep. Idaho National Laboratory (INL), Idaho Falls, ID (United States), 2015.

[439] H. Huang, B. Spencer, and G. Cai. *Grizzly Model of Multi-Species Reactive Diffusion, Moisture/Heat Transfer, and Alkali-Silica Reaction in Concrete*. Tech. rep. INL/EXT-15-36425. Idaho Falls, Idaho 83415: Idaho National Laboratory, 2015.

[440] X. Huang et al. “Evaluation of CANDU NPP containment structure subjected to aging and internal pressure increase”. In: *Nuclear Engineering and Design* 314 (2017), pp. 82–92.

[441] Y.-N. Huang, A. S. Whittaker, and N. Luco. “Seismic performance assessment of base-isolated safety-related nuclear structures”. In: *Earthquake Engineering & Structural Dynamics* 39.13 (2010), pp. 1421–1442.

[442] Y.-N. Huang, A. S. Whittaker, and N. Luco. “A probabilistic seismic risk assessment procedure for nuclear power plants:(I) Methodology”. In: *Nuclear Engineering and Design* 241.9 (2011), pp. 3996–4003.

[443] Y.-N. Huang, A. S. Whittaker, and N. Luco. “A probabilistic seismic risk assessment procedure for nuclear power plants:(II) Application”. In: *Nuclear Engineering and Design* 241.9 (2011), pp. 3985–3995.

[444] Y.-N. Huang et al. “Response of base-isolated nuclear structures for design and beyond-design basis earthquake shaking”. In: *Earthquake Engineering & Structural Dynamics* 42.3 (2013), pp. 339–356.

[445] C. Hudson and S. Seward. *A Compendium of Sources of Fracture Toughness and Fatigue Crack Growth Data for Metallic alloys*. Vol. 14. Int. J. of Fracture, 1978, R151–R184.

[446] C. Hudson and S. Seward. “A Compendium of Sources of Fracture Toughness and Fatigue Crack Growth Data for Metallic Alloys”. In: *Int. J. of Fracture, Part II* 20 (1982), R59–R117.

[447] M. Hudson, I. Idriss, and M. Beikae. *QUAD4M A Computer Program to Evaluate the Seismic Response of Soil Structures Using Finite Element Procedures and Incorporating a Compliant Base*. Tech. rep. Center for Geotechnical Modeling Department of Civil & Environmental Engineering University of California Davis, 1994.

[448] I. Hughes and T. Hase. *Measurements and their uncertainties: a practical guide to modern error analysis*. Oxford University Press, 2010.

[449] T. Hughes. *The Finite Element Method*. Prentice-Hall, 1987.
[450] T. Hughes. "Analysis of Transient Algorithms with Particular Reference to Stability Behavior". In: *Computational Methods for Transient Analysis*. Ed. by T. Belytschko and T. Hughes. Elsevier Science Publishers B.V., 1983, pp. 67–155.
[451] F. Hunkeler, C. Merz, and A. Griesser. "Langzeiterfahrung in der Schweiz". In: *Conference on Alkali Silica Reaction*. 2005.
[452] M. Hussain, S. Pu, and J. Underwood. "Strain Energy Release Rate for a Crack Under Combined Mode I and Mode II". In: *ASTM, STP 560* (1974), pp. 2–28.
[453] L. Hutton and D. M. Boore. "The ML scale in southern California". In: *Bulletin of the Seismological Society of America* 77.6 (1987), pp. 2074–2094.
[454] IAEA. *Evaluation of Seismic Safety for Existing Nuclear Installations*. Tech. rep. NS-G-2.13. Vienna: International Atomic Energy Agency, 2009.
[455] ICOLD. *Lessons from dam incidents, Complete edition*. Tech. rep. Paris, France: International Commission on Large Dams, 1974.
[456] ICOLD. "A2. Imminent failure flood for a concrete gravity dam". In: *5th International Benchmark Workshop on Numerical Analysis of Dams*. Denver, CO, USA, 1999.
[457] ICOLD. *Bulletin on risk assessment in dam safety management*. Tech. rep. Paris, France: International Commission on Large Dams, 2005.
[458] N. Ihekwaba, B. Hope, and C. Hansson. "Carbonation and Electrochemical Chloride Extraction From Concrete". In: *Cement and Concrete Research* 26.7 (1996), pp. 1095–1107.
[459] R. Iman and W. Conover. "A distribution-free approach to inducing rank correlation among input variables". In: *Communications in Statistics-Simulation and Computation* B11 (1982), pp. 311–334.
[460] C. Inglis. "Stresses in a Plate Due to the Presence of Cracks and Sharp Corners". In: *Trans. Inst. Naval Architects* 55 (1913), pp. 219–241.
[461] A. Ingraffea and C. Manu. "Stress Intensity Factor Computation in Three Dimension with Quarter-Point Elements". In: *Int. J. num. Meth. Engng.* 15.10 (1980), pp. 1427–1445.
[462] S. Inoue et al. "Effect Of Rupture Of Shear Reinforcement On Shear Capacity Of ASR Damaged Reinforced Concrete Beams". In: *Proceedings of the 13th International Conference on Alkali-Aggregate Reaction in Concrete*. Ed. by Broekmans, MA and Wigum, BJ. 2008.
[463] Institution of Structural Engineers. *Structural effects of alkali-silica reaction. Technical guidance on the appraisal of existing structures*. Tech. rep. Report of an ISE task group, 1992.
[464] K. Ioannidou, R. Pellenq, and E. Del Gado. "Controlling local packing and growth in calcium–silicate–hydrate gels". In: *Soft Matter* 10.8 (2014), pp. 1121–1133.

[465] I. Ioannou and T. Rossetto. "Empirical Fragility". In: *Encyclopedia of Earthquake Engineering*. Ed. by M. Beer et al. Springer Berlin Heidelberg, 2014, pp. 1–12.
[466] G. Irwin. "Analysis of Stresses and Strains Near the End of a Crack Traversing a Plate". In: *Transactions ASME, J. Appl. Mech.* 24 (1957).
[467] G. Irwin. "Plastic Zone Near a Crack and Fracture Toughness". In: *Proc. 7th Sagamore Conf.* 1960, p. 63.
[468] F. Jalayer. "Direct probabilistic seismic analysis: implementing non-linear dynamic assessments". PhD thesis. Palo-Alto, CA: Stanford University, 2003.
[469] F. Jalayer, R. De Risi, and G. Manfredi. "Bayesian Cloud Analysis: efficient structural fragility assessment using linear regression". In: *Bulletin of Earthquake Engineering* 13.4 (2015), pp. 1183–1203.
[470] F. Jalayer, P. Franchin, and P. Pinto. "A scalar damage measure for seismic reliability analysis of RC frames". In: *Earthquake Engineering and Structural Dynamics* 36 (2007), pp. 2059–2079.
[471] S. Jankovic and B. Stojadinovic. "Probabilistic performance-based seismic demand model for {R/C} frame buildings". In: *Proceeding of the 13th World Conferance on Earthquake Engineering*. Vancouver, B.C., Canada, 2004.
[472] Japanese Society of Civil Engineers. *Dynamic Analysis and Earthquake Resistant Design; Volume 2 Methods of Dynamic Analysis*. Section 4.2. Balkema, 2000.
[473] JATR. *Boeing 737 MAX Flight Control System; Observations, Findings, and Recommendations*. 2019.
[474] F. Javanmardi, P. Leger, and R. Tinawi. "Seismic Water Pressure in Cracked Concrete Gravity Dams: Experimental Study and Theoretical Modeling". In: *ASCE J. of Structural Engineering* 131.1 (2005), pp. 139–150.
[475] F. Javanmardi, P. Leger, and R. Tinawi. "Seismic Water Pressure in Cracked Concrete Gravity Dams: Experimental Study and Theoretical Modeling". In: *ASCE Journal of Structural Engineering* 131 (2005), pp. 139–150.
[476] N. Jayaram, T. Lin, and J. Baker. "A Computationally Efficient Ground-Motion Selection Algorithm for Matching a Target Response Spectrum Mean and Variance". In: *Earthquake Spectra* 27 (2011), pp. 797–815.
[477] F. L. Jeang and N. M. Hawkins. *Nonlinear Analysis of Concrete Fracture*. Structures and Mechanics Report. Seattle, WA: Department of Civil Engineering, University of Washington, 1985.
[478] Y. Jenq and S. P. Shah. "Two parameter fracture model for concrete". In: *Journal of engineering mechanics* 111.10 (1985), pp. 1227–1241.
[479] J. Jeppsson. "Reliability-based assessment procedures for existing concrete structures". PhD thesis. Lund University, 2003.
[480] M. Jirasek and Z. Bažant. *Inelastic Analysis of Structures*. John Wiley, Chichester, 2001.
[481] S. Joe and F. Y. Kuo. *Notes on generating Sobol sequences*. 2008.
[482] C. A. Jones and L. Heitman. *Study of Post tensioning Methods*. Tech. rep. NUREG/CR-7208. U.S. Nuclear Regulatory Commission, 2015.

[483] D. Jones. *Principles and Prevention of Corrosion*. Prentice-Hall, 1995.
[484] B. Ju and W. Jung. "Evaluation of Seismic Fragility of Weir Structures in South Korea". In: *Mathematical Problems in Engineering* 2015 (2015), p. 10.
[485] J. Kabanda, O.-S. Kwon, and G. Kwon. "Time and frequency domain analyses of the Hualien Large-Scale seismic test". In: *Nuclear Engineering and Design* 295 (2015), pp. 261–275.
[486] V. Kadkhodayan, M. Aghajanzadeh, and H. Mirzabozorg. "Seismic Assessment of Arch Dams Using Fragility Curves". In: *Civil Engineering Journal* 1.2 (2015), pp. 14–20.
[487] K. Kaila and H. Narain. "A new approach for preparation of quantitative seismicity maps as applied to Alpide belt-Sunda arc and adjoining areas". In: *Bulletin of the Seismological Society of America* 61.5 (1971), pp. 1275–1291.
[488] M. Kaplan. "Crack Propagation and The Fracture of Concrete". In: *Journal of the American Concrete Institute* 58.5 (1961), pp. 591–610.
[489] A. Kappos. "Seismic damage indices for RC buildings: evaluation of concepts and procedures". In: *Progress in Structural Engineering and Materials* 1 (1997), pp. 78–87.
[490] A. Kappos et al. "A hybrid method for the vulnerability assessment of R/C and URM buildings". In: *Bulletin of Earthquake Engineering* 4.4 (2006), pp. 391–413.
[491] E. Karacabeyli. "Lateral Resistance of Nailed Shear Walls Subjected to Static and Cyclic Displacements". In: *Research Report, FPS 49th Annual Meeting*. Portland, OR, USA, 1998.
[492] J. X. Kasperson and R. E. Kasperson. *The social contours of risk: publics, risk communication and the social amplification of risk*. Vol. 1. Earthscan, 2005.
[493] E. Katsaragakis. "On the Compressive Strength of Concrete Damage by Previous Transverse Tension and Cracking". In: *Studies and Research, Annual Review of Structural Concrete*. Vol. 29. Politecnico of Milan, 2009.
[494] A. Kazantzi, D. Vamvatsikos, and D. Lignos. "Seismic performance of a steel moment-resisting frame subject to strength and ductility uncertainty". In: *Engineering Structures* 78 (2014), pp. 69–77.
[495] A. Kelly. *Strong Solids*. second. Oxford University Press, 1974.
[496] J. G. Kemeny. "Report of the President's commission on the accident at Three Mile Island". In: *The need for change: The Legacy of TMI* (1979).
[497] K. Kenkyusho. *SuperFLUSH/3D*. 1995.
[498] R. Kennedy and M. Ravindra. "Seismic fragilities for nuclear power plant risk studies". In: *Nuclear Engineering and Design* 79.1 (1984), pp. 47–68.
[499] R. Kennedy et al. "Probabilistic seismic safety study of an existing nuclear power plant". In: *Nuclear Engineering and Design* 59 (1980), pp. 315–338.
[500] D. Kent and R. Park. "Flexural Members with Confined Concrete". In: *Journal of the Structural Division, ASCE* 97.ST7 (1971).

[501] C. Kesler, D. Naus, and J. Lott. “Fracture mechanics-its applicability to concrete”. In: *Proceedings of the Society of Materials Science Conference on the Mechanical Behavior of Materials*. Conf Paper. 1972.

[502] A. I. Khuri and S. Mukhopadhyay. “Response surface methodology”. In: *Wiley Interdisciplinary Reviews: Computational Statistics* 2.2 (2010), pp. 128–149.

[503] J. H. Kim, I.-K. Choi, and J.-H. Park. “Uncertainty analysis of system fragility for seismic safety evaluation of NPP”. In: *Nuclear Engineering and Design* 241.7 (2011), pp. 2570–2579.

[504] G. Kirsch. “Die Theorie der Elastizitat und die Bedurfnisse der Festigkeitslehre”. In: *Zeit Verein Deutsch Ing* 42 (1898), pp. 797–807.

[505] J.-U. Klügel. “Problems in the application of the SSHAC probability method for assessing earthquake hazards at Swiss nuclear power plants”. In: *Engineering Geology* 78.3-4 (2005), pp. 285–307.

[506] J. Knowles and E. Stenberg. “On a class of conservation laws in linearized and finite elastostatics”. In: *Arch. Rat. Mech. Anal.* 44 (1972), pp. 187–211.

[507] A. Kostinakis, A. Athanatopoulou, and K. Morfidis. “Correlation between ground motion intensity measures and seismic damage of 3D R/C buildings”. In: *Engineering Structures* 82 (2015), pp. 151–167.

[508] I. Koutromanos et al. “Numerical modeling of masonry-infilled RC frames subjected to seismic loads”. In: *Computers and Structures* 89 (2011), pp. 1026–1037.

[509] H. Krawinkler. “Chanllenges and Progress in performance-based earthquake engineering”. In: *International Seminar on Seismic Engineering for Tomorrow*. Tokyo, Japan, 1999.

[510] J. Kreider and A. Rabl. *Heating and Cooling of Buildings*. Hightstown, NJ: McGraw-Hill, Inc, 1994.

[511] P. Kronenberg, C. Hammerschlag J.G. andMerz, and B. Houriet. *A9 - Viaducs de Chillon; Diagnostic relatif à la réaction alcali-granulats du béton*. Tech. rep. TFB & Holcim & gvh, 2013.

[512] M. Kuhn and K. Johnson. *Applied predictive modeling*. Vol. 26. Springer, 2013.

[513] M. Kumar, A. S. Whittaker, and M. C. Constantinou. “Extreme earthquake response of nuclear power plants isolated using sliding bearings”. In: *Nuclear Engineering and Design* 316 (2017), pp. 9–25.

[514] M. Kumar et al. “Seismic probabilistic risk assessment for seismically isolated safety-related nuclear facilities”. In: *Nuclear Engineering and Design* 313 (2017), pp. 386–400.

[515] R. Kumar. “Decision tree for the weather forecasting”. In: *International Journal of Computer Applications* 76.2 (2013), pp. 0975–8887.

[516] S. Kumar, P. Raychowdhury, and P. Gundlapalli. “Response analysis of a nuclear containment structure with nonlinear soil–structure interaction under bi-directional ground motion”. In: *International Journal of Advanced Structural Engineering (IJASE)* 7.2 (2015), pp. 211–221.

[517] S. Kunnath, A. Reinhorn, and R. Lobo. *IDARC version 3: A program for the inelastic damage analysis of RC structures, Technical Report NCEER-92-0022*. Tech. rep. State University of New York, Buffalo NY: National Center for Earthquake Engineering Research, 1992.

[518] B. Kupfer and K. Gerstle. "Behavior of Concrete under Biaxial Stresses". In: *ASCE Journal of the Engineering Mechanics Division* 99.4 (1973), pp. 853–866.

[519] Y. Kurama and K. Farrow. "Ground motion scaling methods for different site conditions and structure characteristics". In: *Earthquake Engineering and Structural Dynamics* 32 (2003), pp. 2425–2450.

[520] D. Lallemant, A. Kiremidjian, and H. Burton. "Statistical procedures for developing earthquake damage fragility curves". In: *Earthquake Engineering and Structural Dynamics* 44 (2015), pp. 1373–1389.

[521] E. N. Landis. "Damage variables based on three-dimensional measurements of crack geometry". In: *Strength, fracture and complexity* 3.2-4 (2005), pp. 163–173.

[522] J. Lapajne and P. Fajfar. "Seismic hazard reassessment of an existing NPP in Slovenia". In: *Nuclear engineering and design* 175.3 (1997), pp. 215–226.

[523] C. Larive. *Apports Combinés de l'Experimentation et de la Modélisation à la Comprehension del'Alcali-Réaction et de ses Effets Mécaniques*. Tech. rep. *In French*. Paris: *Ecole Normale des Ponts et Chaussées*, 1998.

[524] H Le Chatelier. "Sur les changements de volume qui accompagnent le durcissement des ciments". In: *Bulletin Societe de l'encouragement pour l'industrie nationale* 5 (1900).

[525] T. D. Le Duy, D. Vasseur, and E. Serdet. "Probabilistic Safety Assessment of twin-unit nuclear sites: Methodological elements". In: *Reliability Engineering & System Safety* 145 (2016), pp. 250–261.

[526] G. Lebon, V. Saouma, and Y. Uchita. "3D rock-dam seismic interaction". In: *Dam Engineering* 21 (2010).

[527] Leclerc, M. and Léger, P. and Tinawi, R. *CADAM User's manual, version 1.4.3*. Tech. rep. Department of Civil, Geotechnical, and Mining Engineering, École Polytechnique de Montréal, 2001.

[528] H. Lee et al. "Simplified model and seismic response of integrated nuclear containment system based on frequency adaptive lumped-mass stick modeling approach". In: *KSCE Journal of Civil Engineering* 19.6 (2015), pp. 1757–1766.

[529] J. Lee and G. Fenves. "Plastic-damage model for cyclic loading of concrete structures". In: *Journal of engineering mechanics* 124.8 (1998), pp. 892–900.

[530] A. Leemann. *Personal Communication*. EMPA/Switzerland, 2019.

[531] Y. Lei et al. "Rethinking the relationships of vulnerability, resilience, and adaptation from a disaster risk perspective". In: *Natural hazards* 70.1 (2014), pp. 609–627.

[532] Q. Li and Q. Ren. "Research on determining solid structure critical load and failure mode". In: *Engineering Failure Analysis* 32 (2013), pp. 113–123.

[533] Q. Li, C. Wang, and B. R. Ellingwood. "Time-dependent reliability of aging structures in the presence of non-stationary loads and degradation". In: *Structural Safety* 52 (2015), pp. 132–141.

[534] X. Li et al. "Irreversible desiccation shrinkage of cement paste caused by cement grain dissolution and hydrate precipitation". In: *Materials and Structures* 50.2 (2017), p. 104.

[535] Y Li et al. "Resilience and sustainability: an integrated method for quantitative assessment of a bridge–a case study". In: *WIT Transactions on The Built Environment* 164 (2016), pp. 25–37.

[536] Li, F. Z. and Shih, C. F. and Needleman, A. "A Comparison of Methods for Calculating Energy Release Rates". In: *Engineering Fracture Mechanics* 21.2 (1985), pp. 405–421.

[537] J. Liaudat et al. "ASR expansions in concrete under triaxial confinement". In: *Cement and Concrete Composites* 86 (2018), pp. 160–170.

[538] A. Liel et al. "Incorporating modeling uncertainties in the assessment of seismic collapse risk of buildings". In: *Structural Safety* 31 (2009), pp. 197–211.

[539] H. Lilliefors. "On the Kolmogorov-Smirnov test for normality with mean and variance unknown". In: *Journal of the American Statistical Association* 62.318 (1967), pp. 399–402.

[540] L. Lin and J. Adams. "Lessons for the fragility of Canadian hydropower components under seismic loading". In: *Proceedings of the 9th Canadian Conference on Earthquake Engineering*. Ottawa, Ontario, Canada, 2007, pp. 1762–1771.

[541] L. Lin and J. Adams. "Seismic vulnerability and prioritization ranking of dams in Canada". In: *Proceedings of the 14th World Conference on Earthquake Engineering*. Beijing, China, 2008.

[542] T. Lin and J. Baker. "Conditional Spectra". In: *Encyclopedia of Earthquake Engineering*. Ed. by M. Beer et al. Berlin, Heidelberg: Springer Berlin Heidelberg, 2014, pp. 1–13.

[543] A. Liners. "Microcracking of concrete under compression and its influence on tensile strength". In: *Materials and structures* 20.2 (1987), pp. 111–116.

[544] J. Liu et al. "Stability assessment of the Three-Gorges Dam foundation, China, using physical and numerical modeling - Part I: physical model tests". In: *International Journal of Rock Mechanics and Mining Sciences* 40 (2003), pp. 609–631.

[545] A. Løkke and A. Chopra. *Response spectrum analysis of concrete gravity dams including dam-water-foundation interaction*. Tech. rep. Berkeley, CA: Pacific Earthquake Engineering Research Center Headquarters at the University of California, Berkeley, 2013.

[546] A. Løkke and A. K. Chopra. "Response spectrum analysis of concrete gravity dams including dam-water-foundation interaction". In: *Journal of Structural Engineering* 141.8 (2014), p. 04014202.

[547] W. R. Lorman. "The theory of concrete creep". PhD thesis. University of Colorado, 1939.

[548] Los Angeles Times. *How San Onofre's new steam generators sealed nuclear plant's fate*. 2013.

[549] A. Lupoi and C. Callari. "The Role of Probabilistic Methods in Evaluating the Seismic Risk of Concrete Dams". In: *Protection of Built Environment Against Earthquakes*. Ed. by M. Dolšek. Springer, 2011, pp. 309–329.

[550] A. Lupoi and C. Callari. "A probabilistic method for the seismic assessment of existing concrete gravity dams". In: *Structure and Infrastructure Engineering* 8 (2012), pp. 985–998.

[551] P. Lura, O. M. Jensen, and K. Van Breugel. "Autogenous shrinkage in high-performance cement paste: An evaluation of basic mechanisms". In: *Cement and concrete research* 33.2 (2003), pp. 223–232.

[552] P. Lynn and A. Ingraffea. "Transition Elements to be used with Quarter-Point Crack-Tip Elements". In: *Int. J. num. Meth. Engng.* 11 (1977), pp. 1031–1036.

[553] J. Lysmer and L. Drake. "A Finite Element Method for Seismology". In: *Methods in Computational Physics* 11 (1972), pp. 181–216.

[554] J. Lysmer and R. Kuhlemeyer. "Finite dynamic model for infinite media". In: *Journal of the Engineering Mechanics Division* 95.4 (1969), pp. 859–878.

[555] J. Lysmer and R. Kuhlemeyer. "Finite Element Model for Infinite Media". In: *ASCE Journal of Engineering Mechanics* 95.EM 4 (1969), pp. 859–877.

[556] J. Lysmer, T. Udaka, and H. Seed. *FLUSH A computer Program for Approximate 3D Analysis of Soil-Structure Interaction Problems*. Tech. rep. UCB/EERC-75/30. Earthquake Engineering Research Center, University of California: Berkeley, CA., 1975.

[557] K. Mackie and B. Stojadinovic. *Seismic demands for performance-based design of bridges*. Tech. rep. CA, US: Pacific Earthquake Engineering Research Center, University of California Berkeley, 2003.

[558] K. R. Mackie et al. "Sustainability metrics for performance-based seismic bridge response". In: *Journal of Structural Engineering* 142.8 (2015), p. C4015001.

[559] K. Mackie and B. Stojadinovic. *Fragility basis for California highway overpass bridge seismic decision making*. Pacific Earthquake Engineering Research Center, University of California, Berkeley, 2005.

[560] I. Magne, L. Granger, and P. Guinet. "Prévision du fluage et du gonflement du caisson UNGG de Saint-Laurent". In: *Revue française de génie civil* 2.1 (1998), pp. 123–142.

[561] S. Malla. "Earthquake safety assessment of arch dams based on nonlinear dynamic analyses". In: *Proceedings of the 12th International Benchmark Workshop on Numerical Analysis of Dams*. GRAZ, AUSTRIA, 2013.

[562] S. Malla and M. Wieland. "Analysis of an arch gravity dam with a horizontal crack". In: *Computers and Structures* 72 (1999), pp. 267–278.

[563] S. Malla and M. Wieland. "Analysis of an arch-gravity dam with a horizontal crack". In: *Computers & Structures* 72.1 (1999), pp. 267–278.

[564] L. Malvar and J. Crawford. "Dynamic Increase Factors for Concrete". In: *Twenty-Eighth DDESB Seminar*. Orlando, FL., 1998.

[565] J. Mander et al. “Incremental dynamic analysis applied to seismic financial risk assessment of bridges”. In: *Engineering Structures* 29 (2007), pp. 2662–2672.

[566] S. B. Manyena and S. Gordon. “Bridging the concepts of resilience, fragility and stabilisation”. In: *Disaster Prevention and Management* 24.1 (2015), pp. 38–52.

[567] D. Marchese et al. “Resilience and sustainability: Similarities and differences in environmental management applications”. In: *Science of the Total Environment* 613 (2018), pp. 1275–1283.

[568] S. Marelli, R. Schobi, and B. Sudret. *UQLab user manual - Structural Reliability*. Tech. rep. Report UQLab-V0.92-107. Chair of Risk, Safety and Uncertainty Quantification, ETH Zurich, 2016.

[569] S Marelli and B Sudret. *Report UQLab-V0.9-104: UQLab user manual–Polynomial chaos expansions*. Tech. rep. Chair of Risk, Safety & Uncertainty Quantification, ETH Zürich, 0.9-104 edition, 2015.

[570] S. Marelli and B. Sudret. “UQLab: A framework for uncertainty quantification in Matlab”. In: *Vulnerability, Uncertainty, and Risk: Quantification, Mitigation, and Management*. 2014, pp. 2554–2563.

[571] F. J. Martin. *Slide presentation - Concrete Durability: Rebar Corrosion*. Personal communication. 1996.

[572] H. Martins Gomes and A. Miguel Awruch. “Reliability of reinforced concrete structures using stochastic finite elements”. In: *Engineering Computations* 19.7 (2002), pp. 764–786.

[573] M. Mashayekhi and H. Estekanchi. “Investigation of strong-motion duration consistency in endurance time excitation functions”. In: *Scientia Iranica* 20 (2013), pp. 1085–1093.

[574] M Mashayekhi, H. Estekanchi, and H Vafai. “Simulation of Endurance Time Excitations Using Increasing Sine Functions”. In: *Int. J. Optim. Civil Eng* 9.1 (2019), pp. 65–77.

[575] M. Mashayekhi, H. E. Estekanchi, and H. Vafai. “Simulation of endurance time excitations via wavelet transform”. In: *Iranian Journal of Science and Technology, Transactions of Civil Engineering* 43.3 (2019), pp. 429–443.

[576] M. Mashayekhi et al. “Development of hysteretic energy compatible endurance time excitations and its application”. In: *Engineering Structures* 177 (2018), pp. 753–769.

[577] M. Mashayekhi et al. “Simulation of Cumulative Absolute Velocity Consistent Endurance Time Excitations”. In: *Journal of Earthquake Engineering* (2018), pp. 1–26.

[578] J. Masuero and G. Creus. “Crack growth initiation in concrete-like materials in the presence of creep”. In: *Nuclear Engineering and Design* 156 (1995), pp. 209–218.

[579] E. Matheu and S. Garner. *Folsom Dam Outlet Works Modification Project; Simplified Three-Dimensional Stress Analysis of Monolith 12*. Tech. rep. ERDC/GSL TR-05-14. US Army Corps of Engineers, Engineer Research and Development Center, 2005.

[580] MATLAB. *version 9.1 (R2016b)*. Natick, Massachusetts: The MathWorks Inc., 2016.

[581] R. McGuire. "Probabilistic Seismic Hazard Analysis and Design Earthquakes: Closing the Loop". In: *Bulletin of the Seismological Society of America* 85 (1995), pp. 1275–1284.

[582] D. McHenry. "A new aspect of creep in concrete and its application to design". In: *Proc. ASTM*. Vol. 40. 1943, pp. 1069–1084.

[583] M. McKay, R. Beckman, and W. Conover. "A comparison of three methods for selecting values of input variables in the analysis of output from a computer code". In: *Technometrics* 21.2 (1979), pp. 239–245.

[584] F. McMillan. *Shrinkage and time effects in reinforced concrete*. 3. University of Minnesota, 1915.

[585] C. Medel-Vera and T. Ji. "Seismic probabilistic risk analysis based on stochastic simulation of accelerograms for nuclear power plants in the UK". In: *Progress in Nuclear Energy* 91 (2016), pp. 373–388.

[586] C. Medel-Vera and T. Ji. "Seismic risk control of nuclear power plants using seismic protection systems in stable continental regions: The UK case". In: *Nuclear Engineering and Design* 307 (2016), pp. 377–391.

[587] K. Mehrotra, C. K. Mohan, and S. Ranka. *Elements of artificial neural networks*. MIT press, 1997.

[588] R. Melchers. "Simulation in time-invariant and time-variant reliability problems". In: *Reliability and Optimization of Structural Systems' 91*. Springer, 1992, pp. 39–82.

[589] R. E. Melchers. *Structural reliability analysis and prediction*. John Wiley & Son Ltd, 1999.

[590] Z. Micovic et al. "A non-traditional approach to the analysis of flood hazard for dams". In: *Stochastic environmental research and risk assessment* 30.2 (2016), pp. 559–581.

[591] H. Mihashi and F. Wittman. "Stochastic approach to study the influence of Rate Loading on Strength of Concrete". In: *Heron* 25.3 (1980).

[592] C. Miller et al. *Recommendations for Enhancing Reactor Safety in the 21st Century; The Near-Term Task Force Review of Insights from the Fukushima Dai-Ichi Accident*. 2011.

[593] Mills-Bria, B. and Nuss, L. and Dixon, L. and Powell, C. and Harris, D. and O'Connell, D. *State-of-Practice for the Nonlinear Structural Analysis of Dams at the Bureau of Reclamation*. Tech. rep. Draft. Bureau of Reclamation, 2003.

[594] S. Mindess and F. Young. *Concrete*. Prentice-Hall, Inc., 1981.

[595] H. Mirzabozorg. Personal Communication. 2013.

[596] H. Mirzabozorg et al. "Mathematical Modeling and Numerical Analysis of Thermal Distribution in Arch Dams Considering Solar Radiation Effect". In: *The Scientific World Journal* 2014 (2014).

[597] S. Mirzahosseinkashani and M. Ghaemian. "Seismic fragility assessment of concrete gravity dams". In: *Proceedings of the 29th Annual USSD Conference*. Nashville, Tennessee, US, 2009.

[598] F. Miura and H. Okinaka. “Dynamic Analysis Method for 3D Soil-Structure Interaction Systems with the Viscous Boundary Based on the Principle of Virtual Work”. In: *Japanese Journal of Civil Engineering* (1989), pp. 395–404.

[599] F. Miura and K. Toki. “Estimation of Natural Frequency and Damping Factor for Dynamic Soil Structure Interaction Systems”. In: *Proceedins of the 3rd Int. Conf. on Soil Dynamics and Earthquake Engineering*. 1987, pp. 73–87.

[600] T. Miyagawa et al. “Fracture of reinforcing steels in concrete structures damaged by alkali-silica reaction-field survey, mechanism and maintenance”. In: *Journal of Advanced Concrete Technology* 4.3 (2006), pp. 339–355.

[601] A. Modica and P. Stafford. “Vector fragility surfaces for reinforced concrete frames in Europe”. In: *Bulletin of earthquake engineering* 12.4 (2014), pp. 1725–1753.

[602] J. Moehle and G. Deierlein. “A Framework methodology for performance-based earthquake engineering”. In: *Proceeding of the 13th World Conferance on Earthquake Engineering*. Vancouver, Canada, 2004.

[603] W. K. Mohanty and A. K. Verma. “Probabilistic seismic hazard analysis for Kakrapar atomic power station, Gujarat, India”. In: *Natural hazards* 69.1 (2013), pp. 919–952.

[604] B. Möller, W. Graf, and M. Beer. “Safety assessment of structures in view of fuzzy randomness”. In: *Computers and Structures* 81.15 (2003), pp. 1567–1582.

[605] A. Mood, F. Graybill, and D. Boes. *Introduction to the theory of statistics 3rd ed*. Ed. by McGraw-Hill. 1974.

[606] A. Morales-Torres et al. “Building fragility curves of sliding failure of concrete gravity dams integrating natural and epistemic uncertainties”. In: *Engineering Structures* 125 (2016), pp. 227–235.

[607] MPR-ML16216A242. *MPR-4273, Revision 0, Seabrook Station - Implications of Large-Scale Test Program Results on Reinforced Concrete Affected by Alkali-Silica Reaction. July 2016 (ML16216A242))*. Online; accessed2018-10-15. 2016.

[608] MPR-ML19170A332. *MPR-4273, Rev. 1, Seabrook Station - Implications of Large-Scale Test Program Results on Reinforced Concrete Affected by Alkali-Silica Reaction*. 2016.

[609] S. Multon. “Evaluation expérimentale et théorique des effets mécaniques de l’alcali-réaction sur des structures modèles”. PhD thesis. Université de Marne la Vallée, France, 2004.

[610] S. Multon and F. Toutlemonde. “Effect of Applied Stresses on Alkali-Silica Reaction Induced Expansions”. In: *Cement and Concrete Research* 36.5 (2006), pp. 912–920.

[611] D. F. Munger et al. “Interim tolerable risk guidelines for US Army Corps of Engineers dams”. In: *Managing our Water Retention Systems: Proceedings of the 29 th Annual United States Society on Dams Conference*. 2009, pp. 1125–1141.

[612] A. Muntasir Billah and M. Shahria Alam. “Seismic fragility assessment of highway bridges: a state-of-the-art review”. In: *Structure and Infrastructure Engineering* 11.6 (2015), pp. 804–832.

[613] Y. Murakami. *Stress Intensity Factors Handbook*. (2 Vols). Pergamon Press, 1987.

[614] Y. Murazumi et al. “Study of the influence of alkali-silica reaction on mechanical properties of reinforced concrete members”. In: *18th International Conference on Structural Mechanics in Reactor Technology (SMIRT 18)*. SMIRT18-H03-3. Beijing, China, 2005, pp. 2043–2048.

[615] Y. Murazumi et al. “Study of the influence of Alkali-Silica Reaction on structural behavior of reinforced concrete members”. In: *18th International Conference on Structural Mechanics in Reactor Technology (SMIRT 18)*. SMIRT18-H03-2. Beijing, China, 2005, pp. 2036–2042.

[616] S. K. Murthy. “Automatic construction of decision trees from data: A multi-disciplinary survey”. In: *Data mining and knowledge discovery* 2.4 (1998), pp. 345–389.

[617] M. Nakajima et al. “Evaluation of seismic hazard curves and scenario earthquakes for Korean sites based on probabilistic seismic hazard analysis”. In: *Nuclear engineering and design* 237.3 (2007), pp. 277–288.

[618] N. Nakamura. “Seismic response analysis of deeply embedded nuclear reactor buildings considering frequency-dependent soil impedance in time domain”. In: *Nuclear Engineering and Design* 238.7 (2008), pp. 1845–1854.

[619] N. Nakamura et al. “Study of ultimate seismic response and fragility evaluation of nuclear power building using nonlinear three-dimensional finite element model”. In: *Nuclear Engineering and Design* 240.1 (2010), pp. 166–180.

[620] S. Nakamura et al. “Study on the influence of irregular ground and adjacent building on the seismic response of nuclear power plant building”. In: *Proc. 15 the World Conference of Earthquake Engineering*. 2012.

[621] A. Natekin and A. Knoll. “Gradient boosting machines, a tutorial”. In: *Frontiers in neurorobotics* 7 (2013), p. 21.

[622] National Research Council. *Dam and levee safety and community resilience: A vision for future practice*. National Academies Press, 2012.

[623] J. Nau and W. Hall. *An Evaluation of Scaling Methods for Earthquake Response Spectra*. Tech. rep. Urbana, IL: Department of Civil Engineering, University of Illinois, 1982.

[624] NDT Resource Center. *Some NDT/NDE Technologies*.

[625] S. Nemat-Nasser and M. Hori. *Micromechanics: Overall Properties of Heterogeneous Materials*. Elsevier Science Publishers, North-Holland Series in Applied Mathematics and Mechanics, 1993.

[626] A. Neville. *Creep of concrete: plain, reinforced, and prestressed*. North-Holland Publishing Company, 1970.

[627] J. Newman and I. Raju. *Stress Intensity Factors Equations for Cracks in Three Dimensional Finite Bodies*. Tech. rep. ASTM ATP 791, 1983, pp. I–238–I–265.

[628] I. Newton. *Methodus fluxionum et serierum infinitarum Methods of Seriesand Fluxions, in D.T. Whiteside The Mathematical Papers of Isaac Newton*. Vol. III. Cambridge University Press, 1664-1671, pp. 43–47.

[629] NextEra. *License Renewal Application*. 2010.

[630] NextEra-ML12087A194. *Seabrook Station Updated Final Safety Analysis Report*. Revision 12. ??

[631] NextEra-ML121160422. *Impact of Alkali Silica Reaction on Seabrook Concrete Structure*. 2012.

[632] NextEra-ML13151A328. *Response to Confirmatory Action Letter*. 2013.

[633] NextEra-ML16216A240. *Seabrook, License Amendment Request 16-03 - Revise Current Licensing Basis to Adopt a Methodology for the Analysis of Seismic Category I Structures with Concrete Affected by Alkali-Silica Reaction. Attachment 1 Markup of UFSAR Pages Enclosed. (73 page(s), 8/1/2016)*. 2016.

[634] NextEra-ML16216A240. *Seabrook, License Amendment Request 16-03 - Revise Current Licensing Basis to Adopt a Methodology for the Analysis of Seismic Category I Structures with Concrete Affected by Alkali-Silica Reaction.* ADMAS access number ML16216A250. 2016.

[635] NextEra-ML18141A785. *Seabrook Station - Approach for Determining Through-Thickness Expansion from Alkali-Silica Reaction*. Redacted Document. 2016.

[636] NextEra-ML19205A489. *Testimony of NextEra Witnesses Michael Collins, John Simons, Christopher Bagley, Oguzhan Bayrak, and Edward Carley ("MPR Testimony")*. 2019.

[637] V. Ngala and C. Page. "Effects of Carbonation on Pore Structure and Diffusional Properties of Hydrated Cement Pastes". In: *Cement and Concrete Research* 27.7 (1997), pp. 995–1007.

[638] G. Nikishkov and V. Vainshtok. "Method of Virtual Crack Growth for Determining Stress Intensity Factors K_I and K_{II}". In: *Strength of Materials* 12 (1980), pp. 696–701.

[639] Nikishkov, G. P. and Atluri, S. N. "Calculation of Fracture Mechanics Parameters for an Arbitrary Three-dimensional Crack, by the 'Equivalent Domain Integral' Method". In: *International Journal of Numerical Methods in Engineering* 24.9 (1987), pp. 1801–1821.

[640] NOAA. *Satellite and Information Servis (NESDIS)*. 2013.

[641] T. Nokland and T. Aven. "Review and discussion of uncertainty taxonomies used in Risk Analysis". In: *Safety, Reliability and Risk Analysis: Theory, Methods and Applications, Vols. 1* 4 (2009), pp. 1207–1215.

[642] A. Nour et al. "Probabilistic seismic safety assessment of a CANDU 6 nuclear power plant including ambient vibration tests: Case study". In: *Nuclear Engineering and Design* 304 (2016), pp. 125–138.

[643] A. Nozari and H. Estekanchi. “Optimization of endurance time acceleration functions for seismic assessment of structures”. In: *International Journal of Optimization in Civil Engineering* 1 (2011), pp. 257–277.

[644] NRC. *Individual Plant Examination of External Events (IPEEE) for Severe Accident Vulnerabilities - 10CFR 50.54(f)* . Tech. rep. Generic Letter No. 88-20, Supplement 4. Nuclear Regulatory Commission, 1991.

[645] NRC. *Concrete Degradation by Alkali-Silica Reaction*. Online; accessed2018-07-03. 2011.

[646] NRC. *U.S. Nuclear Regulatory Commission Regulations: Title 10,Code of Federal Regulations; PART 54 Requirements for renewal of operating licenses for nuclear power plants*. 2015.

[647] "NRC-ADAMS". *Agency wide Documents Access and Management System (ADAMS)*. Last accessed October 2018. 2018.

[648] NRC-CU Grant. *Experimental and Numerical Investigation of Alkali Silica Reaction in Nuclear Reactors*. Tech. rep. Grant and Cooperative Agreement NRC-HQ-60-14-G-0010, 2014.

[649] NRC-ML 102861026. *Crystal River Nuclear Plant - Special Inspection Report 05000302/2009007*. Tech. rep. Nuclear Regulatory Commission, 2010.

[650] NRC-ML 12054A735. *FOIA/PA No. 2013-0332; Partial. Group E (Records Being Released in Their Entirety).*

[651] NRC-ML 12054A735. *Order Modifying Licenses With Regard To Requirements For Mitigation Strategies For Beyon D·Design·Basis External Events (Effective Immediately)* . 2012.

[652] NRC-ML12131A431. *Seabrook Station Safety Performance in 2011 & Seabrook Station Safety in light of the Alkali-Silica Reaction Occurring inPlant Structures* . 2011.

[653] NRC-ML12160A374. *Safety Evaluation Report With Open Items Related to the License Renewal of Seabrook Station*. Tech. rep. United States Nuclear Regulatory Commission, 2012.

[654] NRC-ML12199A300. *Seabrook Advisory Committee on Reactor Safeguards presentation slides*. 2012.

[655] NRC-ML19261A762. *NRC Staff Testimony of Angela Buford, Bryce Lehmanm and George Thomas*. 2019.

[656] NRC-ML19312B609. *Official Transcript of Proceedings; NextEra Energy Seabrook, LLC Seabrook Station, Unit 1; Docket Number: 50-443-LA-2;ASLBP Number:17-953-02-LA-BD01*. Newburyport, Massachusetts, 2019.

[657] NRC Office of Public Affairs. *Reactor License Renewal*. Online; accessed2018-07-09. 2018. URL: `\url{https://www.nrc.gov/docs/ML0506/ML050680253.pdf}`.

[658] NuclearEnergy Insider. *Crystal River to be decommissioned 50 years early*. 2019.

[659] NUREG 1150. *Severe Accident Risks: An Assessment for Five U.S. Nuclear Power Plants*. 1990.

[660] NUREG-1737. *Software Quality Assurance Procedures for NRC Thermal Hydraulic Codes*. Tech. rep. NUREG-1737. U.S. Nuclear Regulatory Commission, 2000.

[661] NUREG-2201. "Probabilistic Risk Assessment and Regulatory Decision making: Some Frequently Asked Questions ". In: *Washington, DC: US Nuclear Regulatory Commission* (2016).

[662] NUREG/CR-6706. *NUREG/CR-6706: Capacity of Steel and Concrete Containment Vessels With Corrosion Damage*. 2001.

[663] L. Nuss, N. Matsumoto, and K. Hansen. "Shaken, But Not Stirred - Earthquake Performance of Concrete Dams". In: *Proceedings of the 32nd USSD Annual Meeting and Conference: Innovative Dam and Levee Design and Construction for Sustainable Water Management*. New Orleans, Louisiana, 2012.

[664] O. Nuttli. *The relation of sustained maximum ground acceleration and velocity to earthquake intensity and magnitude*. Tech. rep. Vicksburg, Mississippi: U.S. Army Corps of Engineers, Waterways Experiment Station, 1979.

[665] T. O'Hara and J. Jacobson. *Standardization of the cumulative absolute velocity*. Tech. rep. Electric Power Research Inst., 1991.

[666] G. Ökten, M. Shah, and Y. Goncharov. "Random and deterministic digit permutations of the Halton sequence". In: *Monte Carlo and Quasi-Monte Carlo Methods 2010*. Springer, 2012, pp. 609–622.

[667] A. Olsson and G. Sandberg. "Latin hypercube sampling for stochastic finite element analysis". In: *Journal of Engineering Mechanics* 128.1 (2002), pp. 121–125.

[668] M. O'Rourke and P. So. "Seismic fragility curves for on-grade steel tanks". In: *Earthquake spectra* 16.4 (2000), pp. 801–815.

[669] M Ortiz. "Microcrack coalescence and macroscopic crack growth initiation in brittle solids". In: *International Journal of Solids and Structures* 24.3 (1988), pp. 231–250.

[670] F. Ouchterlony. *Suggested Methods for Determining Fracture Toughness of Rock Material*. Tech. rep. International Society for Rock Mechanics, Commission on Testing Methods, 1986.

[671] A. B. Owen. "Controlling correlations in Latin hypercube samples". In: *Journal of the American Statistical Association* 89.428 (1994), pp. 1517–1522.

[672] D. Owen and A. Fawkes. *Engineering Fracture Mechanics*. Pineridge Press, Swansea, U.K, 1983.

[673] J. Padgett and R. DesRoches. "Sensitivity of seismic response and fragility to parameter uncertainty". In: *Journal of Structural Engineering* 133 (2007), pp. 1710–1718.

[674] J. Padgett, B. Nielson, and R. DesRoches. "Selection of optimal intensity measures in probabilistic seismic demand models of highway bridge portfolios". In: *Earthquake Engineering and Structural Dynamics* 37 (2008), pp. 711–725.

[675] J. Pan, Y. Xu, and F. Jin. "Seismic performance assessment of arch dams using incremental nonlinear dynamic analysis". In: *European Journal of Environmental and Civil Engineering* 19.3 (2015), pp. 305–326.

[676] J. Pan et al. "Numerical prediction of swelling in concrete arch dams affected by alkaliaggregate reaction". In: *European Journal of Environmental and Civil Engineering* 17.4 (2013), pp. 231–247.

[677] R. Pang et al. "Seismic fragility for high CFRDs based on deformation and damage index through incremental dynamic analysis". In: *Soil Dynamics and Earthquake Engineering* 104 (2018), pp. 432–436.

[678] P. Panyakapo. "Cyclic Pushover Analysis procedure to estimate seismic demands for buildings". In: *Engineering Structures* 66 (2014), pp. 10–23.

[679] V. Papadakis, M. Fardis, and C. Vayenas. "Effect of Composition, environmental factors and cement-lime mortar coating on concrete carbonation". In: *Materials and Structures* 25.149 (1992), p. 293.

[680] V. Papanikolaou and A. Elnashai. "Evaluation Of Conventional And Adaptive Pushover Analysis I: Methodology". In: *Journal of Earthquake Engineering* 9 (2005), pp. 923–941.

[681] P. Paris and F. Erdogan. "A Critical Analysis of Crack Propagation Laws". In: *ASME J. of Basic Engineering* 85.3 (1963), pp. 528–534.

[682] J.-b. Park et al. "Seismic analysis of the APR1400 nuclear reactor system using a verified beam element model". In: *Nuclear Engineering and Design* 313 (2017), pp. 108–117.

[683] Y. Park and A. AH-S. "Mechanistic seismic damage model for reinforced concrete". In: *Journal of Structural Division, ASCE* 111 (1985), pp. 722–739.

[684] Y. Park, A. AH-S., and Y. Wen. "Seismic damage analysis of reinforced concrete buildings". In: *Journal of Structural Engineering* 111 (1985), pp. 740–757.

[685] L. Parrott. "Some effects of cement and curing upon carbonation and reinforcement corrosion in concrete". In: *Materials and Structures* 29.3 (1996), p. 164.

[686] M. Parry et al. *Climate change 2007: impacts, adaptation and vulnerability*. Vol. 4. Cambridge University Press Cambridge, 2007.

[687] R. Patev and C. Putcha. "Development of fault trees for risk assessment of dam gates and associated operating equipment". In: *International Journal of Modelling and Simulation* 25.3 (2005), pp. 190–201.

[688] PEER. *Ground Motion Database*. Last viewed November 2014. Pacific Earthquake Engineering Research Center, 2014.

[689] PEER. *PEER Ground Motion Database*. Accessed: 2018-07-16. 2017. URL: \url{http://ngawest2.berkeley.edu/}.

[690] F. Perotti, M. Domaneschi, and S. De Grandis. "The numerical computation of seismic fragility of base-isolated Nuclear Power Plants buildings". In: *Nuclear Engineering and Design* 262 (2013), pp. 189–200.

[691] P. Petersson. *Crack Growth and Development of Fracture Zones in Plain Concrete and similar Materials*. Tech. rep. TVBM 1006. Lund, Sweden: Lund Institute of Technology, 1981.

[692] Q. T. Phung, N. Maes, and D. Jacques. "Current concerns on durability of concrete used in nuclear power plants and radioactive waste repositories". In: *Congrès International de Géotechnique–Ouvrages–Structures*. Springer. 2017, pp. 1107–1121.

[693] G. Pickett. "The effect of change in moisture-content on the creep of concrete under a sustained load". In: *Journal Proceedings*. Vol. 38. 1942, pp. 333–356.

[694] S Pietruszczak. "On the mechanical behaviour of concrete subjected to alkali-aggregate reaction". In: *Computers & structures* 58.6 (1996), pp. 1093–1097.

[695] A. Pitarka et al. "Three-dimensional simulation of the near-fault ground motion for the 1995 Hyogo-ken Nanbu (Kobe), Japan, earthquake". In: *Bulletin of the Seismological Society of America* 88.2 (1998), pp. 428–440.

[696] K. Pitilakis, S. Karapetrou, and S. Fotopoulou. "Consideration of aging and SSI effects on seismic vulnerability assessment of RC buildings". In: *Bulletin of Earthquake Engineering* 12 (2014), pp. 1755–1776.

[697] R. L. Plackett and J. P. Burman. "The design of optimum multifactorial experiments". In: *Biometrika* 33.4 (1946), pp. 305–325.

[698] J. Planas and M. Elices. "Asymptotic Analysis of a Cohesive Crack: 1. Theoretical background". In: *International Journal of Fracture* 55 (1992), pp. 153–177.

[699] N. M. Plum. *Tentative Recommendations for the Prevention of Alkali Aggregate Reactions*. Danish Building Research Institute, 1961.

[700] K. Porter. "An overview of PEER's performance-based earthquake engineering methodology". In: *Proceedings of the 9th International Conference on Applications of Statistics and Probability in Civil Engineering (ICASP9)*. San Francisco, CA, 2003.

[701] K. Porter. "When addressing epistemic uncertainty in a lognormal fragility function, how should one adjust the median?" In: *Proceedings of the 16th World Conference on Earthquake Engineering*. Santiago, Chile, 2017.

[702] K. Porter, R. Kennedy, and R. Bachman. "Creating Fragility Functions for Performance-Based Earthquake Engineering". In: *Earthquake Spectra* 23 (2007), pp. 471–489.

[703] K. Porter. "A Beginner's Guide to Fragility, Vulnerability, and Risk". In: *Encyclopedia of Earthquake Engineering*. Ed. by M. Beer et al. Springer Berlin Heidelberg, 2015, pp. 1–29.

[704] F. Pourkamali-Anaraki and S. Becker. "A Randomized Approach to Efficient Kernel Clustering". In: *IEEE Global Conference on Signal and Information Processing* (2016), pp. 207–211.

[705] F. Pourkamali-Anaraki and S. Hughes. "Kernel compressive sensing". In: *IEEE International Conference on Image Processing*. 2013, pp. 494–498.

[706] G. Powell and R. Allahabadi. "Seismic damage prediction by deterministic methods: Concepts and procedures". In: *Earthquake Engineering and Structural Dynamics* 16 (1988), pp. 719–734.

[707] S. Poyet et al. "Chemical modelling of Alkali Silica reaction: Influence of the reactive aggregate size distribution". In: *Materials and Structures* 40 (2007), pp. 229–239.

[708] Presidential Policy Directive. *Presidential Policy Directive – Critical Infrastructure Security and Resilience*. Last viewed January 2018. White House, 2013.

[709] K. L. Priddy and P. E. Keller. *Artificial neural networks: an introduction*. Vol. 68. SPIE press, 2005.

[710] M. B. Priestley. "Evolutionary spectra and non-stationary processes". In: *Journal of the Royal Statistical Society. Series B (Methodological)* (1965), pp. 204–237.

[711] Progress Energy Florida. *Petition To Determine The Reasonableness And Prudence Of Its Decisions On The Cr3 Steam Generator Replacement Project Leading Up To The October 2,2009 Delamination*. 2011.

[712] Progress Energy Florida (ML102861026). *Crystal River Unit #3 Containment Delamination Update*. Accessed: July 2019. 2009.

[713] J. Proulx et al. "An experimental investigation of water level effects on the dynamic behaviour of a large arch dam". In: *Earthquake engineering & structural dynamics* 30.8 (2001), pp. 1147–1166.

[714] W. Puatatsananon and V. Saouma. "Nonlinear Coupling of Carbonation and Chloride Diffusion in Concrete". In: *Journal of Materials in Civil Engineering* 17.3 (2005), pp. 264–275.

[715] L. G. Pujades et al. "Parametric model for capacity curves". In: *Bulletin of Earthquake Engineering* 13.5 (2015), pp. 1347–1376.

[716] R Core Team. *R: A Language and Environment for Statistical Computing*. R Foundation for Statistical Computing. Vienna, Austria, 2015.

[717] T. Ragg, H. Braun, and H. Landsberg. "A comparative study of neural network optimization techniques". In: *Artificial Neural Nets and Genetic Algorithms*. Springer. 1998, pp. 341–345.

[718] M. R. Rajashekhar and B. R. Ellingwood. "A new look at the response surface approach for reliability analysis". In: *Structural Safety* 12.3 (1993), pp. 205–220.

[719] P. Rajeev, P. Franchin, and P. Pinto. "Increased Accuracy of Vector-IM-Based Seismic Risk Assessment?" In: *Journal of Earthquake Engineering* 12 (2008), pp. 111–124.

[720] S. Ramamoorthy, P. Gardoni, and J. Bracci. "Probabilistic Demand Models and Fragility Curves for Reinforced Concrete Frames". In: *Journal of Structural Engineering* 132 (2006), pp. 1563–1572.

[721] M Ramu and R. V. Prabhu. "Metamodel based analysis and its applications: A review". In: *Acta Technica Corviniensis-Bulletin of Engineering* 6.2 (2013), p. 25.

[722] C. E. Rasmussen and C. Williams. “Gaussian Processes for Machine Learning Cambridge”. In: *MA: the MIT Press.[Google Scholar]* (2006).

[723] C. E. Rasmussen and H. Nickisch. “Gaussian processes for machine learning (GPML) toolbox”. In: *Journal of machine learning research* 11.Nov (2010), pp. 3011–3015.

[724] D. Rea, C.-Y. Liaw, and A. K. Chopra. “Mathematical models for the dynamic analysis of concrete gravity dams”. In: *Earthquake Engineering & Structural Dynamics* 3.3 (1974), pp. 249–258.

[725] Reclamation. *Design of Gravity Dams*. Tech. rep. U.S.Department of the Interior, Bureau of Reclamation, 1976.

[726] N. Regulations. *NRC Title 10, Code of Federal Regulations; Part 50*. Vol. 2. 50-199. Nuclear Regulatory Commission, Office of Administration, Division of Rules, 1987.

[727] R. Reich. “On the Marriage of Mixed Finite Element Methods and Fracture Mechanics: An Application to Concrete Dams”. PhD thesis. University of Colorado, Boulder, 1993.

[728] Q. Ren and B. Wang. “Discussion on slenderness coefficient of arch dams”. In: *Journal of Hohai University (Natural Sciences)* 1 (2003), pp. 1–4.

[729] P. Renault. “Approach and challenges for the seismic hazard assessment of nuclear power plants: the Swiss experience.” In: *Bollettino di Geofisica Teorica ed Applicata* 55.1 (2014).

[730] S. Rezaeian and A. Der Kiureghian. “A stochastic ground motion model with separable temporal and spectral nonstationarities”. In: *Earthquake Engineering & Structural Dynamics* 37.13 (2008), pp. 1565–1584.

[731] S. Rezaeian and A. Der Kiureghian. “Simulation of synthetic ground motions for specified earthquake and site characteristics”. In: *Earthquake Engineering & Structural Dynamics* 39.10 (2010), pp. 1155–1180.

[732] S. Rezaeian and X. Sun. “Stochastic ground motion simulation”. In: *Encyclopedia of Earthquake Engineering*. Ed. by M. Beer et al. Berlin, Heidelberg: Springer Berlin Heidelberg, 2014, pp. 1–15.

[733] R. Riddell. “On ground motion intensity indices”. In: *Earthquake Spectra* 23 (2007), pp. 147–173.

[734] R. Riddell and J. Garcia. “Hysteretic energy spectrum and damage control”. In: *Earthquake Engineering and Structural Dynamics* 30 (2001), pp. 1791–1816.

[735] G. Rizzo et al. “Tree-based models for inductive classification on the Web Of Data”. In: *Web Semantics: Science, Services and Agents on the World Wide Web* 45 (2017), pp. 1–22.

[736] J. Rodriguez et al. “Contribution to Theme A of the Benchmark Workshop: Effect of Concrete Swelling on the Equilibrium and Displacements of an Arch Dam”. In: *Proceedings of the XI ICOLD Benchmark Workshop on Numerical Analysis of Dams*. Valencia, Spain, 2011.

[737] M Rogovin and G. Grampton. “the Nuclear Regulatory Commission (NRC) Special Inquiry Group (1980), Three Mile Island: A report to the Com-

mission and the public (NUREG/CR-1250, 1)". In: *Washington, DC: US Nuclear Regulatory Commission* (1980).

[738] P. Romanski and L. Kotthoff. *Package 'FSelector'*. Last viewed October 2018. 2018.

[739] D. Rooke and D. Cartwright. *Compendium of Stress Intensity Factors*. London: HMSO, 1976.

[740] A. Ross. "Concrete creep data". In: *Structural Engineer* 15.8 (1937), pp. 314–326.

[741] T. Rossetto et al. "Evaluation of existing fragility curves". In: *SYNER-G: Typology Definition and Fragility Functions for Physical Elements at Seismic Risk*. Springer, 2014, pp. 47–93.

[742] N. Roussouly, F. Petitjean, and M Salaun. "A new adaptive response surface method for reliability analysis". In: *Probabilistic Engineering Mechanics* 32 (2013), pp. 103–115.

[743] J.-S. Ryu et al. "Seismic response analysis of soil–structure interactive system using a coupled three-dimensional FE–IE method". In: *Nuclear Engineering and Design* 240.8 (2010), pp. 1949–1966.

[744] B. T. P. SA. "The viaducts of Chillon (Switzerland)". In: *La Technique des Travaux* 47 (1971), pp. 47–60.

[745] A. Saetta, B. Schrefler, and R. Vitaliani. "The Carbonation of Concrete and the Mechanism of Moisture, Heat and Carbon Dioxide Flow Through Porous Materials". In: *Cement and Concrete Research* 23 (1993), pp. 761–772.

[746] A. Saetta, B. Schrefler, and R. Vitaliani. "2-D Model for Carbonation and Moisture/Heat Flow in Porous Materials". In: *Cement and Concrete Research* 25.8 (1995), pp. 1703–1712.

[747] J. W. Salamon. *Seismic Induced Loads on Spillway Gates, Phase I - Literature Review*. Tech. rep. DSO-11-06. Denver, Colorado: U.S. Bureau of Reclamation, 2011.

[748] V. Saouma. *Synthesis of NUREG/CR-6906; SAND2006-2274P Containment Integrity Research at Sandia National Laboratories; An Overview*. Tech. rep. Internal Document. Boulder, CO, 2017.

[749] V. Saouma, ed. *Diagnosis & Prognosis of AAR Affected Structures; State-of-the-Art Report of the RILEM Technical Committee 259-ISR. in-print*. Springer Nature, 2020.

[750] V. Saouma, L. Perotti, and T. Shimpo. "Stress Analysis of Concrete Structures Subjected to Alkali-Aggregate Reactions". In: *ACI Structural Journal* 104 (2007), pp. 532–541.

[751] V. E. Saouma et al. "A mathematical model for the kinetics of the alkali–silica chemical reaction". In: *Cement and Concrete Research* 68 (2015), pp. 184–195.

[752] V. Saouma. "Reliability Based Nonlinear Fracture Mechanics Analysis of a Dam". In: *Dam Engineering* 16.3 (2005), pp. 219–241.

[753] V. Saouma. *KumoNoSu, a 3D Interactive Graphics Mesh Generator for MERLIN; User's Manual*. 2009. URL: \url{http://civil.colorado.edu/~saouma/pdf/kumo.pdf}.

[754] V. Saouma. *Numerical Modeling of Alkali Aggregate Reaction*. 320 pages. CRC Press, 2013.

[755] V. Saouma. *Effect of AAR on Shear Strength Panels*. Tech. rep. Final Report to NRC, Grant No. NRC-HQ-60-14-G-0010, Task 1-C. University of Colorado, Boulder, 2017.

[756] V. Saouma. *Probabilistic Based Nonlinear Seismic Analysis of Nuclear Containment Vessel Structures with AAR*. Tech. rep. Final Report to NRC, Grant No. NRC-HQ-60-14-G-0010, Task 3-B. University of Colorado, Boulder, 2017.

[757] V. Saouma. *Critical Review of the Root Cause Investigation of Crystal River Delamination*. 2019.

[758] V. Saouma and G. Fava. "On Fractals and Size Effects". In: *International Journal of Fracture* 137 (2006), pp. 231–249.

[759] V. Saouma and M. Hariri-Ardebili. *MERLIN Validation & Application of AAR Problems*. Tech. rep. University of Colorado, Boulder, 2019.

[760] V. Saouma, D. Natekar, and E. Hansen. "Cohesive Stresses and Size Effects in Elasto-Plastic and Quasi-Brittle Materials". In: *International Journal of Fracture* 119 (2003), pp. 287–298.

[761] V. Saouma and L. Perotti. "Constitutive Model for Alkali Aggregate Reactions". In: *ACI Materials Journal* 103.3 (2006), pp. 194–202.

[762] V. Saouma, L. Perotti, and Y. Uchita. "AAR Analysis of Poglia Dam with Merlin". In: *8th ICOLD Benchmark Workshop on Numerical Analysis of Dams*. Wuhan, China, 2005.

[763] V. Saouma and D. Schwemmer. "Numerical Evaluation of the Quarter Point Singular Element". In: *International Journal of Numerical Methods in Engineering* 20 (1984), pp. 1629–1641.

[764] V. Saouma and E. Sikiotis. "Stress Intensity Factors in Anisotropic Bodies Using Singular Isoparametric Elements". In: *Engineering Fracture Mechanics* 25.1 (1986), pp. 115–121.

[765] V. Saouma, R. Sparks, and D. Graff. *Development Of ASR Concrete Mix for Large Scale Testing*. Tech. rep. Report to the Nuclear Regulatory Commission, Grant No. NRC-HQ-60-14-G-0010. University of Colorado, Boulder, 2016.

[766] V. Saouma and G. Tussiwand. "Fracture Mechanics of a Solid Rocket Motor Using an AP-HTBP Based Composite Propellant; Part 2: Application". In: *Journal of Propulsion and Power* (2006). Submitted for Publication.

[767] V. Saouma, J. Červenka, and R. Reich. *Merlin Finite Element User's Manual*. 2010.

[768] V. Saouma et al. "Effect of aggregate and specimen size on fracture properties of dam concrete". In: *ASCE, Journal of Materials in Civil Engineering* 3.3 (1991), pp. 204–218.

[769] V. Saouma et al. "A Simplified 3D Model for Rock-Structure Interaction with Radiation Damping and Free Field Input". In: *Bulletin of Earthquake Engineering* 9 (2011), pp. 1387–1402. DOI: s10518-011-9261-7.

[770] V. Saouma et al. *AAR Expansion; Effect of Reinforcement, Specimen Type, and Temperature*. Tech. rep. Report to the Nuclear Regulatory Commission, Grant No. NRC-HQ-60-14-G-0010. University of Colorado, Boulder, 2016.

[771] V. E. Saouma and M. A. Hariri-Ardebili. "Seismic capacity and fragility analysis of an ASR-affected nuclear containment vessel structure". In: *Nuclear Engineering and Design* 346 (2019), pp. 140–156.

[772] Saouma, V.E. *Numerical Modeling of AAR*. 324 pages. CRC Press, 2014.

[773] F. Sarott et al. "Diffusion and adsorption studies on hardened cement paste and the effect of carbonation on diffusion rates". In: *Cement and Concrete Research* 22 (1992), pp. 439–444.

[774] N. Saxena, D. Paul, and R. Kumar. "Effects of slip and separation on seismic SSI response of nuclear reactor building". In: *Nuclear Engineering and Design* 241.1 (2011), pp. 12–17.

[775] P. B. Schnabel, J. Lysmer, and H. Seed. *SHAKE A Computer Program for Earthquake Response Analysis of Horizontally Layered Sites*. Tech. rep. UCB/EERC-72/12. Earthquake Engineering Research Center, University of California: Berkeley, CA., 1972.

[776] B. Schölkopf, A. J. Smola, F. Bach, et al. *Learning with kernels: support vector machines, regularization, optimization, and beyond*. MIT press, 2002.

[777] S. Schroer and M. Modarres. "An event classification schema for evaluating site risk in a multi-unit nuclear power plant probabilistic risk assessment". In: *Reliability Engineering & System Safety* 117 (2013), pp. 40–51.

[778] R. Scott and N. Morgan. *Feasibility and Desirability of Constructing Very Large Centrifuges for Geotechnical Studies*. Tech. rep. Pasadena, CA: California Institute of Technology, 1977.

[779] Scrivener. Personal Communication. 2003.

[780] SEAOC. *Performance-based seismic engineerin, SEAOC Vision 2000 Committee*. Tech. rep. Sacramento, CA: Structural Engineers Association of California, 1995.

[781] A. Sextos et al. "Seismically induced uplift effects on nuclear power plants. Part 1: Containment building rocking spectra". In: *Nuclear Engineering and Design* 318 (2017), pp. 276–287.

[782] J. Shank. "Plastic Flow of Concrete at High Overlaod". In: *Journal Proceedings*. Vol. 45. 2. 1949, pp. 493–498.

[783] N. Sharma, A. Tabandeh, and P. Gardoni. "Resilience analysis: a mathematical formulation to model resilience of engineering systems". In: *Sustainable and Resilient Infrastructure* (2017), pp. 1–19.

[784] B Shen. "The mechanism of fracture coalescence in compression—experimental study and numerical simulation". In: *Engineering Fracture Mechanics* 51.1 (1995), pp. 73–85.

[785] C. Shen et al. "Earthquake induced by reservoir impounding and their effect on Hsinfengkiang Dam". In: *Scientia Sinica* 17.2 (1974), pp. 239–272.

[786] C. Shih, H. de Lorenzi, and M. German. "Crack Extension Modelling with Singular Quadratic Isoparametric Elements". In: *Int. J. Fract.* 12 (1976), pp. 647–651.

[787] H. Shimizu et al. “Investigaiton of Safety Margin for Turbine Generator Foundation Affected by Alkali-Silica Reaction Based on Non-Linear Structural Analysis”. In: *18th International Conference on Structural Mechanics in Reactor Technology (SMIRT 18)*. SMIRT18-H03-4. Beijing, China, 2005, pp. 2049–2059.

[788] H. Shimizu et al. “Study on Material Properties in Order to Apply for Structural Analysis of Turbine Generator Foundation Affected by Alkali-Silica Reaction”. In: *18th International Conference on Structural Mechanics in Reactor Technology (SMIRT 18)*. SMIRT18-H03-5. Beijing, China, 2005, pp. 2055–2060.

[789] M. Shinozuka and Y Sata. “Simulation of nonstationary random process”. In: *Journal of the Engineering Mechanics Division* 93.1 (1967), pp. 11–40.

[790] N. Shome. “Probabilistic Seismic Demand Analysis of Nonlinear structures”. PhD thesis. Stanford University, Stanford, 1999.

[791] N. Shome et al. “Earthquakes, records, and nonlinear responses”. In: *Earthquake Spectra* 14.3 (1998), pp. 469–500.

[792] T. W. Simpson et al. “Metamodels for computer-based engineering design: survey and recommendations”. In: *Engineering with Computers* 17.2 (2001), pp. 129–150.

[793] Simpson Gumpertz & Heger-ML16216A243. *SG&H Report 160268-R-01 Development of ASR Load Factors for Seismic Category I Structures (Including Containment) at Seabrook Station. Seabrook, NH Revision 0 (Seabrook FP# 101039)*. 2016.

[794] Simpson Gumpertz & Heger-ML16279A049. *Evaluation and Design Confirmation of As-Deformed CEB, 150252-CA-02," Revision 0, July 2016.* 2016.

[795] F. Slate and S. Olsefski. “X-Rays for Study of Internal Structures and Microcracking of Concrete”. In: *Journal of the American Concrete Institute* 60 (1963), pp. 575–587.

[796] V. Slowik and V. Saouma. “Water pressure in propagating concrete cracks”. In: *ASCE Structural Engineering* 126 (2000), pp. 235–242.

[797] I. M. Sobol’. “On the distribution of points in a cube and the approximate evaluation of integrals”. In: *Zhurnal Vychislitel’noi Matematiki i Matematicheskoi Fiziki* 7.4 (1967), pp. 784–802.

[798] P. G. Somerville et al. “Modification of empirical strong ground motion attenuation relations to include the amplitude and duration effects of rupture directivity”. In: *Seismological Research Letters* 68.1 (1997), pp. 199–222.

[799] I. Soroka. *Concrete in Hot Environments*. London: E&FN SPON, 1993.

[800] B. Soysal, B. Binici, and Y. Arici. “Investigation of the relationship of seismic intensity measures and the accumulation of damage on concrete gravity dams using incremental dynamic analysis”. In: *Earthquake Engineering and Structural Dynamics* (2015).

[801] B. W. Spencer and H. Huang. “Coupled Physics Simulation of Expansive Reactions in Concrete with the Grizzly Code”. In: *Proceedings of the 18th*

International Conference on Environmental Degradation of Materials in Nuclear Power Systems–Water Reactors. Springer. 2019, pp. 1347–1357.

[802] A. Srivastava. *Generalized event tree algorithm and software for dam safety risk analysis*. Tech. rep. Utah State University, Utah: All Graduate Theses and Dissertations, Paper 32, USU, 2008.

[803] T. Stanton. "Expansion of Concrete Through Reaction Between Cement and Aggregate". In: *Proceedings of ASCE* 66 (1940), pp. 1781–1811.

[804] D. Stark and G. De Puy. "Alkali-silica reaction in five dams in southwestern United States". In: *Special Publication* 100 (1987), pp. 1759–1786.

[805] R. Stevens and F. Guiu. "The Application of the J Integral to Problems of Crack Bridging". In: *Acta Metall. Mater* 42.6 (1994), pp. 1805–1810.

[806] J. R. Stewart. *Verification Methods and NRC Regulations: A Brief Overview*. Tech. rep. Sandia National Lab.(SNL-NM), Albuquerque, NM (United States), 2009.

[807] L. G. Straub. "Plastic flow in concrete arches". In: *Transactions of the American Society of Civil Engineers* 95.1 (1931), pp. 613–678.

[808] L. Struble and S. Diamond. "Swelling Properties of Synthetic Alkali Silica Gels". In: *Journal of the American Ceramic Society* 64.11 (1981), pp. 652–655.

[809] B. Sudret. "Uncertainty propagation and sensitivity analysis in mechanical models–Contributions to structural reliability and stochastic spectral methods". In: *Habilitationa diriger des recherches, Université Blaise Pascal, Clermont-Ferrand, France* (2007), p. 18.

[810] B. Sudret. "Global sensitivity analysis using polynomial chaos expansions". In: *Reliability Engineering & System Safety* 93.7 (2008), pp. 964–979.

[811] R. Swain et al. *Hydrologic Hazard Curve Estimating Procedures*. Tech. rep. U.S. Department of the Interior Bureau of Reclamation, 2004.

[812] R. Taborda and D. Roten. "Physics-based ground-motion simulation". In: *Encyclopedia of Earthquake Engineering*. Ed. by M. Beer et al. Berlin, Heidelberg: Springer Berlin Heidelberg, 2014, pp. 1–33.

[813] H. Tada, P. Paris, and G. Irwin. *The Stress Analysis of Cracks Handbook*. Hellertown, PA: Del Research Corporation, 1973.

[814] T. Takagkura et al. "Structural soundness for turbine-generator foundation affected by alkali-silica reaction and its maintenance plans". In: *18th International Conference on Structural Mechanics in Reactor Technology (SMIRT 18)*. SMIRT18-H03-5. Beijing, China, 2005, pp. 2055–2060.

[815] T. Takakura et al. "Investigation on the expansion value of turbine generator foundation affected by alkali-silica reaction". In: *8th international conference on structural mechanics in reactor technology*. 2005.

[816] T. Takakura et al. "Structural soundness for turbine-generator foundation affected by alkali-silica reaction and its maintenance plans". In: *19th International Conference on Structural Mechanics in Reactor Technology (SMIRT 19)*. IASMiRT, 2007.

[817] T. Takatura et al. "Investigation of the expanded value of turbine generator foundation affected by alkali-silica reaction". In: *18th International*

Conference on Structural Mechanics in Reactor Technology (SMIRT 18). SMIRT18-H03-7. Beijing, China, 2005, pp. 2061–2068.

[818] T. Takatura et al. "Vibration measurement and simulation analysis on a reinforced concrete structure with alkali-silica reaction". In: *18th International Conference on Structural Mechanics in Reactor Technology (SMIRT 18)*. SMIRT18-H03-1. Beijing, China, 2005, pp. 2026–2035.

[819] Tampa Bay Times. *Settlement likely to end inquiries into Duke Energy nuclear plants*. 2014.

[820] L. Tang and L. Nilsson. "Chloride Binding Capacity and Binding Isotherms of OPC Pastes and Mortars". In: *Cement and Concrete Research* 23 (1993), pp. 247–253.

[821] Tang, T.M. "Concrete Degradation of the Containment of Tihange 2 NPP in Belgium Status as of December 2012". In: *OECD/NEA/CSNI Workshop IRIS_2012 Improving Robustness Assessment Methodologies for Structures Impacted by Missiles*. Ed. by N. Orbovic and A. Blahoianu. 2013.

[822] K. Tanioka and H. Yadohisa. "Effect of data standardization on the result of k-means clustering". In: *Challenges at the Interface of Data Analysis, Computer Science, and Optimization*. Springer, 2012, pp. 59–67.

[823] E.-i. Tazawa and S. Miyazawa. "Influence of cement and admixture on autogenous shrinkage of cement paste". In: *Cement and concrete research* 25.2 (1995), pp. 281–287.

[824] E.-i. Tazawa, S. Miyazawa, and T. Kasai. "Chemical shrinkage and autogenous shrinkage of hydrating cement paste". In: *Cement and concrete research* 25.2 (1995), pp. 288–292.

[825] P. Tekie and B. Ellingwood. "Seismic fragility assessment of concrete gravity dams". In: *Earthquake Engineering and Structural Dynamics* 32 (2003), pp. 2221–2240.

[826] K. Terzaghi and L. Rendulic. "*Die wirksame flächenporosität des betons* Effective fluid porosity of the concrete". In: *Zeitschrift des Osterreichischen Ingenieur-und Architekten-Vereines Austrian Journal of Architects and Engineers* (1934), pp. 1–9.

[827] K. Terzaghi. "Simple tests determine hydrostatic uplift". In: *Engineering News Record* 116.6 (1936), pp. 872–875.

[828] B. Thacker et al. *Concepts of Model Verification and Validation*. Tech. rep. LA-14167. Los Alamos National Laboratory, 2004.

[829] M. Thakur and D. Kumar. "A hybrid financial trading support system using multi-category classifiers and random forest". In: *Applied Soft Computing* 67 (2018), pp. 337–349.

[830] M. Thomas, B. Fournier, and K. Folliard. *Alkali-Silica Reactivity Field Identification Handbook*. Tech. rep. FHWA-HIF-12-022. United States. Federal Highway Administration. Office of Pavement Technology, 2011.

[831] F. Thomes. "A Conception of Creep of Unreinforced Concrete, and an Estimation of the Limiting Values". In: *Structural Engineer* 11.2 (1933).

[832] L Torlay et al. "Machine learning–XGBoost analysis of language networks to classify patients with epilepsy". In: *Brain informatics* 4.3 (2017), p. 159.

[833] P. Tothong and N. Luco. "Probabilistic seismic demand analysis using advanced ground motion intensity measures". In: *Earthquake Engineering and Structural Dynamics* 36 (2007), pp. 1837–1860.
[834] C. Townsend. "Control of Cracking in Mass Concrete Structures. Engineering Monograph No. 34". In: *Water Resources Technical Publication. US Department of the Interior. Bureau of Reclamation* (1965).
[835] G. Troxell, J. Raphael, and R. Davis. "Long-term creep and shrinkage tests of plain and reinforced concrete". In: *ASTM Proc.* 58 (1958), pp. 1101–1120.
[836] B. Trunk. *Einfluss der Bauteilgrsse auf die Bruchenergie von Beton (Effect of specimen size on the fracture energy of concrete)*. Tech. rep. In German. Freiburg, Germany: Building Materials Report N 11, Aedificatio Verlag, 2000.
[837] B. L. Turner et al. "A framework for vulnerability analysis in sustainability science". In: *Proceedings of the national academy of sciences* 100.14 (2003), pp. 8074–8079.
[838] C.-M. Uang and V. Bertero. "Evaluation of seismic energy in structures". In: *Earthquake Engineering and Structural Dynamics* 19 (1990), pp. 77–90.
[839] F. Ulm et al. "Thermo-Chemo-Mechanics of ASR Expansion in Concrete Structures". In: *ASCE J. of Engineering Mechanics* 126.3 (2000), pp. 233–242.
[840] W. E. S. US ACROPS. "Investigation of creep in concrete; review of literature on creep in concrete". In: *Structural Engineer* Misc. Papers Vicksburgh, Miss.1 (1955), p. 22.
[841] USACE. *Gravity Dam Design*. 1995.
[842] USACE. *Earthquake design and evaluation of concrete hydraulic structures*. Tech. rep. EM 1110-2-6053. Washington D.C., USA: Department of the Army, U.S. Army Corps of Engineers, 2007.
[843] USACE. *Safety of Dams-Policy and Procedures*. Tech. rep. EM 1110-2-1156. Washington D.C., USA: Department of the Army, U.S. Army Corps of Engineers, 2014.
[844] USACE-USBR. *Best Practices in Dam And Levee Safety Risk Analysis*. Tech. rep. Denver, Colorado: A Joint Publication by U.S. Department of the Interior, Bureau of Reclamation, and U.S. Army Corps of Engineers, 2015.
[845] USBR-manual. *Dam safety risk analysis, Best practices training manual, Version 2.2*. Tech. rep. Denver, Colorado: U.S. Department of the Interior Bureau of Reclamation in coorporation with the U.S. Army Corps of Engineers, 2011.
[846] USGS. *PSHA Interactive Deaggregation Tool, U.S. Geological Survey*. 2003.
[847] USGS. *Unified Hazard Tool*. 2017.
[848] R. N. Vaishnav. "Correlation of creep of concrete with its dynamic properties". PhD thesis. University of Illinois at Urbana-Champaign, 1961.
[849] D. Vamvatsikos and C. Cornell. "Incremental dynamic analysis". In: *Earthquake Engineering and Structural Dynamics* 31 (2002), pp. 491–514.
[850] D. Vamvatsikos and C. Cornell. "Applied incremental dynamic analysis". In: *Earthquake Spectra* 20 (2004), pp. 523–553.

[851] D. Vamvatsikos and C. Cornell. "Developing efficient scalar and vector intensity measures for IDA capacity estimation by incorporating elastic spectral shape information". In: *Earthquake Engineering and Structural Dynamics* 34.13 (2005), pp. 1573–1600.

[852] D. Vamvatsikos and M. Fragiadakis. "Incremental dynamic analysis for estimating seismic performance sensitivity and uncertainty". In: *Earthquake Engineering and Structural Dynamics* 39 (2010), pp. 141–163.

[853] R Van der Have. *Random Fields for Non-Linear Finite Element Analysis of Reinforced Concrete*. 2015.

[854] E. Vanmarcke. *Random fields: analysis and synthesis*. World Scientific, 2010.

[855] Červenka, J. "Discrete Crack Modeling in Concrete Structures". PhD thesis. University of Colorado, Boulder, 1994.

[856] A. K. Verma, S. Ajit, and H. P. Muruva. "Seismic PSA of Nuclear Power Plants". In: *Risk Management of Non-Renewable Energy Systems*. Springer, 2015, pp. 177–254.

[857] M. Vořechovský and D. Novák. "Correlation control in small-sample Monte Carlo type simulations I: A simulated annealing approach". In: *Probabilistic Engineering Mechanics* 24 (2009), pp. 452–462.

[858] A. Vosooghi and M. Saiidi. "Experimental fragility curves for seismic response of reinforced concrete bridge columns". In: *ACI Structural Journal* 109.6 (2012), pp. 4825–834.

[859] D. Wald, G. Martinez, and O. Bayrak. "Expansion behavior of a biaxially reinforced concrete member affected by alkali-silica reaction". In: *Structural Concrete* (2017).

[860] D. J. Wald and T. I. Allen. "Topographic slope as a proxy for seismic site conditions and amplification". In: *Bulletin of the Seismological Society of America* 97.5 (2007), pp. 1379–1395.

[861] D. Wald. "ASR Expansion Behavior in Reinforced Concrete – Experimentation and Numerical Modeling for Practical Application". PhD thesis. Austin, TX: University of Texas, Austin, 2017.

[862] E. Walker. "The Effect of Stress Ratio During Crack Propagation and Fatigue for 2024-T3 and 7075-T6 Aluminum". In: *Effects of Environment and Complex Load History on Fatigue Life*. Ed. by M. Rosenfeld. ASTM STP 462. 1970.

[863] P. F. Walsh. "Crack Initiation in Plain Concrete". In: *Mag. of Concr. Res.* 28 (1976), pp. 37–41.

[864] P. Walsh. "Fracture of Plain Concrete". In: *Indian Concrete J.* 46.11 (1972), 469–470 and 476.

[865] G. G. Wang and S. Shan. "Review of metamodeling techniques in support of engineering design optimization". In: *Journal of Mechanical Design* 129.4 (2007), pp. 370–380.

[866] G. Wang et al. "A general definition of integrated strong motion duration and its effect on seismic demands of concrete gravity dams". In: *Engineering Structures* 125 (2016), pp. 481–493.

[867] J. Wang and H. Morikawa. “Study on shear behavior of deteriorated RC beams due to alkali-silica reaction”. In: *37th Conference on Our World in Concrete and Structures, Singpore*. 2012.

[868] J.-T. Wang et al. “Seismic fragility of arch dams based on damage analysis”. In: *Soil Dynamics and Earthquake Engineering* 109 (2018), pp. 58–68.

[869] M. Wang and S. Shah. “Reinforced concrete hysteresis model based on the damage concept”. In: *Earthquake Engineering and Structural Dynamics* 15 (1987), pp. 993–1003.

[870] W. Wang, C. Gu, and T. Bao. “Safety Monitoring Index of High Concrete Gravity Dam Based on Failure Mechanism of Instability”. In: *Mathematical Problems in Engineering* 2013 (2013), pp. 1–14.

[871] Y. Wang et al. *Performance-based fire engineering of structures*. CRC Press, 2012.

[872] Z. Wang et al. “Random Forest based hourly building energy prediction”. In: *Energy and Buildings* 171 (2018), pp. 11–25.

[873] WASH-1400. *An assessment of accident risks in us commercial nuclear power plants*. NTIS, 1975.

[874] Z. Wei et al. “Failure analysis of high-concrete gravity dam based on strength reserve factor method”. In: *Computers and Geotechnics* 35 (2008), pp. 627–636.

[875] A. Wells. *Application of Fracture Mechanics at and Beyond General Yielding*. British Welding Research Ass., Report M13, 1963.

[876] G. West. *Alkali-aggregate reaction in concrete roads and bridges*. Thomas telford, 1996.

[877] M. Westberg. “Reliability-based assessment of concrete dam stability”. PhD thesis. Lund University, 2010.

[878] H. Westergaard. “Water Pressures on Dams During Earthquakes”. In: *Transactions ASCE* 59.8 (1933), pp. 418–433.

[879] H. Westergaard. “Water pressures on dams during earthquakes”. In: *Transactions of the American Society of Civil Engineers* 98 (1933), pp. 418–433.

[880] H. Westergaard. “Bearing Pressures and Cracks”. In: *J. Appl. Mech.* 61 (1939).

[881] O. Wheeler. “Spectrum Loading and Crack Growth”. In: *J. of Basic Engineering* 94 (1972), pp. 181–186.

[882] A. Whittaker, R. Hamburger, and A. Mahoney. “Performance-based engineering of buildings for extreme events”. In: *Proc., Steel Building Symp. Blast and Progressive Collapse Resistance*. 2003, pp. 55–66.

[883] wikipedia. *Action (physics)*. http://en.wikipedia.org/wiki/Action_(physics). Last viewed June 2015. 2015.

[884] J. Willenborg, R. Engle, and R. Wood. *A Crack Growth Retardation Model Using an Effective Stress Concept*. Tech. rep. Air Force Flight Dynamics Laboratory Report, AFFDL-TM-71-1-FBR, 1971.

[885] E. Wilson. *The Use of the Response Spectrum Method in Earthquake Engineering must be Terminated*. Accessed: 2018-10-12. 2014.

[886] F. Wittmann and L. Brieger. “Numerical Simulation of Carbonation of Concrete”. In: *Material and Science Restoration* (1986).

[887] F. Wittmann et al. “Fracture Energy and Strain Softening of Concrete as Determined by Means of Compact Tension Specimens”. In: *Materials and Structures* 21 (1988), pp. 21–32.

[888] J. Wolf. *Soil-Structure Interaction Analysis in Time Domain*. New York: Prentice-Hall Inc., 1988.

[889] T. Wolff. “Analysis and Design of Embankment Dam Slopes: A Probabilistic Approach”. PhD thesis. Purdue University, 1985.

[890] S. Wong, R. Hobbs, and C Onof. “An adaptive response surface method for reliability analysis of structures with multiple loading sequences”. In: *Structural Safety* 27.4 (2005), pp. 287–308.

[891] X. Wu et al. “Top 10 algorithms in data mining”. In: *Knowledge and information systems* 14.1 (2008), pp. 1–37.

[892] Y. Xi and Z. Bažant. “Modeling Chloride Penetration in Saturated Concrete”. In: *J. of Materials in Civil Engineering* 11.1 (1999), pp. 58–65.

[893] D. Xiu and G. E. Karniadakis. “The Wiener–Askey polynomial chaos for stochastic differential equations”. In: *SIAM journal on scientific computing* 24.2 (2002), pp. 619–644.

[894] J. Xu et al. *Assessment Of Seismic Analysis Methodologies For Deeply Embedded NPP Structures*. Tech. rep. Brookhaven National Laboratory (US), 2005.

[895] Y. Yamamoto. “Stochastic model for earthquake ground motion using wavelet packets”. PhD thesis. Palo-Alto, CA: Stanford University, Stanford, 2011.

[896] Y. Yamamoto and J. W. Baker. “Stochastic model for earthquake ground motion using wavelet packets”. In: *Bulletin of the Seismological Society of America* 103.6 (2013), pp. 3044–3056.

[897] D. Yang, J. Pan, and G. Li. “Non-structure-specific intensity measure parameters and characteristic period of near-fault ground motions”. In: *Earthquake Engineering and Structural Dynamics* 38 (2009), pp. 1257–1280.

[898] X. Yao, A. Elnashai, and J. Jiang. “Analytical seismic fragility analysis of concrete arch dams”. In: *Proceedings of the 15th World Conference on Earthquake Engineering*. Lisbon, Portugal, 2012.

[899] Y. Yazdani and M. Alembagheri. “Seismic vulnerability of gravity dams in near-fault areas”. In: *Soil Dynamics and Earthquake Engineering* 102 (2017), pp. 15–24.

[900] B. D. Youn and K. K. Choi. “A new response surface methodology for reliability-based design optimization”. In: *Computers & Structures* 82.2 (2004), pp. 241–256.

[901] R. Youngs et al. “Strong ground motion attenuation relationships for subduction zone earthquakes”. In: *Seismological Research Letters* 68.1 (1997), pp. 58–73.

[902] Q. Yu et al. “Comparison of Main Models for Size Effect on Shear Strength of Reinforced and Prestressed Concrete Beams”. In: *Structural Concrete* (2016).

[903] A. Yücel. “Seismic Analysis of Concrete Gravity Dams Including Dam-Foundation-Reservoir Interaction”. MA thesis. Turkey: Middel East technical University, 2013.

[904] C. Zangar. “Hydrodynamic Pressures on Dams Due to Horizontal Earthquakes”. In: *Proceedings of Society of Experimental Stress Analysis* 10 (1953), pp. 93–102.

[905] F. Zareian and H. Krawinkler. *Simplified performance based earthquake engineering, Report No. 169*. Tech. rep. Stanford University, 2009.

[906] F. Zareian et al. “Basic concepts and performance measures in prediction of collapse of buildings under earthquake ground motions”. In: *The Structural Design of Tall and Special Buildings* 19 (2010), pp. 167–181.

[907] I Zentner et al. “Numerical methods for seismic fragility analysis of structures and components in nuclear industry-Application to a reactor coolant system”. In: *Georisk* 5.2 (2011), pp. 99–109.

[908] I. Zentner, M. Gündel, and N. Bonfils. “Fragility analysis methods: Review of existing approaches and application”. In: *Nuclear Engineering and Design* 323 (2017), pp. 245–258.

[909] D. Zhang et al. “Time-Dependent Reliability Analysis Through Response Surface Method”. In: *Journal of Mechanical Design* 139.4 (2017), p. 041404.

[910] G. Zhang, B. E. Patuwo, and M. Y. Hu. “Forecasting with artificial neural networks:: The state of the art”. In: *International journal of forecasting* 14.1 (1998), pp. 35–62.

[911] S. Zhang et al. “The effects of strong motion duration on the dynamic response and accumulated damage of concrete gravity dams”. In: *Soil Dynamics and Earthquake Engineering* 45 (2013), pp. 112–124.

[912] Y. Zhang et al. “Treatment of Seismic Input and Boundary Conditions in Nonlinear Seismic Analysis of a Bridge Ground System”. In: *16th ASCE Engineering Mechanics Conference*. University of Washington, Seattle, 2003.

[913] C. Zhao and J. Chen. “Numerical simulation and investigation of the base isolated NPPC building under three-directional seismic loading”. In: *Nuclear Engineering and Design* 265 (2013), pp. 484–496.

[914] W. Zhao and Z. Qiu. “An efficient response surface method and its application to structural reliability and reliability-based optimization”. In: *Finite Elements in Analysis and Design* 67 (2013), pp. 34–42.

[915] H. Zhong et al. “Seismic failure modeling of concrete dams considering heterogeneity of concrete”. In: *Soil Dynamics and Earthquake Engineering* 31 (2011), pp. 1678–1689.

[916] H. Zhong, N.-l. Wang, and G. Lin. “Seismic response of concrete gravity dam reinforced with FRP sheets on dam surface”. In: *Water Science and Engineering* 6.4 (2013), pp. 409–422.

[917] F. Zhou. “Time-dependent Crack Growth and Fracture in Concrete”. PhD thesis. Division of Building Materials Lund Institute of Technology, 1992.

[918] H. Zhou, J. Wan, H. Jia, et al. "Resilience to natural hazards: a geographic perspective". In: *Natural Hazards* 53.1 (2010), pp. 21–41.

[919] Y. Zhou, N. Su, and X. Lu. "An elastic spectral value-based intensity measure for the incremental dynamic analysis of tall buildings". In: *Proceedings of the 5th Kwang-Hua Forum on Innovations and Implementations in Earthquake Engineering Research*. Shanghai, China, 2012.

[920] B Zhu. "Prediction of water temperature in deep reservoirs". In: *Dam Engineering* 8 (1997), pp. 13–26.

[921] H. Zhu et al. "Physical modelling of sliding failure of concrete gravity dam under overloading condition". In: *Geomechanics and Engineering* 2 (2010), pp. 89–106.

[922] K. E. Zicko, D. A. Bruce, and R. A. Kline Jr. "The stabilization of Gilboa Dam, New York, using high capacity rock anchors: addressing service performance issues". In: *Ground anchorages and anchored structures in service, Proceedings of the International Conference, London. London: Thomas Telford*. 2007, pp. 153–65.

[923] O. Zienkiewicz, D. Kelly, and P. Bettess. "The sommerfeld (radiation) condition on infinite domains and its modelling in numerical procedures". In: *Computing Methods in Applied Sciences and Engineering, 1977, I*. Ed. by R. Glowinski, J. Lions, and I. Laboria. Vol. 704. Lecture Notes in Mathematics. Springer Berlin / Heidelberg, 1979, pp. 169–203.

[924] O. C. Zienkiewicz, R. L. Taylor, and P. Nithiarasu. *The Finite Element Method for Fluid Dynamics*. 6th. Elsevier Butterworth-Heinemann, 2005.

[925] O. C. Zienkiewicz, R. L. Taylor, and J. Zhu. *The Finite Element Method for Solid and Structural Mechanics*. 6th. Elsevier Butterworth-Heinemann, 2005.

[926] O. Zienkiewicz. *The Finite Element in Structural and Continuum Mechanics*. First. McGraw-Hill, London, 1967.

[927] G. van Zijl, J. Rots, and R. deBorst. "The Physical Role of Crack Rate Dependence in the Long-Term Behaviour of Cementitious Materials". In: *IUTAM Symposium on Theoretical and Numerical Methods in Continuum Mechanics of Porous Materials*. Ed. by W. Ehlers. 2001, pp. 321–328.

Index

h convergence, 267
p convergence, 267
r convergence, 267
1:6 scale Model
  Pretest Calculations, 764
28 Days Compressive Strength, 883

AAR
  Applications, 831
  Concrette Pores, 209
  Constitutive Model, 205
  Degradation, 214
  Example
    R/C Structure, 831
  Retardation, 208
  RH, 208
  Strain Redistribution, 210
  Volumetric Expansion, 208
Abaqus, 233, 795
Acceleration Root Mean Square, 464
Activation Energies, 207
Adaptive POA, 508
Adaptive Remeshing, 267
Age-adjusted Effective Modulus, 101
Aging, 94
Aging Concrete Information System, 215
Aleatory Variability, 366
Anagram, 25
Analysis
  Code Selection, 768
  Model Development, 768
  Results Interpretation, 772
Analytical Evaluation, 864
Analytical Fragility Curve, 533
Annual Probability of Failure, 586
Annualized Life Loss, 592
Approximate Numerical Solution, 272
Arch Dam Damage Index, 555
Arias Intensity, 461, 464
Arrhenius, 207
Arrhenius Equation, 196
Artificial Damping, 132
Artificial Neural Networks, 442
As-low-as-reasonably-practicable, 596
ASME, 762
ASR
  Finite Element Modeling, 291
  Prediction Past Expansion, 222
ATENA, 234
Attenuation Model, 476
ATU, 606
Auto-correlation Function, 411
Autogenous Shrinkage, 93
Average Annual Life Loss, 586, 596
Axisymmetry, 27

Baker Intensity, 469

Basemart
  High Stiffness, 769
Basemat
  Irregularities, 769
Basemat, 761
Basic Creep, 94
Bauschinger Effect, 57
Beam Shear tests, 857
Beyond Design Basis Loads, 752
Binding Capacity, 188
Bivariate Distribution, 147
Bivariate Normal Distribution, 148
Body Force, 13
Body Force, 28
Boeing 737 MAX, 869
Bojorquez Intensity, 469
Boundary Conditions, 28, 37
Bounded Spectrum Intensities, 467
Box-Behnken Experimental Design, 423
Bracketed Duration, 462
Bravo 1 Tunnel, 871
Brookhaven National Laboratory, 871
Bubble Function, 254
Building Deformation Aging Management, 860
Building Deformation Assessment, 863
Bureau of Reclamation, 215, 346

Calcium Carbonates, 192
Calcium Hydroxide, 194
Calibration, 234
Capacity Analysis
  Guidelines, 765
Capacity Curve, 501
Capacity Diagram, 501
Capacity Function, 501
Carbon Dioxide, 192
Carbonation, 192
Case studies, 217
Category I, 864
Cauchy Strain, 19
Cauchy Stress Tensor, 15
Cauchy Tetrahedron, 14
Cauchy's Equation of Motion, 22
CEB Analysis
  Goals and Planning, 766
Central Composite Design, 422
Central Difference, 121
Central Tendency, 141
Characteristic Intensity, 466
Characteristic Length, 155, 179
Characteristic time, 207
Chemical Bonds, 55
Chemical Hydration, 92
Chemical Prestressing
  Modelling, 894
Chemical Prestressing, 878
Chemical Shrinkage, 93
China Syndrome, 761
Chloride Isotherm, 188
CI, 882
Circular Hole, 63
Cloud Analysis, 522
Cloud Based Fragility, 544
Code Verification, 234
Code-based Approach, 871
Coefficient of Variation, 142
Cohesive Crack Model, 154
Collapse Fragility Curve, 534
Combined Capacity Function, 526
Compressive Meridian, 52
Compressive strength, 216
Computational Power, 766
Computer Model, 235
Conceptual Model, 235
Concrete
  Fracture Energy, 156, 232
Concrete Creep Coefficient, 232
Concrete Elastic Modulus, 232
Concrete Mix, 856
Concrete Strength
  Compressive, 232
  Tensile, 232
Concrete-Rock Interface, 321
Condition Of Incompressibility, 21
Conditional Mean Spectra, 487
Conditional Probability, 137

Conditional Probability Distribution, 147
Conditional Spectra, 487
Conditional Stability, 129
Confidence, 235
Confidence Level, 591
Confinement, effect of, 216
Consequences Categories, 591
Conservation Laws, 19
Conservation of Energy, 22
Conservation of Momentum, 21
Consistency Condition, 60
Consistent Mass Matrix, 122
Constitutive Equations, 25
Constitutive Models, 771
Constitutive Operator, 274
Containment Capacity Analyses, 768
Containment Design, 762
Continuity Equation, 21
Continuous Fragility Function, 532
Continuous Random Variables, 138
Continuum Mechanics, 15
Convection, 32
Conventional POA, 508
Convergence, 279
Convergent Boundaries, 106
Cordova Intensity, 468
Corps of Engineers, 346
Correlation Coefficient, 142
Corroborative Modulus Expansion, 861
Cosenza-Manfredi Intensity, 466
Covariance, 142
Covariance Matrix, 414
Crack Dependent DI, 559
Crack Growth Curve, 75
Crack index, 832
crack index, 860
Crack Inspections, 75
Crack Instability, 160
Creep, 91, 880
Creep Coefficient, 96
Creep Strain, 94
Crude Monte Carlo Simulation, 391, 394
Crystal River 3
  Computer Model, 794
  Delaminatin Explained, 801
  Detailed Model, 798
  Failure Mode Group 1, 798
  Failure Mode Group 7, 800
  Finite Element Modelling, 794
  Global Model, 796
  Model Assessment, 802
Cumulative Absolute Displacement, 465
Cumulative Absolute Velocity, 465
Cumulative DI, 550
Cumulative Distribution Function, 139
Cumulative Inelastic Area, 578
Cumulative Inelastic Duration, 578
Cyclic POA, 515
Cyclic Pushover Procedure, 512

Dam
  Poglia, 613
dam
  Isola, 605
Damage Index, 547
Damage Measure, 452
Damage Probability Matrix, 532
Damage Spatial Distribution Ratio, 579
Damage Spectrum, 550
Damage Tolerance Assessment, 75
Damage Variable, 547
Damping, 460
Data Gathering, 228
Data Mining, 230
Data preparation, 606
Decision Tree Regression, 440
Decision Variable, 452
Deconvolution
  1D, 324
  3D, 325
  Simplification, 325
Defense-indepth, 762
Demand Capacity Ratio, 578
Design of Experiment, 419

Design Philosophy, 68
Destructiveness Potential, 464
Detailed Evaluation, 864
Deterministic DI, 550
Deterministic Seismic Hazard Analysis, 479
Direct Consequences, 584
Direct Cost, 587
Direct Integration, 389
Directional Expansions, 862
Discrete Random Variables, 137
Dislocation, 56
Displacement Based DI, 555
Displacement Based Pushover Analysis, 508
Displacement Dependent DI, 556
Divergence Theorem, 12
Divergent Boundaries, 106
Downtime Measure, 384
Drucker-Prager, 52
Drying Creep, 94
Drying Shrinkage, 93
Dummy Index, 4
Dyadic Notation, 5

Earth's Layers, 103
Earthquake, 103
Earthquake Damage, 105
Earthquake Energy, 115
Earthquake Location, 111
Earthquake Magnitude, 113
Economic Considerations, 587
Economical DI, 550
Edge Effect, 876
EDP Based Fragility, 538
Effective Mass Matrix, 125
Effective Modulus, 101
Effective Peak Values, 467
Effective Stresses, 28
Eigenvalues, 127
Einstein, 766
Einstein's Notation, 4
Elastic properties, 215
Elastic Rebound Theory, 106
Elastic Response Spectra, 458
Elasto-Plastic Fracture Mechanics, 79
Elements
  Beam, 770
  Brick, 770
  Containment, 770
  Continuum, 770
  Shell, 770
Elliptic Equation, 35
Elliptical Hole, 64
Embedded Reinforcement, 288
Empirical Fragility Curve, 533
Endurance Time Acceleration Function, 523
Endurance Time Analysis, 523
Endurance Time Excitation Functions, 492
Energy Based Pushover Analysis, 508
Energy Dependent DI, 560
Engineering Demand Parameter, 452
Engineering Judgment, 773
Engineering Shear Strain, 18
Environment Consequences, 587
Environmental Conditioning Facility, 857
Epicentre, 108
Epistemic Uncertainty, 366
Equation
  Cauchy, Motion, 36
  Darcy, 33
  Diffusion, 36
  Faraday, 202
  Fourrier, 186
  Heat, 37
  Helmholtz, 34
  Inglis, 65
  Kozeny-Carman, 190
  Laplace, 37
  Poisson, 35
  Westergaard, 67
Equation of Motion, 21, 458
Equivalent Domain Integral, 303
Equivalent Static Lateral Force, 515
Error, 235

ETA Curve, 524
Event Tree Analysis, 573
Exclusion Distance, 761
Expectations, 140
Experimental Cyclic Test, 513
Experimental Fragility Curve, 533
Explicit Analysis, 121
exposure, 195
Extended Capacity Function, 525
Extreme Gradient Boosting, 442
Extreme Learning Machine, 443

F-N Chart, 586
Factored Load Combinations, 864
Failure
  Functional, 763
  Structural, 763
Failure Criteria, 773
Failure Criterion
  Global, 769
  Local, 769
Failure Function, 312
Failure Index, 589
Failure Likelihood Categories, 591
Failure Probability, 389
Failures, 763
Faraday's Law, 202
Fatigue Crack Propagation, 88
Fault Mechanisms, 107
Fault Rupture, 105
Fault Tree Analysis, 573
FERC, 346
Ferguson Structural Engineering Laboratory, 855
Ficititous crack, 876
Fick Law, 186, 187
Fictitious Crack, 310
Fidelity, 235
Film Coefficient, 32
Final Safety Analysis Report, 326
Finite Element
  Assessment of Results, 230
  Convergence, 266, 267
  Crystal River, 794
  Equilibrium & Compatibility, 266
  Fundamentals, 237
  Loads and B.C., 231
  Material Properties, 232
  Mesh Verification, 235
  Modelling, 227, 230
  non-linear, 269
  Problem Definition, 228
  Software Selection, 233
  Structured-Unstructures Meshes, 229
  Study, 229
  Tabulation Loads, 232
First Generation of PBEE, 449
First Law, 34
First Order Reliability Method, 389
Flood Overload Factor, 506
Flow, 32
Flow Rule, 59
Fluid Structure Interactions, 345
Flux, 20
Flux, 33
Focal Depth, 108
Force-based Failure Assessment, 888
Forced Based Pushover Analysis, 508
Forces, 13
Foundation PFM, 571
Fourier Amplitude Spectrum, 457
Fourier Phase Spectrum, 458
Fourier Spectra, 456
Fourier Transform, 457
Fourrier Transform, 322
Fractal Cracks, 164
Fractional Factorial Design, 422
Fracture Concrete, 153
Fracture Control Plan, 77
Fracture Mechanics, 63
Fracture Process Zone, 174
Fracture Properties, 71
Fragility, 381
Fragility Curve, 529
Fragility Curves, 753
Fragility Function, 529
Fragility Surface, 530
Free Index, 4

Free Vibration, 132
Full Factorial Design, 421
Functional Failure Modes, 767
Fundamental Laws, 19

Gauss-Divergence Theorem, 12
Gaussian Process Regression, 444
Generalized Linear Model, 535
Geometric Nonlinearities, 772
Geometric Symmetries, 770
Global Model, 769
Global Radiation, 41
Goodness-of-fit, 426
Gravity Dam Damage Index, 550
Green Theorem, 12
Grizzly, 234
Ground Motion Dependent Compound IMs, 465
Ground Motion Dependent Scalar Intensity Measures, 463
Ground motion Duration, 460
Ground Motion Frequency Content, 456
Ground Motion Prediction Equation, 476
Ground Motion Time History, 455
Guidelines, 765
Gumbel Distribution, 146
Gutenberg Richter Recurrence Law, 474

Halton, 369
Halton Sequence, 395
Hariri-Saouma Intensity, 468
Harmonic Functions, 35
Hazard, 376
Heat Transfer, 31
Heuristic Fragility Curve, 533
Higher Order LSED, 421
Hillerborg, 154, 310
Historical Context, 760
Historical Seismic Damage in Dams, 565
Hooke's Law, 25
Hooke's Law, 26
Hour-glass, 770
Housner Intensity, 467
Hsinfengkiang Dam, 566
Hughe's Method, 130
Hybrid Damage Index, 551
Hybrid Fragility Curve, 533
Hybrid Load Vector, 510
Hydraulic conductivity, 349
Hydro Pressure Overload Factor, 506
Hydrostatic Pressure Dependent, 51
Hydrostatic Pressure Independent, 50
Hygrothermal Strain, 93
Hypocentral Distance, 478
Hypocentre, 108

ICOLD, 613
IDA Based Fragility, 538
Ikata No.1 Nuclear Power Station, 786
IM Based Fragility, 537
IM Efficiency, 470
IM Hazard Compatibility, 471
IM Practicality, 470
IM Proficiency, 470
IM Sufficiency, 471
Imminent Failure Mode, 601
Impetus, 14
Implicit, 122
Importance Sampling, 392
In-plane Shear, 856
Incoherence, 117
Incremental Dynamic Analysis, 517
Incremental loads, 609
Incremental Risk, 585
Incremental-iterative, 276
Indicial Notation, 4
Indirect Consequences, 584
Indirect Cost, 587
Individual Risk, 586
Induced Earthquakes, 104
Initial Stiffness, 280
Inner Product, 6
Integration by Part, 12
Intensity Based Performance Assessments, 453
Intensity Measure, 452

Interface Transition Zones, 174
Internal Cracks, 884
Internal Forces, 121
Internal humidity, 880
Invariant Multi Mode Vectors, 509
Invariant Single Load Vectors, 508
Invariants, 10
Ion Diffusion, 202
Irreducible Uncertainty, 235
Isoparametric Element, 294
Isoparametric Elements, 242
Issue Evaluation Study, 591

J Integral, 81
J integral, 299
Jacobian, 294
Jacobian Matrix, 278
Joint Probability Distribution, 146
Joyner-Boore Distance, 477

K-Nearest Neighbor, 435
Kinematic Equation, 271
Kinetics, 206
Koyna Dam, 565
Kozeny-Carman Equation, 190
Kuhn-Tucker, 60
Kurtosis, 142

Laboratory Observations, 53
Lagrangian Interpolation Function, 244
Lame's Constants, 25
Laplace Equation, 35
Laplacian, 12
Large Scale Testing Program, 856
Latency time, 207
Lateral Rigid Body Motion, 342
Latin Hypercube Sampling, 369, 391, 395
Latin Square Experimental Design, 421
Law of Large Numbers, 136
Leak Before Break, 74
Leakage, 767
Leave-One-Out, 429
Lexical Uncertainty, 366
License Renewal Rule, 853
Life Safety Measure, 384
Life Safety Risk, 586
Linear Regression in Transferred Space, 543
Linearization, 274
Liner Tearing, 764
Liquefaction, 105
Load History, 276
Local and Global DI, 550
Localization, 160
Lognormal Distribution, 144
Lognormal Fragility Function, 537
Loss Of Containment, 767
Loss Of Coolant Accident, 853
loss of Life Factor, 590
Love Waves, 108
LS-Dyna, 233

Machine Learning, 430
Machine Learning Classification, 434
Machine Learning Regression, 439
Margin For Future Expansion, 888
margin of safety, 897
Marginal Distribution, 146
Massive R/C structure, 831
Material Coordinates, 18
Mathematical Model, 229
Mathematical Model, 235
Maximum Likelihood Estimation, 540
Mean, 141
Mechanics
Review, 3
Median, 141
Merlin, 234, 835
Metamodeling, 418
Method of Moments, 539
Mineralogy, 883
Mixed Mode Crack Propagation, 72
Modal Pushover Analysis, 509
Model, 235
Model Complexity, 231
Model Revision, 235

Modified Mercalli Intensity, 111
Modified Modal Pushover Analysis, 509
Modified-Newton, 280
Mohr-Coulomb, 52
Moment Magnitude, 461
Monotonic POA, 514
Monte Carlo Simulation, 369
Mozart, 25
MPR Associates, 855
MSA Based Fragility, 541
Multi Adaptive Regression Splines, 444
Multi Record IDA, 520
Multiple-Component Ground Motions IMs, 470
Multiple-Period Intensities, 468
Multivariate Correlation, 370
Multivariate Distributions, 146
Multivariate Normal Distribution, 148

Naive Bayes Classifier, 438
Natural Earthquakes, 103
Newton's Methods, 276
Nitrogen Gas, 764
Non-breach Risk, 585
Normal Distribution, 143
Normalized Empirical Error, 429
Notation
  Indicial, 3
  Tensor, 5
  Voigt, 5
NRC and NextEra, 869
Nuclear Power Engineering Corporation, 765
Numerical Cyclic Loading, 514
Numerical Integration
  Explicit, 272

Occurrence Time, 482
Octahedral Stress, 10
Openings, 770
Optimal IM Selection, 470
Out-of-Plane Expansion, 860
Overlayed shell elements, 891

Pacoima Dam, 566
Parabolic Equation, 35
Parallel Failure Modes, 575
Parallel Systems, 373
Passivity, 183
Passivity and PH, 199
PBEE Framework, 448
Performance Based Earthquake Engineering, 446
Performance Based Engineering, 445
performance Based Engineering, 499
Periodic Risk Analyses, 590
PFM Classification, 571
PFMA Arch Dams, 569
PFMA Buttress Dams, 571
PFMA Criteria, 579
PFMA Gravity Dams, 569
PFMA Index, 578
PFMA Initiators, 568
PFMA Linear System, 578
PFMA Nonlinear System, 580
PGA, 455
PGD, 456
PGV, 456
Plackett-Burman Experimental Design, 423
Plane Strain, 27
Plane Stress, 28
Plastic Capacity, 889
Plastic Zone Size, 79
Plate Tectonics, 105
Poisson's Equation, 35
Poisson's Probability Model, 482
Polynomial Chaos Expansions, 426
Polynomial Metamodel, 425
Pore Pressure, 28
Position, 16
Potential Failure Locations, 767
Potential Failure Mode Analysis, 565, 567
Potential Failure Modes, 773
Power Spectral Density Function, 458
Prediction, 235
Predictor, Corrector, 281

Primary Waves, 108
Principal Values, 9
Probabilistic Analysis, 232
Probabilistic Seismic Demand Analysis, 522
Probabilistic Seismic Demand Model, 470
Probabilistic Seismic Hazard Analysis, 479
Probability, 135
Probability Distribution, 137
Probability of Failure, 373
Probability Of Failure, 767, 889
Probable Maximum Flood, 599
Probable Maximum Ground Acceleration, 326
Pseudo Response Spectra, 459
Pushover, 601
Pushover Based Analysis, 507

Quantitative PFMA, 577
Quantitative Risk Analyses, 593
Quarter Point Singular Elements, 293
Quasi-harmonic Equation, 35
Quasi-Random Method, 369

Radiation, 32, 607
Ramberg Osgood Equation, 519
Random Fields, 409
Random Forest, 441
Random Response Spectrum Method, 398
Random Variable, 136
Randomized Complete Block Design, 420
Rasmussen Report, 761
Rate Theory, 57
Rayleigh Damping, 122
Rayleigh Waves, 108
Rayleigh-Ritz, 244
Reaction Vector, 283
Reality Check, 229
Recurrence Relationship, 473
Reduced Integration, 770
Reducible Uncertainty, 235
Relative Humidity, 880
Relaxation, 880
Reliability, 371
Reliability Index, 372
Reliability Index, 889
Repair Cost Measure, 384
Residual Forces, 283
Residual Risk, 586
Residual Strength Diagram, 75
Resilience, 384
Response Spectrum, 458
Response Spectrum Analysis, 515
Response Spectrum Method, 896
Response Surface Method, 425
Retardation
  AAR, 208
Rezaeian and Der Kiureghian Modal, 489
Riddell-Garcia Intensity, 466
Rigid Body Limit Equilibrium, 599
Risk, 379, 583
Risk Analysis, 585
Risk Assessment, 584, 595
Risk Based Profile System, 589
Risk Based Terminology, 371
Risk Communication, 584
Risk Evaluation, 584
Risk Guidelines, 596
Risk Index, 590
Risk Informed Decision Making, 583
Risk Management, 584
Risk Matrix, 592
Risk Measures, 586
Risk Significance, 767
Risk Types, 585
Rock-Free Field Rocking, 320
Role of Reviewers, 870
Root Cause Investigation, 853
Round-off, 267
Rupture Distance, 477
Rust Production, 202

Safety Evaluation Report, 853
Safety Factor DI, 555
Safety Margin, 372
Saint-Laurent, 809

Salieri, 25
Sampling Techniques, 367
Sandia
  First Study, 761
  Tests
    Preliminary Work, 762
Sanity Check, 228, 772
Scenario Based Performance Assessments, 454
Screening Evaluation, 864
Screening Level Risk Analyses, 588
Seabrook
  Box Limits, 873
  Building Deformation Aging Management, 880
  Building Deformation Assessment, 888
  Finite Element Analysis, 865
  Internal cracking, 878
  Measurement Uncertainties, 887
  Nonlinear Analysis, 891
  Out-of-Plane, 874, 883
  Possible delamination, 876
Seabrook Station Unit 1, 851
Secant Newton, 280
Second Generation of PBEE, 451
Second Order Reliability Method, 390
Secondary Waves, 108
Seepage Analysis, 349
Sefid-rud Dam, 567
Seiches, 105
Seismic & AAR, 835
Seismic Belt, 103
Seismic Hazard Curves, 483
Seismic Hazard Deaggregation, 485
Seismic Hazard Map, 484
Seismic loads, 896
Seismic Probabilistic Risk Assessment, 326
Seismic Source Model, 475
Seismic Waves, 108
Seismogenic Depth, 478
Seismogenic Distance, 477
Seismological Duration, 462
Self-straining Loads, 863
Semi-Quantitative Risk Analyses, 590
Semi-Supervised Learning, 430
Sensitivity Analysis, 366
Series Failure Modes, 575
Series System, 373
Severity Zones, 860
Shaking Intensity, 111
Shaking Intensity Rate, 466
Shear Capacity, 858
Shear Modulus, 26
Shear Transfer Mechanisms, 874
Shear Wave Velocity, 326
Shell Elements, 891
Shih Kang Dam, 565
Shrinkage, 93
Significant Duration, 461
Simplified Methods, 768
Simpson Gumpertz & Heger, 855
Single Record IDA, 517
Singular Element, 295
Singularities, 236
Size Effect
  Bažant, 160
  Saouma, 163
Size Effect, 880
Size-reduced-strength, 161
Skewness, 142
Slenderness, 577
Sliding Safety Factor, 601, 700
Smeared Crack, 209
Smeared Rebar, 771
Snap-Back, 154
Sobol, 369
Sobol Sequence, 396
Social Incremental Risk, 596
Societal Risk, 586
Softening Diagram, 155
Solar Declination, 43
Solar Radiation, 41
Solution Strategy, 771
Source to Site Effect, 116
Spatial Coordinates, 18
Spatial Correlation, 370

Specific Energy Density, 464
Specific Heat, 33
Spline Interpolation, 518
Splitting Crack, 876
Standard Deviation, 142
Standards Based Approach, 583
Star Experimental Design, 422
Statistics, 141
Steam Generator Replacement, 815
Stefan-Boltzman, 41
Stiffness Matrix, 240
Stochastic DI, 550
Stochastic Ground motion
  Simulation, 488
Storativity, 350
Strain
  Linear Operator, 19
Strains, 18
  Eulerian, 18
Strength Reserve Factor, 504
Stress
  Geometric Representation, 16
  Hydrostatic, 15
Stress Concentrations, 63
Stress Intensity Factors, 66, 69
Stress Singularity, 66
Stress-based Failure Assessment,
  888
Stressor, 501
Structural Crack, 857
Structural Integrity Test, 804
Structure-Dependent Spectral IMs,
  468
Structure-Independent Spectral IMs,
  467
Structured Mesh, 229
Submarine, 761
Sum of Squared Error Minimization,
  542
Supervised Learning, 430
Support Vector Machine, 436
Support Vector Regression, 439
Surface measurements
  Internal cracks, 881
Surface Waves, 108
Sustainability, 387
System identification, 219, 610

Taguchi Experimental Design, 424
Tangent Elastic Modulus, 58
Tangent Stiffness Matrix, 120, 274,
  275
Target Response Spectra, 486
Taylor's Series, 276
Temperature
  Modeling, 772
Temperatures
  300°C, 772
Temporal Correlation, 370
Tendons, 796
Tensile Meridian, 52
Tensile strength, 216
Tension-stiffening, 771
Tensor
  Stress, 14
Tensor, 5
Tensors, 5
Tests
  NUPEC-NRC, 765
  Sandia
    Reinforced Concrete, 763
Thermal analysis, 607, 615
Thermodynamics, 78
  First Principle, 22
Thermodynamics, 92
Three Mile Island, 761
Threshold Factor, 887
Through Thickness Expansion, 861
Time Based Performance
  Assessments, 454
Time Dependent Strength
  Degradation, 504
Time Discretization, 123
Time Invariant Reliability, 373
Time Variant Reliability, 375
Time-dependent Inelastic Strains, 91
Tolerable Risk, 595
Tonti Diagrams, 44
Tools And Methods, 766
Tornado Diagram, 366, 367

Total Ground motion Duration, 461
Total Risk, 594
Traction, 13
Traction Vectors, 14
Transfer Function, 323
Transform Boundaries, 106
Transformation
  Tensors, 8
  Vectors, 7
Transient Dynamic Analysis, 119
Transient Pressure, 767
Transverse Isotropy, 27
Tree Bagging, 441
Tresca, 50
Truncated IDA Based Fragility, 540
Tsunamis, 105
Turbine Generator Foundation, 786
Two Step Analysis, 319

Uh Dam, 565
Uncertainty Quantification, 365
Uniform Distribution, 143
Uniform Hazard Spectra, 486
Univariate Distributions, 143
Unscalable Intensity Measures, 463
Unsupervised Learning, 430
Uplif
  Dynamic, 351
Uplift
  Static, 345
Upper Bound Pushover Analysis, 510

Validation, 234
Vamvatsikos Intensity, 468
Variable Amplitude Loading, 88
Variance, 142
Variational Formulation, 119
Vector Based IMs, 469
Vector Fields, 13
Verification, 234
Verification & Validation, 234, 890
Virtual Work, 237
Virtual Work, 123
Viscous Boundaries, 328
Voigt Notation, 15
Voigt Notation, 5
Volumetric Strain, 883
von Mises, 51
Vulnerability, 383

Wave Equation, 326
Wave Equation of Motion, 109
Weakest Link, 231
Weibull Distribution, 145
Westergaard, 352
Wetting Zones, 857
Work-Hardening, 57

Yamamoto and Baker Model, 490
Yield Condition, 49
Yield Function, 49
Yield Stress, 57
Yield Surface, 49

Zangar, 354

Author

COMSOL, xlii, 236
Červenka, J., xliv, 234, 310, 349, 600, 608, 672, 721, 822, 838, 839
Haha, M. Ben, 207
Ökten, Giray, 395
Červenka, J., 310
Červenka, V., 819
209-Creep, ACI Committee, 97, 99

Ababneh, A., 187, 190
ABAQUS, 560
Abdelhamid, H., 688
ABS, 376
Abuhaikal, M., 91
Acharya, S., 807
ACI, 101
ACI 318, 889
ACI 318-71, 864, 866, 871, 889
ACI 349, 232, 806
ACI 365, 868
ACI-ASCE 423.10R-16, 880
Adams, J., 688
Agarwal, Pankaj, xlviii, 555, 556, 688
Aghajanzadeh, Meisam, 688
AH-S., Ang, 466, 549
Ahmadi, M.T., 567
Ahmed, Tarig, 858
Ajit, Srividya, 756
Alekseev, S.N., 194, 195
Alembagheri, M., 512, 513, 520, 555
Alembagheri, Mohammad, 688
Allahabadi, R., 548, 558
Allaix, Diego Lorenzo, 425
Allen, T. I., 820
Alnaggar, Mohammed, 785
Altarejos-Garcia, L., 379
Alves, SW, 398
Amirpour, A., 555
ANCOLD, xlv, 380, 382
Anderson, T.L., xl, xliii, 86, 304, 305, 307, 308
Ando, K, 758
Andonov, A, 507
Andonov, Anton Georgiev, 507
Ang, A.H.S., 554
Ansari, Md Imteyaz, 688
Ansari, Md. Imteyaz, xlviii, 555, 556, 688
ANSYS, 622, 713, 734
Antoniou, S., 508
Apostolov, K, 507
Apostolov, Kiril Stoev, 507
Applied Technology Council, 453, 454, 483, 488, 698, 756
Araya, R., 464
Ares, Antonio Fernandez, 756
Arias A., 464
Arici, Y., 520

Army Corps of Engineers, 366, 659
Arnstein, A, 92
Arrhenius, S., 207
ASCE 4-16, 320, 751, 752, 756, 868, 896, 897
ASCE/SEI 43-05, 752, 756
ASCE/SEI 7, 552, 889
ASCE/SEI-41-13, 514
Aschheim, M.A., 508
Ashar, Hansraj, 755, 759, 892, 895, 896
Aslam, M., 356
ASME, 755
ASME III, BPVC, 752, 756
ASTM C469, 232, 884
ASTM C496, 232
ASTM C512, 232
ASTM, C39, 232
ATC, 467
ATC-13, 384, 447, 533
ATC-14, 447
ATC-40, 447
ATC-58, 697
Athanatopoulou, A., 470
Atkinson, Gail M, 476
Attiogbe, Emmanuel K, xli, 174, 176
Augusti, G., 500
Aven, T., 370
Awruch, A.M., 688
Ayyub, Bilal M, 385, 391
Azarbakht, A., 520

béton, Fédération internationale du, 97
Bažant, Ž and Xiang, Y., 178
Bažant, Ž. and Gettu, R., xlii, 178, 179
Bažant, Z., xl, lix, 93, 170, 171, 177, 178, 880
Bažant, Z.P., 99, 100, 157, 160, 171, 179, 187, 189, 191, 192, 205, 321, 347, 773, 880
Babuska, I., 306
Bach, Francis, 436
Bachman, R., 534, 543, 544
Baecher, G.B., 377, 574
Baecher, Gregory B, 412
Baker, J., 469, 521
Baker, J.W., 487, 488, 534, 535, 541, 543, 673, 759
Baker, Jack, 487
Baker, Jack W, 488, 490–492, 723
Banon, H., 548, 558
Bao, T., 501
Barak, Sasan, 417, 724, 728
Barbato, M., 500
Barenblatt, G.J., 80, 155
Barsoum, R.S., 293
Basili, M., 405
Basu, U., 339
Bathe, K.J., xlii, 227, 252, 256, 282
Baušys, Romualdas, 758
Baweja, S., 99, 100
Baweja, Sandeep, 100
Bayrak, O., lvi, 856–860, 862, 863, 874, 877
Bayrak, Oguzhan, 858, 878
Bazant, Z. P., 201
Bazant, Z.P., 504
Bazant, Zdenek P, 100
Bažant, Z.P., 94
Bažant, Zdeněk P, 92, 99
Becker, Stephen, 437
Beckjord, Eric S, 755
Beckman, R.J., 391, 395
Becq-Giraudon, E., 157
Beeby, Andrew W, 97
Beer, M., 366
Behnken, Donald W, 423, 693
Beikae, M., 327
Belytschko, T., 130, 227
Ben-Ftima, M., 205
Benboudjema, F., 187, 190
Benesty, Michael, 442
Benjamin, J., 368
Bentz, E.C., xli, 163, 879, 880
Bernier, C., 688
Bernier, Carl, 688
Bertero, R.D., 446, 447, 499

Bertero, V.V., 446, 447, 499, 549, 550, 552
Bertero, Vitelmo V, xl, 109
Berveiller, Marc, 428
Bettess, P., 329
Bhattacharjee, S.S., 697
Bielak, J., 339
Binici, B., 520
Bishop, Christopher M, 437, 440
Blackburn, W.S., 87
Blaikie, Piers, 383
Blatman, Géraud, 427–429
Blejwas, T., 762
Blight, G.E., 194
Bocchini, Paolo, xlv, 385, 387, 388
Boer, R., 345
Boes, D.C., 849
Bojorquez, E., 381, 469, 521, 530
Boles, Michael A, 560
Bolisetti, Chandrakanth, 757
Bolt, Bruce A, 462, 495
Bommer, Julian J, 461, 495
Bonfils, Nicolas, 758, 759
Bonstrom, Holly, 386
Boodagh, P, 417, 696
Booker, Stephen, 788
Boore, David M, lx, 113, 476, 477
Boruff, Bryan J, 383
Bournazel, J.P., 208, 880
Boussinesq, Joseph, 236
Bowles, D.S., 377, 574
Bowles, David S, 380
Box, George EP, 423, 426, 693
Boyer, D., 571
Bozorgnia, Y., 465, 549, 550
Bozorgnia, Yousef, xl, 109, 495
Bracci, J., 523, 544
Bradley, B.A., 467
Bradley, Brendon A, 487, 759
Braun, Heinrich, 443
Braverman, J., 758
Breiman, Leo, 442
Breitung, Karl, 390
Brieger, L., 196
Broek, D., 164
Brokaw, J.T., 368
Bruce, Donald A, xlix, 599, 600
Bruhwiler, E., 205
Brundtland, Gro Harlem, 387
Bruneau, M., 385
Bruneau, Michel, 385
Bryant, L.M., 368
Brühwiler, E., 156
Buckingham, E., 872
Buford, A., 882
Burley, Eldon, 858
Burman, J Peter, 423
Burton, H., 536, 679
Båth, Markus, 640

Cabral, Denise Cunha, 758
Cai, G., 205, 234
Cakmak, A.S., 549
Callari, C., 688, 699
Campbell, K.W., 465
Campbell, Kenneth W, 495
Capra, B., 208, 880
Carbone, Vincenzo Ilario, 425
Carol, I. and Bažant, Z.P. and Prat, P.C., 312, 314
Carpinteri, A., 178
Cartwright, D.J., 69
Casagrande, A., 345
Casarotti, C., 508
Cavazzuti, Marco, 419, 421, 423, 424, 428
CEB, 212
Cedolin, L., 156, 321, 347, 773
Celarec, D., 525, 679
Celik, O.C., 525
Cengel, Yunus A, 560
Cervenka, J., 288, 665, 672, 772, 808, 817, 819, 839
Chakrabarti, P., 565, 569
Chana, P.S., 858
Chandler, A.M., 449
Chandra, J.M., 665, 672, 808, 817
Charvet, I., 536
Chen, Jianyun, 758
Chen, Tianqi, 442

Chen, W.F., 50
Cherepanov, G.P., 165
Chern, J. C., 99
Cheung, P.C., 513, 514
Chiorino, MA, 97
Chiu, C., 813
Choi, In-Kil, 757–759
Choi, Kyung K, 425
Chopra, A K., 398, 515
Chopra, A.K., 402–405, 407, 408, 501, 508–510, 515, 565, 569, 688, 697
Chopra, Anil K, xlvii, 398, 515–517
Chopra, O.K., 788
Choudhury, Deepankar, 757
Choun, Young-Sun, 757
Christian, John T, 412
Christiano, P., 339
Chudgar, A.K., 672, 688
Chwang, Allen T, 511
Chénier, JO, 775
Ciampoli, M., 500
Cimellaro, G.P., 385
Cimellaro, Gian Paolo, 385
Civil Engineers), JSCE (Japan Society of, 97
Clark, P.W., 513
Clough, R.W. and Penzien, J., 523
Coleman, Justin L, 757
Comi, C., 506
Committee, ACI, 96, 99
Concrete, Volume Changes in, 97, 99
Conover, W.J., 369, 391, 395, 842
Constantinou, M.C., 513, 514
Constantinou, Michael C, 758
Construction, Japanese-Ministry of, 463
Cordova, P.P., 468
Cornel, C.A., 820
Cornelissen, H., 156
Cornell, A., 541
Cornell, A.C., 470, 679
Cornell, AC., 470, 471
Cornell, C Allin, 489
Cornell, C.A., 368, 468, 469, 501, 518–521, 534, 538, 677, 678, 759
Corotis, Ross B, 386
Cosenza, E., 466, 549
Council, Applied Technology, 513
Courant, R., 126, 231
Crawford, J.E., 177
Creus, G.J., 178
Cunningham, Mark A, 755
Cusatis, Gianluca, 785
Cutter, Susan L, 383, 385
Cyganiewicz, J., 589, 590

D'Ambrisi, Angelo, 501
Darwin, D., lvi, 878, 883
Darwin, David, xli, 174, 176
Dashti, S., 466
Davis, R.E., 94
de Araújo, J., 688
De Biasio, M., 469
De Ceukelaire, L., 194
De Grandis, Silvia, 758
De Puy, GW, 880
De Risi, R., 759
deBorst, R., 178
Dei Poli, S., 156
Deierlein, G., 449
Deierlein, Gregory G, 756
Del Gado, E., 92
deLorenzi, H.G., 304, 306
Dennis, J.E., 219, 220, 272
Deodatis, George, 385
Der Kiureghian, A., 534
Der Kiureghian, Armen, 393, 412, 488–490, 723, 759, 821
Der-Kiureghian, A., 365
Desai, Sarika S, 757
Deschenes, Dean J, 858, 878
DesRoches, R., 470, 523, 525, 544
Dewey, R., 346, 347
Di Luzio, Giovanni, 785
Di Sarno, Luigi, 473
Diamond, S., 214
Diana, TNO, 234

Ding, Shifei, 443
Dipasquale, E., 549
Ditlevsen, O., 365
Ditlevsen, Ove, 372
Dolan, C., lvi, 878, 883
Dolen, T., xlii, lix, 215–218
Dolšek, M., 520, 525, 537, 679, 759
Domaneschi, Marco, 758
Dong, Y., 527
Douglas, J, 476
Downing, Thomas E, 383
Drake, L.A., 329
Draper, Norman Richard, 426
Duda, H., 156
Dugdale, D.S., 80, 155
Duron, Z., 659

Ebeling, R.M., xliv, 346
Ebisawa, K, 758
Efron, Bradley, 428
El Mohandes, F., 205
Elices, M., 157
Ellingwood, B., 552, 699, 889
Ellingwood, B.R., 381, 525, 529, 688, 699, 847
Ellingwood, Bruce R, 375, 385, 425, 758
Elnashai, A.S., 508, 688
Elnashai, Amr S, 473
Engle, R.M., 88, 89
EPRI, 754–756, 892
EPRI-1014099, 465
EPRI-NP-5930, 465
Erberik, M.A., 532
Erdogan, F., 88
Erdogan, F. and Sih, G.C., 72
Eshelby, J.D., 81
Esposito, Floriana, 440
Esposito, Rita, 893
Estekanchi, H.E., 523
Estekanchi, HE, 493
Estekanchi, Homayoon E, 493
Esteva, L., 470, 471

Fajfar, P., 466, 508, 757, 759
Fajraoui, Noura, 427
Fan, Junliang, 442
Fanelli, M., 577
Faravelli, Lucia, 425
Fardis, M.N., 193
Farmer, Frank R, 755
Farrow, K.T., 467
Fatehi, Ali, 756
Fava, G., 161, 164, 880
Fawkes, A.J., xliii, 300, 301
Fedele, R., 506
Federal Register, 882
Felippa, C., xxxix, xliii, 46, 258
FEMA, lx, 448, 449, 508, 595
FEMA P-750, 756
FEMA-PFM, 567, 575
Fenton, Gordon A, 411
Fenves, G., 398, 515, 688, 697, 795, 797, 805, 808
Fenves, Gregory, 398
Fenves, Gregory and Chopra, Anil K, 398
FERC, xliv, xlviii, xlix, 346–348, 499, 566, 567, 570, 572, 583, 584, 588, 589, 594, 595, 597, 600, 649, 650, 669, 713
FHWA, 860, 882, 885, 893
Field, E.H., 820
Filiatrault, A., 513, 514
Filiatrault, André, 109, 475
Filunger, P., 345
Fischinger, M., 466
Folliard, K.J., 861
Folliard, Kevin J, 858, 878
Forasassi, G, 757
Foreman, R.G., 88
Fotopoulou, S.D., 527
Fournier, B., 861
Fragiadakis, M., 502, 525, 759
Franchin, P., 381, 529, 534
Frangopol, D.M., 527
Frangopol, Dan M, 385
Frano, R Lo, 757
Freeman, S.A., 501, 508
Friedman, Jerome, 430, 441, 444
Friedman, Jerome H, 435, 437, 444

Friedrichs, K., 126, 231
Fumal, Thomas E, lx, 476, 477
Furgani, L., 405

Gabriel-Martin, Ivan, 377
Gallagher, R.H., 295
Garcia, J.E., 466
Gardoni, P., 523, 544
Gardoni, Paolo, 380, 385
Garner, S., 659
Gdoutos, E.E., 167, 169
German, M.D., 298
Gershenfeld, Neil, 443
Gershenfeld, Neil A, 443
Gerstle, KH, 212
Ghaemian, M., 512, 513, 517, 520, 552, 555, 688
Ghaemmaghami, A.R., 517, 552
Ghanaat, Y., 566, 569, 578, 672, 688, 714
Ghanem, Roger G, 427, 428
Ghasemi, A., 579
Ghobarah, A., 448, 513
Ghosh, J., 527, 530
Gibson, R.E., 345
Giorgi, P., 508
Giovenale, P., 470, 471
Giuriani, E., 156
Gocevski, V., liv, 775, 776, 784
Goel, R.K., 501, 508–510
Goncharov, Yevgeny, 395
Goodman, R.E. and Taylor, R.C. and Brekke, T.C., 808
Gopalaratnam, V. S., 156
Gordon, Stuart, 386
Gouda, V.K., 199
Graf, W., 366
Graff, D., 870
Grampton, GT, 755
Granger, L., 809
Graves, H., 753
Graybill, F.A., 849
Griesser, A., 887
Griffith, A.A., 171
Griffiths, D Vaughan, 411
Gu, C., 501
Guestrin, Carlos, 442
Guimarães, Antônio César Ferreira, 758
Guinet, P., 809
Guiu, F., 166
Gulikers, J., 201
Gunay, S., 534, 547
Gundlapalli, Prabhakar, 757
Guo, A., 527
Gutenberg, Beno, 115, 473
Gündel, Max, 758, 759

Haberman, S., 853
Haimes, Yacov Y, 386
Hakata, T, 758
Hakata, Tadakuni, 758
Hall, JF, 398
Hall, W.J., 464
Hallquist, J., 233
Halton, John H, 369, 395
Hamburger, R., 446, 449, 451, 499, 500
Hamburger, R.O., 470, 679
Hammerschlag J.G. andMerz, C., lv, lxi, 837, 838
Han, Guoyi, 383
Hansen, E., 161, 163
Hansen, E.J., 187, 198
Hansen, Eric J., 198
Hansen, K.D., 565
Hansen, Will, 93
Hansson, C.M., 194
Hao, M., 463
Harbitz, Alf, 392
Hardy, Greg, 756
Hariri-Ardebili, M A, 705
Hariri-Ardebili, M A., 518, 570, 571, 579, 684, 697
Hariri-Ardebili, M., 819, 837
Hariri-Ardebili, M.A, 291
Hariri-Ardebili, M.A., 370, 468, 499, 510, 517–520, 522–524, 580, 651, 671, 674, 676, 680, 682, 683, 688, 699, 721, 759

Hariri-Ardebili, MA, 393, 417, 500, 696, 712, 733, 759
Hariri-Ardebili, Mohammad Amin, lxi, 365, 393, 417, 590, 671, 687, 688, 690, 693, 703, 708, 720, 724, 729, 739, 816
Harr, M.E., 369
Harrald, John R, 376, 590
Hartford, D.N.D., 377, 574
Hartford, DND, 377
Hase, Thomas, 884
Haselton, C., 539
Haselton, C.B., 452
Hasgur, Z, 489
Hashemi, A., 326
Hasofer, Abraham M, 389
Hastie, T.J. and Tibshirani, R.J., 521
Hastie, Trevor, 430, 435, 437, 441, 444
Hawkins, N. M., 156
Hayward, D.G., 893
He, Tong, 442
Heitman, L.A., 790
Hellen, T.K., 87
Henshell, R. D., 293
Hernandez-Montes, E., 508
Hertlein, Bernard H., 199
Hessheimer, M.F. and Dameron, R.A., 751, 754, 759, 892
Hilber, H, 130, 660
Hill, Peter, 595
Hill, PI, 377
Hillerborg, A., 79, 154, 174, 310, 805
Ho, D.W.S., lix, 194–196
Hobbs, DW, 92
Hobbs, RE, 425
Hope, B.B., 194
Hordijk, D., 156
Hori, M., xli, 171–174
Hori, Muneo, 180
Hoseyni, Seyed Mojtaba, 758
Hoshiya, M, 489
Hossain, Faisal, 385
Houriet, B., lv, lxi, 837, 838
Housner, G.W., 467
Housner, George W, 511
Houst, Y.F., 194
HSE, xlv, 380, 381
Hsu, T.C., 54, 174
Hu, Michael Y, 443
Huaizhi, S., 575
Huang, Gao, 443
Huang, Guang-Bin, 443
Huang, H., 205, 234
Huang, Hai, 234
Huang, Xu, 758, 759
Huang, Yin-Nan, 758, 759
Hubler, M. H., 94
Hudson, C.M., 71
Hudson, M., 327
Hughes, Ifan, 884
Hughes, Shannon, 437
Hughes, T., 130, 660
Hughes, T.J.R., 227
Hughes, T.R., 130
Hunkeler, F., 887
Hussain, M.A., 180
Hussein, M., 688
Hutton, LK, 113

IAEA, 752
ICOLD, 398, 571, 583, 595
Idriss, I.M., 327
Ihekwaba, N.M., 194
Iliev, Alexander, 507
Iman, R., 369, 391, 842
Inglis, C.E., 64, 171
Ingraffea, A.R., 298
Inoue, S., 878
Institution of Structural Engineers, 175, 884
Ioannidou, K., 92
Ioannou, I., 536
Iori, I., 156
Irwin, G., 69, 166
Irwin, G.R., 66, 80
Ivanov, F.M., 194, 195

Jacobson, JP, 495

Jacques, Diederik, 810
Jalayer, F., 381, 470, 522, 529, 534, 538, 541, 544, 679, 691, 759
Jankovic, S., 523, 544
Japanese Society of Civil Engineers, 329
JATR, 869
Javanmardi, F., 351, 364, 512
Jayaram, N., 487, 488, 673, 759
Jeang, F. L., 156
Jendele, L., 819
Jensen, Ole Mejlhede, 93
Jeppsson, Joakim, 375
Ji, Tianjian, 758
Jia, Huicong, 383
Jiang, H., 575
Jiang, J.Q., 688
Jin, F., 517
Jirasek, M., xl, 93
Jirásek, Milan, 92, 99
Joe, Stephen, 396
Johnson, Kjell, 442
Jones, C. A., 790
Jones, D.A., 199, 201, 202
Jordan, T.H., 820
Joyner, William B, lx, 476, 477
Ju, B.S., 688
Jung, W.Y., 688

Kabanda, John, 757
Kadkhodayan, Vandad, 688
Kaila, KL, 474
Kanoglu, Mehmet, 560
Kaplan, M.F., 153
Kappos, A.J., 533, 547
Karacabeyli, E., 513
Karapetrou, S.T., 527
Karniadakis, George Em, 427
Kasai, Tetsurou, 94
Kasperson, Jeanne X, 383
Kasperson, Roger E, 383
Katsaragakis, E., 178
Kazantzi, A.K., 525
Ke, Jyh-Bin, 393, 412
Kearney, V., 88
Keller, Paul E, 442
Kelly, A., 171
Kelly, D., 329
Kemeny, John George, 755
Kenkyusho, K.K., 330
Kennedy, R., 534, 543, 544
Kennedy, R.P., 529, 756, 758
Kent, D.C., 878
Kesler, C., 153
Khuri, André I, 425
Kianoush, M R., 518, 570, 571, 697
Kim, Jung Han, 759
Kinali, K., 381, 529
Kiremidjian, A., 536, 679
Kirsch, G., 64
Kline Jr, Robert A, xlix, 599, 600
Klügel, J-U, 757
Knoll, Alois, 442
Knowles, J.K., 87
Korobokis, G.A., 858
Kostinakis, A., 470
Kotthoff, L., 728
Koutromanos, I., 512
Krawinkler, H., 446, 448
Kreider, J., xxxix, lix, 40, 41, 44
Kronenberg, P., lv, lxi, 837, 838
Kuhlemeyer, R.L., 328, 651, 662
Kuhn, Max, 442
Kumar, Deepak, 441
Kumar, Manish, 758
Kumar, Rajesh, 441
Kumar, Ram, 757
Kumar, Santosh, 757
Kunnath, S.K., 549
Kuo, Frances Y, 396
Kupfer, BH, 212
Kurama, Y.C., 467
Kwon, Gunup, 757
Kwon, O., 508
Kwon, Oh-Sung, 757

Lai, Kwan-Ling, 391
Lallemant, D., 536, 679
Lam, N.T.K., 449
Landis, Eric N, xlii, 175, 176

Landsberg, Heiko, 443
Lapa, Celso Marcelo Franklin, 758
Lapajne, J.K., 757, 759
Larive, C., lix, 205–208, 213, 214
Le Chatelier, H, 94
Le Duy, Tu Duong, 758
Lebon, G., 330
Leclerc, M. and Léger, P. and Tinawi, R., 346, 352
Lee, Huseok, 757
Lee, J., 795, 797, 805, 808
Leemann, A., 885, 887
Leger, P., 351, 364, 512, 697
Lei, Yongdeng, 383
Lemaire, Maurice, 428
Lewis, R.K., lix, 194–196
Lewy, H., 126, 231
Li, F. Z. and Shih, C. F. and Needleman, A., 304
Li, G., 467
Li, Q., 506
Li, Quanwang, 375
Li, X., 92
Li, Y, 388
Li, Y.N., 177, 178
Liaudat, Joaquín, 893
Liaw, C-Y, 398
Liel, A.B., 525
Lignos, D.G., 525
Lilliefors, H.W., 678
Lin, Gao, 688
Lin, L., 688
Lin, T., 673, 759
Lin, Ting, 487
Lind, Niels C, 389
Liners, A.D., 177, 178
Liu, J., 506
Liu, W.K., 130, 227
Lobo, R.F., 549
Lombardi, G., 577
Lorenzi, H.G. de, 298
Lorman, William Rudolph, 94
Los Angeles Times, 789
Lott, J., 153
Lu, X., 468
Luco, N., 470, 471, 531
Luco, Nicolas, 758, 759
Lupoi, A., 688, 699
Lura, Pietro, 93
Lynn, P.P., 298
Lysmer, J., 328, 329, 651, 662
Løkke, A., 402–405, 407, 408
Løkke, Arnkjell, xlvii, 515–517

Mackie, K., 465
Mackie, K.R., 534
Mackie, Kevin R, 388
Madsen, Henrik O, 372
Maes, Norbert, 810
Magne, I., 809
Mahmoud, B., 688
Mahoney, A., 449, 499, 500
Malla, S., 552, 569, 570, 607
Malvar, L.J., 177
Mander, J.B., 519
Manfredi, G., 466, 549, 759
Manu, C., 298
Manyena, Siambabala Bernard, 386
Marchese, Dayton, 388
Marelli, S, 429
Marelli, S., 372, 374
Marelli, Stefano, xlvi, 418, 427
Martin, Farrel J., 201
Martinez, G.A., lvi, 856–860, 862, 863, 874, 877
Martinez-Pereira, Alejandro, 461, 495
Martins Gomes, H., 411
Mashayekhi, M, 493
Mashayekhi, M., 523
Mashayekhi, Mohammadreza, 493, 496, 497, 759
Masuero, J.R., 178
Matheu, E., 659
MATLAB, 394, 396–398, 403–405, 407, 408, 503, 691, 730
Matsumoto, N., 565
McClelland, D., 377, 574
McGuire, R.K., 520, 697
McHenry, Douglas, 94

McKay, M.D., 391, 395
McMillan, F.R., 91
Medel-Vera, Carlos, 758
Mehrotra, Kishan, 443
Melchers, R.E., 373
Melchers, Robert E., 375
Menon, D., 807
Merz, C., 819, 837, 887
Meyer, C., 205
Mezzi, Marco, 501
Micovic, Zoran, 377
Miguel Awruch, A., 411
Mihashi, H., 178
Miller, A., 306
Miller, C., 752
Mills-Bria, B. and Nuss, L. and Dixon, L. and Powell, C. and Harris, D. and O'Connell, D., 658
Mindess, S., 156
Mirzabozorg, H., xxxix, lx, 38, 205, 524, 555, 579, 626, 651
Mirzabozorg, Hasan, 688
Mirzahosseinkashani, S., 688
Miura, F., 329, 330, 335
Miyagawa, Toyoaki, 878, 879
Miyazawa, Shingo, 93, 94
Mlakar, P.F., 368
Modarres, Mohammad, 728, 758
Modica, A., 530
Modry, S., 194, 195
Modéer, M., 79, 154, 174, 310, 805
Moehle, J., 449
Mohan, Chilukuri K, 443
Mohanty, William K, 757
Monteiro, R., 688
Mood, A., 849
Morales-Torres, Adrián, 688
Moran, B., 130, 227
Morfidis, K., 470
Morgan, N., lxii, 872
Morikawa, Hidenori, 858, 876
Mosalam, K.M., 534, 547
MPR-ML16216A242, 856–859, 861, 862
MPR-ML19170A332, 881, 888
Mukhopadhyay, Siuli, 425
Multon, S., 208, 209, 213, 893
Munger, Dale F, 595
Muntasir Billah, A.H.M., 384, 533
Murakami, Y., 69
Murazumi, Y., 786, 787
Murphy, Colleen, 380
Murphy, Joseph A, 755
Murthy, Sreerama K, 440
Muruva, Hari Prasad, 756
Möller, B., 366

Najjar, L.J., 191
Nakajima, Masato, 757
Nakamura, Naohiro, 757
Nakamura, Soshi, 757
Narain, Hari, 474
Narayanan, RS, 97
Natekar, D., 161, 163
Natekin, Alexey, 442
National Research Council, xlv, lx, 386–388
Nau, J.M., 464
Naus, D., 153
NDT Resource Center, xl, 75, 76
Nemat-Nasser, S., xli, 171–174
Nemat-Nasser, Siavouche, 180
Neville, A.M., 91
Newman, J.C., 70
Newton, I., 276
NextEra, 853
NextEra-ML12087A194, 864
NextEra-ML121160422, 866
NextEra-ML13151A328, 853, 866
NextEra-ML16216A240, 855, 863, 864, 886, 890
NextEra-ML18141A785, lxi, lxii, 856, 861–863
NextEra-ML19205A489, 878
Ngala, V.T., 194
Nickisch, Hannes, 444
Nielson, B.G., 470, 523, 544
Nikishkov, G. P. and Atluri, S. N., 309

Nikishkov, G.P., 309
Nilson, A.H., lvi, 878, 883
Nilsson, L.O., 188
Nithiarasu, P., 227
NOAA, 606
Nokland, T.E., 370
Noori, Mohammad, 688, 693
Nour, Ali, 757
Novák, D., 526
Nozari, A., 523
NRC, 752, 753, 755
NRC Office of Public Affairs, 753
NRC-CU Grant, 870
NRC-ML 102861026, liv, lv, 789, 797–799, 802–804, 813
NRC-ML 12054A735, 752, 853
NRC-ML12131A431, 854
NRC-ML12160A374, 853
NRC-ML12199A300, 854
NRC-ML19261A762, 856
NRC-ML19312B609, 870–873, 884–886, 891
NuclearEnergy Insider, 789
NUREG 1150, 755
NUREG-1737, 891
NUREG-2201, 755
NUREG/CR-6706, 817
Nuss, L.K., 565
Nuss, L.K.m, xliv, 346
Nuss, Larry K, 365, 590, 671
Nuti, C., 405
Nuttli, O.W., 465

O'Hara, TF, 495
O'Rourke, M.J., 536
Okinaka, H., 330
Olsefski, S., 54
Olsson, A.M.J., 370, 391, 411
Onof, C, 425
Ortiz, M, 180, 181
Ouchterlony, F., 71
Owen, Art B, 391
Owen, D.R.J., xliii, 300, 301

Padgett, J., 527
Padgett, J.E., 470, 523, 525, 530, 544
Page, C.L., 194
Pan, J., 205, 467, 517
Pang, Rui, 688
Panyakapo, P., 512
Papadakis, V.G., 193
Papanikolaou, V.K., 508, 772, 819, 839
Paris, P., 69, 166
Paris, P.C., 88
Park, Jin-Hee, 759
Park, Jong-beom, 757
Park, R., 513, 514, 878
Park, Y.J., 466, 549
Parrott, LJ, 195
Parry, Martin, 383
Patev, R.C., 672, 688
Patev, RC, 377
Patuwo, B Eddy, 443
Paul, DK, 757
Pauley, T., 513, 514
Paultre, P., 688
PEER, 723, 725, 820
Pellenq, R.J.M., 92
Perego, U., 506
Perotti, Federico, 758
Perotti, L., 205, 506, 613, 819
Petersson, P.E., 79, 154, 156, 174, 310, 805
Petitjean, Frank, 425
Petrini, F., 500
Pfeiffer, P.A., 171
Phung, Quoc Tri, 810
Pickett, Gerald, 94
Pietruszczak, S, 779
Pinho, R., 508
Pinto, P.E., 381, 529, 534
Pitarka, Arben, 489
Pitilakis, K.D., 527
Plackett, Robin L, 423
Planas, J., lix, 157, 170, 171, 880
Plum, N. M., 831
Porter, K., xlvi, 451, 452, 500, 501, 534, 543, 544, 759
Porter, K.A., 499, 518, 519, 522, 688
Porter, Keith, 383, 384, 529, 530, 532

Pourkamali-Anaraki, Farhad, 365, 437, 703, 720, 729
Powell, G.H., 548, 558
Poyet, S., 875
Prabhu, Raja V, 418
Presidential Policy Directive, 384
Priddy, Kevin L, 442
Priestley, Maurice B, 489
Progress Energy Florida, 789
Progress Energy Florida (ML102861026), liv, 752, 789–794, 813
Proulx, Jean, 398
Pu, S.L., 180
Puatatsananon, W., 187, 192
Pugliese, G, 757
Pujades, Luis G, 503
Putcha, CS, 377

Qiu, Zhiping, 425

R Core Team, 442
Rabl, A., xxxix, lix, 40, 41, 44
Ragg, Thomas, 443
Rajashekhar, Malur R, 425
Rajeev, P., 534
Raju, I.S., 70
Ramamoorthy, S., 523, 544
Ramu, M, 418
Ranka, Sanjay, 443
Raphael, J.M., 94
Rasmussen, C Edward, 444
Rasmussen, Carl Edward, 444
Ravindra, M.K., 756, 758
Raychowdhury, Prishati, 757
Rea, Dixon, 398
Reclamation, 345
Regulations, NRC, 890
Reich, R., xliv, 234, 310, 346, 347, 349, 600, 608, 672, 721, 822, 838, 839
Reich, R.W., 281
Reiner, M, 92
Reinhardt, H., 156
Reinhorn, A.M., 385, 549
Reinhorn, Andrei, 385
Reinhorn, Andrei M, 385, 756
Ren, Q., 506, 577
Renault, Philippe, 757
Rendulic, L., 345
Rezaeian, Sanaz, 488–490, 723, 759, 821
Richter, Charles F, 473
Richter, Charles Francis, 115
Riddell, R., 466, 518
Rigden, Stephen, 858
Rizzo, Giuseppe, 440
Rodriguez, J., 205
Roelfstra, P.E., 194
Rogovin, M, 755
Romanski, P., 728
Rooke, D.P., 69
Roosen, Charles B, 444
Rosati, G. P., 156
Ross, AD, 94
Rossetto, T., 533, 536
Roten, Daniel, 488, 489
Rots, J.G., 178
Roussouly, Nicolas, 425
Ryu, Jeong-Soo, 757

SA, Bureau Technique PIGUET, 837
Sadeghazar, M., 523
Sadouki, H., 205
Saetta, A., 194, 196, 202
Saiidi, M.S., 533
Salamon, Jerzy W., 511
Salaun, M, 425
salazar, F, 733
Sandberg, G.E., 370, 391, 411
Saouma, V E., 504, 684
Saouma, V., 205, 207, 222, 291, 506, 760, 809, 876, 891
Saouma, V.E., xliv, xlvii, 154, 161–164, 187, 192, 198, 205, 234, 291, 293, 298, 310, 330, 346, 347, 349, 370, 468, 499, 505, 510, 512, 517–520, 522–524, 580, 600, 608, 613, 665, 671, 672, 674, 676, 680, 682, 683, 688, 699, 700, 721,

754, 759, 808, 813, 817, 819, 822, 837–839, 870, 880, 892, 893
Saouma, VE, 500, 759
Saouma, Victor E, 393, 688, 816
Saqib, Mohd, 688
Saragoni, R., 464
Sarott, F.A., 194
Sata, Y, 489
Saxena, Navjeev, 757
Saydam, D., 527
Schiffman, R.L., 345
Schnabel, P. B., 329
Schnabel, R.B., 219, 220, 272
Schobi, R., 372, 374
Schrefler, B., 194, 196, 202
Schroer, Suzanne, 758
Schwemmer, D., 293
Schölkopf, Bernhard, 436
Scott, R., lxii, 872
Scotta, R., 508
Scrivener, xlii, 209
SEAOC, 447
Seed, H.B., 329
Seo, Jeong-Moon, 757
Serdet, Emmanuel, 758
Seward, S.K., 71
Sextos, AG, 320, 757
Seyed-Kolbadi, S M., 697
Seyed-Kolbadi, S Mahdi, 688, 693
Shah, Manan, 395
Shah, P. S., 156
Shah, S.P., 549
Shahria Alam, M., 384, 533
Shan, Songqing, xlvi, 419
Shank, JR, 94
Sharma, Neetesh, 385
Shaw, K. G., 293
Shen, B, 180, 181
Shen, C.K., 567
Shibata, K, 758
Shih, C.F., 298
Shimizu, H., 787
Shimpo, T., 506
Shinozuka, Masanobu, 489
Shirley, W Lynn, 383
Shome, N., 468, 522
Siew, Chee-Kheong, 443
Sikiotis, E.S., 298
Simpson Gumpertz & Heger-ML16216A243, 865
Simpson Gumpertz & Heger-ML16279A049, lvi, lxi, lxii, 855, 860, 861, 865–867, 875, 887, 889, 891, 894–896
Simpson, Timothy W, xlvi, 419
Slate, F.O., 54
Slowik, V., 512
Smola, Alexander J, 436
So, P., 536
Sobol', Il'ya Meerovich, 369, 396
Somerville, Paul G, 476
Soroka, I., 195
Soysal, B.F., 520
Spanos, Pol D, 427, 428
Sparks, R., 870
Spencer, B., 205, 234
Spencer, Benjamin W, 234
Srivastava, A., 377, 575
Stafford, P.J., 530
Standardization, International Organization for, 96, 99
Stanton, T.E., 217
Stark, David, 880
Stenberg, E., 87
Stevens, R.N., 166
Stewart, James R, 234, 890
Stojadinovic, B., 465, 523, 534, 544
Straub, L. G., 94
Struble, L., 214
Su, N., 468
Sudret, B, 429
Sudret, B., 372, 374
Sudret, Bruno, xlvi, 417, 418, 427–429, 739
Sun, Xiaodan, 488
Swain, R.E., 507

Tabandeh, Armin, 385
Taborda, Ricardo, 488, 489

Tada, H., 69, 166
Takagkura, T., 787
Takakura, Takeo, liv, 786, 787
Takatura, T., 786, 787
Tampa Bay Times, 788, 815
Tang, L., 188
Tang, T.M., lv, 810
Tanioka, K., 435
Taylor, R., 130, 660
Taylor, R. L., 227, 332
Tazawa, Ei-ichi, 93, 94
Tekie, P.B., 552, 688, 699
Terzaghi, K., 345
Terzaghi, Karl, 345
Thacker, B.H., 234
Thakur, Manoj, 441
Thomas, M., 861
Thomes, FC, 94
Tibshirani, Robert, 430, 441, 444
Tibshirani, Robert John, 435, 437
Tinawi, R., 351, 364, 512
Toki, K., 329, 335
Torlay, L, 442
Tothong, P., 470, 471, 531
Toutlemonde, F., 893
Townsend, CL, 39
Tracy, F.T., xliv, 346
Troxell, G.E., 94
Turner, Billie L, 383
Tussiwand, G., 154

Uang, C.-M., 552
Uchita, Y., 330, 613
Udaka, T., 329
Ulm, F., 205, 207
Underwood, J.H., 180
US ACROPS, Waterways Experimental Station, 94
USACE, xlviii, 345, 512, 569, 578, 579, 585, 587, 652, 714
USACE-USBR, xlix, 591, 592
USBR-manual, xlviii, 483, 566, 572
USGS, xlv, 379, 486, 820

V.V., Bertero, 446
Vafai, A., 523
Vafai, H, 493
Vafai, Hassan, 493
Vainshtok, V.A., 309
Vaishnav, Rameshchandra Navalshanker, 95
Vamvatsikos, D., 468, 469, 501, 502, 518–521, 525, 538, 677, 678, 759
Van Breugel, Klaas, 93
Van der Have, R, xlv, 410, 411
Van Nieuwenburg, D., 194
Vanmarcke, Erik, xlv, 409, 410
Vasseur, Dominique, 758
Vayenas, C.G., 193
Vecchio, F.J., 205
Veneziano, D., 548, 558
Verma, Ajit Kumar, 756
Verma, Akhilesh K, 757
Vidic, T., 466
Vitaliani, R., 194, 196, 202
Vosooghi, A., 533
Vořechovský, M., 526

Wald, D., lvi, 856–860, 862, 863, 874, 877
Wald, D. J., 820
Wald, D.M., 856, 857, 874, 881
Walker, E.K., 88
Walsh, P. F., 153
Walsh, P.F., 153, 171
Wan, Jinhong, 383
Wang, B., 577
Wang, Cao, 375
Wang, G Gary, xlvi, 419
Wang, Gaohui, 495
Wang, Jian, 858, 876
Wang, Jin-Ting, 688
Wang, M.L., 549
Wang, Na-li, 688
Wang, W., 501
Wang, Y., 500
Wang, Zeyu, 441
Wanitkorkul, A., 513, 514
WASH-1400, 755
Wei, Z., 504

Wells, A.A., 81
Wen, Y.K., 466
Wen, Z., 575
West, Graham, 831
Westberg, Marie, 706
Westergaard, H.M., 66, 352, 353, 511
Wheeler, O.E, 89
Whittaker, A., 449, 499, 500
Whittaker, Andrew S, 757–759
Wieland, M., 552, 569, 607
wikipedia, 562
Willenborg, J., 89
Willford, Michael R, 756
Williams, CKI, 444
Wilson, E., 753, 896
Wittman, F.H., 178
Wittmann, F.H., 156, 194, 196, 209
Wolf, J.P., 329
Wolff, T.F., 369
Wong, SM, 425
Wood, R.A., 89
Wu, X., 435

Xi, Y., 187, 189, 190, 192
Xie, L.L., 463
Xiu, Dongbin, 427
Xu, Jim, 757
Xu, L.J., 463
Xu, Y., 517

Yadohisa, H., 435
Yamamoto, Y., 488, 490, 492
Yamamoto, Yoshifumi, 488, 490–492, 723
Yang, D., 467
Yao, X.W., 688
Yazdani, Yadollah, 688
Youn, Byeng D, 425
Young, F., 156
Youngs, RR, 476
Yu, Q., 94, 773
Yücel, A.R., 688

Zangar, C.N., xliv, 354, 355, 511
Zareian, F., 446, 539
Zentner, I, 758, 759
Zentner, Irmela, 758, 759
Zhang, Dequan, 425
Zhang, Guoqiang, 443
Zhang, H., 50
Zhang, S., 555
Zhang, Y., 329
Zhao, Chunfeng, 758
Zhao, Weitao, 425
Zhong, H., 552, 699
Zhong, Hong, 688
Zhou, F.P., 177, 178
Zhou, Hongjian, 383
Zhou, Y., 468
Zhu, B, 39, 40
Zhu, H., 506
Zhu, J.Z., 227, 332
Zhu, Qin-Yu, 443
Zi, G., 205
Zicko, Kessi E, xlix, 599, 600
Zienkiewicz, O., 329
Zienkiewicz, O. C., 227, 332
Zienkiewicz, O.C., 295
Zijl, G.P. van, 178

Appendix A
Testing Method for Concrete Fracture Properties

Abstract
Though increasingly adopted in one form or another, Hillerborg's concrete fracture model has yet to be supported by a "standard test" for the fracture energy, G_F.
In this chapter, the authors articulate a testing method that is uniquely suitable for core testing, as we are much more likely to need fracture parameters for safety assessment of existing structures rather than for new ones.

Surprisingly, there is not yet a "standard" to test concrete fracture energy. ACI Committee 446 has been trying to develop such a code for many years, but none has yet emerged. In so far, the only ACI publications pertaining to the fracture of concrete are [13] and [14]. The International Association of Fracture of Concrete and Concrete Structures (IA-FraMCoS) has neither issued such a code.
Based on the first author's experience, a testing method is hereby proposed. The basic principle behind the west splitting test (WST) is the controlled opening of a crack by a controlled movement of a wedge. It is a closed loop, servo-controlled test, Figure A.1.
The major advantages of the proposed WST method are:

1. Easiest method to perform tests on concrete cores recovered from sites.
2. Can be performed on specimens, prismatic or cylindrical, cast in place or on cores recovered from existing structures.
3. Has a substantially longer ligament length per unit weight of concrete as compared to other tests (and in particular compared to the three point bending beam test).
4. Self-weight effect can be neglected for usual sizes (20 x 20 x 10 cm prismatic specimen) [236].
5. Test set-up and specimen geometry can be easily adapted for larger or smaller specimen sizes [836].
6. Has been used for over 25 years by researchers and practitioners in the U.S., Europe, and Japan with specimens ranging from 5 cm up to 3.2 m in size on various types of concretes, mortars, advanced cementitious materials, and rock.
7. The interpretation of the tests results for the determination of G_F as well as the tensile softening diagram is straightforward and requires only very simple calculations.
8. Can be used to measure most fracture properties of concrete: G_F, G_f, K_{Ic}, K_{IC}^S-CTOC$_c$, and f_t' [478].

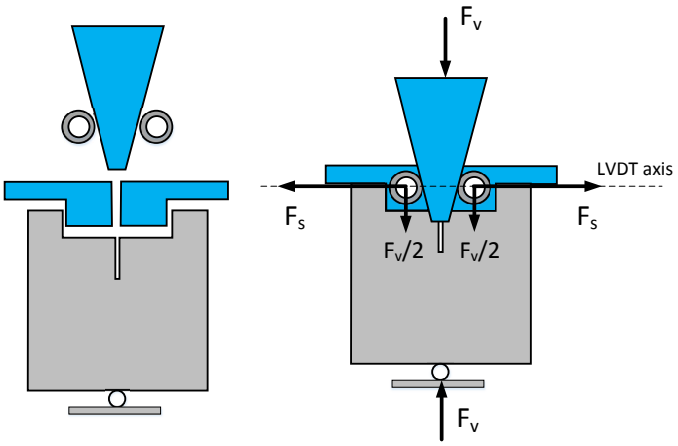

Fig. A.1: Test set-up and acting forces, for a prismatic specimen

This test method introduces, through a wedge, a controlled lateral opening displacement to induce stable crack growth in a prismatic or cylindrical specimen, Figure A.2.
From the splitting force-average crack opening displacement response of the specimen, the specific fracture energy is determined.

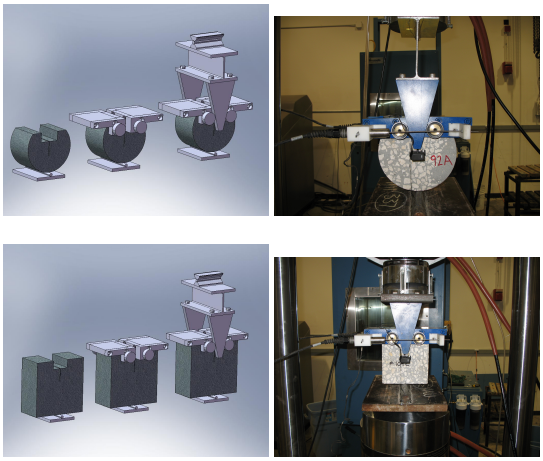

Fig. A.2: Principle of the Wedge Splitting Test Set-up

In a first approximation, the derivation of the tensile softening diagram can be based on the regressions performed on extensive data sets for different types of concretes at quasi-static imposed displacement rates [156].
The uniaxial tensile strength, f_t, should be preferably determined experimentally by means of a uniaxial tensile test. If adequate software modules are available, f_t and the tensile softening diagram can also be indirectly determined by means of an inverse analysis using a FEM simulation of the experimental specimen response.
The geometry of the specimens and the test set-up given in this document are suitable for concretes with a maximum aggregate size (D_{max}) less than or equal to 32 mm. For concretes with a D_{max} superior to 32 mm, the test set-up and specimen geometry can be easily accommodated, [836] [236].
The values of the specific fracture energy, G_F, and tensile softening diagram obtained with the specimen geometry according to Figure A.2 are defined as the reference values for the concrete's fracture properties. For different ratios between the ligament length and the D_{max} as well as between the specimen width and the D_{max}, size effects are to be expected.

A.1 Apparatus

The testing apparatus is described next:

Testing System: The testing system consists of frame, actuator, force cell, controller, and data acquisition equipment as a minimum. Whereas it is preferable to have a closed-loop servo-controlled machine, this is not essential.

Force Cell: The force measuring device shall have sufficient capacity and shall be accurate to within 1.0% of the peak force measured in the test. The device shall be calibrated in accordance with ASTM E4 [64].

Displacement Measurement Devices: Two displacement measuring devices shall be used for measuring the displacements in the axis of the horizontal splitting force, one on each side of the specimen (COD1 on side 1, COD2 on side 2). The displacement measurement devices shall be of a type having sufficient capacity to enable the complete splitting of the specimen in two halves and shall be accurate to within 1.0% of the displacement measured while the specimen is at peak force.

Test Setup: The principle of the wedge splitting test set-up is shown in Figure A.1 with the successive steps, from 1 to 3, of mounting of the test for a prismatic specimen. The test set-up between the actuator or force cell and the specimen consists of a beam with wedges, plates equipped with roller bearings, and a rounded support.

A.2 Test Specimens

The wedge splitting test specimen can be either prismatic or cylindrical, cast in molds or taken as cores from the structure. Dimensions are shown in Figure A.3 where h_1 is 130 and 85 mm for closed loop control of COD and stroke control, respectively.

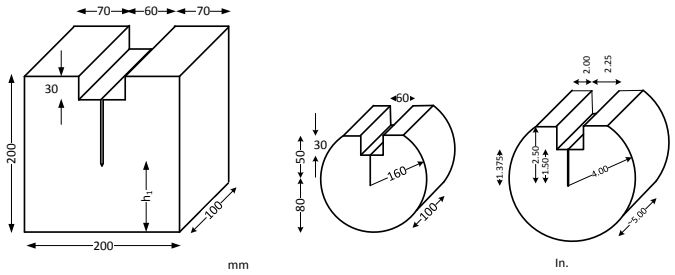

Fig. A.3: Dimensions of the specimens for the wedge splitting test (all dimensions in mm)

The specimens shall be prepared and cured in accordance with Practices ASTM C31 [58], ASTM C42 [60], and ASTM C192 [57]. The groove and notch shall be cast or cut into the specimen.
In order to force a straight path of the crack propagation, a 5 mm deep groove can be cut on both sides of the specimen on the surface following the plane of the ligament, Figure A.4(a). Instrumentation should be carefully installed through a temporary support, Figure A.4(b).

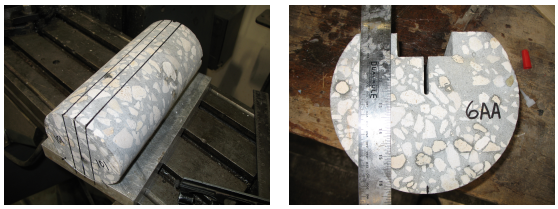

(a) Cutting

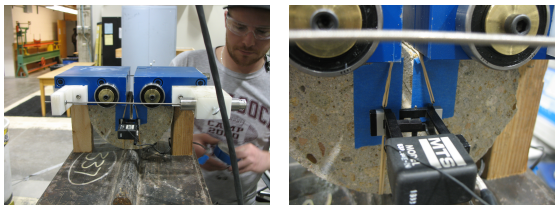

(b) Instrumentation

Fig. A.4: Specimen preparation

A.3 Procedure

Procedure for the test is as follows:

1. Moist-cured specimens shall be tested as soon as possible after removal from moist storage.
2. Test specimens shall be kept moist by any convenient method during the period between removal from moist storage and testing.
3. Place displacement measuring systems on both sides of the specimen.
4. Place specimen on the rounded support, Figure A.4(a)
5. Carefully insert the wedge between the roller bearings.
6. Bring the wedges in contact with the roller bearings until faire and perform the test in either one of two test control modes:
   a. Under COD control in a closed loop, servo-controlled test system at a COD rate of 0.1 mm/min.
   b. Under stroke control at a stroke (cross-head) displacement rate of δ_v equal to 0.2 mm/min.
7. Figure A.1 illustrates the test set-up with a (prismatic) specimen with the forces induced by the imposed COD or crosshead displacement. The resultant splitting force acts at 10 mm below the top side of the specimen.
8. For fracture toughness test, perform an unload/reload at the same rate as loading, Figure A.5:

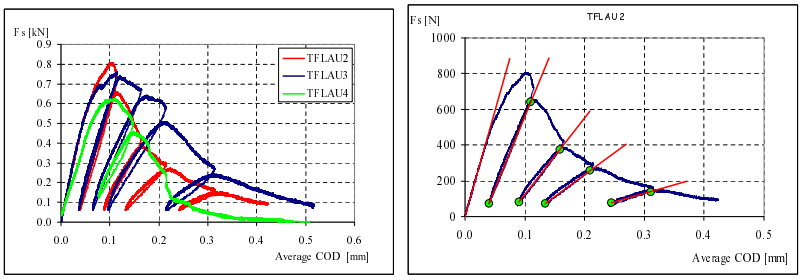

Fig. A.5: Representative Experimental Load-COD Curve

   a. Close to the peak load.
   b. At least 4 times in the post-peak zone.

Measured values should include as a minimum:

1. Vertical force, F_v, as a function of time.
2. Crack Opening Displacements, COD_1 and COD_2, on both sides of the specimen as a function of time.

Additional (optional) instrumentation includes acoustic emission sensors to correlate (micro)crack formation with AE noise.

A.4 Calculation

From the same test setup, and possibly modified loading procedures, one can measure many different fracture properties.

A.4.1 Fracture Energy G_F

Evaluation of fracture energy, G_F, is relatively straightforward:

1. Determine the (horizontal) splitting force acting on the roller bearing, F_S, from:

$$F_S = \frac{1}{2\tan\alpha} \tag{A.1}$$

$$F_V = \frac{1}{2\tan 15^o} F_V = 1.866 F_V \tag{A.2}$$

2. Determine the average of the two displacements measured:

$$COD = \frac{COD_1 + COD_2}{2} \tag{A.3}$$

3. Plot F_S in terms of average COD and, if necessary, extrapolate curve to zero F_S.
4. Determine the ligament area, A_{Lig}, corresponding to the projected area of the crack on the ligament.
5. Determine the work of fracture, W_F, as the area under the $F_S - COD$ curve (Figure A.6).

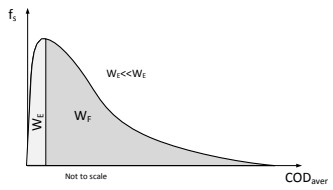

Fig. A.6: Definition of the work of fracture and specific fracture energy

6. Determine the specific fracture energy G_F:

$$G_F = \frac{W_F}{A_{Lig}} \tag{A.4}$$

A.4.2 Tensile Softening Diagram

Whereas this standard focuses on the determination of G_f, application of G_F in advanced numerical simulations of structural concrete requires the tensile softening diagram in terms of the concrete uniaxial tensile strength, f_t, and G_F.
The uniaxial tensile strength, f_t, shall be preferably determined independently by means of a uniaxial tensile test. Alternatively, f_t can be estimated by means of a tensile splitting test in accordance with ASTM C496 [62].
From the knowledge of G_F and f_t, the uniaxial tensile softening diagram can be represented as a first approximation by the following bilinear curve, which is valid for concretes with a D_{max} between 8 and 32 mm, Figure A.7.

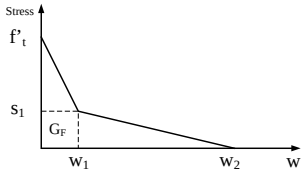

Fig. A.7: Bilinear softening diagram

Brühwiler and Wittmann [155] found that for 1 inch maximum size aggregate:

$$s_1 = 0.4 f_t' \tag{A.5}$$

$$w_1 = 0.8 \frac{G_F}{f_t'} \tag{A.6}$$

$$w_2 = 3 \frac{G_F}{f_t'} \tag{A.7}$$

For structural concrete, Wittmann et al. [887] determined

$$s_1 = \frac{f_t'}{4} \tag{A.8}$$

$$w_1 = 0.75 \frac{G_F}{f_t'} \tag{A.9}$$

$$w_2 = 5 \frac{G_F}{f_t'} \tag{A.10}$$

where f_t' is the uniaxial tensile strength.

A.4.3 Fracture Energy G_f

The fracture energy, G_f, is defined in Figure A.8.

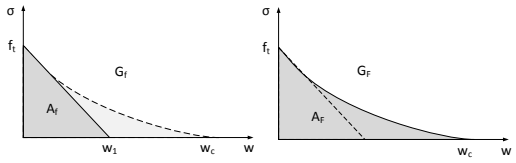

Fig. A.8: G_F *vs* G_f

A.4.4 Fracture Toughness

Though it is widely accepeted that linear elastic fracture mechanics is not applicable to concrete in general, it may be applicable in some special instances. This includes very large specimens and smaller ones subjected to very slow loading [104].
The determination of the fracture toughness requires not only the maximum load but also the corresponding crack size. However, in rock, as in concrete, the tip of the crack may not be easily identifiable due to the heterogeneity introduced by the fine grains. Hence, the concept of an elastic equivalent crack length has to be used to determine the fracture toughness. This is determined through the compliance method which combines finite element calibration with analysis of experimental data.
This finite element analysis of the geometry, with $E = 1$, is conducted in two parts. First, a unit horizontal load is applied at the location of the wedges, and the initial normalized compliance is determined. In this case C_n^0 is simply equal to the COD_{F_S} measured along a unit splitting force F_S.
Subsequently, geometries with increasing crack lengths (again with $E = 1$) are also subjected to a unit F_S and analyzed. For each analysis (crack length, a), we compute the fracture toughness and the compliance. These analyses results are then tabulated, and a least square best fit is performed to determine $a_{eff} = a_{eff}(C_n)$ and $K_{Ic} = K_{Ic}(a_{eff})$, where a_{eff} is the effective crack length.
Figures A.9(a) and A.9(b) show representative normalized and actual compliance and stress intensity factor curves.
Test interpretation proceeds as follows:

1. From the first unload-reload cycle, determine the effective elastic modulus from

$$E_{eff} = \frac{C_n^0}{C_{exp}^0} \tag{A.11}$$

   Where C_n^0 is the normalized compliance (obtained from the pre-test calibration) and C_{exp}^0 is the initial experimental compliance given by

$$C_{exp}^0 = \frac{COD_{F_S}}{F_S} \tag{A.12}$$

   where COD_{F_S} is the crack mouth opening displacement measured along the splitting force F_S.

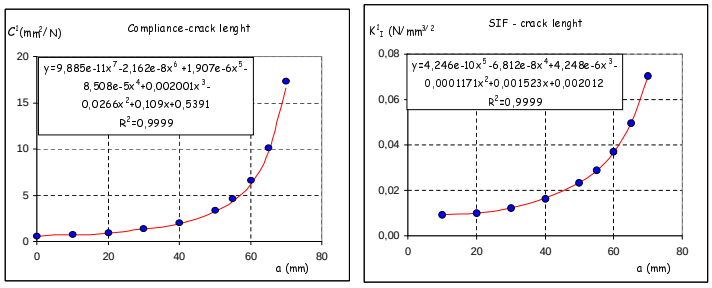

(a) Calibration/noirmalized

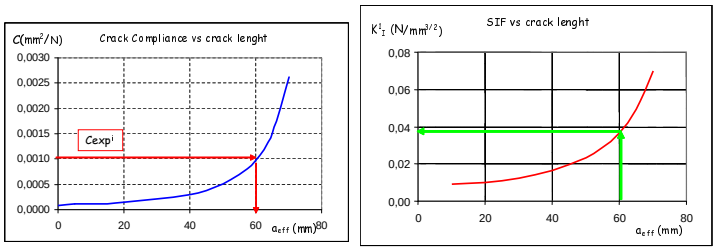

(b) Actual

Fig. A.9: Compliance and stress intensity factors in terms of crack length a

2. Having determined the effective elastic modulus, the normalized compliance is determined from $C_n = E_{eff} C_{exp}$.
3. For each of the subsequent post-peak responses, determine:

   a. The experimental compliance, C_{exp}.
   b. The corresponding elastic equivalent (or effective) crack length from

$$a_{eff} = a_{eff}(C_n) \tag{A.13}$$

   c. The fracture toughness for this particular crack length

$$K_{Ic} = K_{Ic}(a_{eff}) \tag{A.14}$$

4. Plot the determined fracture toughnesses in terms of effective crack length, and determine the average value. It should be noted that as a_{eff} approaches the ligament length (distance from tip of the notch to the bottom of the specimen), there will be a small decrease in K_{Ic}.

A.5 Report

Report the following information:

1. Identification number.
2. Specifications of the material.
3. Specimen age.
4. Specimen dimensions, Figure A.10(b).



Fig. A.10: Measuring specimen dimensions

5. Whether the notch was cast or cut-in.
6. Test control method (stroke displacement or COD control) and displacement rate.
7. Description of the fracture surface, especially any unusual appearance or significant deviation from a vertical plane centered on the pre-notch tip.
8. Splitting force *vs.* average COD curve.
9. Work of fracture (W_F) and specific fracture energy (G_F).

A.6 Additional Illustrations

Technical drawings for the WST apparatus are shown in Figure A.11. Though the test method lends itself for core based specimens, should it be desirable to have a prismatic test specimen (due to possible anisotropy), Figure A.12 illustrates the process.

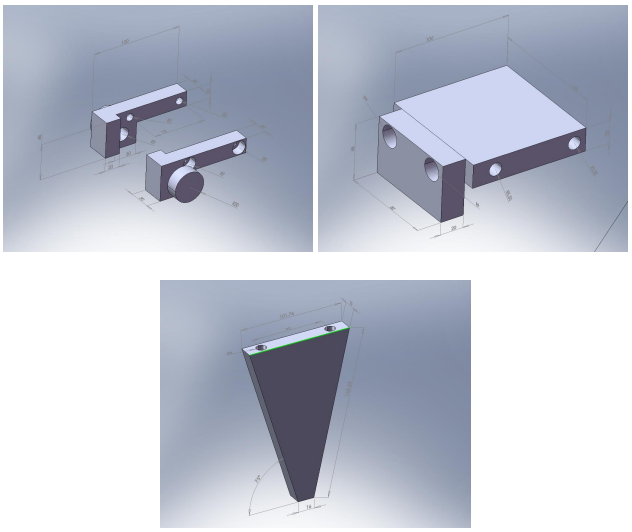

Fig. A.11: Wedge Splitting Test Parts dimensions

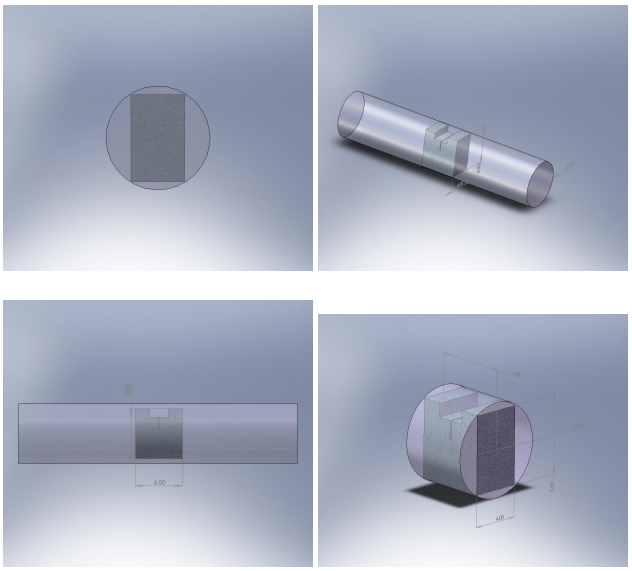

Fig. A.12: From cores to small prismatic specimens

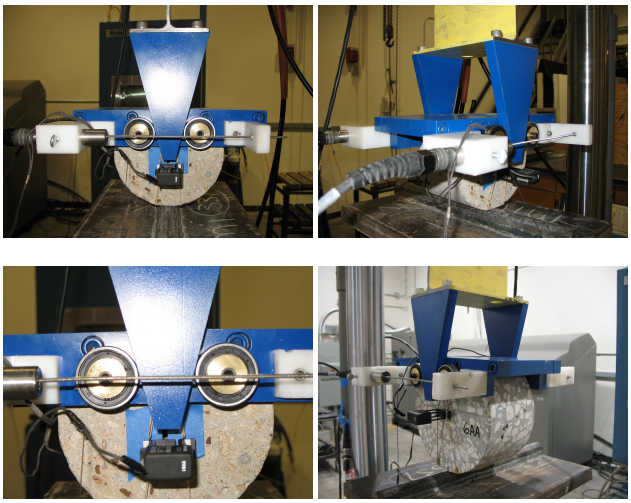

Fig. A.13: Details of the specimens

Appendix B
Computational Tools for Probabilistic Analyses

B.1 Motivation

The finite element (FE) based deterministic analyses need a series of programs:

- Pre-processor: The FE analysis requires the discretization of a structure into a mathematical representation. The discretized structure is then subjected to the governing differential equation with essential (displacement) and natural (traction) boundary conditions. KumoNoSu is a graphical front end to two programs, i.e. 1) T3D a mesh generator and 2) T3D2Merlin which enables definition of material, boundary conditions, and loads.
- Processor: The discretized structure subjected to the essential and natural boundary conditions is then transferred to the main processor (called Merlin) to be analyzed.
- Post-processor: Spider is a general purpose 3D post-processor for static and dynamic nonlinear FE analysis results. It is an OpenGL implementation under Windows.

Figure B.1 shows the interaction among the three programs and the input/output file(s) for each one. They can be summarized as:

- KumoNoSu uses: 1) `.bd` (includes all geometric information of model), 2)`.t3d` (includes all meshing information), and 3) `.ctrl` (includes material property, boundary condition, loads, analysis information), and generates `.inp` (includes all the nodes, elements, material, loads, boundary condition, analysis information) for processor (Merlin). The generated FE descritization can be saved in the form of `.eps`, `.jpeg`, and `.EMF`.
- Merlin uses `.inp` and generates: 1) `.out` (includes all the requested analysis results), 2) `.pst` (includes post-processing data for regular FE analysis), `.rtv` (includes post-processing data for Real Time View of a lengthy dynamic analysis), and 3) `.eig` (includes post-processing data to display the results of an eigenvalue analysis).
- Spider uses one of `.pst`, `.rtv`, or `.eig` and displays the results. Results can be saved in the form of `.eps`, `.jpeg`, and `.EMF`.

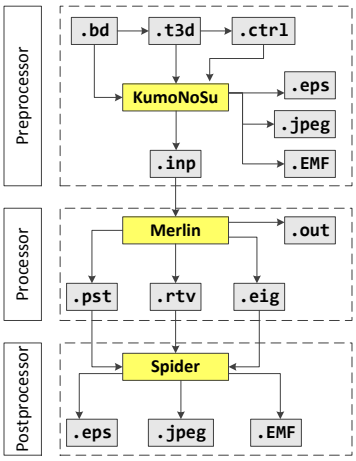

Fig. B.1: Interaction among KumoNoSu, Merlin and Spider

B.2 Probabilistic Performance Assessment of Structures

The group of programs in Figure B.1, are only able to perform a single deterministic analysis. This should be expanded to be used within the context of the probabilistic methods. For this purpose, the Matlab-based algorithm is developed, and is called PPACS (Probabilistic Performance Assessment of Concrete Structures). It includes many Matlab scripts and functions and facilitates the probabilistic assessment of structures. Figure B.2 shows the general algorithm of this program and interaction among different programs. This algorithm is applicable for any type of structure and any probabilistic model (load, material, time). Major steps and features are:

- Use KumoNoSu to build a initial finite element model based on information from the physical model. Hypothetical material property or load magnitude may be used in this step to develop a deterministic `test.inp`.
- The generated `test.inp` file is then broken to different sub-blocks, i.e. `Block-10.inp`, `Block-20.inp`, ...; each one includes specific information about the FE model (e.g. analysis type, nodes, elements, material, loads, boundary condition).
- `P0.m` is used to determine the user-defined input parameters for FE model. This includes: ground motions for dynamic analysis, material property and its distributional model for uncertainty quantification, time-dependent aging, etc.
- `P1.m` uses all input blocks (i.e. `Block-10.inp`, ...) and input data from `P0.m` (`Material.mat`, `GroundMotion.mat`, ...) to generate N new input files, `test-N.inp` which have the desired probabilistic model.
- `P2.m` runs the Merlin N times and generates N `test-N.pst` and `test-N.out` (if requested, `test-N.rtv` and `test-N.eig` also) files. Each of the N `test-N.pst` can be separately read by Spider and provide required graphical output.

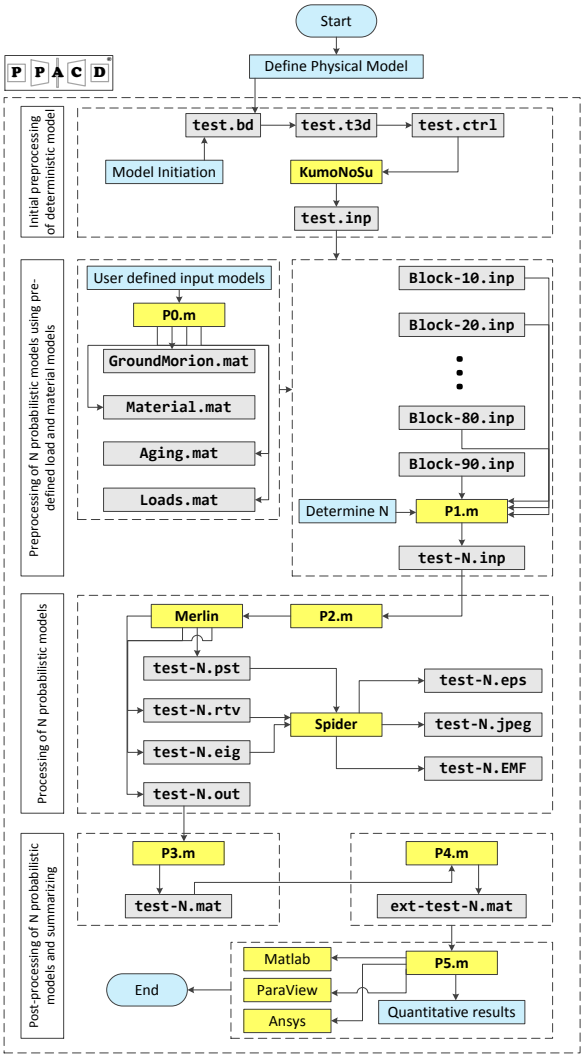

Fig. B.2: Interaction among different programs in Matlab-based code

- `P3.m` uses N `test-N.out` files (in the form of ASCII) and coverts them to `test-N.mat` files (in the form of Binary).
- `P4.m` further process the N `test-N.mat` files and generates N `ext-test-N.mat` files. This step includes process of the results for a specific structure, define the limit states, etc.
- `P5.m` uses the N `ext-test-N.mat` files and applies the probabilistic operations on them (e.g. different fractile, regression, probability of exceedance, ...). The

final results can be either represented quantitatively (tabulated or central values) or graphically. Currently, this program uses either 1) Maltab, 2) ParaView, or 3) Ansys to show the contour plots on the FE model.

B.3 Detailed Steps

Each of the general scripts, i.e. `P0.m` to `P5.m`, are explained in the context of PBEE.

B.3.1 `P0.m`

This script provides a set of appropriate ground motions to be used in dynamic analyses. The general steps and features are:

- Select the type of performance assessment: 1) intensity-based performance assessment (IBPA) assuming that the dam is subjected to a specific intensity of shaking (e.g. specific target response spectrum), 2) scenario-based performance assessment (SBPA) assuming that the dam is subjected to a specific $< R_{rup}, M_w >$ scenario (earthquake intensity is uncertain parameter), or 3) time-based performance assessment (TBPA) assuming the uncertainty in R_{rup}, M_w and the intensity of motion.
- Select between the real (recorded) ground motions and the synthetic one (which is suitable for dam sites where there are not enough recorded signals).
- In the case of real ground motions, either use the direct ground motion selection through PEER online tool, or use a set of Matlab codes developed by Baker research group. In both cases, the selected ground motions are saved in the form of `GMList.xlsx`. The same procedure should be performed for synthetic ground motions.
- The selected ground motions can be truncated (e.g. [5%, 95%] A_I, or [5%, 75%] A_I) using `GM_Truncat.m`.

B.3.2 `P1.m`

Figure B.4 shows different types of uncertainty analyses that can be performed. Three sources of uncertainty in performance assessment of structures are:

- Mechanical (material): For an existing containment vessel structure, this refers to uncertainty in determination of material property and also different random variables (RV) in the constitutive model.
- Hydrologic: Refers to uncertainty in pool elevation and should be quantified based on a hydrologic hazard curve.
- Seismic: Refers to record-to-record variability of the input ground motions and should be quantified based on a seismic hazard curve.
- Time: Refers to time-dependent degradation of the material, e.g. alkali-aggregate reaction and creep.

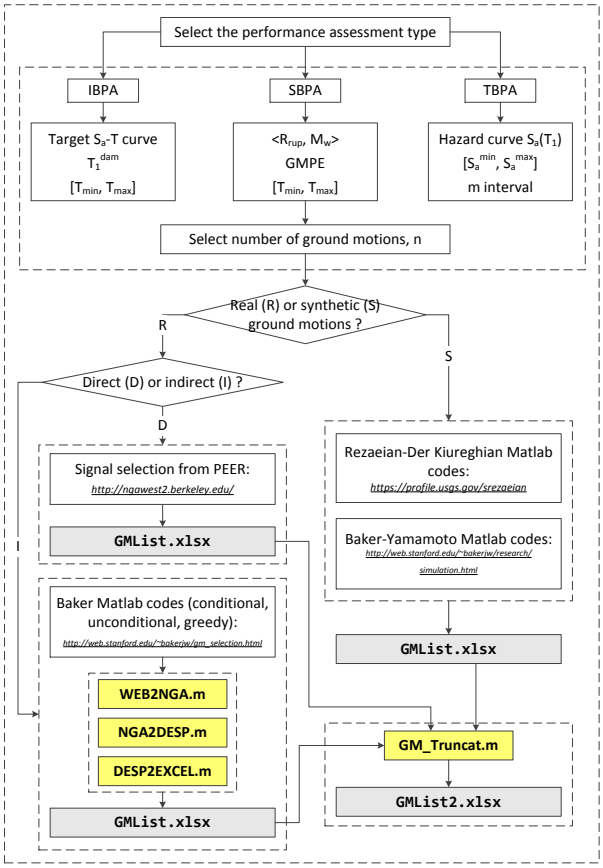

Fig. B.3: General algorithm in `P0.m`

First degree uncertainty refers to incorporating only one of the three sources. Subsequently, 2nd and 3rd degree uncertainty refer to the simultaneous effect of two or three uncertainty sources.

Seismic analysis is performed in two steps: 1) static analysis with all the body forces and hydrostatic forces and 2) through a "restart," a dynamic analysis is initiated from the preceding static one. Thus, two sets of `.inp` and `.out` files will be generated for each analysis. Hereafter, the static input file corresponds to N^{th} analysis and refers to `test-N_dyn1.inp` and the dynamic one refers to `test-N_dyn2.inp`.

Figure B.5 shows the general algorithm to generate input files for static analysis. Based on Figure B.2, the initially generated input file should break into different sub-blocks as:

- `Block-Sta-10.inp`: title and definition
- `Block-Sta-20.inp`: control block, includes number of increments, ...

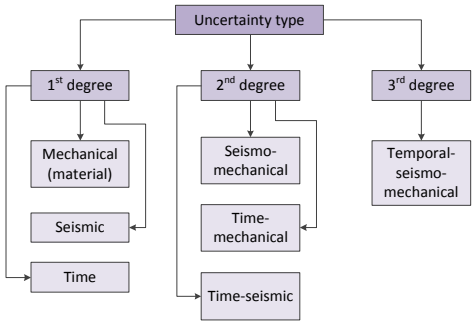

Fig. B.4: Different types of uncertainties in PPACS

- `Block-Sta-30.inp`: element group, includes element types and material property
- `Block-Sta-40.inp`: mesh group, includes nodal mass and damping, master/slave crack
- `Block-Sta-50.inp`: analysis control, includes iterations, error, ...
- `Block-Sta-60.inp`: body forces
- `Block-Sta-70.inp`: uplift model (if any)
- `Block-Sta-80.inp`: displacement boundary condition
- `Block-Sta-90.inp`: hydrostatic pressure (if any)

In Figure B.5, `RandomProperty.m` reads a user defined Excel file storing relevant data for the probabilistic based simulation and then generates N samples based on either crude Monte Carlo Simulation (MCS) or Latin Hypercube Sampling (LHS), Figure B.6.
In both cases the correlated or uncorrelated modes are possible, Figure B.7.
Sampling is based on a distributional model (e.g. normal, lognormal, etc.) predefined by the user for each RV. Moreover upper and lower bounds can be defined to truncate the distributional model.
Figure B.8(a) shows 500 samples for each of three RVs based on LHS. There is a weak correlation between Mat_1 and Mat_2 and also Mat_1 and Mat_3; however, the correlation is strong between Mat_2 and Mat_3. On the other hand, Figure B.8(b) shows an un-symmetric truncation of a normal distribution in the range [18, 38] GPa.
Figure B.9 shows the general algorithm to generate input files for dynamic analysis. Similar to static analysis, Figure B.9, there are nine blocks which define the `test-N_dyn2.inp`; however, some of them are empty in dynamic analysis (e.g. material, mesh) because they are already defined though the static input file. The user selects the type of dynamic analysis and a `Groundmotion.mat` file is generated which includes all the required seismic input with their specifications. Five types of analysis are:

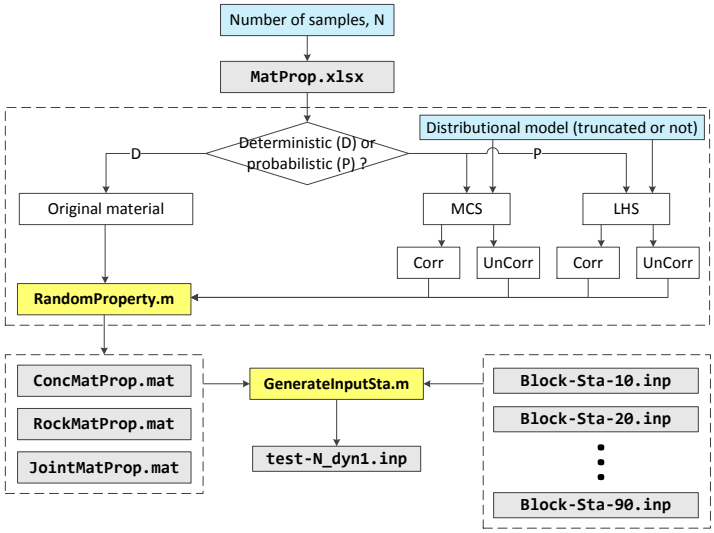

Fig. B.5: General algorithm in `P1Sta.m`

	NRV	RandType	Mean	COV	Activation	STD	BoundLimit	LowerB	UpperB	Property	Unit
Concrete	1	Normal	1	0.2	0	0	0.5	0	0	Thickness	m
Concrete	2	Normal	2.40E-06	0.05	0	0	0.5	0	0	Mass density	Gg/m^3
Concrete	3	Normal	9.90E-06	0.2	0	0	0.5	0	0	Coefficient of thermal expansion	1/C^o
Concrete	4	Normal	36,000	0.2	1	7,200	0.5	18,000	54,000	Elastic/Young's modulus	Pa
Concrete	5	Normal	0.2	0.2	0	0	0.5	0	0	Poisson's ratio	-
Concrete	6	Normal	0	0.2	0	0	0.5	0	0	Fracture toughness (LEFM)	
Concrete	7	Normal	0	0.2	0	0	0.5	0	0	Critical energy release rate (LEFM)	
Concrete	8	Normal	5,000,000	0.15	1	750,000	0.5	2,500,000	7,500,000	Tensile strength	Pa

(a) Concrete properties

	NRV	RandType	Mean	COV	Activation	STD	BoundLimit	LowerB	UpperB	Property	Unit
AAR	1	Normal	1	0.2	0	0	0.5	0	0	Model No.	-
AAR	2	Normal	0.005	0.2	1	0.001	0.5	0.0025	0.0075	Maximum volumetric strain	-
AAR	3	Normal	10.97	0.2	1	2.1932	0.5	5.483	16.449	Characteristic time	ATU
AAR	4	Normal	87.16	0.2	1	17.43	0.5	43.58	130.75	Latency time	ATU
AAR	5	Normal	5,400	0.2	0	0.0	0.5	0.0	0.0	Activation energy for char	^{o}K
AAR	6	Normal	9,400	0.2	0	0.0	0.5	0.0	0.0	Activation energy for lat	^{o}k
AAR	7	Normal	0.1	0.2	0	0.0	0.5	0.0	0.0	Residual red. Factor tension	-
AAR	8	Normal	0.8	0.2	0	0.0	0.5	0.0	0.0	Fraction of tension pre-AAR	-
AAR	9	Normal	-58.7	0.2	1	-11.74	0.5	-29.35	-88.05	Compressive strength	MPa
AAR	10	Normal	5.9	0.2	1	1.18	0.5	2.95	8.85	Tensile strength	MPa
AAR	11	Normal	-2.0	0.2	0	0	0.5	0	0	Shape factor for Gamma_c	-
AAR	12	Normal	10.1	0.2	1	2.02	0.5	5.05	15.15	Reference temperature test	^{o}C
AAR	13	Normal	-8.0	0.2	0	0.0	0.5	0.0	0.0	Upper comp. stress limit	MPa
AAR	14	Normal	0.69	0.2	1	0.138	0.5	0.345	1.035	Reduction factor Young	-
AAR	15	Normal	0.48	0.2	1	0.096	0.5	0.24	0.72	Reduction factor tensile	-

(b) AAR properties

Fig. B.6: User defined Excel file with distribution models, mean, standard deviation and L/U bounds.

- Single ground motion (SGM): only a single ground motion is used for the all N samples. If $N = 1$, this results to single deterministic analysis, and if N = "large number" this is either a sensitivity or material uncertainty assessment.
- Cloud analysis (CLA), Figure B.10(a): N (un-scaled) ground motions are applied to N samples. If all the samples have the same characteristics, this method

NRV	1	2	3	4	5	6	7	8	9	10	11	12	13	14	15
1	1														
2	0	1													
3	0	0	1												
4	0.2	0	0.5	1											
5	0	0	0	0	1										
6	0	0	0	0	0	1									
7	0	0	0	0	0	0	1								
8	0	0	0	0	0	0	0	1							
9	0.8	0	0	0.5	0	0	0	0	1						
10	0	0	0	0	0	0	0	0	0.8	1					
11	0	0.5	0	0	0	0	0	0	0	0	1				
12	0	0	0	0	0	0	0	0.1	0	0	0	1			
13	0.4	0	0	0	0.7	0	0	0	0	0	0	0	1		
14	0	0	0	0	0	0	0	0	0	0	0	0.4	0	1	
15	0	0	0	0	0	0	0	0	0	0.3	0	0	0	0.7	1

Fig. B.7: User defined Excel file with possible correlation coefficients.

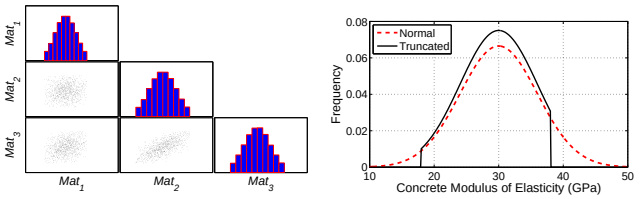

(a) Correlation among RVs (b) Unsymmetry truncation of normal distribution

Fig. B.8: Sampling the material properties based on algorithm in figure B.5

only shows the record-to-record variability. However, if samples are different, it accounts for epistemic uncertainty also.

- Endurance time analysis (ETA), Figure B.10(b): Only three samples are required for three acceleration functions.
- Multiple stripe analysis (MSA), Figure B.10(c): N ground motions are applied in m levels (n=N/m for each level).
- Incremental dynamic analysis (IDA), Figure B.10(d): N ground motions are incrementally scaled in N/n levels and applied to the dam.

B.3.3 `P2.m`

Having the $2N$ input files (static + dynamic), `P2Sta.m` and `P2Dyn.m` are executed, sensationally. They run the Merlin (main processor) 2N times and generate `test-N_dyn1.out` and `test-N_dyn2.out`. Note that `test-N_dyn1.out` is used as part of the input file for dynamic analysis.

B.3.4 `P3.m`

`P3Dyn.m` converts N `test-N_dyn2.out` ASCII files to `test-Dyn-N.mat` Binary files. `P3Dyn.m` is computationally expensive, especially for long duration ground motions with a small time step. It can be run on both PC and supercomputer (CU's

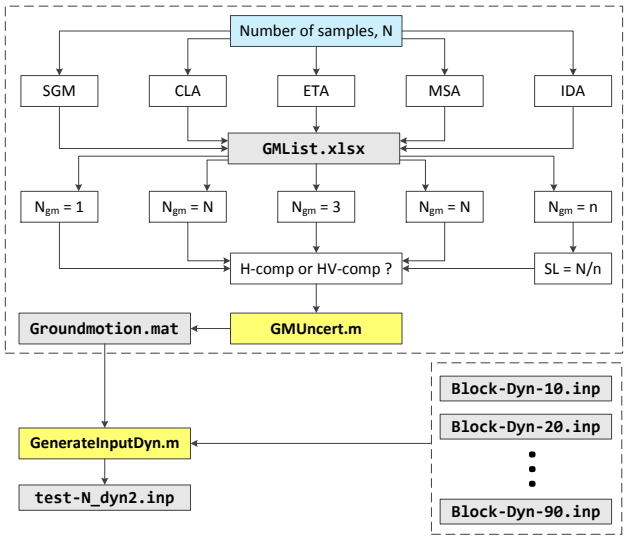

Fig. B.9: General algorithm in `P1Dyn.m`

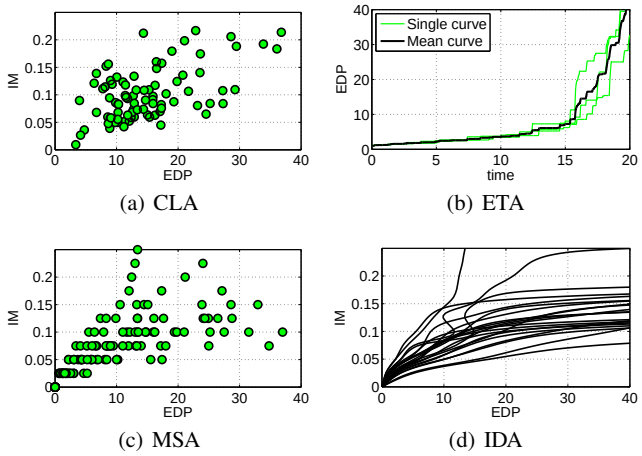

(a) CLA (b) ETA

(c) MSA (d) IDA

Fig. B.10: Different types of dynamic analysis methodologies in PPACS

184-teraflop Dell supercomputer called Janus is used for some of the analyses; it is currently ranked 164 among the world's top-500 supercomputer sites).

B.3.5 P4.m

P4Dyn.m processes the raw data from N test-Dyn-N.mat files and generates N ext-test-Dyn-N.mat files. In the context of PBEE, two major sets of post-processing are required: 1) processing the ground motion intensity measures (IM) and 2) processing the engineering demand parameter (EDP). Figure B.11 shows the seven category of IMs that are computed for any ground motion in P4Dyn.m. For each category, there are several individual IMs that will be explained later.

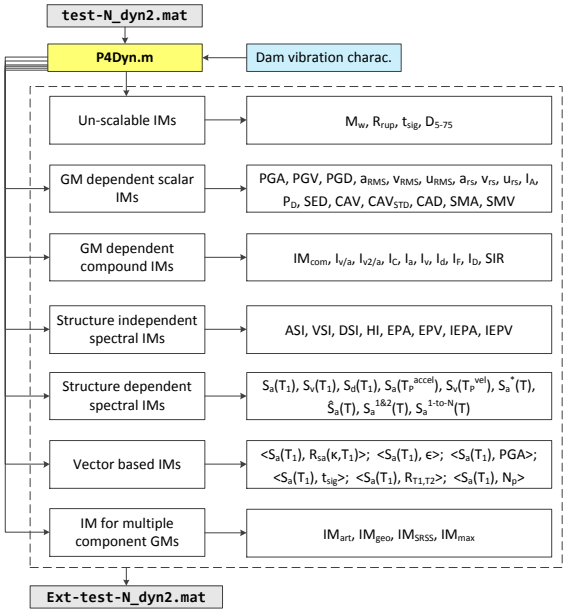

Fig. B.11: Treatment of IMs in P4.m

B.3.6 P5.m

P5.m uses N ext-test-Dyn-N.mat files and applies the probabilistic operations which depends on the type of analysis:

- CLA:
  - Determination of histograms and best fit to IM parameters
  - Determination of optimal IM in terms of efficiency, sufficiency, proficiency, and practicality
  - Determination of optimal vector IM
  - Determination of fragility curves and surfaces

- IDA:
  - Determination of capacity curves
  - Summary of capacity curve into central values and fractiles
  - Determination of optimal IM parameter
  - Determination of fragility curves